

CONNECTIONS VIII

8th
International Workshop on
Connections in
Steel Structures



Northeastern University
Civil and Environmental Engineering

MAY 24–26, 2016

CONNECTIONS IN STEEL STRUCTURES
VIII

Proceedings of the Eighth International Workshop

held at

Hilton Boston Back Bay Hotel
Boston, Massachusetts, USA
May 24–26, 2016

Edited by

Charles J. Carter
Jerome F. Hajjar

© AISC 2016

by

American Institute of Steel Construction

All rights reserved. This book or any part thereof must not be reproduced in any form without the written permission of the publisher.

The AISC logo is a registered trademark of AISC.

ISBN 978-1-56424-019-4

The information presented in this publication has been prepared following recognized principles of design and construction. While it is believed to be accurate, this information should not be used or relied upon for any specific application without competent professional examination and verification of its accuracy, suitability and applicability by a licensed engineer or architect. The publication of this information is not a representation or warranty on the part of the American Institute of Steel Construction, its officers, agents, employees or committee members, or of any other person named herein, that this information is suitable for any general or particular use, or of freedom from infringement of any patent or patents. All representations or warranties, express or implied, other than as stated above, are specifically disclaimed. Anyone making use of the information presented in this publication assumes all liability arising from such use.

Caution must be exercised when relying upon standards and guidelines developed by other bodies and incorporated by reference herein since such material may be modified or amended from time to time subsequent to the printing of this edition. The American Institute of Steel Construction bears no responsibility for such material other than to refer to it and incorporate it by reference at the time of the initial publication of this edition.

Printed in the United States of America

FOREWORD

This book presents the proceedings of the 8th International Workshop on Connections in Steel Structures. The workshop was held at the Hilton Back Bay Hotel in Boston, Massachusetts, USA during the period 24-26 May, 2016 under the auspices of the American Institute of Steel Construction and the European Convention for Constructional Steelwork.

The seven preceding international workshops were held in Cachan, France, in 1987; Pittsburgh, Pennsylvania, USA in 1991; Trento, Italy, in 1995; Roanoke, Virginia, USA, in 2000; in Amsterdam, The Netherlands, in 2004; in Chicago, Illinois, USA in 2008; and in Timisoara, Romania in 2012. Proceedings for these workshops are available by searching for “Connections” in AISC’s “Education Archives” at www.aisc.org/continuinged.

The American Institute of Steel Construction (AISC) and the European Convention for Constructional Steel (ECCS) have supported the holding of these workshops, thus making them possible. Financial support for the 8th Workshop was provided by the American Institute of Steel Construction and Northeastern University.

The American Institute of Steel Construction and Northeastern University were the official hosts of this workshop. Outstanding work by the staff of both AISC and Northeastern University made the workshop possible. The contributions of Janet Cummins, Madeja Metcalf, Sadie Brown, Eric Martin, Victoria Cservenyak, and Keith Grubb of AISC and Mariah Nobrega, Joe Hebert, Carolina Venegas, Megan Kleber, and Arianna Kaplan of Northeastern University are gratefully acknowledged. In addition, the participation of the individuals who served as session chairs contributed significantly to the smooth running of all three days of the workshop.

Finally, the support and technical contributions of the 70 participants from 20 countries who presented 64 technical papers must be acknowledged. Without their commitment to research, design, and construction of structural steel connections worldwide, none of this would have been possible. It is expected that the continued commitment of these participants and others to come in the future, will result in another successful workshop in Coimbra, Portugal in 2020.

Charles Carter
Jerome Hajjar
Reidar Bjorhovde

September 2016

**The 8th International Workshop on
Connections in Steel Structures**

was sponsored by

American Institute of Steel Construction, Chicago, Illinois, USA

European Convention for Constructional Steelwork, Brussels, Belgium

Northeastern University, Boston, Massachusetts, USA

CONTENTS

Technical Opening of Workshop

- Keynote Lecture: The Evolution of Steel Construction and the Role of the Syntheses of Research, 1963-2016 (lecture only)**.....no paper
Lawrence A. Kloiber, LeJeune Steel Company, Minneapolis, MN, USA

Design of Steel Connections

- Chapter J and K of the AISC Specification: A Move away from Prescriptive Requirements**..... 1
Larry S. Muir, AISC, Atlanta, GA, USA
- Upcoming Changes to AISC 341 – Seismic Provisions for Structural Steel Buildings** 11
James O. Malley, Degenkolb Engineers, San Francisco, CA, USA; Leigh Arber, AISC, Chicago, IL, USA
- Current Status of ISO/DS 17607 (lecture only)**.....no paper
Bjørn Aasen, Norconsult AS, Sandvika, Norway
- Pre-Engineered Standardized Industry Structural Steelwork Connections - A New Zealand Perspective**..... 19
Kevin A. Cowie, Steel Construction New Zealand Inc., Auckland, New Zealand
- An Engineering Approach to the Evaluation of the Transformation Parameter β** 33
Ana M. Girão Coelho, Newcastle University, Newcastle upon Tyne, UK
- Detailing Connections – An Integrated Approach from Inception to Fabrication**..... 45
Preetam Biswas and Georgi I. Petrov, Skidmore, Owings and Merrill, LLP, New York, NY, USA; Ronald B. Johnson, Skidmore, Owings and Merrill, LLP, Chicago, IL, USA

Bolt Behavior in Steel Connections

- Recent Investigations into the Slip Factor of Slip-Resistant Connections**57
Natalie Stranghöner, Nariman Afzali and Jörn Berg, University of Duisburg-Essen, Essen, Germany; Peter de Vries, Delft University of Technology, Delft, the Netherlands
- Deformation Capacity, Stiffness and Bearing Strength at Bolt Holes**..... 69
Primož Može, University of Ljubljana, Ljubljana, Slovenia
- Injection Bolts Update on Research and Applications**..... 79
A.M. (Nol) Gresnigt and Peter de Vries, Delft University of Technology, Delft, the Netherlands

CONTENTS (cont'd.)

Behavior of Single-Bolted Lap-Splice Joints at Elevated Temperatures.....	91
<i>Erica C. Fischer, Degenkolb Engineers, Seattle, WA, USA; Amit H. Varma, Purdue University, West Lafayette, IN, USA; Qiaqia Zhu, KPFF Consulting Engineers, Seattle, WA, USA</i>	
The Behavior of Double-Lap Splice Bolted Steel Connections with Fiber-Reinforced Polymer Fills.....	101
<i>Kara D. Peterman, Julieta Moradei and Jerome F. Hajjar, Northeastern University, Boston, MA, USA; James D'Aloisio, Klepper Hahn and Hyatt, East Syracuse, NY, USA; Mark Webster, Simpson Gumpertz and Heger, Waltham, MA, USA</i>	
Structural Safety Check for Products Made of Cast Steel.....	111
<i>Max Spannaus, Thomas Ummenhofer and Peter Knöedel, KIT Steel & Lightweight Structures, Karlsruhe, Germany</i>	
Analysis of Steel Connections	
Single Lap Friction Connection in Tubular Sections.....	123
<i>Milan Veljkovic and Marko Pavlovic, Delft University of Technology, Delft, the Netherlands; Carlos Rebelo and Luís Simões da Silva, University of Coimbra, Coimbra, Portugal</i>	
Energy Dissipation in Centric Bolted Gusset Plate of Braces	133
<i>Maël Couchaux, INSA of Rennes, Rennes, France; Pierre O. Martin, CTICM, Saint-Aubin, France; Xavier Thollard, Tractebel, Gennevilliers, France; Philippe Rivillon, CSTB, Champs-Sur-Marne, France</i>	
Generally Loaded Connections by Component Based Finite Element Method.....	143
<i>František Wald, Lukáš Gödrich and Marta Kurejková, Czech Technical University in Prague, Prague, Czech Republic; Luboš Šabatka, Drahoš Kolaja and Jaromír Kabeláč, IDEA RS, Brno, Czech Republic; Miroslav Bajer, Martin Vild and Josef Holomek, Brno University of Technology, Brno, Czech Republic</i>	
Implementation of a Component Model for the Cyclic Behavior of Steel Joints	153
<i>Luís Simões da Silva, Ashkan Shahbazian, Filippo Gentili and Hugo Augusto, University of Coimbra, Coimbra, Portugal</i>	
Approach to Macro-Modeling of 3D Tubular Column-to-Beam Joint: An Extension of Component Method for Joint Modeling.....	163
<i>Yukihiro Harada, Chiba University, Chiba, Japan, and Luís Simões da Silva, University of Coimbra, Coimbra, Portugal</i>	
Moment-Rotation Behaviour of Bolted Moment End-Plate Connections.....	173
<i>Chen Zhu, Kim J. R. Rasmussen and Hao Zhang, University of Sydney, Sydney, Australia</i>	

CONTENTS (cont'd.)

- A Numerical Study on the Influence of Skew and Slope on RBS
and WUF-W Connections205
*Kevin E. Wilson, Structural Affiliates International Inc., Nashville, TN, USA; Gian A.
Rassati and James A. Swanson, University of Cincinnati, Cincinnati, OH, USA*

Braced Frame Steel Connections

- Establishing and Developing the Weak-Axis Strength of Plates
Subjected to Applied Loads215
*Charles J. Carter, AISC, Chicago, IL, USA; Larry S. Muir, AISC, Roswell, GA, USA; Bo
Dowsell, ARC International, LLC, Birmingham, AL, USA*
- Behavior, Testing and Modeling of Beam-Column Angle Connections.....225
*Thierry Béland and Robert Tremblay, École Polytechnique de Montréal, Montréal,
Québec, Canada; Joshua G. Sizemore and Larry A. Fahnestock, University of Illinois at
Urbana-Champaign, Urbana, IL, USA; Cameron R. Bradley, Tufts University, Medford,
MA, USA; Eric M. Hines, LeMessurier Consultants, Boston, MA, USA*
- Synchronizing Beam and Brace Connection Design in Chevron Braced
Frame Systems.....235
Patrick J. Fortney, Cives Engineering Corporation, Roswell, GA, USA
- Effect of Gusset Plate Connections on Seismic Performance of
Concentrically Braced Frames.....245
*Charles W. Roeder, Dawn E. Lehman, Jeffrey Berman and Andrew Sen, University of
Washington, Seattle, WA, USA*
- Seismic Design of Brace Connections for Steel Concentrically Braced
Frames of the Conventional Construction Category.....255
*Sophie Decaen, Ali Davaran, Robert Tremblay and Alexandre Gélinas, École
Polytechnique de Montréal, Montréal, Québec, Canada*
- Cyclic Behavior of Composite Beam, Column, and Gusset Plate
Connection under Multiple Loads from Frame and Damper Actions265
*Kazuhiko Kasai, Tokyo Institute of Technology, Yokohama, Japan; Yoriyuki Matsuda,
Tokyo University of Science, Chiba, Japan*
- Performance of Weld-Retrofit Beam-to-Column Shear Tab Connections.....275
*Colin A. Rogers, Matthew Marosi and Jacob Hertz, McGill University, Montréal, Québec,
Canada; Dimitrios Lignos, École Polytechnique Fédérale de Lausanne, Lausanne,
Switzerland; Robert Tremblay and Marco D'Aronco, École Polytechnique de Montréal,
Montréal, Québec, Canada*

CONTENTS (cont'd.)

Tubular Steel Connections

- Surrogate Modeling for Rotational Stiffness of Welded Tubular Y-Joints285
Markku Heinisuo, Timo Jokinen, Teemu Tiainen and Kristo Mela, Tampere University of Technology, Tampere, Finland; Marsel Garifullin, Peter the Great St. Petersburg Polytechnic University, St. Petersburg, Russia
- Experimental Evaluation of the Directional Strength-Enhancement Factor for Fillet Welds to CHS.....295
Kyle Tousignant and Jeffrey A. Packer, University of Toronto, Toronto, Ontario, Canada
- Load Bearing Capacity of Adhesively Bonded Tubular Steel Joints305
Matthias Albiez and Thomas Ummenhofer, KIT Steel & Lightweight Structures, Karlsruhe, Germany
- The Connection Conundrum: An Industry in Transition..... 317
Lawrence Griffis, Walter P Moore and Associates, Inc., Austin, TX, USA
- Performance-Based Design and the Load-Deformation of Welded Tubular Connections in Offshore Jacket Structures 327
Kai Wei, Andrew T. Myers, Jerome F. Hajjar and Matthew A. Spencer, Northeastern University, Boston, MA, USA; Sanjay R. Arwade, University of Massachusetts Amherst, Amherst, MA, USA

Bolted Steel Connections

- Fracture Characteristic of Bolted Connections under Block Shear 337
Hussam N. Mahmoud and Huajie Wen, Colorado State University, Fort Collins, CO, USA
- Load-Bearing Capacity of H-Shaped Beam to RHS Column Connections Using Blind Bolts 347
Guo-Qiang Li, Lian Duan, Jiehua Zhang and Jian Jiang, Tongji University, Shanghai, China
- Experimental Investigation of High Capacity End Plate Moment Connections363
Matthew R. Eatherton and Thomas M. Murray, Virginia Tech, Blacksburg, VA, USA; Nonish Jain, Walter P Moore, Washington D.C., USA
- Progress in the Characterization of Three-Dimensional Semi-Rigid Steel Connections 373
Eduardo Bayo, Beatriz Gil, Rufino Goñi and Javier Gracia, University of Navarra, Navarra, Spain
- Finite Element Simulation and Assessment of the Strength of Riveted and Bolted Gusset-Plate Connections in Steel Truss Bridges.....383
Donald W. White, Georgia Institute of Technology, Atlanta, GA, USA; Y. D. Kim, Texas A&M University – Commerce, Commerce, TX, USA; Yavuz Menten, MMI Engineering, Houston, TX, USA; Roberto T. Leon, Virginia Tech, Blacksburg, VA, USA

CONTENTS (cont'd.)

Application of Weathering Steel in Bridges.....	393
<i>Dieter Ungermann, Dennis Rademacher and Annika Peters, TU Dortmund University, Dortmund, Germany; Susanne Friedrich and Peter Lebelt, Institut für Korrosionsschutz Dresden GmbH (Institute for Corrosion Protection), Dresden, Germany</i>	
Structural Integrity of Steel Connections	
T-Stub Joint Component Subjected to Impact Loading.....	403
<i>João Ribeiro and Aldina Santiago, University of Coimbra, Coimbra, Portugal; Constança Rigueiro, Polytechnic Institute of Castelo Branco, Castelo Branco, Portugal</i>	
Deformation Limits and Rotational Capacities for Connections under Column Loss.....	413
<i>Jonathan M. Weigand and Joseph A. Main, National Institute of Standards and Technology, Gaithersburg, MD, USA</i>	
Enhanced Connections for Improved Robustness of Steel Gravity Frames	423
<i>Jonathan M. Weigand and Joseph A. Main, National Institute of Standards and Technology, Gaithersburg, MD, USA</i>	
Steel Gravity Connections Subjected to Large Rotations and Axial Loads.....	433
<i>Jonathan M. Weigand, National Institute of Standards and Technology, Gaithersburg, MD, USA; Jeffrey W. Berman, University of Washington, Seattle, WA, USA</i>	
Modeling of Double-Angle Connections for Robustness Evaluation of Steel Gravity Frames	443
<i>Jonathan M. Weigand and Joseph A. Main, National Institute of Standards and Technology, Gaithersburg, MD, USA; Judy Liu, Oregon State University, Corvallis, OR, USA</i>	
Estimating Collapse Capacity of Steel Moment Connections Subjected to Column Removal.....	453
<i>Ramon Gilsanz and Akbar Mahvashmohammadi, Gilsanz Murray Steficek, New York, NY, USA; John Abruzzo, Thornton Tomasetti, San Francisco, CA, USA</i>	
Experimental Investigations of Composite Joints and their Behaviour during the Loss of a Column	465
<i>Nadine Hoffmann and Ulrike Kuhlmann, University of Stuttgart, Stuttgart, Germany</i>	
Experimental Research on the Behavior of Steel Moment Frame Connections under Column Loss Scenario	475
<i>Florea Dinu, Ioan Marginean, Dan Dubina and Andreea Sigauan, Politehnica University Timisoara, Timisoara, Romania; Ioan Petran, Technical University of Cluj-Napoca, Cluj-Napoca, Romania</i>	

CONTENTS (cont'd.)

Robustness of WUF-B Moment Connections in Steel Frame after Column Removal	487
<i>Yiyi Chen, Wei Wang and Ling Li, Tongji University, Shanghai, China</i>	

Composite Steel/Concrete Connections

Characterization of Load Paths in Composite Steel Deck Diaphragms and Collectors.....	497
<i>Robert B. Fleischman, Anshul Agarwal, Alexander T. Walsh and Luis F. Valdez, University of Arizona, Tucson, AZ, USA</i>	
Effect of Composite Beam Action on the Hysteretic Behavior of Fully-Restrained Beam-to-Column Connections under Cyclic Loading	507
<i>Dimitrios Lignos, Swiss Federal Institute of Technology, Zürich, Switzerland, and Ahmed Elkady, McGill University, Montréal, Québec, Canada</i>	
State-of-the-Art Report on Connections for Composite Special Moment Frames (C-SMF)	517
<i>Zhichao Lai and Amit H. Varma, Purdue University, West Lafayette, IN, USA</i>	
Seismic Performance and Design of CFST Column to Steel Beam Connections	527
<i>Wei Li and Lin-Hai Han, Tsinghua University, Beijing, China</i>	
Modeling of Innovative Re-Centering Connections for Circular CFT Columns.....	537
<i>Y. Gao, HOK, New York, NY, USA; Roberto T. Leon, Virginia Tech, Blacksburg, VA, USA</i>	
Self-Centering Beam-Column Connections Using Large Size Superelastic SMA Bars.....	547
<i>Wei Wang, Jia Liu, Cheng Fang and Yiyi Chen, Tongji University, Shanghai, China</i>	

Seismic Design for Steel Connections 1

Seismic Behaviour of Moment Resisting Frames with Dissipative Double Split Tee Joints.....	557
<i>Massimo Latour, Vincenzo Piluso and Gianvittorio Rizzano, University of Salerno, Fisciano, Italy</i>	
Prequalification Tests on Bolted Beam-to-Column Joints with Haunches.....	569
<i>Aurel Stratan, Cosmin Maris, Cristian Vulcu, Dan Dubina and Calin Neagu, Politehnica University of Timisoara, Timisoara, Romania</i>	
European Qualification of Seismic Resistant Steel Bolted Beam-to-Column Joints: the Equaljoints Project.....	579
<i>Raffaele Landolfo, University of Naples Federico II, Naples, Italy</i>	

CONTENTS (cont'd.)

T-Stub Response and Loading Rate	589
<i>Nadia Baldassino, Martina Bernardi and Riccardo Zandonini, Università degli Studi di Trento, Trento, Italy</i>	
Built-up T-Stub Moment Connection	599
<i>Ricardo Herrera, Juan F. Beltrán, Claudio Alarcón and Constanza Salas, University of Chile, Santiago, Chile</i>	
Innovative Tube-Based Moment Connections for Seismic Applications.....	609
<i>Jason McCormick and Dan Wei, University of Michigan, Ann Arbor, MI, USA</i>	
Experimental Analysis and Design of Friction Joints Equipped with Sprayed Aluminum Dampers	619
<i>Massimo Latour, Vincenzo Piluso and Gianvittorio Rizzano, University of Salerno, Fisciano, Italy</i>	

Seismic Design for Steel Connections 2

The Seismic Response of Embedded Column Bases— Tests and Strength Model	631
<i>Amit Kanvinde, University of California, Davis, CA, USA; David Grilli, Wiss Janney Elstner Associates, Inc., Emeryville, CA, USA</i>	
The Influence of Gravity Framing on the Performance of Steel Buildings Subjected to Seismic Loads.....	641
<i>John P. Judd, University of Wyoming, Laramie, WY, USA; Finley A. Charney, Virginia Tech, Blacksburg, VA, USA; Francisco X. Flores, University of Cuenca, Cuenca, Ecuador</i>	
High Strength Steels in Seismic Resistant Building Frames: Innovative Solutions for Beam-to-Column Joints.....	651
<i>Dan Dubina, Cristian Vulcu and Aurel Stratan, Politehnica University of Timisoara, Timisoara, Romania</i>	
Seismic Collapse Study of a Self-Centering Steel Moment Resisting Frame System.....	663
<i>James M. Ricles, Richard Sause and Omid Ahmadi, Lehigh University, Bethlehem, PA, USA</i>	
Self-Centering Steel Plate Shear Walls with Newz-Breakss Post-Tensioned Rocking Connection	673
<i>Daniel M. Dowden and Michel Bruneau, University at Buffalo, Buffalo, NY, USA</i>	

Workshop Participants.....	683
----------------------------	-----

Author Index	685
--------------------	-----

CHAPTER J AND K OF THE AISC SPECIFICATION: A MOVE AWAY FROM PRESCRIPTIVE REQUIREMENTS

Larry S. Muir
American Institute of Steel Construction, Atlanta, Georgia 30340, USA
muir@aisc.org

ABSTRACT

This paper discusses the ways in which AISC has moved away from, or tried to avoid further, prescriptive requirements related to connection design in Chapters J and K of the 2016 AISC *Specification for Structural Steel Buildings*. Items discussed include changes to the application of the directional strength increase for fillet welds, the design provisions for bolted joints, the application of the existing *Specification* provisions for concentrated forces to members other than wide-flange sections, and the design of rectangular HSS connections.

INTRODUCTION

The committees tasked with writing our codes must balance many considerations. Safety is of course paramount. Other considerations are usability, transparency, simplicity, economy, and technical purity. Over the last 9 decades the AISC *Standard Specification for Structural Steel for Buildings* (hereafter referred to as the *Specification*) has evolved.

One significant change is immediately obvious. The *Specification* has grown. The *Specification* published in 1923 consisted of 12 pages including the title page and introductory material. By 1989 Chapter J, addressing connection design, spanned 18 pages. Chapter J of the 2010 *Specification* contains 35 pages. Combined Chapters J and K, addressing connections to hollow structural sections, consist of 58 pages – nearly five times the page count of the entire 1923 specification.

Some of this growth in page count can be attributed to an increase in materials and processes addressed in the *Specification*. The first mention of welding appeared in 1941. High-strength bolts were introduced in 1963. Hollow structural sections were more formally addressed in 1997. Each of these obviously required new or amended provisions. In some cases they also led to an increase in the limit states that must be considered. For examples, riveted connections possessed relatively low strength and for a majority of the conditions only the number of rivets required had to be calculated, and the geometry required to accommodate the rivets in the joint precluded many possible failure modes. However, as the design strength of bolts was increased, other limit states were discovered and had to be considered.

The author believes that some of the growth has occurred due to misguided and sometime counter-productive attempts to improve usability and simplicity, often at the expense of transparency. In the process of updating Chapters J and K of the 2016 *Specification* an attempt was made to reduce the frequency of prescriptive requirements appearing in these chapters. Additional guidance was provided in Commentary and the *Manual* to aid users in applying the provisions and to provide transparency.

BEARING AT BOLT HOLES AT EDGE BOLTS

Prior to the 1999 *Specification* prescriptive edge distances were provided. It was generally assumed that for edge distances in excess of these values edge bearing or bolt tear-out through the edge was not a concern. The strength of a bolt group was the minimum of the bolt strength based on either shear rupture of the bolt or bearing of the plies multiplied by the number of bolts in the group. Since the bearing strength was independent of the spacing or the edge distance, the design strength for each bolt was the same.

The 1999 *Specification* introduced an explicit edge bearing/bolt tear-out check in the form of $1.2L_c t F_u$, Where L_c is the clear distance, t is the thickness of the ply, and F_u is the tensile strength of the ply. Since the edge distance required to ensure the historical bearing limit state, $2.4dt F_u$, governs is larger than the edge distances that were historically prescribed, this edge bearing condition often governs. Between 1999 and 2010 the *Specification* indicated that the bearing resistance of the group was as the sum of the bearing resistances of the individual bolts.

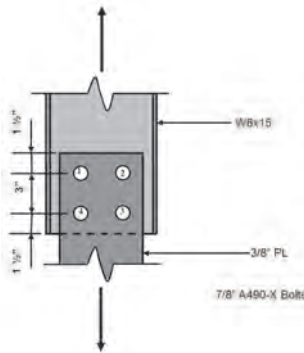


Figure 1 – Bolted Connection

It was theorized that in some unusual cases considering bearing and bolt shear separately could significantly over-estimate the strength of the bolted connection. The 2010 *Specification* therefore included a User Note stating, “The force that can be resisted by a snug-tightened or pretensioned high-strength bolt or threaded part may be limited by the bearing strength at the bolt hole per Section J3.10. The effective strength of an individual fastener may be taken as the lesser of the fastener shear strength per

Section J3.6 or the bearing strength at the bolt hole per Section J3.10. The strength of the bolt group is taken as the sum of the effective strengths of the individual fasteners.”

The difference between the two models can be seen in the analysis of the connection in Figure 1. If bearing on each of the plies is taken as the minimum of $1.2L_c t F_u$ or $2.4dtF_u$, the predicted strength of the connection is 79.6 kips. The model suggested by the User Note predicts a strength of 69.8 kips. This is about a 14% difference. The pre-1999 model, neglecting the effect of the edge distance, predicts a strength of 100 kips. It must be recognized that none of the models are exact. The Commentary to the 2016 *Specification* explicitly recognizes this fact and states, “The group strength is a function of strain compatibility dependent on the relative stiffness of the bolts and connected parts. For typical connections such as shear connections shown in Part 10 of the Steel Construction Manual, the lowest of the limit strengths applied to the group is a satisfactory approximation. For groups outside the range shown in Part 10 of the Manual the sum of the effective strengths of the individual fasteners should be evaluated unless more exact methods are used.”

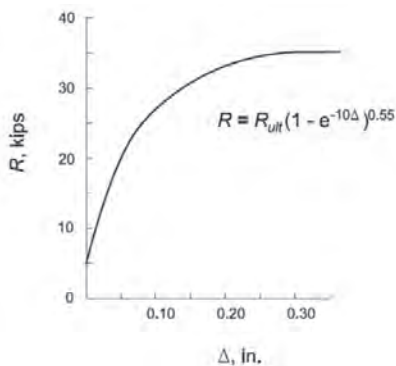


Figure 2 - Load-deformation relationship of a bolt loaded in shear (AISC 2010b)

The model described in the User Note is rational and believed by the committee to provide a lower bound estimate of the connection strength for most practical conditions. However, it may be possible to define a condition for which the model is not safe. Figure 2 shows the behavior of a single bolt in shear that is assumed in the instantaneous center of rotation method as implemented in the AISC *Manual*. The load-deformation relationship is based on empirical data for $\frac{3}{4}$ in.-diameter ASTM A325 bolts in double shear. The reported 0.34 in. deformation is the total deformation of the bolt and the plies. For joints where one of the bolts has a very small edge distance, the full strength of the other bolts may be limited based on the deformation that can occur before the edge bolt is lost. This sort of interaction based solely on the geometry of the joint is not accounted for in the User Note model. Edge distances of this magnitude would be rare in practice, but are not explicitly prohibited under the *Specification*.

Committees can neither anticipate nor account for every conceivable condition.

FILLET WELD STRENGTH

For more than half a century engineers have known that a fillet weld loaded transverse to its longitudinal axis is considerably stronger than a fillet weld loaded parallel to its longitudinal axis. However consideration of this fact was not included in the AISC *Specification* until the 1993 *Specification*. It is impossible to know with certainty why this decision was delayed for so long, but it is likely that simplicity and conservatism were favored over economy and technical purity. Even when the directional strength increase was permitted, the procedure to do so was placed in an Appendix. Another 12 years passed before it made its way out of the Appendix and into Chapter J. Even at this point it continued to evolve as the Committee realized the impact of the decision.

Appendix J of the 1993 *Specification* seemed to allow two different options. The first option calculated the strength of a fillet weld as $F_w = 0.60F_{EXX}(1.0 + 0.50 \sin^{1.5}\theta)$. The second utilized the “instantaneous center of rotation method to maintain deformation compatibility and non-linear load deformation behavior of variable angle loaded welds”. The description of the method was followed by three-quarters of a page of equations that are indecipherable without referencing the AISC Manual of *Steel Construction*, which essentially repeated the same information with an accompanying discussion. Despite the fact that two seemingly independent provisions were provided, the first provision was simply a subset of the second where deformation compatibility is inherent.

The 2005 *Specification* included four options:

1. Neglect the directional strength increase with no consideration of compatibility.
2. A provision for a “linear weld group loaded in-plane through the center of gravity”.
3. The “instantaneous center of rotation method”.
4. A provision for “fillet weld groups concentrically loaded and consisting of elements that are oriented both longitudinally and transversely to the direction of applied load, the combined strength” that provided the results of option 2 for the condition considered.

The 2010 *Specification* clarified that the simplifications, options 2 and 4, only applied to groups with uniform leg size, since this fact had been previously overlooked, another illustration of the difficulty of anticipating every possible configuration.

It is also interesting to note that while a special case was added to address a common condition, a critical consideration, deformation compatibility, was no longer even mentioned. Over time the provision had shifted from explicitly being a method to

achieve certain performance criteria to seemingly a set of equations into which values are to be plugged in order to get an answer.

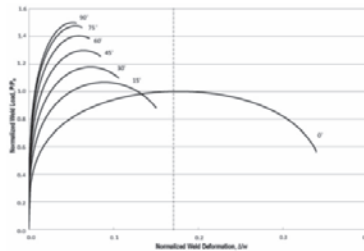


Figure 3 - Load-deformation relationship of fillet welds (AISC 2010b)

Figure 3 shows the behavior of welds that is assumed in the instantaneous center of rotation method as implemented in the *AISC Manual*. The method described in the *Manual* essentially determines a critical element and then calculates the available strength of the other elements assuming that the deformation, and therefore the strength, of each weld element varies linearly with the distance from the instantaneous center. The limiting deformation assumed in the *Manual* procedure is the ultimate deformation obtained at the predicted rupture strength of the critical weld element. However, it has been pointed out that due to the arching shape of the load-deformation curves for some conditions a larger strength can be predicted for the group, if the deformation and strength of the critical element is assumed to be something less than the ultimate. The *Specification* should not prohibit, or even discourage, such rational models.

It is also not uncommon for users to believe that the *Specification* requires the use of the inelastic, instantaneous center of rotation method and/or its simplifications. The AISC Steel Solutions Center, which provides technical support for the users of the AISC *Specification* and other standards, has had reports of engineers and authorities having jurisdiction (building officials) rejecting the use of elastic models, since they are not explicitly addressed in the *Specification* - despite the fact that an elastic model will predict a strength that is significantly lower than the instantaneous center of rotation method presented in the *Manual*.

The Steel Solutions Center has also received comments from engineers questioning the perceived requirements based on technical grounds. For instance the model underlying *Specification* equation J2-10b, $0.85 R_{nw} + 1.5 R_{nwt}$, assumes that the elements delivering the load to the welds are equally stiff. Engineers sometimes feel that the *Specification* is requiring them to assume an unrealistic and counter-intuitive force distribution. A common case is a wide-flange section welded all around and subjected to a force parallel to the web as shown in Figure 4. It is usually assumed that the entire load is carried by the web. However, the *Specification* has been interpreted as requiring the use of equation J2-10b, assuming all of the vertical welds are longitudinally loaded

and the horizontal welds are transversely loaded. For a column section, where the flange width is roughly equal to the depth of the section, the corresponding, and obviously incorrect, result is that the welds to the flanges carry about 80% of the load

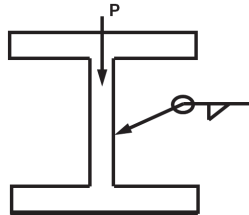


Figure 4 – Wide-flange section with all around weld

The 2016 *Specification* more concisely presents the intent. It permits the directional strength increase to be neglected with no consideration of compatibility and permits the directional strength increase to be considered “if strain compatibility of the various weld elements is considered”. Rather than requiring a specific process, it provides guidance:

The instantaneous center method is a valid way to calculate the strength of weld groups consisting of weld elements in various directions based on strain compatibility.

FILLET WELD TERMINATIONS

From 1969 through to the 2016 the *Specification* provisions addressing fillet weld terminations have changed with nearly each edition. Until the 2016 *Specification* the requirements have been prescriptive. The earlier editions seemed to favor weld returns. The latter editions seemed to favor stopping short. Over the course of fifty years the conditions addressed have included: lap joints in which one connected part extends beyond an edge of another connected part that is subject to calculated tensile stress, connections where flexibility of the outstanding elements is required, transverse stiffeners to plate girder webs 3/4 in. thick or less, transverse stiffeners to plate girder (without thickness criteria), fillet welds that occur on opposite sides of a common plane, cyclic forces of frequency and magnitude that would tend to cause a progressive fatigue failure initiating from a point of maximum stress at the end of the weld, brackets, beam seats (and similar connections), framing angles, simple end-plate connections

The 2016 *Specification* includes a performance-based requirement, “Fillet weld terminations shall be detailed in a manner that does not result in a notch in the base metal subject to applied tension loads. Components shall not be connected by welds where the weld would prevent the deformation required to provide assumed design conditions.” The requirement reflects the intent, and the intent has never changed. However, by eliminating the specific cases, the user can and must use judgment to determine the conditions for this a specific weld termination is appropriate. A User Note

and the Commentary provide further guidance to aid the user in satisfying the intent of the *Specification*.

CONCENTRATED LOADS

Section J10 of the *Specification* addresses limit states related to single- and double-concentrated forces applied normal to the flange(s) of wide flange sections and similar built-up shapes. During the development of the 2016 *Specification* the committee wrestled with two unrelated issue related to this section.

The first involved a special case of the limit state referred to as web crippling. Generally when the concentrated compressive force to be resisted is applied at a distance from the member end that is less than half the depth of the member, the strength is significantly reduced. However, the committee agreed that this reduction was unnecessary when the web was supported by the presence of connection, such as occurs at a gusseted vertical brace connection where the gusset plate applies a load to the web which is attached to the column using a framed connection. After struggling to sufficiently define the various conditions that could exist and all of the consideration within the constraints of specification-type language, the committee opted instead for a statement in the Commentary to address the situation.

The second issue involved members that could not be considered “wide flange sections and similar built-up shapes” yet might be subjected to similar concentrated loads. It is not uncommon for engineers to adapt these limit states to other members, so it was felt this should be addressed in some manner. There are difficulties related to formally including such members in J10. First, a specific inclusion of some sections could be interpreted as an implicit prohibition on other sections. Second, there is little data available related to these limit states applied to other sections. Applying the limit states to other members is likely sufficient in many instances, but delineating the limits in a technically rigorous way was impossible. Again the committee chose not to change the *Specification* itself, but rather to provide guidance. A User Note was added to point people to the Commentary, where the user can find guidance related to specific sections and further background related to the limit states. An abridge portion of the Commentary:

The provisions in J10 have been developed for use with wide flange sections and similar built-up shapes. With some judgment they can also be applied to other shapes...

When applied to members with multiple webs, such as rectangular HSS and box sections, the strength calculated in this section should be multiplied by the number of webs.

Flange local bending assumes a single concentrated line load applied transverse to the beam web. It is not generally applicable to other shapes or other loading

conditions. For instance, point loads, such as those delivered through bolts in tension are typically addressed using yield line methods (Dowswell EJ 2013).

The web local yielding provisions assume that concentrated loads distributed into the member at a 2.5:1 stress gradient. This model is likely appropriate for conditions beyond rolled wide flanges. For example, it could be used to determine the local yielding strength for channels where the concentrated load is delivered opposite the web. It has also been applied to HSS where k is typically taken as the outside corner radius. If the radius is not known, it can be assumed to be $1.5t$, as implied in Section B4.1b(d). If a fillet weld is present at the juncture of the web and the flange, the load can be distributed to a length equal to 2.5 times the flange thickness plus the weld size each side.

Web local crippling has been applied to HSS members assuming t_f and t_w are both equal to the design wall thickness and the depth, d , is equal the flat dimension of the HSS sidewall. When the radius is not known it is typically assumed to be $1.5t$, leading to a depth of $H-3t$. For box sections d and h can be taken as the clear distance between the flanges. Equations J10-4, J10-5a, and J10-5b assume restraint between the flange and the web, which may not be present if small and/or intermittent welds are used to join the elements of built-up sections.

Web compression buckling has been applied to HSS members assuming t_f and t_w are both equal to the design wall thickness and the depth, d , is equal the flat dimension of the HSS sidewall. For box sections d and h can be taken as the clear distance between the flanges. Equation J10-8 assumes pinned restraints at the ends of the web, so fixity is not required at the web-to-flange connection. A continuous fillet weld design to resist shear flow between the elements should be sufficient.

The web panel zone shear equations are applicable to rolled wide flange sections and similar built-up shapes. The J10.6 equations neglect web stability. For deep members with thin webs stability should not be neglected. See Chapter G and AISC Design Guide 16...

HSS CONNECTIONS

In 1997 AISC introduced the *Specification for the Design of Steel Hollow Structural Sections*, which included provisions related to connection design. In 2005 the information presented was moved into the *Specification for Structural Steel Buildings*. In 2010 AISC published the Design Guide 24: Hollow Structural Section Connections. There was significant overlap between the design guide and the *Specification*. There was also significant overlap between the HSS provisions in Chapter K of the *Specification* and provisions of Chapter J. Figure 5 presents a categorization of the limit states related to rectangular HSS presented in the 2010 Specification. The orange shading indicates limit states derived from limit states contained in Section J10.

Though the presentation of Chapter K in the 2010 *Specification* was user-friendly, it was not transparent and users of the *Specification* often did not understand the limitations inherent in the equations. Based on questions received at the Steel Solutions Center misuse was common. Even relative to limit states that engineers commonly checked for wide-flanges, such as web local yielding and web crippling, proximity to the end of a member was often not properly considered. The plastification check for longitudinal through plates, which was simply presented as twice the strength of that for a plate welded to the face of the HSS, implicitly assumed continuity at the penetration, an assumption that is often not satisfied with common details used in practice.

Other limit states (shaded yellow in Figure 5), such as plastification (derived from a yield line analysis) and punching shear, were presented exclusively in Chapter K though they are equally applicable to other conditions. The 2016 *Specification* consolidated these checks in Chapter J, adding Section J10.9 which states, “When a force is applied transverse to the plane of a plate element, the nominal strength shall consider the limit states of shear and flexure in accordance with Sections J4.2 and J4.5.” and a User Note which states, “The flexural strength can be checked based on yield-line theory and the shear strength can be determined based on a punching shear model. See AISC *Steel Construction Manual Part 9* for further discussion.”

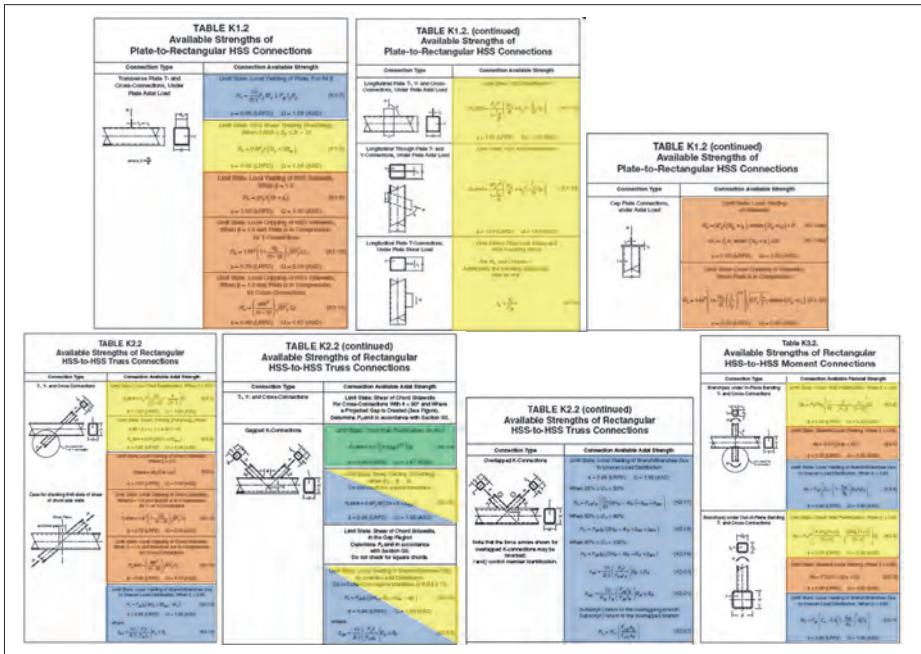


Figure 5 – Classification of 2010 Chapter K provisions

SUMMARY

In the process of updating Chapters J and K of the 2016 *Specification* an attempt was made to reduce the frequency of prescriptive requirements appearing in these chapters. Additional guidance was provided in Commentary and the *Manual* to aid users in applying the provisions and to provide transparency.

REFERENCES

AISC (1923), *Standard Specification for Structural Steel for Buildings*, American Institute of Steel Construction, New York, NY.

AISC (1941), *Specification for the Design, Fabrication and Erection of Structural Steel Buildings*, American Institute of Steel Construction, New York, NY.

AISC (1963), *Specification for the Design, Fabrication and Erection of Structural Steel Buildings*, American Institute of Steel Construction, New York, NY.

AISC (1989), *Specification for Structural Steel Buildings—Allowable Stress Design and Plastic Design*, American Institute of Steel Construction, Chicago, IL.

AISC (1993), *Load and Resistance Factor Design Specification for Structural Steel Buildings*, American Institute of Steel Construction, Chicago, IL.

AISC (1997), *Specification for the Design of Steel Hollow Structural Sections*, American Institute of Steel Construction, Chicago, IL.

AISC (2005), *Specification for Structural Steel Buildings*, ANSI/AISC 360-05, American Institute of Steel Construction, Chicago, IL.

AISC (2010a), *Specification for Structural Steel Buildings*, ANSI/AISC 360-10, American Institute of Steel Construction, Chicago, IL.

AISC (2010b), *Steel Construction Manual*, 14th Ed., American Institute of Steel Construction, Chicago, IL.

AISC (2016), *Specification for Structural Steel Buildings*, ANSI/AISC 360-16, American Institute of Steel Construction, Chicago, IL.

Packer, J., Sherman, D. and Leece, M. (2010), *Hollow Structural Section Connections*, Design Guide 24, AISC, Chicago, IL.

UPCOMING CHANGES TO AISC 341 – SEISMIC PROVISIONS FOR STRUCTURAL STEEL BUILDINGS

James O. Malley
Senior Principal, Degenkolb Engineers, San Francisco, California 94104, USA
malley@degenkolb.com

Leigh Arber
American Institute of Steel Construction, Chicago, Illinois 60601, USA
arber@aisc.org

ABSTRACT

American Institute of Steel Construction (AISC) document 360, Specification for Structural Steel Buildings, is the basic reference for the design, fabrication and erection of structural steel buildings and other “building-like” steel structures in the United States. When applied in conjunction with AISC 360, AISC 341, Seismic Provisions for Structural Steel Buildings, is the standard reference document for the seismic design of steel structures throughout the United States. Balloting is complete to update AISC 341-16 (AISC, 2016b) that will be incorporated with ASCE 7-16 (ASCE, 2016) and AISC 360-16 (AISC 2016a) into the 2018 International Building Code. The document will have significant technical modifications including new material specifications, use of steel braced diaphragms, new column splice details, requirements for SCBF gusset plate welds, and application of demands on columns that participate in intersecting frames. In addition, significant new provisions related to the seismic design of multi-tier braced frames will be provided. A new composite shear wall system has also been developed. This paper will summarize the changes proposed for AISC 341-16 focusing on connection detailing issues related to seismic design.

INTRODUCTION

The 2016 AISC Seismic Provisions introduce a number of new and updated provisions while remaining mostly unchanged from the 2010 edition. The overall organization of the standard is the same, with Chapters A-D containing analysis and connection requirements that apply to all seismic force-resisting systems, Chapters E-H addressing moment and braced frame and their composite counterparts, and Chapters I, J, and K

covering fabrication and erection, QA/QC, and prequalification and qualification testing. The most significant changes include provisions for multi-tiered braced frames, an option to use partial-joint penetration welds in SMF column splices, and clearer provisions for continuity plates, doubler plates, and associated welding. Other changes include new and updated R_y values, new provisions for horizontal truss diaphragms, a new application of composite plate shear walls using concrete-filled steel panel walls, a requirement to consider simultaneous inelasticity in shared columns in orthogonal seismic force-resisting systems, updated welding requirements for SCBF gusset-plate edge welds, and a few updates to prequalification of moment frame connections.

NEW PROVISIONS FOR MULTI-TIER BRACED FRAMES

Multi-tiered braced frames are defined as braced frames with two or more levels of bracing between diaphragms or locations of out-of-plane support. This type of frame, shown schematically in Figure 1, was considered a K-braced frame in the 2010 Provisions and therefore prohibited. In the 2016 Provisions, this bracing configuration is permitted within the definition of either an OCBF, an SCBF, or a BRBF, and carries an extra set of requirements in each case. Generally, these requirements include providing a strut in the plane of the frame at each tier level, torsionally bracing the columns, and designing the strut, column, and connections for amplified forces, which might be forces based on the capacity of the brace or on the ASCE 7 overstrength factor. The commentary explains some of the typical issues with this system, including stability of the column and the tendency for inelastic behavior to concentrate in one tier. The commentary also refers to the ongoing research on these systems.

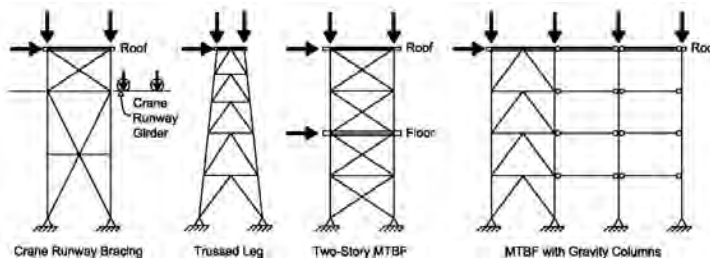


Figure 1 – Multi-Tier Braced Frame Configurations

NEW PROVISION FOR PARTIAL JOINT PENETRATION COLUMN SPLICES

Previous to the 2016 edition of the Seismic Provisions, all Special Moment Frame (SMF) column splices, if welded, were required to be complete-joint-penetration groove welds. In the 2016 edition, partial joint penetration (PJP) welds are now permitted, thereby saving significant costs in welding and erection. Section E3.6g includes provisions for this weld, which require that the flange connection have a tapered transition between column shafts and that the effective throat of the weld be at least 85% of the thickness of the thinner flange. The PJP splice provision allows for several options including single- or double-bevel groove welds, depending on the member thickness, and whether web access holes are provided or not. Companion requirements for nondestructive evaluation of these welds are also included. Industry efforts are underway to validate proper approaches to these evaluations, since ultrasonic testing of PJP welds is not routinely done, due at least partially to the difficulty that can arise in interpreting results of the weld scans.

MODIFIED REQUIREMENTS FOR WELDING OF STEEL MOMENT FRAME PANEL ZONES

The 2016 Seismic Provisions clarify reinforcement and welding at SMF panel zones, which is often a difficult location to determine the flow of forces and avoid congestion. First, the decision about whether continuity plates are required more explicitly points to AISC *Specification* J10 local limit states in the column, although a prescriptive minimum is also required. The flange force, which wasn't specifically addressed in the 2010 Provisions, may be determined by the engineer or according to the User Note in Section E3.6f.1. The thickness of the continuity plate is as required for strength but not less than 75% of the beam flange thickness, whereas in the 2010 Provisions it was required to be 100% of the beam flange thickness for two-sided connections. Also at the panel zone, the requirements for doubler plates are more well-defined, with separate sections with and without continuity plates and whether the doublers are extended beyond or fitted between the continuity plates, as shown in Figure 2. This section of the Seismic Provisions makes reference to AWS D1.8 (AWS, 2009), which now includes a useful prequalified groove weld at the doubler-to-column location as shown in Figure 3.

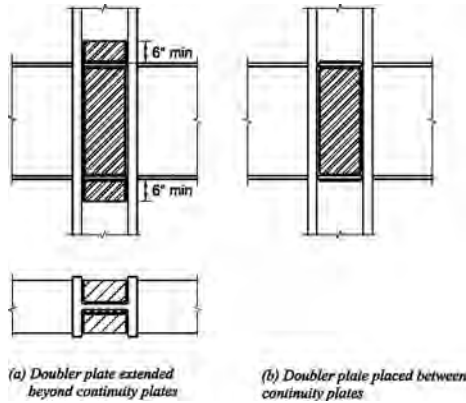


Figure 2 – Doubler Plate Configurations

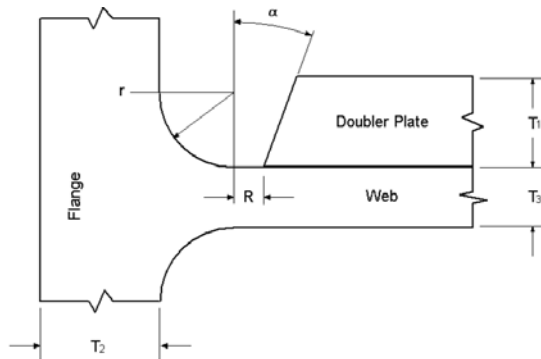


Figure 3 – AWS D1.8 Doubler Plate Weld Definition

USE OF ASTM 1085 FOR HSS SHAPES

For the 2016 Seismic Provisions, values of R_y , the ratio of the expected yield stress to the specified minimum yield stress, were reviewed and minor updates and additions have been made. A new ASTM specification for HSS, A1085, was introduced in 2013 and uses $F_y = 50$ ksi and design wall thickness equal to the nominal thickness. In the 2016 Seismic Provisions, the R_y value for A1085 is given as 1.25 and the R_y for A500 Gr. C has been modified from 1.4 to 1.3. These changes will make HSS more attractive options as the yielding elements in seismic force-resisting systems.

NEW PROVISIONS FOR STEEL BRACED DIAPHRAGM DESIGN

A new Section B5 has been added to address diaphragms, chords, and collectors, and particularly horizontal truss diaphragms composed of structural steel members. The requirements for this truss diaphragm include designing the members and connections for overstrength seismic loads (Ω_o), with exceptions for ordinary systems designed as three-dimensional systems, and for cases where the diaphragm truss members are designed to act as yielding elements.

NEW PROVISIONS CONCRETE ENCASED COMPOSITE PLATE SHEAR WALLS

Another completely new section has been added to the 2016 Seismic Provisions: Section H7, on composite plate shear walls – concrete filled (C-PSW/CF). This system is a second application of the C-PSW system, the other being the concrete encased option (C-PSW/CE) as addressed in Section H6. Concrete-filled C-PSW are highly ductile, easily and quickly constructed, and provide redundancy in the building. Two types of wall, with and without boundary elements, are shown in Figure 4.

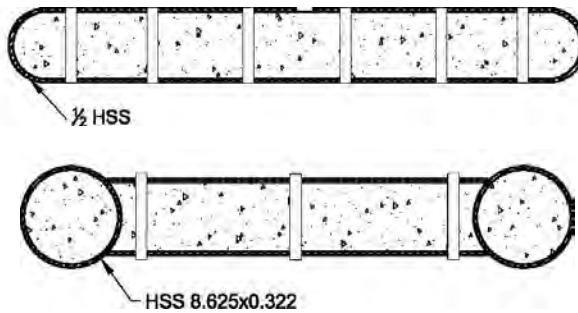


Figure 4- Configurations of Concrete Encased Composite Plate Walls

IDENTIFICATION OF ADDITIONAL CONSIDERATIONS FOR COLUMN DESIGN

Many engineers are familiar with the requirement in ASCE 7 to combine 100% of the seismic forces in one direction with 30% of the forces in the orthogonal direction when a column or other element participates in seismic resistance in both directions. This would be an appropriate approach for elastic response for a “diagonal” event. However, it is recognized that high R factor systems can yield at much lower demands than the elastic

response spectrum would imply. The column design could therefore result in a non-conservative size by applying the 100/30 rule. To more properly consider the demands on these columns in steel systems, Section D1.4a of the Seismic Provisions adds that determination of the required axial strength for columns that are common to intersecting frames shall consider the potential for simultaneous inelasticity from all such frames. Columns that are part of ordinary systems are exempt from this consideration. The commentary to this section explains that the possibility of simultaneous yielding of orthogonal frames depends on the configuration and design and the story drift at which yielding is expected. It is likely that low-rise construction may be more susceptible to taller frames, since it is unlikely that all stories of a frame will be simultaneously yielding. A corresponding requirement is included in Section E3.4a for special moment frames when performing the “strong-column/weak-beam” check to ensure that beams are the weaker element.

REVISED PROVISIONS FOR SCBF GUSSET PLATES CONNECTIONS

In Special Concentrically Braced Frame (SCBF) gusset plates where the brace is designed to buckle out of the plane of the frame, the gusset-to-column-flange and gusset-to-beam-flange welds now have an explicit strength requirement. The welds are required to have an available strength equal to $0.6R_yF_yt_p$, where R_y , F_y , and t_p are properties of the gusset plate, or the welds may be designed to have available strength to resist gusset-plate edge forces corresponding to compression in the brace combined and gusset plate weak-axis flexure. The commentary explains that accurate prediction of maximum stresses at large drifts is difficult, and therefore it is advisable to proportion the welds to be stronger than the gusset plate allowing local yielding in the plate to protect the weld.

CHANGES TO MOMENT FRAME DESIGNATIONS AND PRE-QUALIFICATIONS

Finally, there have been a few changes to moment frames and prequalification. Section E3.2 has been modified to state that special moment frames (SMF) may provide inelastic deformation capacity not only through the typical behavior of flexural yielding of beams but also by yielding of beam-to-column connections, where substantiated by analysis and testing. This revision opens the door to partially-restrained prequalified connections, including one type which will be included in AISC 358-16 (AISC 2016c). Another change to testing requirements is the inclusion of prequalification and qualification for beam-to-column connections not only for steel systems but composite systems as well. Sections K1 and K2 now cover C-SMF and C-IMF as well as their steel counterparts.

SUMMARY

Overall, the 2016 Seismic Provisions has not introduced major changes to the way seismic force-resisting systems are analyzed and designed. The familiar concepts of ductility, capacity design, and analyzing the SFRS as a whole have remained intact. A number of changes and additions have been made to reflect new information and responses to user input from the steel industry. We hope that the 2016 Seismic Provisions will be well-received by the industry as transparent, beneficial to steel construction, and working towards the goal of keeping steel structures safe.

REFERENCES

AISC (2016a), Specification for Structural Steel Buildings, ANSI/AISC 360-16, American Institute of Steel Construction, Chicago, IL.

AISC (2016b), Prequalified Connections for Special and Intermediate Steel Moment Frames for Seismic Applications, ANSI/AISC 358-16, American Institute of Steel Construction, Chicago, IL.

AISC (2016c), Prequalified Connections for Special and Intermediate Steel Moment Frames for Seismic Applications, ANSI/AISC 358-16, American Institute of Steel Construction, Chicago, IL.

ASCE (2016), Minimum Design Loads for Buildings and Other Structures, SEI/ASCE 7-10, American Society of Civil Engineers, Reston, VA.

AWS (2009), Structural Welding Code—Seismic Supplement, ANSI/AWS D1.8/D1.8M:2009, American Welding Society, Miami, FL.

PRE-ENGINEERED STANDARDIZED INDUSTRY STRUCTURAL STEELWORK CONNECTIONS - A NEW ZEALAND PERSPECTIVE

Kevin A. Cowie
Steel Construction New Zealand Inc., Auckland, New Zealand
kevin.cowie@scnz.org

ABSTRACT

Structural steelwork needs to be designed in a manner appropriate to optimizing the value adding processes used in its manufacture. This will result in the specification of more cost effective structural building solutions for the construction market. By using pre-engineered industry normal connections, the structural engineer can minimise design time and optimize fabrication cost. Design expertise can be devoted to solving non-standard connection configurations. The fabricator can develop efficient practices for manufacturing connections based on industry normal practice.

Steel Construction New Zealand Inc. has developed for the New Zealand structural steelwork industry standardized pre-engineered connections. The pre-engineered connections are widely used within the entire New Zealand structural steelwork industry and have been instrumental in getting to the current high market share for steel. This paper will provide an overview of the pre-engineered connections and describe how these provides New Zealand structural engineers with a rapid and cost-effective way to specify the majority of structural steelwork connections.

INTRODUCTION

Structural steelwork needs to be designed in a manner appropriate to optimizing the value adding processes used in its manufacture. This will result in the specification of more cost effective structural building solutions for the construction market. Structural engineers, as a design profession, play an important role in society by developing construction solutions that most effectively utilize the resources available to society.

Fabricated structural steelwork is a value added product. It requires skilled design, management, labour and machine time to be added to the raw material of steel plate and sections, to produce a highly versatile, customized building product.

A small number of generic connection types are used for the vast majority of steelwork fabrication. By using pre-engineered industry normal connections, the structural engineer can minimise design time and optimize fabrication cost. Design expertise can be devoted to solving non-standard connection configurations. The fabricator can develop efficient practices for manufacturing connections based on industry normal practice.

Steel Construction New Zealand Inc. (SCNZ) has developed, for the New Zealand structural steelwork industry, standardized pre-engineered connections. This is published as *Steel Connect: Structural Steelwork Connection Guide, SCNZ 14.1:2007, SCNZ 14.2:2007*, (Hyland et al., 2008/2010) in hardcopy format and also available on the SCNZ website. The guide is widely used within the entire New Zealand structural steelwork industry and has been instrumental in getting to the current high market share for steel.

This paper will provide an overview of the *Structural Steelwork Connection Guide* (referred as the Guide from this point) and describe how the Guide provides New Zealand structural engineers with a rapid and cost-effective way to specify the majority of structural steelwork connections, in accordance with accepted fabrication industry norms. Also covered will be how specification of these connections facilitates the development of reliable cost estimates by designers, fabricators, consulting quantity surveyors and constructors. Potential future developments of the Guide will be provided.

OVERVIEW OF THE NEW ZEALAND STRUCTURAL STEELWORK INDUSTRY STANDARDIZED PRE-ENGINEERING CONNECTIONS

The *Structural Steelwork Connections Guide* contains 12 generic connections types and over 14,000 connections. The connections types are shown in figures 1- 3. Missing from the figures is the bolted beam splice (BBS) connection type.

Limit State Design Capacities Method

A limit states design method has been used throughout the Guide. Connection design capacities are calculated in accordance with the New Zealand Steel Structures Standard, NZS3404:1997 (SNZ, 2007). Factored limit state design actions on connections are calculated in accordance with the New Zealand Structural Design Actions Standard, AS/NZS 1170 (SNZ, 2013).

Connection are Designed for Seismic Ductility Demands

Beam to column face moment connections are required to possess design capacity sufficient to satisfy the ductility demands of primary members in frames of varying levels of seismic ductility. Under design seismic events the connection components will be subjected to over-strength actions developed in the members. The over-strength actions are related to frame ductility category, material variability and strain hardening. In the Guide three frame ductility categories are referenced. These include:

Ductile Frames:	$3 < \mu \leq 6.0$
Limited Ductile Frames:	$1.25 < \mu \leq 3.0$
Elastic Frames:	$\mu = 1.0$

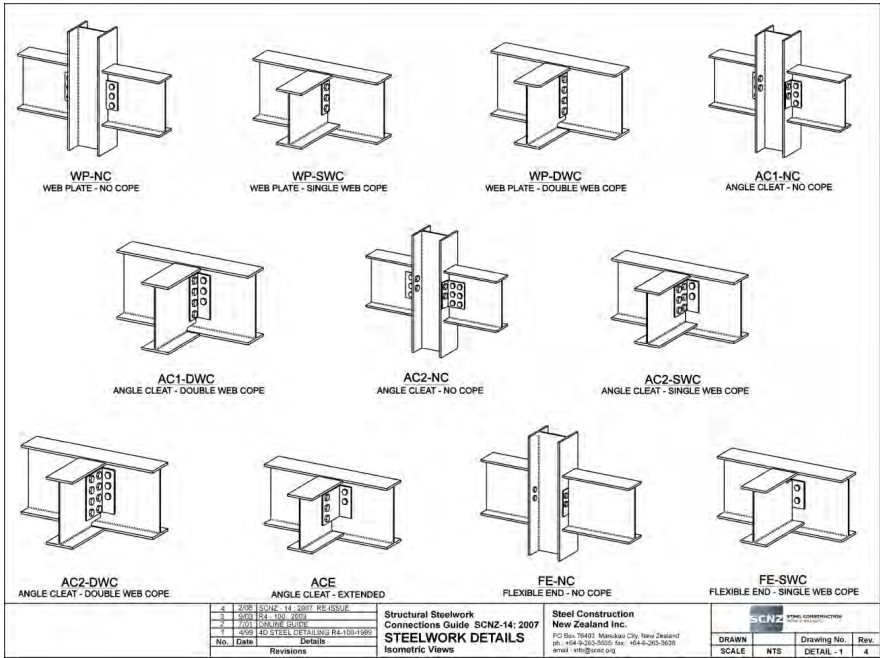


Figure 1: Isometric Drawing of Connection Types

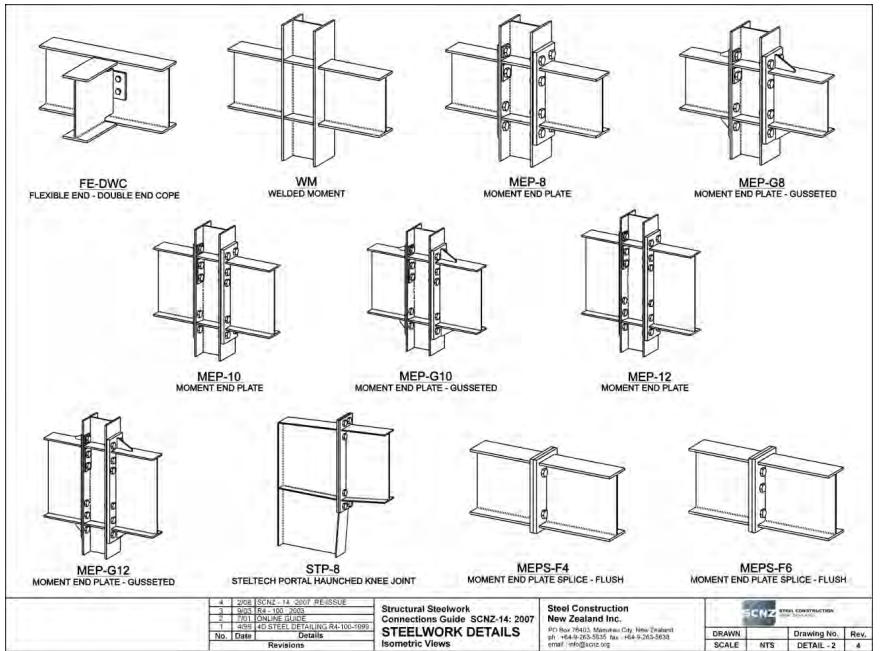


Figure 2: Isometric Drawing of Connection Types

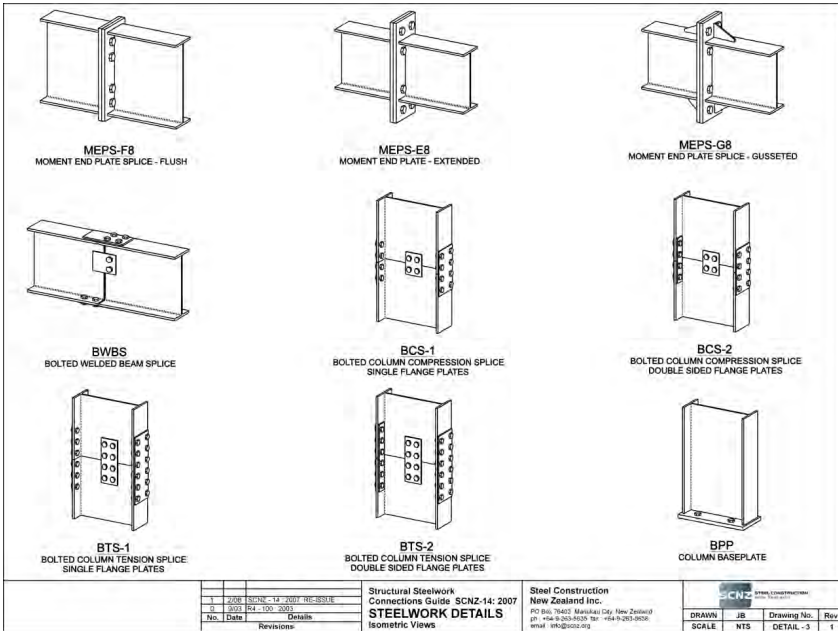


Figure 3: Isometric Drawing of Connection Types

The design procedures recognize that even nominally pin ended shear connections in non-seismic frames will be required to sustain rotational demands induced by building displacements under seismic loadings. Beam and column splices in seismic resisting frames will also be required to sustain enhanced design actions resulting from the development of over-strength actions in plastic hinge zones in primary members of the frames.

Connections are Designed for Fire Ductility Demands

Through the use of fire engineering design approaches in New Zealand there is increasing use of steelwork beam elements without passive fire protection in buildings. Typically columns still require some level of passive fire protection, except in areas with low levels of fire development risk such as car parking structures.

Damage to connections occurs to steel beam connections as the steel shrinks as it cools. To prevent collapse resulting from this sort of behaviour, welds are designed to develop the tensile design capacity of the element connected, whether that is a cleat or an element of a steel section. This prevents the weld being the weakest link and distributes plastic deformation, developed on cooling, into the plate or section element where it can be more readily accommodated.

Steel Material Properties

Capacity design approaches are used for many of the moment resisting connections in the Guide. These assume the use of AS/NZS 3679.1 (SAA/SNZ, 1996) G300

sections and NZ Steel 300MOD welded sections with a supplier's material variation factor, as defined in NZS3404:1997 (SNZ, 2007), less than 1.20. This is traditionally met by Australian and New Zealand produced steels.

Connection cleats are AS/NZS 3678 (SAA/SNZ, 1996) G250 for all connections except end plates for moment end plate connections, for which AS/NZS 3678 G350 is preferred. The use of G250 plate ensures maximum ductility can be developed in connections and simplifies material ordering and tracking through fabrication. End plate connections benefit directly from the use of G350 plate as significant thickness reduction can be achieved using the stronger plate. If an end plate thickness can be kept below 25mm the plate holes can be punched rather than drilled and the plate can be more easily handled in the fabrication process.

Welding

Welds for connections are specified as Structural Purpose, SP, using electrodes with a minimum tensile strength of 480 MPa, in accordance with AS1554.1 (SAA, 2004). This ensures that the weld is compatible with both grade 250 and 350 steels. It is common practice amongst steel fabricators to standardise on a single welding consumable for structural work so as to economise and avoid mismatching errors. Full strength, symmetrical, double sided fillet welds are used where possible in preference to full penetration butt welds. Where fillet welds with leg lengths greater than 12mm would be required by calculation, complete penetration butt welds are specified. This reflects the current crossover in welding economy between butt welds and fillet welds.

Bolting

Bolts are specified as Property Class 8.8 high strength bolts in accordance with AS/NZS 1252:1996 (SAA/SNZ, 1996). Typically M20 bolts are used where ever possible to encourage efficiencies from standardization.

Angle Cleat: AC, Web Plate: WP, Flexible End Plate: FE

Simple shear-only connections are a very economical way to connect steelwork together. The Guide contains three generic shear-only connections: angle cleat (AC); web plate (WP); and flexible end plate (FE). When first published the Guide contained only web plate and flexible end plate connections. The angle cleat connections were introduced in the 2003 version of the Guide following feedback from New Zealand fabricators who were asking for simple shear only connections that did not require any welding.

The simple shear-only connections are designed for the following objectives:

- Possess design capacity to satisfy gravity ultimate limit state loads
- Provide twist restraint to the supported and supporting beams about their respective longitudinal axes, consistent with the restraint provisions of NZ Steel Structures Standard NZS3404:1997 (SNZ, 2007) and HERA report R4-92.
- Have sufficient rotation ductility to accommodate gravity load and seismic drift induced rotations of 0.030 radians, without collapse.

- Have sufficient ductility to accommodate thermal strains induced by extreme fire events without collapse.

The typical limiting conditions for the angle cleat connections are: shear of the cleat or bolts; block shear around bolt groups in support leg and beam web; shear / flexural yield of coped section.

AC and WP connection depths are typically greater than half the supported beam depth. To prevent the possibility of bolt shear under extreme seismic drift induced rotations and fire conditions, the cleat thickness is limited to half the bolt diameter and the bolt group capacity is greater than the lowest limiting flexural condition of the cleat or beam web.

Extended Angle Cleat (ACE) connections that allow beam to beam connections to be made without the need to cope the incoming beam into the flange of the supporting sections are included in the guide. These connections are typically limited by the flexural capacity of the bolt group in the supported beam.

The typical limiting conditions for web plate connections are : shear or flexural yield of the cleat or web; tearing yield of cleat or beam web adjacent to an extreme bolt; block shear / tension yield of the beam web; bolt shear.

Welds of cleats to the supports have design tensile capacity greater than the design tension yield capacity of the cleat plate. This improves connection performance under high thermal strain conditions during fire.

The typical limiting conditions for flexible end plate connections are : shear of the cleat or bolts; block shear of a block extending 20mm into the web and as deep as the end plate; shear / flexural yield of coped section.

For FE connections welds of cleats to the beams have design capacity greater than that the resultant action due to development of over-strength of 1.2 times the flexural yield of the end plate under tensile load and direct shear. This is to ensure ductile performance of the connection under seismic and fire conditions.

In FE connections the beam web adjacent to the top of the cleat is designed to have sufficient capacity to resist combined shear and local longitudinal tension, using a Von Mises based stress criterion. To prevent transverse tensile tearing in the web below the bottom edge of the end plate, block transverse shear and tensile yield capacity is assessed based upon a web block 20mm wide and as deep as the end plate. Compression yield strength is assessed to develop along the top edge of the web block shear element as long as two local web buckling criteria are satisfied. The first of these is that the top flange is laterally restrained at that location by a concrete slab or other means. The second criterion is that the clear web depth to web thickness ratio between the top of the cleat and the underside of the flange, is less than or equal to 17.5.

The end plate in FE connections is maintained as flexible by limiting the thickness of the endplate as a function of the bolt gauge.

Welded Moment: WM

The Welded Moment connections are designed for the following objectives:

- A beam to column face welded connection possessing design capacity sufficient to satisfy the demands of primary members in frames of varying levels of seismic ductility category. These include ductile frames with $3 < \mu \leq 6.0$, limited ductile frames with $1.25 < \mu \leq 3.0$, and elastic frames with $\mu = 1.0$. Seismic flexural over-strength actions are to be combined with shear loads equal to 60% design shear yield capacity of the section.
- The connection is to maintain integrity under fire conditions.

The typical limiting conditions are: flexure or shear of the section.

The welds are sized to develop the design capacity of the web and flanges so as to enhance ductile behaviour under fire conditions. It is considered that the welds should be able to develop the section capacity of the section to cope with shrinkage stresses that may develop during fire cooling phases.

The welds of the flanges may be either complete penetration butt welds or symmetrical fillet welds placed either side of the flanges. Complete penetration butt welds to the flanges are suitable for all members in elastic, limited ductile and ductile frames, without specific design. However these welds must not be ground flush, but should maintain minimum butt weld reinforcement in accordance with AS/NZS 1554.1.

Where fillet welds are specified these are designed to develop the corresponding over-strength design capacity of the flange of the section acting as a primary member in a frame of the given seismic ductility demand category. Welds to the web are designed to develop the design tension capacity of the section web.

Compression and tension stiffeners and flange doubler plates to the supporting column are not specified but will often be required in order to develop the design reactions from the connection.

Connection specifications are only listed for those sections that comply with the corresponding material and section geometry requirements for primary members in seismic frames of the stated ductility demand.

Moment End Plate: MEP

The Moment End Plate (MEP) connections are designed as rigid beam-end connections for beam to column joints. MEP connections allow column assemblies to be fabricated without welded branch stubs. This improves transportation efficiency and minimizes the number of fabricated moment resisting joints and splices in a frame. Moment End Plate connections incorporating end plates extended beyond the beam flanges with and without gussets to stiffen the outstand are included in the guide. The connection typically occurs within the seismic hinge zone of the member and so must cope with inelastic demands. In the guide connections are designed to satisfy the flexural and shear ultimate limit state loads for primary members of limited ductile, $1.25 < \mu \leq 3.0$ and elastic, $\mu = 1.0$, seismic

ductility demand category frames. The design method draws upon the approach set out by the BCSA & SCI in their publication “Joints in Steel Construction: Moment Connections”, P207/95 (SCI, 1995). The method is modified to account for the over-strength actions expected to develop in connections located adjacent to plastic hinge zones in rigid seismic resisting frames.

The MEP connections are designed to ensure endplates, welds and bolts have sufficient design capacity to accommodate over-strength actions resulting from the development of significant plastic deformation in primary members of limited ductile frames. For connections subject to only elastic demand the endplates and bolts need only to accommodate design actions. However the welds to the flanges and webs are designed to develop the design capacity of the web and flange to enhance ductile behaviour under fire conditions.

The connections in the Guide are tabulated with design moment capacities limited by either the top or bottom bolt group design tension capacities. One bolt group is assumed to resist all section flexural tension forces so as to develop the required moment design capacity. Bolt prying effects are accounted for through the assessment of three potential failure modes that incorporate prying effects. The other bolt group is assumed to resist only shear actions.

The connections are designed to ensure reliable rigid connection rotational stiffness characteristics. To ensure adequate frame rigidity in connections with end plates less than 20 mm thick, the minimum plate thickness and bolt combination required to develop the required design capacity should not be limited by mode 1 behaviour. This is in conjunction with a maximum bolt offset from the beam flange, web or gusset plate of 60 mm.

The column-side aspects of the beam to column joint are not covered in the guide but do need to be considered by the designer. Bolt row design capacities and the resulting connection design moment capacity is assessed assuming that the beam end connection capacity is not limited by column-side limit states .

The welds of the flanges may be either complete penetration butt welds or symmetrical fillet welds placed either side of the flanges. Complete penetration butt welds to the flanges are suitable for all members, without specific design. However these welds should not be ground flush, but maintain minimum butt weld reinforcement in accordance with AS / NZS 1554.1.

Moment End Plate Splice: MEPS

Extended end-plate splices with a total of eight, ten or twelve bolts are tabulated. The Moment End Plate Splices, MEPS, are required to possess design capacity sufficient to resist flexural and shear ultimate limit state loads in locations away from potential yielding regions in seismic resisting members. While not required to develop inelastic deformations themselves, the splices need to be designed to resist actions resulting from the development of over-strength actions elsewhere in the frame.

Like the beam to column Moment End Plate, MEP, connection, either the top or bottom bolt group is assumed to resist all design flexural tension forces. The other bolt group is assumed to resist shear actions. The endplates for MEPS connections are sized assuming equal thickness end plates. The design method is similar to that used for MEP connections.

The welds of the flanges are designed as either complete penetration butt welds or symmetrical fillet welds placed either side of the flanges. Complete penetration butt welds to the flanges are suitable for all members, without specific design. The welds are sized to develop the design capacity of the web and flanges so as to enhance ductile behaviour under fire conditions.

Flush Plate: MEPS-F

Flush end-plate splices with a total four, six or eight bolts located on the inside face of the flanges are tabulated in the guide.

As with the MEPS connections they should possess design capacity and ductility to resist flexural and shear ultimate limit state loads in locations away from potential yielding regions. They should also respond in a ductile manner under fire conditions. The endplates for MEPS-F connections are sized assuming equal thickness end plates. The design provisions are similar to those for the MEPS.

The welds of the flanges may be either complete penetration butt welds or symmetrical fillet welds placed either side of the flanges. The flange welds shall have design capacity not less than that of the section flange. Complete penetration butt welds to the flanges are suitable for all members, without specific design. Welds to the web shall be designed to develop the design tension capacity of the section web.

Bolted Welded Beam Splice: BWBS, Bolted Beam Splice: BBS

The Bolted Welded Beam Splice (BWBS) and Bolted Beam Splice (BBS) are designed for the following objectives:

- Possess design capacity to satisfy gravity and seismic design actions derived from relevant design or over-strength actions of primary members of seismic resisting frames.
- The splices are located away from potential seismic yielding regions of the member.
- Maintain ductile performance under fire restraint conditions

The typical limiting conditions are: shear of the web cleat or bolts; tension yield of the flange plates, shear of flange bolts or welds.

These connections are designed for doubly symmetrical I sections only. All flexural actions are resisted by the flange plate couple. All shear actions are resisted by the web cleat.

For BWBS the flange and web cleats are welded to one side of the connection and bolted to the other. The eccentricity used for the design of the web bolt group is less than that used for the design of the weld group. This recognizes that the weld group

is more rigid than the bolt group and the cleat may transfer shear across the splice in single curvature rather than the bolt group forcing double curvature, as in a splice bolted both sides.

Weld groups are designed in accordance with NZS3404:1997 cl 9.8.1.1, the "General method of analysis". Superposition of in-plane direct shears and moment resisting shear couples is used. Direct shear is applied at the weld centroid, and distributed evenly over the total weld length. The moment induced transverse and longitudinal shears are assumed to act at right angles to the x or y direction radius from that point to the weld group instantaneous centre of rotation, and are taken as proportional to that radius.

For the BBS connections pairs of web cleats are set out central to and either side of the beam section. A single row of web bolts is used each side of the splice. Single flange plates located on the outer face of the beam flanges are used for BBS1 connections. For BBS2 connections, flange plates of equal thickness are located on both faces of the beam flanges.

To maintain ductile behaviour under fire restraint and seismic overload conditions the welds to the flange plate are sized to have design capacity greater than the design tensile capacity of the plate. The flange bolt group is similarly designed to have design capacity greater than the flange or flange plate design tensile capacity. It is considered that the web cleat will be protected if the flange splice maintains integrity under seismic overload and fire events.

Bolted Compression Splice, BCS, Bolted Tension Splice: BTS

The Bolted Compression Splice (BCS) and Bolted Tension Splice (BTS) are designed for the following objectives:

- Possess design capacity to satisfy gravity and seismic actions based on design or capacity design derived seismic axial, moment and shear ultimate limit state loads.
- The splices are located away from potential seismic yielding regions of the member and are assumed to be protected by appropriate passive fire protection.

The typical limiting conditions are: shear of the web cleat or bolts; tension yield of the flange plates; and shear of the flange bolts.

The splices are assumed to be located away from potential column yielding regions, at places of minimum ductility demand.

All resultant tensile forces from flexural actions are resisted by the flange plate couple. All shear actions are resisted by the web splice. All compression load resulting from axial and flexural actions is resisted by direct full contact end bearing of the abutting sections.

Pairs of web cleats are set out central to and either side of the column section web. A single row of web bolts is used each side of the splice for the BCS connection.

The web cleat depth is not less than half the section depth. Bolt gauge is set out from the centre-line of the plates and flanges.

Single flange plates located on the outer face of the column flanges are used for BCS1 and BTS1 connections. For BCS2 and BTS2 connections, flange plates of equal thickness are located on both faces of the column flanges.

For stiffness compatibility of the splice with the connected sections, the combined thickness of splice plates should typically be not less than half the thickness of the web or flange spliced.

A minimum loading condition is that the fasteners, splice plates and section shall be sufficient to transmit a force equal to 15% of the section design capacity in direct compression only.

To minimise slip during construction flange splices are detailed with a minimum of two rows of bolts in the flanges, each side of the splice. The flange splice is designed to resist a minimum serviceability load of 15% of section moment capacity by the flange bolts in friction tension mode.

Base Plate Pinned: BPP

The Base Plate Pinned (BPP) connections are designed for the following objectives:

- Possess design axial compression and shear capacity to support ultimate limit state design loads.
- To have sufficient lateral shear resistance provided by the holding down bolts to provide full twist and lateral translation restraint for the axial design load.
- The connection is assumed to be nominally pinned.

The typical limiting conditions are: bearing capacity of the mortar bedding and concrete foundation; flexural /shear capacity of the steel base plate; shear capacity of the weld between the base plate and the column end; and shear capacity of the holding down bolts.

All column ends are assumed prepared for full end contact bearing in accordance with NZS3404:1997. This is typically achieved by cold saw cutting. Holding down bolts are designed to have a shear capacity greater than a shear force equal to 5% of the design axial compression load. Greater shear loads may require shear blocks to be welded to the underside of the base plate.

The welds of the column to the base plate are SP welds, designed to resist the prescribed design action and transfer a minimum of 15% of column section capacity. Bearing area and design capacity of the concrete foundation under the base plate is derived in accordance with the provisions of the New Zealand Concrete Standard, NZS3101:1995 section 8.3.5.

Effective pressure distribution under the base plate is approximated to actual by using an overlapping pressure block approach. This results in the peak limiting bearing stresses occurring under the web to flange intersection points. For slender compression elements the effective stress blocks in the base plate correspond to the

effective stress distributions in the elements used in the Cold Formed Steel Structures Standard, AS/NZS 4600. Therefore portions of slender elements some way from stiffening elements are not considered to contribute axial capacity to the column or develop bearing strength in the base plate. The central portion of column webs and the outer tips of open I and channel sections are typically affected. For circular hollow sections the principle of overlapping stress blocks is approximated by assuming that the internal bearing stress annulus under the plate is fully overlapped and that the outer stress annulus is not.

HOW THE PRE-ENGINEERED CONNECTIONS ARE USED AND SPECIFIED

As mentioned above steel building structures tend to incorporate a limited number of generic connection types. The detailed design of the connections is often not done until late in the structural design process. However, usually the structural engineer will know what type of connection should be used for a given type of structural element, e.g. secondary floor beam, and the relative level of load that it will be required to transmit.

This is the same level of knowledge the engineer needs to effectively use the *Structural Steelwork Connection Guide* and select appropriate connections at preliminary design stage. At the final design stage the engineer can use the guide to verify actual connection design capacities against final calculated design actions.

A system of connection labelling is used that can be used on drawings to communicate the engineer's requirements to the fabricator and quantity surveyor. A minimum load rating based on percentage of design section axial, moment and shear yield capacity is included in the connection label. Section capacity is defined in accordance with NZ Steel Structures Standard NZS3404:1997(SNZ, 2007).

For example, BTS 30/30/15, describes a bolted tension splice capable of resisting a minimum of 30% of the section design axial tension capacity, combined with 30% design section moment capacity and 15% design section yield capacity. In many cases the connection design capacity will exceed this minimum percentage load rating.

The engineer may therefore also specify the load rating requirements for the connection in terms of applied ultimate limit state load required to be resisted. For example, WP 130KN, describes a Web Plate connection capable of resisting 130 KN of applied ultimate limit state shear.

For preliminary design the percentage load rating designation provides a quick and effective way to provide sufficient information to estimators, fabricators and quantity surveyors, for cost estimates to be prepared with confidence. For final design the engineer may wish to take advantage of the full design capacity of the various connections and specify them by specific load as appropriate.

Connections of a type can be differentiated from each other on the basis of whether copes are required or other detailing features that will affect fabrication pricing.

The percentage load designation system used in the Guide is consistent with that used in the SCNZ developed *On-line Structural Steelwork Estimating Guide* (SCNZ, 2003). Therefore structural steelwork drawings that use this system wherever possible make cost estimating work significantly easier.

An estimate may be prepared, using the *On-line Structural Steelwork Estimating Guide*, by summing the total number of connections in the project and multiplying by the relevant price / connection, then adding to that price the allowances for supply of main sections, surface coatings, transport, erection and preparation of shop drawings.

FUTURE DEVELOPMENTS

The *Structural Steelwork Connection Guide* was first published in 1989, with the last significant update over a decade ago in 2005. SCNZ is currently reviewing the Guide and considering how the Guide can be of further benefit to the New Zealand steel construction industry.

The design procedure for each of the connection types will be reviewed in light of recent research and changes to design standards. One item requiring further review is the block shear provisions. The New Zealand Steel Structures Standard, NZS 3404, contains no specific block shear provisions. The standard block shear provisions in the Guide differ from current international standards.

New types of connections are being considered for possible inclusion in the Connection Guide. These include extended web plate connections, parallel flange channel (PFC) connections and column moment baseplate.

The connection guide is currently available in hard copy table format and as an on-line searchable connection format. The review of the connection guide will consider improvements in the delivery of the connection details. SCNZ will consider providing a library of standard connections to detailing software providers as there have been a number of requests in the past for such a library.

CONCLUSION

Structural engineers have an important role to play in developing a cost effective construction industry in New Zealand. Fabricated structural steelwork is an important value added building product that requires a designer to optimise connection fabrication cost as well as material supply cost. The pre-engineered structural steelwork connection developed by SCNZ provides the structural engineer with the necessary tools to quickly specify connection requirements for the large majority of structural framing requirements in building construction. The use of industry-normal connections by the structural engineer assists other parties in the construction chain measure and estimate steel construction cost, achieve productivity gains in manufacture and foster confidence, innovation and economy in the New Zealand construction industry. SCNZ review of the pre-engineering steelwork connections

being undertaken will ensure that the pre-engineered connections remain technically correct and continue to promote efficiency within the steelwork construction industry.

REFERENCES

Hyland, C., Cowie, K., and Clifton, C (2008), *Structural Steelwork Connections Guide Design Procedures*, SCNZ Report 14.1:2007, Steel Construction New Zealand Inc., Manukau, New Zealand

Hyland, C., Cowie, K., Bird, G., (2010), *Structural Steelwork Connections Guide Connection Tables*, SCNZ Report 14.2 : 2007, Steel Construction New Zealand Inc., Manukau, New Zealand

SAA / SNZ, (1996), *Structural Steel Hot-rolled plates, floorplates and slabs*, AS/NZS 3678: 1996, Standards Australia / New Zealand, Homebush / Wellington

SAA / SNZ, (1996), *Structural Steel Part 1: Hot-rolled bars and sections*, AS/NZS 3679.1:1996, Homebush / Wellington

SAA, (2004), *Structural Steel Welding Standard, Part 1: Welding of Steel Structures*, AS 1554.1: 2004, Standards Australia, Homebush

SAA/SNZ, (1996), *High-Strength Steel Bolts with Associated Nuts and Washers for Structural Engineering*, AS/NZ1252: 1996, Standards Australia / New Zealand, North Sydney

SCNZ, *Online Structural Steelwork Estimating Guide*, SCNZ-21, Steel Construction New Zealand Inc., Manukau, New Zealand

SCI, (1995), *Joints in Steel Construction: Moment Connections*, P207/95, Steel Construction Institute, United Kingdom

SNZ, (2007), *Steel Structures Standard (Incorporating Amendments 1 and 2)*, NZS 3404:1997, Standards New Zealand, Wellington, New Zealand

SNZ, (2013), *Structures Design Actions Set*, AS/NZS 1170 Set incorporating AS/NZS 1170.0:2002, AS/NZS 1170.1:2002, AS/NZS 1170.2:2011, AS/NZS 1170.3:2003, NZS 1170.5:2004, Standards New Zealand, Wellington, New Zealand

SNZ, (2006), *Concrete Structures Standard*, NZS 3101:2006, Standards New Zealand, Wellington

AN ENGINEERING APPROACH TO THE EVALUATION OF THE TRANSFORMATION PARAMETER β

Ana M. Girão Coelho
(ana.girao-coelho@ncl.ac.uk) Newcastle University, UK

ABSTRACT

The paper presents a finite element analysis of unstiffened welded connections, in double-sided configurations, in which the two beams do not meet at the same level. The results are used to propose a simple and reliable estimation of the transformation parameter β that accounts for the influence of the column web panel in shear.

INTRODUCTION

In current European Standard EN 1993, part 1.8 – EN 1993-1-8 (CEN 2005), the stiffness and resistance of column web panels in double-sided beam-to-column joints are evaluated using the so-called transformation parameter β (Guisse and Jaspart 1995, Jaspart 1997). This coefficient is related to the web panel internal actions and can be calculated from the moments at each side of the web panel. The β parameter ($0 \leq \beta \leq 2$) is currently limited to the same-depth beams which meet at the same level. In many practical double-sided joints, beams will not be of the same depth, or at the same height. EN 1993-1-8 is silent on such joints.

As a result, several research projects were carried out to investigate the behaviour of double-sided non-symmetrical welded connections (Jordão et al. 2013, Bayo et al. 2015), but did not produce any design guidance for the evaluation of the transformation parameter β . By using a more practical approach, purely based on engineering judgement, Brown (2013) recently proposed some values for β . Essentially, his proposals recognise that where externally applied tension on one side of the column aligns closely with externally applied compression on the other, there will be significant shear in the column web – an onerous condition – and high values are suggested for β . Where there is greater separation, the situation is less onerous. If the externally applied forces are both either tension or compression, they serve to cancel each other to some degree, which is a less onerous situation, and thus low values are suggested for β . This method however has not been checked against test results.

Motivated by these gaps, this paper complements previous research by presenting the results of 106 nonlinear finite element simulations on unstiffened welded joints in double-sided configurations, in which the two beams do not meet at the same level. The commercial finite element code Abaqus/Standard (2015) is used for this purpose. The finite element models are formulated to represent the joint geometry, the material constitutive laws, boundary and load conditions, and capture the three-dimensional global structural behaviour. An elastoplastic material response is assumed. The various parameters varied numerically include the (i) member relative sizes, (ii) beam load ratio, (iii) gap between beams, and (iv) beam overlapping ratio. Results are discussed from a resistance point of view and will serve as a basis to validate the proposed values for β (Brown 2013).

VIRTUAL TEST CONFIGURATIONS AND PARAMETERS

The geometries of the analysis configurations utilized in this research are derived from the geometry of previous welded beam-to-column joints tested by Jordão et al. (2013). Different analysis configurations are created by changing some of the attributes of the specimens. Important geometric parameters are varied over the practical range of interest in order to evaluate the strength behaviour of the column web panel.

A generic configuration for the finite element numerical tests performed in this research is shown in Fig. 1. Specific characteristics and attributes modelled in these studies are as follows:

1. All tests involve double-sided welded connections with beams of the same depth framing into the column.
2. The column ratio $d_c/t_{w,c} < 60(235/f_{y,cw})^{1/2}$ to preclude shear buckling (d_c : clear depth of the web, $t_{w,c}$: thickness of web, and $f_{y,cw}$: yield stress of column web, in N/mm²).
3. Residual stresses due to welding are not accounted for.
4. The material is mild steel grade S355 and the values of the key properties are taken from Jordão et al. (2013), see Fig. 2.

Variables considered in the parametric studies are:

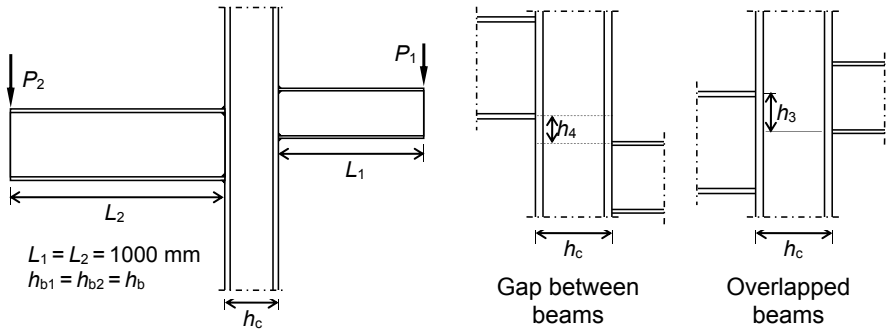


Fig. 1: Configuration and key dimensions

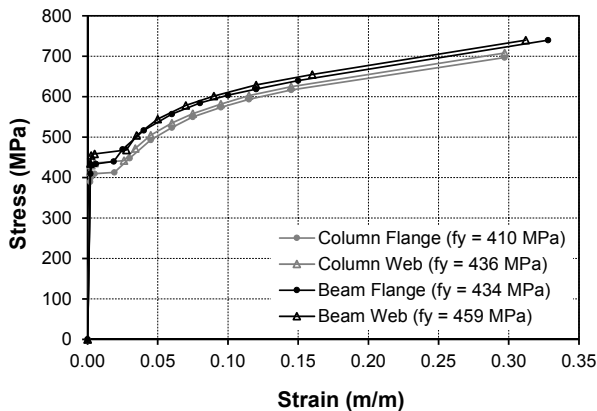


Fig. 2: Stress-strain characteristics (Jordão et al. 2013)

1. Load ratio P_2/P_1 (range of variation: 1, 0, -1, corresponding to the following values for the transformation parameter: $\beta=0$, $\beta \approx 1$, $\beta \approx 2$, respectively, see CEN 2005).
 2. Ratio h_b/h_c (range of variation: 0.8, 0.83, 1, 1.33, 1.67, 2) – series H.
 3. Gap ratio h_4/h_c (range of variation: 0, 0.25, 0.5, 1) – series G.
 4. Overlap ratio h_3/h_c (range of variation: 0.25, 0.50, 0.80, 1.00, 1.33) – series O.
- Specific values for the above variables are given in Table 1.

FINITE ELEMENT MODEL

A three-dimensional model is proposed to generate the nonlinear moment-rotation response of the welded connections. The experimental work and test results of Jordão et al. (2013) are used for validation (specimen labelled IS-0 in the current work).

Table 1. Summary of finite element parametric studies

Test	Load ratio	Member sections			Gap ratio	Overlap ratio
	P_2/P_1	Beam	Column	h_b/h_c	h_4/h_c	h_3/h_c
<i>Initial study set</i>						
IS-0/1/2	1/0/-1	IPE400	HE240B	1.67	–	–
<i>Series H</i>						
H1-0/1/2	1/0/-1	IPE400	HE200B	2.00	–	–
H2-0/1/2	1/0/-1	IPE400	HE300B	1.33	–	–
H3-0/1/2	1/0/-1	IPE400	HE400B	1.00	–	–
H4-0/1/2	1/0/-1	IPE400	HE500B	0.80	–	–
H5-0/1/2	1/0/-1	HE200B	HE240B	0.83	–	–
<i>Series G ($G_i = G1, G2, G3, G4$ for $h_4/h_c = 0, 0.25, 0.50, 1.00$, respectively)</i>						
G1-0/2	1/-1	IPE400	HE240B	1.67	0	–
G2-0/2	1/-1				0.25	
G3-0/2	1/-1				0.50	
G4-0/2	1/-1				1.00	
G_i -H1-0/2	1/-1	IPE400	HE200B	2.00	0 to 1	–
G_i -H2-0/2	1/-1	IPE400	HE300B	1.33	0 to 1	–
G_i -H3-0/2	1/-1	IPE400	HE400B	1.00	0 to 1	–
G_i -H4-0/2	1/-1	IPE400	HE500B	0.80	0 to 1	–
G_i -H5-0/2	1/-1	HE200B	HE240B	0.83	0 to 1	–
<i>Series O ($O_i = O1, O2, O3, O4, O5, O6$ for $h_3/h_c = 0.25, 0.50, 0.80, 1.00, 1.33, 1.67$ respectively)</i>						
O1-0/2	1/-1	IPE400	HE240B	1.67	–	0.25
O2-0/2	1/-1					0.50
O3-0/2	1/-1					0.80
O4-0/2	1/-1					1.00
O5-0/2	1/-1					1.33
O_i -H1-0/2	1/-1	IPE400	HE200B	2.00	–	0.25 to 1.67
O_i -H2-0/2	1/-1	IPE400	HE300B	1.33	–	0.25 to 1.00
O_i -H3-0/2	1/-1	IPE400	HE400B	1.00	–	0.25 to 0.80
O_i -H5-0/2	1/-1	HE200B	HE240B	0.83	–	0.25 to 0.50

Mesh Description

The welded connection is generated with reduced integration, first order shell elements with hourglass control, and with a finite strain thick shell formulation. The welds connecting the beams to the column are not explicitly modelled: the welds are modelled as part of the beam material, and then connected to the column flange by fully coupling all the degrees-of-freedom at the interface. Therefore, partial separation of the weld from the base metal is not possible.

The mesh density was varied to determine the most efficient modelling scheme that also compared well with the experimental results. A mesh sensitivity study was conducted with respect to the degree of discretization in order to capture the overall behaviour and the local stresses in the column web. It was found that the finite element mesh depicted in Fig. 3, with an element side length of 5 mm along the column web and for the height of the beams, complies with the requirements for a reliable simulation and also satisfies the convergence requirements.

Boundary and Load Conditions

Appropriate boundary conditions that are consistent with the actual column restraints are applied. Displacements in the x and z directions, and rotations in y and z directions are restrained at both hinges. Supports restraining vertical movement in the y direction are also added to the bottom hinge. Displacements in the lateral x direction are restrained along the beam end stiffeners.

The load is applied monotonically by imposing incremental vertical displacements at the cantilevered beam tip during the analysis to achieve the required range of joint bending moments, and the moment ratio at each side of the web panel.

Modelling Verification

The validation example IS-0 is a symmetrical welded connection with balanced loading, for which collapse is governed by instability of the column web panel in compression. The obtained moment (i.e. the applied beam load multiplied by the distance to the column web centre) versus beam end displacement curve is plotted in Fig. 4 as a

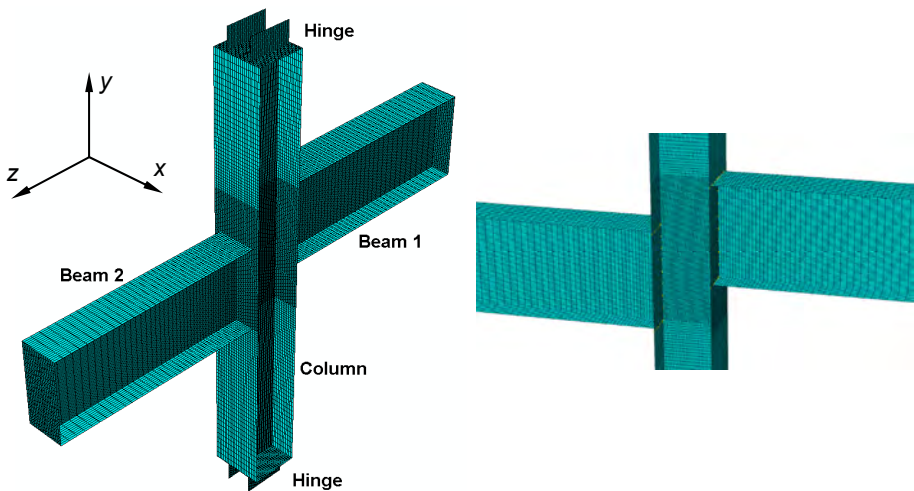


Fig. 3: Finite element mesh (e.g. O3, 34600 shell elements)

solid dark line and compared with the experimental stress (solid grey line) and the finite element results (grey line with markers) of Jordão et al. (2013), who used the commercial code Lusas (FEA 2011). For the model developed in this work, the corresponding von Mises stress plots, at specific load levels on the loading history, i.e. at maximum load, and for a beam displacement of 60 mm (15% h_b , level at which the instability of the column web is very clear), are illustrated in Fig. 5.

The overall agreement with the experimentally observed behaviour is very good, with the latter curve marginally softer in the elastic domain than the numerical predictions. The difference in maximum resistance prediction is merely 0.8%. This provides confidence in the finite element modelling methodology being employed.

PARAMETRIC STUDIES: PRINCIPAL RESULTS

Using the capability of the predicting non-symmetric double-sided welded connection response with the validated finite element modelling approach discussed above, it is possible to evaluate the effect of gap and overlap ratios. A summary of the modelling results is shown in Table 2, in terms of a connection “pseudo-plastic” resistance M_{Rp} to that of the corresponding symmetric double-sided welded connection with balanced moments, $M_{Rp,\beta=0}$. The term “pseudo-plastic” is adopted from Jaspart (1997) and is used below because in some cases the instability phenomenon precedes full plasticity.

The effect of each variable is discussed in the following subsections.

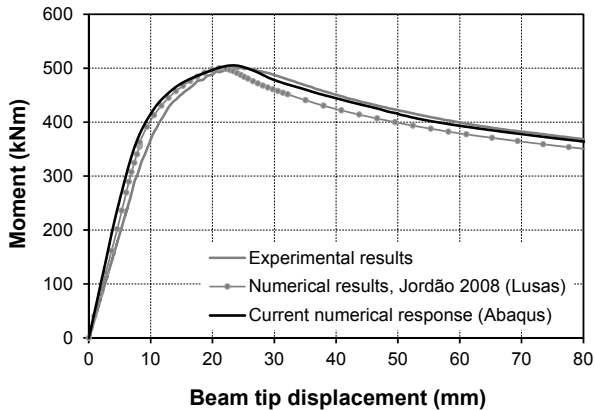


Fig. 4: Moment-rotation plot resulting from implementing the developed finite element model (IS-0) and comparison with existing data

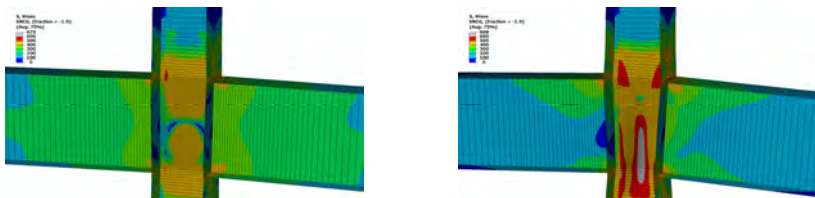


Fig. 5: Test IS-0, von Mises stress contours in the web panel at maximum load level (left) and subsequent collapse (right)

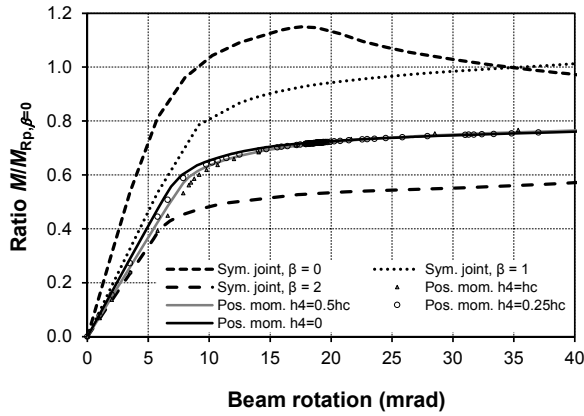
Effect of the Gap Ratio

The comparison results are shown in Table 2 and Figs. 6 and 7 for three representative tests, and the balanced and unbalanced loading cases, respectively. The representative tests are (i) $G_i-0/2$ that use the same member sections as the initial reference tests IS-0/2, (ii) $G_i-H3-0/2$ that uses a deeper slender column, and (iii) $G_i-H5-0/2$ that uses a shorter beam. The following observations are made:

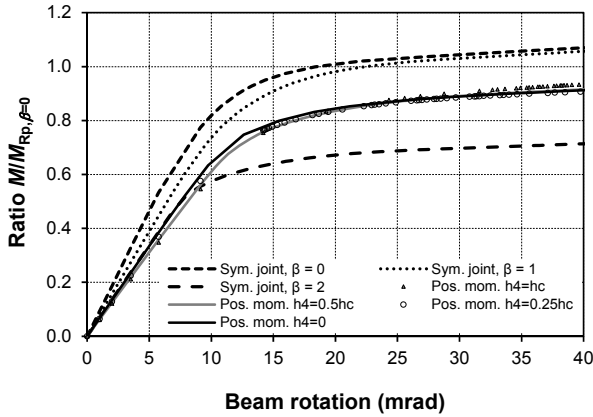
1. For those configurations with beams at the same height (labelled in the graphs as “Sym. joint”, the load-carrying capacity increases as β decreases, i.e. as shear becomes more predominant in the column web panel.
2. The responses for $\beta = 0$ and $\beta = 1$, for the double-sided configuration with symmetric loading and for the single-sided configuration, respectively, are similar for tests that use deep slender columns (e.g. $G_i-H3-0/2$) or short beams (e.g. $G_i-H5-0/2$), because the component “beam flange in compression” is critical.
3. The strength capacities always exceed the “pseudo-plastic” resistance; this indicates that there is a large margin of reserve post-yield (or post-buckling) strength in the column web.
4. The curve labelled in the graphs as “Sym. joint, $\beta = 1$ ” corresponds, in fact, to the single-sided test configuration. In these configurations, the approximate value of β suggested in EN 1993-1-8 is unitary, if the beneficial effect of the shear force in the column is neglected (otherwise, $\beta < 1$). Additionally, the virtual tests carried in this work are

Table 2. Modelling results: “pseudo-plastic” resistance ratio $M_{Rp}/M_{Rp,\beta=0}$

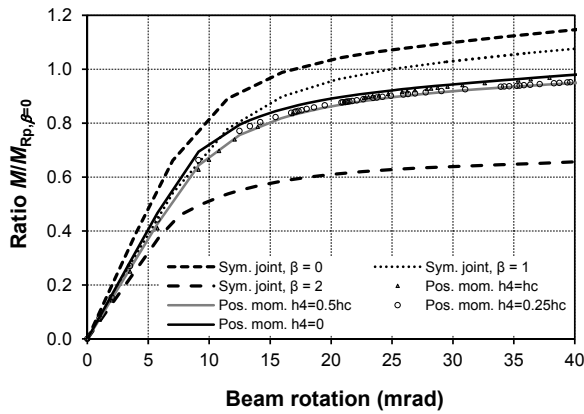
Test		Test		Test		Test		Test	
<i>Initial study set</i>		<i>Series G: symmetric moments</i>		<i>Series G: opposite moments</i>		<i>Series O: symmetric moments</i>		<i>Series O: opposite moments</i>	
IS-0	1.00	G1-0	0.66	G1-2	0.87	O1-0	0.70	O1-2	0.83
IS-1	0.84	G2-0	0.65	G2-2	0.92	O2-0	0.70	O2-2	0.75
IS-2	0.48	G3-0	0.65	G3-2	0.92	O3-0	0.77	O3-2	0.64
<i>Series H</i>		G4-0	0.65	G4-2	0.90	O4-0	0.85	O4-2	0.58
		G1H10	0.59	G1H12	0.76	O5-0	0.95	O5-2	0.50
H1-0	1.00	G2H10	0.59	G2H12	0.80	O1H10	0.60	O1H12	0.80
H1-1	0.70	G3H10	0.59	G3H12	0.81	O2H10	0.61	O2H12	0.72
H1-2	0.45	G4H10	0.60	G4H12	0.82	O3H10	0.67	O3H12	0.64
H2-0	1.00	G1H20	0.72	G1H22	0.85	O4H10	0.71	O4H12	0.58
H2-1	0.90	G2H20	0.73	G2H22	0.92	O5H10	0.83	O5H12	0.50
H2-2	0.55	G3H20	0.71	G3H22	0.92	O6H10	0.95	O6H12	0.44
H3-0	1.00	G4H20	0.71	G4H22	0.95	O1H20	0.71	O1H22	0.80
H3-1	0.95	G1H30	0.83	G1H32	0.90	O2H20	0.75	O2H22	0.70
H3-2	0.62	G2H30	0.83	G2H32	0.98	O3H20	0.85	O3H22	0.59
H4-0	1.00	G3H30	0.83	G3H32	1.00	O4H20	0.90	O4H22	0.53
H4-1	1.00	G4H30	0.83	G4H32	1.00	O1H30	0.80	O1H32	0.77
H4-2	0.84	G1H40	1.00	G1H42	0.93	O2H30	0.82	O2H32	0.67
H5-0	1.00	G2H40	0.98	G2H42	0.93	O3H30	0.90	O3H32	0.58
H5-1	0.91	G3H40	0.98	G3H42	0.95	O1H50	0.89	O1H52	0.68
H5-2	0.60	G4H40	0.98	G4H42	0.95	O2H50	0.95	O2H52	0.60
		G1H50	0.85	G1H52	0.80				
		G2H50	0.85	G2H52	0.90				
		G3H50	0.85	G3H52	0.95				
		G4H50	0.85	G4H52	0.95				



a) Test Gi-0

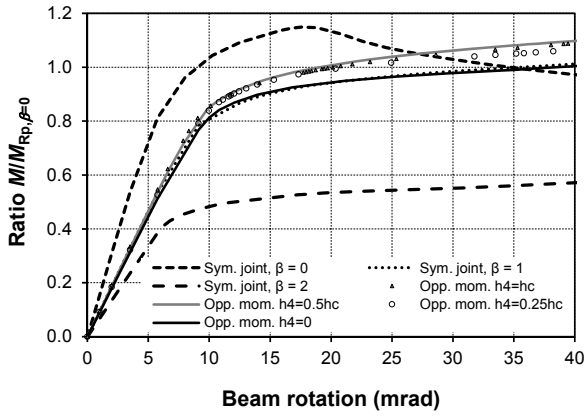


b) Test Gi-H3-0

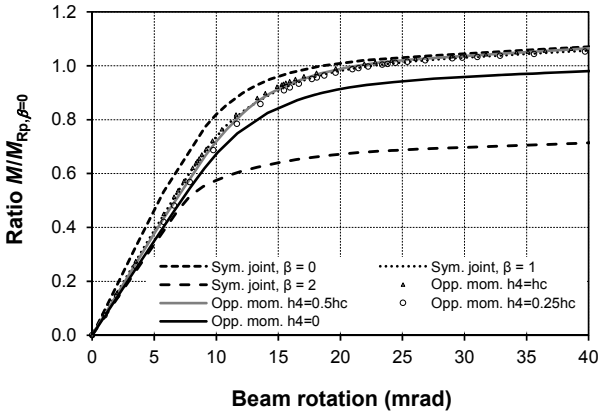


c) Test Gi-H5-0

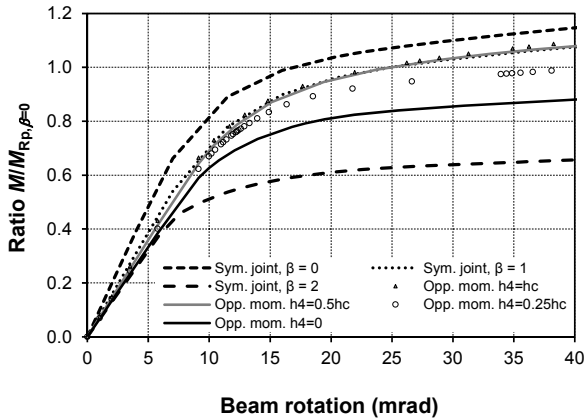
Fig. 6: Non-dimensional moment-rotation plots for test series G with load ratio of 1



a) Test G_i-2



b) Test G_i-H3-2



c) Test G_i-H5-2

Fig. 7: Non-dimensional moment-rotation plots for test series G with load ratio of -1

characterized by quite short columns, of the order of $L_c \approx 4h_b$ (Jordão et al. 2013). In these cases, the exact value for β is $1 - (h_b - t_{fb})/L_c \approx 0.75$ (Faella et al. 2000).

5. In the case of symmetrical beam loading, see Fig. 6, the curves are seen to be practically coincident, as well as the resistance predictions (Table 2), and in all cases “1” $< \beta < 2$. (“1” appears here between inverted commas because this is not an exact value, for the reasons explained above).

6. For non-symmetrical beam loading, see Fig. 7, the predictions for beams with a gap are systematically close to the curve for $\beta \approx “1”$.

Effect of the Overlap Ratio

Figures 8 and 9 and Table 2 compare the strength behaviour for overlapped beams (representative cases identical to the above). Comparisons demonstrate that:

1. The variation in (“pseudo-plastic” and ultimate) resistance due to larger overlap ratio values is quite significant.

2. For beam load ratios of $P_2/P_1 = 1$ (positive moments in both sides of the column web), “1” $< \beta < 2$, corresponding $\beta \approx “1”$ to higher overlap ratio values.

3. For beam load ratios of $P_2/P_1 = -1$ (moments of opposite signs in both sides of the column web), again “1” $< \beta < 2$, now with $\beta \approx “1”$ corresponding to lower overlap ratio values.

DESIGN IMPLICATIONS

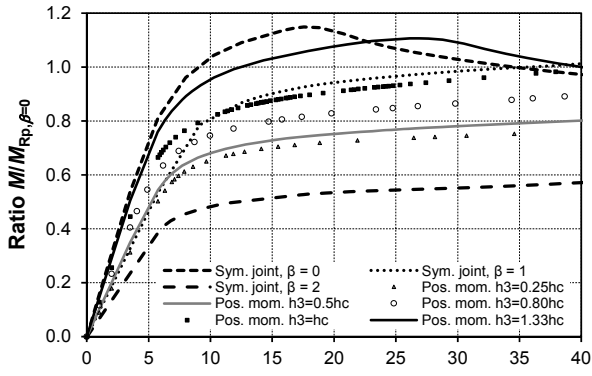
Numerical values for the transformation parameter β are proposed below, based on the results of the 106 tests described and discussed in this paper, and the original proposals from Brown (2013). Tables 3 and 4 set out safe estimations for β for inclusion in EN 1993-1-8. From these values, probably the least straightforward is the proposed $\beta = 1$ for double-sided connections with positive moments and a gap between the two beams. As discussed above, the curves are seen to be practically coincident and $0.75 < \beta < 2$, with $\beta \approx 0.75$ being a more precise value for our single-sided joints. A unitary transformation parameter ultimately corresponds to a case where the two joints can be analysed separately. A careful analysis of the stress contours obtained in this numerical study suggests that this is precisely the case. For illustration, Fig. 10 shows von Mises stress contours for two test joints.

Table 3. Transformation parameter for configurations with a gap between beams

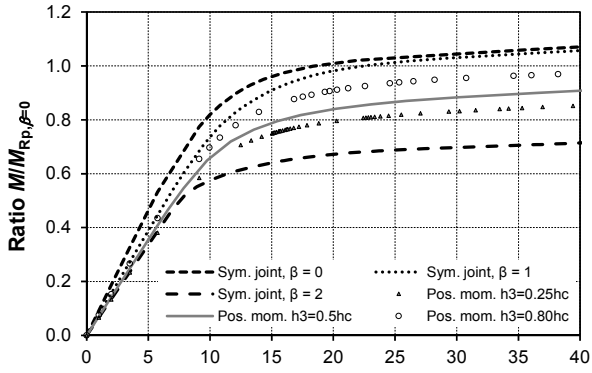
Positive moments	For any gap	$\beta = 1$
Moments of opposite sign	For any gap	$\beta = 1$

Table 4. Transformation parameter for configurations with overlapped beams

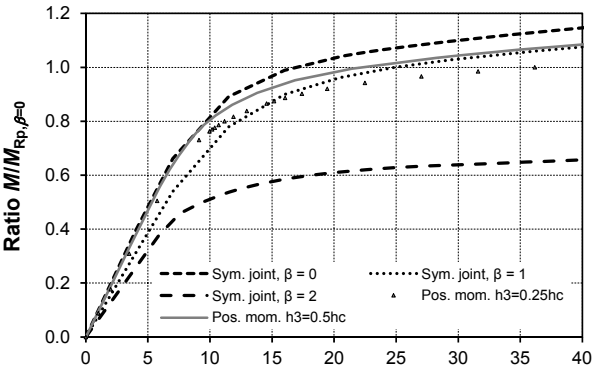
Positive moments	When $h_3 > 0.5h_c$		$\beta = 1$
	When $h_3 \leq 0.5h_c$		$\beta = 2$
Moments of opposite sign	When $h_b \leq h_c$	For any overlap ratio	$\beta = 2$
	When $h_b > h_c$	$h_3 > 0.5h_c$	$\beta = 2$
$h_3 \leq 0.5h_c$		$\beta = 1$	



Beam rotation (mrad)
a) Test O_i-0

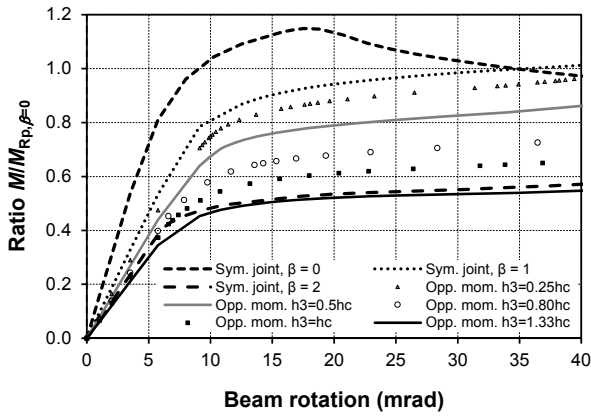


Beam rotation (mrad)
b) Test O_i-H3-0

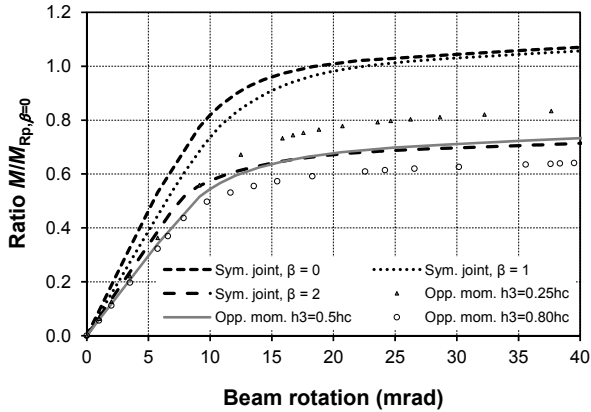


Beam rotation (mrad)
c) Test O_i-H5-0

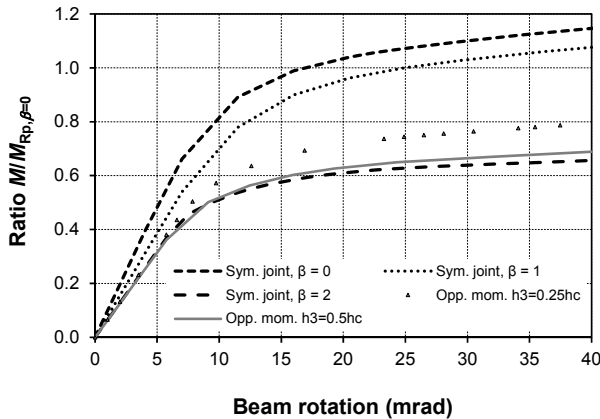
Fig. 8: Non-dimensional moment-rotation plots for test series O with load ratio of 1



a) Test O_i-2



b) Test O_i-H3-2



c) Test O_i-H5-2

Fig. 9: Non-dimensional moment-rotation plots for test series O with load ratio of -1

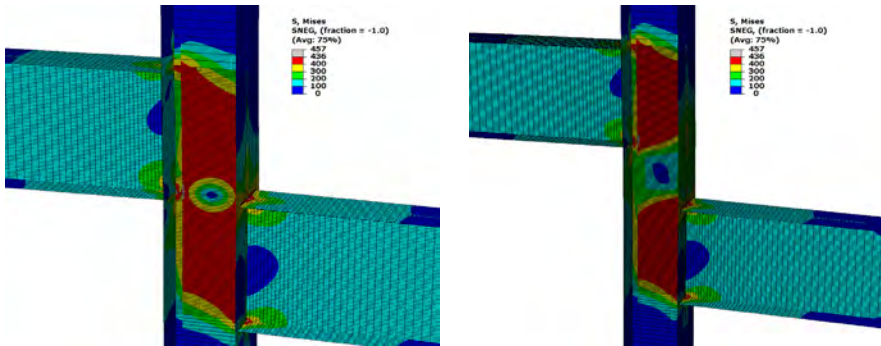


Fig. 10: von Mises stress contours in the web panel at “pseudo-plastic” resistance level for G1-0 ($h_4 = 0$) (left) and G3-0 ($h_4 = 0.50 h_c$) (right)

SUMMARY

Findings from a comprehensive finite element analysis of non-symmetrical double-sided joint configurations are summarized in this paper. The main design implications are extracted and can be extended to the case of bolted joints as well. Suggestions for the transformation parameter β are made for future inclusion in EN 1993-1-8.

REFERENCES

- Abaqus Manual, Version 6.14 (2015). Dassault systems, <http://www.simulia.com>.
- Bayo E., Loureiro A. and Lopez M. (2015). “Shear behaviour of trapezoidal column panels I: experiments and finite element modelling”. *Journal of Constructional Steel Research*, Vol. 108 (pp. 60-69).
- Brown D. (2013). “Web panel resistance: observations on EN 1993-1-8”. *The Steel Construction Institute – internal document*, (presented at the 102th ECCS/TC10 meeting in Liège, April 2013).
- CEN - European Committee for Standardization (2005). *EN 1993 Design of steel structures, Part 1-8: Design of joints*, Brussels.
- Faella C., Piluso V. and Rizzano G. (2000). *Structural steel semi-rigid connections – theory, design and software*, CRC press, Boca Raton.
- FEA (2011). LUSAS: *Finite element analysis system*, Version 14.5-4, Produced by FEA Ltd., Kingston-upon-Thames.
- Guisse S. and Jaspert J.P. (1995). “Stress interaction in column webs”. *Proceedings of the IX International Conference on Metal Structures*, Poland (pp. 147-156).
- Jaspert J.P. (1997). “Contributions to recent advances in the field of steel joints. Column bases and further configurations for beam-to-column joints and column bases”. *Post-doctoral thesis*, University of Liège (<http://orbi.ulg.ac.be/handle/2268/30425>).
- Jordão S., Simões da Silva L. and Simões R. (2013). “Behaviour of welded beam-to-column joints with beams of unequal depth”. *Journal of Constructional Steel Research*, Vol. 91 (pp. 42-59).

DETAILING CONNECTIONS – AN INTEGRATED APPROACH FROM INCEPTION TO FABRICATION

Preetam Biswas PE, Associate Director,
Skidmore, Owings and Merrill, LLP, 14 Wall Street, New York, NY 10005,
preetam.biswas@som.com

Ronald B. Johnson SE, SECB, Associate Director,
Skidmore, Owings and Merrill, LLP, 225 S Michigan Av, Chicago, IL 60604,
ronald.johnson@som.com

Georgi I. Petrov, PE, AIA, Associate
Skidmore, Owings and Merrill, LLP; 14 Wall Street, New York, NY 10005,
georgi.petrov@som.com

ABSTRACT

Extreme fast track building construction schedules has resulted in a shorter time from project conception to the completion of construction. In addition, 3D digital modelling tools now available to designers mean that structures are more complex and have unique geometries, which were inconceivable a few years back. Coupled with a desire to build big but at the same time build economical has led to the need for the development of design and detailing procedures that yield simplified connections that make them affordable and constructible. The Integration of the design, detailing and fabrication process for steel structures has not only helped to drastically reduce the time-frame for project realization, but has also enhanced quality and enabled the creation of optimal structures with efficient use of materials and a reduction of carbon footprint.

INTRODUCTION

With more than 50% of the human population living in cities, the demand for space has been increasing exponentially. Going vertical and avoiding large sprawling cities provide one of the most sustainable solutions to rapid urbanization. Compact cities improve the standard of living for their inhabitants by reducing travel times and increasing access to public transportation. Very often however, large transportation infrastructure and nodal hubs occupy large tracts of uninhabitable and non-desirable land in the heart of urban centers which otherwise would be financially very lucrative for developers. Building departments of big cities worldwide are allowing construction using the air-rights above transportation infrastructure to maximize appropriate use of valuable real estate. However, this also results in the design of complex structures with unique and challenging interface with foundation systems. To deal with cost escalation in real estate, developers have capitalized on such opportunities for utilization of previously

deemed 'unusable areas' since cost premiums, if any, associated with it far outweighs the overall financial gains.

Increasingly, developers worldwide have also initiated marketing that hinges on creating 'first of kind', 'tallest', 'grandest', 'superior spatial experience', 'column-free spans' etc as the mode to beat out competition. These promises then translate into demand for heroic structures that push the boundary of conventional systems. However, it would be a mistake to assume that these desires are always supported by developers willing to implement appropriate increase in the project budget. On the contrary, such superfluous demands are not restricted to unique projects but are included in the narrative of more and more regular projects. In other words, in most cases economical solution with easy to build structural system becomes the most appropriate medium to bridge the gap between project aspirations and budgetary constraints.

Along with this comes the increasing demand for reduced wait period between project conception and final completion. On one hand contractors have been grappling with demand in reduced construction time and on the other hand designers have been tasked with production of optimal and cost efficient design solutions within a constricted design phase. One solution, which is being increasingly implemented is the overlapping of the design and construction phases of projects.

COMPLEX GEOMETRY AND DIGITAL MODELLING

Some of the unique and evolving geometries in new generational design concepts were inconceivable a few years back. Much of this progress can be credited to the digital modelling tools available for designers capable of creating these unique geometry. Although these tools have developed over many years, their impact in the final architectural products has become more prominent lately because of the ability of the design tools to easily communicate with software guiding the actual building process. The simplicity of the information exchange between platforms however has to be a conscious decision of the users in order to eliminate the possibility of mismatch between digital model and fabricated product.

The history of digital modeling tool stretches back to the 1970s with the emergence of the first graphics programs. By the late 1980's and early 1990's computer aided design CAD packages, which could generate complex geometry using non-uniform rational basis splines (NURBS) began to appear. The mathematics behind NURBS has been known since before the inventions of the computer, but their utility in CAD and graphics was quickly recognized (Piegl 1991). They offer a number of useful features, for example the ability to represent both standard shapes such as conics and surfaces of revolution, as well as free form curves and surfaces. Their control points allow for easy manipulation and their evaluation is fast and computationally simple. Rhinoserous (often referred to as Rhino) Robert McNeel & Associates has emerged as one of the most popular NURBS CAD programs.

Another computational tool, which emerged in the early 1990s was Constraint driven design (CDD) - also referred to as parametric design (Aish 1992, Shea et.al. 2005). Early software packages include Pro/Engineer (ProE) by Parametric Technology and

Catia by Dassault Systems. These tools were first explored in the aeronautics and automotive industries, most famously in the design of Boeing's 777 wide-body jet airliner (Norris 1995). Architects and other designers began to explore the possibilities of parametric software initially, as a means to allow computer aided manufacturing (CAM) of geometrically complex forms, such as the curving walls and roofs of the Guggenheim Museum in Bilbao. More recently the new CDD CAD system by Robert McNeel & Associates called Grasshopper has greatly enhanced the efficiency with which architects and engineers collaborate in the design of complex systems. Grasshopper, which runs as a plug-in for Rhino, is a graphical algorithm editor that facilitates the creation of associative models via a visual interface while requiring little knowledge of programming or scripting.

These simplified programming tools at the hands of designers have led to some degree of ease in the creation of eccentric geometries. As always, these eclectic and complicated geometries also need a rational structural system supporting them in order to make them buildable.

ADAPTATION OF STEEL STRUCTURES FOR CONSTRUCTABILITY

Integrating the design of the general structure and the design and detailing of connections allows for a more effective use of modern steel fabrication machinery. Computerized CAD/CAM design makes the fabrication of even quite complicated geometries to be relatively easy.

Computerized cutting machines allow for very precisely formed edges which in many cases eliminates or at least minimizes the need for additional grinding or milling after cutting. The greater accuracy in fit-up makes even complex geometries with curved shapes possible. Figure 1 shows an example of what is possible for large scale concrete filled columns sloping in both directions.

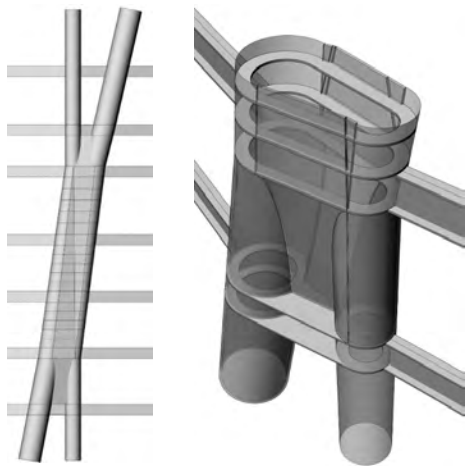


Figure 1: Concrete Filled Tube Column Joint

The use of automated welding machines can produce 3 plate welded beams and girders at a cost very similar to that of a rolled shape. This means that beams can be configured with a geometry which optimizes the efficiency of the member and simplify connections. For example top flanges of composite beams can be smaller than the bottom flange or flanges can be wider so that bolted connections are easier. Similarly columns can be built-up as either 3 plate welded sections or box sections with lighter weight than cover plated rolled sections and usually at lower fabrication costs. Built-up sections can also be proportioned to have thinner plates

High strength steels in addition to potentially reducing the overall material, i.e. purchase cost of the steel, can also reduce fabrication costs by eliminating the need for cover plates. Where complete penetration welds are required, high strength steel with reduced pre-heating and post-welding requirements simplifies the fabrication process and reduces fabrication time.

OPTIMIZATION THROUGH SIMPLIFICATION OF GEOMETRY

Although 3D software and modern fabrication techniques allow very complex geometries to be feasible, the least cost and best engineering solution is the still in developing the simplest configuration possible. Integrating the design and detailing allows options for the connection configurations to be explored at the same time as the member design. Discovering conflicts or challenging connections early in the design process allows member sizes and positions to be adjusted to simplify the connection resulting in an overall more efficient solution.

While it is true that in some cases the best solution to a complex connection is evolved by discretizing the work-point geometries, both horizontally and vertically, of different structural elements framing into a connection; in some cases, the simplification of geometry is required at a macro level, through rigorous and logic driven definition of global geometry of a complex shape.

One such example is a structure which has a faceted roof with 142 unique facets that intersect at unique angles (Besjak et.al. 2013). Here the success lay in defining the geometry through as few parameters as possible and by keeping the count of distinct elements to a minimum. The entire geometry was defined through the vertices called as nodes with work-point described in 3D space. Straight lines joining the nodes defined the planes. Straight primary members ran along the facet edges with secondary members connecting their midpoints and running within the plane of each facet. The complexity of the geometry was resolved entirely in nodes with seven unique node types with a few different parameters that resolved the entire faceted geometry.

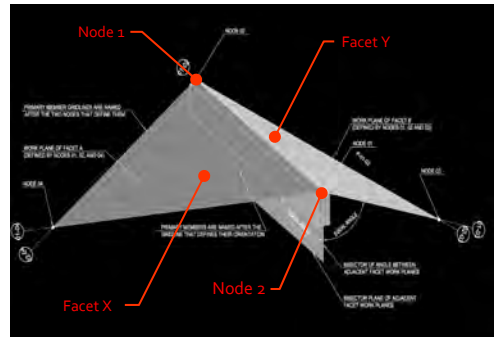


Figure 2: Primary Geometry Definition.

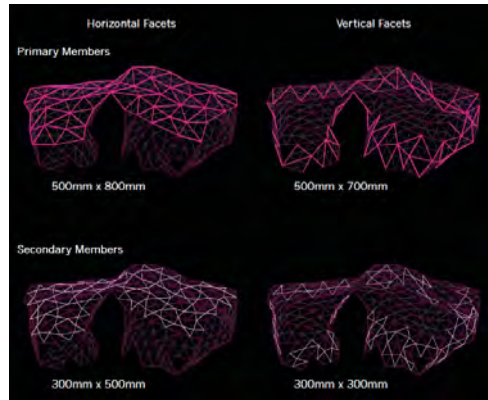


Figure 3. Faceted Roof Primary and Secondary Member Types and Sizes.

To maximize the efficiency of fabrication and installation the entire structure consisted of only two sizes for the primary members and correspondingly two sizes for the secondary members. This allowed for quick installation in that there was only one type of bolted field connection between primary members and nodes and similarly one type of bolted field connection between secondary members and primary members.

CONNECTION CONFIGURATION FOR EASE OF FABRICATION AND ERECTION

When configuring complex joints the most important consideration is how it will be fabricated. This is even more important than the member size or the sizing of the connection itself since the first consideration need to be that the connection can in fact be constructed and erected. For open sections, this is usually not a problem, but with closed sections, the type and configuration of welds needs to be such that each step of the assembly can be completed prior to the next step. Each weld should allow the welder access at about a 45 degree angle. Where assemblies are large, members may need to be increased in size so that there is enough width for the welder to reach far enough inside. It is invaluable during the configuration of large connection assemblies to have the involvement of an experienced fabricator who has had direct experience on the shop floor.

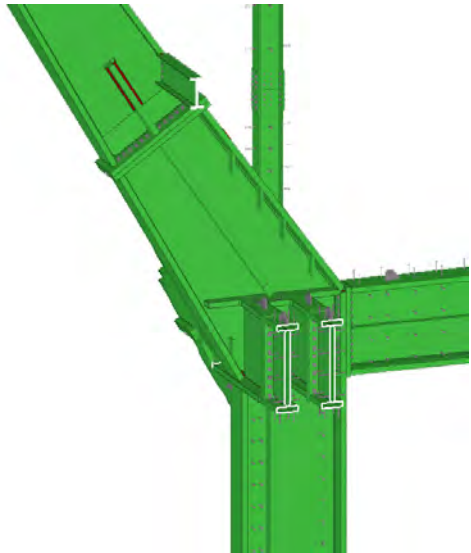


Figure 4: Complex Nodal Connection

Welds should not cross over each other. It is also important to include the weld access holes for CJP welds.

Access for bolting also needs to be considered. Again avoiding box sections simplifies the design. Where box sections are required, one solution is to stop one set a plates short of the connection this is often practical because box column sections are usually used to control slenderness so the full box is not required on the ends. Where the box section is necessary at the connections for torsion or other reasons, then hand holes are required to be provided.

CONNECTION GEOMETRIES FOR REDUCED COST AND IMPROVED QUALITY

The first and most important step in design and detailing connections is the selection of appropriate members during the design stage. Automated structural design tools usually select for the least weight but this procedure will rarely be the most cost

effective solution since the least weight member will often have a more complex connection. For example, HSS sections as bracing members are generally least weight but double angles, although heavier, are simpler to fabricate and easier to erect. The design process should be a continual consideration to balance the weight efficiency of the structure with cost and time for the fabrication and erection. Integrated design and detailing facilitates this process.

Although there are no hard and fast rules for member selection and connection detailing, the following are some “rules of thumb” which can assist in creating a more cost effective solution and a more structurally robust structure.

Shear Connections

- Standardize shear connections.
- Choose member sizes and connection types which allow a single vertical row of bolts.
- Use double angle connections for heavier loads.
- Consider having all fabrication welding on either the columns or the beams—not both. Shops often have separate fabrication lines for welding and bolt hole punching/cutting. By having the member utilize only one line reduces costs.

Moment Connections

- Field connections should be bolted and designed for the actual design moments.
- Limit connection design moments to 70% to 80% of the member capacity in order to avoid net section capacity problems.
- Avoid shallow, heavy rolled sections as moment connected beams. Where shallow members are needed, use built-up sections with relatively wide flanges in order to maximize the net area at bolted connections.
- Moment connected beams should have a minimum of a 7 inch wide flange to allow adequate net area at the connection.
- Avoid complete joint penetration welds.
- Avoid box section and web cover plated columns. Where rolled sections will not be adequate for the load, use built-up 3 plate sections which will dramatically simplify the connections.

Trusses

- As much as possible make the tension plates/members of a connection continuous and make the interrupted members those in shear or compression.
- Highly loaded truss members should use nodes at the connections (Figure 5).
- Nodes and the connecting members should have a minimum of 18 inches clear between flanges to facility access for welding. In



Figure 5: Transfer Truss Bottom Chord

principle the distance between flanges should be at least $\frac{2}{3}$ the depth that welder will need to reach in to make the weld.

- Use built-up sections for heavy truss members—this allows more flange width for bolts.
- Force transfers at welded joints should be in shear with fillet welds or for thick plates, partial penetration welds.
- Use direct bearing connections for compression members and bolted flange connections for tension members. Note that the gusset plates shown in Figure 5 do not have any welds in the direction of the tension force transfer and the compression truss web member has an end plate connection.
- Consider rotating members 90 degrees for heavy trusses—this minimizes welding or even possibly allows a fully bolted connection (Figure 6)
- Detail connections for a continuous, direct load path to the support—avoid shifting forces transverse to the load path.
- Limit flange thickness to 2 inches if possible and 3 inches maximum. Use built-up if these limits will be exceeded. These limits minimize the amount material required at CJP welds, enhance the net area capacity at bolted joints and increase access at joints for welding



Figure 6: Long Span Truss Bottom Chord

OPTIMIZATION OF MATERIAL THROUGH EFFICIENCY OF CONNECTIONS

The design of connections is vitally important in capturing fully the potential savings in material and time that are provided by form-finding and optimization exercises. Although computing techniques for modeling and analysis, described below, have matured in the past decade it is still essential that the design begin as it always has, by sketching with pencil and paper. It is important in the very early stages to test ideas that are only approximate but contain the essential features. The computer forces the designers to be precise, however is it often useful to be able draw various views and plans of a connection that may not be exact and fully consistent with each other. Sketching by hand is also important because the design process is always a collaborative venture. Sitting as a team to bounce ideas while sketching together is still an essential first step in the design process. Once the general typology of a connection is worked out the next step is to draw the connection in a general purpose CAD program. This step adds precision while still allowing for making quick adjustments.

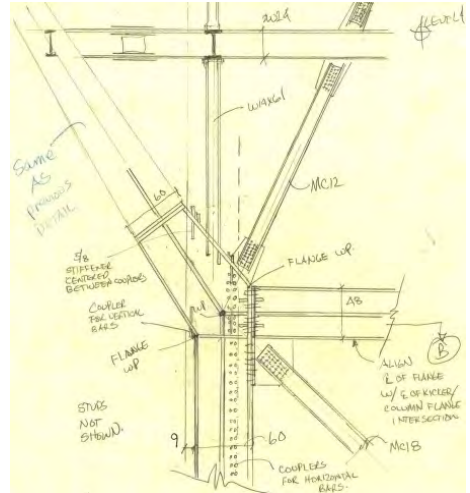
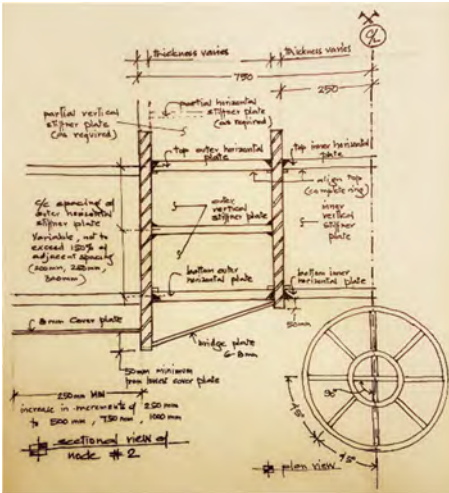


Figure 7: Initial Hand Sketches of Connections

If there are many connections in the project with the same typology but different geometry, it is useful to invest the time to build a parametric model of the connection that can be adapted to various geometries. ProE and Catia remain the two best modeling tools for this purpose. If on the other hand the project is composed of nodes with unique typology modeling directly in Tekla is a common option.



Figure 8. Node 3D solid FE mesh

Connections that reconcile complicated geometry are usually too complex to be analyzed by traditional hand calculations thus a 3D finite element (FE) analysis is usually required. The choice of using 2D shell elements versus 3D solid elements is important, because it determines how the model is built. Although most modern general purpose analysis programs have some meshing capability, the geometry has to be prepared and cleaned in order to get good results. Meshing a connection using shell elements is easier and faster and in most cases is sufficient to demonstrate that the connection has the required strength.

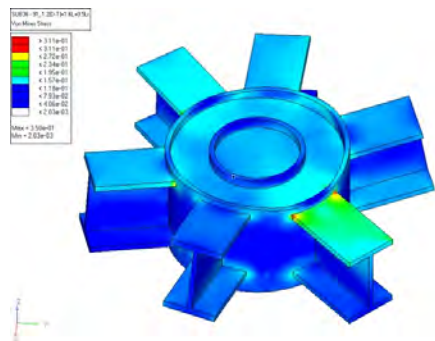


Figure 9. Node Von Mises Stress Analysis

Most connections built out of plate steel lend themselves to analysis with 2D elements. However, careful attention must be paid in preparing the geometry since a geometry model that is composed of the middle surfaces of the plates has to be generated. On the other hand a 3D solid model is inherently more accurate in modeling the state of stress in a complex connection. Solid models however require more time and skill to mesh. Two of the leading software packages for both 2D and 3D FE analysis are HyperMesh by Altair Engineering, Inc. and Strand7 by Strand7 Pty Ltd.

Once the connection has been meshed successfully, special attention has to be paid to loading the model correctly. The overall building analysis model usually applies the member forces at the work points where the connecting elements meet, which is a typically a significant distance from the actual face of the connection. One solution is to transfer the forces to the correct location using rigid links. At SOM this is achieved by the use of in-house scripts that reads the forces from the analysis model and applies them to the connection model (Besjak et.al 2013). For each model the Von Mises stress at each element is checked, and verified to be less than a certain percentage of the yield strength of the steel used.

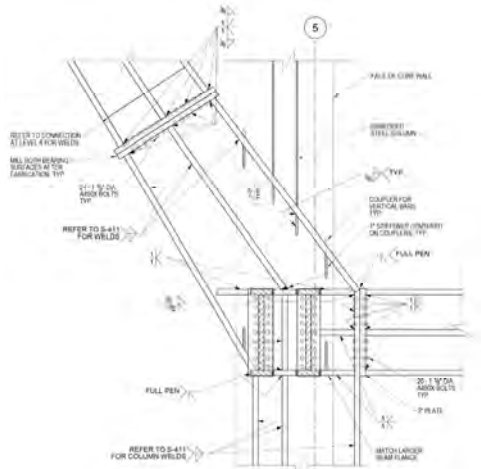


Figure 10. Documentation of Complex Node

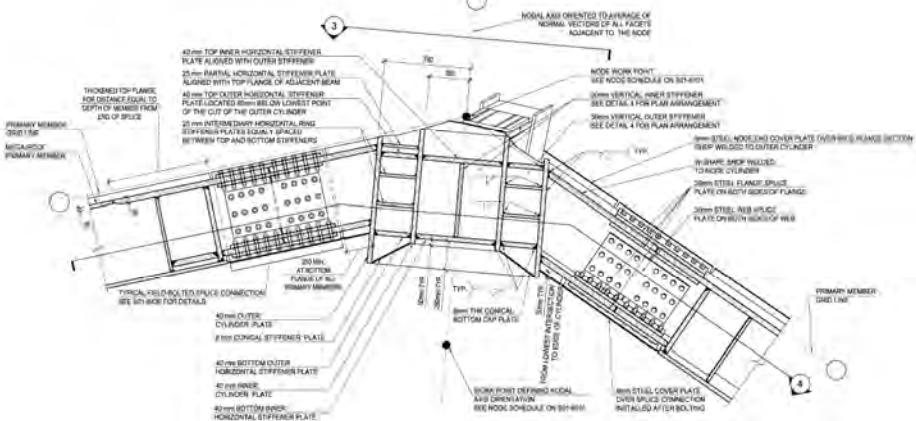


Figure 11. Documentation of Node design

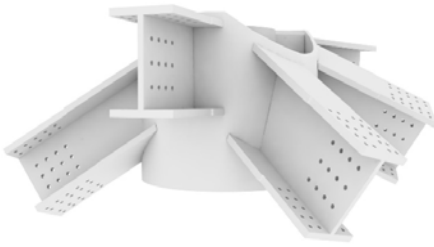


Figure 12. Node 3D model



Figure 13. Node Fabrication



Figure 14: Node being positioned on site



Figure 15: Connecting members to node



Figure 16: The completed Structure

DIGITAL INFORMATION EXCHANGE

The way that complex designs are communicated to the fabricators and erectors is being transformed by the development of novel digital tools. Two dimensional drawings are still required to meet contractual and legal obligations and as a permanent record of the design, however increasingly the relevant information, needed by the fabricator to construct the structure, is being transferred digitally in the form a three dimensional model. The traditional approach where the designer finished a complete set of 2D construction documents and then hands them over to the steel fabricator to develop 2D shop drawings using an unconnected CAD model is insufficient to convey complex geometry. For more than a decade the industry standard for detailing steel structures in 3D, has been Tekla Structures by Tekla Corporation. It is a powerful tool for generating and tracking both simple and complex steel connections. Generating shop drawings from a Tekla model is now becoming the standard practice. However how the final Tekla model is created is evolving. For projects with intricate geometry or a compressed schedule or both, the design engineers are building part or the entire Tekla model before handing it over to the steel fabricator for final preparation of shop drawings. Additionally Tekla allows the work to proceed on a shared server where the current model exists in the “cloud”. In this configuration, any changes, substitutions, or additional of temporary steel to be used by the fabricator and erector, can then be reviewed by the design team even before the production of the final shop drawings.

Similarly the shop drawings are also moving towards a fully digital exchange. They still arrive as 2D drawings to be used as the record set, however it has become standard practice that they are produced directly from the 3D Tekla model. Although still printed out for record, increasingly the delivery, mark-up, and return of shop drawings is being done entirely via digital files, mainly pdf. When the 3D connections are intricate, curving, or complex, the 2D drawings may become hard to read, thus the real evaluation for the accuracy of the design can only be done by reviewing the actual 3D Tekla model.

The ability to incorporate user defined parameters makes the Tekla model a useful tool to follow the progress of each piece of the structure. Color coding the pieces provides an easy to understand 3D graphical report on the status of the project and helps to identify problem areas and zones which require the attention of the project team.

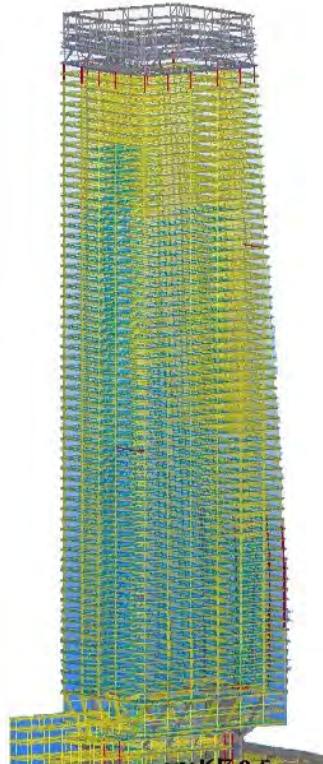


Figure 17: Tekla model showing the status of each member

CONCLUSION

Harnessing the benefits of cloud based 3D modelling and information exchange, the process of approval of fabrication drawings could be reduced drastically. Coupling this with web based conference with the ability to share and work on a single model in real-time meant that comments and decisions that would affect the final outcome of the structure and connections which would typically take weeks and months could be resolved in a couple of hours. Early in the design phases, constructability related input from the fabrication detailer back to the design team results in definition of connection geometry that accurately represents the final assembly. This results in analysis and design of true assemblies which incorporate material loss due to access holes etc. at the design stage itself. This obviously translates into optimum use of material, labor and time. Hyper fast track projects which capitalizes in design and construction integration process, along with efficient use of material is truly a response to the needs of the construction industry today.

REFERENCES

- Aish, Robert, "Computer-aided design software to augment the creation of form", in: Francise Penz (ed.), *Computer in Architecture*, Longman, 1992.
- Besjak, Charles, Preetam Biswas, Georgi I. Petrov, Blake Altshuler, "King Abdullah Financial District Conference Center", Proceedings of Structures Congress 2013, Pittsburgh, PA, 2-4 May 2013.
- Besjak, Charles, Preetam Biswas, Alexandra Thewis, Raymond Sweeney, Damayanti Chaudhuri. "Chhatrapati Shivaji International Airport—Integrated Terminal Building". *Structural Engineering International*. January 2013. pg 8.
- Shea, Kristina, Aish, R., and Gourtovaia, M. "Towards integrated performance-driven generative design tools." *Automation in Construction* 14 (2005) pg. 253–264.
- Norris, Guy. "Boeing's Seventh Wonder." *IEEE Spectrum*. October 1995. pg. 20-23.
- Piegl, Les. "On NURBS: a survey" *IEEE Computer Graphics and Applications*. January/February 1991 vol.11 n.1, pg 55-71.

ACKNOWLEDGEMENT

Charles Besjak PE, SE, FAIA, Director of Structural Engineering,
Skidmore, Owings and Merrill, LLP, 14 Wall Street, New York, NY 10005,
charles.besjak@som.com

RECENT INVESTIGATIONS INTO THE SLIP FACTOR OF SLIP-RESISTANT CONNECTIONS

Natalie Stranghöner, Nariman Afzali, Jörn Berg
University of Duisburg-Essen, Institute for Metal and Lightweight Structures, Essen,
Germany
natalie.stranghoener@uni-due.de, nariman.afzali@uni-due.de, joern.berg@uni-
due.de

Peter de Vries
Technical University of Delft, Stevin II Laboratory, Netherlands
p.a.devries@tudelft.nl

ABSTRACT

Deformations in slip-resistant connections have to be prevented either for serviceability or ultimate limit state reasons. For this reason, EN 1090-2 specifies slip factors for often used surface conditions. For deviating surface conditions, slip factors have to be determined experimentally according to Annex G of EN 1090-2. Current practice shows that the slip test procedure according to EN 1090-2 is not clear in detail and allows several interpretation possibilities. This potentially leads to different slip factors for identical surface conditions. In the frame of the present contribution, the influences of different surface conditions, preloading levels and loading velocity on the slip resistance behaviour of connections are presented. This paper attempts to present an overview on the ongoing research activities on slip factors of slip-resistant connections achieved in the frame of the European RFCS-research project SIROCO and in industrial projects.

INTRODUCTION

Bolted slip-resistant connections according to (EN 1993-1-8, 2009) are used in different type of steel structures such as lattice towers, cranes, bridges as well as wind turbine towers. These structures can be subjected to heavy impact loads, significant load reversal or fatigue. The mechanical performance of these structures depends on slip resistance behaviour of the connections. For this reason, the design slip resistance $F_{s,Rd}$ in the ultimate limit state (ULS) resp. $F_{s,Rd,ser}$ in the serviceability limit state (SLS) according to EN 1993-1-8 is calculated considering the preload in the bolts $F_{p,C} = 0,7 f_{ub} A_s$ (with f_{ub} : tensile strength of the bolt and A_s : tensile stress area of the bolt), the surface condition of the clamped parts specified by the slip factor μ , the number of interfaces n , the size of the holes (k_s) and the applied tensile force $F_{t,Ed}$ (ULS) resp. $F_{t,Ed,ser}$ (SLS), see Eq. (1):

$$F_{V,Ed,(ser)} \leq F_{s,Rd,(ser)} = \frac{k_s \cdot n \cdot \mu \cdot (F_{p,C} - 0,8 \cdot F_{t,Ed,(ser)})}{\gamma_{M3}(= 1,25) \text{ resp. } \gamma_{M3,ser}(= 1,10)} \quad (1)$$

(EN 1090-2, 2011) specifies slip factors for often used surface conditions. For deviating surface conditions, slip factors have to be determined experimentally according to Annex G of EN 1090-2. Current practice shows that the slip test procedure according to EN 1090-2 is not clear in detail and allows several interpretation possibilities.

This potentially leads to different slip factors for identical surface conditions. Furthermore, a survey of existing investigations regarding the determination of slip factors on the basis of international guidelines/standards has shown that most of the achieved slip factors for (almost) identical surface conditions are not comparable at all. The main reasons are:

- different testing procedures (compression test, tension test, test arrangement etc.), e. g. (RCSC, 2009), Annex G of EN 1090-2, (TL-TP-KOR-Stahlbauten, 2002) etc,
- different preload levels in the bolts,
- measuring of the preload in the bolt at beginning of testing (yes/no),
- constantly measuring of the preload in the bolts during testing (yes/no),
- application of different measuring methods of the coating thickness,
- calculation of the slip factor considering the different preloads in the bolts: nominal preload, preload at start of testing or actual preload at slip of the connection,
- different determination points of the slip load: at 0.15 mm slip (EN 1090-2), at 0.3 mm slip (Gruintjes and Bouwman, 1984), at 0.5 mm slip or at the highest peak of the load-deformation-curve, if it occurs before 0.5 mm (RCSC),
- different positions of the measurement devices for the slip deformation,
- only static slip tests (yes/no),
- creep tests / extended creep tests (yes/no),
- slip factor calculated as minimum value, mean value or 5%-fractile etc.

Currently a comprehensive European RFCS research project is going on (SIROCO), in which various aspects of the EN 1090-2 test procedure are evaluated by conducting experiments on bolted slip-resistant connections with different preload levels and varying conditions of the faying surfaces. The research comprises both carbon and stainless steel slip-resistant connections. For the latter one, in a first step the preloading behaviour is investigated with the aim to develop reliable preloading conditions. The present contribution gives an overview on the ongoing research activities on slip-factors of slip resistant connections made of carbon steel achieved in the frame of SIROCO with regard to the influence of the preload level and the loading velocity.

SLIP FACTOR TEST PROCEDURE ACCORDING TO EN 1090-2

EN 1090-2 prescribed a generalized experimental procedure to obtain the slip factor. The test procedure consists of a three step test procedure as shown in Fig. 1. Four tests must be conducted under an incremental tensile loading condition at normal speed. The duration of the tests shall be 10 min to 15 min. The question arises: how much is the normal load and how is it possible to predict the duration of the test before testing?

The individual slip value μ_i , the mean value μ_m and the standard deviation S_μ shall be derived from the following equations:

$$\mu_i = \frac{F_{si}}{4F_{p,C}}, \mu_m = \frac{\sum \mu_i}{n}, S_\mu = \sqrt{\frac{\sum (\mu_i - \mu_m)^2}{n-1}} \quad (2), (3), (4)$$

The slip loads F_{si} are defined as the load at which a slip of 0.15 mm is observed. The next question arises: Does this criterion cover all load-slip-behaviours? This evaluation criterion is different in other standards and recommendations. RCSC and ECCS T10 (Gruintjes and Bouwman, 1984) recommended 0.5 mm resp. 0.3 mm.

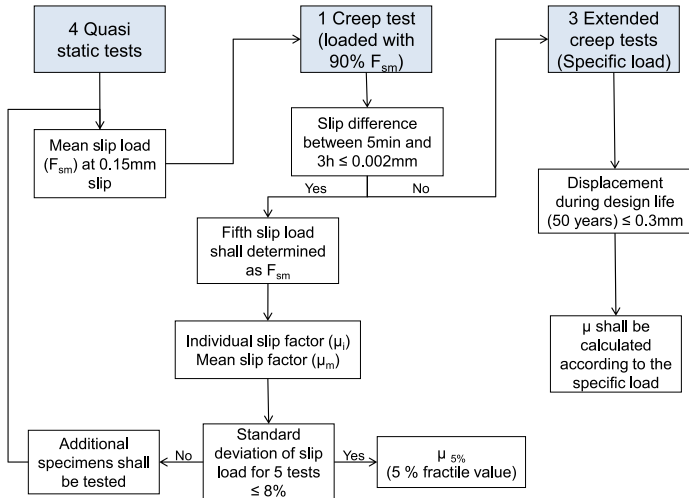


Fig. 1. Three step test procedure according to EN 1090-2, Annex G

With the fifth test specimen, a creep test has to be carried out with 90% of the mean slip load F_{sm} from the first four tests. Optimally, the test shall last 3 hours to investigate the behaviour of the joint under sustained loads. If the difference between the recorded slip at the end of 5 min and 3 hours after the full load application does not exceed 0.002 mm, the slip load for the specimen under long term condition must be specified as for the previous four tests. If the difference between the slips exceeds 0.002 mm, at least three extended creep tests must be performed. The standard deviation S_{Fs} of the ten slip load values which are obtained from the five specimens should not exceed 8% of the mean value, otherwise additional specimens have to be tested.

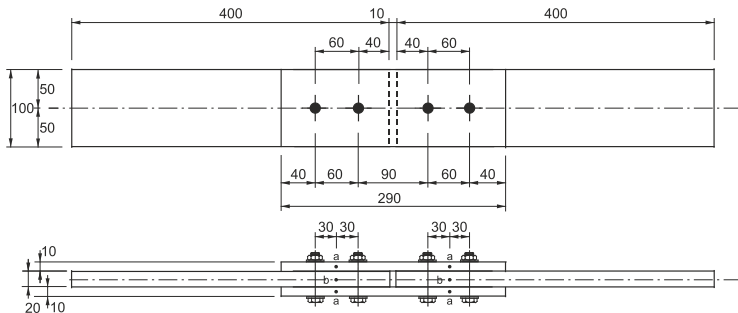


Fig. 2. The test specimen geometry for the determination of the slip factor according to EN 1090-2, Annex G, test specimens for M20 bolts

EXPERIMENTAL INVESTIGATIONS

General

The aim of the presented study was to investigate the influence of different surface conditions, preload levels and loading velocities. All specimens were made of steel S355J2C+N and the specimen geometry was chosen as M20-test-specimens according to EN 1090-2, see Fig.2. The slip displacements were measured in two dif-

ferent positions: CBG (center bolts group) and PE (plate edges) positions. CBG and PE positions consist of 8 (LVDTs 1-8) and 4 (LVDTs 9-12) displacement transducers respectively, as shown in Fig. 3 (b).

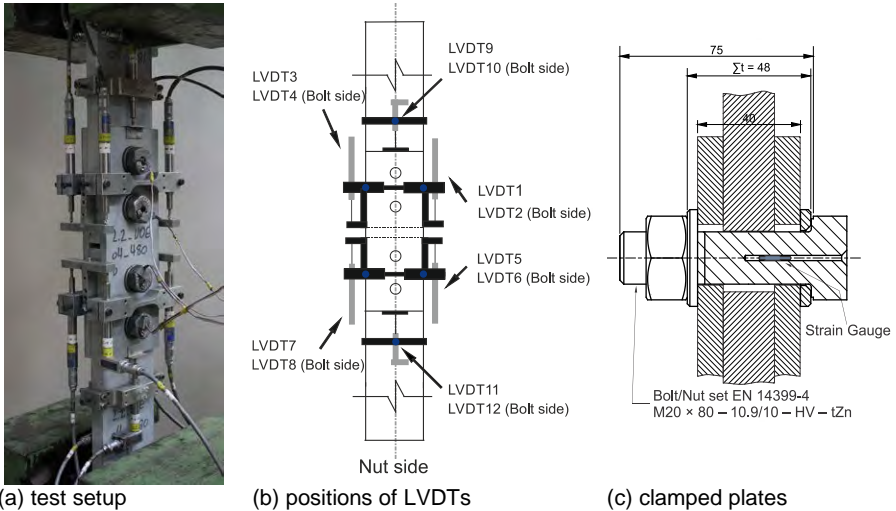


Fig. 3. Test setup, positions of displacement transducers (LVDTs) as well as Clamped plates of a bolted connection with bolts with implanted strain gauge

Measuring the slip displacement at the PE position may lead to a large difference in the slip load when a specific slip criterion is used, since the measured displacements in PE position include the strains of the inner plate between the CBG and PE positions, see also (Stranghöner et al., 2015). In presented paper, the slip factors are evaluated based on the measured slip displacement in CBG position for all four sliding planes, (Stranghöner et al., 2014). In order to investigate the influence of different surface conditions and preload levels, the tests were performed by applying an incremental tensile displacement with a velocity of about 0.01 mm/s. For investigating the influence of different loading velocities on the slip resistant behaviour of the connection, two different test setups (two different clamping lengths) were selected. By increasing the clamping length the loss of preload before and during the test will decrease which potentially lead to different slip factors for identical surface treatments, (Stranghöner et al., 2015).

Influence of different surface conditions

The influence of a blasted/uncoated surface (GB), alkali-zinc silicate coating (ASI), zinc (Zn-SM) and aluminium (Al-SM) metalized and a combination of zinc metalized - alkali-zinc silicate coating (ASI - Zn-SM) on the slip resistance of bolted connections was investigated. As shown in Table 1, different test series were selected with approximately the same clamping length (GB-I, ASI-I, AL-SM-I, Zn-SM-I and ASI - Zn-SM-I) in order to eliminate the effect of clamping length on the loss of preload, (Stranghöner et al. 2015). For each test specimen four M20 HV bolts class 10.9 were instrumented with a strain gauge, see Fig. 3(c), with a preloaded level of $F_{p,c} = 172$ kN. Fig. 3(a) shows the test setup used for the comparative study to investigate the

influence of different surface conditions. The slip load F_{Si} was determined at 0.15 mm slip or at the highest peak before. As shown in Table 1, the static slip factor were evaluated by considering the initial preload when the tests started $\mu_{init,mean}$ and the actual preload at slip $\mu_{actual,mean}$, see Eq. 1.

Table 1. Test programme regarding different surface conditions and preload levels and mean slip factor results

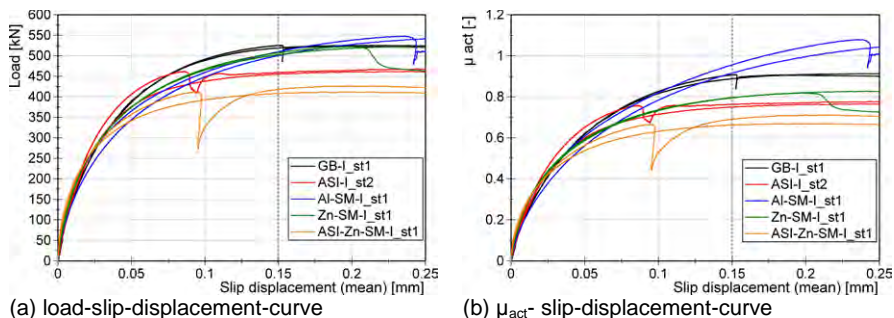
Series ID	Surface preparation		$\Sigma t^{(4)}$ [mm]	Bolt size (Md x l) ⁽⁵⁾ [mm]	Preload [kN]	Number of tests st/ct/ect ⁽⁶⁾	$\mu_{ini,mean}^{(7)}$	$\mu_{act,mean}^{(8)}$	$V_{(\mu_{act})}^{(9)}$
	Sa ⁽¹⁾ / Rz ⁽²⁾ [μ m]	DFT ⁽³⁾ [μ m]					st/st+ct [-]	st/st+ct [-]	st/st+ct [%]
Grit blasted surfaces (GB)									
GB-I	Sa 2½ / 80	-	52	M20 x 80	$F_{p,c}/172$	2/-/-	0.74/-	0.86/-	5.0/-
Alkali-zinc silicate coating (ASI)									
ASI-I	Sa 2½ / 80	60	52	M20 x 80	$F_{p,c}/172$	2/-/-	0.70/-	0.77/-	2.9/-
ASI-II	Sa 2½ / 80	60	48	M20 x 75	$F_{p,c}^*/160$	4/1/1	0.69/0.68	0.79/0.78	1.1/3.3
Aluminium spray metalized coating (Al-SM)									
Al-SM-I	-	360	52	M20 x 80	$F_{p,c}/172$	4/1/-	0.73/0.73	0.93/0.92	2.7/3.9
Zinc spray metalized coating (Zn-SM)									
Zn-SM-I	Sa 3 / 100	140	52	M20 x 80	$F_{p,c}/172$	2/-/-	0.73/-	0.82/-	2.7/-
Zn-SM-II	Sa 3 / 100	164	48	M20 x 75	$F_{p,c}^*/160$	4/-/2	0.74/-	0.83/-	2.2/-
Zn-SM-III		164	48	M20 x 75	$0.9 F_{p,c}^*/144$	4/-/2	0.80/-	0.92/-	1.3/-
Combination of alkali-zinc silicate and zinc spray metalized coating									
ASI – Zn-SM-I	Sa 2½/100 – Sa 3/100	55 – 170	48	M20 x 75	$F_{p,c}/172$	4/1/2	0.63/0.62	0.71/0.70	3.9/5.5
ASI – Zn-SM-II	Sa 2½/100 – Sa 3/100	55 – 170	48	M20 x 75	$0.9 F_{p,c}^*/144$	4/1/-	0.69/0.67	0.77/0.76	3.7/5.2

⁽¹⁾ Sa: surface preparation grade | ⁽²⁾ Rz: roughness | ⁽³⁾ DFT: dry film thickness (Coating thickness) | ⁽⁴⁾ Σt : clamping length | ⁽⁵⁾ d: bolt diameter, l: bolt length | ⁽⁶⁾ st: static test/ct: creep-/ect: extended creep test | ⁽⁷⁾ $\mu_{ini,mean}$: calculated slip factors as mean values considering the initial preload when the tests started | ⁽⁸⁾ $\mu_{act,mean}$: calculated slip factors as mean values considering the actual preload at slip | ⁽⁹⁾ V: Coefficient of variation for μ_{act}

It can be seen from Table 1 that the highest initial and actual slip factors were achieved for GB- and Al-SM-surface conditions respectively. Fig. 4 (a) shows typical load-slip displacement curves. Approximately same slip loads (F_{Si}) are achieved for both GB and Al-SM-surfaces. The higher actual slip factor for Al-SM can be explained by significantly higher losses of preload for AL-SM-surfaces during the tests.

Influence of different preload levels

One of the objectives of the presented research was to investigate the influence of different preload levels on the determination of the slip factor. For this purpose several tests with different preload levels ($F_{p,c}$, $F_{p,c}^*$ and $0.9 F_{p,c}^*$) were performed. Herein, $F_{p,c}^*$ is defined as $F_{p,c}^* = 0,7 f_{yb} A_s = 160$ kN (with f_{yb} : yield strength of the bolt and A_s : tensile stress area of the bolt) and $0,9 F_{p,c}^* = 144$ kN.



(a) load-slip-displacement-curve (b) μ_{act} - slip-displacement-curve
 Fig. 4. Influence of different surface conditions on the slip-load behaviour and actual slip factors

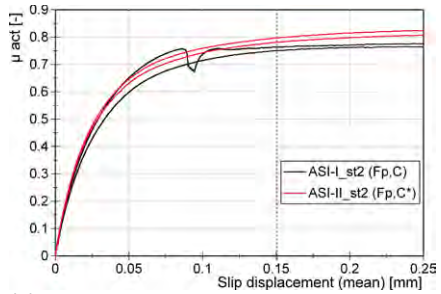
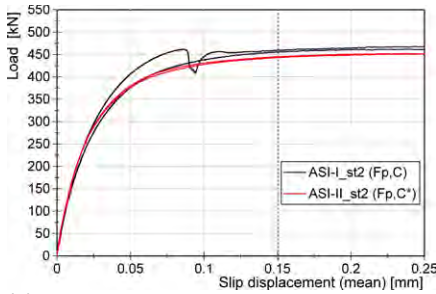
The influence of different preload levels for ASI-surface condition is shown in Fig. 5. The results show that the slip load increases slightly with increasing preload. However, only a minor difference can be observed for the actual slip factor. The actual slip factor for the specimens with preload level of $0.9 F_{p,C}^*$ ($\mu_{act,mean} = 0.79$) is slightly higher than the $\mu_{act,mean}$ values obtained from the specimens with $F_{p,C}$ ($\mu_{act,mean} = 0.77$), see Table 1. It can also be seen in Fig. 6 that the highest actual slip factor is achieved for Zn-SM-III with a preload level of $0.9 F_{p,C}^*$ ($\mu_{act,mean} = 0.92$) in comparison to Zn-SM-II with a preload level of $F_{p,C}^*$ ($\mu_{act,mean} = 0.83$) and Zn-SM-I with preload level of $F_{p,C}$ ($\mu_{act,mean} = 0.82$). Fig. 7 also confirms this phenomenon. The results show that in ASI-Zn-SM series, $\mu_{act,mean} (0.9 F_{p,C}^*) = 0.77$ is higher than $\mu_{act,mean} (F_{p,C}) = 0.71$. These behaviours confirm that a higher static slip factor can be achieved by a lower preload level (lower surface pressure), see Fig.8.

For all coated surfaces, creep tests were failed and extended creep tests are necessary. Evaluating the slip displacement – log time curve based on the results of the creep tests is an effective way to get more information about creep sensitivity of the coated surfaces. As shown in Fig. 9, for both surface conditions (ASI and Al-SM), the slip displacement – log time curves are presented based on the results of creep tests at $0.9 F_{Sm}$. The duration of the creep test is short in comparison to the extended creep test. For this reason, it is not possible to consider these curves as passed extended creep tests. However, both type of coatings (specifically Al-SM) show relatively great slip resistance behaviours with high loading levels under the long term creep test.

One extended creep test was performed for ASI-II with a constant load level of $0.8 F_{Sm}$, see Fig. 9(a). The result shows, the slip is less than 0.3 mm when extrapolated to 50 years and the test is considered as a passed extended creep test and the nominal slip factor can be calculated as following:

$$\mu_{nom,ASI}(F_{p,C}^*) = \frac{0.8 \times F_{Sm}}{4 \times F_{V,nom}} = \frac{355.6 \text{ kN}}{4 \times 160 \text{ kN}} = 0.56 [-] \quad (4)$$

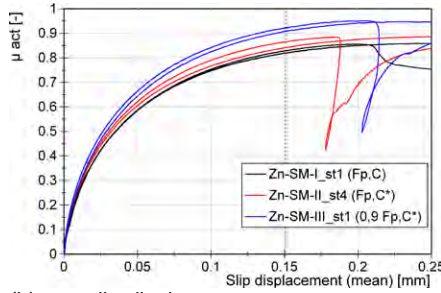
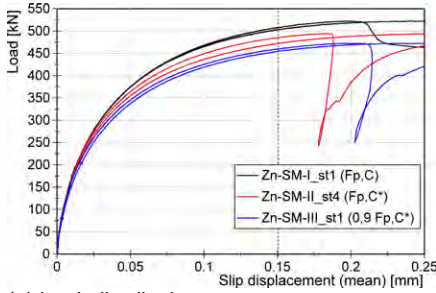
Four extended creep tests were performed for Zn-SM-surface condition with two different preload levels of $F_{p,C}^*$ and $0.9 F_{p,C}^*$, see Fig. 10(a). The extrapolated displacement – log time curves of the extended creep tests show that for a constant load level of $0.6 F_{Sm}$, the slip is less than 0.3 mm when extrapolated to 50 years. Herewith, they are considered as passed. The nominal slip factor for Zn-SM-II and III (with preload levels of $F_{p,C}^*$ and $0.9 F_{p,C}^*$) based on $0.6 F_{Sm}$ can be calculated as following:



(a) load-slip-displacement-curve

(b) μ_{act} -slip-displacement-curve

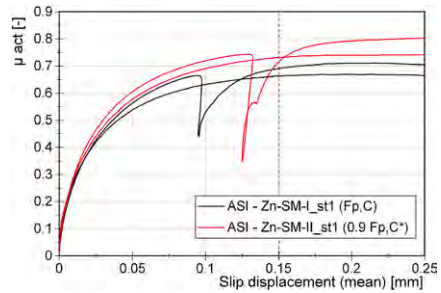
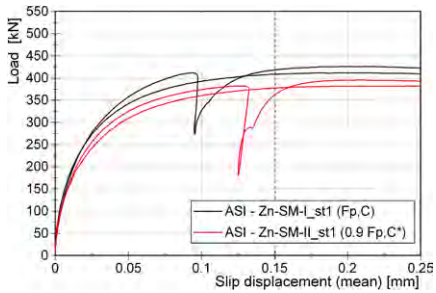
Fig. 5. Influence of different preload levels for ASI-surface condition



(a) load-slip-displacement-curve

(b) μ_{act} -slip-displacement-curve

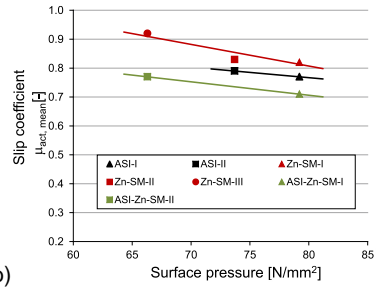
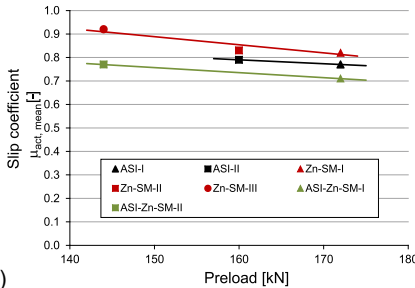
Fig. 6. Influence of different preload levels for Zn-SM-surface condition



(a) load-slip-displacement-curve

(b) μ_{act} -slip-displacement-curve

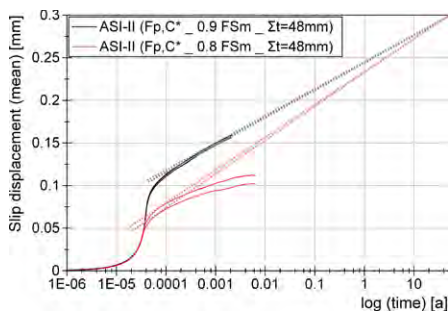
Fig. 7. Influence of different preload levels for ASI-Zn-SM-surface condition



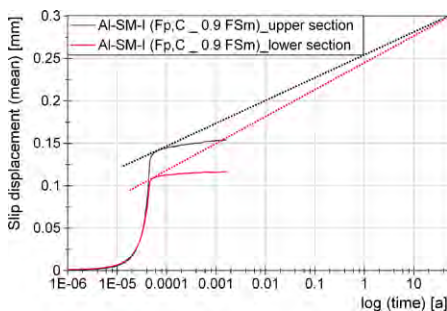
(a)

(b)

Fig. 8. Influence of different preload levels (a) and surface pressures (b)

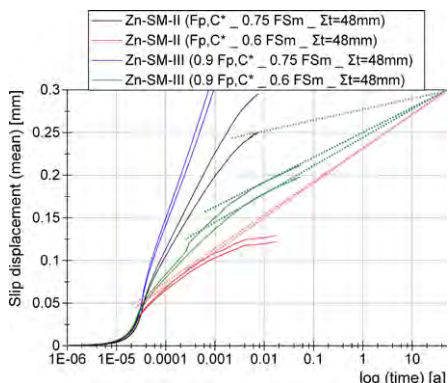


(a) ASI-surface condition (each colour represent the upper/lower section of the specimen)

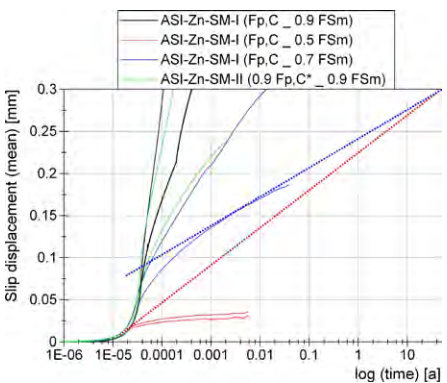


(b) AI-SM-surface condition

Fig. 9. Results of the extended creep tests of the series ASI and AI-SM



a) Zn-SM-surface condition



b) ASI - Zn-SM-surface condition

Fig. 10. Results of the extended creep tests of the series Zn-SM and ASI - Zn-SM considering different load and preload levels (each colour represent the upper and lower section of the specimen)

$$\mu_{\text{nom,Zn-SM}}(F_{p,C^*}) = \frac{0,6 \cdot F_{Sm}}{4 \cdot F_{v,\text{nom}}} = \frac{280,8 \text{ kN}}{4 \cdot 160 \text{ kN}} = 0,44 \text{ [-]} \quad (5)$$

$$\mu_{\text{nom,Zn-SM}}(0,9 F_{p,C^*}) = \frac{0,6 \cdot F_{Sm}}{4 \cdot F_{v,\text{nom}}} = \frac{276,6 \text{ kN}}{4 \cdot 144 \text{ kN}} = 0,48 \text{ [-]} \quad (6)$$

The extended creep test for ASI - Zn-SM-I with a preload level of $F_{p,C}$ and $0.7 F_{Sm}$ was passed for one part of the test specimen and failed for the other part, see Fig. 10(b). In the next step, the load level was reduced to $0.5 F_{Sm}$. The result shows the extended creep test with this load level is clearly passed, but it is still possible to get higher slip factors by performing the test with a higher load level. The nominal slip factor for ASI - Zn-SM-I based on $0.5 F_{Sm}$ can be calculated as following:

$$\mu_{\text{nom,ASI-Zn-SM}}(F_{p,C}) = \frac{0,5 \cdot F_{Sm}}{4 \cdot F_{v,\text{nom}}} = \frac{215,7 \text{ kN}}{4 \cdot 172 \text{ kN}} = 0,31 \text{ [-]} \quad (7)$$

Influence of the loading velocity

The test program for the comparative study regarding the test duration of the static slip tests is presented in Table 2. Three different surface conditions (GB, ASI and Zn-SM) were tested for four different test durations of the static slip tests with 152 mm clamping length (for the Zn-SM surface condition five different test durations were selected). Two of the test durations were chosen within the given test durations of time Annex G (10 to 15 minutes). One test duration was significantly longer, but still short compared to the duration of a creep test. For each type of coating, one test series was performed with the same test duration and different clamping length (52 mm). The duration of a test is defined as the time it takes from starting of the test to load the connection at each side of the specimen to the level at which the slip criterion is reached. A threshold value of 0.15 mm for the displacement between the centre and side plates at the centre of the bolt groups (CBG) was set. For each test specimen four HV bolts M20, class 10.9 were instrumented with a strain gauge and a preload level of $F_{p,C} = 172$ kN. The bolts were selected in two different lengths (180 mm and 80 mm) in combination with especially produced load cells and without any adapter (two washers under the bolt head), see Fig. 11 for the tests setup with adapter.

Table 2. Test program regarding the loading velocity and mean slip factor results

Speed [mm/s]	Surface preparation		Σ^4 [mm]	Bolt size (Md x l) ⁵⁾ [mm]	Test duration [min]	Number of tests st/ct/ect ⁶⁾	$\mu_{ini,mean}$ ⁷⁾ st/st+ct [-]	$\mu_{act,mean}$ ⁸⁾ st/st+ct [-]	V (μ_{act}) ⁹⁾ st/st+ct [%]
	Sa ¹⁾ / Rz ²⁾ [μ m]	DFT ³⁾ [μ m]							
Grit blasted surfaces (GB)									
0.01	Sa 2½ / 80	-	152	M20 x 180	5	8/2/-	0.72/-	0.79/-	2/-
0.005			52	M20 x 80	10	4/0/-	0.67/-	0.81/-	2/-
0.005			152	M20 x 180	11	6/2/-	0.77/-	0.84/-	1/-
0.0025			152	M20 x 180	24	4/0/-	0.79/-	0.85/-	3/-
0.001			152	M20 x 180	64	4/0/-	0.82/-	0.88/-	1/-
Alkali-zinc silicate coating (ASI)									
0.01	Sa 2½ / 80	60 60	152	M20 x 180	5	6/2/-	0.70/-	0.76/-	1/-
0.005			52	M20 x 80	9	4/2/-	0.68/-	0.75/-	1/-
0.005			152	M20 x 180	10	6/2/-	0.71/-	0.76/-	3/-
0.0025			152	M20 x 180	19	6/0/-	0.70/-	0.76/-	2/-
0.001			152	M20 x 180	49	6/2/-	0.72/-	0.78/-	1/-
Zinc spray metalized coating (Zn-SM)									
0.01	Sa 3/ 100	140	152	M20 x 180	6	6/2/-	0.76/-	0.82/-	2/-
0.005			52	M20 x 80	10	4/0/-	0.74/-	0.83/-	4/-
0.005			152	M20 x 180	11	6/2/-	0.76/-	0.83/-	3/-
0.0025			152	M20 x 180	20	4/0/-	0.72/-	0.78/-	3/-
0.001			152	M20 x 180	45	4/0/-	0.69/-	0.75/-	2/-
0.0005	152	M20 x 180	95	4/2/-	0.69/-	0.74/-	1/-		

¹⁾ Sa: surface preparation grade | ²⁾ Rz: roughness | ³⁾ DFT: dry film thickness (Coating thickness) | ⁴⁾ Σ : clamping length | ⁵⁾ d: bolt diameter, l: bolt length | ⁶⁾ st: static test/ct: creep-/ect: extended creep test | ⁷⁾ $\mu_{ini,mean}$: calculated slip factors as mean values considering the initial preload when the tests started | ⁸⁾ $\mu_{act,mean}$: calculated slip factors as mean values considering the actual preload at slip | ⁹⁾ V: Coefficient of variation for μ_{act} | * Nominal level of preload: $F_{p,C} = 172$ kN (M20).

All resulting static slip factors, presented in Table 2, are high compared to values known from literature. This is caused by the long bolt length due to the increased clamping length, see also (Stranghöner et al. 2015). As the objective of this test program is only to quantify the influence of the test duration on the result of a slip factor test, the differences between the slip factors found for the various test series are of

interest. The results show that the static slip factors for grit blasted surfaces tend to higher values for prolonged test duration, in the event that the static slip factors for zinc spray metalized surfaces tend to lower values for prolonged test duration. Beside these results, the test duration has no great influence on ASI-specimens, see Fig. 12, 13 and 14.

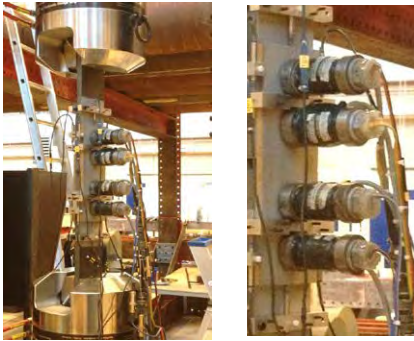


Fig. 11. Test setup with adapter

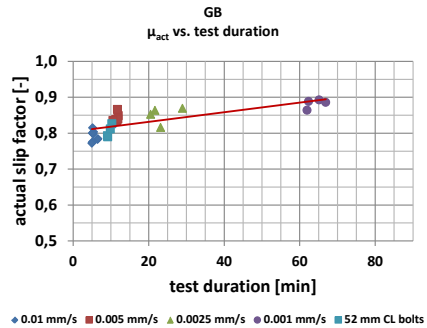


Fig. 12. Slip factors for different test duration of short term tests (GB)

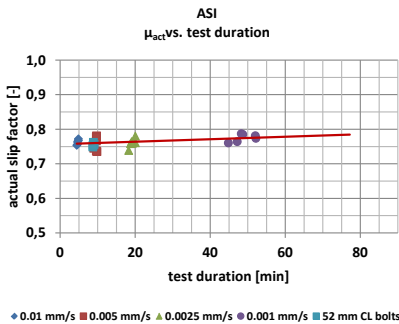


Fig. 13. Slip factors for different test duration of short term tests (ASI)

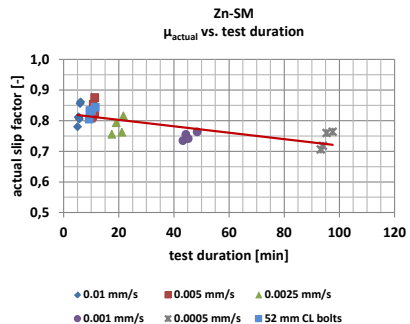


Fig. 14. Slip factors for different test duration of short term tests (Zn-SM)

CONCLUSIONS

The influence of different surface conditions, preload levels and loading velocities on the determination of slip factors for bolted slip-resistant connections were investigated in the frame of the RFCS research project SIROCO. The mean slip factors achieved for Al-SM-surface condition in static slip tests are relatively high compared to other coated surfaces. The slip load increases with increasing preload load level. The highest static slip factor can be achieved by the lowest preload level. Furthermore, grit blasted and Zn-SM surfaces respectively tend to higher and lower slip factor values for prolonged test durations. For ASI-Zn specimens, no influence of the test duration on the slip coefficient could be observed. The research activities are still ongoing.

ACKNOWLEDGMENTS

The authors thank the Research Fund for Coal and Steel (RFCS)/European Commission for funding the research project "Execution and reliability of slip resistant connections for steel structures using CS and SS" SIROCO (RFSR-CT-2014-00024).

REFERENCES

EN 1993-1-8 (2009), EN 1993-1-8:2005 + AC:2009, "Eurocode 3: Design of steel structures – Part 1-8: Design of joints".

EN 1090-2 (2011), EN 1090-2:2008+A1:2011, "Execution of steel structures and aluminium structures – Part 2: Technical requirements for steel structures".

Gruintjes, T. J. J., Bouwman, L. P. (1984), "Slip factors of structural connections formed with high-strength friction grip bolts and with contact surfaces treated in various ways." Faculty of Civil Engineering and Geosciences, TU Delft. (identisch zu ECCS-TC 10: Slip factors of connections with H.S.F.G. bolts, No. 37, www.eccspublications.eu)

RCSC - Research Council on Structural Connections (2009), "Specification for Structural Joints Using High-Strength Bolts." Chicago, Illinois: s.n., 2009.

Stranghöner, N., Afzali, N., Berg, J., Schiborr, M., Bijlaard, Frans S. K., Gresnigt, A. M., Vries, P. de, Glienke, R., Ebert, A. (2015). "Influence of different testing criteria on the slip factor of slip-resistant connections." Proceedings of the Nordic Steel Construction Conference 2015, Tampere, Finland, September.

Stranghöner, N., Schiborr, M., Glienke, R. (2014). "Procedure test of slip-resistant connections according to EN 1090-2" Proceedings of the EUROSTEEL 2014, 7th European Conference on Steel and Composite Structures, September 10-12, 2014, Naples, Italy.

TL/TP-KOR-Stahlbauten (2002), "Technische Lieferbedingungen und Technische Prüfvorschriften für Beschichtungsstoffe für den Korrosionsschutz von Stahlbauten", Anhang E, Blatt 85, Verkehrsblatt-Dokument Nr. B5259, Vers. 12/02.

DEFORMATION CAPACITY, STIFFNESS AND BEARING STRENGTH AT BOLT HOLES

Primož Može

University of Ljubljana, Faculty of Civil and Geodetic Engineering, Slovenia

primoz.moze@fgg.uni-lj.si

ABSTRACT

The paper focuses on the available test results of single bolt connections with plate in bolt bearing. The bearing resistance formula in the ultimate limit state that allows much higher bearing stress than traditional provisions is given and confirmed by the presented tests. The available bearing deformation capacity at bolt holes is given for mild as well as for high strength steel. Attention is paid also to the nominally elastic stiffness. Bearing stress in the material is developed due to the contact pressure. Initially, the contact area is very small, causing stress concentrations and yielding of the material at very low loads. Yielding allows embedment of the bolt on a larger contact area. Such behavior is interpreted as nominally elastic behavior, as stress concentrations are eliminated by the yielding of material occurring at early load stage. The paper includes simple design formulas to estimate the available bearing deformation capacity, bearing stiffness and bearing strength at bolt holes.

INTRODUCTION

Bolting is a practical and simple way of connecting elements. However, bolt holes should have sufficient clearance in order to fit the bolts and plates together. Therefore, bolts are not perfectly aligned and bolt holes have to elongate in order to distribute the load between all bolts. The connected plates are in contact with the bolt shank and the load is transmitted by shear on the bolts and high bearing stress in the plates around the bolt holes. Unlike some other materials like glass or FRP composites, steel has the ability of developing significant plastic strain that localizes around the bolt holes, enabling sufficient bolt hole elongations for load redistribution. Henriques et al. (2014) analyzed the ductility requirements for the design of the connections in bolt bearing. They considered the stiffness of the plate in bolt bearing according to Eurocode (CEN, 2005). The stiffness is discussed also in Rex and Easterling (2003). The effect of bearing pressure on the resistance of the connections was carefully studied in the middle of the 20th century (Kulak et al., 2001). The application of high strength steels in steel structures raised the issue of local ductility (Aalberg and Larsen, 2001, 2002, Kim and Yura, 1999, Kouhi and Kortessma, 1990, Može and Beg, 2010, 2011, Može and Beg, Puthli and Fleischer, 2001, Rex and Easterling, 2003, Snijder et al., 1988). The use of high strength steel reopened the question of the effect of the hole misalignment. Henriques et al. (2014) showed that the maximum misalignment is approximately 4.7 mm for bolts larger than M16, which is roughly 15 % to 28 % of bolt diameter. Kulak et al. (2001) provided evidence that the actual hole misalignment is rarely 3.1 mm and is usually smaller than 0.8 mm.

The paper gives the test results of single bolt connections that failed in bolt bearing. Previous test results of different connections that failed in bolt bearing are also presented in order to obtain the bearing deformation, the bearing deformation capacity and the bearing resistance at small hole elongations required to overcome the initial hole misalignment and allow the force distribution.

TESTS OF SINGLE BOLT CONNECTIONS

The objective of the tests was to measure the behavior of plates in bolt bearing, where the bolt is placed far away from the edges. The test program included 10 single bolt connections (series W1) as well as 19 connections with two bolts, positioned perpendicular to the loading direction (series W2). The connection geometries are given in Table 1. The symbols from Table 1 are defined in Fig. 1. The single bolt connections are presented by three sets. The first set, W101 to W104, includes the specimens with constant end distance of $e_1 = 3 d_b$ and the edge distance e_2 increasing from $2.43 d_b$ to $5 d_b$. The second set W108 to W110 has a constant end distance of $e_1 = 5 d_b$ and the edge distance e_2 increasing from $3.36 d_b$ to $7.47 d_b$. The third set W105 to W107 provides the results for end distances between $3 d_b$ to $5 d_b$ in combination with large edge distances. The objective of test series W2 (2 bolts) was to obtain the interaction of two bolts on the bearing behavior. Three sets and four additional specimens to cover the intermediate geometries present series W2. Sets W201 to W205, W208 to W213 and W216 to W219 have constant pitch of $2.2 d_b$, $3.0 d_b$ and $4.0 d_b$, respectively. Generally, the end distance increases from $1.5 d_b$ to $5.0 d_b$.

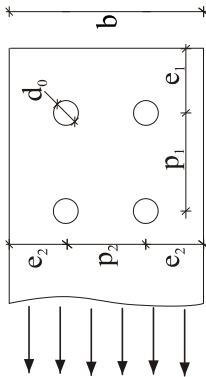


Fig. 1: Test program and results

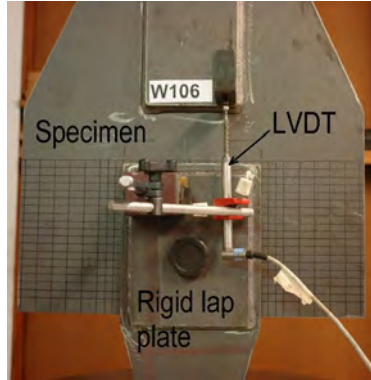


Fig. 2: Test setup and measuring devices

The connections were fabricated from a 10 mm thick steel plate with the following average material characteristics: yield stress $f_y = 342$ MPa, tensile strength $f_u = 447$ MPa. The tensile strength was reached at the uniform strain of 16.3 %, the standard tensile test coupon fractured at 44 %. The cross-section was at fracture reduced by 65 % of the initial size. The connections were designed as lap connections with bolts loaded in double shear. The bolts placed in standard size holes were tightened just to achieve firm contact between the plates. The bolt preloading did not allow any significant friction force development. Therefore, the

load was transferred primarily by bearing and not by friction. Bolts M27 12.9 and the lap plates (twice thicker, sufficient end distance) were designed to remain elastic, thus the failure was always observed in the main plate. The main plate on one side of the connection and the lap plates on the other side were clamped to the testing machine. A relative displacement between the main plate and the lap plate was measured on both sides of the connections by inductive displacement transducer (LVDT – Fig. 2). The tests were carried out at a prescribed displacement rate of 2 mm/min on a testing machine with the capacity of 1 MN.

Table 1: Test program and results

Spec.	Actual relative distances			P_{\max} kN	\bar{P}_{\max}	$\bar{\Delta}_u$	$\bar{\Delta}_{u,80}$
	e_1/d_0	e_2/d_0	p_1/d_0				
W101	3.03	2.43		427	3.55	1.16	1.33
W102	3.00	3.07		443	3.68	1.10	1.37
W103	2.99	4.03		476	3.96	1.08	1.29
W104	3.01	5.01		482	4.00	1.06	1.23
W105	3.49	5.01		536	4.45	1.23	1.43
W106	3.83	7.52		591	4.91	1.08	N.A.
W107	4.44	7.51		657	5.45	1.12	1.45
W108	5.04	3.36		630	5.23	1.19	N.A.
W109	5.00	5.03		613	5.09	1.18	1.72
W110	4.94	7.47		599	4.97	1.06	1.61
W201	1.53	5.03	2.21	485	4.03	0.71	1.10
W202	2.02	5.02	2.21	552	4.58	0.74	1.12
W203	2.36	4.99	2.21	599	4.97	0.79	1.17
W204	3.02	5.03	2.20	686	5.69	1.01	1.22
W205	5.01	5.03	2.22	926	7.69	1.12	N.A.
W206	2.52	5.01	2.51	658	5.47	1.00	1.20
W207	5.02	5.02	2.51	988	8.21	1.20	N.A.
W208	1.53	6.68	3.01	614	5.10	0.90	1.24
W209	2.05	6.69	3.01	672	5.58	0.93	1.18
W210	2.53	6.68	3.01	748	6.21	1.06	1.27
W211	3.01	6.69	3.01	800	6.65	1.12	N.A.
W212	4.01	6.68	2.99	933	7.75	1.08	N.A.
W213	5.01	6.68	3.01	944	7.84	0.95	1.68
W214	3.02	6.70	3.52	869	7.22	1.26	1.54
W215*	5.02	6.71	3.50	997*	8.28*	0.78*	N.A.
W216	2.02	6.67	4.00	758	6.30	0.97	1.27
W217	3.04	6.70	4.01	920	7.64	1.08	0.00
W218*	4.03	6.69	4.02	998*	8.29*	0.91*	N.A.
W219*	5.05	6.70	4.01	1000*	8.30*	0.61*	N.A.
P_{\max}	maximum resistance						
\bar{P}_{\max}	normalized maximum resistance						
$\bar{\Delta}_u$	normalized displacement at maximum resistance (Δ_u / d)						
d	bolt diameter						

TEST RESULTS

The test results are presented in Table 1 in terms of maximum (normalized) resistance and normalized displacements that were reached at maximum resistance. The normalized force is expressed as a multiplier of the ratio between average bearing stress and tensile strength of the plate, while the displacement is normalized by the bolt diameter. Fig. 3 shows photos of W101 and W104 after failure. Plastic deformation of net cross-section observed at W101 led to splitting failure, as the material in front of the bolt tends to split the plate in two parts. The increased width of W104 resulted in bearing failure characterized by a slightly larger resistance and lower deformation capacity (Fig. 4). The deformation capacity of W101 is larger because the net cross-section yielding was also expressed in the hole elongation. Similar may be observed at W108 and W110 in Fig. 5, except the resistance of W108 that failed in a splitting manner is slightly larger than the resistance of W110 that failed in bearing (Fig. 4).

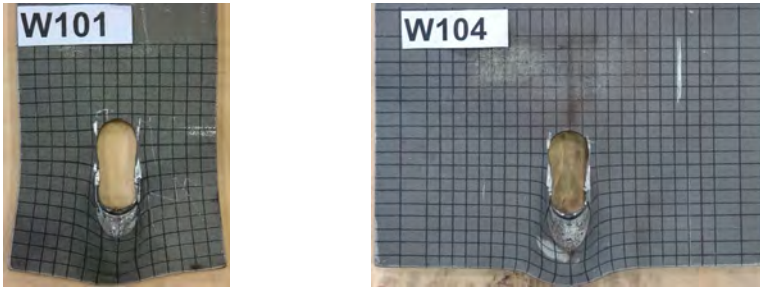


Fig. 3: Failures of W101 ($e_1 = 3db$; $e_2 = 2.4db$) and W104 ($e_1 = 3db$; $e_2 = 5db$)

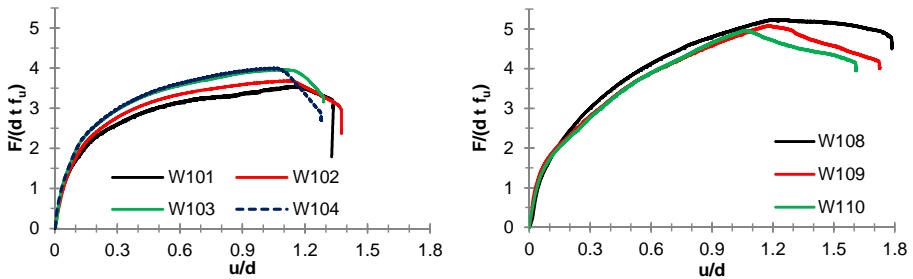


Fig. 4: Response curves for three sets of W1 specimens

The failures of W208 and W212 in Fig. 6 show failures in front of the first bolt and between bolts, respectively. Although the plates are very wide, the yielding of net cross-section around the inner hole observed in both cases tends to split the plate. As expected, all specimens behaved in a very ductile manner, reaching high resistances in bearing.

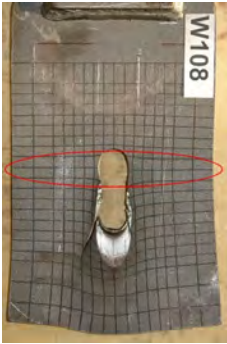


Fig. 5: Failures of W108 ($e_1 = 5db$; $e_2 = 3.4db$) and W110 ($e_1 = 5db$; $e_2 = 7.5db$)

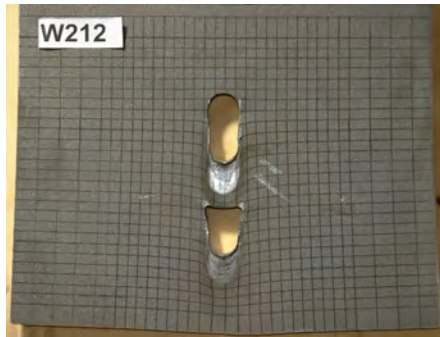


Fig. 6: Failures of W208 ($e_1 = 1.5db$; $p_1 = 3.0db$) and W212 ($e_1 = 4db$; $p_1 = 3db$)

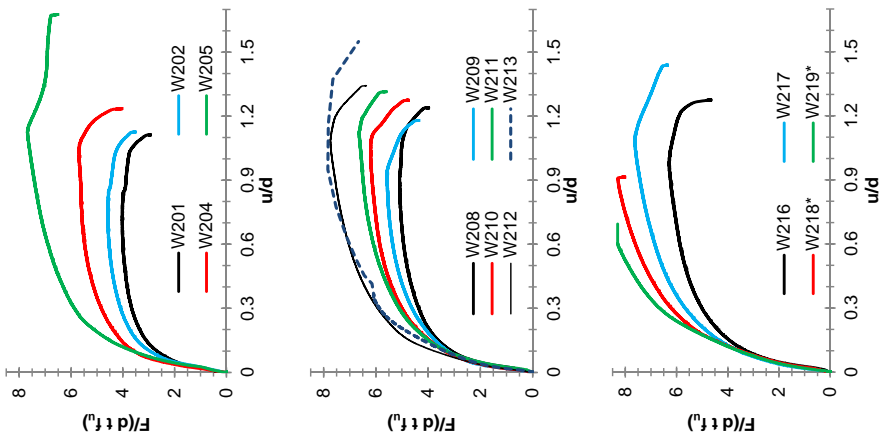


Fig. 7: Response curves for three sets of W2 specimens

BEARING RESISTANCE

Several authors have shown that the bearing resistance check as defined in Eurocode (CEN, 2005) gives conservative results and becomes complicated if the bearing force does not act perpendicular to the edge. In order to simplify the bearing resistance check, the modified formula was presented in (Može and Beg, 2014) and is herein confirmed also for the inner bolt. The modified bearing resistance formula takes into account that the average bearing stress is linearly dependent on end distance e_1 or bolt pitch p_1 , disregarding the effect of edge distance e_2 or bolt pitch p_2 in the direction perpendicular to the bearing force. Thus, the resistance of steel plate in bolt bearing may be defined as:

$$F_b = k_s k_b d t f_u, \quad (1)$$

$$k_b = \begin{cases} \min\left(\frac{e_1}{d_0}; 5\right); & \text{for end bolt} \\ \min\left(\frac{p_1}{d_0} - \frac{1}{4}; 5\right); & \text{for inner bolt} \end{cases} \quad k_s = \begin{cases} 1; & \text{for mild steel S235} \\ 0.9; & \text{for high strength steel S690} \end{cases} \quad (2)$$

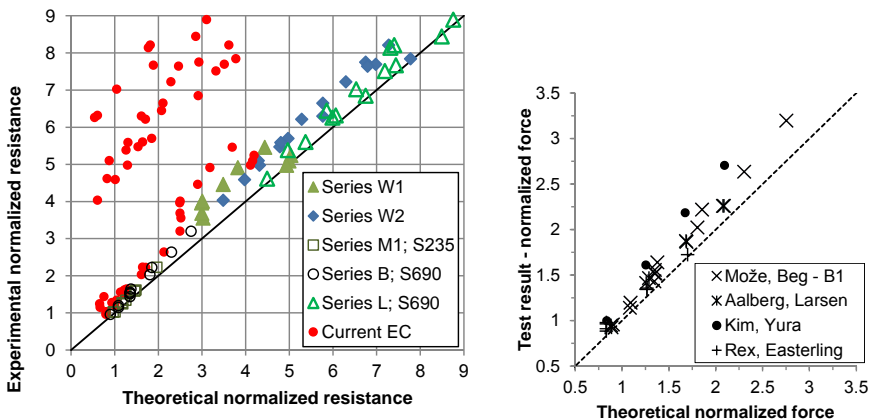


Fig. 8: Proposed bearing resistance in respect to the test results

Hereinafter it is presented that the bearing deformation capacity is also for HSS sufficient to sum up the bearing resistances. This is performed in Fig. 8 (left side) for series L, where the theoretical resistance is represented by equation (1). Series L refers to HSS connections with three or four bolts (Može and Beg, 2011), while series M1 and B refer to single bolt connections (Može and Beg, 2010, 2014). Fig. 8 also shows the calculation of the bearing resistance according to Eurocode. The Eurocode results are very conservative in case of the connections with large end distances or large pitches, mainly due to the upper limitation of the bearing stress to $2.5 f_u$. The right side of Fig. 8 presents the test results for HSS found in literature (Aalberg and Larsen, 2001, 2002, Kim and Yura, 1999, Rex and Easterling, 2003).

The symbols in Fig. 8 that lie just above the symmetry line belong to the splitting failure. The symbols further away from the symmetry line belong to the bolt pull-out or

to the bearing failure. A steel plate with single bolt in bearing and a defined, constant end distance e_1 may fail in net cross-section, if the plate is narrow. In case of intermediate plate widths (widths around $1.33 e_1$), the failure shifts to the splitting type, which is a mixed failure type between net cross-section failure and a bearing failure. The bearing failure will occur in case of wide plates. The net cross-section failure will have the lowest resistance in this case. For this reason, the bearing resistance (1) is defined to correspond to the splitting failures (results close to the symmetry line in Fig. 8).

BEARING DEFORMATION

Bearing deformation in ultimate limit state (ULS) Δ_u is expressed as the bolt hole elongation at maximum resistance. In case of single bolt (series W1) connection, Δ_u is reached at the bolt hole elongation of approximately equal to the bolt diameter. For series W2, the smallest of e_1 and p_1 govern the bearing deformation Δ_u . If some other tests of bolt bearing are considered for mild steel S235 (Može and Beg, 2014) and for high strength steel (HSS) S690 (Može and Beg, 2010, 2011), then a correlation between the maximum resistance and the bearing deformation in ULS Δ_u may be expressed as

$$\Delta_u = \min\left(\frac{e_1}{3}, \frac{p_1}{3}; d\right) \quad \text{for mild steel S235,} \quad (3)$$

$$\Delta_u = \Delta_{u,95} = \min\left(0.9 \frac{e_1}{3}; 0.9 \frac{p_1}{3}; 0.8d\right) \quad \text{for high strength steel S690,} \quad (4)$$

where d is the bolt diameter. The maximum resistance of HSS plates is reached at the beginning of long yield plateau (Može and Beg, 2010) that has a slightly negative gradient. Therefore, it is sensible to define the bearing deformation in ULS $\Delta_{u,95}$ as the bearing deformation at the degradation of maximum resistance by 5%. The upper limit of the bearing deformation for HSS plates is limited to $0.8 d$.

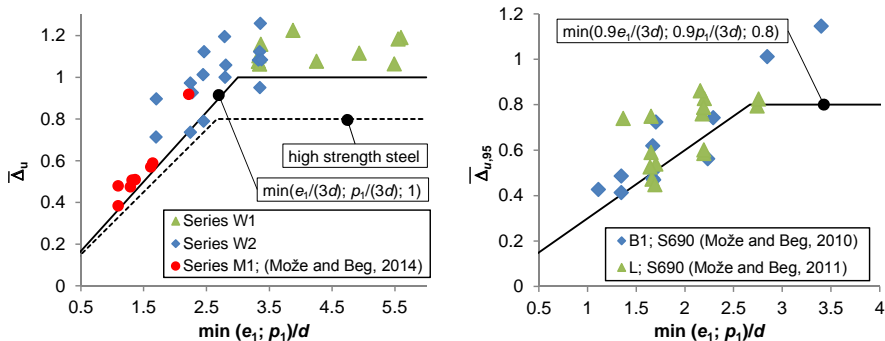


Fig. 9: Comparison of theoretical and experimental bearing deformation in ULS Δ_u for mild (left) and high strength steel (right)

Fig. 9 shows that equations (3) and (4) give very good estimation of bearing deformation in ULS Δ_u . The results in Fig. 9 refer only to bearing failures (single bolt

connections – series M and B1, connections with three or four bolts – series L). Details on the results are given in Može and Beg (2010, 2011, 2014).

The bearing deformation capacity $\Delta_{u,80}$ is defined as the bolt hole elongation at the degradation of maximum resistance by 20 %. The response curves (Fig. 4) for connections with large end distances and pitches are not characterized by a yielding plateau, but on account of crack propagation, the resistance drops after the maximum resistance has been reached. Thus, the deformation capacity $\Delta_{u,80}$ may be assumed equal to the bearing deformation in ULS Δ_u . The deformation capacity is in case of smaller end distances limited by the clear distance (Fig. 10). For mild steel plates, the deformation capacity reaches the maximum value of bolt diameter at the end distance of approximately 1.5 d_b . High strength steel has smaller deformation capacity and maximum capacity is reached with larger end distance (approximately 1.7 d_b) than at mild steel. The deformation capacity may be expressed as:

- for mild steel S235

$$\Delta_{u,80} = \min\left(e_1 - \frac{d_0}{2}; p_1 - \frac{d_0}{2}\right), \quad \text{but} \quad 0.7d \leq \Delta_{u,80} \leq d \quad (5)$$

- for high strength steel S690

$$\Delta_{u,80} = \frac{1}{4} \cdot \min\left(e_1 - \frac{d_0}{2}; p_1 - \frac{d_0}{2}\right) + 0.3d, \quad \text{but} \quad 0.6d \leq \Delta_{u,80} \leq 0.8d. \quad (6)$$

Fig. 10 presents the bearing deformation capacity normalized by bolt diameter experimental results (Može and Beg, 2010, 2011, 2014) and the theoretical capacity represented by equations (5) and (6). The maximum capacity of bolt diameter d or $0.8d$ in case of HSS, which ensures the force distribution between all bolts, is reached with relatively short end distances e_1 or pitches p_1 . The presented bearing deformation capacities are reached only if the resistance in bearing is fully utilized, meaning that the shear resistance of the bolt, the net cross-section resistance as well as the resistance of block shear are sufficient to allow full utilization in bolt bearing.

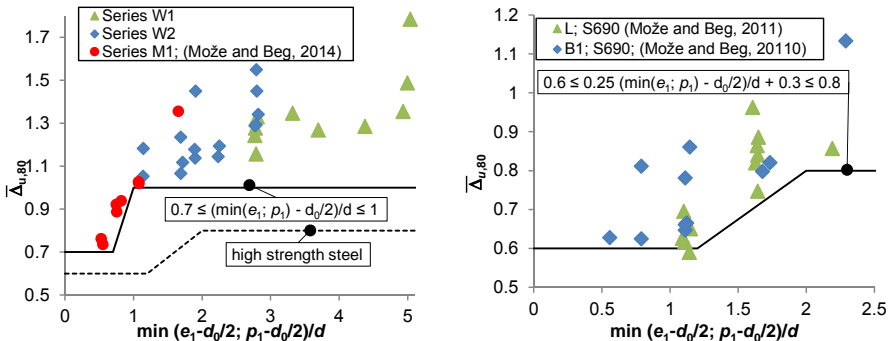


Fig. 10: Comparison of theoretical and experimental bearing deformation capacity $\Delta_{u,80}$ for mild (left) and high strength steel (right)

STIFFNESS OF PLATE IN BOLT BEARING

Bearing stress develops in the material due to the contact pressure. Initially, the contact area is very small, causing stress concentrations and yielding of the material at very low loads. Yielding allows embedment of the bolt on a larger contact area (Kulak et al., 2001). Such behavior is interpreted as nominally elastic behavior, as stress concentrations are eliminated by yielding of the material occurring at early load stage. Stiffness is therefore related to the yield stress. Fig. 11 gives the load displacement curves for various test results that failed in bearing (Može and Beg, 2010, 2014). The curves are plotted in the normalized format. The objective of these tests was to obtain the global behavior. Thus, the initial misalignment is observed at low level of load. Nevertheless, the tests with similar end distances follow more or less the same load path. Furthermore, all results follow the same general curve. The breakaway from the general curve occurs, when the material in front of the bolt yields. The comparison of mild and high strength steel also reveals that HSS connections have a slightly larger stiffness (Može and Beg, 2014). Considering all this, the general curve was constructed for the end distances larger than $2 d_0$ and is presented in Fig. 11.

The bolt hole elongation is important in the serviceability limit state (SLS). The elongation of $0.15 d$ seems appropriate for the definition of the requirement for the SLS. For short distances ($\leq 1.5 d_0$), the load displacement curves just shift from the more or less linear part to the plateau. For larger distances, the average bearing stress is approximately equal to $2 f_u$. Similar was also suggested in literature (Može and Beg, 2011) for the connections with several bolts. Thus, the bearing force for SLS is defined at the hole elongation of $0.15 d$ as:

$$F_{b,ser} = k_{b,ser} dt f_u, \quad (7)$$

$$k_{b,ser} = \frac{\min(0.9 \cdot k_b; 2)}{k_s} \quad (8)$$

Fig. 11 also displays the secant stiffness for the SLS that is given by equation (8). Furthermore, Fig. 11 gives information on the bearing strength in case of hole misalignment. If the misalignment equals to $0.15d$, the shear strength of the bolt should be at least $2f_u dt$.

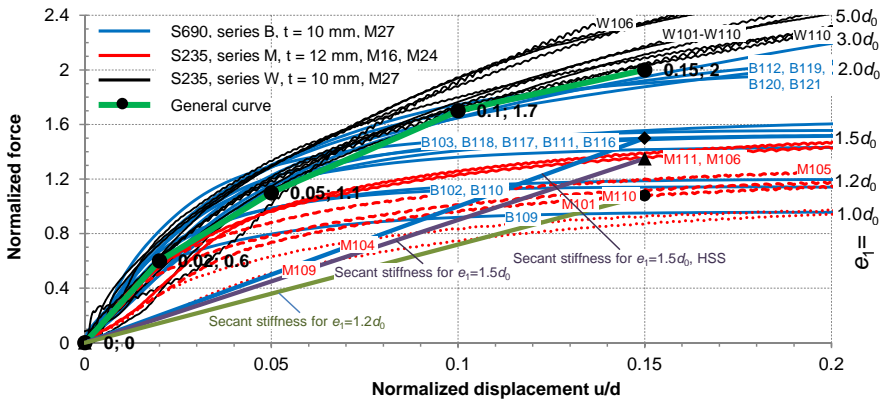


Fig. 11: Normalized load displacement curves for various tests

CONCLUSIONS

The presented test results evidence that the bearing resistance may reach very high average bearing stress as high as $5 f_u$. The elongation of the bolt hole at the ultimate resistance is significant. In ultimate resistance, it reaches the bolt diameter and it becomes more or less constant when the average bearing stress is equal to or larger than $3 f_u$. This is one of the reasons why the upper limit of the bearing strength equal to $2.5 f_u$ (CEN, 2005) or $3 f_u$ (AISC, 2010) could be raised. If the upper limit is too low or if the bearing resistance formula is too conservative, the resistance of the connection may be underestimated even by factor 3 (see Fig. 8). The other reason in favor of the upper bearing strength limit is related to the design of the ductile connection, where the connection is designed to fail in bearing. Such connection will actually fail in bolt shear, but at force larger than the design force.

The presented results also show that the bearing strength is rarely crucial, if standard pitches and end distances are considered. The shear failure of the bolt governs the design when plate thickness-to-bolt diameter becomes larger than 0.25 (Može and Beg, 2014). If the pitches or edge distance in the direction perpendicular to the bearing force are too small, then the block shear or net cross-section failure is critical. The ductility of mild steel as well as of high strength steel plates in bearing allows force redistribution and the summation of the maximum bearing resistances per bolt. The ductility also allows that the bearing strength may be checked for a group of bolts and not necessarily separately for each bolt hole. The paper also gives information on the hole elongations in serviceability limit state and on the shear strength of the bolt for misaligned holes.

REFERENCES

- Aalberg, A. and Larsen, P. K. (2001) *Bearing strength of bolted connections in high strength steel*, translated by Mäkeläinen, P., Kesti, J., Jutila, A. and Kaitila, O., Helsinki: NSCC, 859-866.
- Aalberg, A. and Larsen, P. K. (2002) *The effect of steel strength and ductility on bearing failure of bolted connections*, translated by Lamas, A. and Silva, L. S. d., Coimbra: Universidade de Coimbra, 869-878.
- AISC (2010) 'Specifications for Structural Steel Buildings', *ANS/AISC 360-05*,
- CEN (2005) 'Eurocode 3: Design of steel structures - Part 1-8: Design of joints', *EN 1993-1-8*,
- Henriques, J., Jaspert, J. P. and da Silva, L. S. (2014) 'Ductility Requirements for the Design of Bolted Lap Shear Connections in Bearing', *Advanced Steel Construction*, 10(1), 33-52.
- Kim, H. J. and Yura, J. A. (1999) 'The effect of ultimate-to-yield ratio on the bearing strength of bolted connections', *J Construct Steel Res*, 49(3), 255-270.
- Kouhi, J. and Kortemaa, M. (1990) *Strength tests on bolted connections using high-strength steels (HSS steels) as a base material*, Espoo: Technical Research Centre of Finland.
- Kulak, G. L., Fisher, J. W. and Struik, J. H. A. (2001) *Guide to Design Criteria for Bolted and Riveted Joints*, 2nd ed., Chicago: American Institute Of Steel Construction, Inc.
- Može, P. and Beg, D. (2010) 'High strength steel tension splices with one or two bolts', *Journal of Constructional Steel Research*, 66(8-9), 1000-1010.
- Može, P. and Beg, D. (2011) 'Investigation of high strength steel connections with several bolts in double shear', *Journal of Constructional Steel Research*, 67(3), 333-347.
- Može, P. and Beg, D. (2014) 'A complete study of bearing stress in single bolt connections', *Journal of Constructional Steel Research*, 95, 126-140.
- Puthli, R. and Fleischer, O. (2001) 'Investigations on bolted connections for high strength steel members', *Journal of Constructional Steel Research*, 57(3), 313-326.
- Rex, C. O. and Easterling, W. S. (2003) 'Behavior and modeling of a bolt bearing on a single plate', *Journal of Structural Engineering-Asce*, 129(6), 792-800.
- Snijder, H. H., Ungermann, D., Stark, J. W. B., Sedlacek, G., Bijlaard, F. S. K. and Hemmert-Halswick, A. (1988) *Evaluation of test results on bolted connections in order to obtain strength functions and suitable model factors - Part C: Test data*, Brussels: Commission of the European Communities.

INJECTION BOLTS UPDATE ON RESEARCH AND APLICATIONS

A.M. (Nol) Gresnigt
Delft University of Technology (retired), The Netherlands
Nol@Gresnigt.nl

P.A. (Peter) de Vries
Delft University of Technology, The Netherlands
P.A.deVries@tudelft.nl

ABSTRACT

The present recommended design bearing stress for injection bolts is based on long duration creep tests. This is reasonable for structures with predominantly permanent load as in the initial applications to replace faulty rivets in long span riveted steel bridges. Nowadays, injection bolts are applied in many other types of structures, with less dominant permanent load. For short duration loads much higher design bearing stresses can be allowed.

An overview is given of the research in recent years on statically loaded, fatigue loaded structures and structures with cyclic reverse loading. In order to provide better design guidance for injection bolted connections in various applications, further research on injection bolts is included in the RFCS project SIROCO (2014-2017).

Recent applications of injection bolts are presented, including the application in FRP structures and in an offshore aluminium helicopter deck.

1. INTRODUCTION

The present recommended design bearing stress for injection bolts is based on long duration creep tests. The criterion is that the displacement is not larger than 0.3 mm. This is the same criterion as for high strength friction grip bolts.

Injection bolts have the advantage that in case of overloading no sudden large displacements occur as may happen in high strength friction grip bolted connections when they slip.

In the European Recommendations for Bolted Connections with Injection Bolts (ECCS, 1994) the design bearing stress as determined in long duration testing is used for the serviceability limit state verification. For the ultimate limit state a higher bearing stress is given (factor 1.2), motivated by the above mentioned advantage of injection bolts. The factor 1.2 was chosen by engineering judgement. It was expected that the chosen values would be sufficient to avoid that the ultimate limit state would govern the design. The Eurocode 3 (EN1993-1-8, 2005) rules are formulated somewhat different, but are essentially the same.

In some applications of injection bolts, such as the glass roof in the Amsterdam Central Railway Station (Figure 8), the short duration wind loads by far dominated the

bearing stress. For the Amsterdam glass roof it was asked whether it would be possible to allow much higher bearing stresses for the short duration loadings.

To answer this question the results of research performed in the University of Ljubljana could gratefully be used. In addition to that, short duration tests were performed in the Stevin Laboratory of Delft University of Technology. The test results together with test results from the research in Ljubljana were sufficient to allow much higher bearing stresses for the glass roof in Amsterdam. Results of this research were published in the ECCS-AISC Timisoara workshop (2012). In the next sections 2 and 3, the main results are summarized.

In order to provide better design guidance for injection bolted connections in various applications, further research on injection bolts is included in the Research Fund for Coal and Steel project SIROCO (2014-2017). A summary of the work package 3 on injection bolts is given in section 4. Section 5 gives recent applications of injection bolts.

2. INJECTION BOLTS

Injection bolts (Figure 1) are bolts in which the cavity produced by the clearance between the bolt and the wall of the hole is completely filled up with a two component resin. Filling the clearance of an injection bolt is carried out through a small hole in the head of the bolt. After injection and curing of the resin, the connection is slip resistant. Shear load is transferred through bearing and shear of the bolt.

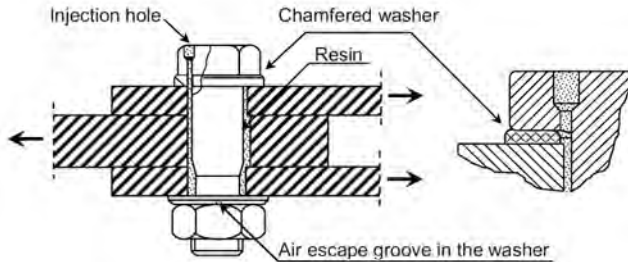


Figure 1. Injection bolt in a double lap joint.

Injection bolts can be manufactured from standard structural bolts. The bolts and washers are adapted to enable the injection of the resin. As compared to other mechanical fasteners, injection bolts have several advantages. Injection bolts may be applied in new structures and in existing structures for repair and strengthening.

Design rules are given in the ECCS Recommendations (1994), which were the starting document for the sections on injection bolts in Eurocode 3 (EN 1993-1-8, 2005). Rules for testing the resin for its bearing strength can be found in EN 1090-2 (2008).

Resins are susceptible to creep-deformation depending on the bearing stress level. In the Fourth International Workshop on Connections in Steel Structures (2000), test results from long duration testing were presented on the two component epoxy resin Araldit SW 404 + HY2404 hardener, now available as RenGel SW 404 + Ren HY 2404.

The main conclusions are:

- Injection bolts are an excellent alternative for replacing faulty rivets in (old) riveted structures.
- Injection bolts can successfully be used for strengthening of (old) structures, especially where welding or HSFG bolting is difficult to apply.
- Ongoing long duration creep tests (more than 5 years) at a bearing stress of 250 N/mm² without exceeding the limit value 0.3 mm displacement.
- High temperature of 70 °C as may occur in bridges has only moderate effect on the deformations. The average creep for ambient temperature (20 °C) was 0.19 mm and for 70 °C it was 0.24 mm (at a bearing stress of 250 N/mm²)
- For the applied resin the allowable bearing stress could be raised from 130 N/mm² up to 200 N/mm².

3. LONG DURATION AND SHORT DURATION HIGH LOADS

In the ECCS-AISC Timisoara workshop (2012), results were reported of test programs in Ljubljana and Delft with short duration monotonic tests and cyclic tests. Figure 2 shows the instrumented test specimens according to EN 1090-2 (2008).

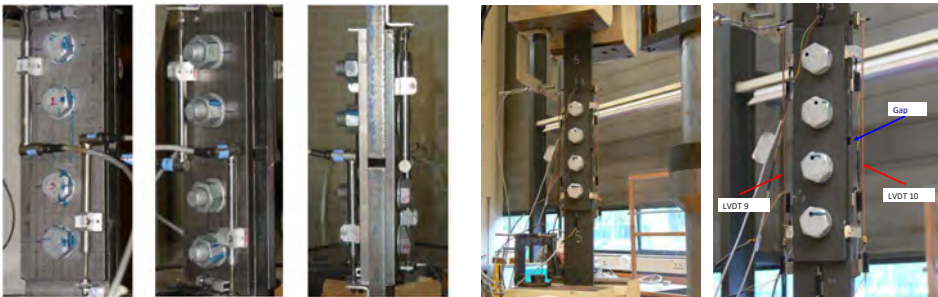


Figure 2. Instrumented test specimens in Ljubljana (left) and in Delft (right).

Selection of test results in Ljubljana, monotonic tests

A selection of test results from the Ljubljana test program is given in Figures 3 to 5. In Figure 3 the effect of preloading is clearly visible.

In Figure 4, the result of the "long duration" creep test according to EN 1090-2 is depicted. It is the tangent extrapolation after three hours with a load equal to 90% of the average resistance from previous short-duration tests. The additional creep limit of 0.002 mm was not exceeded. From the tangent extrapolation to 50 years creep (Figure 4) it is evident that the final creep according to this procedure is less than 0.30 mm.

In Figure 5 the test result of a preloaded connection is depicted. An important difference with the connections with injection bolts is the behaviour after slip. In injection bolted connections the load must increase for further displacements (Figure 3).

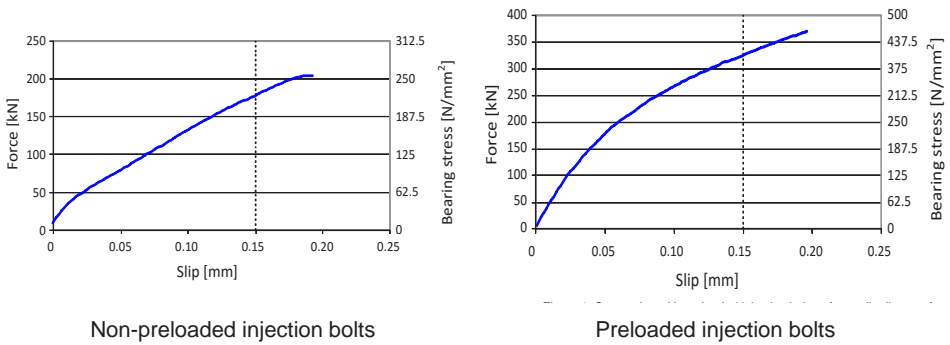


Figure 3. Force – Slip diagrams of monotonic tests (average of 4 measurements).

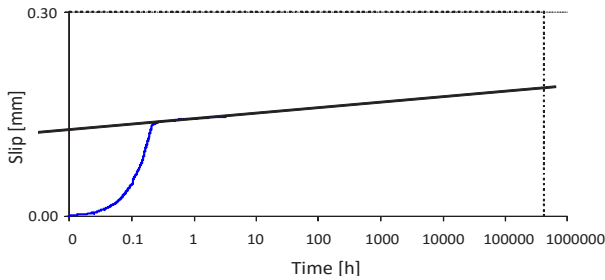


Figure 4. Slip – Time diagram extrapolation to determine the 50 years slip resistance for non-preloaded injection bolts (average of 4 measurements).

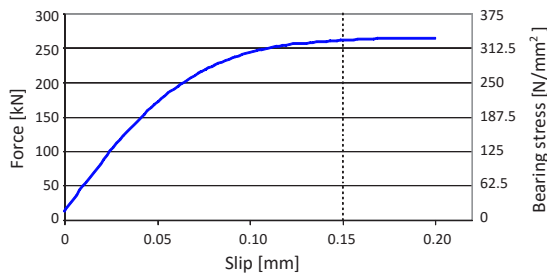


Figure 5. Force – Slip diagram of monotonic testing on a preloaded connection (no injection, average of 4 measurements).

The characteristic values of the slip factor and the bearing resistance of the resin for the corresponding resistance formulas from EN 1993-1-8 were determined as $\mu_k = 0.33$ and $f_{b, \text{resin}} = 200 \text{ MPa}$.

Selection of test results in Ljubljana, cyclic tests

Force-displacement diagrams for two tests are given in Figure 6 and Figure 7. In both cases almost elastic behaviour is observed with narrow hysteresis loops and without visible influence on the loading frequency. In the first 10 to 20 cycles the force amplitude decreases about 10%, but then it remains practically constant (Figure 7). This means that the behaviour of connections with injection bolts at displacement amplitudes of 90% of the allowable slip is very good.

From the short duration cyclic tests it appeared that a much higher bearing stress could be applied without exceeding the deformation limits.

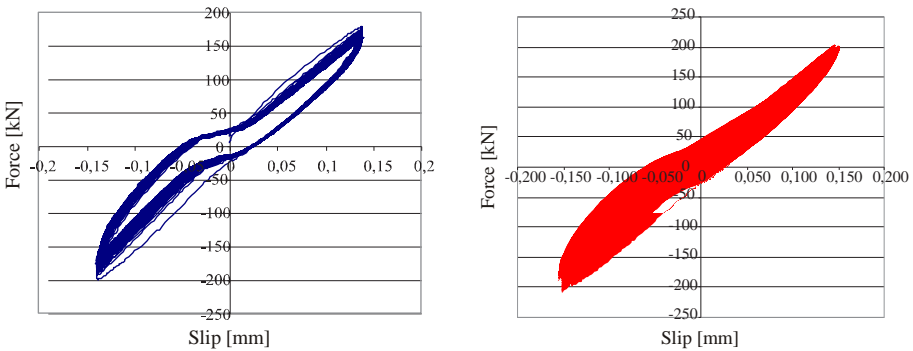


Figure 6. Force-slip diagrams for cyclic tests at 0.05 Hz (left) and at 0,5Hz to 4 Hz (right).

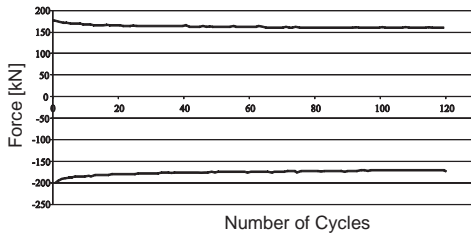


Figure 7. Force amplitudes for cyclic test at 0.05 Hz.

Selection of test results in Delft

In Amsterdam an extension to the railway station is constructed (2011-2013) with a large glass roof (Figure 8). High demands were put on the stiffness of the glass supporting steel structure. Displacements in the bolted connections had to be reduced to very low values. The main reason for that was the safety requirement in case of fire (bus station beneath). To avoid unacceptable levels of uneven heating of the glass, a narrow supporting width of the glass panels was required.

The application of high strength friction grip bolts was problematic because of the need to remove locally the corrosion protection (paint system) and the risk of corrosion traces later on. It was decided to investigate the application of injection bolts M27.

The main load on the roof is wind, which is short duration. It was asked whether it would be safe to allow higher bearing stresses for this load case than the bearing stresses based on long duration creep testing. Injection bolts would be applied in normal size and oversized holes. To answer this question, results of the test programme in the University of Ljubljana were most helpful. The authorities requested for extra testing focusing at the application in Amsterdam.



Figure 8. Artist impression of the extension Railway Station Amsterdam with the glass roof under construction (April 2012, project JSEI).

Six tests were performed on test specimens with M27 bolts as shown in Figure 2. The preparation of the test specimens was done by the contractor guided by the engineering office. The engineering office decided to allow positioning of the bolts in the holes to be what can occur in practice. This resulted in different thicknesses of the resin layers in bearing. The main results of the first test with 10 load cycles are given in Figure 9, where the total elongation on both sides of the connection is measured with LVDT 9 and LVDT 10 as is indicated in Figure 2. Other tests gave similar values.

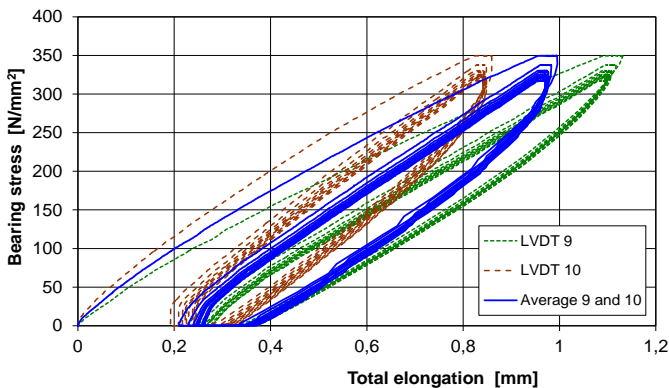


Figure 9. Main results of test 1: Bearing stress – Total elongation, non-preloaded bolts.

The tests were displacement controlled. The maximum average displacement was 0.95 mm. The maximum bearing stress per cycle is given in Figure 10. The decline is the largest in the first cycles and then the average tends to stabilize at about 310 N/mm². It is noted that the last cycle had somewhat smaller displacement than 0.95 mm.

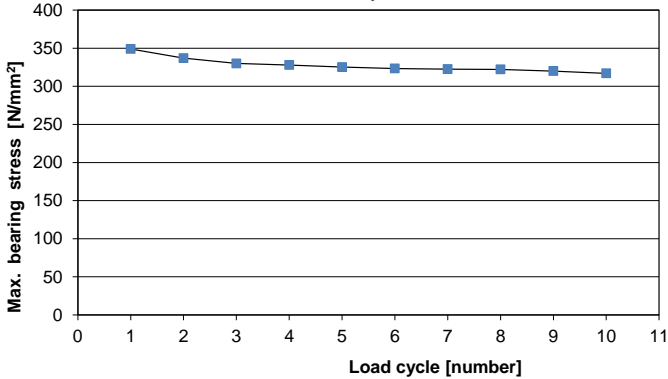


Figure 10. Maximum bearing stress per cycle in test 1.

For a 95% chance of exceeding the design value, the design bearing stress would be 284 N/mm². For the glass roof the following values were adopted:

$$f_{b,resin,long\ duration} = 200\ \text{N/mm}^2 \quad \text{and} \quad f_{b,resin,short\ duration} = 280\ \text{N/mm}^2$$

When short duration and long duration loads are considered in relation to creep, it is noted that in the Eurocode this is only applicable to structures where creep is relatively long duration (concrete, timber).

In injection bolts the creep process is quicker. Wind load is very short duration and will not lead to significant creep, but e.g. snow load and temperature load could be longer duration. In view of this it was decided to consider the following load combinations for the glass roof for the middle long term loads:

$$1.2G+1.0Q_{snow}+0.5Q_{temp} \quad \text{and} \quad 1.2G+1.0Q_{temp}$$

For the short term loads (wind), the standard load combinations were checked with $f_{b,resin}=280\ \text{N/mm}^2$. It was recommended to modify Eurocode 3 part 1-8 and EN 1090-2 accordingly and make a distinction between long duration and short duration load combinations. These findings and other considerations contributed to the motivation for the research on injection bolts in the RFCS project SIROCO in the next section.

4. RESEARCH ON INJECTION BOLTS IN SIROCO

In the RFCS project SIROCO (2014-2017) research is in progress on further development and optimization of connections with injection bolts to achieve slip and creep resistant bolted connections considering various influencing parameters.

The main objectives are:

- Extension and improvement of the design rules in Eurocode 3 Part 1-8 (2005), taking into account various loading conditions.
- Improvement of the test procedures for the design bearing stresses in EN 1090-2 (2008), taking into account various loading conditions.
- Development of guidance on quality assurance of installation and applied resin.

The test program addresses the following:

- a. The creep behaviour for various combinations of long duration load (permanent load) and short duration load (such as wind, snow, traffic), at standard and oversized hole clearances.
- b. The effect of shock load and the effect of alternate loading at various load levels on the creep behaviour, at standard and oversized hole clearances.
- c. The effect of fatigue loading. In preloaded injection bolted connections, part of the load is transferred through bearing and shear, which implies higher stresses in the plates next to the bolt holes than in HSFG bolted connections, resulting in lower fatigue resistance than in HSFG bolted connections. Reference is made to De Jesus et al. (2010) and Van Wingerde et al. (2003).
- d. The influence of the bolt length on the bearing stress distribution and creep to check and if necessary, improve the present design rules on long bolts. Due to bending of the bolts in thick plate packages, uneven bearing stresses occur that have an effect on the creep behaviour. The tests will be accompanied by the development of an analytical model, taking into account the bending stiffness and strength of the bolt and the mechanical properties of the resin.
- e. The influence of the bolt size and hole clearance (i.e. oversized holes). A limited number of tests as in item a. on bolt sizes M16, M36 and M48 is proposed.
- f. Investigation into other resins than Araldite (Rengel) epoxy and how to guarantee their relevant properties like strength, stiffness and creep resistance at various temperatures. It is proposed to select two other resins than the standard resins and to compare their performance to the standard resin. It will also be tried to find a relation between the standard materials properties e.g. as provided by the fabricators of the resins (determined according to relevant standards) and the strength, stiffness and creep performance in an injection bolt.

Non-preloaded injection bolts and preloaded injection bolts are tested. For preloaded injection bolts an extra item to investigate is the behaviour of the bolt loaded in combinations of large normal force with shear force and bending moment. The present rules in EN 1993-1-8 for this load combination on bolts can be optimized for injection bolts. Reference is made to e.g. Renner and Lange (2013).

5. RECENT APPLICATIONS OF INJECTION BOLTS

Several interesting applications of injection bolts are reported such as in FRP bridges, aluminium structures and to repair a crane runway from alternate movements in its bolted connections.

Fibre Reinforced Polymer bridges

At the University of Warwick in the UK, research has been performed into the application of injection bolts in Fibre Reinforced Polymer (FRP) Bridge Engineering. The results from a series of static tests on resin injected bolted joints with pultruded FRP material are reported in Qureshi and Mottram (2012). See also Zafari et al. (2016).

The aim was to characterise a method of connection that could be fatigue and slip resistant. For comparison, tests are also carried out on standard bolted connections without resin with 2 mm clearance holes.

Slip in connections is a major issue in bridge engineering, which has to be controlled if the structural scheme is to perform satisfactorily over its service life. The transfer of force in FRP joints by way of frictional force by using High Strength Friction Grip (HSFG) bolts cannot be relied upon, because the steel bolting is known to lose its pre-tension with time due to the viscoelastic properties of the FRP.

The aim of the preliminary study was to offer a potential solution to developing a suitable slip resistant connection. Tests were conducted on double lap shear connections according to Annex G of EN 1090-2 (2008). The injection bolts and bottom washer were prepared as per Annex K of the same standard. A new top washer has been designed and tested to ensure smooth resin filling in the cavity between the bolts (M16 with 2 mm hole clearance) and the walls of the holes. It was expected that resin injected bolting will provide a mechanical fastening system that has locking capabilities.

The authors indicate that if successful, the outcome of their research will address the challenge of durability and will ensure longer service lives for FRP bridges. The results will also help in preparation of recognised design guidelines for FRP bridges.

Two resins were applied: Araldit RenGel SW404 + HY2404 and Sikadur-30. For the service load range of 0-25 kN, the maximum slip was no more than 0.08 mm at the assumed service load limit. Tensile loading was increased beyond the 25 kN limit to generate slip of more than 0.15 mm for determination of the slip load in accordance with EN 1090-2 (2008). It was found to be 39 kN and 33 kN at top and bottom bolt levels for Araldit RenGel SW404 + HY2404. Similarly, for specimen with Sikadur-30 resin, the slip load was shown to be 40 kN and 42 kN at the two bolt levels (Figure 11).

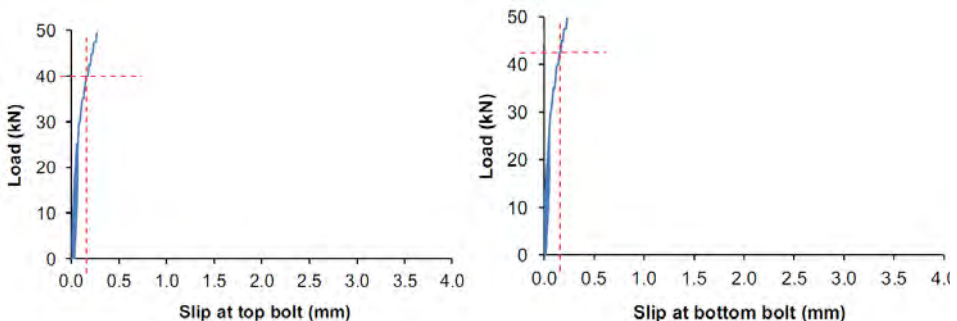


Figure 13. Load slip curve for test M16_18HL_Sika_01 (M16 bolts, 18 mm holes, Sikadur-30 Resin).

Figure 11. Load slip curves according to Qureshi and Mottram (2012).

Another innovative development was a top washer with a new geometry to ensure smooth and rapid passage of the resin into the cavity between the bolt shaft and walls of the connecting FRP material. For a constant radial distribution of the resin around the threaded bolt shaft, an innovative steel bolt centreline location jig was built to precisely position the bolts at the centreline of their holes.

Test results with the resin injected bolting showed this method of connection has promise for FRP bridge engineering in terms of being slip resistant. The next stage in establishing their structural engineering performance is to conduct creep testing to determine the resin's design bearing resistance. Knowing this strength property will then allow specification of the bearing stress range for essential fatigue characterisation.

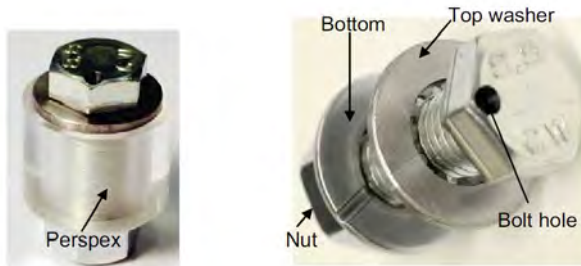


Figure 6. Injection bolted assembly with Perspex to check passage of resin.

Figure 12. Injection bolts with special top washer (Qureshi and Mottram, 2012).

It is noted that at Delft University no bad experiences are known with the washers as prescribed in EN 1990-2 (2008).

Aluminium structures

High strength friction grip bolts in aluminium structures may suffer from decrease of the preload, due to the susceptibility of the aluminium to creep. Another issue is the danger of galvanic corrosion between carbon steel and aluminium.

Stainless steel bolts may be a solution. But also stainless steel may suffer from creep. In the SIROCO project much attention is paid to this problem. Application of injection bolts is recognized as an attractive solution.

A recent application is in an offshore aluminium helicopter deck where HSFG bolted joints showed alternate movement due to loss of pretension. Several thousands of bolts were replaced by injection bolts to solve this problem. A special test program was carried out to investigate its applicability and best execution in view of the special site conditions, in particular the low temperatures that may hamper curing of the resin. Warning up the aluminium during some hours and applying resin with room temperature was prescribed.

Further research in the effect of low temperatures and the effect of partial curing on the bearing resistance is recommended.

Repair of a structure suffering reversal movements

The use of injection bolts has been proposed for solving a problem of loosening of conventional bolt assemblies installed in a roof that supports suspended cranes in the UK. The proposal has been piloted successfully and is favoured as the solution to the problem. This solution would improve the resistance to load reversal that has been modelled and measured. It would also improve the resistance to fatigue and might be an issue over the full design life of the structure.

On site, a number of existing connections were modified which were shown to be experiencing issues with load reversal in service under crane loading (leading to displacements in the connections) which were measured using a variety of LVDTs across the joints and strain gauges in the members. Measurements were taken both before and after remedial works. Two different resins were trailed on site.

Tests were performed with these two different resins, Sika AnchorFix and Sikadur 33. Because of the need to take the cranes out of service as short as possible, Sika AnchorFix appeared to be by far the most appropriate as the curing times were vastly less than the Sikadur 33 and it appeared to provide a more reliable cure (some of the Sikadur 33 samples did not appear to cure properly even in the offsite trials), despite Sikadur 33 showed about 20 % better results for the bearing strength in short duration testing (EN 1090-2, 2008).

Both resins were effective at dramatically reducing slip in the connections to acceptable levels. However the ease of application, curing time and robust curing of the Sika AnchorFix provided confidence that it was the better solution for this application.

During the investigations before the pilot trials, mock-ups were used to establish the practical means of introducing the resin and its ability to penetrate the assembled joint. The preferred solution uses modified washers with holes as the means of introducing the resin rather than a hole in the bolt as illustrated in EN 1090-2. With this method and using the preferred resin, the deformation of the assembly under load has been shown to be within that allowed by the code for fit bolt assemblies.

In terms of the RFCS SIROCO project, further research on the use of resin injection would be welcome if it leads to improved codification of the results, such as Table 8.1 of EN 1993-1-9. For example, the edge distances required in Table 8.1 are larger than those required by EN 1993-1-8. Resin injection is most useful for improving an existing structure (rather than for a new design), and often such structures will have been designed with edge distances for quasi-static loads to Part 1-8.

6. CONCLUDING REMARK

In over 50 years of application, injection bolted connections have performed well. There are no cases known of bad experiences. Continuing research and the development of design rules and rules for execution in Eurocodes has contributed to an increase of applications in many countries, not only in steel structures but also in FRP and aluminium structures. The present research in SIROCO is believed to further increase successful applications.

7. REFERENCES

- ECCS, (1994). *European recommendations for bolted connections with injection bolts*. ECCS publication No. 79, Brussels.
- Gresnigt, A.M., Sedlacek, G., Paschen, M. (2000). *Injection bolts to repair old bridges*. Fourth International Workshop on Connections in Steel Structures, Roanoke, VA, USA.
- Nol Gresnigt, Darko Beg and Frans Bijlaard (2012). *Injection bolts in steel structures with short duration high loads*. Seventh International Workshop on Connections in Steel Structures, 30 May - 02 June 2012 in Timisoara, Romania.
- EN 1993-1-1, (2005). *Eurocode 3, Design of Steel structures. Part 1.1 - General Rules and Rules for Buildings*.
- EN 1993-1-8, (2005). *Eurocode 3 Design of Steel Structures, Part 1-8: Design of joints*.
- EN 1090-2, (2008). *Execution of steel structures and aluminium structures, Part 2: Technical requirements for steel structures*.
- Sedlacek G., Paschen M., Gresnigt A.M. (1997). *Bericht zur Erstanwendung der Injektions-schrauben bei der Hauptträgerstegverstärkung an der Schlossbrücke Oranienburg, Berlin*. Rheinisch-Westfälische Technische Hochschule, Lehrstuhl für Stahlbau, Aachen, Germany.
- Van Lint H.J., Van Wolfswinkel J.C., Gresnigt A.M. (2012), *Besparen op injectie-bouten (Economic design with injection bolts)*. Bouwen met Staal, April 2012, (in Dutch language).
- SIROCO (2014-2017), *Execution and reliability of slip resistant connections for steel structures using carbon steel and stainless steel*. Research Fund for Coal and Steel (RFCS), Grant No RFSR-CT-2014-00024. Coordinated by Prof. Dr.-Ing. habil. Natalie Stranghöner, Universität Duisburg-Essen.
- Renner, A. and Lange, J. (2013), *The influence of the bolt grade on its behaviour under combined tension and shear*. Research and Applications in Structural Engineering, Mechanics and Computation – Zingoni (Ed.). Taylor & Francis Group, London, ISBN 978-1-138-00061-2 (pp.1329-1334).
- Qureshi, Jawed and Mottram, J. Toby (James Toby), (2012), *Resin injected bolted connections: a step towards achieving slip-resistant joints in FRP bridge engineering*. FRP Bridges Conference, London, UK, 13–14 September 2012. Proceedings FRP Bridges pp. 55-66. Permanent WRAP url: <http://wrap.warwick.ac.uk/58223/>.
- Zafari, B., Qureshi, J., Mottram, J.T. and Rusev, R. (2016), *Static and fatigue performance of resin injected bolts for a slip and fatigue resistant connection in FRP bridge engineering*. Structures 7 (2016) pp. 71-84, <http://dx.doi.org/10.1016/j.istruc.2016.05.004>.
- De Jesus, A.M.P., Da Silva, J.F.N., Figueiredo, M.V., Ribeiro, A.S., Fernandes, A.A., Correia, J.A.F.O., Maeiro, J.M.C. (2010), *Fatigue behaviour of resin-injected bolts: an experimental approach*. Iberian conference on fracture and structural integrity.
- Van Wingerde, A.M., Van Delft, D.R.V., Knudsen, E.S. (2003), *Fatigue behaviour of bolted connections in pultruded FRP profiles*. Plastics, Rubber and Composites: Macromolecular Engineering Volume 32, Issue 2, 2003 Special Issue: FRC2002.

BEHAVIOR OF SINGLE-BOLTED LAP-SPLICE JOINTS AT ELEVATED TEMPERATURES

Erica C. Fischer, Ph.D., P.E.
Design Engineer, Degenkolb Engineers
600 University Street, Suite 720, Seattle, WA 98101
efischer@degenkolb.com

Amit H. Varma, Ph.D.
Professor, Purdue University, Robert L. and Terry L. Bowen Laboratory
1040 S. River Road, West Lafayette, IN 47906
ahvarma@purdue.edu

Qiaqia Zhu
Design Engineer, KPFF Consulting Engineers
1601 5th Avenue #1600, Seattle, WA 98101
qzhu@kpf.com

ABSTRACT

A series of lap splice joints were tested to determine the bolt shear and plate bearing behavior of connections at elevated temperatures. Each lap splice joint was constructed from two ASTM A36 plates and connected with one ASTM A325 bolt. The specimens were tested in steady-state conditions at ambient temperature, 400°C, and 600°C. The tearout failure of the specimens occurred suddenly, and there was little or no loss of load carrying capacity prior to this happening. This behavior was not consistent with the softening behavior previous researchers included in their analytical models. For specimens using 6.4mm (0.25inch) thick plates, the maximum load was predicted well using the component models. However, when the plate thickness was increased to 9.5mm (0.375inch), the component model underpredicted the maximum load for the splice plate.

1. INTRODUCTION AND MOTIVATION

Bolted simple connections are used in steel-frame buildings to connect members of the gravity frame together. These connections are popular in U.S. building practices because they provide dimensional flexibility during construction. Inspections for bolted connections are less intensive than welded connections, increasing the speed of construction. Simple bolted connections include: shear-tab, single-angle, and double-angle connections. These connections are designed to resist vertical shear forces at ambient temperatures. During a building fire, composite floor beams of steel-frame buildings deflect excessively which imposes large tensile forces on the connections. Failure of connections can cause the fire to spread to other floors or compartments of

buildings and typically leaves columns unbraced for longer lengths than they were originally designed for.

The behavior of simple connections during building fires has shown that these connections can resist axial forces and negative moment in addition to the shear forces they were designed for (Agarwal et al., 2014). The interaction between the connection components includes slip, contact, elastic-plastic deformation, and separation. The distribution of local stresses throughout the connection is a three-dimensional problem due to the clamping effect caused by the bolts and bending effects. To simulate the effect of fire on full buildings, engineers must incorporate the full connection behavior in a series of nonlinear springs. This behavior includes the axial force-axial displacement-temperature (P - δ - T) relationships for controlling failure modes of the connection; namely: bolt shear fracture, and plate bearing.

Axial load-axial displacement (P - δ) relationships were developed by researchers to aid engineers in predicting the behavior of simple connections at elevated temperatures (Agarwal et al., 2014; Sarraj et al., 2007). However, these relationships were developed using the Eurocode 3 (CEN, 2005) retention factors, and benchmarked against experiments which took place using European grade steel (Burgess et al., 2009). This paper discusses a series of lap splice joints tested for bolt shear fracture and plate bearing. The experiments are performed using U.S. grade steel typically used in U.S. construction practice. The purpose of these tests is to benchmark the component spring models for bolt shear fracture and plate bearing for U.S. building construction and design practices.

A series of experiments were performed on lap spliced joints to examine the axial force-axial displacement (P - δ) relationships at elevated temperatures for bolt shear and plate bearing failure modes. Previous researchers have examined the bolt shear and plate bearing capacity of simple connections at elevated temperatures (Sarraj et al., 2007; Hu and Engelhardt, 2011; Kirby, 1995; Rex and Easterling, 2003; Hanus et al., 2011; Kodur et al., 2012; Hirashima et al., 2014). This research has provided insight into governing failure modes of simple connections subjected to pure axial force at elevated temperatures, in addition to the reduction in bolt shear stress capacity with increasing temperature.

The most commonly used bolts in simple connections are ASTM A325 bolts. These bolts are tempered at a temperature of 427°C to reach their required strength level. Therefore, previous research demonstrates a significant reduction in shear stress (Sarraj et al., 2007; Hu and Engelhardt, 2011; Kirby, 1995) when the bolt temperature is greater than 400°C.

2. DESIGN OF EXPERIMENTS

A series of lap splice joints were tested to determine the bolt shear and plate bearing behavior of connections at elevated temperatures. Each lap splice joint was constructed from two ASTM A36 plates and connected with one ASTM A325 bolt. The specimens were tested in steady-state conditions at ambient temperature, 400°C, and 600°C. Each of these tests used high temperature ceramic fiber heaters to heat the specimen, and Type K thermocouples to measure the temperature distribution on the

plates and through the bolt throughout the test. Both testing series used the same test setup and instrumentation.

2.1 Test setup

The test setup consisted of two steel beams connected by two hydraulic rams and post tensioning bars. Each specimen was loaded in tension to cause either bolt shear or plate bearing failure modes. The bottom beam was post tensioned to the laboratory floor, while the top beam was allowed to move vertically through force applied by the hydraulic rams. Figure 1a shows an elevation view of the loading frame with a specimen inserted. Each specimen was bolted to the top and bottom loading beam through a t-stub connection as shown in Figure 1b. The edge distance, diameter of bolt, and plate thicknesses vary between specimens. Tables 1 and 2 show these dimensions for the bolt shear and plate bearing tests.

Two 305mm x 305mm (12in x 12in) ceramic heaters with a maximum surface temperature of 1250°C were used to heat each side of the specimens at a rate of 15°C/minute. A thermocouple was placed inside of the bolt shank to determine when the target temperature was obtained. Insulation was used to protect the sensor equipment and the loading frame from heat damage. Once the target temperature had been reached, loading of the specimen occurred until bolt shear fracture or tearout failure of the plates.

Table 1 Test matrix and results for lap-splice joints tested for bolt shear failure

Specimen Name	Temperature	Failure Load (P)	Failure axial displacement (δ)
BS-1	Ambient	137 kN (30.8 kip)	5 mm (0.2 inch)
BS-2	Ambient	133 kN (29.9 kip)	6.9 mm (0.27 inch)
BS-3	400°C	102 kN (22.9 kip)	10.7 mm (0.42 inch)
BS-4	600°C	43 kN (9.7 kip)	10.9 mm (0.43 inch)

2.1 Instrumentation

The displacement of the bolt and plates of the lap splice joint were measured using typical voltage sensors. The temperature distribution through the bolt and on the face of both plates was measured using Type K thermocouples. The displacement sensors were attached to metal strips. Two displacement sensors were used at each location in order to account for potential rotation of the upper loading beam of the loading frame. Each displacement sensor was mounted to the lower loading beam. Displacement transducers and string potentiometers were mounted to the bottom loading beam and attached to metal straps welded to the specimen.

Type K thermocouples were used in all elevated temperature tests to capture the high temperatures. Thermocouples were mounted on both the head and tail of the bolt, and both plates of the lap splice joint specimens. In order to measure the temperature at the shear plane of the bolt a 3.2mm (0.125in) diameter hole was drilled through the bolt from the bolt head to a location that was about 3.2mm (0.125in) away from the shear plane. The hole was drilled carefully to not reach the location of the shear plane so the

hole did not affect the shear strength of the bolt. A thermocouple was placed inside this hole to measure the temperature very near to the shear plane. The temperature readings from this thermocouple demonstrated when the temperature distribution through the bolt shank had stabilized and loading could begin in each test.

Table 2 Test matrix and results for lap-splice joints tested for bolt shear failure

Specimen Name	Temperature °C	Bolt Diameter mm (inch)	Plate Thickness mm (inch)	Failure Load (P) kN (kip)	Failure axial displacement (δ) mm (inch)
1-PB-A	Ambient	19 (0.75)	6.35 (0.25)	77.4 (17.4)	5.6 (0.22)
2-PB-400	402	19 (0.75)	6.35 (0.25)	64.4 (14.5)	22.9 (0.9)
3-PB-600	610	19 (0.75)	6.35 (0.25)	30.5 (6.9)	38.8 (1.5)
4-PB-400-7_8	406	22.2 (0.875)	6.35 (0.25)	76.2 (17.1)	27.2 (1.1)
5-PB-600-7_8	605	22.2 (0.875)	6.35 (0.25)	33 (7.4)	25.8 (1)
6-PB-400-3_8	417	19 (0.75)	9.5 (0.375)	100.6 (22.6)	57.1 (2.2)
7-PB-600-3_8	607	19 (0.75)	9.5 (0.375)	46.1 (10.4)	29.9 (1.2)

2.1 Testing protocol

Each specimen was tested under steady state conditions. Heat was applied both surfaces of the specimen. When the target temperature was obtained, load was applied to the specimen as the target temperature was held constant. The tests were terminated when failure occurred in the specimen (bolt shear fracture or tearout failure of the plate) or when the specimen could no longer carry the load. The bolt shear and plate bearing behavior of bolts and plates were evaluated by testing single-bolted lap-splice joints at ambient and elevated temperatures. Each specimen used a 19mm (0.75in) diameter bolt to connect two 12.7mm (0.5in) thick plates. Each specimen was designed with bolt shear as the controlling limit state at ambient temperature. The washers are ASTM F436 and the nuts are ASTM A563 Grade DH. Threads of the bolt were included on the shear plane in each test. The shear strength of the bolt was calculated using Equation J4-4 in the AISC 360-10 *Specification* (AISC, 2010) as 134kN. The target temperature was the temperature of the bolt shank at the shear-plane rather than the temperature on the face of the lap-splice joint.

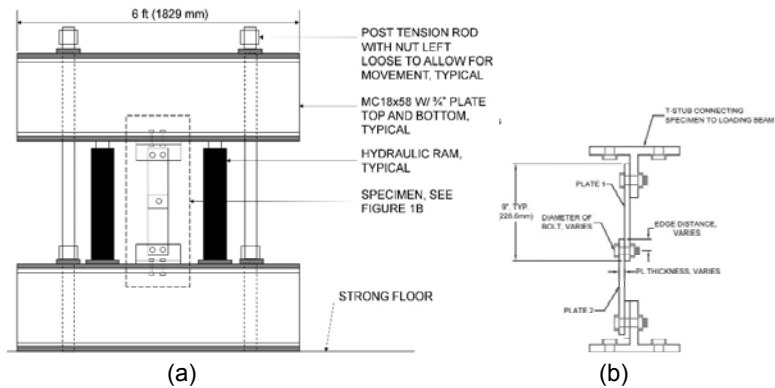


Figure 1 Testing frame for bolt shear and plate bearing lap splice joint (a) Elevation view of test setup with elevation view of specimen dimensions and setup, (b) Profile view of specimen setup

3. BOLT SHEAR TESTS

Four lap splice joint specimens were tested to examine the effect of temperature on the axial force-axial displacement ($P-\delta$) relationship for the bolt shear failure mode, and compare the experimental testing results to the component model developed by Sarraj et al. (2007). Table 1 shows the testing matrix of these four specimens along with failure load and failure axial displacement. Each specimen used a 12.7mm (0.5inch) thick plate with an ASTM A325 19mm (0.75inch) diameter bolt.

Bolt shear fracture is typically categorized as brittle fracture, however, at elevated temperatures bolt shear fracture surface is observed as concave implying a more ductile failure mode than at ambient temperature. The two specimens tested at ambient temperature fractured at measured shear displacements of 5mm and 6.9mm for BS-1 and BS-2 respectively. These two tests served as control specimens for the heated tests. The failure load and failure displacements of these tests were within 5% of one another providing consistency in the testing protocol, and are shown in Table 1.

Limited plate bearing deformation was observed during these experiments. Photographs of the fractured bolts, including the fracture surface from test BS-4 are shown in Figure 2. Failure of specimens BS-1 and BS-2 was defined by sudden bolt shear fracture, however, failure of BS-3 and BS-4 was defined by loss of load carrying capacity of the specimen. After the testing of BS-3 and BS-4, the bolt was not fractured completely. The fracture surface of the bolt in specimens BS-1 and BS-2 was shiny and smooth, but not flat. The fracture surface of the bolt after testing of specimen BS-3 showed blue color and the texture was rougher than the fracture surface of the bolts in the ambient tests. From the load-displacement results, at the both 400°C and 600°C tests, the shear strength and the stiffness of the bolts dropped significantly. The shear displacement of the bolt increased with increasing temperature, indicating increasing

ductility. The shear strength of the bolt and failure displacement of all the tests are listed in Table 1.

Figure 3 shows the retention factors obtained from the tests described in this paper are consistent with those obtained by other researchers (Yu et al., 2009; Kodur et al., 2012). Figure 3 shows that these retention factors agree well with those suggested in Appendix 4 of the *AISC Specification* (AISC, 2010).



Figure 2 Bolt shear fracture for specimen BS-4 (600°C)

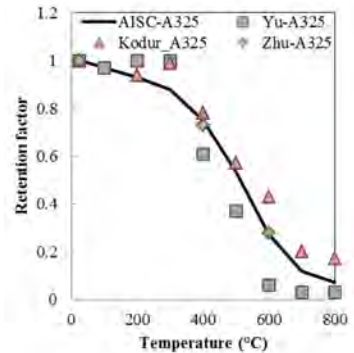


Figure 3 Experimentally measured retention factors for ultimate bolt stress varying with temperature compared with *AISC Specification* (AISC, 2010)

4. PLATE BEARING TESTS

Single-bolted lap splice joints were used to investigate the plate bearing failure mode of single-bolted lap-splice joints varying temperatures. The testing parameters included: (i) temperature, (ii) bolt diameter, and (iii) plate thickness. The experimentally obtained axial load-axial displacement (P - δ) relationships were compared with those developed by Sarraj et al. (2007).

The displacement of the plates and bolts were measured during each of the experiments. The temperature distribution of the plate and bolt was also collected as data during the experiment. Each specimen was heated to a target temperature, and then loaded to failure while the temperature remained constant. Failure of the specimen was categorized as either tear out failure of the plate, or loss of load carrying capacity of the specimen. The testing matrix, maximum axial forces (P), and maximum axial displacements (δ) are shown in Table 2.

The plates in all of the specimens were designed with standard bolt holes with minimum required edge distances prescribed by the AISC *Specification* (AISC, 2010). All steel plates were ASTM A36, with widths of 114mm (4.5inch). The washers were ASTM F436 and the nuts were ASTM A563 Grade DH. The bolt in all the tests was snug-tight only and the washer was installed on the side of the nut. The estimated plate bearing strength and bolt shear strength of the specimens were calculated using AISC Equations J3-6b and J4-4 (AISC, 2010). The retention factors for the tensile strength of the plates were assumed to follow the retention factors developed by NIST researchers (Choe et al., 2014). The retention factors for the bolt ultimate stress were assumed to follow the AISC *Specification* (AISC, 2010).

The two plates in the specimen are referred to as “Plate 1” and “Plate 2”. Figure 1 shows Plate 1 and Plate 2 in each of the specimens. Specimen 7-PB-600-3_8 failed in bolt shear and small bolt hole elongation was observed after the test. Figure 4 shows specimen 3-PB-600 bolt bearing after the completion of testing. Photos of the remainder of the specimens are in Fischer (2015). The photos in Figure 4 show the large bolt hole elongation observed in Specimen 3-PB-600. Specimens 6-PB-400-3_8, and 7-PB-600-3_8 used thicker plates and smaller bolt hole elongation was observed after the testing of these specimens.

The applied load-axial deformation ($P-\delta$) curves for each of the tests are shown in Figure 5. Observation of the plates after the experiment showed the deformation in the plates was not symmetrical. Plate 2 controlled the failure of the control specimen (1-PB-A) and the specimens tested at 400°C, whereas Plate 1 controlled the failure of the specimens tested at 600°C regardless of plate thickness and bolt diameter. As discussed previously, displacement of the plates, bolt head, and bolt nut were considered during the experiments. The displacement of Plate 1 was calculated as the difference in the measured displacement of Plate 1 and the bolt head. Likewise, the displacement of Plate 2 was calculated as the difference in the measured displacement of Plate 2 and the bolt nut.



Figure 4 Lap splice joints after testing for plate bearing failure mode (a) Specimen 3-PB-600, Plate 1, (b) Specimen 3-PB-600, Plate 2

Specimens 1-PB-A and 2-PB-400 failed in tearout failure of Plate 2. Specimen 1-PB-A has fracture on one side of the bolt hole on Plate 2 and was parallel to the direction of loading. Specimen 2-PB-400 had a flared fracture path on both sides of the bolt hole. The retention factor from Eurocode (CEN, 2005) for the steel plate (k_y, T) at 400°C is 1.0, however, the maximum measured load capacity (P_m) of the lap splice joint was reduced by 20% from Specimen 1-PB-A. No shear deformation was observed on the bolts after the test. The test data shows good correlation with the component model, however it shows the failure occurred suddenly instead of the softening of the applied

load-axial displacement ($P-\delta$) presented using the component model created by Sarraj et al. (2007) and further developed by Agarwal et al. (2014).

The test of Specimen 3-PB-600 was stopped when the deformation of the plate exceeded 1.5 times the diameter of the bolt (d_b). Due to this criteria, the test was stopped before tearout failure of the plates. While no bolt shear deformation was observed during the testing of Specimen 2-PB-400, visible bolt shear deformation was observed after testing Specimen 3-PB-600. The maximum measured load capacity (P_m) of Specimen 3-PB-600 was 60% of that of Specimen 1-PB-A. The applied load-axial displacement ($P-\delta$) data is shown in Figure 5. This figure shows the failure displacement of Specimen 3-PB-600 is larger than expected. This can be attributed to the bolt shear deformation that occurred in addition to bolt hole elongation. Compared with Specimens 1-PB-A and 2-PB-400, the bolt hole elongation was more in Specimen 3-PB-600.

The failure mode of Specimen 4-PB-400-7_8 was controlled by tearout failure of Plate 1. The fracture occurred only on one side of the bolt hole and similar to Specimen 2-PB-400 the fracture was flared rather than parallel with the direction of loading. No visible bolt shear deformation was observed after the test. Increasing the diameter of the bolt increased the maximum measured load capacity (P_m) by 18% from Specimen 2-PB-400. The applied load-axial displacement ($P-\delta$) compared with the component model curve for plate bearing, there is good correlation between the test data and the component model. After the experiment was complete the bolt hole elongation of Specimen 4-PB-400-7_8 is much larger than the bolt hole elongation observed after testing Specimen 2-PB-400.

While bolt shear deformation was observed after testing 3-PB-600, no bolt shear deformation was observed when the bolt diameter was increased to 22.2mm (0.875inch). The maximum measured load capacity (P_m) increased by 4% from specimen 3-PB-600, which is negligible when taking into account variation in fabrication and construction of the specimen. The applied load-axial displacement ($P-\delta$) showed that the failure displacement is larger than calculated using the component model relationship. In addition, the softening of the curve that is incorporated into the component model plate bearing relationship was not observed with the test data.

Specimen 6-PB-400-3_8 failed due to tearout failure of Plate 1. Fracture occurred on both sides of the bolt hole in a flared path. No bolt shear deformation was observed after this test. The increase in plate thickness from 6.4mm to 9.5mm increased the maximum measured load capacity (P_m) by 56%. The maximum measured load capacity (P_m) was larger than predicted using the component model. The maximum displacement predicted by the model is consistent with the test data.

The testing of Specimen 7-PB-600-3_8 was stopped when bolt shear fracture occurred. The bolt hole elongation is smaller than the other specimens tested at 600°C. Increasing the plate thickness from 6.4mm to 9.5mm increased the maximum load capacity (P_m) by about 50%. The applied load-axial displacement ($P-\delta$) compared with the component model prediction, similar to specimen 6-PB-400-3_8, the maximum measured load capacity (P_m) is larger than the maximum load predicted by the component model curve; however, the maximum displacement predicted by the model is consistent with the test data.

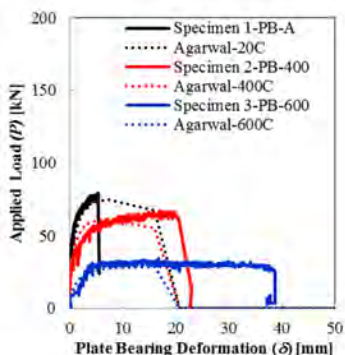


Figure 5 Applied load-axial displacement (P - δ) for lap splice joints tested for plate bearing failure modes compared with component model created by Sarraj et al. (2007), and Agarwal et al. (2014) Specimens 1-PB-A, 2-PB-400, and 3-PB-600

5. SUMMARY AND CONCLUSIONS

This paper presented the experimental investigations of bolt shear and plate bearing failure modes at varying temperature. Parameters such as diameter of bolt and thickness of plate were taken into consideration during this research project. Applied axial force-axial deformation (P - δ) relationships were obtained from the experiments as well as failure modes. Sarraj et al. (2007) developed axial force-axial displacement (P - δ) relationships for the plate bearing and bolt shear fracture failure modes. The bolt shear relationship was benchmarked against experimental tests performed by Yu et al. (2009); however, the plate bearing relationships were not experimentally verified. In addition, these relationships were developed for European building construction with European grade steel.

The results of the experiments performed and described in this paper were compared with the component model developed by Sarraj et al. (2007) and later improved by Agarwal et al. (2014). The comparison showed that the softening behavior showed in the component model curves was not present during the test. The tearout failure of the specimens occurred suddenly, and there was little or no loss of load carrying capacity prior to this happening. For specimens using 6.4mm (0.25inch) thick plates, the maximum load was predicted well using the component models. However, when the plate thickness was increased to 9.5mm (0.375inch), the component model underpredicted the maximum load for the splice plate. The component model also underpredicted the maximum axial displacement for specimens tested at 600°C and using 6.4mm (0.25inch) thick plates.

The lap splice specimens tested in this paper had double curvature of the plates. This curvature caused rotation of the bolt and therefore the displacement data was post processed after the test. Future lap splice tests performed to evaluate the axial load-axial displacement relationships should be designed to limit the curvature of the plates and subsequent rotation of the bolt as this could skew the data results.

REFERENCES

- Agarwal, A., Selden, K. L., & Varma, A. H. (2014). Stability Behavior of Steel Building Structures in Fire Conditions: Role of Composite Floor Systems with Shear-Tab Connections. *Journal of Structural Fire Engineering*, 5(2), 77-96.
- American Institute of Steel Construction, Inc. (2010). Specification for Structural Steel Buildings, ANSI/AISC 360-10. Chicago, IL: AISC.
- Choe, L., Luecke, W., and Gross, J. (2014). "A comparison of two temperature-dependent stress-strain models for structural steel under transient heating conditions", in *8th International Structures in Fire Conference*. Shanghai, China
- European Committee for Standardization (CEN). (2005). Eurocode 3: Design of Steel Structures, Part 1.2: General Rules - Structural Fire Design.
- Fischer, E.C. (2015). *Behavior of Simple (Shear) Connections in Steel-Frame Buildings During Fire* (Doctoral Dissertation). Purdue University Lyles School of Civil and Environmental Engineering. West Lafayette, IN.
- Hanus, F., Zilli, G., & Franssen, J. M. (2011). Behaviour of Grade 8.8 Bolts under Natural Fire Conditions - Tests and Model. *Journal of Constructional Steel Research*, 67(8), 1292-1298.
- Hirashima, T., Esaki, Y., & Ando, S. (2014). "Load-Deformation Behavior of Bolted Double-Splice Friction Joints at Elevated Temperature," in *Proceedings of 8th International Conference on Structures in Fire*. Shanghai, China.
- Hu, G., & Engelhardt, M. D. (2011). Investigations of the Behavior of Steel Single Plate Beam End Framing Connections in Fire. *Journal of Structural Fire Engineering*, 2(3), 195-204.
- Kirby, B. R. (1995). "The Behaviour of High-strength Grade 8.8 Bolts in Fire", *Journal of Constructional Steel Research*, 33, 3-38.
- Kodur, V., Kand, S., & Khaliq, W. (2012). "Effect of Temperature on Thermal and Mechanical Properties of Steel Bolts", *Journal of Materials in Civil Engineering*, 24, 745-774.
- Rex, C. O., & Easterling, W. S. (2003, June). "Behavior and Modeling of a Bolt Bearing on a Single Plate", *Journal of Structural Engineering*, 792-800.
- Sarraj, M., Burgess, I. W., Davison, J. B., & Plank, R. J. (2007). "Finite element modeling of steel fin plate connections in fire", *Fire Safety Journal*, 42, 408-415.
- Yu, H., Burgess, I. W., Davidson, J. B., & Plank, R. J. (2009). "Experimental investigation of the behaviour of fine plate connections in fire", *Journal of Constructional Steel Research*, 65, 723-736.

THE BEHAVIOR OF DOUBLE-LAP SPLICE BOLTED STEEL CONNECTIONS WITH FIBER-REINFORCED POLYMER FILLS

Kara D. Peterman
Northeastern University, Boston, Massachusetts 02115, USA
k.peterman@neu.edu

Julieta Moradei
Northeastern University, Boston, Massachusetts 02115, USA
moradei.j@husky.neu.edu

James D'Aloisio
Klepper Hahn and Hyatt, East Syracuse, New York 13057, USA
jad@khhpc.com

Mark Webster
Simpson Gumpertz and Heger, Waltham, Massachusetts 02453, USA
mdwebster@sgh.com

Jerome F. Hajjar
Northeastern University, Boston, Massachusetts 02115, USA
jf.hajjar@neu.edu

As researchers and practitioners look towards building sustainability, thermal bridges in steel structures become increasingly relevant. In order to mitigate these thermal bridges, structural thermal breaks are necessary to decrease energy loss at the building envelope. Options for improving the thermal insulation in steel buildings include exploring thermally improved materials such as fiber-reinforced polymers (FRP) and stainless steel, along with possible mitigation strategies fabricated from them to provide an effective thermal break without compromising structural integrity. Three-dimensional thermal modeling demonstrates the efficacy of these materials as thermal shims in shelf angles, roof posts, and canopy beams. However, non-steel fills in steel bolted connections are not clearly approved for use in steel structures, and currently, no methodology or test results exist to provide recommendations for their design and implementation. To validate the structural performance of these polymers in steel bolted connections, an array of experiments are conducted to explore these mitigation strategies. Several parameters are experimentally examined in the tests, including: bolt diameter, fill material, fill thickness, and the effect of multiple plies. This work, part of a larger ongoing research effort, aims to determine the behavior of these connections, and establish recommendations for their design and future use.

INTRODUCTION

This study of thermal break strategies for cladding systems in steel structures aims to propose effective structural thermal breaks and validate them through extensive modeling and experimental testing. Thermal bridge mitigation strategies examined in this work range from inserting a thermally-improved shim into the bolted structural connections to replacing the structural member entirely with a thermally-improved member. Two materials explored to date include the use of fiber reinforced polymers (FRPs) and stainless steel. As FRPs differ in mechanical properties to steel, it is necessary to validate the behavior for these FRP fills in bolted steel connections, and under prolonged loading.

The use of steel fills in bolted steel connections has been previously explored by a number of researchers, e.g., Lee and Fisher (1968), Frank and Yura (1981), Dusicka and Lewis (2010), Borello et al. (2009, 2011), and Denavit et al. (2011). This research established that the strength of bolted connections in bearing may be reduced by up to 15%, with the reduction being a function of the thickness of the steel fills (AISC 2005, 2010).

There is limited research on the performance of FRP materials in steel structures, especially subjected to creep. Sa et al. (2011) summarizes previous work in creep experimental studies, which is limited to tension and compression in the plane of the fiber, and bending. However, no studies exist on FRP creep compression performance perpendicular to the plane of the fiber, the typical direction and mode of loading for fills in bolted steel connections.

The work presented here summarizes initial findings on the structural performance of FRP fills in bolted steel connections via thermal modeling, creep testing of FRP materials in compression perpendicular to the fibers, connection testing to establish bolt strength in the presence of shims, and sub-system testing of shelf angle connections. This ongoing research is also exploring the structural and thermal performance of roof posts and canopy beams with a variety of thermal break mitigation strategies.

THERMAL MODELING

Thermal modeling of shelf angles and potential mitigation strategies was completed using the HEAT3 v7.0 software for three-dimensional configurations to demonstrate the efficacy of the thermal break strategies. Steady state thermal analysis was conducted to calculate the effective field of wall U-factor. The results for thermally-improved shims within the shelf angle connections are summarized below.

For the purpose of thermal modeling, all connections are designed to simulate the constructible cladding assemblies, in contrast to the structural test specimens, which are oversized in key components to assure that the primary failure mode of the cladding assembly will not be due to yielding at the connections (this is discussed below). For thermal modeling in HEAT3, surface areas of all materials must be in contact to transmit thermal energy. For example, all hole diameters are modeled with the same diameters as the rods for surface contact between the plates and the rods. Typical thermal gradients of unmitigated and mitigated models are shown in Figure 1.

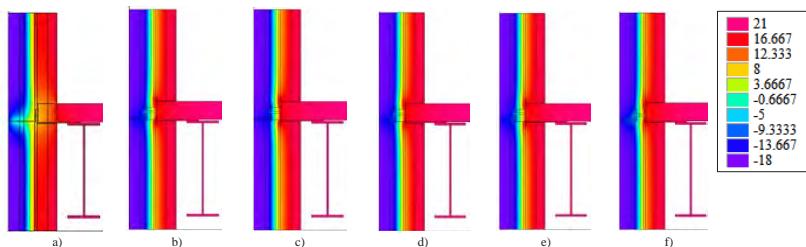


Figure 1: Thermal gradients of a) Unmitigated, b) Vinylester shim with A325 bolts (ΔU -value=50.22%), c) Vinylester shim with A304-SH bolts (ΔU -value=53.16%), d) Proprietary 1 shim (ΔU -value=54.32%), e) Proprietary 2 shim (ΔU -value=54.05%), f) Stainless tube shim (ΔU -value=47.73%) – units in degrees Celcius.

The interior and exterior boundary conditions are based on prescribed values in Normative Appendix A of ASHRAE 90.1-2013 and NFRC 100-2014. An interior ambient temperature of 69.8°F and an exterior ambient temperature of -0.4°F were assumed in accordance with NFRC-2014. These results show that mitigation via thermally improved shims (and by extension, intermittent spacing of the angle along the length due to shimming) improves the thermal conductivity of the system by 47-54%, depending on material. Typical results are tabulated in Table 1 below.

Table 1: Selected thermal modeling results from shelf angle modeling efforts

Unmitigated Model			Mitigated Model				Comparison	
Model Name (-)	Bolt Type (-)	U-Value (BTU/h*R2**F)	Model Name (-)	Shim Material (-)	Bolt Type (-)	U-Value (BTU/h*R2** F)	Δ U-Value (BTU/h*R2**F)	%-Reduction
Shelf Angle Unmitigated 2.5 Inch_S1_V2	A304-SH	0.138	Shelf Angle Mitigated 2.5 Inch_S8_V3	Vinylester shim	A325	0.082	0.056	40.41
Shelf Angle Unmitigated 2.5 Inch_S1_V2	A304-SH	0.138	Shelf Angle FRP 2.5 Inch_S19	FRP angle	A304-SH	0.072	0.066	47.94
Shelf Angle Unmitigated 5 Inch_S4_V2	A304-SH	0.112	Shelf Angle Mitigated 5 Inch_S14.1_V3	Vinylester shim	A325	0.056	0.056	50.22
Shelf Angle Unmitigated 5 Inch_S4_V2	A304-SH	0.112	Shelf Angle Mitigated 5 Inch_S14.2_V3	Vinylester shim	A304-SH	0.053	0.060	53.16
Shelf Angle Unmitigated 5 Inch_S4_V2	A304-SH	0.112	Shelf Angle Mitigated 5 Inch_S17_V3	Proprietary 1 shim	A304-SH	0.051	0.061	54.32
Shelf Angle Unmitigated 5 Inch_S4_V2	A304-SH	0.112	Shelf Angle Mitigated 5 Inch_S18.1_V3	Proprietary 2 shim	A304-SH	0.052	0.061	54.05
Shelf Angle Unmitigated 5 Inch_S4_V2	A304-SH	0.112	Shelf Angle Mitigated 5 Inch_S18.2_V3	Stainless tube shim	A304-SH	0.059	0.054	47.73

CONNECTION TESTING PROGRAM

Double lap splice bolted connections were considered in this experimental program, analogous to the configurations for steel fills in Lee and Fisher (1968), Frank and Yura

(1981), Dusicka and Lewis (2010), Borello et al. (2009, 2011), and Denavit et al. (2011). The test rig is shown in Figure 2. The base of the connection was designed to be essentially rigid and is fixed in the test rig, a 600 kip Forney universal testing machine located at the Simpson Gumpertz and Heger laboratory in Waltham, MA. Monotonic load is applied to the top of the connection at a rate of 1 kip/second. Two bolts were used to decrease variation in the connection strength.

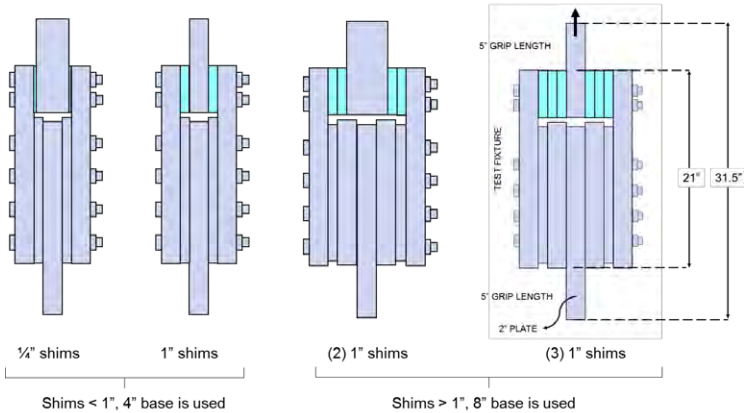


Figure 2: Connection test setup illustrating various shim thickness configurations

The rig base is fixed in the test rig and was designed not to fail. Similarly, the side plates on the outside of the text fixture as well as the interior top plate were designed to force failure into the bolts. To ensure that the interior top plate does not fail, two base fixtures (4 inch base and 8 inch base) were designed so that thicker shims may be tested without compromising strength of the fixture. The interior top plate and side plates are replaced after each test, while the base plates are reused.

The test matrix for the experimental program is shown in Table 2. Bolt material as well as diameter are varied. As stainless steel is less thermally conductive than carbon steel, A304-SH bolts (strain-hardened stainless steel bolts matching closely in strength properties to A325 carbon bolts) were included in the study. FRP shim thickness is also varied from 1/4 inch to 3 inches. Multiple FRP plies are not bonded together (note: 1 inch shims were delivered as two 1/2 inch shims bonded together).

Testing is in progress, but a comparison between the tested specimens (3 inch thick vinylester shims and no shims, each with two 5/8 inch dia. A325 bolts) in Figure 3 demonstrates that peak strength decreases by 37% and stiffness decreases by a factor of 6.5.

The vinylester shims in test C16 ovalized significantly, and delaminated at the bond line at the midpoint of the cross section. This behavior contributed to the overall ductility of the system when compared to test C1 without shims.

Table 2: Connection test matrix (completed tests are shaded)

Test Name	Shim Type	Shim Thickness	Bolt Dia. (in)	Bolt Spec	Hole Size*	Rig Thicknesses	
						Top	Bottom
C1	no shim	-	5/8	A325	11/16	4"	4"
C2	no shim	-	5/8	A304 SH1	11/16	4"	4"
C3	no shim	-	1/2	A325	9/16	4"	4"
C4	polyurethane	1/4"	5/8	A325	11/16	3.5"	4"
C5	vinylester	1/4"	5/8	A325	11/16	3.5"	4"
C6	phenolic	1/4"	5/8	A325	11/16	3.5"	4"
C7	proprietary 1	1/4"	5/8	A325	11/16	3.5"	4"
C8	proprietary 2	1/4"	5/8	A325	11/16	3.5"	4"
C9	vinylester	2x1/2" multiple plies	5/8	A325	11/16	2"	4"
C10	vinylester	1"	5/8	A325	11/16	2"	4"
C11	vinylester	1"	5/8	A304 SH1	11/16	2"	4"
C12	vinylester	1"	1/2	A325	9/16	2"	4"
C13	vinylester	2x1" multiple plies	5/8	A325	11/16	4"	8"
C14	vinylester	2x1" multiple plies	5/8	A304 SH1	11/16	4"	8"
C15	vinylester	2x1" multiple plies	1/2	A325	9/16	4"	8"
C16	vinylester	3x1" multiple plies	5/8	A325	11/16	2"	8"
C17	vinylester	3x1" multiple plies	5/8	A304 SH1	11/16	2"	8"
C18	vinylester	3x1" multiple plies	1/2	A325	9/16	2"	8"

*holes are standard holes (bolt dia. + 1/16")

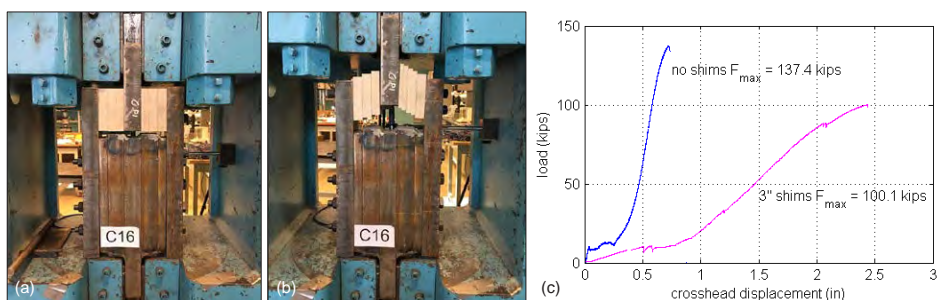


Figure 3: (a) Test C16 (3" vinylester shims, 5/8" dia. A325 bolts) pre-test (b) Test C16 post-test, depicting shim delamination and extent of deformation (c) comparison between no shims case (test C1) and test C16.

MATERIAL CREEP TESTING PROGRAM

The long term behavior of FRP fills is validated via creep testing at the material level. As currently there exists no standard or precedent for creep testing of FRP materials in bearing compression, existing standards for creep testing in tension and compression were referenced to construct the following creep testing protocol. Testing is conducted in a 100 kip MTS testing machine, with load held constant over time and displacements measured over time. Failure typically occurs at approximately the same strain level regardless of the loading and time to failure, until the load is low enough that it is below a threshold such that failure due to creep is not anticipated. Stress ratios ($\sigma_{app}/\sigma_{max}$) are

determined based on the time to failure, t_f . A successful panel of tests consists of tests with t_f in three different logarithmic decades (10^0 , 10^1 , 10^2 , etc), as illustrated in Figure 4.

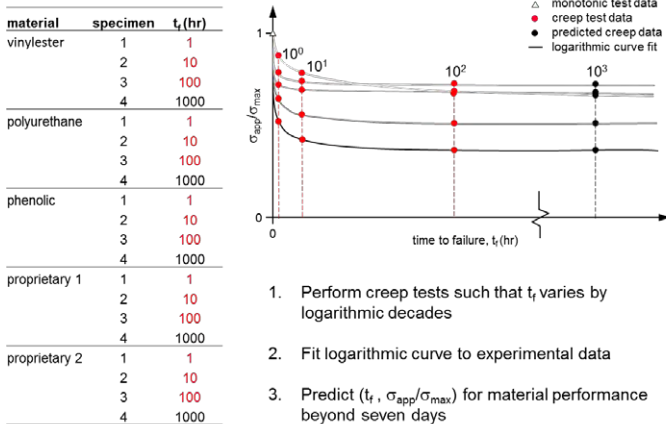


Figure 4: Ideal creep testing matrix and protocol

As each material behaves differently under prolonged loading, the stress ratios that result in failure in each logarithmic decade will differ between the materials tested. The resulting test matrix with time-to-failure results from this work is shown in Table 3 below.

Table 3: Creep results across material types

material	specimen	$\sigma_{app}/\sigma_{max}$	F_{app} (kip)	t_f , time to failure (hr)				
				<10 ⁰	>10 ⁰	>10 ¹	>10 ²	>10 ³
vinylester	3c	0.8	21.28	0.628	-	-	-	-
	1c	0.8	20.98	-	2.79	-	-	-
	2c	0.8	20.93	-	3.30	-	-	-
	5c	0.758	20.78	-	6.23	-	-	-
	6c	0.75	20.10	-	-	13.4	-	-
	4c	0.7	19.11	-	-	-	132	-
polyurethane	1c	0.9	54.68	0.127	-	-	-	-
	2c	0.9	54.45	0.785	-	-	-	-
	3c	0.9	54.01	-	6.09	-	-	-
	4c	0.8	44.03	-	-	36.9	-	-
	5c	0.78	43.46	-	-	-	500+	-
	8c	0.875	12.85	-	-	-	125+	-
phenolic	3c	0.85	12.31	-	1.92	-	-	-
	7c	0.85	12.49	-	9.63	-	-	-
	5c	0.84	12.58	-	-	73.0	-	-
	2c	0.8	12.11	-	-	-	231	-
	1c	0.8	28.15	-	-	16.7	-	-
proprietary 1	2c	0.85	27.84	-	3.08	-	-	-
	3c	0.78	27.16	-	-	-	146	-
	1c	0.8	26.76	0.214	-	-	-	-
proprietary 2	2c	0.7	22.49	-	2.27	-	-	-
	6c	0.69	21.63	-	6.68	-	-	-
	5c	0.65	21.13	-	-	85.4	-	-
	1c	0.8	26.76	0.214	-	-	-	-
	2c	0.7	22.49	-	2.27	-	-	-

*not tested to failure

Time to failure and stress ratio are plotted against each other in Figure 5, with an example logarithmic/power curve fit of the vinylester creep data provided in the inset plot.

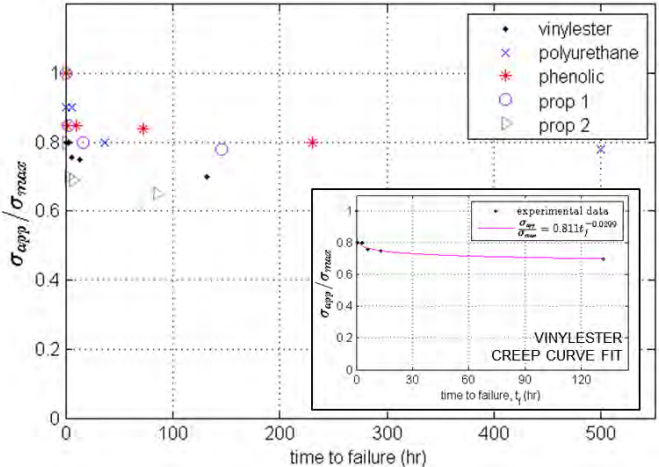


Figure 5: Creep time to failure versus applied stress ratio across tested materials. Inset, power curve fit of vinylester experimental data.

Initial results indicate high variability in tests with high applied stress ratios (85-90% of ultimate stress). Additional repetitions at lower force ratios must be performed to completely characterize the variability of experimental results. Results also indicate an asymptote for each material at which the time to failure dramatically increases; this horizontal asymptote provides an upper boundary of the potential design space for these materials.

SHELF ANGLE SUB-SYSTEM TESTING

To examine the performance of thick FRP shims in shelf angle cladding details, shelf angles with varying bolted connections and thermal break mitigation strategies were examined. As shelf angles are typically deflection-limited, connection strength is non-critical; 5/8" diameter bolts are commonly used. However, in order to observe experimental behavior beyond connection limits, specimens were designed as "designed" (with typical connections) and "over-designed" (with over-sized 1" diameter bolts). Shim material and thickness (corresponding to climate zone insulation specifications) were also varied. Shims were of constant area, 3x4" in size and centered on the shelf angle vertical flange, with the connection bolt passing through the center. The experimental test matrix is shown in Table 4.

Table 4: Shelf angle test matrix (completed tests are shaded)

Test Name	Specimen Type	Mitigation Strategy			Specimen Information			
		Type	Material	Thick (in)	Length	Section	Bolt/Stud Spec	Bolt Dia. (in)*
S1	designed	-	-	-	42	L6x4x5/16	A325	0.625
S2	designed	-	-	-	42	L6x4x5/16	A304-SH	0.75
S3	over-designed	-	-	-	42	L6x4x5/16	A325	1
S4	designed	-	-	-	42	L7x4x3/8	A325	0.625
S5	designed	-	-	-	42	L7x4x3/8	A304-SH	0.75
S6	over-designed	-	-	-	42	L7x4x3/8	A325	1
S7	over-designed	shim	vinylester	1.5	42	L6x4x5/16	A325	1
S8	designed	shim	vinylester	1.5	42	L6x4x5/16	A325	0.625
S9	over-designed	shim	polyurethane	1.5	42	L6x4x5/16	A325	1
S10	over-designed	shim	phenolic	1.5	42	L6x4x5/16	A325	1
S11	over-designed	shim	proprietary 1	1.5	42	L6x4x5/16	A325	1
S12	over-designed	shim	proprietary 2	1.5	42	L6x4x5/16	A325	1
S13	over-designed	shim	vinylester	3	42	L7x4x3/8	A325	1
S14	designed	shim	vinylester	3	42	L7x4x3/8	A325	0.625
S15	over-designed	shim	polyurethane	3	42	L7x4x3/8	A325	1
S16	over-designed	shim	phenolic	3	42	L7x4x3/8	A325	1
S17	over-designed	shim	proprietary 1	3	42	L7x4x3/8	A325	1
S18	over-designed	shim	proprietary 2	3	42	L7x4x3/8	A325	1
S19	over-designed	FRP angle	vinylester	-	42	FRP L6x4x1/2	A325	1
S20	over-designed	tube shim	carbon steel	HSS3x3x3/8	42	L7x4x3/8	A325	1
S21	over-designed	steel shim	carbon steel	3	42	L7x4x3/8	A325	1

*holes are standard holes (bolt diameter + 1/16 inch)

The test rig is depicted in Figure 6. A load beam, designed to simulate loading from brick veneer in a typical installed configuration, compresses the horizontal leg of the shelf angle at a monotonic rate of 0.002 inches/second. Angles are loaded equidistant from the slab plate, regardless of the presence of shims, to maintain wall cavity size between mitigated and unmitigated shelf angles.

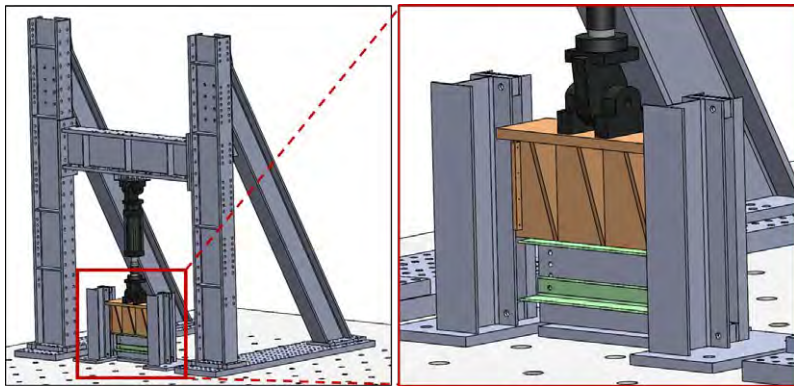


Figure 6: Shelf angle test rig with detail

A comparison of performance for specimens with 3" shims is presented in Figure 7. As the shimmed specimens are loaded nearer to the slab plate, these systems experience an increase in strength and stiffness from the unmitigated details.

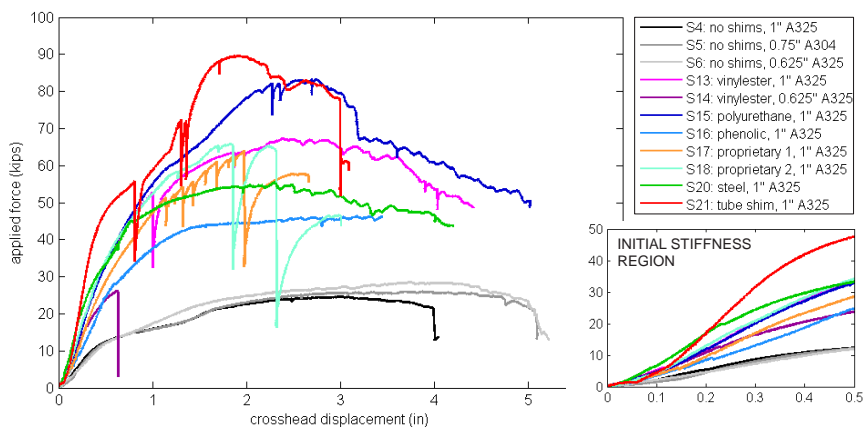


Figure 7: Force-displacement results for climate zone 7 shelf angles (L7x4x3/8) with shim thickness equivalent to required insulation layer (~3").

As Figure 7 illustrates, the unmitigated specimens perform similarly regardless of bolt diameter and material, notably so in the initial stiffness region. Steel shims (representing an intermittently spaced mitigation strategy) and tube shims result in the stiffest mitigated systems. One marked difference between the behavior of these two non-FRP mitigation strategies is that buckling of the tube shim ultimately permits additional deformation of the shelf angle, while the rigidity of the steel shims causes fracture of the shelf angle prematurely; this is borne out in a 38.5% reduction in peak strength of the steel shim specimen relative to the tube shim specimen. Similarly to the steel shims, the polyurethane shims did not fail during testing, resulting in fracture of the shelf angle at the heel. This failure mode is unique among the FRP shimmed specimens in that typically the shims crushed and delaminated while the angle deformed but did not fracture.

CONCLUSIONS & FUTURE WORK

Connection, creep, and shelf angle testing all indicate potential for the use of FRP materials in bolted steel connections and sub-systems. Proposed solutions for thermal bridging in shelf angles demonstrate improved strength and stiffness from the unmitigated cases, in addition to reducing the thermal conductivity of the system between 40 and 50%. Performance of FRP materials under prolonged loads is promising; across the materials examined herein, creep does occur, but only in stress ranges well above typical design regions. Connection testing thus far demonstrates similarity with previous work in bolted steel connections with steel fills with respect to having a stiffness reduction between thick shimmed specimens and specimens without shims. The research summarized in this work is ongoing, with the aim of validating the use of FRP fills in steel bolted connections and in shelf angle cladding details through thermal modeling, sub-system testing, and creep testing, so as to provide design guidance for engineers. Additional tests are required to fully understand the behavior of FRP material under prolonged load. Shelf

angle, roof post, and canopy beam testing is currently in progress to explore the performance of connections with various moment-to-shear ratios and with various types of FRP and proprietary shims.

ACKNOWLEDGEMENTS

This material is based upon work supported by the Charles Pankow Foundation, the American Institute of Steel Construction, the American Composites Manufacturers Association (ACMA), the ACMA-Pultrusion Industry Council, Schöck AG, the National Science Foundation under Grant No. CMMI-0654176, Simpson Gumpertz & Heger Inc., Klepper, Hahn & Hyatt, and Northeastern University. The authors would like to thank Kyle Coleman, Michael McNeil, Kurt Braun, Justin Kordas, Elisa Livingston, Madeline Augustine, and Dennis Rogers of Northeastern University, project team members Pedro Sifre, Mehdi Zarghamee, James Parker, Sean O'Brien, Jason Der Ananian, Nathalie Skaf, and Jessica Coolbaugh of Simpson Gumpertz & Heger and the members of the Industrial Advisory Panel and the ACMA Pultrusion Industry Council Technical Advisory Team. Any opinions, findings, and conclusions expressed in this material are those of the authors and do not necessarily reflect the views of the sponsors.

REFERENCES

- American Institute of Steel Construction (AISC) (2005). Specification for Structural Steel Buildings, ANSI/AISC 360-05, AISC, Chicago, Illinois.
- American Institute of Steel Construction (AISC) (2010). Specification for Structural Steel Buildings, ANSI/AISC 360-10, AISC, Chicago, Illinois.
- Borello D. J., Denavit, M. D., and Hajjar, J. F. (2009). "Behavior of Bolted Steel Slip-Critical Connections with Fillers," Report No. NSEL-017, Newmark Structural Laboratory Report Series, Department of Civil and Environmental Engineering, University of Illinois at Urbana-Champaign, Urbana, Illinois.
- Borello D. J., Denavit, M. D., and Hajjar, J. F. (2011). "Bolted Steel Slip-Critical Connections with Fillers: I. Performance," *Journal of Constructional Steel Research*, Vol. 67, No. 3, pp. 379–88.
- Denavit, M. D., Borello D. J., and Hajjar, J. F. (2011). "Bolted Steel Slip-Critical Connections with Fillers: II. Behavior," *Journal of Constructional Steel Research*, Vol. 67, No. 3, pp. 398–406.
- Dusicka, P. and Lewis, G. (2010). High Strength Steel Bolted Connections with Filler Plate," *Journal of Constructional Steel Research*, Vol. 66, pp. 75–84.
- Frank K. H. and Yura J. A. (1981). An Experimental Study of Bolted Shear Connections," Report No. FHWA/RD-81/148. Federal Highway Administration, U.S. Department of Transportation, Washington, DC, December.
- Lee, J. H and Fisher, J. W. (1968). "Bolted Joints with Rectangular or Circular Fillers," Report No. 318.6., Fritz Engineering Laboratory, Department of Civil Engineering, Lehigh University, Bethlehem, Pennsylvania, June.
- Sa, M. F., Gomes, A. M., Correia, J. R., and Silvestre, N. (2011). Creep Behavior of Pultruded GFRP Elements – Part I: Literature Review and Experimental Study," *Composite Structures*, Vol. 93, pp. 2450–2459.

STRUCTURAL SAFETY CHECK FOR PRODUCTS MADE OF CAST STEEL

Max Spannaus, Thomas Ummenhofer, Peter Knödel
KIT Steel & Lightweight Structures, 76131 Karlsruhe, Germany
max.spannaus@kit.edu; thomas.ummenhofer@kit.edu; peter.knoedel@kit.edu

ABSTRACT

The structural engineer must consider the internal condition of cast steel components during the design phase because this directly influences their calculated load bearing capacity. There is a lack of applicable normative regulations for this purpose, and an overly high quality grade is often specified as a result, increasing manufacturing costs. A current project at the Research Center for Steel, Timber and Masonry at Karlsruhe Institute of Technology (KIT) provides experimental and numerical investigations as a basis to expand existing regulations to address this gap. The aim is to develop an assessment model for the required quality grade considering the stress ratio and component thickness.

1. INTRODUCTION

Regulations for design of steel castings in European and international codes are inadequate for the safe and cost-effective dimensioning of civil engineering structures. The essential difference in comparison to welded structural components made of hot rolled steel is that the structural engineer always has to consider discontinuities and imperfections in the semi-finished cast products. These include blowholes, gas bubbles or inclusions; none of which can be avoided with current casting technology. Therefore manufacturing-related material characteristics and inhomogenities must be taken into account. In doing so, the structural engineer has to determine an allowable defect size and distribution along with a required production grade. Regulations defining a specific defect size or utilization factor depending on the quality grade do not exist in the german National Annex of EC 3 (DIN EN 1993-1-8/NA:2010), except for cast materials with low tensile strength in combination with small wall thickness. Additionally, regulations for verifying sufficient safety against brittle component failure under consideration of such manufacturing-related material faults are lacking.

A standardized concept for future dimensioning and interpretation of components made of cast steel is initiated in a research project by the KIT Steel- and Lightweight Structures group. It is intended to establish a basis for the revision of regulations by means of scientific investigations. This paper highlights the essential contents of this effort (Spannaus 2016).

2. EXPERIMENTAL PROGRAM

2.1. Material

All experimental investigations were performed on two cast materials which represent the lower and upper strengths of steel castings used in civil structures. Specimens representing materials with a low tensile strength were prepared from the material G20Mn5 ($R_e = 300$ MPa) (EN 10340:2007), which is commonly used in civil engineering. Alternatively, the G22NiMoCr5-6 ($R_e = 825$ MPa) (SEW 520:1996) was chosen as a suitable representative of high-strength castings; it is frequently used in tension rod systems and fastening elements.

2.2. Influence of casting defects

In a first step, tensile specimens with real casting defects – inspired by the investigations of (Hardin, Beckermann 2002) – were developed and tested to investigate the influence of manufacturer-related material defects on the load-bearing behavior. Blank castings with different sized material accumulations in the center of the specimen (see Figure 1) were prepared to investigate the widest possible spectrum of different defects. With this material accumulation, the place of the last solidification is deliberately forced into the volume of the subsequently prepared centered tensile specimen. Since the thinner adjacent areas solidify earlier, the medium part is no longer densely fed and a solidification blowhole develops.

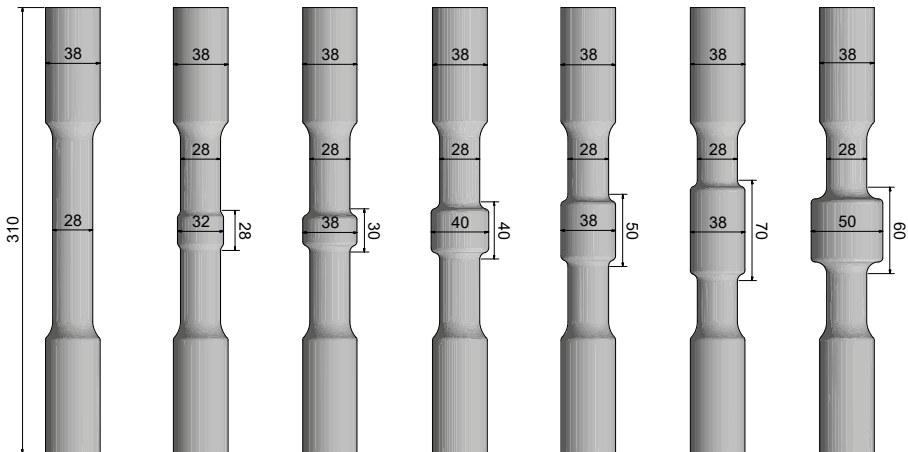


Figure 1. Specimen geometry as casted (Spannaus 2016)

It is necessary to precisely document the internal condition of the test specimen for the subsequent calibration of a calculation model. For this reason, all specimens were investigated using computer tomography after machining of the tensile specimens (diameter \varnothing 20 mm). In Figure 2 the defects are shown for selected specimens.

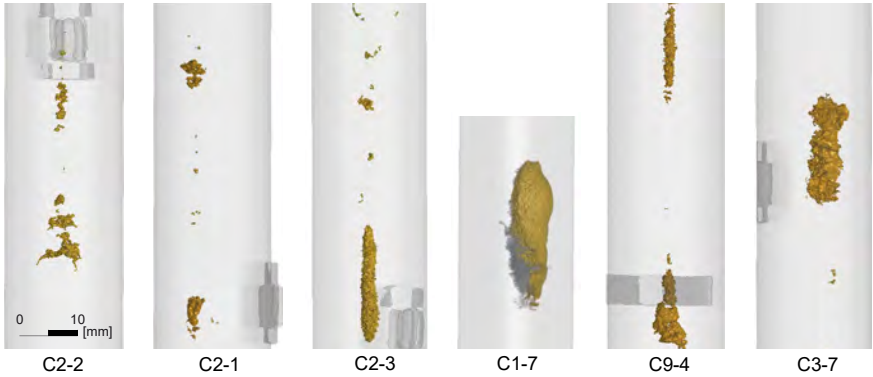


Figure 2. Exemplary overview of detected casting defects

It is shown that a wide spectrum of casting defects was available for further investigations due to the differences in specimen geometries. Defects could be created with a defect size between 2 % and 22 % of the cross section as well as with different defect geometries.

In Figure 3 stress-strain curves of the tensile specimens made of the material G22NiMoCr5-6 are given. They show marked differences in comparison to a flawless specimen.

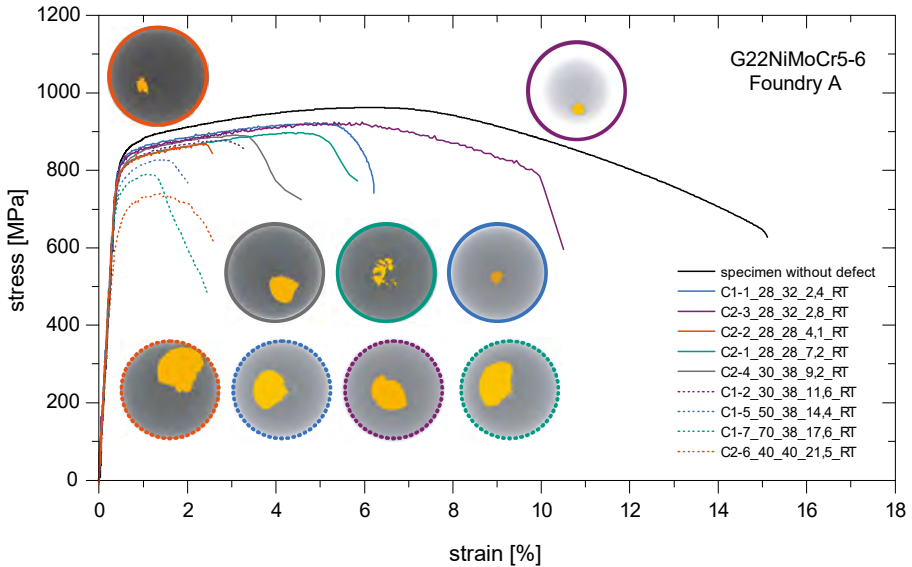
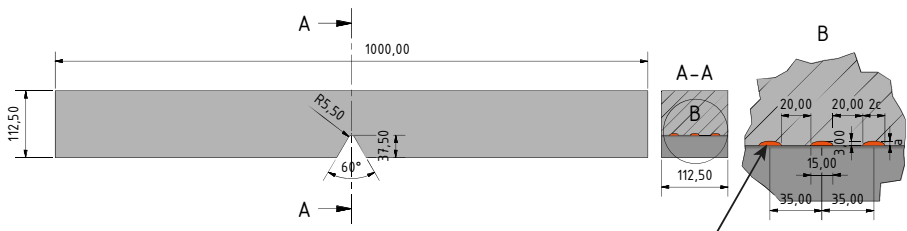


Figure 3. Stress-strain-curves of selected specimens with casting defects compared to a flawless specimen, ambient temperature (Spannaus 2016); the last number of the sample identifier denotes the cross-sectional loss in [%]

The results of the tensile tests show that the defects have particularly negative effects on the elongation at fracture. A small defect (~4 % of the cross section) already lead to a reduction of the elongation at fracture up to 80 %. Furthermore, almost all specimens showed a brittle component failure with a test temperature of -50°C. A numerical design concept based on fracture mechanics failure criterion was chosen based upon the brittle behavior and the crack-like imperfections observed in the nearfield of the defects in the experiments. With a variation of model parameters it is shown that the defect geometry can be neglected with very small cracks (1 mm), and that a casting defect can be conservatively approximated for design purposes as being elliptical, flat and perpendicular to the major principal stress.

2.3. Unfavorable design scenario

Notched 4-point bending specimens with wall thicknesses of 45 mm, 75 mm and 113 mm were tested to experimentally validate the transferability of the achieved results to larger product thicknesses. Since these experimental investigations should depict an unfavorable design scenario regarding brittle fracture behavior, additional cracks were introduced in the specimens to simulate allowable casting defects in the area of the notch. The defect size is based on an allowable defect of quality grade 2 according to the ultrasonic test standard EN 12680-1:2003.



Initial crack shaped as semi-elliptical crack. The a/c - ratio was elected to $a/c = 0,4$.
The crack was first eroded and subsequently enlarged by fatigue loading.

Figure 4. Dimensions and initial defect size of the 4-point bending tests. Exemplary for the plate thickness 112,5 mm (Spannaus 2016)

The results (Figure 5) of the tests performed at -50 °C show that the plastic cross section capacity for the material G20Mn5 is safely achieved for all product thicknesses despite all of the negative influences. The high-strength material G22NiMoCr5-6, however, resulted in a brittle failure of thick-walled specimens at 50 % of the elastic load bearing capacity. These results illustrate that the verification of sufficient safety against brittle fracture is mandatory for products made of cast steel.

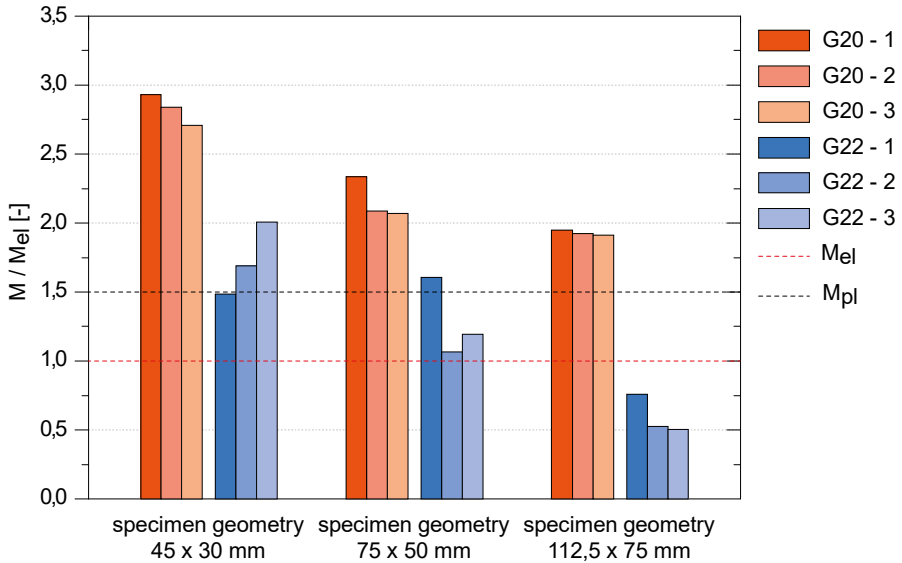


Figure 5. Results of 4-point bending tests (Spannaus 2016)

Based on these results, a reduction factor is derived for the design concept to account for the risk of brittle fracture. This factor depends on temperature, utilization, component geometry and material strength.

3. NUMERICAL INVESTIGATION

Numerical models considering casting defects were calibrated by means of experimental investigations. The defects measured in the CT were transferred into the FEM software ANSYS. In addition, a circumferential crack was modeled in the area of the biggest degradation of the cross section so that a fracture mechanics failure criterion can be applied.

In Figure 6, the results of the calculated and measured elongation at rupture are plotted. Since in practice no information of the defect dimensions and geometry is available when designing the component, each defect was modeled additionally as a plane crack with regard to the subsequent design model. The position of the defect was taken from the CT measurements and the projection area of the defect in longitudinal specimen direction was converted into an elliptic defect with the aspect ratio $a/c = 0.4$. This results in the same net cross section, but with a plane crack. Therefore, in Figure 5, there are two numerically calculated elongations at rupture for each experimental value.

Figure 6 shows that the fracture mechanics model is very suitable for the evaluation of existing defects. Both, the models with volume errors and circumferential crack as well as the models with plane crack give reliable results, assuming a known defect size. These models, however, are not overly conservative.

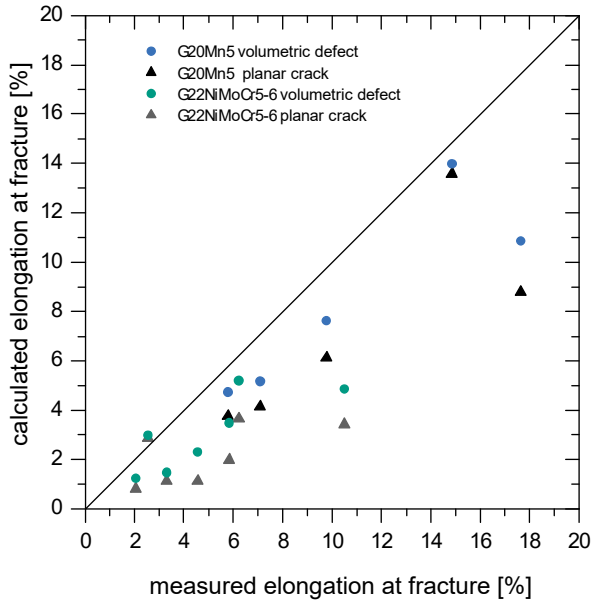


Figure 6. Comparison of measured and calculated elongation at fracture for tensile tests from samples with casting defects (Spannaus 2016)

In addition, a verification method on the basis of FE analyses was developed using EPBM (elastic-plastic fracture mechanics) based on 4-point bending tests. At first, a design crack size (representative for the casting defects) was determined for each quality class. The material parameters that can be estimated numerically were derived from the minimum requirements of the specified delivery quality. On the one hand, this numerical verification method facilitates the ultimate limit state design for complex geometries and components with local stress concentrations with high stress concentration factors, on the other hand, local plastic design is possible despite unfavorably assumed casting defects through the application of EPDM.

In Figure 7, the quarter model for the recalculation of the 4-point bending tests is shown. The measured initial defects from the tests are modeled as plane cracks. In the calculation, the crack tip load in the form of a J-integral was considered for each load step via the cross-checked “CINT-macro” calculation implemented in ANSYS. If the J-integral exceeds the critical value for crack initiation on one of the modeled cracks, in the analysis is assumed to have reached the component’s capacity.

A comparison of the numerically calculated loads with the experimental results (Figure 8) shows very good agreement.

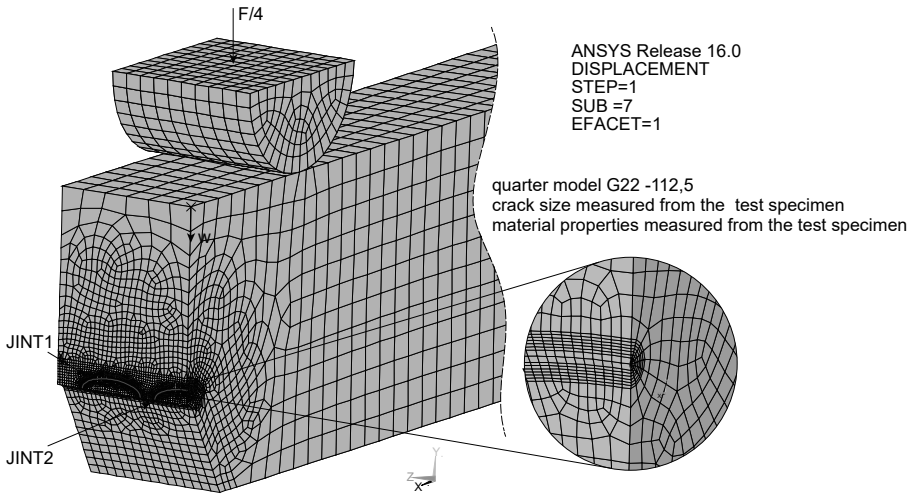


Figure 7. A fracture mechanics limit condition has been chosen as convergence criterion (Spannaus 2016)

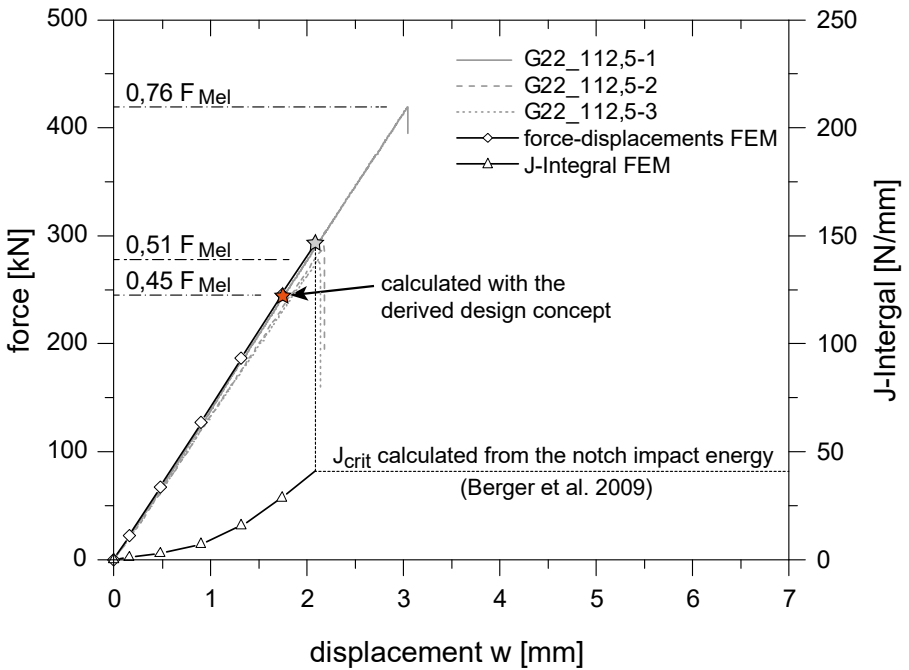


Figure 8. Results of the numerical load bearing analysis using the model according to Figure 7 (Spannaus 2016)

4. DESIGN CONCEPT

During the design and planning phase, neither the geometry of defects nor the position of defects or specific mechanical properties are known to the structural engineer. For this reason, a design scenario on the basis of a worst case defect distribution was derived from the acceptance class of the NDT standards.

First, minimum requirements for each quality class were defined based on the standard for ultrasonic testing (EN 12680). They include requirements on allowable individual defect size, maximum total defect area, minimum defect distance and defect orientation. Finally, a reduction factor R_{GS} for the quality classes 2 to 5 is derived from the resulting allowable defect distributions.

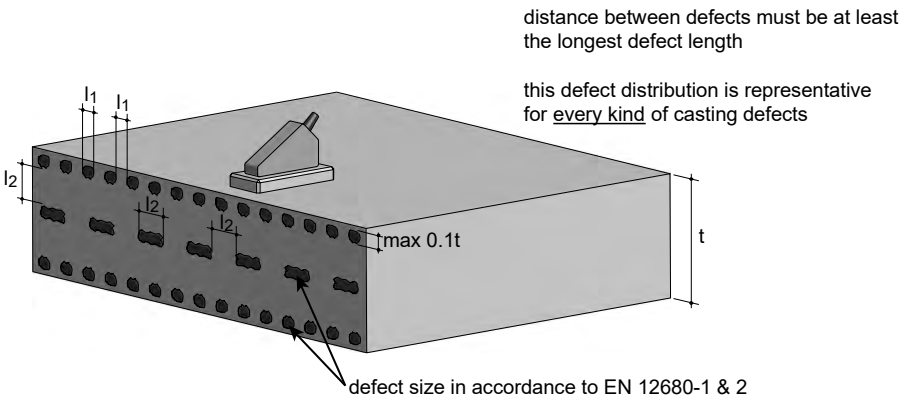


Figure 9. Exemplary demonstration for an assumed defect distribution

The reduction factor R_{GS} considers an increase in the local stresses through a factor $R_{GS,imp}$ based on the total defect range in the stress cross section. Since, according to EN 12680, the allowable individual defect size considerably increases with an increasing quality class, i.e. lower production quality (and thus also the danger of brittle fracture), the load level of different design qualities is standardized using a second factor $R_{GS,frac}$.

$$R_{GS} = R_{GS,imp} \cdot R_{GS,frac} \quad (1)$$

Fracture-mechanical analyses were performed on three reference components. To represent cast components without significant stress concentration factors, a plate with surface crack (reference component 1) as well as a plate with bigger internal cracks (reference component 2) were analyzed. For components with an additional geometric notch, such as given in Figure 4, the reference component corresponding to the brittle fracture verification according to EN 1993-1-10:2010 (non-bearing longitudinal stiffener) was considered (reference component 3). The calculation results used to determine factor $R_{GS,frac}$ for reference component 1 are shown in Figure 10.

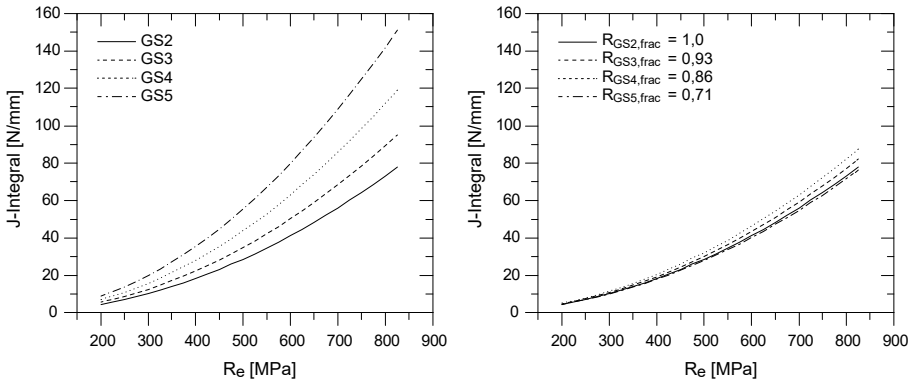


Figure 10. J-Integral for plastic ultimate load with different yield limits for a plate with surface crack. Left: without reduction factor $R_{GS,frac}$, right: with reduced yield strength (Spannaus 2016)

The structural engineer can consider allowable defects according to the ultrasonic standards by reducing the yield limit with the quality class dependent reduction factor R_{GS} , which considers the range and size of defects.

In a second step the brittle fracture verification is provided for all reference components following the method according to EN 1993-1-10:2010 (Sedlacek et al. 2008), which is based on the normalized fracture-mechanical stress (see Figure 10). The initial defect sizes for the verification were derived from ultrasonic test standards and the resistance parameters according to (Berger et al. 2009) were determined. The reduction factor R_{frac} resulting from these calculations was derived considering the reference temperature, thickness, and component utilization of the material and geometry. The results for reference component 3 are reported in Table 1.

With both reduction factors, the structural engineer can define a graded quality requirement for components made of cast steel by using a simple design table.

$$f_{y,d} = R_e \cdot R_{GS} \cdot R_{frac} \quad (2)$$

Following equation 2, the design value for the yield strength results from the characteristics of the technical delivery condition and is reduced by one factor which accounts for the design quality and another factor which considers the danger of brittle fracture.

This method provides conservative results for the material G20Mn5, but facilitates the design of steel cast components without performing fracture-mechanical analyses. For the material G22NiMoCr5-6, the calculated and experimentally determined bearing loads show a very good agreement (cf. Figure 8).

Table 1. Reduction factor R_{frac} for quality grade 2 to 5 for products with additional stress concentrations from component geometry, reference component 3 (Spannaus 2016)

material	thick- nesses [mm]	design temperature T_{Ed} [°C]																			
		10	0	-10	-20	-30	-40	-50	10	0	-10	-20	-30	-40	-50	10	0	-10	-20	-30	-40
		$\sigma_{Ed} = 0,75 \cdot R_e$					$\sigma_{Ed} = 0,50 \cdot R_e$					$\sigma_{Ed} = 0,25 \cdot R_e$									
G20Mn5+QT EN 10340	30						0,97	0,88													
	40						0,94	0,84													
	50						0,90	0,81													
	60						0,97	0,87	0,78												
	70						0,94	0,84	0,76						0,97						
	80						0,91	0,81	0,74						0,94						
	90						0,89	0,79	0,72						0,92						
	100						0,98	0,87	0,78	0,70						0,99	0,90				
	110						0,96	0,85	0,76	0,69						0,97	0,88				
	120						0,94	0,83	0,75	0,68						0,96	0,86				
	130						0,92	0,81	0,73	0,66						0,94	0,85				
	140						0,90	0,80	0,72	0,65						0,92	0,84				
	150	0,98	0,89	0,79	0,71	0,64						0,91	0,82								
	G22Ni- MoCr5-6 SEW 520	30	0,74	0,68	0,60	0,53						0,94	0,83	0,74							
		40	0,71	0,65	0,58	0,51	0,99	0,90	0,80	0,71											
50		0,67	0,62	0,55	0,49	0,95	0,87	0,77	0,68												
60		0,65	0,60	0,53	0,47	0,91	0,83	0,74	0,65												
70		0,62	0,58	0,51	0,45	0,88	0,81	0,71	0,63												
80		0,61	0,56	0,49	0,44	0,85	0,78	0,69	0,61												
90		0,59	0,54	0,48	0,42	0,83	0,76	0,67	0,59												
100		0,57	0,53	0,47	0,41	0,80	0,74	0,65	0,58					0,97	0,94						
110		0,56	0,52	0,45	0,40	0,79	0,72	0,64	0,56					0,92	0,90						
120		0,55	0,51	0,44	0,39	0,77	0,71	0,62	0,55					0,90	0,88						
130		0,54	0,50	0,44	0,38	0,75	0,69	0,61	0,54												
140		0,53	0,49	0,43	0,38	0,74	0,68	0,60	0,53					0,98	0,86						
150		0,52	0,48	0,42	0,37	0,73	0,67	0,59	0,52					0,96	0,85						

no reduction factor

5. CONCLUSIONS AND GENERAL RECOMMENDATIONS

This design concept facilitates a purely stress-based verification that avoids fracture mechanics analysis. In this way, the structural engineer can use simple means to define a quality class requirement based upon the component loading.

In chapter 3 it is shown how load bearing reserves can be considered through numerical analyses. If necessary, an elastic-plastic structural design can be evaluated based on the material toughness. The initial defect sizes and boundary conditions for such analysis are described in (Spannaus 2016).

ACKNOWLEDGEMENT

The investigations presented in this paper were performed within the scope of the IFG-Research Project 17745 N „Load-bearing behavior of welded components made of steels cast considering imperfections and residual stresses” of the Research Association on Welding and Allied Processes of the DVS at the Versuchsanstalt für Stahl, Holz und Steine of Karlsruhe Institute for Technology (KIT). The authors thank the following industrial partners for the design and provision of the specimens, their

cooperation in the project-related steering committees and their advisory support: Stahl- und Hartgusswerk Bösdorf GmbH Leipzig, Friedrich Wilhelms-Hütte Stahlguss GmbH Mülheim an der Ruhr; Schlaich Bergermann Partner Stuttgart, Liebherr-Werk Ehingen, DB Netz AG, Krebs + Kiefer Dresden, Anakon GmbH Karlsruhe, KoRoH GmbH Karlsruhe, BAM Abteilung Bauwerkssicherheit (department of structural safety) Berlin, Ingenieurgesellschaft Peil, Ummenhofer mbH.

REFERENCES

- Berger, C.; Blauel, G.; Hodulak, L.; Pyttel, B.; Varfolomeyev, I. (2009), Bruchmechanischer Festigkeitsnachweis für Maschinenbauteile. 3., überarb. Ausg., Stand 2009. Frankfurt am Main: VDMA-Verlag (FKM-Richtlinie).
- EN 1993-1-8/NA:2010, National Annex - Nationally determined parameters - Eurocode 3: Design of steel structures - Part 1-8: Design of joints.
- EN 10340:2008, Steel castings for structural uses.
- EN 12680-1:2003: Founding - Ultrasonic examination - Part 1: Steel castings for general purposes.
- EN 1993-1-10:2010, Eurocode 3: Design of steel structures - Part 1-10: Material toughness and through-thickness properties.
- Hardin, R. A.; Beckermann, C. (2002), Effect of Shrinkage on Service Performance of Steel Castings. In Steel Founders' Society of America (Ed.), Proceedings of the 56th SFSA Technical and Operating Conference. Chicago, IL, p. Paper No. 4.5.
- Sedlacek, G.; Feldmann, M.; Kühn, B.; Tschickardt, D.; Höhler, S.; Müller, C. et al. (2008), Commentary and Worked Examples to EN 1993-1-10 "Material toughness and through thickness properties" and other toughness oriented rules in EN 1993. First Edition. Luxembourg: Official Publications of the European Communities (Scientific and Technical Research series).
- SEW 520:1996, Hochfester Stahlguß mit guter Schweißbeignung - Technische Lieferbedingungen.
- Spannaus, M. (2016), Beitrag zur Erweiterung der Regelungen für die Bemessung von Erzeugnissen aus Stahlguss unter vorwiegend ruhender Beanspruchung, submitted PhD thesis, Karlsruhe Institute of Technology, Department of Civil Engineering, Geo and Environmental Sciences. Karlsruhe.

SINGLE LAP FRICTION CONNECTION IN TUBULAR SECTIONS

Milan Veljkovic
Delft University of Technology, Delft, the Netherlands
m.veljkovic@tudelft.nl

Marko Pavlovic
Delft University of Technology, Delft, the Netherlands
m.pavlovic@tudelft.nl

Carlos Rebelo
ISISE, Department of Civil Engineering, University of Coimbra, Portugal
crebelo@dec.uc.pt

Luís Simões da Silva
ISISE, Department of Civil Engineering, University of Coimbra, Portugal
luiss@dec.uc.pt

Abstract: A connection between two segments of a steel tubular tower for multi megawatt wind turbines is most commonly designed as a ring flange connection. However, recent research results of EU projects offer a competitive alternative: friction connections with long open slotted holes. The biggest advantage of the friction connection is a rather high fatigue resistance, class 100, compared to 40 to 71 for the ring flange connection, according to EN1993-1-9. Another advantage is speed of the fabrication process leading to the cost reduction to one fifth of the ring flange connection. This paper will address knowledge gained in using friction connection with fitted bolts. Down-scale 4-point bending experiments on connection of 1 m diameter and real-scale single lap-joint are validated by sophisticated FEA using very realistic geometry. Results of experiments and FEA are compared with existing design procedure according to EN1993-1-8 and the criteria of ultimate limit state is discussed.

INTRODUCTION

One of the main objectives of the European Wind Initiative (EWEA, 2013) is to “make onshore wind the most competitive energy source by 2020”. A starting point for structural engineers to reach this target is improvement of the supporting structures of Wind Energy Converters (WEC). Steel tubular towers are the most common supporting structural system for a nacelle and rotor of WEC (DNV/Risø, 2002). They are built of 20 – 30 m high segments, which are traditionally connected by L-shaped ring flange connections with preloaded high-strength bolts, see Figure 1. The design of the tower is governed by the fatigue resistance, as the common ring flange connection between two tower segments belongs to a fatigue design class between 40 and 71 for a typical detail of the ring flange and tower shell connection. according to EN 1993-1-9 (2005). In addition, to relatively costly ring flanges this solution leads to rather thick tower shell.

Ring flange connection

For design purpose, it is assumed that the resistance of the three dimensional tower connection detail, which is loaded dominantly in bending, can be described by the resistance of a segment in tension with a single bolt and bolt row, respectively. The segment width c is equivalent to the arc length between two bolts in the tension zone of the shell, see Figure 1. Applicability of the segment model in the design of the tower connection has been confirmed by Schaumann & Seidel (2000) and Pavlović et al. (2015a).

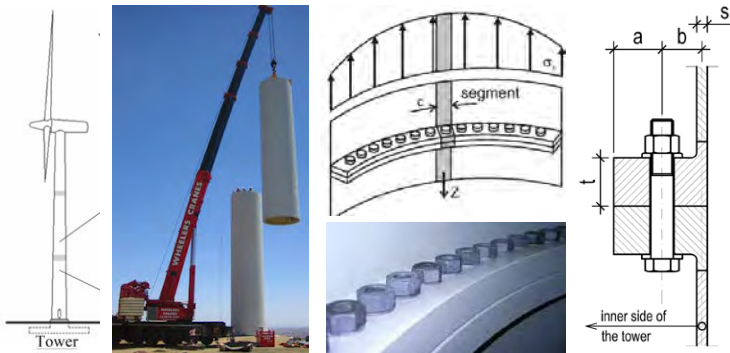


Figure 1. Steel tubular tower for wind energy converter with ring flange connection.

Loading and Fatigue

For design purposes, the life time of a tower is represented by a set of design situations covering the most significant conditions that the wind turbine may experience. The combination of the design situations with pertinent safety factors is operationalized in IEC 61400-1 (2005). Fifteen load cases are used for Ultimate Limit State (U) analyses and seven are used for Fatigue Limit State (F) analyses.

Table 1. Example of loads at the tower bottom (Veljkovic et al. 2015).

Design verification case	F_x (kN)	F_y (kN)	F_z (kN)	M_x (kNm)	M_y (kNm)	M_z (kNm)
Extreme ULS loads	725	958	2220	64538	67796	6476
Fatigue damage equivalent loads: $m = 3$; $N_{ref} = 2.0E+08$	102.6	67.8	28.9	4774	6204	1229

Example of the cross section loads used to design the bottom section of a 80 meters high steel tubular tower supporting a 2.1 MW class IIA turbine are given in Table 1. Fatigue limit state load cases resulting in a fatigue load spectra are converted to Damage Equivalent Load (DEL) using slope of the S-N curve $m_{ref} = 3$ and reference number of cycles $N_{ref} = 2.0E+08$. Furthermore, the fatigue verification is done using the classification method given in EN 1993-1-9 (2005).

Development of the bolt force in function of the segment load shown in Figure 2. It depends on the level of bolt preload, on position of the bolt along the width of the flange, and on the stiffness of the bolt and the clamping package. The segment forces due to damage equivalent loads in towers for WEC are usually in Range 1 resulting in rather small additional bolt force thanks to the preloading. The fatigue resistance of the bolt having nominal detail class 50 according to EN 1993-1-9 (2005) is usually not governing for the design. However, depending on maintenance of the

ring flanges, a rather important opening may occur between. For the sake of validation of FEA, presence of the maximum initial gap of 6.5 mm which has influence variable opening on the third of the circumference of a tower diameter 1 m is investigated by Pavlović et al. (2015). Rapid development of the bolt force even at the lower load levels, see Figure 3, results in reduced fatigue resistance of the bolts. Certainly small tolerances of flanges are needed (ISO 2678-1, 1990) which are achieved by costly machining of the flanges contact surfaces after welding to the tower shell. If such openings are identified in real towers a reparation is needed by inserting lining plates in gaps. This recommendation is based on investigations done in Germany, (Feldman et al. 2011). Almost perfect bolt-force functions could be obtained after retrofitting.

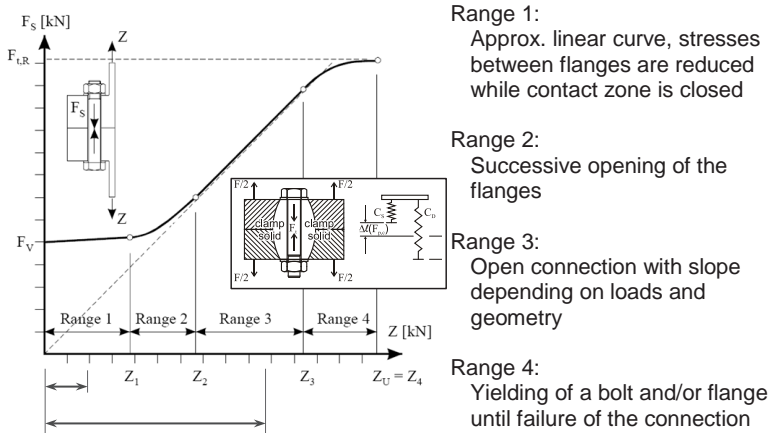


Figure 2. Nonlinear relationship between the bolt force and applied load in segment model for flange connections (Seidel and Schaumann, 2001).

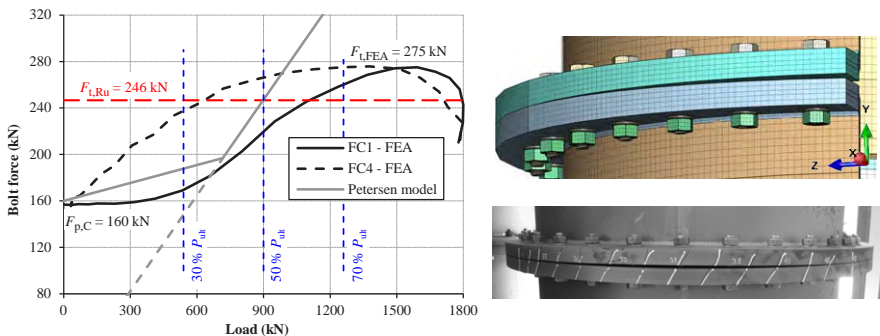


Figure 3. Development of the bolt force in a perfect flange - FC1, and in flange without the initial gap of 6 mm - FC4 (Pavlovic et al., 2015).

Friction connection

Friction connections with normal clearance holes have been used in structural engineering for decades. Their behaviour has been extensively examined by various

researchers and is comprehensively described by Kulak et al. (2001). Slip resistant joints rely on load transfer between the joined elements due to friction, which is ensured by a clamping force provided by preloaded high strength bolts. Friction connections are very efficient for cyclic loading caused by the wind which vary between tension and compression. Due to preloaded bolts and force transfer by friction, the stress concentration does not appear, as it has been confirmed in experiments of the HISTWIN project (Veljkovic et al., 2012). This structural detail belongs to fatigue class 100 according to EN 1993-1-9 (2005).

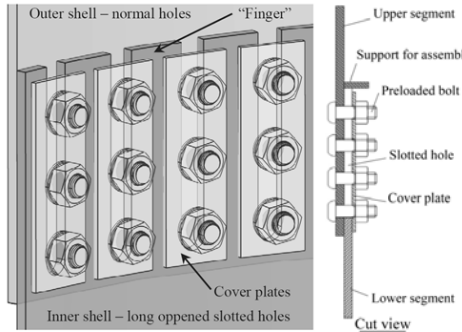


Figure 4. Friction connection with long open slotted holes.

A new type of single-lap friction connection is developed in HISWIN and additionally studied in HISTWIN2 project (Veljkovic et al. 2012, 2014). The main achievement is reduced the production cost and the increase of the fatigue resistance of the connections in WEC towers. The main innovation of the connection is in the substitution of the normal clearance holes on the lower tower section with long open slotted holes with the covered plate, Figure 4. The remaining steel parts between the long open slotted holes are called “fingers” which is based on their visual appearance. At the inside of the tower, cover plates shall be placed to ensure an equal distribution of pressure and to facilitate the speed of the execution process in situ. Bolts are pre-installed in the upper segment and easily slide on the top of the lower segment. This execution technology was proved by feasibility tests, done in Portugal, where 10 mm clearance between two tower segments was provided and shown as sufficient for easy execution of the connection.

Special types of bolts and washers: Tension Control Bolts, BobTail lockbolts, Press-fitted „Knurl“ bolts and Nord-Lock washers are tested to check their appropriateness for execution of the towers. Special attention has been focused on effects of a long term losses of the preloading force (Veljkovic et al. 2012). Long-term losses are very much dependent on testing conditions. The major influence depends on following: ratio between the bolt diameter and the grip length, the total thickness of the primer surface, type of bolts used, existence of the of any minor gap between connected surfaces, type of loading. As an example of possible magnitude of the bolt force losses is estimated approximately about 25% of pretension force after 20 years of the exploitations.

Comparative cost analysis in HISTWIN project showed that up to 80 % reduction of the connection costs in a tower can be obtained by using the novel friction connection with long open slotted holes instead of the classical ring-flange connection.

FEA validation

4-point bending down-scale experiments, on the ring flange connections and the new type of friction connection were performed by RWTH Aachen University within the scope of the HISTWIN project, see Figure 5a. The main objectives of the experiments were as follows: investigate the behaviour of the connection in bending, test the feasibility of the assembling the friction connection and evaluate effects of flanges with parallel flange imperfections. Totally eight specimens were tested on 7.14 m long beams, 8 mm thick shells (S355J2) with diameter of 1 m:

- four with the ring flange connection having 32 M20 bolts and
- four with the friction connection having 24x3 M20 bolts.

Down-scale experiments are validated by using detailed FE model, see Figure 5b (Pavlovic et al. 2015a). Bolts and nuts are modelled with the real thread geometry. The preloading of the bolts is applied by the turning the nuts in the model. Damage material model is used for the bolts in the ring flange connection. This resulted in very good agreement of the overall behaviour between the experiments and FEA for both connection types, see Figure 5c,d.

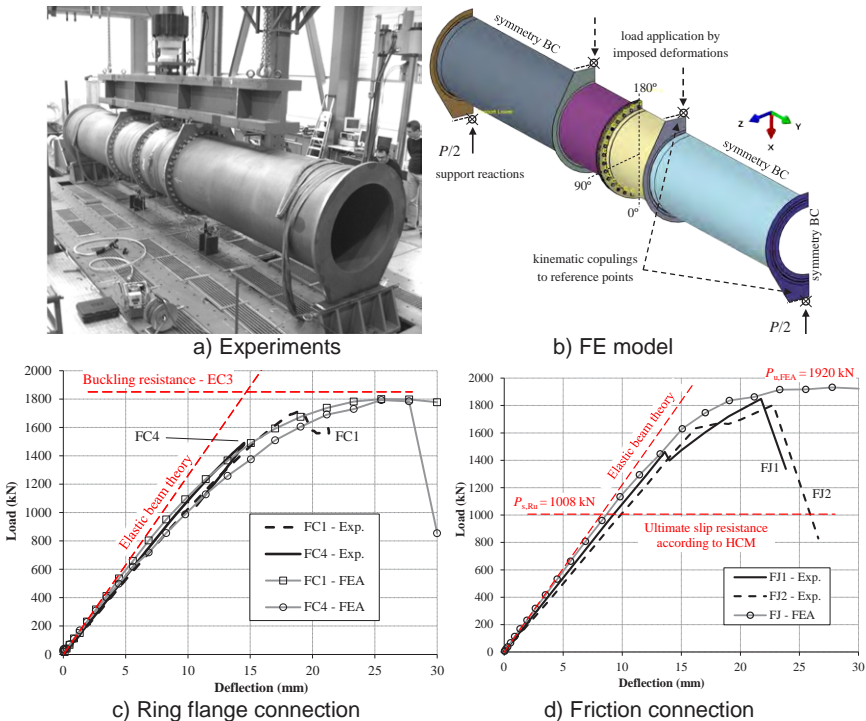


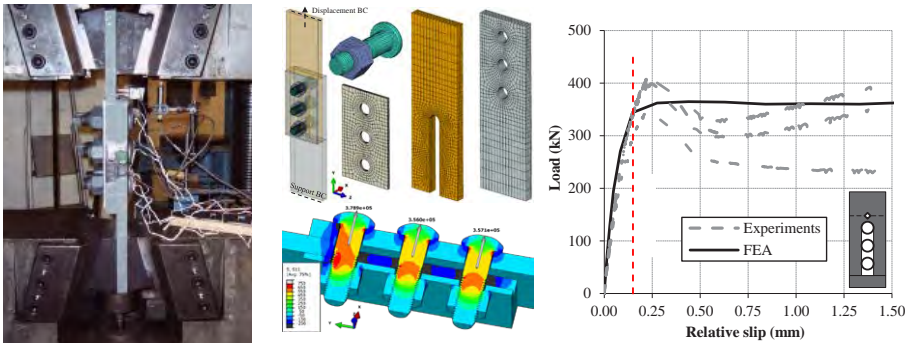
Figure 5. FEA validation of down-scale 4-point bending experiments of tower connections (Pavlovic et al. 2015a).

Series of experiments on the flat plate resembling of the real-scale single lap friction connection with long open slotted holes were performed at Luleå University of Technology within the scope of the HISTWIN project, see Figure 6a. FEA validation using exact geometry of the bolts showed excellent agreement with experiments shown in Figure 6b.

FRICTION CONNECTION

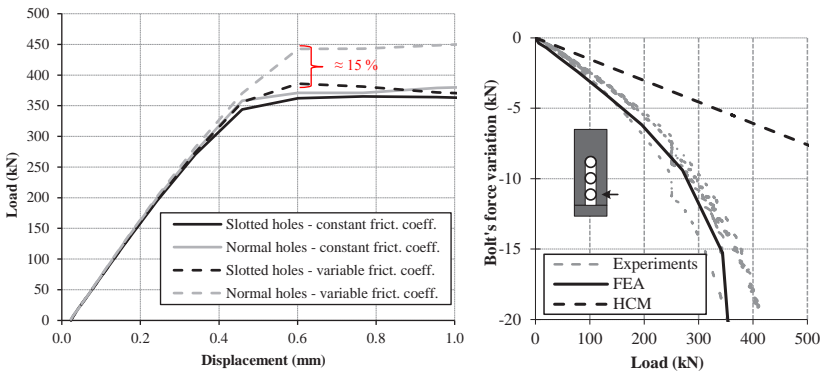
Influence of the hole geometry

The reduction factor k_s used in EN 1993-1-8 (2005) covers the difference between the slip factor determined from the standard friction tests (EN 1090-2, 2008) and the apparent friction coefficient at the ultimate load in a real connection with oversized holes. This factor is studied for open slotted holes in Pavlovic et al. (2015b). Two phenomena are recognized, see Figure 7: a) reduction due to influence of contact pressure on the friction coefficient and b) reduction of the preloading force in the bolt at the ultimate slip load. It is concluded that the same factor $k_s = 0.64$ can be used as for the closed slotted holes given in EN 1993-1-8 (2005). Considering both above mentioned effects the down-scale and the real-scale experiments the recommendation is that the constant value of the friction coefficient used in FEA has to be reduced compared to the slip factor determined in standard friction tests since it depends on the contact pressure. A reduction of 25 % is recommended for the long open slotted holes.



a) Experiments (Husson 2008) b) FEA validation (Pavlovic et al. 2015b)

Figure 6. Investigation of a single lap joint with long open slotted holes.



a) Influence of contact pressure

b) Loss of bolt preload

Figure 7. Influence of the hole geometry on slip factor (Pavlovic et al. 2015b).

Influence of the fingers

In order to achieve easy sliding of the upper segment of the tower to the lower segment of the tower, execution tolerance must be provided in form of gap between these two segments. Bending of the fingers inwards in order to get feasible connection in the full scale have been proposed. The proposal is based on thorough FEA of two possible alternatives: the inwards bended fingers and the smaller radius of the bottom tower segment for 20 - 60 mm, to achieve the "concentric" execution gap of 10 – 30 mm. In both alternatives Heistemann et al. (2014) the closing of the gap imposes residual stresses and imperfections on the fingers. These effects are critical for local buckling of the shell in the vicinity of the connection as well as for the strength of fingers in the connection. Inward bending of the fingers, see Figure 8, results in only 2 % reduction of the bending resistance of the connection with 30 mm concentric gap.

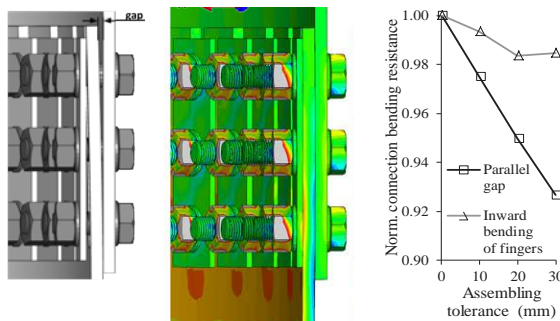


Figure 8. Execution tolerance for the friction connection (Heistemann, 2014).

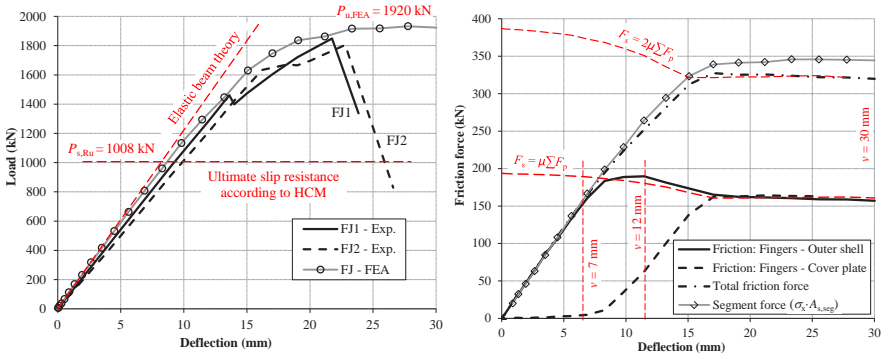
SHEAR TRANSFER IN THE OPEN SLOTTED HOLES

Second friction surface

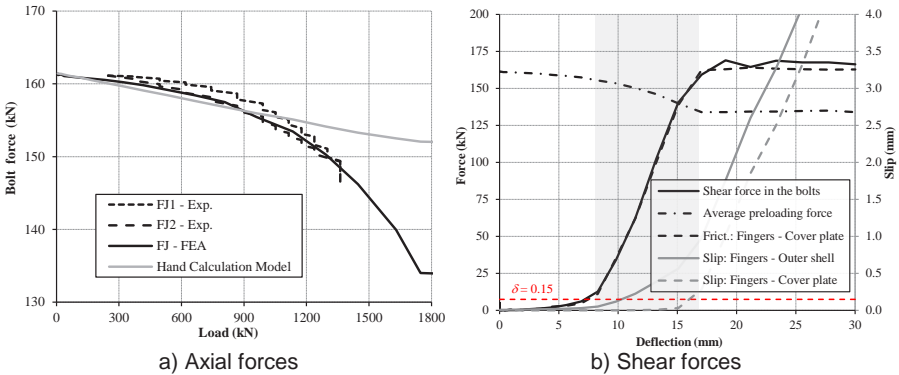
The ultimate resistance of the friction connection corresponds to its ultimate slip resistance. The friction connection with long open slotted holes is a single lap joint, thus providing one friction surface. It has been shown in HISTWIN2 project that the second friction surface is activated after the ultimate limit state is reached. Results of 4-point bending experiments and FEA validation are compared to the characteristic slip resistance according to EN 1993-1-8 (2005) considering one friction surface and reduction due to hole geometry in Figure 9a. Approximately 80 % higher resistance of the connection is obtained in experiments and FEA, than predicted by the codes. Figure 9b shows that the second friction surface is activated at fingers – cover plate interface after the slip at the fingers - outer shell is reached. The nominal slip resistance according to the code occurs at deflection of approximately 7 mm. This deflection corresponds to the slip resistance according to hand calculation model in EN 1993-1-8 (2005) considering one friction surface. The second friction surface in this single lap joint is enabled due to several reasons:

- presence of the cover plates – cover plates must have the same surface treatment as the other faying surfaces (fingers, outer shell)
- relatively short bolts – high bending stiffness of the bolts ensured rigidity to support the cover plate inside the tower.

- fitted bolts are used in experiments – bolts are “clamped” into holes of the outer shell.



a) Load-deflection b) Load transfer within segment in the tension zone
 Figure 9. Slip failure mode in 4-point bending test (Pavlovic et al., 2015).



a) Axial forces b) Shear forces
 Figure 10. Bolt forces in the tension zone of the 4-point bending test (Pavlovic et al., 2015).

Additionally it is interesting to analyse variation of the bolt axial force from FEA, see Figure 10a. The variation is addressed to following:

- contraction of the clamping package in the tension zone due to Poisson's effects,
- development of the shear forces imposed by activation of the second friction surface, see Figure 10b.

This mechanism gives much less bolt force variation compared to the bolt force variation in the ring flange connection, resulting in improved fatigue endurance of the connection.

Requirements for friction connection

After reaching the slip of 0.15 mm in a connection comprising only one bolt row, see Figure 6a, the ultimate resistance of the single lap connection is reached. This proves that the 0.15 mm slip displacement should be used to determine the slip factor in

friction tests. However, in the circular connection, comprising many bolt rows around the circumference, different behaviour is obtained. Figure 10a shows that at the slip of 0.15 mm corresponds to approximately 50 % of ultimate resistance of the connection. This is due to redistribution of the forces between the adjacent bolt rows and activation of the second friction surface.

CONCLUSION

The friction connection with open slotted holes is investigated in recent HISTWIN projects. Great cost benefits are demonstrated in the research projects.. Additional improvements are achieved in the fatigue performance, execution speed compared to the ring flange connections. Furthermore, possible structural benefits in designing the single lap connection in the towers are well documented. The main conclusions are summarized below:

1. Influence of the opened slotted hole geometry on the slip resistance the $k_s = 0.64$ can be used as for the closed slotted holes given in EN 1993-1-8 (2005).
2. Execution tolerances in means of the gap between the upper and lower tower segment up to 30 mm can be achieved by inward bending of the fingers without compromising the resistance of the connection and adjacent tower shell.
3. The single lap friction connection in the tubular section using fitted bolts and the cover plates increases the ultimate resistance of the connection by activating the second friction surface. The effect of the tubular section diameter will be further investigated.

REFERENCES

- DNV/Risø. (2002), Guidelines for Design of Wind Turbines, 2nd Edition. Det Norske Veritas, Risø National Laboratory, Copenhagen.
- EN 1993-1-8 (2005), Eurocode 3: Design of steel structures. Part 1-8: Design of joints. European Committee for Standardization (CEN/TC250), Brussels.
- EN 1090-2 (2008), Execution of steel structures and aluminium structures. Part 2: Technical requirements for steel structures, European Committee for Standardization (CEN), Brussels.
- EN 1993-1-9 (2005), Eurocode 3 - Design of steel structures. Part 1-9: Fatigue. European Committee for Standardization (CEN/TC250), Brussels.
- EWEA (2020), The European Wind Initiative - Wind Power Research and Development to 2020. The European Wind Energy Association, Brussels.
- Feldmann, M., Naumes, J., Pak, D. (2011), Zum Last-Verformungsverhalten von Schrauben in vorgespannten Ringflanschverbindungen mit überbrückten Klaffungen im Hinblick auf die Ermüdungsvorhersage. *Stahlbau* 80: (pp. 21–29).
- Heistermann, C., Veljkovic, M., Simões, R., Rebelo, C., Simões da Silva, L. (2013), "Design of slip resistant lap joints with long open slotted holes". *J. Constr. Steel Res.* 82 (pp. 223–233).

- Heistemann, C. (2014), Resistance of Friction Connections with Open Slotted Holes in Towers for Wind Turbines. Doctoral thesis. Luleå University of Technology, Luleå.
- Husson, W. (2008), *Friction Connections with Slotted Holes for Wind Towers*. Licentiate thesis. Luleå University of Technology, Luleå.
- ISO 2768-1 (1990), SIS - Standardkommissionen i Sverige. SS-ISO 2768-1: Toleranser - Generella toleranser, Del 1: Toleranser för linjära mått och vinkelmått utan direkta toleransangivelser.
- Kulak, G. L. et al. (2001), Guide to Design Criteria for Bolted and Riveted Joints, Second Edition. American Institute of Steel Construction, Chicago.
- Pavlović, M. et al. (2015a), "Connections in towers for wind converters, Part I: Evaluation of down-scaled experiments". *Journal of Constructional Steel Research* 115 (pp. 445–457).
- Pavlović, M. et al. (2015b), "Connections in towers for wind converters, Part 2: The friction connection behaviour". *Journal of Constructional Steel Research* 115 (pp. 458–466).
- Schaumann, P. & Seidel, M. (2000), "Failure analysis of bolted steel flanges", in Zhao, X.L. & Grzebieta, R.H. (ed.). *Proceedings of the 7th International Symposium on Structural Failure and Plasticity (IMPLAST 2000)*, Elsevier, Amsterdam.
- Seidel, M., Schaumann, P. (2001) "Measuring fatigue loads of bolts in ring flange connections", *Proc. Eur. Wind Energy Conf. Exhib. EWEC 2001*, Copenhagen.
- Veljkovic, M. et al. (2012), High-strength tower in steel for wind turbines (HISTWIN), Final report - RFSR-CT-2006-00031, European Commission (RFCS), Brussels.
- Veljkovic M, et al. (2014), Higher steel tubular towers for wind turbines (HISTWIN2). Final report - RFSR-CT-2010-00031, European Commission (RFCS), Brussels.
- Veljkovic M, et al. (2015), High-Strength Steel Tower for Wind Turbines (HISTWIN_Plus). Final report - RFS2-CT-2014-00023, European Commission (RFCS), Brussels.

ENERGY DISSIPATION IN CENTRIC BOLTED GUSSET PLATE OF BRACES

Maël Couchaux
INSA of Rennes, Rennes, France
mael.couchaux@insa-rennes.fr

Pierre O. Martin
CTICM, Saint-Aubin, France
pomartin@cticm.com

Xavier Thollard
Tractebel, Gennevilliers, France
xavier.thollard@gdfsuez.com

Philippe Rivillon
CSTB, Champs-Sur-Marne, France
philippe.rivillon@cstb.fr

ABSTRACT

In dissipative seismic concept according to Eurocode 8, capacity design leads to additional cost for brace connections. In this concept connections don't dissipate energy, this role being dedicated to braces. However connections are able to dissipate by sliding, bearing and block shear. Tests have been performed to observe dissipation in bolted gusset plate connections of brace. These experimental tests are completed by Finite Element Analysis.

1. INTRODUCTION

Considering the seismic design of a steel concentrically braced frame (CBF) according to the dissipative ductility classes of the European standard Eurocode 8, the seismic forces are mainly absorbed by the cyclic yielding of the tension diagonal. The dissipative design is generally efficient for high seismic areas but should always be applied considering specific requirements. For CBFs, this specific capacity design involves that the joints should resist to the yielding of the diagonal. For low to moderate seismicity areas, it implies additional costs and difficulties that can rarely be justified. Less stringent methods for lower dissipation would thus be useful if available.

Previous studies on the behaviour of shear joints have highlighted more or less ductile failure modes: shear of the bolts, local yielding at bolt holes as well as shear block. Under compression, the buckling of the gusset, sometimes following the buckling of the diagonal, limits the resistance of the joint. Under cyclic loads, a significant part of energy is absorbed by the sliding of the joint pieces.

While some of these modes should clearly be avoided in a seismic context because of their low ductility, the other ones could fruitfully be used to absorb a part of the seismic energy if they could be efficiently controlled. In the objective to have a better understanding of the cyclic behaviour of CBF shear joints and having in mind the

development of simplified capacity design rules for low to moderate seismicity areas, a research study has been carried out by CTICM and CSTB, with the support of ArcelorMittal. Experimental tests were developed on two different specimens as well as a numerical model was prepared. The main results of this research project are presented here.

2. EXPERIMENTAL TESTS

2.1 Tests presentation

Monotonic and cyclic tests have been performed in CSTB (Champs-sur-Marne, France) for two geometries of connections of a brace composed of double channel (UPE 200). Interaction between brace and connections being particularly important, the behaviour of the complete structure has been tested (see Figure 1). Specimens have been subjected to monotonic loadings (tension and compression) and cyclic loading (quasi-static). Cyclic tests have performed considering ECCS requirements n°45. Monotonic tests were carried out in order to estimate incremental displacements used during cyclic tests according to ECCS requirements and to evaluate degradation due to cyclic loadings.

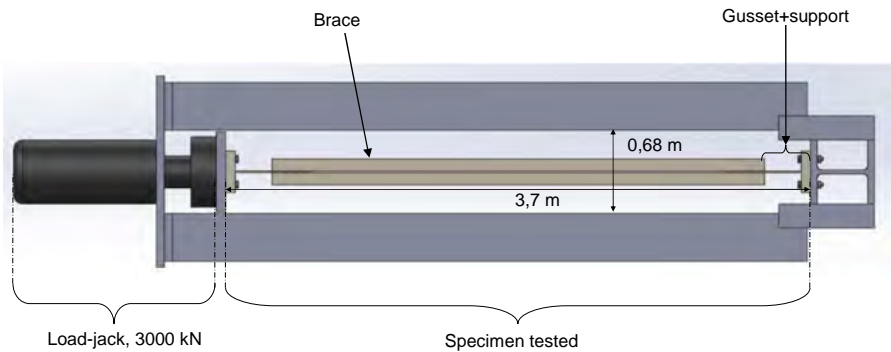


Figure 1 : Test set-up

So as to avoid effect of eccentricity between gusset plates and diagonal bracings, the latter is composed of double channel (see Figure 2). Gusset plates of 10 mm thickness have been designed to get dissipation by bolt hole deformations and block shear. HR preloaded bolts have been designed to observe sliding before the final failure of the connection. Class 8.8 have been used because of a better resilience than class 10.9.

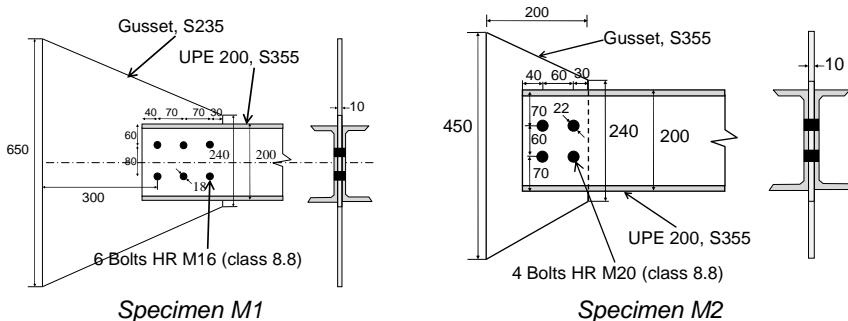


Figure 2 : Geometry of specimens tested (in mm)

Edges and pitches of specimen M2 are close to the minimal value of Table 3.3 of EN 1993-1-8 to privilege yielding by bearing and failure by block shear. By the end, the specimen M1 has been designed to observe the buckling of the gusset plate whereas the brace buckling was expected for the specimen M2.

Displacement transducers have been used to measure longitudinal displacement of connections and transversal displacement of gusset plates and diagonal bracings. The bolts used during cyclic tests have been instrumented with BTM-6C strain gauge to measure axial deformation and to obtain the evolution of preloading by preliminary calibrations.

Tensile tests were carried out on coupons extracted from channels and gussets. It appears that steel have mechanical characteristics clearly superior to nominal ones (see Table 1) particularly steel of gusset of specimen that is closer to S420 than to S235.

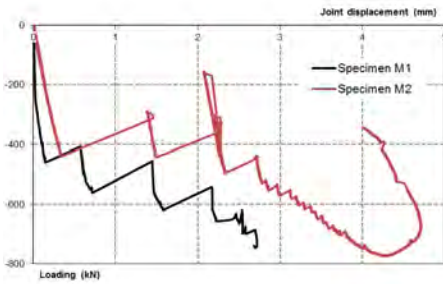
Specimen	Element	Grade/ class	Yield strength	Tensile resistance	Elongation	Necking
			<i>N/mm²</i>	<i>N/mm²</i>	%	%
M1	Gusset	S235	430	516	26,8	59,9
	UPE (web)	S355	473	580	31,8	-
	UPE (flange)	S355	384	522	30,8	-
	Bolt	8.8	874	966	-	-
M2	Gusset	S355	550	580	26	77,3
	UPE (web)	S355	474	580	29,4	63,9
	UPE (flange)	S355	412	568	32,2	67,7
	Bolt	8.8	912	960	26,4	-

Table 1 : Mechanical characteristics of steel

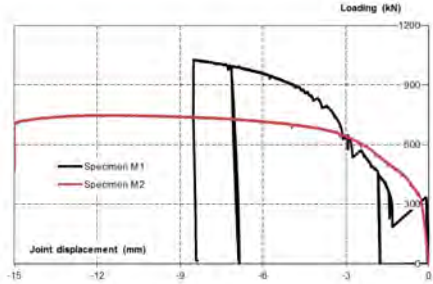
2.2 Tests under monotonic loadings

Tests have been performed under monotonic loadings of compression and tension for each specimen. In tension, failure is due to bolts shear rupture and block shear of the gusset respectively for tests M1 and M2. In compression, buckling of gusset and diagonal bracing are obtained respectively for tests M1 and M2.

The curve of load in function of the axial displacement of the joint is presented in Figure 3. Important losses of preloadings are observed for loading greater than 300-400 kN that correspond to sliding of bolts. These sliding create a huge detonation, associated to the impact of bolts against their hole. The ultimate displacement of specimen M2 is clearly greater than that of specimen M1 insofar as the block shear is more ductile than bolt shear failure.



a- Compression tests



b- Tensile tests

Figure 3 : Monotonic tests – Force-displacement curves

2.3 Tests under cyclic loadings

2.3.1. Loading procedure

The loading procedure is based on the ECCS requirements n°45 but is slightly different because force-control has been used at the beginning of tests in order to be independent of sliding of bolts that depend upon bolt initial positions. A force of 500 kN, greater than sliding resistance, has been applied by steps. The displacement of the load-jack obtained for this force in tension and compression are noted D_t and D_c and used during the next steps of the cyclic loadings (see Table 2).

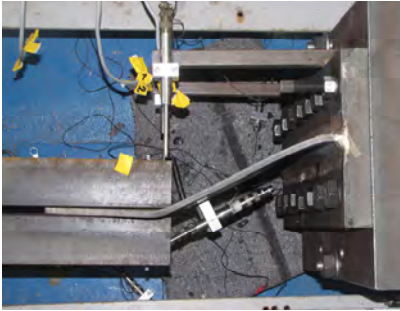
Specimen M1		Specimen M2	
Force/displacement	Cycle(s)	Force/displacement	Cycle(s)
+125 kN	1	+125 kN	1
+250 kN	1	+250 kN	1
+375 kN	1	+375 kN	1
+500 kN	3	+500 kN	1
$1,5D_t/-1,5D_c$	3	$1,5D_t/-1,5D_c$	3
$2D_t/-2D_c$	3	$2D_t/-2D_c$	3
$2,5D_t/-2,5D_c$	3	$2,5D_t/-2,5D_c$	3
$3D_t/-1,5D_c$	3	$3D_t/-3D_c$	3
$5D_t/-1,5D_c$	3	$4D_t/-4D_c$	3
$6 D_t$	-	$5D_t/-5D_c$	3

Table 2 : Cyclic tests – Loading procedure

The measurement of axial deformation of bolts show a loss of 50 % of preloading that starts after the first sliding and increases during the bearing deformations of bolts hole.

2.3.2. Failure modes

The failure mode of the test M1 has been obtained for a tensile force of 1066,8 kN, corresponding to a bolt shear failure (see Figure 4-b). It has nevertheless been preceded by the buckling of the gusset plate (see Figure 4-a).



a- Gusset plate buckling



b- Bolt shear failure

Figure 4 : Cyclic tests – Failure modes of test M1

The failure of the specimen M2 has been obtained for a tensile force of 742,2 kN. The failure mode was a block shear of gusset (see Figure 5-b) but it has been preceded by the buckling of the diagonal bracing (see Figure 5-a). These failure modes are similar to those obtained during monotonic loadings.



a- Brace global buckling



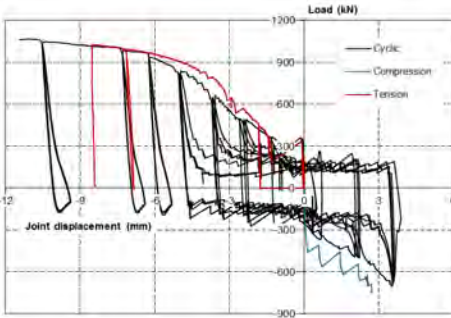
b- Gusset plate block shear

Figure 5 : Cyclic tests – Failure modes of test M2

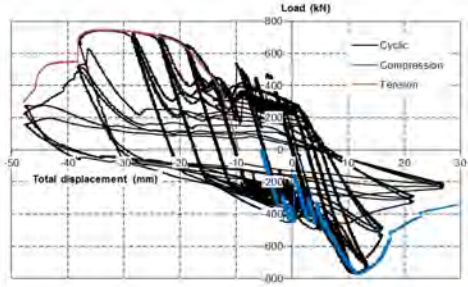
2.3.3. Force-displacements curve

For each specimen, the force displacement curves obtained for cyclic and monotonic loadings (tension and compression) are presented in Figure 6. The curves obtained for monotonic loadings have been translated to compensate the bolt clearance. Cyclic and monotonic curves are similar until the maximal force is reached in tension or compression. After this step, the degradation is more important during cyclic loading of specimen M2.

Sidings are obtained for lower loads during cyclic tests than during monotonic tests. This difference can be explained by the fact that during the first sliding (here in tension), contact surfaces have been cleaned and thus the friction coefficient decreased. Moreover, the loss of preloading during the first sliding leads to an additional reduction of the sliding force.



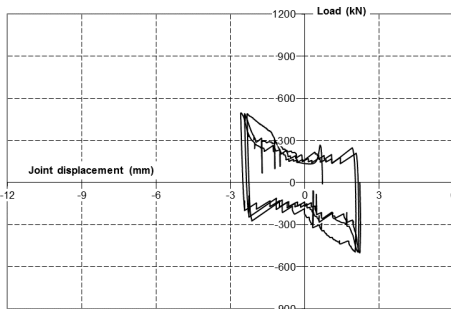
Test M1



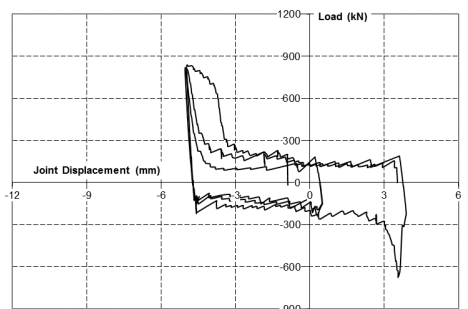
Test M2

Figure 6 : Monotonic and cyclic force-displacement curves

The curves of the force vs. the joint displacement of specimen M1 obtained for two loading rates are presented in Figure 7. For the two cases, sliding appears for a force of 200-300 kN but it developed itself on different lengths. The hole clearances increased during each cycle due to the bolt bearing.



a- Cycles 4 to 6



b- Cycles 10 to 12

Figure 7 : Cyclic test M1 - Force-joint displacement curve

3. NUMERICAL ANALYSIS

3.1 Presentation of the model

The numerical model was built using the Finite Element code ANSYS V14.5. Joints (gusset, bracings, bolts) are generated with three dimensional elements, which are hexahedral bricks (see Figure 8). The dimensions measured before tests are used (Couchaux et al. 2015).

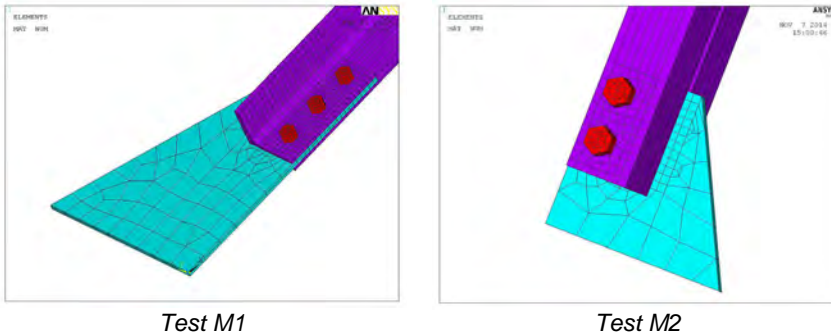


Figure 8 : Meshing of joints modelled

For bolts, a constant effective cross-section is considered over the entire length including the threaded part. The dimension of bolts fulfil the criteria of EN 14399-3 (the product standard of HR bolts). Hole clearances are also considered in order to model the sliding. The preload of bolts is also modelled by the command PSMESH. The washers have been neglected.

Contact elements (CONTACT 174 and 170) are used between truss bar and gusset; bolts and gusset/truss bar. An isotropic Coulomb friction law ($\mu = 0,3$) is considered to reproduce the sliding and sticking conditions between the flange and the bolt head. The contacts are assessed according to the Lagrangian method.

Half of the connection is modelled to take into account the symmetry conditions in loading and geometry. At one end of the truss bar, the gusset is clamped whereas at the other end, all the degrees of freedom are blocked except the longitudinal displacement. The structure is loaded in displacement.

A geometrical imperfection homothetic to the deflected shape of the first buckling mode is applied. The amplitude is set up to $L/200$ and $L/300$ respectively for specimens M1 and M2. L is the length of the element that buckles in the first mode; the length of the gusset plate for specimen M1 and the total length of the brace for specimen M2.

An elastic plastic behaviour of steel is assumed, where the stress-strain relationship is multi-linear. As soon as the deformation level reaches ϵ_u the stress drops to 10 N/mm^2 in order to represent the failure of the element. Two types of stress-strain curve are considered:

- a complex multi-linear curve, for gussets and channel, in which true stress true strain curve are considered particularly to take into account large deformations (Couchaux et al, 2015);
- a simple tri-linear curve for bolts.

The criterion of the yielding surface is Von-Mises with kinematic hardening. Large deformations and great displacements are also heeded.

The effects of low-cycle are not considered in ANSYS V14. Nevertheless, it is not necessary to take account of this phenomenon if the frame of this study, insofar as moderate earthquakes are involved, which contain only a low number of high cycles.

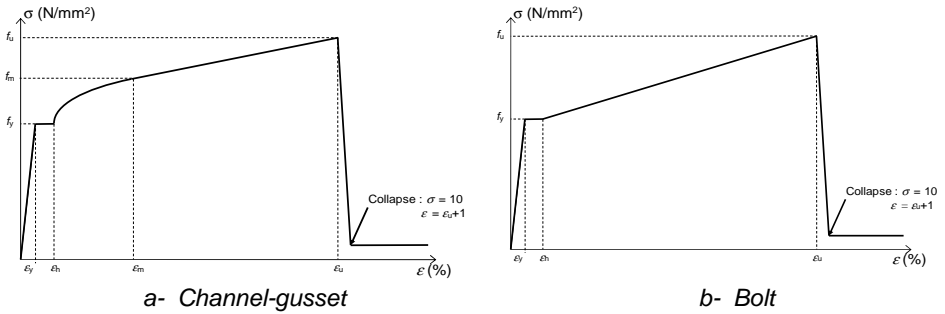
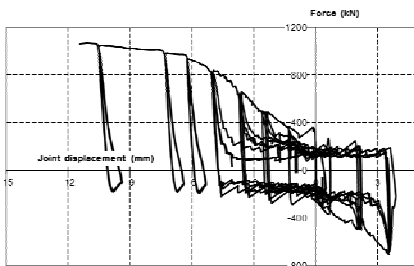


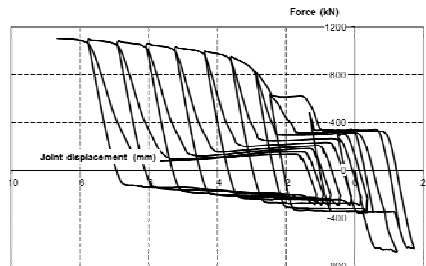
Figure 9 : Stress-strain relationships for steel

3.2 Study of cyclic tests

The cyclic force-displacement curves obtained numerically and by tests are presented in Figure 10 and Figure 11 respectively for specimens M1 and M2. The force-displacement curves obtained numerically are similar to the experimental ones particularly for specimen M2. For test M1, sliding is observed numerically for all cycles contrary to experimental observations. This difference is due to the fact that in numerical simulations, the load after buckling is greater than the sliding resistance.

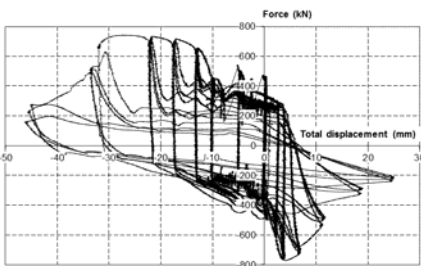


a- Tests

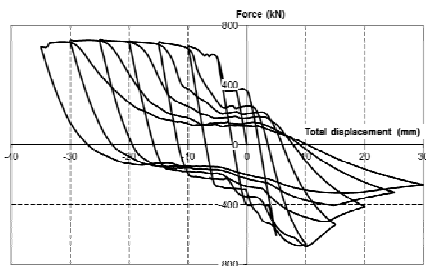


b- Numerical

Figure 10 : Cyclic test M1 – Force-displacement curves



a- Tests

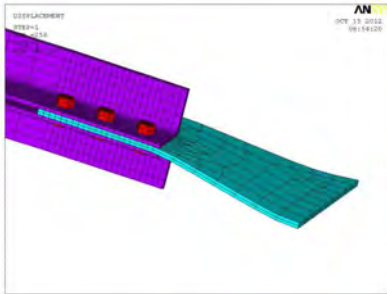


b- Numerical

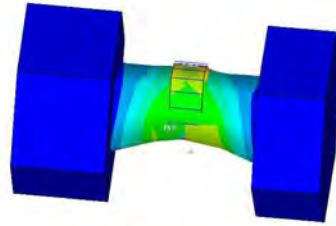
Figure 11 : Cyclic test M2 – Force-displacement curves

The failure modes obtained by tests and numerical analysis (see Figure 12 and Figure 13) are similar:

- in compression, gusset plate buckling and diagonal bracings buckling for tests M1 and M2 respectively,
- in tension, bolt shear failure and gusset plate block shear for tests M1 and M2 respectively.

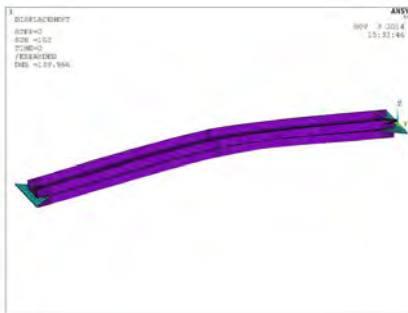


a- Gusset plate buckling

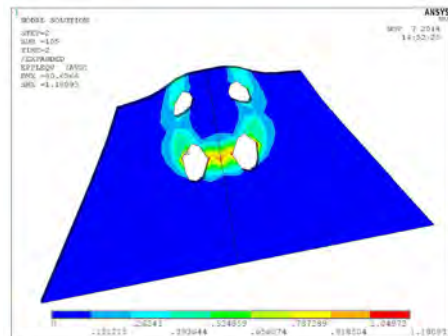


b- Bolt shear failure

Figure 12 : Numerical analysis – Specimen M1 at failure



a- Brace buckling



b- Gusset plate block shear

Figure 13 : Numerical analysis – Specimen M2 at failure

4. CONCLUSION

This research allowed to reveal and to estimate the ductility level of the failure modes of shear bolted CBF joints under cyclic actions. The sliding of the diagonal on the gusset plate, the hole bearing and the block shear have thus proved to be ductile and so to be able to absorb energy during seismic events. On the contrary, the shear of bolts can be considered as a non-ductile mode, preventing any dissipation, and it should then be avoided as far as possible. A premature buckling of the gusset plate disturbs the cyclic behaviour of the joint and can totally restrain the sliding.

The beneficial effect of the sliding should be underlined after this study, as it proved to be an effective part of the energy dissipation, while the phenomenon is often reluctantly perceived by engineers. For the full capacity design of CBF joints in dissipa-

tive diagonals, the Eurocode 8 standard thus allows the sliding during the seismic events.

The numeric modelling set up during the project will be used to add new numeric results for the testing of CBF joints under cyclic actions. The next step would be to define an equivalent behaviour law that would be used to assess the behaviour factor of CBFs using this type of joints for energy dissipation. A European research is currently running on these subjects, and it also includes new experimental tests to cover a wider scope, especially with non-symmetrical joints.

REFERENCES

ECCS (1986), recommended testing procedures for assessing the behaviour of structural elements under cyclic loads, *European Convention for Constructional Steelwork, Technical Committee 1, TWG 13 – Seismic Design*, No. 45.

Rabinovitch, J.S., Cheng, J.J.R. (1993), “Cyclic Behaviour of Steel Gusset Plate Connections”, *Structural Engineering Report No. 191*, Department of Civil Engineering, University of Alberta, Edmonton, Alberta.

EN 1998-1 (2005), Eurocode 8: Design of structures for earthquake resistances. Part 1: General rules, seismic actions and rules for building.

EN 1993-1-8 (2005), Eurocode 3: Design of steel structures. Part 1.8: Design of joints.

Yoo, J.H., Lehman, D.E., Roeder, C.W. (2008), “Influence of connection design parameters on the seismic performance of braced frames”, *Journal of Constructional Steel Research*, Vol. 64, (pp. 608-622).

Nascimbene, R., Rassatib, G.A., Wijesundarac, K.K. (2012), “Numerical simulation of gusset plate connections with rectangular hollow section shape brace under quasi-static cyclic loading”, *Journal of Constructional Steel Research*, Vol. 70, Issue 4, (p177-189).

Couchaux, M., Martin, P.O., Thollard, X., Rivillon, P. (2015), « Assemblages de contreventements par goussets boulonnés centrés sous chargements monotones et cycliques », *Revue Construction Métallique*, Vol.51, No. 3 (in french).

GENERALLY LOADED CONNECTIONS BY COMPONENT BASED FINITE ELEMENT METHOD

František Wald, Lukáš Gödrich, Marta Kurejková
Czech Technical University in Prague, Thákurova 7, 166 29 Praha, Czech Republic
frantisek.wald@fsv.cvut.cz

Luboš Šabatka, Drahoš Kolaja, Jaromír Kabeláč
IDEA RS, s.r.o., U Vodárny 3032/2a, 61600 Brno, Czech Republic
sabatka@idea-rs.com

Miroslav Bajer, Martin Vild, Josef Holomek
Brno University of Technology, Veveří 331/95, 602 00 Brno, Czech Republic
bajer.m@fce.vutbr.cz

ABSTRACT

The paper refers to current development in design of structural steel connections. Today practice is preferring analytical models which assure good prediction for standardised structural solutions. For description of full behaviour were analytical models of resistance equipped by prediction of stiffness, which is called Component method (CM). This paper focuses to the next step of design applying the finite element analyses for distribution of internal forces in joint and the components to analyse connectors itself, Component based finite element method (CBFEM). The material is modelled on design level as bilinear. The proper behaviour of components, e.g. bolts, welds and anchor bolts, is treated by introducing its behaviour in terms of initial stiffness, ultimate resistance and deformation capacity. The linear bifurcation analysis allows to check the slender plates in compression. The internal part of this design procedure is validation and verification including its hierarchy.

1 INTRODUCTION

The structural steel connections are currently designed by experimental, curve fitting, and analytical models. The tests with connections are simple and economical solution for its design. Based on tests and its published databases were prepared design tables for standardised connections. Curve fitting models are known from 1930. Mathematical formulas expressing the influence of geometrical and material parameters are reproducing the behaviour of similar connections well, but are not appointing the questions of the asked safe prediction of resistance. Today are applied in modelling of connections in the performance based seismic design only. The analytical modelling of components of connections are well developed for all connectors, bolts, welds, anchor bolts etc. and summarised in design standards. Zoetemeijer (1985) was the first who equipped the analytical model of resistance with prediction of stiffness. This models prepared for selected types of configuration in known as Component method (CM). The model of stiffness at elastic stage was improved in the work of Steenhius et al., (1994). Description of components behaviour was prepared by Jaspart (2002) for most beam to column connections and by Wald et al. (2008) for column bases. Method implemented in the current European structural standard (EN1993-1-8 2006 and

EN1994-1-1 2010) for steel and composite connections is applied in majority of software for structural steel used in Europe and overseas. The model was generalised by da Silva (2008) and is widely applied for design at elevated temperature during fire, 3D modelling of connections, etc. The procedure starts with decomposition of a joint to components followed by their description in terms of normal/shear force deformation behaviour. After that, components are grouped to examine joint moment-rotational (force-deformation) behaviour and classification/representation in a spring/shear model and application in global analyses. Advantage of the CM is integration of current experimental and analytical knowledge of connections components behaviour, bolts, welds, end plates, flanges, anchor bolts and base plates. This provides very accurate prediction of behaviour in elastic and ultimate level of loading. Disadvantage of component model is that experimental evaluation of internal forces distribution is done only for limited number of joint configurations and its deformation capacity is estimated according to the best engineering practice. Also in temporary scientific papers, description of some components is either not present or has low validity and description of background materials. Models of hollow section connections are described in Ch. 7 of EN1993-1-8 [8], with latest versions in (ISO 2012) and (AISC 2010), by curve fitting procedures. The transfer of curve fitting equations for a different joint geometry and five possible failure modes of RHS, CHS and hollow to open sections connections to CM was prepared by Jaspert & Weynand (2015). The CM is not developed for hand calculation. The analyses of all components in connection and its assembly is focus to preparation of design tools or tables.

Finite element models (FEM) for connections are used from 70s of last century as research-oriented (ROFEM). Their ability to express real behaviour of connections is making them a valid alternative to testing standard and expensive source of knowledge of connection's behaviour. Material model for ROFEM uses true strain stress-strain diagram. Today computational analysis, in particular computational mechanics and fluid dynamics, is commonly used as an indispensable design tool and a catalyst of many relevant research fields. For design-oriented FEM (DOFEM) of connection is logical to use FEM analyses for distribution of internal forces in joint and the components to analyse connectors itself, Component based finite element method (CBFEM), see (Wald et al., 2014). In contrary for standardised joints the FEM may predict the component behaviour and the assembly of internal forces may be done by engineering judgment. The recommendation for design by advanced modelling in structural steel is prepared in Chapter 5 and Annex C of EN 1993-1-5. The material is in DOFEM modelled on design level as bilinear. Strain is recommended to be limited to 5%, see cl. C.8(1) EN1993-1-5. The proper behaviour of bolts, welds and anchor bolts is treated by introducing its behaviour in terms of initial stiffness, ultimate resistance and deformation capacity, which is currently standardised. The linear bifurcation analysis allows to check the slender plates in compression including its design in post buckling stage. The internal part of advanced discrete procedures is Validation & Verification including its hierarchy.

2 VALIDATION & VERIFICATION

Development of modern general-purpose software and decreasing cost of computational resources facilitate this trend. As the computational tools become more readily available and easier to use, even to relatively inexperienced engineers, more scepticism and scrutiny should to be employed when judging one's computational analysis. However for structural connections with thousands experiments available the

validation process may be executed. But even in such situation the verification process performed through benchmark tests gains crucial importance. Seeing the need of making the results of research more transparent to the public, the office of science and technology policy in the United States issued a memorandum stipulating increased access to the results of federally funded scientific research. Such data can be easily verified or used for verification (or benchmarking), of some other work. The trend of making extended data available together with a report or publication persists in order to build confidence in growing number of performed numerical simulations. To achieve this goal it seems even more beneficial at this point to develop a standard set of smaller benchmark tests that can be used as a reference in the verification process of simulations. Native process of computer based design is Validation and Verification (V&V) of models. Comparison of V&V to different engineering application is still to be done. Application of V&V to steel connections research models is limited to a few published benchmark studies, see (Bursi & Jaspart, 1997) and (Virdi et al., 1999).

The detailed procedure for verification of proposed method and its application in design tool IDEA RS Connections, see (IDEA RS, 2015), was prepared in (Wald et al., 2015). The procedure consist of preparation of Benchmark studies for used components, e.g. bolts, welds, slender plates in compression, anchor bolts, and concrete block in compression. Three different types of welded connections were selected for benchmark studies, connections loaded in shear, in bending, and welded to flexible plate. For bolted connections are prepared benchmark studies for T-stub in tension, the splices in shear and the generally loaded end plate connection. For slender plate in compression is studied the triangular haunch in compression, the slender stiffener of column web and the plate in compression between bolts. For hollow section joints are studied the welded joints between CHS members, between RHS and FHR/CHS welded to the open section chords in shape of T, K and TT joints. For column bases are prepared verifications for generally loaded columns of open and hollow sections. Verification of case study consist of description of selected joint, results of CM and CBFEM, differences described in term of global behaviour on the force-deformation/rotation curve, and verification of initial stiffness, resistance, deformation capacity. At the end of each Benchmark study is prepared a Benchmark case to allow the user to check his results. In some cases gives the CBFEM method higher resistance, initial stiffness or deformation capacity. ROFEM model from bricks element validated on own experiments or experiments from literature is used in these cases, to get proper results. CBFEM is approved by this procedure.

3 BEAM TO COLUMN CONNECTION

The major advantage of application of CBFEM is in the design of the generally loaded complex joints as follows. To validate the end plates connections loaded by bending moments to both axes were tests on beam splice joint of two RHS 250x150x16 beams. The beams and plates were designed from S355, with measured $f_{y,exp} = 410$ MPa and $f_{u,exp} = 582$ MPa. End plate P20 – 400 x 300 were connected by M20 8.8 bolts, with the vertical distances 35 – 230 – 100 – 35 mm and horizontal ones 30 – 240 – 30 mm. The beam with connection 500 mm from its centre was loaded in its centre through P20 by hydraulic jack, see Fig. 1. The configuration creates in the connection shear forces and bending moments. The results of the contact imprints on paper placed between the end plates is included on right side of the Figs. The inclination of the specimens varied from 0°; 30° till 45°. The test set up with 0° inclination is documented at Fig. 2.

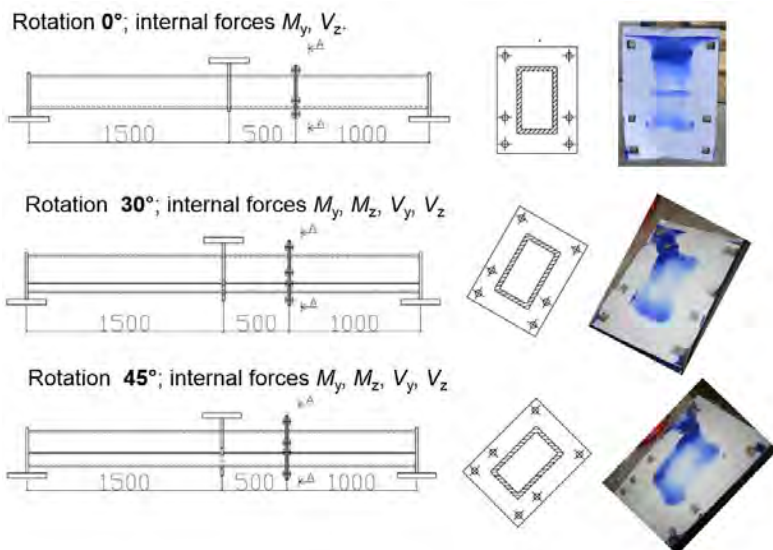


Fig. 1 Position of the beam splice joints on beam, inclination and contact imprints



Fig. 2 The test sample with 0° inclination

The resistances predicted by CM and by CBFEM were compared to experimental results for measured values of material properties, see Fig. 3. For component method is in EN1993-1-8 recommended a liner interaction. The quadratic interaction curve was prepared according to (Neumann, 2014). The calculated results shows a good agreement with the measured ones. In the Fig. 4 is compared the moment - rotational curve modelled by CM and CBFEM to the measured one. The predictions of resistance is adequate of asked quality of design model. The calculated stiffness is higher compared to measure one. The sensitivity study for the change of resistance due to the different plate thickness in Fig. 5 shows the underestimation of the resistance by CM for thin plates with significant influence of membrane action and overestimation of resistance for thick plates, where the resistance of bolts is guided by its bending.

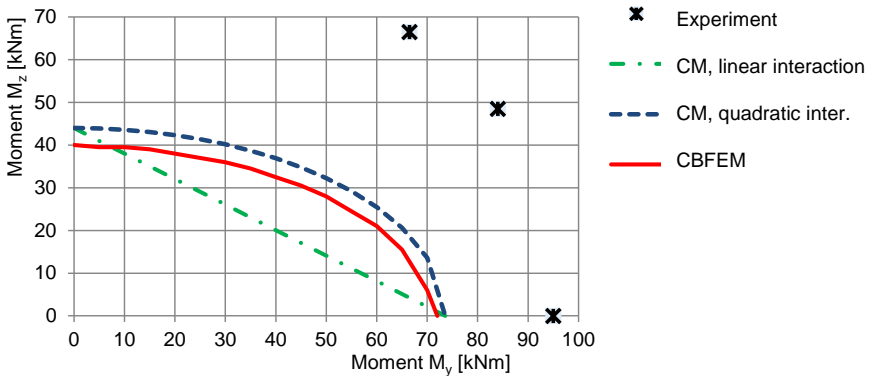


Fig. 3 Comparison of predicted resistances by CM, with linear and quadratic interaction, and by CBFEM to the experimental one

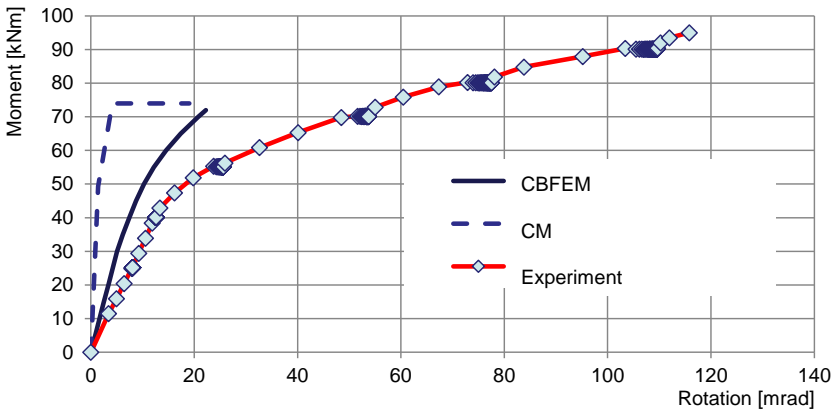


Fig. 4 Comparison of the modelled, by CM and CBFEM, and the measured moment rotational curve

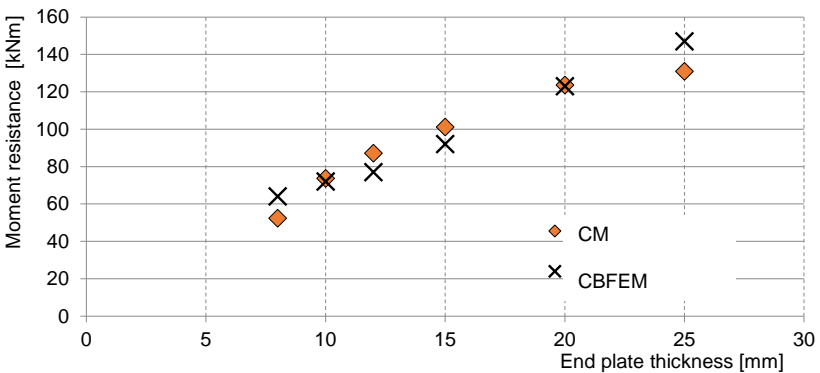


Fig. 5 Influence of the plate thickness to predicted resistance

4 COLUMN BASES

The generally loaded column bases are the useful application of CBFEM. The experimental research on biaxial loading of column base is very scarce, see (Pertola and Heinisuo, 2011). Two experiments were performed at laboratory of Brno University of Technology. The results of loading around the stronger axis are described in (Bajer et al., 2014). Specimens of column HEB 240 anchorage via baseplate 20 mm thick and four anchor bolts M20 grade 8.8, see Fig. 6, were loaded by axial compressive force 400 kN and then horizontal force F_h was gradually increased until the column base was heavily damaged – steel plates yielded, concrete pad heavily cracked and bolts torn. The angle between force F_h and principal axis z was 26.6° .

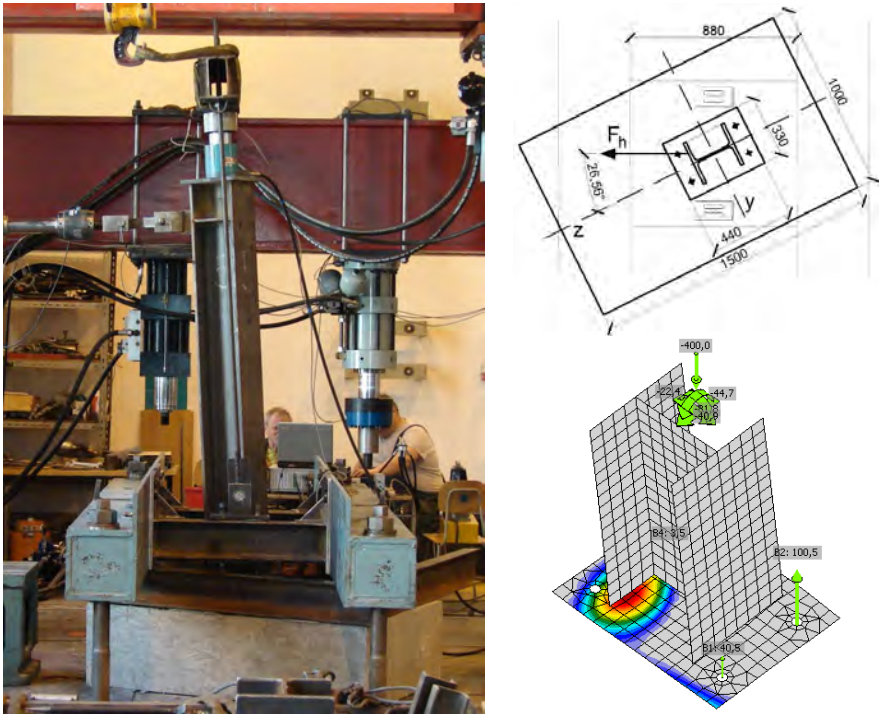


Fig. 6 Test set-up: elevation and plan drawing; CBFEM model

The ROFEM is prepared in Atena 3D code (Červenka & Jendele 2014) where the fracture-plastic material model is prescribed for concrete; material model with von Mises failure criterion for the steel parts and with Mohr-Coulomb criterion for the interfaces. Base plate is modelled by shell elements and anchors as reinforcement elements without any longitudinal bond. The anchors are fixed to the concrete at the location of the anchors heads. Supports of the concrete block are realized by springs. In DOFEM model by CBFEM (Wald et al., 2014) is the steel plates modelled using shell elements, bolts are represented by one dimensional springs and concrete is simplified as Winkler subsoil, see (Bajer et al., 2014).

In Fig. 7 is compared the predicted and measured behaviour on the moment – rotation diagram. The sudden drop in bending moment is caused by rupture of the anchor bolt in Exp. 2. In the experiment, steel plates and anchor bolt yielding and concrete cracking occurred at similar load and the failure modes can hardly be distinguished from each other. However, the failure modes can be assessed separately in ROFEM and in CBFEM. The failure mode of the column base in CBFEM is the concrete cone breakout of the anchor bolt (loaded by tensile force $F_t = 53$ kN) at $M_y = 56$ kNm and $M_z = 28$ kNm. This failure mode has a great scatter of results (Eligehausen et al., 2006) and it is expected that the cracks near anchor head started to propagate even though the experimental curves show no flattening yet. Subsequent failure mode is of the component concrete in compression including grout at $M_y = 88$ kNm and $M_z = 44$ kNm. Then, at $M_y = 100$ kNm and $M_z = 50$ kNm, the resistance of steel of the anchor ($F_{t,Rd} = 120$ kN) was exceeded and after, at $M_y = 102$ kNm and $M_z = 51$ kNm, the plates yielded by more than 5 %. The resistance predicted by CBFEM is more conservative compare to the prediction by ROFEM. The predicted stiffness's are slightly higher then experimental ones. The rotational capacity to weak axes is predicted well.

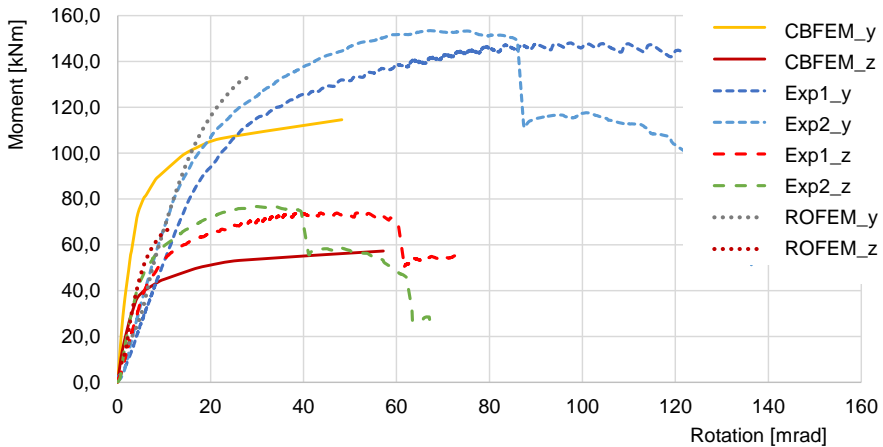


Fig. 7 Moment – rotation diagram of experimental and numerical results

4 CONCLUSIONS

The global analyses of steel structures is today carried out by FEM and all the traditional procedures (like force method, three moment equation, Cremona's pattern, the Cross method or the method distribution moments) are not used any more. In current fast development of software ability will be the connections designed very soon by FEM instead of today used curve fitting and CM. The CBFEM is a competitive solution ready to use.

The asked safety of DOFEM depends on analytical models of plates and connectors, which is introduced in design standards. The comparison of modelling of beam to column extended end plate connection according to (ANSI/AISC 360-10, 2010) and CBFEM documents the applicability of the prediction of connection resistance according to different standard rules. The extended end plate connection P

7/8 21,3 – 7,5 in (vertical distances 1,5 - 3,6 - 19,3 – 2,4 and horizontal 1,7 – 4,0 – 1,7) from steel A36 with bolts M 1 in A325 joints column of cross section W18x97 and the beam W18x50. The connection is loaded by bending moment $M = 252$ kip-ft and shear force $V = 42$ kips. Calculation according to Design Examples v14.1, Example II.B-4 Four-Bolt Unstiffened (Murray & Shoemaker, 2003) gives the capacity $M_u = 273,9$ kip-ft with degree of utilization 0,92. According to the CBFEM is the capacity $M_u = 280$ kip-ft with degree of utilization 0,90, which is limited by bolt capacity $\phi F_{nt} = 53$ kips. Differences are due to the linear distribution of bolt forces along the height of connection in Design guide (Murray, Shoemaker, 2003), compare to the non-linear force distribution in bolts in CBFEM, see Fig. 8. In this worked example reaches strain in the end plate 0,68 % while the limiting strain is 5 %.

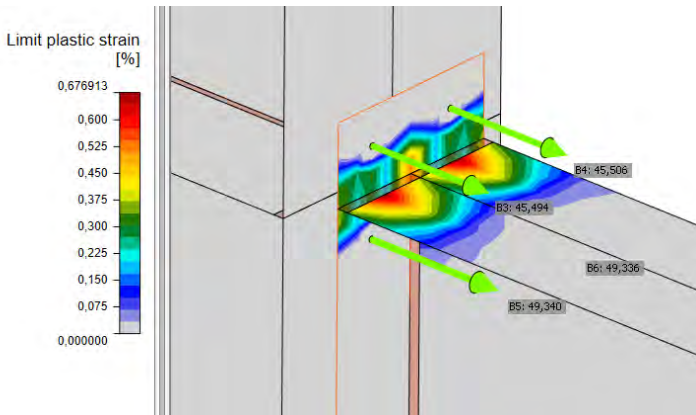


Fig. 8 Strains and bolt forces in the connection according to CBFEM

For proper use of CBFEM is necessary to take care of good V&V procedures to allow of its safe use and proper interpretation of results. The presented results shows the good accuracy of CBFEM verified to CM. In cases, where the CBFEM gives higher stiffness / resistance / deformation capacity. Then needs to verify to ROFEM, which is validated to experiments.

The CB method used in tables and tools limits poor design of structural steel and steel and concrete composite connections by incompetent amateurs. The benchmark cases and correct use of V&V help the improper use of FEM model. The high-quality education remains the background of design of pretty structural connections.

CBFEM is coming step for the structural steel industry to facilitate the vision of a "Smart Factory" in Industry 4.0.

Acknowledgments

The work was prepared under the R&D project MERLION supported by Technology Agency of the Czech Republic, project No. TA02010159.

References

ANSI/AISC 360-10 (2010) Specification for Structural Steel Buildings, AISC, Chicago, 609 p.

Bajer, M., Vild, M., Barnat, J., Holomek, J. (2014), Influence of selected parameters on design optimisation of anchor joint. *Proc. 12th Int. Conf. Steel, Sp. Compos. Struct., CI-Premier Pte Ltd*; 2014, 149–58.

Bursi, O. S., Jaspart, J. P. (1997), Benchmarks for finite element modelling of bolted steel connections, *Journal of Constructional Steel Research*, 43, 1-3, 17-42.

Červenka, J., Jendele, L. (2014), ATENA Program Documentation, Part. Atena Input File Format, Červenka Consulting Ltd.

Da Silva Simoes L. (2008), Towards a consistent design approach for steel joints under generalized loading, *Journal of Constructional Steel Research*, 64, 1059-1075.

Eligehausen, R., Mallee, R., Silva, J.F. (2006), *Anchorage in Concrete Construction*. Ernst & Son.

EN1993-1-5 (2005) *Eurocode 3: Design of steel structures - Part 1-5: Plated Structural Elements*, CEN, Brussels.

EN1993-1-8 (2006) *Eurocode 3, Design of steel structures, Part 1-8, Design of joints*, CEN, Brussels.

EN1994-1-1 (2010) *Eurocode 4, Design of composite steel and concrete structures, Part 1-1, General rules and rules for buildings*, CEN, Brussels.

IDEA RS (2015) Product documentation, www.idea-rs.com.

ISO (2012) IIV XV-1439-13 ISO/FDIS 14346 Static Design Procedure for Welded Hollow-Section Joints – Recommendations.

Jaspart, J.P. (2002), Design of structural joints in building frames, *Prog. Struct. Engng Mater.*, 4, 18-34.

Jaspart, J.P., Weynand, K. (2015), Design of Hollow Section Joints using the Component Method, in ISTS'15, *International Symposium on Tubular Structures*, Rio de Janeiro, 2015.

Murray, T. M., Shoemaker, W. L. (2003), Flush and Extended Multiple-Row Moment End-Plate Connections, *Steel Design Guide 16*, AISC, Chicago, 65p.

Neumann, N. (2014), Design model for combined in-plane and out-of-plane bending of steel joints connecting H or I sections. In *European Conference on Steel Structures Eurosteel 2014*, Naples, 2050-2056.

Perttola, H., Heinisuo, M.. (2011), Test Report, *End Plate Joints of Steel Tubes, Biaxial and Weak Axis Bending*. Research Report 155. Tampere University of Technology.

Steenhuis, M., Gresnigt, N., Weynand, K. (1994), Pre-Design of Semi-Rigid Joints in Steel Frames, In *Second State of the Art Workshop on Semi-Rigid Behaviour of Civil Engineering Structural Connections*, COST C1, Prague, 1994, 131-140.

Virdi, K. S. et al. (1999) *Numerical simulation of semi-rigid connections by the finite element method*, Report of Working Group 6 Numerical simulation COST C1, Brussels.

Wald, F. et al. (2015) *Benchmark Cases for Advanced Design of Structural Steel Connections*, Česká technika – nakladatelství ČVUT. ISBN 978-80-01-05826-8.

Wald, F., Kwasniewski, L. Gödrich, L., Kurejková, M. (2014), Validation and verification procedures for connection design in steel structures. In *Steel, Space and Composite Structures*. Singapore, 111-120.

Wald, F., Šabatka, L., Kabeláč, J., Kolaja, D., Pospíšil, M., Structural Analysis and Design of Steel Connections Using Component Based Finite Element Model (CBFEM), *Journal of Civil Engineering and Architecture*, 10/2015.

Wald, F., Sokol, Z., Steenhuis, M. and Jaspart, J.P. (2008) Component Method for Steel Column Bases, *Heron*, 53, 3-20.

Wald, F., Gödrich, L., Šabatka, L., Kabeláč, J., Navrátil, J. (2014), Component Based Finite Element Model of Structural Connections. In *Steel, Space and Composite Structures*. Singapore, 337-344.

Zoetemeijer, P. (1985), *Summary of the Researches on Bolted Beam-to-Column Connections*. Report 6-85-7, University of Technology, Delft 1985.

IMPLEMENTATION OF A COMPONENT MODEL FOR THE CYCLIC BEHAVIOUR OF STEEL JOINTS

Luís Simões da Silva, Ashkan Shahbazian, Filippo Gentili and Hugo Augusto
ISISE - Department of Civil Engineering, University of Coimbra, Portugal
luiss@dec.uc.pt; shahbazian@uc.pt; filippo.gentili@uc.pt; hugo.augusto@dec.uc.pt

ABSTRACT

Currently, the prediction of the moment-rotation response of steel joints subjected to seismic loading is only possible for the small range of typologies and member ranges that were validated experimentally. This paper presents a general formulation based on the component method for predicting the cyclic response of steel joints. The proposed cyclic component model is based on the static monotonic properties according to Eurocode 3 part 1.8 and appropriate cyclic component laws for the dissipative components. The proposed model has been validated with experimental results on beam-to-column steel joints. In addition, the proposed model has been compared with 3D Finite Element simulations using the software Abaqus. Subsequently, a free access software tool is presented that allows the simulation of the cyclic behavior of steel joints in a user-friendly way. Finally, it is concluded that the proposed model provides good agreement with the observed behaviour for this joint typology and constitutes a generic basis for dealing with the cyclic response of steel joints.

1. INTRODUCTION

Analysing the behaviour of steel joints is complex as several phenomena affect joint behaviour such as material and geometrical nonlinearity, contact and slip between different elements of the joint (Simões da Silva et al, 2002). Dealing with these complexities is possible by using general Finite Element programs. However, general FE packages (i.e. Abaqus unified FEA) need relevant expertise and they are computational expensive and produce results that may be sensitive to the modelling options adopted by the user (Simões da Silva, 2008). One of the simplified methods to deal with the complexity of steel joints is the component method which is the design approach specified in Eurocode 3 part 1.8 (2005). The component method is based on a simplified mechanical model composed of extensional springs and rigid links, whereby the joint is simulated by an appropriate choice of rigid and flexible components. These spring elements represent specific parts of a joint that dependent on the type of loading, contribute to the joints structural behaviour (Weynand et al 1995). In general, each of these components is characterised by a non-linear force-elongation curve, although simpler idealisations are possible. The moment-rotation response of steel joints under cyclic loading is further complicated because of successive static loading and unloading. Therefore, the joint moment-rotation curve is characterised by hysteretic loops with progressive degradation of strength and/or stiffness that leads to the failure of the joint. Earthquakes are typical examples of natural events that impose cyclic loading on the structural members and joints. Due to the level of rotation that is achieved during a seismic event, the cyclic loading and unloading is characterised by repeated incursions in the plastic range that may lead to failure after a small number of cycles, usually denoted low-cycle fatigue.

Unlike static monotonic loading, it is still not possible to predict the moment-rotation response of steel joints under cyclic loading using the component method. Therefore, the usual approach is to develop multi-parameter mathematical expressions that are able to reproduce the range of hysteretic behaviours (moment-rotation) for a given group of steel joint typologies. Subsequently, the values of the parameters are calibrated to satisfactorily correlate to a range of section sizes for a given group of joint typologies (Nogueiro et al, 2007). However, such an approach relies purely on statistical calibration, without a solid physical background. Simões da Silva et al (2009) and Latour et al. (2011) have shown that the component method approach is able to accurately reproduce the cyclic moment-rotation response of steel joints, while also reducing the empirical nature of mathematical curve fitting by providing a mechanical basis to the process. However, the Latour model fails to provide a general implementation that is consistent with the well-proven component models for the static monotonic behaviour of steel joints. In addition, it is not able to address directly joint configurations with multiple bolt rows because it lumps all components in two levels only.

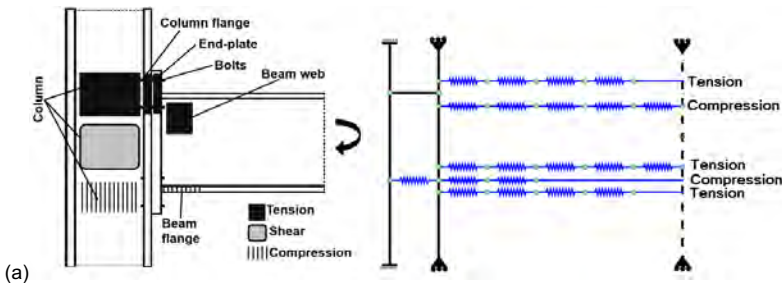
The relevance of this problem was recently further recognised in the on-going European project “EQUALJOINTS”, whereby the development of a cyclic component method is specifically addressed. It is the objective of this paper to extend the component model for the behaviour of steel joints subject to cyclic loading.

2. CYCLIC COMPONENT MODEL

2.1 Introduction

Figure 1 illustrates the active components in a typical external end-plate beam-to-column steel joint and its component assembly for static monotonic loading (Figure 1a for hogging bending and Figure 1b for sagging bending).

Eurocode 3 part 1.8 (2005) provides a simple procedure for the evaluation of the initial stiffness and the plastic resistance of beam-to-column steel joints. In addition, the component models in Figure 1 also allow the calculation of the full nonlinear moment-rotation response of a joint, given an adequate characterisation of the nonlinear behaviour of each component (Gervásio et al, 2004). The nature of the component method implies that all components are associated with a specific stress resultant, besides representing a specific part of the joint. Hence, the component models for hogging and sagging bending are different, as shown in Figure 1.



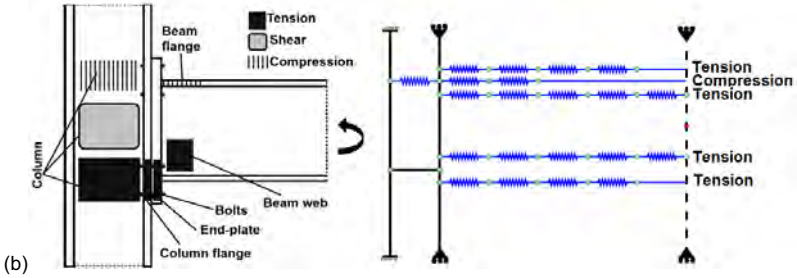


Figure 1. Component models for double-extended end-plate steel beam-to-column joint for (a) hogging and (b) sagging bending moments.

In the context of the behaviour of steel joints subject to both bending moment and axial force, Lima et al. (2004) proposed a component model for M-N interaction that overcomes the above problem by defining components that present distinct behaviour in tension and compression that only become active in tension or in compression, as illustrated in Figure 2. This strategy was successfully implemented for static monotonic loading and a freeware software “NASCon” (Borges, 2003) was developed. However, for cyclic loading, additional aspects need to be considered.

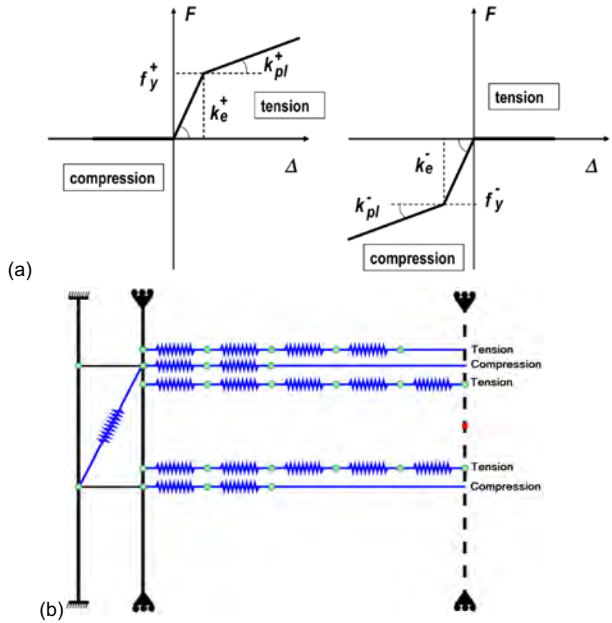


Figure 2. Component model for extended end-plate steel joints subject to both bending moment and axial force: (a) typical component behaviour and (b) component assembly for M-N interaction (Lima et al, 2004).

2.2 Framework and assumptions

The development of a cyclic component model should represent all the phenomena that were described previously. Thus, in addition to the possibility of load reversal at any level of rotation, the model must be able to reproduce the hysteretic behaviour including the degradation of the performance of the joint as the number of cycles increases.

Following the general framework described in Simões da Silva et al. (2009), it is noted that the number of components that are active in a beam-to-column joint subject to load reversal is large but only a small number of components concentrate most of the dissipative behaviour, henceforth called “critical” components. Hence, the following assumptions were adopted in the development of a cyclic component model:

- Hysteretic behaviour is only modelled for a small number of dissipative components (critical components);
- The remaining components are assumed to behave elastically and may be modelled as linear elastic;
- The critical components are defined on the basis of the prior evaluation of the rotational behaviour both for hogging and sagging bending moments under static monotonic loading;
- The force-deformation laws of the components associated with tension or compression are defined with respect to the appropriate effective widths that reflect the geometry of the joint and, in particular, the spacing of the bolt rows based on the Eurocode 3 part 1.8.
- The force-deformation laws of the critical components represent the hysteretic behaviour of the corresponding component, as defined in section 2.3, with an appropriate implementation of tension only (positive force) or compression only (negative force) behaviours.

The identification of the critical components and the evaluation of the cyclic response is carried out according to the following procedure:

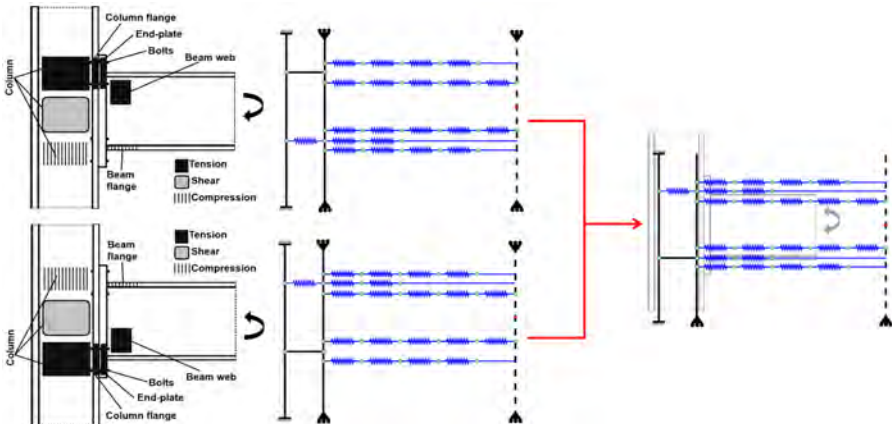


Figure 3. Proposed cyclic component model.

- Step 1: Determination of the moment-rotation curves under static monotonic conditions for hogging and sagging bending, respectively, using appropriate component models (e.g. Figure 1) based on the Eurocode 3 part 1.8 and a component characterisation that accounts for the post-limit stiffness (obtained, for example, from Simões da Silva et al (2002)).

- Step 2: Determination of the “yielding” sequence of the various components until failure, for hogging and sagging moments.
- Step 3: Selection of the critical dissipative components.
- Step 4: Determination of the moment-rotation curves under static cyclic conditions using appropriate cyclic component models (Figure 3).

Without loss of generality, the cyclic component model (Figure 3) presented in this paper is restricted to external node joints, in order to avoid the additional complexity related to the column web panel in internal node joints (Jordão et al, 2013).

2.3 Mechanical characterisation of the cyclic behaviour of the components

In accordance with the assumptions and the detailed procedure for the cyclic model presented in the previous section, two groups of components need to be characterised: (i) critical dissipative components, and (ii) elastic components. Both groups contribute towards the deformation of the joint but only the first group provides energy dissipation. In addition, the force-elongation laws of all the components should be implemented, where appropriate, with tension only or compression only behaviours.

Many authors have investigated the cyclic behaviour of selected zones in steel joints and proposed semi-empirical laws to describe their behaviour (Simões da Silva et al 2009; Swanson et al 2000; Kim et al, 2002; Piluso et al, 2008; Iannone et al, 2011). Focussing on the most common dissipative components, the column web panel in shear exhibits a stable behaviour, with hardly any noticeable stiffness or strength degradation and no pinching effect. The same type of behaviour may be observed for the column web panel under direct transverse stresses (Latour et al, 2011). In contrast, the T-stub in tension behaves asymmetrically and it is characterised by extensive pinching, accompanied by the development of compressive forces when pushed back to the zero-displacement level.

In this paper, two types of critical dissipative components are considered: Type 1 (column web panel in shear), illustrated in Figure 4a and Type 2 (tensile/compressive only components), depicted in Figure 4b.

All other components will have linear elastic force-elongation behaviour, with tension only or compression only behaviours, as shown in Figure 2a.

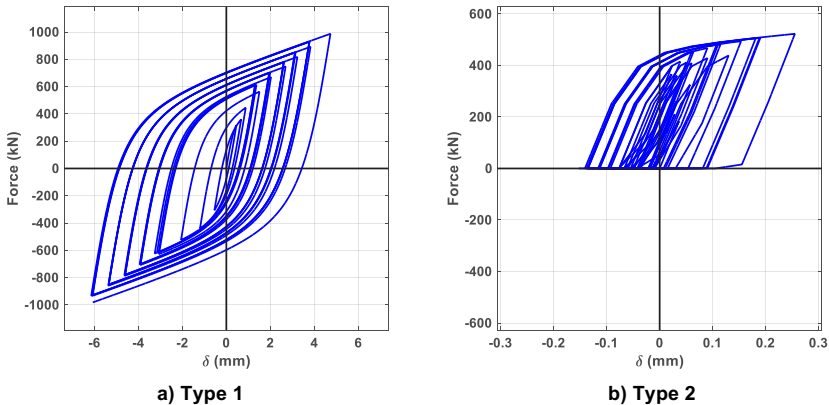


Figure 4. Mechanical behaviour of critical components.

3 COMPUTATIONAL IMPLEMENTATION

The cyclic component model described in section 2 was implemented in a purposely-developed FE program (Shahbazian et al, 2016). The current implementation covers a generic external node beam-to-column steel joint with arbitrary dimensions falling within the limits of application of Eurocode 3, part 1.8 regarding moment-resisting connections. Consequently, the user is free to define the component assembly, with an arbitrary number of bolt rows and the desired active components. Because of the nonlinear nature of the calculations, an algorithm was developed based on a displacement control incremental iterative procedure (Borges, 2003). The program currently provides the three types of component force-deformation laws described in the previous section: the two dissipative types and the elastic non-dissipative type.

4 VALIDATION

4.1 Introduction

A set of experimental tests carried out at the University of Coimbra (Borges, 2003) was used to validate the cyclic component model presented in this paper. The tested joints were designed aiming to study the behaviour of double extended end-plate bolted beam-to-column partial-strength external joints under cyclic loading conditions. The experimental programme comprised thirteen external double-extended bolted end-plate joints, see Table 1. It was divided in four groups, whereby the column section size and/or the beam size were varied, as well as the presence of axial force in the column in J2 group. The first test for each group had the loading applied monotonically, complemented by two tests with cyclic loading, except in the first group which includes one additional cyclic test, with arbitrary loading. The columns were 3.0 *m* high and the beams were approximately 1.2 *m* long. The loading was applied in the vertical direction, at the end of the cantilever beam by means of a 100 *ton* hydraulic actuator.

Table 1: Bolted beam-to-column double extended end-plate joints test programme.

Group 1 (J1)	Beam	Column	type	Bending	Axial
Test J-1.1	IPE360	HEA320	Monotonic	M-	-
Test J-1.2	IPE 360	HEA 320	Cyclic	M-/M+	-
Test J-1.3	IPE 360	HEA 320	Cyclic	M-/M+	-
Test J-1.4	IPE 360	HEA 320	Cyclic	M-/M+	-
Group 2 (J2)	Beam	Column	type	Bending	Axial
Test J-2.1	IPE360	HEA320	Monotonic	M-	N- (800 kN)
Test J-2.2	IPE 360	HEA 320	Cyclic	M-/M+	N- (1200 kN)
Test J-2.3	IPE 360	HEA 320	Cyclic	M-/M+	N- (800 kN)
Group 3 (J3)	Beam	Column	type	Bending	Axial
Test J-3.1	IPE360	HEB320	Monotonic	M-	-
Test J-3.2	IPE 360	HEB 320	Cyclic	M-/M+	-
Test J-3.3	IPE 360	HEB 320	Cyclic	M-/M+	-
Group 4 (J4)	Beam	Column	type	Bending	Axial
Test J-4.1	HEA280	HEA320	Monotonic	M-	-
Test J-4.2	HEA 280	HEA 320	Cyclic	M-/M+	-
Test J-4.3	HEA 280	HEA 320	Cyclic	M-/M+	-

The cyclic loading strategy, for the cyclic tests consisted on 2 distinct cyclic histories, both with gradual increase of the cyclic amplitude in the elastic range followed by

constant amplitude loading with two different levels. The tests were carried out in displacement control, with constant speed of 0.02 mm/sec for the monotonic tests, 0.2 mm/sec for the first cyclic tests and 0.4 mm/sec for the second cyclic tests. The experimental test results were complemented by advanced numerical models using solid elements (Figure 5) developed in Abaqus (Augusto et al, 2016).

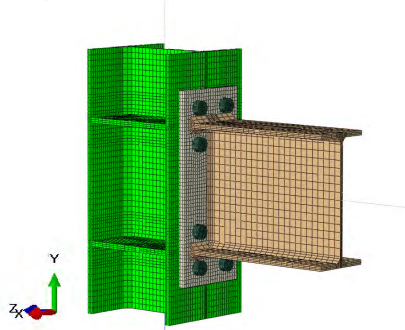


Figure 5. FE model.

4.2 Component model assembly and identification of critical components

Based on Eurocode 3, part 1.8 (2005) the following components should be considered for double extended end-plate joints: (1) Column web panel in shear; (2) Column web in compression; (3) Column web in tension; (4) Column flange in bending; (5) End-plate in bending; (7) Beam flange in compression; (8) Beam web in tension and (10) Bolts in tension. Selecting tests J3 for illustration and with reference to the component models of Figure 1, because of the double symmetry of the joints, the behaviour under hogging and sagging bending moments is identical. Step 1 leads to the moment-rotation curve depicted in Figure 6, that shows good agreement between experimental, FE and component method results, the latter obtained with the software tool briefly described in section 3.

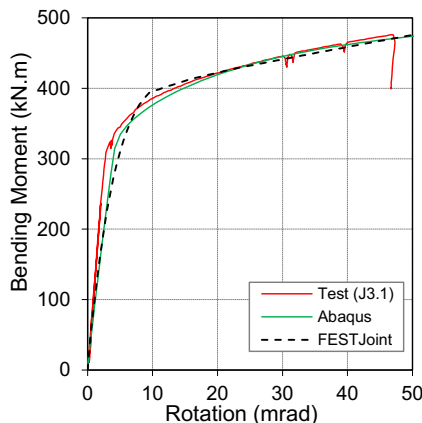


Figure 6. Moment-rotation response of J3.1

According to Step 2 of the procedure defined in section 2.2, the following critical dissipative components were identified: end-plate in bending, column web panel in

shear and column flange in bending (Nogueiro, 2009). Hence, these 3 components should be modelled as dissipative components in Step 4.

4.4 Cyclic response

Teste J3.2 exhibits a stable behaviour without pinching. Figure 6 shows the cyclic component model that is applicable for cyclic conditions.

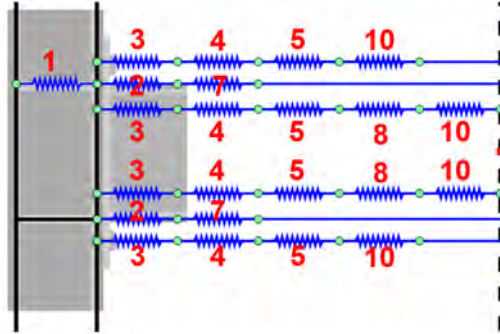


Figure 6. Cyclic component model for double-extended end-plate beam-to-column joint (schematic).

Figure 7 shows the load history for test J3.2. Test J3.2 followed the ECCS cyclic protocol. Figure 8 compares the component model, the experimental and the FE results for J3.2. Good agreement is noted both at the joint level (Figure 8a) and component level (Figure 8b). It is noted that, despite considering hysteretic behaviour for end-plate in bending, there is no pinching effect in the global behaviour of the joint, as was also seen in the test.

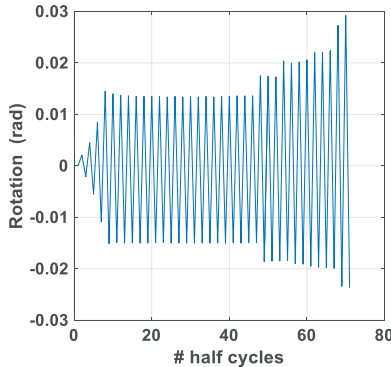


Figure 7. Rotation history for J3.2.

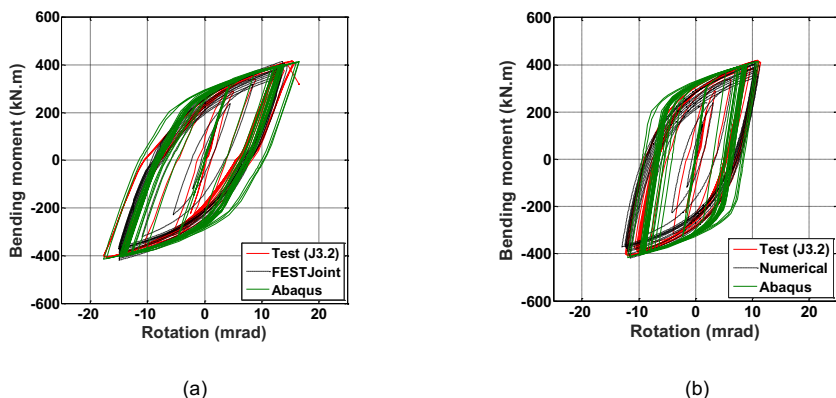


Figure 8. J3.2: (a) overall behaviour and (b) column web panel in shear.

CONCLUSIONS

This paper describes a component based methodology for the prediction of the cyclic behaviour of beam to column steel joints. By adhering to the principles of the component method, this model incorporates the static monotonic component properties specified in Eurocode 3 part 1.8. This component-based methodology is able to generate cyclic bending moment-response of steel joints with sufficient accuracy and to identify the failure modes of the joint. The proposed approach was validated with cyclic tests performed at the University of Coimbra and showed acceptable agreement.

The following conclusion may be drawn:

- Despite the apparent simplicity of the methodology, guaranteeing numerical stability of the component models is not an easy task. Specific guidance is necessary for those willing to implement cyclic models.
- The behaviour of tension only or compression only dissipative components is a crucial feature of the cyclic component model and, combined with the implementation of springs in parallel with zero stiffness paths constitutes the key aspect of this paper that was not previously exploited in the literature.
- The running speed of a cyclic component implementation makes it the only viable option to perform global analysis of frames incorporating the dissipative behaviour of joints, as the “time cost” of running advanced FE models makes them prohibitive in practical applications.

Finally, the component model is currently undergoing a thorough calibration and validation in the context of the RFCS project EQUALJOINTS.

ACKNOWLEDGEMENT

The work was funded by the European Commission’s Research Fund for Coal and Steel (RFCS) through the research project “EQUALJOINTS RFSR-CT-2013-00021”, and by the Portuguese Foundation for Science and Technology (FCT) through project UID/ECI/04029/2013.

REFERENCES

- Augusto, H., Simões da Silva, L., Rebelo, C. and Castro, J.M. (2016) Characterization of web panel components in double-extended bolted end-plate steel joints. *Journal of Constructional Steel Research* 116, 271–293.

- Augusto, H.; Castro, J.M.; Rebelo, C.; Simões da Silva, L. (2014) A contribution to the extension of the component method to beam-to-column connections subjected to cyclic loading. Proceedings of EUROSTEEL 2014. Naples, Italy.
- Borges LAC. (2003). Probabilistic evaluation of the rotation capacity of steel joints. MSc thesis. Coimbra, Portugal: University of Coimbra.
- Eurocode 3 (2005). Design of Steel Structures: Design of joints. Part 1-8: CEN.
- Gervásio H, Simões da Silva L, Borges L. (2004). Reliability assessment of the post-limit stiffness and ductility of steel joints. *Journal of Constructional Steel Research*. 60:635-48.
- Iannone F, Latour M, Piluso V, Rizzano G. (2011). Experimental Analysis of Bolted Steel Beam-to-Column Connections: Component Identification. *Journal of Earthquake Engineering*. 15:214-44.
- Jordão S, Simões da Silva L, Simões R. (2013). Behaviour of welded beam-to-column joints with beams of unequal depth. *Journal of Constructional Steel Research*. 2013;91:42-59.
- Kim KD, Engelhardt MD. Monotonic and cyclic loading models for panel zones in steel moment frames. *Journal of Constructional Steel Research*. 2002;58:605-35.
- Latour M, Piluso V, Rizzano G. (2011). Cyclic Modeling of Bolted Beam-to-Column Connections: Component Approach. *Journal of Earthquake Engineering*;15:537-63.
- Lima LRO, Simões da Silva L, Vellasco PCGdS, de Andrade SAL. (2004). Experimental evaluation of extended endplate beam-to-column joints subjected to bending and axial force. *Engineering Structures*. 2004;26:1333-47.
- Nogueiro P, Simões da Silva L, Bento R, Simões R. (2007). Numerical implementation and calibration of a hysteretic model with pinching for the cycling response of steel joints. *International Journal of Advanced Steel Construction*. 3:128-53.
- Nogueiro PNG (2009). Cyclic behaviour of steel joints (in Portuguese). PhD Thesis. University of Coimbra.
- Piluso V, Rizzano G. (2008). Experimental analysis and modelling of bolted T-stubs under cyclic loads. *Journal of Constructional Steel Research*. 64:655-69.
- Simões da Silva L, Rebelo C, Mota L. (2009). Extension of the Component Method to End-Plate Beam-to-Column Steel Joints Subjected to Seismic Loading. In: Topping BHV, Neves, LFC, Barros RC (eds). *Trends in Civil and Structural Engineering Computing*. Stirlingshire, UK: Saxe-Coburg Publications; p. 149-67.
- Simões da Silva L, Santiago A, Real PV. (2002) Post-limit stiffness evaluation of the ductility of steel joints. *Computers and Structures*.80:515-31.
- Simões da Silva L. (2008) Towards a consistent design approach for steel joints under generalized loading. *Journal of Constructional Steel Research*. 64:1059-75.
- Swanson JA, Leon RT. (2000). Bolted steel connections: Tests on T-stub components. *Journal of Structural Engineering-Asce*. 126:50-6.
- Weynand K, Jaspert J-P, Steenhuis M. (1995). The stiffness model of revised Annex J of Eurocode 3. Proceedings of the 3rd International Workshop on Connections; p. 441-52.

APPROACH TO MACRO-MODELING OF 3D TUBULAR COLUMN-TO-BEAM JOINT: AN EXTENSION OF COMPONENT METHOD FOR JOINT MODELING

Yukihiro Harada

Department of Architecture, Graduate School of Engineering, Chiba University, Japan
yharada@faculty.chiba-u.jp

Luís Simões da Silva

ISISE, Department of Civil Engineering, University of Coimbra, Portugal
luisss@dec.uc.pt

ABSTRACT

In Japan, square hollow-section tubular columns are widely used for steel building structures, and continuity plates (diaphragms) are inserted in the column tube at the tubular column-to-beam joints. Several studies have been conducted on omitting the diaphragm to simplify the fabrication of the tubular column-to-beam joints. Some of the previous studies revealed that the out-of-plane behavior of the tubular column faces depended on the other faces' conditions; this observation means that a single rotational spring cannot properly model the joint behavior. To overcome this difficulty, the authors propose a new "2-D spring" element to describe the correlation among the column faces' behavior. The feasibility of the proposed joint modeling is roughly verified by referring to previous related studies.

INTRODUCTION

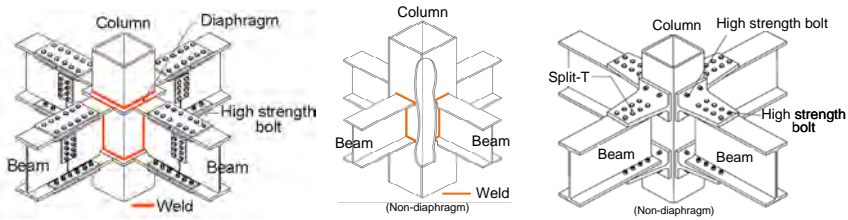
In Japan, square hollow section columns are usually used for multi-story steel building structures, and inserting diaphragm plates (continuity plates) into the column tube at the column-to-beam joints is a popular method of construction (Figure 1(a)). Although this type of column-to-beam joints can be regarded as rigid enough, it has a disadvantage in that lots of full penetration weld is necessary; thus, the fabrication of the joints becomes labor-intensive and less cost-effective.

To overcome the above disadvantages, tubular column-to-beam joints without diaphragm plates have been studied by many engineers and researchers, mainly in the 1990's. One of the authors of this paper previously conducted a series of subassembly loading tests on non-diaphragm tubular column-to-beam joints (Fujita et al., 2001, Harada et al., 2002) (Figure 1(b), (c)).

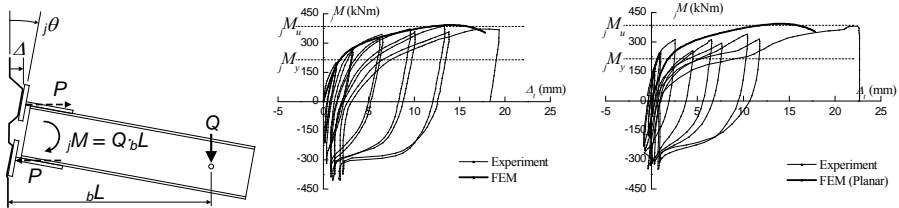
This type of non-diaphragm joint should be designed as semi-rigid, not rigid, owing to local out-of-plane deformation of the column plate at the beam flange (Figure 2(a)). The simplest way to model this semi-rigid beam-end joint may be to model the joint as a

single rotational spring (Figure 3) by regarding the locally deformed portion as a deformable component (CEN, 2005). However, observing the subassembly test results revealed that the apparent local stiffness of the column plate changes depending on the other column plates' conditions (Figure 2(b), (c)); the local stiffness of the beam-end connection of the spatial subassembly is much larger than that of the planar subassembly (Harada et al., 2002). This means that modeling by simple one-dimensional springs cannot exactly describe the out-of-plane behavior of the column faces and that modeling to incorporate the interaction among multiple column faces' out-of-plane deformation behavior is necessary.

The objective of this paper is to present a new modeling methodology to incorporate interaction among adjacent semi-rigid beam-end connections for conducting 3-D frame analysis including non-diaphragm tubular column-to-beam joints.



(a) Through-diaphragm type (b) Welded beam-end type (c) Bolted double split-tee type
Figure 1. Square hollow-section column-to-beam joints



(a) Out-of-plane deformation at beam-end (b) jM - Δ relationship (planar subassembly) (c) jM - Δ relationship (spatial subassembly)
Figure 2. Local behavior of bolted double split-tee beam-end joints (Harada et al., 2002)

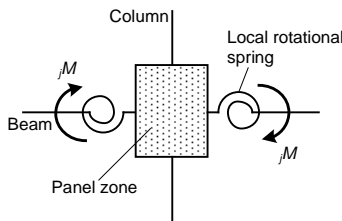


Figure 3. Rotational spring model for beam-end local deformation

OUTLINE OF MACRO-MODELING OF TUBULAR COLUMN-TO-BEAM JOINTS

The deformable tubular column section can be modeled as a planar frame; we call it a cross-section frame hereafter (Figure 4). If tensile or compressive forces through the beam flanges acting on the column faces are approximated as concentrated forces acting on the cross-section frame, then the force-deformation relationship for the cross-section frame will represent the correlation among the column faces' behavior. This force-deformation relationship defines a new type of structural element; here, we define this new element as a "2-D spring" element.

Formulation of 2-D Spring Elements

Let us derive the force-deformation relationship from the cross-section frame. The cross-section of the square tube is modeled by a square plane rigid framework with four equal members with the same length (D), which corresponds to the column width, and the same flexural rigidity (EI) (Figure 4). This cross-section frame is supported by four pin supports at the four corners (this means that the cross-section's overall distortion is neglected here). When the cross-section frame is loaded concentrically at the center of only one column face (say, north-side face), the out-of-plane deformations of the four column faces (i.e., north-, east-, south-, and west-side faces) are derived as follows, by solving this indeterminate moment frame (the detailed computation is omitted here):

$$\delta_N = \frac{17D^3}{1536EI} N_N, \quad \delta_E = \delta_W = -\frac{6D^3}{1536EI} N_N, \quad \delta_S = \frac{3D^3}{1536EI} N_N. \quad (1)$$

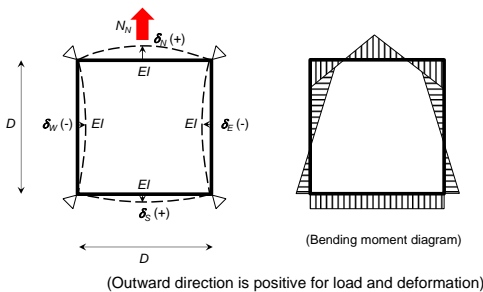


Figure 4. Cross-section frame model (when only one column face is loaded)

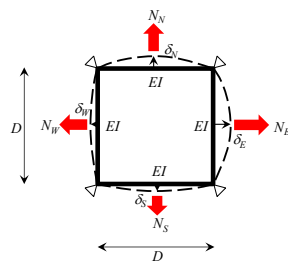


Figure 5. "2-D spring" element based on the cross-section frame model

Equation (1) describes the influence of the one column face's out-of-plane deformation to the other. By superposing this solutions for all four column faces (Figure 5), we derive the following matrix equation, equation (2), to describe the correlation among the four column faces' behavior; interactions among out-of-plane force-deformation relationships of the four tubular column faces can then be described by a 4×4 flexibility matrix $[F]$ in equation (2).

$$\begin{bmatrix} \delta_N \\ \delta_S \\ \delta_E \\ \delta_W \end{bmatrix} = [F] \begin{bmatrix} N_N \\ N_S \\ N_E \\ N_W \end{bmatrix}, \quad [F] \equiv \frac{D^3}{1536EI} \begin{bmatrix} 17 & 3 & -6 & -6 \\ 3 & 17 & -6 & -6 \\ -6 & -6 & 17 & 3 \\ -6 & -6 & 3 & 17 \end{bmatrix} \quad (2)$$

This equation can be rewritten as the following stiffness equation.

$$\begin{bmatrix} N_N \\ N_S \\ N_E \\ N_W \end{bmatrix} = [K] \begin{bmatrix} \delta_N \\ \delta_S \\ \delta_E \\ \delta_W \end{bmatrix}, \quad [K] \equiv [F]^{-1} = \frac{12EI}{7D^3} \begin{bmatrix} 67 & 3 & 21 & 21 \\ 3 & 67 & 21 & 21 \\ 21 & 21 & 67 & 3 \\ 21 & 21 & 3 & 67 \end{bmatrix} \quad (3)$$

This stiffness equation describes the four column faces' load-deformation relationship. By the 4×4 stiffness matrix $[K]$ in equation (3), we can define one structural element, which represents four column faces' action. We call this element the "2-D spring" element. This element can be a substitute for the simple rotational spring elements at the four column faces.

Decomposition of Modes of Column Faces' Deformation

By solving eigenvalues (λ_i) and eigenvectors (\mathbf{x}_i) for the stiffness matrix $[K]$ in equation (3), the following three distinct deformation modes are obtained:

$$\text{Mode 1: } \lambda_1 = 112, \mathbf{x}_1 = \begin{bmatrix} 1 \\ 1 \\ 1 \\ 1 \end{bmatrix}, \quad \text{Mode 2: } \lambda_2 = 28, \mathbf{x}_2 = \begin{bmatrix} 1 \\ 1 \\ -1 \\ -1 \end{bmatrix}, \quad \text{Mode 3: } \lambda_3 = 64, \mathbf{x}_3 = \begin{bmatrix} 1 \\ -1 \\ 0 \\ 0 \end{bmatrix}, \begin{bmatrix} 0 \\ 0 \\ 1 \\ -1 \end{bmatrix}.$$

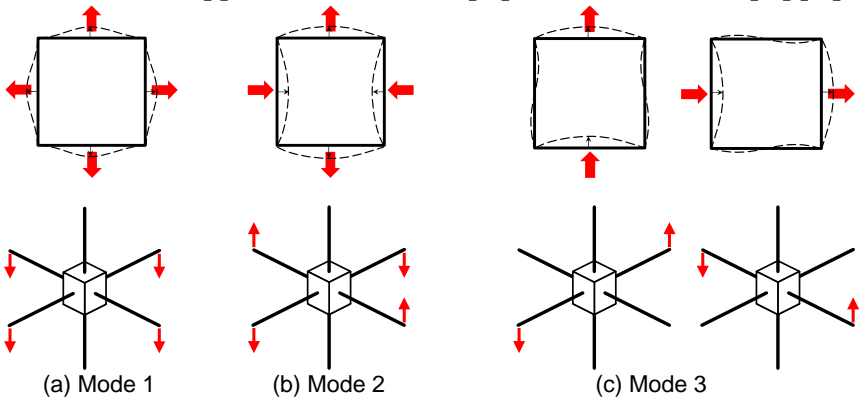


Figure 6. Decomposed modes of column faces' deformation and corresponding loading conditions

These deformation modes corresponding to the obtained eigenvectors \mathbf{x}_i are depicted in Figure 6. Since all the absolute values of non-zero elements in the eigenvectors \mathbf{x}_i are equal to unity, the modal apparent local stiffness (k_{Mi}) of a single column plate can be directly obtained with the corresponding eigenvalues, λ_i , as follows; these local stiffnesses will represent the fundamental mechanical property of the 2-D spring element.

$$k_{M1} = \lambda_1 \frac{12EI}{7D^3} = 192 \frac{EI}{D^3}, \quad k_{M2} = \lambda_2 \frac{12EI}{7D^3} = 48 \frac{EI}{D^3}, \quad k_{M3} = \lambda_3 \frac{12EI}{7D^3} = \frac{768}{7} \frac{EI}{D^3} \left(\approx 109.7 \frac{EI}{D^3} \right) \quad (4)$$

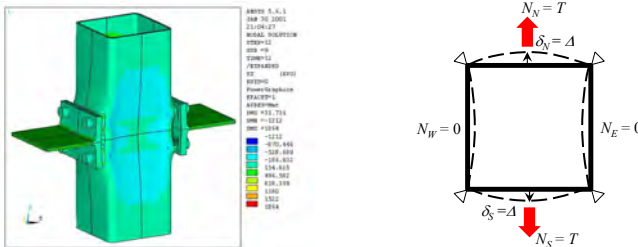
EXAMPLES OF 3D TUBULAR COLUMN-TO-BEAM JOINTS MODELING

Let us show that the apparent local stiffness changes in accordance with the difference of the column faces' loading condition. The referred loading conditions are those shown in previous experimental studies; they are (i) tensioned in opposite column faces, (ii) tensioned only in one column face with other faces constrained, (iii) tensioned in one column face with the opposite faces constrained, and (iv) tensioned in the adjacent two column faces with the other faces constrained. The condition (i) corresponds to that of tensile tests of beam-flange-tubular column joints (Harada et al., 2003). The condition (ii) corresponds to that of concrete filled tubular column-to-beam joints (L. A. P. Silva et al., 2003). The conditions (iii) and (iv) correspond to those of subassemblage loading tests of bolted double split-tee type of tubular column-to-beam joints (Figure 1(c))(Harada et al., 2002).

Local Tensile Test of Beam Flange-Tubular Column Joint

This loading condition (Figure 7(a)) can be described by the 2-D spring model with $N_N = N_S$ (represented by T) and $N_E = N_W = 0$ (Figure 7(b)).

Substituting the conditions into equation (2) obtains the following equation:



(a) Loading condition (b) Loading condition in the 2-D spring model

Figure 7. Loading condition of local tensile test of beam flange-tubular column joint

$$\begin{bmatrix} \Delta \\ \Delta \\ \delta_E \\ \delta_W \end{bmatrix} = \frac{D^3}{1536EI} \begin{bmatrix} 17 & 3 & -6 & -6 \\ 3 & 17 & -6 & -6 \\ -6 & -6 & 17 & 3 \\ -6 & -6 & 3 & 17 \end{bmatrix} \begin{bmatrix} T \\ T \\ 0 \\ 0 \end{bmatrix} \quad (5-1)$$

(By symmetry of the loading, $\delta_N = \delta_S$ holds, so they can be represented by Δ (Figure 7).)

From the first and second rows of equation (5-1), the following force-deformation relationship can be obtained.

$$\Delta = \frac{20D^3}{1536EI} T \quad (5-2)$$

The apparent stiffness of an out-of-plane deformation (k_{tensile}) is then derived as the following.

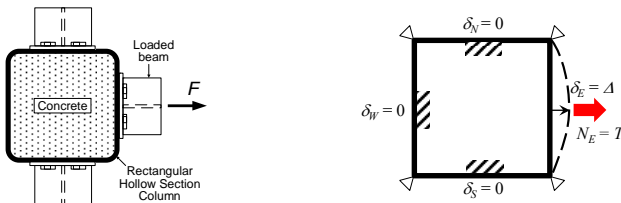
$$k_{\text{tensile}} = \frac{T}{\Delta} = \frac{384}{5} \frac{EI}{D^3} \left(\approx 76.8 \frac{EI}{D^3} \right) \quad (5-3)$$

Concrete-filled tube tensioned in one direction

This loading condition (Figure 8(a)) can be described by the 2-D spring model with $\delta_N = \delta_S = \delta_W = 0$ (Figure 8(b)); this is because the inward out-of-plane deformation can be considered to be restrained by infill concrete.

Substituting the loading conditions into equation (3) obtains the following equation:

$$\begin{bmatrix} N_N \\ N_S \\ T \\ N_W \end{bmatrix} = \frac{12EI}{7D^3} \begin{bmatrix} 67 & 3 & 21 & 21 \\ 3 & 67 & 21 & 21 \\ 21 & 21 & 67 & 3 \\ 21 & 21 & 3 & 67 \end{bmatrix} \begin{bmatrix} 0 \\ 0 \\ \Delta \\ 0 \end{bmatrix} \quad (6-1)$$



(a) Loading condition (b) Loading condition in the 2-D spring model

Figure 8. Loading condition of local tensile test of beam flange-concrete-filled tubular column joint

From the third row in equation (6-1), like in the previous section, the apparent stiffness of an out-of-plane deformation (k_{CFT1}) is derived as follows:

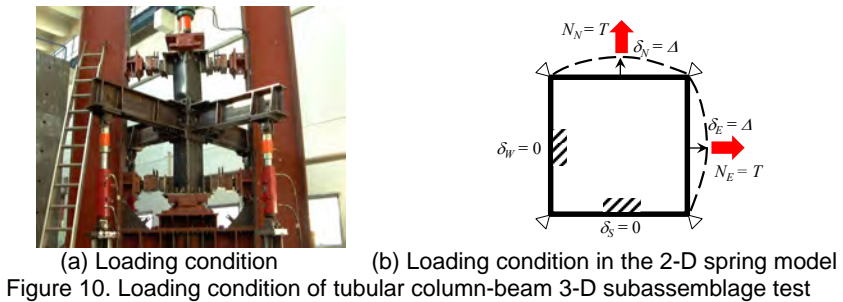
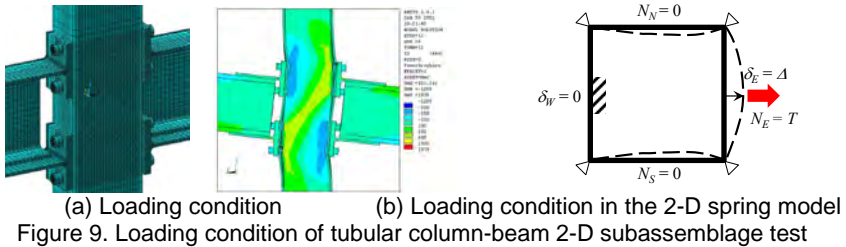
$$k_{CFT1} \equiv \frac{T}{\Delta} = \frac{804}{7} \frac{EI}{D^3} \left(\approx 114.9 \frac{EI}{D^3} \right). \quad (6-2)$$

Split-tee-tube connection under seismic conditions in one or two directions

For the split-tee-tube connection under one-direction lateral loading, this loading condition (Figure 9(a)) can be described by the 2-D spring model with $N_N = N_S = 0$, and $\delta_W = 0$ (Figure 9(b)); this is because the outward out-of-plane deformation at the west-side column face is in contact with the split-tee's flange, so the out-of-plane deformation there becomes very small.

Substituting the loading conditions into equation (2) obtains the following equation:

$$\begin{bmatrix} \delta_N \\ \delta_S \\ \Delta \\ 0 \end{bmatrix} = \frac{D^3}{1536EI} \begin{bmatrix} 17 & 3 & -6 & -6 \\ 3 & 17 & -6 & -6 \\ -6 & -6 & 17 & 3 \\ -6 & -6 & 3 & 17 \end{bmatrix} \begin{bmatrix} 0 \\ 0 \\ T \\ N_W \end{bmatrix}. \quad (7-1)$$



From the fourth row of equation (7-1), the following relationship is obtained:

$$N_W = -\frac{3}{17}T. \quad (7-2)$$

Then, from the third row of equations (7-1) and (7-2), the following relationship is obtained:

$$\Delta = \frac{D^3}{1536EI} \left(17T + 3 \cdot \left(-\frac{3}{17}T \right) \right) = \frac{35D^3}{3264EI} T. \quad (7-3)$$

This relationship results in the apparent stiffness of an out-of-plane deformation (k_{ST2}).

$$k_{ST2} \equiv \frac{T}{\Delta} = \frac{3264}{35} \frac{EI}{D^3} \left(\approx 93.3 \frac{EI}{D^3} \right). \quad (7-4)$$

For the split-tee-tube connection under two-direction lateral loading, i.e., the most general seismic loading condition in real building structures, this loading condition (Figure 10(a)) can be described by the 2-D spring model with $N_N = N_W (= T)$, and $\delta_S = \delta_W = 0$ (Figure 10(b)); this is because the outward out-of-plane deformation at the south- and west-side column faces are in contact with the split-tees' flanges.

Substituting the conditions into equation (3) obtains the following equation:

$$\begin{bmatrix} T \\ N_S \\ T \\ N_W \end{bmatrix} = \frac{12EI}{7D^3} \begin{bmatrix} 67 & 3 & 21 & 21 \\ 3 & 67 & 21 & 21 \\ 21 & 21 & 67 & 3 \\ 21 & 21 & 3 & 67 \end{bmatrix} \begin{bmatrix} \Delta \\ 0 \\ \Delta \\ 0 \end{bmatrix}. \quad (8-1)$$

From the second and fourth rows of equation (8-1), the following force-deformation relationship can be obtained:

$$T = \frac{1056EI}{7D^3} \Delta. \quad (8-2)$$

This relationship results in the apparent stiffness of an out-of-plane deformation (k_{ST4}), and this result corresponds to the observation that the apparent local stiffness under 3-D loading is roughly twice as large as the apparent stiffness under 2-D loading (Figure 2(b), (c)).

$$k_{ST4} \equiv \frac{T}{\Delta} = \frac{1056}{7} \frac{EI}{D^3} \left(\approx 150.9 \frac{EI}{D^3} \right) \quad (8-3)$$

$$\frac{k_{ST4}}{k_{ST2}} = \frac{1056}{7} \bigg/ \frac{3264}{35} \approx 1.62 \quad (8-4)$$

DISCUSSIONS AND COMMENTS

Figure 11 shows the outline of the 2-D spring elements' application to the square hollow section column-to-beam joint. There are two deformable portions in each column face, corresponding to the upper and lower flanges of the beam member, and the differences in the out-of-plane deformations of the upper and lower portions generate the beam-end local rotations. In addition, a shear-deformable element should be placed to describe shear deformation in a panel zone of the column-to-beam joint.

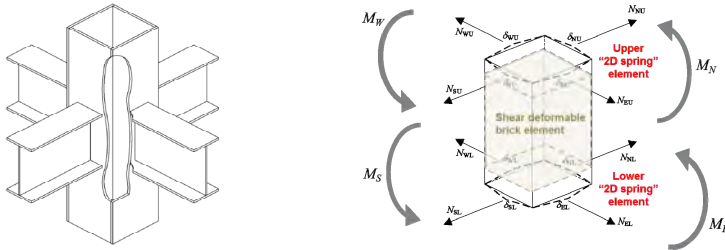


Figure 11. Outline of 2-D spring elements' application to 3-D square hollow section column-to-beam joint

Let us mention the conformity of the 2-D spring element to the component method for semi-rigid connection. A joint modeling framework for 3-D semi-rigid frames based on the component method was previously proposed (Simões da Silva, 2008, Gentili et al., 2015), and so it would be desirable that the 2-D spring element be directly incorporated in the modeling framework. Unfortunately, the 2-D spring element does not conform to the component modeling methodology, since the component method essentially describes the joint's behavior by simply arranging 1-D spring elements in serial and/or in parallel. However, the intent of the 2-D spring element may be approximated by ignoring some of relatively insignificant deformation modes (shown in Figure 6) and by introducing appropriate constraints for some degrees-of-freedom; this point will be investigated further.

The methodology presented here will be also applicable to circular tubular columns (although the ratios among the modal stiffnesses (k_{Mi} in equation (4)) will vary depending on the section form), and this type of joint modeling for 3-D frame analysis has the potential to be used to design steel frames with semi-rigid column-to-beam connections. However, this study is still in its preliminary stage, and so the following problems remain unsolved:

- Consideration of yielding of the column faces on formulation of the 2-D spring element
- Consideration of a section's distortion in the 2-D spring element's formulation
- Determination of flexural rigidity (EI) in the cross-section frame
- More rigorous verification of the cross-section frame modeling
- Modeling for the case that the positions in height of four beam flanges are different.

REFERENCES

- Fujita, K., Harada, Y., and Morita, K. (2001) "Evaluation of local rotational stiffness and strength of beam-to-column connection reinforced by increasing column thickness", *Tubular Structures*, Vol. 9 (pp. 483–492).
- Harada, Y., Arakaki, T., and Morita, K. (2002) "Structural Behaviour of RHS Column-to-H Beam Connection with High Strength Bolts", *International Journal of Steel Structures*, Vol. 2, No. 2 (pp. 111–121).
- Harada, Y., Nakagawa, H., and Morita, K. (2003) "Out-of-Plane Behavior of Column Skin Plate in RHS Column-to-Split-T Tensile Connection with High-Strength Bolts", *Journal of structural and construction engineering (Transactions of A. I. J.)*, No. 567, (pp. 173-180) (in Japanese).
- CEN – European Committee for Standardization. (2005) *EN 1993-1-8. Eurocode 3: Design of steel structures, Part 1-8: Design of joints*.
- L. A. P. Silva, L. F. N. Neves, and F. C. T. Gomes (2003) "Rotational Stiffness of Rectangular Hollow Sections Composite Joints", *Journal of Structural Engineering*, Vol. 129, No. 4 (pp. 487-494).
- Simões da Silva, L. (2008) "Towards a consistent design approach for steel joints under generalized loading", *Journal of Constructional Steel Research*, Vol. 64 (pp. 1059–1075).
- Gentili, F., Costa, R., and Simões da Silva, L. (2015) "Definition and implementation of a simplified model for steel connections in an open source software", *Eighth International Conference on Advances in Steel Structures*, Lisbon, Portugal, July 22-24 (Paper No. 129).

MOMENT-ROTATION BEHAVIOUR OF BOLTED MOMENT END-PLATE CONNECTIONS

Chen Zhu

University of Sydney, Sydney, NSW 2006, Australia
czhu7452@uni.sydney.edu.au

Kim J. R. Rasmussen

University of Sydney, Sydney, NSW 2006, Australia
kim.rasmussen@sydney.edu.au

Hao Zhang

University of Sydney, Sydney, NSW 2006, Australia
hao.Zhang@sydney.edu.au

ABSTRACT

The paper summarises research recently conducted at the University of Sydney on developing a joint model based on the component method for predicting the full-range behaviour of steel connections, including elastic, inelastic, post-ultimate and post-fracture response. The overall context of this work is to produce models for connections that are sufficiently simple and accurate that they can be implemented in beam-element based finite element models of steel frames.

The paper first summarises the Generalised Component Method for predicting the full-range behaviour of each component and the complete joint model. Having set out the equilibrium and compatibility equations, the Method is applied to bolted moment end plate connections and compared to recent tests carried out at Sydney University on these joints. Particular attention is paid to the buckling of the column web plate by presenting a component model specifically developed for this part of the bolted moment end plate connection.

INTRODUCTION

Conventional design of structural steel joints simplifies the connection characteristics into one of three cases: ideally pinned, fully rigid or linear semi-rigid. However, in reality, no joint behaves in exactly these ways and should be treated as nonlinear semi-rigid. Inaccurate modelling of the joint characteristics may lead to an ineffective and potentially unsafe design. Therefore, the consideration of nonlinear semi-rigid joint behaviour is important for the future development of structural design methodologies, such as design by Geometric and Material Nonlinear Analysis with Imperfections (GMNIA), also referred to as advanced analysis.

da Silva et al. (2000) suggested a Component Method type of procedure to find closed-form equations for the nonlinear moment-rotation ($M-\theta$) curve of steel joints. The method employs a technique (da Silva and Girao Coelho, 2001) to reduce a complex steel joint into a two spring system and an energy-based analysis to solve the equilibrium and compatibility equations for the two spring system. The method presented concerns the nonlinear pre-ultimate behaviour of joints.

However, the ductility of steel joints not only constitutes pre-ultimate behaviour but also post-ultimate behaviour. The latter may prove important in large deformation analyses, including progressive collapse analyses, and is the focus of this paper.

In order to extend da Silva's method to the post-ultimate range, Lewis (2010) introduced a method to formulate a post-ultimate spring using negative spring stiffness. Based on this method, a generalised component method based model can be devised. It uses a multi-spring system (*Figure 1*) and is potentially applicable to any type of joints. This generalised connection model will be introduced in Section 1.

The basic input variables for the component method are the spring models describing the behaviours of the individual components, including the elastic, inelastic and post-ultimate stiffnesses as well as the elongation before fracture (ductility). For example, a bolted moment end-plate connection model includes 10 individual components. The spring models of all 10 components must be obtained before creating the component model. The most commonly used models for the individual components can be found in Eurocode 3 (2006b). However, Eurocode 3 only provides linear models for individual components which do not suffice for obtaining full-range connection behaviour.

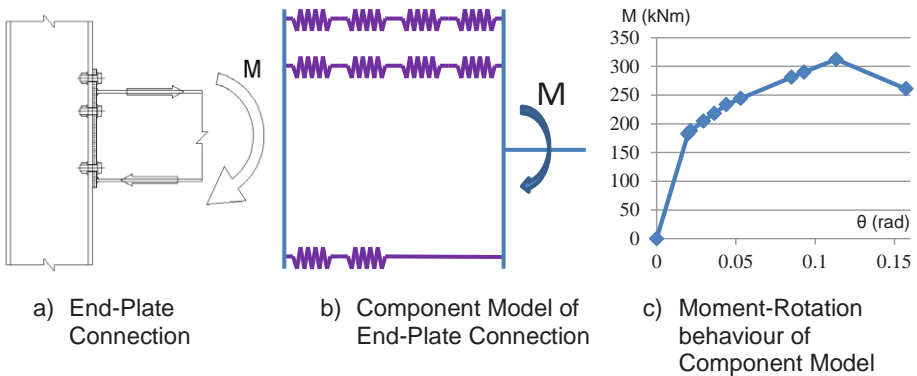


Figure 1: Example of the Component Based Model for Predictating the Moment-Rotation Behaviour of an End-Plate Connection

In bolted end-plate connections, end-plate bending and column web buckling are considered to be the major components influencing the overall connection behaviour. Therefore, the full range behaviour of these two components must be established. The

end-plate bending component can be considered as idealised T-stub (Eurocode3, 2006b) which can be modelled by Swanson’s T-stub model (Swanson and Leon, 2001). However, the column web buckling component has not been covered by existing research. Therefore, a proposed full range force-displacement model for the column web buckling component is introduced in Section 2.

In Section 3, six bolted moment end-plate connections are modelled by the proposed full range component model. Subsequently, the model predictions are compared with the corresponding experimental $M-\theta$ results, indicating good agreement. Of the six connections, three of them are from the University of Sydney (USyd Tests) (Zhu, 2016) and the other three are obtained from Girão Coelho et al. (2004). They all have different column, beam, bolt, backing plate and end-plate combinations, covering the prevalent failure modes of the bolted moment end-plate connection. Thus, the paper provides a generalised model to predict the full range moment-rotation behaviour of bolted moment end-plate connections.

SECTION 1: GENERALISED COMPONENT METHOD

1.1 Energy Method Based Formulation for an Individual Spring

First, based on da Silva’s work (da Silva et al., 2000) and Lewis’ work (Lewis, 2010), a spring with tri-linear behaviour can be reproduced by three springs, each with linear behaviour (Figure 2).

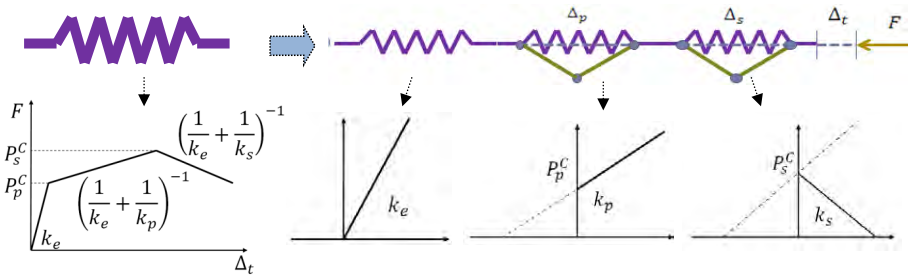


Figure 2: Use three springs to reproduce the tri-linear behaviour of an individual spring. Note the spring with stiffness k_s is the softening spring and its stiffness k_s is negative.

Three different types of springs are shown in Figure 2, viz. an elastic spring, a plastic spring and a softening (post-ultimate) spring. Their stiffnesses are represented by k_e, k_p and k_s respectively. The plastic and softening springs feature “preload” displacements which will prevent deformation before the applied force reaches their corresponding critical loads, P_p^C or P_s^C , as shown in Figure 2.

The potential energy for the *elastic* spring, Π_e , can be written as:

$$\Pi_e = \frac{1}{2}k_e(\Delta_t - \langle\Delta_p\rangle - \langle\Delta_s\rangle)^2 \quad (1.1)$$

where,

$$\langle\Delta_p\rangle \equiv \begin{cases} 0, & F < P_p^C \\ \Delta_p, & P_p^C \leq F < P_s^C \\ \Delta_p^*, & F = P_s^C \text{ and subsequent } F < P_s^C \end{cases} \quad (1.2)$$

$$\langle\Delta_s\rangle \equiv \begin{cases} 0, & F < P_s^C \\ \Delta_s, & F = P_s^C \text{ and subsequent } F < P_s^C \end{cases} \quad (1.3)$$

In Eqns. (1.2-1.3), k_e is the stiffness of the elastic spring, Δ_t is the total displacement of the three-spring series, Δ_p is the displacement of the plastic spring which is a variable, Δ_p^* is the displacement of the plastic spring just at the critical load (P_s^C) which is a constant, F is the applied force, P_p^C is the critical load of activation of the plastic spring and P_s^C is the critical load of activation of the softening spring.

The potential energy for the *plastic* spring, Π_p , is given by (da Silva and Girao Coelho, 2001):

$$\Pi_p = \frac{1}{2}k_p\left(\frac{P_p^C}{k_p} + \langle\Delta_p\rangle\right)^2 \quad (1.4)$$

The potential energy of the *softening* spring, Π_s , can be written as:

$$\Pi_s = \frac{1}{2}|k_s|\left(\frac{P_s^C}{|k_s|} + \langle\Delta_s\rangle\right)^2 - |k_s|\langle\Delta_s\rangle^2 \quad (1.5)$$

So, the total potential energy, Π , of the tri-linear spring is

$$\Pi = \Pi_e + \Pi_p + \Pi_s \quad (1.6)$$

1.2 Derivation of the Equations for the F- Δ Behaviour of a Spring Series Considering Post-Ultimate Softening

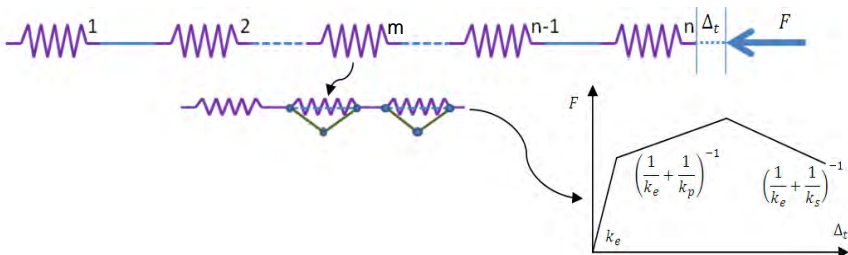


Figure 3: A series of n springs. Each spring with tri-linear behaviour can be reproduced by an elastic spring, a plastic spring and a softening spring.

Consider a series of n springs (Figure 3). Its total energy can be written as:

$$\begin{aligned} \Pi = & \frac{1}{2} \left(\sum_{i=1}^n \frac{1}{k_{ei}} \right)^{-1} \left(\Delta_t - \sum_{i=1}^n \langle \Delta_{pi} \rangle - \sum_{i=1}^n \langle \Delta_{si} \rangle \right)^2 \\ & + \sum_{i=1}^n \frac{1}{2} k_{pi} \left(\frac{P_{pi}^C}{k_{pi}} + \langle \Delta_{pi} \rangle \right)^2 + \sum_{i=1}^n \left[\frac{1}{2} |k_{si}| \left(\frac{P_{si}^C}{|k_{si}|} + \langle \Delta_{si} \rangle \right)^2 - |k_{si}| \langle \Delta_{si} \rangle^2 \right] - F \Delta_t \end{aligned} \quad (1.7)$$

where, k_{ei} is the stiffness of the i^{th} individual elastic spring, Δ_{pi} is the displacement of the i^{th} plastic spring, Δ_{si} is the displacement of i^{th} softening spring, k_{pi} is the stiffness of the i^{th} plastic spring, k_{si} is the stiffness of the i^{th} softening spring, P_{pi}^C is the critical load of activation of the i^{th} plastic spring, P_{si}^C is the critical load of activation of the i^{th} softening spring, and F is the applied force.

Assume that $P_{p1}^C < P_{p2}^C < \dots < P_{pm-1}^C < P_{pm}^C < P_{s1}^C < \dots$ whereby, the first plastic spring will be activated when the applied force reaches P_{p1}^C . The second plastic spring will be activated once the applied force reaches P_{p2}^C , and as the applied force increases, other plastic springs will be activated one after the other until the m^{th} plastic spring is activated. Then, as the applied force keeps increasing, it eventually reaches the critical load of the first softening spring which is the ultimate load of both the spring and series of springs. From this point, the resistance of the first softening spring reduces as the total displacement keeps increasing. This sequence of events leads to two assertions:

1. If the critical load of a softening spring is larger than P_{s1}^C , it will never be activated.
2. All springs except the first softening spring will unload once P_{s1}^C has been reached. The unloading stiffness is equal to the elastic stiffness and plastic springs have no deformation during this process.

Based on these two assertions, the energy equation can be simplified. Then, using the minimum total potential energy principle to find the springs' stationary positions with respect to all variables, a system of equations can be obtained:

$$\frac{\partial \Pi}{\partial \Delta_t} = \left(\sum_{i=1}^n \frac{1}{k_{ei}} \right)^{-1} (\Delta_t - \sum_{i=1}^m \Delta_{pi}) - F = 0 \quad (1.8)$$

$$\frac{\partial \Pi}{\partial \Delta_{p1}} = \left(\sum_{i=1}^n \frac{1}{k_{ei}} \right)^{-1} (\sum_{i=1}^m \Delta_{pi} - \Delta_t) + k_{p1} \Delta_{p1} + P_{p1}^C = 0 \quad (1.9)$$

$$\frac{\partial \Pi}{\partial \Delta_{p2}} = \left(\sum_{i=1}^n \frac{1}{k_{ei}} \right)^{-1} (\sum_{i=1}^m \Delta_{pi} - \Delta_t) + k_{p2} \Delta_{p2} + P_{p2}^C = 0 \quad (1.10)$$

•
•
•

$$\frac{\partial \Pi}{\partial \Delta_{pm-1}} = \left(\sum_{i=1}^n \frac{1}{k_{ei}} \right)^{-1} (\sum_{i=1}^m \Delta_{pi} - \Delta_t) + k_{pm-1} \Delta_{pm-1} + P_{pm-1}^C = 0 \quad (1.11)$$

$$\frac{\partial \Pi}{\partial \Delta_{pm}} = \left(\sum_{i=1}^n \frac{1}{k_{ei}} \right)^{-1} (\sum_{i=1}^m \Delta_{pi} - \Delta_t) + k_{pm} \Delta_{pm} + P_{pm}^C = 0 \quad (1.12)$$

By rearranging these equations, the $F - \Delta$ relationship for a series of springs can be obtained as:

$$F = \langle K^j \rangle (\Delta_t + \langle C^j \rangle) \quad (1.13)$$

$$\langle K^j \rangle \equiv \begin{cases} K_e^j = \left(\sum_{i=1}^n \frac{1}{k_{ei}} \right)^{-1}, & F < P_{p1}^C \\ K_p^j = \left(\sum_{i=1}^n \frac{1}{k_{ei}} + \sum_{l=1}^m \frac{1}{k_{pi}} \right)^{-1}, & P_{p1}^C \leq F < P_{s1}^C \\ K_s^j = \left(\sum_{i=1}^n \frac{1}{k_{ei}} + \frac{1}{k_{s1}} \right)^{-1}, & F = P_{s1}^C \text{ and subsequent } F < P_s^C \end{cases} \quad (1.14)$$

$$\langle C^j \rangle \equiv \begin{cases} C_e^j = 0, & F < P_{p1}^C \\ C_p^j = \sum_{i=1}^m \frac{P_{pi}^C}{k_{pi}}, & P_{p1}^C \leq F < P_{s1}^C \\ C_s^j = \sum_{i=1}^m \frac{P_{s1}^C - P_{pi}^C}{k_{pi}} + \frac{P_{s1}^C}{k_{s1}}, & F = P_{s1}^C \text{ and subsequent } F < P_s^C \end{cases} \quad (1.15)$$

where the superscript j on the terms K^j , K_e^j , K_p^j , K_s^j , C^j , C_e^j , C_p^j , and C_s^j represents the different stiffness stages as exemplified in Figure 4.

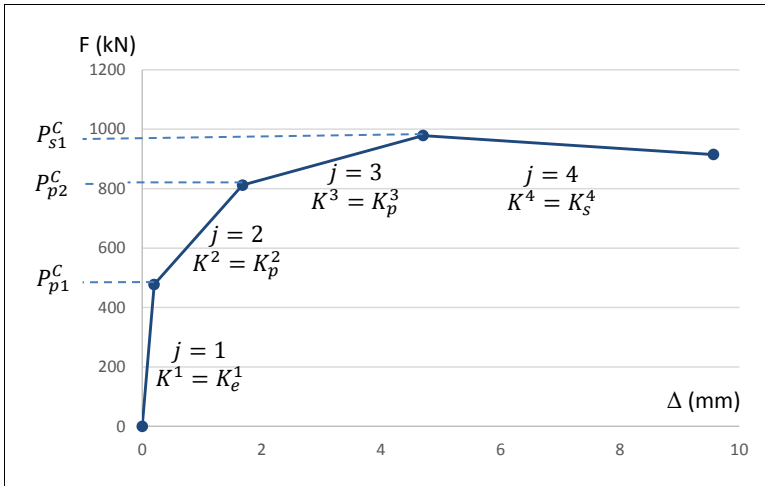


Figure 4: Example of the $F - \Delta$ curve of a spring series.

1.3 Derivation of the M- θ Equation for a Multi-spring System

A multi-spring system with N linear series of springs (Figure 5) is now considered. In this system, there are l spring series in the elastic or plastic stage and m spring series in the post-ultimate stage such that $m + l$ is equal to the total number of the series of springs (N).

Since all spring series have multi-linear behaviour (Figure 4), their combined behaviour can be also represented by a multi-linear curve, as shown in Figure 6 where the superscript $k = 1, 2 \dots 5$ represents the k^{th} segment ($M^k(\theta)$) of the $M - \theta$ curve. Each

segment, $M^k(\theta)$, is defined by a unique stiffness value (K_i^j) and preloading constant (C_i^j) for each spring series ($i = 1, 2 \dots N$), which are contained in the vectors,

$$\mathbf{K}^k = \{K_i^j, i = 1, 2, \dots, N\} \quad (1.16)$$

$$\mathbf{C}^k = \{C_i^j, i = 1, 2, \dots, N\} \quad (1.17)$$

The i^{th} spring series may be either in the elastic ($K_i^j = K_e^j, C_i^j = C_e^j$), plastic ($K_i^j = K_p^j, C_i^j = C_p^j$) or post-ultimate range ($K_i^j = K_s^j, C_i^j = C_s^j$) range, as defined in Eqns. (1.14, 1.15).

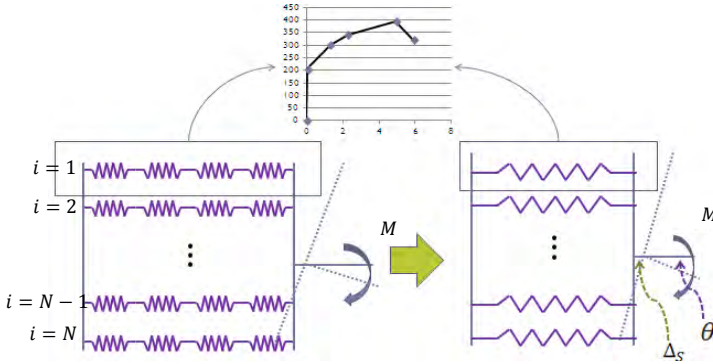


Figure 5: Multi-spring system. Each series of springs may have a multi-linear $F-\Delta$ curve which can be obtained by the method introduced in Section 1.2. Each of these series of springs can be treated as single springs with multi-linear $F-\Delta$ behaviour.

The energy expression for the system on the k^{th} linear curve of the multi-spring system can be written as:

$$\Pi^k = \sum_{i=1}^N \frac{1}{2} |K_i^j| a_i - M^k \theta, \quad K_i^j \in \mathbf{K}^k \text{ and } C_i^j \in \mathbf{C}^k \quad (1.18)$$

$$a_i = \begin{cases} (\Delta_s + h_i \sin \theta + C_e^j)^2, & K_i^j = K_e^j \\ (\Delta_s + h_i \sin \theta + C_p^j)^2, & K_i^j = K_p^j \\ (\Delta_s + h_i \sin \theta + C_s^j)^2 - 2(\Delta_s + h_i \sin \theta)^2, & K_i^j = K_s^j \end{cases}$$

where the stiffness (K_i^j) and preloading constant (C_i^j) of the i^{th} spring series are contained in \mathbf{K}^k and \mathbf{C}^k respectively, Δ_s is the displacement at the zero height of the rotating section on which the applied moment acts (Figure 5), h_i is the height of the i^{th} spring measured from the centroid of the beam, θ is the rotation of the joint, and M^k is the applied moment on the k^{th} linear curve.

Equation (1.18) is differentiated with respect to Δ_s and θ , and the minimum total potential energy principle is used to find the stationary position of the spring system. Two equations are obtained:

$$\frac{\partial \Pi^k}{\partial \Delta_S} = \sum_{i=1}^N K_i^j \Delta_S + \sum_{i=1}^N K_i^j h_i \sin \theta + \sum_{i=1}^N K_i^j C_i^j = 0 \quad (1.19)$$

$$\frac{\partial \Pi^k}{\partial \theta} = \sum_{i=1}^N K_i^j (\Delta_S h_i \cos \theta + h_i^2 \sin \theta \cos \theta + C_i^j h_i \cos \theta) - M^k = 0 \quad (1.20)$$

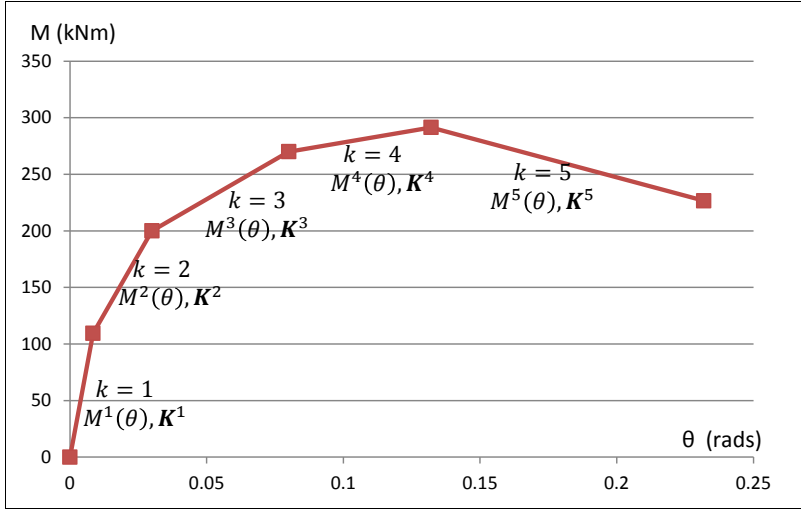


Figure 6: Example of the $M - \theta$ curve of a multi-spring system

By rearranging Eqns. (1.19-1.20), an expression for $M^k(\theta)$ can be obtained:

$$M^k(\theta) = \left\{ \sum_{i=1}^{N-1} \sum_{ii=i+1}^N K_i^j K_{ii}^j (h_i - h_{ii}) [(h_i - h_{ii}) \sin \theta + (C_i^j - C_{ii}^j)] \right\} \cos \theta / \sum_{i=1}^N K_i^j \quad (1.21)$$

In Section 1.5, the energy for each linear curve (V^k) is required for obtaining the total energy of the multi-linear curve. The energy of the k^{th} linear curve can be obtained from:

$$V^k = -\frac{a1^k (\cos 2\theta_1 - \cos 2\theta_0)}{4} + a1^k (\sin \theta_1 - \sin \theta_0), \quad (1.22)$$

where,

$$a1^k = \sum_{i=1}^{N-1} \sum_{ii=i+1}^N K_i^j K_{ii}^j (h_i - h_{ii})^2 / \sum_{i=1}^N K_i^j$$

$$a2^k = \sum_{i=1}^{N-1} \sum_{ii=i+1}^N K_i^j K_{ii}^j (h_i - h_{ii}) (C_i^j - C_{ii}^j) / \sum_{i=1}^N K_i^j$$

in which θ_0 is the rotation at the beginning of the k^{th} linear curve and θ_1 is the rotation at the end of the k^{th} linear curve.

By adding the energy of each linear curve, the total energy of the multi-linear curve can be obtained (Eqn. (1.23)), which is demonstrated in Figure 7,

$$V(\theta_f) = \sum_{k=1}^{N_k} V^k, \quad (1.23)$$

where N_k is the total number of segments contained in the multi-linear curve and θ_f is the rotation at the fracture a component.

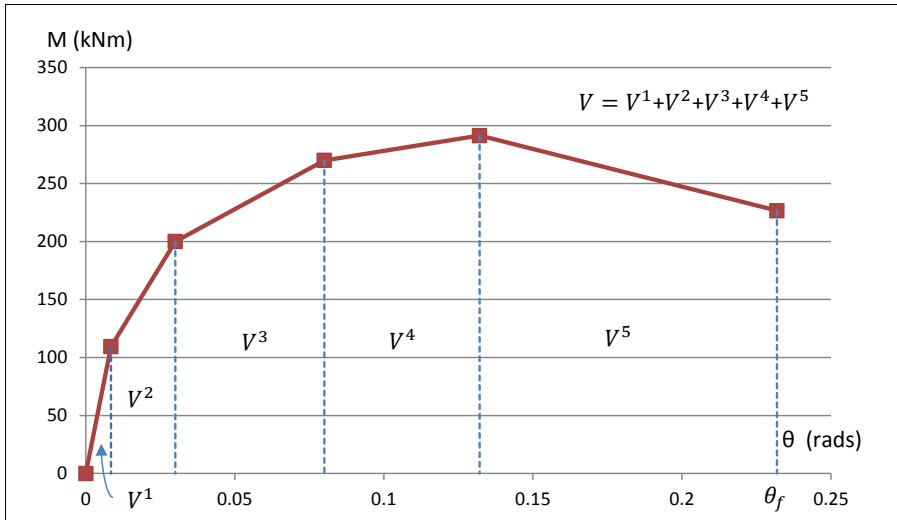


Figure 7: The total energy (V) of the multi-spring system

1.4 Instantaneous Centre of Rotation (ICR)

In Eqn. (1.21), although the F - Δ curves of all spring series are known, the K and C terms are not uniquely defined because the loading condition (compression, tension and unloading) of each individual spring series is unknown at this stage of analysis. In order to determine the (K , C)-terms, the consideration of the instantaneous centre of rotation (ICR) is required. The ICR allows the moving direction of any point on the rotating section to be determined as demonstrated in Figure 8.

The loading condition of any series of springs can be analysed based on the instantaneous moving direction and its deformation history (Table 1).

Table 1

	Tension	Compression
Deforming towards right	Tension	Compression Unloading
Deforming towards left	Tension unloading	Compression

The displacement of a point on the rotating section can be represented by:

$$\Delta_i = \Delta_S + h_i \sin \theta \quad (1.24)$$

where Δ_i is the displacement of a point on the rotating section and h_i is the height of this point.

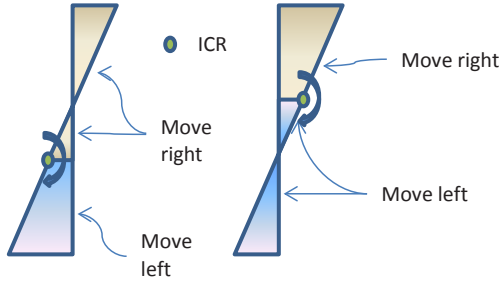


Figure 8: The moving direction of any point on a rotating section

By substituting Eqn. (1.19) into Eqn. (1.24) for Δ_S ,

$$\Delta_i = \left(-\frac{\sum_1^N K_i^J h_i}{\sum_1^N K_i^J} + h_i \right) \sin \theta - \frac{\sum_1^N K_i^J C_i^J}{\sum_1^N K_i^J} \quad (1.25)$$

The expression for the height (h_{ICR}) of the ICR can now be derived. Let Δ_{ICR} represents the longitudinal distance from the ICR to the original section. Since the ICR is independent of the section rotation (θ), Δ_{ICR} is a constant for a certain current condition, i.e.

$$\Delta_{ICR} = \left(-\frac{\sum_1^N K_i^J h_i}{\sum_1^N K_i^J} + h_{ICR} \right) \sin \theta - \frac{\sum_1^N K_i^J C_i^J}{\sum_1^N K_i^J} = \text{constant} \quad (1.26)$$

Thus, Δ_{ICR} can be a constant and independent of θ if, and only if,

$$h_{ICR} = \frac{\sum_1^N K_i^J h_i}{\sum_1^N K_i^J} \quad (1.27)$$

thus providing the expression for height of the ICR.

1.5 Post-fracture Behaviour

In a multi-spring system, the fracture of a spring series may not lead to failure of the whole system because the rest of the system may sustain further rotation at lower resistance level. It is therefore of interest to consider the behaviour of a multi-spring system after the fracture of one or more of its series of springs.

Fracture of a spring series usually causes a sudden loss of force in the system, violates static equilibrium and induces dynamic effects. How this dynamic behaviour affects the system is of no particular interest since eventually the system will be restored to static equilibrium. Some elastic energy is converted to kinematic energy in the process, which will be assumed to be small and ignored in the analysis.

It is possible to determine the new static equilibrium point by the energy method (Figure 9). Each of the distinct equilibrium paths associated with one, two, three, etc. fractured components is referred to as a “stage”.

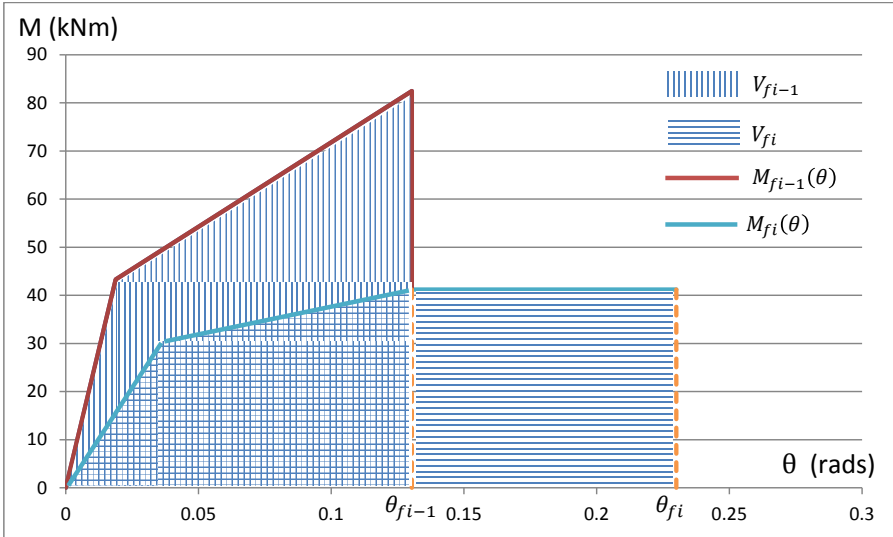


Figure 9: Example of the post-fracture model. The drop in resistance is caused by fracture of a component(s) of a spring series. The $M - \theta$ curve of the post-fracture system is shown in blue.

Two assumptions are made in the application of the energy method in the post-fracture range:

- 1) After the fracture of a component, it is assumed that the new static equilibrium point is located on the $M - \theta$ curve of a new multi-spring system with one spring series less than the non-fractured system, (or previous fractured system).
- 2) The total energy possessed by the post-fracture system just after returning to static equilibrium is assumed to equal the total energy possessed by the original system at incipient component fracture.

When applying the post-fracture model to end-plate connections where end-plate cracking usually dominates the fracture behaviour, two specific assumptions must be made based on experimental observations:

- 1) Because of the complex deformations of the joint, the bolt deformation and crack propagation are observed to always be asymmetric to the centreline of the end-plate, which causes the asymmetrical fracture initiated by either bolt failure or by end-plate failure at the same row. In the spring model, this behaviour induces an unbalanced

force distribution on the left and right parts of the same spring series, and hence, the fracture of a spring series usually occurs on one half of the spring series after the other. At each fracture stage, it is assumed that fracture of a spring series only halves its stiffness and resistance, i.e. the values of k_e, k_p, k_s, P_p^c and P_s^c for the end plate component are halved when fracture first occurs on one half of the end plate and then reduced to zero when fracture occurs on the other half.

- 2) For other components than the end plate, after a major crack(s) occurs, the stiffness is assumed equal to zero, i.e. the resistance of the post-fracture system is assumed to be constant during each post-fracture stage.

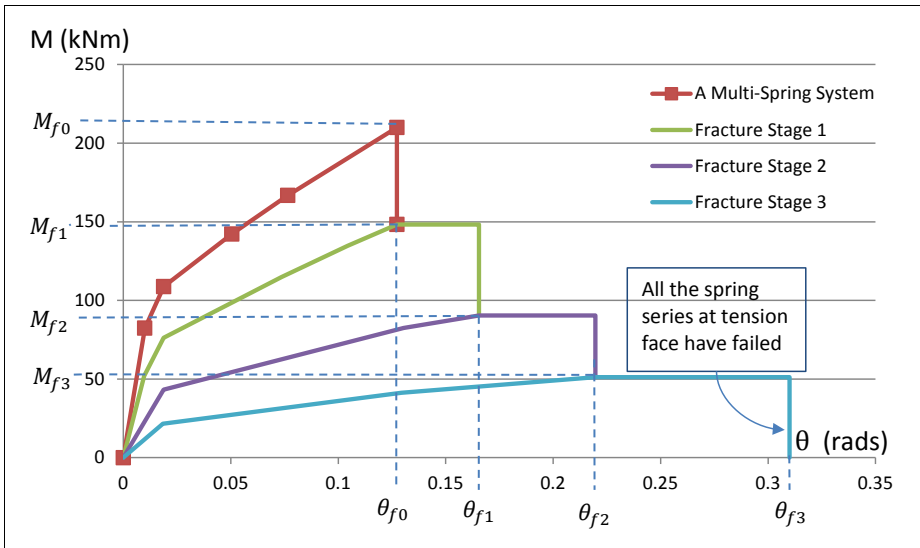


Figure 10: Example of the post-fracture model.

Based on these assumptions, the post-fracture model can be obtained using the following steps:

- 1) The component model detects a component fracture in a spring series.
- 2) The total energy of the multi-spring system model at the incipient fracture stage, $V_{f_{i-1}}(\theta_{f_{i-1}})$, is calculated using Eqn. (1.23) in which $\theta_{f_{i-1}}$ is the incipient fracture rotation. The subscript fi represents the fracture stage, as demonstrated in Figures 9-10.
- 3) The stiffness and strength of the fractured spring series is reduced by 50% in the post-fracture system model.
- 4) The total energy of the new post-fracture system (V_{fi}) at the incipient fracture rotation ($\theta_{f_{i-1}}$) of the old system, $V_{f_{i-1}}(\theta_{f_{i-1}})$ is then calculated using Eqn. (1.23).
- 5) The rotation of the new post-fracture system, θ_{fi} , can be calculated using Eqn. (1.28).

6) Repeat Steps 1 to 5 until all tension spring series have failed.

The rotation of the i^{th} new post-fracture system, θ_{fi} , can be calculated as:

$$\theta_{fi} = \frac{V_{fi-1}(\theta_{fi-1}) - V_{fi}(\theta_{fi-1})}{M_{fi}(\theta_{fi-1})} + \theta_{fi-1} \quad i = 1, 2 \dots \quad (1.28)$$

where, $M_{fi}(\theta_{fi-1})$ is the moment of the new multi-spring model at the incipient fracture stage.

An example of a post-fracture analysis is shown in *Figure 10*. Three stages of component fracture occurred in the simulation and for each stage, the post-fracture system behaviour is demonstrated.

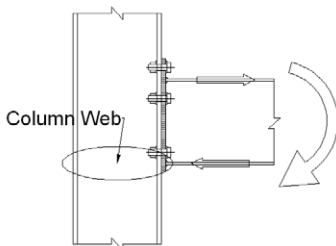
1.6 Summary

The proposed method extends the Component Method to the post-ultimate range, and thus enables the full range moment-rotation relationship of steel joints to be predicted. The method can be used to solve spring models with any number of springs and does not pose numerical difficulties. It is potentially applicable to all types of joints.

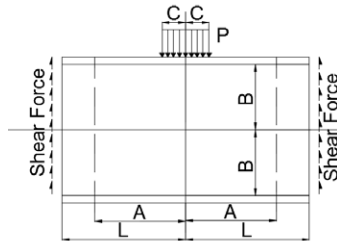
SECTION 2: COLUMN WEB COMPONENT

2.1 General

The column web is a major component of steel joints. It bears most of the compression force transmitted from the beam flange in compression (*Figure 11a*) when the steel joint is subject to bending. Therefore, the behaviour of the steel joint will be greatly affected by the behaviour of the column web component, which has not been well understood and is often not considered in design. For example, in Eurocode 3 Part 1-8, this component is essentially considered as an infinitely stiff link. The Code suggests stiffening this component if prone to buckling.



a) Column Web Component



b) Loading Condition of the Component

Figure 11: The Column Web Component and Its Idealised Loading Condition

While thus Eurocode 3 favours a strong or stiffened column web, in practice, a weaker unstiffened column web may be suitable when it can sustain sufficient large compression forces in the post-buckling range (*Figure 12*). In this range, the resistance may increase significantly depending on the plate slenderness. Moreover, it can provide larger ductility in the post-ultimate range which is usually desirable in structural design. Therefore, it is of interest to devise a model which can predict the full range behaviour of the column web component

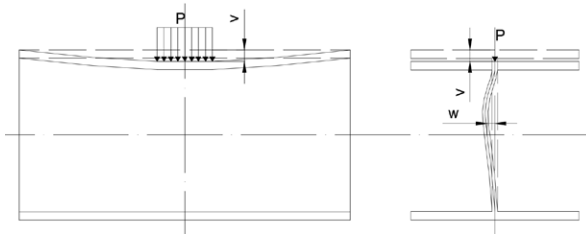


Figure 12: Buckling Behaviour of the Column Web Component Subject to Patch Loading

2.2 Related Literature

Since existing research has focused on the bearing load of strong or stiffened columns, few techniques for modelling the detailed behaviour of unstiffened column webs can be found in the literature. However, a closely related research field is steel girders subject to patch loading (*Figure 11b*), for which several applicable models, such as the elastic buckling analysis and methods for predicting ultimate strength, can be found.

For the elastic buckling analysis, Khan and Walker (1972) devised a viable analytical method for the plate subject to patch loading. Their elastic buckling analysis can be extended to the elastic and inelastic post-buckling ranges by adding the second order stress function and inelastic Young's modulus as will be described in the Section.

A slender column web will reach its ultimate load in the post-buckling range. The most robust design method for predicting the ultimate load is given in Eurocode 3 (2006a). It adopts a plate buckling approach and is readily understood by practicing engineers. Compared to other methods, it is the most accurate method for predicting the strengths obtained in the USyd tests (Zhu, 2016).

For the post-ultimate range, Roberts' mechanism model can be employed (Shahabian and Roberts, 1999). The model assumes the girder collapses due to web folding at the ultimate load (*Figure 12*) and that web buckling is the major contributor to post-ultimate deformations. With modifications to suit the column web component, it can accurately predict the post-ultimate behaviour observed in experiments.

2.3 The Proposed Model

The proposed model includes three parts: a) Elastic and inelastic post-buckling analyses, b) Determination of ultimate resistance and corresponding displacement, and c) Determination of post-ultimate force-displacement relationship.

2.3.1 Elastic Post-Buckling Analysis

The total energy of the column web component can be written as:

$$\Pi = U_b + U_m + U_f - W_p \quad (2.1)$$

The web plate bending energy U_b can be obtained from classical plate theory (Eqn. (2.2)).

$$U_b = \int_{-B}^B \int_{-A}^A \frac{D}{2} \left\{ \left(\frac{\partial^2 w_1}{\partial x^2} + \frac{\partial^2 w_1}{\partial y^2} \right)^2 + 2(1-\nu) \left[\left(\frac{\partial^2 w_1}{\partial x \partial y} \right)^2 - \frac{\partial^2 w_1}{\partial x^2} \frac{\partial^2 w_1}{\partial y^2} \right] \right\} dx dy \quad (2.2)$$

where D is the rigidity of web plate and w_1 is the first order web deflection.

The web plate membrane energy U_m consists of three parts as shown in Eqns (2.3-2.6), in which U'_m is an additional term suggested by Khan and Walker (Khan and Walker, 1972) when a statically admissible stress field (Eqns. (2.10-2.16)) is applied.

$$U_m = U_{m1} + U_{m2} + U'_m \quad (2.3)$$

$$U_{m1} = \int_{-B}^B \int_{-A}^A \frac{t_w}{2} \left[\frac{\partial^2 F}{\partial y^2} \left(\frac{\partial w}{\partial x} \right)^2 + \frac{\partial^2 F}{\partial x^2} \left(\frac{\partial w}{\partial y} \right)^2 + 2 \frac{\partial^2 F}{\partial x \partial y} \frac{\partial w}{\partial x} \frac{\partial w}{\partial y} \right] dx dy \quad (2.4)$$

$$U_{m2} = \int_{-B}^B \int_{-A}^A t_w \left[\frac{\partial^2 F}{\partial y^2} \frac{\partial u}{\partial x} + \frac{\partial^2 F}{\partial x^2} \frac{\partial v}{\partial y} + \frac{\partial^2 F}{\partial x \partial y} \left(\frac{\partial v}{\partial x} + \frac{\partial u}{\partial y} \right) \right] dx dy \quad (2.5)$$

$$U'_m = - \int_{-B}^B \int_{-A}^A \frac{t_w}{E} \left[\left(\frac{\partial^2 F_0}{\partial y^2} + \frac{\partial^2 F_0}{\partial x^2} \right) \left(\frac{\partial^2 F_2}{\partial x^2} + \frac{\partial^2 F_2}{\partial y^2} \right) \right] dx dy \quad (2.6)$$

In Eqns. (2.4-2.5), F is the stress function which can be expressed as $F = F_0 + F_2$, where F_0 and F_2 are the fundamental term and the second order term of the stress function, respectively.

The strain energy of the flange U_f can be obtained from:

$$U_f = \int_{-A}^A \frac{EI_f}{2} \left\{ \frac{\partial^2 v_f(x)}{\partial x^2} \right\}^2 dx \quad (2.7)$$

where v_f is the deflection of the flange plate. The work done by the applied patch load can be written as:

$$W_p = Pv \quad (2.8)$$

where v is the average displacement over the loading area in the y -axis direction and P is total applied patch loading.

In Eqns. (2.1-2.8), F , v and w are the unknown terms which will be determined in Sections 2.3.2-2.3.4 Then, in Section 2.3.5, the total energy Π (Eqn. (2.1)) will be minimised to obtain the buckling load and the force-displacement relationship in the elastic post-buckling range.

2.3.2 Out-of-Plane Displacement w

The out-of-plane displacement w (Figure 12), is adopted from Khan and Walker's method (1972) and given in Eqn. (2.9). Its shape is close to the experimental observations made during the USyd tests.

$$w = w_1 = q_1 t_w \left(\cos \frac{\pi x}{2A} \right) \left(\cos \frac{\pi y}{2B} + \frac{1}{4} \sin \frac{\pi y}{B} \right) \quad (2.9)$$

In Eqn. (2.9), A is the half-length of the buckling area (Figure 11b), as per (Khan and Walker, 1972), B is the half depth of web plate, t_w is thickness of web plate, and q_1 is the amplitude factor for the deflection w .

2.3.3 Stress Function F

In order to achieve sufficient accuracy in the post-buckling analysis, the stress function will not only include the fundamental term, F_0 , but also the second order term, F_2 . For F_0 , Khan and Walker (1972) suggested the following statically admissible stress field (Eqns (2.10-2.16)),

$$\frac{\partial^2 F_0}{\partial y^2} = \frac{P}{t_w} \left(-\frac{3L}{8B^3} \right) y \left(2 - \frac{C}{L} - \frac{x^2}{CL} \right), \quad |x| \leq C \quad (2.10)$$

$$\frac{\partial^2 F_0}{\partial y^2} = \frac{P}{t_w} \left(-\frac{3L}{4B^3} \right) y \left(1 - \frac{|x|}{L} \right), \quad |x| > C \quad (2.11)$$

$$\frac{\partial^2 F_0}{\partial x^2} = \frac{P}{t_w} \left(-\frac{1}{8C} \right) \left(2 + \frac{3y}{B} - \frac{y^3}{B^3} \right), \quad |x| \leq C \quad (2.12)$$

$$\frac{\partial^2 F_0}{\partial x^2} = 0, \quad |x| > C \quad (2.13)$$

$$\frac{\partial^2 F_0}{\partial x \partial y} = \frac{P}{t_w} \left(\frac{3}{8BC} \right) x \left(1 - \frac{y^2}{B^2} \right), \quad -C \leq x \leq C \quad (2.14)$$

$$\frac{\partial^2 F_0}{\partial x \partial y} = \frac{P}{t_w} \left(\frac{3}{8B} \right) x \left(\frac{y^2}{B^2} - 1 \right), \quad x < -C \quad (2.15)$$

$$\frac{\partial^2 F_0}{\partial x \partial y} = \frac{P}{t_w} \left(\frac{3}{8B} \right) x \left(1 - \frac{y^2}{B^2} \right), \quad x > C \quad (2.16)$$

where C is half the length of applied patch load and L is half the length of web plate.

The second order field stress function F_2 , can be obtained from a perturbation analysis as set out by (Budiansky, 1974). The governing equation can be written as:

$$\nabla^4 F_2 = E \left[\frac{\partial^2 w_1}{\partial x^2} \cdot \frac{\partial^2 w_1}{\partial y^2} - \left(\frac{\partial^2 w_1}{\partial x \partial y} \right)^2 \right] \quad (2.17)$$

By using Eqn. (2.9) for the buckling displacement (w_1), F_2 can be obtained as,

$$F_2 = C_1 \cos \frac{\pi x}{A} + C_2 \cos \frac{\pi y}{B} + C_3 \cos \frac{2\pi y}{B} + C_4 \sin \frac{3\pi y}{2B} + C_5 \cos \frac{\pi x}{A} \sin \frac{\pi y}{2B} \quad (2.18)$$

$$C_1 = \frac{5E q_1^2 t_w^2 A^2}{128 B^2} \quad C_2 = \frac{E q_1^2 t_w^2 B^2}{32 A^2} \quad C_3 = \frac{-E q_1^2 t_w^2 B^2}{2048 A^2}$$

$$C_4 = \frac{E q_1^2 t_w^2 B^2}{162 A^2} \quad C_5 = \frac{E q_1^2 t_w^2}{32 B^2 A^2} \left(\frac{1}{A^2} + \frac{1}{4 B^2} \right)^{-2}$$

2.3.4 Average Displacement over the Loading Area

By integrating the y -axis strain, the displacement of the web plate at the top flange junction can be found as,

$$v_f(x) = \int_{-B}^B \left(\frac{1}{E} \left(\frac{\partial^2 F_0}{\partial x^2} + \frac{\partial^2 F_2}{\partial x^2} - v \frac{\partial^2 F_0}{\partial y^2} - v \frac{\partial^2 F_2}{\partial y^2} \right) - \frac{1}{2} \left(\frac{\partial w_1}{\partial y} \right)^2 \right) dy \quad (2.19)$$

So, the average y -axis displacement at loading area, v , can be obtained as,

$$v = \frac{1}{2C} \int_{-c}^c v_f(x) dx = \frac{B}{2CEt_w} P + \left(\frac{10\pi t_w^2 A \sin\left(\frac{\pi C}{A}\right)}{64BC} + \frac{5\pi^2 t_w^2}{64B} \right) q_1^2 \quad (2.20)$$

By re-arranging Eqn. (2.20), q_1^2 can be expressed in terms of v and P ,

$$q_1^2 = C_{q12} v + C_{q11} P \quad (2.21)$$

$$C_{q12} = \frac{64BC}{5\pi t_w^2 \left(2A \sin\left(\frac{\pi C}{A}\right) + \pi C \right)} \quad (2.22)$$

$$C_{q11} = \frac{-32B^2}{5\pi E t_w^3 \left(2A \sin\left(\frac{\pi C}{A}\right) + \pi C \right)} \quad (2.23)$$

2.3.5 Total Energy and Force-Displacement Relationship

By substituting Eqn. (2.9) into Eqn. (2.2), the web plate bending energy can be obtained:

$$U_b = q_1^2 \frac{E\pi^4 t_w^5 (17B^4 + 40B^2 A^2 + 32A^4)}{6144B^3 A^3 (1 - \nu^2)} = C_{Ub} q_1^2 \quad (2.24)$$

Similarly, by substituting Eqns. (2.9-2.16, 2.18) into Eqns. (2.3-2.6) and integrating Eqn. (2.3) by parts, the web plate membrane strain energy can be simplified to:

$$U_m = C_{Um1} P^2 + C_{Um2} P q_1^2 + C_{Um3} q_1^4 \quad (2.25)$$

Where,

$$C_{Um1} = a_{cum} \left(10702 \left(1 + \nu - C^2 - \frac{C^2 \nu}{3} - \nu CL \right) A^3 B^6 \pi^3 + 5351 \left(1 + \nu - C^2 - \frac{C^2 \nu}{3} - 2.5CL - \nu CL \right) A^5 B^4 \pi^3 + 668.9 \left(1 + \nu - C^2 - \frac{C^2 \nu}{3} - 10CL - \nu CL \right) A^7 B^2 \pi^3 + 6625 A^3 B^8 \pi^3 + 3312 A^5 B^6 \pi^3 + 414.1 A^7 B^4 \pi^3 + 111.5 A^7 C^4 \pi^3 + 278.7 A^{10} C \pi^3 + 10702 (1 + \nu) A^4 B^6 C \pi^3 + 5351 (1.833 + \nu) A^6 B^4 C \pi^3 + 668.9 (4.332 + \nu) A^8 B^2 C \pi^3 - 278.7 A^7 C^3 L \pi^3 + 836.1 A^8 C L^2 \pi^3 + 1784 (C^4 + 2.5 C^3 L) A^3 B^4 \pi^3 + 891.8 A^5 B^2 C^4 \pi^3 - 836.1 A^9 C L \pi^3 + \right) \quad (2.26)$$

$$13377A^4B^4CL^2\pi^3 - 2230A^5B^2C^3L\pi^3 + 6689A^6B^2CL^2\pi^3)$$

$$C_{Um2} = a_{cum} \left(-26754 \left((1 + \nu) \sin\left(\frac{c\pi}{A}\right) + \nu \right) A^6 B^4 E t_w^3 + 293.6(1 + \nu) AB^8 CE t_w^3 \pi + 146.8(1 + \nu) A^3 B^6 CE t_w^3 \pi + 13396 \left(1 + \nu + 2(1 + \nu) \cos\left(\frac{c\pi}{A}\right) \right) A^5 B^4 CE t_w^3 \pi \right) \quad (2.27)$$

$$C_{Um3} = \frac{a_{cum}(3.402A^8 CE^2 t_w^6 \pi^7 + 41.85B^8 CE^2 t_w^6 \pi^7 + 20.93A^2 B^6 CE^2 t_w^6 + 74.47A^4 B^4 CE^2 t_w^6 \pi^7 + 27.22A^6 B^2 CE^2 t_w^6 \pi^7)}{a_{cum}} \quad (2.28)$$

$$a_{cum} = 1/2230A^3B^3CEt_w\pi^3(4B^2 + A^2)^2$$

By substituting Eqn. (2.19) into Eqn. (2.7), the flange bending energy can be obtained:

$$U_f = q_1^4 \frac{25b_f E \pi^8 t_w^7}{24576 B^2 L^3} = C_{Uf} q_1^4 \quad (2.29)$$

Similarly, by substituting Eqn. (2.20) into Eqn. (2.8), the work done by the applied patch load can be obtained:

$$W_p = \frac{B}{2CEt_w} P^2 + \left(\frac{5\pi t_w^2 A \sin\left(\frac{\pi C}{L}\right)}{32BC} + \frac{5\pi^2 t_w^2}{64B} \right) q_1^2 P = C_{WP1} P^2 + C_{WP2} q_1^2 P \quad (2.30)$$

By substituting Eqns. (2.24-2.30) into eqn. (2.1), the total energy of the system can be re-written as:

$$\Pi = C_{Ub} q_1^2 + C_{Um1} P^2 + C_{Um2} P q_1^2 + C_{Um3} q_1^4 + C_{Uf} q_1^4 - C_{WP1} P^2 - C_{WP2} q_1^2 P \quad (2.31)$$

By applying the principle of stationary energy for Π with respect to q_1 and then substituting Eqn. (2.21) for q_1^2 , the buckling load and the elastic post-buckling force-displacement relationship can be obtained:

$$P = K_{p-b} \nu + P_{cr} \quad (2.32)$$

$$K_{p-b} = - \frac{2(C_{Um3} + C_{Uf})C_{q12}}{C_{Um2} - C_{WP2} + 2(C_{Um3} + C_{Uf})C_{q11}} \quad (2.33)$$

$$P_{cr} = - \frac{C_{Ub}}{C_{Um2} - C_{WP2} + 2(C_{Um3} + C_{Uf})C_{q11}} \quad (2.34)$$

where K_{p-b} is the elastic post-buckling stiffness and P_{cr} is buckling load.

2.3.6 Inelastic Post-Buckling Stiffness

In the inelastic post-buckling range, the post-buckling stiffness gradually reduces due to material yielding. This gradual yielding bending behaviour can be modelled using a simplified model in which a reduced Young's modulus, E_y (Eqn. (2.35)) is substituted for the elastic Young's modulus in the elastic post-buckling analysis (Zhu, 2016).

$$E_y = \frac{5}{18} E \quad (2.35)$$

The reduction factor (5/18) applied to the elastic modulus was found by trial and error and found to reasonably accurately capture the integral effect of yielding on the moment-rotation curve for a wide range of configurations of bolted end-plate connections.

2.3.7 Ultimate Strength and Corresponding Displacement

The provisions of Eurocode 3 allow the ultimate strength P_u to be easily predicted with adequate accuracy. Its corresponding displacement can then be calculated using the elastic and inelastic post-buckling stiffnesses. The point at the end of the elastic post-buckling range is defined as the yield point. In the proposed method, it is assumed that elastic post-buckling dominates the first two thirds of the post-buckling range. By this assumption, the displacement at the yield point v_y can be obtained as,

$$v_y = \frac{2(P_u - P_{cr})}{3K_{p-b}} \quad (2.36)$$

After the yield point, the inelastic post-buckling stiffness applies to the remaining one third of the post-buckling range. The displacement v_u corresponding to the ultimate load point P_u can be obtained as,

$$v_u = v_y + \frac{(P_u - P_{cr})}{3K_{p-b,y}} \quad (2.37)$$

where $K_{p-b,y}$ is the inelastic post-buckling stiffness.

2.3.8 Post-Ultimate Behaviour

After the applied patch load reaches the ultimate load of the column web component, the web will collapse under decreasing load. This collapse behaviour usually progresses gradually and is associated with folding of the column web and bending of the top flange (Figure 13). In order to model this behaviour, a new model, which is based on Roberts' mechanism model (Shahabian and Roberts, 1999), is proposed.

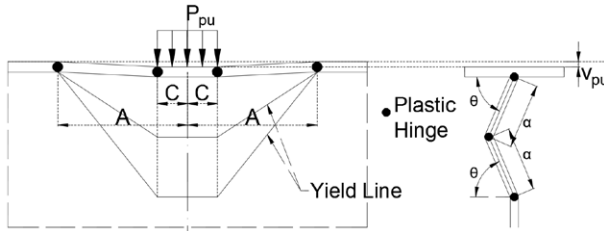


Figure 13: Collapse Model in Post-ultimate Range

Based on the virtual work method introduced by Shahabian and Roberts (1999), the incremental post-ultimate resistance and displacement can be expressed in terms of the angle of web folding, θ (Eqns. (2.38-2.39) and Figure 13).

$$P_{pu} = P_u + (4A + 4t_f)M_w \left(\frac{1 - \eta_{\theta + \Delta\theta}}{\alpha \cos(\theta + \Delta\theta)} - \frac{1 - \eta_{\theta}}{\alpha \cos\theta} \right) \quad (2.38)$$

$$\eta_\theta = \frac{t_w}{t_w + 2\alpha \cos \theta} \qquad \eta_{\theta+\Delta\theta} = \frac{t_w}{t_w + 2\alpha \cos(\theta + \Delta\theta)}$$

$$v_{pu} = v_u + 2\alpha[\sin \theta + \sin(\theta + \Delta\theta)] \qquad (2.39)$$

where, P_{pu} is the resistance in the post buckling range, v_{pu} is the displacement corresponding to P_{pu} and M_w is plastic moment per unit length of the web plate.

Based on the experimental observations made during the USyd tests, half the depth of the folding web, α , can be defined as the distance from the top edge of the web to the maximum deflection point. It can therefore be obtained by equating the first derivative of the deflection function (Eqn. (2.39)) to zero,

$$\alpha = 0.76143667B \approx \frac{3}{4}B. \qquad (2.40)$$

The initial angle of the folding web θ_0 can be defined as:

$$\theta_0 = \text{asin}\left(1 - \frac{v_u}{2\alpha}\right) \qquad (2.41)$$

Starting from $\theta = \theta_0$, the post-ultimate curve can be obtained by solving Eqns. (2.38-2.39).

2.3.9 Comparison with Test Results

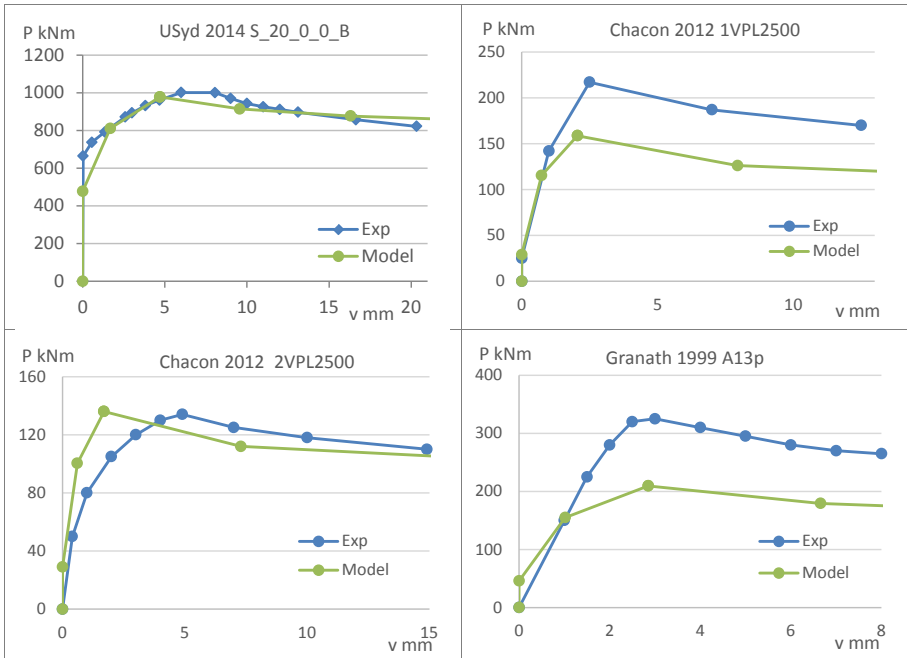


Figure 14: Comparison between the presented model and experiments.

Three sets of experimental data are compared to predictions obtained using the presented model for the column web plate. The tests include those conducted at the University of Sydney (Zhu, 2016) and those reported by Granath and Lagerqvist (1999) and Chacón et al. (2013). The presented model is seen to be in reasonable agreement with the experiments (Figure 14).

SECTION 3: COMPONENT MODEL VALIDATION

3.1 End-plate Connection Tests

Six bolted moment end-plate connections from the USyd tests (Zhu, 2016) and Girão Coelho et al. (2004) are analysed by proposed component model for predicting the full range moment-rotation curve and failure modes. The specimen properties are summarised in Tables 2-8, and the comparison between model predictions and experimental results are shown in Section 3.2.

Table 2: Column and Beam Sections

Test	Column		Beam	
	Profile	Steel Grade	Profile	Steel Grade
S10_0_0	310UC 96.8	AS 350	310UB 46.2	AS 350
S10_0_0_B	310UC 96.8	AS 350	310UB 46.2	AS 350
S20_0_0_B	310UC 96.8	AS 350	310UB 46.2	AS 350
FS1a/b	HE340M	EN S355	IPE300	EN S235
FS2a/b	HE340M	EN S355	IPE300	EN S235
FS3a/b	HE340M	EN S355	IPE300	EN S235

Table 3: End-plates

Test	End-plate			
	Width (mm)	Height (mm)	Thickness (mm)	Steel Grade
S10_0_0	270	400	10	AS 350
S10_0_0_B	270	400	10	AS 350
S20_0_0_B	270	400	20	AS 350
FS1a/b	150	400	10	EN S355
FS2a/b	150	400	15	EN S355
FS3a/b	150	400	20	EN S355

Although there were 13 tests in the USyd tests series, only three “standard” tests were modelled, referred to as S10_0_0, S10_0_0_B and S20_0_0_B. They all employed a standard rig in which the loading direction was in-plane and perpendicular to the specimen beam. The other 10 tests employed non-standard loading arrangements including bi-axial bending, lateral bending and combined axial load and bending. The

non-standard loading arrangements are not considered in the proposed component model and hence no comparisons between these tests and model predictions are made.

The three standard USyd tests employed a relatively small column to assess the effects from column web buckling on the compression face, and large, strong bolts to allow large end-plate bending deformations on the tension face. By varying the thickness of the end-plates, two failure modes, end-plate bending and column web buckling, could be achieved. Specimen S10_0_0 employed a 10mm end-plate that is vulnerable to bending. Similarly, specimen S10_0_0_B also employed a 10mm end-plate, but with 20mm backing plates on the column flange bending component to reduce the deformation of that component. Since the 10mm end-plates were susceptible to bending, both of these tests suffered large end-plate bending deformation, and eventual cracking in the heat affected zone (HAZ) at the weld toe at failure. On the other hand, specimen S20_0_0_B employed a 20mm end-plate with 20mm backing plates on the column flange bending component. Therefore, its tension face was rigid and failure occurred on the compression face due to column web buckling.

On the contrary, Girão Coelho et al. (2004) employed a strong column and medium size bolts. The strong column used in these tests was a rigid component and little deformation was observed in each test. Therefore, the tests all failed at the tension face by either end-plate bending or bolt fracture. Specimens FS1a and FS1b were nominally identical tests employing 10mm end-plates. They both failed due to end-plate bending. Specimens FS2a and FS2b were also nominally identical tests, in this case employing 15mm end-plates. They both failed due to combined end-plate bending and bolt fracture. Specimens FS3a and FS3b were nominally identical tests employing 20mm end-plates. They both failed due to bolt fracture. In combination, the Usyd and Girao Coelho tests featured all the common failure modes of the bolted moment end plate connection.

Table 4: Bolt Hole Positions (mm), (refer to Figure 15 for nomenclature)

Tests	e_{ep}	e_{cf}	e_x	m	m_2	m_x	α^a	w	p
S10_0_0	65	82.5	36	61.7	25.6	25.6	7.2	140	203
S10_0_0_B	65	82.5	36	61.7	25.6	25.6	7.2	140	203
S20_0_0_B	65	82.5	36	61.7	25.6	25.6	7.2	140	203
FS1a/b	30	109.5	30	38.25	34.85	34.85	5.35	90	205
FS2a/b	30	109.5	30	38.25	34.85	34.85	5.35	90	205
FS3a/b	30	109.5	30	38.25	34.85	34.85	5.35	90	205

^a α is a correlation factor for the effective length of the inner end-plate bending component. It can be obtained from figure 6.11 of Eurocode3 (2006b)

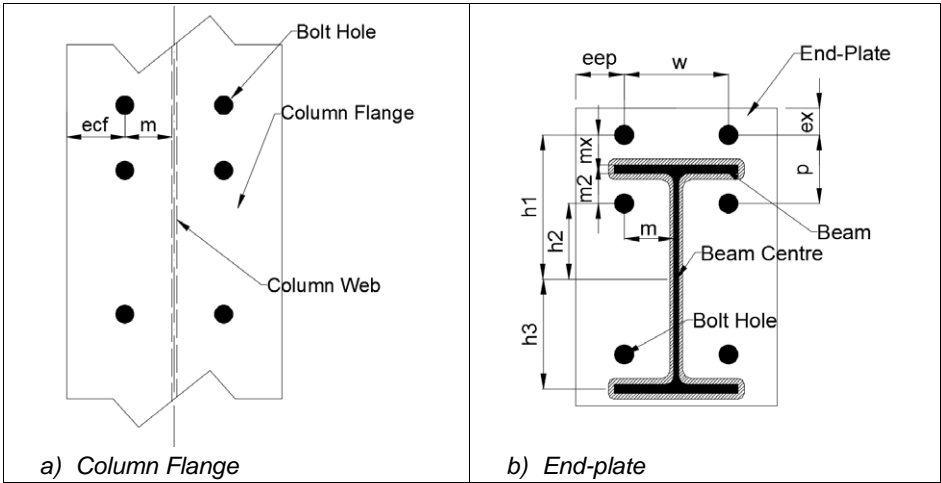


Figure 15: Bolt-Hole Position and Height of Spring Rows

Table 5: Bolts and Welds (mm), (t_w and t_f are the leg lengths of web and flange fillet welds, respectively)

Test	Bolt		Bolt Hole d_{bh}	Welds	
	Bolt Size	Bolt Grade		t_w	t_f
S10_0_0	M24	8.8	26	6	8
S10_0_0_B	M24	8.8	26	6	8
S20_0_0_B	M24	8.8	26	6	8
FS1a/b	M20	8.8	22	4	6
FS2a/b	M20	8.8	22	4	6
FS3a/b	M20	8.8	22	4	6

Table 6: Height of Each Spring Row, (Distances are measured from the centroid of the beam, see Figure 15)

Test	h_1	h_2	h_3
S10_0_0	193.5	103.5	-147.5
S10_0_0_B	193.5	103.5	-147.5
S20_0_0_B	193.5	103.5	-147.5
FS1a/b	192.5	102.5	-147.5
FS2a/b	192.5	102.5	-147.5
FS3a/b	192.5	102.5	-147.5

Table 7: Mechanical Properties for Columns and Beams (MPa)

Test	Column		Beam	
	f_y	f_u	f_y	f_u
S10_0_0	396	512	396	512
S10_0_0_B	396	512	396	512
S20_0_0_B	396	512	396	512
FS1a/b	335	530	316.24	462.28
FS2a/b	335	530	316.24	462.28
FS3a/b	335	530	316.24	462.28

Table 8: Mechanical Properties for End-plates, Bolts and Welds (MPa)

Test	End-plate		Bolt		Welds
	f_y	f_u	f_y	f_u	f_u
S10_0_0	429	556	640	830	480
S10_0_0_B	429	556	640	830	480
S20_0_0_B	429	556	640	830	480
FS1a/b	340.12	480.49	856	914	480 ^a
FS2a/b	340.12	480.49	856	914	480 ^a
FS3a/b	340.12	480.49	856	914	480 ^a

^a According to Girão Coelho et al. (2004), the welds used for specimens FS1a/b, FS2a/b and FS3a/b were full strength 45°-continuous fillet welds, and basic, soft and low hydrogen electrodes used for the welding process. However, specification of the electrodes was not provided. Since basic, soft and low hydrogen electrodes used also used for the USyd tests, it is assumed that the weld ultimate strength of the Girão Coelho tests is the same as that used for the USyd tests.

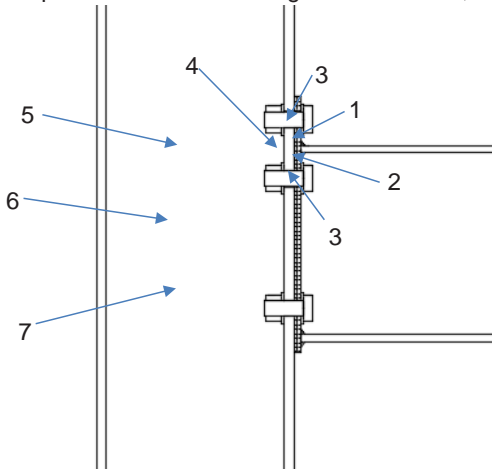
3.2 Model Predictions

By using the connection properties specified in Tables 2-8, models for the individual components can be obtained. Linear models for bolts, column flange in tension and column web shear panel are obtained from Eurocode3 (2006b). A full range model for the column web in compression is obtained using the model presented in Section 2. Full range models for end-plate bending and column flange bending components are obtained using Swanson's T-stub model (Swanson and Leon, 2001).

The full range models can be simplified into bi-linear and tri-linear models. The end-plate bending component model is represented by a bi-linear model in which fracture occurs at the ultimate load (Figure 17a). On the other hand, the column web in compression component is represented by tri-linear model because of its ductile behaviour in the post-ultimate range (Figure 17b).

By converting full range component models (multi-linear models) to bi-linear or tri-linear models, as applicable (Figure 17), the input data (elastic, plastic and softening stiffness and corresponding critical loads) for each spring model (Section 1) can be obtained (Tables 9-14). Note that since Girão Coelho et al.'s tests (Girão Coelho et al., 2004)

employed an oversized column (*Table 2*), the column web in tension and column web in compression components behaved extremely rigidly. For this reason, the stiffnesses for these two column components are set to be rigid for tests FS1, FS2 and FS3.



1. Outer End-Plate Bending
2. Inner End-Plate Bending
3. Bolt in Tension
4. Column Flange Bending
5. Column Web in Tension
6. Column Web Shear Panel
7. Column Web in Compression

Figure 16: End-Plate Joint and the Components It Contains

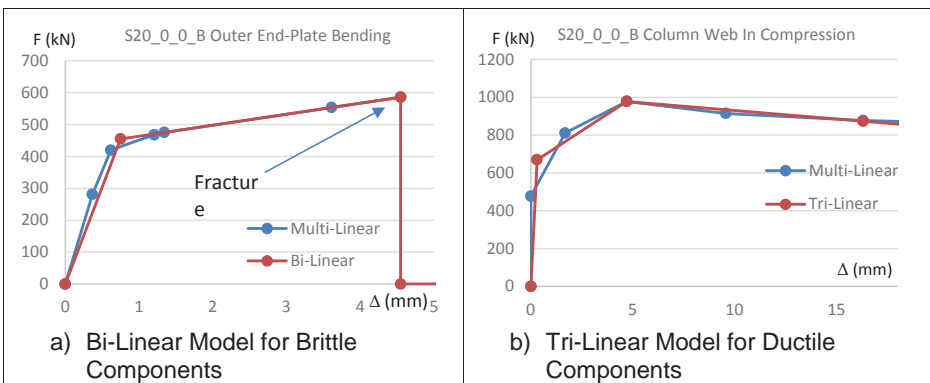


Figure 17: Examples of Converting Multi-Linear Models to Bi-Linear/Tri-Linear Models

Table 9: Specimen S10_0_0 (See Figure 16 for Component No.)

Row	Component	h (mm)	k_e (N/mm)	k_p (N/mm)	k_s (N/mm)	P_p^C (N)	P_s^C (N)
1	1 and 3	193.5	4.40E05	5.78E04	-	2.20E05	3.89E05
1	4 and 3	193.5	1.00E05	6.55E03	-	1.20E05	5.86E05
1	5	193.5	8.79E05	-	-	-	-
2	2 and 3	103.5	6.29E05	3.59E04	-	4.40E05	5.86E05
2	4 and 3	103.5	1.00E05	6.55E03	-	1.20E05	5.86E05
2	5	103.5	8.79E05	-	-	-	-
3	7	-147.5	2.23E06	7.01E04	-9.03E03	6.70E05	9.79E05
3	6	-147.5	9.61E05	-	-	-	-

Table 10: Specimen S10_0_0_B (See Figure 16 for Component No.)

Row	Component	h (mm)	k_e (N/mm)	k_p (N/mm)	k_s (N/mm)	P_p^C (N)	P_s^C (N)
1	1 and 3	193.5	4.40E05	5.78E04	-	2.20E05	3.89E05
1	4 and 3	193.5	1.14E05	9.54E03	-	1.60E05	5.86E05
1	5	193.5	8.79E05	-	-	-	-
2	2 and 3	103.5	6.29E05	3.59E04	-	4.40E05	5.86E05
2	4 and 3	103.5	1.14E05	9.54E03	-	1.60E05	5.86E05
2	5	103.5	8.79E05	-	-	-	-
3	7	-147.5	2.23E06	7.01E04	-9.03E03	6.70E05	9.79E05
3	6	-147.5	9.61E05	-	-	-	-

Table 11: Specimen S20_0_0_B (See Figure 16 for Component No.)

Row	Component	h (mm)	k_e (N/mm)	k_p (N/mm)	k_s (N/mm)	P_p^C (N)	P_s^C (N)
1	1 and 3	193.5	6.07E05	3.45E04	-	4.55E05	5.89E05
1	4 and 3	193.5	1.14E05	9.54E03	-	1.60E05	5.86E05
1	5	193.5	8.79E05	-	-	-	-
2	2 and 3	103.5	9.28E05	2.50E05	-	4.52E05	5.86E05
2	4 and 3	103.5	1.14E05	9.54E03	-	1.60E05	5.86E05
2	5	103.5	8.79E05	-	-	-	-
3	7	-147.5	2.23E06	7.01E04	-9.03E03	6.70E05	9.79E05
3	6	-147.5	9.61E05	-	-	-	-

Table 12: Specimen FS1a/b, (mean values of a- and b-tests; See Figure 16 for Component No.)

Row	Component	h (mm)	k_e (N/mm)	k_p (N/mm)	k_s (N/mm)	P_p^c (N)	P_s^c (N)
1	1 and 3	192.5	1.00E05	7.82E03	-	5.00E04	2.16E05
1	4 and 3	192.5	5.79E05	8.72E04	-	4.19E05	4.48E05
1	5	192.5	Rigid	-	-	-	-
2	2 and 3	102.5	1.50E05	1.25E04	-	1.50E05	4.48E05
2	4 and 3	102.5	5.79E05	8.72E04	-	4.19E05	4.48E05
2	5	102.5	Rigid	-	-	-	-
3	7	-147.5	Rigid	-	-	-	-
3	6	-147.5	Rigid	-	-	-	-

Table 13: Specimen FS2a/b, (mean values of a- and b-tests; See Figure 16 for Component No.)

Row	Component	h (mm)	k_e (N/mm)	k_p (N/mm)	k_s (N/mm)	P_p^c (N)	P_s^c (N)
1	1 and 3	192.5	1.77E05	1.72E04	-	1.10E05	3.24E05
1	4 and 3	192.5	5.73E05	8.92E04	-	4.30E05	4.48E05
1	5	192.5	Rigid	-	-	-	-
2	2 and 3	102.5	2.07E05	1.59E04	-	3.00E05	4.48E05
2	4 and 3	102.5	5.73E05	8.92E04	-	4.30E05	4.48E05
2	5	102.5	Rigid	-	-	-	-
3	7	-147.5	Rigid	-	-	-	-
3	6	-147.5	Rigid	-	-	-	-

Table 14: Specimen FS3a/b, (mean values of a- and b-tests; See Figure 16 for Component No.)

Row	Component	h (mm)	k_e (N/mm)	k_p (N/mm)	k_s (N/mm)	P_p^c (N)	P_s^c (N)
1	1 and 3	192.5	1.39E05	1.66E04	-	2.50E05	4.32E05
1	4 and 3	192.5	5.52E05	8.31E04	-	4.20E05	4.48E05
1	5	192.5	Rigid	-	-	-	-
2	2 and 3	102.5	3.18E05	1.58E04	-	3.50E05	4.48E05
2	4 and 3	102.5	5.52E05	8.31E04	-	4.20E05	4.48E05
2	5	102.5	Rigid	-	-	-	-
3	7	-147.5	Rigid	-	-	-	-
3	6	-147.5	Rigid	-	-	-	-

The ultimate strength of the end-plate bending component is determined by the initiation of cracking, which usually occurs in the HAZ of the end-plate, and is a function of the

strength of the welding material. A simplified method to determine the ultimate strength when major cracking occurs is proposed:

$$F_{T,cr} = 0.6t_{ep}l_{eff}f_{uW} \quad (3.1)$$

in which t_{ep} is the end-plate thickness, l_{eff} is effective length obtained from Eurocode 3 (2006b) and f_{uW} is the ultimate tensile strength of the welds.

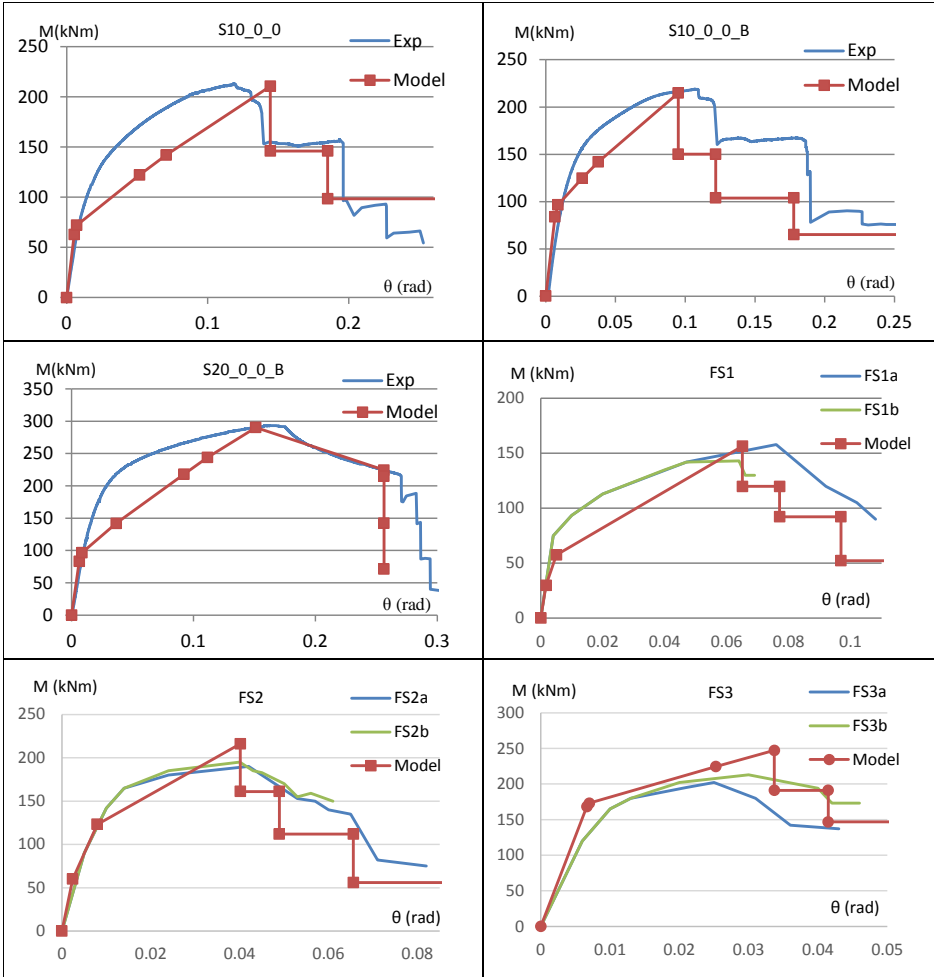


Figure 18: Model Predictions vs Experimental Results

By applying the spring models for each of the individual components, the component models for the six end-plate connections can be obtained. *Figure 18* shows the model predictions and experimental results. The presented models are seen to be in reasonable agreement with the experiments.

In addition, the component fracture sequence can be obtained (*Tables 15-17*). The fracture sequence predictions for specimens S10_0_0 and S20_0_0_B are accurate. The predictions for the FS1 and FS3 test series are roughly correct as seen by comparing the failure modes of each test in each series. For the FS2 series, the prediction for the second stage fracture is slightly different from the experimental observation. In the second fracture stage of FS2, the 1st row end-plate bending failure occurs slightly earlier in the model prediction than the 2nd row bolt failure observed in the test. For this connection geometry, a small variation in material property may cause a different fracture sequence. For specimen S10_0_0_B, the 2nd stage and 3rd stage predictions do not agree with the experimental results. The actual failure in these two stages was a mixture of the beam flange pulling out (*Figure 19b*), end-plate bending and bolt fracture where the beam flange pulling out fracture mechanism is not included in the model. However, the fracture rows in these two stages roughly agree with the experimental observation.

3.3 Summary

The presented full range component model is shown to be in reasonable agreement with experiments for the ultimate moment and the moment-rotation curves in the elastic, inelastic and post-ultimate ranges. Moreover, the presented model predictions of the component fracture sequence are seen to be in good agreement with experimental observations. It was demonstrated that some improvement can be achieved by including the fracture of the HAZ zone in the model as this dominates the end-plate bending behaviour in the large deformation range.

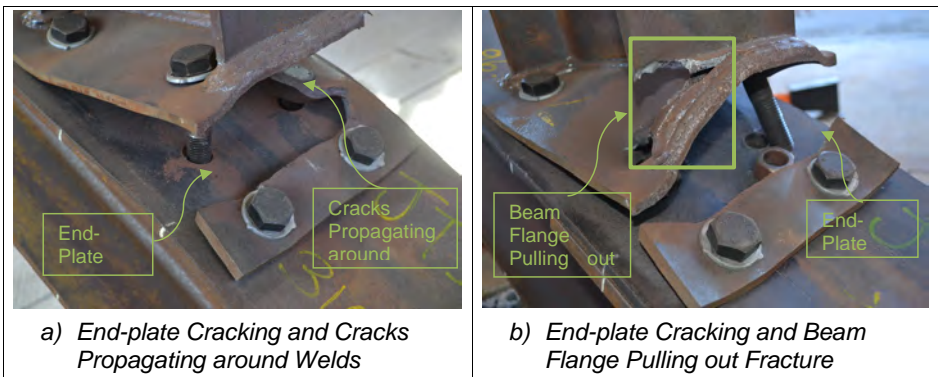


Figure 19: the End-Plate Failure Modes: a) S10_0_0 and b) S10_0_0_B

Table 15: First stage fracture prediction

Tests	1 st Stage Fracture Component	
	Model Predictions	Experimental Results
S10_0_0	Half End-plate in Row 1 Cracking	Half End-plate in Row 1 Cracking
S10_0_0_B	Half End-plate in Row 1 Cracking	Half End-plate in Row 1 Cracking
S20_0_0_B	Row 3, Column Web Buckling	Row 3, Column Web Buckling
FS1a/b	Half End-plate in Row 1 Cracking	Row 1 End-plate Cracking
FS2a/b	Half End-plate in Row 1 Cracking	Row 2 Bolt Failure /Row 1 End-Plate Cracking
FS3a/b	One Bolt in Row 2 Failure	Both Bolts in Row 2 Failure

Table 16: Second stage fracture prediction

Tests	2 nd Stage Fracture Component	
	Model Predictions	Experimental Results
S10_0_0	All End-plate in Row 1 Cracking	All End-plate in Row 1 Cracking
S10_0_0_B	All End-plate in Row 1 Cracking	Row 2 Bolt Stripping /Row 1 End-plate Cracking
S20_0_0_B	One Bolt in Row 1 Failure	One Bolt in Row 1 Failure
FS1a/b	All End-plate in Row 1 Cracking	-
FS2a/b	All End-plate in Row 1 Cracking	Row 2 Bolt Failure /Row 1 End-Plate Cracking
FS3a/b	The Other Bolt in Row 2 Failure	Both Bolts in Row 2 Failure

Table 17: Third stage fracture prediction

Tests	3 rd Stage Fracture Component	
	Model Predictions	Experimental Results
S10_0_0	Half End-plate in Row 2 Failure	Half End-plate in Row 2 Cracking
S10_0_0_B	Half End-plate in Row 2 Failure	Beam Flange Pulling out
S20_0_0_B	The Other Bolt in Row 1 Failure	The Other Bolt in Row 1 Failure
FS1a/b	One Bolt in Row 2 Failure	-
FS2a/b	One Bolt in Row 2 Failure	-
FS3a/b	One Bolt in Row 1 Failure	-

CONCLUSIONS

The paper presents a method to extend the Component Method to the post-ultimate range and thus enables the full range moment-rotation relationship of steel joints to be predicted. It accounts for fracture of the individual components and can generate the fracture sequence of the connection including the overall connection ductility, i.e.

rotation at full fracture. The method can be used to create spring models with any number of springs and does not cause numerical difficulties in solving the derived equations. The method is potentially applicable to all types of joints.

As an example of the application of the model, six bolted moment end-plate connections were modelled by the proposed method and compared to the experimental results. For each end-plate connection, both the full range moment-rotation behaviour and component fracture sequences were predicted with good accuracy. The comparison included all likely failure modes of bolted end-plate connections.

REFERENCES

- BUDIANSKY, B. 1974. Theory of Buckling and Post-Buckling Behavior of Elastic Structures. *Advances in Applied Mechanics*, 14, 1-65.
- CHACÓN, R., MIRAMBELL, E. & REAL, E. 2013. Transversally stiffened plate girders subjected to patch loading. Part 1. Preliminary study. *Journal of Constructional Steel Research*, 80, 483-491.
- DA SILVA, L. S. & GIRAO COELHO, A. M. 2001. A ductility model for steel connections. *Journal of Constructional Steel Research*, 57, 45-70.
- DA SILVA, L. S., GIRAO COELHO, A. M. & NETO, E. L. 2000. Equivalent post-buckling models for the flexural behaviour of steel connections. *Computers & Structures*, 77, 615-624.
- EUROCODE3 2006a. EN 1993-1-5: Plated Structure Elements. *Eurocode 3: Design of steel structures*.
- EUROCODE3 2006b. EN 1993-1-8: Design of joints. *Eurocode 3: Design of steel structures*.
- GIRÃO COELHO, A. M., BIJLAARD, F. S. K. & SIMÕES DA SILVA, L. 2004. Experimental assessment of the ductility of extended end plate connections. *Engineering Structures*, 26, 1185-1206.
- GRANATH, P. & LAGERQVIST, O. 1999. Behaviour of girder webs subjected to patch loading. *Journal of Constructional Steel Research*, 50, 49-69.
- KHAN, M. Z. & WALKER, A. C. 1972. Buckling of plates subjected to localised edge loading. *The Structural Engineer*, 50, 225-232.
- LEWIS, K. 2010. The component method of joints. *Master thesis, School of Civil Engineering, University of Sydney, Sydney, Australia*.
- SHAHABIAN, F. & ROBERTS, T. M. 1999. Buckling of slender web plates subjected to combinations of in-plane loading. *Journal of Constructional Steel Research*, 23.
- SWANSON, J. A. & LEON, R. T. 2001. Stiffness Modeling of Bolted T Stub Connection Components. *Journal of Structural Engineering*, 127, 498-505.
- ZHU, C. 2016. Full Moment Rotation Behaviour of Steel Structural Joints. *Ph.D. dissertation, School of Civil Engineering, University of Sydney, NSW, Australia [In Preparation]*.

A NUMERICAL STUDY ON THE INFLUENCE OF SKEW AND SLOPE ON RBS AND WUF-W CONNECTIONS

Kevin E. Wilson
Structural Affiliates International Inc., Nashville, Tennessee 37205, USA
kwilson@saii.com

Gian A. Rassati
University of Cincinnati, Cincinnati, Ohio 45221, USA
gian.rassati@uc.edu

James A. Swanson
University of Cincinnati, Cincinnati, Ohio 45221, USA
james.swanson@uc.edu

ABSTRACT

Connections in intermediate and special moment frames for seismic resistance can be readily selected from a set of prequalified details that is based by far and large on experimental testing of specimens with orthogonal beam-to-column connection configuration. Architects often choose moment resisting frames for their unobtrusiveness and sometime push common conventions by prescribing beam-to-column connections that have beams framing at odd angles to the columns, either in plan or in elevation. In the absence of explicit guidance from the standards, engineers are often forced to require qualification testing of such non-orthogonal connections, in order to ensure their applicability within the limits of the specifications. This study expands on a scant body of knowledge in this matter, considering numerical simulations of two popular prequalified beam-to-column configurations and examining their response as the skew angle or the slope angle of the beam varies from 0° to 45° . Detailing considerations are made and recommendations are presented for each connection configuration indicating when more in-depth studies are advisable as the skew or slope angles increase.

INTRODUCTION AND BACKGROUND

Steel moment resisting frames (MRFs) are widely used lateral force resisting systems for seismic areas. Architects appreciate the expressive latitude provided by this unobtrusive system, which affords wide open floor spaces with minimal impact in elevation, and are often pushing the limits of this system by envisioning structures that require beams to frame into columns at angles other than 90° , either in plan (skewed connections), or in elevation (sloped connections), or both. On the other hand, structural designers are

bound by ANSI/AISC 341 (2010) to either select a moment connection detail from a set of prequalified connections prescribed in ANSI/AISC 358 (2010) and its supplements (2011, 2014) or to perform qualification testing of other connection details following the requirements of Chapter K of ANSI/AISC 341 (2010). The prequalified connections implicitly assume that beams and columns form right angles with respect to each other both in plan and in elevation, as they are based on collections of experimental results that invariably have been obtained from specimens with orthogonal configurations. Only in the upcoming 2016 edition of ANSI/AISC 358 there will be some commentary language suggesting some limits to the skew angle and to the slope angle of a beam framing into a column, based chiefly on two extant studies: Prinz and Richards (2015) and Ball et al. (2010).

In 2015, Prinz and Richards performed an analytical-only study focused on Reduced Beam Section (RBS) connections in skewed configurations. As part of the study, the researchers considered three beam and column combinations: W14x132 columns connected to W24x131 beams, W18x86 columns with W24x131 beams, and W31x173 columns with W36x150 beams. The skew angles considered were of 0, 10, 20, and 30°. The researchers concluded that the presence of skew causes columns to undergo a twisting deformation that increases with the increase of the skew angle. Interestingly, large skew angles which cause large column twists are also connected to a reduced demand in the RBS region of the beam, leading to a better response at high deformations. Skew angles up to 10° do not lead to a much different behavior than that of an orthogonal connection. The researchers recognized that the published study is not completely adequate to draw general conclusions on the effects of skew in RBS connections.

Ball et al. (2010), followed by Kim et al. (2010), Ball (2011), and Kim et al. (2016) report on the results of a qualification testing and ancillary studies performed during the design of the LAX airport Tom Bradley International Terminal, which contains beam-to-column RBS connections in which the beams are sloped at 28° with respect to the horizontal. The qualification testing proved compliance with the requirements of ANSI/AISC 341 (2010), although the researchers noted how the failure of the connection took place in a mode that had never been witnessed for an RBS detail. Further numerical studies brought the researchers to identify stress concentrations near the heel of the connection which ultimately led to fracture, although fracture took place after the prescribed 40mrad of rotation. Additionally, the researchers recommended that the RBS cut be made perpendicular to the beam section (unequal distance of the RBS cut from the column face) instead of parallel to the column section (equal distance of the RBS cut from the column flange measured perpendicularly to the column), in order to limit the additional strain demands at the heel of the connection. Additionally, the researchers recommended that a more thorough study be conducted to arrive to a holistic set of recommendations for non-orthogonal configurations.

In 2015, Wilson published what is the foundation for the study presented in this paper, expanding on the state-of-the-art by investigating numerical approaches to the high-definition simulation of both skewed and sloped beam-to-column connections using RBS and Welded Unreinforced Flange – Welded Web (WUF-W) details. The present paper

builds on the preliminary results of that study, reporting on the response of RBS and WUF-W connections at slope or skew angles of 0° through 45° in 5° increments. The orthogonal configurations match experimental specimens in literature, for validation and comparison purposes, and the results from the non-orthogonal configurations are then compared to those baselines for the sake of consistency. The paper will discuss the modeling approach and the validation study, followed by a presentation of the analytical results for skewed and sloped configurations of the two connection details chosen. Conclusions and recommendations will follow.

MODELING AND VALIDATION

The RBS and WUF-W configurations that were chosen for the baseline model with a beam framing orthogonally into the column were taken from the literature background that was originally used by AISC's Connection Prequalification Review Panel (CPRP) to prequalify those details for use in intermediate and special moment frames.

The RBS experimental test chosen was reported in Engelhardt et al. (1998) and indicated as specimen DB4, consisting of a W36x194 beam framing into a W14x426 column. The experimental test of the WUF-W detail was recently reported in Morrison et al. (2012), consisting of a W30x148 beam framing into a W14x257 column.

Both experimental tests have been modeled in ABAQUS (2014) in three dimensions using 8 node brick elements with reduced integration and hourglass control as the mainstay finite element of choice. The whole column and beam, including connecting elements such as bolts and shear tabs have been modeled, and restraints compatible with those used experimentally have been applied. Welds were not modeled explicitly in this study, but multi-point constraints were used to positively connect elements together where welds were used. A monotonic analysis was performed, including material and geometric nonlinearities, by applying a displacement equal to the largest experimental displacement to the appropriate location near the tip of the beam, and results were compared against the experimental moment-rotation curves, as shown in Figure 1.

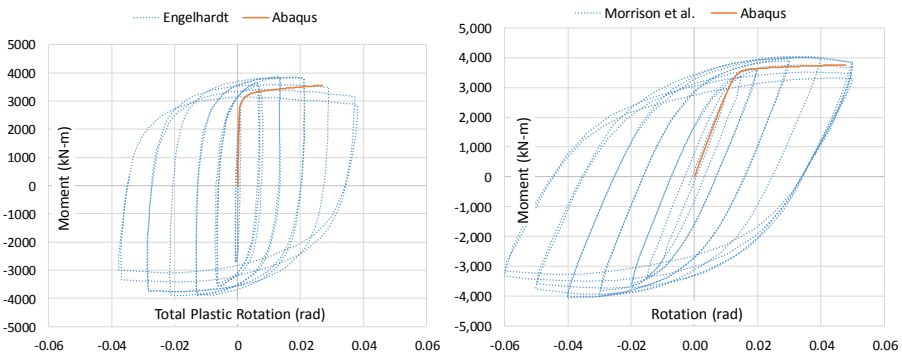


Figure 1. Response comparison between analytical modeling and physical testing. Moment vs. Plastic Rotation for RBS (left) and Moment vs. Rotation for WUF-W (right)

In both cases, the numerical simulation is successful in predicting the elastic stiffness of the experimental specimens, as well as their yielding and post-yielding behavior as well as in reproducing their experimentally observed response up to failure. Overall, the accuracy of the prediction was deemed satisfactory for the purpose of examining the difference in demands and response when modifying the skew or slope angle of the beam. In particular, the equivalent plastic strain demands were carefully studied for the purpose of highlighting the differences in the non-orthogonal configurations.

NUMERICAL RESULTS

Overall, two response measures were investigated in this study: the moment-rotation response of the connection and the evolution of the equivalent plastic strains. The former provides information on the effects of skew and slope angles on connection stiffness and capacity. The latter was investigated with attention to the distribution of strain demands and their potential migration closer to demand-critical welds, column webs, and other sensitive locations of the connection region. The results in this section are presented first for the RBS configurations, followed by those for the WUF-W configurations.

RBS Connections.

For RBS connections, a further subdivision of the test matrix was performed to account for differences in behavior depending on whether the RBS cut is produced parallel to the column or perpendicular to the beam, for both skewed and sloped configurations. The different configurations are shown in Figure 2 for skewed connections and in Figure 3 for sloped connections. There is no guidance in ANSI/AISC 358 (2010) as to how to detail the RBS cut for a non-orthogonal configuration, so in principle both details are acceptable for the purposes of the present study: consequently, configurations with both details were simulated for all the cases of skew and slope that were considered.

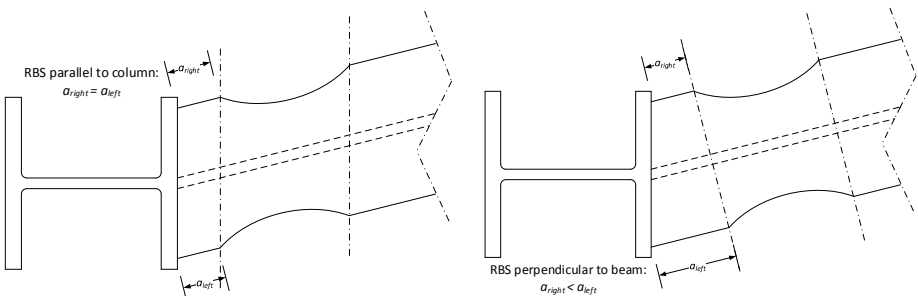


Figure 2. Configurations of RBS cut for skewed connections.

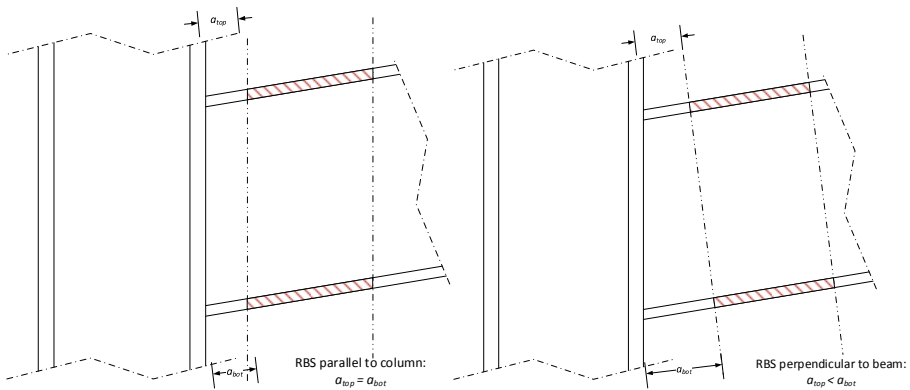


Figure 3. Configurations of RBS cut for sloped connections

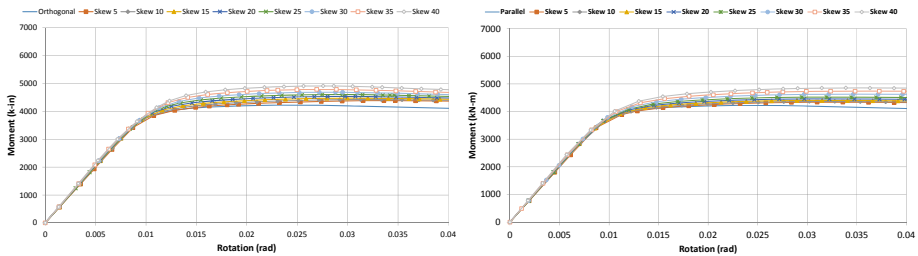


Figure 4. Moment-rotation curves for RBS perpendicular to beam (left) and parallel to column (right).

Considering the skewed configurations first, a comparison can be made among the moment-rotation response of RBS connections, shown in Figure 4 for both cases of cut perpendicular to the beam and parallel to the column. Both approaches to the detailing of the RBS cut yield similar results, showing minimal effects on initial stiffness and on the onset of yielding and some slight increase in the plastic moment capacity of the connection (approximately a 1% increase for each additional 5° of skew). Another difference between RBS cuts perpendicular to the beam and parallel to the column is a slight tendency of the former to show negative stiffness at large rotational demands. Overall, the response in terms of moment-rotation curve results quite similar for both configurations of RBS cut.

Considering the equivalent plastic strain demands, for the sake of brevity only the results for the orthogonal configurations and the skewed configurations at 15° and 30° will be presented. The complete details can be found in Wilson (2015). A comparison of the equivalent plastic strains for the case of the RBS cut perpendicular to the beam is shown in Figure 5, where it can be seen that plastic strain demands are successfully confined

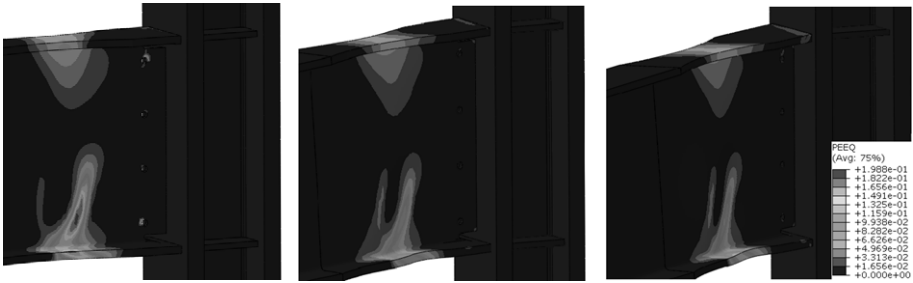


Figure 5. Equivalent plastic strain (PEEQ) for skewed RBS connection configurations. Orthogonal (left), 15° skew (middle), 30° skew (right)

within the RBS region up to a 30° skew, at which point plastic strain demands start appearing on the beam flanges near the acute angle of the connection, reaching 8% of the maximum observed plastic strain demand in the orthogonal configuration. Skews in excess of 30° start showing larger plastic demands near the beam-column interface. A similar response is shown by the configurations with RBS cut parallel to the column section, with more severe plastic strain demands at the beam-column interface becoming noticeable after a 10° skew is exceeded.

Similar considerations were made for the case of RBS connections with beams framing into the column at a slope. In this case, two situations were considered: the response of the connection to a positive moment (downward beam slope, upward beam tip displacement) and that to a negative moment (downward beam slope, downward beam tip displacement). Figure 6 shows the moment-rotation curves for the case of an RBS cut perpendicular to the beam section for both positive and negative moments. In this case, a clear impact of the slope angle on the apparent stiffness of the connection is evident, and it can be explained when considering that a vertical cross-section of the beam increases in depth and size as the angle of slope increases. Also, a marked increase in the plastic capacity of the connection is noted. The most notable difference between the cases of negative and positive moment is that the latter shows a clear capacity peak, followed by a softening behavior, as some buckling occurs in the RBS region. A similar behavior is noted for the case of the RBS cut parallel to the column.

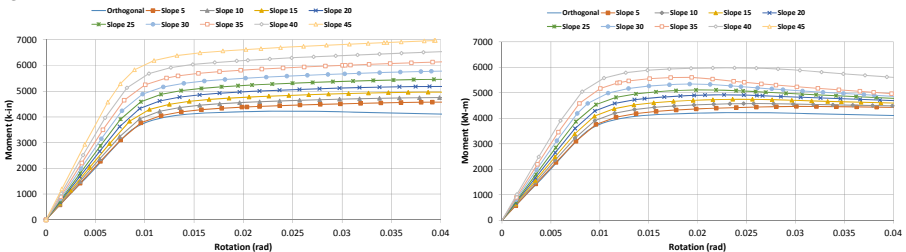


Figure 6. Moment-rotation curves for RBS cut perpendicular to beam – negative moment (left) and positive moment (right)

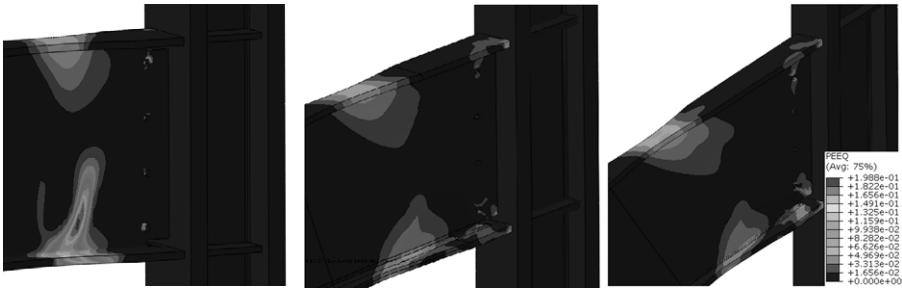


Figure 7. Equivalent plastic strain (PEEQ) for sloped RBS connection configurations under negative moment. Orthogonal (left), 15° slope (middle), 30° slope (right)

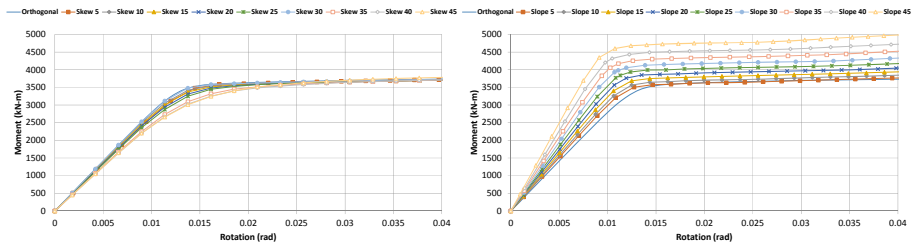


Figure 8. Moment-rotation curves for WUF-W – skewed connections (left) and sloped connections under negative moment (right)

Focusing on the plastic strain demands, Figure 7 shows the comparison between the orthogonal, the 15° and the 30° slope configurations subject to a negative moment when the RBS cut is perpendicular to the beam. For small strains, the RBS cut is successful in confining the plastic demands within its region. As the slope angle increases, plastic strain demands begin occurring on the flanges near the column, especially near the acute angle. Once the slope exceeds 15°, the localized strain demands exceed 60% of the maximum plastic strain observed in the orthogonal configuration, and keep increasing with the slope. For positive moments, the behavior improves slightly, showing no signs of plastic demands outside of the RBS region up to 30° slopes. Similar observations can be made for the case of the RBS cut made parallel to the column for both negative and positive moments, with a reduced range of slopes in which the behavior is favorable.

WUF-W Connections.

A similar set of analyses was run for the case of WUF-W connections. The moment-rotation curves for both skewed and sloped configurations under negative moment are shown in Figure 8. When the connection is skewed, there is no difference in initial stiffness, although the onset of yielding is hastened as the skew angle increases, resulting in a smoother transition between the elastic and the plastic regions. There is no visible impact of skew on the moment capacity of the connections. For sloped connections, the

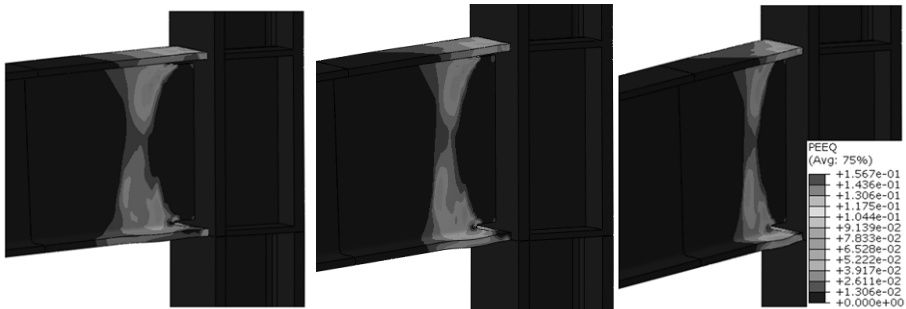


Figure 9. Equivalent plastic strain (PEEQ) for skewed WUF-W connection configurations. Orthogonal (left), 15° skew (middle), 30° skew (right)

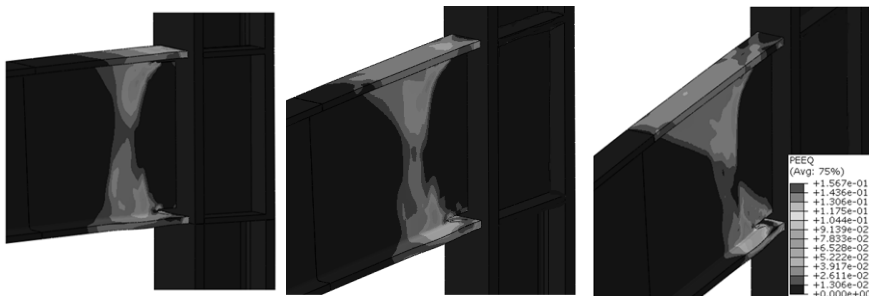


Figure 10. Equivalent plastic strain (PEEQ) for sloped WUF-W connection configurations under negative moment. Orthogonal (left), 15° skew (middle), 30° skew (right)

considerations that can be made are similar to those for the RBS case: the initial stiffness is proportional to the angle of slope, as is the apparent connection capacity, increasing by approximately 4% every additional 5° of slope. When subject to positive moment, the only visible difference is the onset of a slight softening at large rotations.

Focusing on the equivalent plastic strains of skewed WUF-W connections, Figure 9 shows results for the orthogonal, 15° skew, and 30° skew configurations, scaled to the maximum demand noted in the orthogonal case. The strain demands localize near the acute angle formed between beam and column. Plastic hinging occurs at a location appropriate for a WUF-W connection, but as the skew angle increases higher strain demands originate closer to the beam-column interface. The overall trend shows the plastic hinge forming closer and closer to the beam-column interface, suggesting the potential for possible weld failures due to increased stress triaxiality conditions.

When examining the case of sloped WUF-W connections, it can be seen that the plastic hinge tends to remain perpendicular to the beam longitudinal axis. Consequently, as can be seen in Figure 10, the plastic strain demand increases rapidly closer to the column at the bottom flange of the beam (i.e., the acute angle, or the heel of the connection) as the slope increases. This phenomenon is observed regardless of the sign of the applied

moment. On the other hand, the top flange strain demand (i.e., at the toe of the connection) spreads over a larger area as the slope angle increases, thus decreasing the peak plastic strain intensity over that region.

RECOMMENDATIONS AND CONCLUSIONS

The analytical study presented confirms the results in literature and broadens the spectrum of configurations investigated, pointing at possible issues in the expected behavior of RBS and WUF-W connections when configured with a skew or a slope. Table 1 below summarizes the recommended actions for non-orthogonal connections, based on the results of the present study.

Table 1. Recommendations for non-orthogonal moment connections

Configurations	<10°	<30°	<45°
WUF-W sloped	OK	More Work Needed	More Work Needed
WUF-W skewed	OK	More Work Needed	More Work Needed
RBS // sloped	OK	More Work Needed	N/A
RBS ⊥ sloped	OK	More Work Needed	N/A
RBS // skewed	OK	More Work Needed	More Work Needed
RBS ⊥ skewed	OK	OK	More Work Needed

Ultimately, while for deviations from orthogonality of up to 10° the response of the connections investigated does not deviate appreciably from the expected behavior, as skew and slope angles increase the increasing plastic strain demands near the beam-column interface give rise to a possible concern on the performance of the welds. The only exception to this is represented by the case of the skewed RBS connection with the cut perpendicular to the beam, which appears to be able to concentrate plastic demands within the reduced section for skews up to 30°. It is recommended that experimental testing be conducted for skewed and sloped configurations exceeding 10° in order to gather measurable evidence of the influence of non-orthogonality of connections on their expected response. Further numerical studies are ongoing, including the implementation of material damage criteria to simulate fracture initiation in the connections, but the need for experimental testing seems to be unavoidable in these situations, especially considering the scant database of known responses.

REFERENCES

ANSI/AISC 358 (2010), *Prequalified Connections for Special and Intermediate Steel Moment Frames for Seismic Applications*, American Institute of Steel Construction, Chicago, IL

ANSI/AISC 358s1 (2011), *Prequalified Connections for Special and Intermediate Steel Moment Frames for Seismic Applications Including Supplement No. 1*, American Institute of Steel Construction, Chicago, IL

ANSI/AISC 358s2 (2014), *Prequalified Connections for Special and Intermediate Steel Moment Frames for Seismic Applications Supplement No. 2*, American Institute of Steel Construction, Chicago, IL

ANSI/AISC 341 (2010), *Seismic Provisions for Structural Steel Buildings*, American Institute of Steel Construction, Chicago, IL

Prinz G.S. and Richards P.W. (2015), "Demands on Reduced Beam Section Connections with Out-of-Plane Skew", *Journal of Structural Engineering*, 142(1):04015095

Ball S.C., Uang C.M., Kim D.W. and Sim H.B. (2010), "Cyclic Testing of Steel Non-orthogonal RBS Moment Connections for LAX Tom Bradley International Terminal Modernization Program", in *Proceedings of 79th Annual Convention*, Structural Engineers Association of California, Sacramento, CA

Ball S.C. (2011), "Steel Non-Orthogonal Reduced Beam Section Moment Connections – A Case Study", *The Structural Design of Tall and Special Buildings* 20(S1):14-29

Kim D.W., Sim H.B. and Uang C.M. (2010), *Cyclic Testing of Non-Orthogonal Steel Moment Connections for LAX TBIT Modifications*, Report No. TR-09/04, Department of Structural Engineering, University of California San Diego, La Jolla, CA

Kim D.W., Ball S.C., Sim H.B. and Uang C.M. (2016), "Evaluation of Sloped RBS Moment Connections", *Journal of Structural Engineering* (online publication date 14 Jan 2016), permalink: [http://dx.doi.org/10.1061/\(ASCE\)ST.1943-541X.0001459](http://dx.doi.org/10.1061/(ASCE)ST.1943-541X.0001459)

Engelhardt M.D., Winneberger T., Zekany A.J. and Potyraj, T.J. (1998) "Experimental Investigation of Dogbone Moment Connections", *Engineering Journal*, 4th Quarter, American Institute of Steel Construction, Chicago, IL

Morrison M., Schweizer D. and Hassan T. (2012). *Cyclic Testing of WUF-W (Control Specimen)*, Network for Earthquake Engineering Simulation (distributor), Dataset, DOI:10.4231/D3TB0XV0D

Wilson, K.A. (2015). *A Finite Element Investigation of Non-Orthogonal Moment Connections in Steel Construction*, MS Thesis, University of Cincinnati, Cincinnati, OH

ESTABLISHING AND DEVELOPING THE WEAK-AXIS STRENGTH OF PLATES SUBJECTED TO APPLIED LOADS

Charles J. Carter
AISC, Chicago, IL, 60601
carter@aisc.org

Larry S. Muir
AISC, Roswell, GA, 30076
muir@aisc.org

Bo Dowswell
ARC International, LLC, Birmingham, AL, 35201
bo@arcstructural.com

ABSTRACT

When a plate is subjected to applied loads and significant out-of-plane deformation, the demand on the connection may exceed that derived from calculations due to the applied loads only. Where inelastic behavior is acceptable, the intent may be to ensure ductile behavior. For plates with fillet-welded edge connections this can be accomplished by sizing the fillet welds to develop the strength of the plate.

One specific example of this arises when a brace in a special concentrically braced frame (SCBF) is subject to compression and buckles out-of-plane. Bending of the gusset plate may demand more of the gusset plate edge connection than the calculated forces that result on the gusset edge due to the brace force specified in Section F2.6c.2 of AISC 341-16 (AISC, 2016). If not accounted for in the weld size, the uncalculated weak-axis moment on the welds from out-of-plane bending of the gusset plate might cause rupture of the fillet welds to govern the behavior of the system.

The method provided in this paper is suitable to determine the minimum size of fillet welds necessary to prevent weld rupture as out-of-plane deformations occur. It can be used for fillet-welded gusset plate edges in special concentrically braced frames (SCBF) to satisfy the exception provided in Section F2.6c.4 of AISC 341-16.

INTRODUCTION

When a plate is subjected to applied loads and significant out-of-plane deformation, the demand on the connection may exceed that derived from calculations due to the applied loads only. Where inelastic behavior is acceptable, the intent may be to ensure ductile behavior. For plates with fillet-welded edge connections this can be accomplished by sizing the fillet welds to develop the strength of the plate.

One specific example of this arises when a brace in a special concentrically braced frame (SCBF) is subject to compression and buckles out-of-plane. Resulting weak-axis bending of the gusset plate may demand more of the gusset plate edge connection than the calculated forces that result on the gusset edge due to the brace force specified in Section F2.6c.2 of AISC 341-16 (AISC, 2016). If not accounted for in the weld size, the uncalculated weak-axis moment on the welds from out-of-plane bending of the gusset plate might cause rupture of the fillet welds to govern the behavior of the system.

Section F2.6c.4 of AISC 341-16 – a new provision at the time of writing of this paper – provides a fairly simple approach that can be used to determine an appropriate fillet weld size to preclude this concern. It allows the required shear strength for the welds to be taken equal to $0.6R_yF_yt_p/\alpha_s$ (i.e., the expected shear strength of the plate), where these variables are defined in AISC 341-16. A user note is provided to further simplify this for common steel grades and double-sided fillet welds: a weld size of $0.62t_p$ is sufficient for a 36 ksi gusset plates and 70 ksi weld metal, and a weld size of $0.74t_p$ is sufficient for 50 ksi gusset plates and 70 ksi weld metal.

An exception also is provided to recognize that a weak-axis flexural hinge in the gusset plate edge can be used to protect the fillet welds. It recognizes that the forces present from the brace consume a portion of the expected strength of the gusset plate edge. This paper explains how to calculate the portion consumed, the remainder of the gusset plate strength that must be developed, and the corresponding fillet weld size that will do so. In most cases, this approach will produce a smaller required fillet weld size than the other option provided in Section F2.6c.4 of AISC 341-16.

INTERACTION ON THE GUSSET PLATE EDGE

A yield mechanism can be used in the gusset plate to determine the maximum weak-axis bending moment that can exist in the presence of the gusset plate edge forces that result from the force in the brace. Using the generalized interaction equation recommended by Dowswell (2015), the total utilization of the gusset plate in shear, compression, and strong- and weak-axis bending can be expressed as:

$$\left(\frac{P_u}{\phi R_y P_y}\right)^2 + \left(\frac{V_u}{\phi R_y V_p}\right)^4 + \left[\left(\frac{M_{ux}}{\phi R_y M_{px}}\right)^{1.7} + \left(\frac{M_{uy}}{\phi R_y M_{py}}\right)^{1.7}\right]^{0.59} \leq 1 \quad (1)$$

where:

P_u = gusset edge compression force due to brace compression force specified in Section F2.6c.2, kips.

V_u = gusset edge shear force due to brace compression force specified in Section F2.6c.2, kips.

M_{ux} = gusset edge strong-axis moment due to brace compression force specified in Section F2.6c.2, kip-in.

M_{uy} = gusset edge weak-axis moment due to deformations from brace buckling, kip-in.

$\phi R_y P_y = 0.9 R_y F_y L t_p$, the expected compression strength of the gusset plate edge, kips.

$\phi R_y V_p = 1.0(0.6 R_y F_y L t_p)$, the expected shear strength of the gusset plate edge, kips.

$\phi R_y M_{px} = \frac{0.9 R_y F_y L^2 t_p}{4}$, the expected strong-axis flexural strength of the gusset plate edge, kip-in.

$\phi R_y M_{py} = \frac{0.9 R_y F_y L t_p^2}{4}$, the expected weak-axis flexural strength of the gusset plate edge, kip-in.

R_y = ratio of the expected yield stress to the specified minimum yield stress, F_y .

F_y = specified minimum yield stress, ksi.

L = length of fillet welds on gusset plate edge, in.

t_p = gusset plate thickness, in.

Because all variables in Equation 1 except M_{uy} are known for a given gusset plate, it is convenient to rewrite it at the point of equivalency as follows:

$$M_{uy \max} = \frac{0.9 R_y F_y L t_p^2}{4} \left[(1 - P'^2 - V'^4)^{1.7} - M_x'^{1.7} \right]^{0.59} \quad (2)$$

where:

$$P' = \frac{P_u}{0.9 R_y F_y L t_p} \quad (3)$$

$$V' = \frac{V_u}{0.6 R_y F_y L t_p} \quad (4)$$

$$M_x' = \frac{4 M_{ux}}{0.9 R_y F_y L^2 t_p} \quad (5)$$

Equation 2 provides the maximum weak-axis moment, $M_{uy \max}$, that can be delivered to the welds by the gusset plate in the presence of P_u , V_u , and M_{ux} .

In the above formulations, the expected yield strength, $R_y F_y$ is used rather than the minimum specified yield strength, F_y . To not use R_y would reduce the denominator in the calculations of the compression, shear and strong-axis flexural strength ratios – and also reduce the calculated value of the remaining weak-axis flexural demand, $M_{uy \max}$. $R_y F_y$ also is used in the denominator of the weak-axis flexural strength ratio as provided

in Section A3.2 in AISC 341-16, because all of these ratios are determined for the same element in the interaction equation.

DESIGN REQUIREMENTS FOR GUSSET PLATE EDGE FILLET WELDS

The four required strengths at the gusset plate edge (P_u , V_u , M_{ux} , and $M_{uy \max}$) can be used to design fillet welds that will fully develop the edge of the gusset plate and preclude weld rupture. All four effects produce shear on the effective throat of the fillet weld. The effects of P_u , M_{ux} , and $M_{uy \max}$ all are oriented transverse to the fillet weld, while the effect of V_u is oriented parallel to the weld axis. Accordingly, the maximum weld force per unit length due to the combination of all four effects can be expressed as follows:

$$f_u = \sqrt{f_{uv}^2 + (f_{up} + f_{um_x} + f_{um_y})^2} \quad (6)$$

where:

$$f_{uv} = \frac{V_u}{2L}, \text{ kips/in.} \quad (7)$$

$$f_{up} = \frac{P_u}{2L}, \text{ kips/in.} \quad (8)$$

$$f_{um_x} = \frac{2M_{ux}}{L^2}, \text{ kips/in.} \quad (9)$$

$$f_{um_y} = \frac{M_{uy \max}}{(t_p + 0.5w)L}, \text{ kips/in.} \quad (10)$$

w = weld size, in.

The corresponding weld design strength per in. is:

$$\phi r_n = 1.392D(1.0 + 0.5 \sin^{1.5} \theta) \quad (11)$$

where:

$$\theta = \tan^{-1} \left(\frac{f_{up} + f_{um_x} + f_{um_y}}{f_{uv}} \right) \quad (12)$$

D is the number of sixteenths in the weld size, and the basic weld strength of $1.392D$ is determined as explained in Part 8 of the AISC *Steel Construction Manual* (AISC, 2011). Because the quantity in Equation 11 must equal or exceed the quantity in Equation 6, the minimum weld size can be determined as:

$$D_{min} = \frac{f_u}{1.392(1.0 + 0.5 \sin^{1.5} \theta)} \quad (13)$$

This weld size is sufficient to develop the gusset plate, and therefore it is unnecessary to also apply the “Richard” 1.25 weld ductility factor used to address hot spots in cases where the welds do not develop the gusset plate (AISC, 2011).

Note that Equation 10 is based upon a moment arm equal to the distance between centroids of the effective throats of the fillet welds taken at 45 degrees in the welds ($t_p + 0.5w$); see Figure 1. Although some references illustrate the use of the weld area centroids – a moment arm of $t_p + 0.67w$ in this case – the calculations in this paper are made relative to the centroids of the effective throats and the moment arm of $t_p + 0.5w$ is used for consistency. This equation is directly useful when checking a design, as shown in Examples 1 and 2 at the end of this paper, but requires iteration when designing a connection.

Iteration can be minimized by assuming a weld size; a reasonable starting assumption is $w = t_p/2$, in which case $t_p + 0.5w = 1.25t_p$. Alternatively, the weld size can be ignored in design and the moment arm taken as t_p if the resulting penalty is not objectionable.

COMPARISON TO TEST DATA

Table 1 shows the available testing (Johnson, 2005; Roeder, 2015) by which the suitability of the foregoing method can be judged. Predicted and actual test results are shown as GY & BR for gusset yielding and brace rupture; WR for weld rupture. The former is the desired behavior; the latter is undesirable.

Note that weld tearing as testing progresses is not preventable and should not be confused with weld rupture. The geometric deformations of the specimens during testing will cause tearing starting at the ends of the welds. As long as the specimen remains viable and the brace continues to function through the testing until brace fracture, it is an acceptable result. The key concept here is that the weld tearing cannot be unstable and result in complete weld rupture. Rather, weld tearing must be stable so that gusset yielding can occur and, ultimately, brace rupture will limit the test.

Tests are available on both sides of the prediction point of the method, and as can be seen in Table 1, the prediction of the method provided in this paper is correct for all tests shown. The testing by Roeder (2015) and the two edge connections in test HSS 01 (Johnson, 2005) are most relevant because they are all within 1/16 in. – the smallest increment of weld size – of the prediction of the method.

Also provided in Table 1 is a comparison to the use of the $0.6R_yF_yt_p/\alpha_s$ provision from Section F2.6c.4 of AISC 341-16. This provision is easier to use, but requires a larger weld size than the method provided in this paper. Adjusting from weld size to weld volume to better reflect the impact on the cost of welding, the difference is from 25% to 200% in the cases shown in Table 1.

CONCLUSIONS

The method provided in this paper is suitable to determine the minimum size of fillet welds necessary to prevent weld rupture as out-of-plane deformations occur. It can be used for fillet-welded gusset plate edges in special concentrically braced frames (SCBF) to satisfy the exception provided in Section F2.6c.4 of AISC 341-16.

REFERENCES

- AISC (2011), *Steel Construction Manual, 14th Edition*, AISC, p. 8-8, Chicago, IL.
- AISC (2012), *Seismic Design Manual, 2nd Edition*, AISC, Chicago, IL.
- AISC (2016), *Seismic Provisions for Structural Steel Buildings*, ANSI/AISC 341-16, AISC, Chicago, IL.
- Dowswell, B. (2015), "Plastic Strength of Connection Elements," *Engineering Journal*, AISC, Vol. 52, No. 1, 1st Quarter, pp. 47-65, Chicago, IL.
- Johnson, S.M. (2005), *Improved Seismic Performance of Special Concentrically Braced Frames*, Masters Thesis, University of Washington, Seattle, WA.
- Muir, L.S. and W.A. Thornton (2014), *Vertical Bracing Connections – Analysis and Design*, AISC Design Guide 29, AISC, Chicago, IL.
- Roeder, C. (2015), Three SCBF test reports provided to AISC, University of Washington, Seattle, WA.

Table 1. Summary of Available Test Data and Results

	Roeder SCBF 1	Roeder SCBF 2	Roeder SCBF 3	Johnson HSS 01		Johnson HSS 02		Johnson HSS 03		Johnson HSS 04		Johnson HSS 05	
				(beam edge)	(column edge)	(beam edge)	(column edge)	(beam edge)	(column edge)	(beam edge)	(column edge)	(beam edge)	(column edge)
General Parameters													
L , in.	20	18	17.375	35	29	24	20	24	20	24.5	20.375	24	20
t_{pl} , in.	0.6	0.625	0.625	0.5	0.6	0.5	0.5	0.5	0.5	0.5	0.5	0.5	0.375
w , in.	5/16	1/4	1/4	3/16	3/16	1/2	1/2	1/16	7/16	7/16	1/16	5/16	5/16
F_{ext} , ksi	70	70	70	70	70	70	70	70	70	70	70	70	70
F_y , ksi	50	50	50	50	50	50	50	50	50	50	50	50	50
R_y	1.1	1.1	1.1	1.1	1.1	1.1	1.1	1.1	1.1	1.1	1.1	1.1	1.1
Gusset Edge Forces													
P_{ax} , kips	84.8	88.6	83.5	84.1	49.1	71.2	84.6	71.2	84.6	71.2	84.5	68.1	52.1
V_{ax} , kips	116	106	92.8	139	124	115	97.7	115	97.7	116	100	106	93.1
M_{ax} , kip-in.	7	59.1	0	6.43	0	73.5	0	73.5	0	10.7	0	6.82	0
Calculated Parameters													
P'	0.171	0.150	0.155	0.0787	0.0694	0.120	0.110	0.120	0.110	0.118	0.108	0.153	0.140
V'	0.352	0.286	0.259	0.255	0.259	0.290	0.296	0.290	0.296	0.287	0.297	0.367	0.377
Mx'	0.00283	0.0236	0	0.000954	0	0.00201	0	0.00201	0	0.00288	0.00234	0.00255	0
$M_{y, max}$, kip-in.	59.1	84.4	81.6	101	88.9	72.6	60.6	72.6	60.6	74.2	61.8	40.0	33.4
f_{ox} , kips/in.	2.90	2.64	2.67	2.11	2.14	2.40	2.44	2.40	2.44	2.37	2.45	2.27	2.33
f_{oy} , kips/in.	2.12	2.32	2.40	0.974	0.847	1.49	1.37	1.49	1.37	1.46	1.34	1.42	1.30
f_{max} , kips/in.	0.0350	0.265	0	0.0118	0	0.0248	0	0.0248	0	0.0357	0.0289	0.0237	0
f_{max} , kips/in.	4.50	6.25	6.26	5.16	5.16	4.04	4.04	4.21	4.22	4.22	4.22	3.14	3.14
f_{oy} , kips/in.	7.26	9.41	9.07	6.49	6.38	6.05	5.93	6.21	6.09	6.18	6.10	5.12	5.02
θ , radians	1.16	1.25	1.27	1.24	1.23	1.16	1.15	1.17	1.16	1.18	1.16	1.11	1.09
D_{obs} , 16ths	3.63	4.62	4.44	3.19	3.14	3.02	2.97	3.09	3.04	3.07	3.05	2.58	2.55
w_{obs} , in.	1/4	5/16	5/16	1/4	1/4	1/4	3/16	1/4	1/4	1/4	1/4	3/16	3/16
Results													
Is $w \geq w_{obs}$?	Yes	No	No	No	No	Yes	Yes	Yes	Yes	Yes	Yes	Yes	Yes
By how much?	1/16" >	1/16" <	1/16" <	1/16" <	1/16" <	1/4" >	5/16" >	3/16" >	3/16" >	3/16" >	3/16" >	1/8" >	1/8" >
Prediction	GY & BR	WR	WR	WR	WR	GY & BR	GY & BR	GY & BR	GY & BR	GY & BR	GY & BR	GY & BR	GY & BR
Actual Behavior	GY & BR	WR	WR	WR	WR	WR	WR	GY & BR	GY & BR	GY & BR	GY & BR	GY & BR	GY & BR
Method works?	Yes	Yes	Yes	Yes	Yes	Yes	Yes	Yes	Yes	Yes	Yes	Yes	Yes
Alternative 0.6R_yF_yt_{pl}/α Comparison													
D_{obs} , 16ths	5.93	7.41	7.41	5.93	5.93	5.93	5.93	5.93	5.93	5.93	5.93	4.45	4.45
w_{obs} , in.	3/8	1/2	1/2	3/8	3/8	3/8	3/8	3/8	3/8	3/8	3/8	5/16	5/16
Size increase	1/8	3/16	3/16	1/8	1/8	1/8	3/16	1/8	1/8	1/8	1/8	1/8	1/8
% vol. increase	25%	56%	56%	25%	25%	25%	200%	25%	25%	25%	25%	78%	78%

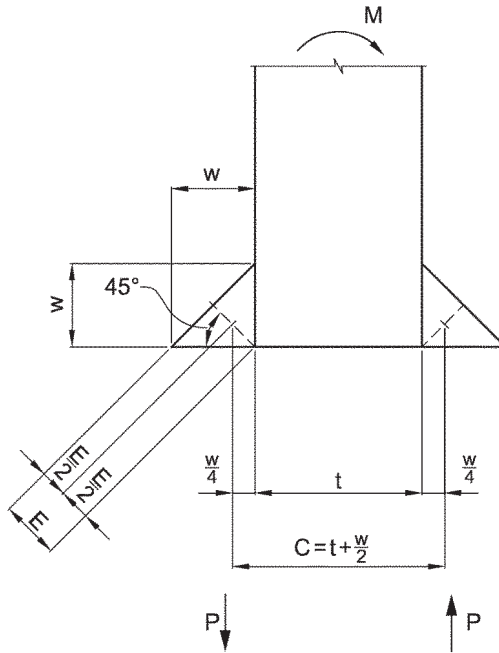
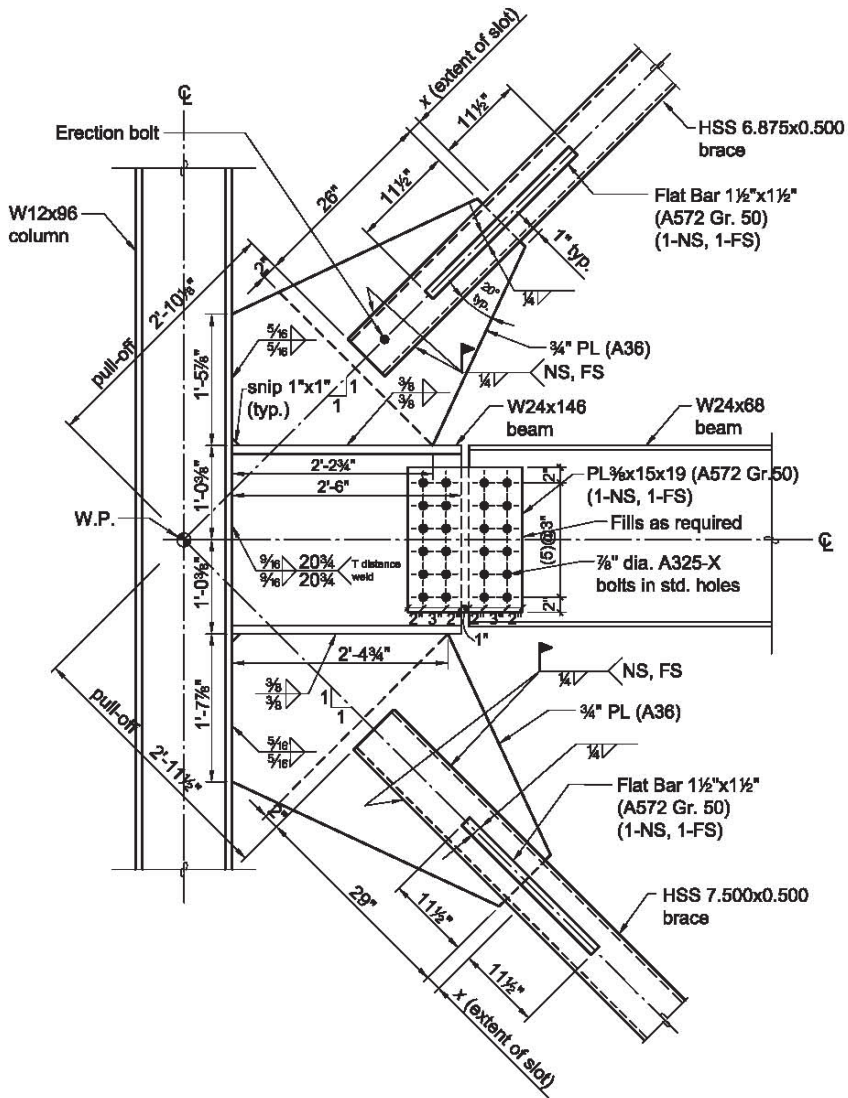


Figure 1. Moment arm for weak-axis bending.



Note: A325-X bolts are to be pretensioned with slip-critical faying surfaces.

Fig. 5-33. Geometry and completed design for Example 5.3.10.

Figure 2. Replication of Figure 5-33 of the AISC *Seismic Design Manual*, 2nd Edition.

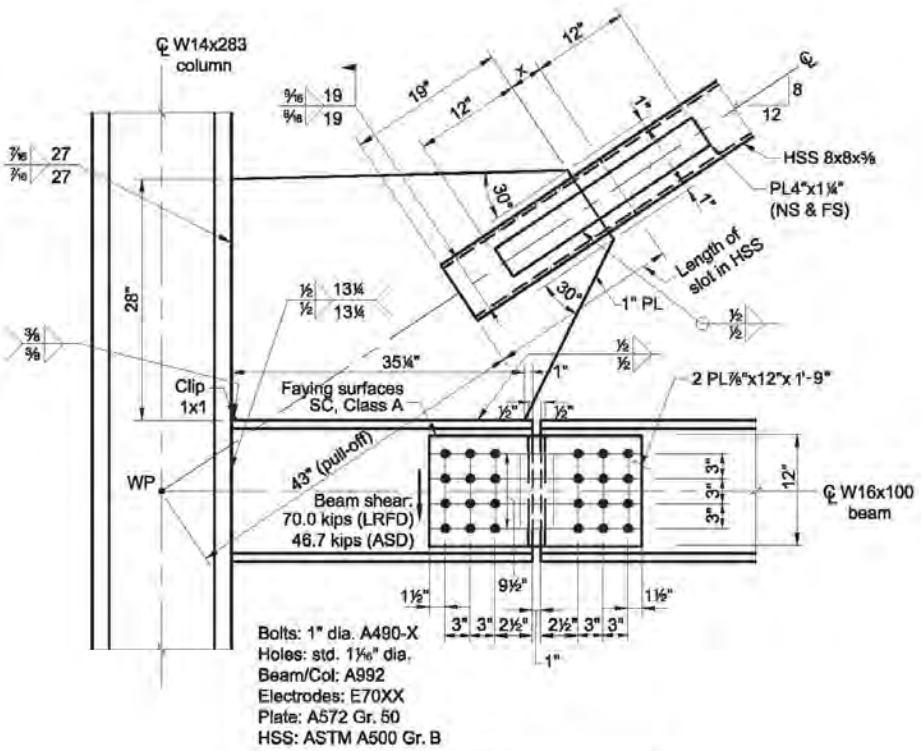


Fig. 6-1. High-seismic design with hinge (moment release)

Figure 3. Replication of Figure 6-1 of AISC Design Guide No. 29.

BEHAVIOR, TESTING AND MODELING OF BEAM-COLUMN ANGLE CONNECTIONS

Thierry Béland

École Polytechnique de Montréal, Montreal, Québec H3C 3A7, Canada
thierry.beland@polymtl.ca

Joshua G. Sizemore

University of Illinois at Urbana-Champaign, Urbana, Illinois 61801, USA
sizemor2@illinois.edu

Cameron R. Bradley

Tufts University, Medford, Massachusetts 02155, USA
cameron.bradley@tufts.edu

Robert Tremblay

École Polytechnique de Montréal, Montreal, Québec H3C 3A7, Canada
robert.tremblay@polymtl.ca

Eric M. Hines

LeMessurier Consultants, Boston, Massachusetts 02135, USA
Tufts University, Medford, Massachusetts 02155, USA
ehines@lemessurier.com

Larry A. Fahnestock

University of Illinois at Urbana-Champaign, Urbana, Illinois 61801, USA
fhnstck@illinois.edu

ABSTRACT

Angles are versatile components that are used extensively in steel construction for gravity and braced frame connections. The double angle configuration is commonly employed, and although it has received attention in a variety of past studies, the objectives and parameter ranges considered in these studies have varied considerably. To establish a consistent and comprehensive database of cyclic behavior for double angle connections, an integrated research program was initiated, comprising angle component and beam-column connection numerical models and full-scale tests. The angle component tests establish fundamental monotonic and cyclic behavioral characteristics of a wide range of angles, which then support validation of angle component models. These angle component models are subsequently implemented in connections for numerical earthquake simulations of steel-framed buildings. In this research, accurate modeling of angle connections is critical for evaluating seismic stability and collapse prevention in low-ductility braced frame systems that are used extensively in Eastern North America.

INTRODUCTION

Angles are used extensively in steel construction since they are a versatile and economical component for creating connections between steel members with bolts and/or welds. Angle connections are most commonly used in the double angle configuration, as shown in Figures 1a and 1b for gravity frame and braced frame connections, respectively. Top and/or seat angles can also be added to a double angle connection, as shown in Figure 1c, to enhance flexural strength and stiffness. Although double angle connections do possess flexural strength and stiffness, they are commonly idealized as pinned connections for analysis and design. Neglecting the flexural contribution of double angle connections is reasonable for common loading scenarios involving wind and gravity, but for more extreme scenarios – such as when seismic stability or progressive collapse resistance are critical – the flexural contribution of these connections may be significant.

The present study is focused on establishing a consistent, comprehensive database of cyclic behavior for double angle connections using integrated angle component and beam-column connection numerical models and full-scale tests. The angle component tests define fundamental monotonic and cyclic behavioral characteristics of a wide range of angle geometries, which then support validation of angle component models. These angle component models are subsequently implemented in connection models for numerical earthquake simulations of steel-framed buildings. As these numerical simulations show, beam-column angle connections, both in gravity and braced frames, contribute to reserve capacity in concentrically-braced frames (CBFs). Reserve capacity is defined as secondary strength, which is inherently more flexible than the primary lateral force resisting system (LFRS). This reserve capacity is activated after significant damage to the primary LFRS. In CBFs, this damage is typically some form of brace-related failure, such as buckling or fracture.

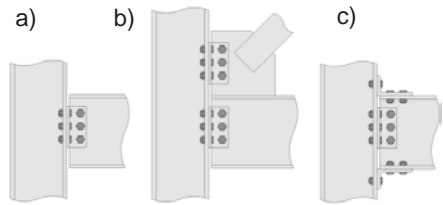


Figure 1 – Angle Connections

This research on beam-column angle connections is part of a comprehensive research program comprising design studies, numerical simulations and full-scale testing, which aims to understand at a fundamental level the influence of reserve capacity on the seismic performance of low-ductility steel CBFs up to the point of collapse. The project is targeted at developing cost-effective strategies for both assessing existing structures and designing new structures so that seismic stability and collapse prevention can be ensured, particularly in regions of moderate seismicity, such as Eastern North America.

BACKGROUND

Over the past few decades, various analytical, numerical and experimental programs have been conducted to characterize the cyclic behavior of bolted angle connections.

Astaneh-Asl et al. (1989) performed 6 full-scale cyclic tests on connections comprising welded-bolted double web angles and found that an increase of bolt rows increased moment capacity and initial stiffness, but also decreased ultimate rotation. The reported failure modes were bolt fracture and angle fracture near the fillet. Abolmaali et al. (2003) performed 20 tests on full-scale double web angle connections, among which 12 were bolted-bolted and 8 were welded-bolted. The bolted-bolted angles were more flexible and exhibited more pronounced hysteretic pinching due to bolt slip and hole elongation. Overall, these double web angle connections exhibited ductile behavior under cyclic loading. Kishi and Chen (1990) showed that the strength and stiffness of double web angle connections can be enhanced by adding top and seat angles. Shen and Astaneh-Asl (1999) studied the influence of geometrical parameters (angle thickness, bolt diameter and bolt position relative to the angle fillet) on the nonlinear behavior of 8 bolted angle component specimens. The observed ultimate strength was two to three times larger than the yield strength due to the combined effect of material strain hardening and geometrical hardening at large deformations. The most influential parameters were the angle thickness and the distance between the column bolts and the angle fillet. Fracture was always observed near the fillet, either in the column leg for thin angles, or in the beam leg for thick angles. Other similar studies demonstrated comparable failure modes (Garlock et al., 2003, Yang and Tan, 2013). Kishi and Chen (1990) introduced the parameter g_2 to quantify the flexural span of the angle column leg, given by the distance between the edge of the bolt head and the end of the fillet. Although prior research on angles is valuable, the lack of a consistent experimental database across a wide range of parameters motivated the present research program.

ANGLE COMPONENT TESTS

Experimental Setup

An extensive angle experimental program of 140 tests was conducted in the structural engineering laboratory at Polytechnique Montreal from June to October 2013 and March to July 2014. The main objective of this experimental program was to characterize at a component level the behavior of bolted-bolted angles under monotonic and cyclic loadings for 19 different angle geometries. In a building, lateral loading conditions cause beam end rotation, which translates into a tensile force pulling connection angles away from the column, as illustrated in Figure 2a. To simulate a similar behavior in the laboratory, the experimental setup comprised a pair of angles bolted to a plate, which was in turn fixed to the actuator (Figure 2b and 2c). To minimize eccentricity effects, angles were tested in pairs similar to prior studies (Shen and Astaneh-Asl, 1999, Garlock et al., 2003, Yang and Tan, 2013).

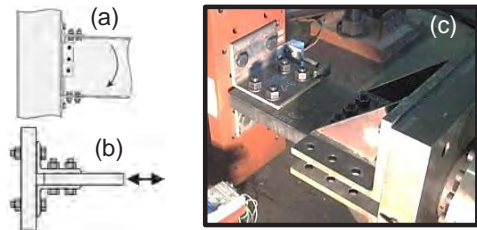


Figure 2 – Angle Test Configuration

The study performed by Shen and Astaneh-Asl (1999) showed that the inelastic behavior of bolted angles is primarily dependent on two geometric parameters: the distance between the angle fillet and the column bolts, and the angle thickness (t). Therefore, a parametric study was developed by varying the thickness of the angles from 8 to 19 mm (5/16" to 3/4") and the column bolt gauge from 64 to 114 mm (2.5" to 4.5"). A test matrix of 19 test cases was assembled as shown in Table 1. The ratio g_2/t , as defined by Kishi and Chen (1990) and shown in Figure 3, was used as a key parameter to develop this test matrix. The g_2/t ratio varied from 1.25 to 8.00 for the angle geometries studied.

Table 1 – Angle Test Matrix

t g _c	7.9 mm		9.5 mm		12.7 mm		15.9 mm		19.1 mm	
	Test Case	g_2/t	Test Case	g_2/t	Test Case	g_2/t	Test Case	g_2/t	Test Case	g_2/t
64 mm	19	3.80	1	2.67	3	1.38	-	-	-	-
76 mm	-	-	2	4.00	4	2.38	5	1.70	6	1.25
89 mm	-	-	7	5.33	9	3.38	11	2.50	13	1.92
102 mm	-	-	8	6.67	10	4.38	12	3.30	14	2.58
114 mm	-	-	15	8.00	16	5.38	17	4.10	18	3.25

Since this parametric study aimed to characterize the ultimate failure behavior of the angles, the bolts were designed to avoid bolt failure and to develop the ultimate capacity of the angles. For every specimen with a thickness of 7.9 mm and 9.5 mm, 19 mm (¾") diameter A325 bolts were used, while 25 mm (1") diameter A490 bolts were used for all other test cases. Every bolt was pre-tensioned and the width of the angles was kept consistent at 203 mm (8").

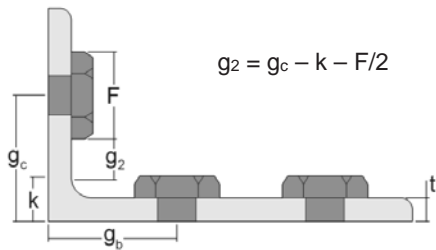


Figure 3 – Angle Geometric Parameters

Angle behavior

All specimens exhibited ductile behavior and nominally bilinear response under monotonic tension loading and two distinct failure modes were observed. The first failure mode is characterized by a fracture in the column leg at the location of the first plastic hinge near the fillet as illustrated in Figure 4a for Specimen TC10 ($g_2/t = 4.38$). This failure mode occurred primarily in slender angles with a g_2/t larger than 2.5. The greater flexibility of the slender angles led to large displacements and geometrical hardening, which is caused by an increasing axial demand on the column leg. This geometrical hardening is generally accompanied by the beam leg uplift from the plate, as illustrated in Figure 4a. The second failure mode, shown in Figure 4b for Specimen TC4 ($g_2/t = 2.58$), is characterized by fracture in the beam leg near the fillet, where the section is subjected to

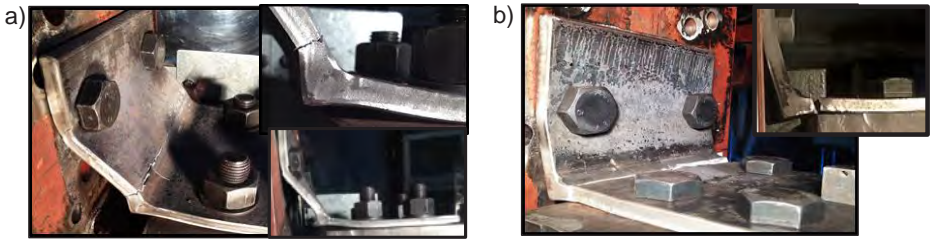


Figure 4 – Angle Failure Modes

tension and bending due to the stiff region of the fillet. This behaviour was observed primarily in stockier angles with a g_2/t ratio lower than 3.0 and at smaller displacements. Significant geometrical hardening was not observed in the stocky angles due to smaller displacements and the column leg acting as a cantilever beam after the first plastic hinge.

Figure 5a presents the monotonic response of two test cases with the same thickness, 12.7 mm, but with a column gage of 76 mm for TC4 and 102 mm for TC10. Because of its slightly shorter column leg flexural span, TC4 presents a larger ultimate strength but a reduced ductility. These observations can be generalized into trends for a given thickness, as the ultimate strength generally decreased while the ultimate displacement increased with an increase of g_2/t , as shown in Figure 5b and 5c, respectively, for the static monotonic cases. These trends are more pronounced for thicker angles.

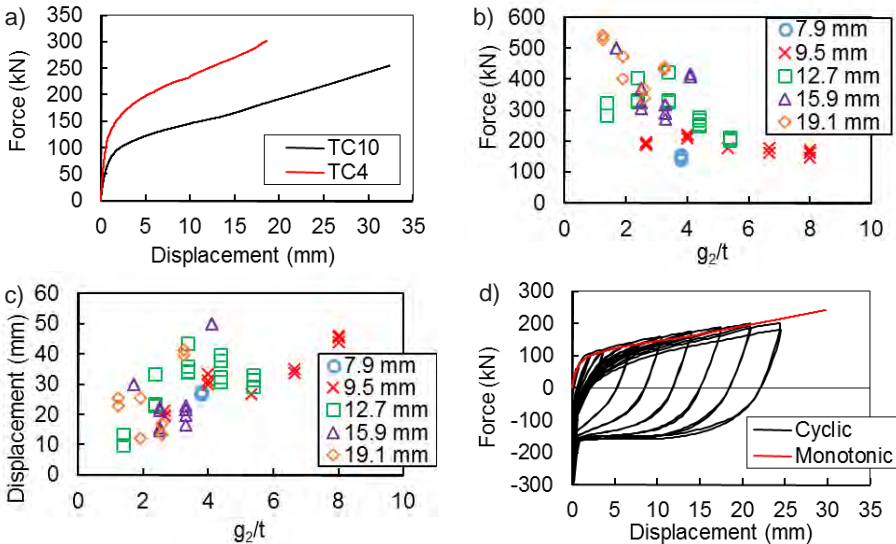


Figure 5 – Angle Experimental Data

Figure 5d shows a typical cyclic response (TC10) under stepwise incremented deformations. As larger displacements are imposed on the angles, the loading stiffness reduces, while the unloading stiffness remains nearly the same. Despite the progressive softening and reduction in yield strength upon reloading, the hysteretic response was generally stable with positive post-yield stiffness. Monotonic curves provide a good approximation of the backbone curve of the cyclic data; however, specimens typically showed smaller deformation capacities under cyclic loading compared to monotonic.

ANGLE MODELS

The comprehensive experimental characterization of angle component behavior provides the basis for accurately modeling beam-column angle connections and studying their impact on the seismic response of buildings. A computationally efficient angle model was developed and implemented in *OpenSees* for conducting nonlinear static and dynamic analyses. This model represents an angle connection with a nonlinear zero-length element that contains fibers with angle segment cyclic load-deformation characteristics, which were obtained from either full-scale testing or detailed component-level cyclic numerical angle simulations. Figure 6 illustrates the basic configuration of this model for a typical double web angle beam-column connection.

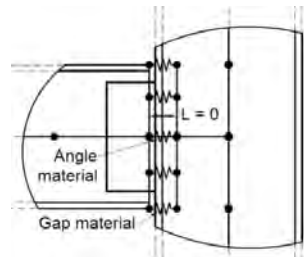


Figure 6 – Schematic of Angle Connection Model

SEISMIC BUILDING RESPONSE

To illustrate the effect that connection behavior has on the global structural system, a series of response history analyses were conducted using a three-story prototype building designed for Boston, Massachusetts (Bradley, 2016) per the AISC *Specification* (AISC, 2005). The building was designed using the $R = 3$ provision with a chevron CBF used as the LFRS. Select members and connections were adapted from the designs presented by Bradley (2016).

Prototype Building

The prototype building consists of a rectangular floor plan 45.7 m by 53.3 m (150' by 175'), with 5 equally-spaced bays in each direction with widths of 9.1 m (30') and 10.7 m (35'), respectively. All three stories have a height of 4.6 m (15'), and there are two interior braced frame bays oriented in each direction. Columns were selectively rotated to insure a balanced proportion of strong- and weak-axis orientation in both directions. The wider braced frame configuration—with 10.7 m bays and beams rather than girders—was the focus of this investigation into seismic response. Bracing members in the 10.7 m bays are HSS9x9x1/4 in Story 1, HSS8x8x1/4 in Story 2, and HSS6x6x1/4 in Story 3. The Level 2 and Level 3 beam sizes in the braced bay are W12x40, and the roof beam is a W12x26.

Beam sizes in the gravity bays range from W16x31 and W18x35 for the lower level interior and exterior beams, respectively, to W12x53 and W12x58 for the respective interior and exterior roof beams. The braced bay includes continuous W12x53 columns, while the remaining columns in the gravity bays are W12x50 for interior columns and W12x40 for exterior columns. A more detailed discussion of the prototype frame and its design is provided by Bradley (2016).

All gravity connections throughout the building consist of 2L4x4x1/4 beam-column double web angles with 3 rows of 19 mm A325 bolts (Figure 1a). Braced frame connections are double angle beam-column-gusset connections (Figure 1b): 2L4x4x5/8 angles are used at Level 2, 2L4x4x1/2 at Level 3, and 2L4x4x3/8 at the roof. Each of the braced frame double angle connections uses 3 rows of 19 mm A325 bolts for the beam-column component. The Level 2 and 3 braced frame angle connections additionally contain a gusset-column component with 3 rows of 19 mm A325 bolts.

Model Description

The numerical model used in the dynamic analyses was constructed using the finite element framework *OpenSees* (McKenna, 1997). Angle connections were modeled using the approach developed by the authors. The brace-gusset connections were modeled using a hysteretic material, with rotational capacity and stiffness calculated using fundamental equations derived by Hsiao et al. (2012). Brace initial imperfection of L/1000 at brace mid-length was modelled with a half-sine wave distribution. Both the brace imperfection and gusset plate hysteretic properties were artificially modeled in-plane, allowing for the building to be modeled in two dimensions rather than three, appreciably reducing computational costs without significant loss of accuracy, as demonstrated by Terzic (2013).

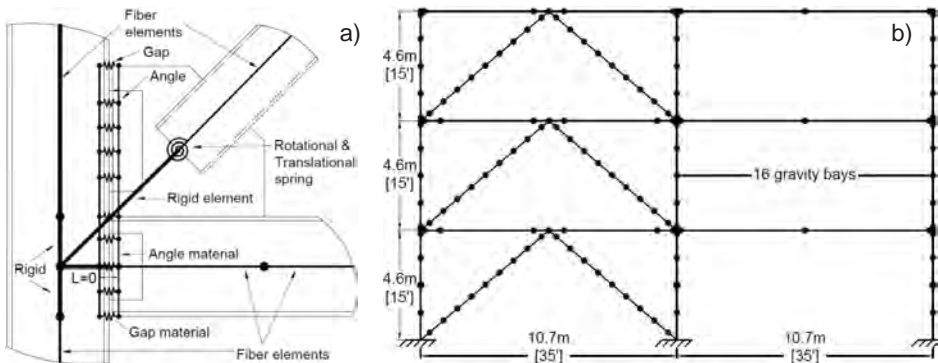


Figure 7 – Building Numerical Model

A fiber-based cross section was used along with the *Steel02* material designation in *OpenSees* to define the cyclic behavior for all beams, columns, and braces. Brace low-cycle fatigue was modeled using an empirical equation proposed by Karamanci and

Lignos (2014) to approximate failure strain for the *Fatigue* material designation in *OpenSees*. Fixed column bases were assumed for the braced bay. An idealized bracing connection schematic from the numerical model is shown in Figure 7a. Symmetry was employed to reduce computational costs, which allowed for modeling only half of the prototype building: a single braced bay with 16 additional gravity bays and columns (Figure 7b). Using the frame design loads (Bradley, 2016), gravity loads were applied accordingly at each level prior to running all analyses.

Dynamic Analyses

The prototype building was subjected to a suite of 15 Site Class B MCE-level ground motions (GMs) developed by Hines et al. (2009) for Boston. Two cases were considered for each GM: (1) all beam-column and beam-column-gusset connections modeled as pins; and (2) all connections modeled using the authors' angle model. The maximum story drifts observed during each ground motion for the two model variations (pinned connections, realistic connections) are presented in Table 2.

Table 2 – Maximum Story Drift (%) Observed for Unscaled Ground Motions

Connection Model	Ground Motion														
	1	2	3	4	5	6	7	8	9	10	11	12	13	14	15
Pinned	1.1	1.1	1.4	1.2	1.6	1.5	0.4	0.5	1.5	1.6	2.0	1.2	1.0	2.2	0.5
Realistic	0.7	0.7	1.2	0.7	1.4	2.1	0.5	0.8	1.3	1.6	1.6	1.7	1.3	1.3	0.4

As the table indicates, collapse was avoided for all 15 unscaled GMs regardless of how the connections were modeled. Because the model did not collapse when using a scale factor of 1 on the GMs, the reserve capacity attributable to the use of the authors' angle model is not obvious. Interestingly, although maximum story drifts occurred predominantly in the pinned-connection model (10 of 15 GMs), there were several cases (5 of 15 GMs) in which larger drifts were observed in the realistic-connection model. This is owing to the highly nonlinear response of these low-ductility systems; slight changes in stiffness can alter demand early in dynamic response, which subsequently significantly alters the evolution of the remainder of the analysis, potentially changing not just the magnitude of drift, but also the story and direction in which maximum drift occurs.

To better test the realistic connection model influence in regards to collapse prevention, select GMs were scaled in intensity until they caused collapse in the pinned-connection building model. These scaled GMs were then applied to the realistic-connection building model. Figure 8 shows the response for two GMs scaled by a factor of 2.0. The pinned-connection building model underwent significant drifts within stories that experienced brace buckling, and without any connection stiffness these drifts grew mostly uninhibited. When the realistic-connection building model was subjected to the scaled GMs shown, collapse was prevented, demonstrating the ability of realistic connections to enhance seismic stability. Thus, the impact of realistic connection modeling that considers the

flexural contribution of double angle connection is seen in two ways: (1) realistic connection modeling is required to accurately predict drift and other demands even during GMs that do not lead to collapse; and (2) with pinned connections, a model will not capture the connection reserve stiffness and strength, which could prevent collapse.

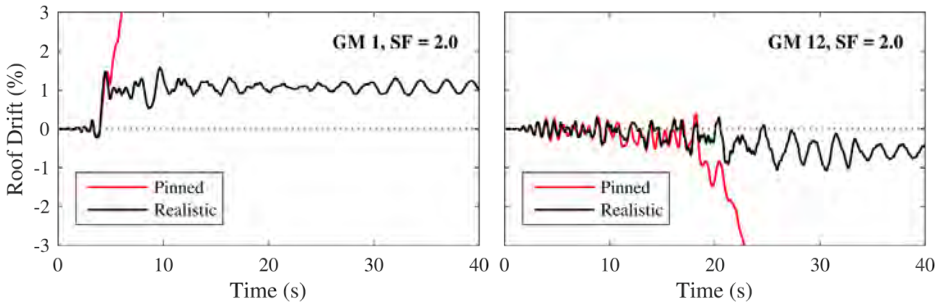


Figure 8 – Dynamic Response of Building Models

CONCLUDING REMARKS

Double angle gravity and braced frame connections are used extensively in steel-framed buildings, and these connections influence seismic stability and collapse prevention in low-ductility braced frame systems that are used extensively in Eastern North America. The research presented in this paper systematically characterized angle monotonic and cyclic response at the component level. These tests demonstrated that all angles across a wide range of geometries and bolt positions exhibited ductile behavior, and that the ratio of flexural span to angle thickness, g_2/t , was the parameter with greatest influence. The tests cover a range of g_2/t from 1.25 to 8 and show that ultimate strength was negatively correlated with g_2/t whereas deformation capacity was positively correlated with g_2/t . An efficient and accurate numerical model to simulate angle connection behavior was developed for use in nonlinear static and dynamic building analysis. A set of representative earthquake simulations was conducted for a building in Boston employing $R = 3$ CBFs as the lateral force resisting system. The simulated behavior of this building illustrated the appreciable effect that angle connections can have on dynamic response. Ongoing work, as part of the project *Reserve Capacity in New and Existing Low-Ductility Braced Frames*, is quantifying reserve capacity obtained from angle connections as well as other sources and developing a design framework that employs these reserve capacity mechanisms to prevent seismic collapse in non-ductile CBFs.

ACKNOWLEDGEMENTS

This study is supported by the US National Science Foundation (Grant No. CMMI-1207976), the American Institute of Steel Construction (AISC) and the Natural Sciences and Engineering Research Council of Canada. The authors acknowledge the technical

staff of the Structural Engineering laboratory of Polytechnique Montreal. Test specimen materials and fabrication were provided by AISC, Nucor, Unytite and ADF Group.

REFERENCES

- Abolmaali, A., Kukreti, A. R. and Razavi, H. (2003), "Hysteresis behavior of semi-rigid double web angle steel connections" *Journal of Constructional Steel Research*, Vol. 59, No. 8 (pp. 1057-1082).
- American Institute of Steel Construction (AISC). (2005). *Seismic Provisions for Structural Steel Buildings*. ANSI/AISC 341-05. Chicago, IL.
- American Society of Civil Engineers. (2005). *Minimum design loads for buildings and other structures*. ASCE 7-05. Reston, VA.
- Astaneh-Asl, A., Nader, M. N. and Malik, L. (1989). "Cyclic behavior of double angle connections" *Journal of Structural Engineering*, Vol. 115, No. 5 (pp. 1101-1118).
- Bradley, C. (2016). "Experimental investigation of post-elastic failure mechanisms in low-ductility braced frames and the implications for collapse performance." M.S. thesis, Tufts University, Medford, MA.
- Chen, W. F. and Kishi, N. (1989). "Semirigid steel beam-to-column connections - data-base and modeling" *Journal of Structural Engineering*, Vol. 115, No. 1 (pp. 105-119).
- Garlock, M., Ricles, J. and Sause, R. (2003). "Cyclic Load Tests and Analysis of Bolted Top-and-Seat Angle Connections" *Journal of Structural Engineering*, Vol. 129, No. 12, (pp. 1615-1625).
- Kishi, N. and Chen, W. F. (1990). "Moment-rotation relations of semirigid connections with angles" *Journal of Structural Engineering*, Vol. 116, No. 7, (pp. 1813-1834).
- Hines, E. M., Appel, M. E. and Cheever, P. J. (2009). "Collapse performance of low-ductility chevron braced steel frames in moderate seismic regions" *AISC Engineering Journal*, Vol. 46, No. 3, (pp. 149-180).
- Hsiao, P. C., Lehman, D. E. and Roeder, C. W. (2012). "Improved analytical model for special concentrically braced frames" *Journal of Constructional Steel Research*, Vol. 73 (pp. 80-94).
- Karamanci, E. and Lignos, D. G. (2014). "Computational approach for collapse assessment of concentrically braced frames in seismic regions" *Journal of Structural Engineering*, Vol. 140, No. 8.
- McKenna, F. (1997). "Object oriented finite element programming frameworks for analysis, algorithms and parallel computing." Ph.D. dissertation, Univ. of California at Berkeley, CA.
- Shen, J. and Astaneh-Asl, A. (1999). "Hysteretic behavior of bolted-angle connections" *Journal of Constructional Steel Research*, Vol. 51, No. 3 (pp. 201-218).
- Terzic, V. (2013). "Modeling SCB frames using beam-column elements." Retrieved from <http://opensees.berkeley.edu/wiki/images/d/de/ModelingSCBF.pdf>
- U.S. Geological Survey. (2013). "Design Maps Summary Report". Retrieved from <http://geohazards.usgs.gov/designmaps/us/application.php>
- Yang, B. and Tan, K. (2013). "Robustness of bolted-angle connections against progressive collapse: Mechanical modelling of bolted-angle connections under tension" *Engineering Structures*, Vol. 57 (pp. 153-168).

SYNCHRONIZING BEAM AND BRACE CONNECTION DESIGN IN CHEVRON BRACED FRAME SYSTEMS

Patrick J. Fortney, Ph.D., P.E., S.E., P.Eng
Cives Engineering Corporation, Roswell, Georgia 30076, USA
pfortney@cives.com

ABSTRACT

In V-type and inverted V-type braced frame systems, there are several reasons why an unbalanced summation of vertical components of the brace forces can exist. This unbalanced force, along with connection geometry and the location of the work point along the span of the beam can impart significant shear and bending moment to the beam. The forces acting at the gusset-to-beam interface of the connection create a complicated distribution of forces that typical frame analysis may not capture. Thus, it is important that the effect of brace connection geometry is known or approximated at the time the beam size is selected.

This paper provides discussion related to the distribution of brace forces within the brace connection region, the effect of the connection force distribution on the beam demands, and also possible methods for accounting for the effects of the connection during the analysis and design of the braced frame beam.

INTRODUCTION

In V-type and inverted V-type braced frame configurations, also known as chevron braced frames, it is common that the summation of the vertical components of the brace forces do not sum to zero, creating an unbalanced vertical force acting on the beam. This unbalanced vertical force can induce significant shear and bending demand in the beam (Johnson, 2014; Fortney and Thornton, 2015). This unbalanced force can be a result from a required analysis such as that required by the AISC Seismic Provisions (AISC 341-10), or an imaginary load case resulting from working with enveloped loads gathered from many different load combinations. Johnson (2014) accurately pointed out that the mechanism analysis required in seismic design imparts relatively large demands on the beam; however, no discussion was presented in regard to how to determine those demands. Fortney and Thornton (2015) provide discussion in regard to the effect of the gusset on the beam demands.

In the presence of an unbalanced vertical load, the frame beam is typically sized from an analysis assuming that the unbalanced load acts as a concentrated load with a line of action that passes through the beam-braces work point; a *Pab/L* analysis if you will. This analysis ignores any affects that the brace-to-beam connection geometry may

have. Depending on several factors such as brace geometry, brace forces, location of work point along the span of the beam, and others, this typical Pab/L analysis may not capture the demands required for the beam.

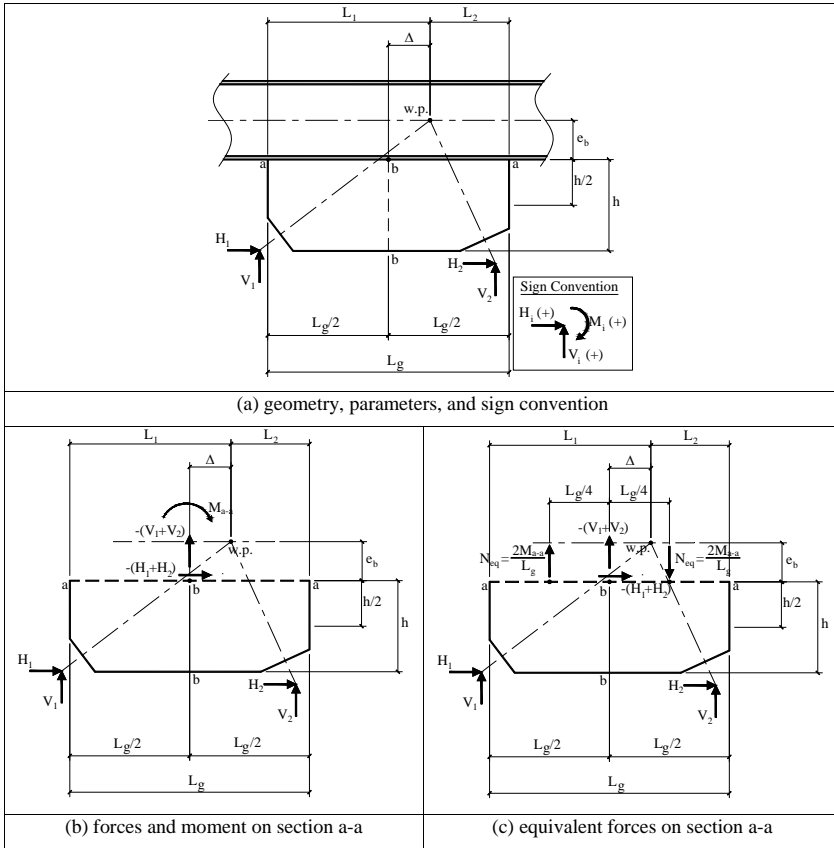


Figure 1: Free body forces on gusset-beam interface – bottom braces

The brace-to-beam connection itself has an influence on the demands imparted to the beam. The force distribution at the gusset-to-beam interface is given by Fortney and Thornton (2015) for a brace framing to the bottom side of the beam. This paper presents similar equations for the gusset-to-beam interface forces for braces framing to the top side of the beam. Together, these interface forces will be used to discuss, evaluate, and compare the beam demands using typical Pab/L analysis to an analysis that accounts for all the geometric effects of the connection.

GUSSET FORCE DISTRIBUTION – BOTTOM BRACES

The equations used to describe the force distribution in a brace connection with braces framing to the bottom side of the beam were derived in Fortney and Thornton (2015). These equations are shown here as they will be used in support of the discussion presented in this paper. Figure 1 can be used as reference for the parameters used in these equations. Figure 1 and Equations 1-4 show the gusset-beam interface forces, as these are the forces applicable to the discussion at hand. For the complete set of free body diagrams and equations, refer to Fortney and Thornton (2015).

Forces Acting on Section a-a on Beam Flange

$$H_{a-a} = (H_1 + H_2) \quad (1)$$

$$V_{a-a} = (V_1 + V_2) \quad (2)$$

$$M_{a-a} = -(V_1 + V_2)\Delta + (H_1 + H_2)e_b \quad (3)$$

$$\Delta = \frac{1}{2}(L_1 - L_2) \quad (4)$$

GUSSET FORCE DISTRIBUTION – TOP BRACES

The equations used to describe the force distribution in a brace connection with braces framing to the top side of the beam can be derived in a similar manner as that done for braces framing to the bottom side of the beam. Equations 5-8 describe the forces acting on Section a-a at the beam flange. See Figure 2 for the parameters used. The complete set of Equations used to describe the complete force distribution will be presented in a paper currently being prepared by Fortney and Thornton (2016) for publication. Only the forces acting on Section a-a are applicable to the discussion presented in this paper.

Forces Acting on Section a-a, on the Beam Flange

$$H_{a-a} = H_1 + H_2 \quad (5)$$

$$V_{a-a} = V_1 + V_2 \quad (6)$$

$$M_{a-a} = -(H_1 + H_2)e_b - (V_1 + V_2)\Delta \quad (7)$$

$$\Delta = \frac{1}{2}(L_1 - L_2) \quad (8)$$

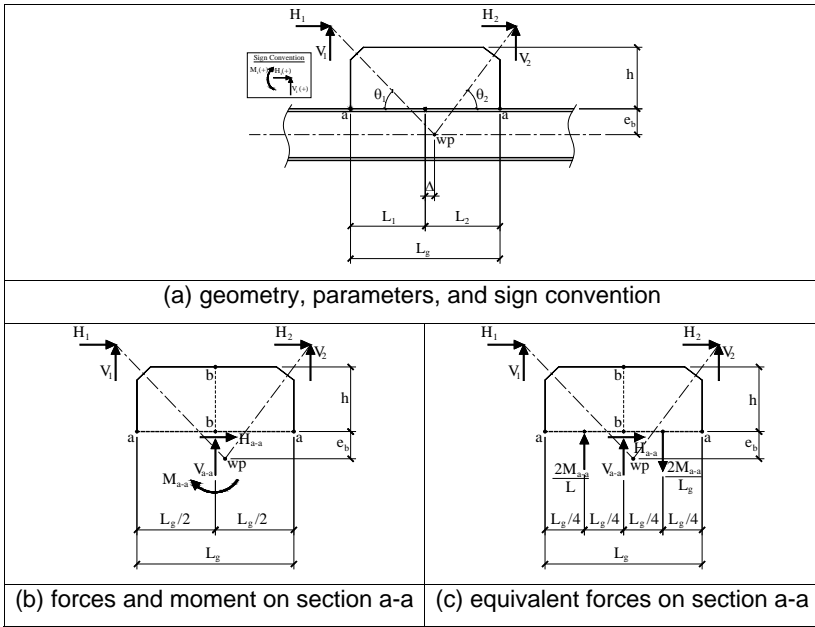


Figure 2: Free body forces on gusset-beam interface – top braces

BEAM SHEAR AND BENDING – $\Sigma V=0$

The connection geometry has an effect on beam shear and moment that a typical Pab/L analysis may not capture. Take the simple case shown in Figure 3a. The summation of the vertical components of the brace forces is zero. So the only forces acting at the gusset-beam interface are the summation of the horizontal components of the brace forces and M_{a-a} . Since the $\Sigma V=0$ ($P=0$), a Pab/L analysis gives that the braces impart zero shear and bending to the beam. However, because of the connection geometry, and the resulting gusset-to-beam interface forces, shear and bending is imparted to the beam along the connection region. Note that for this case, there is no beam shear or bending outside of the connection region. Figure 3b shows the beam shear and moment occurring along the connection region. The beam shear and bending shown in Figure 3a exists even when the ΣV is not equal to zero, and is not captured with a Pab/L analysis. These shear and moments should be superimposed on the effects caused by an unbalanced vertical force.

The maximum beam shear and moment for the case shown in Figure 3 is given in Equations 9 and 10.

$$V_{\max} = \left(\frac{4M_{a-a}}{L_g^2} \right) \left(\frac{L_g}{2} \right) = \frac{2M_{a-a}}{L_g} \quad (9)$$

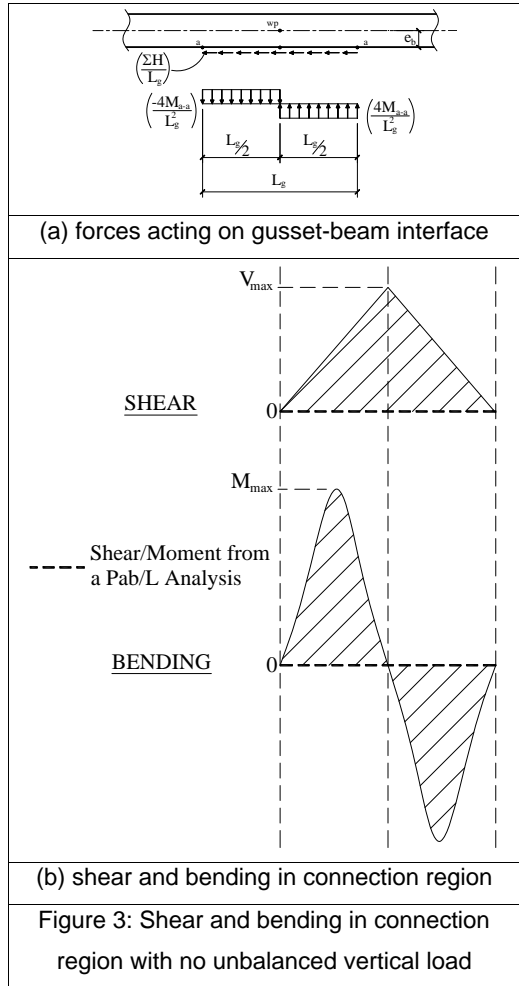
$$M_{\max} = - \left(\frac{\sum H e_b}{L_g} \right)^2 \left(\frac{L_g}{8M_{a-a}} \right) \quad (10)$$

EXAMPLE PROBLEM

Figure 4 shows a 1-bay, two-story, braced frame with a V-type configuration at the top of the first level beam and an inverted V-type configuration at the bottom of the first level beam. For this example, the two mechanism load cases required by AISC Seismic Provisions (AISC 341, 2010) for this type system will be evaluated. Figures 4a and 4b show the brace forces required for compression braces at the expected buckling strength ($1.14F_{cre}A_g$) and at the expected post-buckling strength (30% of $1.14F_{cre}A_g$), respectively. The tension braces are loaded at the braces' expected tension strengths ($R_yF_yA_g$).

For this example, only the mechanistic brace loads are considered. Adding in other superimposed loads such as gravity will only muddy up the conversation. In actual practice all appropriate loads need to be considered. For the purposes of comparing a *Pab/L* analysis to an analysis that includes brace connection geometry, only the brace loads are considered.

The brace connection geometry used for the connection to the first level beam is shown in Figure 5.



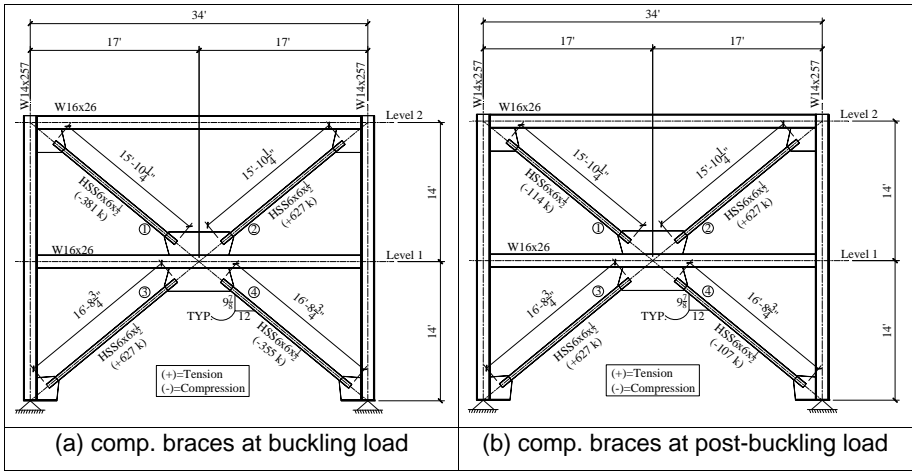


Figure 4: Two mechanistic load cases required by AISC 341-10 (tension brace forces at expected tension strength)

Performing a *Pab/L* Analysis

The vertical components of the brace forces are tabulated in Table 1. The signs associated with the tabulated values are consistent with the sign convention used to derive the equations for the connection force distribution.

From Table 1, it can be seen that the net summation of vertical components is 16.0 kips downward and 4.0 kips downward for the buckling and post-buckling load cases, respectively. The buckling case will produce the larger beam shear and moment demand using a *Pab/L* analysis. The span of the beam, *L*, is 34.0 ft. and the *a* and *b* dimensions are both 17.0 ft. This gives a beam shear and moment demand equal to

$$V_{req} = \frac{16.0k}{2} = 8.0k$$

$$M_{req} = \frac{(16k)(34ft)(12in / ft)}{4} = 1,632kip - in$$

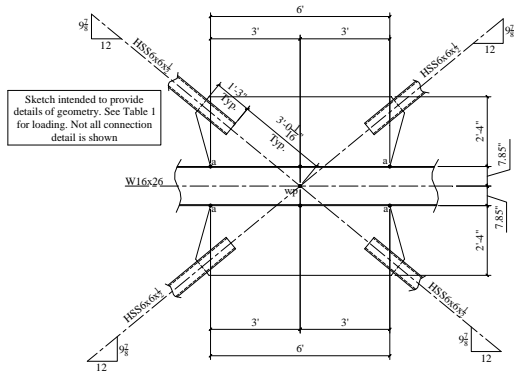


Figure 5: Brace connection geometry

A W16x26 has available shear and flexural strength (ϕV_n , ϕM_n) of 106 kips and 1,992 kip-in, respectively. $\phi V_n=106 \text{ k} > V_{req}=8.0 \text{ kips}$ and $\phi M_n=1,992 \text{ k-in} > M_{req}=1,632 \text{ k-in}$, so this beam satisfies the *Pab/L* type of analysis.

Table 1: Vertical Components of Brace Forces (units of kips)

Load Case	Top Braces		Bottom Braces		$(\Sigma V)_t$	$(\Sigma V)_b$	$(\Sigma V)_{total}$
	1	2	3	4			
Buckling	-242	398	-398	226	156	-172	-16.0
Post-Buckling	-72.0	398	-398	68.0	326	-330	-4.00

Beam Analysis Using Gusset Interface Loads

Figures 6a and 6d show the gusset-beam interface loads calculated using the equations presented previously (Equations 1-8) for both load cases. Figures 6b and 6e show the interface loads distributed over the gusset interfaces, and Figures 6c and 6f show the net distributed loads.

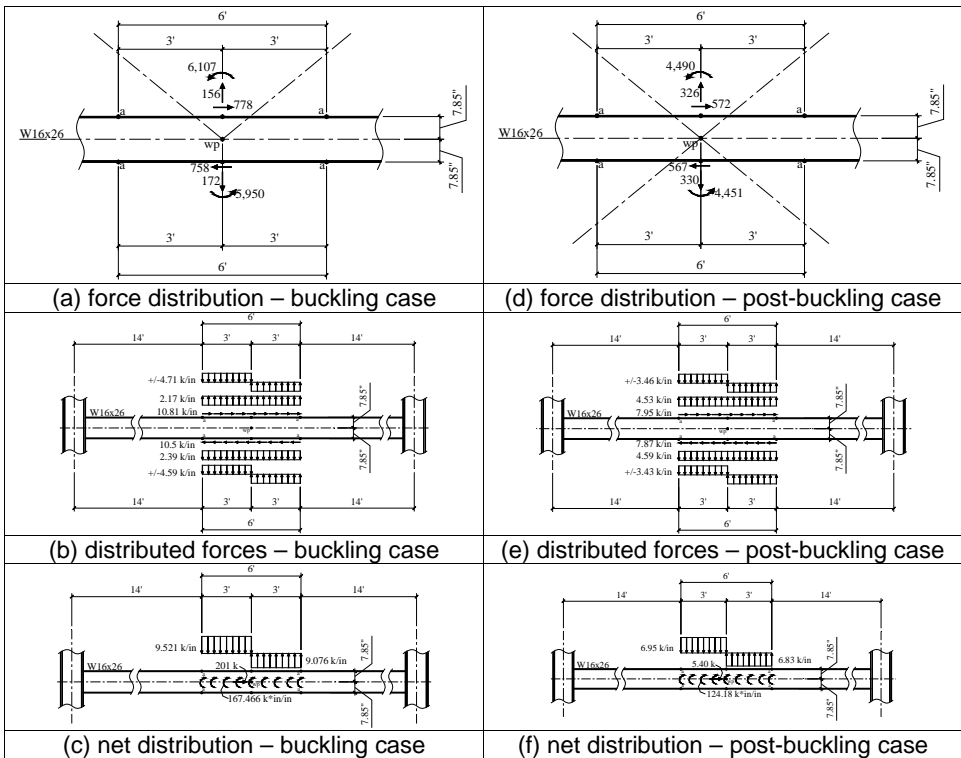


Figure 6: Brace force distributions on beam

Figures 7a and 7c show the beam shear diagrams for both load cases and Figures 7b and 7d show the beam moment diagrams. These diagrams show the beam shear and moment determined using a *Pab/L* analysis along with the analysis resulting from the beam analysis using the loads distributed along the gusset-beam interface. For the buckling load case, the *Pab/L* analysis significantly underestimates the beam shear. Beam shear is 41.9 and 124 times larger using the loads applied at the gusset interface relative to that arrived at using a *Pab/L* analysis for the buckling and post-buckling load cases, respectively. The *Pab/L* analysis will always significantly underestimate the beam shear, regardless of loading, geometry, and connection type.

The W16x26 beam was sized using the buckling load case. Therefore, the W16x26 has sufficient flexural strength for the post-buckling load case although, as can be seen in Figure 7d, the moment is 3.63 times larger than that predicted by the *Pab/L* analysis. The moment is 1.81 times larger than that predicted by the *Pab/L* analysis for the Buckling load case (see Figure 7b). Furthermore, the beam selected is not sufficient for bending for the buckling load case; $M_{req}=2,961$ kip-in compared to $\phi M_r=1,992$ kip-in. There are cases where a *Pab/L* analysis will sufficiently capture the moment required determined using the gusset-beam interface forces. Fortney and Thornton (2016) are currently preparing a paper that will provide a more detailed discussion on this point. However, this example clearly demonstrates the possibility of significantly underestimating the demand on the beam when the interface forces are not considered.

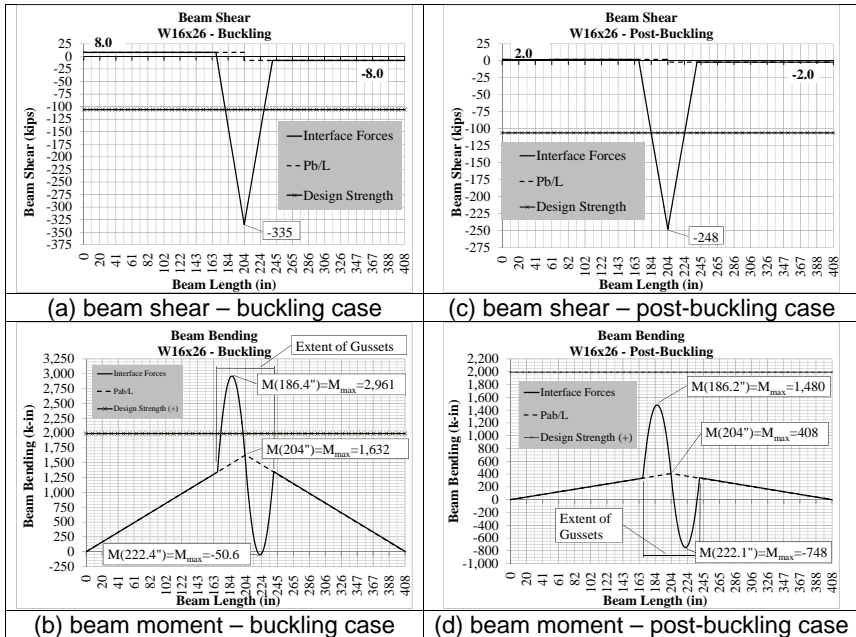


Figure 7: Beam shear and moment diagrams

Pab/L ANALYSIS COMPARED TO THE EFFECT OF THE GUSSET

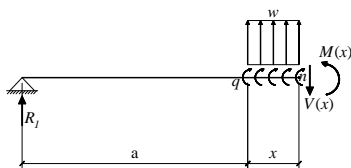


Figure 8: Free body diagram cut within the left half of the gusset region

Figure 8 shows a free body diagram that can be used to write equations, $V(x)$ and $M(x)$, to describe the beam shear and moment distribution. In Figure 8, the uniformly-distributed load, w , is the net transverse effect of the braces framing in from the top and bottom of the beam, and is calculated using the sign convention established for the gusset force distribution.

$$w = -\left(\frac{4M_{a-a}}{L_g^2}\right)_t - \left(\frac{4M_{a-a}}{L_g^2}\right)_b + \left(\frac{\sum V}{L_g}\right)_t + \left(\frac{\sum V}{L_g}\right)_b \quad (11)$$

Referring to Figure 8, the uniformly distributed moment acting at the gravity axis of the beam, q , is the net effect of the horizontal forces acting eccentrically ($e=\theta_b$) to the gravity axis of the beam at the gusset-beam interfaces at the top and bottom of the beam.

$$q = \left[(\sum H)_t - (\sum H)_b \right] \left(\frac{e_b}{L_g} \right) \quad (12)$$

The moment distribution, $M(x)$, is determined by summing moments about point n .

$$\begin{aligned} \sum M_n = 0 &= R_1(a+x) + 0.5wx^2 + qx - M(x) \\ M(x) &= \underbrace{R_1 a}_{\substack{\text{Pab/L} \\ \text{Analysis}}} + \underbrace{R_1 x + 0.5wx^2 + qx}_{\text{Effect of Gusset}} \end{aligned} \quad (13)$$

To determine where the moment is maximum, the derivative of $M(x)$ with respect to x is determined and set equal to zero.

$$\begin{aligned} \frac{d}{dx} M(x) = 0 &= R_1 + wx + q \\ x &= \frac{-R_1 - q}{w} \end{aligned} \quad (14)$$

Thus, M_{max} is,

$$M_{max} = M \left(x = \frac{-R_1 - q}{w} \right)$$

$$M_{max} = \underbrace{R_1 a}_{Pab/L} + \underbrace{(R_1 + q) \left(\frac{-R_1 - q}{w} \right) + 0.5w \left(\frac{-R_1 - q}{w} \right)^2}_{\text{Effect of Gusset}} \quad (15)$$

The shear distribution, $V(x)$, is written as follows,

$$\sum F_V = 0 = R_1 + wx - V(x)$$

$$V(x) = \underbrace{R_1}_{\substack{Pab/L \\ \text{Analysis}}} + \underbrace{wx}_{\text{Effect of Gusset}} \quad (16)$$

Shear is always maximum at $x=L_g/2$, substituting into Equation 16 gives,

$$V_{max} = R_1 + 0.5wL_g \quad (17)$$

Examination of Equation 15 allows the observation that if the sum of the terms that represent the gusset effect have an opposite sign to that of $R_1 a$ that the Pab/L analysis will adequately capture the moment demand on the beam. If both have the same sign, then Equation 15 can be used to evaluate the flexural demand on the beam. A Pab/L analysis will not be sufficient in this case. In regards to shear demand, the Pab/L analysis will always significantly underestimate the shear demand. Equation 17 should be used to evaluate shear. Typically, the gusset geometry is not known at the time the beam size is being selected. The equations presented in this paper can be used assuming a reasonable gusset length, L_g . Fortney and Thornton (2015) recommend that a good rule of thumb is to assume that L_g be approximated as 1/6 of the span of the beam.

REFERENCES

AISC 341, (2010). "Seismic Provisions for Structural Steel Buildings," *American Institute of Steel Construction*, Chicago, IL.

Johnson, J., (2014). "How Big is that Beam?," *Structure Magazine*, pp. 44-45.

Fortney, P.J., and Thornton, W.A. (2015). "The CHEVRON EFFECT – Not an Isolated Problem," *Engineering Journal, American Institute of Steel Construction*, V. 52, N0.2, pp. 125-163.

Effect of Gusset Plate Connections on Seismic Performance of Concentrically Braced Frames

Charles W Roeder
University of Washington, Seattle, WA 98195-2700
croeder@uw.edu

Dawn E. Lehman
University of Washington, Seattle, WA 98195-2700
delehman@uw.edu

Jeffrey Berman
University of Washington, Seattle, WA 98195-2700
jwberman@uw.edu

Andrew Sen
University of Washington, Seattle, WA 98195-2700
adsen@uw.edu

ABSTRACT

Concentrically braced frames (CBFs) are used for seismic design of buildings throughout the US. Currently special concentrically braced frames (SCBFs) are used with extensive capacity based design detailing requirements. Approximately 25 years ago, braced frames were designed without ductile detailing, and these systems are termed non-seismic braced frames (NCBFs). Many NCBFs remain in service throughout the US. An extensive experimental and analytical research program on the seismic performance of braced frames to improve the seismic performance of current SCBFs, to evaluate the performance of older NCBFs, and to develop economical retrofit strategies of deficient NCBFs is in progress. More than 50 large-scale braced frames have been tested. Nonlinear analytical models are developed to predict inelastic performance including fracture and prediction of structural collapse. The models are then used to evaluate seismic performance of the systems and to compare these results to seismic design requirements. This research is summarized and methods for improving seismic performance of CBFs are provided.

INTRODUCTION

Concentrically braced frames (CBFs) are stiff, strong systems, which are used for seismic design, but their design requirements have evolved in the past 25 years. Prior to 1988, CBFs were designed for factored design loads with little consideration of inelastic deformation and capacity based design. The *AISC Seismic Provisions* (AISC 2010) address these deficiencies through extensive capacity based detailed design provisions. Research has been performed on SCBFs designed by current and recent

provisions, and this research shows that significant improvements in the seismic performance of SCBFs can be achieved by making modest changes to the SCBF gusset plate designs. This research is summarized, the proposed changes to the capacity based design provisions are noted, and the benefits of those changes are demonstrated.

Older CBFs don't meet current requirements, and are regarded as non-seismic CBFs (NCBFs). Many NCBFs will remain in service for years to come, and an understanding of their seismic performance is needed. Experimental and analytical research on the seismic performance and retrofit of NCBFs is now in progress. The research to date shows that some deficiencies have a serious detrimental effect on the seismic performance of NCBFs. Other deficiencies to the current SCBF provisions have serious impact, and in some cases offer limited benefit to seismic performance. Economical and practical retrofits have been developed and evaluated for some deficiencies. These results are summarized and documented here.

CURRENT DESIGN PROVISIONS

Prior to 1988, CBFs were designed for reduced seismic loads, but the connections and other elements were designed with very limited special detailing requirements and no consideration of capacity based design. Today, the capacity based design provisions of the *AISC Seismic Provisions* (AISC 2010) are used with the reduced seismic design loads provided by ASCE 7 (ASCE 2010). The reduced forces are used to economically design the braces, and the expected capacities of the braces in compression ($P_{uc}=1.14F_{cre}A_g$) and tension ($P_{ut}=R_yF_yA_g$) are used to evaluate most other aspects of SCBF design. A_g is the gross cross-sectional area of the brace, R_y is the ratio of the expected yield strength to the minimum specified yield strength, and F_y , and F_{cr} are the stresses associated with yielding and brace buckling. Columns, column splices and gusset plate connections must develop these expected brace forces. Beams in chevron CBFs (see Fig. 1a) must also be designed for the vertical unbalanced load occurring after tensile yield and post-buckling deterioration of the brace. Gusset plate geometry must permit brace buckling end rotation. In addition, the designer must:

- Satisfy local and global slenderness limits for the brace and other members.
- Ensure that the tensile brace sustains no more than 70% of the lateral force demand.
- Size the gusset plate (GP) (or other connection) to develop P_{ut} and P_{uc} .
- Design columns and column splices to resist the minimum of the amplified seismic load or the summation of expected brace forces.

Further discussion of the design of GP and its attachments to adjacent beams, columns, and braces provide insight into SCBF response under reversed cyclic loading. Figure 1 shows typical design checks required for gusset plates. They are intended to ensure that (1) brace fracture does not occur at the net section adjacent to the gusset-to-brace connection, (2) the gusset or brace does not fail in block shear, (3) the welds or bolts joining the brace to the GP and the GP to the beams and columns are sufficient to sustain the brace yield force, (4) the GP does not buckle or fail in tension, and (5) the GP connection can accommodate the brace end rotation or moment that results from brace buckling. Bolts and welds are typically sized by the Whitmore width, Uniform

Force Method (UFM), and end rotation is permitted by the $2t_p$ linear clearance method. This design process is generally rational, but the method suggests that conservatism in gusset plate design is very desirable. However, research shows that this suggestion is one of several shortcomings of the method.

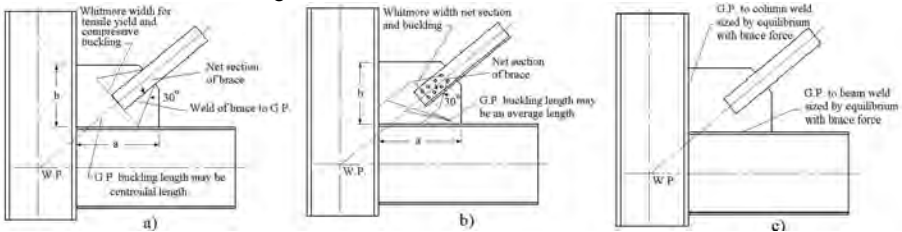


Figure 1. Typical SCBFGusset Plate Design Checks

PERFORMANCE OF CURRENT SCBF SYSTEM

More than 39 single bay CBF assemblages (see Fig. 2a) and 6 multi-story braced frames (see Fig. 2b) were tested (Johnson, 2005; Herman, 2007; Kotulka 2007, Lehman et al. 2008, Lumpkin 2009), and extensive nonlinear analyses were performed. This research provides considerable insight into the seismic performance of the SCBF systems. The frames were full-scale simulations of modest sized CBFs such as may be used in a 2 to 4 story frame or the upper levels of a taller structure. Beam and column sizes and brace configuration were varied in some tests, but GP connection performance was the focus of most tests, and specimens were varied to evaluate:

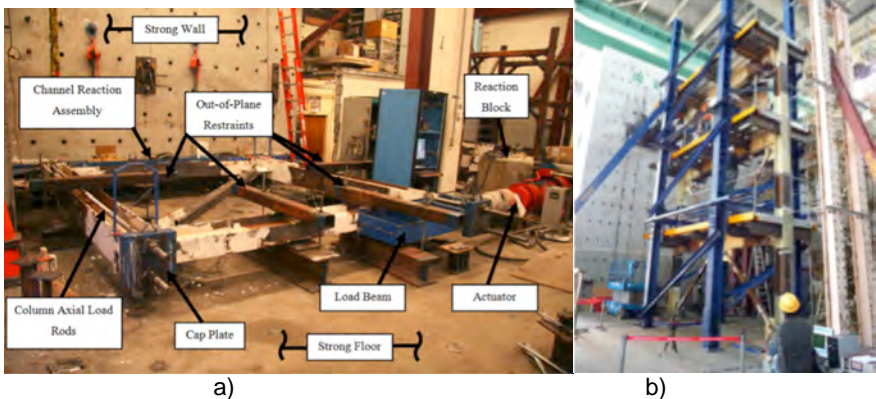


Figure 2. Typical Test Setups, a) Single-Story Single Bay, U of Washington, b) Multi-Story, NCEE

- current design procedures,
- different failure modes for CBFs and GP connections,
- different brace cross sections,
- weld requirements between the GP and framing members,

- connection clearance models for brace end rotation,
- GP thickness and relative stiffness of framing members,
- tapered and rectangular GPs, and
- bolted and welded connections.

The specimens were subjected to a cyclic inelastic deformation history based upon the ATC-24 testing protocol (ATC, 1992).

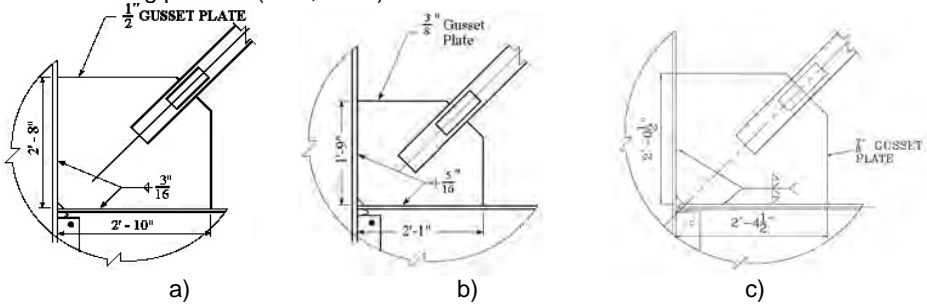


Figure 3. GP design; a) Spec. A, b) Spec. B, c) Spec. C

It is not possible to discuss all tests here, but 3 typical specimens are discussed and compared to illustrate key observations from this research. Figures 3 and 4 show the connection details and force-deformation behavior of the 3 specimens. Figures 3a and 4a show the connection details and behavior for Specimen A, which was designed using the current AISC uniform force method with the UFM and the $2t_p$ clearance method (AISC 2005). The brace yielded in tension and buckled in compression, but the ductility was limited. Sudden fracture of the fillet welds (see Fig. 5a) joining the gusset plate to the beam and column occurred, because the AISC demand critical welds were designed to achieved the expected resistance of the brace with the UFM with no consideration of deformation demands on the GP. The research shows that it is essential to design these welds to develop the plastic capacity of the GP rather than the expected capacity of the brace. The $2t_p$ linear clearance model results in relatively large GPs, which cause significant local yield deformation in the beam and column as shown in Fig. 5d, and an alternate elliptical clearance method (Lehman et al 2008) (see Fig. 6) was developed based on the observed patterns of GP yield. The local yield deformation of the beams and columns is increased with stiff, strong GPs, and decreased with thinner GPs obtained from modified design methods.

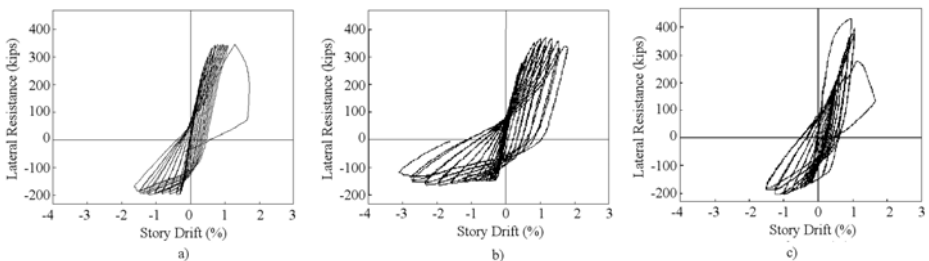


Figure 4. Force-deflection behavior; a) Spec. A, b) Spec. B, and c) Spec. C.

Specimen B (and most other specimens in the test program) used the $8t_p$ elliptical clearance method and welds were designed to develop the plastic capacity of the plate as shown in Figs. 3b and 3c. The elliptical clearance provided optimal connection performance with ample end rotation for brace buckling, thinner, more compact GPs, and reduced local yielding of the beams and columns adjacent to the GP as seen in Fig. 4b. The brace sustained large out-of-plane deformation as shown in Fig. 5b and ultimate fracture occurred in the buckled region as illustrated in Fig. 5c. Specimen C employed the same brace and column as Specimen B, but the gusset plate connection was conservatively designed. The brace fractured as with Specimen B, but the fracture occurred at a much smaller deformation level as shown in Fig. 4c. All rectangular and tapered gusset plates experienced crack initiation as illustrated in Fig. 5e, but if the welds were sized to develop the tensile yield capacity of the GP and used AISC Demand Critical weld electrodes the cracks remained stable and did not fracture.

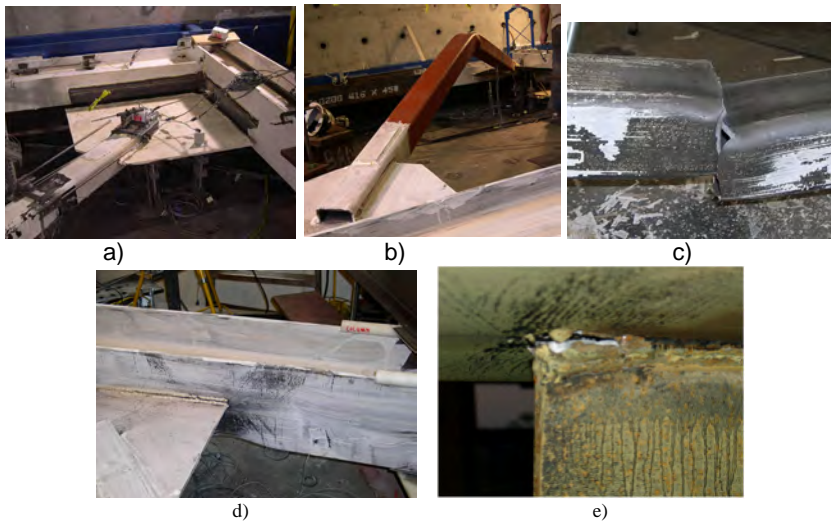


Figure 5. Photos of test results; a) Weld fracture of Spec. A, b) Out-of-plane buckling deformation c) Brace fracture, d) Local Yielding in Column, and e) Weld Crack Initiation.

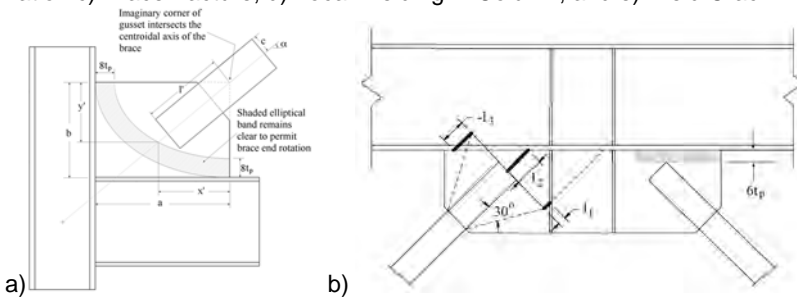


Figure 6. Clearance Models, a) Elliptical Corner GP, b) Midspan GP

IMPROVED SEISMIC PERFORMANCE OF SCBF SYSTEM

This research led to a number of important design recommendations called the Balanced Design Procedure (BDP) (Roeder et al 2011). The BDP is a capacity based design procedure where the yield mechanism and failure modes of Fig. 7 are evaluated, but rather than providing conservative resistance to meet these behaviors, the resistances are balanced to assure a desirable sequence of yield behavior. The method has many similarities with current SCBF design, but there key differences including:

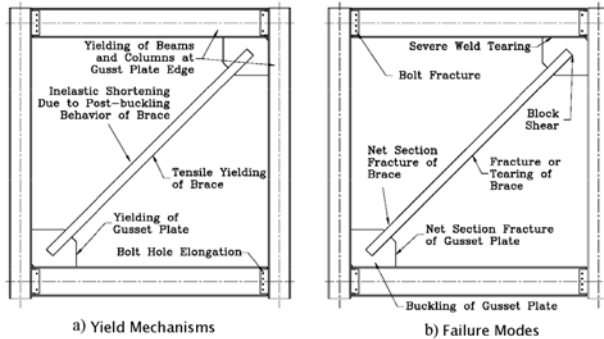


Figure 7. Yield mechanisms and failure modes

- 1) The welds joining the gusset plate to the beam and column are designed to achieve the plastic capacity of the GP rather than the expected resistance of the brace as used in the UFM.
- 2) The $8t_p$ elliptical clearance for corner GPs and $6t_p$ parallel clearance model of midspan GPs (see Fig. 6) permits smaller, more compact gusset plates, which reduces the size of the relatively rigid connection stiffness zone and reduces damage to welds and local yielding of the beam and column adjacent to the GP, while permitting rotation induced by brace buckling.
- 3) Yielding in the Whitmore width of the GP is a desirable yield mechanism, since it reduces damage to the welds and local yielding and deformation of the beams and columns adjacent to the gusset, but it should be delayed until after initial yielding and buckling of the brace.
- 4) Relaxation of the block shear requirements for GPs is required and is appropriate based upon statistical analysis of past GP block shear behavior. The relaxation is an integral part of reducing GP thickness and geometry to increase inelastic deformation capacity.
- 5) The strength and stiffness of the GP connection must be adequate to develop the expected resistance of the brace, but extra strength and stiffness cause early brace fracture and reduced inelastic deformation capacity.
- 6) Wide flange braces achieve larger inelastic deformations than HSS tubes, but they increase deformation demands on the gusset plate connections.

The research shows that this Balanced Design Procedure increases the inelastic deformation capacity 46% compared to the current SCBF criteria.

INVENTORY OF OLDER BRACED FRAMES

Braced frames designed prior to about 1990 do have the current capacity based design requirements and are noted as NCBFs in this paper. A recent detailed review of 13 NCBFs built in seismic regions before about 1990 (Sloat 2014) showed that older NCBFs have serious multiple deficiencies, when compared to current SCBF requirements, and the demand-to-capacity ratios (DCRs) for these deficiencies often were very large.

None of the gusset plate connections could develop the expected capacity of the brace nor did they have allowance for brace end rotation. The connections failed for many different reasons including tensile strength, net section, bolt shear and bearing, and weld resistance. Approximately 70% of these NCBFs had chevron bracing, which is preferred by architects in the US. However, chevron bracing is seldom used for current SCBFs, because the beam becomes extremely large due to the unbalance brace force requirement. Virtually all chevron NCBF beams failed the current beam strength requirements with DCRs as large as 8.0. Slenderness limits for seismic compactness are important for capacity based design, and most braces, beams and columns failed these slenderness limits with ratios up to 2.0 or larger. A wide range of bolted and welded connections (see Fig. 8) also were used in these older NCBFs

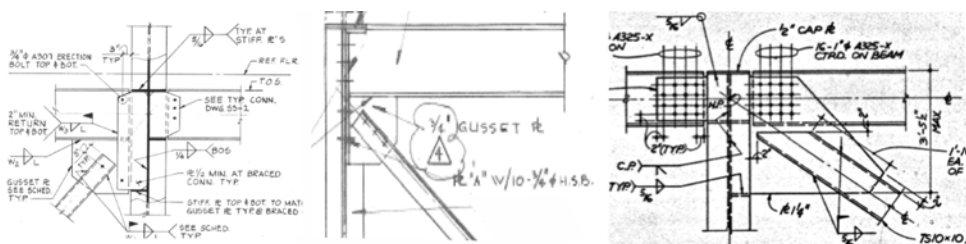


Figure 8. Typical Connection Details

RESEARCH ON OLDER NCBFs

An extensive test program to evaluate NCBF performance and to investigate potential retrofit methods is in progress. Eighteen full-scale NCBF test specimens that were 2-story chevron braced frames (see Fig. 9a) (Sen 2014) or single story diagonal braced frames (see Fig. 9b) (Sloat 2014, Johnson 2014, Ballard 2015) have been evaluated. Individual specimens were designed to have specific deficiencies or economical retrofits for evaluation based upon the inventory noted earlier.

The test results are too extensive to describe in detail, but they clearly show that some deficiencies have more severe impact on seismic performance than others. Further, they show the importance of considering and balancing yield mechanisms and failure modes, because significant inelastic deformation came for unanticipated sources. Figure 10a shows the lateral shear force vs. story drift plot of a specimen with diagonal bracing, which meets current SCBF design criteria. It achieves good inelastic performance, while Fig. 10b shows that a specimen, which does not satisfy SCBF compactness criteria, has brace fracture at a small deformation. The specimen of Fig. 10c is identical to that of Fig. 10b except the slender HSS tube brace is filled with

concrete to restrain local cupping deformation that precedes brace fracture. This significantly increases inelastic deformation capacity.

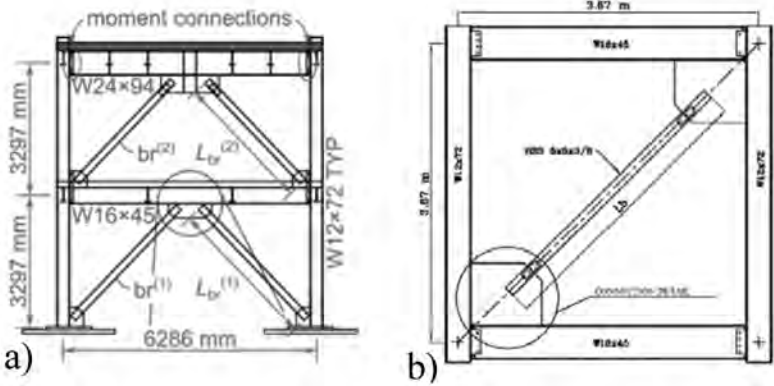


Figure 9. Typical Test Specimens

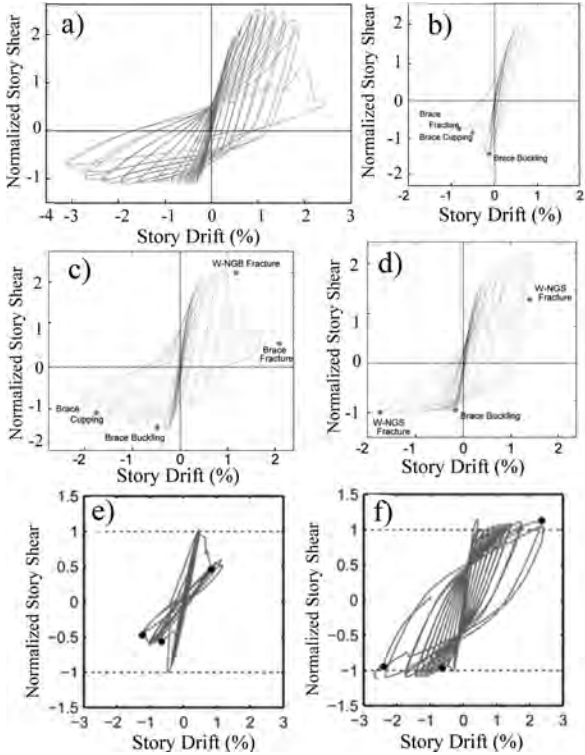


Figure 10. Typical Test Results

Weld deficiencies were common, and weld fracture often occurred at relatively small inelastic deformations as shown in Fig. 10d. Figures 10a through 10d had diagonal braces, and have unbalanced resistance in tension and compression. As a result, diagonal braces are used in pairs. Figures 10e and 10f have balanced behavior because these specimens are chevron NCBFs. Figure 10e has very slender HSS braces and fractures at a small story drift as previously shown in Fig. 10b. However, the chevron NCBF of Fig. 10f failed SCBF beam strength requirements but still had relatively good behavior. This suggests this deficiency is less severe than some others.

CONCLUSIONS

This review of ongoing research summarized a wide range of recent research on the seismic performance of braced frames. It has shown that the Balanced Design Procedure has been developed. This BDP encourages yielding in the gusset, and strives toward thinner, more compact gusset plates thereby assuring an average 46% increase in the inelastic deformation capacity of braced frames under seismic load. The method employs an elliptical clearance model for end rotation due to out-of-plane brace buckling, and requires that the welds joining the gusset plate to beams and columns develop the plastic capacity of the gusset rather than the expected capacity of the brace through the UFM. Many older CBFs were designed prior to current SCBF capacity based design requirements, and the deficiencies with respect to current SCBF requirements are very large in some cases. However, the research shows that some deficiencies are much more severe problems than others, and these deficiencies typically result in sudden brittle fractures, at very small drift ranges. Some other deficiencies have relatively minor detrimental effect on seismic performance, and some apparently deficient systems resulted in seismic performance quite comparable to that achieved with SCBF systems. These effects appear to be very consistent with Balance Design Procedure proposed for new structures, because their yield behavior was related to yield mechanisms that increase story drift without increasing the likelihood of failure. This research continues and further results will be presented in the future.

ACKNOWLEDGEMENTS

The work was funded by the National Science Foundation through research grants CMS 0301792, CMS 0619161, and CMS 1208002. Supplemental financial support and material donations were provided by the American Institute of Steel Construction and coordinated by Tom Schlafly. In addition, the research team received advice from many practicing consultants. This advice and financial support is greatly appreciated. Many large-scale CBF tests and nonlinear analyses have been performed as part of this research. The experimental research discussed in this paper was performed at the University of Washington, the University of California, Berkeley, the University of Minnesota and the National Center for Research in Earthquake Engineering (NCREE) in Taipei, Taiwan.

REFERENCES

- AISC (2010a). "Seismic Provisions for Structural Steel Buildings." *AISC/ANSI 341/10*, American Institute of Steel Construction, Chicago, IL.
- ASCE (2010). "Minimum Design Loads for Buildings and Other Structures." *ASCE/SEI 7/10*. American Society of Civil Engineers, Reston, VA.
- Ballard, R. (2015) "Impact of connection type on system performance of non-seismic concentrically braced frames," MS Thesis, University of Washington, Seattle, WA.
- Herman, D. "Further improvements on and understanding of SCBF systems," MS Thesis, University of Washington, Seattle, WA.
- Johnson, M.M. (2014). "Seismic evaluation of bolted connections in non-seismic concentrically braced frames." MS thesis, Univ. of Washington, Seattle, WA.
- Johnson, S. M. (2005) "Improved seismic performance of concentrically braced frames," MS Thesis, University of Washington, Seattle, WA.
- Kotulka, B.A. (2007) "Analysis for a design guide on gusset plates used in concentrically braced frames," MS Thesis, University of Washington, Seattle, WA
- Lehman, D.E., Roeder, C.W., Herman, D., Johnson, S., and Kotulka, B. (2008) "Improved seismic performance of gusset plate connections," ASCE, *Journal of Structural Engineering*, Vol. 134, No. 6, pgs 890-901.
- Lumpkin, E.J. (2009) "Enhanced seismic performance of multi-story special concentrically braced frames using a balanced design procedure," MS Thesis, University of Washington, Seattle, WA.
- Roeder, C.W., Lumpkin, E.J., and Lehman, D.E. (2011). "A balanced design procedure for special concentrically braced frame connections." *Journal of Constructional Steel Research*, 67(11), 1760-1772.
- Sloat, D.A. (2014). "Evaluation and retrofit of non-capacity designed braced frames." MS thesis, Univ. of Washington, Seattle, WA.
- Sen, A.D. (2014). "Seismic performance of chevron concentrically braced frames with weak beams." M.S. thesis, Univ. of Washington, Seattle, WA.

SEISMIC DESIGN OF BRACE CONNECTIONS FOR STEEL CONCENTRICALLY BRACED FRAMES OF THE CONVENTIONAL CONSTRUCTION CATEGORY

Sophie Decaen, Ali Davaran, Robert Tremblay, and Alexandre Gélinas
Department of Civil, Geological & Mining Engineering, École Polytechnique, Canada
sophie.decaen@gmail.com; dr_davaran@yahoo.co;
robert.tremblay@polymtl.ca; alexandre.gelinas@polymtl.ca

ABSTRACT

In Canadian design practice, steel concentrically braced frames of the Conventional Construction category (Type CC) are often preferred as they require only minimum special seismic design and detailing requirements. This article examines the seismic response of this framing system for two-storey buildings located in Victoria, BC, and Montreal, QC. Site class C (soft rock or firm ground) and E (soft soil) are considered at each location. The frames have HSS bracing members with single-shear bolted lap splice connections and the study focuses on the buckling response of the braces and failure modes developing in brace connections. Satisfactory seismic response was obtained when brace connections were designed to resist amplified seismic loads in tension and compression. Other brace connection design approaches resulted in undesirable brace buckling modes and/or failure of brace connections. The seismic demand is generally higher for the frame located on a class E site in Victoria.

1. INTRODUCTION

Concentrically braced frames with an X-bracing configuration are commonly used to resist lateral loads in medium- and low-rise steel building structures in Canada. The bracing members in these frames are typically made from HSS members with field bolted connections (Figure 1). At mid-connections, X-braced frames typically have one continuous brace member and one discontinuous brace member. Brace connections can be either double-shear or single-shear lap splice connections. For lighter brace axial load applications, the second type is preferred as it is much easier to fabricate and assemble on site.

In Canada, seismic design of building structures must be performed in accordance with the provisions of the National Building Code of Canada (NBCC) (NRCC, 2010) and steel frames must meet the special seismic requirements contained in the CSA S16 standard for the design of steel structures (CSA, 2009). For steel braced frames, seismic provisions are given for three categories: Type CC (conventional construction), Type LD (limited ductility), and Type MD (moderately ductile). Each frame category is assigned a ductility-related force modification factor R_d reflecting its lateral inelastic deformation capacity: 1.5, 2.0, and 3.0, respectively, for Types CC, LD and MD braced frames. In CSA S16, strict compliance to capacity design principles and special detailing rules must be satisfied for Type LD and Type MD braced frames so that the intended ductile response associated with the higher R_d values can be achieved. Conversely, Type CC braced frames essentially rely on

the inherent ductility of steel and other sources of energy dissipation that exists in traditional steel construction (e.g., friction). Hence, capacity design need not be applied for these frames and fewer seismic detailing rules apply. As a consequence, even if it implies larger seismic loads compared to Types LD and MD frames, Type CC is often selected because it is easier to design and fabricate.

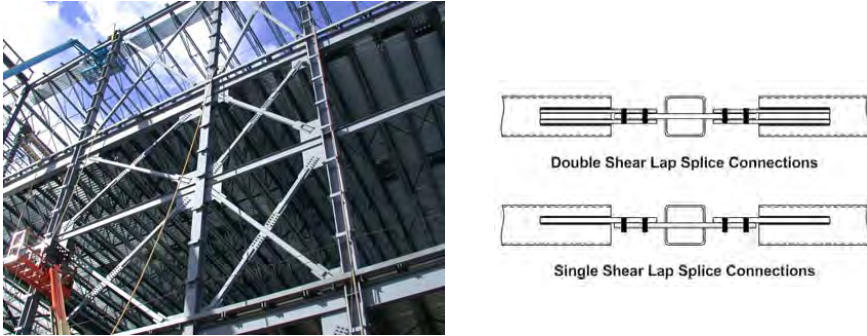


Figure 1: Concentrically X-braced frame with HSS bracing members and field-bolted lap splice connections (connection at braces intersection shown).

As illustrated in Figure 2, full-scale cyclic testing of X-braced frame (Davaran et al. 2012; Gélinas et al. 2013) showed that braces in X-bracing with single-shear lap splice connections can buckle in a three hinge mechanism that mainly involves plastic rotation in the brace connection plates. This “three-hinge buckling mode” is mainly attributed to the eccentricity present in the connection and it is more frequent in the discontinuous brace. It occurs before flexural buckling of the braces and therefore reduces the frame lateral strength. It induces large strains in the plastic hinges forming in the plates, which can lead to premature low-cycle fatigue failure of the connections (Figure 2d). Davaran et al. (2014a) proposed a method to predict the axial compressive strength associated to this buckling mode. Davaran et al. (2014b) developed a numerical model capable of reproducing this instability failure mode and studied its impact on the seismic response of a two-storey braced frame building.

The tests also revealed other failure modes that may occur in brace connections, including tension failure at the net section of connecting plates or bracing members. This paper presents the results of nonlinear response history analyses performed on two-storey Type CC steel braced frames designed with single-shear brace connections. The numerical models used can predict failures due to low-cycle fatigue in connecting plates as well as net section failures. Four different design approaches are considered for the brace connections. The structures were assumed to be located on site classes C and E in both western and eastern Canada to also study the influence of ground motions on frame response.

2. DESIGN OF THE PROTOTYPE BUILDINGS

2.1 Seismic Design of Type CC Low-Rise Steel Braced Frames

In the NBCC, the minimum seismic design load V is given by:

$$[1] \quad V = \frac{S(T_a)M_v I_E W}{R_d R_o} \leq \frac{2 S(0.2s) I_E W}{3 R_d R_o}$$

, where $S(T_a)$ is the design spectrum, T_a is the structure fundamental period used in design, M_v is a factor that accounts for higher mode effects on base shear, I_E is the importance factor, W is the seismic weight, and R_d and R_o are respectively the ductility- and overstrength-related force modification factors. The design spectrum is built from uniform hazard spectral (UHS) ordinates established for a probability of exceedance of 2% in 50 years and modified for local site conditions. For steel braced frames, T_a is equal to $0.025 h_n$, where h_n is the building height. Alternatively, the period T_1 from dynamic analysis can be used for T_a up to an upper limit $T_a = 0.05 h_n$. For low-rise buildings of the normal risk category, M_v and I_E are equal to 1.0. The seismic weight includes the dead load plus 25% of the roof snow load. As mentioned, R_d is equal to 1.5 for Type CC steel seismic force resisting systems (SFRSs). For these structures, R_o is set equal to 1.3 to reflect the dependable system overstrength resulting from the use of resistance factors in design, the difference between nominal and actual steel yield strengths, and the fact the next available (greater) size is selected for the structure components. As indicated in Equation 1, V need not exceed 2/3 times the value calculated at a period of 0.2 s.

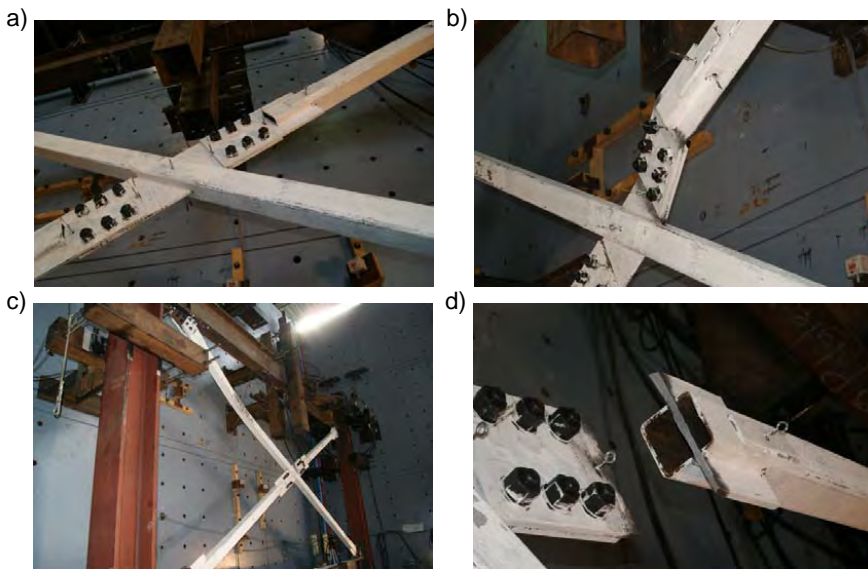


Figure 2. Behaviour of single-shear lap splice connections in steel X-braced frames: a) Connection; b) Buckling of connection in the discontinuous HSS; c) Buckling of the continuous HSS; and d) Failure at mid-connection (Davaran et al. 2012).

For Type CC frames located in moderate and high seismic zones, CSA S16 requires that all connections along the lateral load path be either designed and detailed such that their governing failure mode is ductile or designed for seismic induced axial forces amplified by $R_d = 1.5$. In the second case, the connection design loads need not

exceed the probable yield strength of the members being joined. In this study, these two connection design options are referred to as CCM and CCS, respectively.

CSA S16 includes several requirements for connections subjected to tension forces but no guidance is provided to assess the connection compressive resistance. Consequently, brace connections in practice are often only verified for limit states associated to tension. In this article, the connections so-designed are designated as T/O CCM or T/O CCS (T/O = Tension/Only). The AISC Guide No. 24 (Packer et al., 2010) proposes a method to verify the capacity of single-shear lap joints under compression. In this approach, axial-flexure interaction is verified for each individual plate in the regions outside of the plate overlap segment assuming a moment equal to the axial load times the distance between the centre lines of the connected plates. The connections designed to satisfy this additional interaction check in compression are referred to as T/C CCM and T/C CCS (T/C = Tension/Compression).

2.2 Design of the Prototype Buildings

The structures studied are two-storey office buildings located in two moderate seismic regions of Canada: Victoria, British Columbia, in the west, and Montreal, Quebec, in the east. At both locations, site classes C (soft rock or firm ground) and E (soft soils) were considered. The design gravity loads and the design spectrum $S(T)$ at all sites are given in Figure 3. The properties of the building structures are also shown in Figure 3. The buildings have a square footprint and lateral loads in each direction are resisted by two single-bay, tension-compression X-braced frames, one in each exterior wall. The structure response in the E-W direction is examined herein. For all cases studied, the braced frame width (7.5 m) and storey heights (4.087 m) were set equal to those of the test frame used in the aforementioned full-scale test program so that direct comparison with experimental results could be made for the calibration of the numerical models. For each location and site class, the building plan dimension D_n was varied to achieve a demand-to-capacity ratio close to 1.0 at both storeys with available brace sizes.

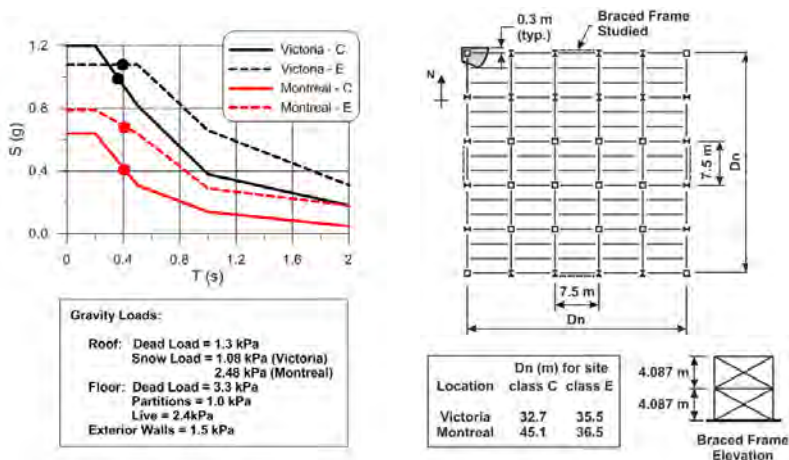


Figure 3: Design loads and building properties.

Characteristics of the final designs are presented in Tables 1 and 2. The computed periods T_1 are given in Table 1. For both structures in Montreal, the period T_a had to be limited to the upper limit $T_a = 0.05 h_n = 0.41$ s. The periods T_a and corresponding S values are plotted in the design spectra of Figure 3. Seismic effects were determined from dynamic (response spectrum) analysis and the design base shear V_d was taken as the minimum between the base shear from analysis multiplied by I_E/R_dR_o and 0.8 times the force V from Equation 1. V_d values are given in Table 1. The minimum $0.8V$ governed for the class C site in Montreal, leading to higher lateral overstrength for this structure. Accidental torsional effects were determined by moving the centre of mass by 5% D_n in the analysis. The bracing members are CSA G40.21-350W HSS members with $F_y = 350$ MPa. Columns are ASTM A992 W shapes. Final sizes are given in Table 1. Braces were governed by compression under seismic loads plus concomitant gravity loads ($D + 0.5L + 0.25 S$). A brace effective length equal to $0.9 \times 0.5 = 0.45$ times the centre length dimension was adopted to reflect the brace net length excluding end connections (0.9) and the out-of-plane and in-plane support provided by the tension acting braces (0.5).

Table 1: Braced frame design

Location	Site Class	T_1 (s)	T_a (s)	V_d (kN)	Level	Brace Sizes	Column Sizes
Victoria	C	0.37	0.37	2685	2	HSS127x127x4.8	W200x52
					1	HSS152x152x8.0	W200x52
	E	0.39	0.39	2789	2	HSS127x127x4.8	W200x52
Montreal	C	0.57	0.41	2341	1	HSS152x152x8.0	W200x52
					2	HSS127x127x4.8	W200x52
	E	0.47	0.41	2321	1	HSS178x178x4.8	W200x52
					2	HSS127x127x4.8	W250x49
					1	HSS178x178x4.8	W250x49

Table 2: Properties of the mid-connections: bolts $n_b \times d_b$ and plate sizes $b \times t$

Brace Sizes	T/O CCM	T/O CCS	T/C CCM	T/C CCS
HSS 127x127x4.8	4x19.1 290x6.4	6x19.1 152x19.1	6x19.1 254x19.1	6x19.1 254x25.4
HSS152x152x8.0	4x28.6 435x7.9	6x28.6 305x19.1	6x22.2 305x31.8	6x25.4 430x31.8
HSS178x178x4.8	4x25.4 385x7.9	6x25.4 254x19.1	6x19.1 254x31.8	6x25.4 305x38.1

Brace connections are single-shear lap splices. The two plates are G40.21-350W steel ($F_y = 350$ MPa) and have the same thickness and width. They are connected with two parallel rows of ASTM A325 bolts. For the same connection type (T/O vs T/O, CCM vs CCS), the same number of bolts, n_b , bolt diameters, d_b , and plate cross-section dimensions, $b \times t$, were required for a given brace size. These properties are given in Table 2. In their study, Castonguay and Tremblay (2010) observed that failure by bolt bearing was more ductile compared to tension failure on net section, shearing of bolts or weld failure. Connections T/O CCM were therefore sized so that bolt bearing governed failure in tension. The T/O CCS connections were designed to resist tension loads determined with seismic loads amplified by 1.5, without verifying the ductility of the governing failure mode. After design completion, calculations showed that net section failure of the plates was critical for all three brace sizes with this connection. Bearing failure was also targeted for the T/C CCM designs; however, it was not possible to obtain realistic plate sizes that would fail in bearing while satisfying the axial-flexure interaction check in compression. The connections were then designed to satisfy the axial-flexure limit state without consideration of ductility. That

modified design is referred to as T/C CCxM. The same approach was used for the T/C CCS connections except that the design axial loads were amplified by 1.5. In all connections, a free length of 25 mm was left between the end of the splice plates and the ends or edges of the HSS members. The through plates used at the brace ends were also same as the lap splice plates required at mid-connections.

3. RESPONSE HISTORY ANALYSIS

3.1 Numerical Model

The seismic nonlinear response history analyses were performed with the OpenSees computer program (McKenna 2011) using a two-dimensional numerical model similar to that developed by Davaran et al. (2014a). As shown in Figure 4a, the model included the bracing members and columns of the braced frame studied as well as the gravity columns stabilized by the frame. Braces and columns were modelled with 10 *Force-Based Beam-Column* elements with fibre discretization of the members' cross-sections (Figure 4b). The *Steel02* material with kinematic and isotropic hardening properties was assigned to the section fibres. Distributed plasticity, inelastic buckling and tension yielding could then be reproduced for the brace members (Aguero et al. 2006).

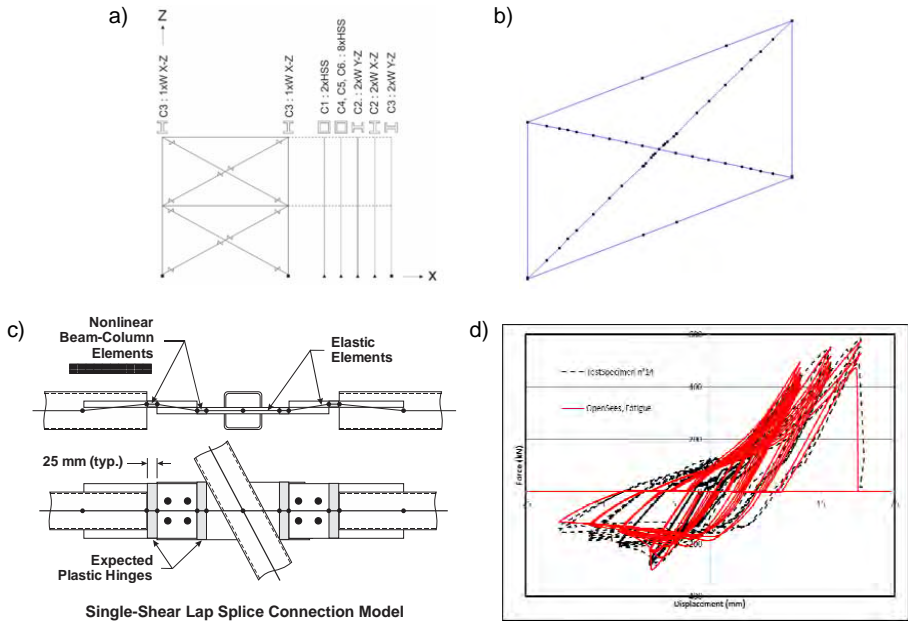


Figure 4: Numerical model: a) Braced frame elevation; b) 3D view of a braced frame storey; c) Mid-connection model; and d) Validation of the connection fatigue model.

Force Based Beam-Column elements were also used for the plate segments of the single-shear splices where plastic hinging was expected to form in the three-hinge brace buckling mode (Figure 4c). Plate eccentricities in the connections were explicitly reproduced in the model. Axial-flexure induced strains developing in the plates in

these critical regions could then be predicted and low-cycle fatigue failure was considered for the fibres of the splice plate elements. The fatigue model by Uriz et al. (2008) was adopted for this purpose. It assumes linear damage accumulation and the parameters m and ε_0 were respectively set equal to -0.3 and 0.213, as was required to adequately reproduce plate failure observed in the tests (Figures 2 and 4d). *ZeroLength* elements with nonlinear material properties were also implemented in the connections to predict tension failure on net section, bolt shear failure, and inelastic deformations due to bolt bearing. For these three failure modes, inelastic deformation capacities prior to connection failure were based on test data by Castonguay and Tremblay (2010) and Jiang (2013). Bolts in Type CC frames are installed in the snug tight condition and bolt slip (± 1.5 mm) at low load (50 kN) was also included in all connection models. A probable yield strength of 460 MPa was assigned to the material used for the bracing members. The yield strength for the plates and columns was set to 385 MPa. Bolt shear resistances were based on nominal properties. Additional detail on the numerical model can be found in Decaen (2015).

For each location and site class, the structure was subjected to an ensemble of 10 representative ground motion time histories scaled to match the 2% in 50 years design spectra of Figure 3. The ground motions were then further amplified by the ratio of the seismic design forces resisted by the braced frames determined with and without considering accidental in-plane torsion effects. P-delta effects induced by the structure dead load plus 50% of the floor live load and 25% of the roof snow load were included in the analyses. Mass proportional damping corresponding to 3% of critical damping in the fundamental mode was assigned to the model.

3.2 Analysis results

Brace connection failures observed in the analyses are presented in Table 3: F = low-cycle fatigue of connection splice plates, and B = bolt shear. The number of ground motion records producing failure are also given in the table (e.g., F(10) = low-cycle fatigue failure in 10 records). For each connection design, all observed failures are of the same type. Table 3 also provides the buckling modes experienced by the continuous (C) and discontinuous (D) braces in compression. Buckling modes for each brace are illustrated in Figure 5a. Buckling of the continuous braces typically initiated in Mode 1 and then migrated to Mode 2 as tension developed in the discontinuous braces so that the latter could provide sufficient out-of-plane support for the continuous brace. Mode 5 involving a three-hinge mechanism was also observed for the continuous braces. For the discontinuous braces, buckling of the individual brace segments occurred in either flexure (Mode 3) or the three-hinge mechanism. The latter involved one brace segment (Mode 4) or both brace segments (Mode 6).

Connections T/O CCM were designed to resist in tension the non-amplified seismic brace forces and were therefore the weakest among the four connection types. In all frames with these connections, ductile bolt bearing deformations initiated in the first response cycles, as anticipated in design. Thereafter, both the discontinuous and continuous braces experienced three-hinge buckling modes with plastic rotation in the splice plates. Buckling was more pronounced in the discontinuous braces with buckling occurring on average at approximately 30% of the brace probable compressive resistances, C_u (Figure 5b). The continuous braces could sustain much higher compression loads up to 0.75 C_u before buckling. For the Victoria sites, plastic rotations in the splice plates induced low-cycle fatigue failure in brace connections under every ground motions. Although less frequent, similar failure was observed for the Montreal structures. The reduced damage in Montreal is due to the smaller displace-

ment demands imposed by the high frequency ground motions expected in eastern Canada and the higher lateral overstrength for the Montreal building on site class C.

Table 3: Brace connection failure modes and brace buckling modes

Location/Site class	T/O CCM	T/O CCS	T/C CCxM	T/C CCS
Victoria C	F(10) C5-D4	F(2) C1&2-D4	B(2) D3&4	- C1-D3
Victoria E	F(10) C5-D6	F(7) C1&2-D4	B(7) D3&4	- C1-D3
Montreal C	F(1) C5-D4	F(1) C1-D4	- D3	- C1-D3
Montreal E	F(6) C5-D6	F(4) C1&2-D4	B(5) D3&4	- C1-D3

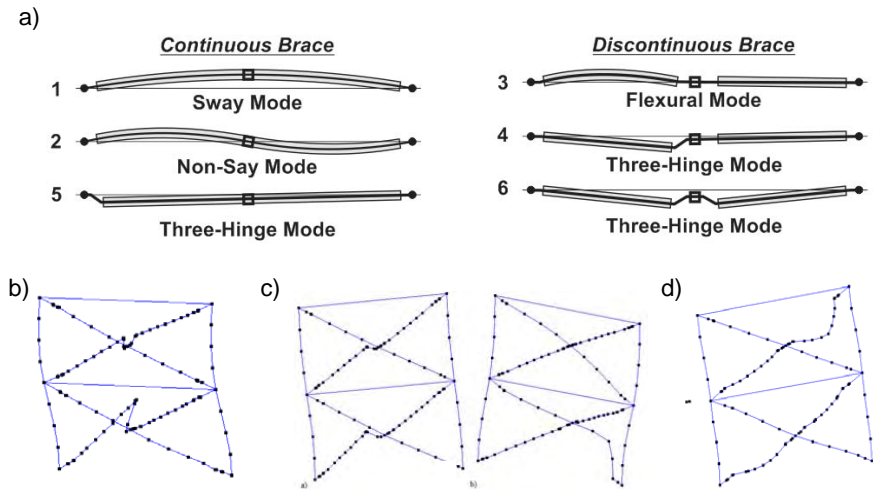


Figure 5: a) Brace out-of-plane buckling modes; b) Buckling of discontinuous braces with connections T/O CCM; c) Buckling of braces with connections T/O CCS; and d) Flexural buckling of discontinuous braces with connections T/C CCS.

In frames with T/O CCS connections designed for amplified tension loads, buckling of the discontinuous braces still occurred in the three-hinge mode but at higher loads corresponding to, on average, 60% of the brace probable compressive resistances (Figure 5c). The higher flexural stiffness of the connections resulted in Mode 2 buckling for the continuous braces (Figure 5c). For these frames, low-cycle fatigue failure took place in connections of the discontinuous braces. In Table 3, the demand is also generally less severe for the structures located in eastern Canada compared to western Canada. For both regions in Canada, failure for the building on the site class C site was less frequent than for the building on the class E site.

Large storey drifts and occurrences of structural collapse were observed after connection failure for the structures with T/O CCM connections. For instance, for the structure on site class C in Vancouver, collapse occurred in one of the 10 motions and peak storey drifts exceeded the code limit of 2.5% times the storey height under 6 ground motion records. To further investigate the risk of structural collapse caused by fatigue failure in brace connections, the structure was subjected to 8 additional ground motions and 5 more collapse occurrences were obtained (total of 6/18), confirming that connection failure may have severe consequences on life safety.

Mixed response was obtained when the brace connections were designed to resist compression (T/C CCxM) without consideration of ductility. The design resulted in much thicker splice plates compared to T/O connections and both flexural and three-hinge buckling modes were observed for the discontinuous braces, depending on the brace size, the storey and the brace segment. When buckling Mode 4 took place, plastic rotations were limited and fatigue failure did not occur. Bolts reaching their shear strengths in the connections limited the tension forces in all braces. This bolt response also limited the compression forces in the continuous braces so that buckling of these braces was prevented. Except for the frame on class C site in Montreal, the inelastic deformation demand on the bolts was sufficient to cause bolt shear failure under several ground motions (Table 4). In general, however, building drifts remained acceptable and structural collapse was not observed.

Connections T/C CCS were the strongest as they were designed to resist in compression the amplified seismic brace forces. Braces buckled only in flexure (Figure 5d) and no connection failure was observed. In all frames, brace compression loads exceeded the forces considered in connection design due to the use of probable brace yield strength in analysis and the high rotational stiffness of the connections that increased the brace buckling strength (K less than 0.45 assumed in design). In all cases, the AISC design approach for single-shear lap splices used with factored plate resistances was sufficient to prevent the three-hinge buckling mechanism from occurring. Peak tension loads in braces were also larger than the design values; however, bolt slip and inelastic shear deformations of the bolts were sufficient to accommodate the seismic demand without failure.

4. CONCLUSIONS

Nonlinear response history analysis was performed on two-storey steel X-braced frames of the Conventional Construction (Type CC) category designed in accordance with Canadian seismic provisions. The frames were located on site classes C and E in Victoria, BC, in western Canada and Montreal, QC, in eastern Canada. Brace connections were field bolted lap splices acting in single-shear. They were designed to exhibit a ductile failure mode (CCM) or resist seismic loads amplified by $R_d = 1.5$ (CCS). Connections were also designed for tension (T/O) or tension and compression (T/C). Cyclic inelastic response of the bracing members and failure of brace connections were explicitly considered in the numerical models used in the analyses. The results showed that:

- The seismic demand was found to be more severe in western Canada, especially for the frame built on soft soil site class E.
- Low-cycle fatigue failure of brace connection plates can be predicted using fibre section discretization of the plates with linear damage accumulation.
- Connections designed to resist amplified brace loads in tension and compression (T/C-CCS) led to satisfactory braced frame performance with flexural brace buckling and no connection failure. Other connection design approaches resulted in undesirable three-hinge brace buckling modes and/or failure of brace connections.
- The analyses showed that fatigue failure of connections designed to resist non-amplified brace loads only in tension (T/O-CCM) could lead to structural collapse.

ACKNOWLEDGEMENTS

This research was funded by the Natural Sciences and Engineering Research Council (NSERC) of Canada.

REFERENCES

- Aguero, A., Izvernari, C., and Tremblay, R. (2006), "Modelling of the Seismic Response of Concentrically Braced Steel Frames using the OpenSees Analysis Environment," *Int. J. of Advanced Steel Constr.*, 2006; Vol. 2, No. 3 (pp. 242-274).
- Castonguay, P., and Tremblay, R. (2010), Seismic performance of concentrically braced steel frames of the conventional construction category. GRS Research Report No. SR10-03, Dept. of Civil, Geological and Mining Eng., Ecole Polytechnique, Montreal, QC (266 p.).
- CSA. (2009), *CSA S16-09, Design of Steel Structures*, Canadian Standards Association, Mississauga, Ontario, 2014.
- Davaran, A., G elinas, A., and Tremblay, R. (2014a). "Inelastic Buckling Analysis of Steel X-Bracing with Bolted Single Shear Lap Connections," *J. Struct. Eng.*, ASCE, 10.1061/(ASCE)ST.1943-541X.0001141,
- Davaran, A., Decaen, S., and Tremblay, R. (2014b), "Numerical Simulation of the Seismic Response of Steel X-Braced Frames with Single Shear Bolted Connections," *Proc. 10th Nat. Earthquake Eng. Conf.*, Anchorage, AK (Paper No. 1350).
- Davaran, A., G elinas, A., and Tremblay, R. (2012), "Experimental Seismic response of Slotted Connections at the Intersection of HSS Braces in X-Bracing Systems," *Proc. VIIth Int. Workshop on Connections in Steel Structures*, Timisoara, Romania (Paper No. 6-1).
- Decaen, S. (2015). *Am elioration du comportement sismique des assemblages   cisaillement simple des contreventements concentriques en X en acier de construction conventionnelle (Type CC)*, M.Sc. Thesis, Dept. of Civil, Geological and Civil Eng., Polytechnique Montreal, Montreal, Canada (222 p.) (*In French*)
- G elinas, A., Tremblay, R., and Davaran, A. (2013), "Buckling response of bolted mid-connections in steel X-Bracing. *Proc. CSCE 2013 Annual Conf.*," Montreal, QC, Paper No. GEN-104.
- Jiang, Y. (2013), *Numerical and experimental seismic assessment and retrofit of steel tension-only double angle braced frames designed before the implementation of detailing provisions for ductile seismic response*. M.Sc. Thesis, Dept. of Civil, Geological and Civil Eng., Polytechnique Montreal, Montreal, Canada (221 p.)
- McKenna, F. (2011), "OpenSees: A framework for earthquake engineering simulation," *Computing in Science and Engineering*, Vol. 13, No. 4 (pp. 58-66).
- NRCC. (2010). *National Building Code of Canada (NBCC)*, 13th ed., National Research Council of Canada, Ottawa, Ontario.
- Packer, J., Sherman, D., and Lecce, M. (2010), *Hollow Structural Section Connections - Steel Design Guide No. 24*, AISC, Chicago, IL.
- Tremblay, R., Bruneau, M., Driver, R., Metten, A., Montgomery, C.J., and Rogers, C. (2010), "Seismic Design of Steel Structures in accordance with CSA-S16-09," *Proc. 9th US Nat. and 10th Can. Conf. on Earthquake Eng.*, Toronto, ON (Paper No. 1768).
- Uriz, P., F.C. Filippou, and Mahin, S.A. (2008), "Model for Cyclic Inelastic Buckling of Steel Braces," *J. of Struct. Eng.*, ASCE, Vol. 134, No. 4 (pp. 619-628).

CYCLIC BEHAVIOR OF COMPOSITE BEAM, COLUMN, AND GUSSET PLATE CONNECTION UNDER MULTIPLE LOADS FROM FRAME AND DAMPER ACTIONS

Kazuhiko Kasai

Professor, Tokyo Institute of Technology, Yokohama, Japan
kasai@serc.titech.ac.jp

Yoriyuki Matsuda

Assistant Professor, Tokyo University of Science, Chiba, Japan
matsuda_y@rs.tus.ac.jp

Abstract: During an earthquake, members of a frame with brace-type dampers are subjected to cyclic forces from the damper and frame having distinct phases and dependencies on the story drift. Many cyclic tests simulating such multiple load effects are conducted for various subassemblies consisting of the slab, beam, column, and gusset plate connections.

Two actuators apply the target story drift step-by-step, and one oil jack applies the damper force. The target damper force is calculated using the values at the previous step for global and local deformations affecting damper deformations. Data analysis method decomposes the recorded strains into the frame action and damper action components, based on phase difference between the two actions.

The paper discusses stiffness and strength of the subassembly, local buckling of the beam flange and web, stress concentration, yielding, and failure of the components, effects of various stiffeners around the connection, and supplemental analysis results.

1. INTRODUCTION

1.1 General

Due to the seismic disasters from the 1995 Kobe earthquake and several major earthquakes that occurred later, there has been significant increase in building owners' desire for higher seismic performance of buildings in Japan. For a steel building under a major earthquake, the practice now typically limits the story drift angle to 0.01 rad or less, in order to prevent serious damage to the frame and to maintain functional continuity of the building. Response-control systems are recognized to show such performance.

Due to these circumstances, most of response-control design specifications in Japan consider elastic frames for a major (design basis) earthquake, including direct design methods to size dampers satisfying the target drift (e.g. JSSI 2002-2014). While adopting these, steel specifications for response control (AIJ 2014) accepts inelastic behavior to some limit: For the target drift angle of 0.01 rad or less typically, the lateral stiffness of the frame is required not to decrease considerably, and local plastic rotations of the members are required to be within the specified range in order to enable post-quake use of the frame without repair. Accordingly, the response control objective differs from that in the US where much larger drift is accepted.

1.2 Objectives and Scopes

The AIJ specifications would promote response control system for the steel buildings, distinguishing it from the conventional seismic-resistant systems. The system is considered as combined “undamped frame” and “damped frame” (e.g., Fig. 1), and damage control for the latter considers large axial force in the beams and columns. The specifications, however could not properly include significant effects of the slab-girder interactions, in spite that most steel buildings use composite beams.

Key issues involving slab-girder interaction effects are; stiffness and strength of the beams affecting responses of other members and frame, strains of beam bottom flange, and strain concentrations in the gusset plate or beam splice. Mahin et al. (2004) demonstrated premature tearing failure of the gusset plate connection of a frame without slab, and alerted importance of investigating such a failure. Rational estimation methods are needed for pre- and post-yield stiffness, plastic rotation, extent of yielding, and consequent damage in both frames.

The above issues are being investigated at Tokyo Institute of Technology (TIT), and objective of this paper is to highlight some of the experimental and analytical results. Sec. 2 describes the experimental method, a compact test system that can efficiently load the specimen, and various subassembly specimens consisting of beam, column, and gusset plate connections with or without slab (Fig. 2). Sec. 3 explains the test results. Sec. 4 explains briefly on the on-going analytical work.



Fig.1 Full-scale building specimen

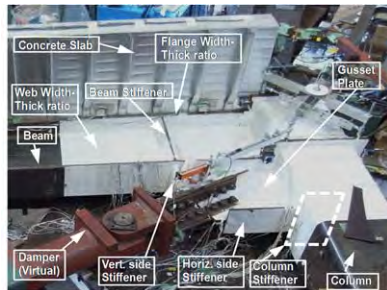


Fig.2 Full-scale subassembly specimen

2. TEST METHOD AND SPECIMENS

2.1 Loading Method Simulating Frame and Damper Actions

As Fig. 3a shows, the damped frame with a typical brace-type damper develops combined bending moment and axial force in the members. The beam shown by thick line is under positive bending and positive (tensile) axial force, and this case will be called as “positive loading case”, and vice versa. Fig. 3b shows the case of harmonically applied story drift, and Q_f and Q_d are called as “frame action” and “damper action”, respectively. While frame action mostly produces harmonically varying beam moment, the damper action produces mostly the beam axial force that has different phase and history depending on the damper type (Fig. 3b).

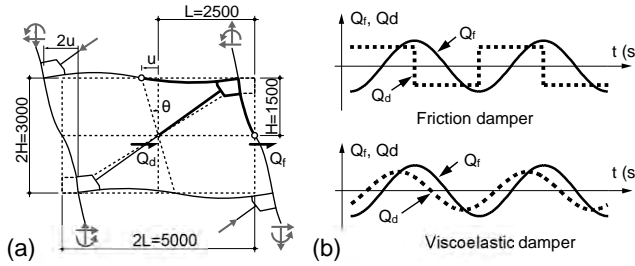


Fig.3 Story drift of and shear forces of frame and dampers

Figs. 4 and 5 show the loading method for the full-scale subassembly representing one-quarter portion (Fig. 3a) of the frame. It is a simplified hybrid scheme combining physical test of the subassembly with applied damper force whose target magnitude is obtained from analysis of the damper assumed. At each time step, the displacement control for the story drift and force control for damper force are performed as follows:

At first, the story drift angle $\theta = u/H$ (Figs. 4 & 5b) is incremented while keeping damper force F_d constant, where $2u$ and $2H$ = drift and height of the original frame, respectively (see Fig. 3a). After reaching target θ , change u_a of added component length is measured (Fig. 4a). Note that $u_a < u \cos \beta$ due to axial deformations of beam, gusset plate, and others, where β is the inclination angle of the virtual damper.

At second, for the u_a measured, a mathematical model for the damper and any elastic component connected in series is used to calculate corresponding value of F_d . The virtual damper can be of any damper type, as long as it is numerically modeled.

As depicted by Fig. 5b, the test applies two cycles of $\theta = \pm 1/800, \pm 1/400, \pm 1/200, \pm 1/100, \pm 1/67, \text{ and } \pm 1/50$ rad (0.00125, 0.0025, 0.005, 0.01, 0.015 and 0.02 rad), respectively. After completing these 12 cycles, repeated cycles of either $\theta = \pm 1/50$ rad (0.02 rad) or $\pm 1/33$ rad (0.03 rad) are applied until failure (see Table 1 footnote).

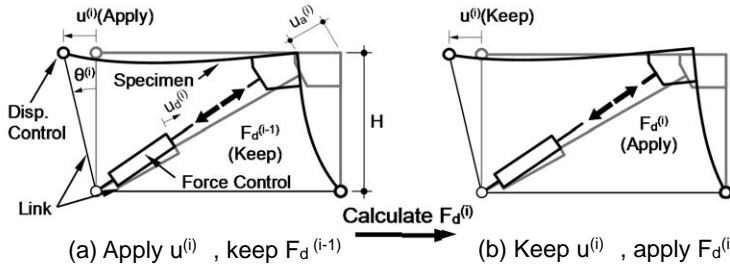
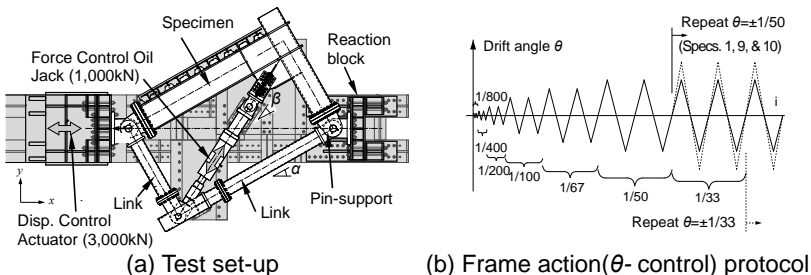


Fig.4 Loading method at i -th step



(a) Test set-up

(b) Frame action(θ - control) protocol

2.2 Specimens and Instrumentations

The beam is a built-up section of typically BH-500×250×12×22, and the column a square box section □-400×400×19 (Fig. 6). For the typical beam, yield stresses of the flange and web are 343 and 354 MPa, and corresponding yield moment and axial force are 1012 kNm and 571 kN, respectively. Stiffeners are at five locations of the beam, column, and gusset plate. The slab consists of corrugated metal deck of 75mm high and top concrete of 85mm thick, and its width 1450mm corresponds to the effective width (AIJ 2010). Fig. 7 shows the locations of normal strain gages and rosette strain gages in the beam (sections A, B1 to 3, C1 to 4), gusset plate (G1 to 6), panel zone (P1 to 4), and column (sections E1 to 2 and F1 to 3), respectively.

Table 1 summarizes total of 17 specimens tested. Specimens 1 to 11 are without slab. Specimens 1, 2, 3, and 9 commonly have the standard details mentioned above, and the first three are loaded by virtual damper forces of steel, viscoelastic, and friction dampers, respectively. Specimen 9 has no damper force. For the other specimens up to 11, steel damper is assumed, and the flange and/or web thickness are reduced, some stiffeners are omitted, gusset plate is removed or made thinner, or beam splice is provided near the gusset plate. Specimens 12 to 17 are with slab.

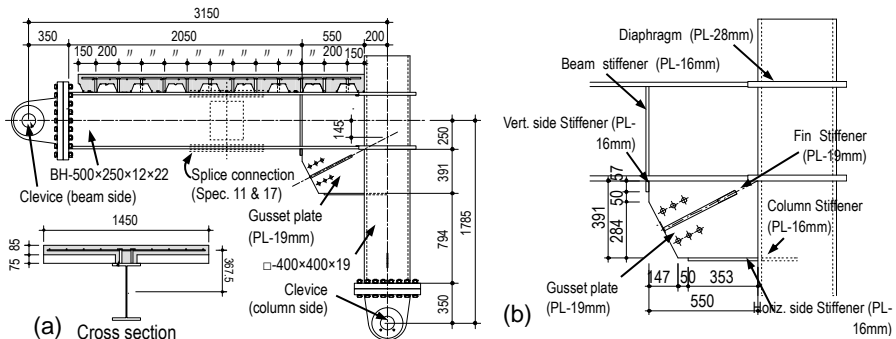


Fig.6 Typical detail of specimen with/without concrete slab

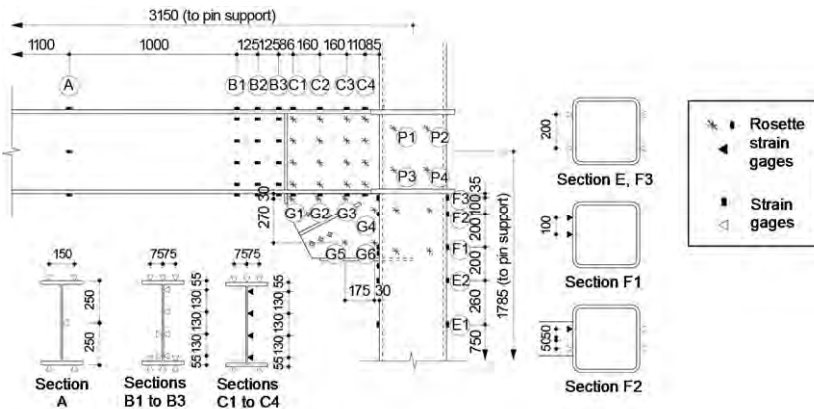


Fig.7 Locations of strain gages in the steel portion

Table 1 List of 11 bare frame and 7 composite frame subassembly specimens

Spec.	tw (mm)	tf (mm)	Damper force	Kf (kN/mm)	Qf,peak (kN)	Nf	Comments
1	12	22	Steel	32.9	802 , -767	106*	Steel damper modeled. Benchmark test
2	12	22	VE/Steel	35.3	909 , -837	47	VE damper modeled. Steel damper for fatigue test
3	12	22	Friction	53.8	1009 , -921	16	Friction damper modeled
4	9	22	Steel	31.2	861 , -703	30	Thinner web. Semi-compact section
5	9	16	Steel	26.8	719 , -562	17	Thinner web and flange. Non-compact section
6	12	22	Steel	31.3	857 , -801	18	Thinner gusset plate. Reduced from 19 to 9mm
7	12	22	Steel	24.3	784 , -757	45	Without column & horiz. Stiffeners
8	12	22	Steel	26.8	861 , -764	43	Without column, beam, horiz, or vert. stiffeners
9	12	22	No damper	36.2	992 , -915	128*	Spec. 1 without damper force
10	12	22	No damper	25.9	705 , -709	122*	Without gusset plate, stiffeners, & damper force
11	12	22	Steel	38.2	975 , -963	1	Beam splice with high-strength bolts
12	12	22	Steel	39.9, 35.4	1018 , -845	31	Spec. 1 & 2 with slab. Corrugated across the beam
13	12	22	Steel	40.7, 36.4	980 , -856	46	Spec. 1 & 2 with slab. Corrugated along the beam
14	12	22	Steel	40.0, 35.8	1125 , -941	13	Spec. 1 & 2 with flat slab 160 mm thick. Thickest
15	9	22	Steel	37.9, 34.6	874 , -713	27	Spec. 4 with slab. Corrugated across the beam
16	12	22	Steel	31.5, 29.4	1004 , -863	61	Spec. 7 with slab. Corrugated across the beam
17	12	22	Steel	41.9, 38.9	1069 , -909	3	Spec. 11 with slab. Corrugated across the beam

* $\theta = \pm 1/50$ was repeated for specimen 1, 9 and 10 only.

Note that the member sections of the 17 specimens are larger than those of the full-scale building (Fig.1) tested using world's largest shake table at E-defense (e.g., Kasai et al. 2009, 2011, 2012). Additional 8 specimens identical to the portions of the building were also tested, and the results will be reported elsewhere.

3. TEST RESULTS

3.1 Simulation of Dampers and Response-Control Systems

Fig. 8 plots the story drift angle θ up to $\pm 1/50$ rad, virtual damper shear Q_d , frame shear Q_f , and system shear $Q_d + Q_f$. Target damper shear is also plotted together with Q_d . Three virtual dampers, steel, viscoelastic, and friction dampers are considered (specimens 1 to 3), respectively. Fig. 8 shows accurate simulation of the damper force, essential for the detailed tests of various subassembly specimens.

3.2 Load-Deformation Characteristics of Frames w/wo Composite Effects

Fig. 9 shows comparative behaviour of selected specimens. The skeleton curve for ${}_sQ_f$ and ${}_s\theta$ (upper Fig. 9) is obtained by choosing a portion of hysteresis curve with Q_f larger than those of the previous cycles, and by connecting the curves together up to cycles of $\theta = \pm 1/33$ rad. Hysteresis curves Q_f vs θ (middle Fig. 9) and curves for peak force ${}_pQ_f$ vs. number of cycles N until failure (lower Fig. 9) are also plotted. Specimen1 was tested up to $\theta = \pm 1/50$ (Fig. 5b), thus the curves from the identical specimen 2 is substituted for the cycles of $\theta = \pm 1/33$ rad.

With the slab of corrugated metal deck (specimen 12), frame stiffness and maximum strength are 1.21 and 1.12 times that without slab (specimen 1) in the positive loading case (Sec. 2.1) producing positive moment and axial force. With the

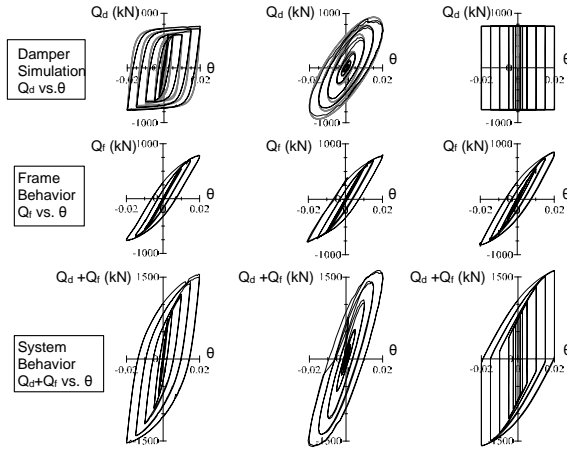


Fig. 8 Test results for damper, frame, and system action
 — Recorded — Target (only Q_d)

flat slab that is two times thicker (specimen 14), the stiffness is similar, but strength is 1.24 times, and are 1.54 and 1.60 times those of the bare frame without gusset plate (specimen 10, Table 1). For the negative loading case, slab changed the stiffness and strength by 1.1 times approximately (Fig. 9). Since the slab causes upward shift of the beam neutral axis, eccentricity of the damper axial force from the panel zone center increases, amplifying bending deformation of the composite beam. This had the effect

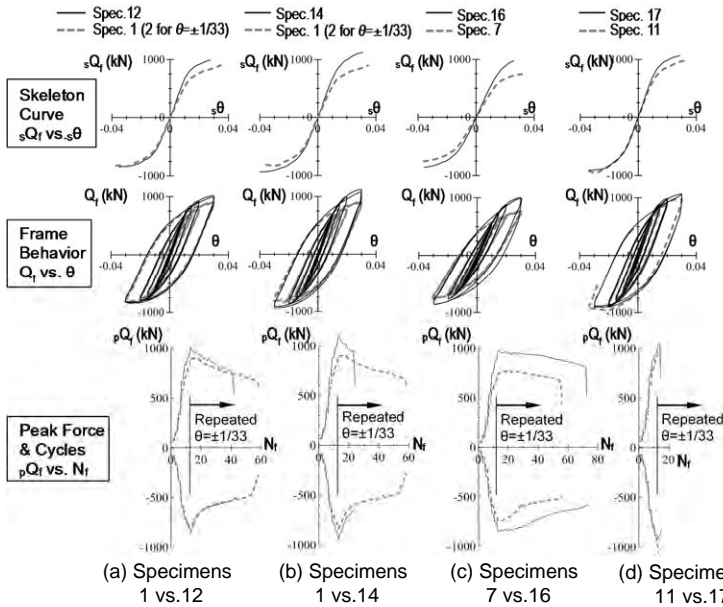


Fig. 9 Skeleton curves, hysteresis, peak forces, and number of cycles

of counteracting the increase of beam bending stiffness.

The subassembly with no stiffeners (specimen 7) is the most flexible among all, but shows the largest increase of stiffness by the slab (Fig. 9c & Table 1). Absence of the column and horizontal stiffeners (Figs. 2 & 6b) caused out-of-plane bending and yielding of the column face, especially when the beam is stiffened by the slab: Beam inelastic deformation was substantially reduced, resulting in the largest number of cycles to failure ($73-12=61$, see Table 1 & Fig. 9c) where repeated $\theta = \pm 1/33$.

In contrast, brittle failure occurred as shown by Fig. 9d: beam splice confined inelastic strains in the area between the splice and gusset plate (Fig. 6a), causing significant strain-hardening and higher connection force. Specimens 11 and 17 show similar hysteresis curves (Fig. 9d), since the slab area cut out by the splice is large near the critical area, and both failed at the smallest number of cycles of 1 and 3 only. Specimens 14 (Fig. 9b) and 13 also showed high forces (Table 1), and failed at the third and fourth smallest number of cycles of 13 and 16, respectively (Table 1).

3.3 Beam Strains Due to Combined Moment and Axial Force

Fig. 10 shows the strains at beam sections A, B1, B3, C1, and C4 (see Fig. 7) of specimens 1 (without slab) and 12 (with slab) under $\theta = \pm 1/400$. The position of the neutral axis is high due to positive moment and positive axial force (Fig. 10), and is even higher with the slab. Since Fig. 10 mostly shows plane section, the standard beam formula considering slab effective width (AIJ 2010) estimates well the steel strains. It needs improvement for negative loading case especially at $\theta = \pm 1/200$, although not shown. It also cannot predict the strain concentration at the bottom flange near the gusset plate (section B3).

In the identical specimens 1 to 3, the bottom flange at B3 had initial compressive strain of about 1/3 times the yield strain of 1673×10^{-6} and showed yielding at the first cycle, but became elastic with strain offset at the second cycle of $\theta = \pm 1/200$. Thus, subtracting the offset and considering strain histories at cycles of $\pm 1/100$, yield drift angle is estimated to be $\pm 1/155$ (0.065) rad, much smaller than the target (e.g. $\pm 1/100$). This would be common problem for a beam whose lower flange is connected to the brace (Fig. 3a), and its effect on low-cycle fatigue (Sec. 3.1) is being studied.

Note also that, for the same value of θ , the composite beam shows about the same bottom flange strain as the non-composite beam (Fig. 10). This is because; (1) the beam stiffened by the slab carries less deformation by redistributing deformation to column and other portions, and (2) larger moment of inertia reduces curvature, overcoming increase of flange strain caused by higher neutral axis and larger forces.

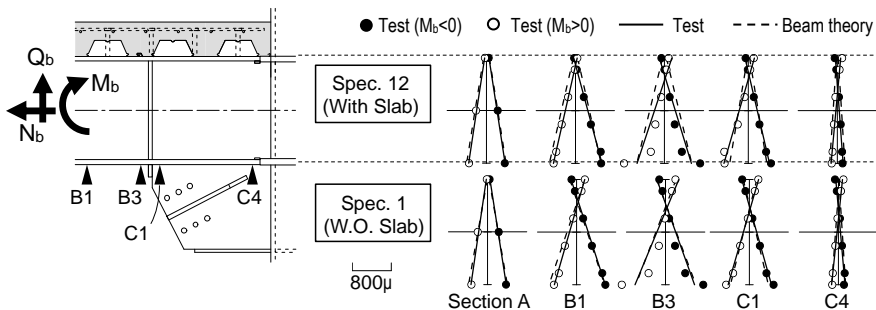


Fig.10 Strain distributions at $\theta = \pm 1/400$ w/o slab (specimens 12 vs.1)

4. DATA ANALYSIS AND SIMULATION

The writers' methods are being used to understand the strain variations as well as internal forces and deformations shared by the steel beam, panel zone, gusset plate, and concrete slab. Sec. 4.1 describes the data analysis method clarifying contributions from frame and damper actions. Composite beam and gusset plate are analyzed as examples. Sec. 4.2 discusses detailed structural analysis using practical line elements arranged to reflect important features of the subassembly.

4.1 Strain Decomposition Considering Frame and Damper Actions

For the beam in Fig. 11, strain $\epsilon \approx \epsilon_F + \epsilon_D$, where ϵ_F and ϵ_D are the frame and damper action components, respectively. The target condition of elastic behaviour is assumed, thus, $\epsilon_F = \lambda_1 \theta$ and $\epsilon_D = \lambda_2 F_d$. The λ_1 and λ_2 are the weights, and they are obtained by the least square method minimizing the error R_ϵ :

$$R_\epsilon = \sum_i [\epsilon^{(i)} - (\lambda_1 \theta^{(i)} + \lambda_2 F_d^{(i)})]^2 \quad (1)$$

where $\epsilon^{(i)}$, $\theta^{(i)}$, and $F_d^{(i)}$ are recorded values, and $(i) =$ step number. After Also, the new data of frame and damper action components $\epsilon_F^{(i)}$ and $\epsilon_D^{(i)}$ are created as follows:

$$\epsilon_F^{(i)} = \lambda_1 \theta^{(i)}, \quad \epsilon_D^{(i)} = \lambda_2 F_d^{(i)}, \quad \epsilon_S^{(i)} = \epsilon_F^{(i)} + \epsilon_D^{(i)} \quad (2a-c)$$

where $\epsilon_S^{(i)}$ should coincide with the recorded $\epsilon^{(i)}$ if the there is no error.

For the subassembly (Fig. 7), Eq. 1 is used twice by separating the cases of the slab in compression and in tension. At each step and for each strain of location 1 to 4 (Fig. 11 top), λ_1 and λ_2 are obtained and $\epsilon_F^{(i)}$ and $\epsilon_D^{(i)}$ created using Eqs. 2a & b. By linear regression (Fig. 11 top), the slope showing curvature and stable values of e' and e'' are obtained. At the same cross section, in the same manner as Eq.1, recorded N^n and M^n are also decomposed into $N_F^{(i)}$ and $N_D^{(i)}$. $M_F^{(i)}$ and $M_D^{(i)}$, respectively. Thus, one extracts all deformation and force quantities of the same

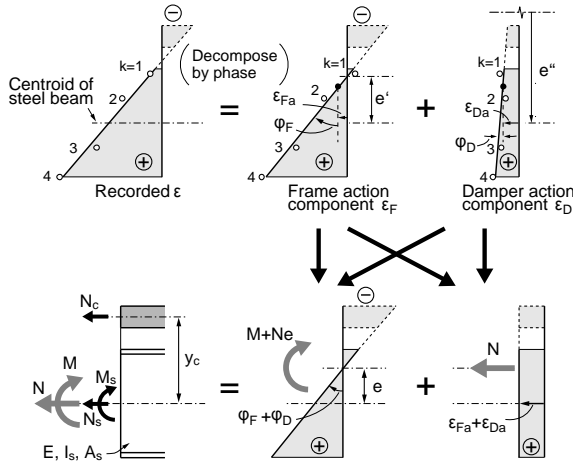


Fig. 11 Composite beam internal forces and steel strains, at i -th time step

action (i.e., same phase), and finally estimates the slab effective width, internal forces $M_s^{(i)}$, $N_s^{(i)}$, and $N_c^{(i)}$, and neutral axis position e (Fig. 11 bottom).

Accuracy was verified by comparing the $\epsilon_s^{(i)}$ (Eq. 2) with the recorded $\epsilon^{(i)}$ (Eq. 1), comparing $N_c^{(i)} + N_s^{(i)}$ with $N^{(i)}$ and so on. This method allows deeper look at the recorded data (e.g. Fig. 10), and use them to find, for instance, effect of slab and/or cross sectional change (i.e., gusset plate), their variations along the span, difference between positive and negative loadings, strain concentrations, and dependencies of any response on the two actions. It differs from the approach in Sec. 3.3 using the beam formula with assumed effective slab width. It was also modified to estimate $M^{(i)}$ and $N^{(i)}$ of composite beams in both undamped and damped frames of the full-scale building in Fig. 1 (Kasai & Matsuda 2015).

Fig. 12 shows the example application to the gusset plate of the same subassembly at $\theta = 1/200$ and simulated steel damper force $F_d = 647$ kN. Strains in three directions are recorded per rosette gage, and each of them is decomposed into ϵ_F and ϵ_D using Eqs.1 and 2. Fig. 12 shows principal strains before and after decomposition, respectively. At $\theta = 1/200$, the frame action is clearly dominant. Since damper yielding occurs when $\theta \approx 1/400$, the increase of F_d is small. Considering these and frame hysteresis (Figs. 8 & 9), the strain will be almost twice at target $\theta = 1/100$, and gusset yielding occurs at the corner shown (yield strain is about 1700×10^{-6}). In this manner, the method utilizes the data to interpret the behaviour, and can predict other cases by simply scaling the frame and damper actions separately.

Gusset plate yielding earlier than beam yielding causes premature tearing failure. This occurred to the gusset plate of Specimen 6 (Table 1) which was 9 mm thick, only 0.47 times the others. The axial stress considering only F_d and Whitmore distribution still satisfies allowable stress. Fig. 12 indicates that frame action is much more critical.

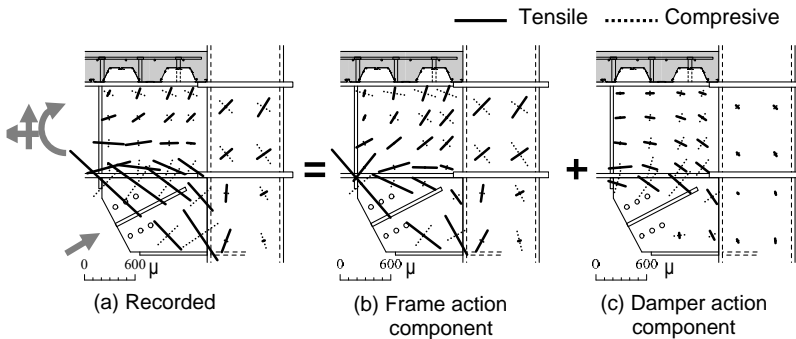


Fig.12 Decomposition of principal strains recorded at $\theta=+1/200$, $F_d=-647$ kN

4.2 Analysis of Subassembly by Simple Analytical Elements

As explained, the behaviour of the composite subassembly under the multiple loading effects is very complex. Tests looking at only global behaviour does not clarify the mechanisms, and efforts to find internal stresses and deformations of the subassembly are needed. Pursuant to this, together with the above study, the writers have been performing detailed nonlinear analysis using simple and available analytical elements. The analysis results agrees well with those of experiments (e.g., Fig.13) as well as 3D finite element analysis, as will be reported elsewhere.

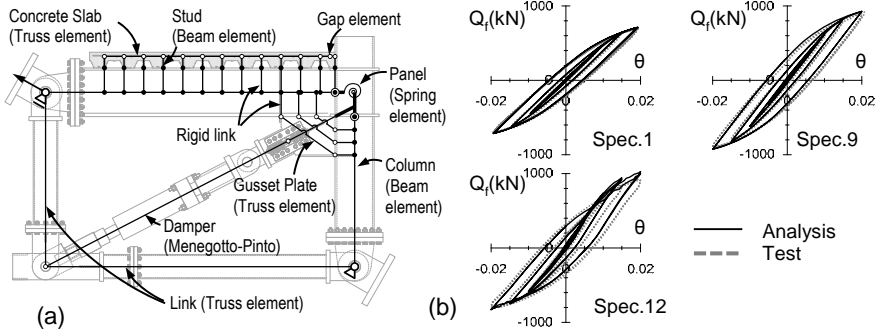


Fig.13 Analysis of specimens 1 (no slab), 9 (no damper), and 12 (with slab)

5. CONCLUSIONS

The response control effectiveness depends on both dampers and frames. A variety of dampers are available, and their properties and behavior are predictable through reasonably accurate mathematical model. On the other hand, for rational approach of performance-targeted design, many unresolved issues remain in both undamped and damped frames, requiring revisit of some past studies.

References:

- Architecture Institute of Japan (2014). Recommended Provisions for seismic damping systems applied to steel structures (in Japanese).
- Architecture Institute of Japan (2010). Design recommendations for composite constructions (in Japanese).
- Japan Society of Seismic Isolation (2002-2014). Manual for Design and Construction of Passively-Controlled Buildings, 1st - 3rd editions (in Japanese).
- Kasai, K., Matsuda, Y. (2015). Seismic Behaviour of Composite Beam under Damper and Frame Force of Shifted Phase; Finding from Full-scale Tests of buildings and subassemblies, *6th Conference on Advances Experimental Structures Engineering, Keynote Paper*, Urbana-Champaign, IL, US.
- Kasai, K., Matsuda, Y., Motoyui, S., Kishiki, S. (2015). Fundamental study using new test loading scheme for steel frame subassembly with damper connection details. *J. Struct. Constr. Eng.*, No.708, pp. 309-319 (in Japanese).
- Kasai, K. et. al. (2012). Test results for building with steel dampers, 3D shake table tests on full scale 5-story steel building with dampers Part2. *J. Struct. Constr. Eng.*, No.673, pp. 499-508 (in Japanese).
- Kasai, K., et al. (2009). Full-scale tests of passively controlled 5-story steel building using E-Defense shake table Part 1. *The 8th International Conference on Behaviour of Steel Structures in Seismic Areas, Keynote Paper*, Philadelphia, PA.
- Mahin, S., Uriz, P., Aiken, I., Field, C., Ko, E. (2004). Seismic Performance of buckling restrained braced frame systems, *13th World Conference on Earthquake Engineering*, Vancouver, Canada.
- Lee CH. (2002). Seismic design of rib-reinforced steel moment connections based on equivalent strut model. *Journal of Structural Engineering*. Vol.128 No.9, pp. 1121–1129.

PERFORMANCE OF WELD-RETROFIT BEAM-TO-COLUMN SHEAR TAB CONNECTIONS

Colin A. Rogers; Matthew Marosi; Jacob Hertz

*Department of Civil Engineering & Applied Mechanics, McGill University, Canada
colin.rogers@mcgill.ca; matthew.marosi@mail.mcgill.ca; jacob.hertz@mail.mcgill.ca*

Dimitrios Lignos

*School of Architecture, Civil & Environmental Engineering, École Polytechnique
Fédérale de Lausanne, Switzerland
dimitrios.lignos@epfl.ch*

Robert Tremblay; Marco D'Aronco

*Department of Civil, Geological & Mining Engineering, École Polytechnique, Canada
robert.tremblay@polymtl.ca; marco.daronco@polymtl.ca*

ABSTRACT

Single plate shear tab connections are a simple means to connect beams to their supporting members. The tab is fillet-welded to the supporting column in the fabrication shop, and then field bolted to the beam web on the construction site. Situations may arise on site in which the bolt holes do not align. Instead of reaming holes or refabricating the connection, a cost efficient alternative is to use a weld-retrofit connection between the beam web and the shear tab. The AISC recommends that this retrofit approach not be taken due to concerns with the rotational ductility of the connection; however, no test-based performance evaluation was available for the weld-retrofit connection. The intent of the paper is to summarize the laboratory phase of a research project in which various weld-retrofit schemes of shear tab connections were evaluated. The connection performance is compared with nominally identical bolted shear tab connections.

1. INTRODUCTION

Single plate steel shear tab connections are commonly used to connect beams to their supporting column members. The tab is fillet-welded to the column in the fabrication shop; the beam web is then field bolted to the shear tab on the construction site. It is possible that during the steel erection process the bolt holes in the beam web and shear tab do not align (Figure 1) due to detailing or fabrication errors, as well as construction miss-alignment. Instead of reaming holes or refabricating the connection, a cost efficient and expeditious alternative is to use a weld-retrofit connection between the beam web and the shear tab. The American Institute of Steel Construction (AISC) does not recommend that this retrofit approach be applied due to concerns with the rotational ductility of the connection; however, no test-based evidence was available that demonstrated the response to loading of this weld-retrofit connection. Hence, a research project was initiated in which various weld-retrofit schemes of shear tab connections were evaluated by means of full-scale laboratory

testing. The connection performance in terms of overall behaviour, shear resistance and rotation capacity is compared with nominally identical bolted shear tab connections. The scope of the study comprised 13 beam-to-column connection specimens of various size W-shape members, original bolt configurations, and weld-retrofits (Figure 2). This was complemented by 7 matching tests of the original bolted shear tabs (Figure 2). Two of the weld-retrofit specimens consisted of replacement tabs having only two bolt holes to aid in erection; the remaining, contained the full allotment of bolt holes. All beams and columns were of ASTM A992 Grade 50 material, while the tabs were of ASTM A572 Grade 50 steel. The weld retrofit was done in the laboratory after the column and beam had been installed in the test frame; a certified welder with extensive experience in the steel fabrication industry completed the fillet welds of various patterns. Shielded metal arc welding (SMAW) with E49 (E70) stick electrodes was used, as would commonly be done on a construction site. In contrast, E71T flux core electrodes were used for all shop fabricated tab-to-column flange welds with an additional CO₂ shielding gas. This paper describes the design of the retrofit fillet welds and the testing program, as well as the observed and measured performance. Note that this research addresses the expected demands on a shear tab connection under the regular gravity loading scenario; it did not take into account the higher rotational demands on shear tab connections resulting from progressive collapse, i.e. loss of a column, nor the demands that might occur during a maximum considered seismic event for a pin connected structure.



Figure 1: Misaligned bolted shear tab connection requiring retrofit (courtesy of DPHV)

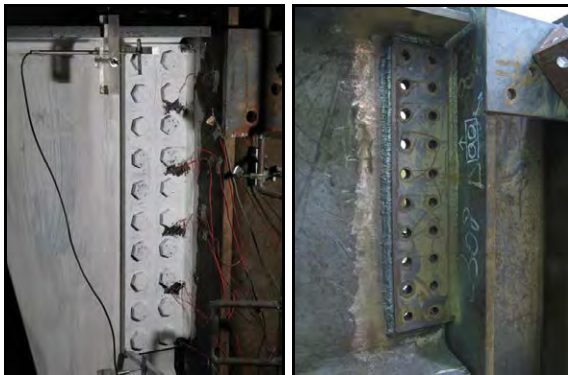


Figure 2: Typical bolted shear tab connection with matching weld-retrofit detail

1.1 Background Information on the North American Shear Tab Design Method

The design procedures for conventional and extended bolted beam-to-column shear tab connections in North America are best documented in the 14th Edition of the AISC Steel Construction Manual (2010) and best described for extended configurations by Muir and Hewitt (2009). Extensive testing of bolted shear tab connections by a variety of researchers dates back to the work of Lipson (1968); a detailed review of the relevant literature is found in the thesis of Creech (2005). Numerical evaluations of shear tab performance have also been carried out by various researchers (Sherman & Ghorbanpoor 2002). Connections are designed for block shear rupture, bolt bearing, bolt shear, shear yielding of the plate and shear rupture of the plate. For extended shear tab connections, the eccentricity of the bolt group is considered in determining the demand on the fasteners. The maximum allowable thickness of the plate is calculated to ensure ductility in the connection. The flexural yielding strength of the plate must also be checked, in addition to plate buckling.

2. WELD-RETROFIT SHEAR TAB TEST PROGRAM

2.1 Overview

The weld-retrofit shear tab test program involved 7 bolted connections and 13 weld-retrofit connections (Table 1, Figure 3). Each of the original bolted shear tab connections was initially designed by Marosi (2011), Marosi et al. (2011), Hertz (2013) and Hertz et al. (2015) following the method documented in the 14th Edition of the AISC Steel Construction Manual (2010), and then tested under gravity loading accounting for shear and rotational demands. The calculated factored resistance of these connections was taken as the starting point for the design of the weld detail for the retrofitted connections. For example, the resistance of the full "C" weld for configuration 1 was designed to have the same factored resistance as the corresponding bolted connection.

Table 1: Summary of weld-retrofit shear tab test specimens

Config.	Beam	Column	Shear Tab Thickness (mm)	Original Bolted Connection			Weld Retrofit	
				Bolt ^{a,b} Config.	Bolt ^a Size (mm)	Weld ^c Size (mm)	Weld ^d Config.	Weld ^d Size (mm)
1	W310x60	W360x196	6	1x3	19	6	Full C	4.8
2	W310x60	W360x196	6	1x3	19	6	Partial C	6.35
3	W310x60	W360x196	10	2x3	19	6	Full C	6.35
4	W310x60	W360x196	10	2x3	19	6	Partial C	7.9
5	W610x140	W360x196	8	1x6	22.2	6	Partial C	7.9
6	W610x140	W360x196	8	1x6	22.2	6	L	7.9
7	W610x140	W360x196	16	2x6	22.2	10	Partial C	11.1
8	W610x140	W360x196	16	2x6	22.2	10	L	14.3
9	W920x223	W360x196	10	1x10	25.4	6	Partial C	7.9
10	W920x223	W360x196	22	2x10	25.4	14	Partial C	15.9
11	W310x74	W360x196	9.5	2x3	19	6.35	Partial C	9.5
12	W610x140	W360x196	8	Temp. ^e	22.2	6	Partial C	6
13	W610x140	W360x196	16	Temp. ^e	22.2	11	Partial C	11

^aConfiguration & bolt size for the original bolted connection; threads excluded. Bolt holes 1/16" (2mm) larger. ^b#vertical rows x #bolts per row. ^cWeld from shear tab to column flange (weld both sides of plate). ^dRetrofit weld shape from beam web to shear tab. ^eHoles were provided only for two temporary installation bolts. ^fThe 'a' distances were (Figure 3) #1-4 51mm, #5-8 63mm, #9,10,12,13 64mm, #11 152mm.

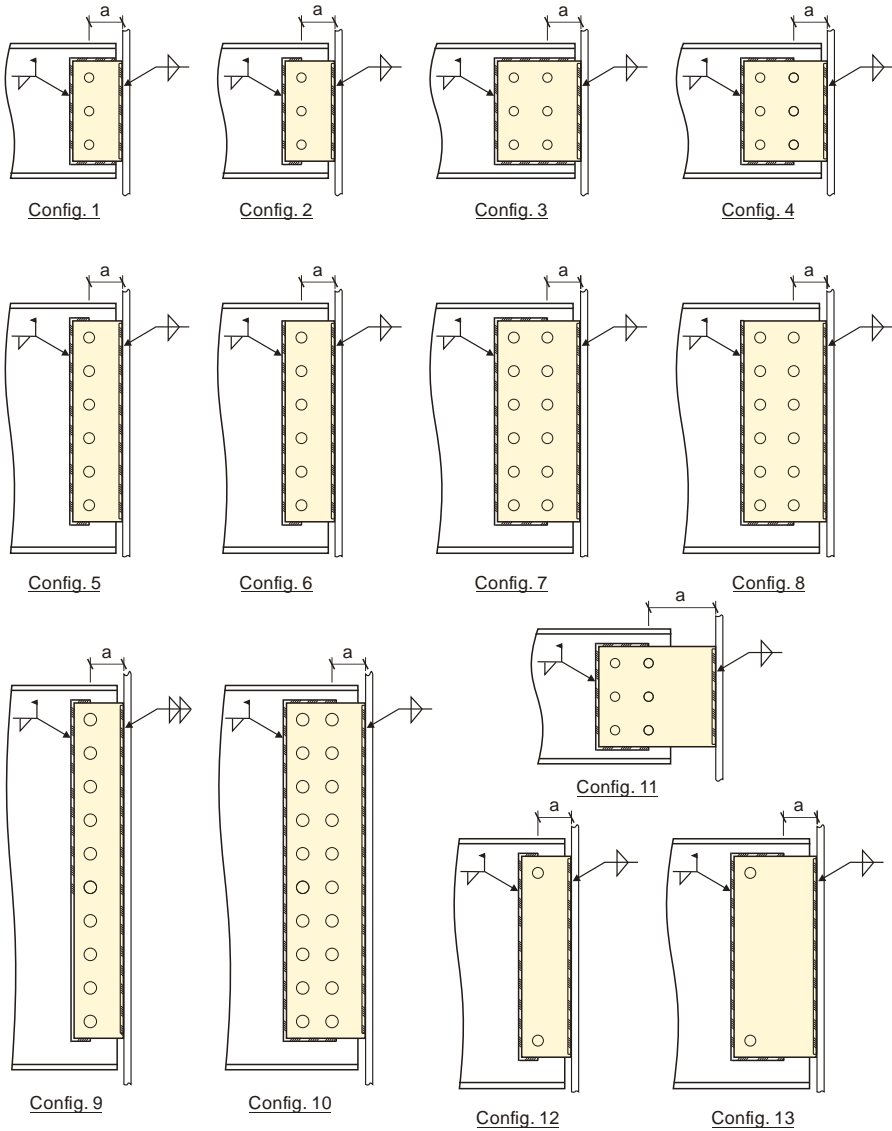


Figure 3: Detail drawings of weld-retrofit shear tab connections

2.2 Weld-Retrofit Design and Fabrication Methodology

The design checks were carried out using the conventional and extended shear tab design procedures, where applicable, of the AISC Steel Construction Manual (2010) to determine predicted resistances for the single and double row shear tab specimens (Marosi 2011, Hertz 2013). The AISC conventional design approach, for example, does not apply to connections when multiple rows of bolts are present. Because the design was done prior to materials testing, overstrength values of $1.1F_y$ and $1.1F_u$ were initially

assumed as the probable yielding and ultimate strengths of the shear tabs when checking to ensure that the shear tabs would fail prior to inelastic deformations taking place in the test beams. ASTM A325 snug tight bolts were used for design.

Practicing structural engineers were consulted concerning the design of the retrofit-weld connections to determine what types of retrofits may be used on construction sites. The weld group shapes included a “Full C”, a “Partial C” and an “L” (Figure 3). The logic behind using the “Full C” shape weld was to utilize the maximum space available for the weld. The “Partial C” shape weld was used because past tests had demonstrated that most of the deformation in the shear tab occurred over the ‘a’ distance, and hence it was decided to avoid placing a weld in this location to allow similar deformations to occur. The “L” shaped weld was chosen to facilitate the on-site welding procedure, where it was anticipated to be difficult to weld in the confined space between the top of the shear tab and the underside of the upper flange of the beam. Once the weld group shapes had been identified, the predicted factored resistance of the respective bolt group was set equal to the predicted factored resistance of the weld group, to determine the size of the fillet weld. This procedure was enabled for all specimens by using the instantaneous centre of rotation (ICR) method as it is provided in the Canadian Institute of Steel Construction (CISC) Handbook (2010), which is based on the Canadian Standards Association (CSA) S16 Design Standard (2009). The eccentricities used in calculating these weld group resistances were taken as the distance from the face of the column to the centroid of the respective weld group. Typical weld-retrofit specimens and the in-lab fabrication of a retrofit weld are depicted in Figure 4.

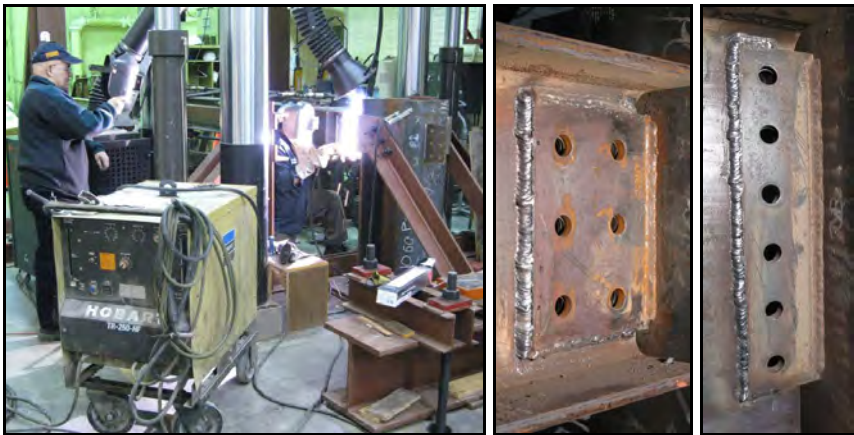


Figure 4: Photographs of representative weld-retrofit shear tab connections prior to testing (Test Configurations 3 & 5)

2.3 Laboratory Testing Procedures

Each connection was tested using a cantilever approach, whereby the beam was supported at one end by the shear tab connection to a column. Two hydraulic actuators were operated in displacement control to apply a shear force at the test connection and to simulate rotation by lowering the end of the test beam. Figure 5 shows an overview of the test beam and column, as well as the lateral bracing frames and beam end actuator support frame. Figure 6 contains photographs of a typical specimen in place. The actuator in the foreground provided the end reaction and lowered the beam end as the test

was carried out; the blocking under the beam end was removed prior to testing. Given the anticipated capacity of Configuration 10 in Figure 3, this actuator was replaced with hydraulic jacks (Marosi 2011). Lateral bracing frames were erected along the length of the beam to prevent the occurrence of lateral torsional buckling. A target rotation of the beam (relative to the face of the column) was chosen to be equal to 0.02 rad for the W310 sections and 0.015 rad for the W610 & W920 sections, to be reached at a probable ultimate shear resistance of the shear tab determined using a resistance factor of 1.0, and material properties of $1.1F_y$ and $1.1F_u$ in the calculations. The lower rotation target was applied to the deeper beams because it was anticipated that smaller mid-span deflections would occur in a real single-span loading scenario due to each beam's higher moment of inertia. A full description of the test setup and loading protocols is available in the works of Marosi (2011), Hertz (2014) and D'Aronco (2014).

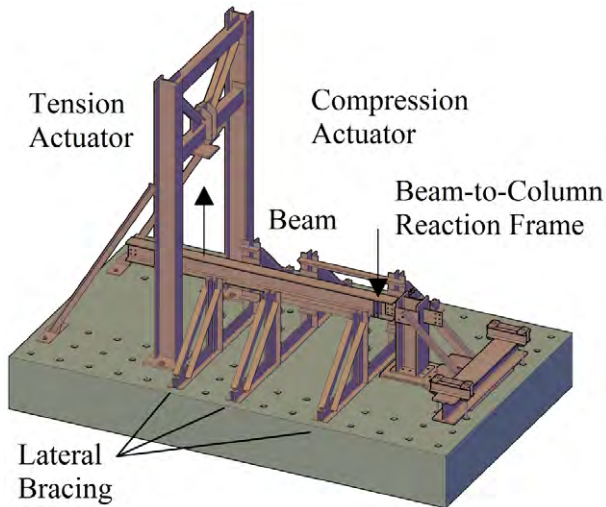


Figure 5: Schematic drawing of beam-to-column shear tab connection test setup

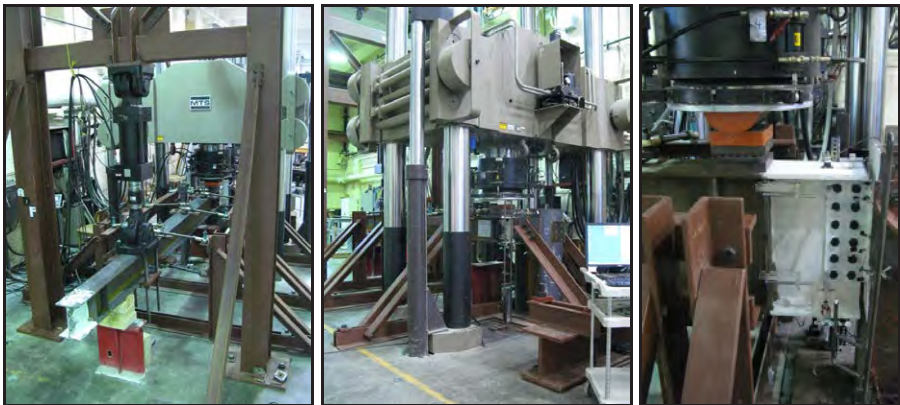


Figure 6: Photographs of beam-to-column shear tab connection test setup

2.4 Discussion of Test Results

Photographs of representative connection Configurations 1 and 7 are provided in Figure 7. The post-test deformations for both the bolted and weld-retrofit connections are shown. Note the similarity in terms of location of inelastic damage / yielding to the shear tab, which was most extensive over the 'a' distance. In the case of Configuration 1 ("Full C" weld) the horizontal welds between the end of the beam web and the centreline of the vertical bolt row fractured, effectively transforming this weld group into a "Partial C" shape. The remaining portion of the retrofit weld was unaffected. Configuration 7 comprised a "Partial C" weld shape, which was not damaged during loading; inelastic deformations were limited to the shear plate. Similar behaviour can also be seen for the other "Partial C" weld shape specimens in Figure 8, including Configuration 11, which possessed a long 'a' distance.

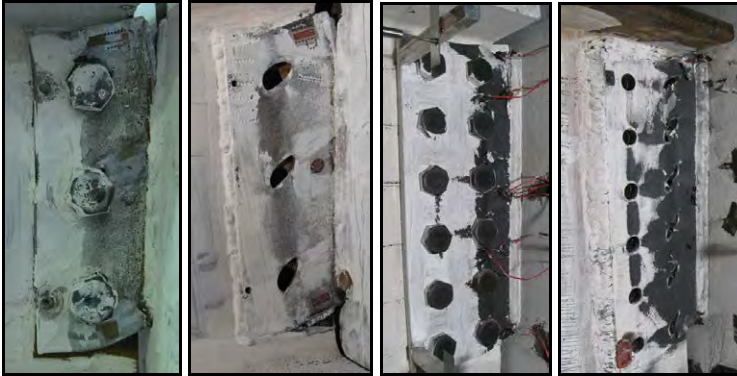


Figure 7: Photographs of post-test deformations for representative bolted and welded connections (Test Configurations 1 & 7)

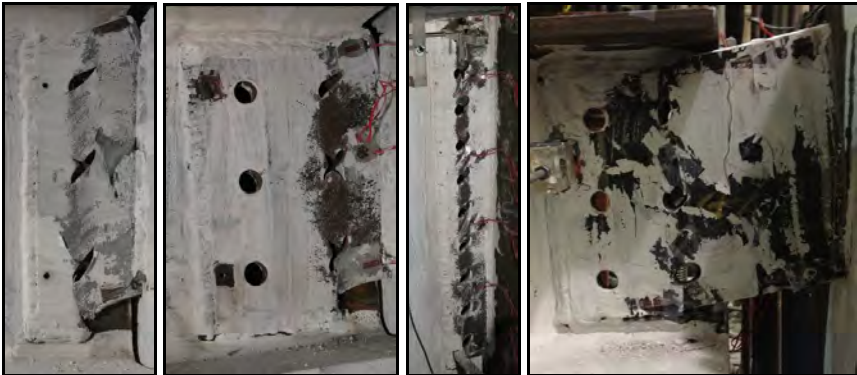


Figure 8: Photographs of post-test deformations for welded connections "Partial C" weld (Test Configurations 2,4,9 & 11)

Pre and post-test photographs of the two "L" shape weld-retrofit specimens are provided in Figure 9. The response was similar to that observed for the "Partial C" connections. Note however, the greater extent of inelastic damage in Configuration 8 compared with Configuration 7 (Figure 7), whereby the plate yielding extended

past the ‘a’ distance. The retrofit welds for these specimens were not damaged. The welder involved in fabricating these two specimens, in addition to those having a horizontal weld along the top of the shear tab, commented that this top weld presented no difficulties during the in-lab fabrication.



Figure 9: Photographs of post-test deformations for welded connections “L” shape weld (Test Configurations 6 & 8)



Figure 10: Photographs of post-test deformations for welded connections “Partial C” weld on replacement shear tab plate (Test Configurations 12 & 13)

The final two weld-retrofit configurations, for which the original shear tab was removed and replaced with a plate that only contained two bolt holes to aid in installation, are depicted pre and post-testing in Figure 10. Although the retrofit welds remained largely undamaged for these specimens, the overall inelastic action of the shear tab was less compared with the other specimens that contained the original bolt holes. Nonetheless, these specimens were able to reach the target rotation demand, as did all other specimens, without any sudden failure. Given that the failure section of the shear tab was greater in area than the connections with the original bolt holes, the ultimate resistance exceeded that of other similarly sized weld-retrofit test specimens.

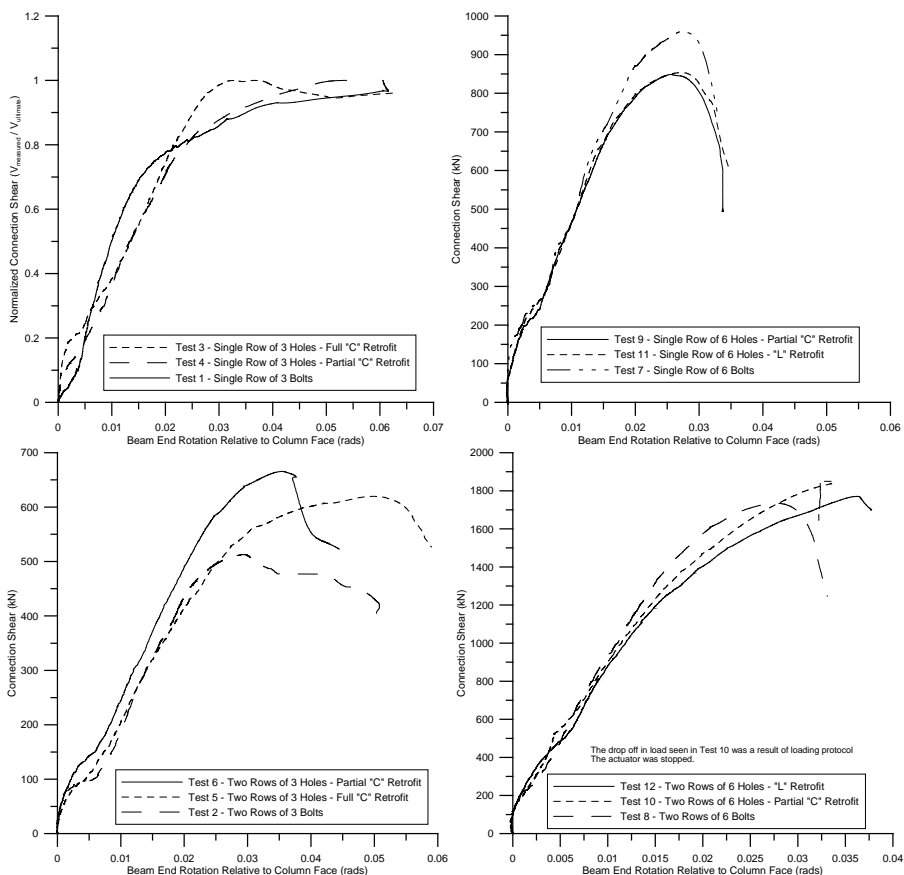


Figure 11: Graphs of connection shear versus rotation for representative bolted and weld-retrofit shear tab connection tests

Representative graphs showing the relationship between the measured connection shear resistance and the rotation between the beam end and column face are provided in Figure 11. Each graph includes the results for the original bolted connection, as well as the two matching weld-retrofit connections. Note: Tests 1, 3 & 4 are Configurations 1 & 2; Tests 7, 9 & 11 are Configurations 5 & 6; Tests 2, 5 & 6 are Configurations 3 & 4; Tests 8, 10 & 12 are Configurations 7 & 8. In all cases, the weld-retrofit specimens were able to reach the same rotation capacity as their matching bolted shear tab connection. Furthermore, the ultimate resistance levels attained by the weld-retrofit connections are similar to their bolted shear tab connection counterparts. Moreover, the connections all reached the force level associated with the AISC predictions.

3. CONCLUSIONS

The laboratory results demonstrated that these weld-retrofit connections can reach resistance and rotation levels consistent with equivalent bolted shear tab con-

nections. There is no advantage to using the “Full C” shape weld group; in contrast, the authors recommend the use of the “Partial C” shape weld since it does not restrict the deformation of the shear tab over the ‘a’ distance. The “L” shape weld does provide for adequate performance; however, given that the welder for this study did not find the installation of the top horizontal section of a retrofit weld to be difficult, one is not obliged to specify this shape. Given that the scenario presented herein is a retrofit solution to lack-of-fit on the construction site, using the original shear tab with all of its bolt holes is advised. The weakened section is advantageous in terms of maintaining the ductility of the shear tab connection. Using replacement shear tabs without bolt holes does raise the connection resistance.

ACKNOWLEDGEMENTS

The authors would like to thank the ADF Group Inc. and DPHV Structural Consultants for their technical and financial support, as well as the Natural Sciences and Engineering Research Council of Canada.

REFERENCES

AISC, Steel construction manual, 13th Edition. American Institute of Steel Construction. Chicago, 2005.

AISC, Steel construction manual, 14th Edition. American Institute of Steel Construction. Chicago, 2010.

CISC, Handbook of Steel Construction, 10th Edition. Canadian Institute of Steel Construction. Markham, 2010.

CSA, Design of Steel Structures S16. Canadian Standards Association. Mississauga, 2009.

Creech DD, Behavior of single plate shear connections with rigid and flexible supports. M.Sc. Thesis, North Carolina State Univ. Raleigh, 2005.

D’Aronco M, Behaviour of double and triple vertical rows of bolts shear tab connections and weld retrofits. MASc Thesis, Dept. of Civil, Geological & Mining Eng., Ecole Polytechnique. Montreal, 2014.

Marosi M, Behaviour of single and double row bolted shear tab connections and weld retrofits. MEng Thesis, Dept. of Civil Eng., McGill Univ. Montreal, 2011.

Marosi M, D’Aronco M, Tremblay R, Rogers CA, Multi-row bolted beam to column shear tab connections. 6th European Conference on Steel and Composite Structures, Budapest. 2011, 555-560.

Hertz J, Testing of extended shear tab connections subjected to shear. MEng Thesis, Dept. of Civil Eng., McGill Univ. Montreal, 2014.

Hertz J, Lignos D, Rogers CA, Full-scale experimental testing of extended beam-to-column and beam-to-girder shear tab connections subjected to shear. STESSA 2015 – 8th International Conference on the Behaviour of Steel Structures in Seismic Areas, Shanghai. 2015, Paper No. 118.

Lipson SL, Single-angle and single-plate beam framing connections. Proceedings of Canadian Structural Engineering Conference. Toronto, 141-162, 1968.

Muir LS, Hewitt CM, Design of unstiffened extended single-plate shear connections. *AISC Engineering Journal* 2009, 46 (2), 67-79.

Sherman DR, Ghorbanpoor A, Design of extended shear tabs. American Institute of Steel Construction Final Report, Univ. of Wisconsin. Milwaukee, 2002.

Surrogate modeling for rotational stiffness of welded tubular Y-joints

Markku Heinisuo
Tampere University of Technology, Tampere, FI-33720, Finland
markku.heinisuo@tut.fi

Marsel Garifullin
Peter the Great St.Petersburg Polytechnic University, St.Petersburg, 195251,
Russia
273marcel@gmail.com

Timo Jokinen
Tampere University of Technology, Tampere, FI-33720, Finland
timo.jokinen@tut.fi

Teemu Tiainen
Tampere University of Technology, Tampere, FI-33720, Finland
teemu.tiainen@tut.fi

Kristo Mela
Tampere University of Technology, Tampere, FI-33720, Finland
kristo.mela@tut.fi

During optimization of tubular structures a wide range of joint geometries and profile alternatives are explored. Determining the rotational stiffness of joints for each design alternative would require computationally intensive finite element analyses (FEAs) which would render the optimization procedure inapplicable. Use of an approximate surrogate model of the joint response leads to significant reduction of computational effort required in optimization. In this paper surrogate models for initial rotational stiffness of welded tubular Y-joints are presented. At sample and validation points, the joints were analyzed using comprehensive FEA. The surrogate model was determined by the Kriging method. The surrogate model calculations were done using ooDACE toolbox in Matlab. The article also studies the effect of fillet welds on initial rotational stiffness.

INTRODUCTION

Tubular structures with welded joints are used in the wide range of structural applications. The most typical application is a tubular truss. The structural analysis model is frequently constructed using beam finite elements, and the braces are connected to the chords using hinges. In reality, the welded joint does not behave as a hinge when it is loaded by a moment. The joint has resistance against the moment, but in the joint area deformations may occur both at the brace and at the chord, so the stiffness against the moment has to be taken into account in the global analysis of the structure. In (Boel, 2010) and (Snijder et al., 2011) it has been shown that the rotational stiffness of a welded tubular joint is the main

parameter when considering buckling of members of tubular trusses. The local design model of Y-joint based on (Boel, 2010) is shown in Figure 1 and the quantity C is the initial rotational stiffness of the joint, denoted as $S_{j,ini}$ in (EN 1993-1-8, 2005).

In (EN 1993-1-8, 2005) the moment resistance is given for the joint where the angle between the brace and the chord is 90 degrees. In (Grotmann and Sedlacek, 1998) has been proposed a method for determining the initial rotational stiffness for this case. Design methods for other angles are still lacking.

The rotational stiffness of the joint can be calculated using comprehensive finite element analysis (FEA). This approach is not suitable in practice when different design alternatives are explored, and especially when structural optimization is performed, where hundreds or thousands of repeated structural analysis is carried out. In order to avoid these computationally heavy calculations surrogate models (or meta models) have been developed. The idea of surrogate modeling is to approximate structural responses by suitable functions that can be evaluated quickly without FEA. In (Díaz et al., 2012) the optimum design of steel frames is presented using semi-rigid joints and surrogate models. The standard steps in the surrogate modeling are: design of experiments, surrogate model construction, and model validation.

This article describes the construction of a surrogate model for initial rotational stiffness of welded tubular Y-joints with square hollow section (SHS) profiles. After the model has been constructed, the effect of the full strength fillet weld size is analyzed.

REQUIREMENTS OF EUROCODES

The joints of this study comply with the Eurocodes, and steel grades up to S700 are included (EN 1993-1-8, 2005), (EN 1993-1-12, 2007). The parameters characterizing the behavior of welded SHS Y-joints are: chord dimensions b_0 , t_0 ; brace dimensions b_1 , t_1 ; angle φ between the brace and the chord; weld type: fillet weld or butt weld. The axial load of chord is a parameter, but not considered here.

The profiles included in the study were taken from the catalogue of Ruukki (Ongelin and Valkonen, 2012), meaning cold-formed tubes. The chord size varies from 100x100x4 mm to 300x300x12.5 mm. The size of the brace is limited by $0.25 \leq b_1/b_0 \leq 0.85$ (EN 1993-1-8, 2005). Moreover, the conditions $b_1/t_1 \leq 35$ and $10 \leq b_0/t_0 \leq 35$ must be satisfied, and all sections must belong to cross-section class 1 or 2 with respect to compression. This last requirement reduces substantially the set of applicable profiles of higher steel grades, especially S700. The angle φ between the brace and the chord varies in the range $30 \leq \varphi \leq 90$ degrees. Full strength fillet welds are employed, with weld size a related to the wall thickness of the brace as shown in Table 1 (Ongelin and Valkonen, 2012).

Table 1. Full strength fillet weld sizes

Brace material	S355	S460	S500	S550	S700
Weld size a	$1.15t_1$	$1.50t_1$	$1.60t_1$	$1.62t_1$	$1.64t_1$

FINITE ELEMENT MODELING

The FEA program Abaqus was used for analysis with C3D8 brick elements for tubes and welds. All sections were modeled with round corners, according to EN

10219-2 (2006). Two-layered mesh was created with solid hexahedral elements being refined near the joints, as shown in Figure 1. Butt welds were modeled as “no weld” by using TIE constraint of Abaqus. Fillet welds were modeled as steel and using TIE constraint where the welds were in contact with the chord. The material does not have influence on the stiffness of joints with butt welds. In case of fillet welds the material of the brace affects considerably on the weld sizes (Table 1). The material model was elastic: the modulus of elasticity was 210000 MPa and Poisson’s ratio 0.3.



Figure 1. Design model and FEA model for Y-joint.

The FEA models were *validated* with the tests (Tuominen and Björk, 2014) in (Haakana, 2014). *The verification* was done in three steps (Heinisuo et al., 2015): moment load in two opposite directions, use of shell elements instead of bricks and varying the type of brick elements from 8 to 20 nodes. The proposed FEA model performed well, and the fillet welds could be modeled using the exact geometry. The initial rotational stiffness C was calculated from FEA by extracting the frame behavior from the FEA results, as described in (Haakana, 2014).

SURROGATE MODELING

As a first surrogate model, linear regression was tried, but its performance, measured by the error term R^2 (Díaz et al., 2012) was not satisfactory. Then, Kriging was employed, with the ooDACE toolbox for Matlab (Ulaganathan et al., 2015). The results of this method are reported here.

Two types of surrogate models were constructed: single model (one model for all sample points) and multi-model (with an independent model for every b_0). The idea of implementing the second approach was that the variable b_0 is discrete, getting its values from the Ruukki’s catalogue, with no intermediate values among them. Both types gave similar results and were used for the final model.

The most popular space filling sampling technique is the Latin Hypercube Sampling (LHS) proposed by (McKay et al., 1979). However, in this research engineering justification was used for the definition of the sample points.

The rotational stiffness of Y-joint depends on four variables: chord width b_0 , chord thickness t_0 , relative brace width $\beta=b_1/b_0$ and angle φ between a chord and a brace. The effect of brace thickness t_1 on rotational stiffness was found to be very weak and was ignored. Numerical values had to be given to t_1 when completing Abaqus analysis.

There were 3 values (minimum, middle and maximum) for variables β and φ . Overall, 285 sample points were distributed evenly and covered the whole area of our interest, see Table 2.

Table 2. Sample points

b_0	β	t_f	t_0	C [kNm/rad]	t_0	C [kNm/rad]	t_0	C [kNm/rad]						
100	0.400	4	4	55	27	23	6	174	85	72	10	1082	406	345
100	0.600	4	4	215	86	68	6	634	262	211	10	4007	1229	1013
100	0.800	4	4	1135	442	343	6	2847	1107	891				
110	0.364	4	4	44	23	20	5	83	43	37	6	140	72	62
110	0.545	4	4	150	63	50	5	272	116	94	6	450	193	158
110	0.818	4	4	1457	568	439	5	2349	948	751	6	3536	1389	1117
120	0.333	4	5	70	37	33	7.1	203	106	92	10	638	291	253
120	0.583	4	5	364	150	121	7.1	1009	422	345	10	3197	1155	953
120	0.833	5	5	2923	1170	923	7.1	6637	2532	2047				
140	0.286	4	5	53	30	27	7.1	152	85	76	10	453	231	205
140	0.571	5	5	353	143	117	7.1	944	399	328	10	2646	1075	891
140	0.786	5	5	2097	794	618	7.1	4846	1954	1569				
150	0.267	4	6	81	47	42	8.8	262	146	130	12.5	1004	433	382
150	0.533	5	6	448	191	158	8.8	1372	593	494	12.5	5046	1897	1586
150	0.800	6	6	3785	1471	1149	8.8	9697	3742	3034				
160	0.250	4	6	73	44	39	8.8	236	135	122	12.5	862	397	353
160	0.563	5	6	559	232	190	8.8	1677	714	590	12.5	5884	2242	1866
160	0.750	6	6	2493	943	735	8.8	6531	2617	2111				
180	0.278	4	7.1	148	85	76	8.8	280	158	141	12.5	946	467	415
180	0.556	6	7.1	896	378	309	8.8	1617	693	571	12.5	5165	2134	1774
180	0.833	7.1	7.1	8286	3312	2600	8.8	13374	5401	4322				
200	0.250	4	7.1	123	74	66	8.8	233	138	124	12.5	750	402	360
200	0.550	5	7.1	869	367	295	8.8	1566	673	546	12.5	4910	2040	1672
200	0.800	7.1	7.1	6690	2589	2020	8.8	10763	4362	3457				
220	0.273	4	8	203	118	105	10	395	226	203	12.5	840	454	405
220	0.545	7.1	8	1157	490	402	10	2131	922	762	12.5	4347	1899	1580
220	0.818	7.1	8	11157	4415	3474	10	18372	7443	5944				
250	0.280	4	8.8	285	164	146	10	416	237	212	12.5	859	472	422
250	0.560	7.1	8.8	1718	721	589	10	2429	1034	848	12.5	4815	2094	1731
250	0.800	7.1	8.8	12549	4943	3876	10	16880	6768	5384				
260	0.269	4	8.8	267	155	139	10	389	226	203	12.5	798	448	402
260	0.538	7.1	8.8	1496	639	524	10	2118	916	755	12.5	4175	1842	1527
260	0.846	8.8	8.8	20765	8271	6441	10	26909	10941	8628				
300	0.267	5	10	390	227	205	12.5	774	445	401				
300	0.533	8	10	2136	908	747	12.5	4114	1795	1486				
300	0.833	10	10	27313	10664	8367	12.5	45620	18624	14858				

The use of this data did not give physically reasonable results using ooDACE, although at the sample points the results were exact; for a detailed discussion, see (Garifulin et al., 2016). In some points the stiffness was “oscillating” with respect to the angle and the symmetry condition at the angle 90 degrees was not fulfilled. To avoid computationally expensive FEA we implemented “pseudo” sample points. They were defined using polynomial fourth order extrapolations for stiffness to enforce the stiffness values to behave properly near the boundaries of the

variables. These pseudo points were calculated by extending the sample space for the angle φ to 20, 25, 95 and 100 degrees, the variable β to 0, 0.01, 0.9 and 0.95, the variable t_0 to 0, 0.1 mm, and two values over the upper bound. Overall, 1869 pseudo points were added, resulting with 285 sample points to the total number of 2154 points. After adding these pseudo points the surrogate model behaved physically appropriately.

For the validation of the surrogate model the following rule has been proposed as a criterion of acceptance (Diaz et al., 2012): $R^2 \geq 0.85$ for validation points amounting approximatively to one third of the number of sample points. For objective assessment of the model, 48 randomly chosen validation points (different than the sample points) were computed by Abaqus. The validation indicated that, although all the models had $R^2 \geq 0.95$, large absolute errors, as computed by Eq. (1), were observed.

$$Error = \frac{|C_{FEM} - C_{SURR}|}{C_{FEM}} \quad (1)$$

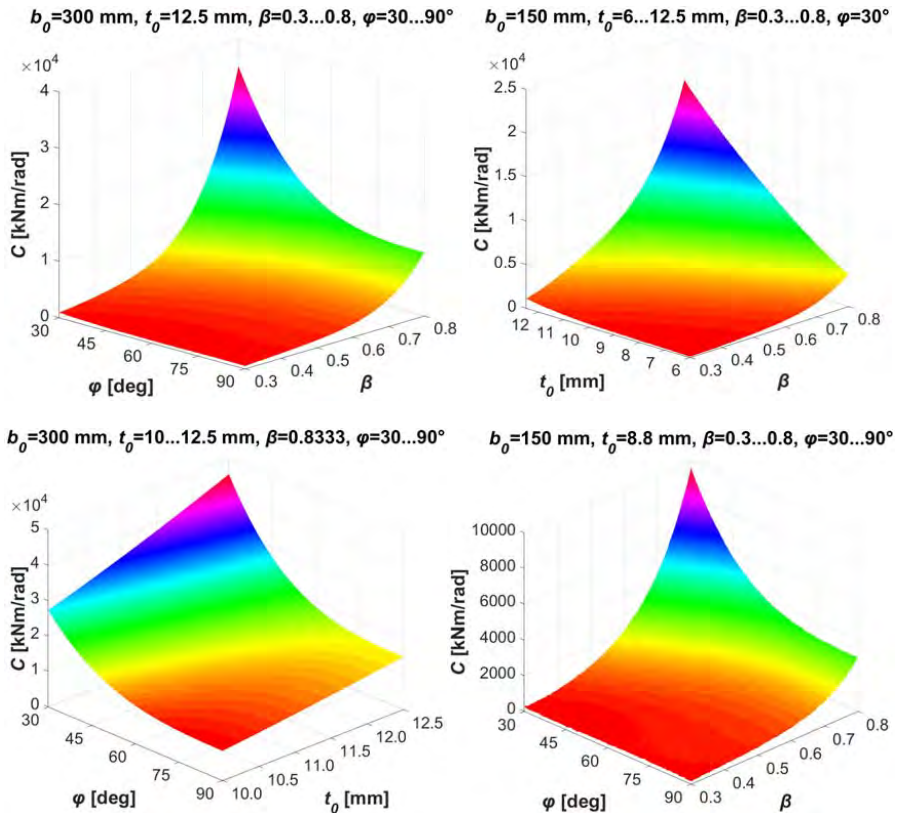


Figure 2. Behavior of the final surrogate model with respect to the variables.

The first validation using 2154 sample points showed the following results: average error 8 % and maximum error 28 %, 16 points with error higher than 10 %. This meant that the accuracy of the model required improvement.

It was concluded that all inaccurate cases were connected to the points for which β was predicted (only β or together with other variables). Graphical analysis showed that C - β curves had considerable differences from their real values, thus causing serious loss of accuracy, up to 28 %. To improve the curves additional pseudo points we included which were determined using polynomial second and fourth order interpolations of stiffness. The same procedure was conducted also for C - φ curves. Constructing the surrogated model using these additional pseudo points increased the accuracy.

To have the best performance, a complex model was created, containing for every chord profile a surrogate model. For solving this task, every chord was analyzed separately to choose the surrogate model with the best performance. Then all the models were collected in one Matlab file and a complex surrogate model was created, available for downloading on (Research Centre of Metal Structures, 2016). Examples of using the final surrogate model are given in Figure 2.

Validation of the final model demonstrated the average error 4 %, maximum 16 % and only 4 cases where the error was greater than 10 %, see Table 3 and Figure 3. This was the best surrogate model obtained in this study.

Table 3. Validation of the final surrogate model

Chord		Brace		FEM		Surrogate model		Chord		Brace		FEM		Surrogate model	
b_0	t_0	β	φ	C	C	$Error$ [%]		b_0	t_0	β	φ	C	C	$Error$ [%]	
100	8	0.800	79	1838	1735	5.6		180	10	0.389	59	405	391	3.4	
100	6	0.400	42	115	122	6.2		180	12.5	0.667	33	8504	9029	6.2	
100	10	0.400	80	349	348	0.4		180	10	0.500	40	1085	1096	1.1	
100	8	0.500	89	300	285	5.0		180	10	0.611	60	1415	1470	3.9	
110	5	0.364	34	71	72	1.4		200	8.8	0.250	69	130	129	1.0	
110	6	0.364	55	76	75	1.2		200	12.5	0.400	62	855	811	5.1	
110	6	0.364	50	82	81	0.9		200	8	0.300	57	138	131	4.8	
110	5	0.818	88	746	748	0.3		200	7.1	0.600	66	448	518	15.5	
120	5.6	0.583	80	170	171	0.8		220	8.8	0.545	71	569	547	3.9	
120	7.1	0.750	83	1098	1111	1.2		220	12.5	0.455	58	1195	1247	4.4	
120	8.8	0.833	42	6030	6726	11.6		220	10	0.409	37	703	819	16.4	
120	7.1	0.500	39	399	387	3.0		220	8	0.727	62	1757	1974	12.4	
140	7.1	0.357	90	106	113	6.5		250	12.5	0.720	60	6397	6163	3.7	
140	6	0.786	89	977	1017	4.1		250	10	0.600	90	1073	1086	1.2	
140	7.1	0.500	40	393	400	1.7		250	12.5	0.600	87	2199	2170	1.3	
140	6	0.500	30	349	366	4.8		250	8.8	0.280	72	151	151	0.2	
150	7.1	0.533	47	405	400	1.2		260	10	0.846	79	8820	8802	0.2	
150	7.1	0.800	89	1643	1783	8.5		260	12.5	0.577	67	2135	2115	0.9	
150	6	0.400	71	84	77	8.0		260	12.5	0.308	73	498	522	4.8	
150	7.1	0.267	39	104	105	0.9		260	12.5	0.692	51	6208	6222	0.2	
160	8.8	0.750	86	1946	2102	8.0		300	12.5	0.833	33	39163	40996	4.7	
160	10	0.313	76	244	243	0.3		300	12.5	0.467	56	1290	1396	8.2	
160	8.8	0.500	85	416	438	5.3		300	12.5	0.833	85	14946	14908	0.3	
160	8.8	0.438	81	303	321	6.0		300	12.5	0.600	86	2247	2338	4.1	

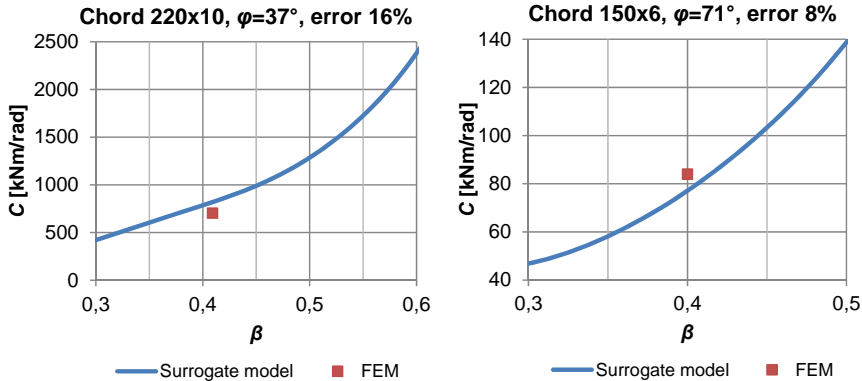


Figure 3. Errors of the surrogate model.

The largest errors seemed to appear when the parameter β is predicted, and especially with large values of β , because the stiffness is increasing rapidly when the value of β is increasing. The use of engineering judgement was, perhaps, not the correct choice for sampling. The use of LHS may lead to better results.

FILLET WELD EFFECT

The weld size of the full strength fillet weld is very large, as is shown in Table 1. Thus, it is interesting to examine the effect of the weld size to the rotational stiffness of the joint. In order to estimate the rotational stiffness of tubular joints with fillet welds the following formula is proposed, see Figure 4:

$$b_{eq} = b_1 + 2\sqrt{2}a \cdot k_{fw} \quad (2)$$

where k_{fw} is a correlation coefficient. This equivalent width of the brace b_{eq} can be used when calculating the rotational stiffness of the joint with no weld, e.g. using the surrogate model.

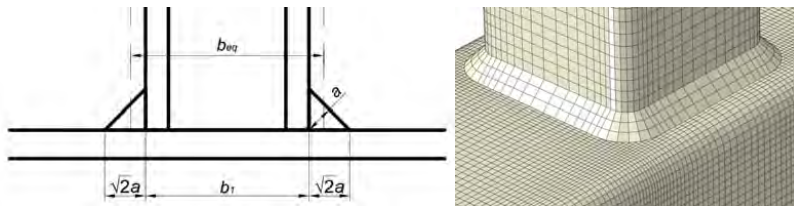


Figure 4. Equivalent brace width, b_{eq} , and FEA model with weld.

To calculate the correlation coefficient the following algorithm was applied:

1. Calculate rotational stiffness for joints with fillet welds using FEA.
2. Calculate rotational stiffness for joints with butt welds and equivalent brace widths using FEA. Equivalent brace width was first determined randomly and then refined through iterations to get the same stiffness as in step 1.
3. Calculate correlation coefficient k_{fw} from Eq. (2).

Exact correlation coefficients k_{fw} were calculated for a number of joints. For simplicity we propose using instead of the exact values k_{fw} the discrete values $k_{fw,dis}$ of correlation factors: 0.6 for S355 steel and 0.7 for S700 steel. For the discrete values rotational stiffness C_{dis} was also calculated and the loss of accuracy was analyzed. All results are presented in Table 4.

Table 4. Discrete correlation coefficients and related errors in stiffness

b_0 [mm]	t_0 [mm]	b_1 [mm]	t_1 [mm]	φ [°]	Material	k_{fw} [-]	C [kNm/rad]	$k_{fw,dis}$ [-]	C_{dis} [kNm/rad]	Error [%]
100	4	40	4	90	S355	0.74	378	0.60	34	9.4
100	7.1	40	4	90	S355	0.60	187	0.60	186	0.0
100	7.1	50	4	90	S355	0.58	321	0.60	327	1.8
110	4	80	4	90	S355	0.63	368	0.60	351	4.1
150	6	40	4	90	S355	0.70	56	0.60	54	4.0
150	7.1	40	4	90	S355	0.65	91	0.60	89	2.2
150	12.5	40	4	90	S355	0.43	465	0.60	507	7.9
150	12.5	60	4	90	S355	0.42	936	0.60	1025	9.0
150	7.1	100	4	90	S355	0.50	848	0.60	918	7.1
150	6	110	4	90	S355	0.51	913	0.60	987	7.7
200	12.5	50	4	90	S355	0.43	413	0.60	437	5.6
200	12.5	110	4	90	S355	0.46	2000	0.60	2126	5.8
200	7.1	140	7.1	90	S355	0.64	1549	0.60	1478	4.8
250	12.5	70	4	90	S355	0.51	478	0.60	488	2.2
250	12.5	150	7.1	90	S355	0.58	3198	0.60	3246	1.4
250	8.8	180	7.1	90	S355	0.62	3079	0.60	3018	1.9
300	12.5	80	5	90	S355	0.57	458	0.60	462	0.8
300	12.5	200	7.1	90	S355	0.57	5026	0.60	5115	2.0
200	7.1	50	4	60	S355	0.64	91	0.60	90	1.3
200	7.1	50	4	30	S355	0.58	157	0.60	158	0.8
200	12.5	50	4	60	S355	0.36	455	0.60	492	8.1
200	12.5	50	4	30	S355	0.34	858	0.60	950	10.5
200	7.1	140	7.1	60	S355	0.63	1973	0.60	1901	3.3
200	7.1	140	7.1	30	S355	0.69	5519	0.60	4961	9.9
120	4	80	4	90	S700	0.72	300	0.70	293	2.8
150	6	100	4	90	S700	0.61	665	0.70	735	10.3
200	7.1	50	4	90	S700	0.79	92	0.70	89	3.8
200	7.1	120	7.1	90	S700	0.73	951	0.70	923	3.7
250	8.8	70	4	90	S700	0.74	187	0.70	185	1.4
250	8.8	160	7.1	90	S700	0.71	2059	0.70	2038	1.1
300	12.5	180	7.1	90	S700	0.66	3741	0.70	3857	3.2

The average error resulting from using the discrete values of correlation coefficient instead of the exact ones was 4.6%, and the maximum error was 10.8%. This justifies the use of discrete values.

The influence of full strength fillet welds on the rotational stiffness can be illustrated by comparing the stiffness of a fillet welded joint with the stiffness of a butt welded joint. This comparison is depicted in Figure 5 for S355 and S700 joints with varying section dimensions (the cases are arranged in ascending order of β).

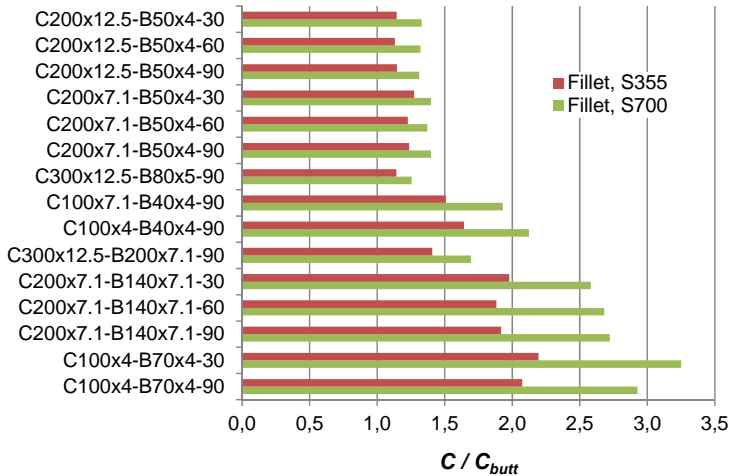


Figure 5. Stiffness of fillet welded joint (C) related to the stiffness of butt-welded joint (C_{butt})

Looking at the results of the analysis the following conclusions can be made:

1. Fillet welds increase considerably the rotational stiffness of welded joints, in average 1.5 times for S355 steel grade and 2.0 times for S700.
2. The influence of welding is more noticeable for small sections. This might be explained by the fact that for small sections the difference between weld size and chord width is not as high as for large sections.
3. The increase of rotational stiffness is higher for sections with high β . This might be explained by a nonlinear C - β curve on which a considerable growth for high values of β is observed.

CONCLUSIONS

So far, there exist no analytical method to calculate the initial rotational stiffness for welded tubular Y-joints for different angles φ . Therefore, the sample point data presented in this study is valuable in the verification of such a method. For example, the component method, which is presently available in the Eurocode for I- and H-sections, provides a general approach for developing analytical expressions for stiffness of tubular joints (Jaspart and Weynand, 2015). Moreover, the surrogate model developed based on the sample points can be utilized for optimization of tubular frames and trusses, as it avoids resorting to time-consuming FE analyses. Improving the accuracy of the surrogate model can be tried by various means. For example, Latin hyper cubes or Monte Carlo simulation can be employed for generating the sample points, and surrogate models other than Kriging can be applied.

Exploiting the considerable effect of full strength fillet weld on the rotational stiffness in design should be examined more closely especially for high strength steel, where notably larger fillet weld size is required for the full strength property.

REFERENCES

- Boel, H. (2010), *Buckling Length Factors of Hollow Section Members in Lattice Girders*. Ms Sci thesis. Eindhoven University of Technology, Eindhoven.
- Díaz, C., Victoria, M., Querin, O.M. and Martí, P. (2012), "Optimum design of semi-rigid connections using metamodels", *Journal of Constructional Steel Research*, Vol. 78 (pp. 97–106).
- European Committee for Standardisation, (CEN). (2006), *Cold formed welded structural hollow sections of non-alloy and fine grain steels. Part 2: Tolerances, dimensions and sectional properties (EN 10219-2:2006)*. Brussels.
- European Committee for Standardisation, (CEN). (2007), *Eurocode 3. Design of steel structures, Part 1-12: Additional rules for the extension of EN 1993 up to steel grades S 700 (EN 1993-1-12: 2007)*. Brussels.
- European Committee for Standardisation, (CEN). (2005), *Eurocode 3. Design of steel structures, Part 1-8: Design of joints (EN 1993-1-8:2005)*. Brussels.
- Garifullin, M., Jokinen, T. and Heinisuo, M. (2016), *Supporting document for surrogate model construction of welded HSS tubular Y-joints*. Publication 164. Tampere University of Technology, Tampere.
- Grotmann, D. and Sedlacek, G. (1998), *Rotational stiffness of welded RHS beam-to-column joints*. Cidect 5BB-8/98. RWTH-Aachen, Aachen.
- Haakana, Å. (2014), *In-Plane Buckling and Semi-Rigid Joints of Tubular High Strength Steel Trusses*. Ms Sci thesis. Tampere University of Technology, Tampere.
- Heinisuo, M., Mela, K., Tiainen, T., Jokinen, T., Baczkiwicz, J. and Garifullin, M. (2015), "Surrogate model for rotational stiffness of welded tubular Y-joints", *Proceedings of the METNET Seminar 2015 in Budapest* (pp. 18–39).
- Jaspart, J.P. and Weynand, K. (2015), "Design of hollow section joints using the component method", *Proceedings of the 15th International Symposium on Tubular Structures*, ISTS 2015 (pp. 405–410).
- McKay, M.D., Bechman, R.J. and Conover, W.J. (1979), "A Comparison of Three Methods for Selecting Values of Input Variables in the Analysis of Output From a Computer Code", *Technometrics*, Vol. 21, No. 2 (pp. 239–245).
- Ongelin, P. and Valkonen, I. (2012), *Structural hollow sections. EN 1993 - Handbook 2012*. Rautaruukki Oyj.
- Research Centre of Metal Structures. (2016), <http://metallirakentaminen.fi/> [Accessed January 29, 2016].
- Snijder, H.H., Boel, H.D., Hoenderkamp, J.C.D. and Spoorenberg, R.C. (2011), "Buckling length factors for welded lattice girders with hollow section braces and chords", *Proceedings of Eurosteel 2011* (pp. 1881–1886).
- Tuominen, N. and Björk, T. (2014), "Ultimate Capacity of Welded Joints Made of High Strength Steel CFRHS", *Proceedings of Eurosteel 2014* (pp. 83–84).
- Ulaganathan, S., Couckuyt, I., Deschrijver, D., Laermans, E. and Dhaene, T. (2015), "A Matlab Toolbox for Kriging Metamodeling", *Procedia Computer Science*, Vol. 51 (pp. 2708–2713).

EXPERIMENTAL EVALUATION OF THE DIRECTIONAL STRENGTH-ENHANCEMENT FACTOR FOR FILLET WELDS TO CHS

Kyle Tousignant

Ph.D. Candidate, Department of Civil Engineering, University of Toronto, Canada
kyle.tousignant@mail.utoronto.ca

Jeffrey A. Packer

Bahen/Tanenbaum Professor of Civil Engineering, University of Toronto, Canada
jeffrey.packer@utoronto.ca

The structural reliability of the $(1.00 + 0.50\sin^{1.5}\theta)$ fillet weld directional strength-enhancement factor is examined, based on a set of laboratory tests on fillet-welded connections between circular hollow sections (CHS) and rigid end-plates. Twelve weld-critical connections were designed and tested to failure by a quasi-static tension load applied axially to the CHS. Measured strengths from the 12 tests, and 21 previous tests on fillet-welded connections between rectangular hollow sections (RHS) and rigid end-plates, are compared to the predicted strengths according to AISC 360 and Eurocode 3.

STATE OF WELD DESIGN FOR HSS

For steel hollow structural section (HSS) connections, recent standards and design guides have outlined two design approaches for proportioning welds. The weld can be designed either: (i) to develop the yield strength of the connected branch, or (ii) to resist the actual forces in the branch. Extensive research at the University of Toronto (Frater and Packer, 1992a, 1992b; Packer and Cassidy, 1995; Packer and Sun, 2011; McFadden and Packer, 2014; Tousignant and Packer, 2015) has shown that, in a typical HSS-to-HSS connection, the connected branch wall and the adjacent weld are loaded in a highly non-uniform manner around the branch perimeter. Hence, designing welds to resist the actual forces in the branch requires the use of weld effective lengths, as pointed out in Annex B of ISO (2013). Weld effective lengths for rectangular HSS-to-HSS connections are given in AISC 360 Chapter K.

American fillet weld design guidance (AISC, 2010; AWS, 2015) permits the use of a $(1.00 + 0.50\sin^{1.5}\theta)$ or “ $\sin\theta$ ” factor to take into account increased capacity of fillet welds loaded non-parallel to the weld axis. The $\sin\theta$ factor is based on fillet-welded lap-splice (Fig. 1a) and cruciform (Fig. 1b) connection tests (e.g. Lesik and Kennedy, 1990). Recently, the use of the $\sin\theta$ factor for fillet weld design in HSS connections has been questioned since: (i) welding can only be performed on one side (the outside) of the HSS wall, and hence welds are subject to a local eccentricity (Fig. 1c); (ii) by the same token, the HSS wall is not externally restrained from rotation; and (iii) unlike in lap-splice connections, fillet welds in HSS connections are often loaded by the HSS in tension (or bending) rather than in shear.

It has been shown, experimentally, that the inclusion of the $\sin\theta$ factor is non-conservative when used in conjunction with current AISC 360-10 Chapter K weld effective length rules (i.e. target reliability levels are not achieved) (Packer and Sun, 2011; McFadden and Packer, 2013, 2014; McFadden et al., 2013; Tousignant and Packer, 2015). Also, there are still concerns about the use of the $\sin\theta$ factor to design fillet welds to HSS, even where the entire weld length is effective.

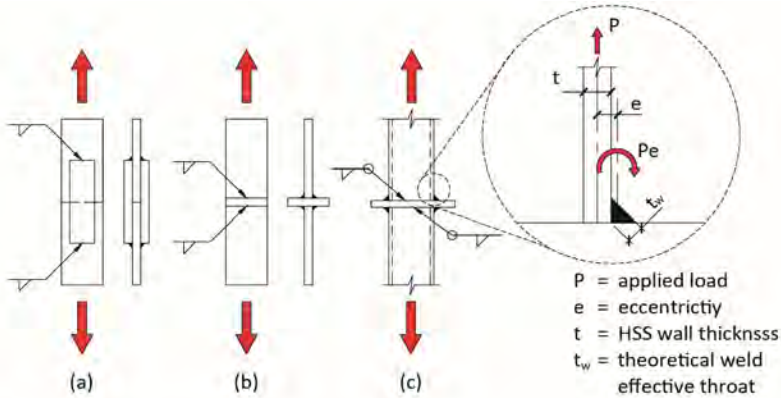


Figure 1. Fillet-welded (a) lap-splice, (b) cruciform, and (c) HSS-to-plate test specimens

CONTEMPORARY FILLET WELD DESIGN

USA

In section J of AISC 360 (AISC, 2010), the design strength (V_r) of a fillet weld is based on shear rupture along the plane of the effective throat, and taken as the product of the nominal stress of the weld metal ($F_{nw} = 0.60F_{EXX}$, where F_{EXX} = ultimate strength of weld metal) and the weld effective throat area (A_w). A resistance factor ($\phi_w = 0.75$) is then applied to obtain $V_r = \phi_w R_n$. The nominal strength (R_n) of the weld is hence:

$$R_n = F_{nw} A_w = 0.60 F_{EXX} A_w \quad (1)$$

For parallel weld elements with a uniform leg size, loaded through the center of gravity, Section J2.4(a) permits the use of the $\sin\theta$ factor when determining F_{nw} . Thus:

$$R_n = F_{nw} A_w = 0.60 F_{EXX} (1.0 + 0.50 \sin^{1.5} \theta) A_w \quad (2)$$

where θ = angle of loading measured from the weld longitudinal axis (in degrees).

Concentrically loaded multi-orientation fillet weld connections are covered under Section J2.4(c). For such connections, R_n is the greater of the following:

$$R_n = R_{nwl} + R_{nwt} \quad (3a)$$

$$R_n = 0.85 R_{nwl} + 1.5 R_{nwt} \quad (3b)$$

where R_{nwl} = nominal strength of all longitudinally-loaded ($\theta = 0^\circ$) fillet welds; and $R_{nwt} =$ nominal strength of all transversely-loaded ($\theta = 90^\circ$) fillet welds, but calculated with $F_{nw} = 0.60F_{EXX}$.

Europe

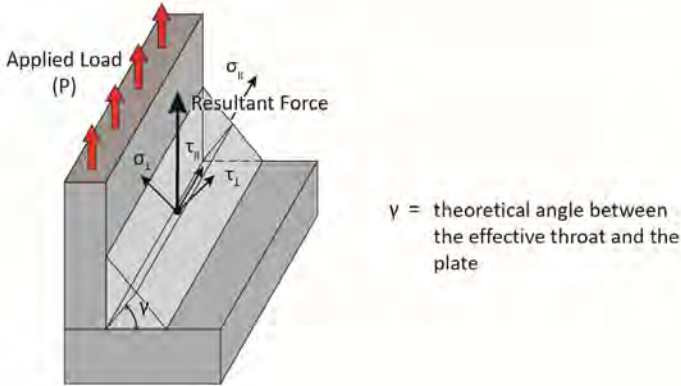


Figure 2. Stress components in the plane of the weld effective throat

According to *Eurocode 3* (EN 1993-1-8) (CEN, 2005), V_r is determined using either the Directional Method or the Simplified Method. The Directional Method requires the resultant design force transmitted by a unit length of weld to be resolved into components parallel and transverse to the longitudinal axis of the weld, and normal and transverse to the plane of the weld throat (Fig. 2). The resistance of the fillet weld is deemed sufficient for design if Eqns. 4a and 4b are satisfied along the weld length.

$$[\sigma_{\perp}^2 + 3(\tau_{\perp}^2 + \tau_{\parallel}^2)]^{0.5} \leq F_u / (\beta_w \gamma_{M2}) \quad (4a)$$

$$\sigma_{\perp} \leq 0.9F_u / \gamma_{M2} \quad (4b)$$

where σ_{\perp} = normal stress perpendicular to the throat; τ_{\perp} = shear stress (in the plane of the throat) perpendicular to the axis of the weld; τ_{\parallel} = shear stress (in the plane of the throat) parallel to the axis of the weld; γ_{M2} = partial safety factor for the resistance of the weld equal to 1.25; β_w = correlation factor for fillet welds (relating F_u to F_{EXX}); and F_u = ultimate strength of the base metal.

If one assumes a design throat area of $A_w = t_w l_w$, where l_w is the weld length, then the ultimate applied load (P_u) can be resolved into components and hence stresses, and R_n and V_r can be determined from Eqn. 4a as follows:

$$\tau_{\parallel} = \frac{P \cos \theta}{t_w l_w}; \sigma_{\perp} = \frac{P \sin \theta \cos \gamma}{t_w l_w}; \tau_{\perp} = \frac{P \sin \theta \sin \gamma}{t_w l_w} \quad (5)$$

$$\frac{P}{t_w l_w} [\sin^2 \theta \cos^2 \gamma + 3(\sin^2 \theta \sin^2 \gamma + \cos^2 \theta)]^{0.5} \leq F_u / (\beta_w \gamma_{M2}) \quad (6)$$

$$P \leq \left(\frac{F_u}{\beta_w \gamma_{M2}} \right) \frac{t_w l_w}{[\sin^2 \theta \cos^2 \gamma + 3(\sin^2 \theta \sin^2 \gamma + \cos^2 \theta)]^{0.5}} = \frac{R_n}{\gamma_{M2}} = V_r \quad (7)$$

For design according to the Simplified Method, the weld is considered to be loaded in pure shear (parallel to the weld axis) regardless of the actual orientation of the applied load. Welds can thus be proportioned according to Eqn. 8, which is a conservative (lower bound) alternative to the Directional Method.

$$V_r = \frac{R_n}{\gamma_{M2}} = \left(\frac{F_u}{\sqrt{3} \beta_w \gamma_{M2}} \right) t_w l_w \quad (8)$$

EXPERIMENTAL PROGRAM

An experimental program was conducted at the University of Toronto to investigate the reliability of using AISC 360 (2010), with and without the $\sin\theta$ factor, and EN 1993-1-8 (CEN, 2005) to predict the strength of welds between CHS and rigid plates. A total of 12 CHS-to-plate connections, with different weld sizes, tube diameter-to-thickness ratios, and angles of 60° or 90° between the CHS and plate (θ_p), were designed and fabricated to fail by weld rupture through the weld throat. Specimens were tested under quasi-static axial tension applied to the CHS member (see Fig. 3).

Mechanical Properties

Specimens were fabricated from cold-formed CHS, made to ASTM A500 Grade C, and 25-mm plate with a nominal yield strength of 350 MPa. Three tensile coupons (TCs) were saw cut from each CHS (at 90° , 180° , and 270° from the weld seam), and from the plate, and tested in accordance with ASTM A370 (2013). The average measured yield stresses determined by the 0.2% offset method (F_y and F_{yp} , for the CHS and plate, respectively) and the average measured ultimate strengths (F_u and F_{up}) are shown in Table 1.

Test welds were made using a semi-automatic flux-cored-arc-welding process, and an E71T-1C electrode (minimum guaranteed tensile strength of 490 MPa). Three all-weld-metal TCs were made per AWS D1.1 (2015), and tested according to ASTM A370 (2015). The average measured yield stress for the weld metal determined by the 0.2% strain offset method (F_{yw}) and the average measured ultimate strength of the weld metal (F_{EXX}) are shown in Table 1.

Table 1. Mechanical properties of the CHS and 25-mm intermediate plate

Connection No.	CHS		Plate		Weld Metal	
	F_y (MPa)	F_u (MPa)	F_{yp} (MPa)	F_{up} (MPa)	F_{yw} (MPa)	F_{EXX} (MPa)
1, 2, 7, 8	421	501	409	566	501	571
3, 4, 9, 10	431	488	409	566	501	571
5, 6, 11, 12	385	450	409	566	501	571

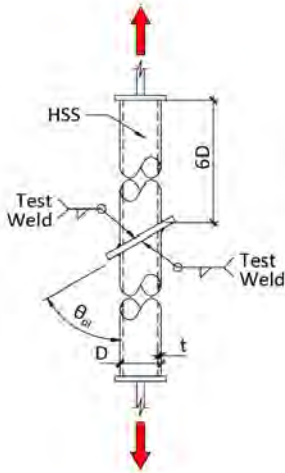


Figure 3. CHS-to-plate test specimen

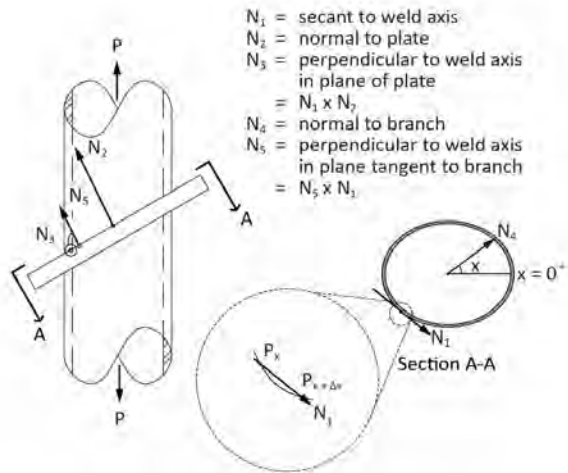


Figure 4. Method used to determine weld geometric properties l_w , Ψ , and θ

Geometrical Properties

Table 2. Average geometrical properties and weld rupture loads

Connection No.	θ_{pl} ($^\circ$)	$D \times t$ (mm \times mm)	t_p (mm)	l_w (mm)	t_w (mm)	w_b (mm)	w_p (mm)	P_u (kN)
1	90 $^\circ$	167.9 \times 6.70	25.0	527	3.90	5.91	5.22	1261
2	90 $^\circ$	167.9 \times 6.70	25.0	527	5.36	8.10	7.19	1279
3	90 $^\circ$	127.4 \times 11.55	25.0	400	6.09	8.60	8.75	1459
4	90 $^\circ$	127.4 \times 11.55	25.0	400	7.12	9.77	10.43	1597
5	90 $^\circ$	101.0 \times 7.34	25.0	318	4.07	5.67	5.91	841
6	90 $^\circ$	101.0 \times 7.34	25.0	318	4.04	5.91	5.58	864
7	60 $^\circ$	167.9 \times 6.70	25.0	569	3.67	5.45	5.33	1450
8	60 $^\circ$	167.9 \times 6.70	25.0	569	3.96	6.12	5.53	1331
9	60 $^\circ$	127.4 \times 11.55	25.0	432	5.06	7.19	7.43	1109
10	60 $^\circ$	127.4 \times 11.55	25.0	432	6.59	9.41	9.68	1479
11	60 $^\circ$	101.0 \times 7.34	25.0	342	3.77	5.73	5.46	776
12	60 $^\circ$	101.0 \times 7.34	25.0	342	3.49	5.19	5.03	803

Prior to testing, welds were manually ground flat, and leg dimensions on the branch and plate (w_b and w_p) were measured at discrete locations along the weld length using a standard (when $\theta_{pl} = 90^\circ$) or skew-T (when $\theta_{pl} = 60^\circ$) fillet weld gage. For each test weld, between 12 and 20 measurements were taken around the branch perimeter. The total weld length (l_w) and the weld length tributary to each measurement were

computed by summing up secants to the weld axis (Fig. 4) with a subtended angle increment (Δx) equal to 1° . The local dihedral angle (ψ) and angle of loading measured from the weld longitudinal axis (θ) were computed using Eqn. 9 (see Fig. 4), with ψ then used to determine t_w in Eqn. 10. Table 2 shows the average measured values of w_b and w_p , and the computed values of t_w and l_w , for each connection.

$$\Psi = \cos^{-1} \left(\frac{N_5 \cdot N_3}{|N_5||N_3|} \right); \theta = \cos^{-1} \left(\frac{P \cdot N_1}{|P||N_1|} \right) \quad (9)$$

$$t_w = \frac{w_b w_p \sin \Psi}{\sqrt{w_b^2 + w_p^2 - 2w_b w_p \cos \Psi}} \quad (10)$$

Test Set-up and Instrumentation

Quasi-static tension was applied to the ends of the CHS branches by a universal testing machine. For each test, load, displacement (over a 50-mm gage length), and longitudinal strain in the branch, adjacent to the weld and in the constant stress region ($3D$ from the weld toe on the branch), were measured. Strain gage readings adjacent to the weld showed that the entire weld length was effective in all tests (i.e. there was uniform load transfer between the branch and the weld), and strain measurements in the constant stress region verified, by virtue of equal strain at all measurement locations, that the specimens were loaded in pure tension (i.e. there were no bending moments caused by misalignments in the test set-up, or by test specimen out-of-straightness). Failure by weld rupture (see Fig. 5) occurred in all tests, and the failure loads (P_u) are given in Table 2. After failure, the broken welds were ground down, and repaired (heavily re-welded), and connections were tested, again, to failure of the weld on the opposite side of the plate.

For connections nos. 1 – 6 (with $\theta_{pl} = 90^\circ$), the load-deformation response of the weld on both sides of the intermediate plate was measured using four equally-spaced linear varying differential transformers. The average weld deformation capacity (Δ/w_b) was found to be 0.101 mm/mm, with the deformation of the test weld (Δ) calculated by taking into account the elastic deformation of the branch within the gage length, and, for every second test, the plastic deformation of the weld from the previous loading procedure. The value of $\Delta/w_b = 0.101$ mm/mm compares well with values given by Butler et al. (1972) for tests on transversely-loaded fillet-welded lap-splice connections.

Post-rupture Macroetch Examinations

After testing to failure, every second connection was saw-cut several times around the branch perimeter in the plane of the local dihedral angle (Ψ). One side of each cut section was surface polished and macro-etch examined, per ASTM E340 (ASTM, 2006), using a 10% nital etchant solution. Employing digital software, the weld leg and theoretical throat dimensions were re-measured, and the actual throat dimension (along the failure plane) (t_{wa}) (Fig. 6) and the angle between the failure plane

and plate (γ_a) for the 90° connections were measured (Table 3). It was found that the actual failure plane did not coincide with the theoretical throat (t_w), but tended towards the weld tension leg (in the direction of the applied load). As a result, t_{wa} was 1.24 times larger, on average, for all connections, than the theoretical effective throat (t_w).

Table 3. Average values of γ_a and t_{wa} determined from macro-etch examinations

Connection No.	1	4	6	8	10	12
γ_a (°)	61.5	70.6	69.7	-	-	-
t_{wa} (mm)	4.73	8.20	5.29	5.05	6.78	4.98
t_{wa} / t_w	1.21	1.15	1.31	1.28	1.03	1.43



Figure 5. Rupture of connection no. 4

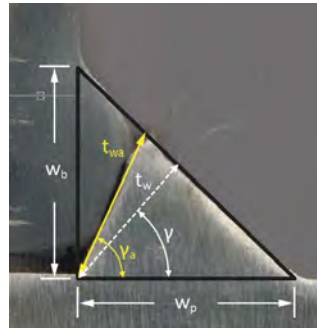


Figure 6. Typical fillet weld macro-etch

ANALYSIS AND RESULTS

Predicted nominal weld strengths (R_n) for the 12 CHS-to-plate connections were computed according to four models: (a) AISC 360-10 without the $\sin\theta$ factor; (b) AISC 360-10 with the $\sin\theta$ factor; (c) EC3 Directional Method; and (d) EC3 Simplified Method.

For models (a) and (d), R_n was determined using the average t_w and l_w values from Table 2 and Eqn. 1 (model (a)) or Eqn. 8 (model (d)), in order to omit all “ $\sin\theta$ effects”. For models (b) and (c), R_n was calculated as the sum of the strengths of “weld components” tributary to each of the 12 – 20 weld dimension measurements. Hence, local average, and not total average, values of t_w , l_w , and θ were used. For model (b), $R_n = 1.5R_{nwt}$ for the 90° connections. Since AISC’s guidance is inexplicit for joints that contain oblique welds ($0^\circ < \theta < 90^\circ$), for the 60° connections R_n was calculated from Eqn. 2. For model (c), R_n was determined from Eqn. 7, with $\gamma = \cos^{-1}(t_w/W_p)$. The lower of F_U and F_{Up} (from Table 1) was used for the ultimate strength of the base metal, and β_w was taken as 0.9 according to Table 4.1 in EN1993-1-8 (2005) for grade S355 (HSS with a nominal yield strength of 355 MPa). Figs. 7a – 7d show the correlation of the actual and predicted weld strengths for the 12 current tests, combined with 21 RHS-to-plate connection tests previously conducted at the University of Toronto (Packer et al., 2015).

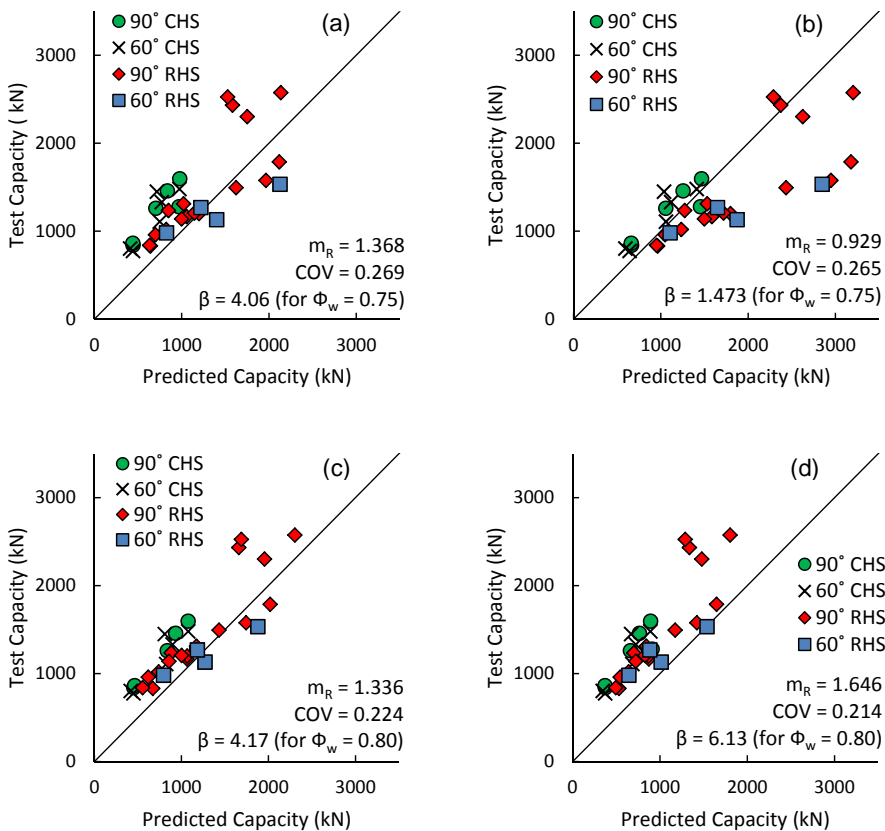


Figure 7. Comparison of actual and predicted strengths for (a) AISC 360-10 without the $\sin\theta$ factor, (b) AISC 360-10 with the $\sin\theta$ factor, (c) EN 1993-1-8 (2005) Directional Method, and (d) EN1993-1-8 (2005) Simplified Method

To assess whether adequate safety margins are inherent in the correlations shown in Figs. 7a – 7d, a simplified reliability analysis was performed. The safety index, β , was determined using Eqn. 11 (Fisher et al. 1978; Ravindra and Galambos, 1978):

$$\beta = -\frac{1}{\alpha \text{COV}} \ln\left(\frac{\Phi_w}{m_R}\right) \quad (11)$$

where α = coefficient of separation taken to be 0.55 (Ravindra and Galambos 1978); m_R = mean of the actual strength-to-nominal strength ratio; and COV = coefficient of variation of m_R (based on the sample standard deviation).

For models (a) and (b), β was calculated using $\phi_w = 0.75$ in Eqn. 11, and compared to the stipulated target safety index of $\beta = 4.0$ (per Chapter B of the AISC Specification Commentary). For models (c) and (d), ϕ_w in Eqn. 11 was taken as $1/\gamma_{M2} = 1/1.25 = 0.80$.

The calculated values of m_R , COV, and β , for each of the four models, are shown in Figs. 7a – 7d. For the aggregate test results, the provisions of AISC 360 (2010) without the $\sin\theta$ factor achieve an acceptable level of safety (LOS) ($\beta = 4.06 \geq 4.0$); however, the provisions of AISC 360 (2010) with the $\sin\theta$ factor do not ($\beta = 1.473 < 4.0$). Using the EN 1993-1-8 Directional Method, the inherent safety index is $\beta = 4.17$, and using the Simplified Method, $\beta = 6.13$. It can thus be concluded that the Directional Method in *Eurocode 3* (CEN, 2005) provides a LOS that is comparable to AISC 360 (2010) without the $\sin\theta$ factor.

CONCLUSIONS

1. When the $(1.0 + 0.50\sin^{1.5}\theta)$ directional strength enhancement factor is used in the strength calculation of fillet welds to HSS, the equations in AISC 360 (2010) lead to predictions which provide an inadequate safety margin against failure.
2. When the $(1.0 + 0.50\sin^{1.5}\theta)$ directional strength enhancement factor is not used in the strength calculation of fillet welds to HSS, the equations in AISC 360 (2010) can be used with adequate safety (reliability) indices being achieved.
3. The Directional Method in *Eurocode 3* (CEN, 2005) provides a level of safety comparable to AISC 360 (2010) without the $\sin\theta$ factor.
4. AISC 360 (2010) guidance for multi-orientation fillet weld groups (i.e. Eqns. 3a and 3b), with elements oriented between $0^\circ < \theta < 90^\circ$, is inexplicit.

REFERENCES

- American Institute of Steel Construction (AISC). (2010). "Specification for structural steel buildings." *ANSI/AISC 360-10*, Chicago, IL.
- American Society for Testing and Materials (ASTM). (2006). "Standard test method for macroetching metals and alloys." *ASTM E340-06*, West Conshohocken, PA.
- American Society for Testing and Materials (ASTM). (2015). "Standard test methods and definitions for mechanical testing of steel products." *ASTM A370-15*, West Conshohocken, PA.
- American Welding Society (AWS). (2015). "Structural welding code – Steel, 23rd. ed." *ANSI/AWS D1.1/D1.1M:2015*, Miami, FL.
- Butler, L. J., Pal, S., and Kulak, G. L. (1972). "Eccentrically loaded welded connections" *J. Struct. Div. ASCE*, 98(ST5), 989-1005.

Comité Européen de Normalisation (CEN). (2005). "Eurocode 3: Design of steel structures – Part 1-8: Design of joints." *EN 1993-1-8:2005*, Brussels, Belgium.

Fisher, J. W., Galambos, T. V., Kulak, G. L. and Ravindra, M. K. (1978). "Load and resistance factor design criteria for connectors." *J. Struct. Div. ASCE*, 104(9), 1427-1441.

Frater, G. S. and Packer, J. A. (1992a). "Weldment design for RHS truss connections. I: Applications." *J. Struct. Eng. ASCE*, 118(10), 2784-2803.

Frater, G. S. and Packer, J. A. (1992b). "Weldment design for RHS truss connections. II: Experimentation." *J. Struct. Eng. ASCE*, 118(10), 2804-2820.

International Organization for Standardization (ISO). (2013). "Static design procedure for welded hollow section joints – Recommendations." *ISO 14346:2013 (E)*, Geneva, Switzerland.

Lesik, D. F. and Kennedy, D. J. (1990). "Ultimate strength of fillet welded connections loaded in plane." *Can. J. Civ. Eng.*, 17(1), 55-67.

McFadden, M. R. and Packer, J. A. (2013). "Effective weld properties for RHS-to-RHS moment T-connections." Phase 1 Report to the American Institute of Steel Construction, University of Toronto, Toronto, Canada.

McFadden, M. R. and Packer, J. A. (2014). "Effective weld properties for hollow structural section T-connections under branch in-plane bending." *Eng. J. AISC*, 51(4), 247-266.

McFadden, M. R., Sun, M. and Packer, J. A. (2013). "Weld design and fabrication for RHS connections." *Steel Construction – Design and Research*, 6(1), 5-10.

Packer, J. A. and Cassidy, C. E. (1995). "Effective weld length for HSS T, Y, and X connections." *J. Struct. Eng. ASCE*, 121(10), 1402-1408.

Packer, J. A. and Sun, M. (2011). "Weld design for rectangular HSS connections." *Eng. J. AISC*, 48(1), 31-48.

Packer, J.A., Sun, M., and Tousignant, K. (2015). "Experimental evaluation of design procedures for fillet welds to hollow structural sections", *J. Struct. Eng. ASCE* DOI: 10.1061/(ASCE)ST.1943-541X.0001467.

Ravindra, M. K. and Galambos, T. V. (1978). "Load and resistance factor design for steel." *J. Struct. Div. ASCE*, 104(9), 1337-1353.

Tousignant, K. and Packer, J.A. (2015). "Weld effective lengths for rectangular HSS overlapped K-connections." *Eng. J. AISC*, 52(4), 259-282.

LOAD BEARING CAPACITY OF ADHESIVELY BONDED TUBULAR STEEL JOINTS

Matthias Albiez and Thomas Ummenhofer
KIT Steel & Lightweight Structures, 76131 Karlsruhe, Germany
matthias.albiez@kit.edu; thomas.ummehofer@kit.edu

ABSTRACT

Tubular structures, due to their constructive and architectural advantages, are largely used in many different areas of structural steel construction. Usually, connections of steel tubulars are realized by the joining procedure welding. When subjected to fatigue loads, cracks start from the weld seams located inside the tubulars, where they are difficult to detect. Within the framework of a research project, it was aimed to investigate to what extent welding can be substituted by adhesive bonding, thus overcoming the fatigue issues.

This paper deals with the concept of adhesively bonded connections between steel tubulars and cast-steel nodes, and their experimental assessment. The emphasis was set onto the conditions prevalent on the building site, as well as on the requirements that result on the adherents, the surfaces and the adhesives. Experiments were conducted on a large variety of different geometries (diameters ranging from 40 mm to 300 mm), with two different adhesives, under static, creep and fatigue loads. Focus of this paper is the experimental investigation of the load bearing capacity of adhesively bonded tubular joints, especially considering geometrical imperfections.

1. INTRODUCTION

Due to creative and structural advantages hollow section steel frameworks are used in many fields of application. Main applications include bridge constructions, crane constructions and wind energy plants (on- and offshore) but also long-span roof structures such as exhibition halls and stadiums. A key factor regarding the durability of hollow section frameworks under fatigue loading is the design of the joints including details of the welds (Figure 1).

Based on current developments of new cast steel materials, welded hollow section joints can alternatively be realized with cast parts. The most significant advantage of cast parts is the almost arbitrary geometrical design of the components. This allows a smoother tension flow and a reduction of tension peaks resulting from notch effects of sharp corners, edges, sharp variations of wall thickness and other constructional details. Furthermore, cast steel components allow an optimized joint design that follows the stress flow ideally and leads to more uniform stress distributions. Fatigue tests on this connection, however, show that fatigue cracks always start from the weld root and are therefore difficult to identify. Thus, higher safety factors are required during the design process such as a classification in low FAT classes. Against this background, the question remains

whether adhesive bonding can be an alternative to welded connections of circular hollow sections.

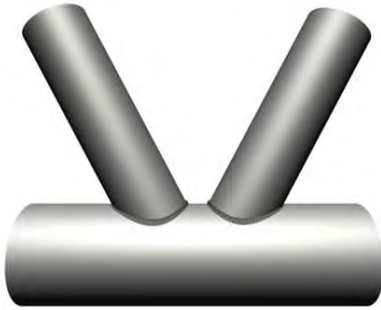


Figure 1. Direct welding of tubulars (Albiez et al. 2013)

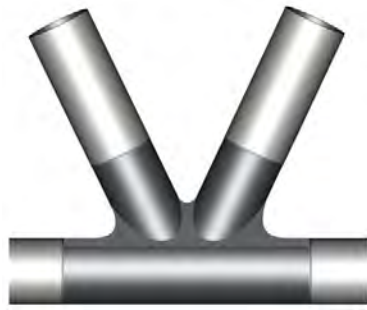


Figure 2. Cast node (Albiez et al. 2013)

In the last years, several bridge structures and building constructions were realized using cast steel components. A famous example for cast steel nodes under static loading is the departure hall at Stuttgart Airport in Germany (Figure 3). At the junction point several hollow sections are connected with the cast steel node using butt welds. Nevertheless, it was observed that fatigue cracks of tubular butt welded specimens subjected to tensile stress always started from the weld root (Puthli et al. 2010). While cracks become visible only at an advanced state of the crack development, they are detected far too late during planned inspections. This implies that visible cracks only appear when the crack has penetrated through the whole wall thickness. This results in low FAT classes (Albiez et al. 2012; Albiez et al. 2015).



Figure 3. Airport Stuttgart (Ummenhofer et al. 2015)



Figure 4. Nesenbach Bridge (Puthli et al. 2010)

Whereas in the field of steel construction adhesive bonding is still of small importance, in other industries, for example in the automotive industry, adhesive bonding today is a central joining technology. In research projects manufacturing and load bearing capacity of adhesively bonded tube joints are investigated for applications in balustrades (Siebert 2006) and pipelines (Boeddeker et al. 2013).

2. STRUCTURAL DESIGN AND RESEARCH FOCUSES

The aim of the research project P884 (Ummenhofer et al. 2015) was the development and systematic investigation of an adhesive bonded joint between cast steel nodes and tubular hollow sections for applications in steel construction. The structural design of the adhesively bonded tubular joint is illustrated in Figure 5. The bonded joint is realized as an overlap joint by putting the hollow section being connected on the cast component. From the difference between the outside diameter of the cast component and the inside diameter of the steel hollow section results a cylindrical gap. This gap is filled with an adhesive using an injection process. The sides of the bonding gap are closed using a sealant. This structural design enables to compensate the significant lower strength of the adhesives compared with structural steel with the larger joining surface as a result of the overlap joint (Albiez et al. 2013).

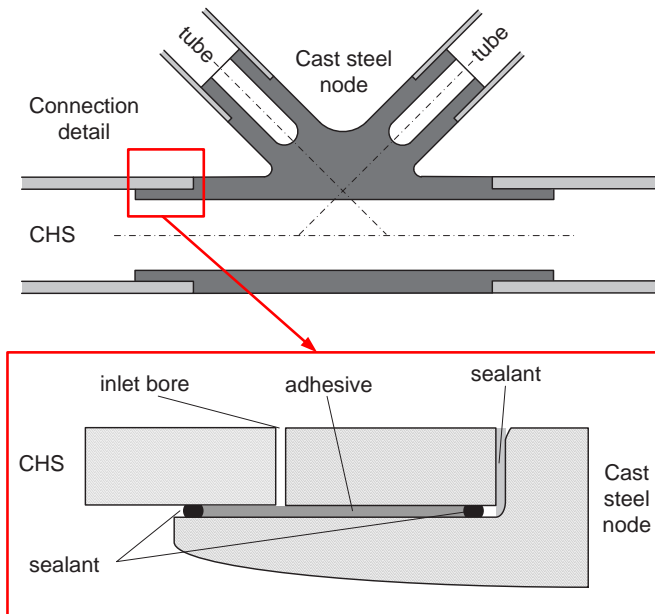


Figure 5. Structural design (Albiez et al. 2013)

Within the scope of the research project P884 mechanical, thermal and medial requirements were initially determined on the bonded connections in applications of civil engineering. It is especially noteworthy that thick-film adhesive bondings in the scale of several millimeters are necessary due to the unavoidable dimensional tolerances of the bonded tubular parts. Therefore, knowledge from the automotive engineering (layer thicknesses considerably less than one millimeter) cannot be transferred to applications investigated in steel construction. Deviations of the nominal thickness of the bonding gap can increase due to assembly imperfections such as “centerline eccentricity” or “canting” and therefore require a detailed investigation. For more details concerning this issue see (Albiez et al. 2012).

Based on the determined requirements preliminary investigations on 24 adhesives were initially conducted. The results of this investigations and technical details in the data sheets resulted in the choice of two commercially available two-component adhesives: the polyurethane adhesive Macroplast 1352 and the epoxy resin adhesive Koemmerling POX EP. The mechanical properties of these adhesives were experimentally investigated in detail on the bulk and on bonded samples. In this context different surface pretreatments were examined as well. One of the principal parts of the research project was the experimental investigation of the load-bearing capacity of adhesively bonded tubular steel joints. An extract of these results is presented in the following section. For more details and a full documentation of results see (Ummenhofer et al. 2015; Albiez et al. 2015).

3. EXPERIMENTAL INVESTIGATION OF TUBULAR JOINTS

Within the scope of the research project P884 (Ummenhofer et al. 2015) extensive experimental investigations were performed to determine the static load-bearing capacity of bonded tubular steel joints. The manufacturing of the bonded connection was carried out according to the following defined process:

- Cleaning of the adhesive surface using methyl ethyl keton
- Blasting of the substrate surfaces with corundum
- Repeated Cleaning of the adhesive surface with methyl ethyl keton
- Application of the joint sealing
- Joining of the two components
- Alignment and centering of the components
- Injection of the adhesive into the joint gap

Different geometrical parameters were varied within the scope of the experimental investigations on adhesively bonded tubular joints. The load-bearing capacity of the bonded connections were investigated for three different adhesive layer thicknesses (2.5 to 6.4 mm), for different tubular hollow section diameters (outside diameter 42.4 to 298.5 mm) and for overlapping lengths between 22.5 mm and 110 mm. Because of the normative demands on the temperature range of application of constructions and the temperature-dependent material behavior of adhesives, the load-bearing capacity of a bonded connection was investigated at -23 °C and +67 °C and after ageing in addition to investigations at ambient temperature. A summary of the results can be taken from (Ummenhofer et al. 2015).

In this paper the experimental investigations on the influence of geometrical imperfections on the load-bearing capacity of bonded tubular hollow sections are presented. For this purpose, adhesively bonded hollow section samples with the defined imperfections „centerline eccentricity“ and „canting“ were manufactured and experimentally investigated. Experimental investigations on reference samples without planned geometrical imperfections were used to quantify the influence of these imperfections.

The geometry of the samples is illustrated in Figure 6. The overlapping length was 27 mm for all presented samples. The tests were conducted using a servo-hydraulic testing machine at a constant testing speed of $v = 0.5$ mm/min (Figure 7). The local deformation between the two bonded parts was recorded during the test.

An optical measuring system was used that enables a three-dimensional determination of the deformations in the area of the investigated tubular section.

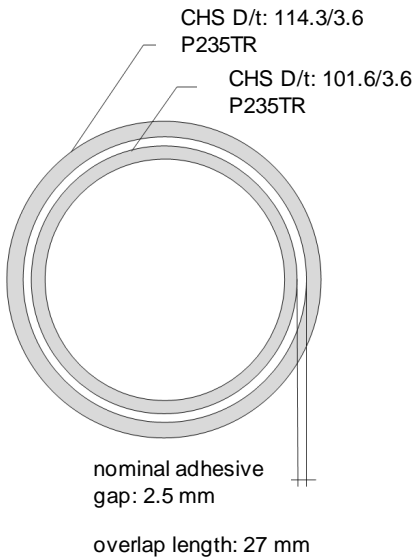


Figure 6. Cross-section adhesively bonded circular hollow sections



Figure 7. Test adhesive bonded tube specimen setup C (Ummenhofer et al. 2015)

At first, the results of the experimental investigations of the reference samples without planned imperfections are presented. Figure 8 illustrates the load-deformation curve of a tensile test of a bonded tubular sample using the adhesive Macroplast 1352, in Figure 9 the load-deformation curve for the used adhesive Kömmerling POX EP is shown. After settlements in the test setup the curves increase almost linearly with constant gradient. The adhesively bonded connection shows brittle failure. This load-bearing and failure behavior was found for all experimentally investigated bonded samples.

The high load-bearing capacity of the connection for both adhesives must be emphasized. For the adhesive Macroplast it amounts to 177.5 kN on the average of five tests with an overlapping length of only 27 mm. The evaluation of the five specimens of this test series results in a mean value of the nominal shear stress in the overlap area of 20.6 MPa with a very low scatter of the test results (standard deviation 0.8 MPa). The load-bearing capacity of the specimens joined with the adhesive Kömmerling POX EP is comparable. The nominal shear stress is 21.9 ± 1.6 MPa on average.

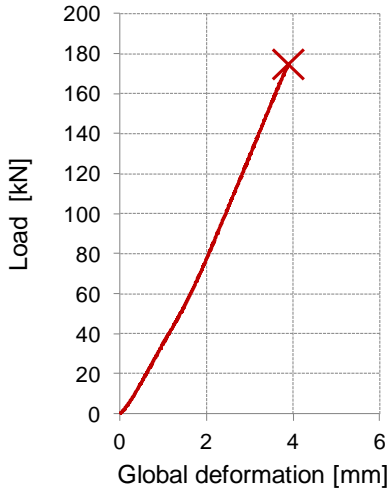


Figure 8. Load-deformation tensile test adhesively bonded CHS joint; adhesive Macroplast 1352

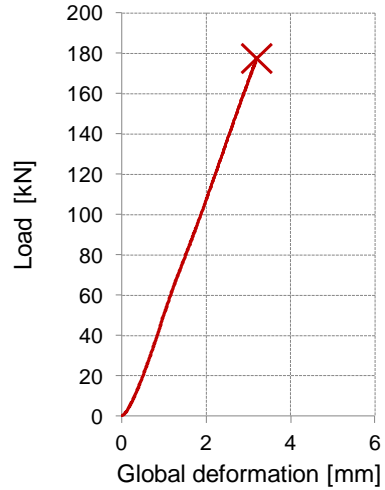


Figure 9. Load-deformation tensile test adhesively bonded CHS joint; adhesive Koemmerling POX EP

In Figures 10a, 10b the fracture appearances of the inner tube and the outer tube are illustrated for the samples bonded with Koemmerling POX EP. A cohesion failure close to the boundary layer (predominantly at the internal tube) combined with an adhesion failure could be determined as the governing failure modes.



Figure 10a: Fracture appearance inner tube (Ummenhofer et al. 2015)



Figure 10b: Fracture appearance outer tube (Ummenhofer et al. 2015)

Bonded hollow section connections were manufactured in addition to the reference samples that show defined incorporated imperfections. The imperfections "centerline eccentricity" and "canting" are schematically shown in Figure 11 and 12. To manufacture samples with centerline eccentricities the inner tube is moved in radial direction with $E = 0.2 \cdot t_a$ or $E = 0.5 \cdot t_a$ (t_a – adhesive gap thickness). This results for an eccentricity of $0.2 \cdot t_a$ in a maximum layer thickness of $t_{a,max} = 3.4$ mm and a minimum layer thickness $t_{a,min} = 2.2$ mm. For the centerline eccentricity of $0.5 \cdot t_a$ adhesive gap thicknesses of $t_{a,min} = 1.4$ mm and $t_{a,max} = 4.2$ mm result.

The samples of further testing series show a canting of the inner tube of 0.75° or 1.50° related to the longitudinal axis of the outer tube. The pivot point is in the center of the overlap area (see Figure 12).

These imperfections might appear small at first sight, they lead, however, to a shift of the endpoint of the tubular of more up to 8 cm with a component length of e.g. 4 m.

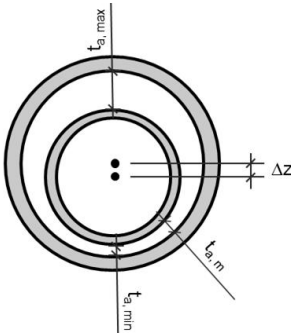


Figure 11. Imperfection: Centerline eccentricity (Albiez et al. 2012)

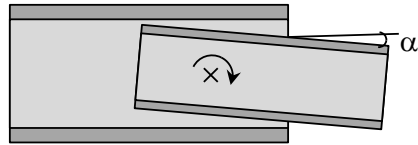


Figure 12. Imperfection: Canting (Albiez 2016)

The results of the tensile tests on the described adhesively bonded tubular hollow sections are presented in the following. For the specimens joined with Macroplast 1352 results from the failure loads of the „imperfection-free“ reference samples a mean value of 20.6 ± 0.8 MPa nominal stress in the overlapping area.

The mean value of the nominal shear stress in the amount of 21.6 ± 1.6 MPa results for the test series with an eccentricity of the centerline of $0,2 \cdot t_a$. This result shows that the adhesively bonded tubular joint has a tolerance against the imperfection eccentricity of the centerline. The evaluation of the tests on bonded hollow section specimens with more than twice of the eccentricity of the centerlines ($E = 0,5 \cdot t_a$) results in a mean value of the nominal stress of 19.0 ± 1.1 MPa. It is determined that the load-bearing capacity of the bonded tubular joints with larger eccentricities of the centerline decreases, in the example of the specimens joined with the adhesive Macroplast, however, only with 8%. These results are illustrated graphically in Figure 13.

A comparable picture is shown for the specimens bonded with the adhesive Koemmerling POX EP (Figure 14). The evaluation of the failure loads of the reference samples results in a mean value of the nominal stress of 21.9 ± 1.6 MPa.

A statistical evaluation of the failure loads of the imperfect specimens with a centerline eccentricity of $0,2 \cdot t_a$ results in a mean value of the nominal shear stress in the adhesive layer of $21.8 \text{ MPa} \pm 2.9 \text{ MPa}$. A significant larger eccentricity of the centerlines of $E = 0.5 \cdot t_a$ results in a mean value of $20.7 \text{ MPa} \pm 1.8 \text{ MPa}$. The tests on tubular joints with the adhesive Koemmerling POX EP also show that bonded connections have a certain tolerance with regard to the applied imperfection. The capacity of the connection decreases with larger imperfections.

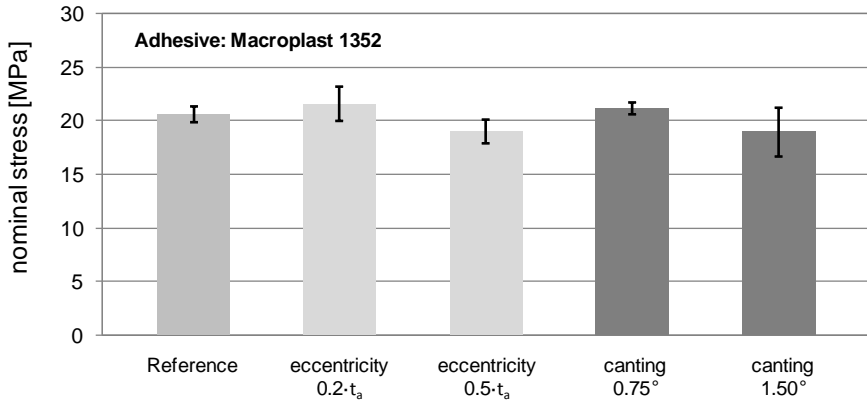


Figure 13: Summary of nominal stresses resulting from experimental testing of adhesively bonded tubular joints with different geometrical imperfections; adhesive Macroplast 1352

The statistical evaluation of the component tests with a canting of $S = 0.75^\circ$ leads to a mean value of 25.0 MPa with a standard deviation of 0.5 MPa. It can be noticed again that the bonded connection is tolerant with regard to the imperfection canting. The tests on bonded tubular specimens with a inserted canting of 1.5° show a higher scatter. The evaluation of the failure loads leads to a mean value of the nominal stress of 20.0 ± 5.1 MPa.

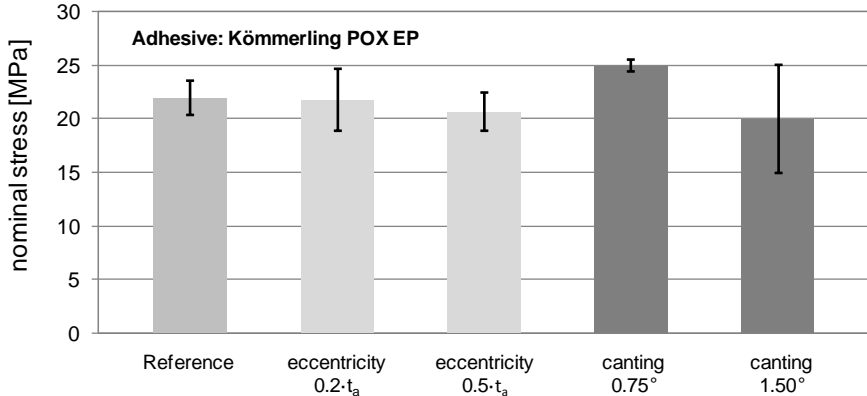


Figure 14: Summary of nominal stresses resulting from experimental testing of adhesively bonded tubular joints with different geometrical imperfections; adhesive Kömmerling POX EP

To summarize, it can be noted that in the presented component tests for both adhesives, nominal stresses of about 20 MPa shear strength were determined. For this reason, the minimum strength of 10 MPa defined in (Ummenhofer et al. 2015) for applications in civil engineering resulting from comparative calculations on real load bearing structures is significantly surpassed. Particular emphasis should be laid

on the low scatters. A tolerance of the bonded connections with regard to the imperfections “centerline eccentricity” and “canting” could be determined. However, with large imperfections a reduction of the load-bearing capacity of the adhesively bonded connection is detectable (Ummerhofer et al. 2015, Albiez 2016).

The knowledge gained within the scope of the research project P884 was applied to the manufacturing and testing of large components in the scale of 1:1. The full scale components consist of a tubular cast steel component (material G20Mn5) with cross-sectional dimensions $D/t = 298.5/30$ mm and a steel hollow section (material S355J0) with the dimensions $D/t = 298.5/12.5$ mm. The cast steel component is graded to a reduced diameter of 265.5 mm in the overlap area, so that an overlapping connection of both tubulars with a nominal bonding gap thickness of 2.5 mm is enabled. The length of the bonding gap is 110 mm. An overview of the dimensions of the full scale components is shown in Figure 15. The manufacturing of the adhesive bond follows the above described process and is shown in Figure 16.

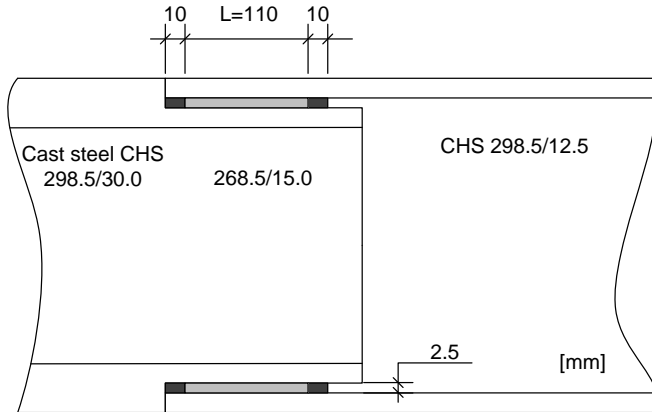


Figure 15: Dimensions full-scale components (Ummerhofer et al. 2015)

After curing of the adhesive the full scale components are experimentally investigated in tensile tests. All tests were performed using a 3.000 kN testing machine and a constant test speed of 0.5 mm/min (see Figure 17).

The load-deformation curve of the experimental test of a full scale component is shown in Figure 18. An almost linear increase of the load is determined with growing path. The bonded connection shows brittle failure. It must be highlighted the maximum load-bearing capacity of the bonded connection of approx. 2,000 kN with an overlapping length of only 110 mm. This corresponds to a nominal stress of 21.2 MPa in the overlapping area. The evaluation of all eight full-scale component tests performed in the scope of the research project P884 leads to a mean value of 19.0 MPa with a very low scatter (standard deviation 1.5 MPa) (Ummerhofer et al. 2015; Albiez et al. 2015, Albiez 2016).



Figure 16: Manufacturing of full-scale components (Ummenhofer et al. 2015)



Figure 17: Testing of full scale-component in 3 MN testing machine

The fracture appearances of the bonded large-scale components are shown in Figure 19. We can determine a mixture between cohesion failure and interface failure at the inner tube. Even with the naked eye, adhering residues are clearly visible in the inner tube.

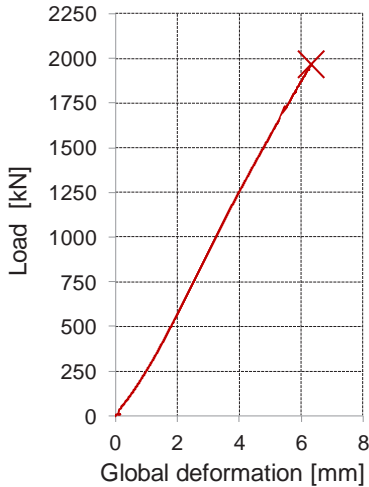


Figure 18: load-deformation-curve full scale component (Ummenhofer et al. 2015)



Figure 19: fracture appearance full scale components (Ummenhofer et al. 2015)

4. CONCLUSION

The results of the research project P884 show that bonded connections of tubular hollow sections represent an efficient alternative to welded or screwed connections in structural engineering applications. In this paper the results of experimental investigations concerning the influence of geometrical imperfections on the load bearing capacity of adhesively bonded tubular joints are highlighted. Furthermore, the results of full scale tests are presented.

5. ACKNOWLEDGMENTS

The project IGF 17199 N of the FOSTA – Forschungsvereinigung Stahlanwendung e.V. was supported by the Federal Ministry of Economics & Energy through the German Federation of Industrial Research Associations (AiF) as part of the program for promoting industrial cooperative research. We thank our research partners Fraunhofer Institute for Manufacturing Technology and Advanced Materials IFAM (Bremen, Germany) and Munich University of Applied Science.

6. REFERENCES

- Albiez, M.; Fricke, H.; Vallée, T.; Bucak, Ö.; Ehard, H.; Ummenhofer, T. (2013): Geklebte Stahlrohr-Stahlgussverbindungen im konstruktiven Stahlbau. *Bauingenieur* Vol. 88 No.10, (pp. 435–441).
- Albiez, M.; Götz, F.; Puthli, R.; Ummenhofer, T. (2012): Numerical and analytical investigation of geometrical imperfections on adhesive bonded cast steel – steel joints. Leroy Gardner (Ed.): *Tubular Structures XIV*: CRC Press, (pp. 249–256).
- Albiez, M.; Ummenhofer, T.; Ehard, H.; Bucak, Ö.; Fricke, H.; Vallée, T. (2015): Adhesive bonded tubular cast steel - steel joints in framework structures. *Proc. METEC & 2nd ESTAD 2015*, Düsseldorf.
- Albiez, M. (2016): Zur statischen Tragfähigkeit geklebter Kreishohlprofilverbindungen im Stahlbau. submitted dissertation, not published yet. Karlsruhe Institute of Technology - Department of Civil Engineering, Geo and Environmental Sciences.
- Boeddeker, Tobias; Flügge, Wilko; Hilgert, Oliver; Kaack, Michael; Andersen, Kenneth (2013): Innovative and competitive new joining technology for steel pipes using adhesive bonding (JoinTec). Publications Office (EUR, 25991). Luxembourg.
- Puthli, Ram; Herion, Stefan; Veselcic, Marian; Hirt, Manfred A.; Nussbaumer Alain; Haldimann, Senta et al. (2010): *Wirtschaftliches Bauen von Strassen- und Eisenbahnbrücken aus Stahlhohlprofilen*: Verlag- und Vertriebsgesellschaft. Forschung für die Praxis FOSTA 591. Düsseldorf.
- Siebert, Marc (2006): *Untersuchung der mechanischen Eigenschaften injektionsgefügter Rundsteckverbindungen*. Shaker (Schriftenreihe des Instituts für Werkstofftechnik Kassel). Aachen.
- Ummenhofer, T.; Albiez, M.; Bucak, Ö.; Ehard, H.; Mayer, B.; Fricke, H. (2015): *Geklebte Stahl-Stahlgussverbindungen am Beispiel von Fachwerkknoten von Rundhohlprofil-Konstruktionen*: Verlag- und Vertriebsgesellschaft. Forschung für die Praxis FOSTA P884. Düsseldorf.

THE CONNECTION CONUNDRUM

An Industry in Transition

Lawrence Griffis, P. E.
Walter P Moore and Associates, Inc., Austin, Texas 78701 USA
lgriffis @walterpmoore.com

Abstract

This paper focuses on a recurring problem that has started to emerge on large commercial projects in the US that contain heavy structural steel members and complex connections. Structural designers often delegate the connection design to fabricators who must then contract with a connection designer separately or, if the expertise exists within the fabrication company, design the connections in house with their own staff. The process becomes very complicated and often very contentious leading to disputes and even expensive litigation. Fast-tracking projects has become a common occurrence in the industry because owners want to accelerate the construction schedule to save time, construction cost and gain an income stream as quickly as possible. The steel industry has now experienced the technical power of a “fully connected computer model” either replacing paper design and shop drawings or supplementing them. This practice, in transition in terms of exactly what constitutes the “contract” for fabrication and erection, has further complicated the design-construction process often leading to disputes and litigation. The paper defines the various problems and recommends some changes that will benefit all parties in the steel industry who are engaged in expensive disputes and litigation because of the current process.

Key Words: fast-track construction process, fully-connected computer models, connections, connection design responsibility, connection design delegation, shop drawings, AISC Code of Standard Practice, pay weight, unit price contracts

Background

In today's marketplace large commercial projects utilizing structural steel as the primary structural framing system are being designed, bid and built using a process that produces a large uncertainty and risk in the financial outcome and schedule of delivery as originally planned and agreed to by the General Contractor or Construction Manager in charge of construction and the Owner. In many cases, these projects result in contentious disputes among the various parties requiring time consuming and expensive mediation or arbitration. Oftentimes, the large financial risks at play lead to litigation requiring even greater uncertainty and risk in the financial outcome.

The purpose of this paper is to describe the process being used, identify the risks among the various parties, provide a critical review of the process and make recommendations for improvement that will benefit all the parties involved. Particular attention will be focused on the design, fabrication and erection of the structural steel members and associated connections of those members.

The Process

While the contractual arrangement among the parties can vary from project to project, the process can be described in outline form as shown in Figure 1.

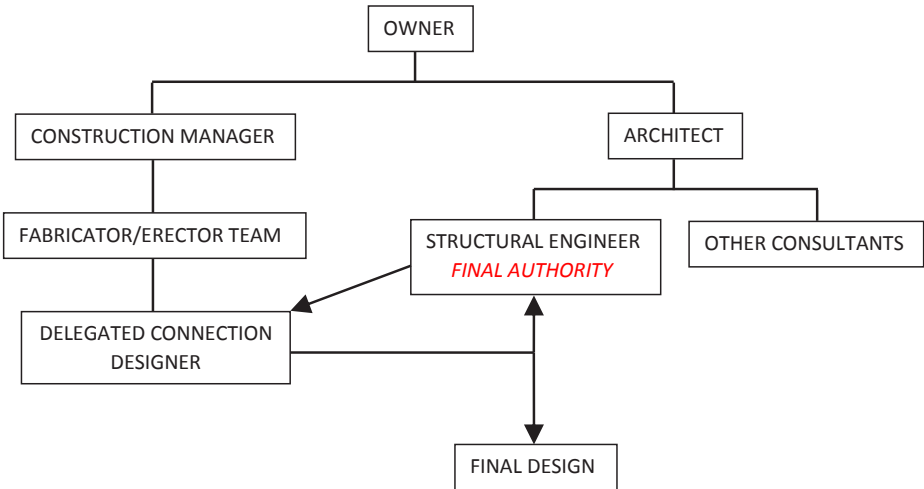


Figure 1. Project Organization – Structural Design

An Owner engages the services of a Construction Manager or General Contractor, designated as the *Owner's Designated Representative for Construction*. This entity is typically in charge of preparing a schedule and budget for the project. This entity is also responsible for receiving bids and negotiating subcontracts with the various subcontractors engaged in the construction. For the purposes of this discussion we will focus on a particular group of subcontractors responsible for fabrication and erection of the structural steel – namely a steel fabricator and erector. The Owner also engages the services of a design team consisting of an architect and group of consultants usually working under the architect. For the purposes of this discussion, we will focus on the

structural engineer in responsible charge of design of the structural steel system. This consultant is often defined as the *Structural Engineer of Record* or, to use terminology defined in the AISC Code of Standard Practice (AISC, 2010), the *Owners Designated Representative for Design*.

Most often on large commercial projects, the design/construction process is *highly accelerated* because the Owner wants to move into the facility as quickly as possible in order to seemingly minimize construction time and money, and to obtain an income stream on the project as soon as possible. The defining characteristics of this process are listed below:

- Super-Fast-Track Projects – Accelerated Schedules
- Owner wants to move in quickly, no time to “delay”
- Structural Engineer rushed to place a *STEEL MILL ORDER* set of drawings
- Drawings are incomplete, usually at Design Development level
- Drawings and connection details are often schematic “stick drawings”
- Often not all members are fully sized or connections designed
- A steel weight (members + connections) is shown in tables on drawings
- A Construction Manager/General Contractor bids to 3 or 4 fabricators
- Fabricators are negotiated hard against each other – until one “wins”
- Project is often labeled as a “Design Assist” contract procedure

A very common theme to the project approach is characterized below:

- The Fabricator is warned that “design is evolving” and incomplete
- Subcontract states that fabricator understands the scope of work, complexity of project and drawing incompleteness
- Fabricator must “accept” the risk of incomplete design
- Fabricator must design the connections as part of his scope of work
- EOR may show a simple Erection Process for steel erection – shored for simplicity
- Fabricator must hire an Erection Engineer to “engineer” the final erection procedure – always more complicated than fully shored
- Any added steel because of erection is “means & methods” at no additional cost to Owner
- Subcontracts usually say change orders are allowed only in the event of a “significant or material change in the scope and character of the work that could not be anticipated”
- Complexity and labor requirements of the steel connections are usually underestimated and not well defined in the initial drawings and the subcontract signed by the fabricator/erector team
- Final connection design and complexity on large complex steel projects almost always creates additional costs for the fabricator/erection team

The added labor for fabrication of the connections increases schedule for fabrication and erection and overall costs leading to disputes and often litigation.

The New Paradigm in Steel Construction – The “Fully Connected Computer Model”

What is a “*fully connected model*”? Its characteristics are as follows:

- A computer model that contains all steel members and all connection material, including bolts, welds, stiffeners, erection aids, etc.
- Often replaces or supplements paper drawings as the basis of a steel subcontract
- Can define “pay weights” for a unit price contract
- Serves as the basis for:
 - Bill of Materials (BOM)
 - Shop Drawings are derived and printed from the model

This new paradigm in the steel industry has created a potentially great advancement for the industry, but has also raised some serious challenges as follows:

- What product, the model or the structural drawings, defines the work to be performed?
- The industry is in transition from paper design drawings or a combination of part models – part design drawings as the contract basis
- Not all models are “fully connected models” – key information may be missing
- Contracts are not always clear as to what defines the work
- Many projects try and use both drawings and models in combination
- Who “owns” and is responsible for the model?
- Creates confusion, disputes and litigation as to “what controls”

A further complication that often arises as to “what is a connection”? This has been and continues to be a potential dispute between engineers and fabricators. What exactly is the distinction between “member reinforcement” (e.g. a stiffener, a doubler plate or other element attached to a member in the connection area to allow the member to carry the prescribed design forces in the member as defined by the engineer of record on the drawings; and, an element that is actually part of the connection itself? In Figure 2 below, what constitutes the “connection” whose member end requires a stiffener plate and/or doubler plate?

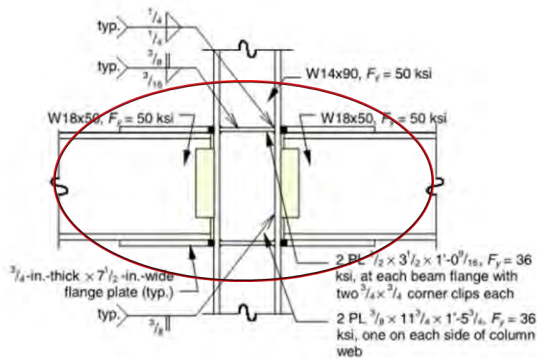


Figure 2. What is the “Connection”?

An engineer of record, who has purposely delegated the connection design to a fabricator, will argue that everything “inside the circle” constitutes the “connection”? Why? In the engineer’s mind, he has delegated the responsibility for connection design to a fabricator because (1) the structural fee that has been negotiated in a competitive solicitation process does not allow the man hours or time to completely design all the connections (2) the *fast-track schedule* established by the owner with the construction manager does not allow time for the engineer to complete the structural drawings with fully designed and detailed connections and (3) the need for member reinforcement is not considered or known until the connection design process has started - a process that the engineer has delegated downstream.

At the same time, the fabricator will argue that any reinforcement for a structural member is part of the member design process, which clearly is part of the structural design and not the connection design – at least in the eyes of the fabricator. Furthermore, how will a bidding fabricator know what to include in his bid if “member reinforcement” is not actually shown and detailed on the structural drawings?

To further complicate this issue, on many large heavy steel projects common in today’s commercial market, it is not clear what part of a complex node of joining large members or trusses constitutes a “member” and what constitutes a “connection”? Refer to Figure 3 for two such examples. Figure 4 shows examples of how complex and also how expensive a complicated node can be on a large project with multiple heavy structural members converging at a common node point.

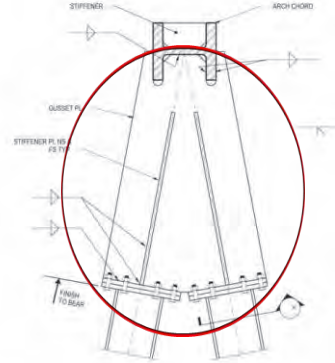
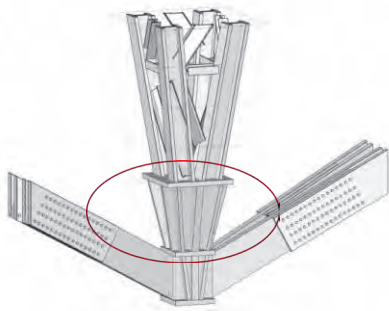


Figure 3. Are the circled elements part of a “member” or “connection”?

One might ask the logical question – “Why does it Matter”? The reason becomes very apparent and also very important from a legal standpoint. If it is a “member” it is the engineer of record’s responsibility. If it is part of the “connection” design that has been seemingly delegated by the engineer to the fabricator, it is a “connection”.

This problem points to the importance of a clear direction that needs to be given in the project specifications by the design engineer, or else a dispute is very likely to result.



Figure 4. Connection Complexity

Another Problem – What is “Pay Weight?”

This becomes an important issue for projects that are set up as unit price contracts to cover the uncertainty involved in un-designed complex (but schematically shown)

connections where the connection design has been delegated to the fabricator. It may also come into play for fixed price contracts where unit prices are specified to be used for pricing change orders. The AISC Code of Standard Practice (AISC, 2010) covers the subject of contract types and pay weights In Section 9. Specifically, Section 9.2 Calculation of Weights defines the rules for calculating weights that are considered the industry standard. For contracts "... stipulating a price per pound for fabricated structural steel that is delivered and/or erected, the quantity of materials for payment shall be determined by the calculation of gross weight of materials as shown on the shop drawings." Section 9.2.2 further specifies that the weights of standard structural shapes, plates and bars shall be calculated on the basis of shop drawings that show the actual quantities and dimensions of material to be fabricated. The following rules are listed for application and clarification:

- a. The weights of all standard structural shapes shall be calculated using the nominal weight per foot and the detailed *overall rectangular dimensions*.
- b. The weights of plates and bars shall be calculated using the detailed *overall rectangular dimensions*.
- c. When parts can be economically cut in multiples from material of larger dimensions, the weight shall be calculated on the basis of the theoretical rectangular dimensions of the material from which the parts are cut.
- d. When parts are cut from standard structural shapes, leaving a non-standard section that is not useable on the same contract, the weight shall be calculated using the nominal weight per foot and the *overall length* of the standard structural shapes from which the parts are cut.
- e. Deductions shall not be made from materials that are removed from cuts, copes, clips, blocks, drilling, punching, boring, slot milling, planing or weld joint preparation.

Figure 5 demonstrates application of the rules for two common conditions. Note that the pay weight includes the enclosed dotted rectangular portions of the material.

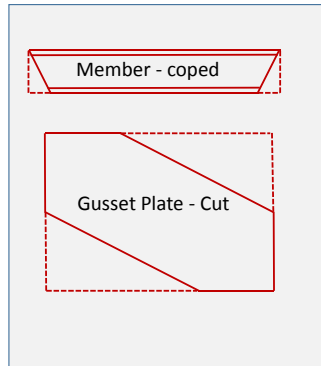


Figure 5. Pay Weights for two common conditions

For projects using fully connected computer models such as found in popular software such as TEKLA, the definition of *Gross Material Weight* closely follows the AISC definition of pay weight. TEKLA considers *gross weight* as follows:

- Weight of members end to end without copes, cuts, holes, bevels deducted
- Weight of all connection plates without cuts, holes or bevels deducted
- For all plates, includes *smallest enclosed rectangle*
- Weld metal not included
- Bolts are included as a separate item
- Very near identical to AISC “Pay Weight” – Fabricator/Industry Standard

The problem arises when the Owner and Construction Manager sometimes try and deviate from this industry standard and substitute terms such “actual weight” or “lifted weight” which have no widespread accepted definition and can have different interpretations. It is strongly suggested that the standard industry term for pay weight be used in all contracts for fabricated structural steel to avoid disputes.

What’s Wrong with the Current Process?

It can be observed in recent years on many large commercial projects that those containing complex heavy steel members where connection design is delegated to the fabricator and based on incomplete or ill-defined connection sketches or “stick diagrams” used to define connections, that disputes are almost inevitable leading to arbitration, mediation and litigation. The design/construction process has seemingly lost sight of how to successfully deliver a large complex steel project. The process is often defined by attempts of the various parties to reduce risk and shove responsibility and liability to the other parties.

Why is the Process Being Set Up in this Way?

The schedule demands that steel mill order drawings be placed before the EOR can complete a final design and before connection design can take place. Many designers are not well trained in connection design and fabricators don't like to be forced into using bad connection designs often depicted on structural drawings. Many structural engineers feel that they cannot get enough compensation or time to perform connection design as part of basic their basic scope of services. Connection design is arduous, complex and time consuming, and often schedule demands do not allow it to happen early in the design process. Many structural engineers do not want the risk for designing connections and feel it has become very specialized and complex. Independent design firms are now being formed to do only connection design to fill the void being created. Schedules are often so compressed (i.e. "super fast-track") that builders believe they can shorten a schedule by delegating connection design. Experience is showing this process is flawed and not often working as anticipated. Disputes and litigation are too often becoming the norm.

A Proposed Solution

Perhaps one solution is to return to the basic premise that *"Engineers should design and contractors should build"*. Shoving design of poorly defined or highly conceptual connections downstream to fabricators can be a flawed practice that really has been shown to complicate the process, create disputes and often extend, not shorten schedules. When disputes arise, the project can be delayed and expensive litigation can result. It is worth noting that delegated connection design for the most part is not permitted in high seismic zones where codes demand the engineer of record completely design and detail all connections on the structural drawings submitted for permit. It is also noted that the bridge industry does not utilize the practice of connection design delegation and the proper time is taken to detail all connections as part of the design drawings.

A better way has been very successfully practiced on some projects as follows:

- Hire the fabricator and erector immediately when the design team is formed. They become part of the "TEAM"
- Negotiate fees up front at a fair market value to ensure fair prices
- Audit the project to ensure fair market prices for material and labor
- Build in incentives for a TEAM APPROACH to finishing a project on time and in budget
- Abandon the common practice of a "low bid mentality" process in construction
- Extend the schedule to allow connection design to be completed before the project is bid
- Manage Client expectations – practice good communication

In the end, an Owner gets what he pays for! Schedule delays, disputes and litigation are avoided.

References:

1. AISC Code of Standard Practice for Steel Buildings and Bridges, American Institute of Steel Construction, Chicago, Illinois, 2010

Performance-based Design and the Load-deformation of Welded Tubular Connections in Offshore Jacket Structures

Kai Wei

Northeastern University, Boston, Massachusetts 02115, USA
k.wei@neu.edu

Andrew T. Myers

Northeastern University, Boston, Massachusetts 02115, USA
atm@neu.edu

Sanjay R. Arwade

University of Massachusetts Amherst, Amherst, Massachusetts 01003 USA
arwade@umass.edu

Jerome F. Hajjar

Northeastern University, Boston, Massachusetts 02115, USA
jf.hajjar@neu.edu

Matthew A. Spencer

Northeastern University, Boston, Massachusetts 02115, USA
spencer.mat@husky.neu.edu

ABSTRACT

Tubular connections in offshore jacket structures are currently designed using strength-based criteria, intended to ensure that the connection behaves elastically during environmental conditions at design recurrence periods. In contrast, performance-based design requires consideration of environmental conditions at recurrence periods well beyond those of current practice, when structural damage is expected and connections are likely to behave inelastically. Performance-based design considers both the occurrence and consequence of structural damage caused by extreme conditions and could improve the performance of offshore structures. This paper assesses the post-elastic behavior and ductility of common connection details for offshore jacket structures based on a survey of experiments and empirical joint models and on nonlinear finite element analyses. The assessment includes common connection details under tension, compression, and bending. The prediction of the inelastic load-deformation response, based on MSL and API, two empirical joint models in the structural analysis program, USFOS, is compared to experiments. As an illustrative example to demonstrate the performance assessment capabilities of this approach, a pushover analysis is carried out for an offshore jacket structure supporting a wind turbine and subjected to extreme wind and wave loading.

1 INTRODUCTION

The Atlantic coast of the U.S. is a natural location for offshore wind energy development because of the abundant wind resource and proximity to major population centers. The most common support structure of fixed-bottom offshore wind

turbines is a monopile, support structure which can be economically installed in water depths up to 30m. In order to also install OWTs in deeper water where winds can be stronger and steadier, a stronger substructure like a jacket is needed instead of a monopile (Bhattacharya et al. 2013). A jacket structure is a steel space frame composed of steel circular hollow sections. Offshore structures located near the U.S. Atlantic coast are exposed to risk of damage from hurricane-induced storm surge, wind and waves (Wang et al., 2005; Sparks 2003). According to the post-hurricane assessment reports of offshore jacket platforms (Energo Engineering Inc. 2005, 2007, 2010), many tubular connection failures have been observed (e.g. cracks at welds, cracks in the chord or brace, punch-through or pull out of brace, buckled members, etc.). In offshore engineering, tubular joints are typically classified as T-, Y-, K- or X-joints according to the geometric orientation of the chords and braces. In most cases, such joints are prepared with complete joint penetration welds connecting the contoured ends of the brace member to the continuous chord member without stiffeners or grout.

The design of the tubular joint connections in offshore jacket structures relies on strength-based criteria. Several empirical and semi-empirical equations have been published to predict ultimate strength for different types of tubular joints considering a wide range of failure modes. For example, Yura et al. (Yura et al., 1980) proposed capacity equations for four types of tubular joint geometries based on a series of 137 tests. Kuobane et al. (Kurobane et al., 1984; Kurobane 1998) and Paul et al. (Paul et al., 1994) studied unstiffened TT and KK joint geometries under symmetric and anti-symmetric brace axial forces and proposed strength equations based on these tests. These experimental studies have provided important insight into the design of jacket connections, however, there are still some challenges in applying these equations to design, such as mismatch between the geometry of the test specimens and the designed connection and the effects of moment-axial force interaction in the member forces that are typically not covered in these studies. Moreover, the above approaches do not provide information on the load-deformation behavior of the connection, an important limitation especially in the context of performance-based design which requires an understanding of the post-elastic behavior of the connections.

Motivated by these limitations, the MSL joint industry project has developed the MSL joint formulation (Dier and Hellan, 2002) which provides fully nonlinear formulae for the load-deformation response of K-, X-, T- and Y-tubular joints subjected to axial force, in-plane bending and out of-plane bending, including interaction between the chord and brace loads. In addition, design guidance for tubular joints in API RP2A (Pecknold et al., 2007) also provides alternative ultimate strength and load-deformation formulations for the design of simple tubular connections based on both the MSL databases and on extended data from finite elements, to increase the range of applicable joint types. Both formulations for joint deformation and strength are implemented in the commercial analysis program USFOS (Holmaas et al., 2006).

To encourage performance-based design of offshore structures, this paper focuses on the post-elastic behavior and ductility of welded tubular connections for jacket structures, and predictions from the API and MSL formulations are compared with experimental data from other researchers. After this comparison, the performance of a hypothetical offshore jacket supporting a wind turbine is evaluated using a static pushover procedure on an analysis model including joint behavior modeled based on the API formulation.

2 MODELING OF WELDED TUBULAR CONNECTIONS

2.1 Joint Modeling in USFOS

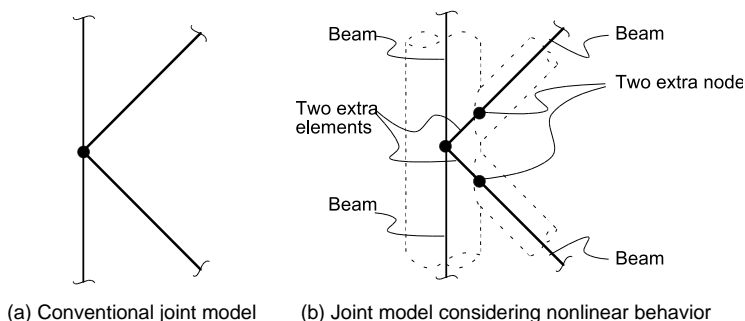


Figure 1 Detail of joint model in USFOS.

In many cases, it is conventional to model connections in jacket structures as rigid (Figure 1a). An alternative joint model, which provides the potential for assessing joint damage (Figure 1b), includes extra elements to represent the behavior of the brace-chord connection. For this alternative model, the ductility of the joint is modeled by selecting parameters for the extra elements according to the selected joint capacity formulation. The nonlinear analyses performed in this study are conducted with the structural analysis program USFOS (Holmaas et al., 2006). In this program, nonlinear joint behavior is modeled with nonlinear spring elements between the brace member and the chord member, as shown in the right of Figure 1b. MSL and API capacity formulae have been implemented in USFOS and either can be selected to model the behavior of the joints. MSL involves three different load-deformation curves, one based on the first crack, one on the mean and one on the characteristic capacity. For consistency of the ultimate capacity results for the MSL and API formulations, the ultimate capacity considered in this study is the load when the first crack appears. More detail of MSL and API formulations can be found in the following references (API, 2005; MSL Engineering Limited, 1999).

2.2 Validation of Applicability of Practical Joint Capacity Formulas

The purpose of this section is to compare the MSL and API joint models with experimental data, in terms of both strength and load-deformation. The first comparison consider four X-joint specimens tested by Noordhoek et al. (Noordhoek et al., 1996). The four specimens include two compression specimens, X355c which is made from grade 355 steel and X500c which is made from grade 500 steel, and two tension specimens, X355t which is made from grade 355 steel and X500t which is made from grade 500 steel. The nominal dimensions of the braces and chords are (370x10 mm) and (450x10 mm). Details of the experimental setup can be found in the report published by Noordhoek et al. (Noordhoek et al., 1996). Table 1 compares the ultimate strength from the tests with the ultimate strength calculated by the MSL and API formulations in USFOS. The ultimate strength results from MSL and API formulations match the experimental data closely.

Table 1 Comparison of ultimate strengths for X-joint specimens (unit: kN).

Specimen	Load pattern	Test	MSL	API
X355c	Compression	661	688	695
X500c	Compression	814	855	863
X355t	Tension	727	701	735
X500t	Tension	802	796	890

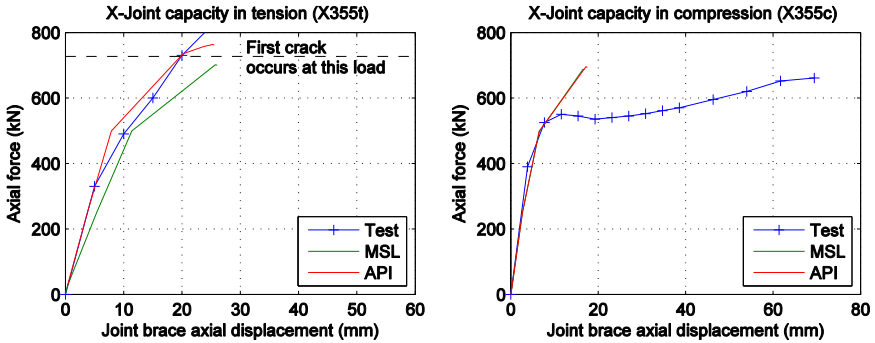


Figure 2 Comparison of the load-deformation curves for X-joints.

Figure 2 compares the load-deformation curves from the MSL and API model with the test data. As shown in Figure 2, the MSL and API formulations predict the deformation accurately for the X355t specimen in tension, while they did not predict the deformation as accurately for the X355c in compression. This is because the failure mode in the test for Specimen X355c involves an indentation of about 50% of the chord diameter, a deformation effect not included by either the MSL or API formulation.

The second comparison between experiments and models is based on tests by Yura et al. (Yura et al., 1978). These tests included T- Y- and K-joint specimens, and five of these are selected here and listed in Table 2. They include one T-joint subjected to out-of-plane bending, one Y-joint subjected to out-of-plane bending, and three K-joints (one subjected to axial force, one subjected to in-plane bending and one subjected to out-of-plane bending). The Y-joint has 30° brace, and the K-joints have a 30° brace and a 90° brace.

Table 2 Specimen identification from the report (Yura et al., 1978).

Specimen Number	Loading	Type of Specimen
G_1	Out-of-plane bending	T
E_1	Out-of-plane bending	Y
C1_2	Axial (90° brace - compression; 30° brace - tension)	K
A2_X	In-plane bending	K
C2_1	Out-of-plane bending	K

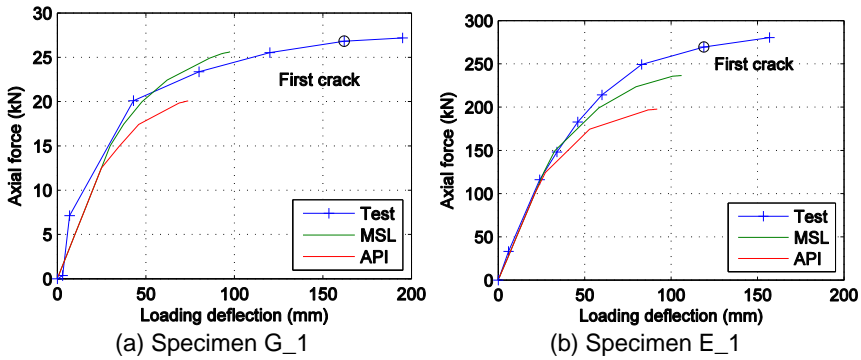


Figure 3 Load-deformation curve for specimens G_1 and E_1.

Figure 3 compares the ultimate strength and load-deformation behavior for the MSL and API formulations compared to test data for T-joint specimen G_1 and Y-joint specimen E_1. Both of these specimens are loaded by out-of-plane bending. In both tests, brace yielding occurred first at the hot spot on the compression side of the brace. After yielding, a crack occurred in the chord at the tension side hot spot. For both tests, the ultimate capacity and deformation prediction of MSL is better than that of API, but both MSL and API predict strength and ductility that is significantly less than the tests.

Figure 4 compares the ultimate strength and load-deformation behavior obtained from MSL and API formulations compared to test data for K-joint specimen C1_2 with 30-degree brace under tension and with 90-degree brace under compression. In both cases, the ultimate strengths of the formulations are similar to the tests. For the tension brace, the results of MSL and API agree with the testing curve. However, for the compression brace, the agreement in terms of load-deformation was worse, similar to the comparison shown in Figure 2 for specimen X355c.

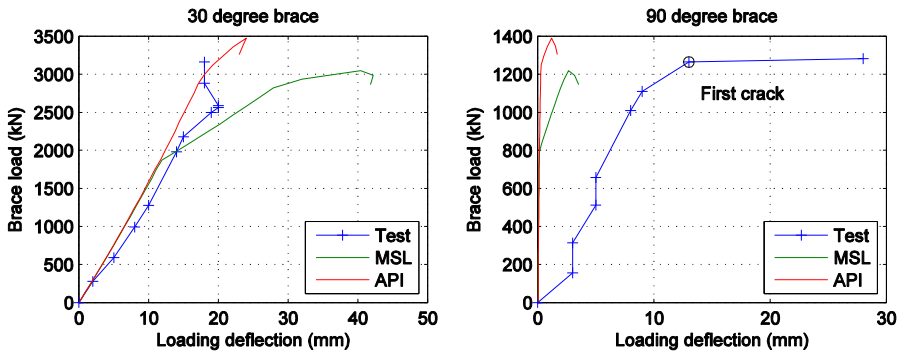


Figure 4 Load-deformation curve for specimen C1_2.

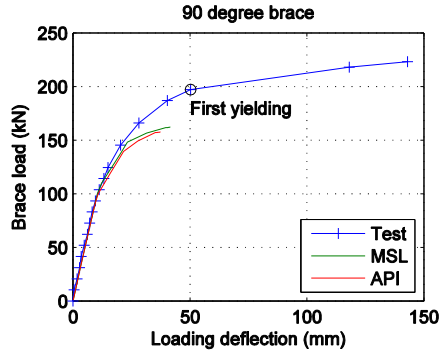
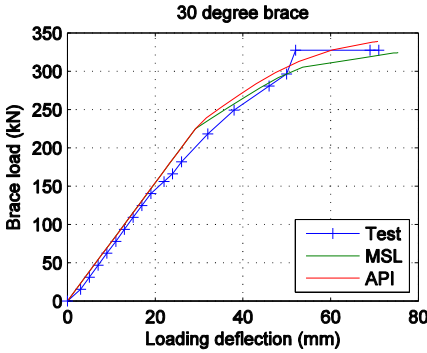


Figure 5 Load-deformation curve for specimen A2_X.

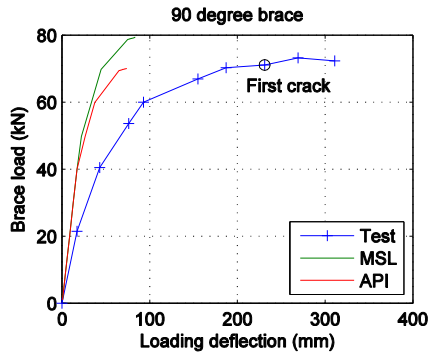
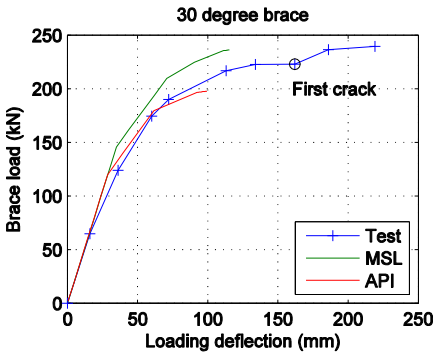


Figure 6 Load-deformation curve for specimen C2_1.

Figures 5 and 6 compare the load-deformation curves obtained from the MSL and API formulations and the testing data for the K-joint specimens under in-plane bending and out-of-plane bending for Specimens A2_X and C2_1 and for both the 30 and 90-degree braces. For both specimens, the results of the MSL and API formulations agree reasonably with the test data for the 30-degree brace, especially so for in-plane bending, while for the 90-degree brace, the formulations have significant differences in stiffness and ductility, for the case of specimen A2_X ultimate strength.

3 EXAMPLE STUDY

Next, this paper illustrates the use of a pushover analysis to assess the structural performance of the NREL 5-MW wind turbine supported by a jacket structure installed in 50 m water depth and subject to extreme environmental loadings. The structure is modeled in USFOS with joint behavior modeled using the API formulation. The jacket design is taken from the UpWind project (Vorpahl et al., 2011). As shown in Figure 7, the rotor-nacelle-assembly (RNA) has a total mass of 350,000 kg and the jacket consists of four legs with four levels of X-braces and cross braces. A concrete deck with a mass of 666,000 kg and plan dimensions of 4.0x9.6x9.6 m is positioned on top

of the jacket and serves as a support platform for the tower of the turbine. See Wei et al. (Wei et al., 2014) for further details on this structure. In this pushover analysis, several simplifying assumptions regarding the structural configuration and loading conditions are made to allow primary attention to be paid to the post-elastic behavior of the jacket. First, the wind and wave loads are assumed to be co-directional and approaching the jacket broadside, second, regular wave kinematics are adopted, and, third, the jacket legs are fully fixed at the mud line without soil-pile interaction.

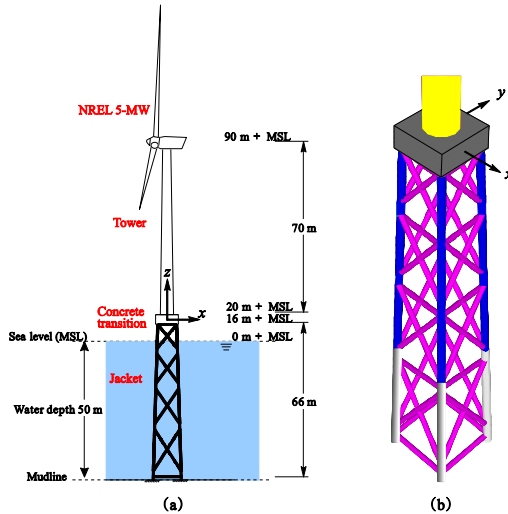


Figure 7 Schematics of the jacket supported OWT: (a) dimensions of reference jacket support structure; (b) 3D view of jacket components.

In order to evaluate the nonlinear performance of the example structure under extreme conditions, a stress-resultant plasticity formulation with plastic hinges combined with the API joint formulation are specified in the model to simulate the nonlinear behavior of both the members and joints. The model is then analyzed with a static nonlinear pushover analysis to estimate damage and assess the performance of the jacket. Wind loads on the turbine and tower and wave loads on the jacket and transition piece are calculated and combined to create the lateral loading in the pushover analysis. The considered extreme environmental conditions are an extreme wave height of 30 m and an extreme wind speed (1min; 10m) of 50 m/s. The analysis was controlled by jacket top displacement until the structure reaches its ultimate state.

Figure 8 shows the pushover curve of the example structure loaded by an extreme wind and wave load pattern. Figure 9 illustrates the locations of damage that occurred due to the extreme environmental loads. The figure shows that the most severe plastic damage occurred in the bottom section of the jacket legs. Additional damage predicted by the models include brace yielding and full plastic hinging of braces in the third and fourth X frame level of the jacket (counted from top to bottom) and buckling of two braces in the second X frame level. None of the joints were predicted to reach their ultimate strength, however yielding was predicted at the joints.

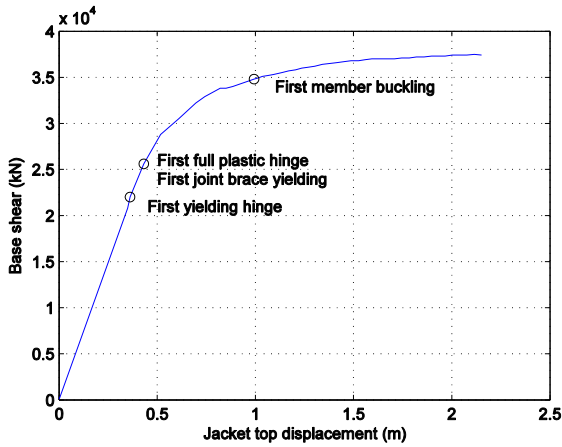


Figure 8 Pushover Curve of OWT jacket under extreme wind and wave loads.

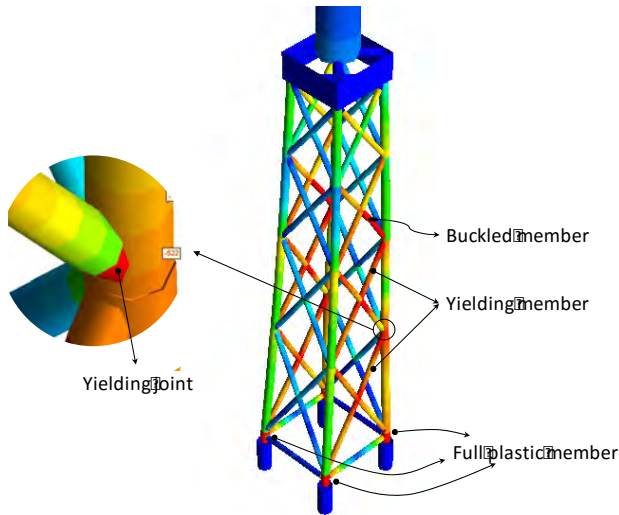


Figure 9 Critical Damages for OWT Jacket under extreme wind and wave loads.

4 CONCLUSION

The current study focuses on the post-elastic behavior and ductility of commonly used connections for offshore jacket structures. The study compares strength and load-deformation behavior predicted from the MSL and API joint formulations, implemented using the finite element analysis program USFOS, with selected experimental results from studies by Noordhoek et al. (Noordhoek et al., 1996) and Yura et al. (Yura et al., 1978) on X-, T-, Y- and K-joints. An example static pushover analysis with plastic hinges and joint capacity formulation based on API was implemented in USFOS for a

jacket structure supporting an offshore wind turbine and subjected to wind and wave loading. The study summarized above supports two conclusions:

(1) The MSL and API joint formulation provides a reasonable approach to estimate the ultimate strength of X-, T-, Y- and K- joint connections, however the predictions for the load-deformation of such connections is less accurate, especially for connections subjected to compression.

(2) The MSL and API joint formulations combined with plastic hinge models can be used to estimate the performance of a jacket structure subjected to extreme loads, considering damage due to member yielding, member plastic hinging, member buckling and joint damage.

ACKNOWLEDGEMENT

This material is based upon work supported by the National Science Foundation under Grant Nos. CMMI-1234560 and CMMI-1234656, the Massachusetts Clean Energy Center, the University of Massachusetts at Amherst, and Northeastern University. Any opinions, findings, and conclusions expressed in this material are those of the authors and do not necessarily reflect the views of the National Science Foundation or other sponsors. The authors would like to thank Dr. Tore Holmas of the USFOS Company for his assistance with this research.

REFERENCES

- API, RP. (2005), Recommended Practice for Planning, Designing, and Constructing Fixed Offshore Platforms-Working Stress Design. In *API RP 2A-WSD 21st Edition*. Washington, D.C.: API Publishing Services.
- Bhattacharya, S., J. A. Cox, D. Lombardi, and D. M. Wood. (2013), "Dynamics of offshore wind turbines supported on two foundations." *Proceedings of the Institution of Civil Engineers-Geotechnical Engineering*, Vol. 166, No. 2 (pp. 159-169).
- Dier, Adrian F., and Oyvind Hellan. (2002), "A non-linear tubular joint response model for pushover analysis." ASME 2002 21st International Conference on Offshore Mechanics and Arctic Engineering, Oslo, Norway.
- EnergO Engineering Inc. (2005), Assessment of Fixed Offshore Platform Performance in Hurricanes Andrew, Lili and Ivan.
- EnergO Engineering Inc. (2007), Assessment of Fixed Offshore Platform Performance in Hurricanes Katrina and Rita.
- EnergO Engineering Inc. (2010), Assessment of Damage and Failure Mechanisms for Offshore Structures and Pipelines In Hurricanes Gustav And Ike.
- Noordhoek, C., A. Verheul, R. J. Foeken, H. M. Bolt and P. J. Wicks. (1996), Static strength of high strength steel tubular joints. ECSC agreement number 7210-MC. 602.
- Holmaas, T., J. Amdahl, and M. R. Emami Azadi. (2006), USFOS, a computer program for ultimate strength analysis of framed structures (with Pile-Soil Module). Norway.
- Kurobane, Y. (1998), "Static Behaviour and Earthquake Resistant Design of Welded Tubular Structures." In *Mechanics and Design of Tubular Structures*. Springer.
- Kurobane, Y., Y. Makino, and K. Ochi. (1984), "Ultimate Resistance of Unstiffened Tubular Joints." *Journal of Structural Engineering*, Vol. 110, No. 2 (pp. 385-400).

MSL Engineering Limited. (1999), JIP - Assessment Criteria, Reliability and Reserve Strength of Tubular Joints (Phase II).

Paul, J. C., Y. Makino, and Y. Kurobane. (1994), "Ultimate Resistance of Unstiffened Multiplanar Tubular Tt-Joints and Kk-Joints." *Journal of Structural Engineering*, Vol. 120, No. 10 (pp.2853-2870).

Pecknold, David, Peter Marshall, and Justin Bucknell. (2007), "New API RP2A tubular joint strength design provisions." *Journal of Energy Resources Technology*, Vol. 129, No. 3 (pp.177-189).

Sparks, P. R. (2003), "Wind speeds in tropical cyclones and associated insurance losses." *Journal of Wind Engineering and Industrial Aerodynamics* Vol. 91 No. 12-15 (pp.1731-1751).

Vorpahl, Fabian, Wojciech Popko, and Daniel Kaufer. (2011), "Description of a basic model of the "UpWind reference jacket" for code comparison in the OC4 project under IEA Wind Annex XXX." *Fraunhofer Institute for Wind Energy and Energy System Technology (IWES)* No. 4 (pp. 1-14).

Wang, D. W., D. A. Mitchell, W. J. Teague, E. Jarosz, and M. S. Hulbert. (2005), "Extreme waves under Hurricane Ivan." *Science*, Vol. 309, No. 5736 (pp. 896).

Wei, Kai, Sanjay R. Arwade, and Andrew T. Myers. (2014), "Incremental wind-wave analysis of the structural capacity of offshore wind turbine support structures under extreme loading." *Engineering Structures*, Vol. 79 (pp. 58-69).

Yura, J. A., L. E. Howell, and K. H. Frank. (1978), Ultimate load tests on tubular connections. In *CESRL Report No. 78-1*: The University of Texas, Austin.

Yura, Joseph A., Nicholas A. Zettlemoyer, and Ian F. Edwards. (1980), "Ultimate Capacity Equations for Tubular Joints." Offshore Technology Conference.

FRACTURE CHARACTERISTIC OF BOLTED CONNECTIONS UNDER BLOCK SHEAR

Hussam N. Mahmoud
Colorado State University, Fort Collins, Colorado 80523, USA
hussam.mahmoud@colostate.edu

Huajie Wen
Colorado State University, Fort Collins, Colorado 80523, USA
huajie.wen@colostate.edu

Abstract: Block shear failure in bolted connections is one of the most complex and least understood failure modes in steel connections. Failure under this mechanism is distinctively characterized by mixture of brittle and ductile fracture, which has been noted recently to be dependent on both stress triaxiality and Lode angle parameter, respectively. In this study, a new analytical fracture model is integrated in numerical finite element simulations to predict fracture in bolted gusset plate and coped beam connections under quasi-static loading. Results from the numerical simulations are compared to their corresponding experimental outcomes in terms of load versus displacement, fracture sequences, and fracture profile. The comparisons show excellent agreement between the simulations and the experimental results. Following the validation step, the numerical results are further employed to propose a new design equation for block shear, which is shown to provide accurate strength predictions based on comparisons with an extensive data set of block shear tests.

INTRODUCTION

Block shear can be considered a special case of ductile fracture in bolted connections. The main failure mechanism in block shear is partial or complete removal of a block of material from the parent component. The failure is typically caused by the presence of varying stress states on distinct tension and shear planes and in some cases with additional inclined failure planes. Undoubtedly, fracturing the connection on a specific failure path will have an impact on the resulting connection response characteristics including strength and ductility. For that reason, the ability to accurately model the failure path can be critical to proper estimation of the true behavior of the connection and the subsequent predictions of a complete structural system response.

Due to its significant importance, the phenomenon of ductile fracture and the associated predictive models continue to be the focus of numerous research studies. Until recently, accurate predictions of this fracture was still a considerably challenging task. This is because historically ductile fracture was thought to be reliant on only the stress triaxiality. However, in the recent decade another stress state parameter, called the Lode angle parameter, was found to have significant influence on predicting ductile fracture, particularly in low and negative triaxiality regimes. Thus, the majority of existing ductile fracture models only considers stress triaxiality. In this study, a newly developed

ductile fracture mode, which was recently developed by Wen and Mahmoud (2015) is introduced where the effect of stress triaxiality and Lode parameter are simultaneously considered. Following the introduction of the model, two examples are provided on numerical simulation of fracture in a gusset plate and a coped beam connection. The simulation results, in terms of failure profile and load versus displacement are compared with their experimental equivalence. Based on various other comparisons between experimental results and numerical finite element simulations (not shown in this paper), a new design equation is proposed for predicting connection strength under block shear. The proposed equation is utilized for predicting strength of 144 connections that have been previously tested. It is shown that the proposed equation results in excellent agreement with the experimental results. A comparison also is performed between the previous tests and existing code equations and it is shown that some codes underestimate the strength while others overestimate it.

DUCTILE FRACTURE MODEL

A three-parameter ductile fracture model was recently proposed by Wen and Mahmoud (2015). Each one of the three parameters are introduced in order to capture unique and independent effects of the stress state parameters, for a wide range of stress states, on predicting the fracture strain. In addition, the inclusion of only three parameters allows for ease of calibration. The proposed ductile fracture model is shown in Equation 1,

$$\bar{\varepsilon}_f(\eta, \bar{\theta}) = c_1 \exp(c_2 \eta) \left[\cos\left(\frac{\pi \bar{\theta}}{6}\right) \right]^{c_3} \quad (1)$$

where c_1 to c_3 are the three parameters requiring calibration, η is the stress triaxiality, and $\bar{\theta}$ is Lode angle parameter. For non-proportional monotonic loading conditions, the two stress state parameters vary with the load path, and the fracture can be obtained using the linear damage evolution rule described in Equation 2, where $\bar{\varepsilon}_p$ is the equivalent plastic strain. The fracture is presumed to occur when the damage D reaches or exceeds a value of 1.

$$D = \int_0^{\bar{\varepsilon}_p} \frac{1}{\bar{\varepsilon}_f(\eta, \bar{\theta})} d\bar{\varepsilon}_p \quad (2)$$

A cut-off region, where fracture will not occur, is assumed to exist. In other words, in the proposed region it is postulated that damage will not accumulate and therefore fracture cannot occur. The cut-off region is defined in Wen and Mahmoud (2015) through Equation 3 and is shown in Figure 1. The relationship between stress triaxiality and Lode angle parameter, for the case of plane stress, has been determined by Wierzbicki and Xue (2005) as shown in Equation 4 and expressed in Figure 1 with a dotted line and labeled "plane stress". Figure 1 also shows the lower and upper bounds of the fracture strain with $\bar{\theta} = 0$ and $\bar{\theta} = \pm 1$, respectively, for various levels of stress triaxiality.

$$\eta + \frac{2}{3} \cos\left(\frac{\pi\bar{\theta} - \pi}{6}\right) \leq 0 \quad (3)$$

$$\cos\left[\frac{\pi}{2}(1-\bar{\theta})\right] = -\frac{27}{2}\eta\left(\eta^2 - \frac{1}{3}\right) \quad (4)$$

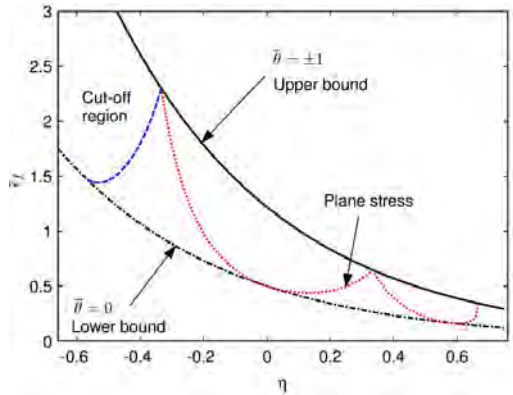


Figure 1: Fracture strain map

NUMERICAL SIMULATIONS

Gusset Plate Connection

Huns et al. (2002) performed laboratory tests on various gusset plate connections; two of which, named T1 and T2, were loaded up to and including failure. The geometrical configuration of the connections and the correspondingly experimental set up of specimen T1, as an example, is shown in Figure 2. The displacement, Δ , shown in the figure represents the monitored displacement during testing. The general purpose finite element program ABAQUS was employed in the numerical simulations. 2-D plane stress elements CPS4R were utilized with a refined mesh size of 1mm×1mm at critical locations. The bolts were modeled using rigid body elements. The bolt/plate interaction was simulated using contact formulation with a friction coefficient of 0.3 (Class C slip factor for untreated hot roll steel, AISC 2010). The computational time was reduced by taking advantage of symmetry where only half geometry models are simulated as highlighted in Figure 2. An example of a numerical model, for specimen T1, is shown in Figure 3. Nonlinear material properties were used with an isotropic hardening rule. In addition, a subroutine, VUMAT, was developed and employed to simulate evolution of damage and the associated fracture. The load in the simulation was applied by imposing displacement boundary conditions on the bolts.

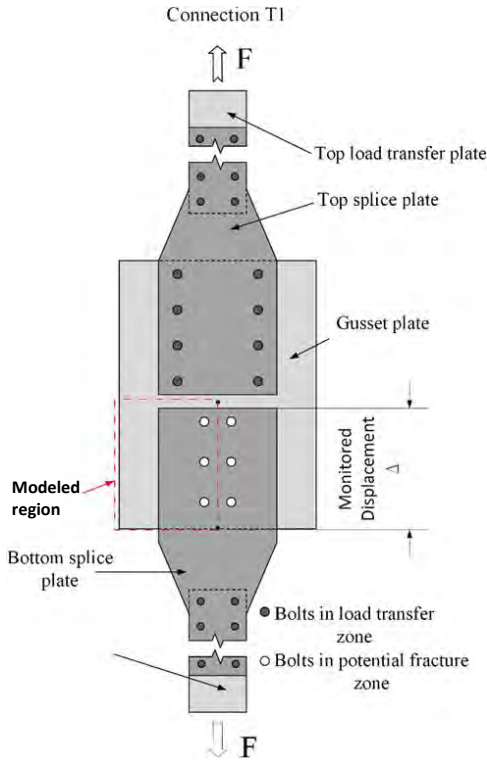


Figure 2. Tests set up for gusset plate connections, after Huns et al., 2002

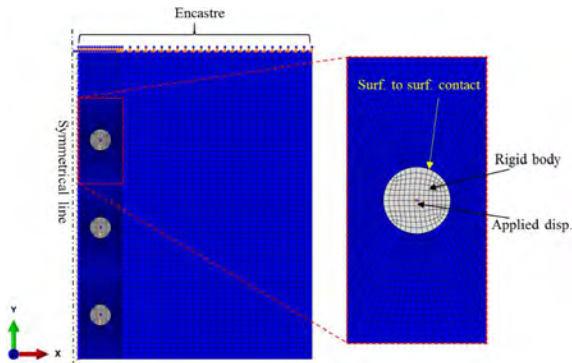


Figure 3. Numerical model for gusset plate connection T1

Parameters of the fracture model are calibrated through trial and error, with initial values from similar steel grades in Wen and Mahmoud (2014). The calibrated damage parameters are shown in Equation 5.

$$\bar{\varepsilon}_f = 0.7506 \exp(-1.9232 \eta) \left[\cos\left(\frac{\pi - \theta}{6}\right) \right]^{-3.3546} \quad (5)$$

A comparison between the simulation results in terms of fracture profile and load versus displacement curve, for specimen T1, is shown in Figure 4 (a) and (b), respectively. As shown in the figure, excellent correlations were achieved. It is worth noting that the peak strength is resulting for connection resistance on the tension and shear planes simultaneously. However, fracture on the tension plane occurs first, which is marked by the sudden drop in load as shown in the load versus displacement curve. In the final fracture propagation stage, the residual strength in the connection is therefore due to resistance from the shear plane.

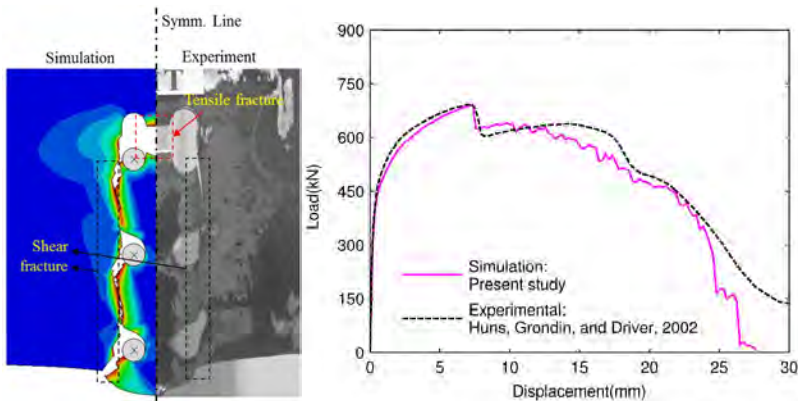


Figure 4. Numerical and experimental comparisons for connection T1 (a) fracture profile and (b) load versus displacement curves (experimental photo from Huns et al. 2002)

Coped Beam Connection

Franchuk et al. (2002) conducted various laboratory tests on coped beam connections with fifteen different cases for connection loaded up to and including failure. A representative sketch of the experimental beam-column connection is shown in Figure 5. The displacement, Δ , which is equal to $\Delta_1 - \Delta_2$, was monitored displacement during the tests. The test setup also included various load cells, as shown schematically in Figure 5, that allowed for calculation of the reaction force so that load versus displacement curves can be plotted.

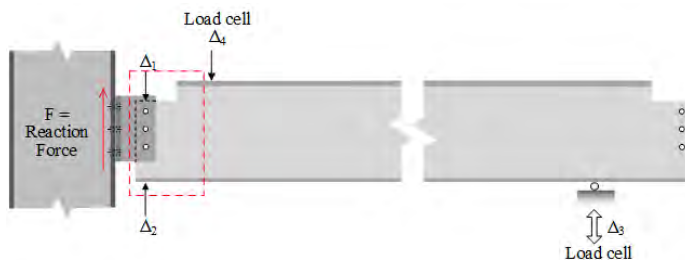


Figure 5: Representative experimental set-up of simulated coped beam connections, after Franchuk et al., 2002

The general numerical modeling approach for the coped beam models is similar to that of the gusset plate described previously. To simulate the connection between the double angles and connected columns, a series of spring systems are used with proper stiffness values representing resistances from various elements as per Rex and Easterling (2003). The representative model with the substituted spring systems is shown in Figure 6.

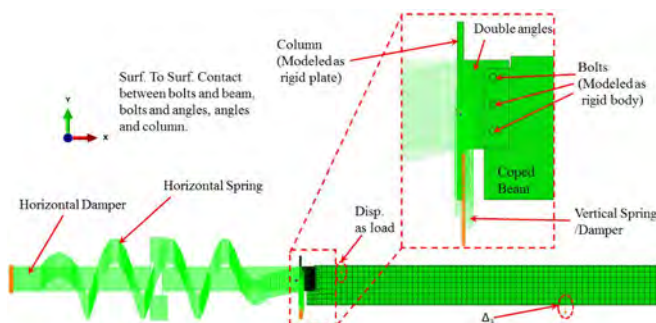


Figure 6: Representative numerical model.

A trial and error process is once again utilized to calibrate the fracture parameters, with values corresponding to similar steel types, calibrated in Wen and Mahmoud (2015), used as initial values. The calibrated damage model can be expressed in Equation 7.

$$\bar{\epsilon}_f = 0.5 \exp(-1.9\eta) \left[\cos\left(\frac{\pi - \theta}{6}\right) \right]^{-6.2} \quad (7)$$

The calibration and simulation protocol are similar to that of the gusset plate connections. A typical example of simulation results, for Specimen F1, was compared to the experimental results for the final fracture profile and load versus displacement curves as shown in Figure 7. Excellent correlations were achieved, not only in the pre-fracture stage, but also in the stage after fracture initiation and until complete failure.

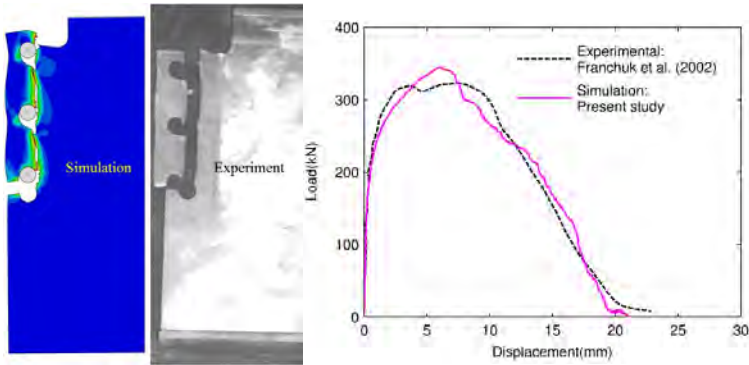


Figure 7. Numerical and experimental comparisons for connection F1 (a) fracture profile and (b) load versus displacement curves (experimental photo from Franchuk et al. 2002)

New Proposed Design Equation

A significant number of simulations were conducted to ensure that the modeling approach is capable of capturing the failure for other connection configurations. The observations from all the simulations were made and used to propose a new design formation for predicting block shear strength. The design equation for block shear failure typically assumes that the tensile and shear plane resist the loading independently, and therefore the strength provided by each plane shall also be determined independently. The 2010 *AISC Specification* (AISC 360-10) includes equations to calculate the strength of elements in tension and shear, expressed respectively in Equation 8 and 9. This is consistent with the block shear strength design equation, except block shear yielding on the gross tension plane is omitted. For the strength on the shear plane, both the yielding and fracturing are considered. The yielding is incorporated with the use of τ_y as $0.6F_y$, which is indicative of the von Mises yield criterion. The ultimate shear strength, defined as $0.6F_u$, appears to be arbitrary. Based on the analysis results, for the steel grades used in the simulations, it is suggested that a value of $0.75 F_u$ be used instead.

$$R_{nt} = \min \left\{ \begin{array}{l} F_y A_{gt} \\ F_u A_{nt} \end{array} \right\} \quad (8)$$

$$R_{nv} = \min \left\{ \begin{array}{l} 0.6F_y A_{gv} \\ 0.6F_u A_{nv} \end{array} \right\} \quad (9)$$

In this present study, two equations are proposed to describe the shear strength under block shear as shown in Equation 10 and 11. The first equation utilizes $0.75F_u$ as the shear strength on the net section where the net section is considered as a shear

fracture plane. In the second equation, $0.6F_u$ is defined to represent a combination of shear yielding and fracture strength with a corresponding shear area taken as $(A_{nv} + A_{gv})/2$. In the design formulation, the smaller value from both terms controls. The full design equation for block shear failure is described in Equation 12. The terms, U_{flv} and U_{ftt} , in Equation 12 are reduction factors for shear and tensile fracture lag respectively, and are less than 1. These terms can be taken as 1 for connections with typical geometry.

$$R_{nv} = 0.75F_u A_{nv} \tag{10}$$

$$R_{nv} = 0.6F_u (A_{nv} + A_{gv})/2 \tag{11}$$

$$R_n = U_{bs} F_u A_{nt} + \min \left\{ \begin{array}{l} 0.75F_u A_{nv} \\ 0.6F_u (A_{nv} + A_{gv})/2 \end{array} \right\} \leq U_{bs} F_u A_{nt} + 0.6A_{gv} (F_u + F_y)/2 \tag{12}$$

A comparison between the predicted strength obtained by the proposed equation and those tested experimentally is shown in Figure 14. The experimental tests (total of 144) included 28 cases from Hardash and Bjorhovde (1984), 73 cases from Udagawa and Yamada (1998), 5 cases from Mullin (2005), 8 cases from Aalberg and Larsen (1999), 5 cases from Rabinovitch and Cheng (1993), and several cases from Swanson and Leon (2000) and Nast et al. (1999). As shown in the Figure 8, the proposed design equation (Equation 12), with all the reduction factors equal to 1, predicts connection strength within about 5% for most of the cases, which could be considered very accurate. Figure 8 also shows the proposed equation to provide better results than the conservative 2010 AISC equation and the non-conservative Canadian code equation.

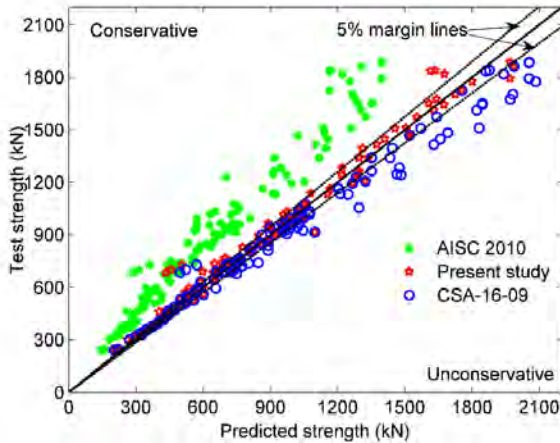


Figure 8. A comparison of the predictions of the proposed design equation and representative current design equations with the numerical and experimental results

Conclusions

In this paper, through the application of a newly developed ductile fracture criterion, numerical simulations are conducted to evaluate the full failure process of a gusset plate and coped beam connection under block shear. The current major code equations for calculating block shear strength are evaluated and analyzed to assess their range of valid estimation with the corresponding failure mechanism. Utilizing the simulation results, new design equations for block shear strength are proposed, and further validated through an extensive comparison against extensive experimental data set.

Based on the simulations and analysis, the following conclusions can be drawn:

1. Excellent agreement is observed between the simulations and experimental results.
2. The current design equations in major codes provide inconsistent predictions of the strength of structural details with the potential for block shear failure.
3. The strength predictions, utilizing the 2010 AISC, seems to be conservative. However, the Canadian code in some cases provides non-conservative predictions.
4. The proposed design equation for the block shear failure correlates exceptionally well with the numerical simulation and experimental results.

References:

- Aalberg, A. and Larsen, P. K. (1999), "Strength and Ductility of Bolted Connections in Normal and High Strength Steels", Department of Structural Engineering, Norwegian University of Science and Technology, N-7034, Trondheim, Norway.
- American Institute of Steel Construction (AISC) (1999), "Load and Resistance Factor Design Specification", Chicago, Illinois.
- American Institute of Steel Construction (2005). "Steel Construction Manual", AISC Inc., Chicago, IL.
- American Institute of Steel Construction (2010). "Steel Construction Manual", AISC Inc., Chicago, IL.
- Canadian Standards Association (CSA) (2009). "CAN/CSA-S16-09 Limit States Design of Steel Structures", Toronto (ON, Canada).
- Franchuk, C. R., Driver, R. G., and Grondin, G. Y. (2002), "Block Shear Behavior of Coped Steel Beams", Structural Engineering Report 248, Department of Civil and Environmental Engineering, University of Alberta.
- Hardash, S. G. (1984), "Gusset Plate Design utilizing Block Shear Concepts", The Department of Civil Engineering and Engineering Mechanics, University of Arizona, Tucson, Arizona.
- Huns, B.B.S., Grondin, G.Y., and Driver, R.G. (2002), "Block Shear Behavior of Bolted Gusset Plates", Structural Engineering Report No. 248, Department of Civil Engineering, University of Alberta, Edmonton, Alta.
- Mullin, D. (2005), "Gusset Plates as Energy Dissipaters in Seismically Loaded Structures", PhD dissertation, Department of Civil and Environmental Engineering, University of Alberta, Edmonton, Alberta.

- Nast, T. E., Grondin, G. Y. and Cheng, J. J. R. (1999) "Cyclic Behavior of Stiffened Gusset Plate-Brace Member Assemblies", Structural Engineering Report 229, Department of Civil and Environmental Engineering, University of Alberta, Edmonton, Alberta.
- Rabinovitch, J. S. and Cheng J. J. R. (1993), "Cyclic Behavior of Steel Gusset Plate Connections", Structural Engineering Report 191, Department of Civil Engineering, University of Alberta, Edmonton, Alberta.
- Rex, C. O., and Easterling, W. S. (2003), "Behavior and Modeling of a Bolt Bearing on a Single Plate", *Journal of Structural Engineering*, 129(6), (pp. 792-800).
- Swanson, J. A. and Leon, R.T. (2000) "Bolted Steel Connections: Tests on T-Stub Components", *Journal of Structural Engineering*, ASCE, Vol. 126, No. 1 (pp. 50-56).
- Udagawa, K. and Yamada, T. (1998) "Failure Modes and Ultimate Tensile Strength of Steel Plates Jointed with High-Strength Bolts", *Journal of Structural and Construction Engineering*, Architectural Institute of Japan, No. 505 (pp. 115-122).
- Wen, H., and Mahmoud, H. (2015), "New Model for Ductile Fracture of Metal Alloys. I: Monotonic Loading", *Journal of Engineering Mechanics* ASCE, Vol. 142, No. 2, 04015088.

Load-bearing Capacity of H-shaped Beam to RHS Column Connections Using Blind Bolts

Guo-Qiang LI

College of Civil Engineering, Tongji University, Shanghai, China
College of Civil Engineering, Shandong Jianzhu University, Jinan, China
gqli@tongji.edu.cn

Lian DUAN

College of Civil Engineering, Tongji University, Shanghai, China
duanlian1215@163.com

Jiehua ZHANG

College of Civil Engineering, Tongji University, Shanghai, China
344808774@qq.com

Jian JIANG

College of Civil Engineering, Tongji University, Shanghai, China
jiangjian_0131@163.com

ABSTRACT

The connection of H-shaped beam to rectangular hollow section (RHS) column using blind bolts is proposed in this paper. The beam is connected to the column by extended endplates. Monotonous static tests are carried out to study the effect of the endplate thickness, bolt strength and column wall thickness on the failure modes and moment-rotation relationships of the proposed connections. The force distribution pattern in bolts is proposed based on the test results. The flexural strength of connections governed by the endplate strength is obtained using the equivalent T-stubs method from EN1993-1-8. A yield line model based on the virtual work principle is proposed for predicting the flexural strength of connections governed by the column wall strength. It shows that the failure mechanism of connections depends on the relative strength between bolts, endplates and column walls, of which the minimum strength can be used to estimate the load-bearing capacity of connections. The principles for the design of H-shaped beam to RHS column connections are finally proposed.

1. INTRODUCTION

Beam-to-column connections play an important role in transforming bending moments, shear forces and axial forces between beams and columns in steel-framed structures. Its performance thus directly affects the strength, stiffness and stability of the whole structure [1].

Rectangular hollow section (RHS) columns and H-shaped beams are commonly used structural components for multi-story steel frame buildings. RHS columns show a better performance than H-shaped columns, by taking the advantages of no weak axis for load-bearing capacity and section moment of inertia, higher torsional resistance and aesthetic appearance.

Previous investigations have focused on fully welded connections of H-shaped beam to RHS column, representing rigid connections. Fig. 1 shows three typical connections: the interior diaphragm, through diaphragm, and external diaphragm connections. However, a number of fracture failures were observed in the welded beam-to-column connections in the 1994 Northridge earthquake and the 1995 Kobe earthquake [2-3], as shown in Fig. 2.

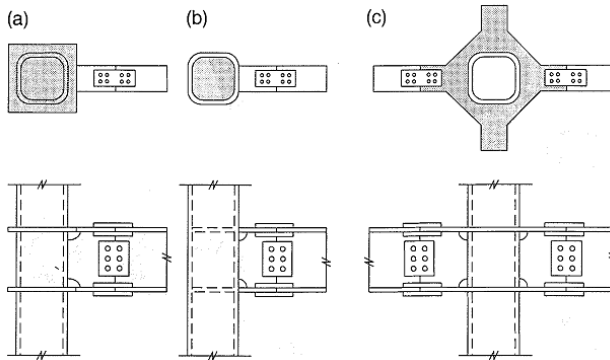


Fig. 1 Typical HSS columns in moment resisting frames: (a) through-diaphragm; (b) interior diaphragm; (c) exterior diaphragm.



Fig. 2 Failure of the beam-to-column welded connections: (a) Northridge earthquake; (b) Kobe earthquake

To avoid the potential fracture failure occurring in the welded beam-to-column connections, bolted semi-rigid connections are applied because of their better

performance than welded connections [4-6]. A large amount of researches have been conducted on connections of H-shaped beam to H-shaped column using conventional bolts. In contrast, the research on connections of H-shaped beam to RHS column is lacking due to the disadvantages and limitations imposed by welding. As an alternative, blind bolts are used to solve these problems. The blind bolts are installed from only one side of structural members, thus making bolted connections available for hollow sections.

Nowadays, the commercial blind bolts are produced by thermal drilling techniques such as flowdrill process, as shown in Fig. 3. The special blind bolts with sleeves such as Holo-Bolt and BoxBolt shown in Fig.4 are designed to expand inside the clearance. Some others with folded gaskets are to unfold inside the tubular column (Fig. 4). Xu et al. [7] improved the sleeved blind bolts by modifying the material properties of the sleeve and configuration of the bolt, as shown in Fig. 6.

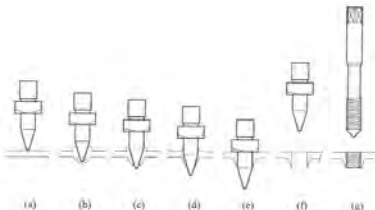
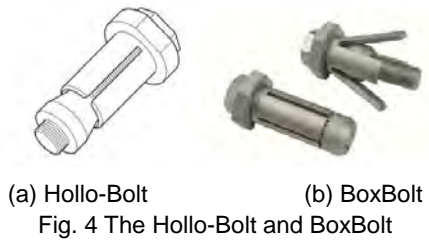


Fig. 3 Sequence of flowdrill process



(a) Holo-Bolt (b) BoxBolt
Fig. 4 The Holo-Bolt and BoxBolt

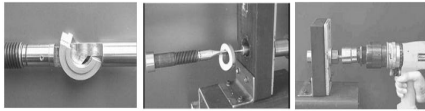


Fig. 5 The installation steps of ONESIDE Fastener



Fig. 6 Chinese STUCK-BOM blind bolt

Recently, there have been several attempts to investigate the performance of connections to tubular columns using blind bolts. Wang et al. [8] studied the static and seismic behavior of flush-end-plate joints to circular or square CFST (i.e. Concrete-filled steel tubular) columns using Holo-bolts. The connections showed good rotation capacity. Liu et al. [9] reported the behavior of open beam-to-tubular column bolted connections with angles subjected to tension and compression. The results showed that the angle thickness and column thickness had significant effects on the initial stiffness and tensile resistance of the connection. France et al. [10-12] conducted a series of monotonic loading tests on end-plate connections for square SHS or CFST columns using flowdrilled bolts. It was proved that the connections had high flexural strength and rotational stiffness. BCSA [13] proposed recommendations for the design of connections of H-shaped beams to RHS columns using Holo-Bolts. The inner end-plated hinge connections and semi-rigid connections were studied. Previous experimental studies have proved the performance of connections of H-shaped beam to RHS column using blind bolts. There is a need for theoretical studies to provide a

solid base for the practical application and design of connections, as shown in Fig. 7. In this paper, experiments are carried out on six connections of H-shaped beam to RHS column using blind bolts subjected to monotonic loading. Theoretical calculation methods of the flexural strength of the connection are proposed.

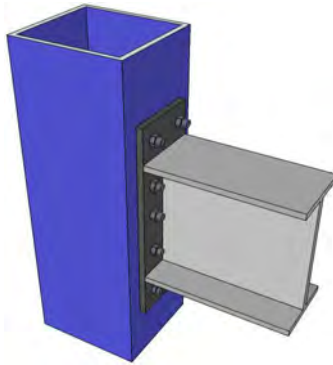


Fig. 7 Connection of H-shaped beam to RHS column using end-plate blind bolts

2. TEST SETUP

2.1 Design of specimens

Table 1 lists a summary of the tested specimens. The three types of connections BR1, BR2 and BR3 were designed for three failure locations at the bolt, endplates and column wall, respectively. Two specimens were prepared for each type of connections. The STUCK-BOM blind bolts in Grade 8.8 M16 were used for the connections of the H-shaped beam to the RHS column. Fig. 8 shows the layout of the tested beam-to-column connection. Fig. 9 shows the installation of the blind bolts.

Table 1 Details of specimens

Specimen	Beam section	Column section	Endplate thickness /mm	Expected failure location
BR1-1 (BR1-2)	HN300×150×6.5×9	□200×12	14	Bolts
BR2-1 (BR2-2)	HN300×150×6.5×9	□200×12	10	Endplate
BR3-1 (BR3-2)	HN300×150×6.5×9	□200×8	14	Column wall

2.2 Material properties

Table 2 lists the measured properties of the steel beams, endplates and columns. The tensile strengths of the blind bolts are shown in Table 3.

2.3 Test process

The test setup was shown in Fig. 10. The RHS column was placed horizontally with two ends fixed. The beam was connected to the column with the other end free. The load was applied by a servo actuator to the flange of the free end of the H-shaped beam. The other end of the actuator was connected to a reaction frame.

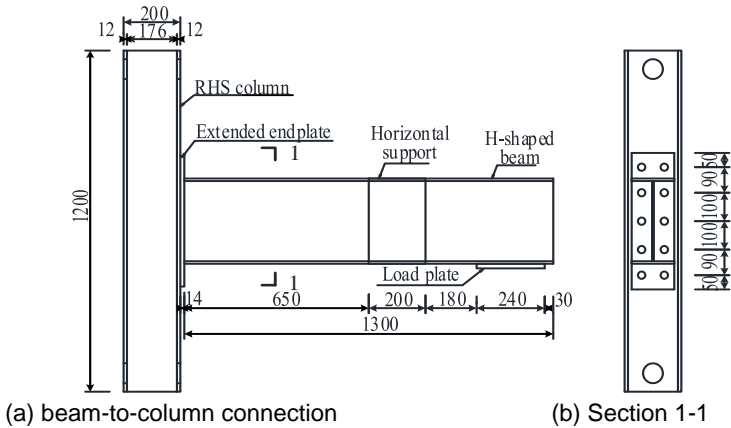


Fig. 8 Layout of specimens



(a) Outside of RHS column

(b) Inside of RHS column

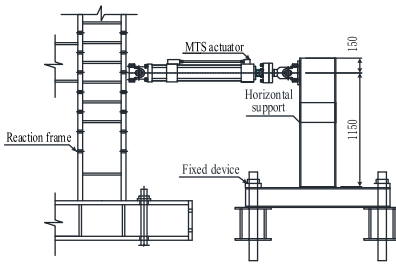
Fig. 9 Connections after installation

Table 2 Material properties of the tested specimens

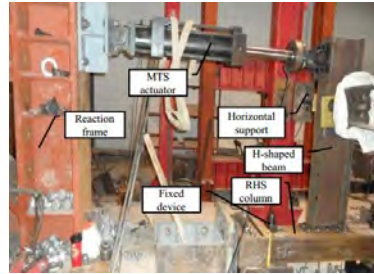
Steel wall thickness t /mm	Steel coupon	Yield stress f_y /MPa	Ultimate stress f_u /MPa	Young's modulus E_s /GPa
9	Steel beam flange	346	480	204
6.5	Steel beam web	338	472	211
10	Endplate	367	529	206
14	Endplate	365	533	202
8	RHS column	341	498	200
12	RHS column	383	534	204

Table 3 Tensile strength of blind bolts

Connection plate thickness t /mm	Yield force $F_{y,b}$ /kN	Ultimate force $F_{u,b}$ /kN
22~26	108	134



(a) Loading device figure



(b) Experimental setup photograph

Fig. 10 Test setup

2.4 Loading system

In order to investigate the behavior of the blind bolted connections under monotonic loading, the test procedure was divided into two phases: preloading and the formal loading. In the preloading phase, all the measurement channels were opened to record the initial readings before the loading. The actuator was then applied in an increment of 3mm displacement and reduced to zero. This process was repeated twice. In the formal loading phase, the actuator was operated by the force control method in a loading speed of 5kN/min before the yielding of connections. The yielding displacement Δ_y was taken as the loading step length after the yielding of connections. The load was applied in the displacement control mode by $0.2\Delta_y/\text{min}$.

During the test, the connection was assumed to fail when one of the following occurs: 1) broken of the bolt; 2) fracture of the end plate or the column wall; 3) fracture of welding.

2.5 Measurement

The deformations of the column and end plate were measured in this test. Displacement gauges were placed on the column wall connected to the end plate, through the holes in the opposite column wall, as shown in Fig. 11.

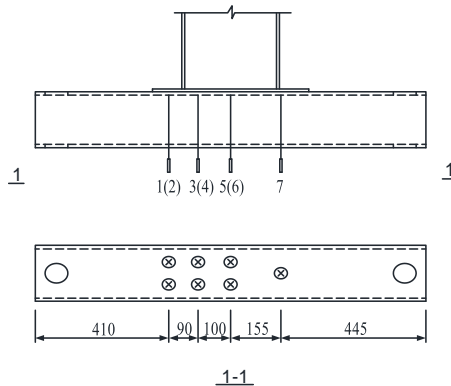


Fig. 11 Arrangement of displacement gauges

3. EXPERIMENTAL RESULTS

3.1 Failure modes

As demonstrated in Figs. 12a and 12b, the Specimens BR1-1 and BR1-2 lost their load-bearing capacities due to the separation between the column wall and flaring sleeves of bolts located outside the tension flange. Figs. 12c and 12d depict the failure of Specimens BR2-1 and BR2-2, respectively. Both the specimens fail due to the fracture of the endplate. Figs. 12e and 12f show the failure modes of Specimens BR3-1 and BR3-2. They failed because of the yielding of the column wall.



(a) Specimen BR1-1



(b) Specimen BR1-2



(c) Specimen BR2-1



(d) Specimen BR2-2



(e) Specimen BR3-1

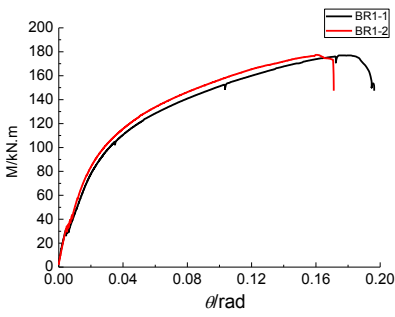


(f) Specimen BR3-2

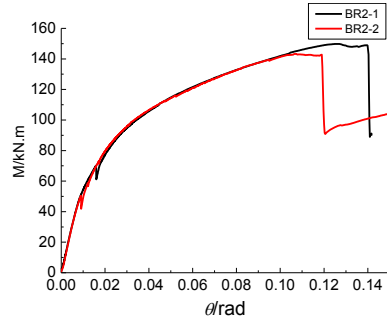
Fig. 12 Failure modes of tested connections

3.2 Moment–rotation relationship

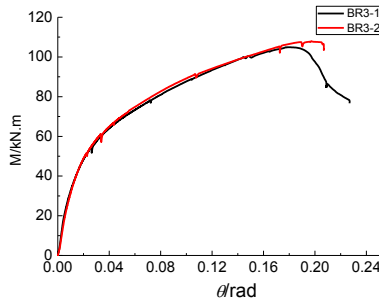
The behavior of beam-to-column connections is characterized by its moment–rotation, $M-\theta$, relationship. The moment (M) is equal to the product of the beam end load (P) and the distance (L_0) from the loading point to the column wall, namely $M = P \times L_0$. Fig. 13 shows the moment–rotation curves of all the connection specimens.



(a) Specimen BR1-1 and BR1-2



(b) Specimen BR2-1 and BR2-2



(c) Specimen BR3-1 and BR3-2

Fig. 13 Moment-rotation curves of tested specimens

4. THEORETICAL STUDY

4.1 Connection strength governed by bolt strength

It is recognized that the force distribution in bolt rows is essential to the moment capacity of connections governed by the bolt strength. Based on the test results, a modified T-shaped bolt-row forces distribution was proposed where the compression is concentrated at the center of the flange, as shown in Fig. 14.

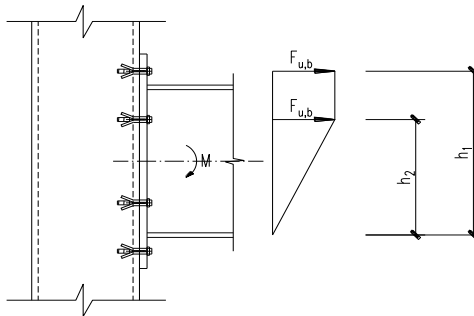


Fig. 14 Modified T-shaped force distribution

The moment capacity of the connection can be calculated by Eq. (1). The comparison between the predicted and measured moment capacities of connections governed by the bolt strength is shown in Table 4. The theoretical predictions agree well with the test results with the error less than 5%. This indicates that the distribution of the forces in bolts is reasonable.

$$M_{bt} = mF_{u,b}(h_1 + h_2) \quad (1)$$

where M_{bt} is the moment capacity of the connection governed by bolt strength; m is the number of bolts; $F_{u,b}$ is the ultimate tensile force in blind bolts; h_1 and h_2 are the distances of the bolt-row above and below the tension flange from the center of the compression flange, respectively.

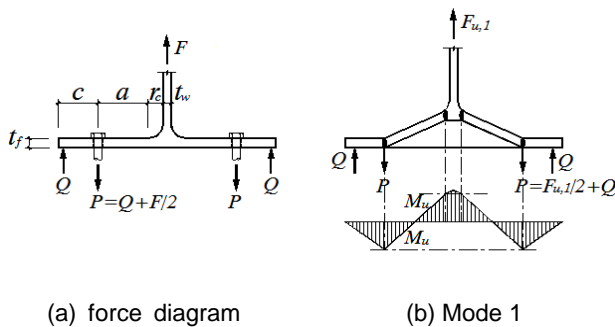
Table 4 Comparisons of capacity governed by bolt strength between predictions and measurements

Specimens	Test data M_t /kN.m	Theoretical calculation M_c /kN.m	M_c / M_t
BR1-1	176.9	171.1	0.967
BR1-2	177.4	171.1	0.964

4.2 Connection strength governed by endplate strength

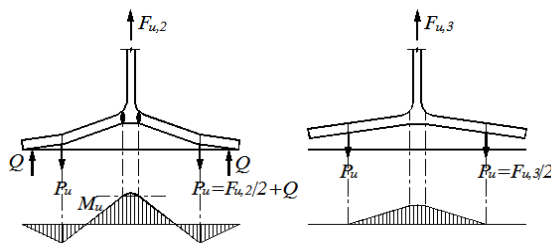
It was observed in experiments that the deformation of endplates above and below the tension flange of beams was larger and yielded earlier than other locations. This is because the load in the tension zone was carried mainly by the bolt-rows above and below the flange. It is reasonable, therefore, to consider the influence of endplate on both sides of the tension flange merely when calculating the moment capacity of connections governed by the endplate strength.

The Eurocode EN 1993-1-8 simplifies the endplate as T-stubs for analyzing the internal forces of connections. It has shown that the relative strength between the bolts, endplates and column walls affects the three possible failure modes of connections illustrated in Fig. 15, i.e. complete yielding of the flange (Mode 1), failure of bolts and yielding of the flange (Mode 2), failure of bolts (Mode 3), respectively.



(a) force diagram

(b) Mode 1



(c) Mode 2 (d) Mode 3

Fig. 15 Failure modes of T-stub model

The stiffness of the endplate is relatively weaker than that of the column wall and blind bolts in H-shaped beam to RHS column connections governed by the endplate strength. This results in a large deformation in the flange of the T-stub, leading to prying forces along its edge after simplifying the single bolt-row into T-stub. It was noted that the endplate had plastic deformation at the root of the flange and around the bolt hole. In addition, the bolts in tension failed by the fracture of shank or pulling out due to its higher load-bearing capacity than that of the endplate. Therefore, the failure mode of the T-stub was similar to Mode 1. Based on mechanical analyses, the tensile strength of T-stub is determined as:

$$(0.5F_{u,1} + Q)a - Q(c + a) = M_{u,1} \quad (2)$$

$$Qc = M_{u,1} \quad (3)$$

$$F_{u,1} = \frac{4M_{u,1}}{a} \quad (4)$$

$$M_{u,1} = 0.25I_{\text{eff},1}t_f^2f_y \quad (5)$$

where Q is the prying force; $M_{u,1}$ is the plastic moment of the T-stub flange for mode 1; $I_{\text{eff},1}$ is the effective length of equivalent T-stub flange in bending for mode 1, determined from Table 5 [14], based on the provision in EN 1993-1-8; t_f is the endplate thickness; f_y is the yield stress of T-stub flange; a and c are measured as specified in Fig.16 and $c \leq 1.25a$ should be satisfied.

Table 5 Effective lengths for equivalent T-stubs

bolt-rows location	Bolt-row considered individually $I_{\text{eff},1}$ /mm	
	Circular pattern	Non-circular pattern
Bolt-row outside tension flange of beam	Smallest of: $2\pi a_x$ $\pi a_x + w$ $\pi a_x + 2c$	Smallest of: $4a_x + 1.25c_x$ $e + 2a_x + 0.625c_x$ $0.5b_p$ $0.5w + 2a_x + 0.625c_x$
First bolt-row below tension flange of beam	$2\pi a$	αa

Note: for the endplate extension, a_x and c_x were used instead of a and c when determining the resistance of the equivalent T-stub flange. The values of w and b_p in Table 5 should be obtained from Fig.16.

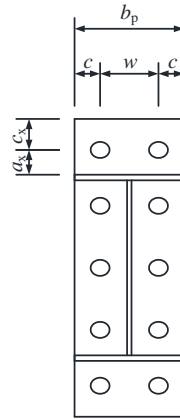
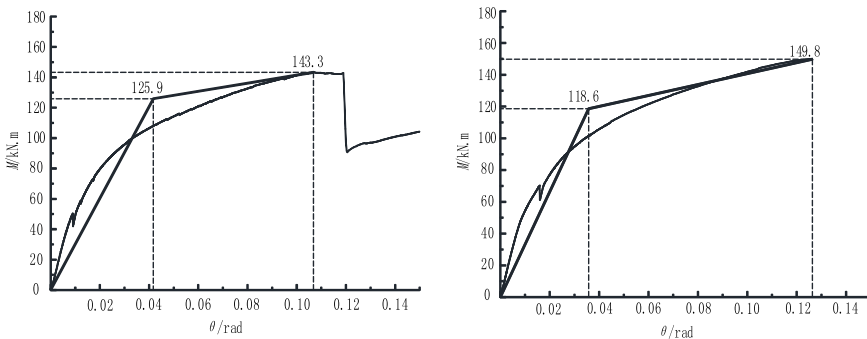


Fig. 16 Dimension of extended endplate

The tensile strength of T-stubs on both sides of the flange are evaluated from Eqs. (4) and (5) in accordance with values given in EN 1993-1-8. The moment capacity of connections governed by the endplate strength is obtained as:

$$M_{ap} = F_{u,1}H \quad (6)$$

The nominal yield point is obtained by the double-line method [15] since there are no obvious yield points in moment-rotation curves, as depicted in Fig.17. The comparison of moment capacities between theoretical predictions and test measurements is illustrated in Table 6. The theoretical predictions of moment capacity governed by endplate strength using equivalent T-stub method are conservative compared to the experimental results, with an error within 10%.



(a) Specimen SB2-1

(b) Specimen SB2-2

Fig. 17 Moment-rotation curves from tests and double line methods

Table 6 Comparisons of capacity governed by endplate strength between prediction and measurement

Specimen	Test results M_{yt} /kN.m	Theoretical calculation M_{yc} /kN.m	M_{yc} / M_{yt}
BR2-1	125.9	118.2	0.939
BR2-2	118.6	118.2	0.997

4.3 Connection strength governed by column wall strength

The yield line theory [16] was adopted to obtain the moment capacity of connections governed by the strength of column walls. Outward deformation of the column wall was observed under four tensile bolt forces around the flange of the beam as the external load increased. Meanwhile the bottom part of column wall around the flange was pushed in. It is reasonable to consider the endplate between the top and bottom flanges as rigid plate regardless of any bending deformation due to the constraints from the flanges and web of beam, as shown in Figs. 12e and 12f. Accordingly, the yield line pattern, shown in Fig. 19, was proposed.

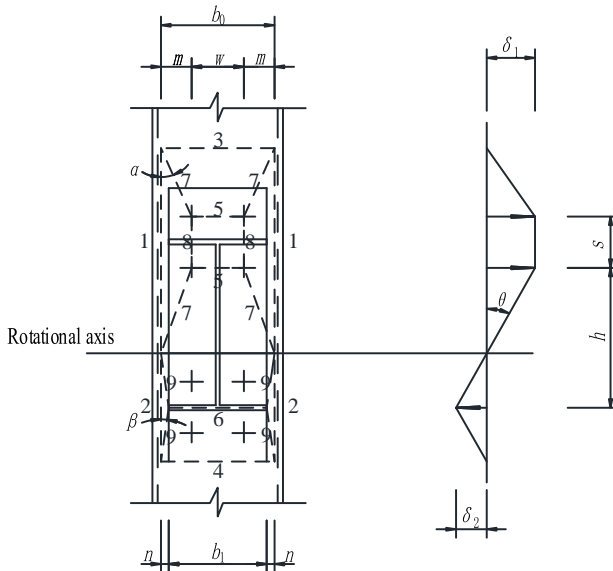


Fig. 19 Yield line model

The work theory was adopted to determine the moment capacity of connections, i.e. the work done from the rotation of yield lines equals to the work done from external loads:

$$M\theta = \sum l_i \varphi_i U_L \quad (7)$$

where M is the external moment; θ is the rotation angle; l_i is the length of yield line; φ_i is the rotation of the region about its axis; U_L is the energy of yield line per unit length, defined as $U_L = \frac{1}{4} t^2 f_y$; t and f_y are the thickness and yield stress of

column wall, respectively.

Defining the parameters illustrated in Fig.19 based on the proposed pattern, and the energy dissipated by yield lines 1 to 9 are deduced as follows:

$$\text{Yield line 1:} \quad U_1 = 2(2 \times m \cot \alpha + s) \frac{\delta_1}{m} U_L \quad (8)$$

$$\text{Yield line 2:} \quad U_2 = 2(2 \times n \cot \beta) \frac{\delta_2}{n} U_L \quad (9)$$

$$\text{Yield line 3:} \quad U_3 = b_0 \times \frac{\delta_1}{m \cot \alpha} \times U_L \quad (10)$$

$$\text{Yield line 4:} \quad U_4 = b_0 \times \frac{\delta_2}{n \cot \beta} \times U_L \quad (11)$$

$$\text{Yield line 5:} \quad U_5 = 2(w \times \frac{\delta_1}{m \cot \alpha}) \times U_L \quad (12)$$

$$\text{Yield line 6:} \quad U_6 = b_L \times \frac{2\delta_2}{n \cot \beta} \times U_L \quad (13)$$

$$\text{Yield line 7:} \quad U_7 = 4(m \times \frac{\delta_1}{m \cot \alpha} + m \cot \theta \times \frac{\delta_1}{m}) \times U_L \quad (14)$$

$$\text{Yield line 8:} \quad U_8 = 2(s \times \frac{\delta_1}{m}) \times U_L \quad (15)$$

$$\text{Yield line 9:} \quad U_9 = 4(n \times \frac{\delta_2}{n \cot \beta} + n \cot \beta \times \frac{\delta_2}{n}) \times U_L \quad (16)$$

Thus, the total energy dissipated by the yield lines is determined as:

$$U = \sum_{i=1}^9 U_i = \left[(8 \cot \alpha + \frac{3b_0}{m} \tan \alpha + \frac{4s}{m}) \delta_1 + (8 \cot \beta + \frac{3b_0}{n} \tan \beta) \delta_2 \right] U_L \quad (17)$$

According to the least work method [10], yielding:

$$\frac{\partial U}{\partial \alpha} = 0 \Rightarrow \tan^2 \alpha = \frac{8m}{3b_0} \Rightarrow \alpha_0 = \arctan \left(\sqrt{\frac{8m}{3b_0}} \right) \quad (18)$$

$$\frac{\partial U}{\partial \beta} = 0 \Rightarrow \tan^2 \beta = \frac{8n}{3b_0} \Rightarrow \beta_0 = \arctan \left(\sqrt{\frac{8n}{3b_0}} \right) \quad (19)$$

In addition, the continuity conditions were supplemented since considering the endplate between top and bottom flanges as rigid plate, represented by:

$$\tan \theta = \frac{\delta_1}{m \cot \alpha} = \frac{\delta_2}{n \cot \beta} \quad (20)$$

Substituting Eq. (7) and Eq. (19) to Eq. (16) and Eq. (6), respectively, yielding:

$$M = \frac{8m \cot^2 \alpha_0 + 8n \cot^2 \beta_0 + 4s \cot \alpha_0 + 6b_0}{m \cot \alpha_0 + n \cot \beta_0} \times H \times U_L \quad (21)$$

where α_0 and β_0 are the included angle between the corner line of column and yield lines 7 and 9, respectively, given by Eq. (18) and Eq. (19). The parameters m , n , s and b_0 are determined as plotted in Fig.19.

The moment capacity of connections governed by column wall strength can be determined by substituting of parameters based on test data into Eq. (21). In conjunction with RHS column connections, which are generally very flexible, an ultimate deformation limit for column wall of 3% of the column width ($0.03b_0$) was

proposed [17]. The comparison of moment capacity between theoretical calculations and test results are illustrated in Table 7. It is distinct that the moment capacity determined by the yield line method is conservative based on the comparison in Table 7.

Table 7 Comparisons of capacity governed by column wall strength between prediction and measurement

Specimen	$0.03 b_0$ /mm	Test results M_{yt} /kN.m	Theoretical calculations M'_{yc} /kN.m	M'_{yc} / M_{yt}
BR3-1	6	55.1	47.8	0.867
BR3-2	6	54.7	47.8	0.874

5. CONCLUSIONS

This paper presents the experimental and theoretical studies on the connections of H-shaped beam to RHS column. The conclusions can be drawn as follows:

(1) A modified T-shaped bolt-row forces distribution was proposed. It is used in the theoretical calculation of moment capacity of connections governed by bolt strengths and its accuracy is validated against experimental results.

(2) The test results show that connections may fail due to the complete yielding of flange when the endplate stiffness is weaker than those of blind bolts and column wall. A generally good agreement is achieved between the test and theoretical results using equivalent T-stub method according to EN 1993-1-8 specification.

(3) A reasonable yield line pattern is applied to extended end-plated connections with blind bolts. The work method is applied to deduce the moment capacity of connections governed by column wall strengths. The predicted capacities are slightly lower than the test results.

(4) The failure mode in terms of endplate bending is adopted in the design of connections rather than those from the fracture of bolts or yielding of column wall. Therefore, it is suggested to make sure that the load-bearing capacity of connections governed by the endplate strength is larger than those of connections governed by bolt and column wall strength.

REFERENCES

- [1] Li, G.Q., Shi, W.L. and Wang, J.F. (2009). Design of Steel Frames with Semi-Rigid Connections. China Building Industry Press, Beijing.
- [2] Miller, D.K. (1998). Lessons learned from the Northridge earthquake. Engineering Structures, 20(4), 249-260.
- [3] Tremblay, R., Filiatrault, A., Bruneau, M., Nakashima, M., Prion, H. G. and DeVall, R. (1996). Seismic design of steel buildings: lessons from the 1995 Hyogo-ken Nanbu earthquake. Canadian Journal of Civil Engineering, 23(3), 727-756.
- [4] Elnashai, A.S., Elghazouli, A.Y. and Denesh-Ashtiani, F.A. (1998). Response of semirigid steel frames to cyclic and earthquake loads. Journal of structural Engineering, 124(8), 857-867.
- [5] Leon, R.T., Hoffman, J.J. and Staeger, T. (1996). Partially restrained composite

connections: a design guide. American Institute of Steel Construction.

- [6] Elghazouli, A.Y. (1996). Ductility of frames with semi-rigid connections. In 11th World Conference on Earthquake Engineering, Acapulco, Mexico, paper (No. 1126).
- [7] Xu Y.B., Li G.Q., Zhang L. (2012). One-way Fastening Bolt: 201210435247.7. China.
- [8] Wang, J.F., Han, L.H. and Uy, B. (2009). Hysteretic behaviour of flush end plate joints to concrete-filled steel tubular columns. *Journal of Constructional Steel Research*, 65(8), 1644-1663.
- [9] Liu, Y., Málaga-Chuquitaype, C. and Elghazouli, A.Y. (2012). Response and component characterisation of semi-rigid connections to tubular columns under axial loads. *Engineering Structures*, 41, 510-532.
- [10] France, J.E., Davison, J.B. and Kirby, P.A. (1999). Strength and rotational response of moment connections to tubular columns using flowdrill connectors. *Journal of Constructional Steel Research*, 50(1), 1-14.
- [11] France, J.E., Davison, J.B. and Kirby, P.A. (1999). Strength and rotational stiffness of simple connections to tubular columns using flowdrill connectors. *Journal of Constructional Steel Research*, 50(1), 15-34.
- [12] France, J.E., Davison, J.B. and Kirby, P.A. (1999). Moment-capacity and rotational stiffness of endplate connections to concrete-filled tubular columns with flowdrilled connectors. *Journal of Constructional Steel Research*, 50(1), 35-48.
- [13] Steel Construction Institute/British Constructional Steelwork Association. (2002). *Joints in Steel Construction: Simple Connections* (No. P212). Publication.
- [14] EN1993, B.S. (2005). 1-8, *Design of Steel Structures—Part 1-8: Design of Joints*.
- [15] Ni, S. G. (1980). Determination of structure ductility coefficient. *Building Structure*, 5, 64-65.
- [16] Johansen, K.W. (1931). Beregning af krydsarmerede Jaernbetonpladers Brudmoment. *Bygningsstatistiske Meddelelser*, 3(1), 1-18.
- [17] Cao, J.J., Packer, J.A. and Kosteski, N. (1998). Design guidelines for longitudinal plate to HSS connections. *Journal of structural engineering*, 124(7), 784-791.

Experimental Investigation of High Capacity End Plate Moment Connections

Matthew R. Eatherton
Virginia Tech, Blacksburg, VA 24061, USA
meather@vt.edu

Nonish Jain
Walter P. Moore, Washington D.C., 20006, USA
nonishj@vt.edu

Thomas M. Murray
Virginia Tech, Blacksburg, VA 24061, USA
thmurray@vt.edu

ABSTRACT

End-plate moment connections are widely used, especially in metal buildings, between rafters and columns or at splice connections in rafters. Most of the connection configurations for which existing design procedures exist do not have more than four bolts or eight bolts at the tension flange for flush and extended end plates, respectively. Three end plate connection configurations with larger moment capacities were experimentally investigated including the six bolt flush unstiffened, eight-bolt extended stiffened, and twelve bolt extended unstiffened configuration. Design procedures including yield line analysis and bolt force models were proposed to calculate moment capacity associated with end-plate yielding, bolt rupture with prying action, and bolt rupture without prying action. The yield moment obtained during thin end plate tests was an average of 5% larger than the predicted end-plate yielding moment capacity and the obtained ultimate moment capacity was 13% larger than the predicted bolt rupture moment capacity on average.

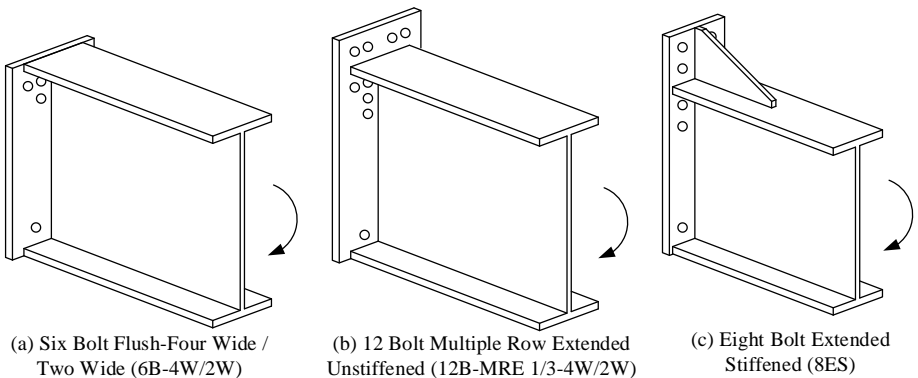
INTRODUCTION

In the United States, end-plate moment connections are commonly used in the low rise metal building industry. An end-plate connection is a rigid connection between a rafter and column or between two segments of a rafter (sometimes referred to as a splice plate connection). End-plate connections can be subdivided into extended and flush end-plates depending on whether the end-plate extends beyond the beam flanges or not. Further, end-plates can be either stiffened or unstiffened, where the stiffeners may be horizontal and located in the web for a flush configuration or vertical and above the flange for an extended configuration.

Over the past three decades, there have been numerous analytical and experimental studies validating the design procedures and behavior of these connections. A partial summary of testing and development of design procedures is presented in (Murray and Shoemaker, 2002) and (Murray, 1988). Based on previous testing and development, the AISC Design Guide 16 (Murray and Shoemaker, 2002) included design

procedures for a total of nine end-plate configurations. More recently, there has been interest by metal building manufacturers in having end-plate connection configurations made available with larger moment capacity. This would allow more flexibility for the pre-engineered metal building industry in the design, detailing, and construction of end-plate connections.

An experimental program was conducted on three end plate moment connection configurations; see Figure 1. Tests were conducted on two new configurations, not currently contained in the AISC Design Guide 16, to produce validated design procedures. The two new end plate connection configurations are the six bolt flush – four wide / two wide (6B-4W/2W) configuration and the 12 bolt multiple row extended unstiffened (12B-MRE 1/3-4W/2W). Additionally, tests were conducted on the eight bolt extended stiffened (8ES) configuration. Although specimens with the 8ES configuration have been tested previously, a review of the literature showed that many of the specimens were designed to produce plastic hinging of the beam, exhibited mixed limit states, and used with rolled beams not exceeding nominal 36 in. depth. These new tests are meant to further validate the 8ES end plate yield line mechanism and bolt rupture prediction equations for deeper sections (56 in. depth).



Note: The two Bolts shown at the compression flange are just representative. The actual number of bolts will depend on the required moment capacity in the other direction.

Figure 1 – Three End Plate Moment Connection Configurations Investigated Herein

Ten full-scale tests were conducted: four specimens for 6B-4W/2W, four specimens for 12B-MRE 1/3-4W/2W, and two specimens for the 8ES configuration. Each test specimen consisted of two built-up rafter sections spliced together at midspan using A325 bolts. Each rafter had end-plates welded to both ends so that it could be used for two tests. The shallow built-up rafter sections were 36 in. deep and the deep rafter sections were either 56 in. deep or 60 in. deep. Additional details about the relevant literature, a fourth configuration that was investigated, and the testing program can be found in the research report by Jain et al. (2015).

BACKGROUND

There are three types of end plate moment connection behavior with distinct controlling limit states. Thin end plate behavior is characterized by end plate yielding and then bolt rupture wherein the bolt forces are affected by prying action. Thick end plate behavior occurs when the plate doesn't exhibit significant yielding and instead, the bolts rupture without prying action. If both the bolts and end plate are designed to be stronger than the plastic moment capacity of the beam, then beam plastic hinging is the controlling limit state. To properly validate the design procedures for all three possible categories of behavior, it is necessary to validate the prediction equations for moment capacity associated with the following limit states: end plate yielding, bolt rupture with prying action, and bolt rupture without prying action.

Validated design procedures for nine end plate configurations are included in the AISC Design Guide 16 (Murray and Shoemaker, 2002). These configurations are either flush end-plate connections (end-plate stops at the outside of the flange) or extended end-plate configurations (end-plate includes bolts outside the flange). The flush configurations have either two bolts or four bolts on the tension side of the connection and can be stiffened or unstiffened. There are five extended end-plate configurations which can be stiffened or unstiffened. The extended end plate configurations have between four and eight bolts at the tension flange. The AISC Design Guide 4 (Murray and Sumner 2003) includes design procedures for three end plate connection configurations intended for seismic and wind applications. Two of the configurations are common between the two design guides, the third is the 8ES configuration.

The eight bolt extended, stiffened end-plate connection is also included in AISC 358-10 (AISC 2010) as a prequalified moment connection for special moment resisting frames. There have been several tests on the connection configuration, but many have focused on developing a plastic hinge in the beam prior to experiencing end-plate yielding or bolt rupture. Experimental programs on the Eight-Bolt Extended Stiffened configuration have been reported by Ghassemieh et al. (1983), Adey et al. (1997, 2000), Sumner et al. (2000), Sumner and Murray (2002), Sumner (2003) and Seek and Murray (2008). Beam depths ranged from 18 in. to 36 in. with end plates between 3/4 in. and 1-3/4 in. and bolt sizes between 7/8 in. and 1-1/4 in. A review of the past tests is contained in Jain et al. 2015.

DESIGN PROCEDURES

The design procedures for end plate moment connections revolve around predicting the moment capacity associated with three key limit states. End plate yielding and bolt rupture with prying action, which are the key limit states for thin end plate behavior, are typically predicted using equations like Eqn. 1 and 2, respectively. The yield line parameter, Y_p , is given in Eqn. 4, 5, and 6 for the yield line mechanisms shown in Figure 2 for the three end plate configurations. It is noted that the yield line parameter in Eqn. 4 is slightly different from that reported in AISC 358-10 (AISC 2010), or AISC Design Guide 4 (Murray and Sumner 2003), but that future editions of those documents are expected to be revised to match Eqn. 4. The moment capacity associated with bolt rupture including prying is often calculated as the maximum value obtained from a series

of scenarios wherein some bolts experience prying action and the rest do not. Details about the scenarios for the three configurations in question are provided in Jain et al. (2015). The limit state of bolt rupture without prying action, which is the characteristic limit state for thick end plate behavior, is predicted using Eqn. 3.

$$\phi M_{pl} = \phi_b F_{yp} t_p^2 Y_p \tag{Eqn. 1}$$

F_{yp} = End plate yield stress
 t_p = End plate thickness
 Y_p = Yield line parameter
 $\phi_b = 0.9$ (Resistance factor for plate bending)

$$\phi M_q = \phi \left[\sum_{\text{some bolts}} (P_t - Q_{\max}) d_n + \sum_{\text{other bolts}} T_b d_n \right] \tag{Eqn. 2}$$

$P_t = A_b F_t$ (Bolt Rupture Strength)
 Q_{\max} = Prying force in bolt
 d_n = Distance from compression flange centroid to bolt
 T_b = Bolt pretension
 $\phi = 0.75$ (Resistance factor for bolt rupture)

Thick end plate behavior

$$\phi M_{np} = \phi P_t \sum N_{bolts} d_n \tag{Eqn. 3}$$

N_{bolts} = bolts in the row

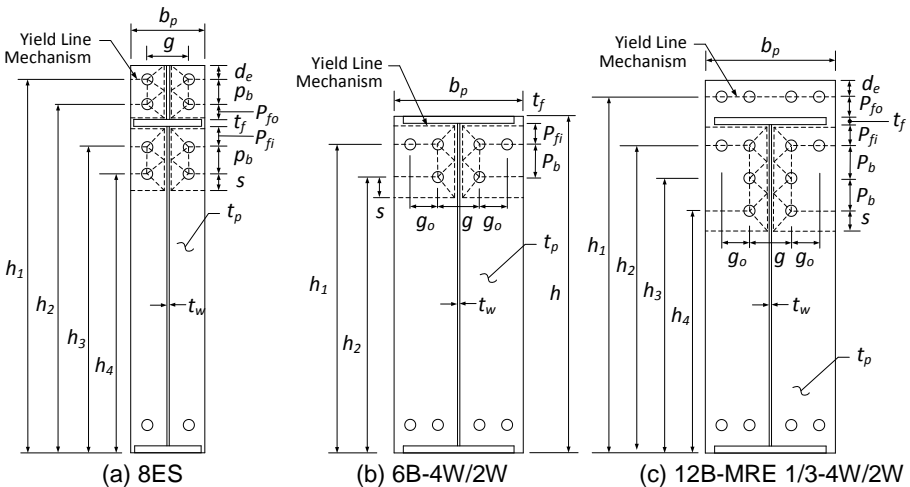


Figure 2 – Yield Line Mechanisms for the Three End Plate Configurations

For 8ES:

$$Y_p = \frac{b_p}{2} \left[h_1 \left(\frac{1}{2d_e} \right) + h_2 \left(\frac{1}{p_{fo}} \right) + h_3 \left(\frac{1}{p_{fi}} \right) + h_4 \left(\frac{1}{s} \right) \right] + \frac{2}{g} \left[h_1 \left(d_e + \frac{3p_b}{4} \right) + h_2 \left(p_{fo} + \frac{p_b}{4} \right) + h_3 \left(p_{fi} + \frac{3p_b}{4} \right) + h_4 \left(s + \frac{p_b}{4} \right) \right] + g \quad \text{Eqn. 4}$$

For 6B-4W/2W:

$$Y_p = \frac{b_p}{2} \left[h_1 \left(\frac{1}{p_f} \right) + h_2 \left(\frac{1}{s} \right) \right] + \frac{2}{g} \left[h_1 (p_f + 0.75p_b) + h_2 (s + 0.25p_b) \right] + \frac{g}{2} \quad \text{Eqn. 5}$$

For 12B-MRE 1/3-4W/2W:

$$Y_p = \frac{b_p}{2} \left[h_1 \left(\frac{1}{p_{f,o}} \right) + h_2 \left(\frac{1}{p_{f,i}} \right) + h_4 \left(\frac{1}{s} \right) - \frac{1}{2} \right] + \frac{2}{g} \left[h_2 (p_{f,i} + 1.5p_b) + h_4 (s + 0.5p_b) \right] + \frac{g}{2} \quad \text{Eqn. 6}$$

EXPERIMENTAL PROGRAM

The test setup is shown in Figure 3. The tested moment connection was located at the center as a splice connection between two rafters. A four-point bending configuration was used to create a region of constant moment at the tested connection. The deeper rafters had a shear span of 18'-0", and the shallower rafters had a shear span of 12'-6". Two servo-hydraulic controlled actuators were used to apply displacement at a rate of 0.10 in./min.



(a) Picture of Test Setup Showing Deeper Specimen

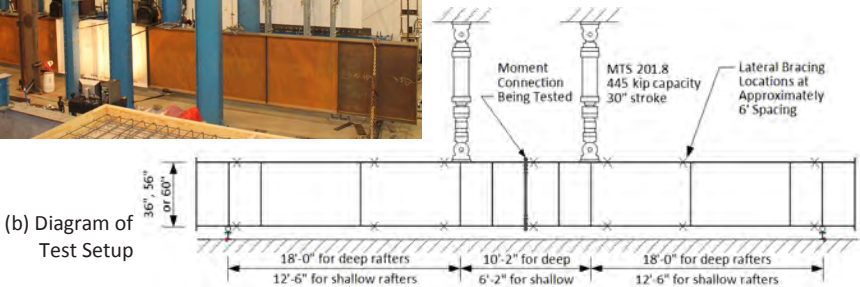


Figure 3 – Picture and Diagram of Test Setup

A total of ten end-plate moment connection tests were performed as shown in Table 1. Specimens were designed to isolate the limit states associated with either thin or thick end plate behavior. Groups of four specimens for the 6B-4W/2W configuration and 12B-MRE 1/3 4W/2W configuration were selected to investigate both thin and thick

end plate behavior for shallower depth rafters ($d=36$ in.) and deeper depth rafters ($d=60$ in.). The group of two specimens for the 8ES configuration was designed to examine thin and thick end plate behavior for deeper depth rafters ($d=56$ in.) only. The resulting end plate designs are shown in Figure 4.

Table 1 - Test Matrix with Geometry

Specimen Identification ¹	Expected Behavior	A325 Bolt Dia., d_b (in.)	No. of Tension Bolts	End-Plate Thickness (in.)	Bolt Pitch, p_b (in.)	Bolt Gage, g_o (in.)	End-Plate Width, b_p (in.)	Flange Width, b_r (in.)	Beam Depth, d (in.)
6B-4W/2W-0.875-1.00-36	Thick	7/8	6	1	3 1/2	4 1/2, 3	14	12	36
6B-4W/2W-1.125-0.75-36	Thin	1 1/8	6	3/4	3 1/2	4 1/2, 3	14	12	36
6B-4W/2W-0.875-1.00-60	Thick	7/8	12	1	3 1/2	4 1/2, 3	14	12	60
6B-4W/2W-1.125-0.75-60	Thin	1 1/8	12	3/4	3 1/2	4 1/2, 3	14	12	60
12B- MRE 1/3 -0.75-1.00-36	Thick	3/4	6	1	3 1/2	4 1/2, 3	14	12	36
12B- MRE 1/3 -1.00-0.75-36	Thin	1	6	3/4	3 1/2	4 1/2, 3	14	12	36
12B- MRE 1/3 -0.75-1.00-60	Thick	3/4	12	1	3 1/2	4 1/2, 3	14	12	60
12B- MRE 1/3 -1.00-0.75-60	Thin	1	12	3/4	3 1/2	4 1/2, 3	14	12	60
8ES-1.00-1.00-56	Thick	1	8	1	3 1/2	5	10	10	56
8ES-1.25-0.75-56	Thin	1 1/4	8	3/4	3 1/2	5	10	10	56

¹ Test Identification: "Conn. type - Bolt dia. - End-plate thickness - Beam depth"

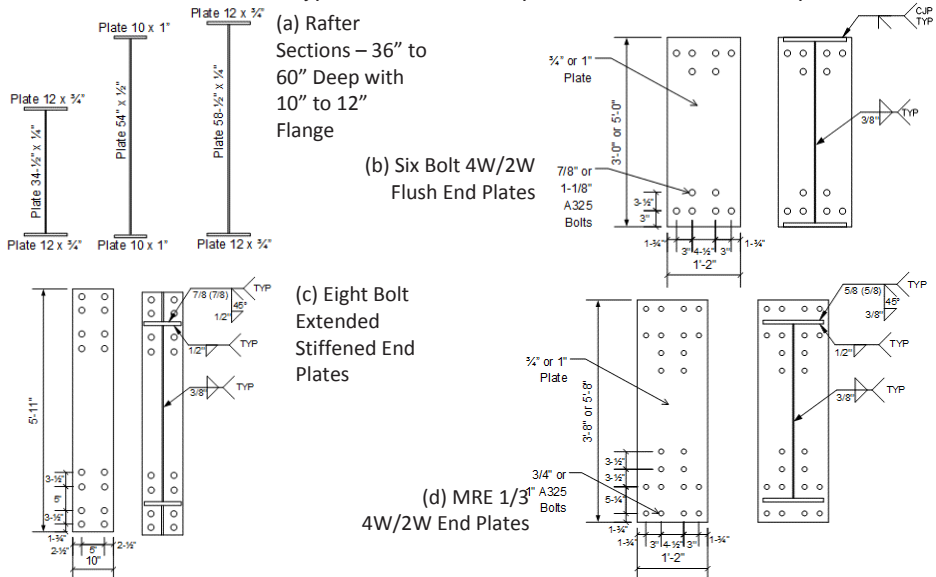


Figure 4 – Rafter and End Plate Designs

A suite of instrumentation was used to measure the behavior of the specimens. Half of the tension bolts were instrumented with strain gages that were calibrated to record bolt axial force. The instrumented bolt locations were selected so that bolt force measurements were available for every bolt position. Four instrumented calipers were used to measure end-plate separation. Five string potentiometers were used to measure vertical displacement of the specimen while the load and displacement from the two actuators were also recorded. Further details of the instrumentation plan can be found in Jain et al. (2015).

EXPERIMENTAL RESULTS

Figures 5, 6 and 7 show selected results from the tests and Table 2 gives measured yield and ultimate moments. The yield moment was obtained as the intersection between lines fit to the initial slope and post-yield slope of the moment vs. end plate separation relationship as demonstrated in Figure 5b.

Specimen 6B-4W/2W-0.875-1.00-36 exhibited thick end plate behavior in that the end plate did not appear to undergo significant inelasticity and bolt rupture without prying action was the observed limit state (absence of prying action was observed by a clear separation between the two end plates at the tension flange prior to bolt fracture). The peak applied moment ($M_u=1030$ k-ft as shown in Figure 5a and given in Table 2) was approximately 20% larger than the predicted moment capacity for bolt rupture without prying action (851 k-ft). This difference is consistent with the ratio of actual bolt ultimate strength divided by the nominal bolt strength that was used in the prediction. Figure 5b shows the end plate separation for specimen 6B-4W/2W-1.125-0.75-36 which was designed to produce thin end plate behavior. The magnitude of end plate separation and variation between end plate separations at different calipers suggests end plate yielding which corroborates the clear end plate distortions observed during the test (see Jain et al. 2015 for details). The predicted end plate yield capacity (calculated using measured end plate yield stress) was within 2% of the measured yield moment as shown graphically in Figure 5b and given in Table 2.

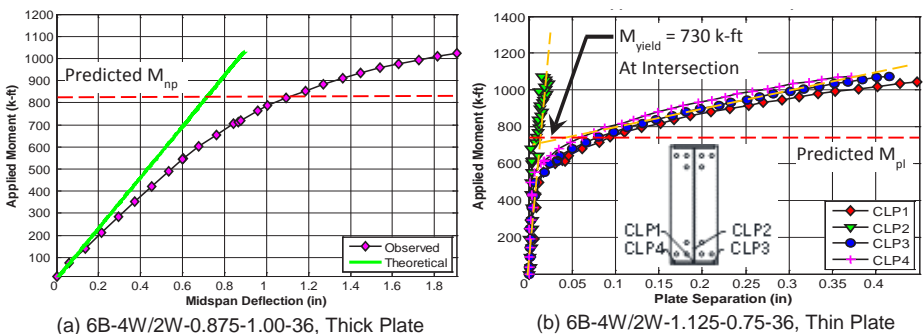


Figure 5 – Selected Results from the 6B-4W/2W Connection Specimens

The 12B-MRE 1/3 4W/2W configuration results showed similar accuracy of the prediction equations. Figure 6a and Table 2 show that the achieved ultimate moment was 15% larger than the predicted moment capacity for bolt rupture without prying action. Again, this is likely related to overstrength of the bolts. Figure 6a shows measurements from the bolt strain gages which exhibit relatively minor increases in strain until the moment overcomes the pretension in the bolts and the end plates separate. Figure 6b shows that the predicted end plate yield moment was within 8% of the experimentally obtained value. Similar to the thick end plate bolt rupture predictions, the ultimate achieved moment was approximately 15% larger than the predicted bolt rupture with prying action for specimen 12B-MRE 1/3-1.00-0.75-36 (see Table 2).

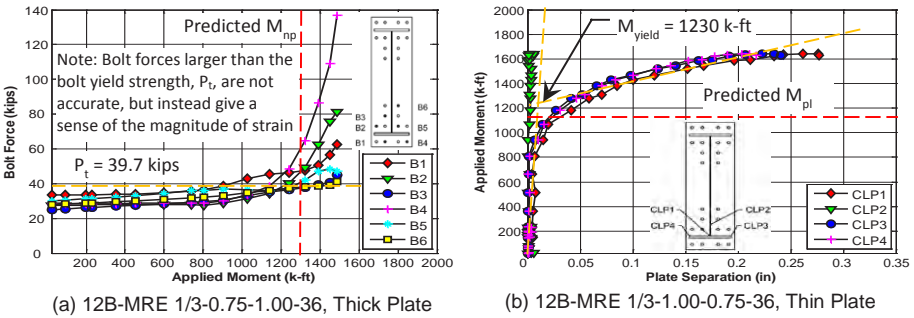


Figure 6 – Selected Results from the 12B-MRE 1/3-4W/2W Connection Separation Specimens

Figure 7a shows the results of the 8ES thick end plate specimen. Little inelasticity was observed in the response prior to bolt rupture at a moment that was approximately 16% larger than the predicted value. The thin end plate specimen exhibited end plate yielding and an experimentally obtained yield moment that was within 4% of the predicted value.

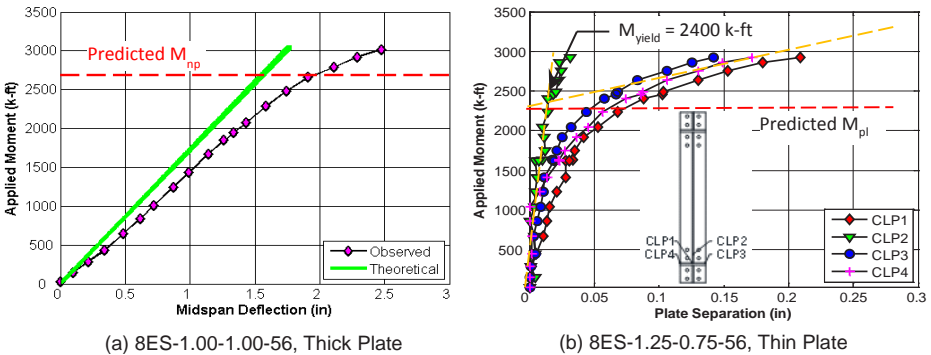


Figure 7 – Selected Results from the 8ES Connection Specimens

The resulting ratios of predicted moment capacity to experimentally obtained moment capacity are provided in Table 2 for the three key limit states of end plate yielding, M_{pl} / M_y , bolt rupture with prying action, M_q / M_u , and bolt rupture without prying action, M_{np} / M_u . Values less than 1.0 indicate that the prediction is conservatively less than the experimentally obtained moment. The predicted end plate yielding moment was on average 5% conservative relative to the experimental yield moment. The bolt rupture limit states had a predicted moment capacity that was 13% less than the ultimate moment on average. This difference is likely related to the use of nominal bolt strength in the prediction.

Table 2 – Results of the Experiments

Specimen	Predicted (kip ft)				Experiment (kip ft)		Ratios		
	M_n	M_{pl}	M_q	M_{np}	M_y	M_u	M_{pl}/M_y	M_q/M_u	M_{np}/M_u
6B-4W/2W-1.125-0.75-36	1630	748	957	-	730	1110	1.02	0.86	-
6B-4W/2W-1.125-0.75-60	3260	1310	1680	-	1400	1980	0.94	0.85	-
6B-4W/2W-0.875-1.00-36	1630	1440	-	851	-	1030	-	-	0.83
6B-4W/2W-0.875-1.00-60	3260	2530	-	1500	-	1730	-	-	0.87
12B-MRE 1/3-1.00-0.75-36	1630	1130	1420	-	1230	1640	0.92	0.87	-
12B-MRE 1/3-1.00-0.75-60	3260	1980	2450	-	2230	2760	0.89	0.89	-
12B-MRE 1/3-0.75-1.00-36	1630	2190	-	1300	-	1490	-	-	0.87
12B-MRE 1/3-0.75-1.00-60	3260	3830	-	2250	-	2490	-	-	0.90
8ES-1.25-0.75-56	3550	2300	2650	-	2400	2920	0.96	0.91	-
8ES-1.00-1.00-56	4160	2630	-	2630	-	3050	-	-	0.86

CONCLUSIONS

This paper examines the design procedures for three end-plate moment connections. Selected configurations were the: eight bolt extended stiffened configuration (8ES), six bolt flush four wide / two wide unstiffened configuration (6B-4W/2W), and twelve bolt multiple row extended four wide / two wide unstiffened configuration (12B-MRE 1/3-4W/2W). Design procedures were presented for each of these end-plate configurations. In particular, equations were provided that predict the moment capacity associated with three limit states including bolt rupture with prying action (M_q), bolt rupture without prying action (M_{np}), and end-plate yielding (M_{pl}).

Ten full-scale experiments (two specimens for 8ES, four specimens for 6B-4W/2W, and four specimens for 12B-MRE 1/3-4W/2W) were conducted to provide data used in evaluating the effectiveness of design equations. It was found that the predicted moment capacities were typically within 10% of the experimentally obtained moment capacities. It was therefore concluded that the proposed yield line mechanisms, bolt models, and design equations were reasonably accurate for the range of parameters tested. Further details about the design procedures and experiments can be found in Jain et al. (2015).

ACKNOWLEDGEMENTS

This project was funded by the Metal Building Manufacturers Association (MBMA). In-kind funding was provided by American Buildings and Bluescope Buildings in the form of donating test specimens. The advice and suggestions by the MBMA connection steering committee throughout the project was invaluable.

REFERENCES

- AISC (2010) ANSI/AISC 358-10 Prequalified Connections for Special and Intermediate Steel Moment Frames for Seismic Applications, Published by AISC
- Adey, B.T., Grondin, G.Y., and Cheng, J.J.R. (1997) Extended End Plate Moment Connections Under Cyclic Loading, Structural Engineering Report No. 216, University of Alberta Department of Civil and Environmental Engineering.
- Adey, B.T., Adey, B.T., Grondin, G.Y., and Cheng, J.J.R. (2000) "Cyclic Loading of End Plate Moment Connections", Canadian Journal of Civil Engineering, Vol. 27, pp. 683-701.
- Ghassemieh, M., Kukreti, A., and Murray, T.M. (1983) Inelastic Finite Element Analysis of Stiffened End-Plate Moment Connections, Report No. FSEL/AISC 83-02, School of Civil Engineering and Environmental Science, University of Oklahoma, Norman, OK.
- Jain, N., Eatherton, M.R., and Murray, T.M. (2015) Developing and Validating New Bolted End-Plate Moment Connection Configurations, Virginia Tech Structural Engineering and Materials Report No. CE/VPI-ST-15/08.
- Murray, T. M. (1988). Recent Developments for the Design of Moment End-Plate Connections. Journal of Constructional Steel Research, 133-162.
- Murray, T. M., & Shoemaker, W. L. (2002) Flush and Extended Multiple-Row Moment End-Plate Connections, AISC Design Guide 16, Published by AISC
- Murray, T.M., and Sumner, E.A. (2003) Extended End-Plate Moment Connections Seismic and Wind Applications, AISC Design Guide 4, Published by AISC
- Seek, M.W., and Murray, T.M., (2008) "Seismic Strength of Moment End-Plate Connections with Attached Concrete Slab", Proceedings of the Connections in Steel Structures VI Workshop, Chicago, IL. June 23-25.
- Sumner, E. A. (2003). Unified Design of Extended End-Plate Moment Connections Subject to Cyclic Loading. Blacksburg, VA: Department of Civil Engineering, Virginia Polytechnic Institute and State University.
- Sumner, E. A., & Murray, T. M. (2001). Experimental Investigation of Four Bolt Wide Extended End-Plate Moment Connections. Blacksburg, VA: Department of Civil Engineering, Virginia Polytechnic Institute and State University.
- Sumner, E. A., Mays, T. W., & Murray, T. M. (2000). Cyclic Testing of Bolted Moment End-Plate Connections. Blacksburg, VA: Virginia Polytechnic Institute and State University.

PROGRESS IN THE CHARACTERIZATION OF THREE-DIMENSIONAL SEMI-RIGID STEEL CONNECTIONS

Eduardo Bayo

University of Navarra, Pamplona, 31009 Navarra, SPAIN

ebayo@unav.es

Beatriz Gil

University of Navarra, Pamplona, 31009 Navarra, SPAIN

bgilr@unav.es

Rufino Goñi

University of Navarra, Pamplona, 31009 Navarra, SPAIN

rgonil@unav.es

Javier Gracia

University of Navarra, Pamplona, 31009 Navarra, SPAIN

jgrarod@unav.es

ABSTRACT

Beam to column connections subjected to loads in the directions of the beams minor axes are usually considered either pinned or rigid for global analysis as well as for resistance and stiffness checks. However, many of these three-dimensional connections exhibit semi-rigid behavior. The consideration of their real semi-rigid behavior (resistance and stiffness) will lead to a more accurate structural analysis and posterior design. There are unresolved issues regarding three-dimensional joints and connections subjected to out-of-plane effects that need further research. This paper describes recent progress in 3D connections through the characterization of the components related to the T-stubs under out-of-plane bending in the major and minor axes. This work comprises: description of experimental results, finite element models and component based mechanical models.

INTRODUCTION

Most of the research on beam-to-column steel connections has been concentrated in its two-dimensional behavior. Except for a small amount of works (Costa Neves et al (2005), Cabrero and Bayo, (2007a and b), Gil and Goñi (2015), Gil et al (2015), Loureiro et al (2012 and 2013) among others) neither three-dimensional joints (that is, columns with beams attached in both the major and minor axis) nor the three-dimensional behavior of connections subjected to out of plane bending and torsion have been researched. In addition, two-dimensional beam to column connections subjected to loads in the beam out of plane direction are usually considered either pinned or rigid for analysis, as well as resistance and stiffness checks.

There are situations in which the three-dimensional or the out of plane behavior as well as the torsional components are needed. Such situations include: internal 3D joints; façade beams when subjected to lateral wind loads; crane girders subjected to both vertical and transversal loads, particularly when they are designed as continuous beams (EC3-6, CEN 2004). Three-dimensional effects can also appear in fire situations and in beams supporting floors with eccentric loads, which induce torsion in the beams. Furthermore, stability checks require the calculation of a critical buckling load (in case of members under compression) and a critical lateral buckling moment (in case of elements under bending). In both cases, the resulting value depends on three factors: the characteristics of the element, the loading and the boundary conditions. Modern codes, including Eurocode 3 (CEN 2005), allow the stability checks to be done by either approximated formulations or by means of advanced method of analysis. The latter become much more accurate if the correct boundary conditions are provided. For this purpose, the minor axis stiffness and strength of the joint must be characterized.

This paper describes recent progress in the characterization of these components considering the general type of three-dimensional joint presented in Fig. 1. The paper includes the description of experimental results, comparison with finite element models, and development of component based mechanical models. Some of the components can be taken from those already defined in EC3-1-8 and in the literature, other new components will have to be defined.



Fig. 1. Type of 3D joint considered in this study.

T-STUBS UNDER OUT OF PLANE BENDING IN MAJOR AXIS

An experimental program was carried out to study the behavior of major axis connections under out of plane bending. Accordingly, the starting point of the research was to analyze the behavior of each component in which the semi-rigid bolted joint is subdivided. A portion of the column and half beam attached to it through half extended end plate constitutes the T-stub as shown in Fig. 2.

The experimental program consisted of five T-Stub specimens depicted in Fig. 2, whose characteristics are summarized in Table 1. The type of steel used was S275 and the bolts used were 10.9 (see Gil and Goñi (2015) for more details).



T-Stub 01



T-Stub 02



T-Stub 03



T-Stub 05

Figure 2. Different T-stub specimens after tests

Test	Column	Beam	End plate (Extended)	Joint
T-stub 01	HEB 160	IPE 300	10 mm	4 bolts \varnothing 16
T-stub 02	HEB 160+ stiffeners	IPE 300	10 mm	4 bolts \varnothing 16
T-stub 03	HEM 160	IPE 300	10 mm	4 bolts \varnothing 16
T-stub 04	HEB 160	IPE 300	-	welded
T-stub 05	HEB 160+ additional plates	IPE 300	10 mm	4 bolts \varnothing 16

Table 1. Tested specimens

All the tested connections exhibited large deformations and high ductile behavior (see Figs. 2 and 3), and none of them reached a complete failure but a yielding of most parts of the joint components. The failure mode depends on the configuration of the joint but is mainly based on the stiffness of the column in the connection zone.

A comparison of general beam-flange moment-rotation curves of the different specimens is also shown in Fig. 3. The joint stiffness and strength are almost the same for T-Stub01 and T-Stub04 because the weakest component and main sources of deformation are the same in both specimens: the column flange and column web. When

stiffeners are added (T-Stub02) to the column or a stiffer column is used (T-Stub03), both the stiffness and strength are highly increased. This increment is higher in the HEM column (T-Stub03) because both the web and the flange are stiffer. When additional plates are added (T-Stub05) the behavior of the joint is improved, although not as much as in the T-Stub02 or T-Stub03 cases. Despite this difference, the design of T-Stub05 serves as a good alternative for three-dimensional joints because it combines good performance with execution advantages.

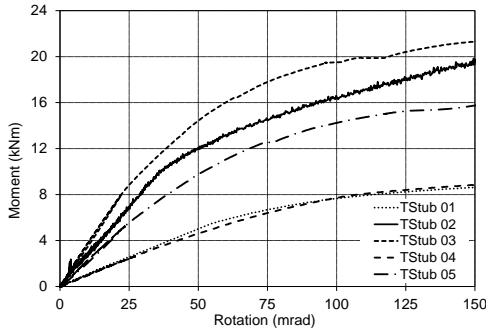


Fig. 3: Comparison of tests beam-flange moment-rotation curves

According to EC3-1-8, clause 5.2, all the tested joints are semi-rigid and partial strength as shown in Table 2. Consequently, more realistic boundary conditions could be taken into account when trying to analyze and optimize the structural elements, instead of considering them as pinned or rigid as it is usually done.

Joint	Classification by stiffness				Classification by strength			
	$S_{j,ini}$ kNm	S_b kNm	$S_{j,ini}/S_b$		$M_{j,Rd}$ kNm	$M_{b,pl,Rd}$ kNm	$M_{j,Rd}/M_{b,pl,Rd}$	
T-Stub01	120	106	1.13>0.5	Semi-Rigid	8.4	17.2	0.47>0.25	Partial Strength
T-Stub02	579	106	2.73>0.5	Semi-Rigid	13.0	17.2	0.76>0.25	Partial Strength
T-Stub03	546	106	5.15>0.5	Semi-Rigid	13.1	17.2	0.70>0.25	Partial Strength
T-Stub04	115	106	1.08>0.5	Semi-Rigid	8.0	17.2	0.47>0.25	Partial Strength
T-Stub05	333	106	3.14>0.5	Semi-Rigid	12.0	17.2	0.70>0.25	Partial Strength

Table 2. Classification by stiffness and strength

A comparison between the moment-rotation curves obtained by the finite element models and the tests is shown in Figs. 4 and 5. The rotations are located in the column flanges, column webs and beam flanges. One may see that there is a good agreement between both sets of curves.

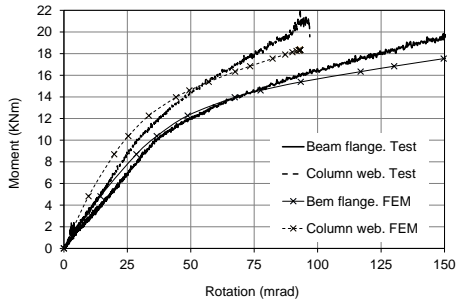
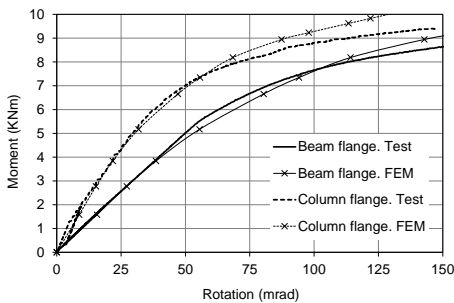


Fig. 4: Comparison between FEM and tests T-Stub01 (left) and T-Stub02 (right)

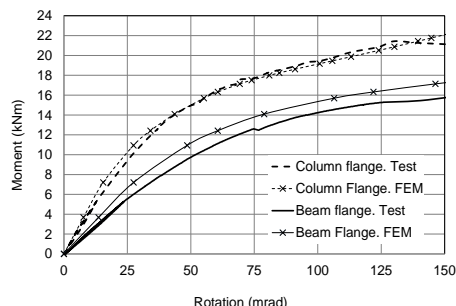
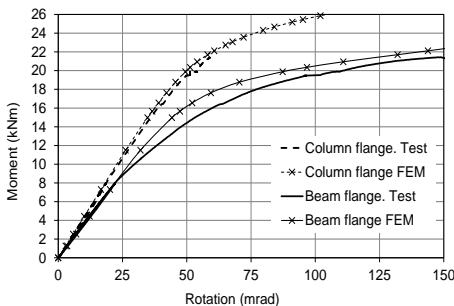


Fig. 5: Comparison between FEM and tests T-Stub03 (left) and T-Stub05 (right)

New components for the T-stub under out of plane bending

The components that are involved in the whole T-Stub are independently studied and characterized based on the component method. New effective lengths and analytical expressions are established for the new components, and also for those already described in Eurocode 3 that needed to be adapted for joints in out-of-plane bending. The components involved in the T-stub are assembled in the proposed mechanical model shown in Fig. 6. The components appearing in this figure are:

- cw,b spring corresponding to the column web in bending, which also includes the column flange in torsion
- cf,b,t spring corresponding to the column flange in bending for the tension zone
- ep,b,t spring corresponding to the end plate in bending for the tension zone
- bf,t spring corresponding to the beam flange in tension
- cf,b,c spring corresponding to the column flange in bending for the compression zone
- ep,b,c spring corresponding to the end plate in bending for the compression zone
- bf,c spring corresponding to the beam flange in compression

In what follows a qualitative description of these components is included. The details of the formulation can be found in Gil et al (2015).

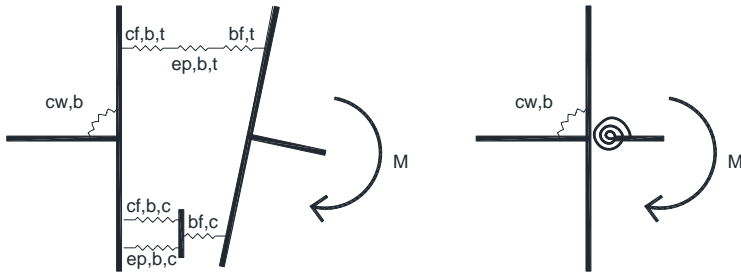


Fig. 6. Mechanical model for a T-stub in out-of-plane bending: complete model (left) and condensed model (right)

Beam flange in compression and buckling

Fig. 7 illustrates how, according to the sign of the moment, the upper part of the beam flange works under tension and the lower part under compression. This component can be characterized from the existing EC3 component for the column web in transverse compression (see clause EC3-1.8, 6.2.6.2 for resistance, and EC3-1.8 Table 6.11 for stiffness) considering a stress dispersion of $\alpha=45^\circ$ (see Fig. 7),

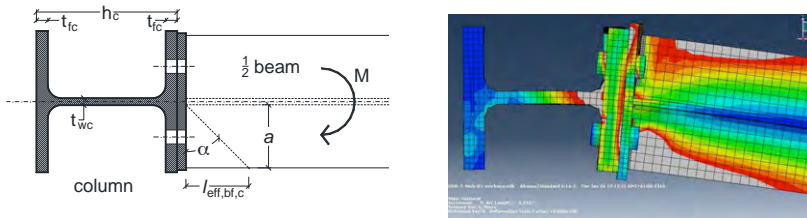


Fig. 7. Beam flange in compression

Column flange in bending

This component consists on two parts: the part under compression and the part under tension. The tension part for an unstiffened column flange in bending has already been defined in EC3, Part 1-8 Clause 6.2.6.4 for the strength and Clause 6.3.2 for the stiffness. These formulae deal with the T-stub behavior corresponding to each bolt row under tension. A different situation arises in the case of a compression zone, for which the plastic mechanism has been identified by means of the test results and finite element simulations. Accordingly, a plastic loading area is established considering a dispersion angle of 45° through the end plate, measured from the welds of the beam flange. The height h_l (see Fig. 8) of this loading area can be obtained from the results of the parametric study. Also, through the finite element simulations and test results, the yielding lines of this component are identified. These lines are similar to those considered in EC3-1.8, table 6.4 for non-circular patterns of a group of two bolts in an unstiffened column flange, for the tension zone.

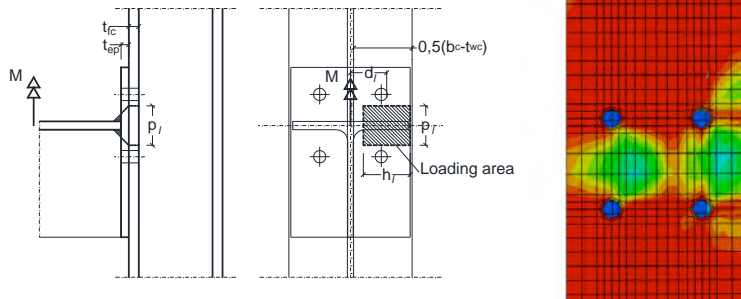


Fig. 8: Column flange in bending for the compression zone

If the column has transverse stiffeners the compression is transmitted directly from the beam flange to the stiffener avoiding bending of the column flange in the compression zone, hence, the stiffness and strength becomes that of the transverse stiffener.

End plate in bending

The strength and stiffness of the end plate in bending in the compression zone is directly obtained from that of the column flange, by replacing the thickness of the column flange by the thickness of the end plate.

Column flange in torsion

The rotation produced in the column side comes mainly from a combination of the rotation of the column web in bending and both column flanges in torsion.

Column web in bending

This component happens to be one of the main sources of deformation and which usually is the first one to yield near the root radius.

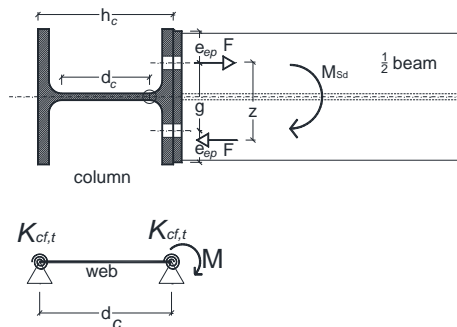


Fig. 9: Column web in bending

The two forces acting on both sides of the column flange (see Fig. 9) generate a bending moment in the column web. This moment is higher at the side of the joint and becomes gradually smaller at the opposite side. A plastic hinge is formed where the root radius meets the column web. If the column has transverse stiffeners, there is no rotation between the column flange and the column web, and the stiffness coefficient of this component becomes infinite.

Comparison between the finite element and the analytical model

The components involved in the T-stub have been assembled to form the proposed mechanical model and a comparison with finite element models is shown in Table 3. The mechanical model predicts the behavior with good accuracy.

Characteristics	Initial stiffness $S_{j,ini}$ kNm		Plastic Moment $M_{j,Rd}$ kNm	
	FEM	Mechanical	FEM	Mechanical
HEB200/IPE300 EP10mm / Bolts 16mm	131.1	123.8	12.8	12.7
HEB180/IPE300 EP10mm / Bolts 16mm	117.5	119.2	10.5	10.6
HEB200/IPE200 EP16mm /Bolts 16mm	98.5	89.4	7.8	7.9
HEB200/IPE270 EP18mm /Bolts 20mm	134.0	116.1	12.9	12.5
HEB260/IPE400 EP20mm /Bolts 24mm	197.8	173.8	18.5	21.3

Table 3. Comparison of the initial stiffness and strength between the finite element model and mechanical model

T-STUBS UNDER OUT OF PLANE BENDING IN MINOR AXIS

An experimental program is currently under way to study the behavior of the minor axis connection under out of plane bending. Several experiments have been performed as shown in Fig. 10, whose characteristics are summarized in Table 4. Finite element models have been developed to perform the parametric analyses necessary to characterize the behavior of the components.

The type of joint is the one depicted in Fig. 1 in which the minor axis beam is attached to the column by means of a plate welded to both column flanges. The advantage of using these supplemental plates is that they provide additional stiffness and resistance to the joint and in addition, they allow for a simpler the execution.

The specimens are formed by a piece of 1200 mm column and half beam of length 500 mm. This beam is connected to the column by means of a T-stub simulating the upper part of bolted extended end plate connection with four bolts. The half beam has a welded plate in one end and a pin in the other which is used to apply the vertical load at a distance of 600 mm from the column flange (see Fig. 10). The column and beam are placed horizontally. Both edges of the column are rigidly fixed to a structure.

The steel grade for sections and plates is steel S275; steel grade for bolts is 10.9 and steel grade for welds is Fe ER 70 S-6 WL G3Si1.

EXPERIMENTAL PROGRAM							
Test	Column	Beam	End plate	Addition al plate	Throat thick.	Steel	Joint
Ts-01m	HEB 160	IPE 200	6 mm	6 mm	4 mm	S275	4 bolts \varnothing 16(10.9)
Ts-02m	HEB 160	IPE 300	10 mm	10 mm	8 mm	S275	4 bolts \varnothing 16(10.9)

Table 4. Tested specimens for minor axis under out of plane bending.

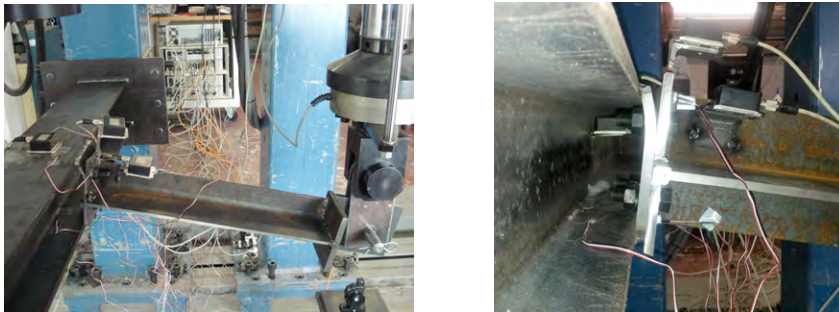


Fig. 10. T-stub experiments for minor axis under out of plane bending

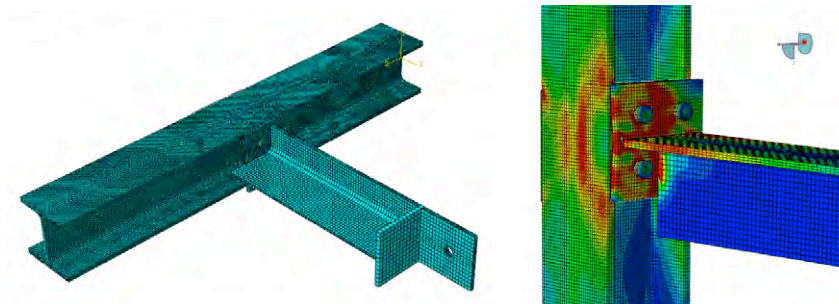


Fig. 11. T-stub finite element models for minor axis under out of plane bending

A comparison between the moment-rotation curves obtained by the finite element models and those obtained with the tests is shown in Fig. 12. The rotations are located in the beam flanges. One may see that there is a good agreement between both sets of curves.

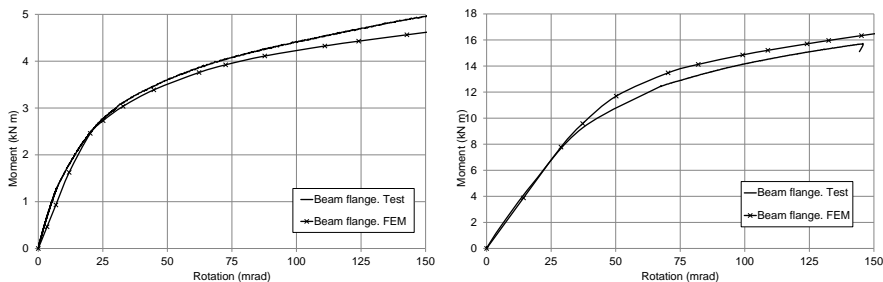


Fig. 12: Comparison between FEM and tests Ts-01m (left) and Ts-02m (right)

REFERENCES

- Cabrero JM , Bayo E. (2007a), "The semi-rigid behaviour of three-dimensional steel beam-to-column joints subjected to proportional loading. Part I. Experimental evaluation", *Journal of Constructional Steel Research*; Vol. 63 (9): (pp. 1241-1253).
- Cabrero JM , Bayo E. (2007b), "The semi-rigid behaviour of three-dimensional steel beam-to-column joints subjected to proportional loading. Part II: Theoretical model and validation", *Journal of Constructional Steel Research*; Vol. 63 (9) (pp.1254-1267).
- CEN. (2005) Eurocode 3: Design of steel structures. Part 1.1: General rules and rules for buildings (en 1993-1-1:2005).
- CEN. (2005) Eurocode 3 : Design of steel structures. Part 1.8: Design of joints (en 1993-1-8:2005).
- CEN. (2004) Eurocode 3 : Design of steel structures. Part 6: Crane supporting structures.
- Costa Neves L, Simoes da Silva L , Vellasco PCG. (2005), "A model for predicting the stiffness of beam to concrete filled column and minor axis joints under static monotonic loading". 4th european conference on steel and composite structures. Hechler BH&O. Maastrich, Druck und Verlagshaus Mainz GmbH Aachen. Vol. C (pp.131-138).
- Gil B , Goñi R. (2015), "T-stub behaviour under out-of-plane bending. I: Experimental research and finite element modelling", *Engineering Structures*; Vol. 98 (pp. 230-240).
- Gil B., Bijlaard F.S.K. , Bayo E. (2015), "T-stub behaviour under out-of-plane bending. II: Parametric study and analytical characterization", *Engineering Structures*; Vol. 98 (pp. 241-250).
- Loureiro A., Moreno A., Gutiérrez R., Reinoso JM. (2012), "Experimental and numerical analysis of three-dimensional semi-rigid steel joints under non-proportional loading". *Engineering Structures*; Vol. 38 (pp. 68-77).
- Loureiro A., López M., Gutiérrez R., Reinoso JM. (2013), "Experimental and numerical analysis of e-stubs in three dimensional joints: A new analytical formulation for the stiffness calculation". *Engineering Structures*; Vol. 53 (pp.1-9).

FINITE ELEMENT SIMULATION AND ASSESSMENT OF THE STRENGTH OF RIVETED AND BOLTED GUSSET-PLATE CONNECTIONS IN STEEL TRUSS BRIDGES

Donald W. White

Georgia Institute of Technology, Atlanta, GA 30332, USA
dwhite@ce.gatech.edu

Y. D. Kim

Texas A&M University – Commerce, Commerce, TX 75428, USA
Debbie.kim@tamuc.edu

Yavuz Mentes

MMI Engineering, Houston, TX 77077, USA
YMentes@mmiengineering.com

Roberto T. Leon

Virginia Tech, Blacksburg, VA 24061 USA
leon@vt.edu

ABSTRACT

This paper presents the development, execution and interpretation of finite element analysis (FEA) test simulation studies of steel truss bridge gusset plates conducted in support of NCHRP Project 12-84, “Guidelines for the Load and Resistance Factor Design and Rating of Riveted and Bolted Gusset-Plate Connections for Steel Bridges.” The research focuses primarily on the buckling and shear failure modes of steel truss bridge gusset plates, including the effects of a wide range of joint geometries and loadings, fastener types, material strengths, combined action of the gussets as chord splice elements along with the force transfer from the truss web members, combined action of gusset and shingle plates, edge stiffening, and section loss due to corrosion. Two groups of equations are developed and applied to estimate the resistances. The equations termed Method 1 are intended as a highly simplified check, whereas the equations termed Method 2 require some additional calculation, but provide improved estimates of the mean resistances. Both of these resistance calculations have been adopted in the AASHTO Manual for Bridge Evaluation, 2nd Edition, with 2015 Interim Revisions.

INTRODUCTION

After the collapse of the I-35W Bridge in Minneapolis, MN in August 2007, the Federal Highway Administration (FHWA) issued guidance on gusset plate design and rating (FHWA 2009) based on the best available information. Early experience showed that while the FHWA Guide represented the best available knowledge on gusset design, it may be overly conservative for some limit state checks. Furthermore, the FHWA Guide

prompted further requests for information on some of calculations to be performed. Therefore, the NCHRP 12-84 research project was launched to develop and improve design and rating methods of gusset plate connections in steel truss bridges. This project included experimental and parametric simulation studies of gusset plate joints. The parametric simulation procedures were evaluated using the experimental test results and an extensive set of simulation studies was performed. As a result of the NCHRP 12-84 project, two gusset strength evaluation procedures, Method 1 (Ocel 2013) and Method 2 (White et al. 2013) were developed based on the experimental and parametric simulation study results. In the following sections, the parametric simulation studies are discussed and the analysis results are assessed. The Method 1 and Method 2 procedures are illustrated and the accuracy of both methods is assessed.

PARAMETRIC TEST SIMULATION STUDIES

Five baseline experimental tests were conducted within the NCHRP 12-84 project. All the specimens were Warren with vertical member configurations with truss members having no chamfer. The following aspects were varied: 1) the length of the gap between the compressional diagonal to the bottom chord, 2) the connection length of the compression diagonal, and 3) fastener types (A370 vs. A490). The different fastener types led to different connection sizes and geometries. These five test specimens were studied in parametric simulation studies with the following variations: 1) gusset thickness, 2) removal of the vertical member, and 3) addition of edge stiffeners.

For the primary parametric simulation studies conducted in NCHRP 12-84, three main truss types were selected: 1) Warren with vertical members, 2) Pratt, and 3) Warren without vertical members. Given the general truss configurations, representative joints were extracted from the following locations in hypothetical steel truss bridges:

- 1) Joints at mid-span,
- 2) Joints at a pier in continuous-span or cantilevered truss construction,
- 3) Joints near a pier in continuous-span or cantilevered truss construction,
- 4) Joints at an inflection point in continuous-span or cantilevered truss construction,
- 5) 90 degree angle corner joints at the simply-supported end of a span,
- 6) Top chord corner joints with a larger than 90 degree angle between the chord and the end diagonal member at the simply-supported end of a span, and
- 7) Bottom chord joints at the start of a haunch over an interior pier in continuous-span or cantilevered truss construction.

Twenty base cases were developed involving the truss configurations and joint locations selected above. This included eight Warren with vertical members, four Warren without vertical members, two Pratt, and six configurations for Cases (5), (6), and (7). After the base cases were studied, the following aspects were varied to investigate their effects on the connection strengths: plate material strengths, combined action of the gussets as chord splice elements along with force transfer from truss web members, combined action of gusset and shingle plates, edge stiffening, and section loss due to corrosion.

The test simulations were performed using Abaqus (Simulia 2010). In all cases, the gusset plates, splice plates, and a partial length of all the members in the vicinity of the test joint were modeled using four-node shell elements (the S4R element). The remainder of the lengths of the truss members was modeled using 2-node linear-order beam elements (the B31 element). Multi-point constraints were used to connect the member cross-section modeled with shell elements to the corresponding end node of the beam element at the transition between the element types.

All joints were modeled in a two-panel subassembly with the test joint placed at either the upper or lower node in the middle of the assembly. All the nodes of the two-panel system except the test joint were restrained in the out-of-plane direction. The horizontal and vertical displacements in the plane of the truss were restrained at the top left node and the vertical displacement was restrained at top right node. In addition, an out-of-plane constraint was applied at one node at the center of the flange splice plate on the outside of the test joint to prevent overall out-of-plane movement of the test joint. The tendency for this overall out-of-plane movement was largest for the joints located at the midspan of the prototype bridge span. However, the out-of-plane reaction at this constraint was found to be small in all the study joints.

The geometric imperfections considered in the simulations included both out-of-flatness and out-of-plane displacement of the gussets at the subject joint, as well as an out-of-alignment of the compression diagonal created by an out-of-plane displacement of the member at the gussets. The value $L_{max}/150$ was used as the out-of-flatness of the gussets where L_{max} is the length of longest free edge adjacent to the compression diagonal. The value $0.1L_{gap}$ was used for the maximum out-of-plane displacement of the compression diagonal at the gussets, where L_{gap} is the smallest length of the gap between the compression diagonal and the adjacent members.

TEST SIMULATION RESULTS

In this section, the simulation results for a representative truss joint are discussed. Figure 1(a) shows the gusset plate geometry of Joint P5-C-WV-NP. It is an upper joint with chamfered members (C) located near a pier (NP) of a continuous Warren truss bridge with vertical members (WV). This joint has a compression diagonal located on the left of the vertical that has a significant chamfer next to the vertical. Figure 1(b) shows the design forces of the truss members, which are the reference loads in the simulation.

Figure 2(a) shows a load-displacement plot from the analysis of P5-C-WV-NP with a gusset plate thickness of 0.4 inches. The plot indicates that P5-C(0.4)-WV-NP reaches its load capacity at the applied load fraction, $P/P_{reference}$ of 0.94 at the first peak. In the NCHRP12-84 research, the maximum load capacity of a test joint was defined as the load level at which a test first reaches either:

- 1) 4% equivalent plastic strain (ϵ_{peq}) over a length equal to the plate thickness at the mid-surface of any of the plates (gusset, shingle, and splice), or
- 2) The first peak load on the load-displacement curve.

The maximum load capacity of a test joint determined based on above criteria is used as R_{test} in the calculation of professional factors R_{test}/R_n , where R_n is the predicted resistance.

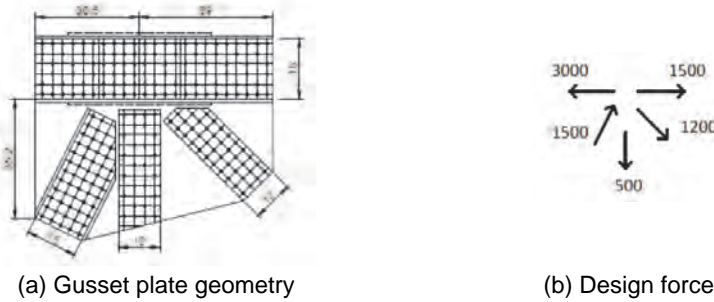


Fig 1. Gusset plate geometry and truss member design forces for P5-C-WV-NP

Figure 2(b) shows the ϵ_{peq} contours at the limit load of this test. These contours show extensive yielding around the entire periphery of the compression diagonal at the strength limit, with the largest concentration of plastic strain occurring at the chamfered and non-chamfered ends of the compression diagonal. In addition, out-of-plane movement of the diagonal and of the long free edge of the gusset is evident at the strength limit. This particular case (P5-C(0.4)-WV-NP) is governed by the Method 1 Partial Shear Partial Yielding (PSPY) and the Method 2 Diagonal Buckling with truncated Whitmore Section (DB-TWS) limit state checks discussed below.

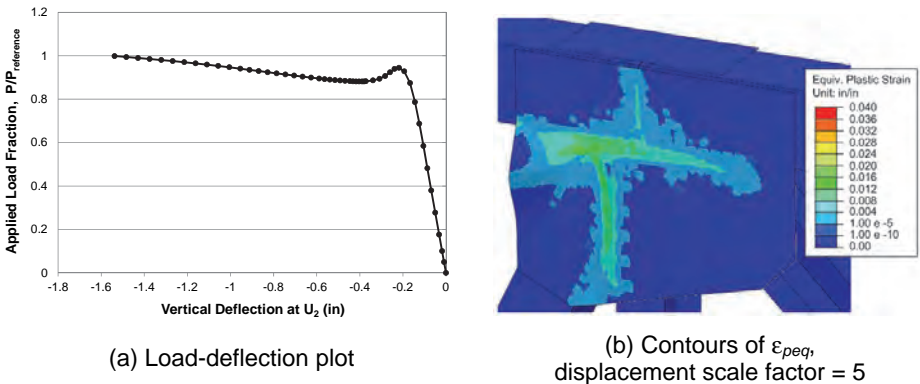


Fig 2. Test simulation results for P5-C(0.4)-WV-NP at limit load

GUSSET PLATE CONNECTION LIMIT STATES

The capacity of gusset plate connections can be governed by the following limit states:

- 1) Chord splice eccentric compression

- 2) Chord splice eccentric tension
- 3) Concentric tension or compression
- 4) Full Shear Plane Yielding (FSPY)
- 5) Diagonal Buckling, full Whitmore section (DB)
- 6) Diagonal Buckling, Truncated Whitmore Section (DB-TWS)

In the NCHRP project 12-84, two methods were proposed to evaluate gusset plate joints for the different limit states listed above except for the limit state (3). In this paper, the proposed procedures for the limit states (4) to (6) are discussed in detail. In general, the first method (referred to as Method 1) involves somewhat simpler calculations. The second method (referred to as Method 2) requires slightly more effort to evaluate the limit states resistance. The research results show Method 2 provides more accurate predictions. Both the Method 1 and 2 resistance calculations have been adopted in the AASHTO Manual for Bridge Evaluation, 2nd Edition, with 2015 Interim Revisions. In the following sections, the Method 1 and 2 limit state calculations are discussed and their professional factors are presented for the experimental and simulated tests.

FULL SHEAR PLANE YIELDING

Method 1: The Method 1 calculation for the Full Shear Plate Yielding (FSPY) resistance is simply the fully-plastic strength of the gusset cross-section using the full length of the shear plane and the gusset thickness. The shear yield strength is taken as $0.58F_y$.

Method 2: Method 2 determines the FSPY resistance by taking 0.9 of the fully-plastic shear resistance. The 0.9 coefficient is a calibration factor associated with the Method 2 FSPY and Diagonal Buckling (DB) models. It was found that the use of 0.9 of the fully-plastic shear resistance along with the Method 2 DB model discussed below led to the smallest coefficient of variation (COV) for the combined checks for these limit states.

DIAGONAL BUCKLING, FULL WHITMORE SECTION

Method 1: The Method 1 Diagonal Buckling (DB) resistance calculation is the equivalent column strength using the Whitmore width. The Whitmore width is calculated as

$$W_{Whitmore} = W_{conn} + 2L_{conn} \tan(30) \quad \text{Eq. (1)}$$

where W_{conn} is the width of the fastener group connecting the diagonal to the gusset and L_{conn} is the length of the connection from the first to the last fastener along this group.

The area of the equivalent column used to evaluate the compression capacity of the gusset, is therefore taken as

$$A_g = 2W_{Whitmore} t_g \quad \text{Eq. (2)}$$

(the factor of two is because the force transfer is via two gusset plates). In Method 1, the length of the equivalent column is taken as L_{mid} , where L_{mid} is taken as the distance along the diagonal from the midpoint of the Whitmore plane at the end of the diagonal to

the adjacent fastener lines. The Method 1 effective length factor for the equivalent column is taken as $K = 0.5$. Given this K factor, the length L_{mid} , and the radius of gyration of the rectangular area $r = t_g/12^{0.5}$, the theoretical Euler elastic buckling stress of the above equivalent column may be written as

$$F_e = \frac{\pi^2 E}{(KL_{mid}/r)^2} = \frac{3.29E}{(L_{mid}/t_g)^2} \quad \text{Eq. (3)}$$

Finally, the value of F_e obtained from Eq. (3) is substituted into the AASHTO LRFD steel column strength equations

$$P_{n,Whitmore} = 0.658^{F_y/F_e} F_y A_g \quad \text{if } F_y/F_e \leq 2.25$$

$$= 0.877 F_e A_g \quad \text{otherwise} \quad \text{Eq. (4)}$$

to determine the Diagonal Buckling (DB) resistance for Method 1.

It was found that the Method 1 DB equations tend to over-predict the resistance of the gussets particularly for joints with tightly-spaced members. These predictions were improved by combining them with a separate Partial Shear Plane Yielding (PSPY) check, which accounts for the reduction in the gusset stiffness due to early shear yielding that occurs between the diagonal and one or both of the adjacent members.

The PSPY check requires the identification of the critical of the two planes along the fastener lines in the two adjacent members. The critical plane is defined as the one that:

- Parallels the chamfer in the diagonal, for cases where only one side of the diagonal is chamfered, or has the greater chamfer, if both sides are chamfered,
- Has the smaller framing angle between the compression diagonal and the adjacent members, if neither side of the diagonal is chamfered, or
- Has the smallest cross-sectional shear area, if the diagonal is unchamfered and the framing angles with the adjacent members are equal.

Once the critical partial shear plane is identified, the PSPY resistance is taken as the compression diagonal axial force developed by assuming its component *tangent to the critical plane* is equal to the shear yield strength of the partial plane, i.e.,

$$P_{n,PartialShear} = \frac{2(0.58F_y L_{PartialShear} t_g)}{\cos \theta} \quad \text{Eq. (5)}$$

where θ is the angle between the compression diagonal and the critical partial shear plane. Given the above calculation associated with the critical plane, the resistance in diagonal compression is taken as the minimum of the strengths from DB and PSPY:

$$P_n = \min(P_{n,Whitmore}, P_{n,PartialShear}) \quad \text{Eq. (6)}$$

Method 2: For cases where the Whitmore section is not truncated by adjacent fastener lines, the Method 2 calculation of the Diagonal Buckling (DB) resistance is very straightforward. The Whitmore section width is given by Eq. (1). The equivalent column length is L_{mid} , which is the same as in Method 1. However, the effective length factor taken as

$K = 0.35$ for Warren trusses with verticals

$$= 0.44 \text{ otherwise} \quad \text{Eq. (7)}$$

These K factors are based on calibration to the results from this research. The fact that these values are smaller than $K = 0.5$ should be no cause for concern. The gusset plate is not an actual column. Its geometry, boundary conditions and stability behavior are far different than an axially loaded prismatic column. Therefore, the equivalent column theoretical elastic buckling stress is

$$F_e = \frac{\pi^2 E}{(KL_{mid}/r)^2} = \frac{6.71E}{(L_{mid}/t_g)^2} \quad \text{Warren trusses with verticals}$$

$$= \frac{4.25E}{(L_{mid}/t_g)^2} \quad \text{otherwise} \quad \text{Eq. (8)}$$

This theoretical stress is then substituted into the column strength equations, Eq. (4) to determine the gusset Diagonal Buckling strength.

DIAGONAL BUCKLING, TRUNCATED WHITMORE SECTION (DB-TWS)

Method 1: In Method 1, the Whitmore section is truncated at intersections with the gusset free edges, and at planes of symmetry. Otherwise, the full Whitmore section is used.

Method 2: Figures 3 and 4 show how Method 2 works with respect to the truncation of the Whitmore section by the fastener lines in adjacent members. The considerations in the Method 2 “Truncated Whitmore Section” (TWS) model are as follows:

- The truncated section width is split generally into three parts, W_L , W_M , and W_R .
- The width between the points where the Whitmore section intersects the adjacent fastener lines, W_M , is referred to as the main “M” part of the Whitmore section. The critical stress on this width, F_{crM} , is exactly as for the cases where the Whitmore section is not truncated by the adjacent fastener lines, except the strength is based on L_M , the distance to the adjacent fastener line from the middle of W_M .
- The other widths, W_L and W_R are the left- and right-hand projections of the fastener lines that truncate the Whitmore section onto the Whitmore plane. The lengths L_L and L_R are the perpendicular distances from the fastener lines that truncate the Whitmore section to the closest fastener lines on the diagonal.
- $K = 0.35$ is used with the lengths L_L and L_R in calculating F_{crL} and F_{crR} , which are taken as critical stresses acting on the widths W_L and W_R .
- We use $0.9F_{crL}$ and $0.9F_{crR}$ as the stresses on W_L and W_R at maximum strength.
- In Fig. 3, the Whitmore section has the normal stresses $0.9F_{crL}$ or $0.9F_{crR}$ on a cut perpendicular to the axis of the diagonal, zero normal stress on a cut parallel to the member axis, and zero shear stress on both of these cuts. This corresponds to an assumed state of shear and compression stress on a cut parallel to the fastener lines on the adjacent members as shown in Fig. 4.

- The DB resistance is determined as

$$P_{n,DB-TWS} = F_{crM}W_Mt_g + 0.9F_{crL}WLt_g + 0.9F_{crR}WRt_g \quad \text{Eq. (9)}$$

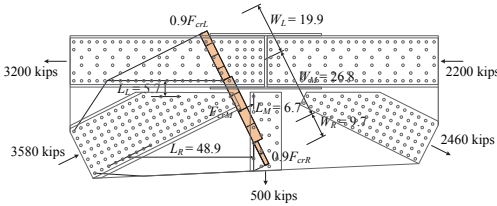


Fig. 3. Method 2 gusset DB-TWS model, shown on P7-C-WV-INF

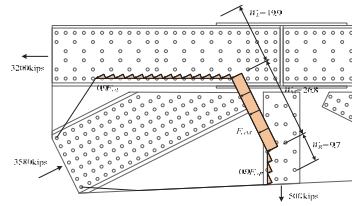


Fig. 4. Assumed state of stress at the bolt lines truncating the Whitmore Section

ASSESSMENT OF THE GUSSET STRENGTH EVALUATION METHODS

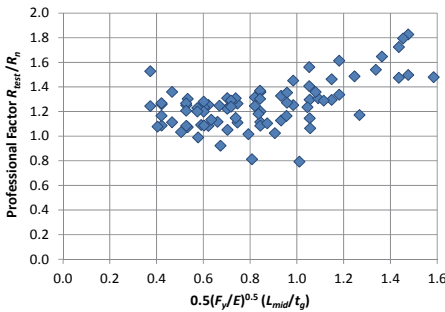
To evaluate the accuracy of the proposed gusset strength evaluation methods, strengths of all the parametric studies are calculated using Methods 1 and 2 and compared to the FEA results. Table 1 summarizes the professional factors for the Method 1 and 2 predictions R_{test}/R_n where R_{test} is the FEA result and R_n is the Method 1 or 2 prediction. In Table 1, NC and C in the Geometry row denote cases with no chamfer and chamfer respectively. Table 1 shows that the mean values of R_{test}/R_n for Method 2 for both no chamfer and chamfer cases are closer to 1.0 than for Method 1. In addition, Method 2 gives a smaller coefficient of variation (COV) as well as maximum and minimum values closer to 1.0 compared to Method 1. For all 147 cases, Method 2 gives R_{test}/R_n values from 0.82 to 1.29 with a mean of 1.09 and COV of 0.09. Method 1 gives a minimum R_{test}/R_n of 0.77 to a maximum of 3.03, a mean of 1.25 and COV of 0.21.

Table 1. Professional factors for Method 1 combined DB or PSPY, Method 2 DB, Method 1 or 2 Diagonal Tension Yielding (DTY), and Method 1 or 2 FSPY.

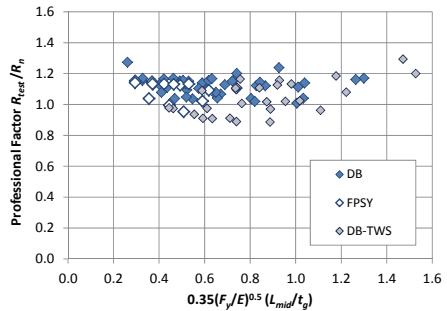
Method	Method 1		Method 2				
	NC	C	NC	NC	NC	C	C
Limit States	DB/PSPY or DTY	DB/PSPY or DTY	DB	FSPY	DB-TWS & DTY-TWS	DB-TWS & DTY-TWS	FSPY
Count	88	59	47	13	28	45	14
Mean	1.30	1.17	1.12	1.09	1.04	1.07	1.11
COV	0.23	0.14	0.05	0.06	0.10	0.10	0.09
Max	3.03	1.62	1.27	1.15	1.29	1.27	1.26
Min	0.79	0.77	1.01	0.95	0.89	0.82	0.96

Figures 5(a) and 5(b) show the distribution of R_{test}/R_n versus the normalized slenderness parameters $0.5(F_y/E)^{0.5} (L_{mid}/t_g)$ and $0.35(F_y/E)^{0.5} (L_{mid}/t_g)$ for 88 No Chamfer cases. The cases in Fig. 5(a) are governed by the Method 1 DB check. The cases in Fig. 5(b) are governed by three Method 2 limit state checks: DB, FSPY, and DB-TWS. One can observe that there is substantial dispersion in R_{test}/R_n for Method1, and that there are two R_{test}/R_n values significantly less than 1.0. However, the Method 2 data for DB is clustered in a relatively tight band mostly between R_{test}/R_n of 1.01 and 1.20. Clearly, Method 2 provides a better prediction for cases governed by DB.

Thirteen tests are governed by the FSPY check in Method 2. Figure 5(b) shows that the R_{test}/R_n distribution for these tests is between 0.95 and 1.15. Figure 5(b) also shows the distribution of R_{test}/R_n for 28 cases governed by the Method 2 DB-TWS check. The mean R_{test}/R_n for these cases is slightly smaller (1.04) and the COV is slightly larger (0.10) compared to the other Method 2 predictions discussed in the above. A significant number of the tests at intermediate plate slenderness values have an R_{test}/R_n close to 0.9. However, the results are better than for Method 1. The smallest R_{test}/R_n value is 0.89 in Fig. 5(b) versus a minimum of 0.79 in Fig. 5(a).



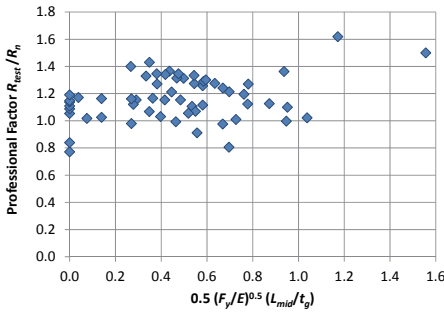
(a) Method 1, DB or PSPY



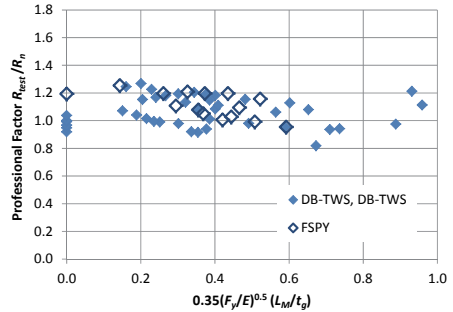
(b) Method 2, DB, FSPY, and DB-TWS

Fig. 5. R_{test}/R_n values for cases with no chamfer

For the chamfered test cases, similar results have been observed. Figures 6(a) and 6(b) show the results from Methods 1 and 2 for the chamfered test cases. Figure 6(a) shows the distribution of R_{test}/R_n versus $0.5(F_y/E)^{0.5} (L_{mid}/t_g)$ for 59 tests governed either by the Method 1 DB, DTY, or PSPY limit state checks, Figure 6(b) shows the R_{test}/R_n distribution for 45 tests governed by the Method 2 DB-TWS or DTY with a Truncated Whitmore Section versus $0.35(F_y/E)^{0.5} (L_{mid}/t_g)$, and the results for 14 tests that were governed by the Method 2 FSPY limit state calculations. As for the No Chamfer cases, Method 2 gives better predictions, with mean R_{test}/R_n closer to 1.0, smaller COV on R_{test}/R_n , and larger minimum R_{test}/R_n values (also see Table 1). Figure 6(a) indicates that there are three Chamfered tests that have an R_{test}/R_n close to 0.8 (minimum value of 0.77), while Fig. 6(b) shows that Method 2 has only one test that has low R_{test}/R_n of 0.82 with all the other tests exhibiting $R_{test}/R_n > 0.90$.



(a) Method 1, governed by DB, DTY, or PSPY



(b) Method 2, governed by DB-TWS, TY-TWS or FSPY

Fig. 6. R_{rest}/R_n values for cases with chamfer

ACKNOWLEDGEMENT

This work was sponsored by the Federal Highway Administration and was conducted in support of the National Cooperative Highway Research Program (NCHRP) Project 12-84. Thanks are extended to Justin M. Ocel and Robert S. Zobel of FHWA for extensive discussions, feedback, and collaboration during the analytical studies as well as their skillful management of the project and execution of the project experimental tests. The opinions, findings and conclusions expressed in this paper are those of the authors and do not necessarily reflect the views of the above individuals and organizations.

REFERENCES

FHWA (2009). "Load Rating Guidance and Examples for Bolted and Riveted Gusset Plates in Truss Bridges", Publication No. FHWA-IF-09-014, US Department of Transportation, Federal Highway Administration, February.

Ocel, J. (2013) "Guidelines for the Load and Resistance Factor Design and Rating of Riveted and Bolted Gusset-Plate Connections for Steel Bridges", Project No. 12-84, Final Report, January.

White, D.W., Leon, R.T., Kim, Y.D., Mentes, Y., and Bhuiyan, M. T. (2013). "Finite Element Simulation and Assessment of the Strength Behavior of Riveted and Bolted Gusset-Plate Connections in Steel Truss Bridges", Report prepared for Federal Highway Administration and NCHRP Transportation Research Board of the National Academies.

APPLICATION OF WEATHERING STEEL IN BRIDGES

Dieter Ungermann
TU Dortmund University, 44221 Dortmund, Germany
dieter.ungermann@tu-dortmund.de

Dennis Rademacher
TU Dortmund University, 44221 Dortmund, Germany
dennis.rademacher@tu-dortmund.de

Annika Peters
TU Dortmund University, 44221 Dortmund, Germany
annika.peters@tu-dortmund.de

Susanne Friedrich
Institut für Korrosionsschutz Dresden GmbH (Institute for corrosion protection),
01217 Dresden, Germany
susanne.friedrich@iks-dresden.de

Peter Lebelt
Institut für Korrosionsschutz Dresden GmbH (Institute for corrosion protection),
01217 Dresden, Germany
peter.lebelt@iks-dresden.de

ABSTRACT

Bridges made of weathering steel offer great advantageous in view of lifetime costs. Reservations are often made in view of bolted connections, where in case of constant moisture at the gaps of the joint the corrosion protection generated by the patina may be disturbed. In addition microclimatic influences like de-icing salt affect the formation of the patina.

The reaction of weathering steel on realistic climatic environmental conditions of bridges was analyzed and tendencies in view of a safe and efficient formation of a patina are shown.

Furthermore tests on slip-resistant connections were carried out, where the roughness of the prestressed connection zone is solely generated by the corroded surface without any additional surface treatment.

INTRODUCTION

Traditional steel bridge design focuses on economic and durable constructions. Due to the need to reduce CO₂ emissions in all sectors of human activities, also the design of ecological bridge solutions with low maintenance costs is getting more and more in

the focus. If painting is used, corrosion protection leads to repeated maintenance actions during the required 100 year lifetime of a bridge. An alternative corrosion protection is ensured by weathering steel and benefits the lifecycle assessment.

Structural steels with improved atmospheric corrosion resistance according to (EN10025-5), the so-called weathering steel, are low alloyed steels, which offer similar mechanical properties in comparison to conventional carbon steel under EN 10025, but their durability is much better. Due to the alloying with copper, chrome, nickel or phosphor, weathering steel develops a corrosion layer with a strong adherence – the patina – under the impact of sulfur dioxide. The patina blocks the penetration of oxygen, water and sulfur oxide. Thereby further corrosion is decelerated under normal atmospheric conditions. The corrosion rate is as low that no additional corrosion protection is needed to ensure the 100 year design life of bridges and therefore only minimal maintenance is necessary.

Figure 1 gives an impression how the corroded surface of weathering steel undergo changes during a two years period. The impression of degradation and naturalness without artificiality is the particular expression of bridges made from weathering steel.



Figure 1: Patina in the course of time (Zaki)

In certain environments the use of weathering steel can lead to durability problems, such as maritime environment, use of de-icing salt, constant wet/damp conditions and atmospheric pollution, which can be avoided by using an additional organic coating.

A recent research project (FOSTA) focused on the development of the patina and its protection effects. The reaction of weathering steel under real atmospheric conditions and laboratory loads was analyzed and quantified.

Bolted connections are the preferred economic connection type because of the high grade of prefabrication and short erection time on site. Bearing-type connections may not be used in bridge engineering due to their minor fatigue resistance. Fitting bolts offer sufficient fatigue resistance, but lead to increased installation costs caused by the production of the required minimum bolt hole tolerances. Taking into account both the fatigue behaviour and an economic fabrication, a slip-resistant connection is the best suitable bolted connection for bridge constructions. The question is what kind of preparation of friction surfaces has to be considered in view of using weathering steel.

With the FOSTA research project, both the evolution of the patina and the slip factors were determined. The aim was to elaborate design guidelines and recommendations for a wider use of weathering steel in bridge design.

WEATHERING TESTS

On the basis of outdoor exposure tests and additional laboratory tests the chemical environment influencing the weathering steel structures' durability were assessed and criteria were examined to evaluate the resistance of the protective patina. For the laboratory tests an aging procedure was established in order to evaluate the corrosion progress quantitatively and qualitatively. Artificially accelerated weathering with a constant condensation atmosphere and a variation of the sulfur dioxide SO₂ according to (EN ISO 3231) introducing drying phases were carried out. One cycle of loading lasted one week. The reduction of air pollution during the last three decades, especially of SO₂ in the ratio of 91.9%, (Um 2014), was taken into account.

The objective was to determine, whether a minimum air pollution of sulfur dioxide is necessary to develop the patina and ensure thus the corrosion protection. In addition the question was, whether the accelerated pollution of the laboratory tests shows corrosion behaviour comparable to the real atmospheric load at bridges. Two different weathering steel grades – S355J2W and S355J2WP – as well as a typical carbon steel DC01 were tested. The chemical configuration of the tested steel grades are given in table 1.

Tested steel	C in %	Si in %	Mn in %	P in %	S in %	Cr in %	Cu in %	Others in %
DC01	0.031	0.01	0.172	0.011	0.009	0.012	0.01	Ni = 0.013 Al = 0.045
S355J2W	0.085	0.16	1.15	0.02	0.02	0.442	0.353	Ni = 0.153 Mo = 0.036 Zr = 0.004
S355J2WP	0.078	0.41	0.353	0.091	0.006	0.786	0.409	Ni = 0.167 Al = 0.031

Table 1: chemical composition of tested steels

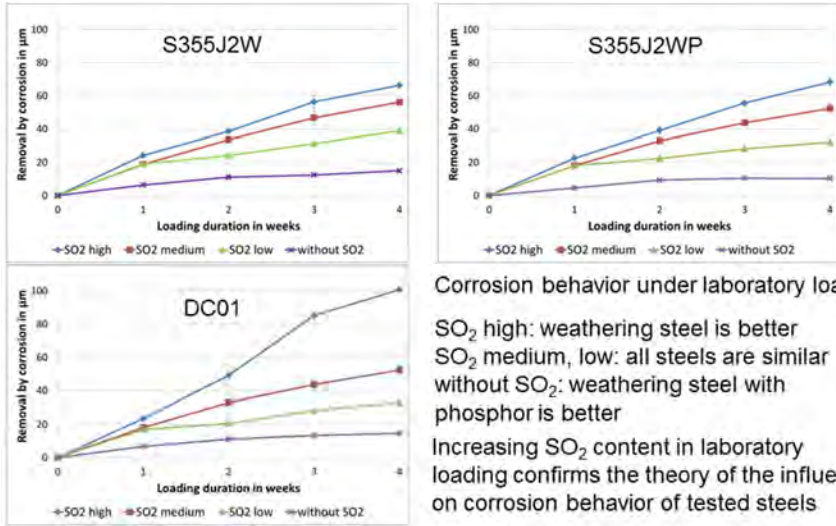
Water vapor without SO ₂	Water vapor and SO ₂ high	Water vapor and SO ₂ medium	Water vapor and SO ₂ low
5 days with ISO 6270-2 CH, 8h + laboratory climate 16h	5 days with ISO 3231, 0,2l SO ₂ , 8h + laboratory climate 16h	3 days with ISO 3231, 0,2l SO ₂ , 8h + laboratory climate 16h	1 day with ISO 3231, 0,2l SO ₂ , 8h + laboratory climate 16h
		2 days with ISO 6270-2 CH, 8h + laboratory climate 16h	4 days with ISO 6270-2 CH, 8h + laboratory climate 16h
2 days laboratory climate	2 days laboratory climate	2 days laboratory climate	2 days laboratory climate

Table 2: chemical composition of tested steels

The best condition for a patina evolution by natural weathering is known to be SO₂ < 50µg/m³·day or < 40mg/m²·day and dry - wet – cycles, but no permanent wetness. For the simulation of natural weathering with different SO₂ contents in the atmosphere,

four different loading tests were performed according to (EN ISO 3231) and (EN ISO 6270-2) with and without SO₂. Each loading comprised four cycles. The specimen were evaluated after each load cycle (one week), **table 2**.

The results of the laboratory loading are given in **figure 2**. The corrosion behaviour, represented by gravimetric measurements – that is the reduction of weight due to corrosion – is shown versus the corrosion time within four cycles.



Corrosion behavior under laboratory loading

SO₂ high: weathering steel is better
 SO₂ medium, low: all steels are similar
 without SO₂: weathering steel with phosphor is better

Increasing SO₂ content in laboratory loading confirms the theory of the influence on corrosion behavior of tested steels

Figure 2: Evaluation of laboratory tests with simulated weathering

For the gravimetric measurement the oxide layers of test specimen were removed by inhibited chemical stripping in hydrochloric acid.

During the laboratory loading, the weathering steel grades under high sulfur dioxide atmosphere showed reduced corrosion degradation rates. Under low and medium sulfur dioxide pollution all three steel grades showed similar degradation and in cases where no sulfur dioxide was added, the weathering steel with the higher phosphor percentage had the smallest degradation. These are first results, which have to be confirmed by further tests and tests over a longer period. Based on the results it should be possible to create a laboratory test for simulating the natural behaviour of weathering steel.

The outdoor exposure testing was carried out in the natural atmosphere of the city Dresden, Germany, using the same three steel grades. Measurements of degradation were carried out after one, two, three and six months. The corrosivity category at the atmospheric test installation of Institut für Korrosionsschutz Dresden (Institute for Corrosion Protection) was measured and calculated with C2 according to (EN ISO 9223). Based on the fixed corrosivity category the typical degradation of steel and weathering steel can be determined by means of literature as shown in **table 3**.

Material	Corrosivity	r_{av} in $\mu\text{m}/\text{yr}$	r_{lin} in $\mu\text{m}/\text{yr}$	Forecast 20 yr's
Weathering steel	C2	$0,1 < r_{av} \leq 2$	$0,1 < r_{lin} \leq 1$	$2 \mu\text{m} < 30 \mu\text{m}$
Carbon steel	C2	$0,4 < r_{av} \leq 8,3$	$0,3 < r_{lin} \leq 4,9$	$7 \mu\text{m} < 132 \mu\text{m}$

Table 3: corrosion rate forecast of tested steels (r_{av} until 10 yr's, $r_{lin} > 10$ yr's)

The measured corrosion rates of the three different steel types with one, two, three and six months natural weathering served as basis for extrapolating rates with respect to a 20 years corrosion period, according to (EN ISO 9224), **figure 3**.

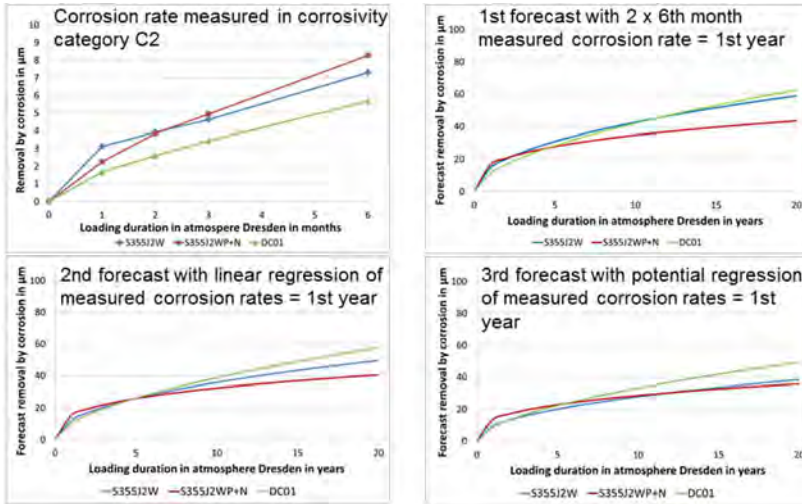


Figure 3: Evaluation of outdoor exposure tests and long-range prognosis

The first results of the outdoor exposure tests are summarized as follows:

- The long term prognosis for the degradation rate of weathering steel, specified as 36 to 50 μm for a 20 year period, are quite high, compared to the forecast for corrosivity category C2. The carbon steel has similar degradation rates between 49 to 58 μm . This is according to the forecast expectations.
- The sulfur dioxide pollution in Dresden was measured in the mean range of 3.58 $\mu\text{g}/\text{m}^3$. Due to the marginal sulfur dioxide pollution the patina could not develop in a sufficient manner to prevent further corrosion.
- The laboratory tests achieve higher degradation rates. The comparison with the outdoor exposure tests shows similar degradation regarding the laboratory tests with low SO_2 concentrations.

The most interesting fact is that the degradation of weathering steel is above the level, which is given in the literature for the low corrosivity category C2. Obviously, also a minimum concentration of SO_2 is required to achieve the protective effect of the patina. Current research activities of Institut für Korrosionsschutz Dresden (Institute for Corrosion Protection) deal with this subject.

Furthermore the corrosion behaviour of weathering steel at different site locations has to be analyzed, because it differs in the macroclimate of sea-, rural- or industrial zones,

but also in microclimate conditions like de-icing salt or constant humidity. Therefore, a database should be established, which includes all relevant data and the special corrosion process. The artificial laboratory tests have to be developed on the basis of this database to allow for a design check of applicability of weathering steel under environmental conditions at the specific site. In the frame of bridge inspection there must be a possibility to verify the degradation and to allow for an expert rating of the patina. Therefore, check criteria for the characterization of the patina have to be established.

Regarding slip-resistant connections, a long lasting corrosion protection is required to avoid corrosion in gaps. If the friction surface is coated, all gaps smaller than 1 mm are closed permanently. If no additional treatment of surface is provided a sealing at the plate edges has to be applied.

SLIP-RESISTANT CONNECTIONS

Introduction

The design of steel structures made of weathering steel is based on (EN 1993). Part 1-8 gives the common rules for the design of connections. The design slip resistance of a preloaded class 8.8 or 10.9 bolt should be taken as:

$$F_{S,Rd} = \frac{k_s \cdot n \cdot \mu}{\gamma_{M3}} \cdot F_{p,c}$$

with: $k_s = 1.0$ for bolts in normal holes
 $n =$ number of friction surfaces
 $\mu =$ slip factor
 $\gamma_{M3} =$ safety factor depending on category B connection (slip resistant at serviceability) or category C connection (slip resistant at ultimate)
 $F_{p,c} = 0.7 \cdot f_{ub} \cdot A_s$ (preloading force of the bolt)

The slip factor μ is obtained either by specific tests for the friction surface in accordance with (EN 1090-2), Annex G or taken from table 18 in EN1090-2. The question was, if anyway a surface treatment has to be applied or if it can be avoided due to the roughness of the corroded surface.

Test setup

A test program was established to verify the behaviour of the corroded surface of weathering steel and to determine an applicable slip factor. After sandblasting a six weeks lasting outdoor weathering of the test specimen was performed. As reference one test series with sandblasted surface according to EN 1090-2, slip category A (roughness after blasting 80 – 90 μm) and another one with coated surface according to EN 1090-2, slip category B (first sandblasted then zinc-silicate coating with thickness 75-100 μm) were prepared, **figure 4**. The test setup is conform to EN 1090-2, Annex G. M20 bolts were used set into $\varnothing 22\text{mm}$ holes to avoid bearing action. Each test series consisted of four test specimens. For each surface three specimens were loaded in a servo-hydraulic machine at normal speed with a test duration of approximately 10 - 15 minutes.

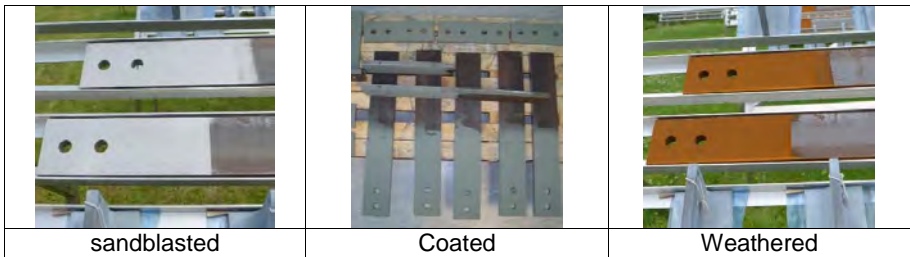


Figure 4: tested surfaces

Besides these short time tests a fourth specimen was used for a long time test in order to investigate possible creep deformations. The load-slip resistance was recorded by means of eight displacement transducers, **figure 5**.

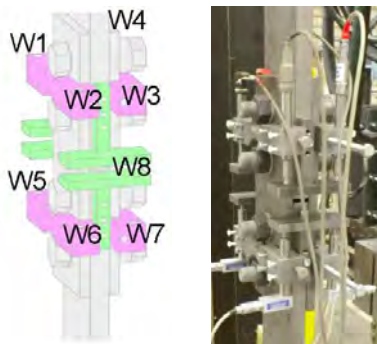


Figure 5: installation of eight-displacement transducer

Therewith it was possible, to record the behaviour of the lower and the upper part of the connection separately, so every test specimen included two independent results. When one part reached the slip load, it was fixed and a further load increase was possible until the second part failed.

The slip was taken as the relative displacement between adjacent points at an inner plate and an outer plate, measured in the direction of the load. The slip load for the connection was reached, when a slip of 0,15mm was measured. All bolts were prepared with strain gauges, which allow for an exact pretensioning of the bolts.

Short time tests

A typical slip deformation curve of a weathered specimen is given in **figure 6**. Slip occurred typically close to the ultimate load. The measured slip factor depends on the inconsistent surface of the weathered steel. In consequence, a great scatter in results occurs, the measured slip factor is between 0.59 and 0.72. **Table 4** gives the summary of the test series, where the characteristic slip factor μ_{stat} is given as 5%-fractile of the measured values. As the preloading of the surface, measured through the strain gauges in the bolts, slightly differ between the beginning of the test and at the ultimate state, an adjusted slip factor μ^*_{stat} with reference to the preload at ultimate state is given.

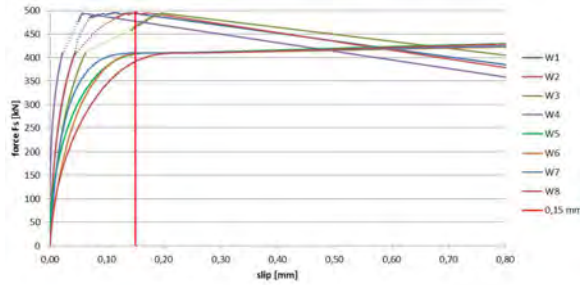


Figure 6 typical slip-force-behaviour of a weathered specimen V_bewitt_k_02

	F_{Sm}	$0,5 \cdot F_{Sm}$	SFS	μ_m	μ^*_m	S_μ	S_{μ^*}	μ_{stat}	μ^*_{stat}
blasted	417,05	208,53	49,36	0,61	0,65	0,07	0,08	0,46	0,49
coated	370,24	185,12	27,85	0,54	0,58	0,04	0,04	0,45	0,48
weathered	454,39	227,19	59,02	0,66	0,72	0,09	0,09	0,47	0,53

Table 4: static tests according to EN1090-2

It can be seen that the highest slip factors were achieved with the weathered surface, but due to the great scatter the fractile-values are reduced. The measured slip factors for the coated surface were the lowest, but due to the small scatter the fractile-values are in the range of the other surface types.

Long time (creep) tests

The aim was to determine a slip factor, which do not cause displacements greater than 0.3 mm during the design life of the structure, usually assumed to 50 years, **figure 7**. In view of the lifetime of bridges the extrapolation of test results was extended to 100 years. The creep load applied in the tests was chosen, considering the previously determined slip factor and a reduction ratio for permanent use in application.

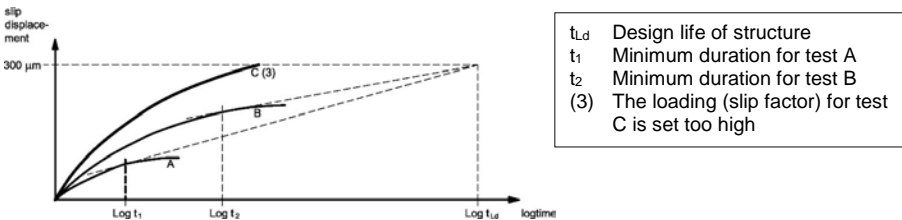


Figure 7: displacement-log time curve for extended creep tests (EN1090-2)

Accounting for efficient and cost reduced creep tests in short time, the test set-up was arranged to perform only one combined creep test for all three surfaces. Therefore, the specimens were arranged lying upon another so that they could be loaded simultaneously, **figure 8**. Therewith the whole duration of the creep tests could be

minimized to ten weeks. All specimens were initially loaded by the same load of 185 kN, which was the mean slip load of the static tests with the coated specimen.

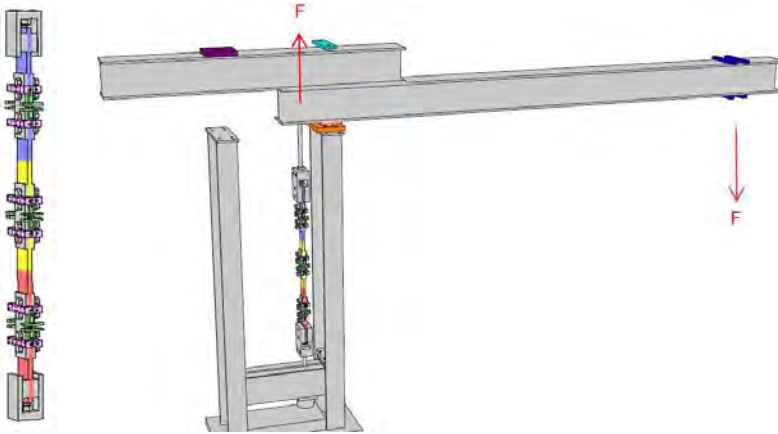


Figure 8: test setup for creep tests

Before the test load was applied, the bolts were preloaded and the loss of preloading was recorded after 72 hours, which was 2.72% for the weathered surface, 3.21% for the sandblasted surface and 4.15% for the coated surface. All bolts were then reloaded to 100% before the creep test began. During the ten weeks test period the loss in preloading decelerated for all specimens and was in the range of 7% at the end. The main loss of preloading caused by flattening of the prestressed surfaces seems to occur immediately after preloading.

As soon as the extrapolation to 100 years indicated deformations less than 0.3mm, the creep load was increased. At load level of 265 kN slip in the lower part of the coated test specimen occurred. At a load level of 345 kN, which corresponds to the mean 70% slip load of the weathered test specimen in the short time tests, the upper part of the coated specimen and the weathered specimen failed. At this load stage the creep test was finished. The deformation of sandblasted specimen of 0.07mm indicated full slip capacity. **Table 5** summarizes the creep test results in terms of allowable slip factors.

	$F_{si,up}$ [kN]	μ_{up}	μ_{up}^*	$F_{si,down}$ [kN]	μ_{down}	μ_{down}^*
blasted	> 345,00	> 0,50	> 0,53	> 345,00	> 0,50	> 0,53
coated	265,00	0,39	0,42	345,00	0,50	0,53
weathered	345,00	0,50	0,53	345,00	0,50	0,64

Table 5: summary results of creep tests

CONCLUSIONS

The corrosion protection of weathering steel depends on the corroded steel surface, the so-called patina. Weathering tests on plates made of weathering steel show that

the quality of the patina predominantly depends on the amount of sulfur dioxide SO₂. A specific amount of SO₂ is necessary to ensure the corrosion protection by the patina. Accelerated laboratory tests show good compliance with outdoor exposure tests, but they have to be refined in view of the macro- and microclimatic influences on the corrosion behaviour.

Tests concerning the slip resistance showed, that the weathered surface of weathering steel produce sufficient slip resistance without any additional treatment. Due to the great scatter in the weathered surface, further test series have to be performed to define slip factors depending on the specific surface characteristics. Especially the development of the slip factor at different periods of pre-weathering has to be examined systematically. As a general test result can be concluded, that a reloading of prestressed bolt after three days is always reasonable to achieve a durable 100% preloading.

ACKNOWLEDGEMENT

The authors gratefully acknowledge the financial support of the Research Association for Steel Application (FOSTA) through project P1150.

REFERENCES

FOSTA P1150: Ungermann, D. et al: Zur Verwendbarkeit von wetterfestem Baustahl im Brückenbau, to be published in 2016, FOSTA, Düsseldorf

Um (2014), Umweltbundesamt, trend graphs in the frame of the German report concerning the atmospheric pollution since 1990

EN 1090-2, 2011, Execution of steel structures and aluminum structures - Part 2: Technical requirements for steel structures

EN 1993-1-8, 2010, Eurocode 3: Design of steel structures - Part 1-8: Design of joints

EN 10025-5, 2011, Hot rolled products of structural steels. Technical delivery conditions for structural steels with improved atmospheric corrosion resistance

EN ISO 3231, 1998, Paints and varnishes. Determination of resistance to humid atmospheres containing sulfur dioxide.

EN ISO 6270-2, 2005, Paints and varnishes - Determination of resistance to humidity - Part 2: Procedure for exposing test specimens in condensation-water atmospheres

EN ISO 9223, 2012, Corrosion of metals and alloys – Corrosivity of atmospheres – Classification, determination and estimation

EN ISO 9224, 2012, Corrosion of metals and alloys – Corrosivity of atmospheres – Guiding values for the corrosivity categories

T-STUB JOINT COMPONENT SUBJECTED TO IMPACT LOADING

João Ribeiro

ISISE - Department of Civil Engineering, University of Coimbra, Portugal
joao.ribeiro@uc.pt

Aldina Santiago

ISISE - Department of Civil Engineering, University of Coimbra, Portugal
aldina@dec.uc.pt

Constança Rigueiro

ISISE – Polytechnic Institute of Castelo Branco, Portugal, Portugal
constanca@ipcb.pt

ABSTRACT

The importance of the ductility of connections for the robustness evaluation of structures has been highlighted in FEMA's report "*Connection performance under impact loads... needs to be analytically understood and quantified for improved design capabilities and performance as critical components in structural frames*". The design of moment-resisting steel joints is nowadays based on the "component method"; this method requires the accurate characterization of each active component. The T-stub model is used to describe the main components providing ductility to the joint due to its high deformation capacity. Nevertheless, connection ductility capacity characterization remains problematic, usually requiring the development of challenging finite-element models.

In this paper, the T-stub evaluation is improved with dynamic increase factors to predict its response when subject to rapidly applied dynamic loads. Exploring and improving an analytical procedure available in the literature, its whole non-linear behaviour is described. The results are compared with FE predictions and experimental results. This "modified analytical procedure" is able to describe the force-displacement response of the T-stub model for both static and dynamic situations with relevant accuracy. Finally, the model is implemented as a stand-alone application with a graphical user interface.

1. INTRODUCTION

Structural connection capacity when subject to impact loads remains a somewhat unclear theme in the robustness assessment of steel structures. Relevant literature in building robustness improvement (Ellingwood *et al.*, 2007) provides little guidance on this matter, forwarding load assessment to EC1-1-7:2006 and connection design to EC3-1-8:2005. However, both of these standards fail to provide accurate guidance of how to deal with connection design to impact loading regimes.

The design of moment-resisting steel joints under monotonic loading is based on the "component method" established in the EC3-1-8:2005. This method requires the accurate characterization (stiffness, resistance and ductility) of each active component (representing a specific part of a joint that makes a contribution to one or more of its structural properties); then, each component is characterised

as a bi-linear spring (force *versus* axial deformation); at the end, all springs are assembled into a connection model and the joint behaviour is calculated.

The T-stub model is used to describe the components in the tension zone of the joint, namely the end-plate in bending, column flange in bending and flange cleat in bending. The formulation to characterize it (design resistance and initial stiffness) is presented in chapters 6.2.4 and 6.3.2 of the EC3-1-8:2005. Concerning the rotational capacity, in chapter 6.4 of the same standard it is referred that the above components, additionally to the column's web in shear, are the components that provide the rotation capacity to a beam-to-column joint in bending. Nonetheless, guidance to predict its post-limit stiffness is still absent as well as its resistance under rapidly applied dynamic loads.

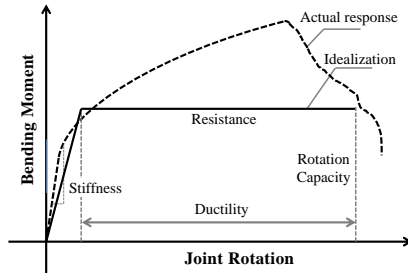


Figure 1 – Moment-rotation response of joint

This paper concerns the development of analytical procedures to describe the non-linear dynamic behaviour of the T-stub model. The analytical procedure based on yield-lines developed by Yu and co-authors (Yu *et al.*, 2009), is improved to account for high strain rate effects through the introduction of a variable to account for the time in which the loading (or displacement) is applied; a dynamic increase factor (DIF) independently affecting the behaviour of each plastic hinge and the bolt is calculated for each analysis increment.

2. ANALYTICAL PROCEDURES TO EVALUATE THE T-STUB RESPONSE

One of the first studies regarding the analytical procedures to evaluate the non-linear force-displacement curve of a T-stub until failure was developed by Faella and co-authors (Faella *et al.*, 2000). It considers the three possible failure modes, as established in EC3-1-8:2005, and thereafter calculates the ultimate rotation of each of the plastic hinges involved in the collapse mechanism. This approach is able to establish the force-displacement response through the integration of the curvature diagrams of each plastic hinge, up to failure of either the flange or the bolt, provided that a failure criterion is defined. Due to the closed form formulation, the authors derived the force-displacement response of T-stub's by calculating the force and displacement for each of the four characteristic points used to establish the material's description (Figure 2); this material description represents the non-linear strain-relationship of steel through 4 different slopes, including a yielding plateau.

Yu and co-authors (Yu *et al.*, 2009) followed an alternative, but similar, procedure to capture the behaviour of end-plate connection under large deformations. One of the main motivations to develop such model was the study of joints subject to elevated temperatures; in this situation, semi-rigid connections' behaviour under large deformations and its ductility capacity (i.e. rotation capacity

and failure mode) are required to establish the structural behaviour. The model consists on deriving the behaviour of simple yield-lines, which take material hardening into account, and use them as basic units to describe the response of end-plate connections.

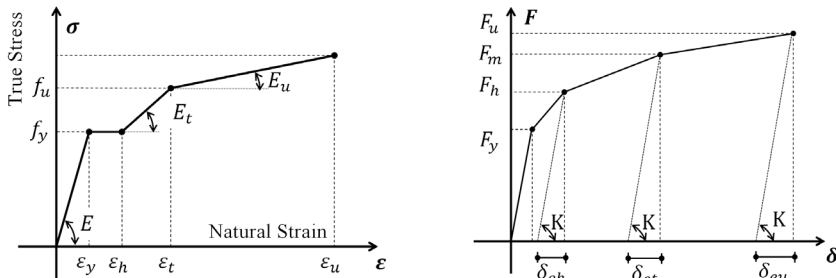


Figure 2 – a) Multi linear material description, and b) corresponding multi linear four forces versus displacement curve (Faella *et al.*, 2000).

Considering the T-stub model as a simplification of the behaviour of end-plate connection, the authors assessed the capabilities of the analytical procedure to describe the force-displacement response ($F - \delta$), by establishing yield-lines where plastic hinges (PH) are usually developed. Figure 3 presents the simplified half T-stub model considered in the analytical procedure where PH_1 represents the plastic hinge next to the weld toe, PH_2 is the plastic hinge in the bolt line, δ_b is the bolt's axial spring displacement, m is the distance between plastic hinges and n the distance between the prying force location and the bolt axis. The procedure is solved following the virtual work's principle of keeping the strain energy a minimum (Eq.(1)).

$$F \cdot \delta = W_{PH1} + W_{PH2} + W_{bolt} \quad (1)$$

The work for each plastic hinge is obtained by integrating the bending moment over the rotation, considering a three-phase elasto-plastic material model in Figure 4b), and a cross-section curvature as a function of the maximum strain in the cross-section; the three curvature diagrams presented in Figure 4a) are considered. The size of each plastic hinge is dependent on the parameter k describing the relative dimension of the plastic hinge length to the plate thickness; the increase of this value generates an increase in the displacement for the same load level. After calibration with experimental results, $k = 2$ has been conservatively adopted (Yu *et al.*, 2009). The bolt is represented by a spring with a similar strain hardening condition up to the bolt's peak force. A post-peak behaviour simulating the gradual necking and its progressive degradation was incorporated but bolt bending remains unaccounted for. 3D effects are taken into account based on the effective width. The model was found to be most appropriate for T-stubs with smaller effective width in which the bolt is able to effectively hold down the plate both in the edges and in the middle. The authors assessed the capabilities of this analytical procedure for a collection of T-stub responses available in the literature. This model is enlarged in the current paper to account for increased strain rate effects on the material.

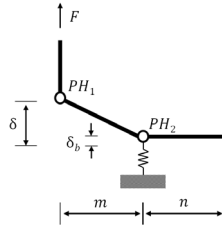


Figure 3 – Yield line model scheme of half the T-stub (Yu *et al.*, 2009)

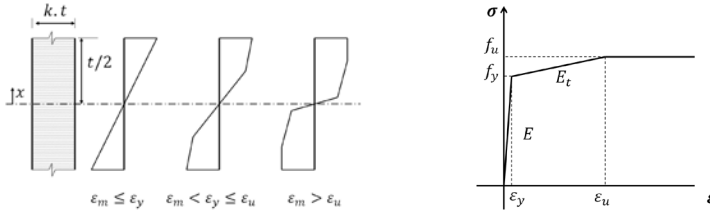


Figure 4 – a) Section stress distributions considered in the model; b) tri-linear material model (Yu *et al.*, 2009).

3. STRAIN RATE EVALUATION

Strain rate is the deformation, *i.e.* strain variation, that a material is subject per time unit, $d\epsilon/dt$. Most ductile materials have strength properties which are dependent on the loading speed, and mild steel is known to have its flow stress affected. The effect of increasing strain rates on the stress-strain relationship of steel are illustrated in Figure 5a). The presented true stress-logarithmic strain curves have been obtained from an experimental program carried out at the University of Coimbra (Saraiva, 2012). A Universal Tensile Machine has been used for the quasi-static tests, based on a displacement control loading at low speed of 0.03 mm/s ($\dot{\epsilon} = 0.001 \text{ s}^{-1}$) to emulate the static response of the steel; for the dynamic properties assessment, compressive Split Hopkinson Pressure Bar (SHPB) tests were conducted at an average strain rate around $\dot{\epsilon} = 600/\text{s}$, which is in the range of impact loading (Riisgard *et al.*, 2007). Steel coupons have been made from the same raw steel plates used to build the tested T-stub specimen: steel grade S355. The results are in line with what is observed by other researchers in similar tests (Jones, 2012):

- i. the yield and ultimate strengths (f_y, f_u) increase beyond the results obtained under quasi-static loading;
- ii. the total strain on rupture (ϵ_u) decreases;
- iii. the elastic modulus (E) remains unchanged for different loading rates.

Usually the effects of elevated strain rates are incorporated on the models by a “dynamic increase factor” (DIF), which will promote the increase of the elastic and ultimate strengths based on the ratio of the strength observed dynamically (σ_{dyn}) and statically (σ), Eq. (2):

$$DIF = \frac{\sigma_{dyn}}{\sigma} \quad (2)$$

Based on the static ($\dot{\epsilon}_0 = 0.001 \text{ s}^{-1}$) and dynamic ($\dot{\epsilon}_0 = 600 \text{ s}^{-1}$) stress-strain relationships, the Johnson-Cook model (Johnson & Cook, 1983) (Eq. (3)) has

been used to describe the DIF_{steel} for intermediate strain rate values (Figure 5b).

$$\sigma = [A + B\varepsilon^n] \cdot [1 + C \ln \dot{\varepsilon}^*] \cdot [1 - (T^*)^m] \quad (3)$$

where: A is the quasi-static yield strength; B and n represent the effects of strain hardening; m is the thermal softening fraction; T^* is a non-dimensional parameter defined based on the melting and transition temperatures to take account for material softening due to temperature variation; ε is the equivalent plastic strain; $\dot{\varepsilon}$ is the strain rate; $\dot{\varepsilon}^* = \dot{\varepsilon}/\dot{\varepsilon}_0$ is the reference dimensionless plastic strain rate (assumed as $\dot{\varepsilon}_0 = 0.001 \text{ s}^{-1}$) and C is the strain rate constant. Calibration of parameter C yielded $C_{steel} = 0.039$ for steel S355. Because no experimental evaluations were performed for the bolt material M20, grade 8,8, a maximum DIF_{bolt} of 1.1 is considered according to the literature (Ellingwood *et al.*, 2007), thus $C_{bolt} = 0.0072$ is found.

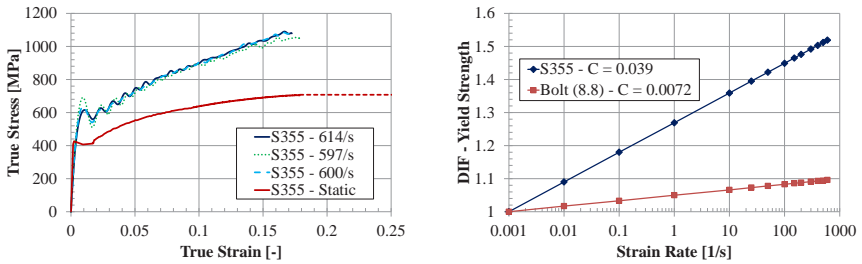


Figure 5 – a) Effects of strain rate on the behaviour of mild steel (Saraiva, 2012); b) Dynamic increase factor (DIF) of the yield strength as function of the strain rate.

4. EXPERIMENTS AND NUMERICAL STUDIES

4.1 Experimental tests

The T-stub typologies used to validate the analytical proposals are extracted from previous experimental and numerical studies carried out at the University of Coimbra (Ribeiro *et al.*, 2015). The experimental specimen consists of a T-stub defined by two plates, the flange and the web, welded by means of a continuous 45° fillet (a_w), as illustrated in Figure 6. Under quasi-static loading, two geometries are considered: T-10 ($t_f = 10 \text{ mm}$) and T-15 ($t_f = 15 \text{ mm}$), while for impact loading, the study is focused only on T-10; for both specimens the steel grade is S355 and the bolts is M20 grade 8,8, fully threaded.

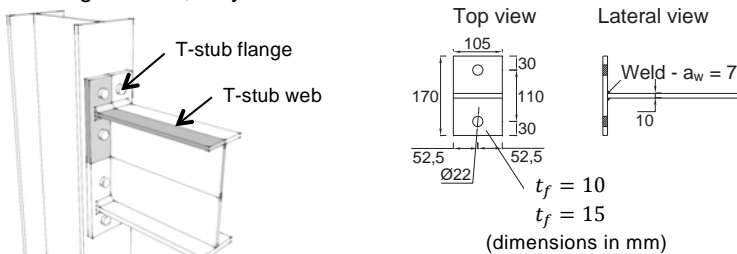


Figure 6 – a) T-stub fragment from a beam-to-column joint; b) T-stub geometry (Ribeiro *et al.*, 2015).

The experimental layout used to perform the experimental tests is depicted in Figure 7. It consists of a very stiff structure (shown in grey colour) anchored to the floor slab of the laboratory; the loading mechanism is based on the principle of a 2nd class lever: the yellow beam (flying beam) is loaded in one end by a loading device (pneumatic cylinder - red colour) and it rotates around the pivot axis in the other end. The tested T-stub (shown in blue in the middle of the testing layout) is limited by two additional pins in its end, assuring the transfer of axial tensile forces only.

During the quasi-static tests, the load is gradually applied under displacement control with a speed of 0.02mm/s until failure; whilst during the impact tests, two different load levels are considered: gas pressures of 12 MPa (Impact #1 of T-10-D120-160) and 16 MPa (Impact #1 of T-10-D160).

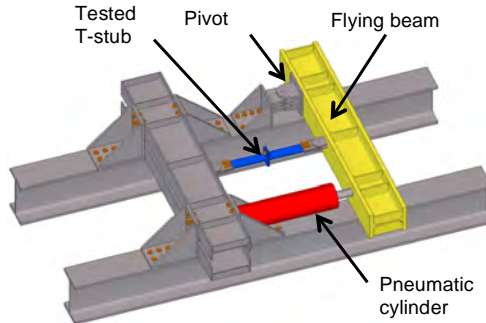


Figure 7 - Experimental test layout.

4.2 Numerical modelling

Numerical evaluation of the response of the T-stub has been carried out with software ABAQUS (Abaqus, 2011) with a dynamic/implicit algorithm.

The T-stub model is a simplified, individualized and symmetric geometry of the tested T-stub presented in the previous section. Figure 8 shows the numerical model's boundary condition and mesh discretization.

Material nonlinearity is included by specifying a non-linear stress-strain relationship for material hardening; von Mises criterion is considered to establish the yield surfaces with the associated plastic flow for isotropic materials. Stress-strain relationship for base steel and bolts has been obtained through uniaxial coupon tests and input in the form of *true-stress – logarithmic plastic strain* curves; strain rate effects discussed in Section 3 for the mild steel and bolts are included following Eq. 8. The welds are assumed to have the same strain-rate sensitivity as the base steel. Figure 9a) presents the material non-linear stress-strain relationship input in the numerical models. Additionally, a failure criterion based on continuum damage mechanics (Lemaitre, 1992) with element deletion technique has been introduced; the intention is to model the material's stiffness degradation (i.e. the softening branch of the stress-strain relationship beyond the ultimate tensile strength (more details are available in Ribeiro *et al.*, 2016).

Concerning the applied loading, a displacement based loading following the experimental scheme, was considered in the quasi-static simulations while, in the dynamic simulations, transient displacement curves (that were measured in the experimental tests) have been applied as a boundary condition (Figure 9b).

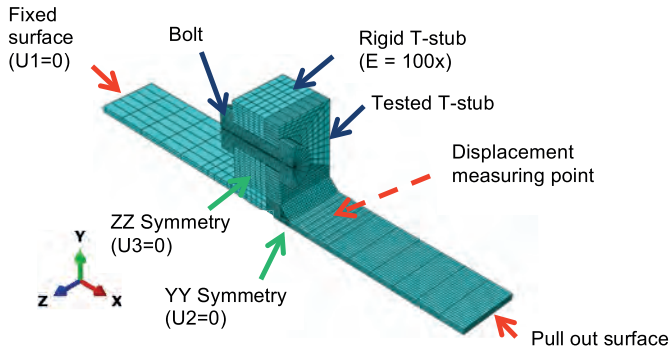


Figure 8 – Numerical model, boundary condition and mesh discretization.

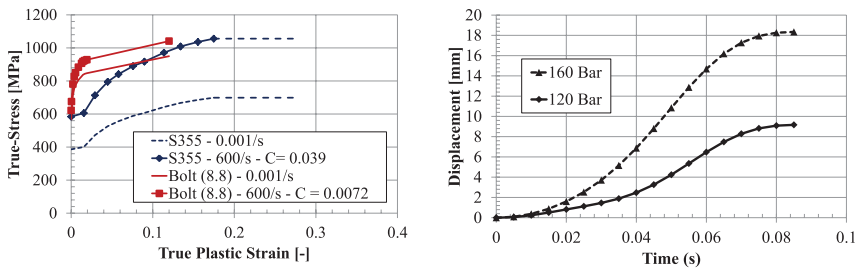


Figure 9 – a) Stress-strain relationship for steel and bolts considering strain-rate sensitivity; b) Dynamic simulations: T-stub displacement curves measured experimentally and used for displacement based loading application in FEA.

5. PROPOSED ANALYTICAL PROCEDURES TO EVALUATE THE T-STUB RESPONSE UNDER IMPACT LOADING

5.1 Analytical approach to evaluate the non-linear response of the T-stub

An analytical approach to evaluate the full response of a T-stub under impact loading is proposed. It is based on the work performed by Yu (Yu *et al.*, 2009) presented in Section 2, but considering a time dependency: $\dot{\epsilon} = d\epsilon/dt$.

Firstly, it is assumed that a total displacement (δ) occurs in a given total amount of time (Δt). Then, the analysis is divided in a “step by step” analysis and the displacement (δ_i) is considered to occur in a time step (Δt_i), calculated by linearly discretizing δ and Δt in the number of computed increments (n). This stepwise development allows the computation of the induced strain rate on each step ($\dot{\epsilon}_i$), by calculating the additional rotation required to meet equilibrium (Eq. (4)), and updating the maximum strain. The added strain for the current step ($\epsilon_{m,(i)}$) is assumed to be developed in the time step (Δt_i) allowing the computation of the strain rate $\dot{\epsilon}_i$. Thus a different DIF for each increment ($DIF_{step,i}$) is calculated and applied in the material strength. The proposed procedure is summarized in the flowchart of Figure 10 (for more information see Ribeiro *et al.*, 2015).

$$\frac{\partial(W_{PH1} + W_{PH2} + W_b)}{\partial \delta_b} + 0 \quad (4)$$

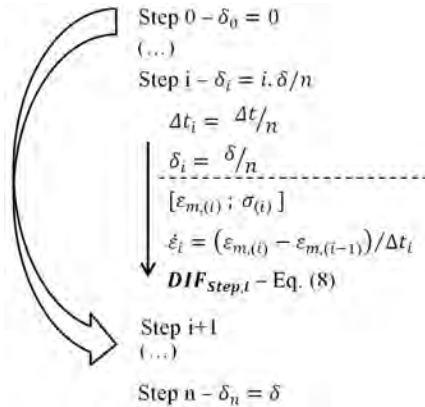


Figure 10 - Application of strain rate effects – Flowchart

5.2 T-stub under quasi-static loading

Figure 11a) compares the quasi-static responses obtained experimentally, numerically and analytically. The triangular markers point out the instant where the maximum force is attained within the analytical procedure. From the results, it is observed that the non-linear approach is able to provide approximate results for estimation of the $F - \delta$ response. For T-10, the analytical model provides rather conservative prediction of the maximum load as the maximum strength is limited by the two plastic hinges developed per flange leg, conditioning the T-stub's displacement to the PH's rotation, thus hindering the bolts' greater resistance to be mobilized. For T-15, this prediction is more accurate, although for a smaller displacement, from which point on a negative stiffness develops as a result of the necking and progressive degradation routine implemented on the bolt spring (Ribeiro *et al.*, 2015).

5.3 T-stub under impact loading

In Figure 11, the T-stub responses (T-10) under impact loading are compared. Static curves are represented by the blue lines, while the red lines correspond to the dynamic curves. Examination of the non-linear analytical curves indicates a good agreement with the experimental and numerical results.

Comparing the peak resistance force values obtained from the non-linear approach, an increase of $256/205 = 24\%$ is observed in the dynamic results. Dynamic effects on the ductility cannot be compared as no failure is observed in the dynamic experimental tests.

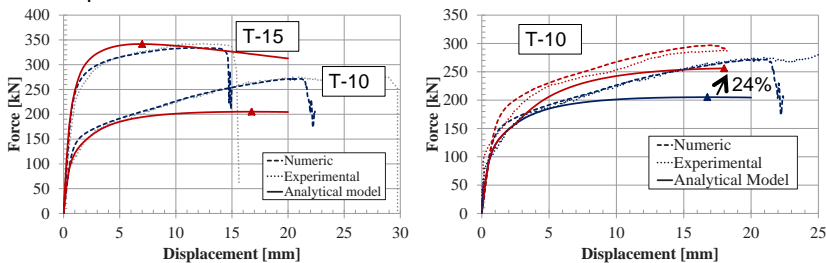


Figure 11 – T-stub $F - \delta$ response: a) quasi-static response; b) dynamic response T-10

6. GRAPHICAL INTERFACE

Looking forward to improve the usage of the developed model, a Graphical User Interface (GUI) has been built. The main objective is to provide means of easily introducing the data required for the calculation process and to visualize the results, within a stand-alone application. The GUI is built using the development platform QT (<http://www.qt.io/>) which includes a set of pre-programmed widgets allowing for a fast and intuitive development. Using the module *Pyuic4* it is possible to convert the generated code to the programming language *python* in which the model has been implemented.

The graphical interface is presented in figures 12 and 13. It consists of four different tabs: i) *Bolt properties*; ii) *T-stub properties*; iii) *Results* and iv) *Help*. The first two allow the user to introduce the geometric and material properties of the bolt and the T-stub (Figure 12); the third presents the loading parameters and the results in the form of force vs. displacement curves (using *matplotlib*) (Figure 13); the *Help* tab provides additional information on the software. This software may be found on the following link: <https://www.dropbox.com/s/mjq2qjaowp6kvni/Impact-T-stub-v01.rar?dl=0>

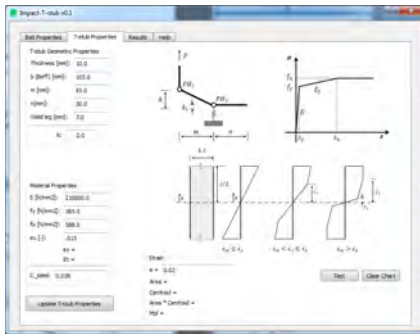


Figure 12 – "T-stub properties" tab

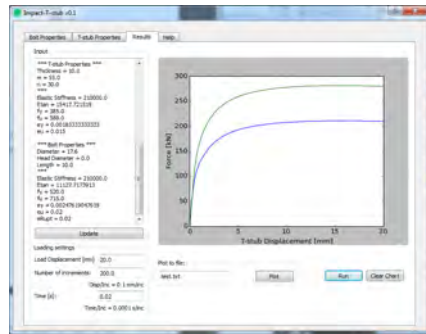


Figure 13 – "Results" tab

7. CONCLUSIONS

An assessment of the T-stub model behaviour subject to rapidly applied loads is performed based on the yield and ultimate strength enhancement through dynamic increase factors by exploring and improving a non-linear analytical approach available in the literature to describe its full response.

Firstly, the T-stub was evaluated for monotonic load cases using a non-linear analytical approach and the results were compared against numerical and experimental ones. Later, the model was modified to take into account the effects of high strain rates on the material's stress-strain relationship, by means of dynamic increase factors. The major contribution of this method is the stepwise calculation which allows the computation of the strain rate at each displacement increment, obtained by the linear decomposition of a pre-defined total time frame. Application of 18 mm displacement in 80 ms, as recorded during experimental testing, are studied for a T-stub flange thickness of 10 mm and conservative results are obtained when compared with non-linear dynamic finite-element analyses and experimental results.

Finally, the model is implemented as a stand-alone application with a graphical user interface.

ACKNOWLEDGMENT

This work was partly financed by FEDER funds through the Competitiveness Operational Programme - COMPETE and by national funds through FCT – Foundation for Science and Technology within the scope of the project POCI-01-0145-FEDER-007633.

REFERENCES

- Abaqus, 2011. *Karlsson & Sorensen, Abaqus Theory Manual*, v.6.11.
- CEN, 2005. *EN 1993-1-8, Eurocode 3: Design of steel structures Part 1-8: Design of joints..*
- CEN, 2006. *EN 1991-1-7, Eurocode 1: Actions on structures. Part 1-7, General actions - Accidental actions.*
- Ellingwood, B. et al., 2007. *Best Practices for Reducing the Potential for Progressive Collapse in Buildings*. NISTIR 7396.
- Faella, C., Piluso, V. & Rizzano, G., 2000. *Structural Steel Semi-Rigid Connections*. Boca Raton: CRC Press.
- Johnson, G. & Cook, W., 1983. *A constitutive model and data for metals subjected to large strains, high strain rates and high temperatures*. The Hague, The Netherlands, Proceedings of the 7th International Symposium on Ballistics, pp. 541-547.
- Jones, N., 2012. *Structural Impact*. Cambridge, UK, : Cambridge University Press.
- Lemaitre, J., 1992. *A Course on Damage Mechanics*. Springer.
- Ribeiro, J., Santiago, A., Rigueiro, C. & Veljkovic, M., 2016. Numerical assessment of T-stub component subjected to impact loading.. *Engineering Structures*, Volume 106, pp. 450-460.
- Ribeiro, J., Santiago, A., Rigueiro, C. & Simões da Silva, L., 2015. Analytical model for the response of T-stub joint component under impact loading.. *Journal of Constructional Steel Research*, Volume 106, pp. 23-34.
- Riisgard, B. et al., 2007. *Dynamic Increase factors for high performance concrete in compression using split Hopkinson pressure bar*. Catania, Italy, 6th International Conference on Fracture Mechanics of Concrete and Concrete Structures.
- Saraiva, E., 2012. *Variação das propriedades mecânicas do aço relacionadas com problemas de impacto em estruturas*.
- Yu, H., Burgess, I., Davison, J. & Plank, R., 2009. Development of a yield-line model for endplate connections in fire. *Journal of Constructional Steel Research*, Volume 65, pp. 1279-1289.

DEFORMATION LIMITS AND ROTATIONAL CAPACITIES FOR CONNECTIONS UNDER COLUMN LOSS

Jonathan M. Weigand

National Institute of Standards and Technology, Gaithersburg, MD 20899 USA
jonathan.weigand@nist.gov

Joseph A. Main

National Institute of Standards and Technology, Gaithersburg, MD 20899 USA
joseph.main@nist.gov

ABSTRACT

For structural steel framing systems subjected to column loss, the ultimate gravity load carrying capacity of the system is often controlled by the rotation and deformation capacities of the connections within the affected bays. Within current design specifications, the potential for disproportionate collapse in structural design is evaluated by notionally removing critical load supporting elements from the structure, and designing the structure to sustain the applicable gravity loads without collapse via the alternative load path analysis method. Steel gravity framing systems subjected to column loss undergo large vertical deflections under gravity loads that induce large rotation and axial deformation demands on the connections. However, the acceptance criteria currently used to evaluate connection failure in alternative load path analysis are based on results from seismic testing that do not reflect the large axial demands imposed on the connections. Recent experimental data have shown that application of these rotation limits to column loss scenarios in steel gravity framing systems can be non-conservative. In this paper, experimental data from steel single-plate shear connections tested under column loss are compared to the rotation limits provided in existing standards, and the factors influencing the widely varying levels of conservatism for different connection geometries are explained. A new approach for calculating acceptance criteria for steel gravity connections under column loss is also introduced. The new approach provides more risk consistency and accounts for the important influence of axial deformation demands on the connections.

INTRODUCTION

Some building owners in the United States (e.g., the General Services Administration and the Department of Defense (DoD)) and certain jurisdictions (e.g., New York City) currently require buildings to be designed to resist disproportionate collapse. To evaluate the potential for disproportionate collapse in design, engineers rely on the alternative load path analysis method (see e.g. DoD (2009)), in which individual load-bearing elements

are notionally removed from the structure, and the remaining structure is designed to support the applicable gravity load combination without collapse. For steel frames designed to support only gravity loads, the steel shear connections play a critical role in ensuring the system robustness and stability. Large-scale tests of steel gravity framing systems under column removal (Johnson et al. 2014; Johnson et al. 2015) have shown that the system robustness depends on the capacity of the connections to resist axial loads after undergoing large rotation and axial displacement demands.

Current acceptance criteria for steel connections, which are used to evaluate connection failure in alternative load path analysis, take the form of rotation limits. These rotation limits are based almost entirely on results from seismic testing. In such seismic tests, the connections are typically subjected to rotation cycles of increasing magnitude until failure. These test conditions (1) result in low-cycle fatigue of the connection components, which is not relevant to column loss, and (2) do not reflect the large axial demands placed on the connections under column loss. While the increased plastic deformations associated with low-cycle fatigue may partially compensate for the lack of axial demands, recent experimental data have shown that direct application of seismic rotation limits to column loss scenarios in steel gravity framing systems can be non-conservative. Thus a better approach for calculating rotation limits for connections under column loss is needed.

In this paper, experimental data from steel single-plate shear connections tested under column loss (Weigand and Berman 2014) are compared to the rotation limits provided in standards for seismic evaluation and retrofit of existing buildings and for alternative load path analysis. Widely varying levels of conservatism are observed for different connections, and the factors contributing to this variability are discussed. To address the issues with the existing acceptance criteria, a new approach for calculating rotation limits for steel gravity connections under column loss is introduced. The new approach accounts for the influence of axial deformation demands on the connections and provides more risk consistency in the evaluation of connection failure under column loss.

COMPARISON OF EXPERIMENTAL DATA WITH CURRENT ROTATION LIMITS

Several existing specifications incorporate rotation limits for various types of steel connections; however, the applicability of these rotation limits to connections subjected to column loss needs to be considered carefully. The American Society of Civil Engineers (ASCE/SEI) 41-13 *Seismic Evaluation and Retrofit of Existing Buildings* (ASCE 2013) provides rotation limits for different connection types derived from tests of connection subassemblies under rotation cycles of increasing magnitude without axial restraint. These rotation limits depend only on the connection type and the depth of the connection bolt group, and thus have a number of deficiencies when considering their applicability to column loss, including the following:

1. they do not account for changes in connection geometry (e.g., changes in bolt diameter, thickness of the shear plate), which strongly influences the connection rotational capacity,

2. they do not include the effects of axial demands on the connections, and
3. they do not account for the effect of span length.

The Unified Facilities Criteria (UFC) 4-023-03 *Design of Buildings to Resist Progressive Collapse* (DoD 2009), which covers buildings under the jurisdiction of the DoD, adopted life-safety rotation limits from ASCE/SEI 41-13 for most connections, but provided reduced rotation limits for specific connection types including welded unreinforced flange, bolted web moment connections, reduced beam section moment connections, and single-plate shear connections. The rotation limits specified for these connection types in the UFC 4-023-03 were reduced relative to ASCE 41-13 based on a series of tests on connections subjected to blast and/or column removal conducted by the U.S. Defense Threat Reduction Agency and analyses performed by Myers, Houghton & Partners (Karns et al. 2008). Fig. 1 shows a comparison between the applicable acceptance criteria and measured rotational capacities for single-plate shear connections under column loss from Weigand and Berman (2014). The uncertainty in the experimental data was estimated as $\pm 1\%$ (Weigand and Berman, 2016). The acceptance criteria, which are shown as dashed lines, include rotation limits from ASCE/SEI 41-13 for both life safety (labeled ASCE 41-LS) and collapse prevention (labeled ASCE 41-CP), as well as rotation limits from UFC 4-023-03 for primary members (labeled UFC-Primary) and for secondary members (labeled UFC-Secondary). The UFC-Secondary line is the same as the ASCE 41-LS line. The equations used to calculate the rotation limits are shown in Table 1.

Fig. 1 shows that the ASCE 41 rotation limits would be unconservative if applied directly to consider column loss (i.e., they would predict larger rotational capacities than single-plate shear connections can actually sustain). The UFC-Primary rotation limits are conservative when compared to the measured rotational capacities, but the amount of conservatism (i.e., the amount that the measured rotational capacities lie above the UFC-Primary line) vary widely for the different connections, which had different geometries (span, plate thickness, thread-condition, etc.). The connections with the least conservatism had either the longest spans or threads included in the shear plane.

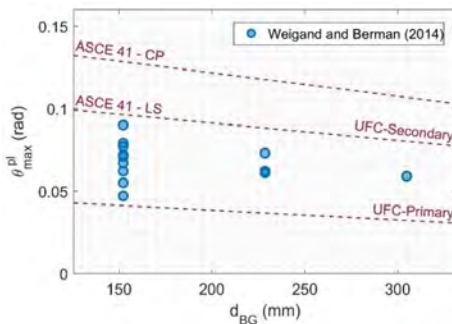


Figure 1: Comparison between rotation limits from ASCE/SEI 41 and UFC 4-023-03 and measured rotational capacities for connections subjected to column loss, as a function of the depth of the bolt group, d_{BG} .

Table 1: Specified Rotational Capacities for Single-Plate Shear Connections from ASCE 41-13 and UFC 4-023-03 (d_{BG} is the depth of the connection bolt group in mm).

Specification	Condition	Rotation Limit
ASCE 41-13	Life-Safety	$\theta_{\max}^{\text{pl}} = 0.1125 - (0.0001063 \text{ mm}^{-1})d_{BG}$
	Collapse Prevention	$\theta_{\max}^{\text{pl}} = 0.1500 - (0.0001417 \text{ mm}^{-1})d_{BG}$
UFC 4-023-03	Secondary Members	$\theta_{\max}^{\text{pl}} = 0.1125 - (0.0001063 \text{ mm}^{-1})d_{BG}$
	Primary Members	$\theta_{\max}^{\text{pl}} = 0.0502 - (0.0000591 \text{ mm}^{-1})d_{BG}$

A new standard, which is intended to specifically address disproportionate collapse, the *ASCE/SEI Standard for Mitigation of Disproportionate Collapse*, is currently under development. However, much of the existing guidance is still based on the ASCE/SEI 41-13 acceptance criteria. The new approach presented in this paper for calculating rotation limits for single-plate shear connections is based on the kinematics of connection response to column loss, and provides capabilities to overcome the deficiencies discussed above.

COMPONENT-BASED ANALYSIS OF FACTORS AFFECTING ROTATION LIMITS

Fig. 1 demonstrates that the amount of conservatism between the measured connection rotational capacities and the rotation limits specified in ASCE/SEI 41-13 and UFC 4-023-03 vary as a function of connection geometry. However, Fig. 1 only includes the specific connection geometries tested by Weigand and Berman (2014). Here, additional connection geometries are considered to answer two key questions:

1. What if the beam spans were longer?
2. What if the bolt threads were included in the shear plane?

Because experimental data are not available for these geometries, a component-based model for single-plate shear connections developed by Weigand (2016) is used to answer these two questions. In the component-based connection model, the connection is discretized into an arrangement of component springs that geometrically resembles the connection, where each component spring embodies a single bolt and characteristic-width segments of the shear plate and beam web (Fig. 2(a)). The component-based connection model was already validated against all 13 of the single-plate shear connection tests from Weigand and Berman (2014), and shown to predict their capacities within an average of 10 % (e.g., see Figs. 2(b) and 2(c)), using only the connection geometry, material properties, and applied loading (see Weigand (2014) for more details).

Fig. 3(a) shows the measured rotational capacities from Weigand and Berman (2014), with span length differentiated by marker color (all except one connection had threads excluded from the shear plane), Fig. 3(b) shows calculated rotational capacities for connections with 3.66 m (12 ft) longer spans (i.e., 12.8 m (42 ft) and 18.3 m (60 ft) spans) and all other connection geometry held constant, Fig. 3(c) shows calculated rotational capacities for connections with threads included in the shear plane, and Fig. 3(d) shows

calculated rotational capacities for connections with threads included and with the 3.66 m (12 ft) longer spans. Comparison of Figs. 3(a) and 3(b) shows that increasing the span would reduce the rotational capacities for all connections, and that one 3-bolt connection rotational capacity would actually fall below the UFC-Primary acceptance criteria. Comparison of Figs. 3(a) and 3(c) shows that including threads in the shear plane would also reduce the rotational capacities for all connections, and that four of the connection rotational capacities would fall below the UFC-Primary acceptance criteria. Including threads in the shear plane had a larger influence on the connection rotational capacities than did increasing the span (inferred by comparing Figs. 3(b) and 3(c)). Fig. 3(d) shows that connections having both threads included in the shear plane and long spans are particularly vulnerable to having rotational capacities that are non-conservative, relative to the UFC-Primary acceptance criteria (seven out of the total thirteen connection rotational capacities fall below the UFC-Primary acceptance criteria). This demonstrated potential for the rotational capacities of realistic connection geometries to be predicted non-conservatively by the most stringent current acceptance criteria (UFC-Primary) motivates the need for a better approach for calculating connection rotational capacities.

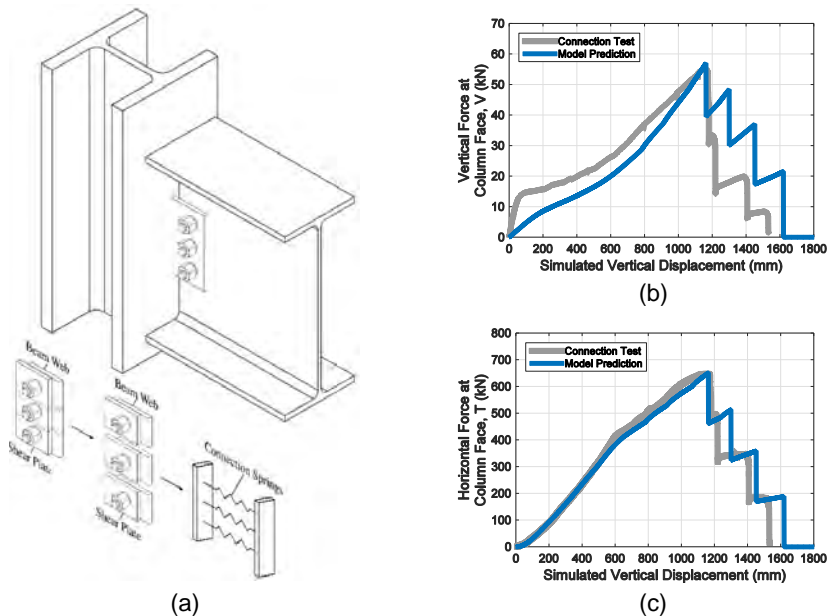


Figure 2: (a) discretization of single-plate shear connection into individual bolt-widths, (b) comparison of predicted vertical force-displacement response with connection data and (c) comparison of predicted horizontal force-displacement response from component-based model with connection data.

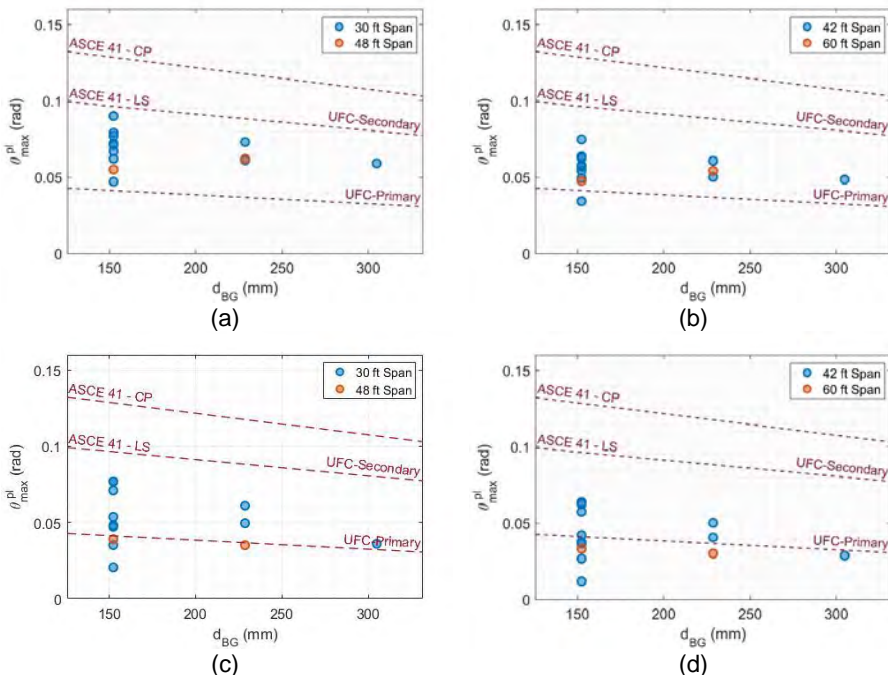


Figure 3: (a) Experimental data; calculated rotational capacities for, (b) increased span lengths and threads excluded from shear plane, (c) threads included in shear plane, and (d) increased span lengths and threads included in shear plane.

ANALYTICAL DERIVATION OF ROTATION LIMITS UNDER COLUMN LOSS

For frames designed to support gravity loads only, loss of a column results in large vertical deflections at the missing column that impose significant rotational demands on the connections. Significant axial demands can also be imposed, depending on the degree of restraint provided by the surrounding structure. Where the connections are discontinuous through the unsupported column (e.g., for a corner column loss scenario) minimal axial restraint is provided, and thus the axial demands are small. However, where the connections span continuously through the unsupported column (e.g., for an interior column loss scenario), the axial restraint provided by the surrounding structure can subject the connections to significant axial deformations in combination with large rotations. Fig. 4(a) illustrates the limiting case of no axial restraint, where the end columns are free to translate horizontally in-plane and the connections are subjected only to monotonically increasing rotation until failure. Fig. 4(b) illustrates the limiting case of perfect axial restraint, where translation of the column ends is prevented.

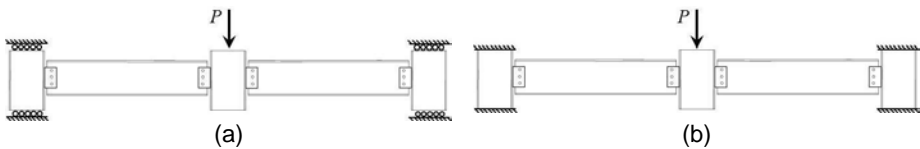


Figure 4: Column loss scenarios with (a) no axial restraint and (b) axial restraint.

The rotational demands imposed on the connections can be calculated in terms of the vertical deflection of the missing column, Δ , as

$$\theta = \tan^{-1} \left(\frac{\Delta}{L_r} \right), \quad (1)$$

where L_r is the distance between the centers of the bolt groups at the ends of the framing members in the undeformed configuration (Fig. 5). For the condition without axial restraint (Fig. 4(a)), no axial demands are imposed on the connections. For the condition with axial restraint (Fig. 4(b)), an axial deformation δ is imposed on each connection (see Fig. 5), which can be calculated as follows:

$$\delta = \frac{L_r}{2} \left[\sqrt{1 + \left(\frac{\Delta}{L_r} \right)^2} - 1 \right]. \quad (2)$$

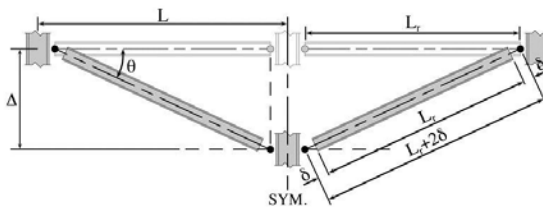


Figure 5: Connection demands based on vertical deflection of the missing column.

For both axial restraint conditions, the axial deformation of each connection spring (see Fig. 2(a)) can be calculated in terms of θ and δ as:

$$\delta_j = \delta + y_j \sin \theta, \quad (3)$$

where y_j denotes the vertical distance from the j^{th} connection spring to the center of the bolt group. Eqs. (1) - (3) are based on the assumption that the beams are rigid relative to the connections, so that the rotations and deformations localize in the connections. This rigid-body assumption is further discussed by Weigand and Berman (2014), including validation of the assumption through comparison with experimental measurements.

For the condition without axial restraint (i.e., $\delta = 0$), the connection spring deformations from Eq. (3) are essentially linear with increasing rotation (Fig. 6(a)). For the condition with axial restraint, δ is calculated from Eq. (2), and larger tensile deformations of the component springs are observed for a given level of rotation (Fig. 6(b)), relative to the case without axial restraint. Because of the dependence of Eq. (2) on the span length, larger span lengths result in increased tensile deformations of the component springs.

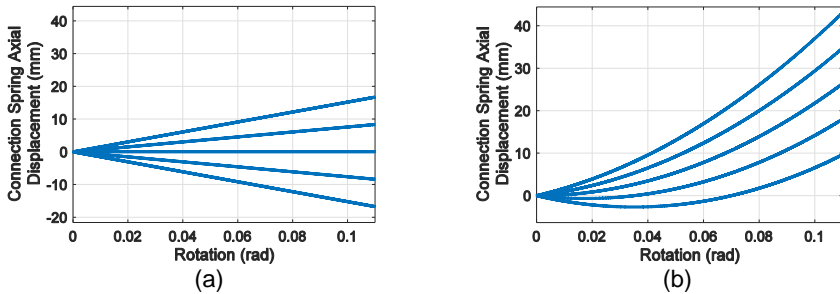


Figure 6: axial deformations of connection segments, δ_j , with (a) $\delta = 0$, and (b) $\delta \neq 0$.

If the limiting axial deformation for a single bolt row of a connection, δ_u , is known, either from experiments or from computational modeling, then the corresponding rotation limit for the connection, θ_u , can be calculated. The rotation limit, θ_u , corresponds to the configuration in which the axial deformation of an extreme bolt row (lowest or highest) reaches δ_u . Setting $y_j = d_{BG}/2$ in Eq. (3) for the extreme bolt row and introducing the small-angle approximation $\sin(\theta) \approx \theta$ allows Eq. (3) to be solved for θ_u , as

$$\theta_u = \frac{2(\delta_u - \delta)}{d_{BG}} . \quad (4)$$

For the condition without axial restraint (i.e., $\delta = 0$), Eq. (4) reduces to $\theta_u = 2\delta_u/d_{BG}$. For the condition with axial restraint, substituting Eq. (2) into Eq. (4), introducing small-angle approximations, and neglecting higher-order terms (see Main and Sadek (2012) for more details), results in a quadratic equation for θ_u that yields the following positive root:

$$\theta_u = 2\sqrt{\left(\frac{d_{BG}}{2L}\right)^2 + \frac{\delta_u}{L}\left(1 + \frac{\delta_u}{L}\right)} - \frac{d_{BG}}{L} . \quad (5)$$

Fig. 7 compares solution curves calculated from Eq. (5) against measured rotation limits for single-plate shear connections subjected to column loss from Weigand and Berman (2014), for 3-bolt and 4-bolt connections with 9.1 m (30 ft) and 14.6 m (48 ft) spans. Fig. 7 verifies that the rigid-body model provides a close approximation to the measured rotation at connection failure, as demonstrated by the close proximity of the connection data (circular markers) to the solution curves. The solution curves are also shown to be slightly conservative relative to the experimental data (i.e., the solution curves are consistently below the experimental data), which is expected based on the rigid-body model and the assumed perfect axial restraint.

By using Eq. (5), along with average measured values of the limiting axial deformation δ_u for different groups of connections tested by Weigand and Berman (2014), rotational capacities can be calculated and compared with the experimental data (Fig. 8). Compared with the wide scatter of the experimental data relative to current rotation limits (Fig. 1), Fig. 8 shows that Eq. (5) provides significantly improved consistency with the experimental data. The improved consistency is achieved by accounting for the influences of axial restraint, span length, and connection geometry, factors which current rotation

limits used in alternative load path analysis do not directly consider. Fig. 8 shows that Eq. (5) is conservative relative to the experimental data for all but one test, with the slight non-conservatism in that case resulting from the use of the average measured value for δ_u . Uncertainty in the deformation limit δ_u is the key factor affecting the uncertainty in the calculated rotational capacities. In selecting appropriate values of δ_u to use in design, uncertainty in the value of δ_u should be considered to ensure consistent reliability.

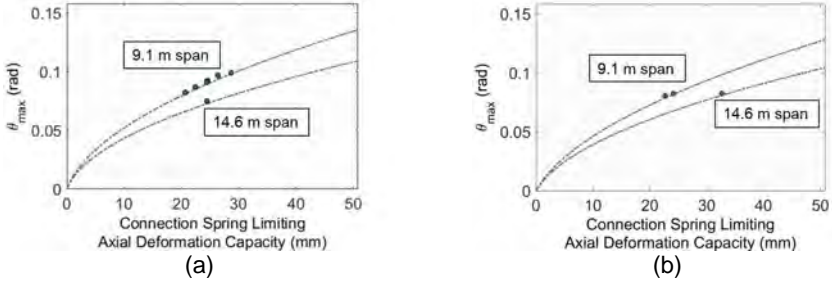


Figure 7: Comparison between Eq. (5) and measured rotational capacities for (a) 3-bolt single-plate shear connections and (b) 4-bolt single-plate shear connections.

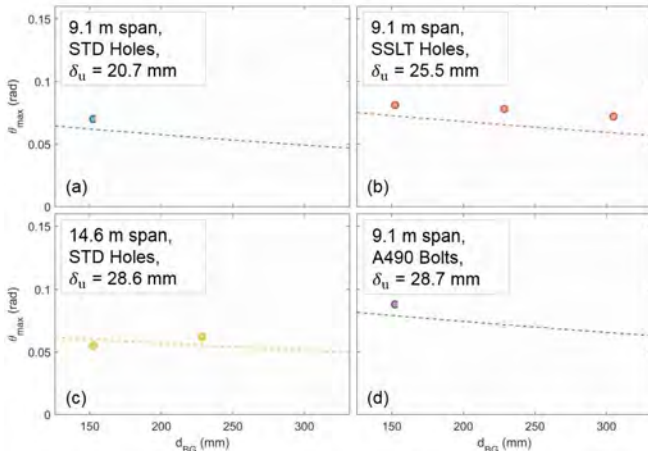


Figure 8: Comparison between Eq. (5) (dashed line) and measured rotational capacities for single-plate shear connections (circular markers).

SUMMARY AND CONCLUSIONS

When evaluating the performance of connections subjected to column loss, it is important to recognize that connections behave differently when subjected to seismic loads than when subjected to column loss. Acceptance criteria in existing specifications, which were developed based on results from seismic testing, may not be appropriate for column loss as they do not capture (1) differences in connection geometry (e.g., bolt diameter, plate

thickness, thread condition), (2) the influence of axial deformation demands on the connections, and (3) the influence of span length. As a result of these deficiencies, current acceptance criteria are not risk-consistent for connections with different geometries, or frames which have different spans.

Results from component-based models of single-plate shear connections showed that there exist connection geometries in which even the most stringent currently specified acceptance criteria (the UFC 4-023-03 rotation limits for primary members) would not be conservative for disproportionate collapse. However, a new approach in which the axial deformation capacities of component-width segments of the connection are used to calculate rotational capacities for the connections can overcome these deficiencies to provide results that are both risk-consistent and capture the influence of axial deformation demands on the connection, including those resulting from span length.

REFERENCES

- ASCE (2013). *Seismic Evaluation and Retrofit of Existing Buildings, SEI/ASCE 41-13*, American Society of Civil Engineers, Reston, VA.
- Karns, J.E., Houghton, D.L., Kim, J. and Hong, J. (2008). *GSA Steel Frame Bomb Blast & Progressive Collapse Test Program*, Contract No. GS-23F-0092P, January, 2008.
- Johnson, E.S. Meissner, and Fahnstock, L.A. (2015). "Experimental Behavior of a Half-Scale Steel Concrete Composite Floor System Subjected to Column Removal Scenarios." *J. Struct. Eng.*, 04015133.
- Johnson, E.S., Weigand, J.M., Francisco, T., Fahnstock, L.A., Liu, J., and Berman, J.W. (2014). "Large-Scale Experimental Evaluation of the Structural Integrity of a Composite Steel and Concrete Building Floor System." *Structures Congress*, Boston, MA.
- Main, J.A. and Sadek, F. (2012). "Robustness of steel gravity frame systems with single-plate shear connections." *NIST Technical Note 1749*, Gaithersburg, MD.
- Weigand, J. M. and Berman, J. W. (2014). "Integrity of Steel Single Plate Shear Connections Subjected to Simulated Column Removal." *J. Struct. Eng.*, 140 (5), 04013114, pp.1-12.
- Weigand, J.M. (2014). "The Integrity of Steel Gravity Framing System Connections Subjected to Column Removal Loading." Ph.D. Dissertation in Civil Engineering, University of Washington, Seattle, WA.
- Weigand, J.M. (2016). "A Component-Based Model for Single-Plate Shear Connections with Pre-tension and Pinched Hysteresis." *J. Struct. Eng.* Under review.
- Weigand, J.M. and Berman J.W. (2016). "Steel Gravity Connections Subjected to Large Rotations and Axial Loads." *Eighth International Workshop on Connections in Steel Structures (Connections VIII)*, Boston, Massachusetts, May, 2016.
- DoD (2009). *Design of Buildings to Resist Progressive Collapse, UFC 4-023-03*. United States Department of Defense.

ENHANCED CONNECTIONS FOR IMPROVED ROBUSTNESS OF STEEL GRAVITY FRAMES

Jonathan M. Weigand

National Institute of Standards and Technology, Gaithersburg, MD 20899 USA
jonathan.weigand@nist.gov

Joseph A. Main

National Institute of Standards and Technology, Gaithersburg, MD 20899 USA
joseph.main@nist.gov

ABSTRACT

Potential vulnerability to collapse under column loss has been identified for steel gravity framing systems with simple shear connections. To address this potential vulnerability, an enhanced connection for steel gravity frames is proposed that incorporates U-shaped top and seat plates with long-slotted holes bolted to the beam flanges. Finite element analyses are used to evaluate the effectiveness of the enhanced connection under column loss scenarios. Addition of the U-shaped slotted plates is shown to increase the vertical resistance of a two-span beam assembly under center column loss to 2.5 times the resistance with conventional connections. Analysis of a composite floor system subject to interior column loss shows that incorporation of the enhanced connections achieves a 90 % increase in the ultimate vertical capacity, relative to the system with conventional connections, under uniform static loading. Under sudden column loss, the ultimate capacity of the floor system with enhanced connections is essentially equivalent to the applicable gravity load combination of $1.2D + 0.5L$, while the system with conventional connections sustains only 56 % of the applicable gravity loading.

INTRODUCTION

Recent full-scale experiments (Lew et al. 2012) and computational analyses (Main and Liu 2013) have demonstrated the effectiveness of seismically designed steel moment frames in redistribution of gravity loads under column removal scenarios. In contrast, computational analyses (e.g., Main 2014) and experimental studies (Johnson et al. 2015) have indicated that steel gravity frames are potentially vulnerable to disproportionate collapse under column loss. Four column removal tests performed on a half-scale steel gravity framing system with composite slab on steel deck, by Johnson et al. (2015), showed that the floor system could only carry between 44 % and 62 % of the applicable gravity load combination of $1.2D + 0.5L$ for extraordinary events from American Society

of Civil Engineers (ASCE) Standard 7-10 (ASCE 2010), where D = dead load and L = live load. To help address this potential vulnerability, researchers have begun to consider two primary approaches for enhancing the robustness of steel gravity frames: (1) enhancing the floor slab capacity through improved slab detailing, and (2) enhancing the connection capacity through improved connection detailing. While previous analyses have shown that the concrete slab on steel deck adds significant capacity under column removal, that capacity is sensitive to small variations in the slab thickness, slab continuity, detailing between deck sheets, and the attachment method to the perimeter framing (Main et al. 2015). Enhancements to the steel gravity connections are potentially more versatile and can be implemented both for new construction and for retrofit of existing structures.

In this study, high-fidelity numerical models of single-plate shear connections were first validated against experimental data from Weigand and Berman (2014) and then used to investigate steel gravity framing systems with enhanced connection detailing. The enhanced connections used U-shaped slotted steel plates, which were welded to the column flange and bolted to the beam flanges, to increase both the flexural capacity of the connection (at small rotations) and the tensile capacity of the connection (at large rotations). High-fidelity analyses were used to evaluate the component-level behavior of the U-shaped slotted plates under axial loading and to evaluate the behavior of the enhanced connections in a two-span beam assembly under center column loss. Reduced-order models were then used to evaluate the effectiveness of the enhanced connections in a two-bay by two-bay composite floor system under interior column loss.

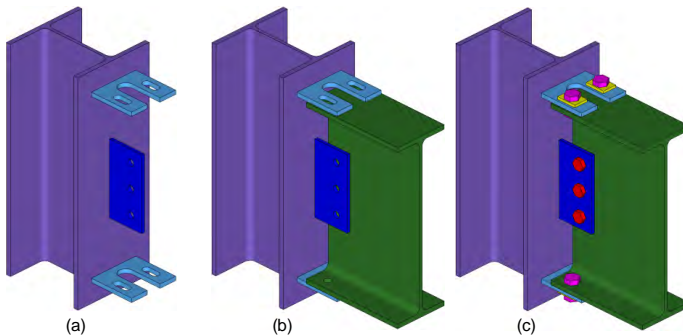


Figure 1: Enhanced single-plate shear connection: (a) U-shaped slotted top and seat plates welded to column; (b) beam in position; (c) bolted with rectangular plate washers.

ENHANCED CONNECTION DETAILS

The enhanced connection configuration includes top and seat plates, which are welded to the column and then bolted to the beam flanges (Figure 1). The top and seat plates have long-slotted holes to permit large slip displacements of the flange bolts prior to the initiation of bearing at the ends of the slots. Each top or seat plate has a U-shaped cutout that serves two purposes: (1) it allows the plate to be placed on either the interior or the

exterior face of the beam flange (exterior placement would be used in new construction while interior placement could be preferable for retrofit in some cases), and (2) it reduces the net section of the plate relative to the shear area of the bolts to ensure that tensile yielding develops in the plate sections adjacent to the slots, thus achieving significant plastic elongation of the slotted portion of the plate prior to tensile rupture (similar in concept to how a reduced beam section connection enhances ductility in flexure). Rectangular plate washers (Figure 1(c)) distribute the bearing stresses induced by pre-tension in the flange bolts. Standard holes are used in the beam flanges.

COMPUTATIONAL MODELING

High-fidelity finite-element modeling of the connections followed the approach described by Main and Sadek (2014) except that reduced-integration solid elements were used, rather than fully integrated elements, in order to better capture the localization of shear strain in the bolts. In the connection region, finely meshed hexahedral elements were used to represent the shear plate, top and seat plates, bolts, plate washers, and the beam (Figure 2). Outside of the connection region, the beam was modeled using shell elements, and nodal constraints were used to enforce compatibility of displacements and rotations at the solid/shell interface. Typical solid element sizes were 1.5 mm (0.06 in) for the bolts and 3 mm (0.12 in) for all other components. Contact was defined between all solid components to transfer forces through the bolted connection, and friction was included, with a static coefficient of friction of 0.34 for all interfaces, corresponding to an average value calculated from the extensive data compiled by Grondin et al. (2007). Piecewise-linear plasticity models were used to model the material behavior, with fracture simulated using element erosion, as described by Main and Sadek (2014). The stress-strain curve used to model the A325 bolts was based on tensile test data reported by Kulak et al. (1986). Stress-strain curves used to model the plates and wide-flange sections were obtained from tensile coupon testing of the actual materials used in single-plate shear connection tests by Weigand (2014), and data from one of these connection tests was used for model validation, as described in the following section.

Model Validation

The modeling approach was validated against results from a connection sub-assembly test conducted by Weigand and Berman (2014), for a 3-bolt single-plate shear connection with a W12x72 column, W21x50 beam, 19.1 mm ($\frac{3}{4}$ in) diameter ASTM A325 bolts, and a 9.5 mm ($\frac{3}{8}$ in) thick ASTM A36 shear plate (Specimen sps3b|STD|34|38|). Figure 2 illustrates the model used in the analysis, which consisted of two loading phases. In the initial phase, pre-tension was introduced in the bolts through thermal contraction, by artificially reducing the temperature of the bolts to achieve an average pre-tension of 185 kN (42 kip) per bolt. In the second phase, displacement-controlled axial and transverse loads were applied to the beam end, replicating the loading conditions used in the test (Weigand and Berman 2014), which imposed a combination of rotational and axial demands on the connection to represent a column loss scenario.

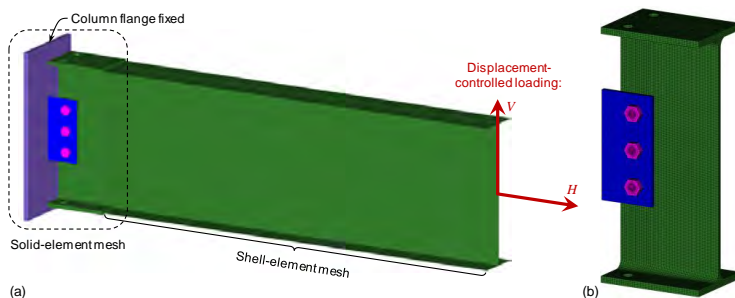


Figure 2: Computational model of specimen sps3b|STD|34|38] from Weigand and Berman (2014): (a) overview of model; (b) solid-element mesh.

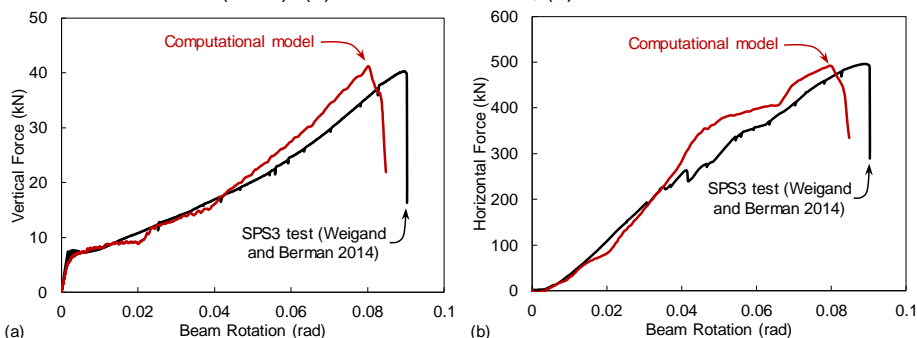


Figure 3: Comparison of computational and experimental results for (a) vertical force and (b) horizontal force vs. beam rotation. (Uncertainties in the experimental measurements are discussed by Weigand and Berman (2016).)

Figure 3 compares the computed vertical and horizontal forces with those obtained experimentally for Specimen sps3b|STD|34|38]. The peak vertical force from the computational model is 2 % greater than the experimental value and the peak horizontal force from the computational model is 1 % less than the experimental value. A somewhat larger discrepancy is observed for the rotation at peak load, for which the computational model underestimated the experimental value by 11 %. These discrepancies give an indication of the degree of uncertainty in the predictions of the computational model.

Component-Level Axial Behavior of U-Shaped Plate with Long-Slotted Holes

Prior to considering the behavior of enhanced connections under column loss, the model shown in Figure 4(a) was used to investigate the component-level behavior of a U-shaped plate with long-slotted holes under axial loading. A rectangular plate with standard holes was also modeled for comparison (Figure 4(b)). Plates made of ASTM A36 steel with a thickness of 12.7 mm (½ in) were considered, which were bolted to the flange of an ASTM

A992 W21×50 beam using two 22.2 mm ($\frac{7}{8}$ in) diameter ASTM A325 bolts. ASTM A36 plate washers with a thickness of 7.9 mm ($\frac{5}{16}$ in) were used for the U-shaped plate with long-slotted holes. One flange of the beam was modeled, including the flange-to-web fillet, and nodes along the toe of the fillet were constrained to permit axial displacements only. Displacement-controlled axial loading was applied to one end of the beam flange, and the opposite ends of the A36 plates were fixed (Figure 4). Prior to axial loading, initial pre-tension of 234 kN (53 kip) was introduced in each bolt through thermal contraction.

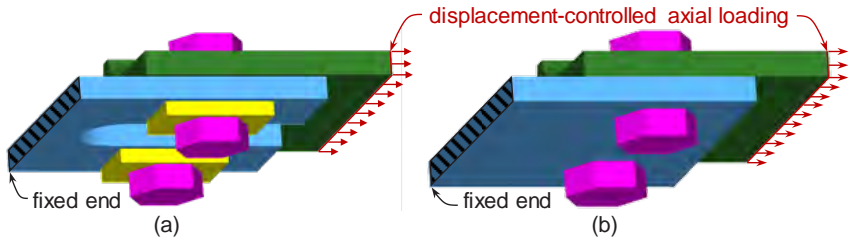


Figure 4: Component-level analysis models: (a) U-shaped plate with long-slotted holes; (b) rectangular plate with standard holes.

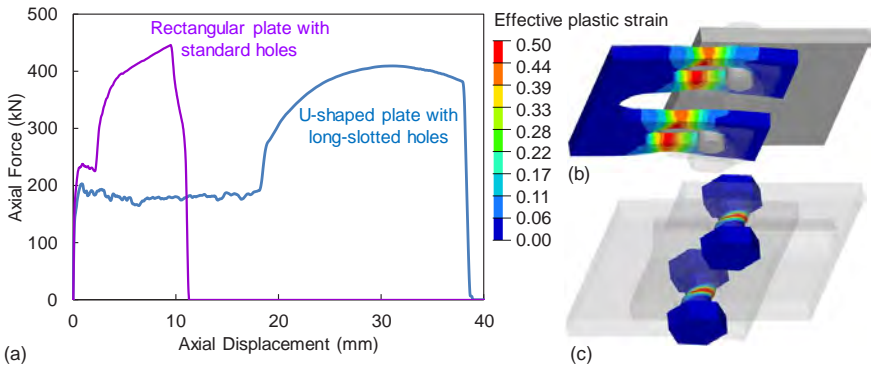


Figure 5: (a) Axial force-displacement results from component-level analyses, along with contours of effective plastic strain just prior to rupture for: (b) U-shaped plate with long-slotted holes; (c) flange bolts for rectangular plate with standard holes.

Figure 5(a) shows axial force-displacement curves obtained from the two models in Figure 4. For the model in Figure 4(a), Figure 5(b) shows contours of plastic strain just prior to tensile rupture of the U-shaped slotted plate, and for the model in Figure 4(b), Figure 5(c) shows contours of plastic strain just prior to shear rupture of the bolts. The peak axial force for the U-shaped slotted plate was slightly less (by 8 %) than that for the rectangular plate with standard holes, because of the intentional reduction in the net section of the U-shaped plate. However, the displacement at tensile rupture for the U-shaped slotted plate (38 mm (1.5 in)) was four times as large as the displacement at bolt

shear rupture for the rectangular plate with standard holes. The substantially larger displacements for the U-shaped slotted plate were developed initially through sliding of the bolts through the long slots (for displacements less than 18 mm (0.72 in)), and subsequently through a combination of bearing deformations, bolt shear deformations, and elongation of the plate legs on each side of the long slots (see Figure 5(b)).

Two-Span Beam Assembly

A two-span beam assembly (Figure 6) was considered to evaluate the effectiveness of enhanced connections in bare steel framing (i.e., no floor slab) under column loss. A computational modeling approach similar to that illustrated in Figure 2 was used to analyze the response of the two-span beam assembly with different types of connections, including the two different types of top and seat plates illustrated in Figure 4. Figure 7(a) compares the results for these connections with those from a conventional single-plate shear connection. Figure 7(a) shows that the additional deformation capacity of the U-shaped plates with long-slotted holes results in a peak vertical capacity that is 46 % greater than that for rectangular top and seat plates with standard holes. Figure 7(a) also shows that the addition of U-shaped slotted top and seat plates results in a peak vertical capacity that is 2.5 times the vertical capacity for a conventional single-plate shear connection. Figure 7(b) shows that pre-tension in the flange bolts provides additional vertical resistance in the initial phase of the response, when the bolts are sliding in the slots, but has an insignificant effect after the onset of bearing deformations at a center column displacement of about 450 mm (18 in).

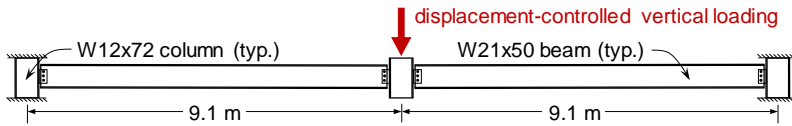


Figure 6: Two-span beam assembly.

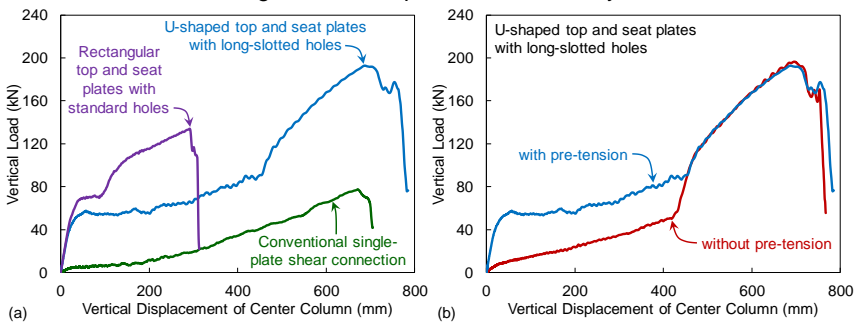


Figure 7: Vertical load-displacement analysis results for two-span beam assemblies: (a) comparison of results for different connection types; (b) influence of pre-tension.

Figure 8 shows that the behavior of the enhanced connections could be accurately represented using a reduced-order modeling approach in which the components of the connection were modeled as nonlinear springs interconnected by rigid links (Figure 9(a)). Such an approach has previously been successfully applied for moment connections (Sadek et al. 2013) and for single-plate shear connections (Main and Sadek 2014). Figure 8 shows that the reduced-order modeling approach captured the peak load from the high-fidelity model within 1 % and the corresponding displacement of the center column within 4 %. In this study, the force-deformation relationships for the nonlinear connection springs were defined using piecewise-linear approximations of results from high-fidelity finite element analysis of the connection components (Figure 9(b) and (c)). However, analytical models for the connection components could also be used, where available, such as the component-based model developed by Weigand (2016) for single-plate shear connections with pre-tension. The use of such a model facilitates parametric studies and optimization of connection configurations, which will be pursued in future studies.

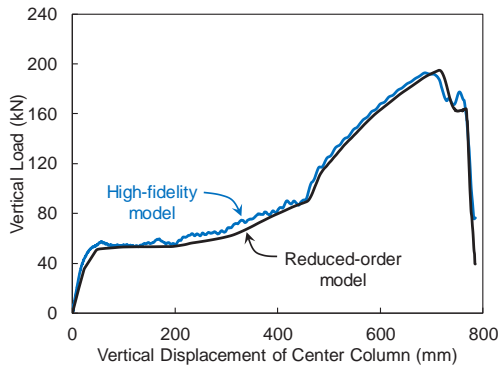


Figure 8: Reduced-order and high-fidelity model results for two-span beam assembly.

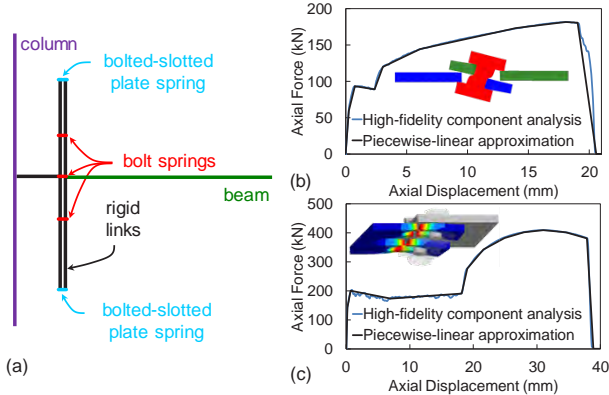


Figure 9: (a) Reduced-order connection model with force-displacement relationships for: (b) single-plate shear connection (one bolt row); (c) U-shaped slotted plate.

Composite Floor System

To evaluate the effectiveness of the enhanced connections in composite steel gravity framing, a prototype two-bay by two-bay composite floor system previously considered by Main (2014) was analyzed under center column loss, both with conventional single-plate shear connections and with enhanced beam-to-column and girder-to-column connections incorporating U-shaped slotted top and seat plates. The modeling approach for the composite floor system, illustrated in Figure 10, followed the approach proposed by Main (2014), in which the girders, beams, and columns were modeled with beam elements, and alternating strips of shell elements were used to represent the ribbed profile of the concrete slab on steel deck, with distinct integration points through the slab thickness for the steel deck, concrete, and welded wire reinforcement. Connections were modeled using a reduced-order approach as illustrated in Figure 9(a). Modeling of the conventional floor system in this study differed from Main (2014) in that a steeper softening modulus was used for the post-ultimate tensile resistance of concrete, as discussed by Main et al. (2015), and improved deformation limits were used for the single-plate shear connections, based on measurements from Weigand and Berman (2014), with a steep drop in resistance when those deformation limits were reached. The enhanced floor system was modeled using the piecewise-linear load-deformation relationship in Figure 9(c) to represent the U-shaped slotted plates.

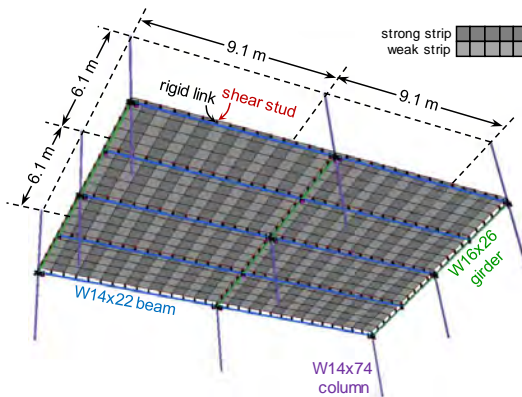


Figure 10: Reduced-order model of a 2-bay by 2-bay composite floor system.

Figure 11(a) shows computed curves of load intensity vs. center column displacement for floor systems with conventional and enhanced connections under uniform static loading with an unsupported center column. Figure 11(b) shows corresponding curves for sudden column loss, which were obtained from the curves in Figure 11(a) using the energy-based approach described by Main (2014). The floor system with conventional connections was unable to sustain the applicable gravity loading of $1.2D + 0.5L$, even under static loading. However, the enhanced connections increased the capacity of the floor system under

static loading by 90 %, resulting in a capacity that significantly exceeded the applicable gravity loading. As proposed by Bao (2014), a robustness index was calculated by normalizing the ultimate capacity under sudden column loss by the applicable gravity loading, whereby robustness indices of 0.56 and 0.99 were obtained for the systems with conventional and enhanced connections, respectively. The enhanced connections thus increased the robustness of the floor system by 76 %, resulting in an ultimate capacity under sudden column loss that was essentially equivalent to the applicable floor loading.

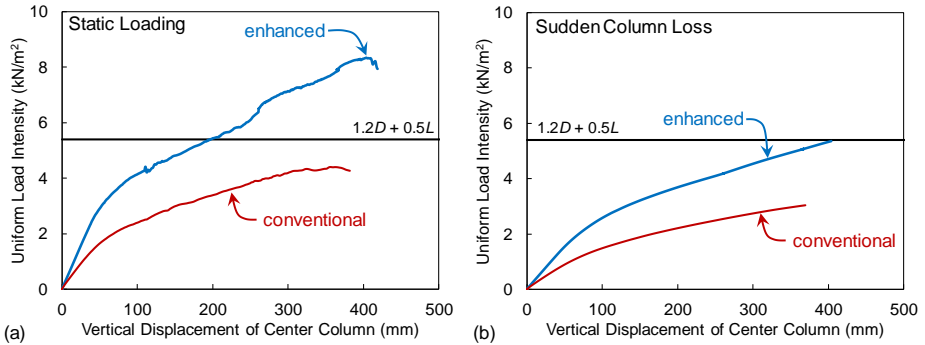


Figure 11: Uniform load intensity vs. center column displacement for floor systems with conventional and enhanced connections: (a) static loading; (b) sudden column loss.

SUMMARY AND CONCLUSIONS

This paper presented an enhanced steel gravity connection that used steel plates, bolted to the upper and lower flanges of the beam and welded to the column flange, to increase the flexural and tensile capacity of the connection. Analysis of the enhanced connection in a two-span beam assembly showed that it had a peak vertical resistance under column loss that was 2.5 times as large as that for a conventional single-plate shear connection. When implemented in system-level analyses of a two-bay by two-bay composite floor system, the enhanced steel gravity connections increased the vertical load-carrying capacity of the system under center column loss by 90 % under static loading. Robustness indices of 0.56 and 0.99 were calculated for the floor systems with conventional and enhanced connections, respectively, indicating that the enhanced connections increased the robustness of the floor system by 76 % and that the ultimate capacity of the enhanced floor system under sudden column loss is essentially equivalent to the applicable gravity loading. Future work will involve experimental evaluation of the performance of the enhanced connections under column loss scenarios and development of design procedures for the enhanced connections.

REFERENCES

- ASCE (2010). *Minimum Design Loads for Buildings and Other Structures*, SEI/ASCE 7-10, American Society of Civil Engineers, Reston, VA.
- Bao, Y, Main, J.A., Lew, H.S., and Sadek, F. (2014). "Robustness Assessment of RC Frame Buildings under Column Loss Scenarios." *Proc., Structures Congress*, Boston, MA, May, 2014.
- Grondin, G., Jin, M. and Josi, G. (2007). "Slip-critical bolted connections – a reliability analysis for design at the ultimate limit state." *Structural Engineering Report No. 274*, University of Alberta.
- Kulak, G.L., Fisher, J.W., and Struik, J.H.A., (1986). *Guide to Design Criteria for Bolts and Riveted Joints*, 2nd Edition, John Wiley & Sons, New York.
- Lew, H.S., Main, J.A. Robert, S.D., Sadek, F., and Chiarito, V.P. (2012). "Performance of steel moment connections under a column removal scenario. I: Experiments," *Journal of Structural Engineering*, 139(1), 98-107.
- Johnson, E.S. Meissner, and Fahnestock, L.A. (2015). "Experimental Behavior of a Half-Scale Steel Concrete Composite Floor System Subjected to Column Removal Scenarios." *Journal of Structural Engineering*, 04015133.
- Main, J.A. (2014). "Composite Floor Systems Under Column Loss: Collapse Resistance and Tie Force Requirements." *Journal of Structural Engineering*, 140(8), A4014003.
- Main, J.A. and Liu, J. (2013). "Robustness of Prototype Steel Frame Buildings against Column Loss: Assessment and Comparisons." *Proceedings of the ASCE/SEI Structures Congress*, Pittsburgh, PA, May, 2013.
- Main, J.A. and Sadek, F. (2014). "Modeling and Analysis of Single-Plate Shear Connections under Column Loss." *J. Struct. Eng.*, 140(3), 04013070.
- Main, J.A., Weigand, J.M., Johnson, E.S., Francisco, T.W., Liu, J., Berman, J.W., and Fahnestock, L.A. (2015). "Analysis of a Half-Scale Composite Floor System Test under Column Loss Scenarios." *Proceedings of the ASCE/SEI Structures Congress*, Portland, Oregon, April, 2015.
- Sadek, F., Main, J.A., Lew, H.S., and El-Tawil, S. (2013). "Performance of Steel Moment Connections under a Column Removal Scenario. II: Analysis." 139(1), 108-119.
- Weigand, J.M. (2016). "A Component-Based Model for Single-Plate Shear Connections with Pre-tension and Pinched Hysteresis." *J. Struct. Eng.* Under review.
- Weigand, J. M. and Berman, J. W. (2014) "Integrity of Steel Single Plate Shear Connections Subjected to Column Removal Loading." *Journal of Structural Engineering*. 140(5), 04013114.
- Weigand, J. M. and Berman, J. W. (2016) "Steel Gravity Connections Subjected to Large Rotations and Axial Loads." *Proc., Eighth International Workshop on Connections in Steel Structures (Connections VIII)*, Boston, Massachusetts, May, 2016.

STEEL GRAVITY CONNECTIONS SUBJECTED TO LARGE ROTATIONS AND AXIAL LOADS

Jonathan M. Weigand
National Institute of Standards and Technology, Gaithersburg, MD 20899, USA
jonathan.weigand@nist.gov

Jeffrey W. Berman
University of Washington, Seattle, WA 98195, USA
jwberman@uw.edu

ABSTRACT

Steel gravity framing systems (SGFSs) rely on connections for system robustness when a column suffers damage that compromises its ability to carry gravity loads. Redistribution of gravity loads through the development of a sustained tensile configuration resulting from large vertical deflections is a key behavior in achieving robustness. Development of such an alternative load path depends on the ability of the gravity connections to remain intact after undergoing large rotation and axial extension demands. These demands are significantly larger than those considered for typical SGFS connection design. This paper presents the results of experiments on steel single-plate shear and bolted angle connections subjected to loading consistent with an interior column removal. The characteristic connection behaviors are described and the performance of multiple connection configurations are compared in terms of their peak resistances and deformation capacities.

INTRODUCTION

Steel gravity framing systems (SGFSs) are present in nearly every steel building constructed in the United States, yet they have been identified as potentially vulnerable to collapse (Foley et al., 2006; Sadek et al., 2008; Main and Sadek, 2012; Weigand, 2014). If the vertical load carrying capacity of a single column is diminished or lost, it is presently unclear if the gravity loads on the structure can be sustained. The notion of a design procedure for achieving structural robustness in SGFSs is in its infancy, and the current body of knowledge lacks experimental data on the behavior and performance of steel buildings subjected to unanticipated loads.

While it would be impractical and prohibitively expensive to directly design for unanticipated loading events (e.g., vehicular impact, blast, or accidental overload), history has shown that some inherent robustness is often present. Research on disproportionate collapse in steel framing has found that ductile connection detailing may improve system robustness under unanticipated loadings. In the event that a column in a SGFS loses the

capacity to support its gravity loads, alternative load paths must develop in the horizontal framing members to support the gravity loads. These load paths develop from large vertical deflections that result in catenary action in the system, and that subject the connections to large rotation and axial extension demands.

The performance of steel gravity connections under seismic loading has been studied experimentally. However, experimental investigations involving the collapse behavior of SGFSs or its components are more limited. Astaneh-Asl et al. (2001a) investigated the collapse resistance of a two-bay gravity system under column removal and showed that an improvement in capacity could be achieved (Astaneh-Asl et al., 2001c) by adding post-tensioning cables. Thompson (2009) tested specimens each consisting of a column stub with symmetrically configured single-plate shear connections tied via short stiffened pinned-end beams to a vertical perimeter frame under an interior column pulldown scenario. Using connection sub-assemblages, Guravich and Dawe (2006) conducted an investigation of four gravity connection types typical to Canadian structural engineering practice to determine if shear connections could sustain significant tensile loads in combination with their design shear capacity. Oosterhof and Driver (2012) also investigated the strength and ductility of common shear connections using sub-assemblages, under combinations of moment, shear, and tension.

To evaluate the structural robustness of SGFSs, a multi-university collaborative experimental program was established to investigate the behavior of the state of current industry practice for gravity framing and work toward developing the next-generation of SGFSs. This program was a collaborative effort which involved contributions from the University of Washington (UW), Purdue University (PU), and the University of Illinois at Urbana-Champaign (UIUC). This paper summarizes experimental results from tests on SGFS connection subassemblies conducted at the UW to evaluate their response to loading consistent with an interior column losing its vertical load carrying capacity. A broad range of single-plate shear and bolted angle connection sub-assembly tests were conducted to characterize connection response to combined loading, and to determine controlling failure mechanisms for various connection geometries.

CONNECTION CONFIGURATIONS

The steel single-plate shear and bolted angle connection sub-assemblages tested in this study were designed to resist the shear demands resulting from a series of prototypical steel gravity framing systems, with gravity loads modeled after the SAC¹ prototype building loads. The prototype systems encompassed a broad range of configurations typical of current industry design practice, and are described in more detail in Weigand et al. (2012). The connection configurations were selected from the prototype system designs and refined to provide a wide breadth of parameter variation.

¹SAC Joint Venture between the Structural Engineers Association of California (SEAOC), the Applied Technology Council (ATC), and the Consortium of Universities for Research in Earthquake Engineering (CUREE)

The typical connection sub-assembly specimen consisted of a 1524 mm (60.0 in) long W12x72 column stub and a 1220 mm (48.0 in) long W21x50 beam stub, connected via a single shear plate (Fig. 1), bolted web angles, or top and seat angles; however, two specimens used W14x90 and W18x35 column and beam stub sections, respectively. The varied connection parameters for the single-plate shear connections included the number of bolts (n_b), bolt diameter (d_b), bolt grade, plate thickness (t_p), horizontal plate edge distance (L_{ehp}) relative to the minimum allowable plate edge distance (L_{emin}), hole type (standard (STD) or short-slotted (SSLT)), eccentricity with respect to the beam centerline, gap between the beam flange and the column flange, and the simulated system span. The varied connection parameters for the bolted angle specimens included the number of bolts on the angle legs bolted to the column flange (n_b), angle column-leg bolt diameter (Col. d_b), angle beam-leg bolt diameter (Bm. d_b), angle leg thickness (t_L), configuration, eccentricity with respect to the beam centerline, and gap between the beam flange and the column flange. The naming convention for the tested specimens consists of a prefix that describes the connection type (e.g., sps (Single-Plate Shear)), followed by the number of bolts (e.g., 3b), the hole type (e.g., STD), the bolt diameter fraction in inches (e.g., 34 corresponds to 3/4 in), plate thickness fraction in inches (e.g., 38 corresponds to 3/8 in), and additional descriptor (e.g., Edge) where applicable. A similar naming convention was used for the bolted angle connections using the bolt diameter fraction, angle thickness fraction, and additional descriptor, where applicable. Table 1 shows the parameter values for the single-plate shear specimens and Table 2 shows the values for the bolted angle specimens.

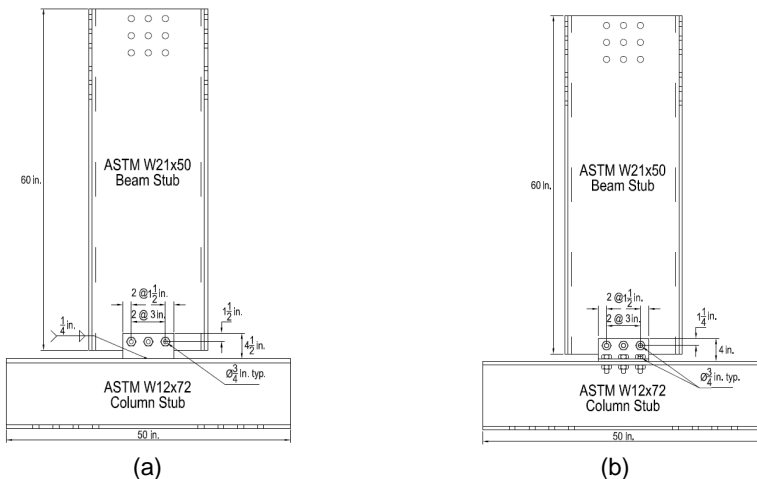


Figure 1. (a) Typical single-plate shear specimen, and (b) typical bolted angle specimen (1 in = 25.4 mm). For both: dimensions vary, see Tables 1 and 2.

Table 1. Single-Plate Shear Connection Test Specimens and Results

Name	Connection Properties						Test Results							
	Span (m)	n_b	d_b (mm)	t_p (mm)	Hole Type	L_{end}/L_{min}	Δ (mm)	θ (rad)	δ (mm)	d_r (mm)	V_{max} (kN)	T_{max} (kN)	V_{max}/V_{Nom}	Failure Location
sps3b STD 34 38 48L	14.6	3	19.1	9.53	STD	1.5	1053	0.075	19.6	24.5	41.2	497	0.099	Bolt
sps4b STD 34 38 48L	14.6	4	19.1	9.53	STD	1.5	1159	0.082	23.8	32.7	55.1	647	0.093	Bolt
sps3b STD 34 38	9.1	3	19.1	9.53	STD	1.5	788	0.090	17.9	20.7	40.2	495	0.097	Bolt
sps3b SSLT 34 38	9.1	3	19.1	9.53	SSLT	1.5	890	0.092	22.7	24.5	44.1	474	0.106	Bolt
sps3b SSLT 34 38 Edge	9.1	3	19.1	9.53	SSLT	1.0	809	0.087	18.8	22.4	32.3	384	0.067	Plate
sps4b SSLT 34 38	9.1	4	19.1	9.53	SSLT	1.5	863	0.093	21.4	24.2	49.6	544	0.083	Bolt
sps5b SSLT 34 38	9.1	5	19.1	9.53	SSLT	1.5	807	0.079	18.7	25.5	60.4	628	0.078	Bolt
sps3b SSLT 34 38 A490	9.1	3	19.1	9.53	SSLT	1.5	943	0.099	25.5	28.7	52.4	527	0.119	Bolt
sps3b SSLT 34 38 Offset ¹	9.1	3	19.1	9.53	SSLT	1.5	906	0.091	23.6	24.4	43.4	435	0.105	Bolt
sps4b SSLT 78 38	9.1	4	22.1	9.53	SSLT	1.3	795	0.081	18.2	22.7	48.7	503	0.081	Bolt
sps3b SSLT 34 14	9.1	3	19.1	6.35	SSLT	1.5	894	0.089	23.0	26.4	38.9	387	0.123	Plate
sps3b SSLT 34 38 Gap ²	9.1	3	19.1	9.53	SSLT	1.5	772	0.067	17.1	19.9	36.9	426	0.089	Bolt
sps3b SSLT 34 14 Weak ³	9.1	3	19.1	9.53	SSLT	1.5	972	0.110	27.1	32.6	38.5	388	0.121	Plate

¹ Shear plate offset 76 mm (3.0 in) from beam centerline.

² Reduced gap of 6.4 mm (1/4 in) between beam flange and column flange.

³ Weak-axis configuration that frames into column web.

Table 2. Bolted Angle Connection Test Specimens and Results

Name	Connection Properties					Test Results							
	n_b	Col d_b (mm)	Bm. d_b (mm)	t_b (mm)	Δ (mm)	θ (rad)	δ (mm)	d_r (mm)	V_{max} (kN)	T_{max} (kN)	V_{max}/V_{Nom}	Failure Location	
ba3b 34 14	3	19.1	19.1	6.35	1175	0.133	37.6	45.3	34.2	282	0.049	Angle	
ba3b 34 12	3	19.1	19.1	12.7	1168	0.132	37.2	41.6	61.1	543	0.067	Bolts	
ba5b 34 14	5	19.1	19.1	6.35	1033	0.117	29.3	46.7	46.4	373	0.041	Angle	
ba5b 34 12	5	19.1	19.1	12.7	1078	0.118	31.9	47.8	93.9	780	0.059	Bolts	
ba3b 1 34	3	25.4	25.4	19.1	1563	0.176	64.6	74.6	134.1	877	0.146	Beam Web	
ba3b 34 14 Offset ¹	3	19.1	19.1	6.35	1074	0.122	31.7	41.1	33.0	258	0.047	Angle	
ba3b 34 12 Offset ¹	3	19.1	19.1	12.7	1086	0.116	32.3	39.6	60.5	533	0.066	Bolts	
ba3b 34 14 Gap ²	3	19.1	19.1	6.35	1080	0.122	32.0	40.5	30.5	258	0.044	Angle	
ba3b 34 12 Gap ²	3	19.1	19.1	12.7	1150	0.122	36.1	41.2	65.2	553	0.071	Bolts	
ba3b 34 14 TopSeat ³	3	19.1	19.1	6.35	542	0.062	8.3	-	42.5	137	0.077	Angle	
ba3b 34 12 TopSeat ³	3	19.1	19.1	12.7	557	0.063	8.7	-	68.9	46	0.108	Bolts	
ba3b 34 14 HConfig ⁴	3	19.1	25.4	6.35	1328	0.15	47.6	52.9 ⁸	44.5	322	0.064	Angle	
ba3b 34 12 HConfig ⁴	3	19.1	25.4	12.7	1216	0.138	40.2	41.7 ⁸	57.8	475	0.063	Beam Web	
ba3b 34 14 BlegWeld ⁵	3	19.1	-	6.35	1067	0.121	31.2	-	27.2	240	0.039	Angle	
ba3b 34 14 ClegWeld ⁶	3	-	19.1	6.35	1125	0.127	34.6	34.1	15.8	130	0.023	Weld	
ba3b 34 14 Weak ⁷	3	19.1	19.1	6.35	1100	0.125	33.2	-	29.5	231	0.042	Angle	
ba3b 34 14 Weak ⁷	3	19.1	19.1	12.7	1373	0.155	50.6	-	79.6	591	0.087	Bolts	

Note: All bolted angle specimens used a simulated span of 9.1 m (30 ft)

¹ Angles offset 76 mm (3.0 in) from beam centerline.

² Reduced gap of 6.4 mm (1/4 in) between beam flange and column flange.

³ Top-and-seat angle configuration.

⁴ Angles had three 19.1 mm (3/4 in) diameter bolts on column legs and two 25.4 mm (1 in) diameter bolts on beam legs.

⁵ Angles bolted to column face and welded to beam web.

⁶ Angles welded to column face and bolted to beam web.

⁷ Weak-axis configuration that frames into column web.

⁸ Value corresponds to fiber centered at beam leg bolt.

TEST SETUP AND LOADING

A self-reacting load frame (Fig. 2) was constructed in the UW Structural Research Laboratory. The reaction frame was capable of delivering combined shear, tension, and flexural loading to the gravity connection sub-assemblages. Three actuators were attached at their bases to the reaction frame and at their heads to a load beam. A single 245 kN (55 kip) actuator was mounted horizontally to the reaction column and attached to the load beam. Two 489 kN (110 kip) actuators were mounted vertically and spanned between the outriggers and the load beam. The outriggers were rigidly fixed to the foundation beams and anchored to the strong floor. Each actuator had swivels at both ends to accommodate in-plane movements while preventing flexural loading of the piston rods. Out-of-plane movements were restrained at the end of the beam stub.

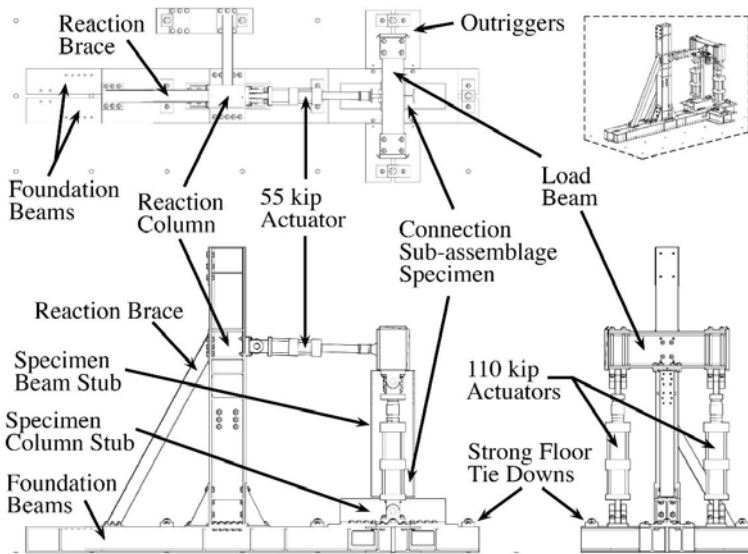


Figure 2. Connection test setup (1 kip = 4.448 kN).

Axial extension and rotation demands were applied quasi-statically to the connection sub-assemblage specimens through the load beam by the three independent actuators fixed to the reaction frame. The actuators were operated in displacement control. The displacements were computed by assuming a simple geometric relation between the extension and rotation demands at the connection and the centerline deflection of the interior column location in a simulated two-span system as shown in Fig. 3(a). The column was assumed to deflect perfectly vertically downward, and all deformations were assumed to occur at the connections about the centers of gravity of the connection bolt groups.

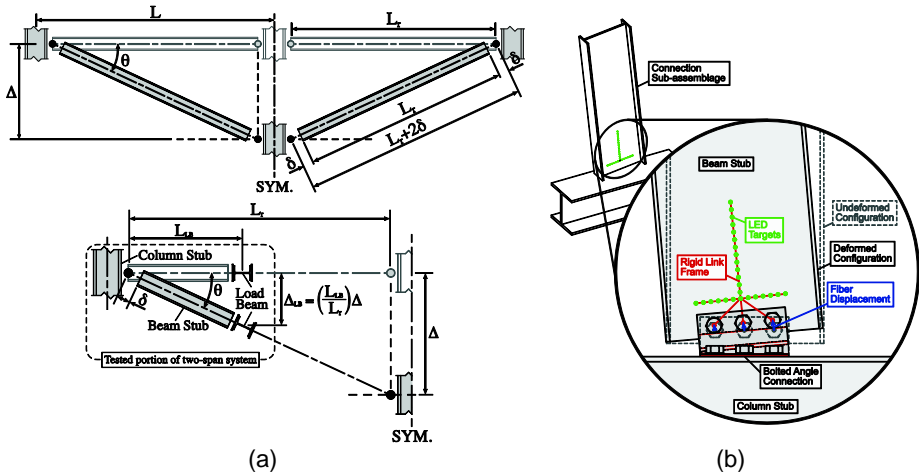


Figure 3. (a) Deformed two-span system used for determining applied rotation and displacement. (b) Fiber displacements computed from light-emitting diode (LED) targets.

Considering these assumptions, the applied rotation, θ , and simultaneously applied axial extension, δ , were:

$$\theta = \tan^{-1}\left(\frac{\Delta}{L_r}\right) \quad (1)$$

$$\delta = \frac{L_r}{2} \left[\sqrt{1 + \left(\frac{\Delta}{L_r}\right)^2} - 1 \right] \quad (2)$$

respectively, where all terms are as shown in Fig. 3. See Weigand and Berman (2014) for more details on the derivation of Eq. (1) and Eq. (2).

EXPERIMENTAL RESULTS

Experimental results are shown in Table 1 and Table 2. The estimated uncertainty in the measured data was $\pm 1\%$, based on repeated calibrations of the instruments over the course of testing. Results presented for each connection include the maximum connection rotation θ , maximum corresponding vertical displacement at the simulated damaged column, Δ , using the span lengths in Table 1 and a 9.1 m (30 ft) span for all bolted angle specimens, the maximum fiber displacement d_f , the maximum shear force at the columns face (aligned with the column), V_{max} , the maximum tension force in the connection (aligned perpendicular to the shear force), T_{max} , the maximum shear force normalized by each connection's nominal strength, V_{max}/V_{Nom} , and the failure mode. Complete discussions of the results may be found in Weigand (2014), Weigand and Berman (2015) and Weigand and Berman (2016).

To account for the combined contributions to bolt and plate deformations from the rotation and axial extension demands, the connection was discretized into individual component-width segments (fibers) each made up of a single bolt and the tributary width of beam web, and shear plate or angle. The locations of the fibers were determined prior to the application of load, with fiber-nodes centered at the light-emitting diode (LED) targets on the connection bolt-heads. One node of each fiber was assumed to be rigidly attached to the fixed specimen column stub, and the other was assumed rigidly attached to the beam web. The kinematic motions of the beam web fiber-nodes were computed by imposing a rigid-link structure onto the grid of LED targets positioned on the beam web (Fig. 3(b)). Experimental fiber displacement profiles were computed as the vectors spanning from the undeformed to the deformed locations of the fiber nodes, and decomposed into axial and shear components.

As shown in Table 1 and Table 2, different failure modes were observed depending on connection configuration and specific parameters (i.e., shear plate thickness, angle thickness, bolt diameter, etc.). Fig. 4 illustrates the progression of deformation and eventual failure for two single-plate shear specimens, one with a thinner plate (sps3b|SSLT|34|14|) that had a tearout failure and one with a thicker plate (sps3b|SSLT|34|38|) that had a bolt shear rupture failure.

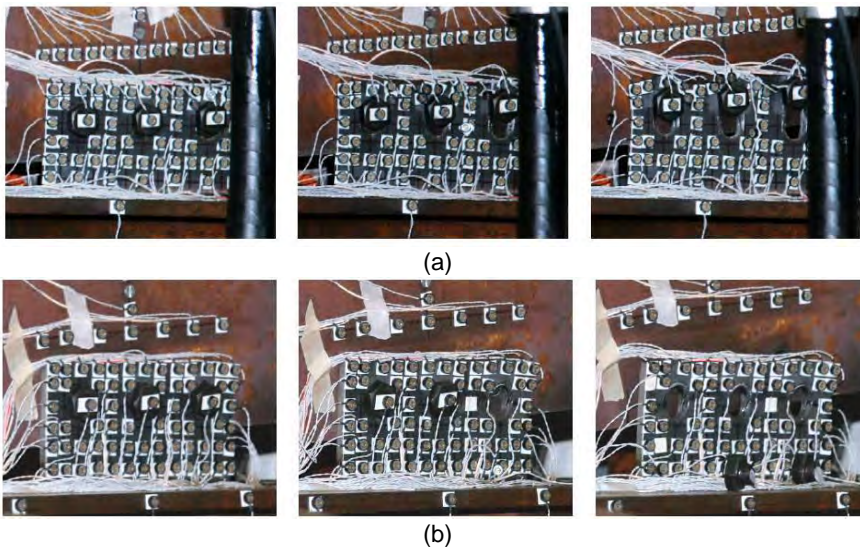


Figure 4. (a) Example of progression of plate tearout rupture in Specimen sps3b|SSLT|34|14| (b) example of bolt shear rupture in Specimen sps3b|SSLT|34|38|

The performance of connection specimens across the parameter space resulted in several key observations for gravity connections subjected to combined rotations and axial deformations. For steel single-plate shear connections:

1. The vertical shear force at the column face at connection failure is much lower than the nominal shear strength of the connection. The presence of tension in the connection greatly reduces the shear capacity. Table 1 illustrates this, as the maximum vertical shear force normalized by the nominal shear strength (V_{max}/V_{Nom}) is typically less than 0.13.
2. Failure is generally controlled by the deformation capacity of the outer fiber. Deeper connections with more bolts have larger strength, but less deformation capacity (both rotation and tension) than shallower connections and their increase in strength is less than the increase in their nominal shear strength. This is illustrated in Fig. 5, which shows test results for three single-plate shear connections with 3 bolts, 4 bolts, and 5 bolts. The increase in vertical shear capacity (see Fig. 5(a)) is not proportional to the increase in nominal strength due to the increased number of bolts (i.e., the 4-bolt and 5-bolt connections achieved smaller percentages of their nominal strengths than the 3 bolt connection, as shown in Fig. 5(b)). Fig. 5(c) shows that the axial displacement capacity of the outer fiber of each connection was the approximately the same.
3. Connections with short slotted holes achieve larger shear forces at the column face than connections with standard holes (e.g., compare results from sps3b|STD|34|38| and sps3b|SSLT|34|38| in Table 1).
4. Binding of the beam and column flanges has a negative impact on connection performance but is unlikely to occur in typical connection configurations due to the large axial deformations at the connections (see Weigand and Berman (2014) for more details).

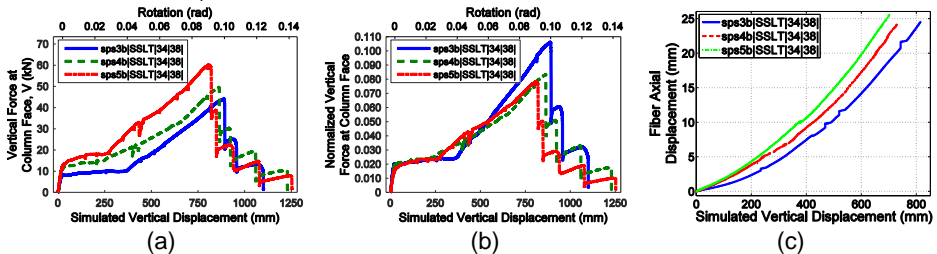


Figure 5. Comparison of (a) vertical force at column face normalized by connection nominal shear strength (b) horizontal force at the column face normalized by the plate tension strength, and (c) the displacement profiles in the outer fiber for 3 bolt (blue), 4 bolt (green) and 5 bolt (red) single-plate shear connections (profiles terminated at connection failure).

The key observations from the results of the tests on bolted angle specimens subjected to combined large rotations and axial deformations are:

1. For each pair of connections that differed only by angle thickness (e.g., Specimens ba3b|34|14| and ba3b|34|12|, Specimens ba5b|34|14| and ba5b|34|12|, etc.), the thicker bolted angle specimens achieve larger vertical force at the column face (Fig 6(a)).

- Increasing the number of bolts reduces the deformation capacity of the connections and results in smaller normalized maximum vertical forces at the columns face as shown in Fig. 6(b).
- Double angle connections with one leg welded (i.e., Specimens ba3b|34|14|BlegWeld and ba3b|34|14|ClegWeld) have reduced strength and ductility relative to bolted-bolted connections (see Table 2).
- Double angle connections have larger deformation capacity, but lower strength than single-plate shear connections with the same nominal shear strength as shown in Fig. 7.

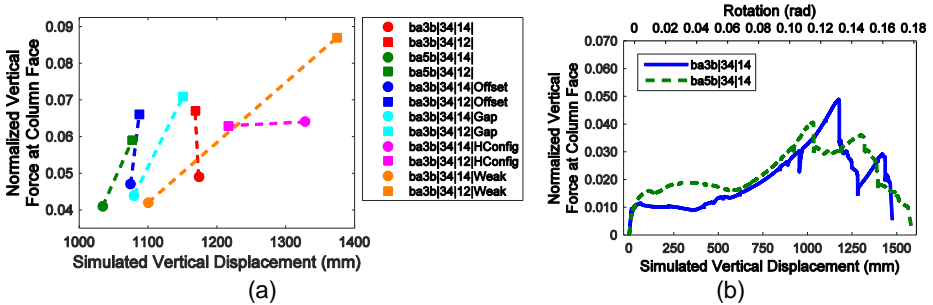


Figure 6. Comparison between (a) vertical capacities of bolted web angle connections with 6.35 mm (1/4 in.) thick and 12.7 mm (1/2 in.) thick angles normalized by connection nominal shear strength (connections of the same configuration but different angle thicknesses are connected via dashed line), and (b) vertical force at column face normalized by connection nominal shear strength for 3 bolt (blue) and 5 bolt (green) double angle connections.

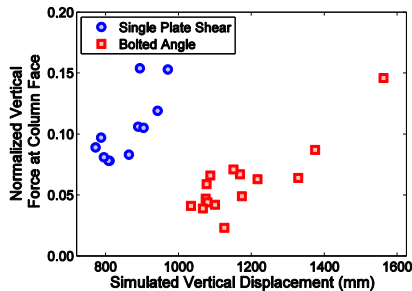


Figure 7. Maximum vertical force at column face normalized by connection nominal shear strength versus the maximum simulated vertical displacement at the removed column for all tested single-plate shear and double angle connections.

SUMMARY AND CONCLUSIONS

Tests on steel gravity framing system connections subjected to combined large rotation and tension were performed to investigate their potential contribution to structural

robustness. These tests showed that such connections are adversely affected by the large deformation demands associated with a column loss scenario and often are able to resist vertical forces at the column face of less than 15 % of their nominal shear strength. The connection strength and ductility are limited by the demands on the outer fiber (i.e., the outermost bolt and tributary plates or angles) and the limiting deformations of those outer fibers were quite consistent across connections with different depths.

ACKNOWLEDGEMENTS

This research was supported by the American Institute of Steel Construction (AISC) and the National Science Foundation under Grant No. CMMI-1000926. The steel wide flange sections used in the experiments were donated by AISC. Any opinions, findings, conclusions, and recommendations are those of the authors, and do not necessarily reflect the views of the sponsors.

REFERENCES

- Astaneh-Asl, A., Jones, B., Zhao, Y., and Hwa, R. (2001). "Progressive collapse resistance of steel building floors." Report No. UCB/CEE-Steel-2001/03, University of California at Berkeley, Dept. of Civil and Environmental Engineering.
- Astaneh-Asl, A., Madsen, E., Noble, C., Jung, R., McCallen, D., Hoehler, M.S., Li, W., and Hwa, R. (2001). "Use of catenary cables to prevent progressive collapse of buildings." Report No. UCB/CEE-Steel-2001/02, University of California at Berkeley, Dept. of Civil and Environmental Engineering.
- Foley, C.M., Martin, K., and Schneeman, C. (2006). "Robustness in structural steel framing systems." Thesis, MU-CEEN-SE-06-01, Marquette University.
- Khandelwal, K., Kunnath, S., El-Tawil, S., and Lew, H. (2008). "Macromodel-based simulation of progressive collapse: Steel frame structures." *J. Struct. Eng.*, 134(7), 1070-1078.
- Main, J. A. and Sadek, F. (2013). "Modeling and analysis of single-plate shear connections under column loss." *J. Struct. Eng.*, 140(3), 04013070.
- Oosterhof, S.A. and Driver, R.G. (2012). "Performance of Steel Shear Connections under Combined Moment, Shear, and Tension." *ASCE/SEI Structures Congress*, Chicago, IL. 146-157.
- Sadek, F., El-Tawil, S., and Lew, H.S. (2008). "Robustness of composite floor systems with shear connections: Modeling, simulation, and evaluation." *J. Struct. Eng.*, 134(11), 1717-1725.
- Thompson, S.L. (2009). "Axial, shear and moment interaction of single plate "shear tab" connections." Thesis, Milwaukee School of Engineering.
- Weigand, J.M. (2014). "The Integrity of Steel Gravity Framing System Connections Subjected to Column Removal Loading." Ph.D. Dissertation in Civil Engineering, University of Washington, Seattle, WA.
- Weigand, J.M. and Berman, J.W. (2014). "Integrity of Steel Single Plate Shear Connections Subjected to Simulated Column Removal." *J. Struct. Eng.*, 140(5), 04013114.
- Weigand, J.M. and Berman, J.W. (2016). "Integrity of Bolted Angle Connections Subjected to Simulated Column Removal." *J. Struct. Eng.*, 142(3), 04015165.
- Weigand, J.M., Meissner, J.E., Francisco, T., Berman, J.W., Fahnestock, L.A., and Liu, J. (2012). "Testing the Integrity of Steel Gravity Frames subjected to Large Vertical Deflections: Components." *ASCE/SEI Structures Congress*, Chicago, IL (March).

MODELING OF DOUBLE-ANGLE CONNECTIONS FOR ROBUSTNESS EVALUATION OF STEEL GRAVITY FRAMES

Jonathan M. Weigand
National Institute of Standards and Technology, Gaithersburg, MD 20899 USA
jonathan.weigand@nist.gov

Judy Liu
Oregon State University, Corvallis, OR 97330 USA
judy.liu@oregonstate.edu

Joseph A. Main
National Institute of Standards and Technology, Gaithersburg, MD 20899 USA
joseph.main@nist.gov

ABSTRACT

Component-based models of bolted double-angle beam-to-column connections have been developed for evaluating the structural robustness of steel gravity frames. The component-based models were developed based on results from high-fidelity finite-element models, which used solid elements to model the bolts, angles, and wide-flange sections, with explicit modeling of contact and friction. Fracture was modeled using element erosion with a plastic-strain-based failure criterion and reduced ductility at the “k-area” of the angle. The high-fidelity analyses were used to investigate the influence of span length on connection failure, including angle deformations at fracture. The component-based approach modeled each bolt row using a nonlinear load-displacement relationship that captured the effects of plastic hinge formation, straightening of the angle legs, and tearing of the angle near the heel. The component-based analysis results were compared with experimental data for double-angle connections subjected to combined rotation and axial extension representative of column loss scenarios.

INTRODUCTION

Bolted double-angle beam-to-column connections are common in steel gravity framing systems and have demonstrated substantial deformation capacity in simulated column loss scenarios (Liu et al. 2012). Component-based connection models provide an efficient framework for modeling the behavior of connections under extreme loads by providing

automatic coupling between the in-plane flexural and axial connection behaviors, a feature that is essential for modeling connections under column removal. The computational efficiency of the component-based modeling approach makes it well suited for evaluating the robustness of entire buildings. This paper presents a component-based model for steel bolted-angle connections that was developed based on insights obtained from high-fidelity finite element analysis. Results from the high-fidelity analyses are first presented, including the influence of span length and observations on angle deformations at failure. The component-based modeling approach is then presented, and predictions of the model are compared to experimental data for bolted angle connections tested under a simulated column loss scenario.

HIGH-FIDELITY FINITE-ELEMENT MODELING

Modeling Approach

The behavior of the bolted double-angle connections was first investigated using high-fidelity finite-element models, as illustrated in Figure 1, which were previously validated through comparisons with experimental data under axial loading and under a column removal scenario (Liu et al. 2012). The models were developed using the LS-DYNA finite-element software package (Hallquist 2007). The double angles, bolts, and wide-flange sections were modeled using 8-node solid elements with selective-reduced integration. The typical element size was about 2.6 mm (0.10 in) in the beam and column near the connecting elements and about 1.3 mm (0.05 in) in the bolts. The element size for the angles was on the order of 1.3 mm (0.05 in) to best capture plastic hinging mechanisms and fracture. The radius of the fillet at the heel of the angle was explicitly modeled. All components were initially in contact; static and dynamic friction coefficients of 0.3 were used.

Piecewise linear plasticity material models, calibrated to match data from tensile coupon tests, were used to model the steel. Finite element models of tensile coupons with appropriate gage length and element size were used to ensure that calculated engineering stress-strain curves corresponded to the test data. The plastic strain limit for each material (e.g., A36, A992) was calibrated to match the elongation at fracture from the tensile coupon tests. Element erosion, or removal of elements upon reaching an effective plastic strain limit, simulated fracture of the steel (Liu et al. 2012).

As proposed by Liu et al. (2012), the fracture strain in the heel of the angle was reduced to 60 % of the measured percent elongation for tensile coupons taken from the angle legs. This reduced the ductility at the critical location in the k-area, the region in the angle leg just past the fillet. The reduction in ductility at the k-area proposed by Liu et al. (2012) was based on comparisons to data from monotonic and cyclic tests of double-angle connections in tension (Garlock et al. 2003, Shen and Astaneh-Asl 1999). Reduced ductility in the k-area of an angle was also supported by coupon test data from Yang and Tan (2012). For W-shapes, Tide (2000) showed that percent elongation values at fracture were significantly smaller for coupons taken from the k-area than for coupons taken from

the web and flanges, because the k-area properties were affected by the rotary straightening process conducted in the mill. It has been acknowledged (Rees-Evans 2011) that rotary straightening and cold-working of steel angles could similarly result in reduced ductility in the k-area of the angles.

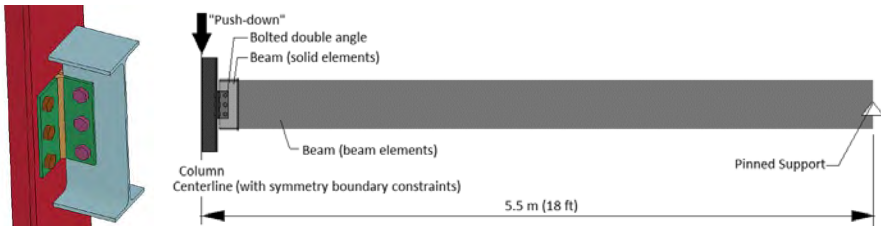


Figure 1: Two-span beam specimen modeled using symmetry boundary constraints

Influence of Span Length on Connection Failure

The influence of span length on failure of double-angle connections was investigated for a two-span beam assembly with exterior pin supports subjected to displacement-controlled vertical loading of the unsupported center column. This configuration corresponds to a full-scale test series conducted by the Defense Threat Reduction Agency and the General Services Administration (Stevens et al. 2011). Only a single span of the assembly was modeled, with symmetry boundary conditions at the column centerline (Figure 1). The beams and column were A992 W16×26 and W10×49 shapes, respectively. The A572 Grade 50, 216 mm (8.5 in) deep angles were L4×3.5×5/16. Three rows of 19 mm (0.75 in) ASTM F1852N tension control (TC) bolts were placed in standard holes at a column-leg gage of 76 mm (3 in) and a beam-leg gage of 64 mm (2.5 in). The bolts had a beam web edge distance of 51 mm (2 in) and the top bolt was located 130 mm (5 in) from the top of beam. As illustrated in Figure 1, high-fidelity modeling was used for the connection, while most of the beam span was modeled with beam elements, using constraints to enforce continuity of displacement and rotation at the interface. Additional details of the model can be found in Liu et al. (2012).

The influence of beam span was investigated by comparing results for the original 5.5 m (18 ft) beam span with results for models with span lengths of 2.7 m (9 ft) and 9.1 m (30 ft), using the same beam cross section and connection in all cases. Plots of computed horizontal reactions versus chord rotations (Figure 2(a)) show that fracture of the double-angle connection occurred at lower chord rotations for longer spans. Due to kinematics of the subassembly, a longer beam span results in greater elongation at the connection for the same beam chord rotation.

Compared to the variation in the chord rotation at failure shown in Figure 2(a), Figure 2(b) shows that the horizontal deformation of the angle at first fracture was only slightly affected by the span length. First fracture occurred at the bottom of the angle at the k-area of the column leg and propagated upward through the angle under continued

loading. While the angle's horizontal deformation at complete fracture increased somewhat with decreasing span, the angle's deformation at first fracture was nearly constant, with values of 37 mm (1.5 in), 34 mm (1.3 in), and 35 mm (1.4 in) for span lengths of 2.7 m (9 ft), 5.5 m (18 ft), and 9.1 m (30 ft), respectively. This consistency in the angle's deformation at fracture supported the use of a component-based modeling approach with a consistent value of angle deformation at failure, regardless of the span length. In the component-based approach, complete fracture of the connection is represented by successive fracture of each component in the connection, which allows the chord rotation at complete fracture to vary with span length as shown in Figure 2(b).

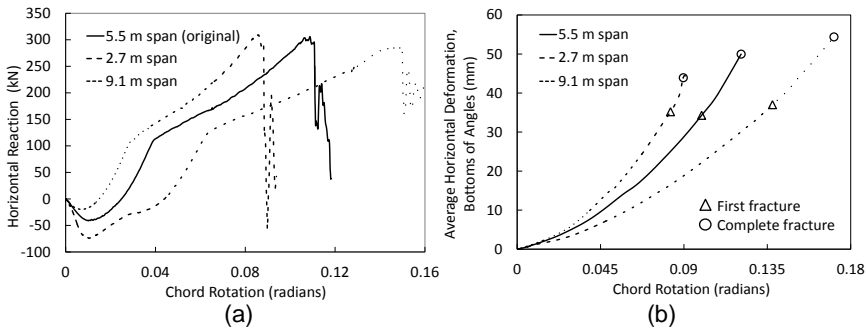


Figure 2: (a) Horizontal reactions versus chord rotation for different beam spans; (b) average horizontal deformation of angle versus chord rotation

Geometry of Deformed Angle

Figure 3 shows the geometry of a single angle in plan view, obtained from a high-fidelity finite element model in which the column leg and the beam leg of the angle were truncated at the centerlines of the column-leg bolts and the beam-leg bolts, respectively, and the angle was idealized as fully fixed at these cross sections. Figure 3(a) shows the initial, undeformed geometry of the angle, where k is the distance between the angle heel and the toe of the angle radius, g_c is the column gage length of the angle (i.e., distance between the angle heel and the centerline of the column-leg bolt), g_b is the beam gage length of the angle (i.e., distance between the angle heel and the centerline of the beam-leg bolt), and t is the angle thickness. Figure 3(b) shows the deformed geometry of the angle, in which the angle deformation along the beam axis, δ , is measured from the column face to the deformed position of the angle heel. The angle lengthens and straightens as it deforms, with two plastic hinges forming in the column leg, as indicated in Figure 3(b). This results in lateral deformation of the beam leg, δ' , and curvatures γ and γ' at the ends of the k -area in the column and beam legs, respectively. As is discussed subsequently, results of the high-fidelity analyses allowed relationships to be established between the curvatures and strains at the k -area, enabling the development of the component-based model.

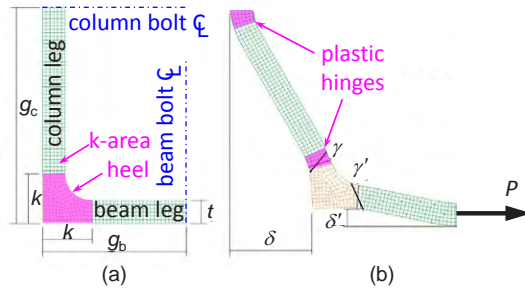


Figure 3: Angle geometry: (a) initial; (b) deformed.

COMPONENT-BASED CONNECTION MODEL

Component-based connection models provide a versatile analytical framework that can be used to model the responses of connections under extreme loads, such as column removal. In the component-based model described in this paper, the connection is discretized into multilinear component springs that are assembled into a configuration representing the geometry of the connection (Figure 4), where each component spring embodies an isolated characteristic-width segment of the two angles.

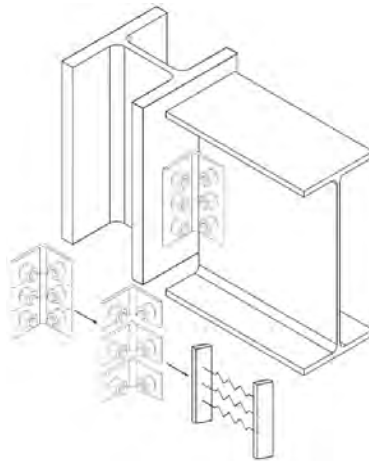


Figure 4: Discretization of bolted angle into characteristic-width angle-segments

Load-Deformation Relationship

As illustrated in Figure 5, the nonlinear behavior of the angle segment is represented through a piecewise-linear relationship between the axial load P and the angle deformation δ (see Figure 3). A single angle is considered with a component width b obtained by dividing the total depth of the angle by the number of bolts. The load

corresponding to one bolt row of a double-angle connection is obtained by doubling P . The yield capacity P_y corresponds to formation of plastic hinges in the column leg of the angle, and the ultimate capacity P_u is associated with fracture of the angle at the k-area.

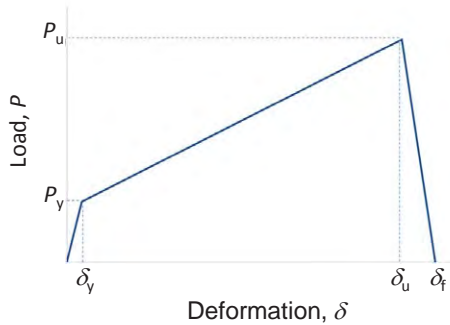


Figure 5: Load-deformation relationship for angle

Plastic Hinge Formation at Yield Load

The yield load, corresponding to the formation of two plastic hinges in the column leg of the angle (Figure 3(b)) is given by

$$P_y = \frac{2M_p}{g_{\text{eff}}}, \quad (1)$$

where $M_p = (bt^2 / 4)F_y$ is the plastic moment capacity of the component-width angle segment, F_y is the yield strength of the angle, $g_{\text{eff}} = g_c - k - d_h / 2$ is the effective gage length of the angle's column leg after formation of the plastic hinges (i.e., the distance between the plastic hinges), and d_h is the diameter of the column-leg bolt holes. The angle deformation at the formation of the plastic hinges, δ_y , can be calculated as

$$\delta_y = \frac{P_y}{K_i}, \quad (2)$$

where K_i is the initial stiffness of the angle segment. The initial stiffness is calculated from the following expression, which was derived by Shen and Astanteh-Asl (2000) based on the geometry of the section of angle between the beam-leg bolt and the column-leg bolt, assuming elastic bending of the angle's column leg:

$$K_i = \frac{12EI}{g_c^3} \left[1 - \frac{3g_b}{4(g_c + g_b)} \right], \quad (3)$$

where E is the modulus of elasticity of steel and $I = bt^3 / 12$ is the moment of inertia of the angle.

Angle Fracture at Ultimate Load

Expressions for the ultimate load P_u (i.e., the load corresponding to initial tearing in the angles) and the corresponding angle deformation δ_u are derived based on the simplified geometry shown in Figure 6, in which the angle's column leg is modeled as a straight-line segment with concentrated plastic hinges at its ends, subjected to axial tension T_u , shear force V_u , and bending moment M_u . The plastic hinge lengths are assumed equal to the angle thickness t .

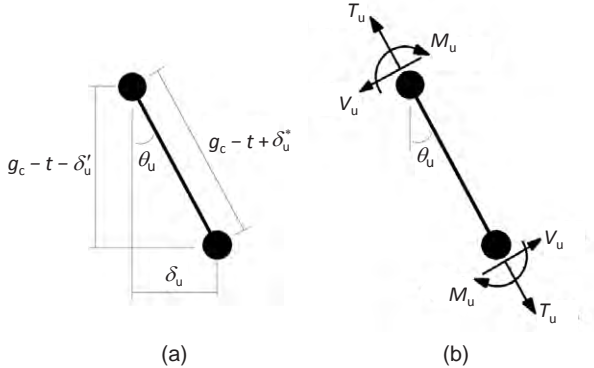


Figure 6: Two-hinge idealization of the angle's column leg at the ultimate load: (a) geometry and (b) free-body diagram.

Equilibrium of forces along the beam axis yields the following expression for P_u :

$$P_u = V_u \cos \theta_u + T_u \sin \theta_u , \quad (4)$$

in which the chord rotation of the angle's column leg, θ_u , can be calculated as

$$\theta_u = \cos^{-1} \left(\frac{g_c - t - \delta'_u}{g_c - t + \delta_u^*} \right) , \quad (5)$$

where δ_u^* is the elongation of the column leg at the ultimate load. The shear and axial tension in the angle's column leg are calculated as

$$V_u = \alpha P_y \quad \text{and} \quad T_u = \alpha b t F_y / 3 , \quad (6a,b)$$

in which $\alpha = 1.2$ is a strain-hardening coefficient. The expression for T_u in Eq. (6b) assumes that the cross-section is fully yielded with a linear strain profile based on observations from high-fidelity models, in which the tensile and compressive strains at the faces of the angle's column leg at fracture (at the toe of the angle radius) were found to be ϵ_{uk} and $\frac{1}{2} \epsilon_{uk}$, respectively, where ϵ_{uk} is the elongation at fracture at the k-area. This observed strain profile can be decomposed into a bending strain of $\frac{3}{4} \epsilon_{uk}$ and an axial strain of $\frac{1}{4} \epsilon_{uk}$, from which the column-leg elongation can be calculated as $\delta_u^* = \frac{1}{2} t \epsilon_{uk}$,

assuming that axial elongation occurs only at the plastic hinges, with plastic hinge lengths of t . As proposed by Liu et al. (2012), in the absence of test data for the k-area, 60 % of the reported elongation from certified mill test reports or tests of coupons from the leg of the angle is recommended for ε_{uk} .

The lateral deformation of the beam leg, δ'_u in Eq. (5), is calculated from the geometry:

$$\delta'_u = (g_b - t) \sin(\gamma'_u(k - t) / 2) \approx \gamma'_u(g_b - t)(k - t) / 2. \quad (7)$$

Based on the observed strain profile at the ultimate load, noted above, the curvature of the angle's column leg at the end of k-area can be calculated as

$$\gamma_u = \frac{3\varepsilon_{uk}}{2t}. \quad (8)$$

The curvature of the angle's beam leg at the end of the k-area, γ'_u in Eq. (7), can be related to the curvature of the angle's column leg, γ_u in Eq. (8), through the following empirical equation, based on the results of high-fidelity finite-element analyses (to be published):

$$\gamma_u / \gamma'_u = r + (r^3 - 1)\left(t - \frac{5}{16}\right) + (r^5 - 1)\left(t - \frac{5}{16}\right)^2, \quad (9)$$

where $r = g_c / g_b$ is the ratio of the angle's gage lengths. Eq. (9) is considered to be applicable for thickness, t , from 6.4 mm (0.25 in) to 15.9 mm (0.63 in), and gages, g_b and g_c , from 51 mm (2.0 in) to 76 mm (3.0 in). Also, g_c should be greater than or equal to g_b . The ultimate deformation of the angle can be calculated from the geometry as

$$\delta_u = (g_c - t - \delta'_b) \tan \theta_u. \quad (10)$$

The failure deformation, at which the load P drops to zero, is taken as $\delta = 1.1 \delta_u$.

Comparisons with Experimental Data

Results of the component-based connection model were compared with experimental measurements from bolted-angle connection tests reported by Weigand and Berman (2015). In that study, the connections were tested under combined rotation and axial deformation demands representative of a column loss scenario, corresponding to displacement-controlled vertical loading of an unsupported center column in a two-span beam assembly. The double-angle connections at both ends of each beam span were assumed to be identical, and the end columns were assumed to be fixed, so that all deformations occurred in the connections and beams. In the component-based modeling, a single beam span was considered, assuming symmetry of the response about the unsupported center column. The load-deformation relationship for single-plate shear connections from Main and Sadek (2014) was used for the compressive response of the connections, with yield and ultimate capacities corresponding to the combined bearing strength at the bolt holes of the two angles' beam legs.

Figure 7 shows a comparison of measured and computed values of the vertical load applied to the unsupported center column and the horizontal reaction at the end column for a double-angle connection with three bolt rows (Weigand and Berman 2015, specimen ba3b|34|14). For that connection test, the thickness of the angles was $t = 6.4 \text{ mm}$ (0.25 in) and the gages of the column leg and the beam leg were $g_c = 76 \text{ mm}$ (3.0 in) and $g_b = 70 \text{ mm}$ (2.8 in), respectively. The measured yield strength of the angle steel was $F_y = 382 \text{ MPa}$ (55.4 ksi). Initial differences between the measured and computed values, for displacements less than about 300 mm (11.8 in), resulted from frictional resistance of the connection due to pre-tensioning of the bolts, which was not considered in the model. The subsequent response, after frictional slippage and loss of pre-tension, is captured fairly well by the component-based model. The peak vertical load and the peak horizontal reaction from the model exceed the measured values by 9 % and by 0.7 %, respectively. The model prediction for the center column displacement at the ultimate vertical load was 7 % less than the experimental value.

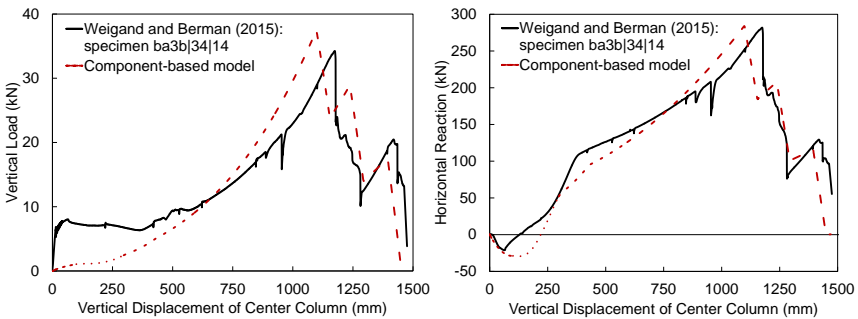


Figure 7: Comparisons of component-based model with experimental measurements for a double-angle connection with three bolt rows (estimated uncertainty in experimental data is less than $\pm 0.5 \%$, based on repeated calibrations of instruments)

CONCLUSIONS

Building on insights obtained from high-fidelity finite element analyses of bolted double-angle connections, a component-based model was developed to capture the response of the connections under the combined axial and flexural loading that occurs in column removal scenarios. The high-fidelity modeling provided key insights on the initiation of angle fracture at a consistent level of deformation and the relationship between strains and curvatures in the angle at the point of fracture. By considering the mechanics of angle deformation associated with the formation of two plastic hinges in the column leg of the angle, equations were developed for the yield capacity and the ultimate capacity of the angle, along with the corresponding deformations. Using these equations, a nonlinear load-displacement relationship was defined to represent the axial response for each bolt row of the angle. Predictions of the component-based model were compared with experimental results for a bolted double-angle connection under a column removal scenario, showing that the model captured the key features of the measured response.

ACKNOWLEDGMENTS

This study was partially supported by the NIST/ UMD-ARRA Fellowship. The authors would like to thank Fahim Sadek of NIST for valuable comments and input on this work.

DISCLAIMER

Certain commercial software or materials are identified to describe a procedure or concept adequately. Such identification is not intended to imply recommendation, endorsement, or implication by NIST that the software or materials are necessarily the best available for the purpose.

REFERENCES

- Garlock, M.M., Ricles, J.M., and Sause, R. (2003). "Cyclic Load Tests and Analysis of Bolted Top-and-Seat Angle Connections," *J. Struct. Eng.*, Vol. 129, Issue 12, pp. 1615-1625.
- Hallquist, J. (2007). *LS-DYNA Keyword User's Manual, Version 971*, Livermore Software Technology Corporation, Livermore, CA.
- Liu, J., Main, J. and Sadek, F. (2012) "Modeling of Double-Angle Shear Connections for Evaluation of Structural Robustness," *Proc., 6th Congress on Forensic Engineering*, San Francisco, CA, October 31 – November 3, 2012, pp. 1081 – 1090.
- Main, J.A. and Sadek, F. (2014). "Modeling and Analysis of Single-Plate Shear Connections under Column Loss," *J. Struct. Eng.*, 04013070, pp. 1-12.
- Rees-Evans, D. (2011). "Re: Steel Angle Question," message to J. Liu, 27 Sept. 2011, e-mail.
- Shen, J. and Astaneh-Asl, A. (1999) "Hysteretic Behavior of Bolted-Angle Connections," *J. Constructional Steel Research*, Vol. 51, pp. 201–218.
- Stevens, D., Crowder, B., Sunshine, D., Marchand, K., Smilowitz, R., Williamson, E., and Waggoner, M. (2011). "DoD Research and Criteria for the Design of Buildings to Resist Progressive Collapse," *J. Struct. Eng.*, Vol. 137, Issue 9, pp. 870-880.
- Tide, R.H.R. (2000) "Evaluation of Steel Properties and Cracking in 'k'-area of W Shapes," *Engineering Structures*, Vol. 22, Issue 2, pp. 128-134.
- Weigand, J. M. and Berman, J. W. (2015) "Integrity of Bolted Angle Connections Subjected to Simulated Column Removal," *J. Struct. Eng.*, 04015165, pp. 1-13.
- Yang, B. and Tan, K.H. (2012) "Numerical Analyses of Steel Beam-Column Joints Subjected to Catenary Action," *J. Constructional Steel Research*, Vol. 70, pp. 1–11.

ESTIMATING COLLAPSE CAPACITY OF STEEL MOMENT CONNECTIONS SUBJECTED TO COLUMN REMOVAL

Ramon Gilsanz
Gilsanz Murray Steficek, New York, New York, 10001, USA
Ramon.Gilsanz@GMSLLP.com

Akbar Mahvashmohammadi
Gilsanz Murray Steficek, New York, New York, 10001, USA
Akbar.mahvash@GMSLLP.com

John Abruzzo
Thornton Tomasetti, San Francisco, CA, 94108, USA
JABruzzo@ThorntonTomasetti.com

The National Institute of Standards and Technology has performed a research study on progressive collapse of steel structures. Prototype ten-story steel buildings have been designed for seismic design category C and D. The designed steel structures had steel welded unreinforced flange-bolted web (WUF-B) and reduced beam section (RBS) connections. Full scale testing has been performed on beam-column assemblies of the designed structures with two beams and three columns to investigate the capacity of the designs subjected to column removal. The study showed that the rotational capacity under monotonic column removal testing is greater than the rotational capacity obtained from seismic tests by about twice for steel structures. Numerical simulations have been performed in the mentioned study to predict the capacity of the structural systems using rigorous nonlinear analysis. This articles presents simple approximate formulas to estimate the collapse capacity of steel WUF-B and RBS connections for design purposes that were developed in Chapter 3 of the Alternative Load Path Analysis (ALPA) Guideline research committee.

INTRODUCTION

The National Institute of Standard and Technology (NIST) is conducting a comprehensive research program to study the vulnerability of structures to disproportionate collapse. Experimental studies were performed on steel and concrete frame systems along with rigorous numerical analysis to predict collapse behavior of steel and concrete frame systems (Sadek et al, 2010). In this article a summary of the experimental study performed by NIST on steel structures with WUF-B and RBS connections is presented. Comparison of the experimental results and the resistance predicted by design codes shows inaccuracy of code prediction. In this article a simple closed form formula is presented to predict the collapse capacity of steel beam-column assemblies subjected to progressive collapse.

EXPERIMENTAL STUDY

NIST performed an experimental study of two full scale steel beam-column assemblies with three steel columns and two beams to define response characteristics under a column removal scenario and provide experimental data for validation of beam-to-column connection models for assessing the robustness of structural systems (Lew et al, 2013). A summary of the experimental study is presented in this section.

Building Plans and Test Specimens

Full scale testing was performed on two steel beam column assemblies including three columns and two beams which represented part of the second floor framing of a 10-story steel frame building. The steel buildings are located in seismic design category (SDC) of C and D with plans as shown in Figure 1. The SDC C building consists of welded unreinforced flange bolted (WUF-B) beam-column connection and the SDC D building consists of reduced beam section (RBS) connection as shown in Figure 2. The steel tests specimens are shown in Figure 3. Figure 4 shows photographs of test specimens subjected to center-column displacement.

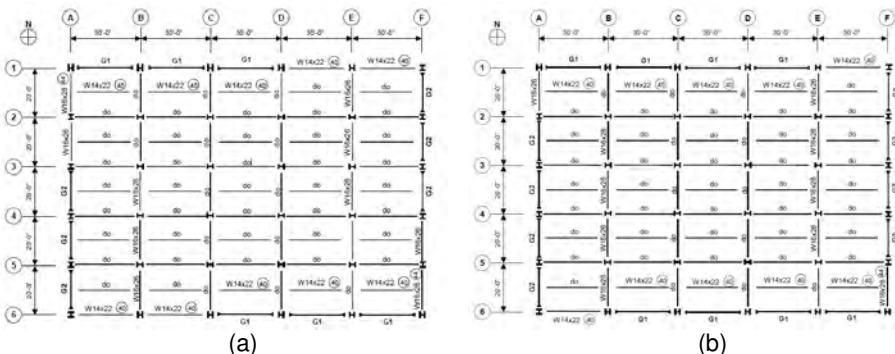


Figure 1. Plan layouts for (a) SDC C and (b) SDC D buildings (Sadek et al, 2013)

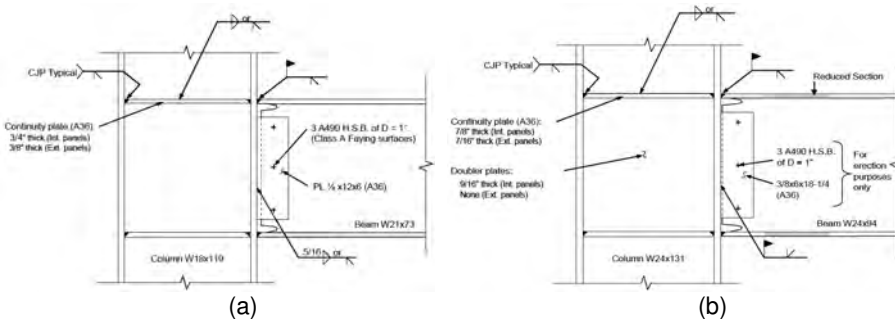


Figure 2. Moment connection details; (a) WUF-B and (b) RBS connection (Lew et al, 2013)

Experimental Results

The failure mode and load-displacement curve of the WUF-B specimen are shown in Figure 5. The WUF-B specimen failed under a deflection of 19.5 in, corresponding chord rotation of 0.081 rad (4.6°) using beam center line to centerline span, and applied force of 200 kip. The failure was characterized by the following sequence (Sadek et al, 2010):

1. Local buckling of the top flanges of the beams near the center column
2. Successive shear failure of the lowest and middle bolts connecting the beam web to a shear tab at the center column
3. Fracture of the bottom flange near the weld access hole.

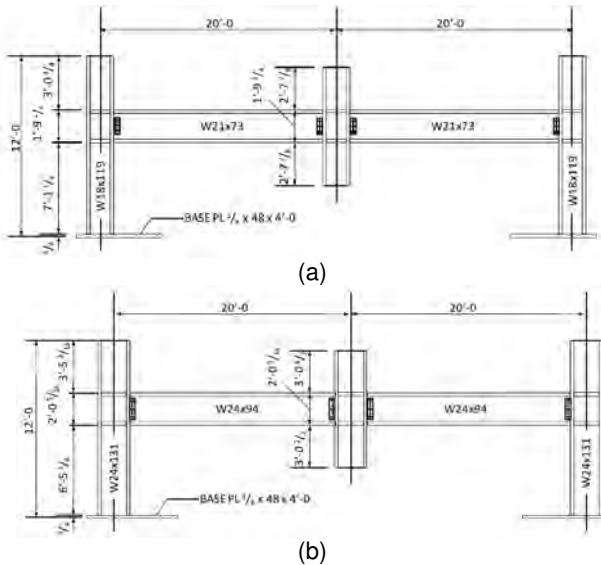


Figure 3. Steel test specimen; (a) SDC C with WUF-B connection (b) SDC D with RBS connection (Lew et al, 2013)

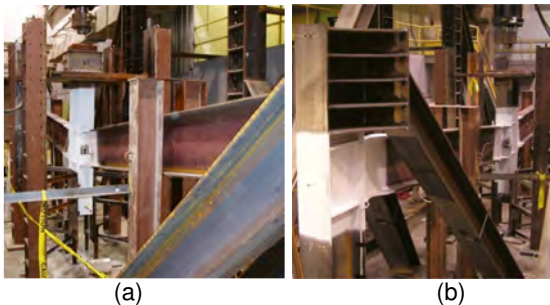


Figure 4. Photographs of test specimens subjected to center-column displacement; (a) WUF-B specimen (b) RBS specimen (Lew et al, 2013)

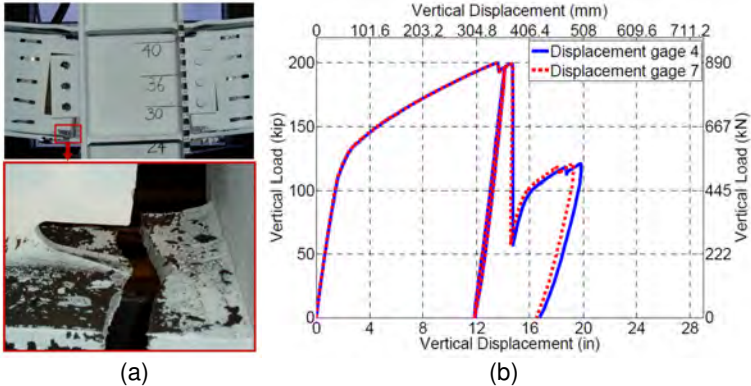


Figure 5. Experimental results of WUF-B specimen; (a) failure mode, (b) applied load versus deflection (Lew et al, 2013)

The failure mode and load deflection curve of RBS specimen are shown in Figure 6. This specimen failed at a vertical displacement of 33.5 in, corresponding chord rotation of 0.14 rad (8) using centerline to centerline beam span, and applied vertical load of 400 kip. The failure initiates by fracture of the bottom flange in the middle of one of the RBSs close to the centerline column which propagates through the web until the specimen cannot carry the applied load (Sadek et al, 2010).

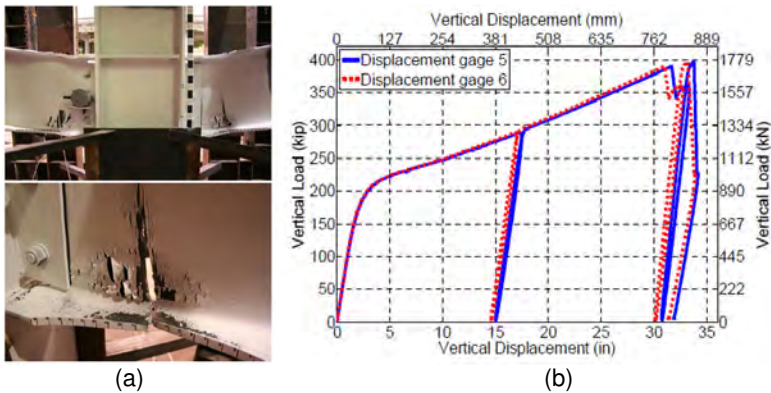


Figure 6. Experimental results of RBS specimen; (a) failure mode, (b) applied load versus deflection (Lew et al, 2013)

SIMPLIFIED CLOSED FORM SOLUTIONS

The actions resisting column removal disproportionate collapse are bending and catenary actions. Figure 7 shows the free body diagram of resisting forces developed at one half of the beam-column assembly subjected to a column removal scenario. The beam-

column assembly is assumed to have rigid-plastic behavior with plastic rotation concentrated at column faces. The parameters in Figure 7 are defined as:

- Δ = the deflection at the removed column center
- $\theta = \Delta/L$ = the beam chord rotation
- F = the applied force at the removed column center
- M = the beam moment at column face
- P = the axial force in the beam
- L = the beam clear span

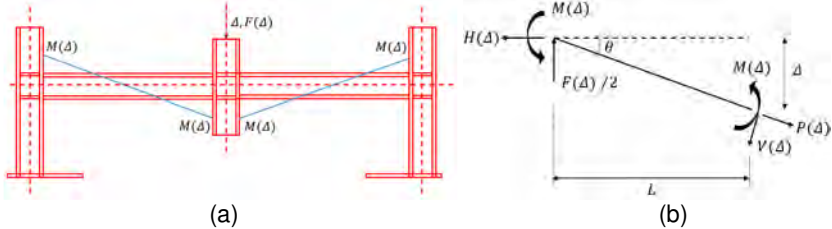


Figure 7. Resisting actions developed after column removal; (a) moment diagram, (b) free body diagram

The bending action resists the applied force by developing bending and consequently shear forces in the section. The catenary action provides resistance by developing truss action as a result of geometric nonlinearity. Using the free body diagram of one half of beam-column assembly shown in Figure 7, the resisting force at vertical displacement of Δ can be written as:

$$F(\Delta) = 2V(\Delta)\cos(\theta) + 2P(\Delta) \cdot \sin(\theta) \quad 1$$

where,

$$V(\Delta) = \frac{2M}{L/\cos(\theta)} \quad 2$$

Substitution of Eq. 2 into Eq. 1 results in

$$F(\Delta) = \frac{4M(\Delta)}{L} \cos^2(\theta) + 2P(\Delta) \cdot \sin(\theta) = 4M(\Delta) \frac{L}{L^2 + \Delta^2} + 2P(\Delta) \cdot \frac{\Delta}{\sqrt{L^2 + \Delta^2}} \quad 3$$

As shown in Eq. 3, the resistance depends on the beam end moments and axial force, which depends on axial deformation and rotation. Accurate prediction of resisting force requires nonlinear analysis (both material and geometric nonlinearity) and a model that captures the failure modes.

Abruzzo (2014) provided an incremental solution for Eq. 3 using concepts of theory of plasticity that can be used as a spreadsheet in engineering offices. He assumed the plastic rotation and plastic axial deformation are concentrated at hinges located at the column faces. At each increment the moment and axial force can be determined at each hinge location using the normality rule. The normality rule states that the ratio of the displacement increments corresponding to load effects must be normal to the yield surface. While a function curve has a unique normal along its length, a piecewise linear representation has unique vectors within straight line portions and then is discontinuous

at the joining points. According to the normality rule at the points of discontinuity the ratio of the displacement increments can take the range between the normal vectors. This makes the computation easier using a spreadsheet. This method provides estimations close to the experimental data (ALPA, 2016).

In this article three simplifying assumptions were made in analysis of steel frame structures, to be able to change the path dependent step by step nature of the problem to a closed form prediction format that can simply predict the resisting force given the displacement:

1. The material was assumed to be rigid plastic with an effective yield stress $F_{y,eff}$ as an average of yield F_y and ultimate F_u stresses, and plastic rotation was assumed to be concentrated at column faces.
2. The yield surface (moment axial force interaction) was assumed to be the simplified yield surface shown below:

$$\begin{aligned} \frac{P}{P_y} + \frac{M}{1.18M_p} &= 1.0, & \text{for } P > 0.15P_y \\ M &= M_p, & \text{for } P \leq 0.15P_y \end{aligned} \quad 4$$

The simplified yield surface is shown in Figure 8 and is known to be a good approximation of the actual yield surface when axial buckling cannot occur (Salmon et al, 2009)

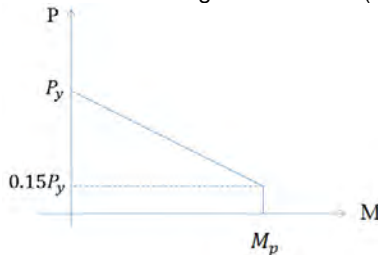


Figure 8. Simplified yield surface

3. The resistance at each point is assumed to be the maximum resistance that can be achieved by using any pair of moment and axial force on the yield surface. In other words the resistance at each deformation is assumed to be the collapse resistance at that deformed geometry.

By applying the assumptions in Eq.3, we can write:

$$F(\Delta) = \max \left(4M(\Delta) \frac{L}{L^2 + \Delta^2} + 2P(\Delta) \frac{\Delta}{\sqrt{L^2 + \Delta^2}} \right) \quad 5$$

where,

$$P(\Delta) = P_y \left(1 - \frac{M(\Delta)}{1.18M_p} \right) \quad 6$$

and

$$P_y = AF_{y,eff} \quad 7$$

$$M_p = ZF_{y,eff} \quad 8$$

Substitution of Eq. 6 in Eq. 5 leads to:

$$F(\Delta) = \max \left(4M_p \frac{L}{L^2 + \Delta^2} + 2P_y \left(1 - \frac{M(\Delta)}{1.18M_p} \right) \frac{\Delta}{\sqrt{L^2 + \Delta^2}} \right) \quad 9$$

This equation is first order with respect to $M(\Delta)$ indicating that the derivative is constant (not zero) and the maximum happens at either of boundary values for $M(\Delta)$, i.e. $M(\Delta)$ and $P(\Delta)$ pairs of zero and P_y , and M_p and $0.15P_y$ (See Figure 9). Therefore substitution of pairs of $M(\Delta) = 0$, $P(\Delta) = P_y$ and $M(\Delta) = M_p$, $P(\Delta) = 0.15P_y$ into Eq. 3 results in:

$$F(\Delta) = \max \left(4M_p \frac{L}{L^2 + \Delta^2} + 0.3 \cdot P_y \frac{\Delta}{\sqrt{L^2 + \Delta^2}}, 2 \cdot P_y \frac{\Delta}{\sqrt{L^2 + \Delta^2}} \right) \quad 10$$

In smaller deformations the resistance is governed by axial force and moment pair of $P(\Delta) = 0.15P_y$ and $M(\Delta) = M_p$, and in larger deformations the resistance is governed the axial force and moment pair of by $P(\Delta) = P_y$ and $M(\Delta) = 0$. The two pairs lead to the same response when:

$$\begin{aligned} F(\Delta) &= 4M_p \frac{L}{L^2 + \Delta^2} + 0.3 \cdot P_y \frac{\Delta}{\sqrt{L^2 + \Delta^2}} = 2 \cdot P_y \frac{\Delta}{\sqrt{L^2 + \Delta^2}} \\ &\xrightarrow{\text{yields}} 4M_p \frac{L}{L^2 + \Delta^2} = 1.7P_y \frac{\Delta}{\sqrt{L^2 + \Delta^2}} \xrightarrow{\text{yields}} \Delta \sqrt{L^2 + \Delta^2} = \frac{4}{1.7} \frac{M_p L}{P_y} \xrightarrow{\text{yields}} \\ &\Delta \sqrt{L^2 + \Delta^2} = 2.35 \frac{ZL}{A} \end{aligned} \quad 11$$

Eq. 10 can be rewritten using Eq. 11:

$$F(\Delta) = \begin{cases} 4M_p \frac{L}{L^2 + \Delta^2} + 0.3 \cdot P_y \frac{\Delta}{\sqrt{L^2 + \Delta^2}}, & \Delta \sqrt{L^2 + \Delta^2} \leq 2.35 \frac{ZL}{A} \\ 2 \cdot P_y \frac{\Delta}{\sqrt{L^2 + \Delta^2}}, & \Delta \sqrt{L^2 + \Delta^2} > 2.35 \frac{ZL}{A} \end{cases} \quad 12$$

The failure point was found using a plastic hinge length and considering bending action only. It was assumed that the test specimen fails when the beam extreme fiber reaches the ultimate strain in the plastic hinge. The failure (ultimate) deformation is calculated as:

$$\Delta_u = \theta_u L = \phi_u l_p L = \frac{\epsilon_u}{0.5d} l_p L \quad 13$$

where,

Δ_u = the ultimate deformation

θ_u = the ultimate chord rotation

ϕ_u = the ultimate curvature corresponding to the curvature with ultimate strain at the extreme fiber

l_p = the plastic hinge length

d = the beam depth

Consequently the failure strength can be found by substituting Eq. 13 into Eq. 12:

$$F_u(\Delta) = \begin{cases} 4M_p \frac{L}{L^2 + \Delta_u^2} + 0.3 \cdot P_y \frac{\Delta_u}{\sqrt{L^2 + \Delta_u^2}}, & \Delta_u \sqrt{L^2 + \Delta_u^2} \leq 2.35 \frac{ZL}{A} \\ 2 \cdot P_y \frac{\Delta_u}{\sqrt{L^2 + \Delta_u^2}}, & \Delta_u \sqrt{L^2 + \Delta_u^2} > 2.35 \frac{ZL}{A} \end{cases} \quad 14$$

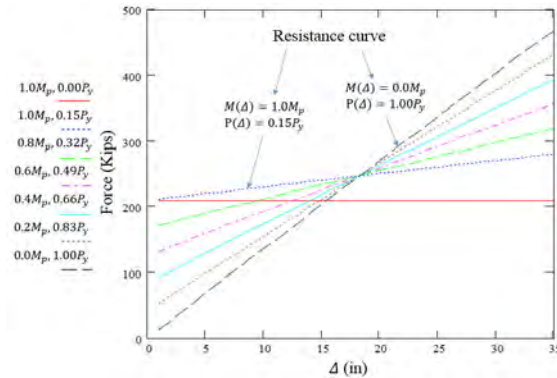


Figure 9. Resistance curve as the envelope of force deformation curves obtained from different pairs of moment and axial force on yield surface

Example 1: Steel WUF Connections

In this example we compare the experimental and analytical predictions of the SDC building test specimen with WUF-B connection detail as shown in Figure 3 (a). Figure 10 (a) compares the experimental force-deformation curve with predictions by FEMA 350 (2000), ASCE 41 (2006), AISC steel design guide 26 (2010), and New York City Building Code (2008). The failure point does not agree with predictions provided by these codes. Figure 10 (b) compares the experimental results, with prediction provided using the simplified approach (Eq. 12). Three different effective stresses of F_y , $(F_y + F_u)/2$, and F_u were used for prediction of resisting force using Eq. 12 with the corresponding labels of F_{GMS_yield} , $F_{GMS_weighted}$, and $F_{GMS_ultimate}$ in Figure 10 (a). The assumption of rigid plastic material (neglecting strain hardening) leads to smaller slope in analytical predictions than the experimental results.

It was observed that using a plastic hinge length l_p equal to a quarter of beam depth $0.25d$ leads to good prediction of ultimate deformation:

$$l_p = 0.25d \text{ for WUF-B connections} \quad 15$$

Substituting Eq. 15 into Eq. 13 the ultimate deformation is found as:

$$\Delta_u = \theta_u L = \phi_u l_p L = 0.5 \epsilon_u L \quad 16$$

The predicted ultimate deformation is shown in Figure 10 (b). The assumption of plastic hinge length equal to 25% of beam depth agrees with the observations from NIST experiment as shown in Figure 11. However there is experimental data that recommend plastic hinge length much greater than $0.25d$ for WUF-B connections (Uang et. al, 2015).

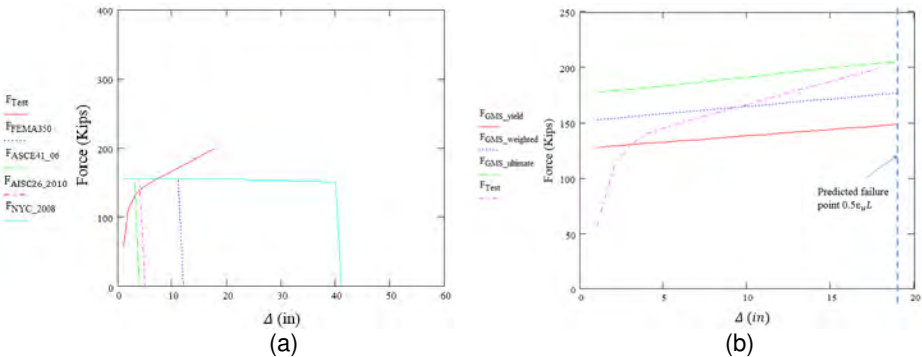


Figure 10. Comparison of WUF-B experimental force-deformation curve with (a) code predictions, (b) Simplified method

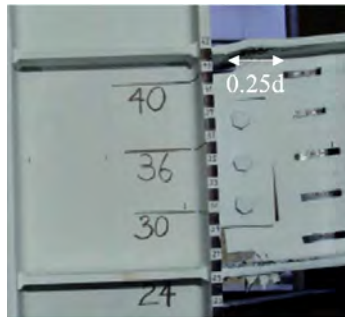


Figure 11. Plastic hinge length of WUF-B connection observed in experiment

Example 2: Steel RBS connections

In this example we compare the experimental and analytical predictions of the SDC building test specimen with RBS connection detail as shown in Figure 3 (b). Figure 12 (a) compares the experimental force-deformation curve with predictions by FEMA 350 (2000), ASCE 41 (2006), AISC steel design guide 26 (2010), and New York City Building Code (2008).

Figure 12 (b) compares the experimental results, with predictions provided using the simplified approach (Eq. 12). Three different effective stresses of F_y , $(F_y + F_u)/2$, and F_u were used for predicting the resisting force using Eq. 12 with the corresponding labels in Figure 12 (b) as F_{GMS_yield} , $F_{GMS_weighted}$, and $F_{GMS_ultimate}$.

It was observed that using a plastic hinge length l_p equal to 60% of the beam depth leads to good prediction of ultimate deformation:

$$l_p = 0.6d \text{ for WUF-B connections} \quad 17$$

Substituting Eq. 15 into Eq. 13, the ultimate deformation can be calculated as:

$$\Delta_u = \theta_u L = \phi_u l_p L = 1.2 \varepsilon_u L \quad 18$$

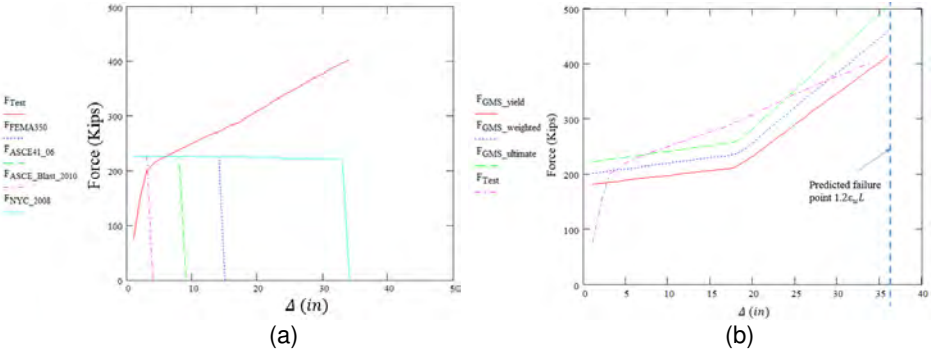


Figure 12. Comparison of RBS experimental force-deformation curve with (a) code prediction, (b) simplified method

The predicted ultimate deformation is shown in Figure 12 (b). The assumption of plastic hinge length equal to 60% of beam depth agrees with the plastic hinge length range in literature, as shown in Figure 13. (Uang, et. al, 2015)

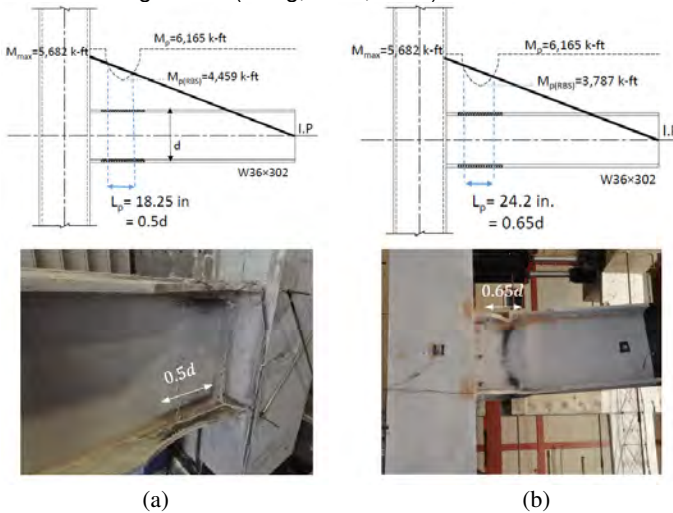


Figure 13. RBS plastic hinge length, (a) with box column and $c = 0.16b_f$, (b) box column and $c = 0.25b_f$ (Uang, et. al, 2015)

SUMMARY AND CONCLUSION

NIST performed two experiments on beam column assemblies with WUF-B and RBS connections that were designed in seismic design category C and D. It was shown that the current design codes do not provide accurate predictions on force-deformation behavior of such assemblies subjected to column removal scenarios. A simplified approach was presented and was shown to predict good estimates of the resistance provided by such assemblies subjected to a column removal scenario.

REFERENCES

- AISC Steel Design Guide 26 (2010), "Design of Blast Resistance Structures", American Institute of Steel Construction.
- ASCE 41-06 (2006), "Seismic Rehabilitation of Existing Buildings", American Society of Existing Buildings.
- FEMA-350 (2000), "Recommended Seismic Design Criteria for New Steel Moment Frame Buildings", Federal Emergency Management Agency.
- Lew, H.S., Main, J., Robert, S.D., Sadek, F., Chiarito, V.P. (2013), "Performance of Steel Moment Connections under a Column Removal Scenario. I: Experiments", *Journal of Structural Engineering*, Vol. 139, (pp. 98-107).
- NYCBC (2008), "New York City Building Code".
- Sadek, F., Main, J., Lew, H.S., Robert, S.D., Chiarito, V.P., El-Tawil, S. (2010), "An Experimental and Computational Study of Steel Moment Connections under a Column Removal Scenario", NIST Technical Note 1669.
- Salmon, C.S., Johnson, J.E., Malhas, F.A. (2009), "Steel Structures, Design and Behavior, Fifth Edition", HarperCollins College Publishers.
- Uang (2015), "Personal communication with Chia-Ming Uang, Gulen Ozkula and Charles Carter", Department of Structural Engineering, University of California, San Diego.
- ALPA (2016), "Alternative Load Path Analysis Guideline for Disproportionate Collapse, Chapter 3 50% Draft".
- Abruzzo (2014), "Mitigation Strategies for Disproportionate Collapse", Thornton Tomasetti Inc.

EXPERIMENTAL INVESTIGATIONS OF COMPOSITE JOINTS AND THEIR BEHAVIOUR DURING THE LOSS OF A COLUMN

Nadine Hoffmann

Institute of Structural Design, Pfaffenwaldring 7, University of Stuttgart, Germany
Nadine.Hoffmann@ke.uni-stuttgart.de

Ulrike Kuhlmann

Institute of Structural Design, Pfaffenwaldring 7, University of Stuttgart, Germany
U.Kuhlmann@ke.uni-stuttgart.de

ABSTRACT

A local damage within a frame structure (e.g. column loss) may lead to a failure of the global structure and therefore to a collapse of the building. To avoid such a global failure through local damage it is necessary to enable a redistribution of loadings within the structure. This means that the development of alternate load paths should be enabled. Such a redistribution of loadings from a pure bending to a bending-membrane-loading causes under certain circumstances large deflections leading to big deformations of the joints.

Tests on composite joints under simultaneous and successive M-N-loading have been performed. The different behaviour of sagging and hogging moment at the joints as well as the influence of these dynamic effects, as they occur in the case of an impact, are worked out.

Additionally two tests on composite frames have been performed with the aim to absorb an additional vertical loading through large deformations activating the catenary effect in the composite frame without receiving a premature failure.

1 INTRODUCTION

In case of a column loss the available loadings in the structure have to be transferred by the members of the residual intact structure. In EN 1991-1-7 different methods are given how to consider a local failure of the structure within the design. The method of alternate load paths represents one of them. The objective is to enable large deformations in the structure and hence redistribute loadings from a pure bending to a bending-membrane-state, leading to a normal force in the joints. Consequently additional loading capacity is activated in the system (Hoffmann et al., 2015).

For such a robust design of the structure sufficient load bearing capacity as well as sufficient rotational capacity have to be provided in beams and joints.

Based on a typical office building as a reference structure details have been extracted as test specimens (see Figure 1), which were designed according to EN 1994-1-1 and EN 1993-1-8.

During a possible loss of a column two different critical joints have to be considered: The joint that is located directly above the lost column (directly affected joint) and the joints that are adjacent to the lost column (indirectly affected joints). The directly affected joint undergoes during the column loss a change of the hogging moment into a sagging moment, whereas the hogging moment in the indirectly affected joint

increases during the column loss. For activation of an alternate load path in the structure all three joints have to contribute to the frame system.

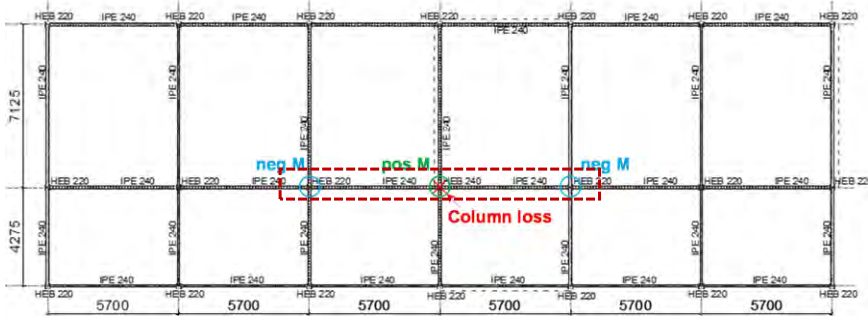


Figure 1. Column loss in a reference structure (Kuhlmann et al., 2016)

2 EXPERIMENTAL INVESTIGATIONS OF COMPOSITE JOINTS

2.1 Experimental programme

In the frame of a German DAST-AiF research project “Robustheit” (Kuhlmann and Hoffmann, 2015a) four tests on composite joints have been investigated. Hence, two tests under sagging moment loading (series JT1) have been performed and two tests under hogging moment loading (series JT2) respectively. In order to observe the behaviour of the joints during the loss of a column and the development of catenary action an additional normal force was applied on the test specimens. The moment loading and the horizontal loading have been applied once successively and in the other cases simultaneously.

Four additional tests on composite joints with a combined M-N-loading have been performed in the frame of the European RFCS research project “RobustImpact” (Kuhlmann et al., 2016). As variants of these tests the loading velocity was increased. An overview on the performed tests is given in Table 1.

Table 1. Overview on the experimental programme on composite joints (Kuhlmann and Hoffmann, 2015a), (Kuhlmann et al., 2016)

Tests	Loading	Number of tests	Positive M (JT1)		Negative M (JT2)	
Composite joint tests	static	4	<i>M/N successive (JT1.1)</i>	<i>M/N simultaneous (JT1.2)</i>	<i>M/N successive (JT2.1)</i>	<i>M/N simultaneous (JT2.2)</i>
Composite joint tests	high speed	4	<i>M/N simultaneous (JT1.3)</i> Speed: 140 mm/s	<i>M/N simultaneous (JT1.4)</i> Speed: 70 mm/s	<i>M/N simultaneous (JT2.1)</i> Speed: 140 mm/s	<i>M/N simultaneous (JT2.2)</i> Speed: 70 mm/s

The loading speed of 140 mm/s corresponds to the displacement velocity at the top of the column during an impact of a car with around 30 km/h to a column, as has been calculated in (Kuhlmann et al., 2016). But of course this velocity of the column head depends on several different factors influencing the response of a column as for example velocity of the impact body, mass height and angle of the impact body as well as resistance of the column and the mass applied on the column head (Kuhlmann et al., 2016).

2.2 Test setup

In order to investigate the load bearing behaviour and the rotational behaviour of the composite joint under combined M-N-loading three hydraulic jacks have been used for the performance of the tests (see Figure 2). A vertical jack above the column that is assumed as lost applying an additional force in order to generate a moment at the joint. Two horizontal jacks are installed at both ends of the test specimens causing the additional normal force in the joint.

In order to minimize the efforts for the construction of the test rig, the test specimens of the tests with hogging moment were turned around so that the vertical force applies the reverse moment to the composite girder. Thus it was possible to use the same test rig for performing all the experimental joint tests.

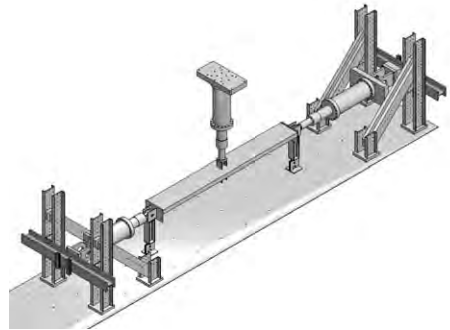


Figure 2. Test setup of composite joint tests (Kuhlmann and Hoffmann, 2015a), (Kuhlmann et al., 2016)

2.3 Performance of the tests

The test specimens were designed through analytical calculations as to achieve a ductile failure of the joints. For joints with sagging moment loading the ductile component *endplate in bending* in mode 2 (yielding of endplate with failure of bolts finally) was decisive and for joints with hogging moment loading a failure of the *rebars in tension* was dominant. All tests are performed deformation controlled up to failure of the test specimen. The failed test specimens of the composite joints are shown in Figure 3. It may be recognized that for the sagging moment loading as well as for the hogging moment loading the expected failure mode occurred.



Figure 3. Composite joints after failure (Kuhlmann and Hoffmann, 2015b)

2.4 Test results

During the tests it could be observed that a redistribution of the present moment loading into a membrane loading was feasible for joints with sagging moment loading as well as for the joints with hogging moment loading (see Figure 4)

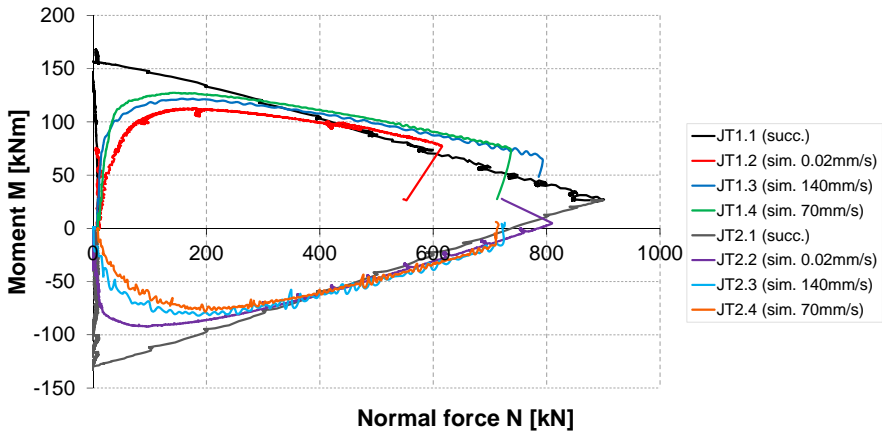


Figure 4. M-N - behaviour of the composite joints

It may be observed that for sagging moment loading the M-N-capacity of the joints is about 30 % higher for the joints with a higher loading velocity, compare JT1.3 with JT1.2. This might be explained by the behaviour of the steel that is under tension for the sagging moment and that is decisive for the joint failure. Through tensile tests with higher loading velocities, it has been confirmed that the steel had higher yielding strengths for higher strain rates (Kuhlmann and Hoffmann, 2015b). For the composite joints with hogging moment loading, it might be stated that the M-N-capacity is slightly lower for higher loading velocities, compare JT2.3 with JT2.2. In this case the influence

of the reinforced concrete that is in tension at hogging moment loading is decisive for the failure.

Considering the moment-rotation curve in Figure 5 of the composite joints it may be observed that for sagging moment loading the loading velocity has a rather small influence, see JT1.2 for a velocity of 0.02 mm/s and JT1.3 for 140 mm/s. For the hogging moment loading the rotational capacity of the joint with higher loading velocity is about 20 % lower than for the static loading, compare JT2.4 with JT2.2. This highlights the influence of the reinforced concrete in tension to the rotational behaviour of the joint.

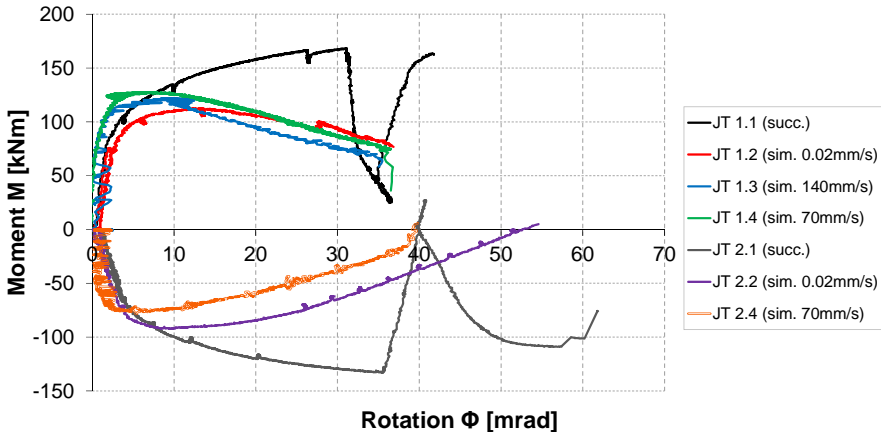


Figure 5. M- Φ - behaviour of the composite joints

It may be observed that for the statically loaded joints with negative bending moments (Tests JT2) the rotational capacity was slightly higher than for the joints with positive bending moment (Tests JT1).

3 EXPERIMENTAL INVESTIGATIONS OF COMPOSITE FRAMES

3.1 Test programme

In addition to the composite joint tests two experimental tests on a 2D-frame structure have been performed in order to investigate the behaviour of the composite frame and the influence of the joints to each other.

In a first experimental frame test FT1 the configuration of the joints was adapted to the reference structure and to the composite joint tests (see Figure 6).

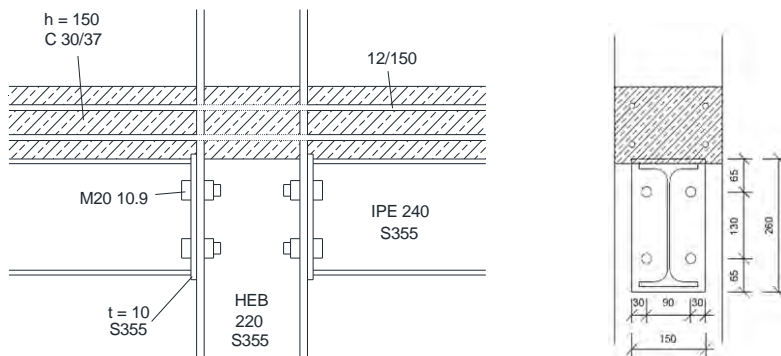


Figure 6. Joint configuration of frame test FT1

For the second experimental test frame test FT2 the configuration of the bolted steel connection of the joints was changed in order to achieve a higher ductility of the joints. Following the recommendations of (Rölle, 2013) on one hand the diameter of the bolts was changed from M20 to M24, on the other hand the distance of the bolt hole to the web of the beam was increased (see Figure 7). The concrete part of the composite frame remained the same than for frame test FT1.

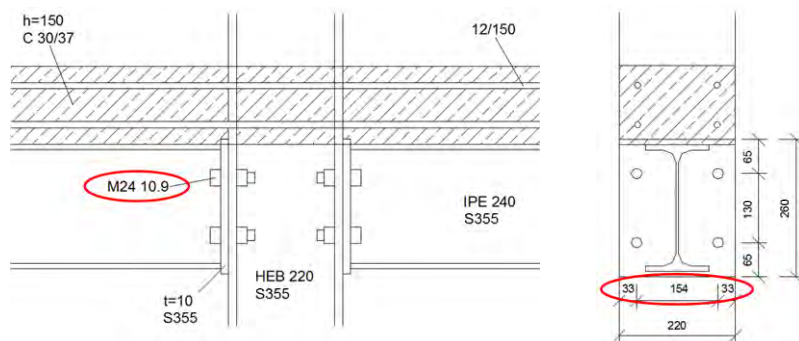


Figure 7. Joint configuration of frame test FT2

Due to these amendments a more ductile behaviour of the component *endplate in bending* should be achieved. This is due to the fact that through the increased distance of the bolt to the web of the beam a greater span of the T-stub in the tension zone can be achieved that enables an increased deformability of the T-stub (Rölle, 2013). Due to this higher ductility of the decisive component larger deformation of the entire joint should be enabled and therefore the deflections of the composite frame should be increased so that the activation of catenary action should be enabled.

3.2 Test setup

The test setup of the composite frame tests was realised analogous to the joint tests with three hydraulic jacks (see Figure 8). One vertical jack applying a moment loading at the position of the middle column that is assumed as lost and two horizontal jacks simulating the stiffness of the intact part of the residual structure. All jacks were again operating displacement controlled.

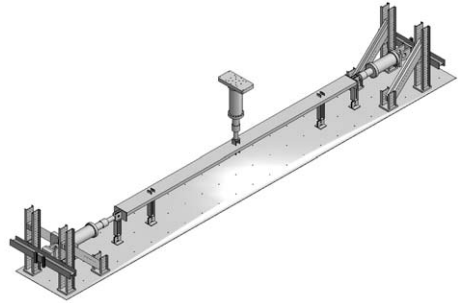


Figure 8. Test setup of composite frame tests

3.3 Performance of the tests

Within the performance of the tests the objective was to realise the most realistic possible simulation of the load history of the frame. Therefore the following testing procedure was defined:

1. Application of a uniformly distributed line load on the concrete slab in order to simulate the existing constant and variable loads acting in reality. During this load step the middle column was replaced by a hydraulic cylinder.
2. Removal of the cylinder at the middle column in order to simulate the loss of the column.
3. Application of an additional vertical loading above the middle column simulating the loads of the upper storeys of the building.
4. Activation of the horizontal jacks after reaching large deflections in order to activate the catenary action.

Whereas during the performance of the first frame test FT1 a premature failure of the bolt under tension at the internal joint occurred, within the second Frame Test FT2 the changed arrangement of the bolts allowed for a vertical deflection of more than 600 mm without a failure of the test specimen.

The deformed test specimen of FT1 is shown in Figure 9. It may be observed that the lower bolts at the middle column, where a sagging moment loading existed, failed due to tension.



Figure 9. Deformed frame test FT1 at the end of the test

It may be observed that the deformation of FT2 is increased compared to the behaviour of FT1, see Figure 9b) and Figure 10b).

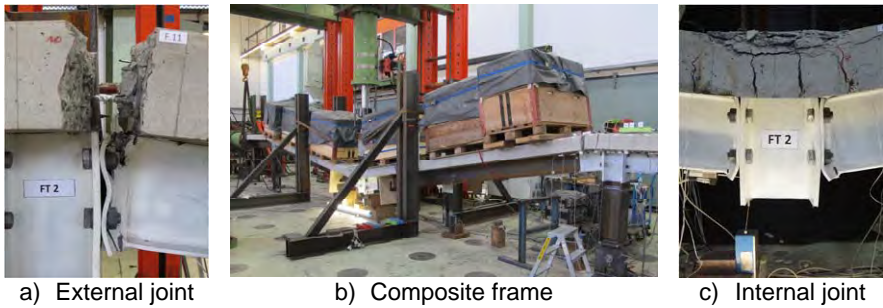


Figure 10. Deformed frame test FT2 at the end of the test

At the end of the tests a failure of the rebars at the external joints Figure 10a) was recognized in the upper as well as in the lower layer of the reinforcement. Nevertheless the steel components of the joint were able to carry the existing loads at the external joint due to large deformations developing at the endplate (see Figure 10 a)).

Due to the sagging moment loading at the internal joint of the composite frame a crushing of the concrete under compression loading could be observed as well as cracks in the lower part of the concrete slab and a gap between endplate and column flange as a result of the tension loading within the steel part of the joint (see Figure 10 (c)). However no complete failure of the external joints occurred.

3.4 Test results

The load-deformation curves of the two frame tests in Figure 11 clearly indicate that for frame test FT1 it was not possible to activate the catenary action.

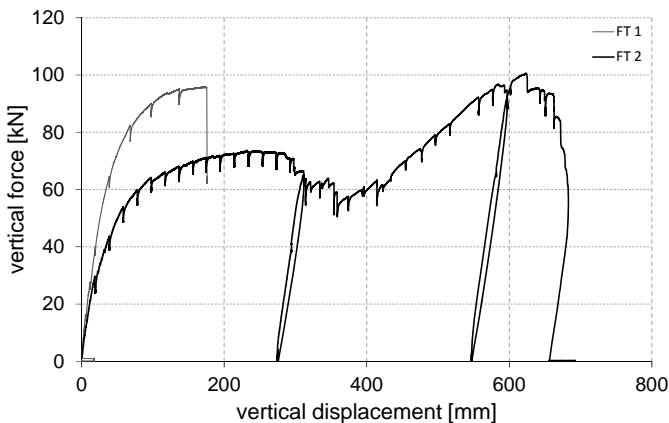


Figure 11. Vertical force-displacement behaviour of the internal joint at the composite frame tests

Due to the minimal modification of the configuration of the bolts and the steel endplate of the joint within the second frame test FT2 larger vertical deflections could be applied and the catenary action with the frame was active. Due to this catenary action hold by the horizontal jacks the applied vertical load could be increased further.

As a result of the changed arrangement of the bolts, see Figure 7, further outward in horizontal direction at the internal joint of the frame test FT2 the stiffness of the composite joint is reduced compared to the stiffness of frame test FT1. As a consequence the applied vertical force at the beginning of frame test FT2 is lower than the applied vertical force in frame test FT1. With the activation of the catenary action this difference regarding the applied vertical forces is compensated.

4 SUMMARY AND OUTLOOK

Within the performed experimental joint tests the possible redistribution of an existing moment loading at the joint into a pure membrane force state could be demonstrated that it is possible to and therefore to carry a catenary action within the frame system. The tests with different loading velocities have shown that the influence of the loading velocity on the behaviour of the composite joints is different under sagging moment loading compared to hogging moment loading at the joint.

The composite frame tests allowed to recognize that with a simple modification of the joint configuration, larger bolt diameter and increase of "bolt" lever arm by increase of endplate, a significant increase of the overall ductility of the joints can be achieved. This follows the recommendations of *Rölle* (Rölle, 2013) developed for steel joints with high ductility. Therefore huge potential exists to achieve a load redistribution in the system by activation of catenary action with only small efforts when designing the ductile joints. Consequently, by this modification existing additional loading capacity is activated in the system.

In order to develop further results in addition to the knowledge obtained from the experimental tests numerical recalculations of the composite joints as well as of the composite frame are necessary to form the basis for parameter studies. Within these numerical investigations the influence of the reinforced concrete slab in tension on the joint behaviour should be investigated especially in view of the rotational capacity of the joint (Hoffmann).

5 ACKNOWLEDGEMENTS

The research project "Robustheit" was financed in the frame of a German DAST/Aif project within the programme to support the „cooperative industrial research (IGF)" of the "Bundesministerium für Wirtschaft und Technologie".

The further work presented here is carried out as a research project by different European partners with a financial grant from the Research Fund for Coal and Steel (RFCS) of the European Community (grant agreement n° RFSR-CT-2012-00029). The authors gratefully acknowledge the financial support. The authors also thank for the colleagues from Université de Liège, University of Trento, RWTH Aachen, ARCELORPROFILE und INSAR Rennes for their fruitful cooperation.

6 REFERENCES

EN 1991-1-7 (2006): *Eurocode 1 – Actions on structures – Part 1-7: General Actions – Accidental actions*. CEN – European committee for standardization.

EN 1994-1-1 (2004): *Eurocode 4 – Design of composite steel and concrete structures – Part 1-1: General rules and rules for buildings*. CEN – European committee for standardization.

EN 1993-1-8 (2005), *Eurocode 3: Design of steel structures – Part 1-8: Design of joints*. CEN – European committee for standardization.

Hoffmann N., Kuhlmann U., Demonceau J.-F., Jaspart J.-P., Colomer C., Hoffmeister B., Zandonini R., Hjjaj M. and Mohler C. (2015), *Robust impact design of steel and composite buildings*. Proceedings of IABSE Workshop, February 11-12, Helsinki , Finland.

Hoffmann N. (planned), phd thesis, Institute of Structural Design, University of Stuttgart.

Kuhlmann U., Hoffmann N., Demonceau J.-F., Jaspart J.-P., Colomer C., Hoffmeister B., Korndörfer J., Zandonini R., Baldassino N., Hjjaj M. and Hanus F. (2016). *ROBUSTIMPACT Robust impact design of steel and composite structures*, RFSR-CT-2012-00029 (in preparation).

Kuhlmann U., Hoffmann N. (2015a), *Außergewöhnliche Bemessungssituationen nach DIN EN 1991-1-7 - Effektive Anwendung und Bemessungsstrategien für Stahl- und Verbundrahmentragwerke*. DAST/AiF research project, No. 17153.

Kuhlmann U., Hoffmann N. (2015b), *Robust impact design of steel and composite structures – Report of the experimental results and preliminary evaluation*. RFSR-CT-2012-00029 ROBUSTIMPACT contribution to Deliverable D.1.

Rölle, L. (2013), *Das Trag- und Verformungsverhalten geschraubter Stahl- und Verbundknoten bei vollplastischer Bemessung und in außergewöhnlichen Bemessungssituationen*. phd thesis, Institute of Structural Design, University of Stuttgart.

EXPERIMENTAL RESEARCH ON THE BEHAVIOR OF STEEL MOMENT FRAME CONNECTIONS UNDER COLUMN LOSS SCENARIO

Florea Dinu

Politehnica University Timisoara, Timisoara, Romania
Romanian Academy, Centre for Advanced and Technical Sciences, Timisoara
florea.dinu@upt.ro

Ioan Marginean

Politehnica University Timisoara, Timisoara, Romania
ioan.marginean@upt.ro

Dan Dubina

Politehnica University Timisoara, Timisoara, Romania
Romanian Academy, Centre for Advanced and Technical Sciences, Timisoara
dan.dubina@upt.ro

Ioan Petran

Technical University of Cluj Napoca, Department of Structures, Cluj Napoca,
Romania
ioan.petran@bmt.utcluj.ro

Andreea Sigauan

Politehnica University Timisoara, Timisoara, Romania
andreea.handabut@student.upt.ro

ABSTRACT

The overall performance of a building structure in case of an accidental loading can be measured by its capacity to survive the hazard without collapse initiation, or, when considered acceptable, the capacity to limit the propagation of damage. Taking advantage of structure's inherent redundancy and available load paths, seismic resistant steel frames are considered appropriate to achieve such objectives. However, there are specific problems, which need to be considered when localized failures, particularly of columns, occur, i.e. large deformations and catenary response of beams. In this study, we investigated the performance of four steel frame beam-to-column connection types following the removal of a column. Acceptance criteria for progressive collapse events were proposed and compared to existing seismic provisions.

INTRODUCTION

Steel framed structures are widely used for multi-storey buildings, offering many advantages over other types of constructions. According to EN 1990 (EN1990, 2002), in order to provide the required capacity, relevant design situations must be selected and applied, based on the conditions of use and on the requirements concerning the performance of the structure. Even not always designed for accidental design

situations, structures must resist any action without being damaged to an extent disproportionate to the original cause. The disproportionality refers to the situation in which failure of one member causes a major collapse, with a magnitude disproportionate to the initial event; this is also known as progressive collapse (NISTIR, 2007). Avoidance or limitation of potential damage may be done by several means, from elimination or reduction of hazard, to selection of a structural form which has low sensitivity to hazards and can survive adequately the accidental removal of an individual member or a limited part of the structure. For the latter option to be effective, it is necessary to provide continuity across the damaged area, and thus to allow the development of alternate loads paths. The alternate path method (AP) provides a formal check of the capability of the structural system to resist the removal of specific members, such as columns. The method does not require the characterization of the threat causing loss of the member. The AP method, with its emphasis on continuity and ductility, is similar to current seismic design practice (NISTIR, 2007). Seismic design procedures can be adopted as reference for progressive collapse design, but several modifications are necessary to accommodate the particular issues associated with progressive collapse. One such issue is the response of members and connections and their qualification for progressive collapse consideration. Thus, seismic resistant moment frames should be designed and detailed so that the required plastic deformations occur primarily in the beams or in the beam-to-column connections (EN1998-1, 2004), (AISC, 2014). If the structure is designed to dissipate energy in the beams, the connections of the beams to the columns should be strengthened and stiffened by using cover plates, haunches. Two examples for such type of connections are Welded Cover Plated Flange connection (CWP) and Haunched End Plate Bolted connection (EPH), respectively. These types of connections are used in practice, even they are not the most cost-effective and simple to execute connections. Alternatively, the section of the beam can be reduced at a distance away from the connection to obtain a favourable mechanism. One such connection is the Reduced Beam Section welded connection, RBS. If properly configured and executed, RBS connection is simpler and more cost effective than CWP and EPH, and has similar performances. If the structure is designed to dissipate energy in the connections, their flexural capacity is a fraction of that of the beams, and the connection is classified as partial strength connection. One example is the unstiffened extended end plate bolted connection (EP). Such connections are widely used in seismic resistant structures, but their use is permitted only if the rotation capacity supplied by the connection is consistent with the global deformation (EN 1998, 2004). If for evaluation of seismic performance of connections and members, cyclic loads with increasing magnitude are applied, without axial loading, in case of progressive collapse, the connection and member experiences one half cycle of loading, often in conjunction with a significant axial load, due to large deformations and catenary response. Unfortunately, only limited experimental research on the performance of steel frame connections under column removal scenarios were conducted so far.

When experimental testing is of concern, the use of connection components and sub-assembly testing are most common solutions, allowing the complete evaluation of the response and validation of computational models. Yang and Tan (Yang & Tan, 2013) tested experimentally the performance of common types of bolted steel beam-column joints under a central-column-removal scenario. The results showed that tensile capacities of beam-column joints after undergoing large rotations usually

control the failure mode and the formation of catenary action. Xu and Ellingwood (Xu and Ellingwood, 2011) investigated the performance of steel frames with partially restrained connections fabricated from bolted T-stubs following damage to load-bearing columns. They reported that frames with strong T-stub connections can resist collapse in damage scenarios involving the notional removal of one column, whereas the robustness of the frames with weak T-stub connections is questionable. They also reported that, in the presence of catenary action of the beams, gravity loads in free-edge columns might induce column buckling. In a similar study, Gong (Gong, 2014) conducted tests on 31 bolted double-angle connections under pure tension load, aiming to develop a method for the robustness design of bolted angle connections. The results showed that to achieve ductile behaviour that would produce a catenary action, the capacity design philosophy should be followed in the robustness design of connections. Thus, for bolted angle connections, tension bolt fracture before angle rupture should be avoided. Structural system testing, involving entire building systems or parts of them are very expensive and difficult, and therefore very few tests have been performed so far. A very recent study (Dinu et. all, 2015, 2016) investigated the capacity of a 3D steel frame structure with extended end-plate bolted beam-to-column connections to support the loss of a central column. A scaled-down specimen with two bays and two spans was constructed and tested under monotonic loading applied to the top of the central column until complete failure. The results showed that connections possessed sufficient strength to resist the catenary forces developing in the beams, with a rotation capacity over 200 mrad.

In the present study, we investigated the capacity of steel frame beam-to-column connections to develop catenary action under column loss and the performance under large deformation demands. Four connection types were designed and detailed to meet the seismic design requirements for special moment frame connections. The specimens, having two spans of 3.0 m each, were subjected to a monotonic loading applied on top of the removed central column until complete failure occurred. The study is part of a research program devoted to the design of structures that can sustain extreme loading events without collapse (CODEC, 2012).

SPECIMENS AND TEST SETUP

Figure 1.a shows the plan layout of the case-study building. The bays and spans each measure 8.0 m. Structure was calculated for the effect of gravity loads (permanent and variable actions) and lateral loads (wind and seismic actions), using the Eurocodes. The dead and live loads were each 4.0 kN/m² and the reference wind pressure was 0.5 kN/m². The structures were located in a low seismicity area, characterized by a design ground acceleration a_g of 0.08 g and a control period T_c of 0.7 s. It should be noted that, the seismic intensity and the response spectrum used in design were those given in the Romanian Seismic Code, P100-1 (2006). High dissipative structural behavior was considered using a behavior factor q of 6.5. An inter-story drift limitation of 0.008 of the story height was used for the seismic design for the serviceability limit state. Various loading cases, including seismic design loads, were used for the structural design of members, connections and details, using the relevant Eurocode parts. No particular accidental design situation was considered in design. The highlighted area indicates the perimeter frame extracted for investigation. Due to space limitation in the laboratory, the frame was scaled down from 8.0 m span to 3.0 m span. Each specimen consists of two steel beams and three columns and

have a length of 6.0 m between the center lines of the marginal columns. Figure 1.b shows the experimental frame, with the test set-up, the specimen and the 100 tones actuator. To consider the restraint from the surrounding elements in the reference structure, horizontal restraints were provided by a strong reaction wall, on one side, and by a brace system, on the other side. Out of plane restraints were also provided along the span of the beams and at the central column. Note that the in-plane rotation of the central column was not restrained. In this study, four specimens were tested, each with a different type of beam-to-column connections but with the same sections for members. In all specimens, beam section was IPE220 while the column section was HEB260 with flanges reduced to 160 mm width. Steel material in plates and profiles was S275 J0 and bolts were grade 10.9 for EP and EPH and 8.8 for CWP. First specimen (CWP) used welded cover plated flange connections. The top and bottom beam flange cover plates are 12 mm thick, width is 130 mm and length is 150 mm. Cover plates were welded with complete joint penetration CJP groove welds to the column flange, and with fillet welds to the top and bottom beam flanges. Beam web connection was made using a bolted shear tab, reinforced with fillet welds to the beam web and column flange. Second specimen (EPH) used extended end plate bolted connections and bottom haunches, with 20 mm thick end plate and six rows of bolts M20 grade 10.9. The height of the haunch is 110 mm while the length is 150 mm (same length as cover plates in CWP). Third specimen (RBS) used reduced beam section connections, with circular radius cuts in both top and bottom flanges of the beam. Dimensions of the reduced zones, calculated according to ANSI/AISC 358-10 (AISC, 2014), are $a=66$ mm, $b=150$ mm and $c=22$ mm. Welds of beam flanges to the column are CJP groove welds. Fourth specimen (EP) used unstiffened extended end plate bolted connections, with 16 mm thick end plate and five rows of bolts M16 class 10.9. Figure 2 shows the construction details of the connections for the specimens, while Figure 3 shows the moment-rotation characteristics of the connections and the classification according to EN 1993-1-8 (EN1993, 2005). The instrumentation included displacement transducers for vertical deflection and joint rotation (see Figure 4). For estimating the axial force in beams, additional transducers were placed on horizontal elements of the in-plane restraining system. As these elements remain elastic, it is easy to estimate the intensity of the axial force in the beams during the test. In addition, strains and displacements were recorded in potential plastic zones of the beams, using a digital image correlation technique DIC, called VIC-3D (VIC-3D, 2016), see Figure 4 (bottom right). DIC is an optical method, which measures deformation on an object's surface (Sutton et. all, 2009). The method tracks the changes in gray value pattern in small neighborhoods called subsets during deformation, see Figure 5. The system has a point-to-point strain accuracy of 0.02%.

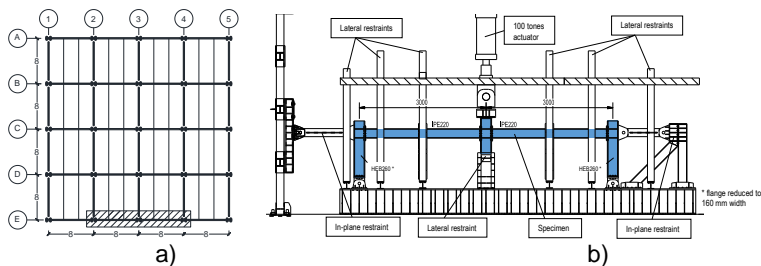


Figure 1. Plan layout of the reference multi-storey building with the position of the specimens extracted for testing (a) and test set-up (b)

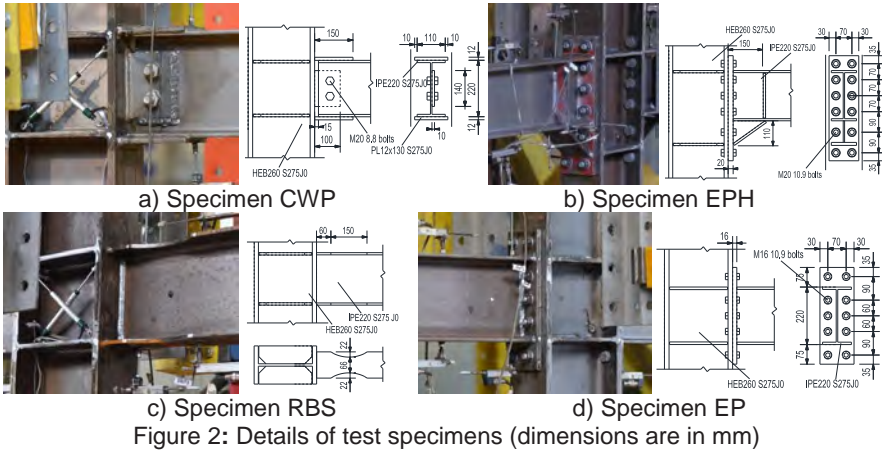


Figure 2: Details of test specimens (dimensions are in mm)

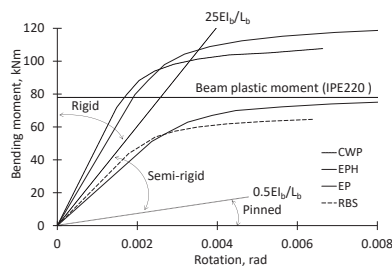


Figure 3. Moment-rotation characteristics of the connections

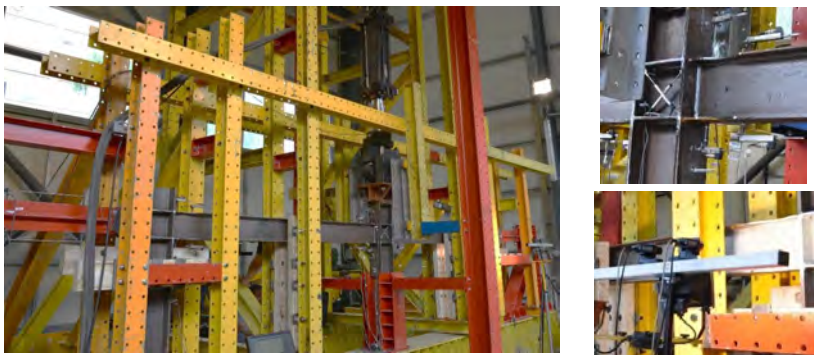


Figure 4. Specimen instrumented for testing

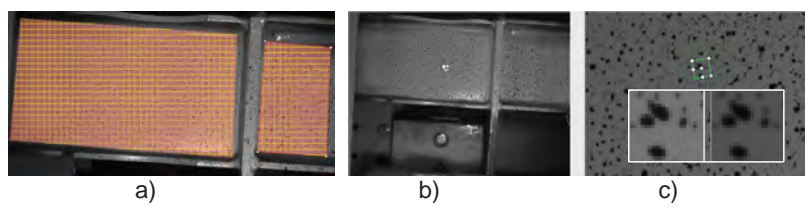


Figure 5. Preparation of the surface for DIC measurements; a) subset size; b) speckle pattern on the surface; c) subset tracking

Before the test, bolts and material coupons from beams, columns, and plates were tested to evaluate the mechanical characteristics of materials. The yield strength and strain, f_y and ϵ_y , the ultimate strength, f_u and the total elongation at maximum stress, A_{gt} , are listed in Table 1. The actual material characteristics were employed in a preliminary push down analysis on the scale-down specimen models to assess their behavior before performing the test. Pre-test simulation was also necessary to approximate the load–displacement curve, ultimate load, and ultimate vertical displacement.

Table 1. Average characteristic values for steel profiles, plates and bolts

Element	f_y (N/mm ²)	f_u (N/mm ²)	ϵ_y (%)	A_{gt} (%)
Beam flange IPE220	351	498	0.17	15.0
Beam web IPE220	370	497	0.18	15.0
Column web HEB 260	402	583	0.19	12.9
Column flange HEB 260	393	589	0.19	13.3
End plate, t = 16 mm	305	417	0.15	17.1
End plate, t = 20 mm	279	430	0.13	12.7
Cover plate, t = 12 mm	315	455	0.15	16.3
Shear tab, t = 10 mm	314	416	0.15	16.7
Bolt, M20 class 10.9	920*	1085	1.75*	12.2
Bolt, M16 class 10.9	965*	1080	1.76*	12.0
Bolt, M20 class 8.8	672*	825	1.78*	12.3

Note: * 0.2% offset yield point

EXPERIMENTAL RESULTS

The vertical force was applied on top of the central column using a displacement control loading protocol, and was gradually increased until failure of the specimen was reached. The amplitude of the force was monitored using the load cell of the actuator. Data from displacement transducers located at beam ends were used to capture the joint rotations R1, R2 and R3, see Figure 6. Because the central column was not prevented from in-plane rotations, the imperfections in the system can lead to different rotations of beam ends R2 and R3. To note that, if the central column is fully prevented from rotating, the deformation demands are evenly distributed between the adjoining beam ends, and therefore the rotation demands are smaller than for the cases presented in this study. The results from the four experimental tests are presented in the next section.

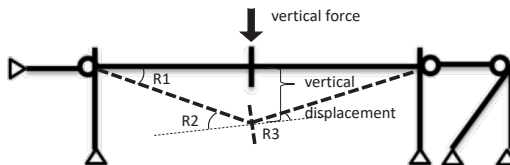


Figure 6. Experimental setup and beam rotation notations schematic representation

A summary of the test results is presented in Table 2. Figure 7 shows global views with specimens after the test and detail photos with the failure modes. The maximum axial force attained in beams, N_{max} , is also compared to the expected ultimate axial resistance corrected due to the presence of bending moment, N_M . A ratio $N_{max}/N_M < 1$ indicates failure is attained in connection not in beam. Figure 8 shows, comparatively, the response parameters for all specimens, i.e. relation between applied vertical force

and vertical displacement and the history of axial force, bending moment and rotation in beams vs. vertical displacement.

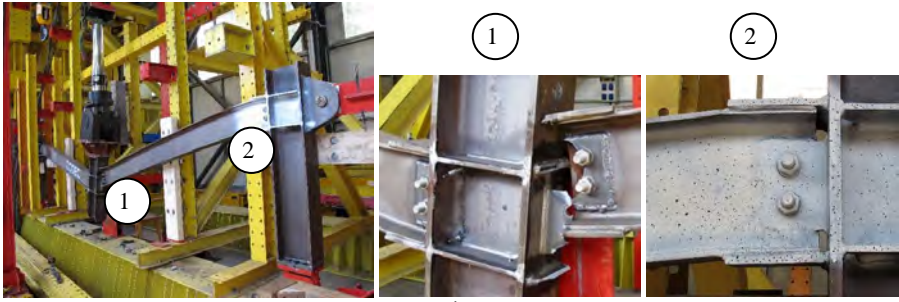
The highest capacity against vertical load is attained by the CWP specimen, which also has the largest deformation capacity, as it attains the largest vertical displacement and joint rotation, respectively. The axial capacity of the connection is sufficient to allow the development of large catenary force in beams, even the failure is due to the fracture in the connection and not in the beam, i.e. $N_{max}/N_M < 1$. This could be explained by the fact that, even the connection was designed with flexural overstrength compared to the beam, and indirectly with axial overstrength, the steel materials in the cover plates were supplied with larger overstrength than the profiles, see Table 1. It is also possible that relatively weak shear tab, which is susceptible to net section fracture, to have initiated and weakened the connection and thus causing the failure. Same conclusion was drawn by Khandelwal and El-Tawil (2011).

The second largest capacity is attained by the EPH specimen, which was also designed with overstrength compared to the connected beam, and failure takes place also in the connection, i.e. $N_{max}/N_M < 1$. A possible solution for improving the axial resistance of the connection is to use stronger bolts or to stiffen the top side of the connection (where the hogging bending is more demanding than the sagging bending). A very good response was provided by the partial strength connection specimen, RBS, which failed in tension due to the fracture of the beam in the reduced area, but after developing large catenary forces in beams ($N_{max}/N_M = 1$). It is therefore worth to note that, when properly designed and detailed, RBS connections can be a cost-effective solution for providing resistance to collapse, compared to the stronger, but more costly connections CWSP or EPH. The second partial strength connection specimen, EP, exhibited the poorest capacity, due to the premature fracture of the bolts before developing any significant catenary force in beams. The ratio $N_{max}/N_M \ll 1$ indicates a very low axial resistance compared to the beam. Therefore, careful attention is necessary in design, particularly with respect to the design of bolts for larger axial forces than those resulted from current flexural-based design. Excepting the EP specimen, which showed limited rotation capacity, the other three specimens demonstrated that rotational capacities are much higher than actually reported in UFC 023 (DoD, 2013), which are based on ASCE 41 Provisions for Seismic Design (Figure 8.c). It is also worthwhile to mention that, with the exception of EP specimen, for which the contribution from catenary action is negligible, for the other three specimens the catenary action developed in beams at the large deflection stage significantly increased the load capacity in the event of a column loss, see Figure 9.

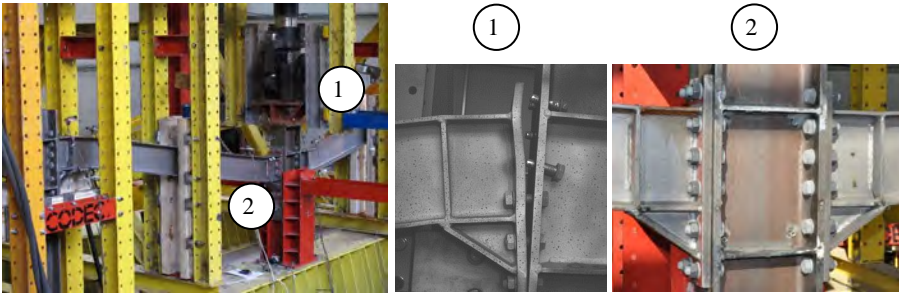
Table 2. Test results for specimens

Test	Maximum applied force F_u [kN]	Maximum rotation in beams [rad]	Maximum axial force in beams N_{max} [kN]	Maximum bending moment in beams M_{max} [kNm]	Expected axial capacity reduced due to bending N_M^a [kN]	N_{max}/N_M
CWP	603	0.193	1230	154	1323	0.93
EPH	477	0.130	1035	156	1060	0.98
RBS	401	0.172	760	147	757	1.00
EP	182	0.079	571	130	1066	0.54

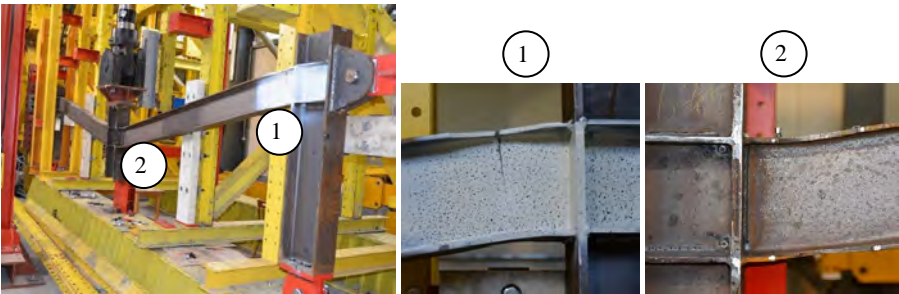
^a - N_M - calculated using linear interaction relationship $N_M = N_{pi}[1 - M/M_{pi}]$, where N_{pi} is axial plastic resistance, M_{pi} is plastic moment resistance



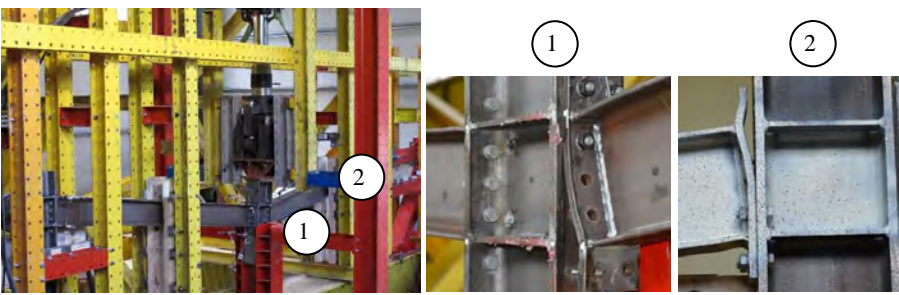
a)



b)



c)



d)

Figure 7. Specimens after the test: a) CWP; b) EPH; c) RBS; d) EP

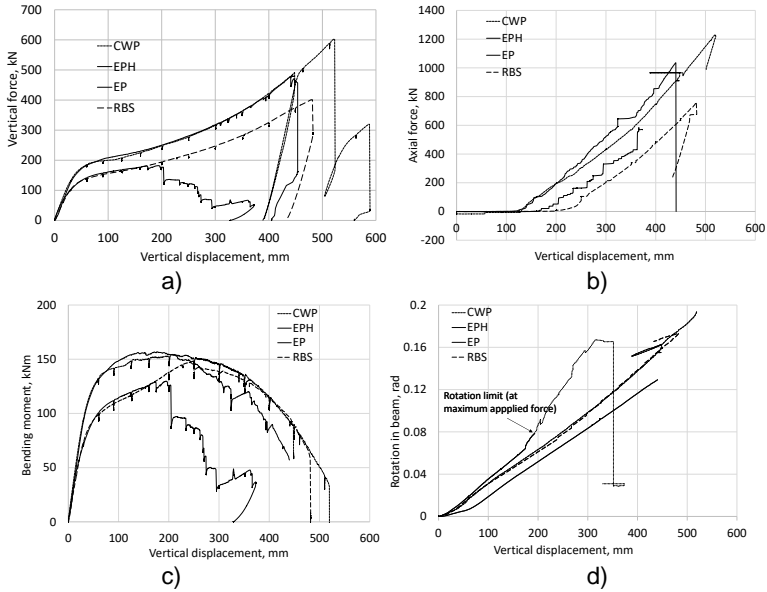


Figure 8. Response parameters for all specimens: a) vertical force vs. vertical displacement; b) axial force in beams vs. vertical displacement; c) bending moment in beams vs. vertical displacement; d) rotation in beams vs. vertical displacement

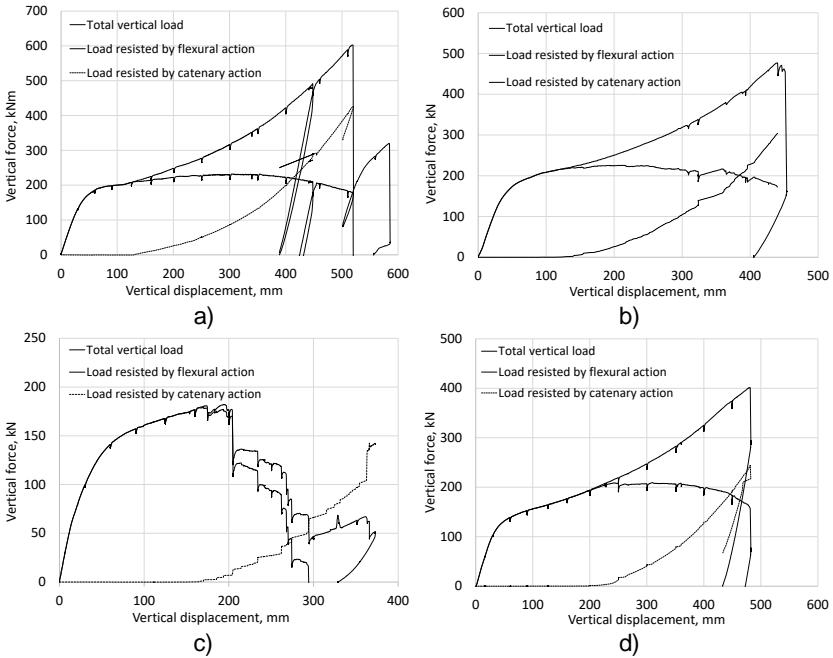
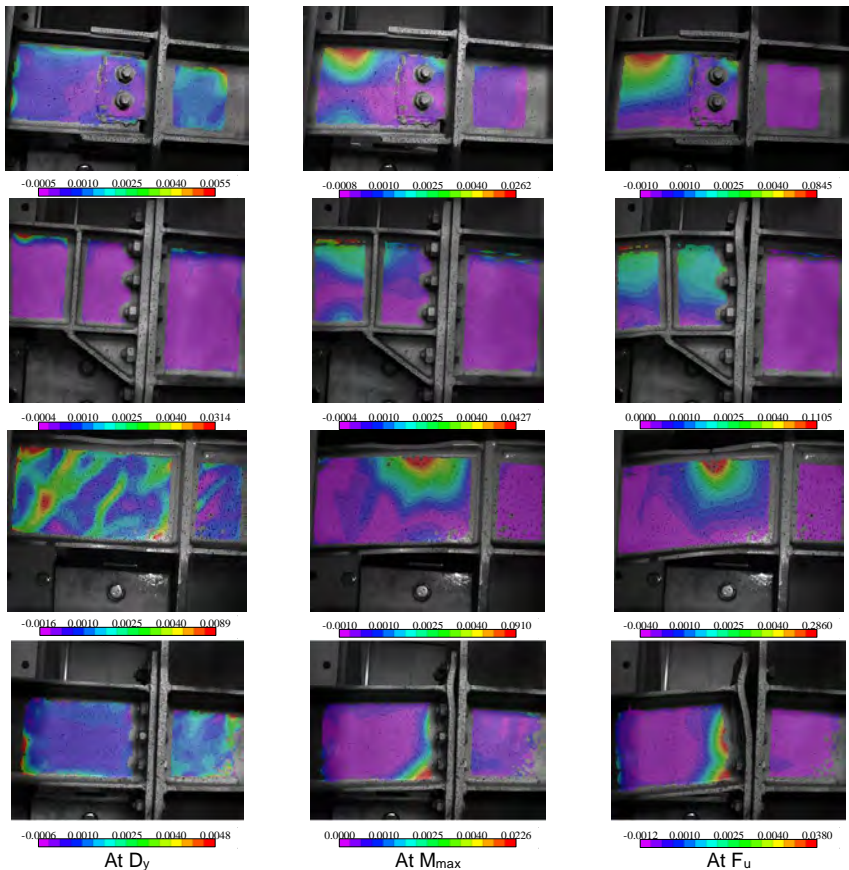


Figure 9. Force-displacement curves of specimens

Figure 10 shows the evolution of strains in beams web, from initiation of yielding to ultimate stage before failure, obtained with VIC-3D software. The principal strain maps are shown as an overlay to the actual deformation state of the specimens during testing. For CWP specimen, the ultimate recorded data indicates strain concentrations (in excess of 0.08) at top flange in tension, near the cover plate. To note that, even the specimen failed due to fracture of the connection (cover plate followed by shear tab), there were also large cracks in the top flange, exactly at the position indicated by the strain concentrations mentioned above.

For EPH and EP, the strains indicated in Figure 10 are not actually the ultimate strains that govern the failure in structures, because the specimens failed due to bolt fracture, where the strains were not possible to monitor. For RBS specimen, the ultimate strains indicated in Figure 10 (equal to 0.2860) are actually the tensile failure strains, because the measurements covered exactly the crack opening and development zone.



Note: for CWP, no strain data were recorded after 448 mm vertical displacements
 Figure 10. Principal strains map in beams web: a) at yield; b) at maximum bending moment in beams; c) at failure

CONCLUSIONS

An experimental program was conducted at PU Timisoara to investigate the performance of four types of moment resisting connections when a column is removed. The specimens were extracted from a six-story moment resisting frame structure, designed to meet the seismic design requirements for special moment frames. The two-span specimens were tested under a monotonically increased vertical force, applied on top of the central column using a displacement control, until failure of the specimens was reached. The specimens using over strength connections (CWP and EPH) showed a good response, experiencing large deformation capacity and catenary response. RBS specimen, where the beam is reduced near the column face, also developed large axial forces in beams before failure, with an ultimate rotation over 170 mrad. The specimen with unstiffened end plate bolted connections showed the poorest behavior and failed before developing significant catenary action in beams. The combined contribution from direct applied axial loads, prying effects and bending due to flexible end plate, finally contributed to bolt fracture, with an ultimate rotation of 79 mrad. Without significant strengthening of the bolts, this connection cannot be used for developing catenary forces and therefore should be used for flexural-based design only. DIC measurements provided valuable information and are currently used for validating detailed FEA models for each specimen.

The results and conclusions presented above are based on a limited number of tests. Therefore, additional studies are necessary to confirm or to adjust the findings. Thus, an extensive numerical parametric study is under development, aiming at investigating the factors that may have a significant impact on the catenary response of connections under extreme loading conditions, e.g. influence of beam depth on the rotation limit, beam web-to-column detail (for welded connections) and strain rate.

ACKNOWLEDGMENTS

Funding for this research was provided by the Executive Agency for Higher Education, Research, Development and Innovation Funding, Romania, under grant PCCA 55/2012 "Structural conception and collapse control performance based design of multistory structures under accidental actions" (2012-2016).

REFERENCES

ANSI/AISC 358-10 (2014). "Prequalified Connections for Special and Intermediate Steel Moment Frames for Seismic Applications", AISC.

CODEC (2016). "Structural conception and collapse control performance based design of multistory structures under accidental actions" CODEC (2012–2016), Executive Agency for Higher Education, Research, Development and Innovation Funding (UEFISCDI), Romania, grant number PN II PCCA 55/2012, the Partnerships Program Joint Applied Research Projects.

Department of Defense DoD (2013). "United Facilities Criteria (UFC): *Design of buildings to resist progressive collapse*". Washington (DC).

Dinu, F., Dubina, D., Marginean, I. (2015) "Improving the structural robustness of multi-story steel-frame buildings", *Structure and Infrastructure Engineering*, Vol 11, No. 8

(pp.1028-1041) doi: 10.1080/15732479.2014.927509.

Dinu, F., Marginean, I., Dubina, D. and Petran and I. (2016). "Experimental testing and numerical analysis of 3D steel frame system under column loss", *Engineering Structures*, Vol. 113 (pp. 59-70), doi: 10.1016/j.engstruct.2016.01.022.

EN 1990 (2002) Eurocode – "Basis of structural design", CEN.

EN 1993-1-8 (2005) Eurocode 3: "Design of steel structures" - Part 1-8: "Design of joints", CEN.

EN 1998-1 (2004) Eurocode 8: "Design of structures for earthquake resistance – Part 1: General rules, seismic actions and rules for buildings", CEN.

Gong, Y. (2014) "Ultimate tensile deformation and strength capacities of bolted-angle connections", *Journal of Constructional Steel Research*, Vol. 100, (pp. 50–59), doi: 10.1016/j.jcsr.2014.04.029.

Khandelwal, K & El-Tawil, S. (2007) "Collapse behavior of steel special moment resisting frame connections", *Journal of Structural Engineering*, 133(5):646–55.

NISTIR 7396 (2007) "Best Practices for Reducing the Potential for Progressive Collapse in Buildings", National Institute of Standards and Technology, Oakland, CA.

P100-1 (2006). Seismic design code. Part 1: "Earthquake resistant design of buildings P100-1/2006" (Buletinul Constructiilor, No. 12-13). INCERC, Bucharest, Romania, Ministry of Transport, Construction and Tourism MTCT (in Romanian).

Sutton, M. A., Orteu, J. J. & Schreier, H. (2009) "Image correlation for shape, motion and deformation measurements: basic concepts, theory and applications", *Springer Science & Business Media*.

VIC-3D Digital Image Correlation Software, Correlated Solutions Inc., 2016.

Xu, G. & Ellingwood, B. (2011) "Disproportionate collapse performance of partially restrained steel frames with bolted T-stub connections", *Engineering Structures*, Vol 33, (pp. 32–43), doi: 10.1016/j.engstruct.2010.09.015.

Yang, B. & Tan, K.H. (2013) "Experimental tests of different types of bolted steel beam–column joints under a central-column-removal scenario", *Engineering Structures*, Vol. 54, 112–130, DOI:10.1016/j.engstruct.2013.03.037.

ROBUSTNESS OF WUF-B MOMENT CONNECTIONS IN STEEL FRAME AFTER COLUMN REMOVAL

Yiyi Chen

Tongji University, Shanghai 200092, China
yiyichen@tongji.edu.cn

Wei Wang

Tongji University, Shanghai 200092, China
weiwang@tongji.edu.cn

Ling Li

Tongji University, Shanghai 200092, China
rabbitmumu@163.com

Abstract: In a column-removal scenario for a building structure, the catenary action will play an essential role for the frame in resisting a progressive collapse. This paper investigates the catenary behavior of welded unreinforced flange - bolted web connection (i.e. WUF-B connection) in plane frames by means of full-scale testing. Two different layouts of bolts at the beam web were considered, with four bolts arranged in one row or two rows in the two specimens, respectively. The results demonstrate that both specimens of the WUF-B moment connection were able to develop an effective catenary action via the bolted web following the primary flexural phase. The failure modes of the bolted web vary with different bolt arrangements under the catenary action. When all (four) bolts were arranged in one row, the lowest bolt bearing area on the web tends to be compressed to fracture before bolt tear-out failure occurs near the weld access hole. When the bolts were arranged in two rows, however, the shear tab cracked at the section across the bolt holes. The former failure mode is deemed to be more robust than the latter under a column removal scenario.

1. INTRODUCTION

As a general guide to preventing disproportionate or progressive collapse in the event of a critical local failure, a structure should be designed to possess an adequate degree of continuity and ductility, in addition to strength [1-3]. Moment-resisting beam-column connections, which hold the critical path of the gravity load in a framed structure, are generally beneficial in terms of the structural redundancy [4]. After the removal of a column, the connection(s) and the adjoining members will typically experience an intensified flexural action stage, followed by a catenary action phase as the deflection becomes large. It has been demonstrated [5-11] that the catenary action mechanism has the potential to considerably supplement and eventually replace the flexural action in carrying the vertical load. However, it can be understood that the realisation of an effective catenary action depends upon two basic conditions, a) a sufficiently large axial tension can develop in the beams, and b) such axial tension can maintain while large deformation advances. In this respect,

the ability of the connections in withholding a necessary degree of integrity into the large deformation regime becomes critically important.

According to the preceding experimental investigation of beam-to-tubular column moment connections under the column removal scenario [11], different connecting methods at the web may provide a similar flexural capacity but they could end up with considerably different catenary action capacity after flexural failure occurred. For a welded-web connection, the flexural action and catenary action mechanisms tend to deteriorate simultaneously because of continuous crack propagation after the bottom flange of the beam section fractured. In contrast, a bolted web connection enables the catenary action to develop more effectively, thanks to the interaction of the beam web with the bolts and shear tabs even after fracture occurs in the bottom flange.

This paper investigates the catenary behaviour of the typical H-beam and square-column moment connections with a bolted web connection, with a particular focus on the influence of different bolt layouts on the structural resistance in the large deformation regime. Two full-scale beam-to-column assemblies with WUF-B connection were designed in detail in accordance with a prototype steel building frame, and they were constructed and tested under a push-down action applied at the unsupported center column location. The experimental results are presented and discussed comprehensively.

2. EXPERIMENTAL PROGRAMME

2.1. Test specimens

The test specimens were designed to represent the beam-to-column connection region in a column removal scenario. For this purpose, a Beam-Joint-Beam (B-J-B) assembly is extracted from the directly affected spans of the frame when a middle column is removed, assuming that the inflection point is located around the mid-span of the original beam members in such a scenario. This configuration allows the full details at the connection to be reproduced, while the column removal scenario can be simulated by a push-down action via a center column, as will be shown in Section 2.2.

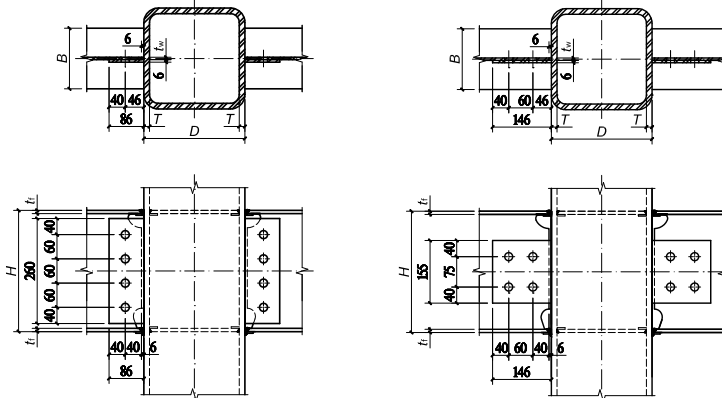
The WUF-B connections between the H-beam and the square hollow section (SHS) column are investigated in this paper. The column cross-section is SHS250X14; the beam cross-section is H300X150X6X8; the thickness of inner-diaphragm is 8mm. The main difference between the two test specimens under consideration, namely SI-WB and SI-WB-2, lies in the arrangement of the web bolts. The span of the beam is $l_0 = 4500\text{mm}$, and the height of the center column is 1100mm.

Fig. 1 illustrates the details of the connections. In each specimen, two H-section beams were connected to the SHS column via the WUF-B connection, and within the joint region two inner-diaphragms were installed inside the column at the locations corresponding to the top and the bottom flanges of the beam. The flanges of the beam and the inner-diaphragms were weld to the column wall. The beam was bolted on the web to a shear tab which was pre-welded to the column, via four M20 Grade-10.9 frictional type high-strength bolts. Four bolts were arranged with two different layouts in the two specimens; Specimen SI-WB had all four bolts arranged in a single row along the depth of the web (see Fig. 1 (a)), whereas Specimen SI-WB-2

had the four bolts arranged in two rows around the mid-height region of the web (see Fig. 1 (b)). The measured material properties of the SHS column and the H-section beams are summarized in Table 1.

Table 1. Material properties of specimens.

Components	Yield strength f_y (MPa)	Tensile strength f_u (MPa)	Elongation δ (%)
Plate of SHS	411	653	28
Corner of SHS	414	748	32
Beam flange	401	668	31
Beam web	407	638	31



(a) Specimen SI-WB

(b) Specimen SI-WB-2

Fig. 1. Details of the WUF-B moment connections with two different bolt layouts

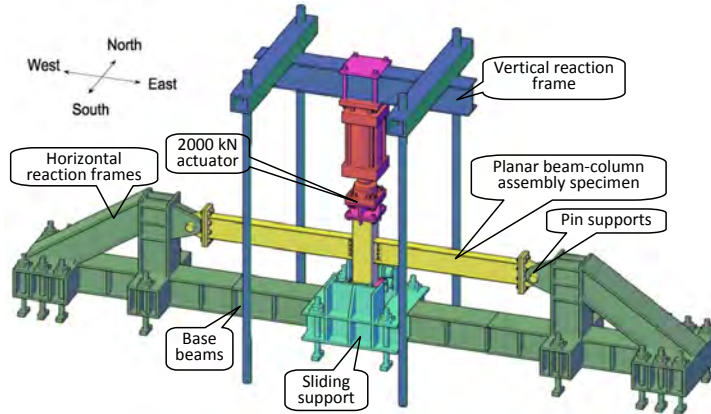


Fig. 2. Test setup.

2.2. Test setup

A purpose-built test setup was employed for the series of tests, as schematically illustrated in Fig. 2. The test specimens were loaded vertically at the top of the center column to simulate the effect following the removal of the middle column below. To avoid complication in the loading condition, the center column was guided at the

bottom end using a sliding support so that only vertical movement was possible. The specimens were pin-supported at the two horizontal ends with latch-type rollers to realise free rotation at the beam ends within the test plane. The tightness and stiffness of the pin supports were assured by using a manufactured strong pin joint connected to the support frame, as illustrated in Fig.2. The distance between the two pin supports was 4500mm. The vertical load was applied in a quasi-static manner with a displacement rate of less than 7mm/min during the tests. The test was terminated once the maximum vertical displacement at the central column was reached.

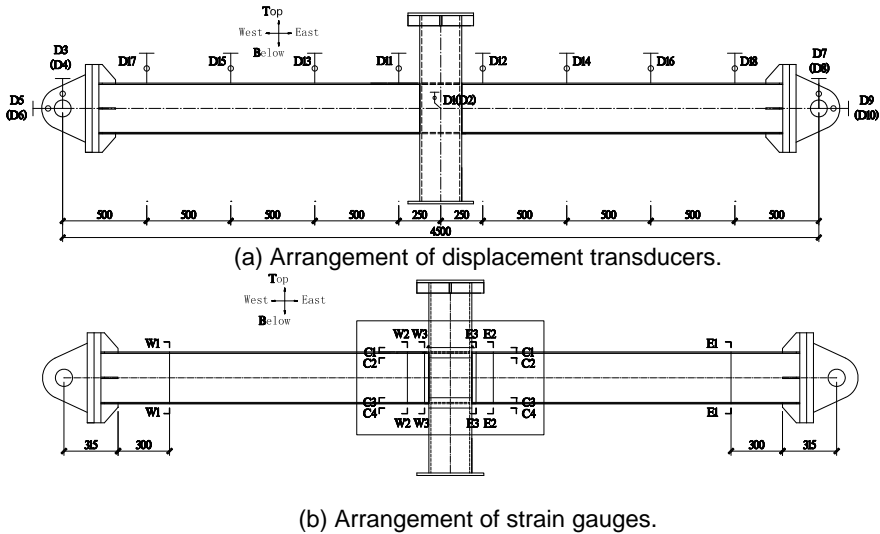


Fig. 3. Arrangements of displacement transducers and strain gauges.

2.3. Instrumentation

Instrumentation was arranged to measure the distribution of displacements along the length of the beam and strains at the critical regions during the tests. Fig. 3 shows the instrumentation arrangement in the two tests. As can be seen from Fig. 3 (a), 18 transducers were used to measure the deflection of the beam-to-column assembly along the beam length and any possible movements of the two pin support rollers. More than 100 strain gauges were used to measure the strains at critical locations on the column wall and at selected sections of the beams, with an overall arrangement as illustrated in Fig. 3 (b). Due to the stiffening effect of the weld on the sections that connected the beam members to the column wall, the nearby Sections W3 and E3 were expected to represent the most critical sections in the beam-to-column assembly under the column removal scenario. The anticipated large strains at the flanges of Sections W3 and E3 were measured by special strain gauges with an effective range of more than 100,000 $\mu\epsilon$. The strains on the Sections W1 and E1 of the beam members (see Fig. 3 (b)), where only elastic response was anticipated, were measured to allow for a calculation of the internal forces at these sections, and hence a deduction of the reaction forces at the pin supports.

3. EXPERIMENTAL RESULTS

3.1. General behavior and failure modes

The measured relationships of the vertical load versus vertical displacement at the center column location from the two tests are shown in Fig. 4. A few key stages of the response are identified on the curves, and the associated damage developments are depicted in the corresponding photographs included in Fig. 5. It is noted that a nominal plastic load, F_p , is employed for the normalisation of the applied load. F_p is calculated as the vertical load corresponding to the state where the full plastic yield moment of the beam section was achieved at the critical location (Sections W3 and E3), and it is found to be 180kN in both specimens. The beam chord rotation θ is evaluated by dividing the applied displacement at the center column by the distance between the centerline to the pin support (effectively half-span length) of 2.25 m.

In the SI-WB specimen (see the black curve in Fig. 4 and the photographs in Fig. 5 (a)), the first significant failure event (point “A1” on the load-displacement curve) took place when local buckling occurred at top flanges near Section W3 and E3, while the displacement reached about 110mm, which corresponded to the beam chord rotation θ of 0.048 rad. After that, the development of sliding between the bolts, webs and shear tabs was evident and even the sound of bolt sliding was continuously heard from the test. The specimen reached a peak load (point “A2”) when the bottom flange (near the weld access hole) at Section E3 fractured, and the corresponding displacement was 234 mm ($\theta = 0.104$ rad). The fracture caused a steep drop of the force from the peak load of 275 kN ($1.54F_p$) to 122 kN ($0.68F_p$). The specimen then saw a gradual pick up of the vertical force, showing an apparent change of the resistance mechanism to a catenary-action dominated regime. Meanwhile at the lower bolts of Section E3 large bearing deformation occurred on the web with the bolt holes deforming into elliptical shapes. Eventually at the center displacement of 345 mm ($\theta = 0.153$ rad), bolt was torn out of the web across the lowest bolt hole and the nearby weld access hole (point “A3”). The test was terminated at this point, and the vertical force had reached 306kN ($1.70F_p$), which exceeded the earlier peak value and was still in an increasing trend.

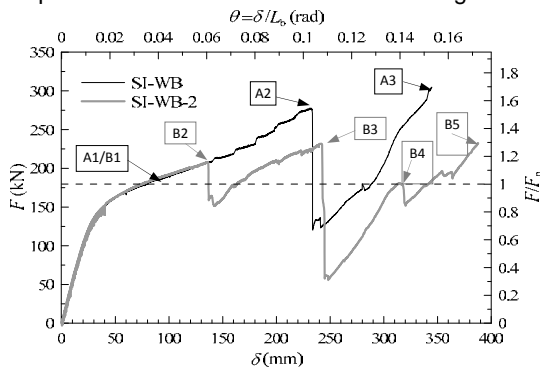
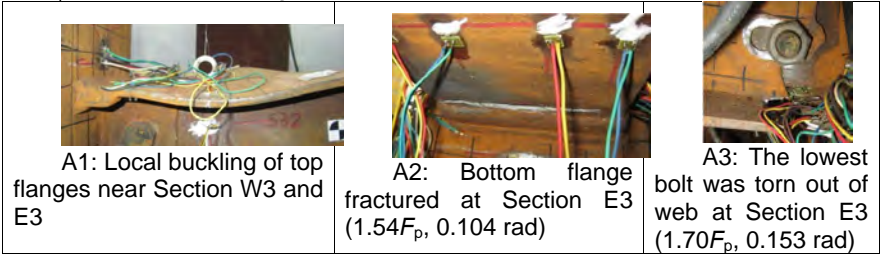


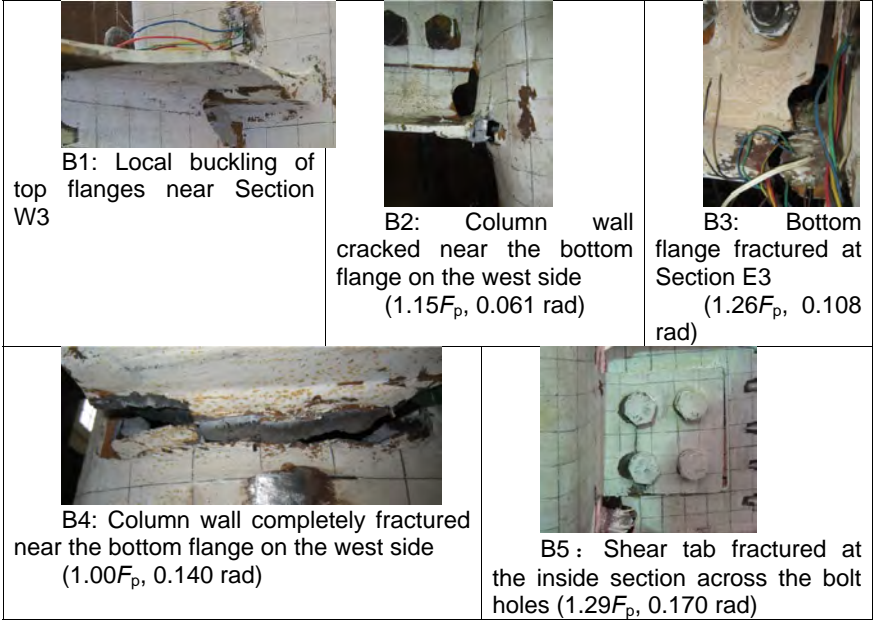
Fig. 4. Vertical load vs. displacement relationships of two specimens.

In the SI-WB-2 test (see the grey curve in Fig. 4 and the photographs in Fig. 5 (b)), the load-displacement development path was identical to that of test SI-WB in the early stage, with the failure initiated from local buckling at top flanges near

Section W3 and E3 (point “B1”). The load still kept increasing until the column wall cracked near the bottom flange on the west side (point “B2”) when the displacement reached 137 mm ($\theta = 0.061$ rad), at which stage the load dropped abruptly from 207 kN ($1.15F_p$) to 158 kN ($0.88F_p$). The rotational constraint exerted by the centre column effectively allowed the bending strength of beam on the other side (east side) to continue developing until the bottom flange (near the weld access hole) at Section E3 fractured (point “B3”). At this point the flexural capacity of the system effectively lost altogether, causing a steep drop of the load from 226kN ($1.26F_p$) to only 57 kN ($0.32F_p$). The corresponding displacement was 243 mm ($\theta = 0.108$ rad).



(a) Specimen SI-WB.



(b) Specimen SI-WB-2.

Fig. 5. Development of damage at key stages of response of the specimens.

With further increase of the displacement, the load gradually picked up at a similar rate as in specimen SI-WB, apparently due to the development of the catenary effect. As a result of large deformation, the crack of the column wall on the west side propagated across the entire width of the bottom flange. The column wall fractured completely across the thickness (point “B4”) when the displacement reached about 316 mm ($\theta = 0.140$ rad), and this was accompanied with a slight dip

of the load from 180kN ($1.00F_p$) to 150 kN ($0.83F_p$). Thereafter the west-side column wall tore up from the two ends of the bottom fracture line; however the vertical resistance was able to increase persistently thanks to the catenary action. Eventually the shear tab cracked vertically through the bolt holes at Section E3 (point "B5"), but the load kept increasing even when the displacement reached 387 mm ($\theta = 0.170$ rad). The test was terminated at this point, and the vertical load had reached 232 kN, or $1.29F_p$, which exceeded the maximum load level reached during the flexural phase of the response.

The failure process in the two specimens shared some general commonalities. In both cases the process may be divided into three distinctive phases, namely a flexure-dominated phase, a flexure-to-catenary transitional phase and a catenary action dominated phase. The transitional phase in both cases came to an end (point A2 for SI-WB and point B3 for SI-WB-2) at about the same level of the vertical displacement, which was around 240mm or 0.1 rad. Whether or not the flexural phase would involve a marked interim stage as evidenced in Specimen SI-WB-2 would depend upon the development of flexural failure in the beams of the two sides and the effectiveness of the rotational constraint exerted by the centre column. However, the severity of the flexural failure tended to have a significant effect on the magnitude of decrease in the vertical load, which in turn affects the vertical load carrying capacity during the catenary action phase for a comparable level of deformation. In the two specimens under consideration, the load carrying capacity in SI-WB-2 was generally lower than that in SI-WB by about 35% in the catenary phase of the response.

Overall, both specimens were able to transit into an effective catenary action following the end of the primary flexural phase, which was marked by fracture at the bottom flange. Such a degree of resilience of the WUF-B connections was apparently attributable to the robustness of the connection mechanism via the bolts while the structure underwent excessively large deformations. This observation echoes the findings from testing a pair of tubular connections where bolted and welded joints were used respectively [11], and it further suggests that a bolted connection is generally favourable for steel frames in resisting progressive collapse.

3.2. Deformation shapes and limit displacements

The shift from a flexural mode of response to a tension-catenary mechanism can be further observed from the change of the deflection shapes in the specimens, as depicted in Fig. 6 for Specimen SI-WB. The deflected profiles exhibited a typical flexural pattern at the early stages of the response. As the deflection increased, the deformation became increasingly concentrated at the connection, and eventually turned into a profile that resembled two straight lines (the beam member) connected to the center column like a hinge. A similar development of the overall deformation was observed in Specimen SI-WB-2.

For general applications, it would be instructive to identify the characteristic deformation limits, as well as the relative peak loads, from the experiments. The results for the two test specimens are summarized in Table 2. From the test data in Table 2, the peak loads in the primary flexural phase were all greater than the theoretical full-plastic load F_p , and this indicates that the flexural capacity in both specimens was well developed before the critical bottom flange fractured. The primary flexural phase apparently ended in both specimens at about the same deflection limit of approximate 0.1 rad in terms of the chord rotation. After a steep

drop of the load, the vertical resistance was able to pick up persistently in the catenary phase, and at about a beam chord rotation of more than 0.15–0.17 rad the vertical load capacity exceeded the flexural peak load.

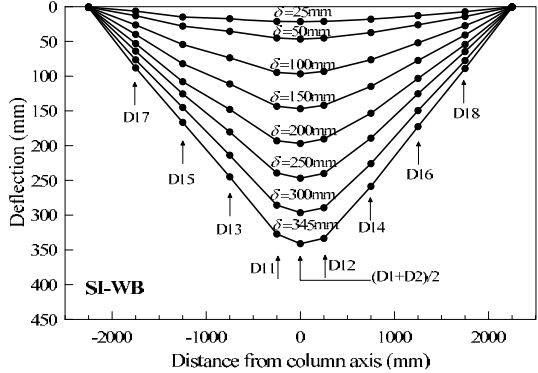


Fig. 6. Deflection profiles of specimen SI-WB.

Table 2. Deformation limits and corresponding vertical loads

Specimen	Characteristic deflection limits		
	1 st peak	2 nd peak	Ultimate state
SI-WB	234mm ($\theta = 0.104$ rad) 275 kN ($1.53F_p$)		≥ 345 mm ($\theta = 0.153$ rad) ≥ 307 kN ($1.71F_p$)
SI-WB-2	137 mm ($\theta = 0.061$ rad) 207 kN ($1.15F_p$)	243 mm ($\theta = 0.108$ rad) 226 kN ($1.26F_p$)	≥ 387 mm ($\theta = 0.170$ rad) ≥ 232 kN ($1.29F_p$)

4. PERFORMANCE OF BOLTED WEB CONNECTION UNDER CATENARY ACTION

The WUF-B connection has been experimentally proven to be generally effective in facilitating the development of the catenary action after a flexural failure. Nonetheless, the actual efficiency of a particular WUF-B connection is still dependent upon the detailed arrangement of the bolts across the web.

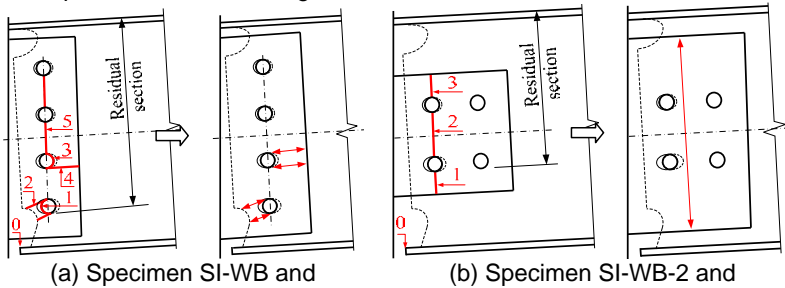


Fig. 7. Potential failure sequences and improvement scheme of the bolted web in the WUF-B connection

Fig. 7 further compares the engagement of the bolted web and the sequence of the failure in the bolt bearing areas between the two bolt arrangements. Within each layout scheme there is always scope for improved performance by enhancing the weak links under each scheme, and this falls into the area of detailing enhancement

and optimization involving many factors such as plate size, plate thickness, edge distances and the height of the shear tab etc. The results presented in this section would help set out a general direction.

With all the bolts arranged across the depth of the web in one single row such as Specimen SI-WB (Fig. 7 (a)), the lowest bolt area is subjected to the severest stress after the bottom flange fracture (point “0”) occurs; as a result, the bolt bearing wall undergoes a compression failure (point “1”) and this is followed by a bolt tear-out failure of the web near the weld access hole (point “2”). A similar stress condition and potential failure then shifts upwards to the next bolt (point “3”), and so forth. Understandably, the bolt tear-out failure of the web could be prevented if the distance from the bolt holes to the edge of the connected components is made sufficiently large (certainly larger than in specimen SI-WB).

When the bolts are arranged in two (or more) rows located around the middle part of the web, such as in Specimen SI-WB-2 illustrated in Fig. 7 (b), the much narrowed shear tab section could turn to be the weakest link, leading to rupture of the shear tab across the bolt holes in a progressive manner starting from the lower bolt upwards. When the shear tab ruptures completely (across points “1” to “3”), the beam will be tied to the column merely by the top flange, which would provide little tensile capacity for the assembly and therefore constitute a complete failure. The damage pattern is featured by the plate crack at the net section, whose section area may be too small to provide a sufficient capacity.

With respect to the associated deformability during the failure process, the failure mode featured by the compression of the bolt bearing area tends to be more ductile than the case involving rupture of the connection plate. From the observations outlined above, it is reasonable to deduce certain measures about the configuration at the bolt connection region to improve the robustness of the WUF-B connections. Clearly, allowing a sufficient distance between the bolt holes and the edge of the connected components would effect to postpone or even avoid bolt tear-out failure, see the improvement drawing in Fig. 7 (a). On the other hand, enlarging the cross section of the connection plate (shear tab) could prevent the rupture of the plate and therefore allow for a ductile failure mode to develop (Fig. 7 (b)).

5. CONCLUSIONS

Full-scale experimental studies have been conducted to investigate the behaviour of WUF-B type of steel moment connections with an inner-diaphragm under a column removal scenario, with a particular focus on the effect of different layouts of the bolts. Two beam-column assemblies were designed, constructed and tested, one with all four bolts at the connection arranged in a single row across the beam web, and the other with the bolts arranged in two-rows around the middle portion of the beam web. The two cases with different bolt layouts exhibited almost identical response until the bottom flange fractured, which signified the end of the flexural action phase. The design with all bolts arranged in a single row over the entire web area (Specimen SI-WB) was able to engage the beam web into action more effectively after the bottom flange failure, allowing for a smoother transition into the centenary action phase than the case with the two-row layout of the bolts (Specimen SI-WB-2). Furthermore, scrutiny of the local failure patterns indicate that further improvements in both cases may be achieved by enhancing the local connection details, in particular a safeguard of the bolt bearing capacity by ensuring a sufficient distance from the bolt holes to the end surface of the beam, and the

prevention of the shear tab rupture by enlarging the section of the connection plate. More specific guides to the design and optimization of such details warrants further parametric analysis and this will be addressed in subsequent studies.

ACKNOWLEDGMENTS

The research presented in this paper was supported by the Natural Science Foundation of China (NSFC) through Grant No. 51008220 and the Ministry of Science and Technology of China through Grant No. SLDRCE09-B-02. Any opinions, findings, conclusions, and recommendations expressed in this paper are those of the authors and do not necessarily reflect the views of the sponsors.

REFERENCES

- [1] General Service Administration. (2003), *Progressive Collapse Analysis and Design Guidelines for New Federal Office Buildings and Major Modernization Projects*. Washington, D.C.
- [2] Department of Defense. (2009), *Design of Buildings to Resist Progressive Collapse*. Washington, D.C. UFC 4-023-03; 2009.
- [3] Ellingwood BR, Smilowitz R, Dusenberry DO, Duthinh D, Lew HS, Carino NJ. (2007), *Best Practices for Reducing the Potential for Progressive Collapse in Buildings*. Rep. No. NISTIR 7396, National Institute of Standards and Technology, Maryland.
- [4] Brett C, Lu Y. (2013), "Assessment of Robustness of Structures: Current State of Research [J]". *Frontiers of Structural and Civil Engineering*, 7(4): 1-13.
- [5] Yi W, He Q, Xiao Y, et al. (2008), "Experimental Study on Progressive Collapse-Resistant Behavior of Reinforced Concrete Frame Structures." *ACI Structural Journal*; 105(4): 433-439.
- [6] Sadek F, Main JA, Lew HS, Robert SD, Chiarito VP, El-Tawil S. (2010), "An Experimental and Computational Study of Steel Moment Connections under a Column Removal Scenario." Rep. No. NIST Technical Note 1669, National Institute of Standards and Technology, Maryland.
- [7] Lee C, Kim S, Lee K. (2010), "Parallel Axial-Flexural Hinge Model for Nonlinear Dynamic Progressive Collapse Analysis of Welded Steel Moment Frames." *Journal of Structural Engineering*, ASCE, 136(2): 165-173.
- [8] Yang B, Tan K H. (2012), "Robustness of Bolted-Angle Connections against Progressive Collapse: Experimental Tests of Beam-Column Joints and Development of Component-Based Models." *Journal of Structural Engineering*, 139(9): 1498-1514.
- [9] Yang B, Tan K H. (2013), "Experimental Tests of Different Types of Bolted Steel Beam-Column Joints under a Central-Column-Removal Scenario." *Engineering Structures*, 54(0): 112-130.
- [10] Liu Y, Málaga-Chuquitaype C, Elghazouli AY. (2012), "Response of Beam-to-Column Angle Connections Subjected to Combined Flexural and Axial Loading." In: Gardner L, editors. *Proceeding of the 14th International Symposium on Tubular Structures*. London.
- [11] Li L, Wang W, Chen YY, Lu Y. (2013), "Experimental Investigation of Beam-to-Tubular Column Moment Connections under Column Removal Scenario." *Journal of Constructional Steel Research*, 88: 244-255.

CHARACTERIZATION OF LOAD PATHS IN COMPOSITE STEEL DECK DIAPHRAGMS AND COLLECTORS

Robert B. Fleischman
University of Arizona, Tucson, Arizona 85721, USA
rfleisch@email.arizona.edu

Anshul Agarwal
University of Arizona, Tucson, Arizona 85721, USA
anshul@email.arizona.edu

Alexander T. Walsh
University of Arizona, Tucson, Arizona 85721, USA
alexanderwalsh@email.arizona.edu

Luis F. Valdez
University of Arizona, Tucson, Arizona 85721, USA
lfvaldezsoto@email.arizona.edu

Diaphragm behavior remains one of the less defined aspects of building response. In an earthquake, inertial forces must be carried through the floor diaphragm to the lateral force resisting system. The floor systems in steel structures are indeterminate assemblages of different materials and geometries, acting at different elevations, and connected by elements which may not be primarily considered for diaphragm action. Complex load paths develop in the floor diaphragm, including interaction with lateral load and gravity load systems. Research has indicated that peak diaphragm forces during an earthquake can significantly exceed the levels prescribed in past codes. As these larger forces will be reflected in upcoming design codes, it is important to better understand how these forces are carried in the floor system to permit efficient and economical designs. This paper presents details of an upcoming analytical program examining the characteristics, behavior, and failure modes of composite steel deck diaphragms.

1. INTRODUCTION

Floor diaphragm behavior remains one of the less defined aspects of building response. In an earthquake, inertial forces must be carried through the floor or roof diaphragm to the primary elements of the lateral force resisting system. The systems that comprise the diaphragm for steel structures are complicated indeterminate assemblages of different materials and geometries, acting at different elevations, and connected by elements which may not be intended for diaphragm action. Complex load paths develop in the floor system as a result not only of diaphragm action, but also interaction with lateral load and gravity load transfer. Research has indicated that due to the building's nonlinear dynamic response, peak diaphragm force magnitudes during an earthquake can

significantly exceed the levels prescribed in past codes. As the large inertial forces will be reflected in upcoming design codes, it is crucial to better understand how these forces are carried in the floor system to permit efficient and economical designs.

This paper presents the details of an upcoming analytical study aimed at examining the load paths in steel diaphragms and collectors for the purposes of better describing the characteristics and behavior of these systems. The analytical study is based on models constructed and calibrated using the results of previous testing of steel composite deck diaphragm components and bays. 2D (vertical plane and horizontal plane) and 3D models have been developed to examine collector action, diaphragm capacity and diaphragm seismic demand. The recently initiated study has the following objectives: (1) Determine global force paths through composite deck diaphragm; (2) Characterize chord and collector load paths within steel floor systems; (3) Establish the response of diaphragm bays within the global diaphragm system; and, (4) Quantify the global properties and seismic performance of the composite steel deck floor system.

2. STEEL DECK DIAPHRAGMS

Diaphragm action is a horizontal in-plane membrane action through which the lateral loads (e.g. from wind or earthquake) are transferred from the floor or roof system to the primary (vertical plane) elements of the Lateral Force Resisting System (LFRS), e.g. shear walls, moment frames, braced frames.

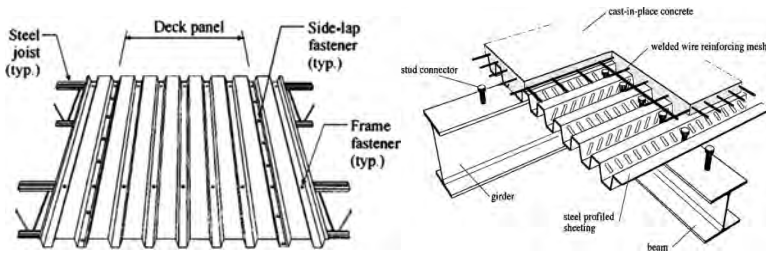


Figure 1. Steel Deck Diaphragms: (a) Bare Metal-Deck (Rogers & Tremblay, 2003a); (b) Composite Steel Deck (Hedao, et al., 2012).

In steel structures, diaphragm shear action is achieved by the floor plate, which for floor systems is typically formed through composite action of the concrete slab with the metal deck (Sabelli, et al., 2011), while for roof systems can often be unfilled metal deck, particularly in low rise buildings (Essa, et al., 2003). The deck is made of corrugated sheets attached to each other through side lap fasteners (welds, screws or button punches) and to the supporting members through deck-to-frame fasteners, e.g. spot welds, screws, powder-actuated or air driven pins, or shear studs (See Fig. 1a). In floor systems, composite diaphragm action is attained through a combination of chemical bond between the slab and deck, mechanical interlock by embossments in the deck profile, and for composite floor systems, steel shear studs welded to the underlying framing that project into the slab (See Fig. 1b). Note the distinction between *composite floor systems*, which employ shear studs for gravity load, and *composite diaphragm action*, acting between the deck and the slab, assumed to occur even in the absence of shear studs.

Steel Diaphragm Design

In design, the floor diaphragm is often treated as a horizontal deep beam, carrying in-plane (horizontal) shear and flexure forces, and “collecting” forces back to the primary vertical plane LFRS elements (See Fig. 2a). In steel structures, the floor or roof deck system is designed to provide the in-plane shear resistance (analogous to a beam web), while the underlying steel perimeter frame members are often counted on to carry in-plane axial or “chord” actions, analogous to a beam flange (Sabelli, et al., 2011).

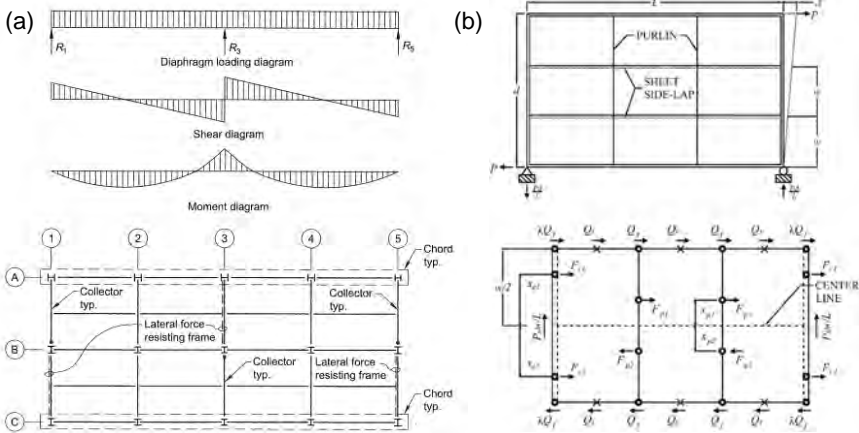


Figure 2. Steel Diaphragms: (a) Diaphragm Internal Forces and Elements (AISC, 2010); (b) Diaphragm Bay and Deck Panel Forces (SDI, 2004).

In modern structures, the primary LFRS elements are often isolated from each other in the floor plan, necessitating the need for “collectors” to bring the diaphragm forces to these elements. Steel floor systems requiring significant collector action will utilize floor system members for this purpose. Thus, chord and collector members are often part of the underlying gravity-load resisting system (GLRS) frame, checked and modified, if needed, for axial force. Due to the reversing nature of the earthquake loads, these elements are designed both as tension members (i.e. connections) and as beam-columns for the limit states of flexural, torsional, flexural torsional and lateral torsional buckling. The lateral and torsional bracing inherent in the floor framing and deck is an important consideration in design, including a “constrained” flexural torsional mode about the top axis. Lateral bracing is ignored for parallel deck ribs. Torsional bracing is often ignored for metal deck while considered continuous for composite deck. For wind or more modest seismic loads, the collector and chord action may instead be provided by reinforcing bars placed within the concrete deck (AISC, 2010).

Metal deck diaphragm shear strength is limited by fastener strength, except for shallow decks with large floor beam spacing where shear buckling controls. Design shear strength is based on edge fastener strength, using an elastic strain distribution for interior fasteners, and providing corner fasteners with reduced capacity due to deck distortion (See Fig. 2b). Tables are provided for individual fastener strength (SDI, 2004).

The design strength of a composite diaphragm is controlled by a modified version of the ACI 318 (2014) diagonal cracking equation based on the thickness of the slab

above the metal deck (SDI, 2004). Counting on this strength requires meeting certain fastener strength requirements to ensure this higher force can be developed, which requires closely spaced fasteners or a lower number of shear studs.

Diaphragm design shear stiffness is based on an effective shear modulus, G' , which incorporates the geometry, end warping restraint and fastener slip. For a typical unfilled deck, G' may be an order of magnitude lower than the G of steel due to the corrugations (SDI, 2004). The added in-plane stiffness provided by the concrete make a composite diaphragm panel significantly stiffer than the unfilled deck (SDI, 2004).

Diaphragm Design Forces

New diaphragm seismic design forces are being adopted in the code (BSSC, 2014) in recognition of large peak diaphragm inertial forces that can develop during a seismic event. These forces can be substantially larger than the design forces prescribed in current code equivalent lateral force (ELF) procedures (ASCE 7, 2010), Fig. 3a,b. Diaphragm forces are underestimated in design because the response modification factor (R) used for LFRS design, which is tied to the fundamental mode is incorrectly applied to diaphragm design, whose acceleration demands are tied to higher modes, Fig. 3c (Rodriguez, et al., 2007). Fig. 3d shows a comparison of the current to the newly proposed ASCE 7 diaphragm design forces. Explicit *diaphragm design force reduction factors* R_s are also being introduced into code (BSSC, 2014). These factors reflect the capacity of diaphragms to accommodate large instantaneous diaphragm forces through overstrength, ductility and redistributive properties. Diaphragm forces also arise due to transfer conditions where vertical plane LFRS elements are offset, for instance at setbacks or podium slabs, or dissimilar, e.g. in a dual system (Sabelli, et al., 2011).

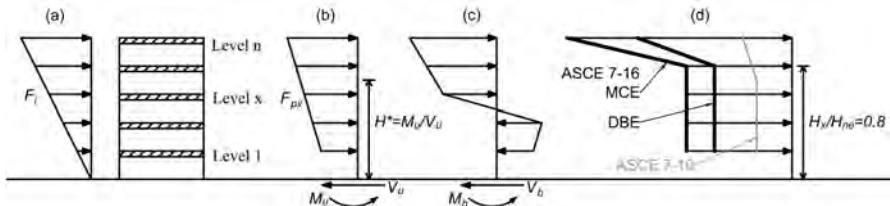


Figure 3. Earthquake forces: (a) ELF design; (b) Diaphragm design; (c) Instantaneous inertial force; (d) Comparison of new to existing diaphragm forces.

3. KEY BEHAVIOR OF COMPOSITE STEEL DECK DIAPHRAGMS

The light weight and constructability of the concrete-filled deck floor systems make them the preferred alternative in steel-frame construction. The concrete slab introduces a stiffer alternate path through which shear forces may travel through the diaphragm, and limits end warping and corner local buckling. For this, composite action with the deck must be maintained and sufficient fasteners provide to develop the slab shear strength.

The fastener properties are often the key factor in describing the diaphragm stiffness, strength, ductility and energy dissipation for metal deck (Essa, et al., 2003). Rogers and Tremblay (2003a, 2003b) performed a series of tests on a variety side lap and frame fasteners under cyclic loading protocols to determine the characteristics of these

elements. The fasteners exhibited a range of strengths and ductility, and detailing recommendations were provided for improved behavior.

Easterling and Porter (1994a) summarized 32 full-scale composite diaphragm tests with main design parameters steel deck/slab thickness, and connector type/number. Three primary limit states were identified: (1) Composite Slab: Diagonal cracking across the diaphragm panel, with a complimentary diagonal (X) crack on reversal leading to a significant drop in load carrying capacity. Longitudinal cracking also occurred in thinner slabs; (2) Deck-Slab Interface: Measurable end slip occurred between the concrete and deck for welded frame fasteners (and not for shear studs), with end warping deformation of the deck contributing to interface separation; (3) Edge Fasteners: The transfer of in-plane load between frame members and the composite slab took place near the edge of the bay. At locations away from the edge, the steel deck and fasteners were found to contribute very little to the diaphragm resistance. Deck orientation had an impact for filled diaphragms, with higher strength for loading perpendicular to ribs; gravity load did not have a significant effect on diaphragm strength and stiffness.

Diaphragm collector beams must be able to accumulate axial load through shear studs and transfer these forces into the seismic resisting system through a dependable, axially stiff load path across all the gravity columns but one that does not develop high moments (See Fig. 4) in the columns (Cowie, et al., 2013).

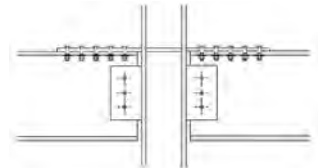


Figure 4. (a) Collector Detail (Cowie, et al., 2013)

Discussion of Load Path

The diaphragm chord transfer, represented simply in design, is actually quite complex. For elements in parallel, forces will follow the stiffest path. Thus, compression chords might be assumed to be carried through the concrete slab at the perimeter; while tension chords can flow either through the steel frame or through reinforcement in the slab if present, depending on their relative stiffness (Cowie, et al., 2013). The deck orientation also matters since ribs parallel to the chord will certainly participate, while ribs perpendicular are assumed not to have a large effect (Cowie, et al., 2013). Gravity load transfer to the chord can induce torsion for an edge (spandrel) beam, and requires proper spandrel beam slab reinforcement (Clifton & El Sarraf, 2005). Note also that the relative stiffness will change during the seismic event as elements soften, yield, slip, crack, or crush. Further, the compression chord region reverses and becomes the tension chord region with each oscillation of the diaphragm in the earthquake.

Though not considered directly in design, it is worth asking how the inertial forces, which originate in both the slab and the framing, find their way to the foundation. Tests performed on isolated diaphragm panels are not reproducing the boundary condition provided by the adjacent slabs. Very little experimental evidence exists to distinguish the strut action (Bull, 1997) that develops in the steel composite slab relative to the transfer into the underlying frame (See Fig. 5). Designing significant collectors and collector connections, often assuming inertial forces are making right angle turns into the LFRS element, without knowledge of the load path spatially in the horizontal plane, nor the percentage of the inertial force carried by the slab vs. the underlying frame at each location may not lead to the most economical, or in cases safe diaphragm designs.

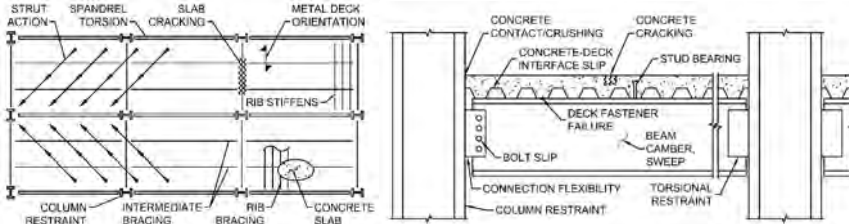


Figure 5. Composite Diaphragms Load Paths: (a) Horizontal-Plane; (b) Vertical Profile

The same elements in the floor system that are providing the diaphragm action are also providing gravity load resistance during the earthquake. It is assumed that the interaction of shear stud diaphragm force and gravity load force can be ignored (Burmeister & Jacobs, 2008), because the horizontal shears due to lateral loads oppose the gravity-induced values for half the beam. These design assumptions rely on sufficient inelastic deformation capacity for plastic redistribution, low cycle fatigue life, and limited degradation of surrounding concrete. Likewise these same framing members are participating, at least secondarily, in the lateral load resistance. This frame action can occur in moment frames that serving as part of the lateral force resisting system, but may also be arise in as secondary lateral resistance provided by the gravity system. While gravity framing is intended to be pinned, and collectors are typically detailed to prevent moment, these connections nonetheless have some partial fixity, particularly when the contributions of the slab are considered. It is unclear how much these systems interact, not only producing force combinations in the diaphragm, but also possibly diaphragm forces acting on connections in the underlying gravity and lateral force resisting framing. Likewise, the concrete slab detail at the column can affect the magnitude of the beam axial force developing due to slab inertial effects in the floor diaphragms (Chaudhari, et al., 2014).

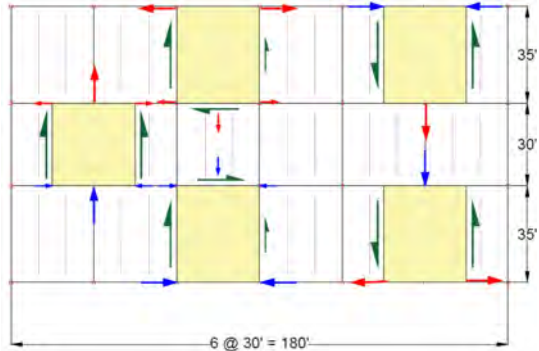


Figure 6. Force Conditions at Different Bays.

4. ANALYTICAL STUDY DESCRIPTION

The analytical models will leverage products from the significant existing past research on components steel diaphragm and composite structures. Key diaphragm components and interfaces are listed in Table 1 along with the existing research and data products to be leveraged in the research. The models developed for the study will rely on these existing data products, component models and research findings.

An evaluation structure (Refer to Fig. 6) has been selected and designed for the analytical study. The evaluation structure represents typical construction, and is both straightforward and generic for easy parameter variation, and also capable of examining

critical conditions. The structure is designed for a site in Los Angeles according to the current design codes (AISC, 2011) (ASCE 7, 2010), as well as in consideration of possible future code changes (BSSC, 2014). Building heights of 4, 8 and 12 will be evaluated. Different steel LFRS types and layouts will be considered, as well as live loading conditions. Both floor and roof diaphragm behavior will be considered.

Table 1. Existing Research and Data Products.

Component	Incorporated in Model	Product	Model/Limit State	Reference
Metal Deck	Continuum 3D steel w/linear geometry and material	Micro deck diaphragm test data Shear Buckling Quasi-static test data for use in calibration	Calibrated FE model Profiled sheet w/intrusion Springs, large defl.	(Vignoli and Noseni, 1997)
	Orthotropic 2D plane stress/w/elastic material	Effective Shear Modulus		(Eisa # et al., 2003)
				(SDI, 2004)
Deck Fasteners	Non-linear degrading hysteretic coupled springs	Test data for direct use	Side-lap fasteners Frame fasteners	(Rogers and Tremblay, 2003a) (SDI, 2004) (Rogers and Tremblay, 2003b)
	Smudged crack modeling	Test data composite slab, Design Equations		(Eastwing and Pyle, 1994a) (Eastwing and Pyle, 1994b) (SDI, 2004)
Concrete Slab	Strut & Tie Models etc.	Analysis/Des. Method	Internal Force Paths	(Blauwendraat & Herzogenboom 1966) (Sud, 1997)
Shear Studs	3D solid modeling, Nonlinear springs and contact elements	Stud Failure modes Test Data	Interface-Slud large Defl. Splitting Failure Combined Forces	(Cusani and Lam, 2012) (Lowe et al., 2014) (Mira and U.; 2010)
	Interface Elements with Cohesive Bond Material	Test Data	Cohesive Bond Model Bond and Connectors Slip strength	(Mira et al., 2014) (Soudki et al., 2013) (S. Owen, 2002)

Analytical Modeling

Analytical models are being developed for steel floor diaphragms and structures. The models include nonlinear material (steel), degrading material (concrete), interface elements (slab to deck), contact elements (slab to column), slip elements (bolted connections), nonlinear geometry (deck distortion) and non-ductile springs (welds, side-lap and deck fasteners). The model functionality has been extended incrementally.

As seen in Figure 7, the models will be expanded from more detailed “micro” models of key local behavior (e.g. shear stud bearing, profiled deck-concrete slip etc.) for solid modeling, to “meso” models of key portions (diaphragm bay, chord or collector, etc.) for nonlinear pushover models, to “macro” models of the entire structure for nonlinear time history analysis (i.e., earthquake simulation). Models for the collector began as two-dimensional plane stress representations (in the vertical plane) and are being extended to three dimensional representations of the floor system.

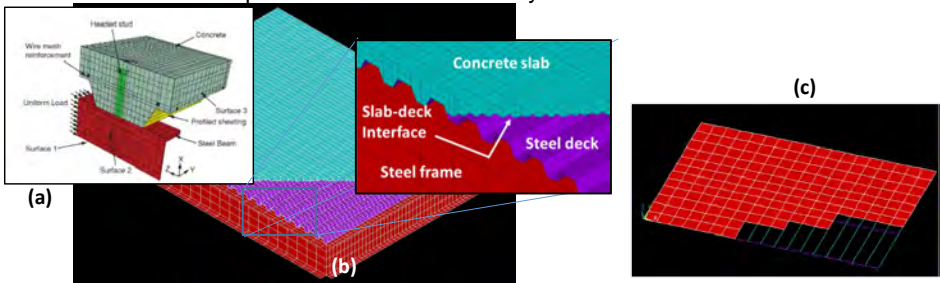


Figure 7. Analytical Models: (a) Micro (Qureshi & Lam, 2012); (b) Meso; (c) Macro.

Analytical Study

The analytical study will have three stages (See Table 2): (1) *Bay Properties*: Models of diaphragm bays will be used to determine diaphragm properties; (2) *Diaphragm Capacity*: models of the entire diaphragm will be used to investigate load paths and steel diaphragm capacity; (3) *Diaphragm Demands*: Design recommendations will be verified

through earthquake simulations of a realistic building structure model. Note that each step involves different analyses: (1) Nonlinear static “pushover” (NP) analyses for determining bay capacity and characteristic properties (stiffness, strength, ductility for shear, axial force); (2) Body force analyses of the floor diaphragm to determine failure sequence and plastic redistribution; and (3) Nonlinear time history (NTH) analysis for determining anticipated demands in the design and maximum considered earthquake (DBE, MCE).

Table 2. Analytical Study Stages.

Study	Title	Structure	Level	Simulation
1	Dia. Properties	Evaluation	Bay	Nonlinear Pushover
2	Diaphragm Capacity	Evaluation	Diaphragm	Body Force
3	Diaphragm Demands	Prototype	Structure	Nonlinear Time History

Table 3 shows the study matrix for the analytical study: (a) using the meso model for the three primary regions of the steel diaphragm: interior shear bay, chord region and collectors, and focusing on parameters related to detailing, behavior, models and design; and (b) for the Macro-model under body force NP analyses focusing on load path and characteristics of the diaphragm system, and nonlinear time histories of the entire structure to determine diaphragm seismic demands.

Table 3. Study Matrix with Parameters Evaluated.

Area		Topic	Meso-Model under Body Force			Area	Topic	Macro-Model
		Diaphragm Region	Interior Bay	Chord	Collector	Diaphragm System: Macro-Model NP/NTH		
DETAILS	ribs parallel/perpendicular		<input type="checkbox"/>	<input checked="" type="checkbox"/>	<input checked="" type="checkbox"/>	LOAD PATH	Horizontal Plane Load Path	<input checked="" type="checkbox"/>
	gravity/moment connections		<input type="checkbox"/>	<input checked="" type="checkbox"/>	<input checked="" type="checkbox"/>		Gravity Column Effect	<input checked="" type="checkbox"/>
	composite/form/unfilled		<input checked="" type="checkbox"/>	<input checked="" type="checkbox"/>	<input checked="" type="checkbox"/>		Transfer Conditions	<input checked="" type="checkbox"/>
BEHAVIOR	tension vs. compression		<input type="checkbox"/>	<input checked="" type="checkbox"/>	<input checked="" type="checkbox"/>	CHARACTERISTICS	System Stiffness/Strength	<input checked="" type="checkbox"/>
	initial state/as damage incurs		<input checked="" type="checkbox"/>	<input checked="" type="checkbox"/>	<input checked="" type="checkbox"/>		Controlling Limit State	<input checked="" type="checkbox"/>
	stability/gravity load effects		<input type="checkbox"/>	<input checked="" type="checkbox"/>	<input checked="" type="checkbox"/>		System Overstrength	<input checked="" type="checkbox"/>
MODEL	2D planar vs. 3D profile		<input checked="" type="checkbox"/>	<input checked="" type="checkbox"/>	<input checked="" type="checkbox"/>	DEMANDS	Failure Sequence/ Plastic Redistribution	<input checked="" type="checkbox"/>
	isolated bay vs. in system		<input checked="" type="checkbox"/>	<input checked="" type="checkbox"/>	<input checked="" type="checkbox"/>		Diaphragm Forces	<input checked="" type="checkbox"/>
	vertical elements (columns)		<input checked="" type="checkbox"/>	<input type="checkbox"/>	<input checked="" type="checkbox"/>		Floor Accelerations	<input checked="" type="checkbox"/>
DESIGN	Stiffness / Strength		<input checked="" type="checkbox"/>	<input checked="" type="checkbox"/>	<input checked="" type="checkbox"/>	Ductility Demands	<input checked="" type="checkbox"/>	
	Overstrength / Redistribution		<input checked="" type="checkbox"/>	<input checked="" type="checkbox"/>	<input checked="" type="checkbox"/>			
	Degradation / Ductility		<input checked="" type="checkbox"/>	<input checked="" type="checkbox"/>	<input checked="" type="checkbox"/>			

5. PRELIMINARY RESULTS AND FUTURE WORK

The analytical research has focused on model calibration to date and results from the studies described are anticipated at the time of the workshop presentation. The objectives of the analytical study to be presented at the workshop are to:

- (1) *Determine the global force paths through composite deck diaphragm*, including: (a) the horizontal-plane spatial distribution of force; (b) the relative participation of the slab, deck, and underlying framing in horizontal force transfer; (c) the paths within the floor system vertical profile; (d) the interaction of inertial and transfer force paths; and (e) the effect of vertical plane elements (gravity system columns, moment frames).

- (2) Characterize the chord and collector load paths within steel building floor systems, including: (a) the efficiency of chords and collectors in a composite steel floor system with respect to diagonal strut transfer mechanisms in the slab; (b) the performance of discrete chords and collectors with different connection, bracing or reinforcing details; and, (c) chords and collectors oriented parallel vs. transverse to decking.
- (3) Establish the response of steel diaphragm bays within the global diaphragm system, including determining the behavior of composite steel diaphragm bays under different boundary conditions and varying levels of shear-flexure-tension combinations.
- (4) Quantify the global properties and seismic performance of the composite steel deck floor system, including characterizing the: (a) shear and flexural stiffness and the shear and flexural strength; (b) the failure sequence and diaphragm system overstrength; (c) the diaphragm ductility and ability to redistribute forces during inelastic response; (d) the seismic demands relative to capacity.

Model Calibration

The models are being calibrated using existing test results prior to the analytical studies. Since there is not an abundance of steel composite deck diaphragm test results in existence, the models are also being calibrated using tests with other focus (e.g., composite gravity and moment frames) that contain portions of the floor system. Figure 8a shows an example of the test on a composite frame (Nakashima, et al., 2007) used to calibrate the components of the collector model (Figure 8b) for the bare frame (Figure 8c) and composite frame (Figure 8d). Likewise, Figure 8e shows a metal deck model being calibrated to (Essa, et al., 2003), and a comparison of fastener response (Fig. 8f) where in each case test results are shown in red and the model response is shown in blue.

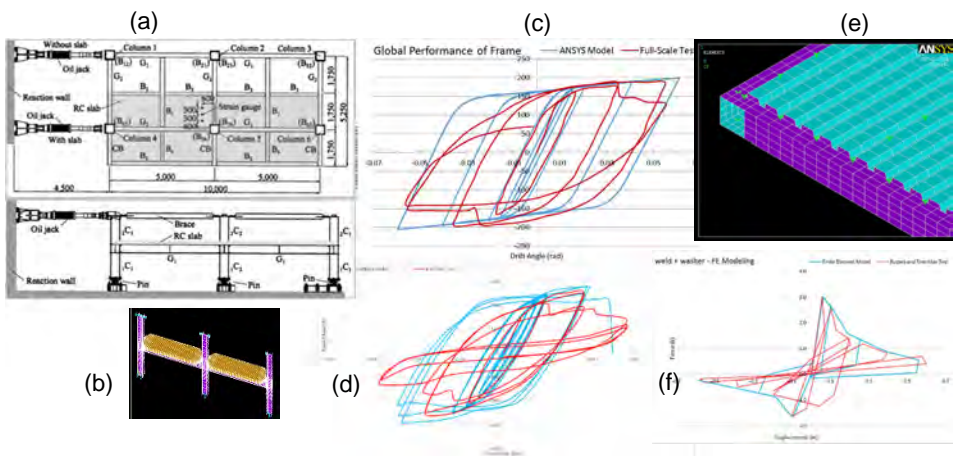


Figure 8. Model Calibration: (a) Test Specimen (Nakashima, et al., 2007); (b) FE Model; (c) Bare Frame Model; (d) Composite Frame Model; (e) Metal Deck Model; and (f) Deck Fastener Calibration (Essa, et al., 2003).

REFERENCES

- ACI 318, 2014. *ACI 318-1: Building Code Requirements for Structural Concrete (ACI 318-14)*, s.l.: American Concrete Institute.
- AISC, 2010. *Seismic Design Manual 2nd ed.* s.l.:s.n.
- AISC, 2011. *Steel Construction Manual 14th ed.* s.l.: s.n.
- ASCE 7, 2010. *Minimum Design Loads for Buildings and Other Structures (ASCE/SEI 7-10)*, s.l.: American Society of Civil Engineers.
- BSSC, 2014. *Diaphragm Design Force Level. Proposal IT06-001 - Revise ASCE/DEI 7-10 Chapters 11&12.* s.l.:Building Seismic Safety Council, Committee IT6.
- Bull, D., 1997. "Diaphragms", *Seismic Design of Reinforced Concrete Structures*, s.l.: Technical report No 20, new Zealand Concrete Society.
- Burmeister, S. & Jacobs, W. P., 2008. Horizontal floor diaphragm load effects on composite beam design. *Modern Steel Construction*, December.
- Chaudhari, T. et al., 2014. *Composite slab effects on beam-column subassemblies: Further development.* s.l., s.n.
- Clifton, G. & El Sarraf, R., 2005. *Composite Floor Construction Handbook*, Namukau City, New Zealand: HERA Report R4-107. N.Z. HERA.
- Cowie, K. et al., 2013. *Seismic Design of Composite Metal Deck and Concrete-filled Diaphragms - a discussion paper.* s.l., s.n.
- Easterling, W. & Porter, M., 1994a. Steel Deck Reinforced Concrete Diaphragms I. *Journal of Structural Engineering*, 120(2), pp. 560-576.
- Easterling, W. & Porter, M., 1994b. Steel Deck Reinforced Concrete Diaphragms II. *Journal of Structural Engineering*, 120(2), pp. 577-596.
- Essa, H., Tremblay, R. & Rogers, C., 2003. Behavior of Roof Deck Diaphragms Under Quasi-Static Loading. *Journal of Structural Engineering*, 129(12), pp. 1658--1666.
- Hedaoo, N. A., Gupta, L. M. & Ronghe, G. N., 2012. Design of composite slabs with profiled steel decking: a comparison between experimental and analytical studies. *International Journal of Advanced Structural Engineering*, 3(1).
- Majdi, Y., Hsu, C.-T. T. & Punurai, S., 2014. Local bond-slip behavior between cold-formed metal and concrete. *Engineering Structures*, Volume 69, pp. 271-284.
- Nakashima, M., Tomohiro, M., Keiichiro, S. & Feng, Z., 2007. Full-Scale Test of Composite Frame under Large Cyclic Loading. *Jrnl of Str Engg*, 133(2), pp. 297-304.
- Qureshi, J. & Lam, D., 2012. Behaviour of Headed Shear Stud in Composite Beams with Profiled Metal Decking. *Advances in Structural Engineering*, 15(9), pp. 1547-1558.
- Rodriguez, M., Restrepo, J. & Blandon, J., 2007. Seismic Design Forces for Rigid Floor Diaphragms in Precast Concrete Building Structures. *Journal of Structural Engineering*, November, 133(11), pp. 1604-1615.
- Rogers, C. A. & Tremblay, R., 2003a. Inelastic Seismic Response of Side Lap Fasteners for Steel Roof Deck Diaphragms. *Jrnl of Str Engg*, 129(12), pp. 1637-46.
- Rogers, C. A. & Tremblay, R., 2003b. Inelastic Seismic Response of Frame Fasteners for Steel Roof Deck Diaphragms. *Jrnl of Structural Engg.*, 129(12), pp. 1647-58.
- Sabelli, R., Sabol, T. A. & Easterling, W. S., 2011. *Seismic Design of Composite Steel Deck and Concrete-filled Diaphragms*, s.l.: NIST.
- SDI, 2004. *Diaphragm Design Manual*, s.l.: Steel Deck Institute.

EFFECT OF COMPOSITE BEAM ACTION ON THE HYSTERETIC BEHAVIOR OF FULLY-RESTRAINED BEAM-TO-COLUMN CONNECTIONS UNDER CYCLIC LOADING

Dimitrios Lignos

School of Architecture, Civil & Environmental Engineering, Swiss Federal Institute of Technology (EPFL), Switzerland
dimitrios.lignos@epfl.ch

Ahmed Elkady

Department of Civil Engineering and Applied Mechanics, McGill University, Canada
ahmed.elkady@mail.mcgill.ca

ABSTRACT

This paper assesses the composite beam effects on the hysteretic behavior of fully-restrained beam-to-column connections as part of steel moment-resisting frames (MRFs) designed in highly seismic regions. A practical approach is developed based on available experimental data to simulate the hysteretic behavior of composite beams including the effects of asymmetric deterioration of the beam flexural strength and stiffness. A system-level analytical study is then performed that evaluates the collapse resistance of steel frame buildings designed with steel MRFs including the composite beam effects. It is demonstrated that when steel MRFs are designed with a SCWB ratio larger than 1.5 a tolerable probability of collapse is achieved over the life cycle of the steel frame building. It is also shown that controlled panel zone yielding can be achieved while reducing the required number of welded doubler plates in beam-to-column panel zone joints.

1. INTRODUCTION

Past experimental studies on fully restrained composite beam-to-column connections reveal that: (a) the flexural strength of a steel beam typically increases especially when the slab is in compression; (b) the strong-axis moment of inertia of a composite steel beam is typically larger than that of the bare steel beam; and (c) the cyclic deterioration in flexural strength and stiffness of a composite beam becomes asymmetric (e.g., Jones et al. 2002; Tremblay et al. 1997; Zhang and Ricles 2006). Experimental studies on steel frame systems (Cordova et al. 2004; Nakashima et al. 2007; Ohsaki et al. 2008) indicate that the neutral axis of a composite steel beam shifts into its upper half due to the presence of the slab. This shift as well as the role of the composite action in delaying local buckling in the top flange is more pronounced when there is beam and slab continuity, which is not evident in typical cruciform subassemblies that their beam ends are free to translate. For the seismic design of steel special moment frames (SMFs) in North America (AISC 2010a), the *moment ratio* rule [also referred to as the strong-column/weak-beam (SCWB) criterion] is employed in order to avoid column flexural yielding. In this check a set of adjustments for strain hardening and the material variability is considered depending on the beam-to-column connection type. However, the contribution of the composite beam effects is typically ignored. There is a perception that this assumption is typically conservative; however,

the considerable flexural strength increase of a beam due to the presence of the slab may shift flexural yielding to occur in the steel column rather than the beam even if the SCWB ratio was employed. The same issue may occur because of the redistribution of forces within a steel SMF due to strength deterioration of the steel beams because of geometric instabilities (i.e., local buckling). The aforementioned issues affect the collapse resistance of steel SMFs when subjected to earthquakes with low probability of occurrence.

This paper quantifies the effects of the composite action on the hysteretic behavior of steel beams as part of fully restrained beam-to-column connections. A rational approach is then developed that captures such effects within a numerical model. Finally, the effects of the composite action on the seismic performance of typical SMFs are investigated through rigorous nonlinear response history analyses based on a set of archetype steel frame buildings designed in the West Coast of the US.

2. NONLINEAR MODELING OF COMPOSITE BEAM-TO-COLUMN CONNECTIONS

This section proposes an approach to capture the effect of the composite action on the hysteretic behavior of beam-to-column connections. For this reason, a set of 22 experiments on interior joint beam-to-column connections was gathered from a searchable W-shape database of steel beams (Lignos and Krawinkler 2011; Lignos et al. 2010). Due to brevity, a detailed description of the test data can be found in (Elkady and Lignos 2014, 2015).

2.1 Modeling of Composite Steel Beams

The modified Ibarra-Medina-Krawinkler (IMK) model (Ibarra et al. 2005; Lignos and Krawinkler 2011) has been calibrated extensively to simulate the hysteretic behavior of bare steel beams (Lignos and Krawinkler 2011, 2013). An example of such calibration is shown in Figure 1a for a bare steel beam with a reduced beam section (RBS). The same numerical model was modified to simulate the asymmetric hysteretic behaviour of a composite steel beam, its residual strength due to local buckling stabilization as well as the ductile tearing due to low cycle fatigue (Lignos et al. 2011). The modified IMK deterioration model is bounded by a backbone curve as shown in Figure 1. This backbone curve is defined based on: (1) the elastic flexural stiffness K_e of the steel beam; (2) the effective yield moment M_y ; (3) the capping-to-effective yield moment ratio M_c/M_y ; and (4) the residual-to-effective yield moment ratio M_r/M_y . From Figure 1, three deformation parameters fully define the backbone curve of the IMK model: (1) the pre-capping plastic rotation θ_p ; (2) the post-capping plastic rotation θ_{pc} ; and (3) the ultimate rotation θ_u . The cyclic deterioration of the flexural strength and stiffness of a steel beam is controlled through the reference energy dissipation capacity (Δ) and the rates of cyclic deterioration in the positive and negative loading directions (D^+ and D^-).

From Figure 1, the differences between the hysteretic behavior of a bare and a composite steel beam can be qualitatively assessed. In brief, due to the presence of the slab, composite steel beams have an asymmetric hysteretic behavior (see Figure 1b). In particular, a higher flexural strength and plastic deformation capacities are observed in the positive loading direction (i.e., slab in compression) than the corresponding parameters in the negative loading direction (i.e., slab in tension). The former is attributed to the restraint that the slab provides to the top flange of a steel beam. The latter is attributed to the beam neutral axis shifting towards its upper flange. In this case, the bottom flange is susceptible to lateral torsional buckling.

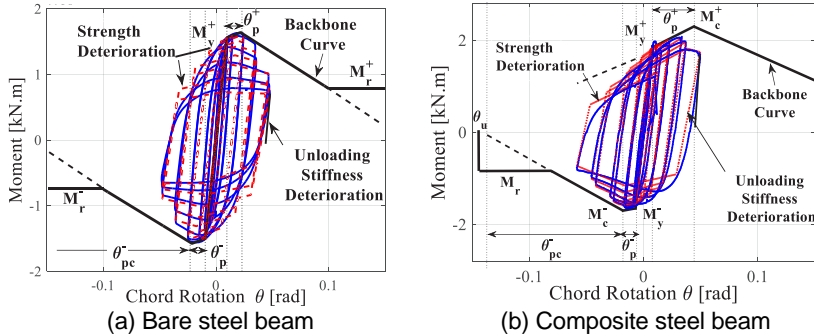


Figure 1: Modified IMK component model [data from Uang and Fan(2001) and Zhang and Ricles 2006)

To quantify these values and develop modeling recommendations for composite beams, the hysteretic response of the modified IMK deterioration model is calibrated with respect to the set of experiments summarized in Elkady and Lignos (2014). The calibrated parameters of the modified IMK deterioration model for both the positive and negative loading directions are summarized in Table 1. From this table, the deformation parameters are normalized with respect to those of the respective bare steel beam. The effective yield flexural strength in the positive and negative loading directions are normalized with respect to the effective flexural strength of the bare steel beam M_y , calculated as $M_y = 1.1Z_xF_{ye}$, in which Z_x is the plastic modulus about the beam’s strong-axis; and F_{ye} is the expected yield stress of the steel material. The 1.1 factor is considered to represent approximately the effects of cyclic hardening on the steel beam flexural strength (Lignos and Krawinkler 2011). Table 1 summarizes the counted mean and coefficient of variation (COV) of the normalized values of each input parameter of the modified IMK model for composite beams. These values can be used to adjust the backbone curve of a bare steel beam to account for the composite action in a practical manner.

Table 1: Normalized deterioration parameters for composite steel beams

Param.	I_c	M_y^+	M_y^-	M_c^+	M_c^-	M_r^+	M_r^-	θ_p^+	θ_p^-	θ_{pc}^+	θ_{pc}^-	Λ	D^+	D^-
Mean	1.4	1.35	1.25	1.30	1.05	0.30	0.20	1.80	0.95	1.35	0.95	1.0	1.15	1.0
COV	0.12	0.13	0.13	0.08	0.02	0.31	0.23	0.32	0.48	0.21	0.13	0.31	0.19	0.0

In brief, when the slab is in compression, the effective yield flexural strength, M_y^+ and capping flexural strength, M_c^+ is larger by 30 to 35% compared to that of the bare steel beam. After the crushing of the concrete slab and the formation of beam flange local buckling, the flexural strength of a composite beam reaches to a residual strength of about 20% to 30% of the respective effective yield strength in the loading direction of interest. If a designer knows the geometric and material properties of the steel deck and concrete slab, the composite beam flexural strength can be directly calculated based on the approach discussed in AISC (2010b). The following assumptions should be considered: (a) full composite action between the concrete slab and the steel beam; (b) the geometry of the reduced beam section for beams with RBS; (c) the effective width of the composite beam as calculated based on AISC

(2010b) (see Section I 3.1a); and (d) the effective stress in the concrete is taken as 0.85 of the specified concrete stress f_c' .

2.2 Modeling of Composite Panel Zones

The “parallelogram model” proposed by Gupta and Krawinkler (2000) is utilized to represent the beam-to-column panel zone joint within a steel moment-resisting frame (MRF). This model simulates the nonlinear relation between the shear force, V and the shear distortion angle, γ within a panel zone. The trilinear backbone curve proposed by Krawinkler (1978) is employed to simulate the backbone curve of a panel zone as shown in Figure 2a. The concrete slab affects the hysteretic behavior of the panel zone. Therefore, the backbone curve of the panel zone should be adjusted for this reason. In particular, the effective depth of the panel zone depends on the loading direction (see Figure 2b). When the slab is in tension the effective depth is similar to that of a bare steel beam-to-column panel zone joint; hence the negative yield flexural strength of the panel zone should be calculated as discussed in Gupta and Krawinkler (2000). When the slab is in compression the effective depth becomes larger than that of the bare steel panel zone joint. The positive yield flexural strength of the panel zone joint can be calculated based on Equation 1,

$$M_y^- = V_y d_{eff}^- = V_y (d_b - t_f) \quad (1)$$

$$M_y^+ = V_y d_{eff}^+ = V_y (d_b - d_{rib} + 0.5t_s - 0.5t_f) \quad (2)$$

in which, d_{rib} is the depth of the ribbed section of the steel deck and t_s is the thickness of the slab. This increase in the effective depth reflects the higher stiffness and yield flexural strength of the panel zone due to the composite action (Kim and Engelhardt 2002). For composite panel zones as part of interior beam-to-column connection joints, their backbone curve remains symmetric because in both loading directions the slab is effective (Elkady and Lignos 2014). However, composite panel zones as part of exterior beam-to-column connection joints have an asymmetric backbone curve.

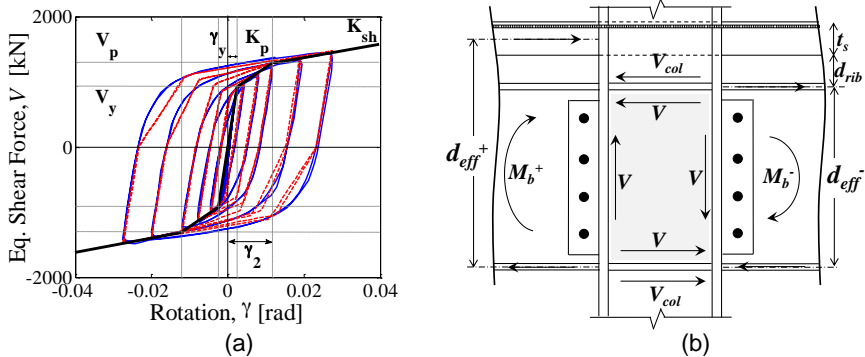


Figure 2: (a) Panel zone hysteretic material model [Data from Jones et al. (2002)]; (b) boundary forces acting on interior composite beam-to-column panel zone joints

The current seismic provisions for steel MRFs in the US (AISC 2010a; b) only consider the bare steel properties when sizing the panel zone thickness (i.e., doubler plate thickness). This implies that beam-to-column panel zone joints as part of steel

MRFs experience larger shear force demands and hence larger plastic deformations than expected. This is discussed in detail in the subsequent sections.

3. EFFECT OF COMPOSITE ACTION ON THE SEISMIC PERFORMANCE OF STEEL FRAME BUILDINGS WITH SPECIAL MOMENT FRAMES

This section discusses an analytical investigation of the seismic performance of archetype steel frame buildings with perimeter SMFs through collapse. The main goal is to assess the composite beam effects on the collapse resistance of the archetypes. The modeling recommendations discussed in Section 2 are utilized for this purpose.

3.1 Description of Archetype Steel Frame Buildings

A set of 2- to 20-story archetype steel frame office buildings that utilize perimeter SMFs is designed according to AISC (2010a; b) and ASCE 7-10 (ASCE 2010). The archetypes are assumed to be located in urban California. The SMFs are designed with typical beams with RBS. Figure 3 shows a typical plan view of the archetypes including an elevation view of one of the SMFs (see Figure 3b). Two dimensional (2-D) analytical model representations of the archetype buildings are developed in the OpenSees simulation platform (Mckenna 1997). The steel beams and columns of the steel SMFs are modelled with elastic beam-column elements. Each element utilizes the modified IMK deterioration model at its ends. For the bare SMFs (noted as B-models) the input parameters of the deterioration model are defined based on earlier work by Lignos and Krawinkler (2011). For the composite SMFs (noted as C-models) the input parameters of the steel beams are defined based on the recommendations presented in Section 2. P-Delta effects are considered with a fictitious leaning column. The Rayleigh model is employed with 2% damping ratio to simulate viscous damping.

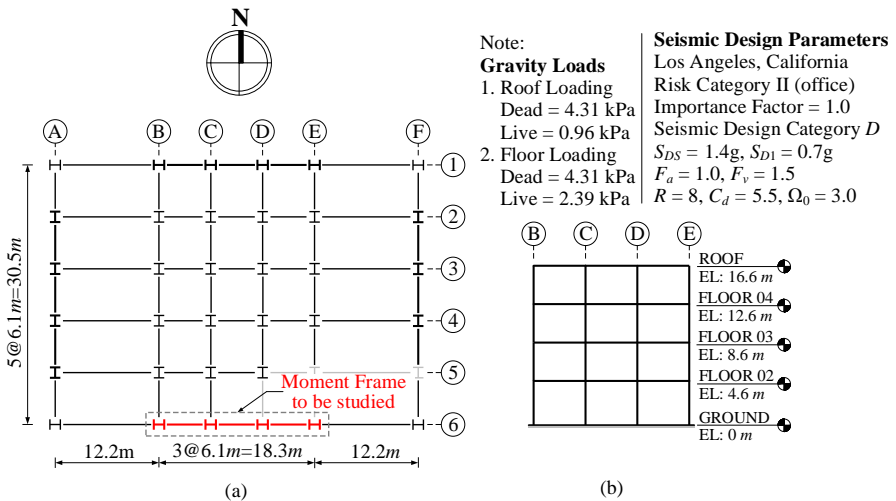


Figure 3: Typical archetype steel frame buildings: (a) plan view; (b) elevation of a four-story SMF

3.2 Collapse Assessment of Archetype Steel Frame Buildings

The dynamic behavior of the archetype buildings is assessed by performing incremental

dynamic analysis (Vamvatsikos and Cornell 2002). Earthquake-induced collapse due to sidesway instability is simulated explicitly. The far field set of 44 ground motions from FEMA P695 (FEMA 2009) is utilized for this purpose. Figure 4a shows the incremental dynamic analysis curves for the 8-story steel SMF (B-model) in the East-West (EW) loading direction in terms of the spectral acceleration of the first mode period $S_a(T_1,5\%)$ of the SMF versus its maximum story drift ratio (SDR). Based on this figure, a collapse fragility curve is constructed for the B-model representation of the 8-story SMF (see Figure 4b). If we repeat the same process with the C-model of the same archetype its collapse fragility curve shifts to the right as shown in Figure 4b. The collapse resistance of the same SMF slightly increases when the composite action is considered.

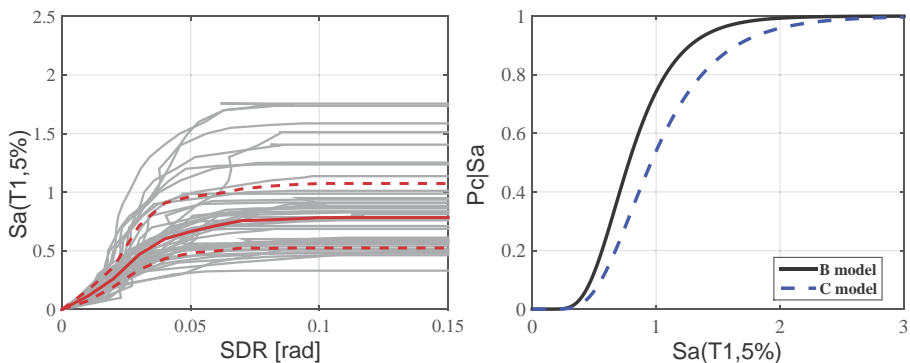


Figure 4: IDA and collapse fragility curves for the 8-story steel SMF

The added benefit of the composite beam action on the overall steel SMF seismic performance can be assessed through the mean annual frequency (MAF) of collapse, λ_c . This metric defines a collapse risk that is estimated by combining the probability of collapse of a steel SMF, given a seismic intensity, with a seismic hazard curve. The mean annual frequency of collapse can be translated to a probability of collapse over the life building expectancy. This value can be compared with the acceptable probability of collapse limit given in ASCE (2010). Figure 5 shows the λ_c values for the five archetypes that were considered in this paper. These values are computed based on the B- and C-models. From this figure, note that when a B-model is employed then mid-rise steel SMFs do not meet the requirements for a probability of collapse less than 1% over 50 years. It is evident that when the composite action is considered the estimated probability of earthquake-induced collapse is somewhat decreased compared to that predicted based on the B-models. This is mainly attributed to three reasons. The first relates to the added lateral stiffness that the composite action provides and therefore P-Delta effects do not easily shift the first order story shear of a steel SMF to zero. The second reason is due to the delay of flexural strength deterioration of a steel beam in the positive loading direction because of the slab restraint. The last reason is related to the higher inelastic demands that the panel zones experience due to the presence of the slab. Note that panel zone shear yielding is a stable yielding mechanism. This indicates the added benefit of a balanced panel zone design (Zhang and Ricles 2006).

The aforementioned issue can be further evaluated in Figure 6 that illustrates the moment-rotation relations of a column, the panel zone and the beam of the second story interior joint of the 8-story SMF for one of the employed ground motions scaled at the collapse intensity. In particular, from Figures 6a to 6c when a B-model is employed (i.e.,

composite action is neglected) most of the plastic deformation concentrates in the steel beam (see Figure 6c). The panel zone and the column essentially remain elastic. However, from Figures 6d to 6f when the nonlinear response history analysis is repeated with a C-model (i.e., composite action is considered) the panel zone yields extensively due to the increased flexural strength of the composite steel beam (see Figure 6e). In addition, flexural yielding occurs in the column (see Figure 6d). From this figure, excessive panel zone yielding at interior joints of steel SMFs should be treated with caution. The reason is that fracture may occur between the bottom flange of the steel beam and the column face. A reasonable approach to control the amount of panel zone yielding as well as to avoid flexural yielding in the steel columns of a steel SMF would be to consider a higher SCWB ratio as part of the design of the steel SMF compared to what is traditionally used in seismic design. This is examined in the following section.

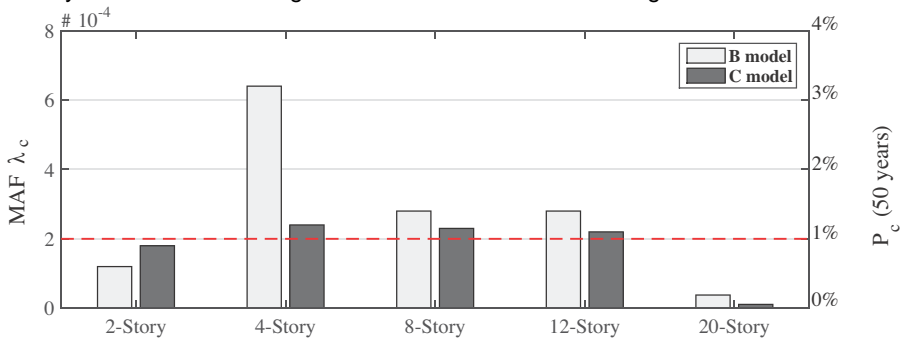


Figure 5: Mean annual frequency of collapse, λ_c for steel SMFs based on B- and C-models

4. EVALUATION OF COMPOSITE SPECIAL MOMENT FRAMES DESIGNED WITH HIGHER STRONG-COLUMN/WEAK-BEAM RATIOS

The archetype steel frame buildings discussed in Section 3.1 are redesigned with a SCWB ratio >1.5 and >2.0 . Because the steel columns of the redesigned SMFs have thicker webs, their panel zones experienced lower levels of shear distortion compared to the original designs. Therefore, the likelihood of bottom flange fracture due to excessive panel zone shear distortion is reduced. Furthermore, the thicker column webs reduce the dependency of the panel zone design on welded doubler plates. Therefore, fabrication costs may be reduced with an average column weight increase of not more than 149kg/m (100lbs/ft). Figure 7 illustrates the dependence of λ_c on the SCWB ratio and the corresponding probability of collapse in 50 years based on the C-models of the archetypes. From this figure, when a SCWB >1.5 is employed then a nearly uniform probability of collapse is achieved for all the archetypes. The probability of earthquake-induced collapse, $P_c(50\text{ years})$ becomes less than 1%, which is the acceptable limit per ASCE/SEI 7-10 (ASCE 2010) given that earthquakes follow a Poisson distribution in time. Because the 3-dimensional effects and the flexibility of the column bases is neglected in the present study it is recommended that the employed SCWB ratio for collapse prevention be at least larger than 2.0.

A higher SCWB ratio would typically lead to the use of heavier column sections compared to the current SCWB criteria. However, a considerable reduction in the required welded doubler plates to satisfy the panel zone strength requirements per AISC (2010a) is achieved. This reduces the fabrication cost and the likelihood of weld-related failures (Ibrahim et al. 2013).

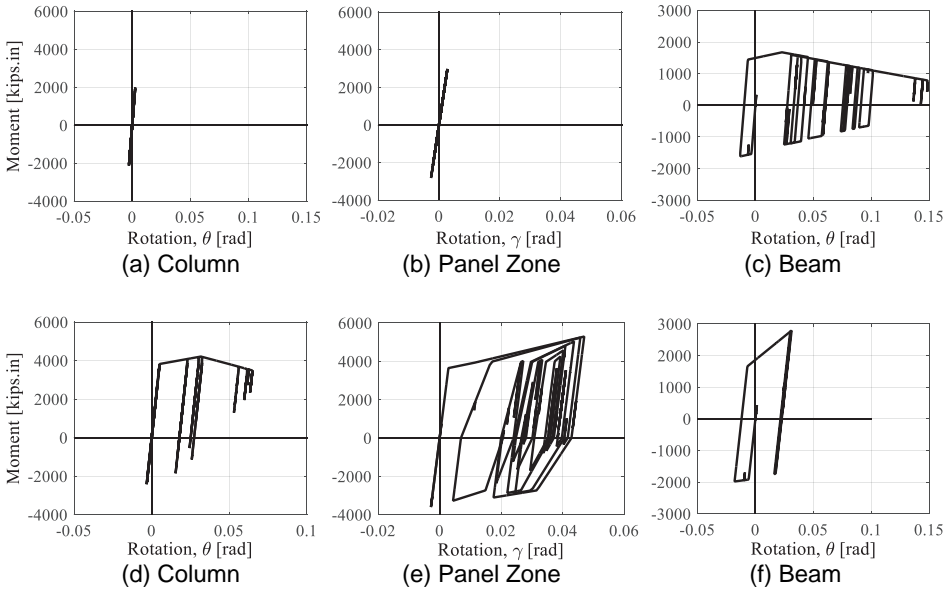


Figure 6: Moment-rotation relation of a second story interior joint at collapse intensity for the 8-story bare model (top) and composite model (bottom)

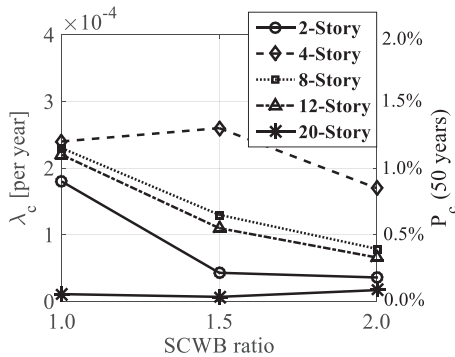


Figure 7: Mean annual frequency of collapse versus SCWB ratio for all composite models representations of the steel archetype buildings

5. CONCLUSIONS

This paper evaluates the effect of the composite action on the hysteretic behavior of fully restrained beam-to-column connections. The assessment is based on available test data from full-scale experiments of such connections. A state-of-the-art deterioration model was calibrated with the available experimental data and a rational approach was developed to simulate the asymmetric hysteretic behavior of composite steel beams and panel zones. This approach was then used to develop analytical model representations of archetype steel frame buildings with special moment

frames (SMFs) designed in highly seismic regions in North America. The main findings are summarized as follows:

- The flexural strength of a composite steel beam can be reasonably computed based on the ANSI/AISC 360-10 (AISC 2010b) provisions if the slab's geometry and material properties are available. Therefore, this value can be directly used in the strong-column/weak-beam (SCWB) ratio computation.
- The pre- and post-capping plastic rotation of a composite steel beam when the slab is in compression increase by 80% and 35%, respectively, compared to those of a bare steel beam. This is due to the lateral restraint that the slab provides to the top flange of the beam.
- When the composite beam effects are considered, excessive panel zone shear distortion was observed in steel SMFs designed with a SCWB > 1.0 (i.e., current code requirement). This is due to the increased flexural strength of composite beams compared to bare ones. Controlled panel zone yielding is achieved only if a SCWB ratio > 1.5 or 2.0 was employed as part of the seismic design process of the SMFs.
- Steel SMFs designed with SCWB ratios > 1.5 or 2.0 achieved less than 1% probability of collapse over 50 years per ASCE/SEI 7-10 (ASCE 2010). The same designs typically utilized columns with thicker webs. This results into lower fabrication costs due to the lesser number of required welded doubler plates in the beam-to-column panel zone joints of the SMF.

ACKNOWLEDGEMENTS

This study is based on work supported by the National Science and Engineering Research Council of Canada (NSERC). Funding was also provided by the Steel Structures Education Foundation (SSEF). The financial support is greatly appreciated. Any opinions, findings and conclusions expressed in the paper are those of the authors and do not necessarily reflect the views of sponsors.

REFERENCES

- AISC. (2010a). *Seismic provisions for structural steel buildings*. Seismic Provisions, American Institute for Steel Construction, Chicago, IL.
- AISC. (2010b). *Specification for structural steel buildings*. Seismic Provisions, American Institute for Steel Construction, Chicago, IL.
- ASCE. (2010). "Minimum Design Loads for Buildings and Other Structures." American Society of Civil Engineers, Reston, Virginia.
- Cordova, P., Chen, C. H., Lai, W., Deierlein, G. G., and Tsai, K.-C. (2004). "Pseudodynamic test of full-scale RCS frame: Part II - analysis and design implications." *Structures 2004*, American Society of Civil Engineers, 1–15.
- Elkady, A., and Lignos, D. G. (2014). "Modeling of the composite action in fully restrained beam-to-column connections: implications in the seismic design and collapse capacity of steel special moment frames." *Earthquake Engineering & Structural Dynamics*, 43(13), 1935–1954.
- Elkady, A., and Lignos, D. G. (2015). "Effect of gravity framing on the overstrength and collapse capacity of steel frame buildings with perimeter special moment frames." *Earthquake Engineering & Structural Dynamics*, 44(8), 1289–1307.
- FEMA. (2009). "Quantification of Building Seismic Performance Factors." Federal Emergency Management Agency (FEMA), Washington, DC.

- Gupta, A., and Krawinkler, H. (2000). "Estimation of seismic drift demands for frame structures." *Earthquake Engineering & Structural Dynamics*, 29(9), 1287–1305.
- Ibarra, L. F., Medina, R. A., and Krawinkler, H. (2005). "Hysteretic models that incorporate strength and stiffness deterioration." *Earthquake Engineering & Structural Dynamics*, 34(12), 1489–1511.
- Ibrahim, O., A., Lignos, D. G., and Rogers, C., A. (2013). "Estimation of residual stresses in thick steel plates due to welding through finite element simulation." CSCE, Montreal.
- Jones, S., L., Fry, G., T., and Engelhardt, M., D. (2002). "Experimental evaluation of cyclically loaded reduced beam section moment connections." *Journal of Structural Engineering*, 128(4), 441–451.
- Kim, K. D., and Engelhardt, M. D. (2002). "Monotonic and cyclic loading models for panel zones in steel moment frames." *Journal of Constructional Steel Research*, North American Special Issue, 58(5–8), 605–635.
- Krawinkler, H. (1978). "Shear in beam-column joints in seismic design of steel frames." *Engineering Journal*, 15(3).
- Lignos, D. G., Chung, Y., Nagae, T., and Nakashima, M. (2011). "Numerical and experimental evaluation of seismic capacity of high-rise steel buildings subjected to long duration earthquakes." *Computers & Structures*, 89(11–12), 959–967.
- Lignos, D. G., and Krawinkler, H. (2011). "Deterioration modeling of steel components in support of collapse prediction of steel moment frames under earthquake loading." *Journal of Structural Engineering*, 137(11), 1291–1302.
- Lignos, D. G., and Krawinkler, H. (2013). "Development and utilization of structural component databases for performance-based earthquake engineering." *Journal of Structural Engineering*, 139(8), 1382–1394.
- Lignos, D. G., Zareian, F., and Krawinkler, H. (2010). "A steel component database for deterioration modeling of steel beams with RBS under cyclic loading." *Structures Congress 2010*, American Society of Civil Engineers, 1241–1252.
- Mckenna, F. T. (1997). "Object-oriented finite element programming: frameworks for analysis, algorithms and parallel computing." University of California, Berkeley.
- Nakashima, M., Matsumiya, T., Suita, K., and Zhou, F. (2007). "Full-scale test of composite frame under large cyclic loading." *Journal of Structural Engineering*, 133(2), 297–304.
- Ohsaki, M., Kasai, K., Matsuoka, Y., and Zhang, J. (2008). "Results of recent E-Defense tests on full-scale steel buildings: Part 2 — collapse simulation and blind analysis contest." *Structures Congress 2008*, American Society of Civil Engineers, 1–8.
- Tremblay, R., Tchegotarev, N., and Filiatrault, A. (1997). "Seismic performance of RBS connections for steel moment resisting frames: Influence of loading rate and floor slab." *STESSA '97*, Kyoto, Japan.
- Vamvatsikos, D., and Cornell, C. A. (2002). "Incremental dynamic analysis." *Earthquake Engineering & Structural Dynamics*, 31(3), 491–514.
- Zhang, X., and Ricles, J. M. (2006). "Experimental evaluation of reduced beam section connections to deep columns." *Journal of Structural Engineering*, 132(3), 346–357.

STATE-OF-THE-ART REPORT ON CONNECTIONS FOR COMPOSITE SPECIAL MOMENT FRAMES (C-SMF)

Zhichao Lai, Ph.D.

Postdoctoral Research Associate, Robert L. and Terry L. Bowen Laboratory, Purdue University
1040 S. River Road, West Lafayette, IN 47906

laiz@purdue.edu

Amit H. Varma, Ph.D.

Professor, Purdue University, Robert L. and Terry L. Bowen Laboratory
1040 S. River Road, West Lafayette, IN 47906

ahvarma@purdue.edu

Abstract

There is a lack of summary of the research on composite special moment frames (C-SMF). As a result, the current AISC Specifications (AISC 360-10 and AISC 341-10) do not include detailed provisions for the design of composite connections. This paper compiles an experimental database of tests conducted on composite connections. Based on the comparisons of the test data, two connections are recommended, i.e., split-tee connection for rectangular CFT composite frames, and through-beam connections for circular CFT composite frames. A design example for the through-beam connection is also presented.

1. INTRODUCTION AND BACKGROUND

Composite special moment frames (C-SMF) usually consists of concrete-filled steel tube (CFT) columns, steel-wide flange beams, and rigid beam-to-column connections. As an innovative and efficient structural system, C-SMF have been widely used around the world, for example, in: (i) 3 Houston Center in Houston, USA, (ii) Wuhan International Financial Center in Wuhan, China, and (iii) Shimizu Super High-Rise in Tokyo, Japan.

Significant research has been conducted to investigate the behavior of composite moment resisting frames (MRFs) and their components (i.e., columns, beams, and connections). For example, experimental tests on CFT-MRFs have been conducted by Matsui (1985), Kawaguchi et al. (1996), Chen et al. (2004), Herrera et al. (2008). Experimental tests on CFT columns have been conducted by many researchers, and summarized independently by Nishiyama et al. (2002), Kim (2005), Gourley et al. (2008), Hajjar (2013), Lai et al. (2014), and Lai and Varma (2015). Experimental tests on various types of connections for C-SMF have also been conducted. These include Kanatani et al. (1987), Yokoyama et al. (1991), Morino et al. (1992), Kawano and Matsui (1996), Alostaz (1997), France et al. (1999), Elremaily (2000), Fujimoto et al. (2000), Koester (2000), Chiew et al. (2001), Peng (2001), Beuteal et al. (2001), Ricles et al. (2004), Shin

et al. (2004, 2008), Fukumoto and Morita (2005), Wang and Guo (2012), Wang et al. (2013), and Tizani et al. (2013) among others.

However, there is a lack of a comprehensive state-of-the-art report to summarize the results and findings from the available research. As a result, current AISC Specifications (AISC 360-10 and AISC 341-10) do not include detailed provisions for the design of composite connections. Therefore, it is difficult for the engineers to use composite connections in design, and the application of C-SMF is limited despite their significant potential benefits.

To address this, the current ASCE Composite Construction Committee proposed a special project, which is aimed to develop a comprehensive state-of-the-art-report that can be used and referenced by engineers to design composite connections. The state-of-the-art-report will enable engineers to design composite structures with detailed guidance and more confidence. As part of this special research project, the authors focus on two specific sub-tasks, i.e., the evaluations of the moment resisting connections for (i) C-SMF with rectangular CFT columns and (ii) C-SMF with circular CFT columns.

In this paper, experimental database on composite connections were first compiled. The database includes 91 test data. Comparisons and discussions of these connections are then presented. Based on the comparisons, two connections are recommended, i.e., split-tee connection for rectangular CFT composite frames, and through-beam connections for circular CFT composite frames. A design example for the through-beam connection is also presented.

2. EXPERIMENTAL DATABASE

Moment connections for CFT composite frames can be categorized into two general types, based on how the steel beam is connected to the CFT column. For example, a moment connection is categorized as Type I if the steel beam is attached to the surface of the steel tube only; a moment connection is categorized as Type II if the steel beam is connected to the CFT column using elements embedded in the panel zone.

Details of Type I connections usually include: (i) welding the beam flanges and (or) web to the steel tube wall, or (ii) using interior or exterior diaphragms to attached the beam to CFT column. Directly welding the beam to the steel tube wall usually results in excessive deformation at the beam flanges near the column face, and cracking or fracture of the steel components near the welding (Alostaz, 1997). Extensive research have been conducted (especially in Japan) using interior or exterior diaphragms, for example, Yokoyama et al. (1991), Morino et al. (1992), Kawano and Matsui (1996), Fujimoto et al. (2000), and Fukumoto and Morita (2005).

Type II connections usually include: (i) split-tee connections (see Fig. 1(a)) using through bolts tested by Kanatani et al. (1987), Koester (2000), and Ricles et al. (2004) among others; (ii) end plate connections using through bolts or blind bolts tested by France et al. (1999) Wang and Guo (2012), and Wang et al. (2013) among others; and (iii) through-beam connections (see Fig. 1(a)) tested by Alostaz (1997) and Elremaily (2000) among others.

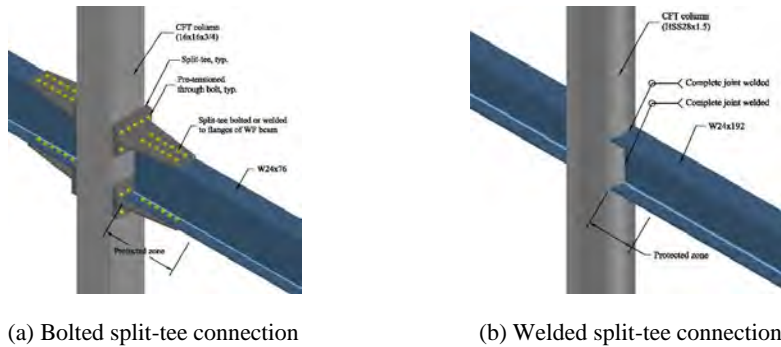


Figure 1. Example of the (a) all-bolted split-tee connection and (b) through-beam connection.

As part of this research, the authors compiled a comprehensive database of tests conducted on moment resisting connections for C-SMF. This database includes five groups of data: Group I has 13 tests on through-beam connections, Group II has 14 tests on split-tee connections, Group III has 36 tests on connections using diaphragms for circular CFT columns, Group IV has eight tests on connections using diaphragms for rectangular CFT columns, and Group V has 20 tests on connections with other details. For the first four groups, the following information was collected where reported: (i) connection location (interior or exterior); (ii) loading type (cyclic or monotonic); (iii) geometric and material properties for the columns (Length L , depth H , width B , flange web thickness t_f and t_w , steel yield strength F_y , and concrete compressive stress f'_c) and beams (Length L , diameter D , tube wall thickness t , and steel yield strength F_y of the flanges and web); and (iv) figures showing connection details and experimental results. The geometric and material properties were not presented for the last group (Group V) due to lack of relative information. For the split-tee connections (Group I), additional information such as the number of bolts, bolt size, and tensile strength F_u are included. For the connections with diaphragms (Groups III and VI), additional information such as the thickness of the diaphragms (t_d), diaphragm opening hole size, and yield stress of the diaphragms are included. Details of all of these information were presented by the authors in Lai and Varma (2016).

Experimental results indicated that Type I connections with interior or exterior diaphragm and all Type II connections provide excellent seismic performance. However, fabrication of the interior or exterior diaphragm is labor extensive, because the column needs to be cut and substantial welding is required. Therefore, Type I connections are not practical to be implemented in the USA, and the corresponding design guidance is not further investigated in this paper. Type II connections are used instead. For Type II connections, split-tee connections (see Fig. 1(a)) and through-beam connections (see Fig. 1(b)) are shown to be most suitable for rectangular and circular CFT columns, respectively. Experimental research of these two connections are briefly presented as follows. Engineers are encouraged to refer to the database

(Lai and Varma 2016) and the corresponding references if they are interested in more details of these two connections or other connections.

Most of the research on split-tee connections for rectangular CFT columns was conducted by Lehigh University and The University of Texas at Austin in a cooperative way. Researchers from Lehigh University (Peng, 2001 and Ricles et al., 2004) focused on the design and development of the steel components of the connection (i.e., tees and through bolts) and other connection details. Two types of details were used in the split-tee connections by Peng (2001) and Ricles et al. (2004). In Type (a), the tee stem was connected to beam flanges using bolts; in Type (b), the tee stem was welded to the beam web. Experimental tests conducted by these researchers indicated that: (i) specimens with both details performed well and the rotational capacity was greater than 0.05 rad; (ii) the shear tab that connected the beam web to the column flange was not necessary; and (iii) beam flanges in type (a) connection should be reinforced to prevent the bolt elongation resulting from the bolt bearing on flanges, and to prevent the fracture of the beam flanges after local buckling occurred.

Researchers from University of Texas at Austin (Koester, 2000) focused on the role of concrete infill within the panel zone in transferring the shear forces. Koester (2000) performed 14 panel zone tests and six full scale tests. The test results showed that the concrete in the panel zone acted as compression strut. Fig. 2 shows the typical moment-rotation response of a wide flange beam that is connected to a rectangular CFT column using split-tee connection.

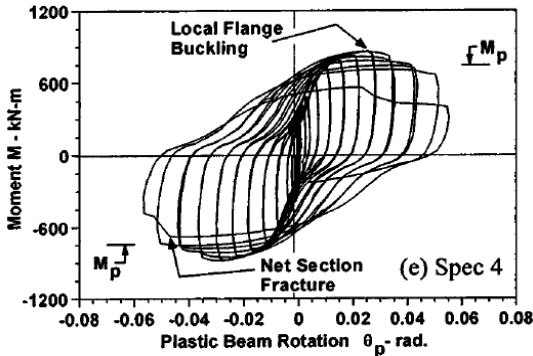


Fig. 2. Typical moment-rotation response (Specimen 4 by Ricles, 2004)

Research on through-beam connections for circular CFT columns was performed by Alostaz (1997) from University of Illinois at Urban-Champaign and Elremaily (2000) from University of Nebraska. Several connection details were studied by Alostaz (1997). It was found that through-beam connections were the most robust connection type. Elremaily (2000) further performed eight tests on through-beam connections with different details. Test results showed that specimens with column-to-beam flexural strength ratio (M_c/M_p) of 1.5 and full penetration welding performed favorably well. Specimens with column-to-beam flexural strength ratio (M_c/M_p) of 2.0 and fillet welding also performed favorably well. The panel zone shear strength

contributed from three parts: shear yielding of the beam web, shear yielding of the steel tube wall, and compression strut of concrete core within the panel zone. Fig. 3 shows the typical moment-rotation response of a wide flange beam that is connected to a circular CFT column using through-beam connection.

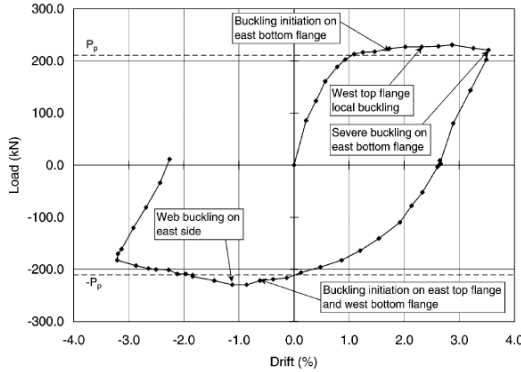


Fig.3 Typical moment-rotation response (Specimen NSF5 by Elremaily, 2000)

3. DESIGN OF MOMENT RESISTING CONNECTIONS

3.1 Split-tee connection

The panel zone shear strength (V_n) of split-tee connections for rectangular CFT columns consists two parts, i.e., the shear strength of the steel tube wall in the panel zone (V_s) and the concrete compression strut (V_c). The design equations proposed by Koester (2000) was used to calculate the panel zone shear zone strength as follows:

$$V_n = V_c + V_s \tag{1}$$

where,

$$V_c = 28Bh\sqrt{f'_c} \tag{2}$$

$$V_s = A_{web} \frac{\sigma_y}{\sqrt{3}} \tag{3}$$

where B and h is the width and depth of the concrete core with the panel zone, f'_c is the concrete compressive strength (in psi), A_{web} is the area of the web of the steel tube, and σ_y is the yield stress of the steel tube.

The design of split-tee connections has been discussed in detail by the authors in a previous paper (Fischer and Varma 2015), and not repeated here for brevity. In that paper, a design example along with detailed flow-chart showing the design procedure was presented.

3.2 Through-beam connection

The panel zone shear strength (V_n) for through-beam connections is consist of three parts: shear yielding of the beam web, shear yielding of the steel tube wall, and compression strut of concrete core within the panel zone. The design equations proposed by Elremaily (2000) was used to calculate the panel zone shear zone strength (V_n) as follows:

$$V_n = V_{wn} + V_m + V_{csn} \quad (4)$$

where V_{wn} , V_m , and V_{csn} are the nominal shear strengths of the web, steel tube wall, and concrete compression strut, respectively:

$$V_{wn} = 0.6F_{yw}d_c t_w \quad (5)$$

where F_{yw} is the yield stress of the beam web, d_c is the column diameter, and t_w is the web thickness.

$$V_m = 0.6F_{yt} \frac{\pi d_c t_t}{2} \quad (6)$$

where F_{yt} is yield stress of the steel tube wall, and t_t is tube wall thickness

$$V_{csn} = 24\sqrt{f'_c} \frac{\pi d_c^2}{4} \quad (7)$$

where f'_c is the concrete compressive strength in psi.

The term $24\sqrt{f'_c}$ is the limiting horizontal shear stress over the horizontal projections of the strut region. Experimental data reported by Sheikh et al. (1990) for connections between steel beams and reinforced concrete columns indicated that the shear stress terms varied from $24\sqrt{f'_c}$ to $36\sqrt{f'_c}$. Elremaily (2000) showed that $24\sqrt{f'_c}$ was a conservative value, and therefore this value was used to calculate the V_{csn} as shown in Equation (7). A design example as presented in the next section can better help engineers designing the through-beam connection.

4. DESIGN EXAMPLE

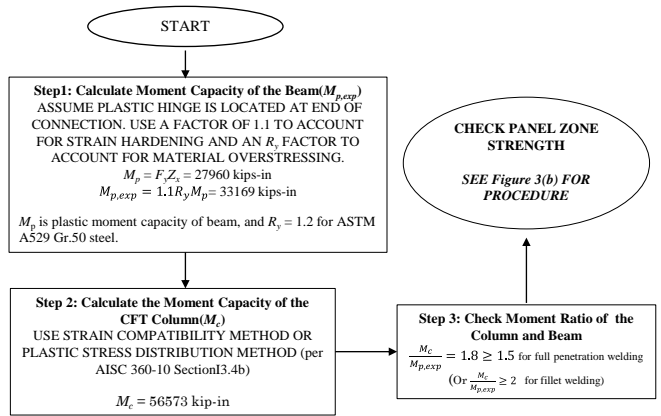
This section presents a design examples that provides guidance for designing through-beam connections of for C-SMF. The connection presented is located at an interior joint in a special moment frame. The frame consists of CFT columns and wide flanged sections for beams. The beam section is a W24x192 and the column section is a HSS28x1.5 with f'_c of 4 ksi.

The through-beam design example presented in this section assumes that plastic hinges form in the WF beams outside of the protected connection zone. The failure modes of through-beam connections are listed below in order, from most ductile to least ductile.

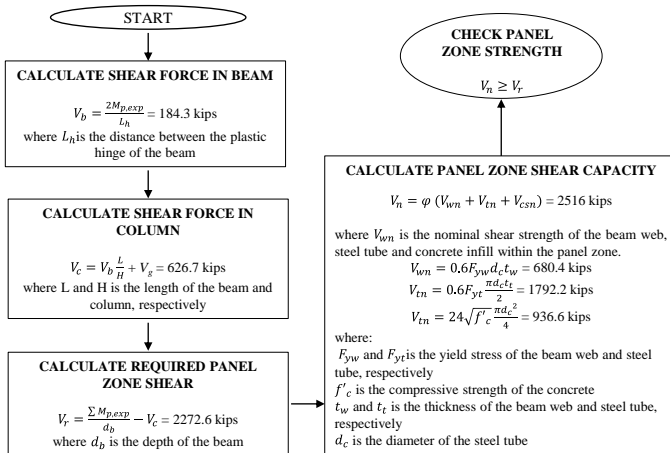
1. Plastic hinge formation in beam
2. Plastic hinge formation in the column
3. Panel zone failure of column

The through The following example presents the design procedure for through-beam connections as shown in Fig. 1(b). This connection is designed and detailed to resist the expected

shear force due to the expected plastic moment capacity of the beam and the gravity loads. The connection is also designed and detailed so that the governing failure modes occur in the order 1-3 listed above from most ductile (desirable) to least ductile. Fig. 4 provides a step-by-step approach for designing this connection. In this example, the beams are W24×192 wide flanged sections that are 30ft in length ($F_y = 50$ ksi, $F_u = 65$ ksi, $R_y = 1.1$), and the CFT column is made from HSS28×1.5 ($F_y = 50$ ksi, $F_u = 65$ ksi,) and filled with normal weight 4 ksi concrete ($f'_c = 4$ ksi). The ratio (P_0/P_n) of the applied axial load (P_0) to the nominal axial compressive strength (P_n) is 0.19. The gravity loads considered on the beam are 0.84kip/ft distributed dead load (w_D) and 0.60kip/ft distributed live load (w_L).



(a)



(b)

Figure 4. Step-by-step approach for designing through-beam connection.

5. SUMMARY AND CONCLUSIONS

This paper summarized the existing experimental tests of the connections for C-SMF. An experimental database that consist of 91 test data on composite connections was compiled. Summary of the existing research indicated that split-tee connection connections are most suitable for C-SMF with rectangular CFT columns, and through-beam connections are most suitable for C-SMF with circular CFT columns. A design example for the through-beam connections was also presented. This design example along with the design example developed by Fischer and Varma (2015) can efficiently help engineers designing the connections for C-SMF.

References

- Alostaz, Y. M. (1997). "Connections to concrete-filled steel tubes [Dissertation]." University of Illinois at Urbana-Champaign.
- Beutel, J., Thambiratnam, D., and Perera, N. (2001). "Monotonic behaviour of composite column to beam connections." *Engineering Structures*, 23(9), 1152–1161.
- Chen, C. H., Hsiao, B. ., Lai, J. W., Lin, M. ., Weng, Y. ., and Tsai, K. . (2004). "Pseudodynamic test of a full-scale CFT/BRB frame: Part 2—Construction and testing." *13th World Conference on Earthquake Engineering*, Vancouver, Canada.
- Chiew, S., Lie, S., and Dai, C. (2001). "Moment resistance of steel I-beam to CFT column connections." *Journal of structural Engineering*, 127(October), 1164–1172.
- Elremaily, A. (2000). "Connections between steel beams and concrete-filled steel tube columns." University of Nebraska.
- Fischer, E. C., and Varma, A. H. (2015). "Design of split-tee connections for special composite moment frames." *Engineering Journal*.
- France, J., Davison, J., and Kirby, P. (1999). "Moment-capacity and rotational stiffness of endplate connections to concrete-filled tubular columns with flowdrilled connectors." *Journal of Constructional Steel Research*, 50(1), 35–48.
- Fujimoto, T., Inai, E., Kai, M., Mori, K., Mori, O., and Nishiyama, I. (2000). "Behavior of Beam-to-Column Connection of CFT Column System." *12th World Conference on Earthquake Engineering*, 2197:1–8.
- Fukumoto, T., and Morita, K. (2005). "Elastoplastic Behavior of Panel Zone in Steel Beam-to-Concrete Filled Steel Tube Column Moment Connections." *Journal of Structural Engineering*, 131(12), 1841–1853.
- Gourley, B. C., Cenk, T., Denavit, M. D., Schiller, P. H., and Hajjar, J. F. (2008). "A synopsis of studies of the monotonic and cyclic behavior of concrete-filled steel tube members, connections, and frames, Report No. NSEL-008, Department of Civil and Environmental Engineering." University of Illinois at Urbana-Champaign, Champaign, IL, USA.
- Hajjar, J. F., Gourley, B. C., Tort, C., Denavit, M. D., and Schiller, P. H. (2013). "Steel-concrete composite structural systems, <http://www.northeastern.edu/compositesystems>." *Department of Civil and Environmental Engineering, Northeastern University*, Northeastern University.
- Herrera, R. A., Ricles, J. M., Asce, M., and Sause, R. (2008). "Seismic Performance Evaluation of a Large-Scale Composite MRF Using Pseudodynamic Testing." *Jornal of Structural Engineering*, 134(February), 279–288.
- Kanatani, H., Tabuchi, M., Kamba, T., Hsiao-lien, J., and Ishikawa, M. (1987). "A study on

- concrete filled RHS column to H-beam connections fabricated with HT bolts in rigid frames.” *Composite Construction in Steel and Concrete*, 614–635.
- Kawaguchi, J., Morino, S., and Sugimoto, T. (1996). “Elasto-plastic behavior of concrete-filled steel tubular frames.” *Composite Construction in Steel and Concrete: Proc., Engineering Foundation Conf*, Irsee, Germany.
- Kawano, A., and Matsui, C. (1996). “New connections using vertical stiffeners between H-shaped beams and hollow or concrete-filled square tubular columns.” *Composite construction in steel and concrete III*, 172–185.
- Kim, D. K. (2005). “A database for composite columns [Thesis].” Georgia Institute of Technology.
- Koester, B. (2000). “Panel Zone Behavior of Moment Connections Between Rectangular Concrete-Filled Steel Tubes and Wide Flange Beams [Dissertation].” The University of Texas at Austin.
- Lai, Z., and Varma, A. H. (2015). “Noncompact and slender circular CFT members: Experimental database, analysis, and design.” *Journal of Constructional Steel Research*, Elsevier Ltd, 106, 220–233.
- Lai, Z., and Varma, A. H. (2016). *Experimental database on connections for composite special moment frames (C-SMF)*. PURR.
- Lai, Z., Varma, A. H., and Zhang, K. (2014). “Noncompact and slender rectangular CFT members: experimental database, analysis, and design.” *Journal of Constructional Steel Research*, 101(10), 455–468.
- Matsui, C. (1985). “Strength and behaviour of frames with concrete filled square steel tubular columns under earthquake loading.” *1st international speciality conference on concrete filled steel tubular structures*, 104–111.
- Morino, S., Kawaguchi, J., Yasuzaki, C., and Kanazawa, S. (1992). “Behavior of concrete-filled steel tubular three-dimensional subassemblages.” *Composite Construction in Steel and Concrete II*, 726–741.
- Nishiyama, I., Morino, S., Sakino, K., Nakahara, H., Fujimoto, T., Mukai, A., Inai, E., Kai, M., Tokinoya, H., Fukumoto, T., Mori, K., Yoshioka, K., Mori, O., Yonezawa, K., Uchikoshi, M., and Hayashi, Y. (2002). *Summary of research on concrete-filled structural steel tube column system carried out under the U.S.-Japan cooperative research on composite and hybrid structures*. Ibaraki Prefecture, Japan.
- Peng, S. W. (2001). “Seismic resistant connection for concrete-filled tube column-to-WF beam moment resisting frames [Dissertation].” Lehigh University, Bethlehem, PA.
- Ricles, J., Peng, S., and Lu, L. (2004). “Seismic behavior of composite concrete filled steel tube column-wide flange beam moment connections.” *Journal of Structural Engineering*, 130(FEBRUARY), 223–233.
- Sheikh, B. T. M., Deierlein, G. G., Yura, J. A., and Jirsa, J. O. (1990). “Beam-column moment connections for composite frames: part 1.” *Journal of Structural Engineering*, 115(11), 2858–2876.
- Shin, K.-J., Kim, Y.-J., and Oh, Y.-S. (2008). “Seismic behaviour of composite concrete-filled tube column-to-beam moment connections.” *Journal of Constructional Steel Research*, 64(1), 118–127.
- Shin, K.-J., Kim, Y.-J., Oh, Y.-S., and Moon, T.-S. (2004). “Behavior of Welded CFT Column to H-Beam Connections with External Stiffeners.” *Engineering Structures*, 26(13), 1877–1887.
- Tizani, W., Wang, Z. Y., and Hajirasouliha, I. (2013). “Hysteretic Performance of a New Blind

- Bolted Connection to Concrete Filled Columns under Cyclic Loading: An Experimental Investigation." *Engineering Structures*, Elsevier Ltd, 46, 535–546.
- Wang, J., and Guo, S. (2012). "Structural Performance of Blind Bolted End Plate Joints to Concrete-Filled Thin-Walled Steel Tubular Columns." *Thin-Walled Structures*, Elsevier, 60, 54–68.
- Wang, J., Zhang, L., and Spencer, B. F. (2013). "Seismic response of extended end plate joints to concrete-filled steel tubular columns." *Engineering Structures*, 49, 876–892.
- Yokoyama, Y., Morita, K., Kawamata, Y., and Matsumura, H. (1991). "Structural behavior of steel-beam to concrete-filled square tube column connections reinforced with inner ring stiffener." *3rd International Conference on Steel-Concrete Composite Structures*, 165–170.

SEISMIC PERFORMANCE AND DESIGN OF CFST COLUMN TO STEEL BEAM CONNECTIONS

Wei Li, Lin-Hai Han

Department of Civil Engineering, Tsinghua University, Beijing 100084, China
iliwei@tsinghua.edu.cn, lhhan@tsinghua.edu.cn

Abstract

This paper summarizes the investigation on the seismic performance and design method of concrete-filled steel tubular (CFST) columns to steel beams connections, where the beam and column are connected by external diaphragm and the reinforced concrete (RC) slabs are attached. Experimental research is conducted with the main experimental parameters of the connection type, the axial load level on the column and the beam section configuration. A finite element analysis (FEA) model for the composite connection under cyclic loading is also established and verified by a set of experimental results. The parametric study is carried out to study the influence of the critical parameters for the composite connections. A hysteretic model is proposed for the panel zone of the composite connection, and is then integrated in a fiber-based connection macro element. It is found that the composite connection has favorable seismic behavior and the proposed simplified models are featured with reasonable accuracy.

Introduction

The concrete-filled steel tubular (CFST) column has being widely used in engineering structures in recent years owing to the column's excellence on earthquake-resistant properties, such as high capacity, high ductility and large energy absorption capacity. The CFST columns are often connected to steel beams in real structural system, and the reinforced concrete (RC) floor slabs are usually attached to steel beams with shear connectors. The photo of the connection before placing the RC slab is shown in Fig.1 (Han and Li, 2010). This type of composite construction is widely used in many engineering practices.

In the past, investigations have been carried out on steel beam to CFST column connections, which involved experimental studies to assess the elasto-plastic behavior of the composite connections (Leon et al., 1998; Schneider and Alostaz, 1998; Elremaily and Azizinamini, 2001; Beutel et al, 2002; Ricles et al. 2004; Wang et al., 2008). Parts of the U.S.-Japan cooperative research program on composite and hybrid structures have also studied the connection details and accompanying design provisions for the steel beam to CFST column connections (Nishiyama et al., 2002).

Previous research mainly concerned about the composite connections consisted of the CFST column and the H-shape steel beam without RC floor slabs, especially on the efficiencies of different forms of diaphragms or connection details to achieve an ideal load transfer mechanism. Some researchers also established nonlinear simplified models (Fukumoto et al. 2005, Cheng et al. 2007). The results showed that connections with external diaphragms have adequate strength, favorable ductility and high energy dissipation capacity. However, the research on the connection with RC slab is rather limited (Nie et al, 2008; Han and Li, 2010). There's still limit information on the behavior of connections consisted of circular CFST column and steel beam with RC slab, especially on the conditions of CFST columns under high axial load levels (such as higher than 0.5). Moreover, behavior of the exterior and interior composite connections could be different, even when same component sections and connection details are applied.

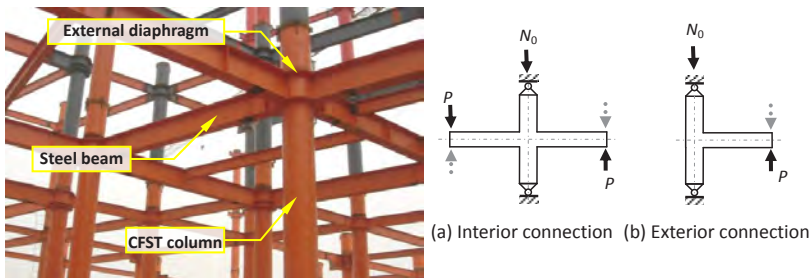


Fig.1 Photo of CFST connection with external diaphragm

The experimental investigation of CFST connections with external diaphragms and RC slabs were thus conducted. The corresponding nonlinear finite element analysis (FEA) model was also established. The simplified model was proposed to predict the shear stiffness, shear strength, shear deformation and the hysteretic rules for the panel zone of the composite connection, and was then integrated in a fiber-based connection macro element.

Summary of experimental Investigation

Specimen design and test program

The composite connection specimens were designed under the assumption that the mid-span of beams and the mid-height of CFST column in the building were hinged. Fig.1 shows the schematic views of connection specimens, where N_0 represents the vertical load received from the upper floor, P represents the load caused by the horizontal earthquake. The prototype of the test specimens were designed referencing the recommendation from DBJ13-51-2003 (2003). The scale factor was approximately 1/2. The parameters of specimens were connection types (exterior and interior connections in a planar frame), the axial load level in the column (defined as N_0 / N_u , where N_0 was the load applied on top of the column, N_u was the plastic

compression resistance of the composite column cross-section), and the beam cross-sectional configuration. Table 1 and Fig.2 show some details of specimens. The material properties can be found in Han and Li (2010).

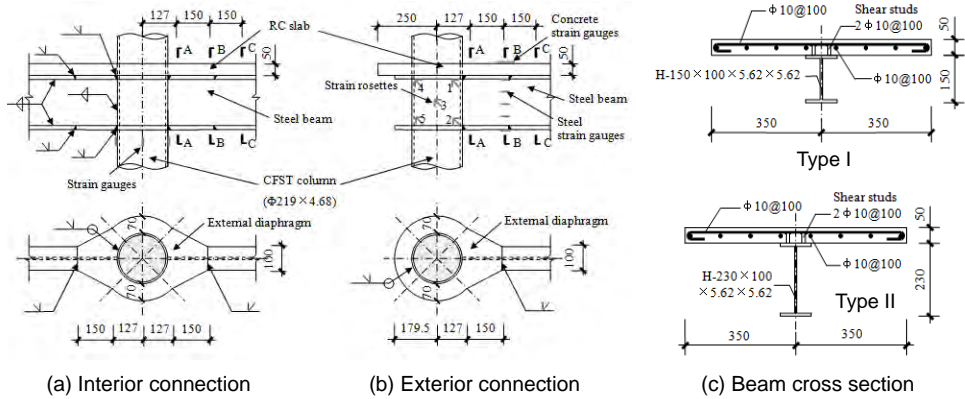


Fig.2 Configuration of specimens

Table 1 Summary of properties of specimens

ID	Type	Beam Type	Axial load level n	N_0 (kN)	Yield Strength* (kN)	Ultimate Strength* (kN)	Failure Mode	Ductility index	Energy dissipation coefficient E
CIJ-1	Int.	Type I	0.33	850	60.5/-52.3	86.3/-73.2	Beam	3.56	0.177
CIJ-2	Int.	Type I	0.66	1700	69.0/-52.8	89.8/-71.7	Beam	3.73	0.184
CIJ-3	Int.	Type II	0.33	850	84.3/-71.2	125.2/-102.4	Column	4.28	0.180
CIJ-4	Int.	Type II	0.66	1700	84.2/-71.1	121.3/-96.6	Column	3.30	0.225
CEJ-2	Ext.	Type I	0.66	1700	66.9/-47.0	101.2/-66.4	Beam	3.37	0.204
CEJ-4	Ext.	Type II	0.66	1700	108.4/-92.3	161.4/-111.4	Beam	2.66	0.196

Note *: The negative value denotes the yield or ultimate strength under hogging moment.

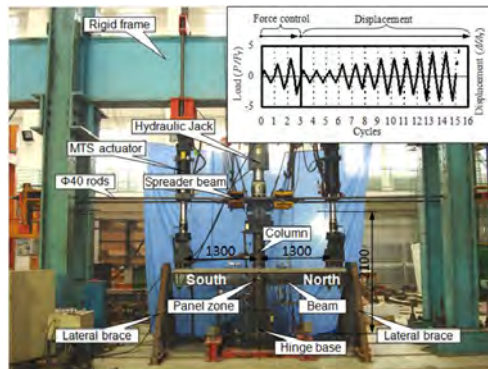


Fig.3 Test setup and loading protocol (unit: mm)

Fig.3 gives a general view of the test setup. The constant axially compressive load,

which represented the reaction received from upper floors was applied on the top of the column. The column ends were restrained from horizontal movement but were allowed to rotate in the loading plane. Cyclic loads in vertical direction were applied at the ends of beam segments by MTS hydraulic rams. The loading history at the end of the beam was generally based on the Chinese code JGJ 101-96 (1997). The load and displacement at the ends of beams were recorded, and strain gauges were arranged to measure the cross-sectional strain distributions and the shear distortion.

Test results and analysis

All composite connections behaved in ductile manners. Table 1 summarizes the experimental results under hogging and sagging moment. Fig.4 shows the typical failure modes of the specimens. The specimens showed two kinds of failure modes. One was the beam failure, featured with the buckling of the beam and damage of RC slab. Fig. 5 shows the crack pattern on the RC slab. The other one was the column failure, where the column was curved and the outward bulging of the steel tube was found near the beam. Diagonal cracks developed in the panel zone concrete for column failure specimens.

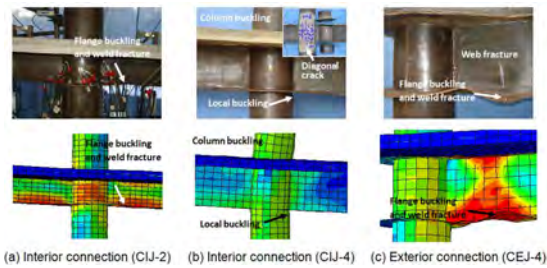


Fig.4 Failure modes of specimens

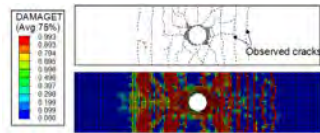


Fig.5 Damage of RC slab (CIJ-1)

Fig.6 shows the measured vertical beam load (P) versus displacement (Δ) hysteretic curves, where the curves show only moderate pinching effect. The exterior and interior connections with the same beam configuration behaved differently in the test. For the interior connections, the strength from both beams was larger than that from the single beam for the exterior connection, and was also larger than that of the column, therefore the column failure occurred. The definition of energy dissipation coefficient E in JGJ101-96 was used to describe the energy dissipation capacity of the specimens. The column axial load level n had a moderate influence on the total energy dissipated ability of interior connections CIJ-1 and CIJ-2, for the column suffered a mild damage in the test. The energy dissipated ability for each cycle was slightly enhanced for connections CIJ-3 and CIJ-4 when n increased, for the concrete stress in CFST column increased with a higher axial load level. The specimen CIJ-4 showed an earlier column failure than CIJ-3 in the experiment, therefore the maximum energy dissipated ability for CIJ-4 was less than that of CIJ-3. More analysis on the connection behavior can be found in Han and Li (2010).

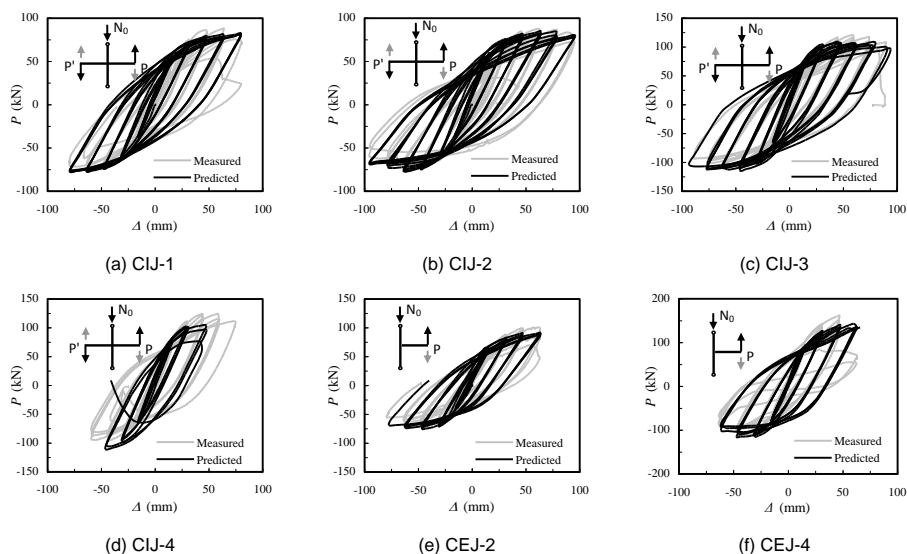


Fig.6 Load versus beam deflection relations of specimens

Summary of Numerical Investigation

FEA modeling

Previously there were several reports for the numerical analysis on CFST column to beam connections, such as Chiew et al., (2001) and Nie et al. (2008). However, most of the analysis did not consider the material damage under cyclic loading. In this study, the analysis was conducted in the ABAQUS/Standard module [9]. The confined concrete stress-strain relationship presented in Han et al. (2007) for the core concrete of CFST in compression was used. The evolution of the tensile damage variable (d_t) and compressive damage variable (d_c) were introduced to represent the damage of concrete. It was assumed in the uniaxial stress-strain plane there exist some geometrical loci defined as “focal points”. Li and Han (2011) proposed a deterioration model for core concrete and slab concrete, where the concept of “focal point” was used. The contact model between the steel and concrete was also established. More details can be found in Li and Han (2011).

The predicted failure modes, ultimate strengths, unloading and reloading stiffness were close to the measured results, as shown in Figs. 4-6. The tensile damage was also plotted and compared with the crack pattern of the RC slab in Fig. 5. However, there were still some differences between the predicted and measured results, due to the severer local buckling steel components and the weld fractured.

Analytical behavior and parametric analysis

Fig. 8 shows three types of failure modes for the composite connection occurred in

the finite element analysis, i.e. the beam failure mode, the mixed failure mode and the column failure mode. The beam failure was characterized as large deformation and plasticity developed on the steel beam and RC slab, while the panel zone and column behaved elastically in general. The mixed failure was characterized as the large deformation and plasticity developed on the panel zone and accompany with a moderate beam and column yielding. The column failure was characterized as an obvious overall deformation of the column and outward buckling of tube wall. The beam failure would happen when the column bending strength was significantly larger than that of the beam ($k_m \leq 0.6$, k_m is the beam to column strength ratio), the column failure might occur when the beam bending strength was larger than that of the column ($k_m \geq 1.2$), and the mixed failure could happen when k_m ranged from 0.6 to 1.2.

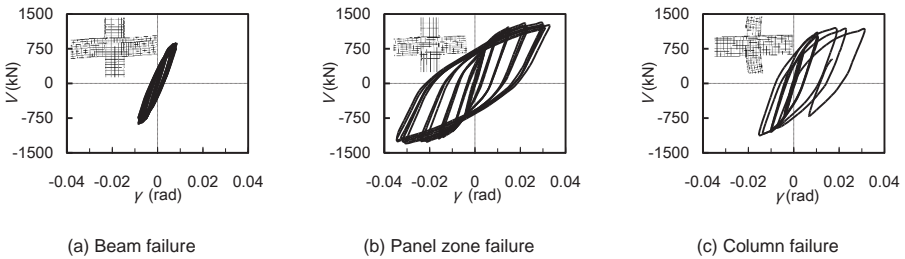


Fig.8 Different failure modes and corresponding V- γ curve

Fig.9 shows the shear strength of CFST connection under different axial load level of panel zone (n_p). The influence of n_p was not significant when n_p was less than 0.5. When n_p was more than 0.5, the shear strength of steel decreased for the yield strength of steel was reached at an earlier stage. For the core concrete, the compressive area of core concrete increased when n_p increased. The connection shear strength decreased significantly when n_p was more than 0.8.

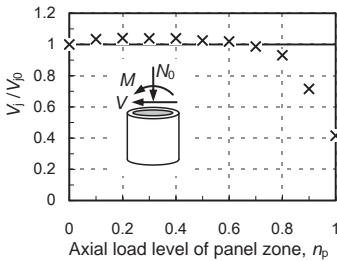


Fig.9 Shear strength of connection under different axial load level

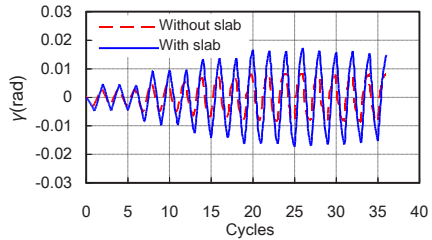


Fig.10 Shear deformation of panel zone w & w/o RC slab

The RC slab could not enhance the shear strength for the connection. However, the shear deformation of the panel zone under the same drift level would increase when the RC slab was attached. Fig.10 shows that the maximum shear deformation of the connection with RC slab ($h_c=100\text{mm}$) increased 122% when compared to bare steel

beam connection under same beam loading displacement, and the failure mode changed from beam failure to mixed failure.

Design Methodology

In the simplified structural analytical model, the beam and the column were usually simulated by using beam elements, and the wall and the floor were usually simulated by using shell elements such as Tort and Hajjar (2007). The connection was usually treated as "common nodes" shared by beam and column elements or a "rigid" one, while the deformation of connection itself was usually neglected. Simplified models for composite connections were necessary in order to obtain accurate results in some key regions with favorable accuracy. Previously, several researchers proposed connection models for the nonlinear analysis of CFST structures, such as Nishiyama et al., (2004), Fukumoto and Morita (2005), Zhao et al. (2010) and Kang et al.(2014).

A trilinear $V_j-\gamma_j$ relation was proposed for the panel zone of circular CFST connection using external diaphragm with RC slab, as shown in Fig.11. The total shear resistance of the panel zone was obtained by the superposition of shear forces from steel tube and core concrete. The descending section of the $V_j-\gamma_j$ relation was not significant in the CFST connection owing to the steel hardening. As a result, the total shear of the panel zone nearly remained the same. The hysteretic rules were also applied for the $V_j-\gamma_j$ relation. More details can be found in Li and Han (2012).

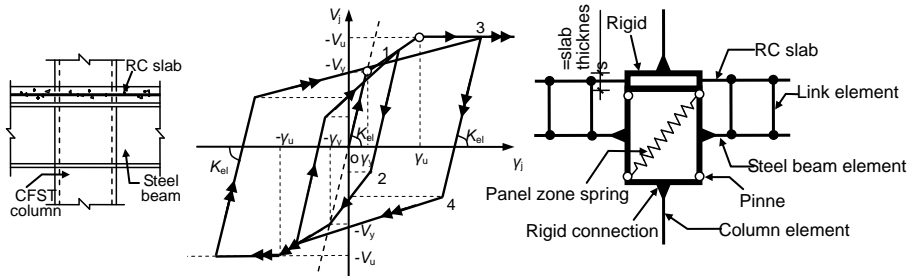
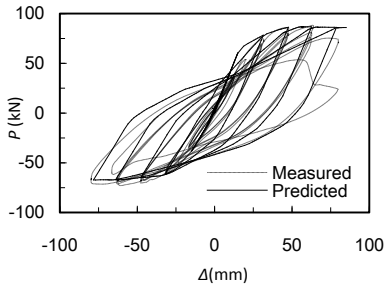
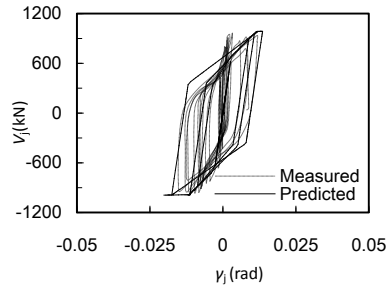


Fig.11 Simplified model for CFST connection with RC slab

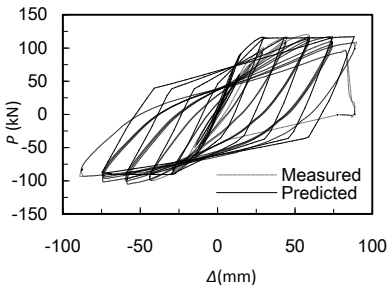
After building the hysteretic model for the panel zone, a macro connection element was established to implement the hysteretic model for the overall structure analysis. The schematic view of the macro connection element for CFST connection is shown in Fig.11. It had various components: the CFST column component, the steel beam component, the RC slab component, the shear stud component and the panel zone component. Fig.12 shows the measured and predicted results of specimens with RC slab (Li and Han, 2012). Both load-deformation relation of beam end and shear-shear deformation of panel zone are compared. In general good agreement is achieved for both global and local behavior of the connection.



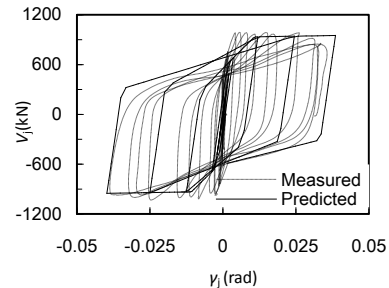
(a) Load-displacement (P - Δ) relation (CIJ-1)



(b) Shear-shear deformation (V_j - γ_j) relation (CIJ-1)



(c) Load-displacement (P - Δ) relation (CIJ-3)



(d) Shear-shear deformation (V_j - γ_j) relation (CIJ-3)

Fig.12 Verification of simplified model

Concluding Remarks

The experimental and numerical investigations were conducted on the CFST column to beam connections with external diaphragm and RC slab. It was found that the interior and exterior composite connections with the same beam section configuration exhibited different failure modes under cyclic loading in the test. The effect of the axial load level was moderate for the composite connection with beam or panel zone failure mode, while it was significant for the connection with a column failure mode. The tested specimens exhibited an average ductility coefficient of 3.57. The proposed FEA model could predict the behavior of the composite connection with a proper precision. Limited parametric study showed that the strength of the steel beam, the thickness of the RC slab and the steel ratio of the CFST column had significant influence on the failure mode of the composite connection, while the slenderness ratio and the dimension of the external diaphragm had minor effects. A simplified model of CFST connection for the structural system analysis was established, where a hysteretic model for panel zone was integrated. The proposed connection model could be applied in the seismic calculation of composite structural system with high efficiency and reasonable accuracy on both overall and local behavior.

Acknowledgement

The research reported in the paper is part of Project 50425823 and 51208281

supported by National Natural Science Foundation of China. The financial support is highly appreciated.

References

- Beutel, J., Thambiratnam, D., and Perera, N. (2002), "Cyclic Behaviour of Concrete Filled Steel Tubular Column to Steel Beam Connections", *Engineering Structures*, Vol. 24, No. 1 (pp. 29-38).
- Cheng, C. T., Chan, C. F., and Chung, L. L. (2007), "Seismic Behavior of Steel Beams and CFT Column Moment-resisting Connections with Floor Slabs", *Journal of Constructional Steel Research*, Vol. 63, No. 11 (pp. 1479-1493).
- Chiew, S.P., Lie, S.T. and Dai, C.W. (2001). "Moment Resistance of Steel I-beam to CFT Column Connections". *Journal of Structural Engineering ASCE*, Vol. 127, No. 10, (pp. 1164-1172).
- DBJ13-51-2003. (2003), *Technical Specification for Concrete-filled Steel Tubular Structures*. Fuzhou: The Construction Department of Fujian Province [in Chinese].
- Elremaily, A., and Azizinamini, A. (2001), "Experimental Behavior of Steel Beam to CFT Column Connections", *Journal of Constructional Steel Research*, Vol. 57, No. 10 (pp. 1099-1119).
- Fukumoto, T., and Morita, K. (2005), "Elastoplastic Behavior of Panel Zone in Steel Beam-to-concrete Filled Steel Tube Column Moment Connections", *Journal of Structural Engineering ASCE*, Vol. 131, No. 12 (pp. 1841-1853).
- Han, L.H., Yao, G.H. and Tao, Z. (2007). "Performance of concrete-filled thin-walled steel tubes under pure torsion". *Thin-Walled Structure*, Vol. 45, No.1 (pp. 24–36).
- Han, L. H. and Li, W. (2010), "Seismic Performance of CFST Column to Steel Beam Joints with RC Slab: Experiment", *Journal of Constructional Steel Research*, Vol. 67, No. 1 (pp. 127-139).
- JGJ101-96. *Specification for Test Methods of Seismic Buildings*. Beijing: Architecture Industrial Press of China, 1997 [in Chinese].
- Kang, L.P., Leon, R.T. and Lu, X.L. (2014), "A General Analytical Model for Steel Beam-to-CFT Column Connections in OPENSEES", *Journal of Constructional Steel Research*, Vol. 100, (pp. 82-96).
- Leon, R. T., Hajjar, J. F., and Gustafson, M. A. (1998), "Seismic Response of Composite Moment-Resisting Connections", I: Performance. *Journal of Structural Engineering ASCE*, Vol. 124, No. 8 (pp. 868-876).
- Li, W., and Han, L. H. (2011), "Seismic Performance of CFST Column to Steel Beam Joints with RC Slab: Analysis", *Journal of Constructional Steel Research*, Vol. 67, No. 1 (pp. 127-139).
- Li, W., and Han, L. H. (2012), "Seismic Performance of CFST Column to Steel Beam

Joint with RC Slab: Joint Model”, *Journal of Constructional Steel Research*, Vol. 73, No. 3 (pp. 66-79).

Nie, J., Qin, K., and Cai, C. S. (2008), “Seismic Behavior of Connections Composed of CFSSTCs and Steel–concrete Composite Beams—Experimental Study”, *Journal of Constructional Steel Research*, Vol. 64, No. 10 (pp. 1178-1191).

Nishiyama, I., Fujimoto, T., Fukumoto, T., and Yoshioka, K. (2004), “Inelastic Force-deformation Response of Joint Shear Panels in Beam-column Moment Connections to Concrete-filled Tubes”, *Journal of Structural Engineering ASCE*, Vol. 130, No. 2 (pp. 244-252).

Nishiyama, I., Morino, S., Sakino, K. et al. (2002), “Summary of Research on Concrete-filled Structural Steel Tube Column System Carried Out Under the US-Japan Cooperative Research Program on Composite and Hybrid Structures”. BRI Research Paper No.147, Building Research Institute, Japan.

Ricles, J. M., Peng, S. W., and Lu, L. W. (2004), “Seismic Behavior of Composite Concrete Filled Steel Tube Column-wide Flange Beam Moment Connections”, *Journal of Structural Engineering ASCE*, Vol. 130, No. 2 (pp. 223-232).

Schneider, S. P., and Alostaz, Y. M. (1998), “Experimental Behavior of Connections to Concrete-filled Steel Tubes”, *Journal of Constructional Steel Research*, Vol. 45, No. 3 (pp. 321-352).

Tort, C. and Hajjar, J. F. (2007), “Reliability-based Performance-based Design of Rectangular Concrete-filled Steel Tube (RCFT) Members and Frames”. Structural Engineering Report No. ST-07-1, University of Minnesota.

Wang, W. D., Han, L. H., and Uy, B. (2008), “Experimental Behaviour of Steel Reduced Beam Section to Concrete-filled Circular Hollow Section Column Connections”, *Journal of Constructional Steel Research*, Vol. 64, No. 5 (pp. 493-504).

Zhao, H. L., Kunnath, S. K. and Yuan, Y. (2010), “Simplified Nonlinear Response Simulation of Composite Steel-concrete Beams and CFST Columns”. *Engineering Structures*, Vol. 32, No. 9 (pp. 2825-2831).

MODELING OF INNOVATIVE RE-CENTERING CONNECTIONS FOR CIRCULAR CFT COLUMNS

Y. Gao
HOK, New York, NY 10018 USA
ygao63@vt.edu

Roberto T. Leon
Virginia Tech, Blacksburg, VA 24061 USA
rleon@vt.edu

ABSTRACT

Circular concrete filled steel tubes are regarded as ideal column members for seismic moment resisting systems as they combine large axial and flexural strength with ductile behavior. However, economic and robust configurations for connections between steel I-sections and circular tubes are not common in the USA due to perceived high fabrication costs. This paper describes a design procedure for an extended stiffened end plate connection, where a combination of through-column mild steel and shape memory alloy rods are used to create a PR re-centering connection. The connection is intended to combine inelastic PR behavior with a re-centering capability to produce a very robust and economic connection. The behavior of this type of connection was implemented into SAP2000 and OpenSEES and studies conducted to demonstrate the benefits of this connection. The new connection configuration can accommodate very large beam sizes and can be easily expanded into a biaxial moment connection.

INTRODUCTION

Circular concrete filled steel tubes (CCFTs) are regarded as ideal frame members in seismic resisting systems, as they combine large axial and flexural capacity with very large ductility (Perea et al., 2014). The synergetic properties of the two materials increase the strength of the confined concrete and avoid premature local buckling of the steel tube, in addition to providing savings in formwork and erection time. However, most common connection configurations for circular concrete filled tubes, which include some form of through plates in the connection (Zhao et al., 2010), are not economic in the US market due to (a) the desire of designers to use only fully restrained connections and its associated (b) high cost of fabrication and field welding. Research indicates that well designed partially restrained connections can supply equal or even better cyclic behavior (Astaneh and Nader, 1996). This paper describes a new connection that incorporates partially restrained and self-centering behavior, and follows developments described at a previous Connections Conference (Hu, 2016). A 3D view of a biaxial implementation of

the proposed connection is shown in Figure 1, while the details of a 2D connection are shown in Figure 2. The connection consists of:

- A CCFT made from either HSS sections or tubes of larger dimensions and higher strengths, such as API sections (API, 2012).
- A reduced beam section (RBS) girder that limits the force input to the connection while maintaining the frame stiffness.
- A stiff extended end plate connection with stiffeners to transfer all girder forces into the through rods. End plates are economical and robust connections (Murray and Meng, 1996)
- The end plates that bear on a rectangular tube, which in turn is connected to the circular column by fillet-welded internal diaphragms and external cover; the space between the tubes is to be filled by a high strength concrete or expansive grout. The size of this space is exaggerated in Figure 3 for clarity purposes; in practice it should range from 2 to 4 inches.
- A series of large diameter rods composed of both shape memory alloys (SMA) and mild steel rods. The design of the mild steel rods minimizes inelastic deformations during moderate seismic events while the design of the SMA rods (Anraves and DesRoches, 2007) provides re-centering after large events. The forces need to be carefully apportioned between the two types of rods and prestressing of either or both types of rods may be needed to maximize performance.

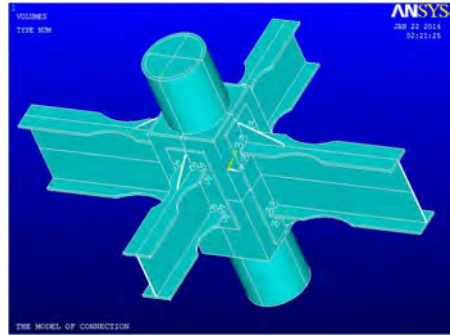


Figure 1. Biaxial connection.

While this connection may appear complex, it compensates for initial costs through shop prefabrication, ease of erection, self-centering characteristics and higher robustness.

The design steps are summarized in the next section. The procedure is deterministic and easy to program, which simplifies the design considerably.

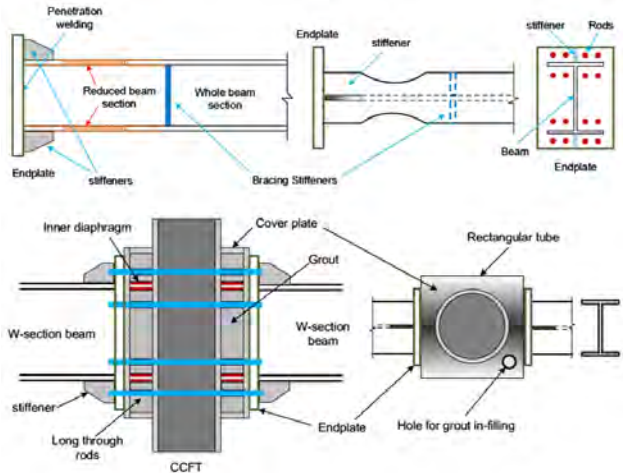


Figure 2. Details of proposed connection.

CONNECTION DESIGN

The design of the connection requires the following steps:

1. Given a beam and CCFT size, determine trial reduced beam section (RBS) dimensions using the criteria given in Section 5.8 of AISC 358 (AISC 358-10, 2010). If a displacement-based design approach is used, as opposed to a strong column-weak beam one, it may not be necessary to utilize a RBS section.
2. Determine ultimate moment demand (M_d) in the plane between the end plate and the square steel tube using the criteria in Section 5.8 of AISC 358.
3. Check the flexural strength of the beam at the face of the square steel tube (M_d in Figure 3) to ensure that the RBS strength controls. This moment is assumed to be reached when the strain in the SMA rods is beyond the 5% strain re-centering limit.
4. Calculate required end plate thickness to transmit M_d using a yield line approach similar (Yu, 2015) to that described in Murray and Meng (1996).
5. Compute target design moment demand ($M_{tar} \approx \gamma M_d$) at the surface of the square tube to be resisted by all rods when maximum strain in SMA rods reaches 5%. The SMA rods will begin to lose their re-centering capacity when the strains exceed 5% and the design requires that yielding begin to occur at the RBS before that strain limit is reached in the SMA rods. The value of γ should range from 0.7 to 0.9, with 0.8 being a reasonable initial trial choice.
6. Calculate the required rod lengths assuming that a deformation of 0.04 radians is required from the end plate rotation when the SMA rods reach 5% strain. The calculation should include any prestressing present in the SMA rods.
7. Calculate the connection design rotation, including the contribution of the RBS section, at M_{tar} based on the selected rod lengths.
8. Calculate moment at the surface of the square tube resisted by all SMA rods when the first SMA rods start phase transformation (ζM_{tar} in Figure 3). A choice needs to be made between how the loads are going to be apportioned between the steel and SMA rods and in which position the SMA and mild steel rods will be placed. A parameter ζ is introduced to determine the portion of total moment capacity supplied by the SMA rods when the maximum strain of SMA rods is 5%; its recommended value ranges from 0.4 to 0.6.
9. Calculate diameter of SMA rods based on one of the possible schemes shown in Figure 4. Details on how to select the best configuration are available in Yu (2015).
10. Calculate required prestressing parameter α for the SMA rods. In order to increase the stiffness of the proposed PR connection, pretension forces should be specified

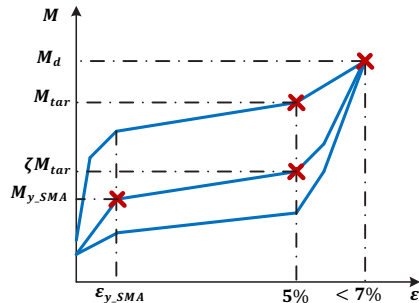


Figure 3. Design space for SMA rods.

for both SMA and steel rods. If the steel rods fully yield during a large seismic loading, the pretension forces in steel rods will be lost totally. After the lateral seismic loading is removed, only the pretension forces in SMA rods are available to resist the beam ends moments caused by the service loads. This capacity should be sufficient so that the connection can re-center, and should be specified as a portion of the beam end moments caused by the gravity loads.

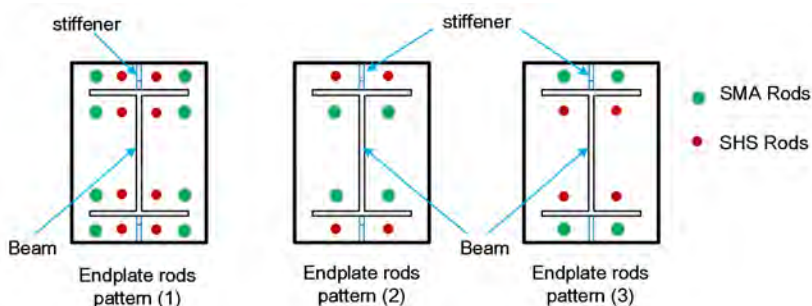


Figure 4 - Possible rod patterns for end plates.

11. Calculate moment capacity supplied by SMA rods with diameters determined from step 9 when the strain in the most strained SMA rods reaches 5%.
12. Calculate the force required to be carried by the mild steel rods as the difference between the total forces and that calculated from the SMA rods in Step 11.
13. Determine the required diameter of the mild steel rods.
14. Calculate, if necessary, the required prestressing for the mild steel rods. The pretension effects of steel rods will be lost totally under large seismic forces, as noted in Step 10, but should be sufficient to provide elastic behavior under both gravity and wind loads. Non-linear dynamic studies have shown that this prestressing, which appears necessary from a static analysis, may not be needed if adequate prestressing is provided by the SMA rods.
15. Check that the connection exceeds M_d at a SMA strain of 7% (Figure 3).
16. Calculate the maximum strain in SMA rods under the ultimate moment to ensure the strain limit of 7% is not exceeded.
17. Calculate shear forces at critical sections of the end plate under M_d .
18. Check shear yielding and shear rupture capacity of the end plate at critical sections.
19. Check shear capacity of rods.
20. Check bearing capacity of end plate holes.
21. Calculate thickness of inner diaphragms and size of fillet welds between the two tubes.
22. Check bearing and other local effects on the tubes' walls.
23. Calculate thickness of beam stiffeners and detail them, if needed.

CONNECTION MODELING

In this section, a 2D simplified spring model (2D-SSM) for uniaxial bending is developed for checking the connection performance using programs such as SAP2000. This type of component model (Rassati al., 2004) aims to capture the main characteristics of the new proposed connection behavior, including self-centering capacity, pretension effects, stiffness softening caused by yielding and sliding of the steel rods, rotation of end plates, and plastic hinges due to RBS and column yielding, among others.

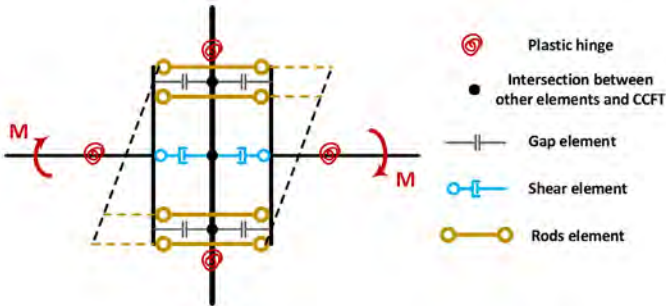


Figure 5: 2D-Simplified spring model for uniaxial bending connection

In Figure 5, the vertical dark bold line in the middle stands for the CCFT column, the other two shorter vertical dark bold lines on both sides of the CCFT column represent the two end plates and the two horizontal dark bold lines are used to simulate two beams on either side of the CCFT column. The four plastic hinge elements in red placed on both beams and the CCFT columns represent the plastic hinges in both the RBS and CCFTs, respectively. The four gap elements in gray are used to model the bearing behavior of both the inner diaphragms and in-filled grout. The two shear elements in blue are adopted to transfer the vertical shear forces from the beams to the CCFT column. The four rod elements in brown are adopted to simulate all rod behavior on four levels and help resist the moment at the ends of beams by supplying tension forces. A detailed description for each element is as follows:

- For the CCFT column, a beam element is used. Three *degrees of freedom (DOFs)* in plane are kept at each node. Elastic cross section properties for the CCFT column are assigned to this element and plastic behavior is allowed only in the two plastic hinges on the top and bottom CCFT columns near the joint.
- For the two end plates, either two rigid link elements or two elastic beam elements with large elastic stiffness for all axial, flexural and transverse DOFs are used. The end plate in the model can therefore be considered as rigid if the end plate is very thick or flexible if it is not.
- For the two beams on both sides of the CCFT column, two linear beam elements are used. The elastic cross section properties of the W-section are assigned to these beam elements. All plastic behavior of the RBSs will be considered within the two plastic hinges on the beams.

- The four plastic hinge elements are classified into two groups. One is the *plastic hinge* of the CCFT *column* (**PHC**), which is located at both ends of each CCFT column. The other is the *plastic hinge of the RBS* (**PHR**), which is located at the center of the RBS cross section on the beams. For the PHRs, only a non-linear moment-rotation curve for the RBS is defined. For the PHCs, the P-M interaction effect for the CCFT column is considered. The plastic hinges details follow Lignos, D.G. and Krawinkler, H. (2013)
- Four gap elements with very large elastic stiffness are used to model the bearing behavior of the inner diaphragms and the infill grout. The gap elements have only axial stiffness in compression. A very large elastic stiffness is assigned to them, so the contribution of the inner diaphragms and the in-filled grout under compression is very small to the overall deformation of the 2D-SSM.
- Two so-called 'shear elements' are defined by using two linear beam elements. This type element is designed to transfer only the vertical shear forces from the beams to the CCFT column, and doesn't provide any axial or flexural capacities. For the proposed connection, the vertical shear forces from the beams are assumed to be resisted by the friction between the end plates and the square steel tube faces, and there are very small relative vertical movements between them. To achieve this aim, a very large elastic transverse stiffness will be assigned to these shear elements.
- There are four so-called 'Rod elements' used in the 2D-SSM. Each of the rod elements is composed of three sub-elements: (1) one 'MultiLinear elastic link element' and one 'MultiLinear plastic link element with Kinematic hysteresis law'; (2) one 'Hook element' and one 'MultiLinear plastic link element with Takeda hysteresis law'; and (3) the combination of the above two types. For all the hook and plastic link elements, only the axial DOF is defined; all others are released. The choice of the 'Rod element' depends on the different rods patterns for the connection configuration shown in Figure 4. Each 'Rod element' should be able to simulate the combined behavior expected of all rods on each level (SMA only, steel only or combination): (1) only the SMA rods behavior with flag-shape pseudoelastic self-centering and pretensioning effect; or (2) only the steel rods behavior with stiffness softening due to yielding and sliding effects and pretensioning effect; or (3) the combination of above two to simulate both SMA and steel rods on that rod level.

A more sophisticated version of this same basic model containing (a) four additional gap elements placed on the two exterior rods levels, and (b) four additional plastic hinges are added at the four intersections between the four gap elements on the two beam flange levels and the two end plates is shown in Figure 6. This model was used in further studies as it was found that it was most efficient to allow the steel rods to start with a small initial gap (ergo, no pretension) and engage only after the SMA had begun their phase transformation.

CONNECTION BEHAVIOR

The behavior of this connection is shown in Figure 7. The key points in the moment-rotation curve for a symmetrical and monotonically increasing deformation history are:

- Point A represents the maximum capacity of the connection at rotation of 0.055 (rad.), which is the rotation of the connection when the maximum moment from the connecting beam is reached as determined from the proposed design procedure.
- Point B represents the maximum capacity of the connection at a rotation of 0.044 (rad.) which is the rotation of the connection when the maximum strain of some SMA rods reaches 5%.
- Point C represents the flexural capacity of the connection supplied by the SMA rods at a rotation of 0.044 (rad.).
- Point D represents the flexural capacity of the connection from the pretension of the SMA rods. The corresponding rotation of the connection is nearly zero.
- Point E represents the flexural capacity of the connection from the pretension of both the SMA and the steel rods. The corresponding rotation is also nearly zero.
- Point F represents the flexural capacity of the connection from only the SMA rods at rotation of 0.0075 (rad.), which is the rotation of the connection when the SMA rods starts to enter its transformation phase.

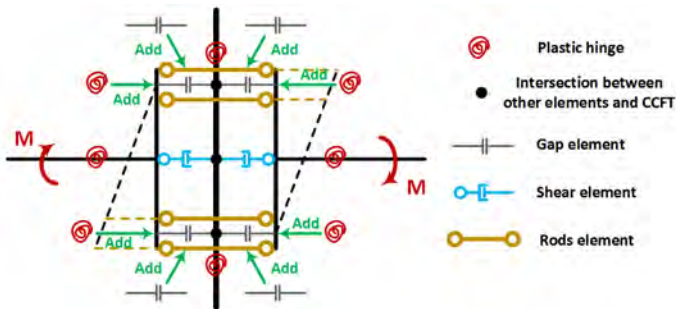


Figure 6 - Improved 2D-SSM for uniaxial bending.

The consistency between the spring model and the design procedure is shown by the trial design of a connection between a A992 W33x130 beam and a built-up A572 Grade 50 24x1-3/8 CCFT with a 30x1 rectangular collar (Table 1). The CCFT and infill were made from 8 ksi concrete. The connection configuration is Type 1 (Figure 4) with 1-1/8" SMA ($\sigma_{tar} \approx 64$ ksi ; $\sigma_{5\%} \approx 74$ ksi ; $\sigma_{7\%} \approx 95$ ksi) prestressed to 40% of $\sigma_{5\%}$ and 1-1/4" ($f_y = 50$ ksi ; $f_u = 65$ ksi) mild steel rods. The connection design was for a 32 ft. span on a heavily loaded library in a high seismic zone. The comparison in Table 1 indicates that the design and the SAP2000 results in Figure 7 have very good correspondence. This indicates that if the connection deformation is not very large, the proposed model is sufficiently accurate to reflect the main characteristics of the real connection behavior. The connection behavior is characterized by three monotonic envelopes that reflect the total strength, the upper strength of the SAM rods only and the lower strength of the SMA rods only. This model tends to underestimate both connection strength and stiffness because it assumes that the bottom row of bolts is carrying some tension.

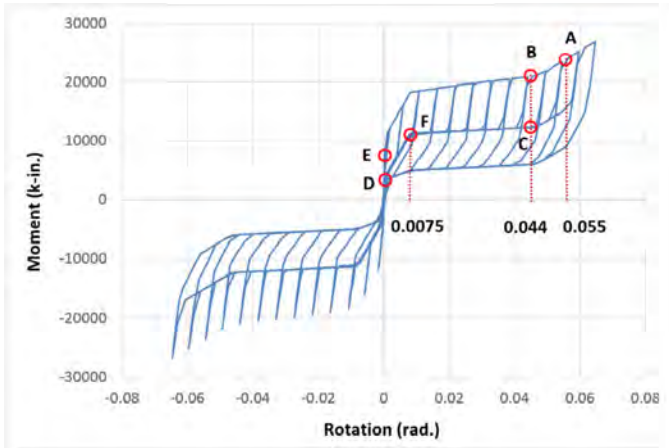


Figure-7: Moment -rotation curve for cyclic load history.

Table 1 - Design vs. SAP2000 moment capacities for connection with W33*130 beam

Point	Characteristic	Rotation (rad)	Design Procedure Moment (kip-in)	SAP 2000 Moment (kip-in)
A	Ultimate capacity	0.0553	25228	23805
B	Capacity when max. strain in SMA rods is equal to 5%	0.0436	21442	20840
C	Capacity from SMA rods at same rotation as Point B %	0.0436	12528	12231
D	Capacity from the SMA rods pretension	0	3378	3258
E	Capacity from the all rods pretension	0	6708	6586
F	Capacity supplied by the SMA rods at phase transformation	0.0075	11019	10821

FRAME BEHAVIOR

The simplified connection model described above was calibrated against detailed finite element studies and implemented in OpenSEES to allow for comprehensive non-linear

dynamic time history frame analyses (Yu, 2015). Figure 8 shows a comparisons of the moment-rotation connection behavior between the proposed connection and an idealized welded SMRF connection located in a lower story of a public library with five stories above the grade and a one story basement designed for a Site Class D soil in a high seismic zone. The plan dimensions of the building are approximately 120 ft. in the N-S direction, and 160 ft. in the E-W direction. The structural system is intended to work within a grid spacing of 32 ft. by 24 ft. with story heights of 14 ft.

Figure 8 indicates that the conventional steel welded frame (Convent. (CCFT)) will have very substantial rotational demands when compared to the proposed connection (SC-Gaps). Figure 9 shows a typical drift response for these frames, indicating that the residual deformations are substantially lower for the frame with the proposed connection (well within the 0.5% criteria for frame repairability), while the idealized SMRF has almost four times as much permanent drift.

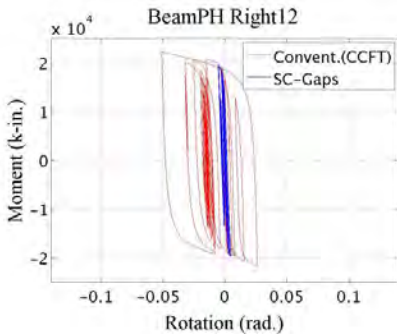


Figure 8 - Moment-rotation behavior of lower story interior connection.

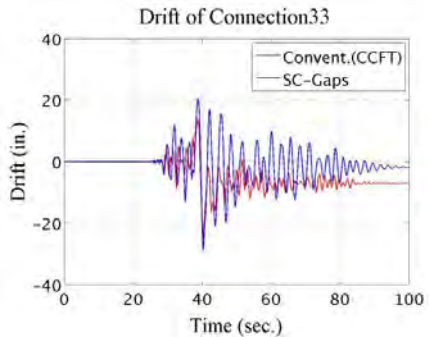


Figure 9 - Drift for strong ground motion time history

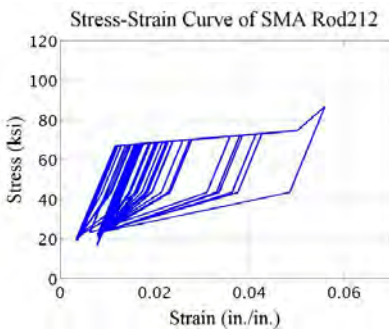


Figure 10 - Typical stress-strain time history for a SMA rod.

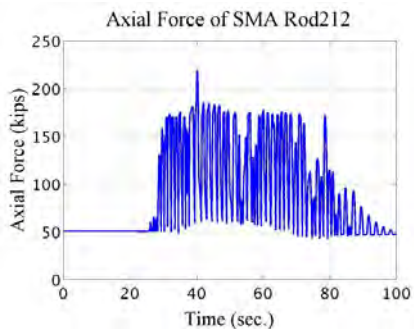


Figure 11 - Force history for a typical SMA rod.

Figure 10 shows a typical stress-strain history for a SMA rod in an interior connection in the lower floors. Because of the severity of the ground motion, the strain has exceeded 5% but not the 7% limit. The resulting permanent drift shown in Figure 9 comes mostly from column yielding at the base of the structure. Figure 11 shows the axial force history, indicating that this SMA rod was being used to the full capacity throughout the load history. An important characteristic of SMA materials is their superior fatigue performance, a key property given the large number of non-linear excursions shown in Figure 11.

CONCLUSION

This paper describes the design and behavior of an innovative connection between steel W shapes and CCFT columns. The connection provides re-centering behavior for large earthquakes and satisfactory elastic performance under moderate ground motions.

REFERENCES

- AISC 358-10 (2010), Prequalified Connections for Special and Intermediate Steel Moment Frames for Seismic Applications, AISC, Chicago.
- AISC341-10, (2010). Seismic Provisions for Structural Steel Buildings, AISC, Chicago. 2010,
- Andrawes, B. and DesRoches,R. (2007) Effect of hysteretic properties of superelastic shape memory alloys on the seismic performance of structures. *Structural Control and Health Monitoring*, 14(2).
- API (2012). API Spec 2B-1: Specification for Fabrication of Structural Steel Pipe (R2012), 6th Ed., American Petroleum Institute, Washington, D.C.
- Hu, J.W. (2016). *Smart Connection Systems: Design and Seismic Analysis*, CRC Press, Boca Raton.
- Lignos, D.G. and Krawinkler, H. (2013). Development and Utilization of Structural Component Databases for Performance-Based Earthquake Engineering, *Journal of Structural Engineering*, 139(8).
- Murray, T.M., and Meng, R.L. (1996). Seismic Loading of Moment End-Plate Connections: Some Preliminary Results, in Connections in Steel Structures III: Behaviour, Strength and Design , R. Bjorhovde et al. (eds.), Elsevier Applied Science, London.
- Nader, M.N. and Asatneh-Asl, A. (1996). Shaking Table Tests of Rigid, Semirigid, and Flexible Steel Frames, *Journal of Structural Engineering*, 122(6).
- Perea, T. Leon, R.T., Hajar, J.F. and Denavit, M.D. (2014). Full-Scale Tests of Slender Concrete-Filled Tubes: Interaction Behavior, *Journal of Structural Engineering*, 140(9).
- Rassati, G.A., Leon, R.T. and Noe, S. (2004). Component modeling of partially restrained composite joints under cyclic and dynamic loading, *Journal of Structural Engineering*, 130(2)..
- Yu, G., (2015), Innovative Self-Centering Connection for CCFT Composite Columns, PhD Thesis, The Graduate School, Virginia Tech, Blacksburg, VA.
- Zhao, X.L., Han, L. H., and Lu, H. (2010). *Concrete-filled tubular members and connections*. CRC, Boca Raton.

SELF-CENTRING BEAM-COLUMN CONNECTIONS USING LARGE SIZE SUPERELASTIC SMA BARS

Wei Wang

Tongji University, Shanghai 200092, China
weiwang@tongji.edu.cn

Jia Liu

Tongji University, Shanghai 200092, China
1332510@tongji.edu.cn

Cheng Fang

Tongji University, Shanghai 200092, China
chengfang@tongji.edu.cn

Yiyi Chen

Tongji University, Shanghai 200092, China
yiyichen@tongji.edu.cn

Abstract: This paper presents two types of practical self-centring connections, namely, connection with all SMA bars (SMA-All) and connection with combined angles and SMA bars (SMA-Angle). Both connections were shown to have stable and controllable hysteretic responses till 5% loading drift. Up to 3% drift, the self-centring performance was satisfactory for both connection types, but beyond which the presence of the angles could lead to accumulated residual drift. Also, due to these angles which contributed to energy dissipation in a manner of material yielding, specimen SMA-Angle generally had higher equivalent viscous damping than specimen SMA-All, but at the cost of increased residual rotation. Importantly, for both connections, the deformation was accommodated by the SMA bolts or angles, whereas no plastic deformation was observed at any other structural members. This confirmed the feasibility of using such connections for highly resilient structures where minimal repair work is required after earthquakes.

1. INTRODUCTION

Prior to the 1990s, steel moment resisting frames with fully restrained welded beam-to-column connections (e.g. connections with welded beam flange and welded/bolted beam web) had long been recognised as an appropriate structural system against seismic loadings. However, it was observed that brittle fractures occurred in a large number of such connections in the Northridge earthquake in 1994 and later in the Kobe earthquake in 1995, even though part of connections didn't fracture immediately in earthquake, these connections still didn't use continuously because of much residual deformation. These seismic damage facts indicated traditional steel moment frames using welded beam-column connections were susceptible to brittle fracture and commonly had large residual deformation after earthquakes. Thus a novel steel structural system incorporating with SMA bars having the capability of self-centring, adequate ductility and dissipating energy was put forward to address such problems.

In seismic engineering, one promising application of large size SMA bars is for self-centring beam-to-column connections. The main idea was to accommodate the

ductility and energy dissipation demands via superelastic deformations of SMA bolts (or other viable SMA components), whilst keeping the remaining major structural members within the elastic range. Adopting this design concept, the post-earthquake repair work on main structural members can be minimal. Abolmaali et al. (2006) examined the cyclic response of T-stub connections equipped with SMA bolts. The specimens showed reasonable self-centring properties, but the energy dissipation ability and ductility were relatively poor. Sepúlveda et al. (2008) carried out a series of tests on end-plate connections using copper-based SMA bolts, where superelastic behaviour with a moderate level of energy dissipation could be exhibited at a drift level up to 3%. Ocel et al. (2004), Penar (2005) and Speicher et al. (2011) conducted a series of physical tests which further proved the efficiency of using SMA tendons for connections with shear tab. More recently, the authors and co-workers launched a series of experimental programmes evaluating the feasibility of incorporating SMA bolts into various beam-to-column connections. Seven proof-of-concept tests were first carried out considering two SMA bolt sizes, i.e. 10 mm and 16 mm diameters. It was found that the specimens with 10 mm diameter SMA bolts performed better than those with 16 mm bolts in terms of both self-centring ductility and ductility. In particular, the 16 mm SMA bolts experienced quite early fracture (Fang et al., 2014). A subsequent study examined the potential of using 8 mm diameter SMA bars for I-beam to tubular column connections, where good self-centring abilities were shown (Wang et al., 2015). Some specimens also considered hybrid bolt arrangements integrating combined SMA and steel bars, but it was found that the presence of the steel bars had limited benefit under repeated load due to bolt relaxation (plastic deformation of steel). It is noted that shear resistance was not considered for these connections. Additional angles were also employed for such connections to provide supplementary shear resistance and energy dissipation source, however, it was found that the self-centring driving force offered by the 8 mm SMA bar group was insufficient to promote deformation recovery, and thus significant residual deformation was still induced (Wang et al., 2015).

This paper presents two practical self-centring connections and conducts two connection experiential tests. One specimen with combined SMA bolts and energy dissipative angles was designed to try a better balance between SMA bars and angles, and the other specimen equipped with four rows of SMA bolts was designed to try a perfect self-centring connection. These two connections both addressed the unreliable shear-resistance issue that existed in the previous proof-of-concept studies ((Wang et al., 2015), (Fang et al., 2014)). A detailed discussion about this two types of connections was made on their key structural performances, including strength, stiffness, ductility, self-centring ability, and energy dissipation capacity.

2. SMA CONNECTION TEST

2.1. Specimens and test setup

The main idea of self-centring connections based on SMA material is to allow 'superelastic hinges' being formed at the beam-to-column intersections, such that the connections can be self-centred and concurrently help dissipate energy. The adjacent beams and columns can remain intact after earthquakes. Based on these objectives, two full-scale specimens, representing two practical steel connection types, were prepared and examined in this paper.

The first specimen was a shear tab connection equipped with four rows of SMA bolts, as shown in Fig. 1. The shear tab was used to provide sufficient shear resistance for the connection, and the bolt holes were slotted to enable a certain level of rotational flexibility. The bending resistance as well as the self-centring driving force were provided by the eight SMA bolts. It is noted that in order to weaken the hindering function from shear tab friction, the beam was attached to column via double shear tabs with shear bolts hand tightened. For the second specimen, the shear tab was removed, and the two internal SMA bolt rows (four bolts) were replaced by four pieces of L100×100×6 angles. The main functions of the angles are mainly three folds: 1) to provide shear resistance for the connection, 2) to offer considerable supplementary energy dissipation via steel yielding, and 3) to provide a certain degree of rotational stiffness. In addition, these angles are replaceable after earthquakes if excessive plastic deformation is developed. Grade 10.9 M16 high strength bolts were employed for the shear tab and angle connections. Details of the geometric properties of the test specimens are illustrated in Fig. 1. For ease of identification, the code for the first specimen is 'SMA-All', and that for the second specimen is 'SMA-Angle'.

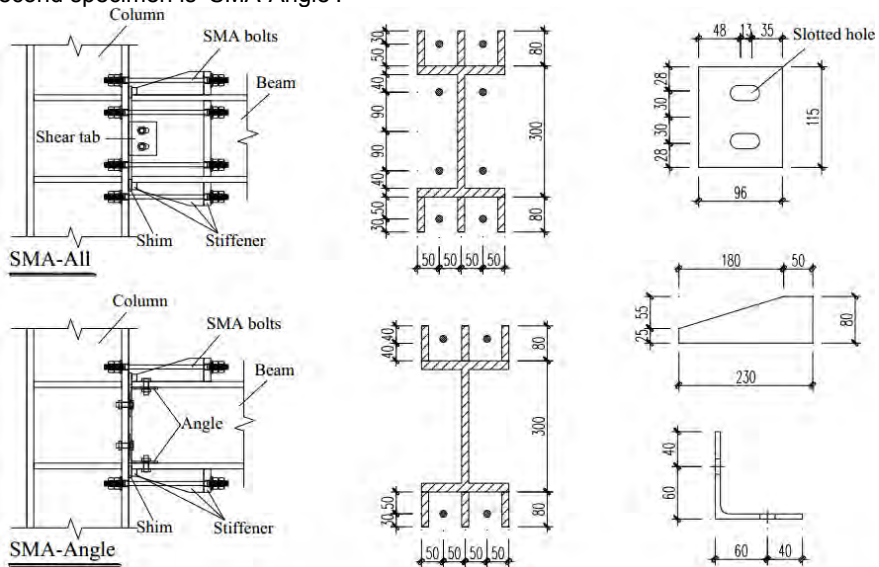
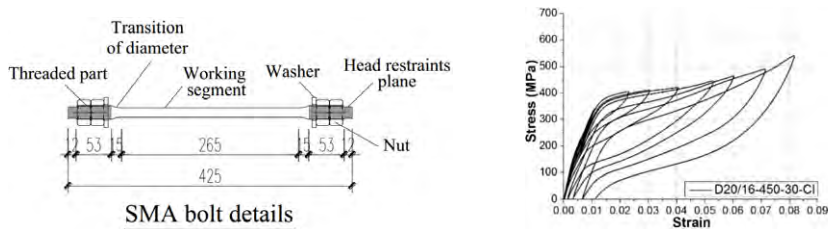


Fig. 1 Details of test specimens



(a) Details property of SMA bolts

(b) Mechanical property of SMA bolts

Fig. 2 Details and mechanical property of SMA bolts

The total length of each SMA bolt was 425 mm, and the detailing of SMA bolts was shown in Fig. 2(a). The original diameter D_1 of the SMA bars was 20 mm, where the two ends of the bar were threaded with a net diameter D_3 of 18.15 mm. The diameter of the reduced/working segment, D_2 , was 14 mm, leading to a D_3/D_2 ratio of 1.30, which could avoid quite early fracture over the net threaded area to ensure adequate ductility of connections compared with D_3/D_2 ratio of around 1.0 (Fang et al., 2014). It is worth mentioning that when increasing SMA bar diameter, it became more difficult to preload SMA bars to prescribed pre-strain because of torsional deformation of SMA bar shank according to relevant research ((Wang et al., 2015), (He, 2012)). In this paper, the SMA bars were cut into two planes parallel to longitudinal axis at each end, where one can apply reverse torque to avoid torsional deformation of reduced segment when preloading SMA bars. And this detailing had been proved much effective when preloading SMA bars. Before conducting connections experiment, the author made a detailed discussion on the heat treatment strategy for large size SMA bars as well as the resulting mechanical properties. The material test results indicated that the optimal heat treatment procedure for the SMA bars with diameters 20 mm was 400 °C for 30 minutes, and then water quenched. For all the SMA bolts considered in the connection tests, the 'optimal' heat treatment procedure based on the material test results was employed, and here gives a representative mechanical test results for dog-bone coupons, as shown in Fig. 2(b).

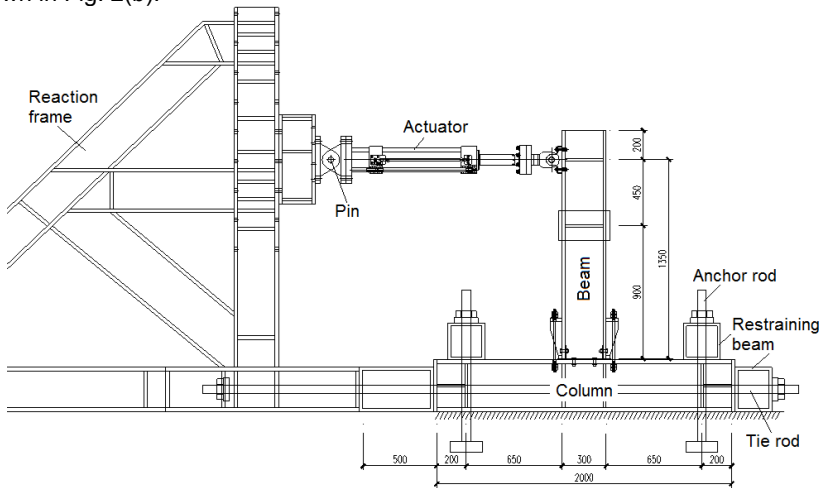


Fig. 3 Test setup

A sub-frame, consisting of a fabricated column, a fabricated beam, and the associated beam-to-column SMA connection, was considered for testing. The beam and column sizes were designed to ensure that the members would remain elastic (and thus damage free) during the loading procedure. Beam flange stiffeners were added to facilitate bolt end fixing as well as to reinforce the steel beams. The test setup was designed such that the cyclic load could be conveniently applied. The column was horizontally placed and fixed to the strong floor via two restraining beams which were used to prevent in-plane column rotation. The vertical steel beam was perpendicularly connected to the column through the SMA connections. A

bidirectional servo-actuator was used to apply the horizontal cyclic concentrated load at the beam tip at a distance of 1350mm from the column flange face. The other end of the servo-actuator was pin-connected to the side column of a triangle reaction frame. Lateral supports were also used to avoid possible out-of-plane movement of the beam. The schematic layout of the test setup is shown in Fig. 3.

2.2. Instrumentations and test procedure

The displacement and deformation conditions of the specimens were monitored via a series of linear variable differential transformers (LVDTs) and strain gauges, as illustrated in Fig. 4. Two LVDTs (#1 and #2) were mounted at the beam tip location to record the drift of the sub-frame, where each LVDT was placed near one edge of the beam flange. The relative shear displacement between the column face and the beam end (connection end) was monitored through LVDTs 3 to 6 to monitor whether shear slippage occurred or not. LVDTs 7 and 8 were placed at the two ends of the column to measure any rigid body column rotation which needs to be deducted from the overall drift. The gap opening and closure condition between the beam and the column face were measured via LVDTs 9 to 12. For local deformation conditions, a series of strain gauges were mounted over the beam cross-sections to ensure that the beam stayed in the elastic range during the loading process, such that the main inelastic deformation demand was accommodated by the elongation of the SMA bolts or the bending deformation of the angles (based on the basic design concept). These strain gauges were also used for calibration purposes, making sure that the beam tip load was applied correctly. Some strain gauges were also placed at the column flange and beam stiffeners to understand their strain developments. Due to relatively complex strain conditions at the angles or shear tab, rosettes were employed to capture the strains along multiple directions, as detailed in Fig. 4. For each SMA bolt, two strain gauges were placed along the shank (reduced) segment at two opposite sides, such that the bolt elongations, including minor bending actions, can be checked during the cyclic loading process.

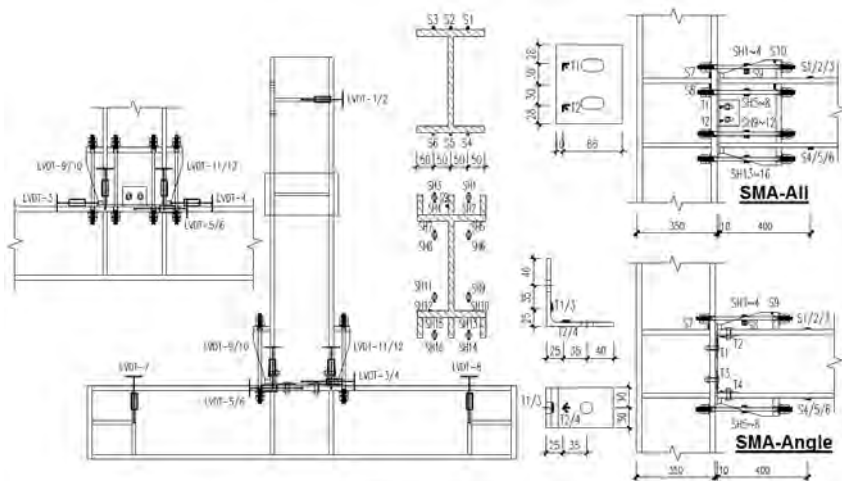
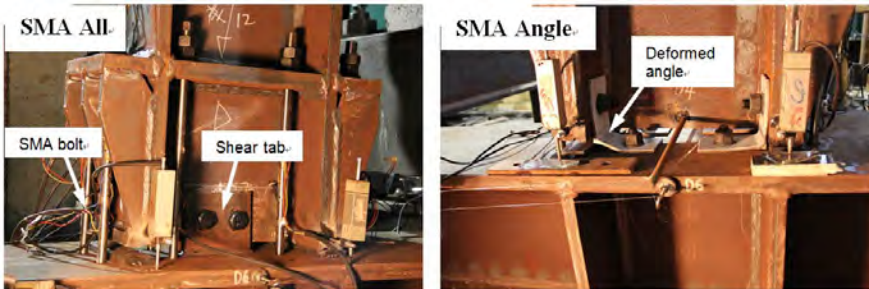


Fig. 4 Instrumentations for test specimens

In order to prevent bolt relaxation, a 1.25% pre-strain, corresponding to the initiation point of forward transformation, was applied to each SMA bolt, where the achievement of the target pre-strain was aided by the readings of the strain gauges mounted at the bolt shank. The high-strength bolts for angles were installed with a snug-tightened condition. After the SMA bolts were pre-strained, the cyclic load was applied by the bidirectional servo-actuator with displacement control. The standard SAC loading protocol (FEMA, 2000), considering drift as the governing parameter for steel connection tests under cyclic loads, was adopted, where the following sequence of drift was employed: 0.375% (six cycles), 0.50% (six cycles), 0.75% (six cycles), 1% (four cycles), 1.5% (two cycles), 2% (two cycles), and then with 1% drift incremental intervals (two cycles per drift level). The test was terminated at the last cycle of 5% drift.

3. TEST RESULTS

Both specimens showed stable and controllable structural responses under the cyclic load till 5% drift. The typical deformation responses of the specimens are shown in Fig. 5. As expected, the deformation was accommodated by the SMA bolts or angles, whereas no visual plastic deformation was observed at any other structural members. For specimen SMA-All, the SMA bolts stayed tightened at 4% drift, indicating proper self-centring function of these bolts. At 5% drift, one external SMA bolt suddenly fractured over the threaded area, and the other three external bolts also experienced relaxation at the end of the test. This suggested that the self-centring driving force provided by the external SMA bolts were almost exhausted at 5% drift, and the connection started to lose its self-centring ability. In addition, minor bending deformation was observed for the SMA bolts after the test, and this was due to the gap opening between the beam and the column face. During the cyclic loading process, the high strength bolts of the shear tab connection moved along the slotted bolt holes, which had little hindering function to connection. According to the readings of LVDTs 3-6, no relative shear slippage was observed between the beam and the column, indicating sufficient shear resistance of the connection.



(a) SMA-All connection

(b) SMA-Angle connection

Fig. 5 Typical deformation mode of connections

When the internal SMA bolts of specimen SMA-All were replaced by energy dissipative angles, i.e. the case of specimen SMA-Angle, a different deformation mode was observed, especially at large drift levels. At 3% drift, all the SMA bolts were fully functional with no bolt relaxation, and the plastic deformation of the angles

could be fully recovered. After 4% drift, a minor 'permanent' gap was induced between the beam end and the column face. This was due to the insufficient self-centring driving force being unable to fully recover the plastic deformation of the angles, and once this happened, the gap was gradually accumulated with further loading cycles, and as a result the beam end tended to move away from the column face. After 5% drift, residual deformation of the angles could be seen, and an approximately 2 mm gap was left between the beam end and the column face. As a result, all the SMA bolts were still kept tightened at this stage. Again, due to the presence of the angles, the connection exhibited adequate shear resistance with no shear slippage being recorded between the beam end and the column face.

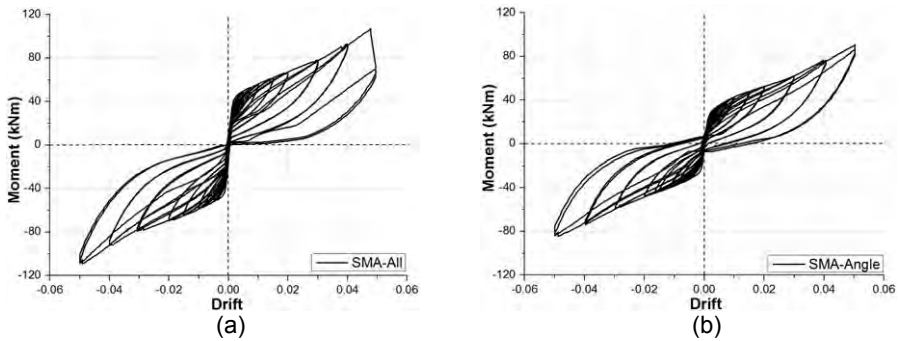


Fig. 6 Moment-drift responses of connections

Fig. 6 shows the moment-drift responses of the two specimens, where the moment was calculated by $M = P \times L$ (P = beam tip load, and L = level arm, i.e. 1350 mm). Both curves exhibited recognizable flag shape hysteretic pattern. The hysteretic curves were generally stable and repeatable, although a certain level of degradation was found. The initial stiffness of specimens SMA-All and SMA-Angle were 28626 kNm/rad and 16790 kNm/rad, respectively. The 'yielding' moments (i.e. due to the initiation of forward transformation of the SMA bolts) of the two specimens were approximately 48 kNm and 31 kNm, respectively, and at 5% drift, the ultimate moments for the two connections could achieve 110 kNm and 88 kNm, respectively. This indicated pronounced 'hardening' of the moment resistance after the inception of the forward transformation of the SMA bolts. The resisting moment of specimen SMA-Angle was generally lower than that of specimen SMA-All, and this was due to the relatively lower load resistance of the angles in bending, compared with the case of SMA bolts in uniaxial tension. Moreover, a certain level of residual rotation was shown for specimen SMA-Angle after 3% drift, which was in line with the test observation, i.e. due to unrecoverable plastic deformation of the angles. For specimen SMA-All, no residual rotation was shown at 4% drift. When 5% drift was being approached, a sudden drop of the curve was shown, echoing the initiation of bolt fracture as observed during the test. Accompanied by successive relaxations of the other external SMA bolts, more evident degradation was observed along the ascending loading branch during the second round of cycle at 5% drift.

4. DISCUSSION OF RESULTS

Both specimens showed satisfactory ductility supply. According to the relevant standards, e.g. AISC (2005), a connection needs to be designed to have a rotational

capacity of 4% and 2% inter-storey drift angles for the criteria of special moment frame (SMF) and intermediate moment frame (IMF), respectively. For Eurocode 8 (2004), it is required that a connection should satisfy the rotational capacities of the plastic hinge region not less than 0.035 and 0.025 radians for structures of ductility class high (DCH) and those of ductility class medium (DCM), respectively. For the current two specimens, no bolt fracture occurred at 4% drift, and the peak moment at each drift level (i.e. skeleton curves) showed no tendency of decrease with incremental drifts, although the ascending branch of the moment-drift responses showed gradual degradation of stiffness with increasing cycles. According to the requirements in AISC and Eurocode 8, the ductility of both specimens well satisfies the requirements for SMF and DCH structures, respectively. It is worth mentioning that the net threaded-to-shank bolt diameter ratio (D_3/D_2 ratio = 1.30) of the current SMA bolts showed reasonably good fractural resistance, recalling that early bolt fracture was observed in the previous study (Fang et al., 2014), where D_3/D_2 ratio was around 1.0. This confirmed the effectiveness of increasing D_3/D_2 ratios for improving the overall ductility of the connection.

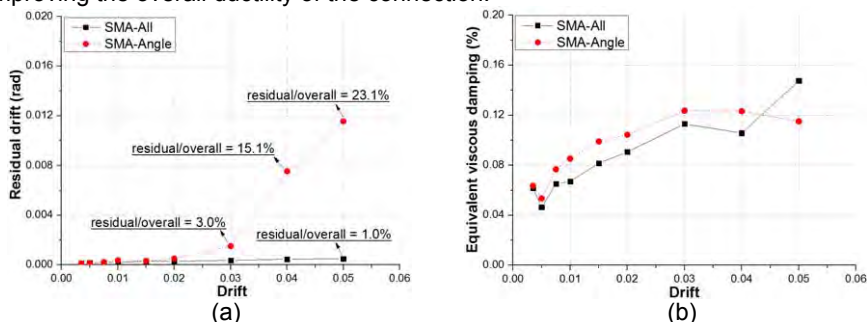


Fig. 7 Discussion of connection test results: a) residual drift, b) EVD

The self-centring ability, which is one of the most important characteristics of the SMA connections, was evaluated via the trend of accumulated residual drift, as shown in Fig. 7(a) (the values for the last cycle at each drift are given). It was confirmed that specimen SMA-All, which was equipped with a series of SMA bolts, exhibited negligible residual drift by the end of the test (the final residual drift only took up 1.0% of the total drift), which achieved the initial design intention. For specimen SMA-Angle under the same incremental loading scenario, the residual drift was almost negligible within 3% drift according to ATC-58 50% Draft (2009), and then a significant increasing in residual drift with increasing drift. It's noted that at 3% drift, the total strain of SMA bolts was approximately 5%, which just responding to three cycles training at 5% strain of SMA bolts before connection tests. Beyond this drift, the residual strain of SMA bolts increased rapidly (He, 2012), which resulting in a significant increasing in residual drift. At 4% drift, which is the deformability requirement for SMFs in AISC (2005), the residual-to-overall drift ratio was 15.1%; in other words, approximately 85% of the rotational deformation could be recovered, which is still a quite encouraging recovery rate and has much improvement compared with other connections (Wang et al., 2015). At 5% drift, the residual drift further increased, and the residual-to-overall ratio finally reached 23.1%. Generally speaking, the large size SMA bolts, which had been subjected to appropriate heat

treatments, could offer sound self-centring driving force for both connection types, especially when the drift was less than 4%.

From the energy dissipation point of view, the trends of equivalent viscous damping (EVD) for the two specimens are shown in Fig. 7(b), where the value of the first cycle for each drift is typically given. In general, the EVD increased with increasing drift level for both specimens. This is because that at small drift levels, the superelasticity of the SMA bolts was not significantly mobilised due to relatively small levels of bolt strain. In addition, the drift partially caused by the elastic deformation of the steel beam in flexural bending might not be negligible at initial loading stages, and this elastic portion of deformation did not contribute to energy dissipation. With increasing number of cycles, the elastic bending deformation of the steel beam became insignificant (compared with total drift), and stable flag shape hysteretic loops were formed, leading to increased EVD. For the two specimens under varying drift levels, the EVD ranged between 4.1% and 14.8%, and it was found that specimen SMA-Angle generally had higher EVD than specimen SMA-All (except at 5% drift). This was due to the presence of the angles which contributed to energy dissipation in a manner of material yielding. However, the EVD was increased at the cost of larger residual deformation, and therefore, it was recommended that larger diameter SMA bolts (or smaller angles) could be employed to effectively utilise the energy dissipation function of the angles without compromising the self-centring ability of the connections at large drifts. This requires more reasonable combination design for SMA bolts and angles, and further investigations may be required on this front.

5. SUMMARY AND CONCLUSIONS

With the available information on heat treatment, two full-scale tests have been carried out to further examine the feasibility of large size SMA bars in practical seismic-resistant beam-to-column connections, where the first specimen was a shear tab connection equipped with four rows of SMA bolts (Specimen SMA-All), and the second specimen employed combined SMA bolts and energy dissipative angles (Specimen SMA-Angle). For both specimens, the deformation was accommodated by the SMA bolts or angles, leaving no plastic deformation developed at any other structural members. This was fully in line with the initial design intention. In addition, both specimens showed good ductility supply, satisfying the requirements for SMF and DCH structures according to the AISC and Eurocode 8 requirements, respectively. From the perspective of self-centring ability, specimen SMA-All showed negligible residual rotation by the end of the test, which indicated perfect self-centring performance for specimen SMA-All; for specimen SMA-Angle, residual drift started to be induced at 4% loading drift, and a final residual drift of around 1.15% was induced at the final cycle (5% drift). Moderate energy dissipation capacity was observed for the two specimens, and the maximum equivalent viscous damping (EVD) achieved 14.8%. Due to the presence of the angles which contributed to energy dissipation in a manner of material yielding, specimen SMA-Angle generally had higher EVD than specimen SMA-All, but at the cost of increased residual rotation. This suggested that an appropriate combination design of SMA bolts and angle size is required for well-balanced self-centring and energy dissipation capacities.

ACKNOWLEDGEMENT

The work presented in this paper is supported by the State Key Laboratory of Disaster Reduction in Civil Engineering of China through Grant No. SLDRCE14-B-05 and the Collaborative Research Project under International Joint Research Laboratory of Earthquake Engineering in China.

REFERENCES

- [1] Abolmaali A, Treadway J, Aswath P, Lu FK, McCarthy E. (2006), "Hysteresis Behavior of T-Stub Connections with Superelastic Shape Memory Fasteners", *Journal of Constructional Steel Research*, Vol.62, No.8(pp.831-8).
- [2] Sepúlveda J, Boroschek R, Herrera R, Moroni O, Sarrazin M. (2008), "Steel Beam-Column Connection Using Copper-Based Shape Memory Alloy Dampers", *Journal of Constructional Steel Research*, Vol.64, No.4(pp.429-435).
- [3] Ocel J, DesRoches R, Leon RT, Hess WG, Krumme R, Hayes JR, Sweeney S. (2004), "Steel Beam-Column Connections Using Shape Memory Alloys", *ASCE Journal of Structural Engineering*, Vol.130, No.5(pp.732-40).
- [4] Bradley W. Penar (2005), "Recentering Beam-Column Connections Using Shape Memory Alloys", Master Thesis, School of Civil and Environmental Engineering, Georgia Institute of Technology.
- [5] Speicher MS, DesRoches R, Leon RT. (2011), "Experimental Results of a NiTi Shape Memory Alloy (SMA)-Based Recentering Beam-Column Connection", *Engineering Structures*, Vol.33, No.9(pp.2448-57).
- [6] Fang C, Yam MCH, Lam ACC, Xie LK. (2014), "Cyclic Performance of Extended End-Plate Connections Equipped with Shape Memory Alloy Bolts", *Journal of Constructional Steel Research*, Vol.94(pp.122-136).
- [7] Wang W, Chan TM, Shao HL, Chen YY. (2015), "Cyclic Behavior of Connections Equipped with NiTi Shape Memory Alloy and Steel Tendons Between H-Shaped Beam to CHS Column", *Engineering Structures*, Vol.88(pp.37-50).
- [8] Wang W, Chan TM, Shao HL. (2015), "Seismic Performance of Beam-Column Joints with SMA Tendons Strengthened by Steel Angles", *Journal of Constructional Steel Research*, Vol.109(pp.61-71).
- [9] He Xiaohui, (2012), "Hysteretic Behavior of New Energy-Dissipated Beam-to-Column Connections in Steel Frame", PHD Thesis, School of Civil Engineering, Harbin Institute of Technology.
- [10] FEMA-350 (2000), "Recommended Seismic Design Criteria for New Moment-Resisting Steel Frame Structures", Federal Emergency Management Agency, Washington, D.C., 2000.
- [11] AISC 2005, "Seismic Provisions for Structural Steel Buildings". American Institute of Steel Construction, Chicago, IL, USA, 2005.
- [12] EN 1998-1:2004, Eurocode 8: "Design of Structures for Earthquake Resistance – Part 1: General Rules, Seismic Actions and Rules for Buildings". Brussels, Belgium, 2004.
- [13] ATC-58 50% Draft (2009), "Guidelines for Seismic Performance Assessment of Buildings", Applied Technology Council, Washington, D.C., 2009.

SEISMIC BEHAVIOUR OF MOMENT RESISTING FRAMES WITH DISSIPATIVE DOUBLE SPLIT TEE JOINTS

Massimo Latour, Vincenzo Piluso, Gianvittorio Rizzano

*University of Salerno, Department of Civil Engineering
Via Giovanni Paolo II, Fisciano (SA)- Italy*

mlatour@unisa.it, v.piluso@unisa.it, g.rizzano@unisa.it

ABSTRACT

Structural seismic systems with low damage connections or easily replaceable connections have received, in recent years, a growing interest from the scientific community on earthquake resistant design. Within this framework, damping devices able to dissipate the seismic input energy, reducing the seismic demands on the structural elements, are particularly interesting. In this paper, the possibility of providing the structure with damping devices by means of properly detailed beam-to-column joints is analysed. In particular, the behaviour of two different joint solutions equipped with damping devices, one of yielding type and one of friction type, are analysed and compared with that of full strength joints involving in plastic range a reduced beam section (RBS connections). Finally, the seismic performance of steel frames equipped with damping devices has been analysed by performing IDA analyses on three steel frames. All these frames have the same geometry and the same structural members, the only variation is due to the examined joint typology.

1. INTRODUCTION

In the seismic design of steel frames the dissipation of the seismic input energy is provided by the plastic engagement of some zones of structural members, the so-called “dissipative zones” which have to be properly detailed in order to assure wide and stable hysteresis loops. In addition, as it is well known, it is important to promote the plastic engagement of the greatest number of dissipative zones, so that both European and American seismic codes suggest the use of member hierarchy criterion aiming to prevent the premature plastic engagement of columns which can lead to a non-dissipative collapse mechanisms, such as storey or partial mechanisms.

As soon as the yielding of columns is prevented, a global dissipative collapse mechanism can be ensured either by the formation of plastic hinges at the beam ends or by yielding of connections, provided that the connecting elements involved in plastic range are able to develop an adequate energy dissipation capacity. Within this framework, beam-to-column joints play a role of paramount importance. In fact, beam-to-column joints can be designed either as Full Strength (FS) or Partial Strength (PS). In the first case, the seismic input energy is absorbed by means of cyclic excursions of the beam ends in plastic range, while, in the second case, the plastic engagement of ductile joint components supplies the required dissipation capacity.

Even though the classical design approach of FS joints is potentially the best solution, because it is based on the good plastic behaviour of beam profiles, the rules for evaluating the joint over-strength, needed to include the effects due to both strain hardening and random material variability, are still today under discussion and the design methods for FS bolted connections able to ensure the full exploitation of the

beam plastic resources are not yet completely satisfactory. Therefore, many studies were aimed to improve the plastic rotation supply of fully welded connections either by strengthening the critical area subjected to fracture or by reducing the bending resistant area of the beam ends by properly cutting the flanges in a zone close to beam-to-column connection, commonly called Reduced Beam Section (Moore et al., 1999), (Carter and Iwankiw, 1999), (Chen et al., 1997), (Grecea et al., 2004).

An alternative design approach consists in the dissipation of the seismic input energy by means of the plastic engagement of dissipative joint components. It is important to underline that last version of Eurocode 8 (CEN, 2005), has explicitly opened the door to the use of PS joints underlining the possible location of the dissipative zones either at the beam ends or in the beam-to-column connections, but not in the columns. The seismic behaviour of semirigid steel frames with PS joints has been already examined by many authors and some proposals for the behaviour factor of semirigid PS frames have been outlined (Aribert and Grecea, 2000), (Astaneh-Asl and Nader, 1994), (Grecea et al., 2004).

Even though the above research efforts allowed to recognize that semi-rigid PS connections can lead to dissipation and ductility capacity compatible with the seismic demand, provided that they are properly designed by means of an appropriate choice of the joint component where the dissipation has to occur, detailed design procedures for the seismic design of semirigid PS frames able to guide the designer up to the complete detailing of beam-to-column joints still deserves additional investigations (Rizzano, 2015).

In recent years, growing interest from the scientific community has been addressed to equip the structure with supplemental damping devices able to dissipate a part of the seismic input energy reducing the seismic demand on the structural elements leading to structural systems able to perform adequately during the seismic events. Many works have been carried out leading to relevant results and to the development of a large number of high dissipation capacity dampers, either of friction type or of yielding type (Aiken et al., 1993), (Constantinou et al., 1998), (Christopoulos and Filiatrault, 2000), (Kim et al., 2007). However, the use of such devices has been mainly suggested within the framework of the design strategy of supplementary energy dissipation.

Starting from the above background, in this paper, the possibility of using steel frames with innovative bolted connections, already investigated in (Latour et al., 2011) and in (Montuori et al., 2015), has been analysed with the aim of providing the structure with damping devices substituting the traditional dissipative zones. These devices are located within the beam-to-column connections by means of properly detailed double split Tee joints. Therefore, the design strategy can be referred as “substitution strategy” rather than supplementary energy dissipation, because the dissipation of the earthquake input energy remains entrusted to the beam ends occurring in specifically designed dampers rather than in plastic hinges.

2. ANALYSED JOINT TYPOLOGIES

With reference to PS connections assembled by means of Tee elements, the work herein presented focuses the attention on two types of Double Split Tee beam-to-column connections conceived to improve the ductility supply and the energy dissipation capacity. The first typology, aiming to improve the cyclic response and the low cycle fatigue resistance of traditional T-stubs (Latour et al., 2011), applies, to the configuration of the T-stub flanges, the concepts usually adopted for ADAS devices. This solution is based on the use of hysteretic dampers located at the beam flange levels. The

second typology is conceived within the same framework, but using friction dampers instead of hysteretic dampers.

An important feature of the tested joints is that they are designed to provide the same flexural resistance which has been selected to provide a ratio between the design resistance of the connection and the design resistance of the connected beam equal to about 0.75. Aiming to compare the behaviour of such typologies with connections designed to assure the complete development of the plastic rotation capacity of the connected beam, also RBS connections have been investigated. To this scope, by keeping the same beam and column sections, RBS connections have been designed according to the provisions suggested in (Moore et al., 1999).

In the following sections, the structural details of the designed connections are given and their cyclic response resulting from experimental tests is presented and discussed.

3 CONNECTIONS WITH HOURGLASS SHAPED TEE ELEMENTS

The energy dissipation capacity of classical tee elements used for assembling beam-to-column connections is improved by means of an appropriate shape of the tee flange where yielding has to occur. To this aim, the basic concepts of plate elements working under double curvature, such as ADAS (Added Damping and Stiffness) devices, are exploited. The tapering of the flange plate section is carried out in the region located between the flange-to-web connection and the bolt. In particular, an hourglass shape of the T-stub flange, as already pointed out in (Latour and Rizzano, 2009), is selected to generate bending actions with a point of contra-flexure located at mid-span of the region between the bolt and the flange-to-web connection. Therefore, the yielding plates possess a shape varying according to the bending moment distribution to promote the spreading of plasticity along the whole hourglass region mentioned above.

In (Latour and Rizzano, 2009) a wide experimental analysis has been performed on dissipative T-stubs, whose flanges have been manufactured with the hourglass shape described above (Fig. 1), pointing out a significant improvement of the low cycle fatigue resistance when compared to traditional T-stubs. In (Latour M., Rizzano G., 2011), an experimental campaign on Double Split Tee Connections with hourglass T-Stubs flanges, has been developed. The design of the Double Split Tee Connection (DSTC) has been performed according to the procedure described in (Latour M., Rizzano G., 2011) by imposing that the weakest joint component has to be the bolted T-stub and designing all the other connecting elements with sufficient overstrength to remain in elastic range. The designed specimen, namely TSJ-XS-CYC07, is depicted in Fig. 1. The T-sub flange is connected to the column flange by means of four M30 bolts class 10.9 while the T-stub stem is connected to the beam flanges by means of eight M20 bolts of the same class.

The experimental tests have been performed at the structural engineering laboratory of the University of Salerno. The testing equipment is constituted by two MTS 243 hydraulic actuators adopted to apply the axial load in the column and to impose the displacement history at the top end of the cantilever beam (Fig.2). The two ends of the horizontally located column are equipped with a steel hinge and a roller bolted to a rigid base which is anchored to the laboratory strong floor by means of high strength DYWIDAG bars. The two actuators have been fixed to a rigid steel braced frame acting as reaction wall. Moreover, in order to prevent the lateral-torsional buckling of the beam, an horizontal frame has been adopted. The loading history is given in terms of drift angle, according to AISC provisions (2005). During the tests many parameters

have been monitored and acquired, in order to get the test machine history imposed by the top actuator and the displacements of the different joint components.

As expected, the behaviour of the specimen during the test evidenced the plastic engage of the T-stubs only, with the development of yielding in the dissipative elements (Fig. 1). The cyclic response obtained from experimental evidence is characterised by the stability of the hysteresis loops where minor strength degradation occurred only after 44 cycles (Fig. 3). However, some pinching of the shape of the hysteresis loops is also observed due to minor yielding and bending of the bolts. Despite of the reduced material located in the mid-span of the hourglass region, the failure of the joint occurred due to the formation of a crack in the unreduced section, located at the flange-to-web connection, and its propagation up to the complete fracture of the flange for a rotation demand equal to about 0.09 rad (Fig. 1b).

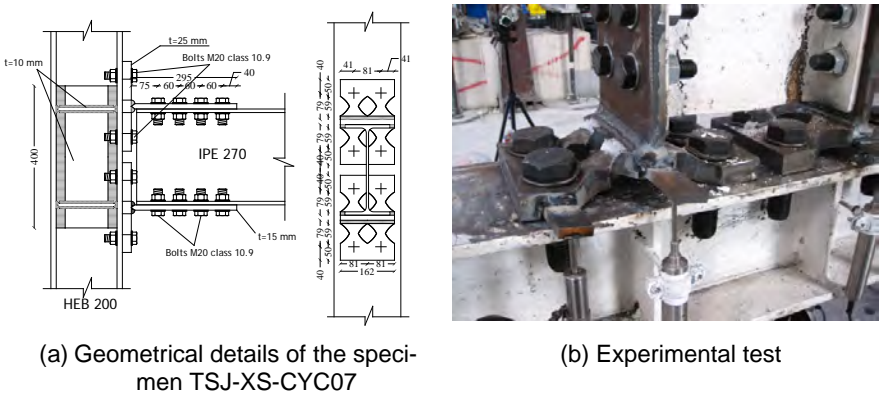


Fig. 1: Geometrical details and experimental test of dissipative DSTC with hourglass T-stub flanges

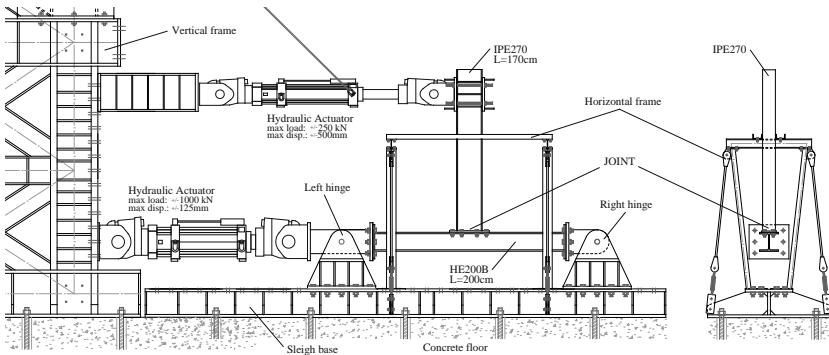


Fig. 2: Experimental test set up

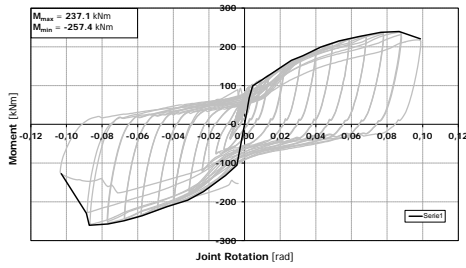


Fig. 3: Cyclic response of the specimen TSJ-XS-CYC07

4 DOUBLE SPLIT TEE CONNECTIONS WITH FRICTION DAMPERS

Friction dampers dissipate the seismic input energy through the slippage of two surfaces in contact on which an adjustable normal action is applied. Obtained hysteresis cycles are similar to that of elastic-plastic dampers with high initial stiffness. This is a great advantage of friction devices, as they can be designed aiming to remain in elastic range under the load combinations corresponding to gravity loads only and to SLS for earthquake actions and to slip under load combinations corresponding to ULS for seismic actions. In this way, the friction devices can be used to work as displacement reducers under SLS conditions and to dissipate the seismic input energy at ULS.

In order to equip beam-to-column connections with friction dampers, double split tee connection have been designed as depicted in Fig. 4 by introducing friction pads between the beam flanges and the web of the tee elements. Rubber friction material has been used. The friction material is also reinforced by means of a thin fiber mesh. The bolts are preloaded with a torque equal to 450 kNm. The length of the slot has been calibrated according to a maximum joint rotation equal to 0.07 rad. The experimental test of the specimen TSJ-F2-CYC09 is depicted in Fig. 5. In agreement with the design criteria, the test does not exhibited any involvement of the joint components in plastic range and, as a consequence, any joint damages. This leads to stable cycles with a moderate hardening behaviour due to the increase of local stresses caused by the beam rotation (Fig. 6).

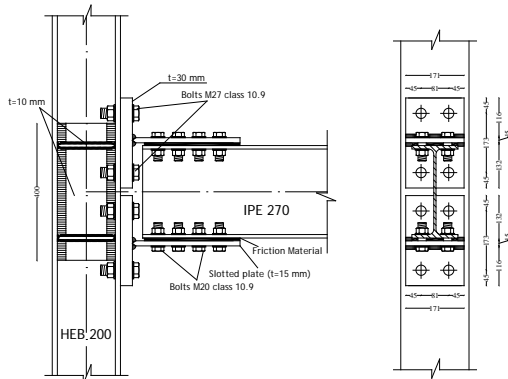


Fig. 4: Geometrical details of TSJ-F1-CYC09

The amount of the energy dissipation capacity of the DSTC equipped with friction dampers can be calibrated by properly detailing the beam end. In fact, in order to increase the energy dissipation capacity it is possible to increase the sliding resistance by means of additional preloaded bolts or to raise the joint moment corresponding to the knee of the moment-rotation curve by increasing the lever arm by means of an haunch at the beam end. It is important to underline that the dissipative joints with friction dampers, after inelastic cyclic rotations up to 0.06 rad, remain without any damage both of the connected members and of the connecting elements.

Comparing the cyclic response of DSTC with hourglass T-stub flanges (Fig. 3) with the response of DSTC with friction pads (Fig. 6), it can be recognised a significant hardening behaviour of the first joint which leads to a greater energy dissipation capacity. However, it has to be underlined that, from a design point of view, the over-strength due to the hardening behaviour of DSTC with hourglass T-stub flanges leads, for this joint typology, to more severe design conditions for the other joint components which have to remain in elastic range.



Fig. 5: Arrangement of DSTC with friction material

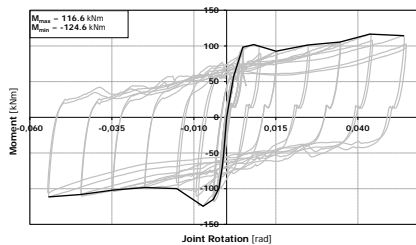


Fig. 6: Moment-Rotation Curves of DSTC equipped with friction dampers

5. FULL STRENGTH JOINT WITH REDUCED BEAM SECTION

The third specimen is a full strength extended endplate connection, so that it is aimed to investigate the energy dissipation capacity of the connected beam. However, aiming to obtain the same flexural resistance of previous specimens, the reduced beam section (RBS) strategy, called also “dog bone”, has been adopted. The three parameters

to be designed, i.e. the distance of the reduced section zone from the face of the column flange, the length of the reduced section zone, and the flange reduction width (Fig. 7), have been designed following the procedure suggested in Moore et al. (1999).

The displacements recorded by LVDT confirmed that, according to the design criteria, the connection component contribution is negligible. Yielding has been concentrated in the reduced beam section zone. The failure mechanism is the one typical of steel members with I section shape. In particular, after yielding of flanges and web and the attainment of the maximum flexural resistance, flange local buckling occurs accompanied by beam web buckling due to compatibility between flange and web out-of-plane displacements (Fig. 7). The shape of the cycles of the whole joint is, as well known from the technical literature, wide and stable, guaranteeing a good energy dissipation capacity and significant plastic rotation supply (Fig. 8).

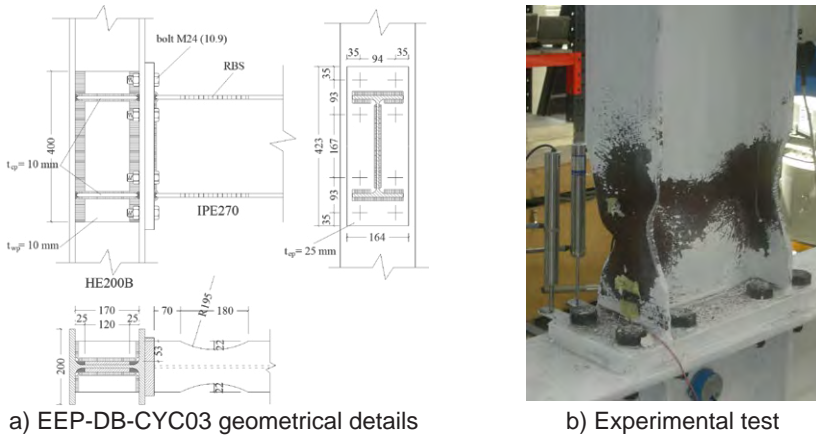


Fig. 7: Geometry of the specimens

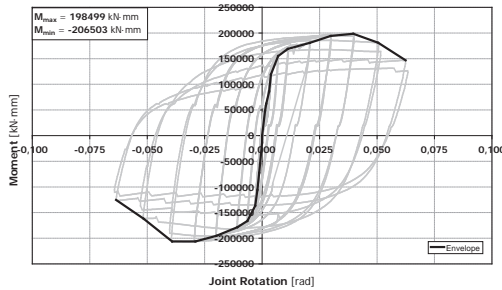


Fig. 8: Moment-Rotation Curves of EEP-DB-CYC03 joint

6. SEISMIC RESPONSE OF STEEL FRAMES WITH ANALYSED JOINTS

In order to analyse the potentialities of the proposed alternative solutions of DSTC, the peak ground acceleration values leading to failure have been evaluated by means of Inelastic Dynamic Analyses (IDA), performed by SeismoStruct 3.0 software, with reference to the 3bays-6storey MR-Frame depicted in Fig. 9, equipped with the joint typologies previously described. The joints have been modelled as rotational inelastic springs at the beam ends characterized by a moment-rotation law accounting for the

stiffness and strength degradation and the pinching phenomena. The hysteretic joint behaviour has been modelled by adopting a Smooth Hysteretic Model (SHM) which allowed a better numerical convergence during the analyses with respect to the Polynomial Hysteretic Model. The parameters of the hysteretic moment-rotation law of the analysed joints have been calibrated by means of best fitting between the experimental curve and the numerical one obtained. Fig.10 shows the good accuracy of the calibrated models.

The member sections of the analysed MR-Frame have been preliminarily dimensioned under design gravity load q , assumed equal to 25.20 kN/m, and by imposing a design value of the beam plastic moment approximately equal to $qL^2/8$, being L the beam span. The column sections have been selected by adopting a rigorous design procedure aimed to guarantee a collapse mechanism of global type (Montuori et al., 2015). In order to assure a frame structural response consistent with the joint rotational behaviour obtained from experimental tests, the values of column and beam material mechanical properties adopted in IDA analyses are assumed equal to those measured in testing beam-to-column sub-assemblages (Iannone et al., 2011). A bilinear elastic-perfectly plastic model characterized by an hysteretic behaviour without any degradation have been adopted for beam and column elements.

The IDA analyses have been performed considering 10 earthquake records selected from PEER database and assuming mass and stiffness proportional damping equal to 3% of the critical value. All accelerograms have been preliminarily scaled to the value of the spectral acceleration corresponding to the fundamental period of vibration of the structure, equal to $T_1=1.6$ sec for frames with EEP-DB-CYC03 or TS-M2-460-CYC09 connections (Fig. 11) and equal to $T_1=1.76$ sec for frame with TSJ-XS-CYC07 connections.

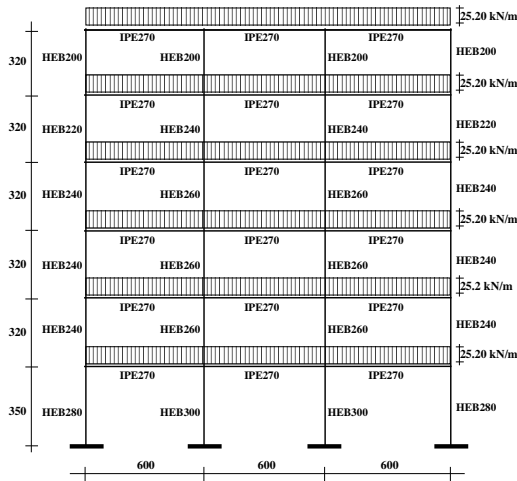
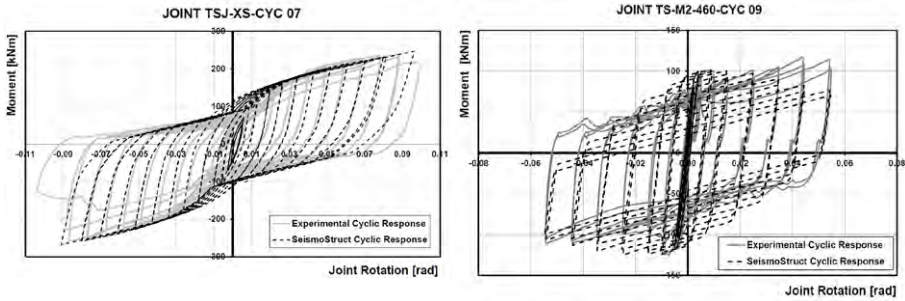
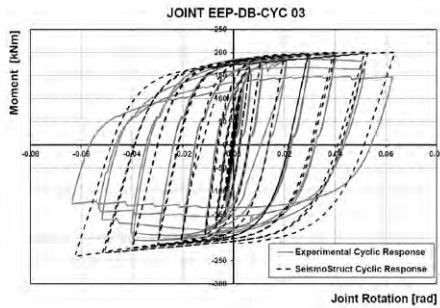


Fig. 9: Analyzed frame



a) Calibration of SHM for the joint TSJ-XS-CYC07

b) Calibration of SHM for the joint TS-M2-460-CYC09



c) Calibration of SHM for the joint EEP-DB-03

Fig. 10: Comparison between the calibrated models and the experimental curves

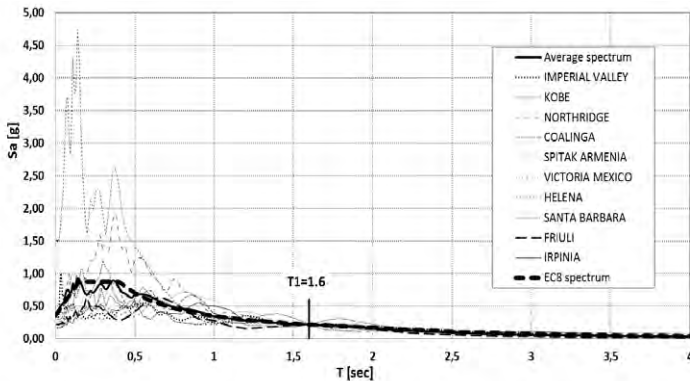


Fig. 11: Earthquake records scaled to the fundamental period of vibration of the structure

The IDA analyses have been performed increasing progressively the spectral acceleration up to achievement of the ultimate condition corresponding to the attainment of the experimental ultimate value of the plastic rotation supply equal to 0.09 rad for

the frame with TSJ-XS-CYC07 connections and equal to 0.06 rad for EEP-DB-CYC03. Conversely, as MR-Frames with TS-M2-460-CYC09 connections practically do not have any limitation in terms of rotational capacity provided that the length of the slotted holes for the sliding of bolts is sufficient, a target maximum interstorey drift equal to 0.1, according to FEMA (2000), has been adopted as ultimate condition against collapse prevention limit state.

The results of IDA analyses are depicted in Fig. 12 and summarized in Table 1. It can be observed that both frames equipped with hourglass shaped tee elements and with friction dampers show a seismic performance better than that of the frame equipped with RBS connections, testifying the good potentialities of the dissipative joints which could represent a more suitable solution for steel frames under destructive earthquakes.

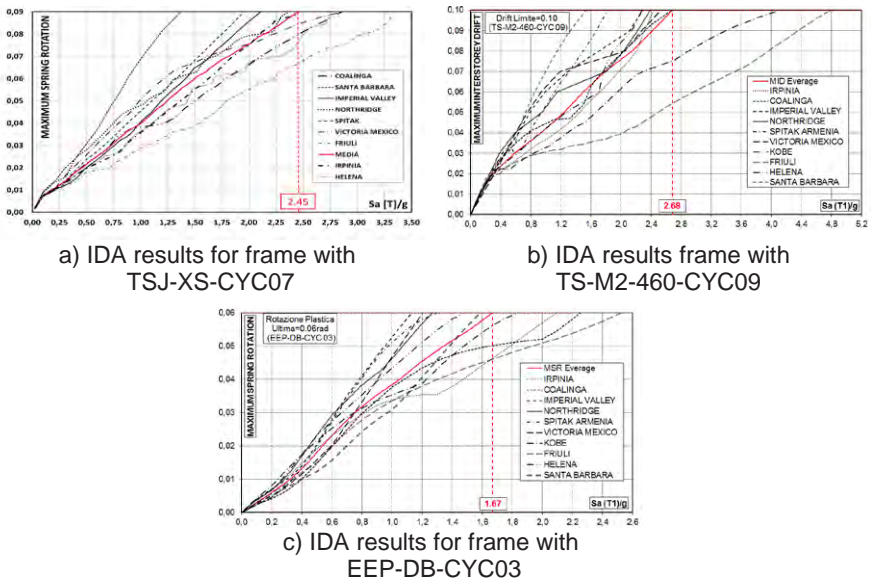


Table 1 – Spectral acceleration values leading to the attainment of the ultimate condition

Earthquake	EEP-DB-CYC03	TSJ-XS-CYC07	TS-M2-460-CYC09
	[g]	[g]	[g]
Coalinga	2.25	2.86	2.67
Imperial Valley	1.13	2.11	2.29
Northridge	1.27	2.37	2.39
Spitak Armenia	1.30	1.96	1.82
Victoria Mexico	1.20	2.88	2.53
Kobe	1.84	-	4.11
Friuli	2.53	3.31	4.78
Helena	1.48	2.76	2.28
Santa Barbara	1.59	1.37	1.54
Irpinia	2.09	2.40	2.43
Average Value	1.67	2.45	2.68

7. CONCLUSIONS

With reference to the seismic behaviour of steel frames with partial strength joints, in this paper two dissipative solutions for Double Split Tee Connections have been proposed with the aim to increase the energy dissipation capacity of classic DSTC. The experimental analysis of the proposed solutions, one belonging to yielding devices and other one to friction devices, allows to underline the following main aspects:

- a. the dissipative Double Split Tee Connections with hourglass shape of the T-stub flanges shows a greater hardening behaviour with respect to the DSTC equipped with friction dampers and, as a consequence, a greater energy dissipation capacity; simultaneously, this leads to a more severe design conditions for the joint components which have to remain in elastic range;
- b. the dissipative Double Split Tee Connections equipped with friction dampers are characterized by stable cycles with low hardening; the amount of the energy dissipation capacity of this connection can be calibrated by properly detailing the beam end by increasing the sliding resistance and/or the lever arm;
- c. the improvement of the number of cycles to failure provided by the dissipative joints, both with hourglass flange shape and with friction pads, is very significant;
- d. the dissipative joints with friction dampers, after inelastic cyclic rotations up to 0.06 rad, remain without any structural damage;
- e. the Incremental Dynamic Analyses performed on a 3bay-6storey steel frame equipped with dissipative Partial Strength Joints constituted by Double Split Tee Connections with friction dampers or Double Split Tee Connections with hourglass shape of the T-stub flanges show a significant improvement of the ultimate value of PGA for both solutions.

REFERENCES

- Aiken ID, Clark PW, Kelly JM. (1993), "Design and Ultimate-Level Earthquake Tests of a 1/2.5 Scale Base-Isolated Reinforced-Concrete Building". *Proceedings of ATC-17-1 Seminar on seismic Isolation, Passive Energy Dissipation and Active Control*. San Francisco. California.
- AISC, (2005): "Seismic Provisions for Structural Steel Buildings", *American Institute for Steel Construction*, Chicago.
- Aribert, J.M., Grecea, D., (2000), "Numerical investigation of the q-factor for steel frames with semi-rigid and partial-strength joints", *Proc. of the Third International Conference STESSA 2000*, Montreal, August 21-24.
- Astaneh-Asl, A. Nader, N., (1994), "Proposed code provision for seismic design of steel semi-rigid and rigid frames", *Proc. of the 5th U.S. National Conference of Earthquake Engineering*, EERI, Chicago.
- Carter, C.J. and Iwankiw, N. (1999), "Improved Ductility in Seismic Steel Moment Frames with Dogbone Connections", *Journal of Constructional Steel Research*, Vol. 46, No. 1-3, Paper No. 253.
- CEN, EN 1998-1-1, (2005), Eurocode 8: Design of structures for earthquake resistance - Part 1: General rules, seismic actions and rules for buildings, *European committee for standardization*.

- Chen, S.J., Chu, J.M., Chou, Z.L. (1997) "Dynamic Behaviour of Steel Frames with Beam Flanges Shaved Around Connection", *Journal of Constructional Steel Research*, Vol. 42, No. 1, pp. 49-70.
- Christopoulos C, Filiatrault A. (2000), "Principles of Passive Supplemental Damping and Seismic Isolation". *IUSS PRESS. Pavia. Italy.*
- Constantinou M.C., Soong T.T., Dargush, G.F. (1998), "Passive Energy Dissipation Systems for Structural Design and Retrofit". *Multidisciplinary Center for Earthquake Engineering Research*, University at Buffalo, State of New York.
- FEMA-350 (2000), "Recommended Seismic Design Criteria for New Steel Moment Frames Buildings", Prepared by *SAC Joint Venture for the Federal Emergency Management Agency*, Washington DC.
- Grecea, D., Dinu, F., Dubina, D. (2004), "Performance criteria for MR steel frames in seismic zones", *Journal of Constructional Steel Research*, Vol. 60, pp. 739-749.
- Kim Y, Oh S., Ryu H., Kang C. (2007), "Hysteretic behaviour of moment connections with energy absorption elements at beam bottom flanges". *ICAS 2007*, Oxford.
- Iannone F., Latour M., Piluso V., Rizzano G. (2011), "Experimental Analysis of Bolted Steel Beam-to-Column Connections: Component Identification", *Journal of Earthquake Engineering*, Vol.. 15 pp.214-244.
- Latour M., Piluso V., Rizzano G. (2011), "Experimental analysis of innovative dissipative bolted Double Split Tee beam-to-column connections", *Steel Construction*, Vol. 4, June.
- Latour M., Rizzano G. (2009), "Monotonic Modelling, Cyclic Behaviour and Fatigue Life of Dissipative T-stubs", *ICASS 2009*, Hong Kong.
- Latour M., Rizzano G. (2011), "Cyclic behaviour of Dissipative Double Split Tee Connections", *Eurosteel 2011*, Budapest.
- Montuori, R., Nastri, E. and Piluso, V. (2015), "Advances on the theory of Plastic Mechanism Control: Close Form solution for MR Frames", *Earthquake Engineering & Structural Engineering*, vol. 4, pp. 1035-1054, 2015.
- Montuori R., Nastri E., Troisi M. and Piluso V. (2015), "Influence of the Cyclic Behaviour of Beam-to-Column Connection on the Seismic Response of Regular Steel Frames", *Proceedings of the XXV CTA*, Salerno, September.
- Moore, K.S., Malley, J.O., Engelhardt, M.D. (1999), "Design of reduced Beam Section (RBS) Moment Frame Connections", *AISC Structural Steel Educational Council*, Moraga, CA.
- Rizzano, G. (2015), "New strategies in the seismic design of bolted beam-to-column connections", Key Note at X Congresso de La Construcao Metalica e Mista, Coimbra, 26-27 november, pp. 11-44.

PREQUALIFICATION TESTS ON BOLTED BEAM-TO-COLUMN JOINTS WITH HAUNCHES

Aurel Stratan, Cosmin Maris, Cristian Vulcu, Dan Dubina, Calin Neagu
*Politehnica University of Timisoara, Dept. of Steel Structures and Structural Mechanics
Timisoara, Romania*

aurel.stratan@upt.ro; cosmin.maris@upt.ro; cristian.vulcu@upt.ro;
dan.dubina@upt.ro; calin.neagu@upt.ro

ABSTRACT

Modern seismic design codes require that the seismic performance of beam-to-column connections in steel moment resisting frames be demonstrated through experimental investigations, which often prove to be expensive and time-consuming. A solution to this problem is the prequalification of typical connections for the design practice, which is common in U.S. and Japan, but currently is missing in Europe. For this reason, a European research project entitled EQUALJOINTS (European pre-QUALified steel JOINTS), is currently underway and aims at seismic prequalification of several beam-to-column connection typologies common in the European practice. The current paper outlines the experimental program performed on 24 bolted extended end-plate connections with haunches investigated at the Politehnica University of Timisoara in the framework of EQUALJOINTS project. The parameters of the experimental program consist in beam/column size, haunch geometry, joint configuration (single-sided and double-sided), panel zone strength, loading protocol (monotonic and cyclic) and beam overstrength.

1. INTRODUCTION

The use of pre-qualified joints is a common practice in U.S. (ANSI/AISC 341-10). Guidelines for design of connections in steel structures are also available in Japan (AIJ-2012). Nevertheless, the standard joints pre-qualified according to codified procedures in U.S. and Japan cannot be extended to Europe, due to differences in materials and section shapes. Moreover, the beam-to-column joint types usually adopted in U.S. and Japan are not commonly used in Europe. As a result, the existing scientific and technical background on pre-qualification may not be directly extended to European context. For this reason, a European research project entitled EQUALJOINTS – European pre-QUALified steel JOINTS (Landolfo et al. 2013), is currently underway and aims at seismic pre-qualification of several beam-to-column connection typologies common in the European practice. The research activities focus on the standardization of design and manufacturing procedures based on different geometric and mechanical parameters of selected joint typologies. Hence, a large experimental program supported

by theoretical and numerical analyses is proposed to provide reliable standard joints that can be easily used by designers.

The current paper outlines the results of experimental tests and numerical simulations on bolted extended end-plate connections with haunches that are investigated at the Politehnica University of Timisoara in the framework of EQUALJOINTS project.

2. EXPERIMENTAL PROGRAM

The aim of the experimental program is to investigate the behavior of bolted connections with haunches under monotonic and cyclic loading. A set of 24 beam-to-column joint assemblies are tested in order to evaluate different parameters that are specific for this type of connection. Single sided and double sided joints were selected from moment resisting frames (MRF) as illustrated in Figure 1. Member sizes were obtained by designing a set of MRFs according to EN 1993-1-1 (2005) and EN 1998-1 (2004). The buildings were representative of low (three storeys) and mid-rise (6 storeys) structures in Europe, with the span of 6 and 8 m. High ductility class (DCH according to EN 1998-1) was adopted, while the seismic loading was characterized by response spectrum type 1 and soil type C. Two seismic hazard levels were considered, with the design peak ground acceleration of 0.35 g and 0.25 g. An interstorey drift limitation of 0.075 times the storey height was considered. Design of MRFs was governed by serviceability and second order effects limitation requirements. Beam size ranged between IPE330 and IPE750, and were designed in S355 steel. Taking into account the limitations of the testing equipment, and the need to cover a full range of representative beam cross-sections, three beam sizes were selected for the pre-qualification program: IPE360, IPE450 and IPE600.

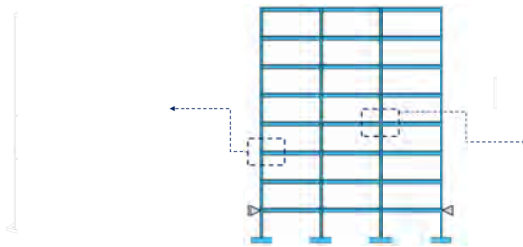


Figure 1. Single-sided and double-sided joints selected from MRF structure

The experimental program, summarized in Table 1, contains three groups of specimens:

- Group 1: full strength & rigid joint, shallow haunch (35° angle), strong web panel;
- Group 2: full strength & rigid joint, steep haunch (45° angle), strong web panel;
- Group 3: full strength & semi-rigid joint, shallow haunch (35° angle), balanced web panel.

Table 1: Experimental program on bolted beam-to-column joints with haunches

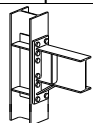
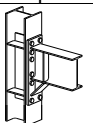
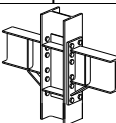
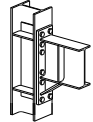
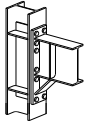
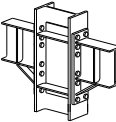
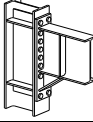
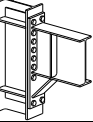
Group 1: single-sided joints		Group 2: single-sided joints		Group 3: double-sided joints	
	EH1-TS-35 IPE 360 HEB 280		EH1-TS-45 IPE 360 HEB 280		EH1-XB-35 IPE 360 HEB 340
	EH2-TS-35 IPE 450 HEB 340		EH2-TS-45 IPE 450 HEB 340		EH2-XB-35 IPE 450 HEB 500
	EH3-TS-35 IPE 600 HEB 500		EH3-TS-45 IPE 600 HEB 500		

Table 2: Description of joint configuration and labelling

Gr.	Conn. type	Joint config.	Haunch geom.	Load protoc.	Beam/column depth		
					1	2	3
1	EH	TS	35°	M	-	EH2-TS-35-M	-
	EH	TS	35°	C1	EH1-TS-35-C1	EH2-TS-35-C1	EH3-TS-35-C1
	EH	TS	35°	C2	EH1-TS-35-C2	EH2-TS-35-C2	EH3-TS-35-C2
	EH	TS	35°	CA	EH1-TS-35-CA	EH2-TS-35-CA	EH3-TS-35-CA
	EH	TSO	35°	C	EH1-TSO-35-C	-	EH3-TSO-35-C
2	EH	TS	45°	M	-	EH2-TS-45-M	-
	EH	TS	45°	C1	EH1-TS-45-C1	EH2-TS-45-C1	EH3-TS-45-C1
	EH	TS	45°	C2	EH1-TS-45-C2	EH2-TS-45-C2	EH3-TS-45-C2
	EH	XB	35°	M	-	EH2-XB-35-M	-
3	EH	XB	35°	C1	EH1-XB-35-C1	EH2-XB-35-C1	-
	EH	XB	35°	C2	EH1-XB-35-C2	EH2-XB-35-C2	-

Note:

- Connection type: Haunched beam to column connection (EH)
- Joint configuration and panel zone: exterior joint with strong column web panel (TS), exterior joint with strong column web panel/strong beam (TSO), interior joint with balanced column web panel (XB)
- Haunch geometry: angle of haunch 35° (35), angle of haunch 45° (45)
- Loading protocol: monotonic (M), cyclic (C1, C2), alternative cyclic protocol (CA)

Group 1 and Group 2 serve for qualifying two alternative haunch geometries (lower and upper limit of reasonable haunch angle) for considered range of beam size. Group 3 investigates joints with balanced panel zone strength, which also leads to a semi-rigid classification of the joint (connection and panel zone). Two supplementary web plates are used for the joints of Group 1 and Group 2, while for Group 3 only one supplementary web plate is used. Additionally, larger column depth increases the range of prequalified column sizes. The complete parameters considered within the experimental program are: loading protocol (monotonic and cyclic), member size, single-sided and double sided connections, strong panel zone / balanced panel zone,

strong beam and haunch geometry. Table 2 makes an overview of the parameters considered within the experimental program and describes the labelling of the specimens. As can be observed, the experimental program covers 24 tests on joint specimens, out of which three tests are performed under monotonic loading: EH2-TS-35-M, EH2-TS-45-M, and EH2-XB-35-M, in order to aid in calibration of finite-element models. All other tests are performed using cyclic loading. The ANSI/AISC 341-10 (2010) loading protocol is adopted for most of tests. Three of the cyclic tests (one for each beam size – CA series) are performed using a cyclic loading protocol developed within the EQUALJOINTS project. The latter is similar to the ANSI/AISC 341-10 protocol, but has less low-amplitude cycles. Two joints (the TSO series) had the same geometry and connection characteristics with the corresponding TS joints, but the beam was fabricated as a built-up member using S460 steel grade, in order to simulate a larger overstrength of the beam, and possibly trigger failure in the connection. These tests are not meant to serve directly for pre-qualification, but to obtain information on the characteristics of the bolted connection.

The analytical design procedure of the bolted connections with haunches was developed based on the component method implemented in EN 1993-1-8 (2005). The design of the joints was performed considering the formation of the plastic hinge in the beam, at the end of the haunch. Further, the components of the joint were designed for an equal or higher capacity in comparison to the fully yielded and strain hardened plastic hinge. Furthermore, based on pre-test numerical investigations (Maris et al. 2015), the assumptions considered in design were as follows: (i) the active bolt rows were those situated near the flange in tension, (ii) the compression center was located at a distance equal to 60% of the haunch depth measured from the bottom flange of the beam.

3. EXPERIMENTAL INVESTIGATIONS

3.1. Test set-up and instrumentation

The experimental test set-up (conceptual scheme and illustration) for the bolted beam-to-column joints is presented in Figure 2. A hydraulic actuator connected at the tip of the column served as loading device. The support at the bottom end of the column was pinned (horizontal and vertical displacements were restrained), while the tip of the beam was connected to a vertical link pinned at both ends – and therefore the vertical displacement at the tip of the beam was restrained, but the horizontal displacement was free. The out of plane deformations of the beam were restrained at both top and bottom flange near the support and at distance of 1.25 times the beam height from the end of the haunch.

The global instrumentation consisted in measuring: the force in the actuator, displacement at the tip of the column, horizontal and vertical displacement at column base and tip of the beam. The local instrumentation was aimed at measuring the deformations within the dissipative zone, connection, and column web panel. Digital image correlation technique was also used in order to investigate the distribution of strains in the beam and column web panel.

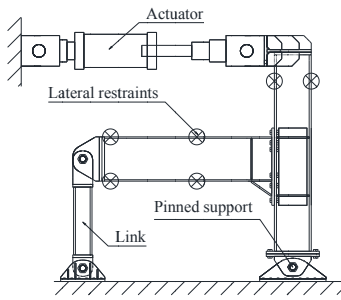


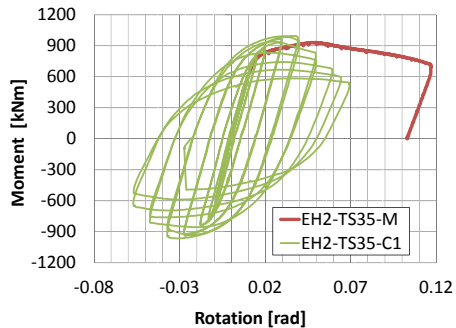
Figure 2. Experimental test set-up – conceptual scheme and illustration

3.2. Test results

At the time of writing this paper, the tests are still under way, 15 out of 24 specimens being already tested. The primary test results for typical specimen (EH2-TS-35-C1) are shown in terms of moment-rotation curve (bending moment computed at column face and chord rotation computed at column centreline) and illustration of the failure mode. Figure 3 shows the response of EH2-TS-35-C1 joint assembly, as well as the comparison of the moment-rotation curve in comparison with the one of the corresponding specimen tested monotonically (EH2-TS-35-M). The yielding was initiated in the beam flanges near the ending of the haunch, and was followed by large plastic deformations – local buckling of flanges and web. No damage was observed within end-plate and column web panel. Consequently, the plastic mechanism considered in the design was confirmed, i.e. formation of the plastic hinge in the beam. The rotation capacity, defined at a drop of 20% of the maximum moment, was 0.05 rad. Similar results were obtained for other specimens.



(a)



(b)

Figure 3. Response of EH2-TS-35-C1 joint assembly: illustration of failure mode (a), and moment-rotation curve, in comparison with the monotonic one EH2-TS-35-M (b)

An important parameter in the design of the connection is estimation of the expected moment in the connection, corresponding to yielded and fully strain hardened plastic hinge in the beam. According to experimental observations, the plastic hinge was considered to be located at a distance equal to half the beam depth from haunch end. The expected moment at the column face was computed as:

$$M_{j,Ed} = \gamma_{sh} \cdot \gamma_{ov} \cdot (M_{pl,Rd} + V_{Ed} \cdot s_h)$$

where $M_{pl,Rd}$ is the plastic moment resistance of the beam; V_{Ed} is the corresponding shear force in the beam; s_h is distance from the column face to the plastic hinge (length of the haunch plus half of the beam depth); γ_{ov} is the material overstrength; and γ_{sh} is a factor accounting for strain hardening, and defined as the ratio between the peak value of the bending moment and the plastic resistance. The last factor was defined as in ANSI/AISC 358 (2011):

$$\gamma_{sh} = (f_u + f_y) / (2 \cdot f_y) \leq 1.20$$

Table 3 shows a comparison between the expected moment in the connection ($M_{j,Ed}$), computed using measured steel characteristics, and the experimental peak moment ($M_{j,Ed, test}$). A very good correlation between the two could be observed.

Table 3: Comparison between maximum bending moment at column face (test under cyclic loading) and analytical value of bending moment

Cross section	EH1-TS (IPE360 beam)		EH1-TS (IPE450 beam)	
Bending moment	hogging	sagging	hogging	sagging
$M_{j,Ed}$ [kNm]	588.1	588.1	1003.2	1003.2
$M_{j,Ed, test}$ [kNm]	578.0	579.1	997.4	974.6
$M_{j,Ed, test} / M_{j,Ed}$	0.98	0.98	0.99	0.97

4. NUMERICAL INVESTIGATIONS

In addition to the experimental program, numerical investigations were performed. The pre-test numerical investigations were realized with the aim to obtain an accurate prediction for response of the beam-to-column joint assemblies. The numerical models of the joints developed at this stage were further used for the calibration based on experimental data. The numerical simulations were performed with the finite element modelling software Abaqus (2014).

4.1 Calibration of the material model

Based on the tensile tests conducted on material samples, a set of numerical simulations were performed for the calibration of the material model. In particular, the engineering stress-strain curve obtained from the test was computed into the true stress – true strain curve using equation C.1 from EN 1993-1-5 (2015). Beyond the ultimate strength, trial values needed to be used for stress and strain in order to obtain a good

comparison with the experimental force-displacement curve, see Figure 4. The calibration procedure was used for the following parts: beam flange and web (IPE450 – S355), end-plate (S355), column flange and web (HEB340 – S355), plates for reconstructed beam (IPE360 / IPE600 – S460). The detailed information regarding the values of the material model for each part can be found in Lee (2015). Additionally, the material properties for bolts (see Maris et al. 2015), were calibrated based on data from a past project (Dubina et al. 2015), in which experimental investigations were performed on T-stubs.

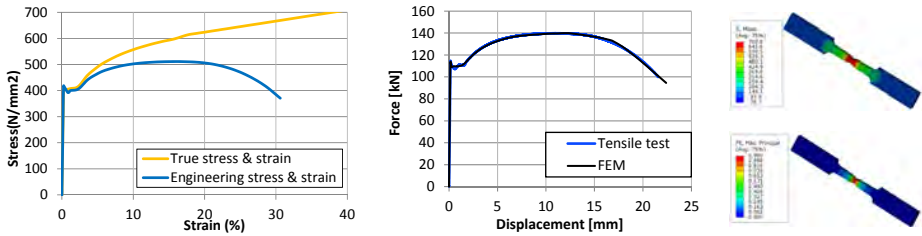


Figure 4. Calibration of the material model (e.g. IPE450 beam flange): engineering and true stress/strain, test vs. simulation, FE model of steel samples illustrating the failure mode

4.2 Calibration of the joint model

The modelling procedure of the beam-to-column joint models is further described. All the components of the steel haunched joint were modelled using solid linear hexahedral elements of type C3D8R. The nominal geometry was used, except for the thickness of some components (e.g. beam, end-plate). A dynamic explicit type of analysis was used due to large contact surfaces within joint models. The tie constraint was used for welded connections, while the contact interaction between different parts of the joint assembly was defined using a normal (hard contact) and tangential (penalty with friction) interaction law. It is to be mentioned that the out-of-plane support system was modelled through a set of elements placed at the level of the beam flanges according to the test set-up, and in addition a small gap was considered based on the observations from the test. Frictionless contact between beam flanges and the lateral support system was applied. The boundary conditions were adopted according to the test set-up (see Figure 5a), i.e. column base was pinned, a double-hinged link was connected to the tip of the beam, and the load was applied through a displacement control at the tip of the column. The pre-stressing of bolts was performed by defining and linking a connector to the bolt nut, respectively bolt rod, and specifying a connector force. Figure 5b illustrates the mesh discretization of the joint assembly.

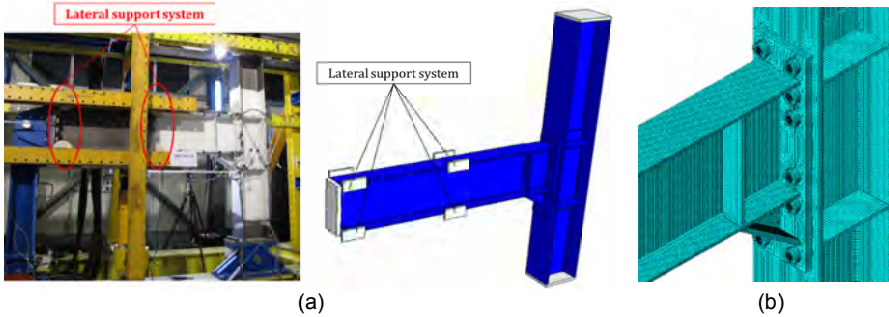


Figure 5. Beam-to-column joint model (EH2-TS35-M): (a) lateral support system, (b) mesh discretization of joint assembly

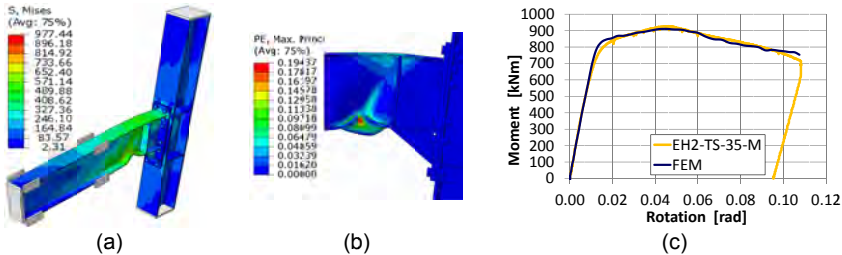


Figure 6. Outcomes from the calibration of EH2-TS-35-M joint model: (a) von Mises stress distribution, (b) plastic strain / failure mechanism, (c) comparison between test and simulation in terms of moment-rotation curve

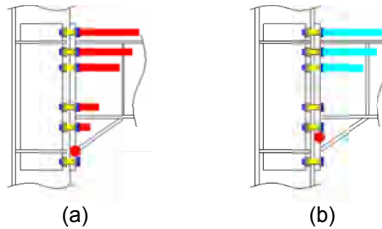


Figure 7. Distribution of bolt forces and compression center: according to EN 1993-1-8 (a) and as observed from numerical simulations (b).

From the calibration process, a set of numerical models were obtained which were capable of reproducing with a good accuracy the response of the joints considering the moment-rotation curve and the failure mechanism, see Figure 6. Consequently, the comparison between test and simulation is further shown in terms of moment rotation curve (with the rotation computed at column centreline, and the bending moment computed at column face). Furthermore, the response of the EH2-TS-35-M beam-to-column joint configuration is presented in terms of stress distribution (von Mises) and plastic strain. As can be observed in Figure 6, the plastic hinge developed

in the beam near the haunch, while the connection zone experienced only elastic deformations. Additionally, the numerical investigations confirmed the yielding sequence observed during the test, namely yielding of the top and bottom beam flanges close to the haunch, followed by large plastic deformations of flanges and web (elongation / local buckling).

Based on the outcomes of the calibrated joint models (with hogging loading), respectively the same joint models subjected to sagging loading, it was observed that only the first three bolt rows are active in resisting the moment in the connection, with the major contribution given by the two are those situated above and below the flange in tension. The design assumption in EN 1993-1-8 (2015) is based on a plastic distribution of bolts, and assumes that all bolts above compression center are active (Figure 7).

Regarding the compression center, it was observed that under hogging loading, the compression center is situated at the haunch flange (as assumed by EN 1993-1-8 (2015)) only in the elastic range. In the plastic range the compression center moves up (Figure 7), changing for different values of loading. Under hogging loading (elastic range), the active haunch height was 100% for the 35° angle haunch, respectively 75% for the 45° angle haunch. Corresponding to yielding and maximum capacity, the active haunch height was ≈80% for the 35° angle haunch, respectively ≈55% for the 45° angle haunch. Under sagging moment, the usual assumption of the position of the compression center at the beam flange was confirmed. Consequently, the actual position of the compression center is not stable, and depends on: load level, haunch angle.

5. CONCLUSIONS

Experimental investigations evidenced a good response of the bolted beam-to-column joints with haunches. The plastic mechanism considered in design was confirmed, i.e. formation of the plastic hinge in the beam. The experimental data from material and joint tests were further used for the calibration of the material and joint models. The comparison between test and simulation evidenced a very good correlation in both moment-rotation curve and failure mechanism (development of plastic hinge in the beam). This allowed for a better understanding of the joint response. Important differences were observed with respect to current design approach of the haunched connection in EN 1993-1-8.

6. ACKNOWLEDGEMENT

The research leading to these results has received funding from the European Community's Research Fund for Coal and Steel (RFCS) under grant agreement no RFSR-CT-2013-00021 "European pre-qualified steel joints (EQUALJOINTS)". This support is gratefully acknowledged.

REFERENCES

- Abaqus (2014). Abaqus Analysis User's Manual, Version 6.14. Abaqus, Inc., Dassault Systèmes Simulia Corp., Providence, RI, USA.
- AIJ-2012. (2012). Recommendation for Design of Connections in Steel Structures. Architectural Institute of Japan.
- ANSI/AISC 341-10. (2010). Seismic Provisions for Structural Steel Buildings. American Institute of Steel Construction.
- ANSI/AISC 358-10. (2011). Prequalified Connections for Special and Intermediate Steel Moment Frames for Seismic Applications, Including Supplement No. 1. American Institute of Steel Construction.
- Dubina D., et al. (2015). High Strength Steel in Seismic Resistant Building Frames (HSS-SERF). Final Report. Directorate-General for Research and Innovation, Unit D.4 – Coal and Steel, RFCS Publications, European Commission, ISBN 978-92-79-44081-6, doi:10.2777/725123.
- EN 10034 (1993). Structural Steel I and H Sections – Tolerances on Shape and Dimensions. CEN – European Committee for Standardization.
- EN 1993-1-1 (2005). Eurocode 3: Design of steel structures - Part 1-1: General rules and rules for buildings. European Committee for Standardisation (CEN).
- EN 1993-1-5 (2005). Eurocode 3: Design of steel structures - Part 1-5: Plated structural elements. CEN – European Committee for Standardization.
- EN 1993-1-8 (2005). Eurocode 3: Design of steel structures - Part 1-8: Design of Joints. CEN – European Committee for Standardization.
- EN 1998-1. (2004). Eurocode 8: Design of structures for earthquake resistance - Part 1: General rules, seismic actions and rules for buildings. European Committee for Standardisation (CEN).
- Landolfo R., et al. (2013). European pre-QUALified steel JOINTS – EQUALJOINTS, RFSR-CT-2013-00021, website: <http://dist.dip.unina.it/2013/12/09/equaljoints/>
- Lee K. (2016). Numerical investigation on seismic behaviours of steel haunch connections, (Dissertation/Erasmus Mundus Programme) Politehnica University of Timisoara. (http://ct.upt.ro/suscos/files/2014-2016/Keunwoo_Lee_Dissertation.pdf)
- Maris C., Vulcu C., Stratan A., Dubina D. (2015). “Experimental program and numerical simulations of bolted beam-to-column joints with haunches”. Proceedings of the 8th International Conference on Behaviour of Steel Structures in Seismic Areas, Shanghai, China.

EUROPEAN QUALIFICATION OF SEISMIC RESISTANT STEEL BOLTED BEAM-TO-COLUMN JOINTS: THE EQUALJOINTS PROJECT

Raffaele Landolfo
University of Naples Federico II, Department of Structures for Engineering and
Architecture
landolfo@unina.it

Abstract

Nowadays, prequalification criteria for seismic resistant beam-to-column joints are missing in Europe. In addition, specific requirements and design rules for these joints are not provided by Eurocodes, which gives rules only for non-seismic joints, even though dissipative joints are allowed by EN1998-1, provided that their effectiveness is verified by testing. Obviously this approach results in expensive and time-consuming design, due to the lack of reliable analytical tools able to predict the seismic performance of such connections. In order to overcome such limitations, the ongoing EQUALJOINTS research project was funded to develop a prequalification procedure for bolted joints typically used in the EU practice, i.e. haunched, extended stiffened and unstiffened end-plate joints. In addition, welded dog-bone joints with heavy profiles are also investigated. Design tools and prequalification charts will be provided on the basis of experimental, numerical and analytical investigations. Those include general requirements, limitations, design procedure and qualification data.

1. Introduction

Nowadays, codified design procedures for steel bolted beam-to-column joints in seismic resistant steel frames are missing in Europe. Analyzing the existing scientific literature a wide data base of experimental results on beam-to-column joints is available (e.g. SERICON and RECON databases). However, none of the existing European studies was aimed at prequalifying specific configurations on the basis of parametric experimental investigations. This lack is mainly evident in the case of dissipative beam-to-column connections, where many issues still remain open. Indeed, at the present time, there are no reliable design tools able to predict the seismic performance of dissipative Beam-to-Column connections in order to meet code requirements. With this regard, EN 1998-1 prescribes design supported by experimental testing, which results in impractical solutions within the time and budget constraints of real-life projects. On the other hand, also for full-strength joints reliable design tools are necessary. Indeed, owing to the variability of steel strength, these connections could not have enough overstrength (e.g. min $1.1 \times 1.25 M_{b,rd}$, being $M_{b,rd}$ the bending strength of the beam), and in such cases their plastic rotation capacity must be prequalified by relevant test and numerically based procedures.

In contrast to current European design methodology, the approach used in other countries with high seismic hazard is based on codified and easy-to-use design tools and procedures. In particular, following the widespread damages observed after Northridge and Kobe earthquakes, North American practice was directed at prequalifying standard joints for seismic resistance. In 1995, the US FEMA and the SAC joint venture initiated a comprehensive 6-year program of investigation, called

FEMA/SAC program, to develop and evaluate guidelines for the inspection, evaluation, repair, rehabilitation, and construction of steel moment frame resisting structures. The US research effort was directed to feed into a specific standard (ANSI/AISC 358-05, 2005) containing design, detailing, fabrication and quality criteria for a set of selected types of connections, which should be prequalified for use with special moment frames (SMF) and intermediate moment frames (IMF). The prequalified connections include the most part of joint typologies used in US practice. Among these, welded-flange-bolted-web connections are the most common solutions in US steel moment-frame design. These connections have groove welds connecting the beam flanges to the column, and an erection plate (or shear tab) shop welded to the column with fillet or groove welds and bolted to the beam web for the transfer of shear force. Other joint typologies implemented in USA practice are the haunched and cover-plated connections. Both of them have similarities because they achieve improved seismic performance by strengthening or reinforcing the connection at the column face in order to avoid fracture at the beam flange weld. This is accomplished by enforcing plastic deformations to the end of the strengthened segment or by a combination of panel zone yielding with flexural plastic deformation at the end of the strengthened zone. In low seismic zones of USA, bolted T-stub connections and double-flange-angle connections are commonly used. Double-flange-angle connections are weaker and more flexible than the T-stub connection. They usually develop no more than 30% to 70% of the plastic bending capacity of connected beams. These connections have many similarities with seated beam connections except that the latter usually have a heavy bottom flange angle and a light top flange angle, while double-flange-angle connections normally have the same angle for the top and bottom.

Similarly to US design approach, also in Japan a prequalification activity was carried out. Japanese columns are usually made of cold formed steel tubes with shop weld placed at a short distance away from the face of the column. The critical location (or hot spot) of the Japanese welded connection occurs at the tip of the flanges, rather than at the center of the flange as noted in US connections. These differences limit the applicability of Japanese research results. Nevertheless, Japanese research suggests that weld access hole details are very important to prevent brittle failure, thus requiring research consideration. The Japanese connection tests are mainly based upon the internal diaphragm connection with tubular connections. Connection details with bolted webs and field-welded flanges are also used with built-up box columns.

Unfortunately, joint typologies commonly used in US and Japanese practices, are quite different from European ones, also employing different ranges of cross sections, material properties, bolt assemblies, etc. Therefore the prequalification procedures obtained in non-European framework are not properly suitable for European joints.

Another important issue limiting the direct application of American prequalification is related to the loading protocol for experimental tests. With this regard, it should be noted that the type of European seismic input, which affects the ductility demand, differs from US earthquakes. In this framework, the ongoing European research project "Equaljoints" aims at filling all these gaps. Indeed, it is characterized as pre-normative research aiming to provide prequalification criteria of steel joints for the next version of EN 1998-1. In detail, the research activity is focusing on the standardization of design and manufacturing procedures with reference to a set of bolted joint types and a welded dog-bone with heavy profiles. The bolted joint

typologies are shown in Fig. 1: (i) haunched joints (see Fig. 1a); (ii) extended stiffened (see Fig. 1b) and unstiffened (see Fig. 1c) endplate joints.

Moreover, with reference to the above mentioned typologies, joints designed to meet two performance levels are investigated: rigid full strength, for severe seismic zones and semi-rigid partial strength for medium-to-severe seismic zones.

To achieve these objectives, a large experimental program supported by theoretical and numerical analyses is currently ongoing. This paper provides an overview of the project and the preliminary results are described and discussed.

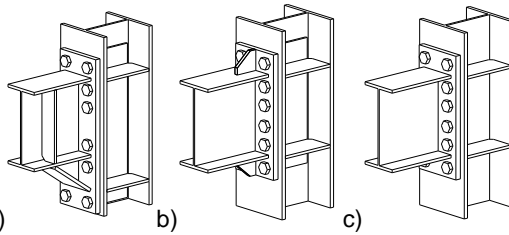


Figure 1. Bolted beam-to-column joints investigated in the framework of EQUALJOINTS project.

2. Partnership

The research group is composed of seven European institutions, i.e. five universities, the European association of steel fabricators, and a steel producer. In detail, the partners and the relative responsible people are indicated in the following:

- University of Naples Federico II – UNINA (R. Landolfo, project coordinator)
- Imperial College – IC (A. Elghazouli)
- University of Coimbra- UC (L. da SILVA)
- University of Liege – ULG (J.P. Jaspart)
- Universitatea "Politehnica" din Timisoara – UPT (D. Dubina)
- The European Convention for Constructional Steelwork - ECCS, (V. Dehan)
- ArcelorMittal Belval & Differdange S.A. (O. Vassart)

It is worth noting that the experimental activity on bolted joints is entirely concentrated within three universities (UNINA, ULG, UPT), while AM is in charge of testing dog-bone joints.

The other academic partners (i.e. IC and UC) are mainly involved with analytical, modelling, numerical investigation and design aspects, in order to support and validate experimental results and to develop loading protocol to be used during tests. AM is in charge of the manufacturing of specimens and together with ECCS is involved in the development of technological recommendations for good practice rules.

3. Research program

The EQUALJOINTS project has threefold objective, which can be summarized as follows:

1. To provide codified seismic pre-qualification charts for a set of steel standard joints, thus aiming to propose relevant criteria for the next version of EN 1998-1;
2. To develop analytical and numerical models for predicting the behavior of beam-to-column joints under cyclic loading, on the basis of a wide experimental campaign;

3. To define technological requirements for fabrication of the codified steel joints and to evaluate the economic benefits related to the costs and construction time of different solutions.

As shown in Fig. 2, the project is divided in four main parts, which are numerical investigation, experimental tests, analytical models and development of design recommendations.

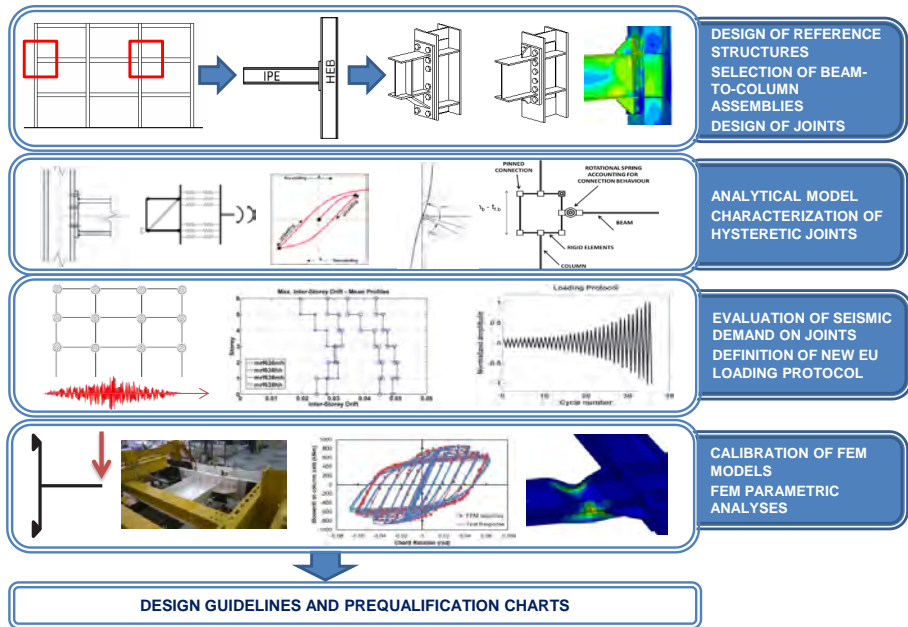


Figure 2. EQUALJOINTS action plan.

In order to achieve the goals of the projects, the research program is formulated in the following working packages:

- *WP1 (leader: IC-Elghazouli) - Selection and design of joint typologies*

This WP is devoted to select and design the joints to be qualified. In particular, they are selected according to common European practice and to be compatible with different structural systems (moment resisting frames and dual frames). The dimensions of column and beam sections are obtained from design calculation of these building structures according to EN 1998-1. Moreover, the influence of loading protocol is investigated. To this aim, a comprehensive set of non-linear time-history analyses has been performed considering two sets of ground motions scaled to match the EC8 spectra. Cumulative and maximum rotation demands provide the basis for the selection of protocol. The design of joint specimens was carried out after a critical review of the existing design and analysis methods as well as on the main outcomes of existing research. Both technological and mechanical aspects are investigated.

- *WP2 (leader: UC-Da Silva) - Analytical Models*

The objective of WP2 is to provide analytical tools to interpret and characterize the behavior of beam-to-column joints subjected to cyclic loading. In particular, analytical

models should characterize the cyclic behavior of the qualified joints, obtaining design guidance for the use of partial strength dissipative joints in seismic regions.

- *WP3 (leader: UNINA-Landolfo) - Numerical Tests*

The research activity of WP3 focuses on finite element simulations. In the first part of the project finite element analyses (FEAs) are devoted to support the experimental activity (e.g. to design the test lab setups). Subsequently, FEAs are performed both before and after the execution of experimental tests in order to investigate the key parameters affecting the joint response and to design the test setup. Moreover, in the post-experimental phase the validation and calibration of finite element models allows to better clarify the joint response and to deepen the understanding of their relevant mechanical behavior. Afterwards, on the basis of validated numerical models a parametric study is carried out in order to extend the research outcomes to a wider range of geometrical and mechanical variations per joint.

- *WP4 (leader: UPT-Dubina): Experimental Tests*

The aim of WP4 is to perform tests on a set of typical steel joints selected and designed within WP1. Experimental tests will be performed in order to demonstrate both the effectiveness and the reliability of the designed joint detailing under seismic/wind simulated loading. In WP4 the failure criteria will be defined for each limit state.

- *WP5 (leader: ULg-Jaspart): Design tools*

Following the results of WP2, WP3 and WP4 activities, within WP5 the main achieved results are collected; the design guidelines are developed. Moreover, this WP will include the recommended detailing of each investigated joint typology, the design methodology and relevant design criteria.

- *WP6 (Leader: UNINA-Landolfo): Coordination, management and dissemination*

WP6 has the fundamental role of planning, managing and coordinating the research activities.

Five deliverables will represent the final outputs of the main parts which the research plan has been subdivided into. The expected deliverables are the following:

1. Reports summarizing the main outcomes of the research versus the assumed objectives;
2. Data base with the experimental results;
3. Best practice guide: document on design and fabrication of seismic-resistant connections;
4. Prequalification procedures: document on recommended prequalification procedures for seismic-resistant connections;
5. Standardized pre-qualified seismic joints charts: document giving full details of recommended design and detailing/fabrication procedures for selected standard connections.

It should be noted that pre-qualified seismic joints charts will provide 'ready to use' design and detailing/fabrication procedures for the selected configurations, its impact is by no means restricted to the selected configurations and it will be considerably wider. In particular, through Items 4 and 5 (i.e. best practice and pre-qualification procedures), this project will open the door for other connections (which are deemed in the future to provide favorable performance and offer practical/cost-effective merits), to be included in updates of the guide.

4. Experimental activity

Tests were performed on a sufficient number of non-identical specimens to validate the ability and reliability of each connection typology to undergo the required interstorey drift angle. The experimental program (summarized in the following table) includes 76 beam-to-column specimens by varying the joint typologies, the performance objectives, the joint configuration (internal/external joints), and the loading protocol (monotonic and two different cyclic loading protocols are used)

Table 1. Experimental program.

EXPERIMENTAL PROGRAM – 76 JOINT SPECIMENS	
BEAM TO COLUMN ASSEMBLIES	SMALL BEAM (IPE 360) – MEDIUM BEAM (IPE450) – DEEP BEAM (IPE600) <i>*DOGBOONE CONNECTION DISEGNEED FOR W-TYPE US PROFILES.</i>
JOINT TYPE	HAUNCHED – EXTENDED STIFFENED ENDPLATE – UNSTIFFENED ENDPLATE - DOGBOONE
JOINT CONFIGURATION	INTERNAL AND EXTERNAL
PERFORMANCE OBJECTIVES	FULL STRENGTH – EQUAL STRENGTH – PARTIAL STRENGTH
LOADING PROTOCOL	MONOTONIC – CYCLIC AISC – CYCLIC PROPOSED
SHOOT PEENING	YES/NO

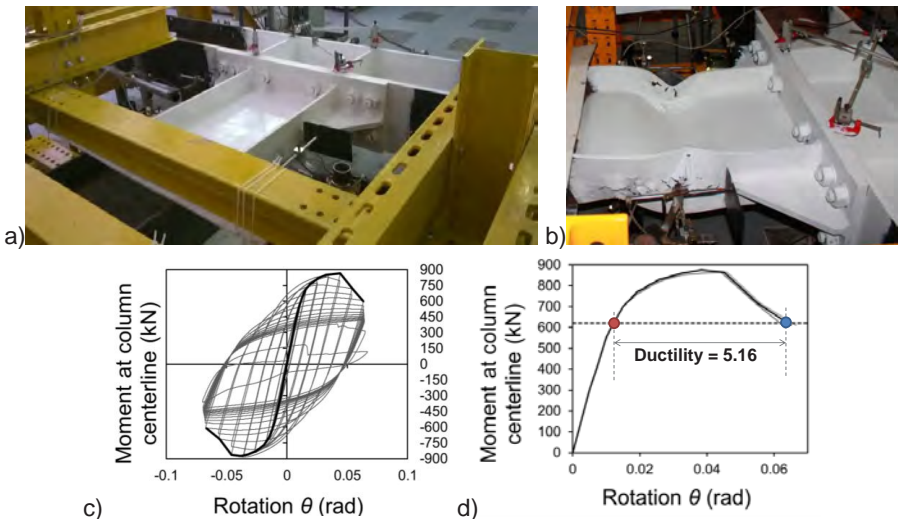


Figure 3: Test setup at UNINA (a); plastic hinge into the beam of a full strength joint tested at UNINA (b); Hysteretic experimental response (c); envelope experimental response curves (d).

In addition, for each “steel type”, monotonic and cyclic coupon tests and Charpy tests will be carried out to characterize the inelastic properties of the material. At the present time, the experimental campaign is started but not yet completed. Figure 3 shows the experimental setup and the results of a test carried out at University of Naples on an exterior full strength extended end-plate joint. As it can be noted the response curve shows stable hysteretic behavior indicating good energy dissipation, showing also a ductility of about 5.16 prior the strength degradation below the plastic

bending moment of the beam profile. The specimen exceeded the qualification limit given by both AISC 341-10 and EN1998-1 provisions. Indeed, the US code qualifies seismic resistant joints for special moment frames at 4% interstorey drift angle without significant strength loss. For EN1998-1 the connection should guarantee a rotation capacity of the plastic hinge region at least equal to 35 mrad for structures of ductility class DCH, namely an interstorey drift ratio equal to 3.5%. It is interesting to note that the cumulative rotation ductility demand (CRD) was larger than 450, which represents a significantly large value especially if compared with the demand generally computed on the basis of seismic analyses on steel frames.

5. Analytical models of cyclic response of joints

Analytical modelling was substantially devoted to revise and to extend the component method in order to predict the cyclic response of joints. Predicting behavior of steel joints is complex as several phenomena affect joint behavior such as material and geometrical nonlinearity. Under cyclic load, this behavior is further complicated by loading and unloading.

At the current stage, the component method is able to accurately predict the monotonic moment rotation response for a wide range of joint configurations by properly combining force-elongation behavior of each component up to the yielding, but EC3 part 1.8 is not applicable for cyclic loading. Therefore, additional tool is needed to predict the joint moment-rotation behavior under cyclic actions.

In order to achieve this objective, the hysteretic behavior of single components must be known. Thereby, the cyclic behavior of mechanical components was investigated on the basis of literature and finite element analyses and the relevant hysteretic response curves were determined.

The mathematical expressions of “Modified Richard Abbott method” (Nogueiro et al., 2009) were used to generate component behavior. An in-house tool has been developed by implementing above expressions. This tool can be accessed from MATLAB FILE EXCHANGE. Figure 4 shows capability to simulate the response of extended end-plate connection by using Richard-Abbott tool for approximating moment-rotation relationship with hardening and force-displacement and also for approximating hysteretic moment-rotation as given by Shamsudin (2014).

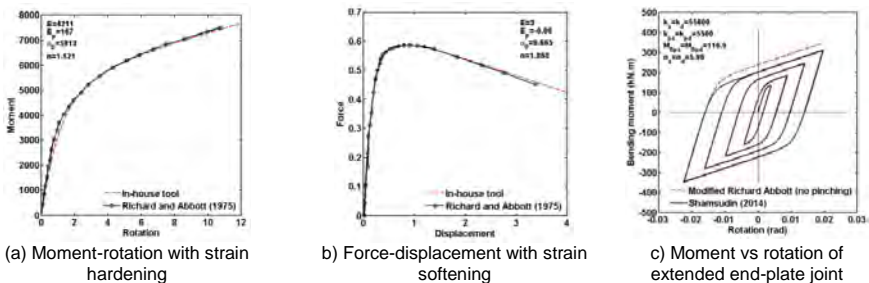


Figure 4: Developed Modified Richard Abbott model vs. experimental results.

6. Loading protocols for European qualification

Among the objectives of the project there is the development of a new loading protocol for prequalification, representative of European seismic demand. The

selection of loading protocol is based on the results of a representative set of non-linear time-history analyses performed on the buildings designed within WP1 using an ensemble of European ground motions, scaled to match the EC8 spectra. The numerical models used to investigate the seismic performance were developed taking into account the cyclic response of the selected joints. Cumulative and maximum rotation demands obtained from the analyses provided the basis for the selection of the protocol in order to represent more accurately design earthquake demands and, if necessary, to make a proposal for upgrading the existing ones.

The basis of the adopted methodology has been presented by Krawinkler et al. (2000) as part of the SAC project research after the 1994 Northridge earthquake. More recently, a set of cyclic loading protocols for European regions of low to moderate seismicity has been developed by Mergos and Beyer (2014) on the basis of nonlinear time-history analyses of a set of single-degree-of-freedom systems, corresponding to various types of structural systems. The latter methodology by Mergos and Beyer (2014), with appropriate adaptations, was basis for the investigation performed in the context of EQUALJOINTS project.

The analyses have been grouped into the following cases: (i) medium seismicity moment resisting frames (MRF-MH), (ii) high seismicity moment resisting frames (MRF-HH), (iii) medium seismicity dual concentrically braced frames (D-CBF-MH) and (iv) high seismicity dual concentrically braced frames (D-CBF-HH). For the ground motion set corresponding to each case, median sequences of normalized amplitudes were derived and subsequently used for constructing a loading protocol representative of the drift demands at each seismicity level. The input signals were extracted from the storeys that sustained the maximum inter-storey drifts, for each frame typology. The selected drift response histories correspond to a seismic intensity level consistent with the near collapse (NC) limit state, as a minimum. The derived median loading protocols for the moment-frame cases is presented in Fig. 5a along with comparative plots of the respective cumulative ductility functions (CDF) (Fig. 5b).

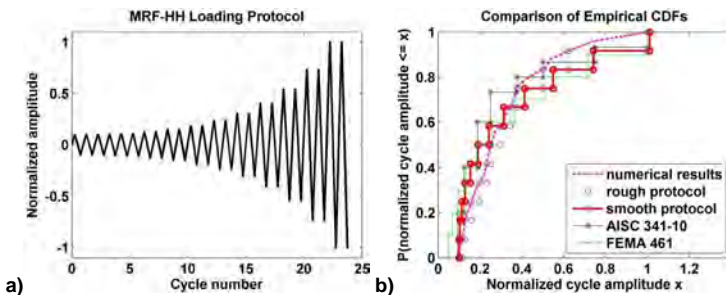


Figure 5: selected loading protocol (a); protocol – comparison of CDF (b).

7. Finite element analyses

All experimental tests were simulated by means of finite element analyses (see Fig. 6). On the basis of models validated against experimental results, parametric numerical analyses were carried out in order to extend test outcomes and to deepen the knowledge of the behavior of examined typologies of joints. In addition, the numerical simulations are also devoted to verify the applicability of the current European steel joint design code against those proposed in the EJ project. To fulfil

these purposes, the number of cases to be investigated was increased by varying both geometrical and mechanical variables which may affect the joint performance. To this aim, on the basis of calibrated models the beam depth-to-column depth ratio, beam flange slenderness, beam width, column flange slenderness, dimension and shape of stiffeners have been varied. In addition, the influence of design criteria, the number of bolt rows, the yield strength of base materials have been varied with respect to the base model for each failure mode.

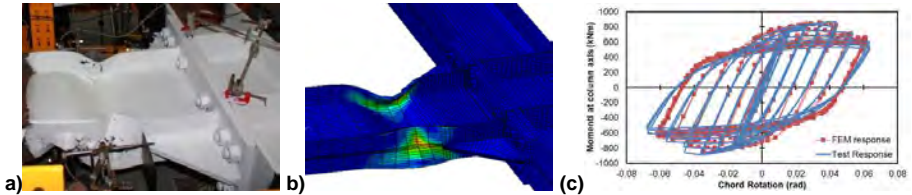


Figure 6: Experimental failure mode (a); simulated failure mode (b); comparison in terms of response curve (c).

8. Experimental database

Experimental and numerical data are being collected by all partners to a database application developed to manage a wide range of data to be further applicable for producing prequalified charts.

In this database all the available recorded data including the organization and source of the data, geometric properties of each element, material properties of each element, geometrical imperfection if available, loading protocols, hysteretic behavior of joint, failure mode and etc. are going to be collected. Figure 7 shows the main graphical user interface of the developed application by UC.

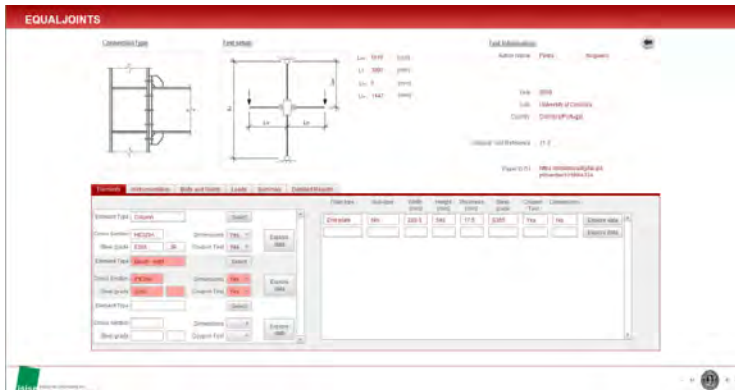


Figure 7: GUI of database application.

9. Conclusion

At the present time, one of the main criticisms of Eurocodes is that there are no reliable design tools able to predict the seismic performance of steel beam-to-column joints to meet code requirements. Indeed for dissipative joints, EN 1998-1 prescribes

design supported by experimental tests, resulting in impractical solutions within the time and budget constraints of real-life projects.

The European research project "Equaljoints (European pre-QUALified steel JOINTS, RFSR-CT-2013-00021) is currently working to introduce in European practice a pre-qualification procedure for the design of moment resisting connection in seismic resistant steel frames, in compliance with EN1998-1 requirements. The project is also intended as a pre-normative research aimed at proposing relevant design criteria to be included in the next version of EN 1998-1.

An overview of the project was provided and the preliminary results were described and discussed.

References

Abaqus Analysis User's Manual, Dassault Systèmes Simulia Corp., Providence, RI, USA. ASNI: American Society For Non Destructive Testing, 2013

American Institute of Steel Construction (AISC) (2010). Seismic Provisions for Structural Steel Buildings, ANSI-AISC 341-10 Standard, American Institute of Steel Construction, Chicago, Illinois, USA.

American Institute of Steel Construction, Inc. (AISC) (2011). Prequalified Connections for Special and Intermediate Steel Moment Frames for Seismic Applications. Standard ANSI/AISC 358-10, Chicago (IL, USA).

CEN (2005). Eurocode 3: Design of steel structures – Part 1-8: Design of joints. European Standard EN 1993-1-8:2005, Brussels.

CEN (2005). Eurocode 8: Design of structures for earthquake resistance – Part 3: Assessment and retrofitting of buildings. European Standard EN 1998-3:2005, Brussels.

Downing, S. D., Socie, D. F. (1982). "Simple rainflow counting algorithms." International Journal of Fatigue, 4(1), 31-40.

Dutta A., Dhar S., Acharyya S.K., (2010). "Material characterization of SS 316 in low-cycle fatigue loading", Journal of Materials Science, Vol. 45, Issue 7, pp. 1782-1789.

ECCS (1986). "Recommended Testing Procedures for Assessing the Behaviour of Structural Elements under Cyclic Loads". European convention for Constructional Steelwork. Publication no. 45.

Krawinkler, H., Gupta, A., Medina, R., Luco, N. (2000). "Loading histories for seismic performance testing of SMRF components and assemblies." Report SAC/BD-00/10, SAC Joint Venture, California, USA.

Mergos, P. E., Beyer, K. (2014). "Loading protocols for European regions of low to moderate seismicity." Bulletin of earthquake Engineering, 12:2507-2530.

Nogueiro, P., Silva, L. S. d., Bento, R., Simões, R. (2009) Calibration of model parameters for the cyclic response of end-plate beam-to-column steel-concrete composite joints. Steel and Composite structures, 9(1), 39-58.

OpenSees (2015). Open System for Earthquake Engineering Simulation, Pacific Earthquake Engineering Research Center, University of California at Berkeley, California USA (opensees.berkeley.edu as of March 10th 2015).

Richard, R. M., Abbott, B. J. (1975) Versatile Elastic-Plastic Stress-Strain Formula. the Engineering Mechanics Division, 1(4), 511-515.

Shamsudin, M. F. B. (2014) Analytical tool for modeling the cyclic behaviour of extended end-plate connections. MSc, University of Coimbra.

T-STUB RESPONSE AND LOADING RATE

Nadia Baldassino
Università degli Studi di Trento, Trento, IT
nadia.baldassino@unitn.it

Martina Bernardi
Università degli Studi di Trento, Trento, IT
martina.bernardi@studenti.unitn.it

Riccardo Zandonini
Università degli Studi di Trento, Trento, IT
riccardo.zandonini@unitn.it

ABSTRACT

Recent studies have drawn the importance of ductility in enabling structural resistance mechanism against progressive collapse. In steel and steel and concrete composite structures, experimental studies have pointed out the central role of the beam-to-column joints in the mechanisms of force transmission towards the undamaged part of the structure. The Università di Trento was recently involved in a European research project aimed at the development of new design concepts against accidental actions, for steel-concrete composite frames. In the framework of these activities, the Authors performed an experimental study focused on the influence of loading rate on the beam-to-column joint performance. The study comprises tests on T-stubs modelling a flush end-plate beam-to-column bolted connection. Both the column flange and the end-plate T-stub responses were investigated. In this paper, the main features of the experimental program and of the tests' results are described and discussed.

INTRODUCTION

The rotation capacity of a steel connection depends on the deformation capacity of the less ductile components. In beam-to-column bolted joint connections a significant part of the inelastic rotation is provided by the column flange and the end-plate. The behaviour of these joint components is efficiently modelled by means of equivalent T-stub (Zoetemeijer, 1974), (Jaspart, 1991), (Faella et al., 2000). The knowledge of the force-displacement curves of the T-stub components would hence enable the approximation of one of the main sources of plastic rotation capacity of beam-to-column bolted joints. The response of T-stubs under tensile quasi static loading has been widely investigated in the recent years. The outcomes of the studies identified simplified relationships based on the possible failure mechanisms of the T-stub's flange for the prediction of the performance. Three possible failure mechanisms are identified: flange yielding without bolt failure (mode 1), yielding of flange and bolt failure (mode 2) and bolt fracture (mode

3). The smallest load between those associated with each one of the three collapse modes defines the T-stub collapse load. The evaluation of the collapse resistance associated with modes 1 and 2 requires the definition of an effective length of the potential yield line mechanisms of the T-stub flanges.

Recent studies have drawn the importance of local ductility in enabling structural resistance mechanism against progressive collapse (Kuhlmann et al., 2016). In steel and steel-concrete composite structures with partial strength connections, the central role of the beam-to-column joints in the mechanism of force transmission from the damaged to the undamaged part of the structure was pointed out. At this aim, joints should possess adequate resources in terms of resistance and inelastic deformation capacity to allow for preventing progressive collapse.

The knowledge related to the robust behaviour of steel and steel-concrete composite structures was up to now based on experimental studies performed in quasi static conditions which do not allow investigation of the structural response in conditions close to the ones occurring during an accidental loading scenario. The dynamic nature, which characterise the phenomena associated with accidental loading, indicates that the design analysis should account for the influence of strain rate. The beam-to-column joints do have a central role in ensuring a robust response of steel and steel and concrete composite structures. Therefore, the consideration of material rate sensitivity stresses the need of studies concerning the influence of strain rate on the joint response.

The Università di Trento was recently involved in a European research project (acronym RobustImpact) aimed at the development of new design concepts for steel-concrete composite frames subject to accidental actions (Kuhlmann et al., 2016). The ability of the structure to transfer the loads from the damaged to the undamaged part is the central issue investigated. The studies of the Trento unit focused on two main problems:

- i) the influence of the biaxial membrane action associated with the concrete slab in a framed structure when the collapse of a column happens;
- ii) the influence of loading rate on the joint performance, with particular reference to the deformation capacity of endplate connections.

This paper focuses on the studies associated with the second issue. The study comprises tests on T-stubs associated to a flush end-plate beam-to-column bolted connection. Both the column flange and the end-plate T-stub responses were investigated. In this paper the main features of the experimental program and of the tests results are described and discussed.

LAYOUT OF THE SPECIMENS

The activities of the RobustImpact project focussed the attention on a typical a five-story steel-concrete composite structure selected as case study (Kuhlmann et al., 2016). In the design phase of the structure, bolted flush-end plate beam-to-column connections (Fig.1 and Fig. 2) and fixed connections at the base were assumed.

Aiming at investigating the influence of strain rate on the response of the beam-to-column joints, among the joint components the attention was focused on the column flange and on the end-plate in bending. A total of 20 tensile tests on unstiffened T-stubs were then planned. Specimens were designed so that compliance with the beam-to-column joints of the case study was met (Fig.1 and Fig. 2).

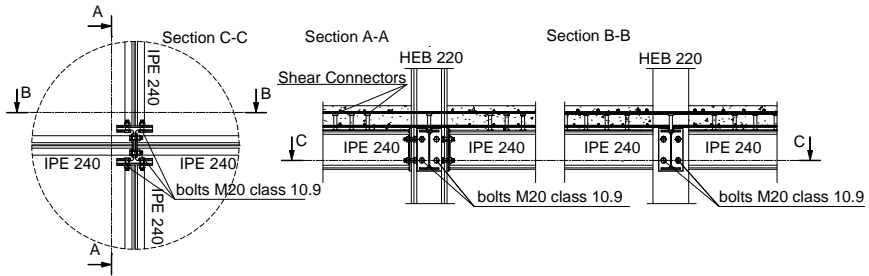


Figure 1: Steel and concrete composite joint

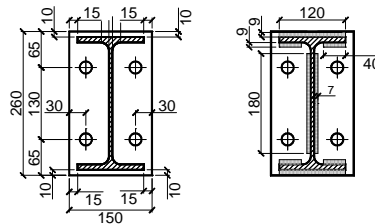


Figure 2: Detail of the beam-to-column joint (measures in mm)

In detail, 10 tests were performed on ‘end-plate’ T-stubs and 10 tests on the ‘column flange’ T-stubs. The design of the specimens’ geometry was performed in accordance to the EN 1993-1-8 (CEN, 2005). In the design analysis, the nominal mechanical properties were considered for the structural steel (S355) and for the bolts (M20 grade 10.9). Table 1 the results of this analysis. A detailed description the T-stub geometry is given in Figure 3.

Joint component	Effective length mm	Collapse mode	Collapse load kN
End-plate	190	Mode 1	186,38
Column flange	162	Mode 2	344,77

Table 1: Theoretical effective length and collapse loads for column flange and end-plate T-stubs

Before testing, the main geometrical dimensions of the specimens were measured in order to point out possible dimensional deviation with respect to the nominal values. The measures indicate deviations in compliance with the fabrication tolerances. In order to allow a more effective analysis of the tests’ results the geometries of bolts, nuts and washers were also measured.

THE TESTS ON T-STUBS

The tests on T-stubs were carried out by connecting the flange of the specimens to a rigid

support. The load was applied through the web so as the force is aligned to the bolts connecting the flange to the rigid support (Figure 4). The bolts connecting the specimens to the rigid support were preloaded with a torque moment of 0,550kNm, so that consistency is achieved with the bolts' preload adopted during 3D tests on the full-scale specimens (Kuhlmann et al., 2016).

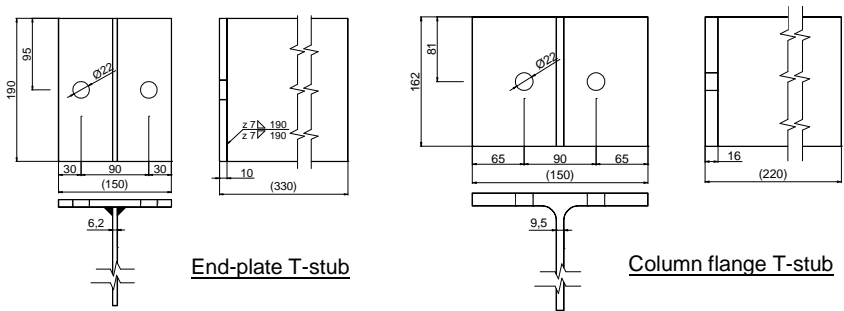


Figure 3: T-stub geometry (measures in mm)

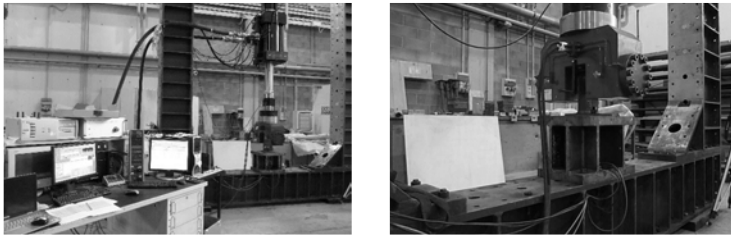


Figure 4: a) The test set-up; b) Detail of a specimen under test

In order to evaluate the influence of loading rate on the T-stub performance, tests were carried out at two different deformation rate (160mm/s and 326,9mm/s). As to this choice, it should pointed out that the loading rate values adopted are in agreement with the range values investigated in another study (Barata et al., 2014). The maximum value of the deformation rate, i.e., 326,9mm/s, was dictated by the equipment's capability. The test series comprised three tests for each deformation rate. For comparison, 3 quasi static tests were additionally carried out (0,07 mm/s).

The load history adopted in the tests is described in Figure 5. The force/displacement was applied via a MTS hydraulic actuator with a maximum capacity in tension of 1000kN. In order to collect data concerning the specimen's deformation capacity, the transducers' set-up was designed so that to monitor the flange displacements at three different locations. Furthermore, in order to get information on the prying effect, in all the tests the bolt shank elongation was also measured with internal strain gauges (Figure 6). In order to evaluate the force acting on the bolts, each bolt before installation was calibrated in the elastic range, so identifying a 'calibration curve' in terms of force-axial strain.

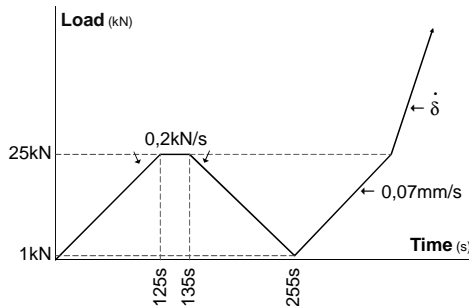
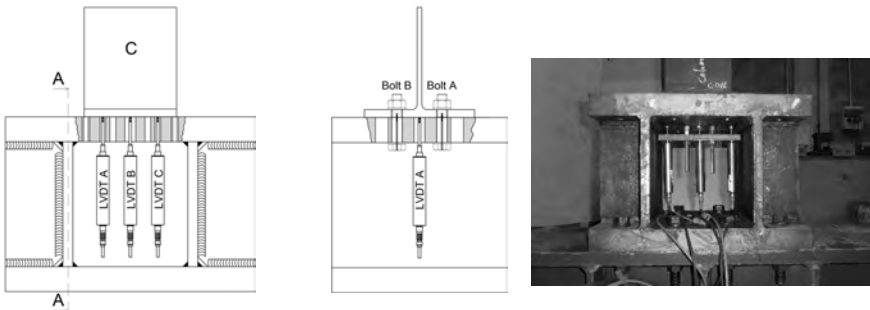


Figure 5: Typical load history (graph not in scale)



Section A-A

Figure 6: Instruments set-up

During the tests, the load, the displacements and the bolt axial deformation were automatically recorded at a frequency of 4800Hz. In case of quasi-static tests, the acquisition frequency was reduced to 200Hz.

For an easier understanding of the test results, Table 2 summarises the tests performed and the related loading condition.

COLUMN FLANGE T-STUB RESULTS

The results of the tests in terms of maximum load are summarised in Table 3. Specimen C-04 was used for checking the test set-up, the related results are hence not included.

In all the tests, it was observed:

- the partial development of a flange mechanism, which appeared more pronounced in tests performed at the lower deformation rate (0,07 mm/s);
- the failure associated with the fracture of the bolts;
- a collapse mode compatible with a collapse mode identified as type 2; i.e., the collapse codified by Eurocode 3 part 1-8 (Table 1)(CEN, 2005).

COLUMN FLANGE T-STUBS			END-PLATE T-STUBS		
ID spec.	Bolts' preload Torque moment kNm	Def. rate $\dot{\delta}$ mm/s	ID spec.	Bolts' preload Torque moment kNm	Def. rate $\dot{\delta}$ mm/s
C-01	0,55	326,90	EP-01	0,55	326,90
C-02	0,55	326,90	EP-02	0,55	326,90
C-03	0,55	326,90	EP-03	0,55	326,90
C-04	Preliminary test		EP-04	0,55	0,07
C-05	0,55	0,07	EP-05	0,55	0,07
C-06	0,55	0,07	EP-06	0,55	0,07
C-07	0,55	0,07	EP-07	0,55	160
C-08	0,55	160	EP-08	0,55	160
C-09	0,55	160	EP-09	0,55	160
C-10	0,55	160	EP-10	Snug tightened	160

Table 2: The tested column T-stubs and end-plate T-stubs

COLUMN FLANGE T-STUBS		
ID specimen	Deformation rate $\dot{\delta}$ mm/s	Maximum load kN
C-01	326,90	487,950
C-02	326,90	502,987
C-03	326,90	510,318
C-05	0,07	458,424
C-06	0,07	441,193
C-07	0,07	465,529
C-08	160	445,350
C-09	160	487,297
C-10	160	479,809

Table 3: Test's results for column T-stubs

As an example of the test's results, Figure 7 presents the outcomes of specimen C-03. In detail, the figure reports:

- i. the load-displacement response as obtained from the three transducers measuring the flange displacements (Fig. 6);
- ii. the load-axial deformation of the bolts (Fig. 6). In the plots, for an intuitive appraisal of the bolts' deformation, the axial deformation (ϵ_y) associated with the nominal yielding strength ($f_{yb}=900\text{MPa}$) is also drawn;
- iii. the overall behaviour as it appears from pictures of the specimen during and at the end of the test, and of the bolts at collapse.

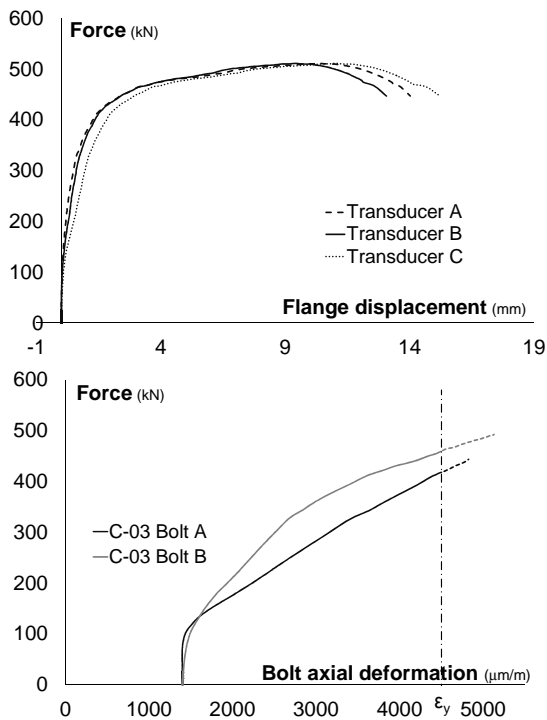


Figure 7: Test' s results for specimen C-03

The load-displacement curves for the central transducer (transducer B in Figure 6) are gathered, for all the tests on the column flange T-stubs, in Figure 8.

The comparison between the force-flange displacements curves (Fig.8) indicates a moderate influence of the deformation rate on the collapse load. The lower collapse loads were observed in quasi-static tests (i.e., $\dot{\delta}=0,07\text{mm/s}$). Furthermore, it appears that collapse loads are not affected by the deformation rate when the two higher values are considered (i.e., $\dot{\delta}=326,90\text{mm/s}$ and 160mm/s). The natural scatter of test results and the limited number of tests does not enable correlating deformation rate and ductility.

END PLATE T-STUB RESULTS

The results of the tests in terms of maximum load are summarised in Table 3. As an example of the results, in Figure 9 the response of test EP_08 is presented.

In all the tests, the following features were observed:

- i. the development of a clear flange mechanism independently of the deformation rate;
- ii. the presence of cracks at the welds between the flange and the web which, in one case, triggered the collapse of the specimen;

- iii. the failure of the bolts triggered by the development of cracks at the welds between the flange and the web. In two cases the simultaneous collapse of the welds and of one of the bolts was observed;
- iv. a collapse mode compatible with a mode type 1 among the collapse modes identified according by Eurocode 3 part 1-8 (Table 1) (CEN, 2005).

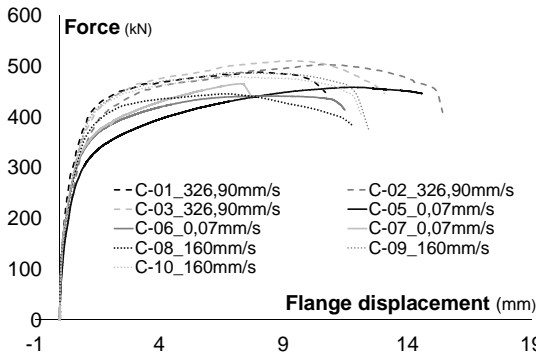


Figure 8: Comparison between test results on column flange T-stubs

END PLATE T-STUBS		
ID specimen	Deformation rate	Maximum load
	$\dot{\delta}$ mm/s	
EP-01	326,90	331,365
EP-02	326,90	396,490
EP-03	326,90	347,270
EP-04	0,07	270,917
EP-05	0,07	302,674
EP-06	0,07	304,240
EP-07	160	321,676
EP-08	160	340,999
EP-09	160	324,570
EP-10*	160	335,102

* Snug tightened bolt

Table 4: Test's results for end-plate T-stubs

The comparison between the load–flange displacement curves of all the end-plate T-stub is presented in Figure 10. The curve related to the test without bolt preloading (specimen EP_10) is also included due to the observed negligible influence of the preloading. The comparison between the curves shows a negligible influence of the deformation rate on both the collapse load and the ductility of the tested specimens. This conclusion is in agreement with the findings of (Pereira, 2012).

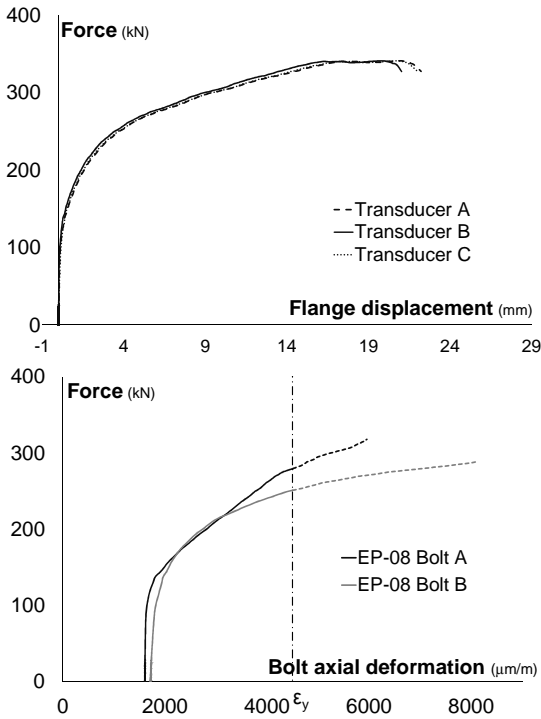


Figure 9: Test's results for specimen EP_08

SUMMARY AND CONCLUSIONS

The dynamic nature, which characterise the phenomena triggered by accidental loads, requires knowledge of the influence of the strain rate. In steel and steel-concrete composite structures the central role of beam-to-column joints and the material rate sensitivity stress the need of studies concerning the influence of strain rate on the joint response. At this aim, a study of the influence of deformation rate on the performance of the components that contribute the most to the deformation capacity of a beam-to-column steel joint, i.e., the column flange and the end-plate, was carried out. The study referred to the steel joints of the reference structures investigated in the project RobustImpact (Kuhlmann et al., 2016). A total of 20 tests, 10 for the column flange and 10 for the end-plate, were performed. For each joint component, quasi-static tests and dynamic tests at two different deformation rate levels were considered.

A preliminary evaluation of the tests' pointed out:

- i. the potential influence of the deformation rate on the collapse load in case of stiff flanges. This is apparent by comparing the response of the column and of the end-plate T-stubs;

- ii. the negligible influence of the deformation rate on the joint component ductility;
- iii. the possibility of referring to the collapse modes identified by Eurocode 3 part 1-8 (CEN, 2005) even in case of high deformation rates;
- iv. the importance of the quality of the welds between flange and web which could result in brittle failures.

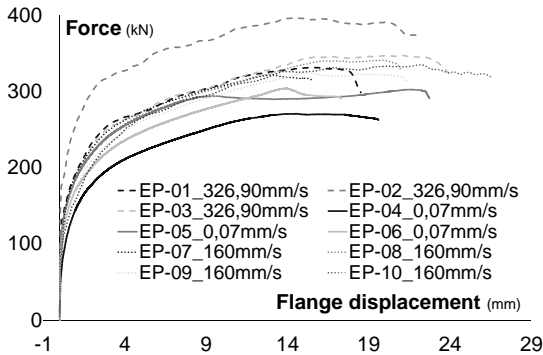


Figure 10: Comparison between test results on column flange T-stubs

These results are consistent with the study by (Pereira, 2012). However, the limited number of tests prevent from getting general conclusions.

REFERENCES

- Zoetemeijer, P. (1974), "A design method for the tension side of statically loaded, bolted beam-to-column connections", *Stevin-Laboratory*, Vol. 20 (1) (pp.3-59).
- Jaspart, J.P. (1991), *Etude de la Semi-Rigidite des Noeuds Poutre-Colonne et son Influence sur la Resistance et la Stabilité des Ossatures en Acier*. Ph.D. Thesis, University of Liege, Belgium.
- Faella, C., Piluso, V. and Rizzano, G. (2000), *Structural Steel Semirigid Connections: Theory, Design and Software*. CRC Press LLC, Boca Raton.
- Kuhlmann, U., Jaspart, J.P., Zandonini, R, Hoffmeister, B., Hanus, F. and Hijaj, M., (2016), *ROBUSTIMPACT Robust design of steel and composite structures*, Contract RFSR-CT-2012-00029, Final report (in print).
- CEN, (2005). EN 1993-1-8, Eurocode 3 Design of joints – Part 1-8: Design of joints, *CEN European Committee for Standardization*, May.
- Barata, P., Santiago, A., Rodrigues, J.P.C. and Rigueiro, C. (2014), "Experimental analysis of a T-stub component subjected to impact loading". Proceedings of Eurosteel 2014, September 10-12, Naples.
- Pereira, M.F. (2012), *Robustness of multi-story steel-composite buildings under column loss: rate-sensitivity and probabilistic framework*. Ph.D. Thesis, Department of Civil and Environmental Engineering, Imperial College, London, pp. 319.

BUILT-UP T-STUB MOMENT CONNECTION

Ricardo Herrera
University of Chile, Santiago, Chile
riherrer@ing.uchile.cl
Juan F. Beltrán
University of Chile, Santiago, Chile
jbeltran@ing.uchile.cl
Claudio Alarcón
University of Chile, Santiago, Chile
claudioalarconoso@gmail.com
Constanza Salas
University of Chile, Santiago, Chile
constanza.salas@ug.uchile.cl

ABSTRACT

The research reported herein is part of a study on the response of a Double Built-up Tee (DBT) beam/column moment connection. The objectives of this research are to identify failure modes associated with this type of connection and establish simplified force-displacement or moment-rotation relations to include the connection in structural models. Four prototype buildings were designed according to the Chilean seismic, considering the flexibility of the connection, and complying with the compactness and strong column-weak beam requirements set forth by the AISC seismic provisions. The prototypes had the same floor plan, story height and bay size, but different number of stories (three, six, nine, and twelve).

A representative beam/column connection was selected from the prototype buildings to generate models and specimens with different controlling limit states. These configurations will be represented numerically through a 3D finite element model, using ANSYS, and experimentally studied by subjecting the specimens to cyclic loads.

INTRODUCTION

Current seismic design specifications for steel structures (AISC, 2010a) require that connections for highly ductile moment resisting frames have a certified inelastic deformation capacity. This certification is obtained through prequalification testing for those connections that have not yet been included in the list of already prequalified connections accepted by AISC (AISC, 2010b). So far, only fully rigid connections have been included in this list, although significant research has been conducted on several partially restrained connections.

One of these connections is the double split tee (DST) connection. Several studies including analytical (Zoetemeijer, 1974; Yee and Melchers, 1986; Piluso et al, 2001a; Yang et al, 2013), numerical (Girão Coelho et al, 2006; Sherbourne and Bahari, 1996;

Mistakidis et al, 1997; Hantouche et al, 2012) and experimental (Smallidge, 1999; Swanson and Leon, 2000; Piluso et al, 2001b; Girão Coelho et al, 2004; Hantouche et al, 2012) research on the response of the T stub and the entire connection led to the inclusion of this connection as a prequalified connection in FEMA 350 (FEMA, 2000). However, most of this research has been conducted on hot rolled spilt tees.

An ongoing research program at the University of Chile is looking at the possibility of using built-up instead of hot-rolled T-stubs. The use of built-up tees presents advantages in terms of material utilization, freedom of sizing, and availability, but it can introduce brittle failure modes associated with the weld between the flange and the stem of the T. So far, the response of the isolated built up tee has been studied under monotonic and cyclic loading (Herrera et al, 2013; Bravo and Herrera, 2014). In this paper, the latest developments of this research program are presented. The objective now is to look at the entire connection by extending the numerical model developed and testing full size specimens. To come up with realistic sizes of beams, columns and connections, a series of prototype buildings are designed and a representative connection is extracted to conduct the numerical and experimental investigations. Included in this paper are the details of the design of these prototypes, a description of the numerical model under development and some preliminary results, and an overview of the experimental program to be conducted.

DESIGN OF PROTOTYPES

Four prototype buildings were designed according to the requirements of the Chilean seismic building code NCh433 (INN, 2009). The buildings had the same floor plan with moment resisting frames located on the perimeter, as shown in Figure 1, a constant story height of 3.5 m, and they differed only in the number of stories (3, 6, 9, and 12). The buildings were destined for housing and assumed to be located on soil type A and seismic zone I, as per NCh433. Structural steel grade ASTM A36 and bolts grade ASTM A490 were considered.

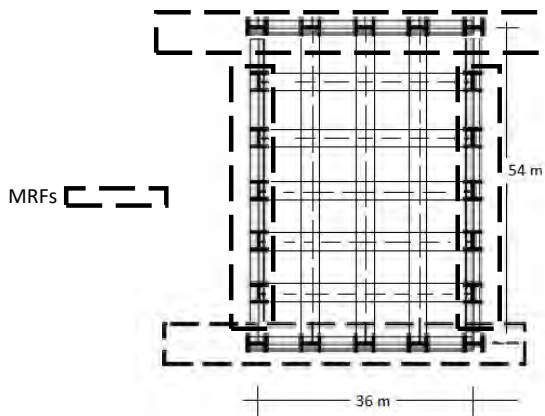


Figure 1: Prototype building floor plan

The design was controlled by drift requirements. NCh433 imposes a limit of 0.2% of the story height for the elastic drift calculated using the design spectrum. This limit becomes even more critical when semi-rigid connections are used. It was found that the main parameter that influenced drift in the prototypes designed was the combined beam/connection flexibility. Therefore, the design was driven by selecting the proper size of beams to control drift, then the connections were sized to not exceed the drift limit, and finally an appropriate column was chosen to comply with strong column/weak beam requirements of AISC 341-10 (AISC, 2010a).

In order to consider the flexibility of the connections in the design, an equivalent stiffness for the beam/connection assembly was used in the design elastic model. This stiffness was calculated using equation (1)

$$EI_{eq} = \frac{1}{\frac{6h}{L_b^2 K_s} + \frac{1}{EI_b}} \quad (1)$$

Where,

EI_{eq} : equivalent flexural stiffness of the beam/connection assembly

EI_b : flexural stiffness of the beam alone, when rigid connections are used

h : story height, equal to 3.5 m for the prototypes

L_b : bay width, equal to 9 m for the prototypes

K_s : connection stiffness, given by Equation (2), recommended in FEMA 350 (FEMA, 2000)

$$K_s = \frac{d_b M_{fail}}{0.9525} \quad (2)$$

Where:

M_{fail} : T stub moment connection capacity

d_b : Beam depth

It must be noted that the use of built up tees allows the designer to size the connection as a fully rigid connection, considering that the sizes of the flange and the stem of the T can be freely selected. However, Piluso et al. (2001a) showed that depending on the relative sizes of the tee, three failure modes can occur, namely: yielding of the tee flange, yielding of the tee flange combined with fracture of the tension bolts, and fracture of the bolts alone.

Designing the connection to be fully rigid would induce mode 3 (fracture of the tension bolts) to occur, which is a brittle and hard to predict failure mode. Therefore, for this study it was decided to design the connection as partially restrained.

Table 1 presents the sizes of the beams resulting from the design of the prototypes. The last two columns on the table present the total number of stories and the specific stories of the prototype where the beam size was used, respectively. Only two sizes of beams were selected for each prototype. No effort was made to optimize the design, because the purpose was to find reasonable beam and connections sizes to study in detail numerically and experimentally.

Four different connection configurations were designed for each beam size, each one looking to achieve a specific limit state, according to FEMA 350 (FEMA, 2000). These designs are shown in Table 2, whereby the first design for each beam size corresponds to the one that induces the formation of the plastic hinge on the beam. The variables in Table 2 correspond to the nomenclature used in FEMA 350, reproduced in Figure 2.

Table 1: Dimensions of beams used in the prototype buildings

Beam size	d mm	b _f mm	t _f mm	t _w mm	Prototype stories	Levels used in
W33x118	900	540	110	90	6	1-4
W36x182	900	540	110	90	9	1-7
W36x194	900	540	110	90	12	1-10
W21x101	800	440	60	17	3	All
W24x94	800	440	60	15	6	5, 6
W24x94	800	440	60	15	9	8, 9
W24x84	800	440	60	13	12	11,12

Table 2: Connection designs for the prototype beams

ID	Beam size	S ₁ [mm]	d _{bolt} [mm]	S ₂ [mm]	S ₄ [mm]	g [mm]	t _{stem} [mm]	a [mm]	t _{f-t} [mm]	g _f [mm]
DBT 1	W 24x94	124	35	105	44	130	20	71	24	12
DBT 2		136	35	125	44	130	12	71	36	12
DBT 3		136	35	105	44	130	12	71	36	12
DBT 4		122	35	105	44	130	20	71	22	12
DBT 5	W 24x84	128	38	115	48	130	24	71	28	20
DBT 6		136	35	125	44	130	10	71	36	10
DBT 7		136	35	105	44	130	10	71	36	10
DBT 8		123	35	105	44	130	22	71	23	14
DBT 9	W 21x101	124	35	105	44	160	22	69	24	14
DBT 10		130	35	130	44	160	14	69	30	14
DBT 11		130	35	105	44	130	14	69	30	14
DBT 12		121	35	105	44	160	20	69	21	14
DBT 13	W36x194	128	38	150	48	160	28	76	28	20
DBT 14		134	38	150	48	160	20	76	34	20
DBT 15		132	38	115	48	160	20	76	32	20
DBT 16		124	38	115	48	160	24	76	24	20
DBT 17	W36x182	128	38	140	48	160	28	76	28	16
DBT 18		130	38	150	48	160	18	76	30	16
DBT 19		130	38	115	48	160	18	76	30	16
DBT 20		123	38	115	48	160	18	76	23	16
DBT 21	W33x118	126	38	115	48	160	20	76	26	12
DBT 22		130	38	150	48	160	12	76	30	12
DBT 23		130	38	115	48	160	14	76	30	12
DBT 24		118	38	115	48	160	16	76	18	12

Notes: N = 4 for all cases

Table 3 presents the type of failure mechanism expected, based on the formulation of Piluso et al (2001), the capacity of each limit state considered, where the numbers in red represent the capacity of the controlling limit state, and the flexural stiffness ratio EI_{eq}/EI_b for all the connection configurations considered. The capacities listed in Table 3 are the moments at the connection when the limit state is achieved: M_{hinge} : moment at formation

of plastic hinge in the beam; M_{nsf} : moment at net section tensile fracture in the T stem; M_{sbf} : moment at shear bolt fracture; M_{shb} : moment at shear block failure; M_{prying} : moment at T flange plastification; M_{tbf} : moment at tension bolt fracture. In the determination of the limit state capacities, nominal yield stress values for an ASTM A36 steel were used for the beam, while values reported by Bravo and Herrera (2014) were used for the built-up tee ($F_y = 318$ MPa, $F_u = 466$ MPa). Nominal strength values were also used for the bolts, considering ASTM A490 material with threads included in the plane of force transfer.

Table 3: Collapse mechanism, limit state capacities, and flexural stiffness ratio

ID	Mech.	M_{hinge} [kN-m]	M_{nsf} [kN-m]	M_{sbf} [kN-m]	M_{shb} [kN-m]	M_{prying} [kN-m]	M_{tbf} [kN-m]	E_{leg}/E_{lb}
DBT 1	I	1636	2314	2940	2195	2852	3390	0.70
DBT 2	II	1675	1375	2972	1523	1766	2981	0.60
DBT 3	II	1643	1375	2949	1317	1766	2981	0.59
DBT 4	I	1635	2313	2938	2195	741	2828	0.44
DBT 5	I	1473	2727	3488	2783	2095	3785	0.72
DBT 6	II	1490	1133	2948	1259	1260	2683	0.58
DBT 7	II	1461	1133	2925	1088	1260	2683	0.57
DBT 8	I	1455	2533	2915	2395	644	2684	0.44
DBT 9	I	1677	2258	2587	2297	3745	3085	0.70
DBT 10	II	1721	1419	2617	1717	2366	2910	0.60
DBT 11	II	1680	1419	2591	1352	2366	2910	0.59
DBT 12	I	1675	2044	2585	2088	1434	2855	0.60
DBT 13	I	5025	6105	5363	6459	6848	6183	0.66
DBT 14	II	5034	4331	5372	4613	5199	5933	0.61
DBT 15	II	4874	4329	5293	3780	4606	5847	0.58
DBT 16	I	4863	5206	5282	4536	2894	5668	0.51
DBT 17	I	4674	6080	5318	6133	7630	6211	0.67
DBT 18	II	4720	3869	5343	4134	4039	5729	0.60
DBT 19	II	4573	3869	5268	3387	4039	5729	0.56
DBT 20	I	4563	3862	5258	3387	2374	5488	0.48
DBT 21	I	2643	3902	4760	3405	4412	5374	0.69
DBT 22	II	2734	2322	4833	2493	3313	5076	0.61
DBT 23	II	2646	2715	4765	2383	3475	5128	0.61
DBT 24	I	2637	3101	4750	2724	1316	4842	0.47

Table 4 lists the results for natural period of the structure, design base shear and minimum base shear required by NCh433 (INN, 2009), and the ratio between minimum and design base shear. The maximum allowed elastic drift for the design spectrum (7 mm according to NCh433) is always larger or equal to the drift of the prototypes. The strong column/weak beam requirement is met for all the prototypes, with ratios ranging from 1.3 for the 12 story prototype to 4 for the 3 story prototype.

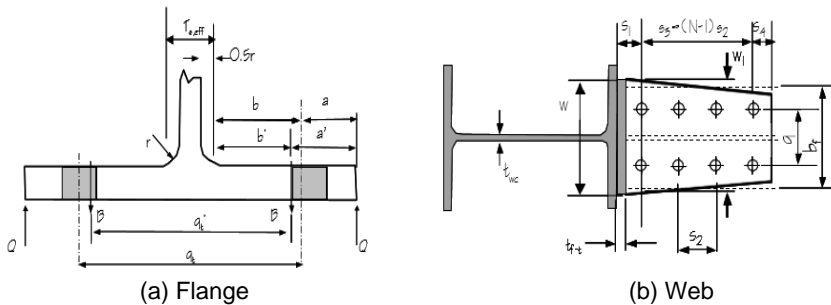


Figure 2: Geometric parameters according to FEMA 350 (FEMA, 2000)

Table 4: Dynamic and design quantities for the prototype structures

Response quantities	Units	Prototype			
		3 story	6 story	9 story	12 story
Fundamental period, T^*	[s]	0.53	1.32	1.74	2.31
Design base shear, V_{b_design}	[kN]	278	261	294	305
Minimum base shear, V_{b_min}	[kN]	417	938	1509	2118
V_{b_min} / V_{b_design}	-	1.50	3.60	5.14	6.95

NUMERICAL MODEL

The finite element model developed is shown in Figure 5. This model is an extension of the model presented by Bravo and Herrera (2014), which represented one half of the T stub. To simplify the model, the column is replaced by a rigid surface with compression-only supports. Solid rectangular 20-node and tetrahedral 10-node elements are used to mesh the T stub and bolts. The beam is divided in three segments indicated in different tones: a segment at the connection, a plastic hinge segment and a nominally elastic segment. A denser mesh is used in the segment where the plastic hinge in the beam is expected. The analysis is conducted under displacement control. The load is applied in two stages; first, the bolts are subjected to a pretension, followed by the application of a vertical displacement at the tip of the beam.

Bilinear stress–strain curves are used to represent the response of the different parts of the model. The nonlinear behavior of the material is modeled using a Von Mises yield criterion with isotropic hardening.

A number of contact conditions are imposed to describe the interaction between the different parts of the model, namely, T stub, bolts, and beam. The model can capture the bearing of the shear bolts on the holes and the ensuing local deformation of the plate around the bearing area. The friction between the beam flange and the T stem is modeled using a “slip-critical standard” contact condition, with a friction coefficient μ of 0.33, assuming Class A surface conditions according to AISC (2010a).

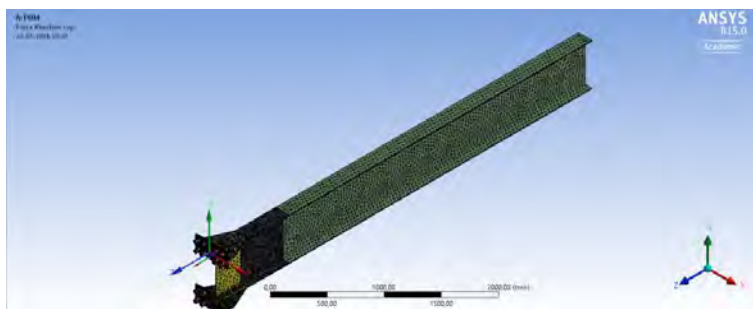


Figure 4: Finite element model of the connection and the beam

In order to preliminarily validate the numerical model, a specimen tested by Smallidge (1999) was modelled and analyzed under monotonic loading. The material properties reported by Smallidge were used for the beam, T stubs, and columns. For the other parts of the model, nominal values were used. The specimen was selected because, although it was built with hot-rolled T stubs, the damage was concentrated in the beam, hence, the effect of the weld should not be relevant in the response of the specimen. Figure 5 shows the comparison between the experimental and numerical results. Because the column was not modelled, it was included as an additional flexibility causing additional vertical displacement at the tip of the beam, assuming elastic response. The model captures adequately the yielding and capacity of the test specimen. The difference in stiffness can be attributed to all the flexibilities in the test setup and the test specimen that cannot be captured by the numerical model, for instance the panel zone deformation, bending of the column flanges, deformation at the supports.

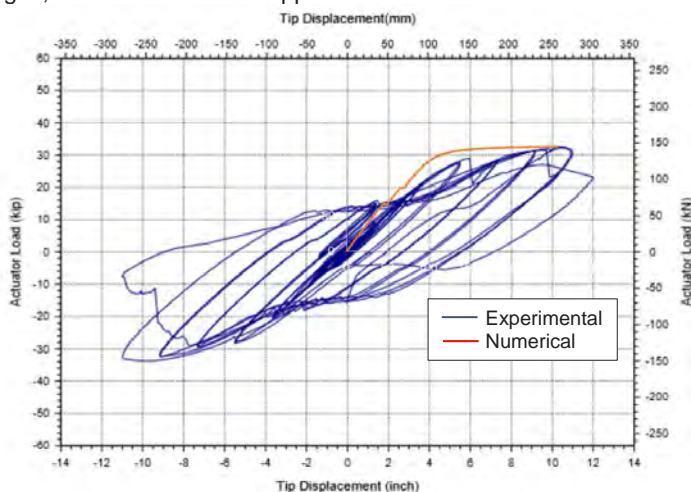


Figure 5: Numerical vs experimental results

Numerical models of all the connection configurations previously presented are being constructed and will be analyzed for a monotonically increasing load, applied under displacement control.

EXPERIMENTAL DETAILS

Based on the results of the design of the prototype structures, one size of beams, columns, and connections was selected as a reference specimen. Three other specimens were generated by varying the sizes of the connections and the columns in order to obtain a specific limit state. The test specimens emulate an interior connection, with one beam on each side of the column. The main characteristics of the four test specimens are listed in Table 5, where the subscripts b and c indicate beam and column dimensions, respectively. Columns are 3595 mm long and beam, 4330 mm long.

Table 5: Test column and beam dimensions

Specimen	d_c [mm]	b_{fc} [mm]	t_{fc} [mm]	t_{wc} [mm]	d_b [mm]	b_{fb} [mm]	t_{fb} [mm]	t_{wb} [mm]
SS-01(DWT1)	800	450	60	35	600	250	16	12
SS-02(DWT2)	800	450	60	35	600	250	16	12
SS-03(DWT1)	800	450	60	18	600	250	16	12
SS-04(DWT1)	800	450	60	25	600	250	16	12

The dimensions of the T stubs are shown in Figure 6. The thickness of the T flange is 50 mm for DWT1 and 25 mm for DWT2.

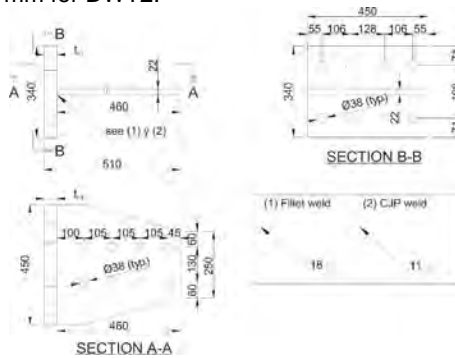


Figure 6: T stub connection dimensions

The load is applied at the top of the column using a 1000 kN actuator driven by a digital controller under displacement control. The AISC testing protocol for prequalification (AISC, 2010a) is followed to conduct the tests. A render of the test setup is shown in Figure 7, with the test specimen in grey. The force-displacement response of specimen SS-01 is shown in Figure 8. The specimen achieved a story drift of 0.04 rad in the East direction with incipient prying of the tees. In the West direction the actuator ran out of stroke at 0.03 rad. No sign of fracture was observed.

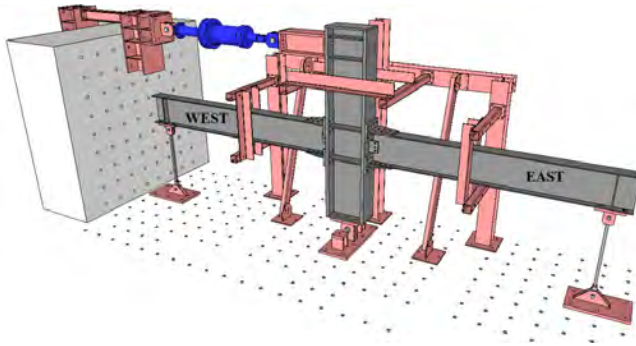
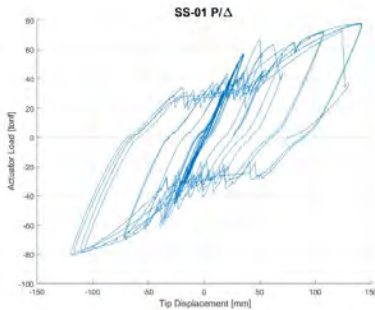
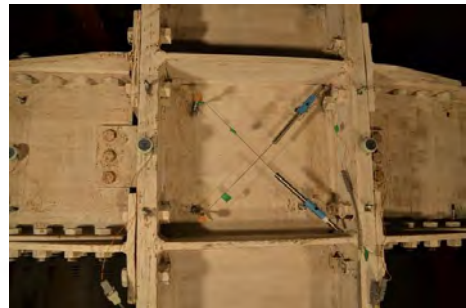


Figure 7: 3D render of experimental setup



(a) Load vs. displacement



(b) Prying at 0.04 rad story drift

Figure 8: Experimental results for test SS-01.

CONCLUSION

The details of a research program being conducted to study the performance of Double built-up T moment connections have been presented. The focus of the study is the numerical simulation and testing of full size connection subassemblages. Four prototype buildings are designed following current seismic design provisions in Chile. The design is feasible, although the sizes of beams and columns result large, due to the stringent displacement limits and minimum base shear requirements. A finite element model capable of reproducing the response of the connection/beam assemblage has been developed and shown to predict adequately the yield and ultimate capacity of the connection. This model will be used to conduct a parametric study for the connection. Finally, an experimental setup has been designed and constructed and testing has started on the specimens, showing an adequate performance under cyclic load. The results from these tests will be used to further validate the finite element model and improve design recommendations for these type of connections.

ACKNOWLEDGEMENTS

The research reported herein was possible thanks to the financial support of the National Council of Science and Technology (Conicyt) of Chile through FONDECYT grant N°1140628.

REFERENCES

- AISC (2010a), *ANSI/AISC 341-10 Seismic provisions for structural steel buildings*, American Institute of Steel Construction, Chicago, IL.
- AISC (2010b), *ANSI/AISC 358-10 Prequalified Connections for Special and Intermediate Steel Moment Frames for Seismic Applications*, American Institute of Steel Construction, Chicago, IL.
- Bravo, M.A. and Herrera, R.A. (2014), "Performance under cyclic load of built-up T-stubs for Double T moment connections", *Journal of Constructional Steel Research*, Vol. 103 (pp. 117-130).
- FEMA (2000), *Recommended Seismic Design Criteria for New Steel Moment-Frame Buildings*, Federal Emergency Management Agency, Washington DC, USA.
- Girão Coelho, A., Bijlaard, F., Gresnigt, N., and Simoes Da Silva, L. (2004), Experimental assessment of the behaviour of bolted T-stub connections made up of welded plates, *Journal of Constructional Steel Research*, Vol. 60 (pp. 269–311).
- Girão Coelho, A.M., Simões da Silva, L., and Bijlaard, F.S. (2006), "Finite-element modeling of the nonlinear behavior of bolted T-stub connections", *Journal of Structural Engineering*, Vol. 132, No. 6 (pp. 918-928).
- Hantouche, E. G., Rassati, G. A., Kukreti, A. R., and Swanson, J. A. (2012), "Built-up T-stub connections for moment resisting frames: Experimental and finite element investigation for prequalification", *Engineering Structures*, Vol. 43 (pp. 139-148).
- Herrera, R.A., Bravo, M., Gómez, G., and Aedo, G. (2013), "Performance of built-up T-stubs for Double T moment connections", *Journal of Constructional Steel Research*, Vol. 88 (pp. 289-295).
- INN (2009), NCh433.Of1996, *Earthquake resistant design of buildings, including 2009 modifications and 2011 Decree 61 (In Spanish)*, Instituto Nacional de Normalizacion, Santiago, Chile.
- Mistakidis, E.S., Baniotopoulos, C.C., Bisbos, C.D., Panagiotopoulos, P.D. (1997), "Steel T stub connections under static loading: an effective 2-D numerical model", *Journal of Constructional Steel Research*, Vol. 44, No. 1–2 (pp. 51–67).
- Piluso, V., Faella, C., and Rizzano, G. (2001a), "Ultimate behaviour of bolted T-stubs. I: theoretical model", *Journal of Structural Engineering*, Vol. 127, No. 6 (pp.694–704).
- Piluso, V., Faella, C., and Rizzano, G. (2001b), "Ultimate behaviour of bolted T-stubs. II: model validation", *Journal of Structural Engineering*, Vol. 127, No. 6 (pp. 686–93).
- Smallidge, J. (1999), *Behavior of bolted beam-to-column T-stub connections under cyclic loading*, Thesis to obtain the degree of M.S. in C.E. School of Civil and Computer Engineering, Georgia Institute of Technology, Atlanta, GA.
- Sherbourne, A.N. and Bahaari, M.R. (1996), "3D simulation of bolted connections to unstiffened columns-I. T-stub connections", *Journal of Constructional Steel Research*, Vol. 40 (pp. 169–187).
- Swanson, J.A. and Leon, R.T. (2000), "Bolted steel connections: tests on T-stub components", *Journal of Structural Engineering*, Vol. 126, No. 1 (pp. 50–56).
- Yang, J.G., Kim, H.K., Park, J.H., and Back, M. C. (2013), "Analytical models for the initial axial tensile stiffness and ultimate tensile load of a T-stub, including the effects of prying action", *International Journal of Steel Structures*, Vol. 13, No. 2 (pp. 341-352).
- Yee, Y. L., Melchers, R. E. (1986), "Moment-rotation curves for bolted connections", *Journal of Structural Engineering*, Vol. 112, No. 3 (pp. 615–635).
- Zoetemeijer, P.A.(1974), "Design method for the tension side of statically loaded, bolted beam-to-column connections", *Heron*, Vol. 20, No. 1 (pp. 1–59).

INNOVATIVE TUBE-BASED MOMENT CONNECTIONS FOR SEISMIC APPLICATIONS

Jason McCormick

University of Michigan, Ann Arbor, Michigan 48109-2125, USA
jpmccorm@umich.edu

Dan Wei

University of Michigan, Ann Arbor, Michigan 48109-2125, USA
danwei@umich.edu

Hollow structural sections (HSS) have been used extensively as truss members and bracing members in systems under static loads due to their high strength-to-weight ratio; good compression, tension, and bending properties; and high torsional stiffness. These properties can further be taken advantage of in low-rise tube-based seismic moment frame systems provided that the beam members meet required width-thickness and depth-thickness requirements and proper connection details are used to limit the occurrence of brittle weld failure. To further optimize the performance of tube-based seismic moment connections, a detailed finite element study is conducted for external diaphragm plate HSS connections and an innovative collar connection. The studies explore the effect of beam size, plate properties, and loading type on the performance of the connection. The results suggest that the beam's wall thickness and depth-thickness ratio play a critical role in the behavior of these tube-based connections.

INTRODUCTION

The high strength-to-weight ratio; good compression, tension, and bending properties; high torsional stiffness; and aesthetic appeal associated with steel hollow structural sections (HSS) can be taken advantage of in low-rise structures through a completely tube-based seismic moment frame. In the United States HSS use in seismic moment frames has been limited by a design approach that traditionally relies on select frames to resist lateral loads leading to a missed opportunity to take advantage of the unique and beneficial properties of HSS. Such a system can lead to a more advantageous response to seismic excitation due to reduced weight and a decrease in lateral bracing requirements resulting from the inherent torsional stiffness associated with HSS members. However, the use of a completely tube-based seismic moment frame has been limited due to a lack of information in regards to member and detailing requirements to meet current seismic practices (i.e. strong column-weak beam design).

Previous studies of HSS beam members have considered their behavior under monotonically increasing loads where they noted the importance of the width-thickness, depth-thickness, and aspect ratio of the HSS beam (Korol and Hubdoba, 1972; Wilkinson and Hancock, 1998). Only recently has studies by Fadden and McCormick

(2012a and 2014a) provided limiting width-thickness and depth-thickness ratios to achieve 80% of the plastic moment capacity out to 0.04 rad. of rotation as is required in the current American Institute of Steel Construction Seismic Design Provisions (AISC, 2010a). These findings combined with studies of Viernedeeel truss connections by Korol et al. (1977) suggest that HSS-to-HSS seismic moment connections are feasible provided proper detailing requirements are developed. To address this limitation and optimize the performance of tube-based seismic moment connections, detailed finite element studies of an external diaphragm plate connection and innovative collar connection are conducted.

REINFORCED HSS-BASED SEISMIC MOMENT CONNECTIONS

An external diaphragm plate and through plate connection are developed based on current seismic design provisions (AISC, 2010a) and current seismic moment frame connection configurations for wide flange beams to HSS columns (Kurobane et al., 2004). For these connections, a design philosophy where yielding of the reinforcing plate or plastic hinging of the beam occurs prior to weld fracture is implemented to ensure the connection develops the plastic moment capacity of the beam (Fadden and McCormick, 2014b). The external diaphragm plate wraps around the column to more efficiently transfer the bending moments in the beam to the sidewalls of the column preventing significant column face plastification. The through plate connection provides a similar load transfer mechanism with a through plate that is installed by cutting the HSS column and welding it in between the segments when they are reattached.

The two reinforced connections were experimentally tested to evaluate whether the design philosophy allowed the connections to meet current seismic design requirements and to provide information necessary to further optimize their performance. Both connections utilized an HSS 254×254×15.9 mm column and HSS 305×203×9.5 mm beam and underwent a loading protocol similar to that required to prequalify seismic moment connections (AISC, 2010a). The resulting normalized moment versus connection rotation results for the external diaphragm plate connection is shown in Figure 2. A similar behavior is seen for the through plate connection. The results show that both of the reinforced connections undergo desirable ductile plastic hinging of the beam prior to local buckling and they are able to maintain 80% of the connection's plastic moment capacity out to a rotation level of 0.04 rad. The majority of the inelastic deformation occurs in the beam member. Further details of these experimental tests and the connection configurations can be found in Fadden et al. (2015). The experimental results suggest the viability of the reinforced connections, but there remains a need to further optimize the design procedure and their performance.

FINITE ELEMENT STUDY OF THE EXTERNAL DIAPHRAGM PLATE CONNECTION

Finite Element Model: A finite element model is developed to further explore the performance of the external diaphragm plate connection by considering the effects of

the beam size and type of loading. A similar approach to modeling the connection as that used by Fadden and McCormick (2014b) is adopted with some changes to increase the accuracy of the model, namely including geometric imperfections in the plastic hinge region of the beam to more accurately capture local buckling. The finite element model is created in Abaqus CAE (Version 6.14-1) and represents an exterior connection in a seismic moment frame with a bay width of 5.8 m and floor height of 3.0 m (Figure 1). Half the height of the column is modeled above and below the beam and pinned end connections are used to represent the inflection points in the column.

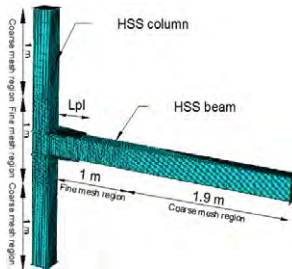


Figure 1. Finite element model for the external diaphragm plate HSS-to-HSS seismic moment connection.

The beam and column members are modeled with S4R shell elements. To improve the efficiency and accuracy of the analysis, the region adjacent to the column face that spans 1.0 m along the beam length utilizes 12.7 mm square elements while for the remaining length of the beam the element size gradually increases from 12.7 mm to 203 mm square elements. The smaller mesh size close the column face was determined based on a convergence study and ensures that the behavior within the plastic hinge region of the beam is accurately captured. The mesh for the column is broken into three segments with the central segment spanning 0.5 m above and below the center point of the connection. This region utilizes 12.7 mm square elements due to the potential for panel zone deformation. The other two segments extend to the ends of the column and have a gradually increasing mesh size from 12.7 mm to 152 mm square elements. The diaphragm plates are modeled with C3D8R solid elements that are 6.35 mm square. Tie constraints are used to simulate the CJP welds between the diaphragm plates and column, the flare bevel groove welds between the HSS beam and plates, and the fillet welds across the top and bottom of the HSS beam at the ends of the diaphragm plate. Since tie constraints are used instead of modeling the welds, weld failure is not considered in the models which is justified based on the design approach of avoiding critical weld failure and the findings of the experimental study (Fadden et al., 2015).

Tensile coupon tests of the flat and corner material of an HSS member (Fadden and McCormick, 2014a) provide the material properties that are incorporated into the finite element models after being converted to true stress-strain values. The measured yield strength and tensile strength of the beam flats are 426 MPa and 558 MPa and they are 416 MPa and 565 MPa for the beam corners. Similarly, the measured yield strength and

tensile strength of the column flats are 415 MPa and 565 MPa and are 416 MPa and 565 MPa for the column corners. All the material models for the beam and column utilize a combined hardening law to better predict cycling effects. The beam and column models are each partitioned into four flat sections and four corner sections with the material properties corresponding to each being applied to capture the cold working effects associated with the HSS manufacturing process. The corner material is applied up to a distance of twice the wall thickness away from the corner. For the diaphragm plate, ASTM A36 steel was assumed using an elastic-perfectly plastic model with a yield strength of 248 MPa. An isotropic hardening rule is used with the plate material model.

Finite Element Model Calibration: The finite element model is validated against the experimental results from the external diaphragm plate connection test (Fadden et al., 2015). The same beam end displacements that were measured during the experimental test are applied to the finite element model. Figure 2 provides a comparison of the experimental and finite element moment-rotation results. The results indicate that the model without geometric imperfections considered in the plastic hinge region over predicts the moment capacity by 3% and sees smaller moment degradation.

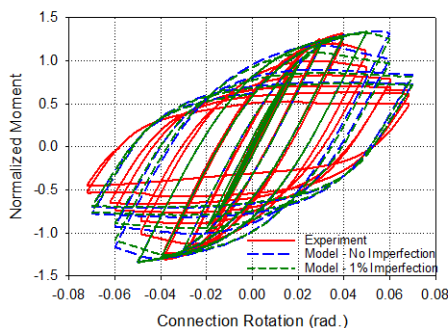


Figure 2. Comparison of the experimental test and finite element model results considering different levels of initial geometric imperfection.

To better simulate the hysteretic behavior observed during the experimental test, an initial geometric imperfection in the beam plastic hinge region is applied by introducing the mode shape obtained from an eigenvalue buckling analysis of the beam. Although larger initial imperfections tend to induce earlier local buckling and larger moment degradation, it is reasonable to utilize an imperfection of 1% of smaller dimension of the HSS beam as this value is the maximum allowable out-of-plane tolerance for ASTM 500 steel (AISC, 2010b). As shown in the Figure 2, the moment-rotation results of the model with a 1% initial imperfection are closer to the experimental result with only 2% difference in the maximum moment capacity. More moment degradation at each cycle is observed compared with the model without an initial imperfection. Based on these findings, all of the finite element models of the external diaphragm plate connections will incorporate a 1% initial geometric imperfection.

Parametric Study: To explore the behavior of the external diaphragm plate HSS-based seismic moment connections and ensure that the beam can achieve its maximum plastic moment capacity based on the design methodology proposed by Fadden and McCormick (2014a), a parametric study with different beam sizes is conducted. All column members are HSS 254×254×15.9 while the beam size is varied between HSS 254×203×6.4 to HSS 406×203×9.52 as shown in the Table 1. The length, L_{pl} , and thickness, t_{pl} , of the external diaphragm plates are determined according to the design procedure presented in Fadden and McCormick (2014b) where the objective is to have plastic hinging of the beam or plate yielding be the controlling limit state.

Along with varying the beam size, two different cyclic loading protocols (Figure 3) are selected to simulate far-field and near-fault type earthquakes. The far-field loading protocol applies increasing beam rotations from 0.0375 rad. up to 0.07 rad. with two repeated cycles at each rotation level. A near-fault ground motion is a pulse-like motion with an initial large amplitude, but short duration that can insight different structural responses than a far-field motion. The near-fault loading protocol shown in Figure 3 is considered with a large initial cycle to a rotation level of 0.06 rad.

Table 1. External Diaphragm Plate Connection Details (Unit:mm)

Beam Size	Plate Length	Plate Thickness
HSS 254x203x6.35	381	12.7
HSS 254x203x9.52	457	15.9
HSS 254x203x15.9	457	25.4
HSS 305x152x6.35	533	12.7
HSS 305x152x9.52	457	15.9
HSS 305x152x15.9	457	22.2
HSS 305x203x6.35	457	12.7
HSS 305x203x9.52	457	19.0
HSS 305x203x15.9	533	28.6
HSS 356x152x9.52	533	15.9
HSS 406x203x9.52	533	22.2

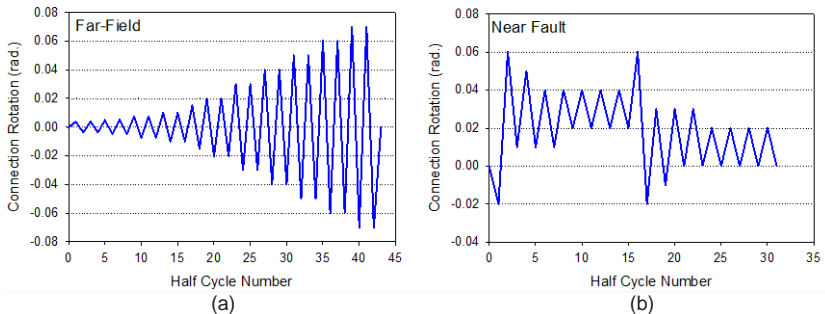


Figure 3. Loading protocols used for the external diaphragm plate connection parametric study: (a) Far-Field and (b) Near-Fault.

Moment-Rotation Results: To investigate the effect of the different parameters on the seismic response of the external diaphragm plate connection, the moment-rotation behavior is considered. The moment, which is calculated as the load applied at the beam tip multiplied by the distance from the beam tip to the center of the connection, is normalized by the beam plastic moment capacity. The beam plastic moment capacity is calculated as the beam's plastic section modulus multiplied by the beam flats' yield strength obtained from the coupon tests used to develop the HSS material model.

The normalized moment-rotation results under the far-field motion show varying degrees of degradation in the moment capacity with continued cycling. The maximum normalized moments range from 0.97 to 1.34 suggesting that the majority of the connection configurations are able to achieve the plastic moment capacity of the beam. For the HSS 305×152×6.35, HSS 305×152×9.52 and HSS 305×152×15.9 beams shown in Figure 4(a), the maximum normalized moments are 1.32, 1.20 and 0.97, respectively. However, the connection with the thinnest beam (HSS 305×152×6.35) reaches its maximum moment capacity at around 0.035 rad. and shows the largest degradation in the maximum moment with cycling. This behavior can be attributed to its large width-thickness ratio, 22.8, and depth-thickness ratio, 48.5. The connection with an HSS 305×152×9.52 beam exhibits more stable hysteretic behavior with little degradation in the moment capacity with cycling. Due to the thicker walls of the HSS 305×152×15.9 beam, yielding of the diaphragm plates controls rather than beam plastic hinging. This limit state leads to a lower moment capacity, but stable hysteresis.

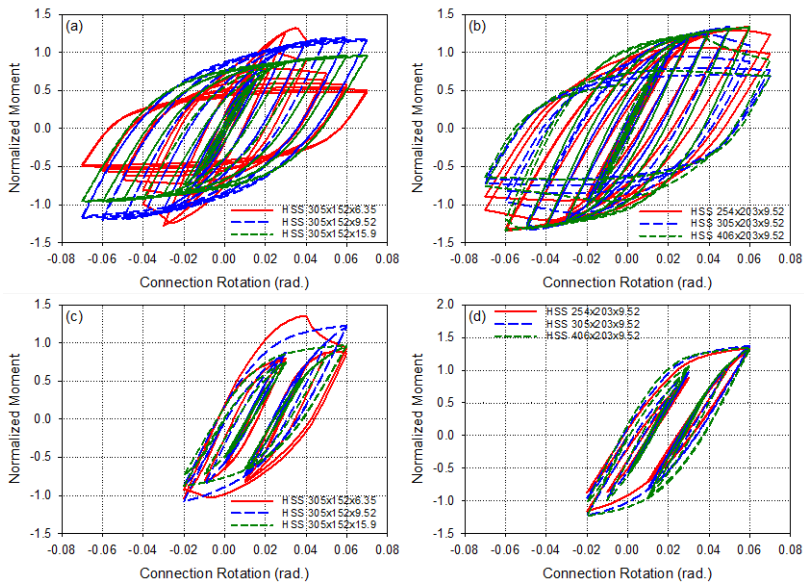


Figure 4. Normalized moment-rotation results for the external diaphragm plates connections: (a,b) Far-Field and (c,d) Near-Fault.

The influence of beam depth and depth-thickness ratio on the performance of the connection can be seen in Figure 4(b) where the normalized moment-rotation behavior for the connections with HSS 254×203×9.52, HSS 305×203×9.52 and HSS 406×203×9.52 beams is provided. The beam depth and depth-thickness ratio has very little effect on the normalized moment capacity, but does significantly influence the degradation of the moment capacity with continued cycling. During the last cycle to 0.07 rad., the maximum moment has decreased by 27%, 49%, and 49% for these connections with increasing beam depth-thickness ratios of 25.7, 31.4, and 42.8.

The influence of a large early pulse associated with a near-fault motion is explored in Figure 4(c) and (d). The maximum normalized moments are 1.36, 1.23 and 0.97, respectively, for the connections with HSS 305×152×6.35, HSS 305×152×9.52 and HSS 305×152×15.9 beams. Similar to what was seen with the far-field motion, the moment capacity of the connection with the HSS 305×152×6.35 beam suddenly drops at around the 0.04 rad. rotation level. Meanwhile, the other two connections with thicker beam walls exhibit more stable hysteretic behavior. The connections with HSS 254×203×9.52, HSS 305×203×9.52 and HSS 406×203×9.52 beams all show similar behavior.

Parameter Effects: To explore the effects of the diaphragm plate thickness and length on the connection’s capacity, the maximum normalized moment for each of the connections is shown in Figure 5 with respect to plate thickness and length. The results again show little influence due to the ground motion type. With increasing plate thickness, the maximum normalized moment in the connections decrease due to a shift from beam plastic hinging to plate yielding, while no clear trend is seen with respect to plate length. The results suggest that the design procedure for sizing the diaphragm plates provides the expected behavior under far-field and near-fault loading scenarios.

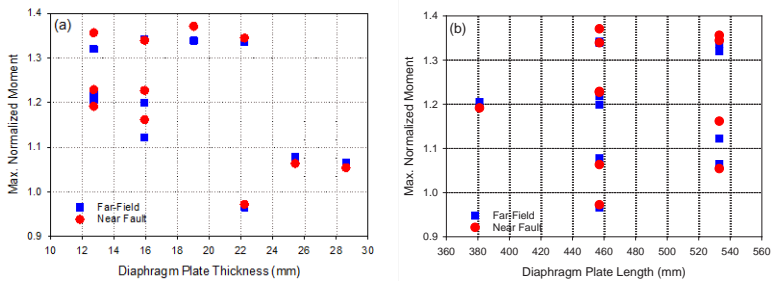


Figure 5. Maximum normalized moment versus (a) plate thickness and (b) plate length for the external diaphragm plates connections.

FINITE ELEMENT STUDY OF AN HSS-BASED COLLAR MOMENT CONNECTION

Although the use of external diaphragm plates leads to a good performance for tube-based moment connections under seismic loads, they can be labor intensive and require a significant amount of field welding. For these reasons, a collar connection concept is introduced to increase construction speed and minimize field welding. Figure 6

provides a schematic of the collar connection. Within the collar connection, the beam endplate, beam, column, and lower collar are shop welded. A gap left between the column face and collar allows the beam endplate to slip into the lower collar in the field. Once the beam is installed, the upper collar is slipped down the column and over the top of the beam endplate and welded. Only fillet welds are required in the field easing the construction process. To further control the load transfer mechanism and location of inelastic deformation, endplate stiffeners also are used.

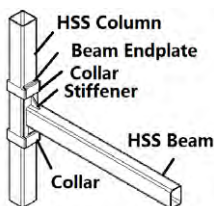


Figure 6. Schematic of the HSS-based collar connection.

Parametric Study: The seismic moment frame configuration used to study the external diaphragm plate connection is used for the HSS-based collar connection finite element study. All of the columns are HSS 254×254×15.9, while eight different beam members are considered (HSS 254×203×9.52, HSS 254×203×15.9, HSS 305×152×6.35, HSS 305×152×9.52, HSS 305×152×15.9, HSS 305×203×6.35, HSS 305×203×9.52, HSS 305×203×15.9). To isolate the effects of different beam width-thickness and depth-thickness ratios, the thickness of the collars, beam endplate and stiffeners are kept at 19 mm. The depth of the collars is 152 mm and the legs of the stiffeners are 152 mm. A gap of 25.4 mm is left between the toe of the stiffener and collar edge. The beam endplate extends 25.4 mm beyond the collar resulting in a total length of 965 mm and 1016 mm for connections with beam depths of 254 and 305 mm, respectively. The effect of loading type is also considered as the two loading protocols used in evaluating the external diaphragm plate connection are used to study the collar connection.

The beam and column are modeled as discussed previously. The models of the collars, beam endplate, and stiffeners are constructed with C3D8R solid elements with a 6.35 mm square element size. The interfaces between the beam and beam endplate, beam and stiffeners, collars and beam endplates, collars and column, beam endplate and column face, and stiffeners and beam endplate utilize tie constraint to represent the welds. As a result, weld failure is not modeled explicitly in the finite element study of the collar connections. The material models used to represent the collars, stiffeners, and beam endplate assume an elastic-perfectly plastic behavior with a yield strength of 248 MPa, which is the minimum required strength for ASTM A36 steel. A combined hardening law is considered for all the material models to account for cyclic load effects.

Moment-Rotation Results: To explore the effects of beam size and loading protocol on the performance of the collar connections, the normalized moment-rotation behavior is considered. The maximum normalized moments ranged from 1.01 to 1.19 suggesting

that all of the connections are able to develop their beam's plastic capacity. In Figure 7(a), the maximum normalized moments for the collar connections with HSS 305×152×6.35, HSS 305×152×9.52 and HSS 305×152×15.9 beams are 1.12 at 0.03 rad., 1.19 at 0.05 rad. and 1.11 at 0.07 rad., respectively. Of these three connections, the beam member with the largest wall thickness showed the most stable behavior with no local buckling observed. The degradation from the maximum moment capacity to the moment capacity during the last rotation cycle is approximately 54% and 28% for the connections with HSS 305×152×6.35 and HSS 305×152×9.52 beams. The findings again can be attributed to the width-thickness and depth-thickness ratios of these beams. Figure 7(b) also shows that an increase in beam depth will increase the degradation of the moment capacity with cycling due to the larger depth-thickness ratio. The findings suggest the viability of the connections for seismic application under large cyclic loads with a better performance observed for a thicker walled beam.

Figure 7(c) and (d) show that similar trends exist for the collar connections when undergoing a near-fault loading. In Figure 7(c), the maximum normalized moments for the connections with HSS 305×152×6.35, HSS 305×152×9.52 and HSS 305×152×15.9 beams are 1.15 at 0.03 rad., 1.22 at 0.06 rad. and 1.09 at 0.06 rad., respectively. The connection with the HSS 305×152×6.35 beam exhibits degradation after reaching its peak moment capacity due to the large depth-thickness ratio, 48.5. In Figure 7(d), the maximum normalized moments are both 1.18 for the collar connections with HSS 254×203×9.52 and HSS 305×203×9.52 beams. Both connections experience little moment degradation and exhibit stable seismic performance under near-fault excitation.

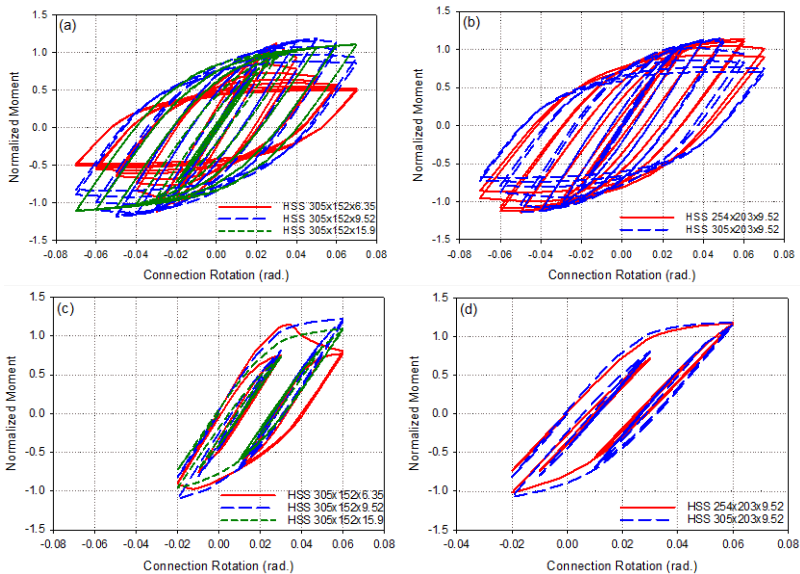


Figure 7. Normalized moment-rotation results for the collar connections: (a,b) Far-Field and (c,d) Near-Fault.

CONCLUSION

A finite element study is conducted to explore the effect of beam size, reinforcing plate dimensions, and loading type on the performance of tube-based external diaphragm plate and collar connections to determine the viability of their design procedures and to optimize their performance. Beam width-thickness ratio, depth-thickness ratio, depth, and wall thickness have the greatest contribution in influencing the connection's behavior while the difference between the behaviors under far-field or near-fault type loadings is minimal. The use of thicker beams also can lead to a shift away from beam plastic hinging and more inelastic behavior in the diaphragm plates or other collar connection elements. Overall, the results suggest that with proper member selection and detailing, the external diaphragm plate and collar seismic connections are viable.

REFERENCES

- AISC. (2010a), *Seismic Provisions for Structural Steel Buildings*. ANSI/AISC 341-10, Chicago.
- AISC. (2010b), *Specification for Structural Steel Buildings*. ANSI/AISC 360-10, Chicago.
- Fadden, M. and McCormick, J. (2012). "Cyclic Quasi-Static Testing of Hollow Structural Section Beam Members", *J. Struct. Eng.*, Vol. 138, No. 5 (pp. 561-570).
- Fadden, M. and McCormick, J. (2014a). "Finite Element Model of the Cyclic Bending Behavior of Hollow Structural Sections", *J. Constr. Steel Res.*, Vol. 94, (pp. 64-75).
- Fadden, M. and McCormick, J. (2014b). "HSS-to-HSS Seismic Moment Connection Performance and Design", *J. Constr. Steel Res.*, Vol. 101, (pp. 373-384).
- Fadden, M., Wei, D., and McCormick, J. (2015). "Cyclic Quasi-Static Testing of Welded HSS-to-HSS Moment Connections for Seismic Applications", *J. Struct. Eng.*, Vol. 141, No. 2 (pp. 04014109-1-14).
- Korol, R.M., El-Zanaty, M., and Brady, F.J. (1977), "Unequal Width Connections of Square Hollow Sections in Vierendeel Trusses", *Can. J. Civ. Eng.*, Vol. 4, No. 2 (pp. 190-201).
- Korol, R.M. and Hudoba, J. (1972), "Plastic Behavior of Hollow Structural Sections", *AISC Proceedings, Journal of the Structural Division*, Vol. 98, No. ST5 (pp. 1007-1023).
- Kurobane, Y., Packer, J.A., Wardenier, J., and Yeomans, N. (2004), *Design Guide for Structural Hollow Section Column Connections, CIDECT Design Guide No. 9*. CIDECT and TÜV, Köln, Germany.
- Wilkinson, T. and Hancock, G.J. (1998), "Tests to Examine Compact Web Slenderness of Cold-Formed RHS", *J. Struct. Eng.*, Vol. 124, No. 10 (pp. 1166-1174).

EXPERIMENTAL ANALYSIS AND DESIGN OF FRICTION JOINTS EQUIPPED WITH SPRAYED ALUMINUM DAMPERS

Massimo Latour, Vincenzo Piluso, Gianvittorio Rizzano

*University of Salerno, Department of Civil Engineering
Via Giovanni Paolo II, Fisciano (SA)- Italy*

mlatour@unisa.it, v.piluso@unisa.it, g.rizzano@unisa.it

ABSTRACT

In this paper, a free from yielding approach based on the application of friction dampers to steel joints is presented. In particular, it is proposed to connect the beam to the column with a classical fixed T-stub fastening the upper flange and a friction damper located at the beam lower flange. The friction damper, composed by a stack of steel plates with one of the inner plates coated with thermally sprayed aluminium, is designed in order to slide for a force level equal to the ratio between the flexural resistance of the connected beam and the lever arm, i.e. the distance between the T-stub and the friction damper. In this way, it is possible to obtain practically full-strength connections able to dissipate the seismic input energy, provided that all the joint components are designed to be over-strength with respect to the actions corresponding to the friction damper sliding force without any damage to the steel elements. In this paper, such approach is validated reporting the results of an experimental campaign developed at the Laboratory of Materials and Structures of the University of Salerno.

1. INTRODUCTION

The design of modern seismic resistant structures is based on a preliminary selection of the so-called dissipative zones which have to be designed to assure, by means of their plastic engagement, the dissipation of the earthquake input energy. Dealing with Moment Resisting Frames (MRFs), it is well known that the dissipative zones can be located at beam ends, by designing full-strength joints, or in joints, by designing the joints to be less resistant than the connected member (CEN 2005a,b,c). To date, the first approach has been widely applied in practical seismic design and surely provides some advantages, such as the development of stable hysteresis loops (Mazzolani & Piluso, 1996) and the prevention of soft storey mechanisms. However, the use of full-strength joints, with the code required over-strength can lead, in some cases, to the detailing of frames which are not cost-effective due to the significant oversizing of connections and columns required by the code in order to promote the plasticization of beams and to respect the members' hierarchy criterion (CEN 2005a). Therefore, in past decades, in order to overcome the drawbacks related to the use of full-strength beam-to-column joints, the use of partial-strength connections has been promoted by many theoretical and experimental research programs (Faella et al., 2000, Jaspart & Demonceau, 2008, Castro et al., 2005, Kim & Engelhardt, 2002, Nogueiro et al., 2009) and, recently, Eurocode 8 has opened the door to their use provided that their plastic rotation capacity is properly demonstrated. Nevertheless, even though the effort provided by the scientific community has already been significant, there are still some issues which deserve

further investigation, such as the codification of design criteria for dissipative joints or the development of new types of dissipative connections easy to replace after a severe seismic event (Latour et al., 2012, Soong & Spencer, 2002, Yang & Popov, 1995).

However, independently of the use of either full-strength or partial-strength beam-to-column joints, the main drawback of the traditional seismic resistant design strategy is intrinsic in the strategy itself. In fact, on one hand the structural damage is essential to dissipate the earthquake input energy but, on the other hand, it is the main source of direct and indirect losses. For this reason, many researchers have focused their attention on the strategy of supplementary energy dissipation with the aim to reduce the structural damage under destructive seismic events and, as a consequence, the direct and indirect losses. Among these works, recently, some of these researches have been devoted to the development of a new design strategy, whose goal is the design of connections able to withstand without any damage not only frequent and occasional seismic events, but also destructive earthquakes such as those corresponding to rare and very rare events. The basic idea of these new researches (Khoo et al., 2014, Khoo et al., 2012, Latour et al., 2011, Latour et al., 2014) is inspired to the strategy of supplementary energy dissipation, but it is based on the use of damping devices under a new perspective. In fact, while passive control strategies have been commonly based on the integration of the energy dissipation capacity of the primary structure by means of a supplementary dissipation coming from damping devices; conversely, the new design strategy is conceived in such a way to substitute the traditional dissipative zones of MRFs, i.e. between the beam ends, by equipping the connections with friction dampers.

Within this framework, in this paper a new beam-to-column connection system is investigated. In particular, it is suggested to modify the classical detail of Double Split Tee Joints (DST) by introducing a symmetrical friction damper at the level of the lower beam flange. With the proposed connecting system, under bending actions, the joint is forced to rotate around the upper T-stub, preventing slab damage, and the energy dissipation supply is provided by the slippage of the lower beam flange on the friction pads, which are made of steel plates coated with thermally sprayed aluminum. In this way, provided that the steel components of the connection are properly over-strengthened, the joint resistance and the rotation capacity can be easily governed by calibrating the preload applied to the frictional interfaces and realizing slotted holes whose length provides an adequate stroke for the dissipative device. In order to validate the proposed approach, the results of an experimental program carried out at the Materials and Structures Laboratory of the Salerno University are presented, reporting the results of preliminary tests aimed at characterizing the frictional properties of new pads and the results of two tests on real-scale external beam-to-column joints.

2. TESTS ON THERMALLY SPRAYED ALUMINUM INTERFACES TO BE APPLIED IN FRICTION DEVICES

The results herein presented are referred to a friction interface composed by 8 mm steel plates coated with a layer of thermally sprayed aluminium sliding on steel (Fig.1). Even though the main field of application of sprayed aluminum is the prevention of corrosion phenomena, its good tribological properties for friction pad applications, which are characterised by high values of the friction coefficient and a low cost of the raw material, have already been evidenced in past experimental works (Ono et al., 1996). In order to evaluate the friction coefficient of the interface a sub-

assemblage composed by a stack of S275JR steel plates has been employed (Fig. 2). In particular, the device used for testing the friction pads is conceived in order to allow the slippage of one of the inner steel plates on the interposed material.

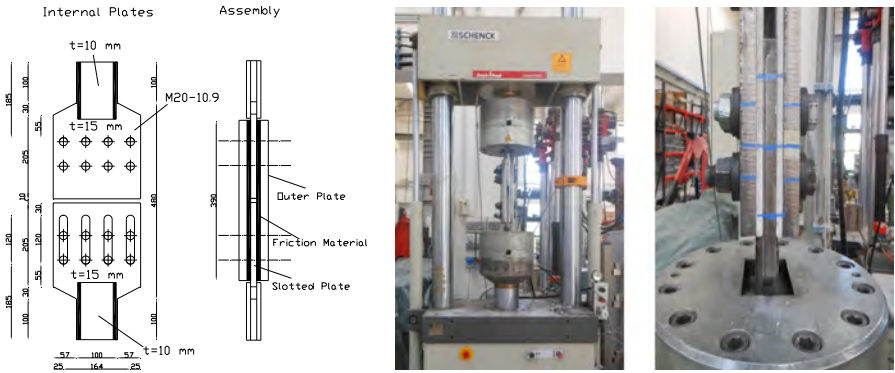


Fig. 1: Specimens' layout

To this scope, such plate is realised with slotted holes, while the other inner and the two outer plates are realised with circular holes according to the detail reported in Fig. 2. The clamping force is applied to the friction pad by means of a maximum number of 8 high strength M20 bolts 10.9 class and, in order to keep constant the preloading applied on the frictional interface during the test, couples of cone annular disc springs working in series have been used in substitution of the classical circular flat washers. The tests have been carried out by means of a universal testing machine Schenck Hydropuls S56 (Fig. 1). The experimental analysis has been carried out in two phases. In the first phase, specimens with friction pads characterized by different values of the thickness of sprayed aluminum coating (50 μm , 150 μm and 300 μm) have been tested. Successively, in the second phase, additional tests have been carried out only on the interface with friction plates with 300 μm of coating, to evaluate also the influence of the applied pressure on the friction coefficient (Table 1).

Table 1 – Summary of the tests performed

Coating Thickness	Number of tightened bolts	Bolt Torque	Number of Cycles of the loading sequence	Amplitude
50 μm	4	200 Nm	10	+/- 15 mm
	8		45	
150 μm	4	200 Nm	10	+/- 15 mm
	8		45	
	4		10	
300 μm	8	200 Nm	20	+/- 15 mm
	4		10	
	4		400 Nm	

In particular, in the first phase, for each test, two different loading sequences have been considered by applying to the bolts a tightening torque of 200 Nm. In the second phase, other two tests have been performed only on the interface with coating

thickness equal to 300 μm considering other two values of the tightening torque equal to 300 Nm and 400 Nm. The main goals of the experimental campaign are, on one hand, the evaluation of the friction coefficient for different values of the normal force acting on the sliding interface and, on the other hand, the assessment of the cyclic response in order to evaluate the stability of the obtained cycles and the energy dissipation capacity. In the following the test results are discussed reporting the obtained values of the friction coefficient. In particular, starting from the test results, the friction coefficient has been determined as:

$$\mu = \frac{F}{n_s n_b N_b} \quad (1)$$

where n_s is the number of surfaces in contact, n_b is the number of bolts, N_b is the bolt preloading force and F is the sliding force. In particular, the bolt preloading force N_b is determined starting from the knowledge of the tightening torque by means of the following expression:

$$N_b = \frac{T_b}{k d_b} \quad (2)$$

where T_b is the value of the tightening torque, k is a factor accounting for the friction arising between bolt head and plate and between bolt shank and nut and d_b is the bolt nominal diameter. In agreement with (UNI-CEI-CNR, 1988) the value of k has been assumed equal to 0.20.

2.1.1 Tests with variable thickness of the coating layer

The results of the tests with variable thickness of the coating layer has pointed out that the behavior of all the interfaces is quite stable with a high energy dissipation capacity, due to the high forces that the employed friction material is able to develop. In particular, all the interfaces exhibited a high initial stiffness and, after reaching the sliding force, began to slide with a force similar to the initial one, evidencing that there is not a significant difference between the static and kinetic coefficient of friction. In addition, after the first cycle, all the subsequent cycles reached a value of the maximum force slightly lower than the initial one, evidencing the role played by the wearing of the friction material of the coated surface (Fig. 2). In particular, in Fig.2 the obtained hysteretic curves for the different values of the coating layer are reported, together with the values of the friction coefficient obtained by means of Eq. 1 are represented versus the cumulated displacement.

Analyzing the results summarized in Table 2, it is possible to observe that, considering all the tested interfaces, the value of the friction coefficient ranges in between 0.37 and 0.59, revealing that thermally sprayed aluminum is able to provide a value of the coefficient of friction higher than the metallic and rubber interfaces tested in past experimental investigations. In particular, the highest value of the friction coefficient was obtained with the thickness of 150 μm and the lowest with the thickness of 50 μm . In addition, the reported tests show that the degradation of the sliding force significantly depends on the thickness of aluminum coating. In fact, considering the first loading sequence (Table 2), in case of 50 μm and 300 μm thickness, the degradation of the sliding force is very low and the ratio between the initial and final friction coefficient is equal to 1.12 and 1.02 respectively. In the first case, probably the result

is due to the lower sliding force that provided a limited consumption of the friction pad. Conversely, a higher degradation was shown by the 150 μm interface, whose initial/final sliding force ratio was equal to 1.22. Therefore, analyzing the results on these tests, for the subsequent phase of the experimental work, only the coating with thickness of 300 μm has been considered. In fact, as result of the first phase tests, this thickness of the coating layer is believed to provide a good compromise between the initial value of friction coefficient and degradation of the sliding force during a cyclic loading history.

Table 2 – Summary of the test results

Thickness of the coating	1 st loading sequence		2 nd loading sequence	
	Initial	Final	Initial	Final
50 μm	0.37	0.33	0.37	0.31
150 μm	0.59	0.48	0.52	0.29
300 μm	0.52	0.51	0.45	0.37

1st Loading Sequence

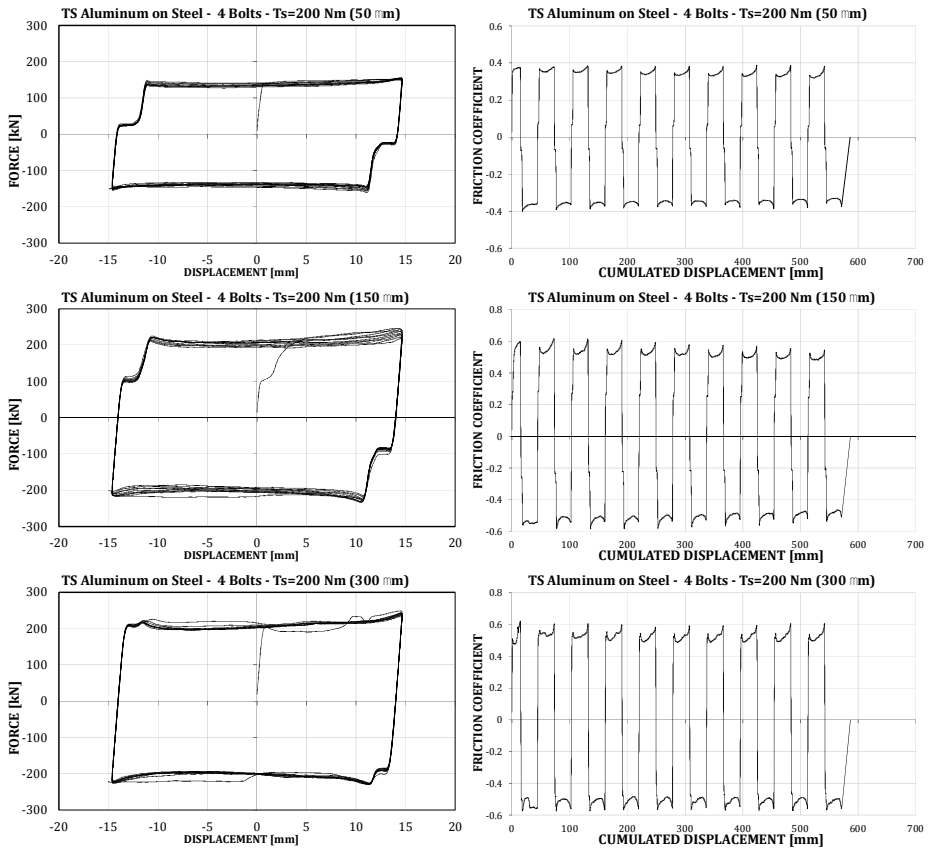


Fig. 2: Experimental results: influence of the thickness of the coating layer

2.1.2 Tests with variable pressure

As aforesaid, in order to evaluate the influence of the tightening pressure on the value of the slip resistance, additional tests have been carried on further specimens having the selected coating thickness of 300 μm . In particular, three different values of the tightening torque have been considered and only one loading sequence of ten cycles with amplitude of ± 15 mm has been adopted. The behavior exhibited by such specimens is reported in Fig. 3. It evidences a response very similar to that reported in previous tests, but reveals that the value of the initial coefficient of friction, for this interface, strongly on the pressure applied on the interface. In fact, as it is possible to observe, as far as the value of the tightening torque increases, the initial value of the friction coefficient decreases (Fig.3). The results obtained in this preliminary phase have been employed in order to design the sliding force of the friction dampers employed in the beam-to-column connections, whose test results are presented in next sections.

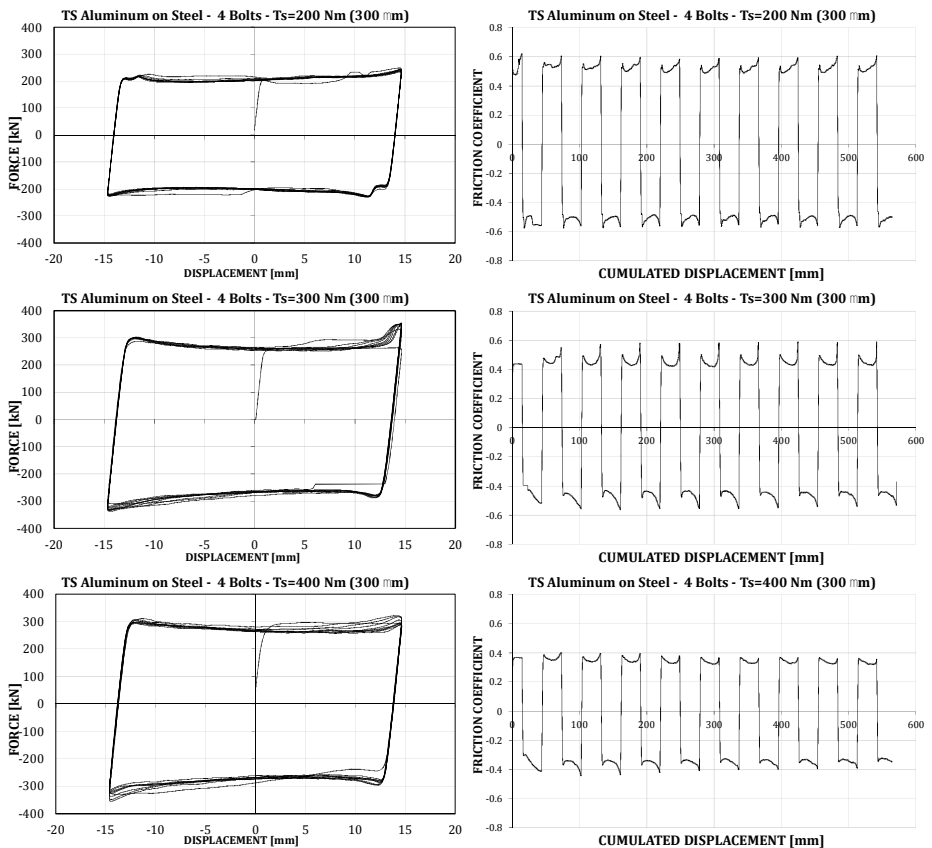


Fig. 3: Experimental results: influence of the applied pressure

3 EXPERIMENTAL TESTS ON BEAM-TO-COLUMN JOINTS

Starting from the results of the preliminary tests on the friction damper, the design of dissipative DST connections equipped with friction pads has been performed. The joint detail proposed in this paper is the modification of the classical detail of a double split Tee beam-to-column connection obtained by substituting the lower T-stub with a friction damper obtained by connecting the beam bottom flange to the column flange by means of three steel angles, composed by welding and by interposing between them and the beam flange one or two friction pads (Fig.4). In this way, the energy dissipation supply of the beam-joint system is provided by the friction damper, while all the other elements of the connection and the beam are designed in order to be completely free from damage. This strategy, as already demonstrated in some preliminary studies on similar prototypes, allows the development of beam-to-column connections with high energy dissipation able to accommodate the required rotations without any damage (Latour et al., 2011). The classical T-stub connection at the top flange level is aimed to fix the center of rotation with the goal of preventing the damage of the reinforced concrete slab.

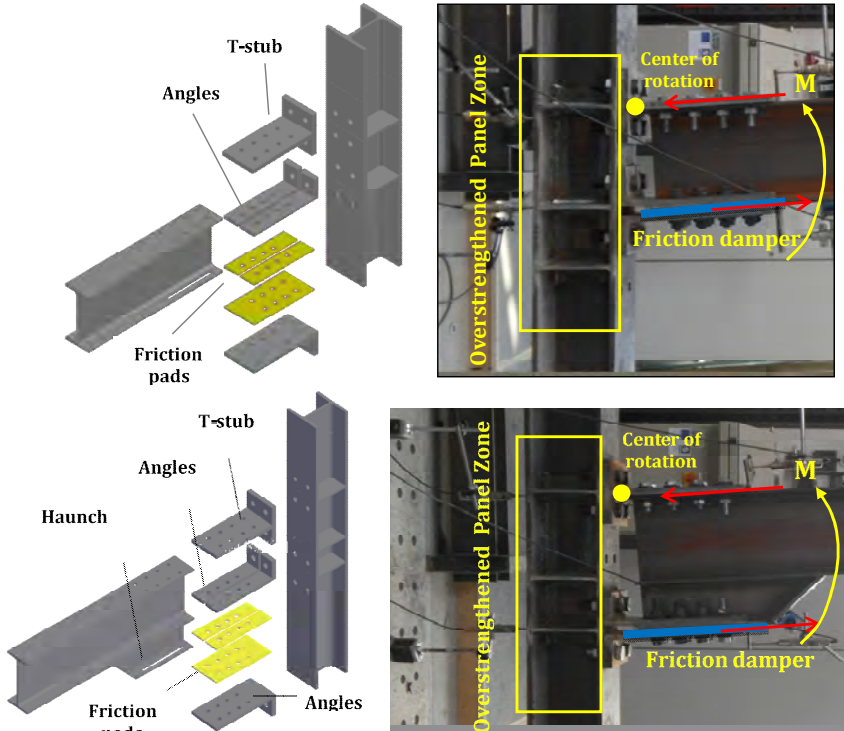


Fig. 4: Beam to column connections with friction damper, with or without haunch

A significant advantage of this joint configuration is that, by controlling the tightening torque applied to the bolts, it is possible to calibrate magnitude of the sliding resistance of the friction damper and, therefore, depending on the lever arm, the magnitude of the bending moment transmitted to the column. It is important to note that, in order to assure that the beam end remains in elastic range, the bending sliding resis-

tance of the connection has to be not greater than the nominal bending resistance of the connected beam. However, in order to maximize the exploitation of the beam under gravity loads and under the internal actions occurring when the structure is subjected to horizontal forces corresponding to serviceability limit states such as wind actions or frequent seismic events having a low return period, the ratio between the bending sliding resistance of the connection and the nominal bending resistance of the connected beam has to be as close as possible to 1.0. In order to satisfy the above design criterion and to maximize the exploitation of the connected beam, the use of a beam end haunch to increase and calibrate the lever arm can also be suggested (Fig.4). In such a way, the beam section is fully exploited, but both the oversizing of the other joint components (such as the panel zone usually requiring supplementary web plates, the beam end requiring reinforcing ribs or cover plates the increase of the bolt diameter, etc.) and the column oversizing (because of beam-column hierarchy criterion) can be significantly limited and/or controlled. Within the experimental activity described in this paper two different joints equipped with the friction damper previously tested under uniaxial loading conditions, have been tested under cyclic loading conditions. In particular, the two joints fasten an IPE 270 beam to an HEB 200 column both made of S275 steel. They are identified as follows:

- TSJ-SA300-320-CYC 12: it is a joint where the upper beam flange is connected to the column by means of a T-stub, while the lower beam flange is fastened to the column by means of a system of three angles. A steel plate with a 300 μm coating of thermally sprayed aluminum is located in between the beam flange and the angles in order to realize the friction damper;
- TSJ-H-SA300-260-CYC 13: it is a joint with a detail very similar to the previous one where, in order to increase the lever arm, the friction damper is applied by means of an additional haunch which is welded to the beam. This allows a proportional reduction of the tightening torque.

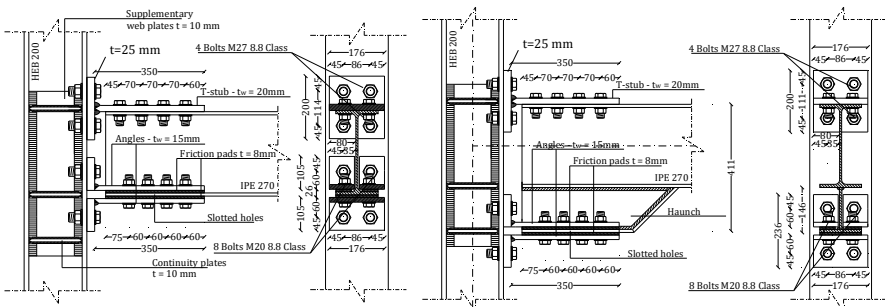


Fig. 5: Left: TSJ-SA300-320-CYC12, Right: TSJ-SA300-260-CYC13

Starting from the experimental results previously reported, the pre-tightening level of the bolts used to pre-load the friction interface of the dampers has been calibrated according to the joint design bending moment which has been assumed equal to the nominal value of the beam plastic resistance (133 kNm). The length of the slots made in the lower flange plate of the beam or in the additional haunch has been calibrated in order to accommodate a maximum value of the joint rotation equal to 40 mrad. The specimens' details are reported in Fig.5.

The experimental tests have been carried out at Materials and Structures Laboratory of Salerno University employing a layout specifically devoted to tests on external joints. The specimens are assembled with the column (HEB 200) in horizontal position, connected to the hinges, and the beam (IPE 270) in vertical position (Fig. 9). The loads have been applied by means of two different hydraulic actuators. The first one is a MTS 243.60 actuator with a load capacity equal to 1000 kN in compression and 650 kN in tension with a piston stroke equal to ± 125 mm which has been used to apply, under force control, the axial load in the column equal to 30% of the squash load. The second actuator is a MTS 243.35 with load capacity equal to 250 kN both in tension and in compression and a piston stroke equal to ± 500 mm which has been used to apply, under displacement control, the desired displacement history at the beam end. In order to avoid the lateral-torsional buckling of the beam an horizontal transversal frame has been conceived to work as a guide which restrains the lateral displacement of the beam. The loading history has been defined in terms of drift angle, according to the testing protocol provided by AISC, 2005.

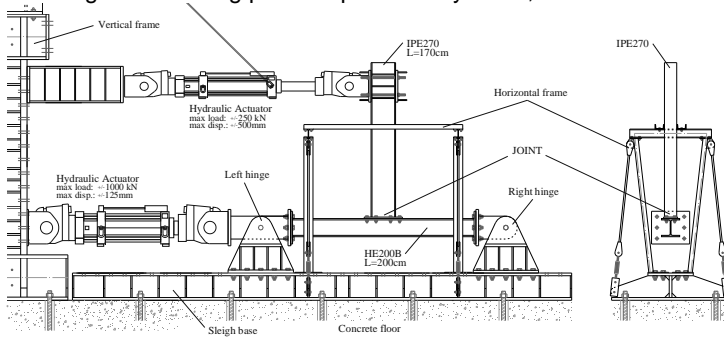


Fig. 6: Experimental setup

4 EXPERIMENTAL RESULTS

As aforesaid the two joints were tested under cyclic loading conditions following the drift history suggested by the AISC loading protocol. As expected, on the basis of the design criteria adopted, in all the experimental tests there has not been any significant damage of the joint components, but only the wearing of the friction pads. Therefore, a very important outcome of the experimental program is the verification that this connection typology can be subjected to repeated cyclic rotation histories, i.e. to repeated earthquakes, by only substituting the friction pads, if needed, and by tightening again the bolts to reach the desired preloading level. In addition, the rotation capacity can be easily calibrated by simply governing the length of the slotted holes. In fact, in all the tests the rotation demand applied to the joint has been completely due to the slippage of the friction damper located at the bottom beam flange. The experimental results are in line with the outcomes of the tests on the friction interfaces pointing out that, as expected, the cyclic behaviour of the joint is mainly governed by the cyclic behaviour of the weakest joint component, i.e. the friction. In fact, in both tests the response has been very similar to that exhibited during the uniaxial tests on the interface. At low force values the joints exhibited an elastic behaviour characterized by a high initial stiffness. In particular, in case of joint TS-H-SA300-260-CYC13 the initial stiffness was sensibly higher due to the increased lever arm provided by the additional haunch. When the force applied at the end of the can-

tilever beam reached a value approximately equal to the design bending moment divided by the beam length, the slippage of the friction dampers started (Fig.7). After the first slippage, the joints hysteretic response was characterized for all the loading/unloading cycles approximately by a parallelogram shape with a slight strength degradation as the number of the cycles of the loading history increases (Fig.8).

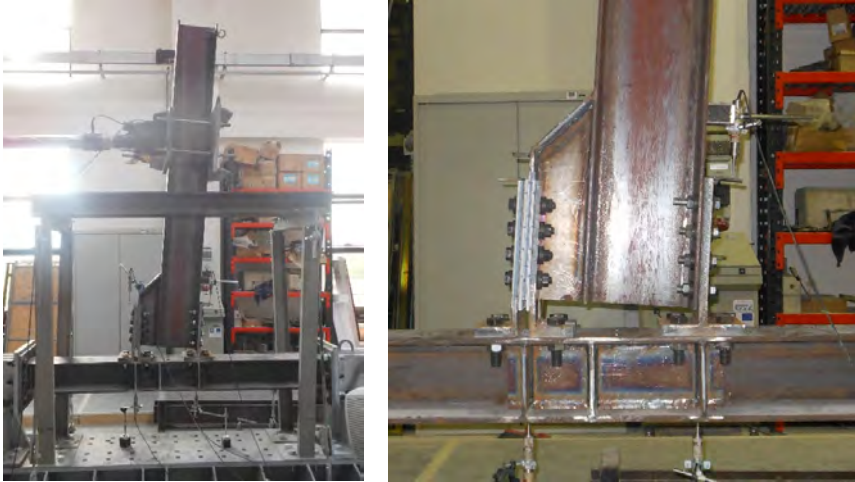


Fig. 7: Sliding motion of the friction damper during the test

By the comparison with the results of the tests carried out on the friction dampers (i.e. the component alone), it is worth noting that the main difference between the hysteresis cycles of the friction DST joint and those observed during the uni-axial tension test is the asymmetric response. This difference is mainly due to the role played by the beam rotation in the kinematic mechanism. In fact, the beam rotation causes two effects that give rise to an increase of the bending moment as far as the beam rotation increases. On one hand, there is an increase of the local pressure on the friction pads due to the reaction force provided by the stem of the fixed T-stub at the top beam flange level and by the stems of the angles at the bottom flange level, that behave in a way similar to a pocket foundation. Because of this pocket foundation effect, the increase of the pressure on the friction pads depends on the direction of the horizontal displacement of the cantilever. Therefore, the asymmetry of the cyclic response is due to the reduction of the friction coefficient when the pressure on the friction pads increases. On the other hand, minor yielding of the tee stems at the stem-to-flange connection of top T-stub and bottom angles contributes to the total bending resistance providing a slight hardening behaviour as experimentally observed (Fig.8). The most important feature of the proposed connection is that, as confirmed by the experimental results, it is able to provide a high dissipative capacity also under values of the rotation significantly greater than the minimum value, equal to 35 mrad, required by Eurocode 8 for frames in High Ductility Class. Furthermore, it is possible to observe from Fig.8 that the resistances of the joints and of the dampers approximately correspond to the design ones. Finally, it is very important to underline that the obtained flexural strength is greater than the plastic resistance of the connected beam, so that practically full-strength connections are obtained without providing any damage to the beam ends.

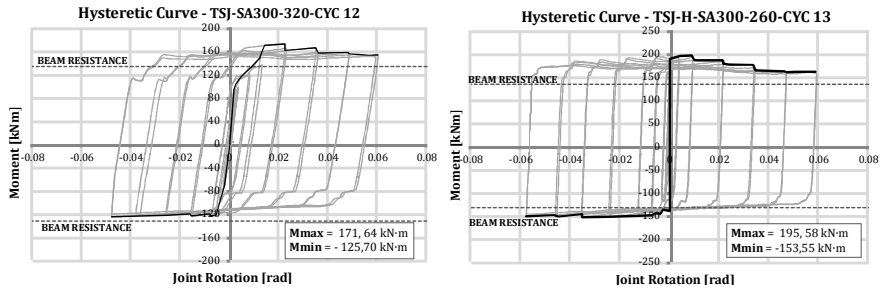


Fig. 8: Moment-Rotation response of the connections

CONCLUSIONS

The results of an experimental program devoted to evaluate the possibility to equip steel joints with friction dampers realized with pads coated with thermally sprayed aluminum have been presented. The work has been carried out in two steps. In the first phase, the behavior of the frictional interface has been evaluated and, successively, tests on two joint configurations have been carried out. The main outcomes of the experimental programs can be summarized as follows:

- The frictional interface “thermally sprayed aluminum on steel” is characterized by high values of the kinematic friction coefficient. In fact, compared to other metallic or rubber materials tested in a past experimental program under the same loading conditions it is able to exhibit values of the friction coefficient significantly greater;
- The friction coefficient of the interface decreases as far as the pressure applied to the interface increases;
- The strategy to be applied to design free from damage friction T-stub connections characterized by a desired moment resistance and rotation supply have been presented. In particular, the bending moment of the connection can be easily calibrated by controlling the tightening torque of the bolts of the friction damper, while the rotation supply of the connection can be controlled by properly designing the length of the slots of the friction damper;
- The results of the tests on the connections substantially confirm those coming out from the tests on the friction dampers, pointing out the ability of the proposed joints to dissipate an high amount of energy without any damage to the structural parts;
- The experimental program dealing with double split friction tee stub joints has confirmed the possibility to obtain yielding-free connections.

REFERENCES

- CEN. Eurocode 8: Design of structures for earthquake resistance - Part 1: General rules, seismic actions and rules for buildings. 2005a.
- CEN. Eurocode 3: Design of steel structures - Part 1-1: General rules and rules for buildings. 2005b.
- CEN. Eurocode 3: Design of steel structures - Part 1-8: Design of joints. 2005c.
- Mazzolani, F. and Piluso, V. Theory and Design of Seismic Resistant Steel Frames. E & FN Spon, an imprint of Chapman & Hall, London, 1996.

- Faella, C., Piluso, V., and Rizzano, G. *Structural Steel Semi-Rigid Connections*. CRC Press, Boca Raton, 2000.
- Iannone, F., Latour, M., Piluso, V., and Rizzano, G. Experimental Analysis of Bolted Steel Beam-to-Column Connections: Component Identification. *Journal of Earthquake Engineering*, 15, 2 (2011), 214-244.
- Jaspart, JP and Demonceau, JF. European Design recommendations for simple joints in steel structures. *Journal of Constructional Steel Research*, 64/7, 8 (2008), 822-832.
- Castro, J.M., Elghazouli, A.Y., and Izzudin, B.A. Modelling of the panel zone in steel and composite moment frames. *Engineering Structures*, 27 (2005), 129-144.
- Kim, K.D. and Engelhardt, M.D. Monotonic and cyclic loading models for panel zones in steel moment frames. *Journal of Constructional Steel Research*, 58 (2002), 605-635.
- Nogueiro, P., Simoes da Silva, L., Bento, R., and Simoes, R. Calibration of Model Parameters for the Cyclic Response of End-Plate Beam-to-Column Steel-Concrete Composite Joints. *Journal of Steel and Composites Structures*, 9, 1 (2009), 35-58.
- Latour, M and Rizzano, G. Experimental Behavior and Mechanical Modeling of Dissipative T-Stub Connections. *Journal of Structural Engineering*, 138, 2 (2012), 170-182.
- Soong, T.T. and Spencer Jr, B.F. Supplemental Energy Dissipation: State-of-the-Art and State-of-the-Practice. *Engineering Structures*, 24 (2002), 243-259.
- Yang, TS and Popov, EP. Experimental and analytical studies of steel connections and energy dissipators. UCB/EERC-95/13, Earthquake Engineering Research Center, Berkeley, 1995.
- Khoo, H, Clifton, G, Macrae, G, and Ramhormozian, S. Proposed design models for the asymmetric friction connection. *EARTHQUAKE ENGINEERING & STRUCTURAL DYNAMICS*, 44, 8 (December 2014), 1309-1324.
- Khoo, H, Clifton, C, Butterworth, J, MacRae, G, Gledhill, S, and Sidwell, G. Development of the self-centering Sliding Hinge Joint with friction ring springs. *Journal of Constructional Steel Research*, 78 (2012), 201-211.
- Latour, M, Piluso, V, and Rizzano, G. Experimental analysis of innovative dissipative bolted double split tee beam-to-column connections. *Steel Construction*, 4, 2 (June 2011), 53-64.
- Latour, M, Piluso, V, and Rizzano, G. Experimental Analysis of Friction Materials for supplemental damping devices. *Construction and Building Materials* (2014).
- Ono, S, Nakahira, K, Tsujioka, S, and Uno, N. Energy Absorption Capacity of Thermally Sprayed Aluminum Friction Dampers. *Journal of Thermal Spray Technology*, 5, 3 (September 1996).
- UNI-CEI-CNR. *Costruzioni di acciaio. Istruzioni per il calcolo, l'esecuzione, il collaudo e la manutenzione*. Steel structures. Instructions of design, construction, testing and maintenance. UNI, 1988.
- AISC. *Seismic Provisions for Structural Steel Buildings*. Chicago, Illinois, 2005.

THE SEISMIC RESPONSE OF EMBEDDED COLUMN BASES – TESTS AND STRENGTH MODEL

Amit Kanvinde,
University of California, Davis, CA 95616, USA
kanvinde@ucdavis.edu

David Grilli,
Wiss Janney Elstner Associates, Inc, Emeryville, CA 94608
dagrilli@ucdavis.edu

Abstract

Embedded Column Base (ECB) connections are commonly used in mid- to high-rise moment frame buildings, when exposed base plate connections cannot economically provide adequate strength or stiffness. Results from five full-scale tests on ECB connections are presented to examine their seismic response. The tests indicate that (similar to composite beam column connections), response is controlled by a combination of the following mechanisms: (1) bearing of the column flanges against the concrete, (2) panel zone shear, and (3) vertical restraint to uplift and rotation of the embedded base plate. A new strength model is presented. The model considers these mechanisms, as well as their interactions. Limitations of the research are discussed along with their implications for design.

INTRODUCTION

For tall buildings with where large column base moments must be resisted by the footing, designers often use “embedded” type base connection (see Figure 1), in which the dominant mechanism of moment resistance is direct bearing between the column and the concrete footing. Significant research has been conducted on exposed type base connections, where the base plate is anchored on top of the footing (Gomez et al., 2010; DeWolf & Sarisley, 1980); however similar research is not available for Embedded Column Base (ECB) connections, such that there are no established approaches to facilitate their design – specifically, AISC Design Guide One (Fisher and Kloiber, 2006), and the SEAOC SSDM (Grilli and Kanvinde, 2013) exclusively address exposed type connections.

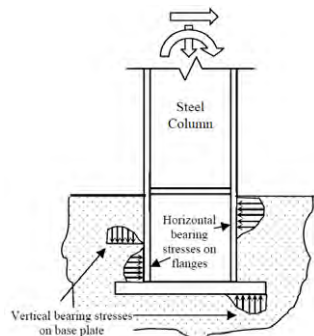


Figure 1: Load transfer in ECB Connections

For the design of ECB connections, practitioners use ad hoc methods based on research on other structural components that show mechanisms similar to those expected in ECB connections, including steel coupling beams in shear walls and composite beam-column connections. However, these components have significant differences with respect to ECB connections, making such adaptation somewhat challenging. Specifically, these pertain to the presence of column axial force and indeterminate interactions between the horizontal bearing and the vertical bearing mechanisms that are shown in Figure 1. Motivated by these issues, this paper presents results from 5 full-scale tests on embedded column base connections representing typical column base connections for moment-frame buildings, such that their failure is controlled by interactions of flexure and axial load. The paper presents these experimental results and briefly outlines a working model for the strength characterization and design of such connections.

EXPERIMENTAL PROGRAM

All tests specimens were cantilever columns loaded laterally in deformation control as per a cyclic loading protocol. This protocol was applied under a constant axial load (either compressive, tensile, or zero). The major variables interrogated were (1) embedment depth (2) column size, including flange width, and (3) axial load. Table 1 summarizes the test matrix, along with key experimental results, whereas Figure 2 shows the test setup with specimen being tested (including both tension and compression setups).

Table 1: Test matrix

Test #	Column Size, (b_f [mm])	Axial load P [kN]	d_{embed} [mm]	Base Plate, $t_p \times N \times B$ [mm]	z [m]	M_{base}^{max} [kN-m]
1	W14x370 (419)	445 (C)	508	51 x 762 x 762	2.84	2579(+)
2	W18x311 (305)			51 x 864 x 711		2613(-)
3	W14x370 (419)	0	762	51 x 762 x 762	3.10	2324(+)
4		445 (C)				2168(-)
5		667 (T)				3741(+)
						3444(-)
						4124 (+)
			3612(-)			
			3800 (+)			
			3464(-)			

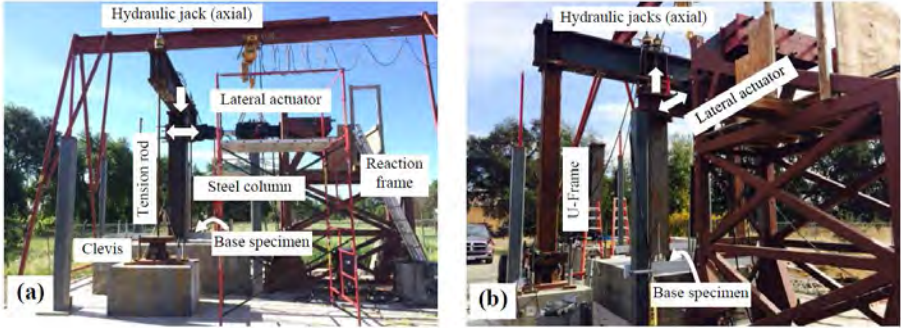


Figure 2: Test setup for (a) specimens with axial compression and (b) specimens with axial tension

All specimens reflected current construction practice. Figures 2a and b show photographs of the test setup for compressive load (Test #1, 2, 4) and tensile axial load (Test #5) respectively. Test #3, which has no axial load, does not have the fixtures for introduction of axial load, which are present in the other tests. Main features of the test setup and specimens are described in Grilli and Kanvinde (2015).

Table 1 summarizes the test matrix. The parameters varied include: (1) the embedment depth, (2) axial load, and (3) the column size. The values for each of these were selected based on a consideration of similarity to full-scale connections, and limitations of the test setup. For all the tests, displacement-controlled cyclic lateral loading was applied according to the SAC loading protocol (Krawinkler et al., 2000) to represent deformation histories consistent with seismic demands in moment frame buildings.

TEST RESULTS

Figures 3a-e show the moment-drift plots for all the specimens, whereas Figure 4 shows photographs of damage and failure. All experiments followed a qualitatively similar progression of damage, with some variations. Small cracks began to form near the corners of the column immediately after the commencement of lateral loading, but this did not affect the load-deformation response, such that linear elastic response was observed until 0.5% drift. After this, gradual nonlinearity in the load deformation curve was observed, accompanied by the opening of a small gap adjacent to the tension flange, accompanied by the growth of the diagonal cracks described previously. This was accompanied by strength degradation as well as pinching response. The pinching response is due to the gapping shown in Figure 4b resulting in unrestrained movement of the column within its “socket,” as it moved through the vertical position.

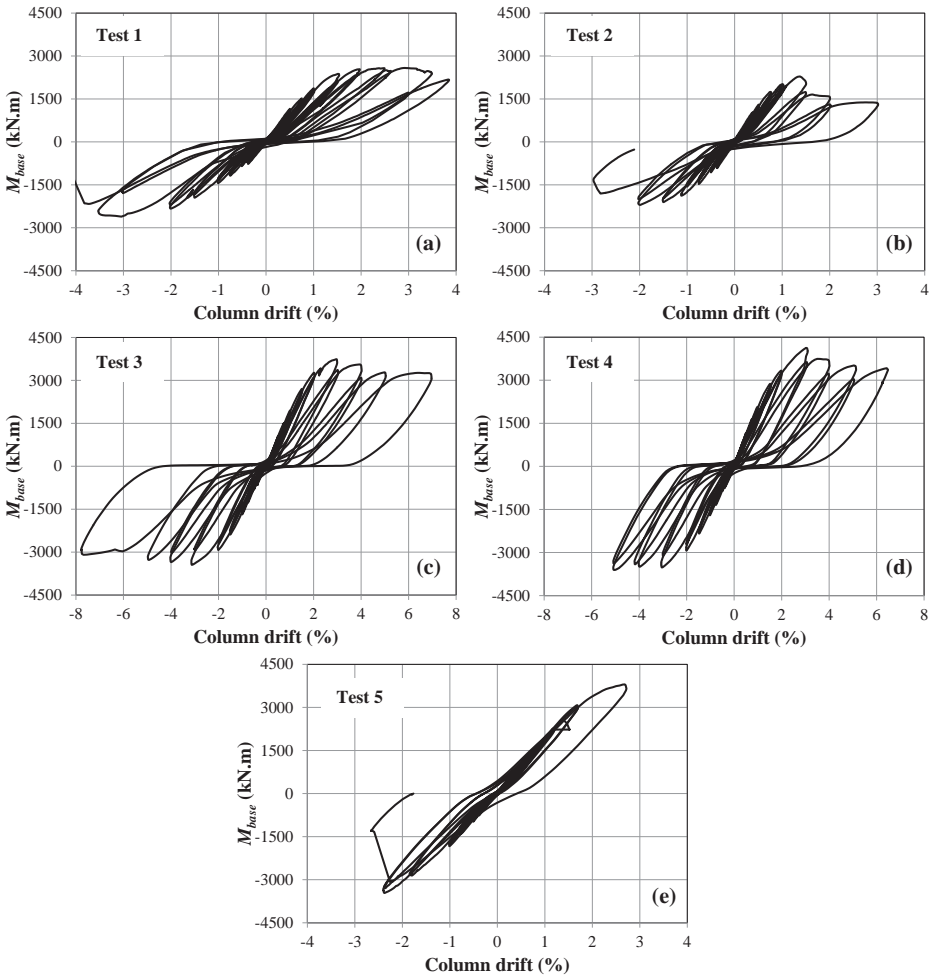


Figure 3: Moment drift plots for all experiments

In Test #1 and #2, with the shallower embedment final failure was accompanied by sudden uplift of a cone of concrete on the tension side of the connection (Figure 4a). For Test #3 and #4 with the deeper embedment, failure was more gradual, as increasing deformations were accompanied by a steady drop in load. This results in a pattern of widespread cracking damage (as shown in Figure 4b), in contrast with the sudden failure shown in Figure 4a.

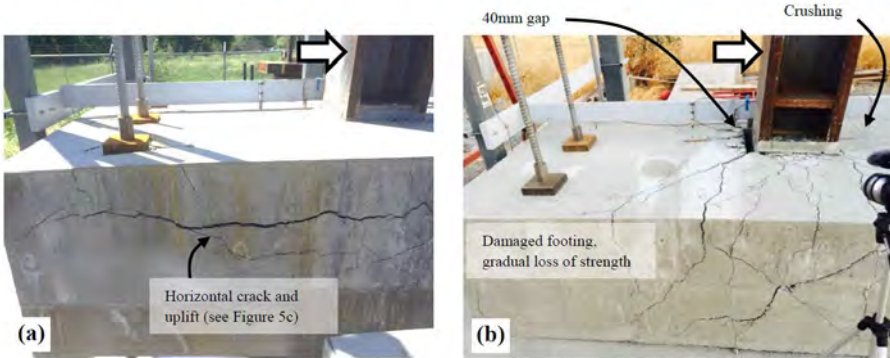


Figure 4: Failure patterns for tests with (a) shallower embedment and (b) deeper embedment

Based on the test results, and visual observations the physics of force transfer is postulated Figure 5 illustrates the assumed physics. Referring to the Figure, it is assumed that compressive axial force is carried by the top stiffener plate, skin friction along the column, and the bottom base plate. Tensile axial force is carried by skin friction, and downward bearing on the bottom base plate. The base moment is resisted through a combination of horizontal bearing stresses against the flanges of the column (Figure 5a) and vertical bearing stresses against the lower base plate (Figure 5b). The horizontal bearing stresses are accompanied by shear in the panel zone. The tension field in the panel zone is responsible for the diagonal shear cracks observed in Figures 4b. The strength model, described in the next section, is based on these mechanisms.

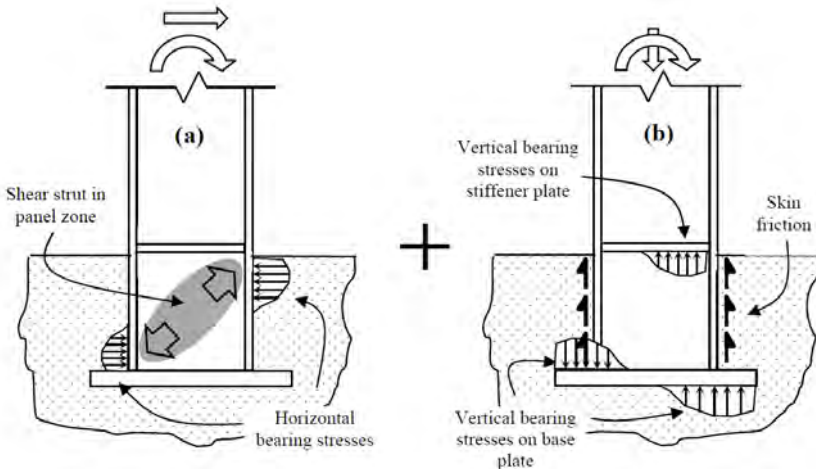


Figure 5: Force resisting mechanisms (a) horizontal bearing and panel zone strut (b) vertical bearing and skin friction

STRENGTH MODEL

The strength model aims to characterize base moments associated with various limit states given the ECB geometry and applied axial force and shear to moment ratio. Specifically, the parameters defining the problem are: the column embedment depth d_{embed} , the column section, axial force P , base plate dimensions t_{plate}, B, N , and the shear-to-moment ratio, in addition to the dimensions of the footing as well as material properties of the steel of the base plate F_y^{plate} and the concrete, i.e., f_c' . Given these parameters, the strength model determine must determine the base moments M_{base} , at which each of the possible limit states is attained, and finally determine the ultimate (or design) moment that can be sustained by the ECB connection.

The complete derivation and mathematical expressions for the strength model are significantly complex, and cannot be suitably described within the scope of this paper. The reader is directed to Grilli and Kanvinde (2015), as well as forthcoming journal articles on the topic. In this article, only the key aspects of the model and some equations are summarized.

Figures 6a and b schematically illustrate the idealized internal forces associated with force and moment transfer from the column into the footing. Specifically, Figure 6a shows compressive axial load transfer, and Figure 6b shows moment and shear transfer.

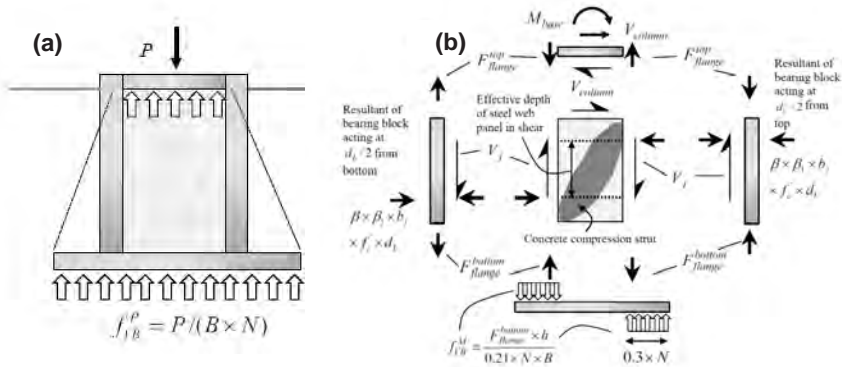


Figure 6: Internal force distribution with respect to (a) axial compression
(b) shear and moment

Following the distribution shown in Figure 6, the model assumes that the base moment may be decomposed into its components resisted by the horizontal and vertical bearing stresses, such that $M_{base} = M_{HB} + M_{VB}$. However, it is noted that this decomposition is an indeterminate one. To resolve this indeterminacy, it is further assumed that the net moment M_{base} is distributed in a constant proportion between the two mechanisms, such that –

$$M_{VB} = \alpha \times M_{base} \quad (1)$$

and,

$$M_{HB} = (1 - \alpha) \times M_{base} \quad (2)$$

Where the ratio α controls the relative contribution of the two mechanisms. The contribution of the vertical bearing stresses will diminish as the embedment depth increases, since most of the moment will be carried by the horizontal bearing stresses; refer Grilli and Karvinde (2015). Once this is determined, a complex hierarchy of failure modes may be established. More specifically, the failure modes associated with the horizontal bearing are:

1. Bearing failure of concrete in front of the flanges.
2. Shear failure of the panel zone, including the strengths of the steel web, compression strut, and compression field.

Vertical bearing results in a different set of failure modes, as shown in Figures 7a-d; these pertain to breakout of the concrete, yielding of the base plate and local crushing of the concrete near the base plate.

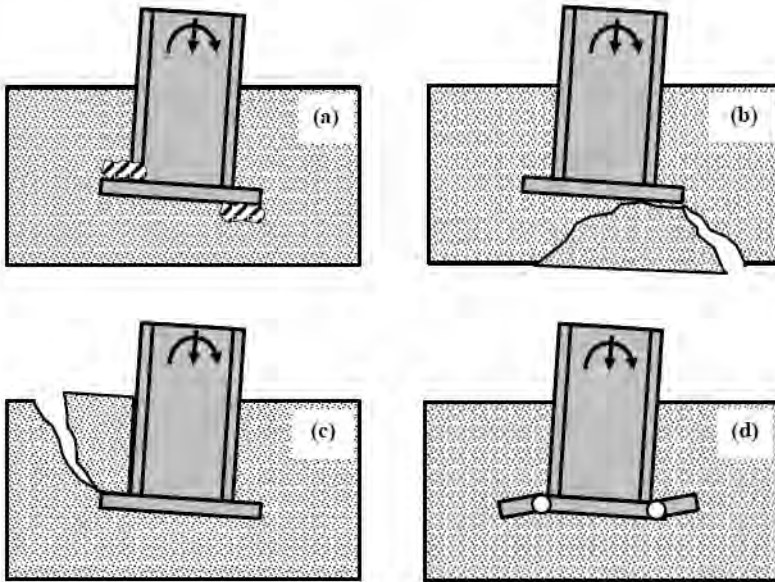


Figure 7: Limit states associated with vertical bearing (a) local crushing (b) and (c) breakout (d) base plate yielding

Once the strengths associated with each possible failure mode are determined, these need to be interpreted within a hierarchy of failure modes that interact in various ways. These interactions arise from (1) shared load paths between two failure modes (e.g., the compressive strut in the shear panel and bearing on the lower base plate), or (2) the nature of failure modes, e.g., some failure modes (horizontal bearing) are ductile allowing for the development of other limit states subsequent to them, whereas others are brittle (breakout of concrete due to vertical uplift) cause immediate loss in connection strength, with no possibility of further loading. The final strength method needs to recognize these interactions. The flowchart presented in Figure 8 below shows a method for explicit consideration of these interactions in calculating connection strength – the terms are explained in greater detail in Grilli and Kanvinde (2015); here only the overview is presented.

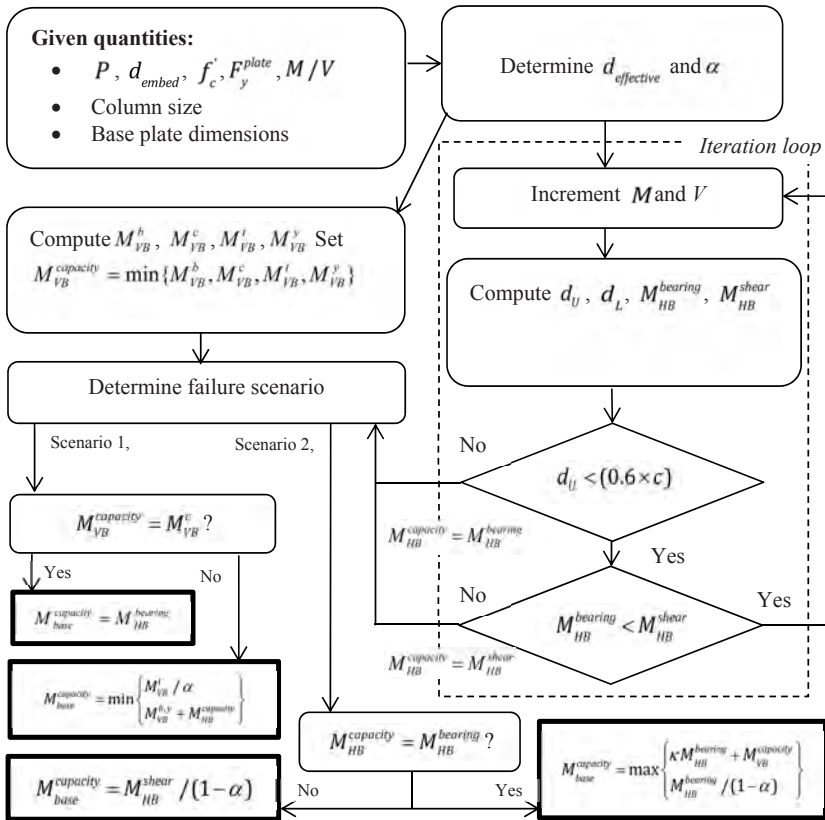


Figure 8: Flowchart for implementing strength characterization method

The method is inspired by physical observations of experimental response, but it is important to acknowledge, that some aspects of the method (coefficients in some formulas) have been empirically calibrated to achieve optimal agreement with test data. The resulting fit with test data is nearly perfect, with an average test to predicted ratio of 1.0, with a coefficient of variation of 6%.

CONCLUSIONS AND LIMITATIONS

The study, and the strength method has many limitations, which must be considered in its interpretation and application. The limitations of the experimental program are inherited by the method as well – these include the examination of one generic detail, the absence of major reinforcement, and a relatively small data set for validation. Extrapolating the method to footing/embedment sizes that are significantly different from the method is potentially erroneous, since the empirical aspects of the method may be sensitive to size. It is also important to recall that the method only addresses failure modes that occur in the immediate vicinity of the embedded connection; and not those triggered by overall foundation failure. It is likely that these are sensitive to foundation type. Future work may involve additional experiments on different details, and finite element simulations for more accurate understanding of internal force transfer. Finally, the method provides deterministic estimates of nominal strength, and resistance ϕ -factors are required to ensure adequate margins of safety against failure. These may be developed through reliability analysis.

ACKNOWLEDGMENTS

The authors are grateful to the Charles Pankow Foundation and the American Institute of Steel Construction for providing major funding for this project. Supplementary funding was provided by graduate fellowships at the University of California, Davis. Gregory Deierlein of Stanford University provided valuable feedback, as did Geoff Bomba of Forell Elsesser Engineers, and Ron Klemencic and Rob Chmielowski of Magnuson Klemencic Associates.

REFERENCES

DeWolf J.T., and Sarisley, E.F. (1980). "Column Base Plates with Axial Loads and Moments," *Journal of the Structural Division, ASCE*, Vol. 106, No. 11, November 1980, pp. 2167-2184.

Fisher, J.M. and Kloiber, L.A. (2006), "Base Plate and Anchor Rod Design," 2nd Ed., *Steel Design Guide Series No. 1*, American Institute of Steel Construction, Inc., Chicago, IL.

Gomez, I.R., Kanvinde, A.M., Smith, C.M., and Deierlein, G.G., (2009), "Shear Transfer in Exposed Column Base Plates," Report Submitted to the American Institute of Steel Construction, Chicago, IL.

Grilli, D.A., and Kanvinde, A.M. (2013). "Special Moment Frame Base Connection: Design Example 8," 2012 IBC SEAOC Structural/Seismic Design Manual, Volume 4, Examples for Steel-Frame Buildings, 255-280.

Grilli, D.A. and Kanvinde, A.M. (2015). "Embedded Column Based Connections subjected to Flexure and Axial loads," Report 3-11 submitted to the Charles Pankow Foundation.

Krawinkler, H., Gupta, A., Medina, R., and Luco, N. (2000), "Loading Histories for Seismic Performance Testing of SMRF Components and Assemblies," SAC Joint Venture, Report no. SAC/BD-00/10. Richmond, CA.

THE INFLUENCE OF GRAVITY FRAMING ON THE PERFORMANCE OF STEEL BUILDINGS SUBJECTED TO SEISMIC LOADS

Johnn P. Judd
University of Wyoming, Laramie, Wyoming 82071, USA
jjudd5@uwyo.edu

Finley A. Charney
Virginia Tech, Blacksburg, Virginia 24061, USA
fcharney@vt.edu

Francisco X. Flores
University of Cuenca, Cuenca, Ecuador
francisco.flores@ucuenca.edu.ec

Abstract: In this paper, the influence of the gravity system on the seismic performance of steel buildings was evaluated using the basic methodologies provided in FEMA P-695, *Quantification of Building Seismic Performance Factors*, and FEMA P-58, *Seismic Performance Assessment of Buildings*. The sequence of analyses was performed on archetype 4-story and 8-story buildings that utilize perimeter moment frames designed for Seismic Design Categories (SDC) C and D. It is shown that by including the gravity framing in the assessment, the predicted life safety of the building was improved due to the effects of reserve lateral strength in the gravity beam connections. For serviceability, the predicted repair costs and associated repair time, as well as the probability of an unsafe placard were generally reduced, but the amount of reduction depended on the SDC and the number of stories. In conclusion, recommendations are provided for the development of a “dual system” concept design procedure.

INTRODUCTION

The current design practice is to ignore the influence of gravity framing in assessing the performance of structures subjected to seismic loads. However, such framing may have a beneficial effect, represented by reduced residual drift (Eatherton and Hajar, 2011), reduced probability of collapse (Flores et al., 2014; Elkady and Lignos 2015), and improved serviceability (Judd and Charney, 2014b). The predicted effect of the gravity framing system in steel buildings depends on the individual behavior of beam and column connections, and how these connections are modelled. Experimental testing and computer modeling have indicated that column base connections, column splice connections and splice locations (Flores et al., 2014), and beam-to-column connections (Judd, 2015) are especially critical. Additionally, the spatial distribution of gravity loads acting through the gravity columns can have a profound influence on the global stability of the building (Flores et al., 2015).

The objectives of this paper are to examine the influence of gravity framing on the predicted life safety and serviceability-level performance of archetype steel buildings, and, based on the results, to develop recommendations for a “dual system” concept.

ARCHETYPE BUILDINGS

Structural Design. The archetype 4-story and 8-story buildings (Fig. 1) were based on buildings designed for the ATC-76 project (NIST, 2010). The ATC-76 archetypes have also been used in several recent studies (e.g. Elkady and Lignos, 2014; Flores et al., 2014). The building used perimeter moment frames, 20-foot bays, a 15-foot first story height (measured to the top of the beam), and a 13-foot upper story height.

The perimeter moment frames were designed for the highest spectral accelerations corresponding to Seismic Design Categories (SDC) C and D, for soil site class D. Moment frame columns were considered fixed at the base. Special steel moment frames (SMF) with reduced beam sections were used. The sizes and details of the SMF designs are provided in the appendix of the ATC-76 report.

The original archetype models did not explicitly include the gravity system, however, so the gravity framing system was developed for this study. The gravity framing was designed for a 90 psf dead load and a 50 psf live load. The roof and floor of the buildings use a 5.5-inch composite slab (2-inch normal weight concrete cover on 3-inch steel deck), and gravity framing beams spaced at 10 feet on center with shear tab connections.

Gravity framing columns were oriented with the strong axis in the same direction as the moment frames (the longitudinal direction of the building), and thus the influence of the gravity system observed in this study represents an upper bound for this building layout. Gravity columns were considered pinned at the base and spliced 4 feet above the third and sixth floors. The sizes of the gravity design are provided by Judd (2015).

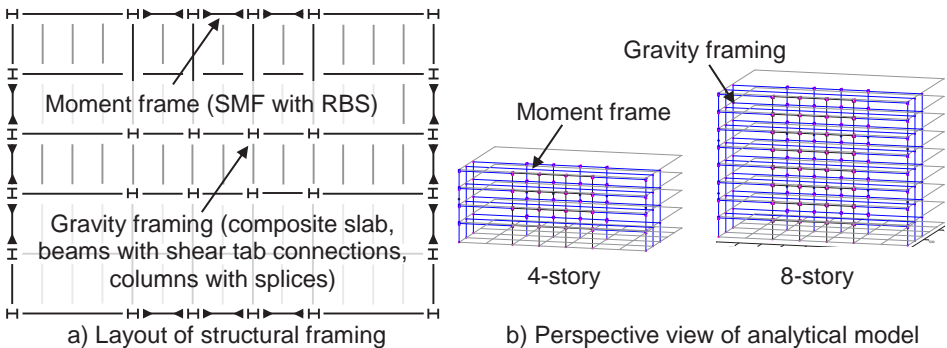
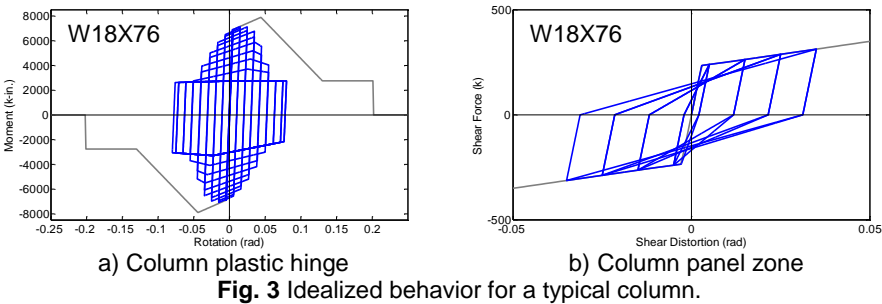
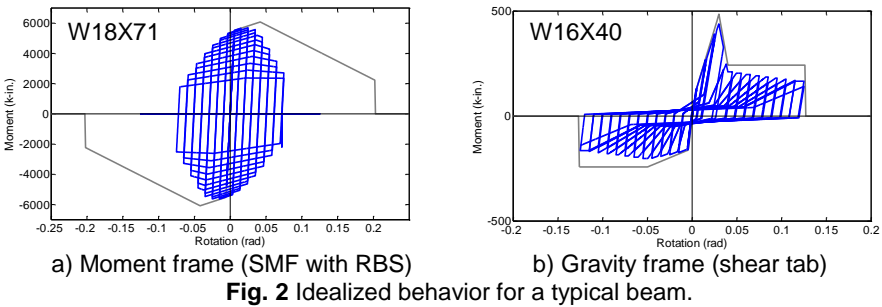


Fig. 1 Archetype building.

Analytical Model. A structural model of the building frame was developed using *OpenSees* (PEER, 2012) finite element software. Beams and columns were modeled using an assembly of linear elastic elements and zero-length nonlinear springs to simulate the formation of plastic hinges in the reduced section of the beams, plastic hinges at the top or bottom of columns, and shear yielding of the column panel zone. Second-order ($P-\Delta$) effects were included by modeling the gravity framing explicitly instead of using a leaning column, and by employing the “corotational” approach, where the local element coordinate frame continuously rotates to capture large displacements.

The moment rotation behavior of SMF connections (Fig. 2a) was represented using the modified Ibarra-Medina-Krawinkler bilinear model. Hysteresis parameters were based on a statistical analysis of experimental test data of bare steel RBS connections (Lignos and Krawinkler, 2011). The effect of composite action between the moment frame and slab was not included, but was considered in a related study (Judd, 2016).

Column plastic hinge behavior (Fig. 3a) was idealized similarly to SMF connection behavior, except column strength was reduced to account for axial load interaction. The reduction in flexural strength was approximated using AISC 360-10 Equations H1-1a and H1-1b and a constant axial load determined resulting from the gravity load plus half the lateral load calculated in a nonlinear pushover analysis.



Column panel zones were explicitly represented using the Krawinkler joint model to represent the combined contributions of the column web and the column flanges (Charney and Marshall, 2006). Shear-distortion behavior (Fig. 3b) was modeled using a tri-linear envelope curve and bilinear hysteresis behavior. Column splices were idealized as pinned connections with no rotational constraint, but the effect of the splice location and strength was considered in a related study (Flores et al., 2014).

In order to investigate the influence of the gravity framing, the moment rotation behavior of the shear tab beam connections (Fig. 2b) was represented using a hysteretic model with pinching (Lowes et al., 2004). Hysteresis parameters were based on test data of shear tab connections (Liu and Astaneh-Asl, 2000), corresponding analytical models [(Liu and Astaneh-Asl, 2004; Wen et al., 2013), and FEMA P-440A (FEMA, 2009a)]. The connections exhibit cyclic degradation of both stiffness and strength, until approximately 10% to 12% drift, after which the rotational stiffness and flexural strength of the connection was zero. The negative-moment capacity boundary (monotonic envelope) was based on the behavior of the bare steel beam.

LIFE SAFETY

Life safety was evaluated using a sequence of analyses following the FEMA P-695, *Quantification of Building Seismic Performance Factors* methodology (FEMA, 2009b). An initial pre-load (gravity) analysis was followed by an Eigen-value analysis to determine the periods and modes of vibration of the building. The computed fundamental period of vibration was used for both referencing spectral accelerations and for estimating damping (taken as 2.5%) that was not explicitly modeled by the component hysteresis. The gravity and vibration analyses were then followed by two nonlinear pushover analyses: a pushover analysis to estimate axial loads in columns, and a subsequent pushover analysis that accounted for axial load interaction.

Nonlinear dynamic response history analyses were conducted using the FEMA P-695 Far-Field normalized ground motion set. The model was subjected to the set of ground motions, incrementally scaled in intensity with respect to the target SDC spectrum, until the ground motions caused the building model to collapse in a side-sway mechanism.

Finally, the collapse fragility was determined by fitting individual collapse points (spectral acceleration at the reference period and corresponding probability of collapse for a one scaled ground motion record) with a curve, assuming a lognormal cumulative distribution function. The median collapse spectral acceleration was increased to account for spectral shape and the total dispersion in collapse capacity, based on record-to-record dispersion measured in the incremental dynamic analyses and epistemic dispersion due to design, test data, and modeling uncertainty.

The results of the life safety evaluation are summarized in Table 1. The computed fundamental period, T_1 was higher than the empirical predictions suggest, but the computed period was in line with prior analyses (NIST, 2010).

Table 1 Life Safety Evaluation

SDC	Model	T_1 (s)	Ω	μ_T	S_{aMCE} (g)	CMR	ACMR	ACMR _{10%}	
<i>4-Story</i>									
C	MF	1.75	4.87	5.06	0.17	3.51	5.13	Pass	
	MF+GF	1.60	5.93	4.92	0.19	4.35	6.31	Pass	
	<i>8-Story</i>								
	MF	3.18	3.45	3.04	0.09	1.98	2.63	Pass	
	MF+GF	2.88	3.93	3.44	0.10	2.61	3.55	Pass	
<i>4-Story</i>									
D	MF	1.46	1.92	6.00	0.62	1.51	2.27	Pass	
	MF+GF	1.36	2.26	5.63	0.66	1.93	2.82	Pass	
	<i>8-Story</i>								
	MF	2.03	2.90	3.54	0.44	1.26	1.71	Fail	
	MF+GF	1.94	3.12	3.57	0.46	1.42	1.94	Fail	

As expected, the gravity framing decreased the computed period of the model. The static overstrength, Ω increased by up to 22%. Gravity framing usually led to a modest increase in period-based ductility, μ_T . The effect of the gravity framing on the collapse margin ratio, CMR and the adjusted collapse margin ratio, ACMR (increased to account for spectral shape) was significant. All buildings passed the 10% probability of collapse given the MCE ground motions, S_{aMCE} criteria, except the 8-story SDC D building which had a 12% probability of collapse (MF) and an 11% probability of collapse (MF+GF).

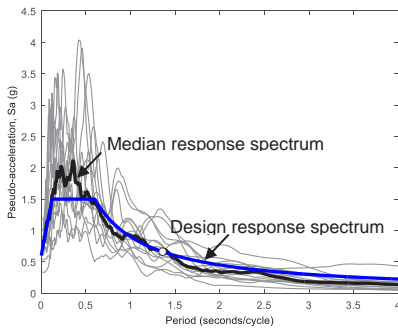
SERVICEABILITY

Serviceability performance was evaluated using the FEMA P-58, *Seismic Performance Assessment of Buildings* methodology (FEMA, 2012a). The service-level hazard was defined as 10% of the Maximum Considered Earthquake (MCE) ground motions for the target SDC, corresponding to approximately a 50% probability of exceedance in 30 years [43-year mean recurrence interval (MRI)] for locations in the western United States (Judd and Charney, 2014a).

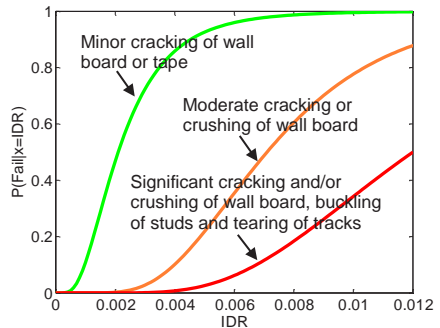
A sub-set of the FEMA P-695 Far-Field ground motions (Table 2) was first normalized using the FEMA P-695 Toolkit (Hardyniec and Charney, 2015) and scaled to the service-level hazard intensity (for example, Fig. 4a). The nonlinear structural response was determined and the repair cost, repair time and likelihood of unsafe placards was then predicted using in the FEMA P-58 software *PACT* (FEMA, 2012b) using 200 Monte Carlo simulations to correlate interstory drifts, floor accelerations, and roof accelerations to structural and non-structural damage (for example, Fig. 4b). Structural components consisted of beam connections, column splices, and base plates. Non-structural components included a variety of items, ranging from mechanical, electrical, and plumbing (MEP) equipment to exterior cladding and partition walls. Quantities of components were estimated using the FEMA P-58 spreadsheet tools and depended on the building stories.

Table 2 Ground motions used for the serviceability analyses

<i>P-695 ID</i>	<i>Record Name</i>	<i>Earthquake</i>	<i>Magnitude</i>
1	Beverly Hills - Mulhol	1994 Northridge	6.7
2	Canyon Country-WLC USC	1994 Northridge	6.7
11	Yermo Fire Station CDMG	1992 Landers	7.3
15	Abbar BHRC	1990 Manjil, Iran	7.4
17	Poe Road (temp)	1987 Superstition Hills	6.5
18	Rio Dell Overpass	1992 Cape Mendocino	7
21	LA - Hollywood	1971 San Fernando	6.6



a) Scaled response spectrum



b) Gypsum wall partitions

Fig. 4 Serviceability analysis (4-story SDC D building).

The median predicted performance is summarized in Table 3. The repair cost is shown as a percentage of the total cost of replacing the building, estimated at 230 dollars/sf for the core and shell and 537 dollars/sf for tenant improvements. The repair cost data in *PACT* was adjusted to reflect the 2013 national average commercial construction costs.

The repair time was estimated using typical construction schedules (392 days for the 4-story buildings, and 462 days for 8-story buildings) based on advice from practitioners (Jarrett et al., 2015). The maximum number of workers per square foot (used to calculate repair time) was one worker per 1,000 square feet (the default value in *PACT*).

The repair costs and repair time were mostly dominated by damage to the gypsum wall partitions. For the 8-story SDC D building, there were other significant contributions to repair costs and repair time. These included bolted shear tab gravity connections, and unanchored chiller and air handling units. For some components sensitive to accelerations, such as the chiller, the gravity system actually increased the probable repair time. However, in general the reserve lateral strength in the gravity framing shear tab connections led to a significant reduction in repair cost and a mild reduction in repair time. The improvement was most dramatic in the 8-story SDC C building.

Table 3 Serviceability Evaluation

<i>SDC</i>	<i>Model</i>	<i>Median Repair Cost (% of building replacement cost)</i>	<i>Median Repair Time (days)</i>	<i>Median Prob. of Unsafe Placard</i>
<i>4-Story</i>				
C	MF	4.8%	28	5%
	MF+GF	4.5%	26	3%
<i>8-Story</i>				
C	MF	4.4%	37	9%
	MF+GF	3.4%	29	0.03
<i>4-Story</i>				
D	MF	4.5%	26	3%
	MF+GF	3.8%	24	5%
<i>8-Story</i>				
D	MF	3.0%	25	1%
	MF+GF	2.5%	21	0%

The probability of an unsafe placard (“red tag”) being placed on the building was mostly attributed to the prefabricated steel stair system that had landings without seismic joints, but there were several other components that contributed to the probability of unsafe placards. Including the gravity framing in the model slightly reduced the probability of a red tag, with the most improvement associated with unbraced fire sprinkler water piping.

DUAL SYSTEM DESIGN CONCEPT

A “dual system” concept design procedure could be developed that explicitly includes the gravity system if the gravity frame columns and gravity beam connections are qualified as part of the seismic force resisting system. The concept is similar to the standard dual system in ASCE 7-10 (ASCE, 2013). For the archetype steel buildings with shear tab connections examined in this study, the predicted life safety performance indicates that the gravity framing system needs to be capable of resisting at least 10% of the prescribed seismic forces to be effective with SMFs. This minimum ratio needs to be verified before implementation of the concept. Qualification of the gravity system would also require a plan for continuous and periodic inspections to assure that the quality of the column splice connections and beam connections meet the strength and ductility requirements assumed for design, similar to the primary system.

The response modification factor, R for the dual system could correspond to the primary seismic force resisting system (for example, R equal to 8 for SMFs), or could be increased based on the predicted performance. In the latter approach, the dual system would be beneficial for SMF systems in which the minimum base shear requirement does not control, allowing the value of R to be increased, perhaps up to a value of 10. The increased R value approach would be viable for buildings 8-stories or fewer on site

class A and B soils. One could go taller with softer soils. Nevertheless, taller buildings would need to be studied before implementation of this approach. For the archetype steel buildings with shear tab connections examined in this study, the influence of the gravity framing was less pronounced on the 8-story SDC D building. The dual system with an increased R value approach is more attractive for intermediate steel moment frames (IMFs) and ordinary moment steel moment frames (OMFs), as well as for concentrically braced frames (CBFs) with R values less than 8.

CONCLUSIONS

The predicted seismic performance of 4-story and 8-story office buildings using perimeter SMFs with reduced beam sections was improved by including the gravity framing. Even though the gravity framing decreased the computed fundamental period—and thus increased the seismic demands on the building—both the static overstrength and the collapse margin ratio (the “dynamic overstrength”) was improved. The most improvement was predicted for the SDC C and 4-story buildings. All buildings passed the FEMA P-695 acceptance criteria of no more than 10% probability of collapse given the MCE ground motions, except the 8-story SDC D buildings (which almost passed).

The influence of the gravity framing generally led to a significant reduction in predicted repair cost, and to a minor improvement in predicted repair time. The improvement was attributed to unanchored or unbraced components of the building and was most dramatic in the 8-story SDC C building. Including the gravity framing also slightly reduced the probability of an unsafe placard being placed on the building. For a number of components sensitive to accelerations, including the gravity system actually increased the predicted repair times.

A dual primary-gravity system design could be developed if the gravity frame columns and gravity beam connections are qualified as part of the seismic force resisting system. A quality assurance program would be needed to evaluate column splices and gravity beam connections. Based on the limited set of buildings examined in this study using shear tab connections, the gravity framing system would need to be capable of resisting at least 10% of the prescribed seismic forces in order to be effective with SMFs. It is anticipated that the R value for the dual system would correspond to the primary seismic force resisting system. It is possible that the R value could be increased for SMF designs where the minimum base shear requirement does not control, or for IMF, OMF, and CBFs in moderate seismic regions, but additional research is recommended before implementing this approach.

REFERENCES

ASCE (2013). Minimum design loads for buildings and other structures. ASCE/SEI 7-10, American Society of Civil Engineers (ASCE), Reston, Virginia.

Charney, F.A. and Marshall, J.A. (2006), "Comparison of the Krawinkler and Scissors models for including beam-column joint deformations in the analysis of moment resisting frames." *Engineering Journal*, Vol. 43, No. 1 (pp. 31–48).

Eatherton, M.R., and Hajjar, J.F. (2011), "Residual drifts of self-centering systems including effects of ambient building resistance." *Earthquake Spectra*, Vol. 27, No. 3 (pp. 719–744).

Elkady, A. and Lignos, D.G. (2014), "Modeling of the composite action in fully restrained beam-to-column connections: implications in the seismic design and collapse capacity of steel special moment frames." *Earthquake Engineering and Structural Dynamics*, Vol. 43, No. 13, (pp. 1935–1954).

Elkady, A. and Lignos, D.G. (2015), "Effect of gravity framing on the overstrength and collapse capacity of steel frame buildings with perimeter special moment frames." *Earthquake Engineering and Structural Dynamics*, Vol. 44, No. 8, (pp. 1289–1307).

FEMA (2009a), *Effects of strength and stiffness degradation on seismic response*. FEMA P-440A, Federal Emergency Management Agency (FEMA), Washington, D.C.

FEMA (2009b), *Quantification of building seismic performance factors*. FEMA P-695, Federal Emergency Management Agency (FEMA), Washington, D.C.

FEMA (2012a), *Seismic performance assessment of buildings, volume 1—methodology* (FEMA P-58-1). Federal Emergency Management Agency (FEMA), Washington, D.C.

FEMA (2012b), *Seismic performance assessment of buildings, volume 3—Performance Assessment Calculation Tool (PACT), version 2.9.65*. Federal Emergency Management Agency (FEMA), Washington, D.C.

Flores, F.X., Charney, F.A., and Lopez-Garcia, D. (2014), "Influence of the gravity framing system on the collapse performance of special steel moment frames." *Journal of Constructional Steel Research*, Vol. 101, No. 10 (pp. 351-362).

Flores, F.X., Charney, F.A., Lopez-Garcia, D., and de la Llera, J.C. (2015), "The influence of accidental torsion on the inelastic dynamic response of buildings during earthquakes," *XI Chilean Congress on Seismology and Earthquake Engineering*, Santiago, Chile.

Hardyniec, A. and Charney, F.A. (2015), "A toolkit for the performance of FEMA P-695 evaluations." *Earthquake Spectra*, doi: <http://dx.doi.org/10.1193/040214EQS044>.

Jarrett, J.A., Judd, J.P., and Charney, F.A. (2015), "Comparative evaluation of innovative and traditional seismic-resistant systems using FEMA P-58." *Journal of Constructional Steel Research*, Vol. 105, No. 2 (pp. 107–118).

Judd, J.P. (2015), *Multi-hazard performance of steel moment frame buildings with collapse prevention systems in the central and eastern United States*. Ph.D. dissertation, Civil Engineering. Virginia Polytechnic Institute and State University, Blacksburg, Virginia.

Judd, J.P. (2016), "Seismic collapse risk of steel-concrete composite moment-frame buildings." *International Colloquium on Stability and Ductility of Steel Structures*, May 30–June 1, Timișoara, România.

Judd, J.P., and Charney, F.A. (2014a). "Performance-based design in the central and eastern United States." *Structures Congress*, Boston, Massachusetts, (pp. 2355-2368).

Judd J.P., and Charney, F.A. (2014b), "Seismic performance of buildings designed for wind." *Structures Congress*, Boston, Massachusetts (pp. 2342-2354).

Lignos, D.G. and Krawinkler, H. (2011), "Deterioration modeling of steel components in support of collapse prediction of steel moment frames under earthquake loading." *Journal of Structural Engineering*, Vol. 137, No. 11 (pp. 1291–1302).

Liu, J., and Astaneh-Asl, A. (2000), "Cyclic testing of simple connections including effects of slab." *Journal of Structural Engineering*, Vol. 126, No. 1 (pp. 32–39).

Liu, J., and Astaneh-Asl, A. (2004), "Moment-rotation parameters for composite shear tab connections." *Journal of Structural Engineering*, Vol. 130, No. 9 (pp. 1371–1380).

Lowes, L.N., Mitra, N., and Altoonash, A. (2004), *A beam-column joint model for simulating the earthquake response of reinforced concrete frames*. PEER Report 2003/10, Pacific Earthquake Engineering Research Center, University of California, Berkeley, California.

NIST (2010), *Evaluation of the FEMA P-695 methodology for quantification of building seismic performance factors*. NIST GCR 10-917-8, National Institute of Standards and Technology (NIST), Gaithersburg, Maryland.

PEER (2012), *Open Systems for Earthquake Engineering Simulation (OpenSees)*, version 2.4.0. Pacific Earthquake Engineering Research Center (PEER), University of California, Berkeley, California.

Wen, R., Akbas, B., and Shen, J. (2013), "Practical moment–rotation relations of steel shear tab connections." *Journal of Constructional Steel Research*, Vol. 88, No. 9 (296–308).

HIGH STRENGTH STEELS IN SEISMIC RESISTANT BUILDING FRAMES: INNOVATIVE SOLUTIONS FOR BEAM-TO-COLUMN JOINTS

Dan Dubina; Cristian Vulcu; Aurel Stratan

*Politehnica University of Timisoara, Dept. of Steel Structures and Structural Mechanics
Timisoara, Romania*

dan.dubina@upt.ro; cristian.vulcu@upt.ro; aurel.stratan@upt.ro;

ABSTRACT

The paper summarizes the RFSR-CT-2009-00024 research project entitled High Strength Steel in Seismic Resistant Building Frames (HSS-SERF), focusing on: aim, partnership, objectives, and the solutions for beam-to-column joints investigated within the project. Further, the paper presents the research activities conducted by the Politehnica University of Timisoara in the framework of HSS-SERF project. Particularly, an experimental program was developed and carried out with the aim to characterize the behavior of two types of moment resisting joints in dual-steel frames of concrete filled high strength steel rectangular hollow section (CF-RHS) columns and mild carbon steel beams. The specific detailing and the design approach for the two joint typologies, i.e. with reduced beam section (RBS) and with cover plates (CP), are presented. The experimental program, test set-up and test results are shown for the investigated beam-to-column joint configurations. In addition, outcomes from the numerical investigation program are presented, as well as the main observations and conclusions.

1. INTRODUCTION

Seismic resistant building frames designed as dissipative structures, must allow for plastic deformations to develop in specific members, whose behavior is expected to be predicted and controlled by proper calculation and detailing. Members designed to remain elastic during earthquake, such as columns, are characterized by high strength demands. Structural systems realized according to the “dual-steel” concept, in which High Strength Steel (HSS) is used within members with a predominantly “elastic” response during earthquake, while Mild Carbon Steel (MCS) is used in dissipative members, can be reliable and cost efficient. Because present European seismic design codes do not cover this specific configuration, an extensive research project, HSS-SERF – High Strength Steel in Seismic Resistant Building Frames (see Dubina et al., 2015), was carried out with the aim to investigate and evaluate the seismic performance of dual-steel building frames. Universities of Stuttgart (Germany), Liege (Belgium), Ljubljana (Slovenia), Naples (Italy), the VTT Technical Research Centre (Finland), GIPAC Ltd. Design Office (Portugal), RIVA Acciaio S.p.A (Italy), Ruukki Construction Oy (Finland), under the coordination of the Politehnica University of Timisoara (Romania) have been involved. One of the objectives was to find reliable structural typologies and

joint/connection detailing for dual-steel building frames, (e.g. of HSS and MCS members), and to validate them by tests and advanced numerical simulations. For this purpose, a number of 18 multi-storey frames were designed (Silva et al., 2011, Tenchini et al., 2014, Dubina et al., 2015). The set of frames, was obtained from the combination of: (i) three structural types (MRF – moment resisting frames, D-EBF – dual eccentrically braced frames, D-CBF – dual concentrically braced frames) – see Figure 1a, (ii) three types of steel-concrete composite columns (FE-WF – fully encased wide flange sections, PE-WF – partially encased wide flange sections, CF-RHS – concrete filled rectangular hollow section tubes) – see Figure 1b, and (iii) two high strength steel grades (S460, S690). The dissipative members (beams from MRF's, braces from D-CBF's, etc.) were realized from S355 steel grade. The choice of composite columns can be justified by the enhanced fire resistance compared to the bare steel column configurations, which leads to a higher robustness of the building framing. In spite of the advantages of steel-concrete composite columns, a problem is related to the beam-to-column connections – for which a special attention needs to be paid. Consequently, the HSS-SERF project attempts to provide and validate a set of innovative solutions on that purpose. The designed frames served as basis for the selection of the dimensions for beam-to-column joint specimens (Figure 1c). The joining solutions were represented by bolted and welded connections.

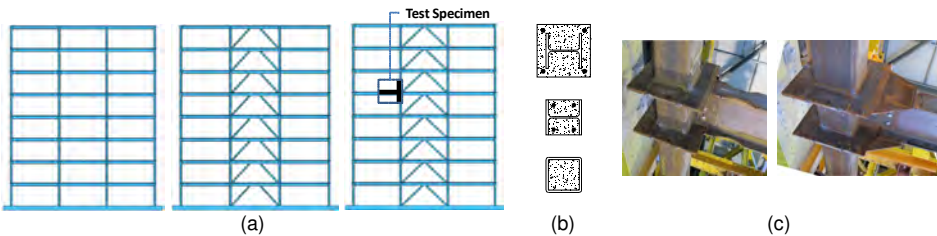


Figure 1. (a) Structural typologies: MRF, D-EBF, D-CBF; (b) cross sections used for columns (FE-WF, PE-WF, CF-RHS); (c) RBS / CP welded beam-to-column joints

The bolted beam-to-column joints (see Figure 2) were analyzed and tested at the University of Liege (Hoang et al., 2014, Dubina et al., 2015), particularly covering three situations: (a) partially encased wide flange column with reinforced end-plate connection; (b) concrete filled tube column with reinforced end-plate connection; (c) concrete filled tube column with end-plate connection and long bolts.

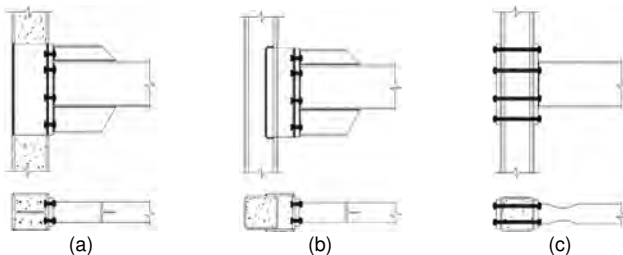


Figure 2. Bolted beam-to-column joints (Hoang et al., 2014)

The welded beam-to-column joints were analyzed and tested at University of Ljubljana (Cermelj and Beg, 2014, Dubina et al., 2015), and Politehnica University of Timisoara (Vulcu et al., 2014, Dubina et al., 2015). The particular configuration of the joints studied at University of Ljubljana was characterized by fully encased wide flange columns and welded connection with rib stiffeners and respectively cover plates (Figure 3a). The beam-to-column joints investigated at the Politehnica University of Timisoara, were characterized by concrete filled tube columns and welded connections with reduced beam section and cover plates – see Figure 3b and Figure 1c.

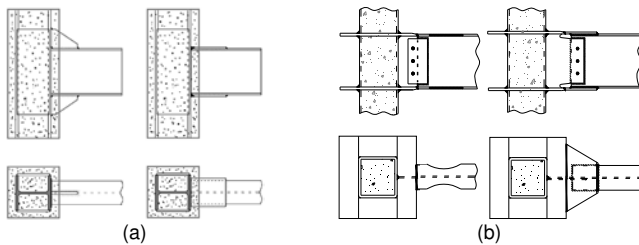


Figure 3. Welded beam-to-column joints:

- (a) rib stiffener & cover plate joints with FE-WF columns (Cermelj and Beg, 2014);
- (b) reduced beam section & cover plate joints with CF-RHS columns (Vulcu et al., 2014)

2. WELDED BEAM-TO-CFT COLUMN JOINTS FOR DUAL-STEEL FRAMES

The research activities conducted by the Politehnica University of Timisoara in the framework of HSS-SERF project were related to the welded beam-to-column joints, involving: mild carbon steel beams, high strength steel rectangular hollow section columns filled with concrete, and two joint typologies – with Reduced Beam Section (RBS), and with Cover Plates (CP) respectively.

2.1 Design and detailing of the beam-to-column joints

The design procedure for the two joint typologies, in principle organized following the “component method” of EN 1993-1-8 (2005), does not make the subject of the current paper, and can be found elsewhere (Dubina et al., 2015). In brief, the first step is related to the selection of component size, and estimation of the expected moment and shear force at the plastic hinge location. Further, the welded connections and joint components are designed and/or checked with the aim of obtaining an equal or higher capacity compared to the design values of the actions, which are computed at the component location based on the expected bending moment and shear force within the plastic hinge.

The RBS joint (see Figure 4ab) connects a wide-flange hot rolled beam with a CFT column using field welding. A reduced beam section is used in order to alleviate stresses in the beam-column connection and control the location of the plastic hinge. An external diaphragm is shop-welded to the column in order to transfer the forces from beam to the side walls of the column. Beam flanges are welded to the external diaphragm using full-penetration butt welds. The preparation details for full penetration welds between external diaphragm and beam flanges are shown in Figure 4c. The solution does not require weld

access holes, and the advantage is that no preparations are necessary for beam flanges. A shear tab bolted connection between the beam web and vertical column stiffener was considered for erection only. The final connection of the beam web is realized using full-penetration weld, using the shear tab as backing plate. The design of the reduced beam section was performed based on provisions from AISC-358 (2010). The design procedure was adapted to the particular joint configuration employing CFT column reinforced with external diaphragm. An illustration of the RBS joint specimen is shown in Figure 1c.

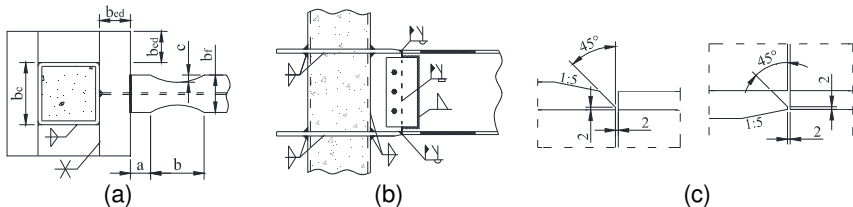


Figure 4. RBS joint configuration: (a) & (b) conceptual scheme, (c) weld preparation details for on-site welded connections (beam flanges to external diaphragm)

The CP joint (see Figure 5ab) connects a wide-flange hot rolled beam with a CFT column using field welding. An external diaphragm is shop-welded to the column in order to transfer the forces from beam to the side walls of the column. Cover plates are used in order to reinforce the beam-column connection, forcing the plastic hinge to form in the beam. The cover plates are welded to the external diaphragm using full-penetration butt welds. The preparation details shown in Figure 5c are based on the weld access-hole details recommended in FEMA-350 (2000). The advantage is that no preparations are necessary for cover plates. A bolted connection between beam web and vertical column stiffener was considered for erection only. The final connection of the beam web is realized using fillet welds. An illustration of the CP joint specimen is shown in Figure 1c.

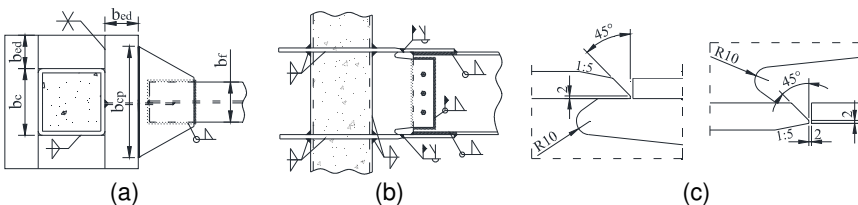


Figure 5. CP joint configuration: (a) & (b) conceptual scheme, (c) weld preparation details for on-site welded connections (cover plates to external diaphragm)

Regarding the two joint configurations, the advantage of the RBS joint consists in simpler fabrication details and lower costs. The disadvantage of this configuration consists in lower strength (and consequently larger deformation demands), as well as susceptibility to lateral torsional buckling. The advantage of the cover plate joint consists in larger strength (and consequently lower deformation demands). This improves the performance of the structure. The disadvantage of this configuration consists in larger fabrication costs. It is to be noted that the details of the reduced beam section are as

follows: $a = 90$ mm, $b = 260$ mm, $c = 35$ mm, $R = 260$ mm (radius). In addition, the weld material grade was used as follows: (i) filler metal G46 – for the connection between S355 component and S460 component, respectively between S460 components, (ii) filler metal G69 – for the connection between S355 component and S690 component, respectively between S690/S700 components.

2.2 Experimental program and specimen configuration

The aim of the experimental program was to validate by tests welded connections in moment resisting frames and dual braced frames designed using the dual-steel concept. The experimental investigations were considering: material sample tests, load introduction tests, and beam-to-column joint tests. The current paper is focused on the investigation of the joint assemblies, while the description and outcomes of the whole experimental program can be found elsewhere (Dubina et al., 2015, Vulcu et al., 2014).

The experimental program on beam-to-column joints with CF-RHS columns is illustrated in Figure 6. The parameters considered in the configuration of the joints are given by the two joint typologies (RBS and CP – see Figure 1c, Figure 6ab), two steel grades for the RHS tubes (S460 and S700), and two intended failure modes (beam and joint components). In addition, two loading conditions were considered, i.e. monotonic and cyclic loading procedure. Considering the two joint typologies and two HSS/MCS combinations, a number of four beam-to-column joints were designed (see Figure 6c). Besides, in order to assess the over-strength of the connection zone and to observe the basic components of the joints, tests were performed on the corresponding joint assemblies, but for which the beam was strengthened (see Figure 6d). The reason was to face the case of unexpected over-strength of MCS beams. The aim of this investigation was to force the development of plastic deformations in connection zone and joint components.

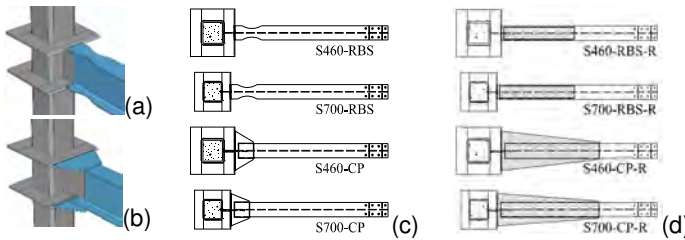


Figure 6. Welded external diaphragm beam-to-column joints with reduced beam section (a), and cover plates (b), designed joint specimens (c), and corresponding joint specimens with reinforced beam (d)

2.3 Test set-up, instrumentation, loading protocols and material properties

The conceptual scheme and illustration of the test set-up are shown in Figure 7. A hydraulic actuator connected at the tip of the beam served as loading device. The column ends were supported using pinned connections, while the beam out of plane deformations were blocked using a lateral support system.

The global instrumentation consisted in measuring: the force in the actuator, displacement at the tip of the beam, horizontal and vertical displacement at column ends.

The local instrumentation was aimed to measure the deformations within the dissipative zone, connection zone, and column web panel. Additionally, with the aim to identify the yielding sequence, the connection zone was prepared by whitewashing. Furthermore, the cyclic loading was performed using the ANSI/AISC-341 (2010) loading protocol. The material properties were obtained for each part of the joint assemblies through material sample tests, i.e. compression tests on concrete cube samples, and respectively tensile and Charpy V-notch impact tests on steel samples (see Dubina et al., 2015).

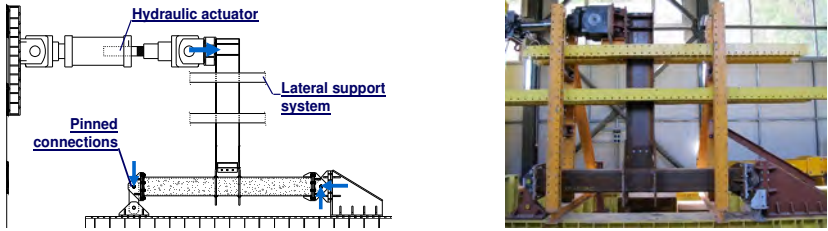


Figure 7. Conceptual scheme (a) and illustration of the experimental test set-up (b)

2.4 Test results

The test results are shown in terms of moment-rotation curve and illustration of the failure mode. Figure 8 illustrates the response of the four designed joints (S460-RBS, S700-RBS, S460-CP, S700-CP) to monotonic and cyclic loading. Failure mode is illustrated only for joints subjected to cyclic loading. The yielding was initiated in the beam flanges within the RBS zone, respectively near the cover plates, and was followed by large plastic deformations – local buckling of flanges and web. No damage was observed in the external diaphragm and column web panel. The response of the corresponding joint specimens with reinforced beam is presented elsewhere (Dubina et al., 2015).

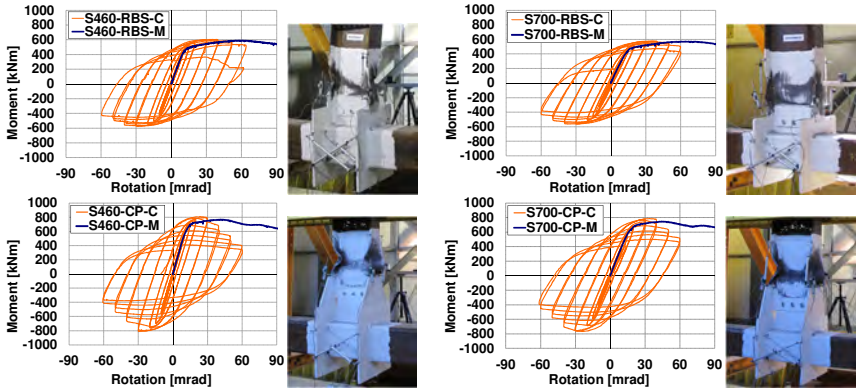


Figure 8. Monotonic & cyclic response of RBS and CP designed joints / illustration of failure mode (cyclic loading)

With regard to the interpretation and evaluation of results, the seismic performance of the joints subjected to cyclic loading was assessed by identifying the joint rotation corresponding to three performance levels (damage limitation – DL, significant damage – SD, near collapse – NC), assumed to be characterized by the following description (based on FEMA 356 (2000)): DL – light damage with the component retaining the initial strength and stiffness; SD – significant damage with some margin against total collapse of the component; NC – heavy damage, with low residual strength and stiffness of the component. The procedure is described elsewhere (Dubina et al. 2015). Figure 9 illustrates the envelope curves and the state of S700-RBS-C and S700-CP-C joints corresponding to the three performance levels. In relation to the seismic performance of the joints, the following observations were made:

- Corresponding to the Significant Damage performance level, all four joint configurations evidenced rotation capacities larger than the 40 mrad (a common code requirement for high-ductility MRF's), and therefore the seismic performance of the joints was considered acceptable;
- The state of the joints corresponding to the three performance levels (see Figure 9) was observed to reflect in a realistic manner the definition related to each performance level as stated above.

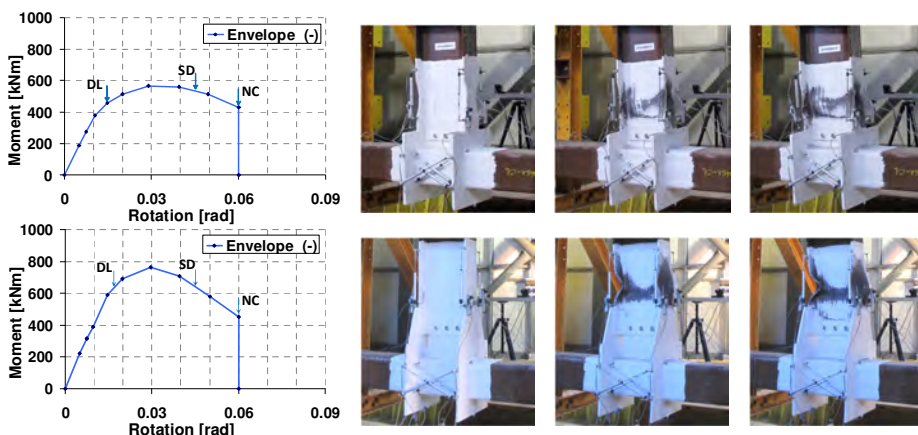


Figure 9. S700-RBS-C / S700-CP-C: envelope curves and state of joint at damage limitation (DL), significant damage (SD), and near collapse (NC) performance levels

3. NUMERICAL INVESTIGATION

3.1 Calibration of numerical models

In addition to the experimental tests, extensive numerical simulations have been performed with the finite element modelling software Abaqus (2011). The first step was represented by the calibration of the numerical models of joint assemblies. Further, the experimental program was extended with the aim to assess the influence of additional parameters on the joint behavior. From the calibration process, see Dubina et al. (2015),

a set of numerical models were obtained which were capable of reproducing with a good accuracy the response of the joints considering the moment-rotation curve and the failure mechanism (see Figure 10).

The monotonic response of the RBS and CP designed joints is illustrated in Figure 10. As can be observed, the plastic hinge developed in the beam, while the cover plates, external diaphragm and column web panel experienced only elastic deformations. Furthermore, the numerical investigations confirmed the yielding sequence observed during the test:

- In case of RBS joints (see Figure 10a): yielding of beam flanges within the RBS zone followed by plastic deformations of flanges and web (elongation / buckling);
- In case of CP joints (see Figure 10b): yielding of beam flanges near the cover plates followed by plastic deformations of flanges and web (elongation / buckling).

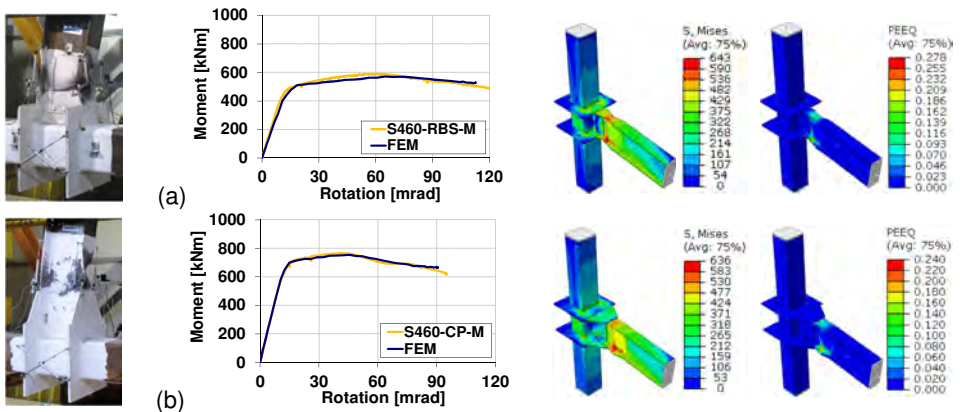


Figure 10. Illustration of failure mode (test), moment-rotation curve (test vs. FEM), von Mises stress distribution, and equivalent plastic strain for joint configurations: (a) S460-RBS, (b) S460-CP.

3.2 Extension of the experimental program

The experimental investigations were conducted on single sided beam-to-column joints. Due to the more complex working conditions of a beam-to-column joint within a 3D building frame, a set of complementary cases were considered for the investigation through FE simulations. The influence of different parameters on the joint behavior was investigated for the following cases: (i) influence of the concrete core – i.e. the response of the joint without concrete core in comparison to the reference joint with CFT column; (ii) influence of the axial force – i.e. the response of the joint with axial force in the column ($N=0.5 \cdot N_{p}$) in comparison to the reference model (without axial load); (iii) response of the joints with two and respectively four welded beams.

The extension of the experimental program lead to the following outcomes:

- The absence of concrete core (FEM NC – “no concrete”) did not affect significantly the response of RBS and CP joints, as only a minor reduction of the capacity was observed (see Figure 13).

- The axial force in the column did not affect the response of the joint (see Figure 12), and the failure mechanism was not affected (plastic hinge developed in the beam).
- Compared to the reference joint model, see Figure 13 and Figure 14, a reduction of the stiffness can be observed for one- and two-way joints. The capacity and the failure mode were not affected, except corresponding to the secondary loading direction of the two-way joint (due to the development of plastic deformations in the column above the external diaphragm). Plastic deformations were not evidenced by the connection zone. Consequently, the joining solution with external diaphragms exhibited a good response for the case of one- and two-way joints.

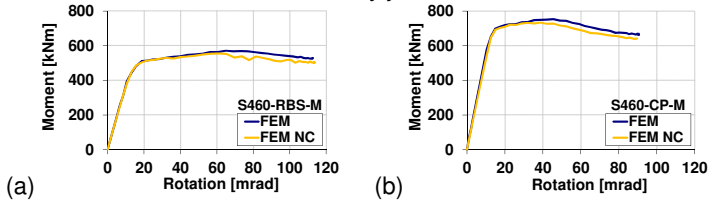


Figure 11. Influence of concrete core: (a) S460-RBS, (b) S460-CP

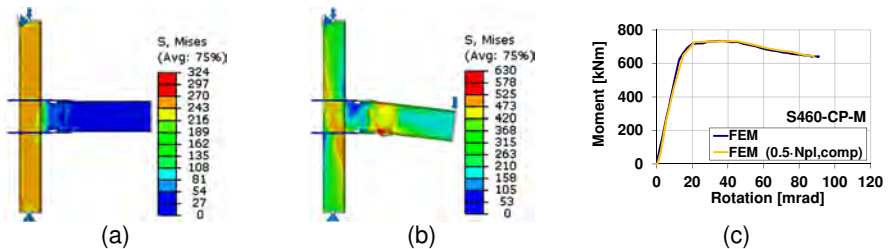


Figure 12. Influence of column axial force (S460-CP joint): (a) joint assembly with axial force in column ($0.5 \cdot N_{pl,Rd}$), (b) same joint with loaded beam; (c) moment-rotation curve

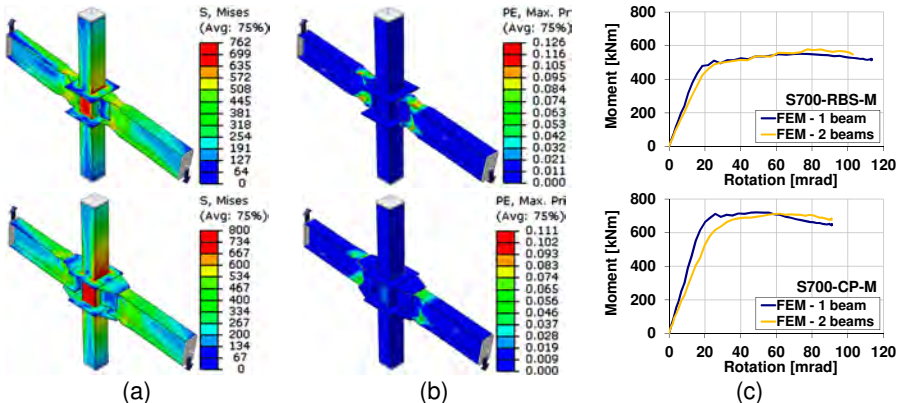


Figure 13. Response of one-way joints: (a) von Mises stress, (b) plastic strain, (c) moment-rotation curve – in case of S700-CP and S700-RBS joint configurations

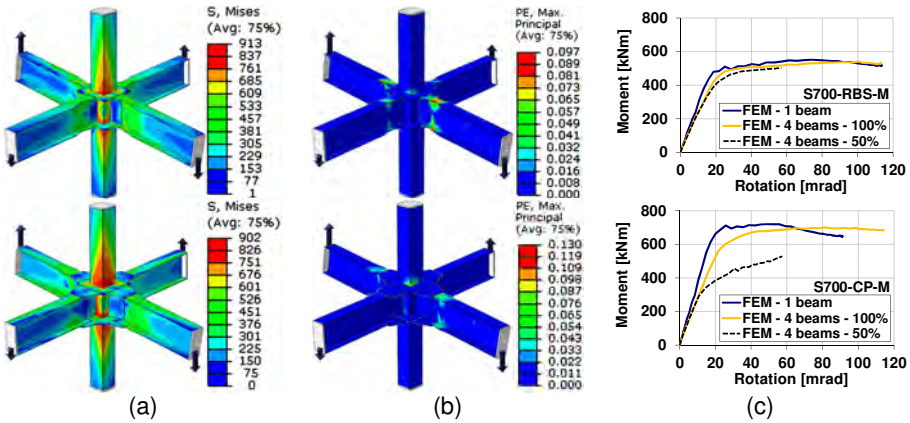


Figure 14. Response of two way joints: (a) von Mises stress, (b) plastic strain, (c) moment-rotation curve – in case of S700-RBS and S700-CP joint configurations

5. CONCLUSIONS

The current paper summarized HSS-SERF research project with the emphasis on: aim, partnership, objectives, and the innovative solutions for the beam-to-column joints investigated within the project. Furthermore, the results presented herein focused on the research activities conducted by the Politehnica University of Timisoara within HSS-SERF project. Particularly, an experimental program was developed and carried out with the aim to characterize the behavior of two joint typologies for dual-steel frames of high strength steel CF-RHS columns. In addition, numerical investigations were performed for the extension of the experimental program with additional cases – for which the experimental investigation was not possible.

The experimental investigations performed on beam-to-column joints under both monotonic and cyclic loading evidenced a good conception and design of the joints (RBS and CP), justified by: elastic response of the connection zone, formation of the plastic hinge in the beam. The current study proved the feasibility of using higher steel grades in non-dissipative members (columns) and joint components. Furthermore, the experimental program allowed the investigation on the seismic performance of the welded beam-to-CFT column joints. As a result, corresponding to the Significant Damage performance level, the RBS and CP joint configurations evidenced rotation capacities larger than the 40 mrad, and therefore the seismic performance of the joints was considered as acceptable.

The numerical investigations were aimed, in the first phase, at predicting with a good accuracy the behavior of the joints in order to avoid unacceptable failure during experimental investigations. Furthermore, the numerical models of the joints were calibrated based on monotonic and cyclic test results, thus obtaining a set of numerical models capable of reproducing with a good accuracy the response of the tested joint assemblies. This led to a better understanding of the joint behavior and allowed for

additional parameters to be investigated numerically, such as: influence of the concrete core, influence of the axial force in the column, response of one-way and two-way joints. The calibration of the joint models lead to several observations:

- The designed failure mechanism was confirmed for both standard designed joints (RBS, CP), and the corresponding joints with artificially strengthened beam: (i) formation of the plastic hinge in the beam, and the elastic response of the joint components, (ii) yielding of joint components (beam flanges near the connection in the HAZ, cover plates, external diaphragm, column web panel).
- The joint models subjected to cyclic loading showed a reasonable match with the experimental data considering the moment-rotation hysteretic loops, and envelope curves (good match considering the initial stiffness, maximum strength and degradation of the capacity). This allowed to evaluate the state of the joint assemblies (e.g. stress, strain) corresponding to the peak amplitudes for each cycle.

The extension of the experimental program lead to the following outcomes:

- The absence of concrete core did not affect significantly the response, as only a minor reduction of the capacity was observed.
- The axial force in the column did not affect the response of the joint, as the moment-rotation curve and the failure mechanism were not affected.
- A reduction of the stiffness was evidenced in case of one- and two-way joints. The capacity and the failure mode were not affected, except corresponding to the secondary loading direction of the two-way joint (due to the development of plastic deformations in the column above the external diaphragm). Plastic deformations were not evidenced within the connection zone. Consequently, the joining solution with external diaphragms exhibited a good response for one- and two-way joints.

As part of HSS-SERF project (see Dubina et al. 2015), the evaluation of the technical and economic efficiency of dual-steel structures compared to conventional ones was performed. For this purpose, a number of 15 frame configurations were selected and designed on a more detailed level, considering the following joint typologies: (i) welded external diaphragm reduced beam section joint, (ii) welded rib stiffened joint, (iii) bolted hammer head joint, (iv) bolted reduced beam section joint with long bolts. Based on the computed price of frames and the price associated with the fabrication of connections, it was observed that the use of higher steel grades in non-dissipative members and connections, lead to cost reduction – justified by the reduction of steel consumption within members and connections and reduction of welding volume. The study contains a comparison between the prices of the four types of joints as well.

6. ACKNOWLEDGEMENT

The present work was supported by the funds of European Project: “High Strength Steel in Seismic Resistant Building Frames”, Grant N0 RFSR-CT-2009-00024.

REFERENCES

- FEMA 350 (2000) – “Recommended seismic design criteria for new steel moment-frame buildings”. Prepared by the SAC Joint Venture for FEMA, Sacramento, California.
- FEMA 356 (2000) “Pre-standard and Commentary for the Seismic Rehabilitation of Buildings”, prepared by Building Seismic Safety Council for FEMA, Washington.
- EN 1993-1-8 (2005). European Committee for Standardization – CEN. Eurocode 3: Design of steel structures. Part 1.8: Design of joints.
- AISC-358 (2010) – “Prequalified Connections for Special and Intermediate Steel Moment Frames for Seismic Applications”. American Institute of Steel Construction.
- Abaqus (2011) Analysis User’s Manual I-V. Version 6.11. USA: ABAQUS, Inc.
- FEMA P-795 (2011) “Quantification of Building Seismic Performance Factors: Component Equivalency Methodology”. Prepared by Applied Technology Council, for Federal Emergency Management Agency and ATC Management & Oversight.
- Silva, L.S., Rebelo, C., Serra, M., Tenchini, A., (2011), “Selection of structural typologies and design of optimized dual-steel multi-storey frames”. Mid Term Report of HSS-SERF Project / (GIPAC): “High Strength Steel in Seismic Resistant Building Frames”, Grant No. RFSR-CT-2009-00024.
- Tenchini, A., D’Aniello, M., Rebelo, C., Landolfo, R., Silva, L.S., Lima, L., (2014). “Seismic Design of Dual-Steel Structures”. In Dubina D., Landolfo R., Stratan A., Vulcu C., (*Editors*), “Application of High Strength Steels in Seismic Resistant Structures”. “Orizonturi Universitare” Publishing House, ISBN: 978-973-638-552-0. (<http://www.steelconstruct.com/site/#> / E-store / Books / Seismic Design).
- Hoang, L., Demonceau, J.-F., Jaspert, J.-P., (2014), “Innovative Bolted Beam-to-Column Joints in Moment Resistant Building Frames: from Experimental Tests to Design Guidelines”. In Dubina D., Landolfo R., Stratan A., Vulcu C., (*Editors*), “Application of High Strength Steels in Seismic Resistant Structures”. “Orizonturi Universitare” Publishing House, ISBN: 978-973-638-552-0.
- Cermelj, B., Beg, D., (2014), “Evaluation of Cyclic Tests on Welded Stiffened Beam-to-Column Joints in Frames with HSS Columns”. In Dubina D., Landolfo R., Stratan A., Vulcu C., (*Editors*), “Application of High Strength Steels in Seismic Resistant Structures”. “Orizonturi Universitare” Publishing House, ISBN: 978-973-638-552-0. (<http://www.steelconstruct.com/site/#> / E-store / Books / Seismic Design).
- Vulcu, C., Stratan, A., Ciutina, A., Dubina, D., (2014). “Experimental Evaluation of Welded Reduced Beam Section (RBS) and Cover Plate (CP) Beam-to-CF-RHS Column Joints”. In Dubina D., Landolfo R., Stratan A., Vulcu C., (*Editors*), “Application of High Strength Steels in Seismic Resistant Structures”. “Orizonturi Universitare” Publishing House, ISBN: 978-973-638-552-0.
- Vulcu, C., Stratan, A., Ciutina, A., Dubina, D., (2014). “Steel-Concrete Connection in Case of Concrete Filled Rectangular Hollow Section Columns”. EUROSTEEL 2014, Naples, Italy, September 10-12, 2014.
- Dubina, D., Vulcu, C., Stratan, A., Ciutina, A., Grecea, D., Ioan, A., et al. (2015), “High Strength Steel in Seismic Resistant Building Frames (HSS-SERF)”. Final Report. Grant No. RFSR-CT-2009-00024 (01.07.2009 – 30.06.2013). Directorate-General for Research and Innovation, Unit D.4 – Coal and Steel, RFCS Publications, European Commission, ISBN 978-92-79-44081-6, DOI: 10.2777/725123, 2015.

SEISMIC COLLAPSE STUDY OF A SELF-CENTERING STEEL MOMENT RESISTING FRAME SYSTEM

James M. Ricles
Lehigh University, Bethlehem, PA 18015, USA
jmr5@lehigh.edu

Richard Sause
Lehigh University, Bethlehem, PA 18015, USA
rsause@lehigh.edu

Omid Ahmadi
Lehigh University, Bethlehem, PA 18015, USA
oma210@lehigh.edu

ABSTRACT

A steel self-centering moment resisting frame (SC-MRF) is a lateral load resisting system with post-tensioned beam-to-column moment connections. When subjected to extreme loads, such as that which occurs during an earthquake, an SC-MRF develops controlled gap opening at the beam-column interfaces. Recent analytical and experimental research has shown that an SC-MRF can achieve the performance objective of remaining free of structural damage under the design earthquake. Little is known about the collapse resistance of an SC-MRF under extreme seismic ground motions. Incremental Dynamic Analysis (IDA) are performed to determine the probability of collapse of a 4-story building with perimeter steel SC-MRFs during an earthquake. A model of the SC-MRF was developed that included both stress-resultant and continuum elements to enable the important limit states, including local buckling in the beams, to be accounted for in the IDA. The results show that the seismic collapse resistance of an SC-MRF system can exceed that of a conventional steel SMRF.

INTRODUCTION

Conventional steel special moment resisting frames (MRFs) are designed to dissipate energy under the design earthquake by developing yielding in the main structural members. This can result in permanent structural damage as well as large residual drift following the earthquake. To avoid permanent structural damage and large residual drift, post-tensioned beam-to-column connections for self-centering (SC) MRF were proposed by Ricles et al. (2001). This innovative lateral resisting system provides not only a softening capability to the frame without causing any structural damage, but also a SC capability that leads to minimal residual drift after the design earthquake. An SC-MRF is characterized by gap opening and closing at the beam-column interface under cyclic loading. The beams are post-tensioned to columns by high strength post-tensioning (PT)

strands oriented horizontally to provide self-centering forces when gap opening occurs (see Figure 1(a)). Energy is dissipated by special energy dissipation devices, rather than by forming inelastic regions in the structural members. Presently, several variations of beam-to-column connections have been proposed for steel moment resisting frames (Garlock et al. (2005), Rojas et al. (2005), Kim and Christopoulos (2008), Wolski et al. (2009)). Recently, to experimentally investigate the performance of an SC-MRF designed in accordance with a performance based design (PBD) procedure, a 0.6 scale 4-story 2-bay SC-MRF with PT connections with web friction devices (WFDs) was designed and tested by Lin et al. (2013a,b). They concluded that SC-MRFs can be designed to perform with minor damage while maintaining self-centering behavior under the maximum considered earthquake (MCE). In this paper the results of a study to investigate the collapse resistance of an SC-MRF with WFDs is presented. The study involved developing nonlinear complex finite element models of a 4-story perimeter steel SC-MRF and performing a series of IDAs to establish the structure's collapse resistance.

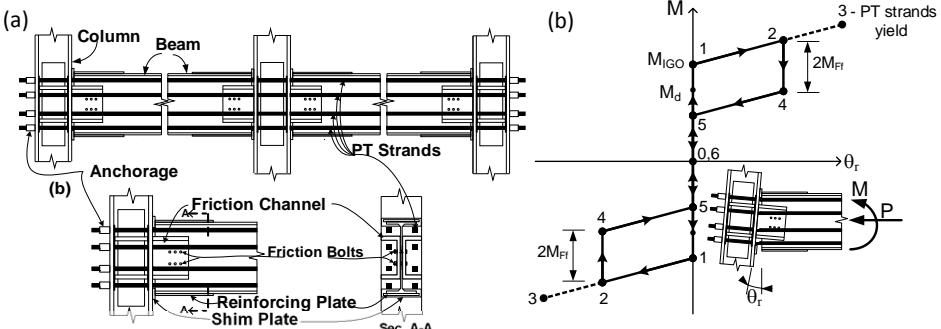


Figure 1 Schematic of (a) elevation of a 2-bay SC-MRF with PT strands, (b) PT-WFD connection, and moment-relative rotation ($M-\theta_r$) of a PT-WFD connection.

CONNECTION BEHAVIOR

Figure 1(b) shows the conceptual moment-relative rotation ($M-\theta_r$) behavior for a post-tensioned SC-WFD connection where θ_r is the relative rotation between the beam and column when gap opening occurs and M is the moment at the connection. The total moment resistance of the connection is provided by the contribution of the PT force in the strands, diaphragm force, and friction force produced by the WFD:

$$M = P d + F_f r \tag{1}$$

In Equation (1), P is the beam axial force and d is the distance from the PT force centroid to the center of rotation (COR) that coincides at the reinforcing plate and the shim plate of the connection. The product $F_f r$ is denoted as the friction moment, M_{Ff} , where r is the distance from the WFD friction force resultant, F_f , to the COR. P is due to the post-tensioning force, T , and an additional axial force, F_{Id} , produced by the interaction of the SC-MRF with the floor diaphragm that transfers the lateral inertia forces to the SC-MRF:

$$P = T + F_{fd} \quad (2)$$

The moment at imminent gap opening, M_{IGO} , occurs at event 1 in Figure 1(b), where the gap opening and the corresponding relative rotation θ_r begins:

$$M_{IGO} = T_0 d + F_f r \quad (3)$$

In Equation (3) T_0 is the initial PT force. The stiffness of the connection after gap opening is associated with the elastic axial stiffness of the PT strands. The connection moment, M , continues to increase as the PT strand force, T , increases with the strand elongation due to the gap opening (event 1 to event 2 in Figure 1(a)):

$$T = T_0 + 2 d \theta_r^{ave} \left(\frac{k_b k_s}{k_b + k_s} \right) \quad (4)$$

In Equation (4), k_b and k_s are the axial stiffness of the beam and the PT strands within one bay, respectively. θ_r^{ave} is the average connection relative rotation for all connections on one floor level. With continued loading, yielding of the strands may eventually occur at event 3. Upon unloading prior to strand yielding, θ_r remains constant but the moment decreases by $2M_{Ff}$ due to the reversal in the friction force in the WFD. Continued unloading reduces θ_r and M to zero with the beam being compressed against the shim plates at event point 6. A similar behavior occurs when the applied moment is reversed. As long as the strands remain elastic and there is no significant beam yielding, the PT force is preserved and the connection will self-center under cyclic loading.

PERFORMANCE BASED DESIGN PROCEDURE

A performance-based design (PBD) procedure by Lin (2012) was used to design the SC-MRF studied in this research. The PBD considers two levels of seismic hazard, namely the design basis earthquake (DBE) and maximum considered earthquake (MCE). Under the DBE, which is equal to two-thirds the intensity of the MCE, and has an approximate 10% probability of being exceeded in 50 years, an SC-MRF system is designed to sustain

minimal structural damage and no significant residual drift. This level of performance would enable immediate occupancy after the DBE, depending on the amount of non-structural damage. In the present research, an SC-MRF system is designed to achieve the collapse prevention (CP) performance level under an MCE level ground motion, where the MCE has a 2% probability of exceedance in 50 years. Different limit states for an SC-MRF are

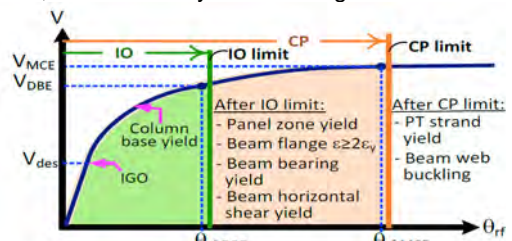


Figure 2. Design objectives related to global response, Lin (2012)

shown in the conceptual base shear-roof drift ($V-\theta_r$) response in Figure 2. Before the Immediate Occupancy (IO) performance level, connection decompression and minimal yielding at the column bases of the SC-MRF is permitted to occur. Panel zone yielding,

beam web yielding, and a beam flange strain greater than twice the yield strain is designed to occur between the IO and CP levels. At the CP level, PT strand yielding, beam web buckling, and excessive story drift are not permitted. The details of the design procedure are given in Lin (2012).

PROTOTYPE BUILDING

The prototype SC-MRF building is a 7x7-bay office building shown in Figure 3(a). The prototype building was designed by Lin (2012). The building is assumed to be located in Van Nuys (Latitude = 34.22° and Longitude = -118.47°), California in the Los Angeles region. The building has four stories above ground and a one-story basement below ground. Each side of the building perimeter contains two 2-bay SC-MRFs as shown in Figure 3(a). The floor diaphragm at each level is attached to only one bay of each SC-MRF. By attaching the floor diaphragm to only one bay, the beam-to-column connections are free to develop gap opening as illustrated in Figure 1(b). The member sizes and number of PT strands at each floor level are summarized in Table 1. All members were assumed to be A572 steel; the PT strands are 7-wire low-relaxation ASTM A416 Grade 270 steel strands with a nominal ultimate strength $F_{u,n}=270$ ksi. The selection of the number of stands was based on limiting the total PT strand force under the MCE to not exceed 90 percent of the nominal total PT strand yield force ($T_{y,n}$). Based on ASTM A416, $T_{y,n}$ is assumed to be equal to $0.9T_{u,n}$, where $T_{u,n}$ is the total nominal PT strand ultimate force capacity. The beam-to-column connections have beam web friction devices (WFDs). The PT strands run parallel to the beams across the two bays of the SC-MRF. Under the DBE level ground motions, the SC-MRF system is designed to sustain minimal structural damage with no significant residual drift. This level of performance would enable immediate occupancy after the DBE, depending on the amount of non-structural damage. Complete details of the design are given in Lin (2012).

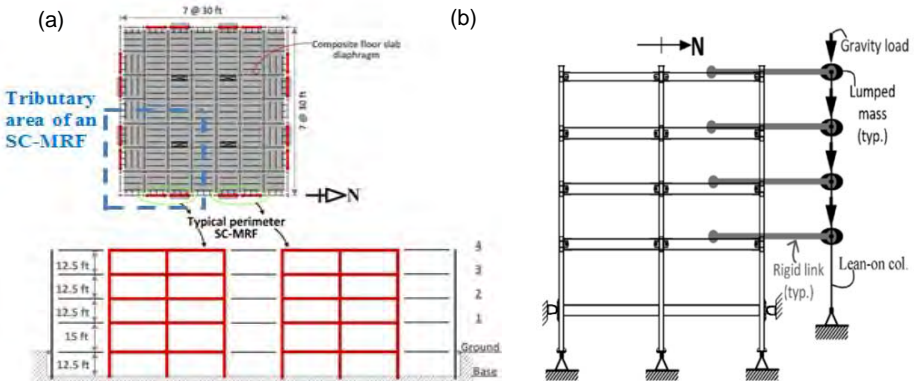


Figure 3. Prototype building: (a) Floor plan and elevation; (b) SC-MRF and gravity frame model

Table 1. Prototype SC-MRF member sizes and PT strands.

Story	Beam	Column		Number of Strands	Strand Area (in. ²)
		Interior	Exterior		
4 th Story	W24x94	W14x193	W14x176	8	0.217
3 rd Story	W30x132	W14x193	W14x176	16	0.217
2 nd Story	W30x148	W14x257	W14x233	24	0.217
1 st Story	W30x148	W14x257	W14x233	24	0.217

FINITE ELEMENT MODEL OF PROTOTYPE BUILDING

The beams in an SC-MRF are subject to large moments combined with appreciable axial force P caused by the PT force and diaphragm force, making the beams susceptible to local buckling. Although the proposed PBD procedure attempts to prevent beam local buckling failure under the MCE level, it likely will occur under ground motions that exceed the MCE hazard level. Beam local buckling at the end of the reinforcing plates is one of the important collapse limit states that must be considered in developing an analytical model of the SC-MRF. The occurrence of local buckling in the beam leads to shortening of the member, which in turn results in a loss of PT force and subsequent moment capacity of a post-tensioned SC-WFD connection. A finite element model was developed for the study that consists of stress-resultant and continuum shell elements in order to model the complete structural system while capturing the important limit states that can occur, including gap opening at the beam-to-column interface, yielding and/or fracture of PT strands, second order (P -delta) effects due to gravity loads imposed on the gravity load frames, and beam local flange and web buckling at the end of the reinforcing plates. The ABAQUS (2011) program is used to develop the model on the basis of its ability of reliably solving complex nonlinear problems.

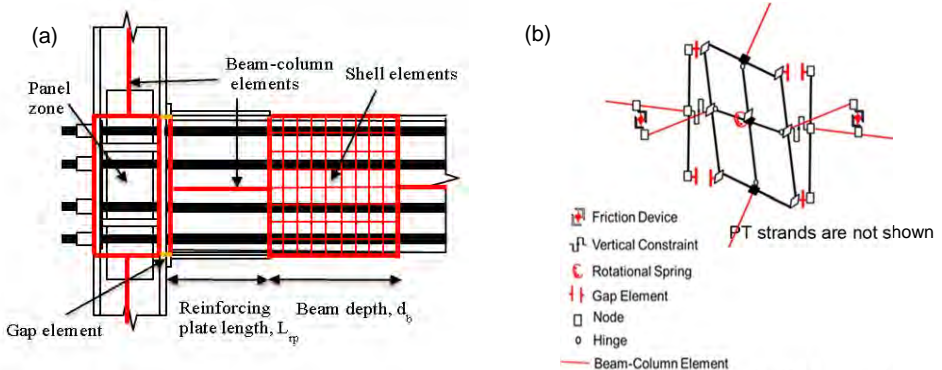


Figure 4. Finite element model: (a) Schematic of SC connection using shell elements at the end of reinforcing plate length, (b) model details of SC-MRF connection.

The building has a symmetric floor plan in both directions. Thus, one of the perimeter SC-MRFs is studied (as shown in Figure 3(b)) under one-directional ground motions. A lean-on column is used (shown in Figure 3(b)) in order to model the P-delta effects due to the gravity load system. The lean-on column nodes, where the lumped seismic mass of each floor are located, are connected with the beam of only one bay at each floor level of the SC-MRF by multi-point constraints (i.e., equal degrees of freedom) in the horizontal direction (Figure 3(b)). The seismic mass is determined based on the tributary area shown in Figure 3(a). In order to develop a computational efficient model, continuum shell elements are used only at the end of the reinforcing plates where beam local buckling is expected to occur (see Figure 4(a)) for ground motions with an intensity beyond the MCE level. The other portions of the members are modeled with stress-resultant beam column elements, as shown in Figure 4(a). Initial imperfections are imposed on the shell elements to initiate any local buckling in the beam. Figure 4(b) shows the SC-MRF connection model details. A kinematic based panel zone model is used with nonlinear shear deformations. The boundary node displacements and rotations are appropriately slaved to the displacements and rotations of two center nodes which are connected with a rotational spring. The two center nodes have the same displacements but independent rotations to simulate the shear deformations in the panel zone. Compression-only gap elements as used to transfer the compressive force between nodes at the beam-column interface, as shown in Figure 4(b). The friction device provides friction force components after gap opening occurs.

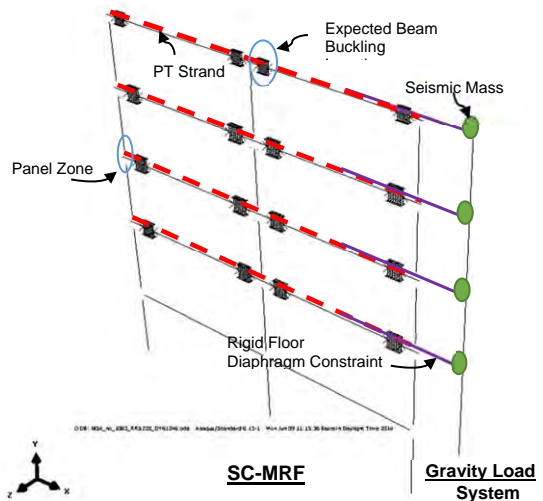


Figure 5. Schematic of SC-MRF model in ABAQUS

Figure 5 shows a schematic of the ABAQUS frame model for seismic collapse resistance evaluation of an SC-MRF. The model was calibrated using tests performed by Ricles et al. (2000), Lin et al. (2013a,b), and Garlock (2005).

COLLAPSE PERFORMANCE EVALUATION

The Incremental Dynamic Analysis (IDA) method was used to assess the collapse capacity under a set of far-field ground motions which included 44 ground motions from FEMA P695 (2009). IDA is a parametric analysis method (Vamvatsikos and Cornell, 2006) in which individual ground motions are scaled to increasing intensities until the structure reaches a collapse point. Collapse fragility curves can be defined through a

cumulative distribution function (CDF). These curves relate the ground motion intensity to the probability of collapse (Ibarra et al., 2002) using the collapse data from the IDA results. The probability of collapse at a given spectral acceleration associated with the fundamental period of the structure, S_T , (defined in FEMA P695) is based on the number of ground motions which cause collapse at that spectral acceleration.

From the fragility curve the median collapse capacity \hat{S}_{CT} can be determined and is associated with the S_T value where half of the ground motions cause the structure to collapse. The ratio between \hat{S}_{CT} and the MCE code-specified spectral acceleration intensity (S_{MT}) at the fundamental period of the structure is the collapse margin ratio, CMR. The CMR is one of the primary parameters used to characterize the collapse safety of a structure, where:

$$CMR = \frac{\hat{S}_{CT}}{S_{MT}} \quad (5)$$

INCREMENTAL DYNAMIC ANALYSIS RESULTS

The results from the IDA for all 44 ground motions are shown in Figure 6. Each data point in Figure 6 corresponds to the result of a non-linear time history analysis of the building subjected to one ground motion record scaled to a prescribed intensity level. Each curve shown in this figure corresponds to a single ground motion scaled to increasing spectral intensity levels. In Figure 6 the vertical axis data is the spectral acceleration, S_T , associated with the 5% damped median spectral acceleration of the far-field record set at the fundamental period of the structure (defined in FEMA P695) and the horizontal axis is the maximum story drift ratio, θ_s , corresponding to each time history analysis. The slope of each IDA curve in general rapidly decreases and flattens out at some S_T level, meaning that at such intensity level, the story drift becomes large with a small increase in ground motion intensity. This phenomenon indicates dynamic instability of the frame. For an individual record, the collapse capacity intensity (S_{aCOL}) of the frame model is the smaller of the S_T value at the end of the corresponding IDA curve where convergence failed in the analysis due to incipient collapse and the S_T value at the transient story drift of 15%.

S_{aCOL} from the IDA curves are ranked in ascending order, each being treated as an equally likely outcome. The collapse fragility curve is obtained by fitting a cumulative distribution function, assuming a lognormal distribution, to the ranked S_{aCOL} data points, as illustrated in Figure 7, where the median of S_{aCOL} at collapse, \hat{S}_{CT} , and associated standard deviation β_{RTR} of the natural logarithm are $\hat{S}_{CT}=2.43g$ and $\beta_{RTR}=0.26$. Figure 7 shows the cumulative distribution function fits reasonably well the trend in the data points.

Different sources of uncertainty affect the fragility curve. Record to record (RTR) variability is the only source of uncertainty (β_{RTR}) considered for deriving the fragility curve shown in Figure 7. In order to compare the above results with criteria from FEMA P695 for acceptable values for collapse resistance, other sources of uncertainty such as the design requirement uncertainty (DR), test data uncertainty (TD), and modeling uncertainty

(MDL) need to be considered to find the total amount of system uncertainty (β_{TOT}), where per FEMA P695:

$$\beta_{TOT} = \sqrt{\beta_{RTR}^2 + \beta_{DR}^2 + \beta_{TD}^2 + \beta_{MDL}^2} \quad (6)$$

FEMA P695 defines a quality rating for the above mentioned uncertainties and translates them into quantitative values of uncertainty. The amount of uncertainty is defined as 0.1, 0.2, 0.35 and 0.5 for superior, good, fair and poor quality rates, respectively. Considering $\beta_{RTR}=0.4$ (FEMA P695), a good quality for modeling and test data, and fair quality for the design requirement (since the design procedure per Lin (2012) has not undergone peer review), results in a value of $\beta_{TOT}=0.6$. The fragility curve corresponding to $\hat{S}_{CT}=2.43g$ and $\beta_{TOT}=0.6$ is shown in Figure 7.

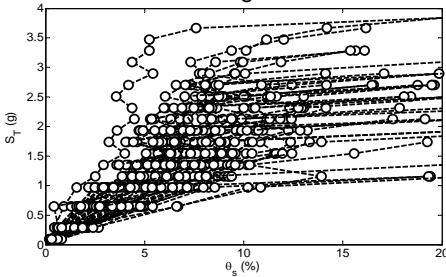


Figure 6. DA results: spectral acceleration vs. maximum story drift ratio ($S_T - \theta_s$) for 4-story SC-MRF.

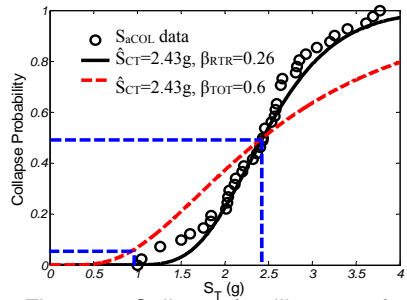


Figure 7. Collapse fragility curve for 4-story SC-MRF.

Acceptable performance is defined per FEMA P695 by the probability of collapse under MCE ground motions being 10% or less on average across a performance group. Performance groups reflect major differences in configuration, design gravity and seismic load intensity, structural period and other factors that may significantly affect seismic behavior. In addition, the average value of an adjusted collapse margin ratio (ACMR) needs to exceed $ACMR_{10\%}$ for the performance group, where $ACMR_{10\%}$ is the adjusted collapse margin ratio based on β_{TOT} and a 10% collapse probability. In addition, for each archetype within a performance group the probability of collapse needs to be 20% or less and the ACMR exceed $ACMR_{20\%}$ (adjusted collapse margin ratio based on β_{TOT} and a 20% collapse probability). The CMR value is modified to obtain an ACMR to account for the effects of spectral shape, where:

$$ACMR = SSF * CMR \quad (7)$$

In Equation (7) SSF is the value for the spectral shape factor. To be conservative, the lower bound value of unity is used for SSF herein. Although one archetype is only included in this study, the ACMR value and probability of collapse under the MCE are compared with the acceptable values stipulated by FEMA P695. Table 2 summarizes the ACMR value and the probability of collapse under the MCE level along with the allowable values in accordance with FEMA P695. The ACMR and probability of collapse under the MCE based on the fragility curve with $\hat{S}_{CT}=2.43g$ and $\beta_{TOT}=0.6$ are found to be 2.52 and 6.18%,

respectively. These values are within the limits per FEMA P695, as shown in Table 2. Seo et al. (2014) found the CMR and probability of collapse under the MCE level to be 1.94 and 10.58%, respectively (values were modified to account for the fundamental period definition in FEMA P695 and sources of uncertainty, considering $\beta_{RTR}=0.4$ and a good quality for modeling, test data and design requirement), for a 4-story SMRF designed for the same location as the SC-MRF used in the present study. These results indicate that the collapse resistance of the 4-story SC-MRF exceeds that of the comparable SMRF.

Table 2. ACMR value and probability of collapse under MCE level for SC-MRF and SMRF, along with the allowable values in accordance with FEMA P695.

System	ACMR	Probability of Collapse under MCE	FEMA P695 Minimum ACMR	FEMA P695 Maximum Probability of Collapse
SC-MRF	2.52	6.18%	ACMR _{10%} =1.96 ⁽¹⁾	10% ⁽¹⁾
			ACMR _{20%} =1.56 ⁽²⁾	20% ⁽²⁾
SMRF	1.94	10.58%	ACMR _{10%} =1.96 ⁽¹⁾	10% ⁽¹⁾
			ACMR _{20%} =1.56 ⁽²⁾	20% ⁽²⁾

⁽¹⁾ Allowable value on average across a performance group (FEMA P695)

⁽²⁾ Allowable value for each archetype within a performance group (FEMA P695)

SUMMARY AND CONCLUSIONS

A series of IDA are performed to investigate the seismic collapse resistance of a 4-story 2-bay steel SC-MRF. The SC-MRF is modeled using an approach that is capable of capturing important limit states beyond the MCE level, including beam flange and web local buckling. Although only one archetype is studied in this research, the results show that a properly designed SC-MRF system using an existing PBD procedure has the potential to enable an acceptable margin against collapse and probability of collapse to be achieved under the MCE in accordance with FEMA P695, where this PBD procedure is based on achieving prescribed performance levels under the DBE and MCE. Furthermore, the collapse resistance of the SC-MRF is found to exceed that of a comparable SMRF. Therefore, in addition to the already established fact that an SC-MRF system can perform in a resilient manner under the DBE, it appears that the SC-MRF in this study has a satisfactory margin against collapse that is comparable, or better than a conventional steel SMRF. To generalize this statement for SC-MRF systems, additional archetypes and performance groups must be considered to qualify the system as having an acceptable resistance to collapse.

ACKNOWLEDGEMENTS

The authors sincerely acknowledge the financial support awarded to the first author through the Department of Civil and Environmental Engineering, Lehigh University during

the course of this study. Any opinions, findings, and conclusions expressed in this paper are those of the authors and do not necessarily reflect the views of the sponsor.

REFERENCES

- ABAQUS, Inc. (2011). ABAQUS Analysis User's Manual, v. 6.11.
- FEMA (2009), Quantification of Building Seismic Performance Factors. *Report FEMA P695*, Federal Emergency Management Agency (FEMA), Washington, D.C.
- Garlock, M., Ricles, J., Sause, R. (2005) "Experimental Studies on Full-scale Post-tensioned Steel Connections," *Jrn of Str Eng*, ASCE; **131**(3): 438–448.
- Ibarra L., Medina R., Krawinkler H. (2002) "Collapse Assessment of Deteriorating SDOF Systems," *Proceedings, 12th European Conference on Earthquake Engineering*, London; Elsevier Science Ltd, paper No. 665.
- Kim H.-J., Christopoulos C. (2008) "Friction Damped Posttensioned Self-Centering Steel Moment-Resisting Frames," *Jrn of Str Eng*; **134**(11): 1768-1779.
- Lin Y-C, (2012) Seismic Performance of a Steel Self-Centering Moment Resisting Frame System with Beam Web Friction Device. Ph.D. Dissertation, Dept. of Civil and Environmental Engineering; Lehigh University, Bethlehem, PA.
- Lin, Y.C., Sause, R., and Ricles J.M. (2013a) "Seismic Performance of a Steel Self-Centering Moment Resisting Frame: Hybrid Simulations under Design Basis Earthquake," *Journal of Structural Engineering*; **139**(11): 1823-1832.
- Lin, Y.C., Sause, R., and Ricles J.M. (2013b) "Seismic Performance of a Large-Scale Steel Self-Centering Moment Resisting Frame: MCE Hybrid Simulations and Quasi-Static Pushover Tests," *Jrn of Str Eng*; **137**(7), pp. 1227-1236.
- Ricles, J.M., Ricles C., Lu L.-W., Fisher J.W., (2000) "Development and Evaluation of Improved Details for Ductile Welded Unreinforced Flange Connection," ATLSS Rpt No. 00-04, Lehigh University, Bethlehem, PA.
- Ricles J.M., Sause R., Garlock M., Zhao C. (2001) "Post-Tensioned Seismic-Resistant Connections for Steel Frames," *Jrn of Str Eng*; ASCE; **127**(2): 113-121.
- Rojas, P., Ricles J.M., Sause R. (2005) "Seismic Performance of Post-tensioned Steel Moment Resisting Frames With Friction Devices," *Jrn of Str Eng*; **131**(4): 529-540.
- Seo, C.Y., Karavasilis, T., Ricles, J.M. and R. Sause, (2014) "Seismic Performance and Probabilistic Collapse Resistance Assessment of Steel MRFs with Viscous Fluid Dampers," *EESD*, **43**(14), 2135–2154, DOI: 10.1002/eqe.2440.
- Wolski M., Ricles J., Sause R. (2009) "Experimental Study of a Self-Centering Beam-Column Connection with Bottom Flange Friction Device," *Jrn of Str Eng*; **135**(5): 479-488.
- Vamvatsikos D., Cornell C.A. (2006) "Direct Estimation of Seismic Demand and Capacity of Multi-Degree of Freedom Systems Through Incremental Dynamic Analysis of Single Degree of Freedom Approximation," *Jrn of Str E*; **131**(4): 589-599.

SELF-CENTERING STEEL PLATE SHEAR WALLS WITH NEWZ-BREAKSS POST-TENSIONED ROCKING CONNECTION

Daniel M. Dowden
University at Buffalo, Buffalo, NY 14260, USA
dmdowden@buffalo.edu

Michel Bruneau
University at Buffalo, Buffalo, NY 14260, USA
bruneau@buffalo.edu

ABSTRACT

This paper presents information on the combined contribution of post-tensioning and beam-to-column joint rocking connections in self-centering steel plate shear walls (SC-SPSW) with the NewZ-BREAKSS connection (i.e., NZ-SC-SPSW). Detailed free-body diagrams presented in this paper provide insights on the basic fundamental kinematic behavior of this Lateral Force Resisting System. Furthermore, the fundamental equations presented provide information suitable to facilitate connection design.

INTRODUCTION

Conventional steel Lateral Force Resisting Systems (LFRS) that comply with current building codes and the AISC seismic provisions (AISC 2010) used in the United States are typically expected to suffer damage during moderate to severe earthquakes. Designed in accordance with prescribed detailing requirements proven by research to ensure ductile response (and protect occupants), these structural systems are not expected to collapse during a severe earthquake, but will likely require repairs following a design level earthquake. Furthermore, the structure could be left with significant residual drifts and visibly leaning following the earthquake (AIJ 1995, Krawinkler et al. 1996, Kawashima et al. 1998, Christopoulos et al. 2003, Pampanin et al. 2003). Thus, although current conventional LFRS can meet the code-specified objective of collapse prevention for standard buildings, structural damage is expected to occur (albeit controlled damage), which could prevent use of the building for a significant repair period after a design level earthquake, and possibly lead to demolition of the building in some cases. This seismic performance is typically expected for conventional LFRS of any material and construction.

Recent research (Winkley 2011, Dowden and Bruneau 2014, Clayton et al. 2015) on Self-Centering Steel Plate Shear Walls (SC-SPSW) has demonstrated that it is possible to design structures to achieve greater performance objectives, by providing frame recentering capabilities after a seismic event, together with replaceable energy dissipating components. This self-centering capability in SPSWs is achieved here by using beam-to-column post-tensioned (PT) moment rocking frame connections, similarly to what was done in past research on self-centering moment frames (e.g., Ricles et al.

2002, Christopoulos et al. 2002, Garlock et al. 2003, Rojas et al. 2005). Because self-centering buildings could economically provide a level of protection designated as available for “immediate occupancy” following an earthquake, this design strategy makes sense from a life-cycle cost perspective. However, to be fully successful, such self-centering strategies need to account for the interaction (due to the PT boundary frame expansion) between the LFRS and the gravity frame.

Towards that goal, this paper presents information on the connection detailing and some connection design aspects of a SC-SPSW detailed with the proposed NewZ-BREAKSS (NZ) rocking connection (Dowden and Bruneau 2011), a beam-to-column joint detail inspired by a moment-resisting connection developed and implemented in New Zealand (Clifton 1996 & 2005, Clifton et al. 2007, MacRae et al. 2008). This PT beam-to-column (a.k.a., horizontal boundary element-to-vertical boundary element or HBE-to-VBE) rocking connection seeks to eliminate PT boundary frame expansion (a.k.a., beam-growth) that occurs in all the other previously researched rocking connections (referenced above). First, a review of the basic kinematics of the NZ-SC-SPSW is presented, from which equations for the beam shear and axial force reactions are obtained from a capacity design approach based on yielding of the SPSW infill web plates. Furthermore, information is presented to facilitate detailing at the corners of the infill web plates to mitigate large tension force demands of the infill web plates with frames with HBE-to-VBE rocking connections.

BASIC KINEMATICS OF THE NZ-SC-SPSW SYSTEM

A SC-SPSW differs from a conventional Steel Plate Shear Wall (SPSW) in that HBE-to-VBE rigid moment connections in a conventional SPSW are replaced by PT rocking moment connections. This allows a joint gap opening to form between the VBE and HBE interface about a rocking point, leading to a PT elongation, this being the self-centering mechanism. The particular NewZ-BREAKSS rocking connection differs in that it eliminates the PT boundary frame expansion typically encountered in the previously researched rocking connections (that rock about both of their beam flanges), by instead maintaining constant contact of the HBE top flange with the VBES during lateral drift. By doing so, when one of the rocking joint “opens”, the rocking joint at the opposite end of the HBE “closes”. As a result, the net gap opening (due to PT boundary frame expansion) is zero over the full length of the HBE. However, in this configuration, the PT elements require their anchorage to the HBE. Also, while the PT at the opening joint will always contribute to frame recentering, the PT element at the closing joint may or may not depending on the relationship between the initial PT force provided and the instantaneous frame drift.

A schematic of the NewZ-BREAKSS detail is shown in Fig. 1. In that figure, it is observed that an initial gap is provided at the bottom of the HBE flanges, which allows rocking about the HBE top flanges only. As a result, during frame sway, an immediate increase and decrease of PT force occurs at the opening and closing joint locations, respectively. Compared to frames with HBE-to-VBE rocking joints that rock about both flanges (a.k.a., Flange-Rocking or FR connections), this results in a reduced PT boundary frame stiffness (due to the relaxation of the PT elements at the closing joints). Also note that in FR connections, both top and bottom HBE flanges are initially in

contact with the VBE), with the benefit that at incipient initiation of joint gap opening (referred to the condition when the “decompression-moment” strength of the joint is reached), the joint stiffness is comparable to that of a rigid moment connection. However, scaled and full-scale tests (Dowden and Bruneau 2014, Dowden et al. 2016) have shown that the absence of a decompression-moment and relaxation of the PT elements at the closing joints, does not have a detrimental effect on the seismic response of NZ-SC-SPSWs.

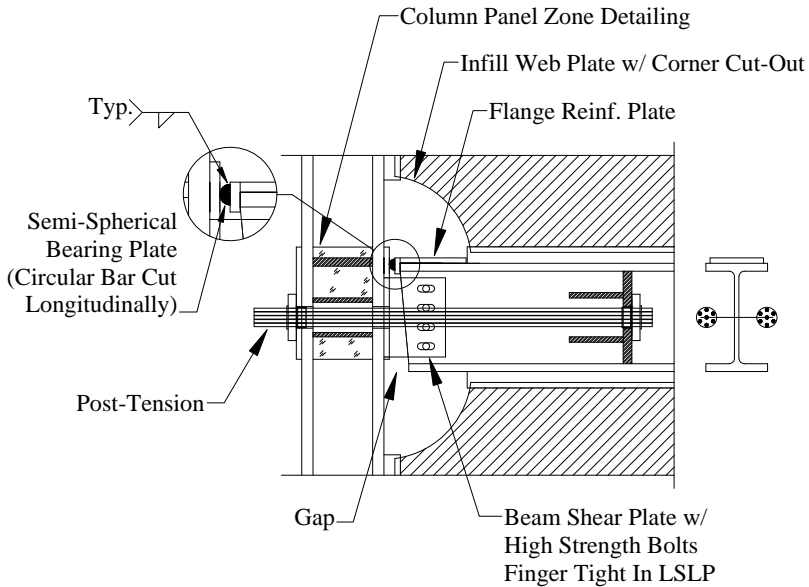


Fig. 1. NewZ-BREAKSS Connection

Furthermore, the base connection of the VBEs for a SC-SPSW should be detailed such to allow free rotation without the formation of a plastic hinge mechanism (in contrast to conventional SPSWs where typically a fixed VBE base connection is assumed). If a plastic hinge is able to form at the base of the VBE member, this could limit the self-centering potential of the PT boundary frame. Furthermore, providing a foundation detail free of damage would also use the SC-SPSW to its full potential. As a result, the only needed replaceable elements after a moderate or design level earthquake would be the infill web plates, as all other elements are designed to remain essentially elastic.

HBE FREE-BODY-FORCE DIAGRAM

To design a typical intermediate NewZ-BREAKSS connection of a SC-SPSW, it is first instructive to review the free-body-diagram (FBD) of a HBE located at an intermediate floor level once the web plate has fully yielded. Figure 2 shows the resultant force FBD of an intermediate HBE (neglecting gravity forces) where: V_i is the story shear force (as

presented in Dowden et al. 2012 for the flange-rocking SC-SPSW) and is assumed to be equally distributed on each side of the frame, W_{bx1} , W_{bx2} and W_{by1} , W_{by2} are respectively the horizontal and vertical force resultants along the length of the HBE, subscripts 1 and 2 respectively denote the level below and above the HBE (here assuming that the force components labeled with subscript 1 are larger than subscript 2 associated with a thicker web plate below the HBE than above), $P_{HBE(VBE)}$ is the horizontal reaction at the rocking point of the yield force resultant of the infill web plate acting on the VBE (as presented in Sabelli and Bruneau 2007), P_s is the PT force, P_{sVBE} is the horizontal reaction of the post-tension force at the rocking point, R_1 is the vertical reaction required for equilibrium of the vertical yield force component of the infill web plate along the HBE, R_2 is the vertical reaction required for equilibrium of the horizontal yield force component of the infill web plate along the HBE, R_3 is the vertical reaction required for equilibrium of the post-tensioned forces acting on the HBE, y is the distance from the HBE neutral axis to the centroid of the PT, d is the depth of the HBE, R is the length of the radius corner cut-out of the infill plate and represents the length of the end segments of the HBEs where the infill web plate is not attached as shown in Fig. 1 (and will be further addressed subsequently), L_1 is the length of the HBE that corresponds to the HBE-to-VBE rocking point to the location of the post-tension anchor at the “opening joint” end of the HBE, L_2 is the length of the HBE that corresponds to the HBE-to-VBE rocking point to the location of the post-tension anchor at the “closing joint” end of the HBE, and L is the clear span of the HBE.

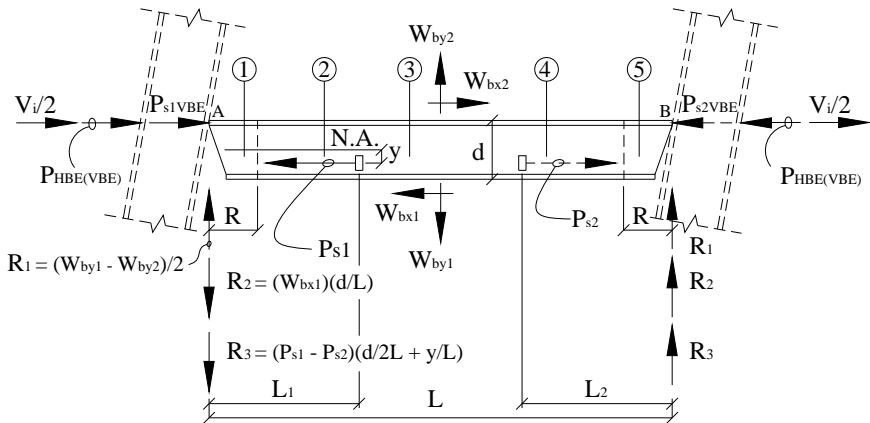


Fig. 2. Complete force resultant free body diagram of HBE

Furthermore, in Figs. 1 and 2, the location of the PT anchor point along the beam will depend on the strain demands of the PT elements at the maximum target drift. The anchor location should be provided such to ensure that the PT strains remain elastic up to that drift demand. Additionally, to clarify the effects of P_{s1} and P_{s2} , each P_s component is composed of two forces; the initial post-tension force P_o , applied prior to drift, and the force induced due to post-tension elongation during building drift, ΔP . For a rightward drift for the condition shown in Fig. 2, from geometry, elongation of post

tension will occur in P_{s1} while “relaxation” of the post-tension element P_{s2} will occur (for reasons described earlier) resulting in the following post-tension forces on the HBE:

$$P_{s1} = P_o + \left(\frac{k_{b1} k_{PT}^*}{k_{b1} + k_{PT}^*} \right) \Delta_{drift} - \frac{k_{PT}^*}{k_{b1} + k_{PT}^*} P_{HBE(VBE)} \quad (1)$$

$$P_{s2} = P_o - \left[\frac{k_{b2} k_{PT}^* + 2(k_{PT}^*)^2}{k_{b2} + k_{PT}^*} \right] \Delta_{drift} - \frac{k_{PT}^*}{k_{b2} + k_{PT}^*} P_{HBE(VBE)} \quad (2)$$

where in equations (1) and (2), k_{b1} and k_{b2} is the HBE axial stiffness along length L_1 and L_2 , respectively. Furthermore, Δ_{loss} is the axial shortening that occurs along the HBE span length between the end of the HBE to the post-tension anchor point locations on the HBE, and Δ_{drift} is the drift induced elongation of the post-tension elements at the HBE-to-VBE joint connection producing the incremental force ΔP and calculated as:

$$\Delta_{loss} = \frac{P_{HBE(VBE)}}{k_{PT}^* + \frac{A_{HBE} E_{HBE}}{L_1}} + \left(\frac{k_{PT}^*}{k_{PT}^* + \frac{A_{HBE} E_{HBE}}{L_1}} \right) \Delta_{drift} \quad (3)$$

$$\Delta_{drift} = \phi_{drift} \left(\frac{d}{2} + y \right) \quad (4)$$

where ϕ_{drift} is the relative HBE-to-VBE joint rotation in units of radians, A_{HBE} is the cross section area of the HBE, E_{HBE} is the modulus of elasticity of the HBE. Furthermore, from Fig. 2, it can be observed that the PT force contributing to HBE axial shortening along the length of the HBEs between PT anchor points, is a smaller fractional value of the tension force in the PT elements due to geometry. This is reflected by the term k_{PT}^* in Eqn. (3) which can be expressed as:

$$k_{PT}^* = \left(\frac{A_{PT} E_{PT}}{L_{PT}} \right) \cdot SF = k_{PT} \cdot SF \quad (5)$$

and from geometry, the scale factor can be approximated as:

$$SF = \left(\frac{h - y}{h + 0.5d} \right) \quad (6)$$

where h is the distance from the bottom of the VBE to the centroid of the HBE, y is the distance of the PT from the HBE centroid, and d is the depth of the HBE.

HBE-to-VBE Shear and Axial Connection Forces

The shear and axial reaction forces used in the connection design of the NewZ-BREAKSS detail can be determined from the free-body-diagram of Fig. 2, where the maximum horizontal compression reaction at the HBE-to-VBE flange rocking point and maximum vertical HBE end reaction occur at points “A” and “B”, respectively, for the rightward drift condition shown in Fig. 2. It then follows, combining the individual forces shown in the FBD, $P_{reaction} = (V_i/2 + P_{HBE(VBE)} + P_{s1(VBE)})$ at point “A” and $V_{reaction} = (R_1 + R_2 + R_3)$ at point “B”. Furthermore, by replacing the force resultants of the infill web plate diagonal tension field forces (i.e., W terms) in Fig. 2 with terms using the equivalent force per unit length quantities (i.e., ω) as defined by Sabelli and Bruneau (2007), the $V_{reaction}$ and $P_{reaction}$ forces can be expressed as:

$$R_A = \frac{(\omega_{by1} - \omega_{by2})(L - 2R)}{2} - \frac{(\omega_{bx1})(L - 2R)}{L}d - (P_{s1} - P_{s2})\left(\frac{d}{2L} + \frac{y}{L}\right) \tag{7}$$

$$V_{Reaction} = R_A - (\omega_{by1} - \omega_{by2})(L - 2R) \tag{8}$$

$$P_{reaction} = \frac{(\omega_{bx1} - \omega_{bx2})(L - 2R)}{2} + (\omega_{cx1} + \omega_{cx1})\left(\frac{h}{2} - \frac{d}{2} - R\right) + P_{s1(VBE)} \tag{9}$$

Accordingly, $V_{reaction}$ can then be used to design the bolted shear plate connection and $P_{reaction}$ can be used to design the HBE flange reinforcement plate and VBE panel zone. Note that equations (7) to (9) are based on a capacity design approach where the web plates have fully yielded. Finally, as shown in Fig. 2, Eqns. (7) to (9) were derived with the assumption that the story force (i.e., V_i) is equally distributed to each side of the frame. For the condition when the story force is delivered to only one side of the frame, Fig. 2 would be modified to show V_i acting at location “A” and $V_i = 0$ at location “B” in that figure (note that the value of the reaction R_2 shown in that figure, would remain unchanged). This would have the effect of increasing the above equations proportionally to V_i versus $V_i/2$.

INFILL WEB PLATE CORNER CUT-OUT DETAIL

As presented earlier, radius corner cut-outs are provided at the infill web plate corner locations. The primary purpose of this detail is to remove the portion of the infill web plate at the corner locations that would otherwise be subjected to excessive tensile strains during lateral frame drift due to the opening of the rocking joint (as schematically shown in Fig. 3).

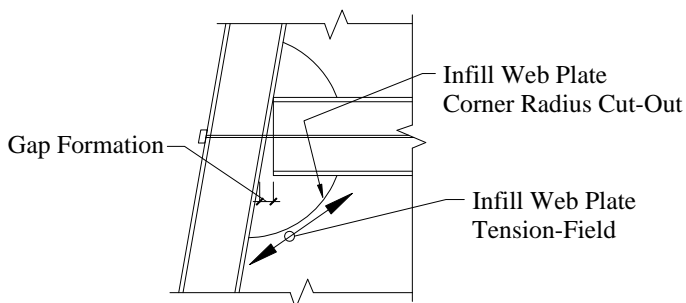


Fig. 3. HBE-to-VBE joint gap formation

To determine the appropriate value of the radius corner cut-out to use in design, a proposed analytical equation describing the infill web plate strain demands was presented by Dowden and Bruneau (2014) as follows:

$$\varepsilon_{Total} = \frac{\gamma \sin 2\alpha}{2} \left(\frac{\frac{d}{R} \tan \alpha + \cos \alpha + \sin \alpha \tan \alpha}{\cos \alpha + \sin \alpha \tan \alpha} \right) \quad (10)$$

Equation (10) represents the total tensile strain on the infill web plate for HBE-to-VBE rocking connections at a distance R away from the HBE-to-VBE flange rocking point, where γ is the gap opening rotation and α is the angle of inclination of the tension field to the vertical axis. To further clarify the effects of Eqn. (10), for the case of $\alpha = 45$ degrees, Eqn. (10) results in the following:

$$\varepsilon_{Total} = Component1 + Component2 = \frac{\gamma d \sqrt{2}}{4R} + \frac{\gamma}{2} \quad (11)$$

where, in Eqn. (11), *Component1* is the contribution of tensile strain from the gap opening and *Component2* is the contribution from lateral frame drift (i.e., a rigid panel sway mechanism). It is observed, that the closer the infill web plate is to the corner (corresponding to a smaller R), the larger the strain demands. In particular, if $R = 0$, the theoretical strain is infinite.

SEISMIC PERFORMANCE

While focus here has been on providing details of the NewZ-BREAKSS connections and free-body-diagrams leading to equations for the design of beams having such connections, it is important to note that quasi-static, pseudo-dynamic, and shake-table tests have demonstrated the adequate seismic performance of SC-SPSWs having this type of connection (Dowden and Bruneau 2014; Dowden et al. 2016). While a

comprehensive presentation of results is not possible here, Fig. 4 shows the third-scale SC-SPSW specimen on the shake table at the University at Buffalo and a plot of residual deformations recorded after earthquakes scaled to 10%, 25%, 50%, 75%, 100%, 120%, 140% (twice), and 50% (again) of the design ground motion and applied successively and in that sequence to the specimen. In all cases, residual drifts were less than the value of 0.2% drift commonly used as an acceptable out-of-plumb tolerance for new construction, confirming the self-centering ability of the system.

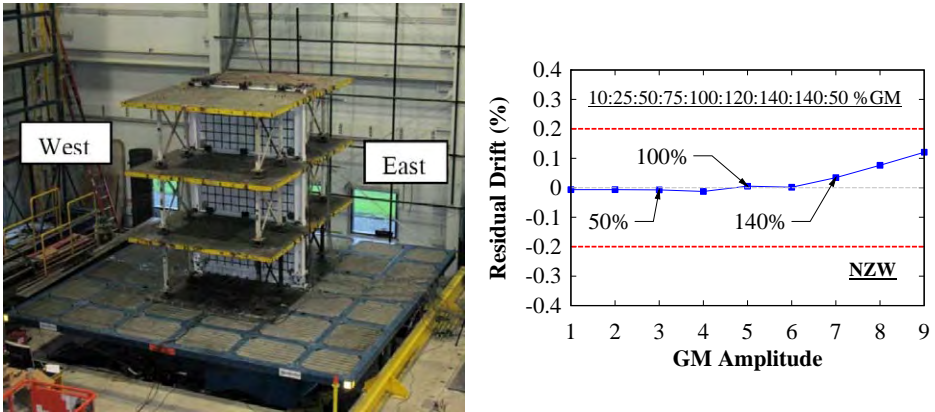


Fig 4: Shake table test: (a) Specimen; (b) Residual drifts

SUMMARY AND CONCLUSIONS

Some aspects of the fundamental behavior of self-centering steel plate shear walls with the NewZ-BREAKSS connection (i.e., NZ-SC-SPSW) were presented. Closed form equations were presented for: (i) HBE axial and shear force reactions for use in connection design based on capacity design principles; and (ii) infill web plate strains for HBE-to-VBE rocking joints.

Recent research shows that SC-SPSWs could be a viable alternative to traditional lateral force resisting systems for buildings located in regions of high seismicity. Towards that purpose, the findings presented here provide an initial step for their design, by establishing some basic kinematics of SC-SPSWs incorporating the NewZ-BREAKSS connection detail.

ACKNOWLEDGEMENTS

Financial support for this study was provided by the National Science Foundation as part of the George E. Brown Network for Earthquake Engineering Simulation under award number CMMI-0830294. Additional financial support for D. Dowden was provided by MCEER. Any opinions, findings, conclusions, and recommendations presented in this paper are those of the authors and do not necessarily reflect the views of the sponsors.

REFERENCES

- AIJ (1995). "Performance of Steel Buildings during the 1995 Hyogoken – Nanbu Earthquake." (In Japanese with English Summary). Tokyo: Architectural Institute of Japan.
- AISC (2010), Seismic Provisions for Structural Steel Buildings, ANSI/AISC 341-05, American Institute of Steel Construction, Chicago, IL.
- Christopoulos, C., Filiatrault, A., Uang, C.M., and Folz, B. (2002). "Posttensioned Energy Dissipating Connections for Moment-Resisting Steel Frame." *Journal of Structural Engineering*, ASCE, Vol. 128, No. 9, pp. 1111-1120
- Christopoulos, C., Pampanin, S., and Priestley, M. J. N. (2003). "Performance-Based Seismic Response of Frame Structures Including Residual Deformations. Part I: Single-Degree of Freedom Systems." *Journal of Earthquake Engineering*, Vol. 7, No. 1, pp. 97-118.
- Clayton, P.M., Dowden, D.M., Li, C.-H., Berman, J.W., Bruneau, M., Lowes, L.N., and Tsai, K.C. (2015), "Self-Centering Steel Plate Shear Walls for Improving Seismic Resilience." *Procs., 8th STESSA Conference on Behavior of Steel Structures in Seismic Areas*, Shanghai, China.
- Clifton, G.C. (1996). "Development of Perimeter Moment-Resisting Steel Frames Incorporating Semi-Rigid Elastic Joints", *New Zealand National Society for Earthquake Engineering Conference*, 1996; pp. 177-184.
- Clifton, G.C. (2005). "Semi-Rigid Joints for Moment Resisting Steel Framed Seismic Resisting Systems." Ph.D. dissertation, Department of Civil and Environmental Engineering, University of Auckland, New Zealand.
- Clifton, G. C., MacRae, G. A., Mackinven, H., Pampanin, S., and Butterworth, J. (2007). "Sliding Hinge Joints and Subassemblies for Steel Moment Frames", *Proceedings of the New Zealand Society of Earthquake Engineering Annual Conference*, Paper 19, Palmerston North, New Zealand.
- Dowden, D.M., and Bruneau, M. (2011). "NewZ-BREAKSS: Post-tensioned Rocking Connection Detail Free of Beam Growth." *Engineering Journal*, AISC, Second Quarter, 153-158.
- Dowden, D.M., Purba, R., and Bruneau, M. (2012). "Behavior of Self-centering Steel Plate Shear Walls and Design Considerations." *Journal of Structural Engineering*, ASCE, Vol. 138, No. 1, pp. 11-21.
- Dowden, D.M., and Bruneau, M. (2014). "Analytical and Experimental Investigation of Self-Centering Steel Plate Shear Walls." *Tech. Rep. MCEER-14-0010*, Multidisciplinary

Center for Earthquake Engineering Research, State University of New York Buffalo, Buffalo, New York.

Dowden, D.M., Clayton, P.M., Li, C.-H., Berman, J.W., Bruneau, M., Lowes, L.N., and Tsai, K.C. (2016). "Full-scale Pseudo-dynamic Testing of Self-Centering Steel Plate Shear Walls." *Journal of Structural Engineering, ASCE*, (In Press).

Garlock, M. (2002). "Design, Analysis, and Experimental Behavior of Seismic Resistant Post-Tensioned Steel Moment Frames." Ph.D. dissertation, Department of Civil and Environmental Engineering, Lehigh University, Bethlehem, PA.

Garlock, M., Ricles, J., and Sause, R., (2005). "Experimental Studies of Full-Scale Posttensioned Steel Connections." *Journal of Structural Engineering, ASCE*, Vol. 131, No. 3, pp. 438-448.

Kawashima, K., MacRae, G.A., Hoshikuma, J.-I., and Nagaya, K. (1998). "Residual Displacement Response Spectrum" *Journal of Structural Engineering, ASCE*, Vol. 124, No. 5, pp. 523-530.

Krawinkler, H., Anderson, J., Bertero V., Holmes, W., and Theil, C. Jr. (1996). *STEEL BUILDINGS. Earthquake Spectra: January 1996*, Vol. 12, No. S1, pp. 25-47.

MacRae, G.A., Clifton, G.C., Mackinven, H., Mago, N., Butterworth, J., and Pampanin, S. (2008). "The Sliding Hinge Joint Moment Connection." *Bulletin of the New Zealand Society for Earthquake Engineering*, Vol. 43, No. 3, pp. 202-212.

Pampanin, S., Christopoulos, C., and Priestley, M. J. N. (2003). "Performance-Based Seismic Response of Frame Structures Including Residual Deformations. Part II: Multi-Degree of Freedom Systems." *Journal of Earthquake Engineering*, Vol. 7, No. 1, pp. 119-147.

Ricles J.M., Sause R., Peng, S., and Lu, L. (2002). "Experimental Evaluation of Earthquake Resistant Posttensioned Steel Connections." *Journal of Structural Engineering, ASCE*, Vol. 128, No. 7, pp. 850-859.

Rojas, P., Ricles, J.M., and Sause, R. (2005). "Seismic Performance of Post-tensioned Steel Moment Resisting Frames With Friction Devices." *Journal of Structural Engineering, ASCE*, Vol. 131, No. 4, pp. 529-540.

Sabelli, R., and Bruneau, M., (2007). "Steel Plate Shear Walls." *AISC Steel Design Guide 20*, American Institute of Steel Construction, Inc., Chicago, Ill.

Winkley, T.B. (2011). "Self-centering Steel Plate Shear Walls: Large Scale Experimental Investigation." M.S. thesis, Dept. of Civil and Environmental Engineering, University of Washington, Seattle, WA.

WORKSHOP PARTICIPANTS

Bjørn Aasen.....	Norconsult AS, Norway
Eduardo Bayo.....	University of Navarra, Spain
Jeffrey W. Berman.....	University of Washington, USA
Preetam Biswas.....	Skidmore, Owings and Merrill, LLP, USA
Reidar Bjorhovde.....	The Bjorhovde Group, USA
Michel Bruneau.....	University at Buffalo, USA
Charles J. Carter.....	American Institute of Steel Construction, USA
Yiyi Chen.....	Tongji University, China
Maël Couchaux.....	INSA of Rennes, France
Kevin A. Cowie.....	Steel Construction New Zealand Inc., New Zealand
Florea Dinu.....	Politehnica University of Timisoara, Romania
Dan Dubina.....	Politehnica University of Timisoara, Romania
Matthew R. Eatherton.....	Virginia Tech, USA
Larry A. Fahnestock.....	University of Illinois at Urbana-Champaign, USA
Erica C. Fischer.....	Degenkolb Engineers, USA
Robert B. Fleischman.....	University of Arizona, USA
Patrick J. Fortney.....	Cives Engineering Corporation, USA
Ramon Gilsanz.....	Gilsanz Murray Stefcick, USA
Ana M. Girão Coelho.....	Newcastle University, UK
Arvind Goverdhan.....	Stanley D. Lindsey & Associates, USA
A.M. (Nol) Gresnigt.....	Delft University of Technology, the Netherlands
Lawrence Griffis.....	Walter P Moore and Associates, Inc., USA
Jerome F. Hajjar.....	Northeastern University, USA
Yukihiro Harada.....	Chiba University, Japan
Ricardo Herrera.....	University of Chile, Chile
Nadine Hoffmann.....	University of Stuttgart, Germany
Johnn P. Judd.....	University of Wyoming, USA
Amit Kanvinde.....	University of California, Davis, USA
Kazuhiko Kasai.....	Tokyo Institute of Technology, Japan
Lawrence A. Kloiber.....	LeJeune Steel Company, USA
Peter Knöedel.....	KIT Steel & Lightweight Structures, Germany
Raffaele Landolfo.....	University of Naples Federico II, Italy
Roberto T. Leon.....	Virginia Tech, USA
Guo-Qiang Li.....	Tongji University, China
Wei Li.....	Tsinghua University, China
Dimitrios Lignos.....	Swiss Federal Institute of Technology, Switzerland

WORKSHOP PARTICIPANTS (cont'd.)

Judy Liu.....	Oregon State University, USA
Hussam N. Mahmoud.....	Colorado State University, USA
Akbar Mahvashmohammadi	Gilsanz Murray Stefcick LLP, USA
Joseph A. Main	National Institute of Standards and Technology, USA
James O. Malley.....	Degenkolb Engineers, USA
Jason McCormick.....	University of Michigan, USA
Kristo Mela.....	Tampere University of Technology, Finland
Primož Može	University of Ljubljana, Slovenia
Larry S. Muir	American Institute of Steel Construction, USA
Andrew T. Myers	Northeastern University, USA
Jeffrey A. Packer.....	University of Toronto, Canada
Ioan Petran.....	Technical University of Cluj-Napoca, Romania
Vincenzo Piluso.....	University of Salerno, Italy
Dennis Rademacher	Technical University of Dortmund, Germany
Kim J. R. Rasmussen	University of Sydney, Australia
Gian A. Rassati.....	University of Cincinnati, USA
James M. Ricles	Lehigh University, USA
Gianvittorio Rizzano.....	University of Salerno, Italy
Charles W. Roeder	University of Washington, USA
Colin A. Rogers.....	McGill University, Canada
Aldina Santiago	University of Coimbra, Portugal
Luís Simões da Silva.....	University of Coimbra, Portugal
Natalie Stranghöner.....	University of Duisburg-Essen, Germany
Aurel Stratan.....	Politehnica University of Timisoara, Romania
Robert Tremblay	École Polytechnique de Montréal, Canada
Thomas Ummenhofer.....	KIT Steel & Lightweight Structures, Germany
Dieter Ungermann	TU Dortmund University, Germany
Amit H. Varma.....	Purdue University, USA
Milan Veljkovic.....	Delft University of Technology, the Netherlands
František Wald.....	Czech Technical University in Prague, Czech Republic
Wei Wang	Tongji University, China
Jonathan M. Weigand.....	National Institute of Standards and Technology, USA
Donald W. White.....	Georgia Institute of Technology, USA
Riccardo Zandonini.....	Università degli Studi di Trento, Italy

AUTHOR INDEX

Abruzzo, J.....	453	Friedrich, S.....	393
Afzali, N.....	57	Gao, Y.....	537
Agarwal, A.....	497	Garifullin, M.....	285
Ahmadi, O.....	663	Gélinas, A.....	255
Alarcón, C.....	599	Gentili, F.....	153
Albiez, M.....	305	Gil, B.....	373
Arber, L.....	11	Gilsanz, R.....	453
Arwade, S.....	327	Girão Coelho, A.....	33
Aasen, B. (lecture only).....	no paper	Gödrich, L.....	143
Augusto, H.....	153	Goñi, R.....	373
Bajer, M.....	143	Gracia, J.....	373
Baldassino, N.....	589	Gresnigt, A.M.....	79
Bayo, E.....	373	Griffis, L.....	317
Béland, T.....	225	Grilli, D.....	631
Beltrán, J.....	599	Hajjar, J.....	101, 327
Berg, J.....	57	Han, L.H.....	527
Berman, J.....	245, 433	Harada, Y.....	163
Bernardi, M.....	589	Heinisuo, M.....	285
Biswas, P.....	45	Herrera, R.....	599
Bradley, C.....	225	Hertz, J.....	275
Bruneau, M.....	673	Hines, E.....	225
Carter, C.....	215	Hoffmann, N.....	465
Charney, F.....	641	Holomek, J.....	143
Chen, Y.....	487, 547	Jain, N.....	363
Couchaux, M.....	133	Jiang, J.....	347
Cowie, K.....	19	Jokinen, T.....	285
D'Aloisio, J.....	101	Judd, J.....	641
D'Aronco, M.....	275	Johnson, R.....	45
Davaran, A.....	255	Kabeláč, J.....	143
de Vries, P.....	57, 79	Kanvinde, A.....	631
Decaen, S.....	255	Kasai, K.....	265
Dinu, F.....	475	Kim, Y.....	383
Dowden, D.....	673	Kloiber, L. (lecture only).....	no paper
Dowswell, B.....	215	Knöedel, P.....	111
Duan, L.....	347	Kolaja, D.....	143
Dubina, D.....	475, 569, 651	Kuhlmann, U.....	465
Eatherton, M.....	363	Kurejková, M.....	143
Elkady, A.....	507	Lai, Z.....	517
Fahnestock, L.....	225	Landolfo, R.....	579
Fang, C.....	547	Latour, M.....	557, 619
Fischer, E.....	91	Lebelt, P.....	393
Fleischman, R.....	497	Lehman, D.....	245
Flores, F.....	641	Leon, R.....	383, 537
Fortney, P.....	235	Li, G.Q.....	347

AUTHOR INDEX (cont'd.)

Li, L.	487	Šabatka, L.	143
Li, W.	527	Salas, C.	599
Lignos, D.	275, 507	Santiago, A.	403
Liu, Jia	547	Sause, R.	663
Liu, Judy	443	Sen, A.	245
Mahmoud, H.	337	Shahbazian, A.	153
Mahvashmohammadi, A.	453	Sigauan, A.	475
Main, J.	413, 423, 443	Simões da Silva, L.	123, 153, 163
Malley, J.	11	Sizemore, J.	225
Marginean, I.	475	Spannaus, M.	111
Maris, C.	569	Spencer, M.	327
Marosi, M.	275	Stranghöner, N.	57
Martin, P.	133	Stratan, A.	569, 651
Matsuda, Y.	265	Swanson, J.	205
McCormick, J.	609	Thollard, X.	133
Mela, K.	285	Tiainen, T.	285
Mentes, Y.	383	Tousignant, K.	295
Moradei, J.	101	Tremblay, R.	225, 255, 275
Može, P.	69	Ummenhofer, T.	111, 305
Muir, L.	1, 215	Ungermann, D.	393
Murray, T.	363	Valdez, L.	497
Myers, A.	327	Varma, A.	91, 517
Neagu, C.	569	Veljkovic, M.	123
Packer, J.	295	Vild, M.	143
Pavlovic, M.	123	Vulcu, C.	569, 651
Peterman, K.	101	Wald, F.	143
Peters, A.	393	Walsh, A.	497
Petran, I.	475	Wang, W.	487, 547
Petrov, G.	45	Webster, M.	101
Piluso, V.	557, 619	White, D.	383
Rademacher, D.	393	Wei, D.	609
Rasmussen, K.	173	Wei, K.	327
Rassati, G.	205	Weigand, J.	413, 423, 433, 443
Rebelo, C.	123	Wen, H.	337
Ribeiro, J.	403	Wilson, K.	205
Ricles, J.	663	Zandonini, R.	589
Rigueiro, C.	403	Zhang, H.	173
Rivillon, P.	133	Zhang, J.	347
Rizzano, G.	557, 619	Zhu, C.	173
Roeder, C.	245	Zhu, Q.	91
Rogers, C.	275		



AMERICAN INSTITUTE OF STEEL CONSTRUCTION
130 East Randolph Street, Suite 2000, Chicago, Illinois 60601
www.aisc.org



CONNECTIONS VIII

Eighth International Workshop on Connections in Steel Structures